

ANALYSIS OF LAWS OF MICROSEISMIC DAMAGE IN A COAL MINE

LI-GANG CHEN, XIAO-GUANG ZANG, YONG-ZHAN PAN, XUE-MIN WU and WEI-HONG HUANG

Qingdao Technological University

Qingdao, 266033, P.R. China

Geological structure characteristics in a coal mine is described and underground mining activity is summarized at first. Then, the characteristics and laws of microseismicity induced by underground mining and geological structure activation are analyzed. The relationship between underground mining and structure activation is derived. Finally, the laws of failure induced by microseismicity in the coal mine are summarized. The result can be used in studying of microseismic phenomena in other mines with similar geological setting.

1 The Characteristics of Geological Structure in Mining Area

The Beipiao coalfield is located in the complex position between the Tianshan -Yinshan zonal structural belt and the new cathaysian system subsidence belt. Subsidiary fractures lie in compound joint positions of Heichengzi of new Cathaysian, the north part of Kezuo depression and NW-trending Pingzhuang and Fuxin depression. It is a coal-forming basin with wave depressions.

1.1 Regional Fault Structure

There are four faults from north to south in the mining area. The Longtan fault is located in the north border of the mining area. The Tayingzi fault is a buried structure. The Jianshanzi fault, more widely disputed in history as the Feilaifeng fault by Mr.Weng initially, is at the present thought to be a pressure wrench fracture. The Nantianmen fault located in the southeast border of the coalfield forming boundary of Hecheng and Kezuo depression plays an important role in the improvement of the coalfield. The common characteristics of four faults are as follows:

Firstly, it is arranged parallel to the direction of the trend. Secondly, the horizontal distance of faults is about 6.5-7.5km and the equidistant distribution is obvious. Finally, the mechanics are characteristic of a compresso-shear fracture fault.

Except the four main fractures mentioned above, there are many small faults consistent to conjugate joints in region whose direction is either NE or NW.

1.2 Fold Structure

The fold structure in the mining area lies between the Longtan fault and the Nantianmen fault. There are many folds parallel to the main faults; for example, the Yudaigou Syncline, Wendengyingzi anticline, Beichengzi Syncline, and the Beipiao Monoclinic.

As far as it is known, the Beipiao coalfield is a monoclinical structure, tendency N 40°-60°E, dip NW $\angle 25^{\circ}$ -75°. It is possible for coal measures to be lifted because of the cut by the Jianzishan fault deep down.

After the formation of coal measures, the evidences show that tertiary laterite and quaternary loess are cut by faults on Nantianmen fracture line affected by crustal movement and new structure.

2 Present Situation and Disaster Analysis of Underground Mining in Mining Area

It was built in 1922 in Beipiao mining area. Before liberation it had six pairs of inclined shafts and a pair of shafts. After liberation, production was expanded gradually and extended to the deep step by step with mined-out the shallow coal seam. Now there are three collieries, i.e. Sanbao mine with a pair of inclined shaft, Guanshan mine with a pair of shafts and Taiji mine with both a pair of shafts and a pair of inclined shafts. The general production capacity designed of three mines is 1920kt/a, but the final capacity is determined 2070kt/a. At present, the mining depth is 722m in Taiji mine and the mining depth is 750m in Guanshan mine.

Taiji Shaft located on the west of coalfield is succeeding mining in the deep based on mining in the shallow with three pairs of inclined shafts. It was constructed in 1966 and produced formally in 1974. The first production level is -550m. Now it is transiting to -700m of the second level with +172.3m for wellhead elevation. The development mode adopts central transportation tunnel in shaft level and district development in rock tunnel.

The mining methods contain short-wall hydraulic mining, longwall mining and storage mining and so on. Roof management is accomplished with roof subsidence naturally.

There are many sorts of natural disaster in Beipiao mining area. The disasters related to mining dynamic reveal conclude coal and gas outburst, impact pressure and rock burst. The occurrence of microseism is frequent in Taiji mining area and microseism is discovered in the west of Guanxishan recently. The maximum gas pressure is up to 81.5kg/cm. It has taken place 1024 times for coal and gas outburst from 1951, and the general amount is 42.4kt. The maximum of them is 1.635kt. Impact pressure happened three times and the maximum intensity is 1.2t. With mining extended to the deep, rock burst phenomenon increased. It is up to 34times include 3 times for shaft driving, 3 times for the level of -400m, 9 times for the level of -550m and 19 times for the level of -700m.

3 The Characteristics and Laws of Microseism in Mining Area

The characteristics and laws of microseism is studied by monitoring of microseism on the basis of epicenter and comprehensive analysis of seismic data include microseism basic parameters. For analysis of the cause and mechanism led to microseism in mining area, seismic station is set up. Microseism is monitored by seismograph[1-3].

3.1 The Characteristics of Microseism in Mining Area

It has some characteristics such as shallow focus and high intensity. The focus depth is about 1~7km through analysis of monitor data for microseism. It was felt in a wide area when $M_s \geq 1.0$. The buildings both ground and underground are destroyed slightly when $1.5 \leq M_s < 2.0$. Damage is significant when $M_s \geq 2$. For example, partial section of underground roadway took place caving and track distorted. Even production is interrupted after microseism took place on April 28, 1977 which intensity is up to 7 degree in the meizoseismal area.

3.2 The Characteristics of Microseism Phase in Mining Area

According to the microseism graph record of Beipiao monitoring station, p-wave period is about 0.2s and s-wave period is about 0.4s. It is likely blasting on the whole, but period surface wave develop well as well as random and amplitude is slow compared with blasting.

Compared with seismic phase recorded by Chaoyang seismic station which distance and magnitude are approximate,, not only P-wave, S-wave and the whole duration of microseism in mining area are shorter than those of natural earthquake but also the period is longer and Short period surface wave develop more better.

3.3 The Characteristics of Seismic Distribution

Microseism epicenter is distributed in Taiji shaft and nearby area according to azimuth location method. Macro examination of damage shows that about 78% of microseism with $M_s \geq 2$ happened on the faults between F8 to F13 in the middle of mine field.

3.4 The Annual Periodic Law of Microseism Activity in Mining Area

Periodicity of the distribution of microseism activity is obvious. Based on analysis of the sequence diagram ($m_s \geq 1.0$) from 1971, there are two active stages and three relative quiet stages for microseism activity. The facts show that the third active stage began in 1987.

3.5 The Characteristics of Monthly Period and Daily Probability for Microseism in Mining Area

Based on statistics analysis of microseism frequency, the probability of microseism occurrence on three months including March, April and August is high every year. According to statistical data for daily microseism frequency with $M_s \geq 1.0$, the probability of microseism occurrence is high at nine to seventeen every day.

3.6 The Law of Regional Stress Field

According to the results of rock stress determination and analysis of earthquake mechanism, stress field in the mining area is nearly horizontal principal compressive stress in a nearly E-W direction consistent with regional principal stress in Liaoxi area. Regional stress effect is major factor of microseism occurrence.

3.7 The Relation between Microseism and Small Faults in Mining Area

Under the control of regional stress field , microseism is closely related to fault structure in mine field due to specific geological zones for Taiji shaft. After microseism happened with $M_s \geq 2.0$, both sides of fault were occurred relative slide. There have happened 13 times for microseism with $M_s \geq 2.0$ on the faults, i.e. F8, F10, F11, F12 and F13.

3.8 The Law of Movement and Deformation

Observation points are set up in the conglomerate roadway of coal measures basement. They move to goaf after exploitation. Two parts of fault has relative displacement after microseism occurrence. The range of surface subsidence enlarged and the subsidence velocity increased affected by microseism.

3.9 Correlation between Microseism in Mining Area and Local Earthquake

A strong linear correlation was observed between strain energy which released by microseism with $M_s \geq 1.0$ every year and the logarithms of local earthquake annual frequency. The regression equation is:

$$\sqrt{E} = -69.997 + 61.77 \log N \quad (1)$$

According to calculation, correlation coefficients are 0.9247 and 0.8162. The former epicenter distance is within 100km, and the latter is within 150km. All these illustrate that local earthquake affected strongly microseism.

3.10 The Precursor Information of Microseism in Mining Area

It is possible to obtain precursor information before microseism occurrence. The phenomena of microseism frequent or small earthquake swarm can be observed before microseism occurrence with $M_s \geq 1.0$. Two parts of fault has relative displacement before microseism occurrence with $M_s \geq 2.0$, displacement post-microseism is opposite compared with before microseism.

3.11 Source Parameter Calculation and Prediction of Microseism in Mining Area

Spectral analysis shows that it is low stress drop event with the scale of source for hectometer magnitude, fault average offset of 0.1—0.3cm, Stress drop to several pa. Medium factor-q is about 300 which are lower than surrounding area. All these show that medium integrity is worse and occurrence of bigger microseism is impossible.

3.12 Imaginary Wave Velocity

Time-space parameter of earthquake can be determined by using of propagation velocity and travel time table of seismic wave.

Average crustal thickness is adopted In J-B travel-time. Parameter error is big for small range. So it is necessary to obtain imaginary wave velocity for improving precision. Imaginary wave velocity in Liaoxi area is obtained based on solving linear equation for more than four S—P data and group solving for several greater earthquakes in 1982 and 1983.

4 Investigation and Analysis of Microseism Damage in Mining Area

There are many sorts of natural disaster, but it was not noticed for starting time of microseism occurrence. People often felled slight shake since 1971, and from that time it increased year by year without obvious damage. Building on the ground and engineering facilities underground were destroyed ,even production is interrupted after microseism took place on April28, 1977 which magnitude is up to 3.8 degree. After that, people pay more attention to microseism

From 1971 to 1986, there happened 1507 times for microseism with 18 times for $M_s \geq 2.0$. Based on the data of microseism for 14 times and investigation of damage situation, analysis results of microseism damage for four representational mining areas are shown in the Table 1[4].

Table 1 Analysis of microseism damage

No.	Occurrence time	Magnitude (Ms)	Macro-location	the situation of the damage On the ground and the underground	the exploitation situation in the vicinity
1	April 28, 1977 06:46 AM	3.8	The range of felt earth-quake was about 70km. The range of meizoseis-	1. About 2km for meizoseismal area 2. Cracks occurred for brick-concrete structure buildings, chimney twist off.	-400 ~ -550 Miming No.4 coal seam.

			mal area was about 2km The epicenter was located on No.10 fault.	3. Cracks in chimney and wall, wall collapsed more than 400 houses in Taiwan Street .449 Overhaul, 12 people injured in Taiji street 4. In Taiji village, 715 houses damaged, 58 houses for serious cracks in the wall 5. Rock falling, both sides of fault relative displacement, track distorting, etc.	Mining area was located on the hanging wall of No.10 fault i.e. west side
2	April 7, 1981 09:30 AM	2.2	The range of felt earthquake included the surface and underground. The epicenter was located on No. 13-2 fault.	1. Shaft station damaged badly in the level of -550, and falling rocks injured 5 workers. 2. Falling rocks was for about 200m ³ , and the largest block was up to 2m in diameter in the level -535 roadway. 3. Both sides of fault had an obvious displacement. 4. Winch room felt strongly and all of electrical power equipment powered cut.	-400 ~ -550 Mining No.4 coal seam Mining area was located on the hanging wall of fault No. 12. No.13-2 fault was in the middle of mining area.
3	December 13, 1981 3:24 PM	2.5	Felt of earthquake was strongly including of ground and underground The epicenter was located on No.12 fault.	1. Transformer substation on the ground power cut. 2. Pressure increased in a large area such as rock roadway, shaft station and the location near to the fault, etc.	Roadway was long 110m with tunneling near to No.12 fault.
4	April 27, 1983 7:26 PM	2.0	Felt of earthquake was strongly including of ground and underground. The epicenter was located on No.12 fault.	1. Rock falling nearby fault No.8 2. Rock falling, floor heave and track distortion affected transportation for 6 hours in the level -550 near to the fault No.8. 3. The surface subsidence was up to 13m. Buildings on the surface were damaged badly after the earthquake.	Coal seam No. 8 and No. 9 Mining area was located on the fault No.8.

Through investigation and analysis of microseism damage in mining area, the characteristics of damage are shown as followed.

On the one hand, the characteristics of buildings damage on the surface are analysed. High and large building for reinforced concrete structure, for example two shaft tower and one chimney which are up to 53m, did not affect by microseism with the magnitudes of 3.8 and intensity of 7. But brick-concrete structure buildings such as hostel, office building, chimney of industrial boiler house and so on are destroyed seriously. Subsequently, these building are destroyed in different degree when $M_s \geq 2.5$. Damage is obvious for masonry structure bungalow and adobe house when $M_s \geq 2.0$.

On the other hand, the characteristics of damage underground are analysed. The phenomena such as relative displacement for both sides of fault, rock falling, floor heave of roadway and so on can be observed in the conglomerate roadway of coal measures basement. For example, observation points in the hanging wall of fault moved to goaf after microseism took place on April 28, 1977 which magnitude is up to 3.8 degree.

5 Dependence between Microseism, Mining Underground and Tectonic Activation

Both significant failure zone and macroscopic epicentral area lay in East Block No.1 to West Block No.1 for 14 times microseism. The position of macroscopic epicenter has a close relation with exploitation area. With the

enlargement of mining area and effect of repeat mining, the phenomena appeared repeatedly for fault activities or continuous activities. Fault activities are related to the position of exploitation area, Most of which are boundary faults activities.

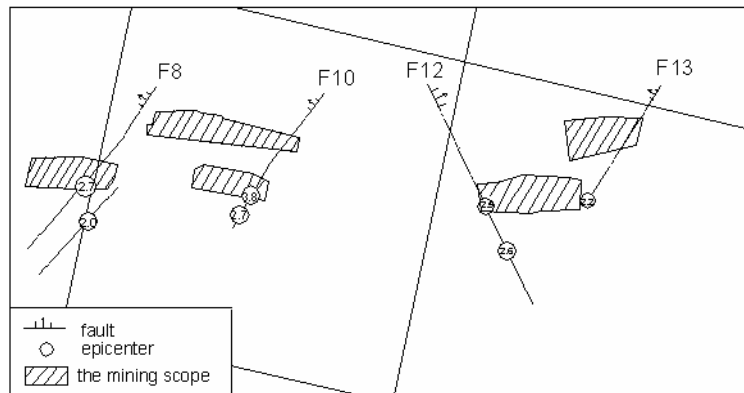


Figure 1 Dependence between microseism, mining underground and tectonic activation

6 Conclusions

Through the observation and study of many years, the characteristics and laws of microseism are understood. Microseism in mining areas is restricted by the regional stress field and is related to slope activities. Under the leading role of the regional stress field, mining activities destroy the equilibrium state of the partial stress field. Thus the fault becomes activated and coal and rock seams produce slight fracture. The energy of active faults is released as microseism. It brings about a certain threat to the safety in production.

Microseism has little relation to the surface deformation, but affects normal laws of movement and deformation on the surface. In addition, the relationship between microseism and deformation underground is significant.

Acknowledgements

The authors thanks for sustain from the National Natural Science Fund of China (No: 50874064; 50804026) and Natural Science Fund of Shandong Province.

References

1. Beipoao Mining Bureau. Comprehensive Report on Study of the Characteristics and Laws of Mine Seismicity in Taiji Mining Area, 1986, 10.
2. Jiang, J.Q. and Zhang, K.Z. Cause and Control Method of Mine Earthquake in Fully Mechanized Top Coal Caving. Chinese Journal of Rock Mechanics and Engineering, 2006, (z1). 3276-3282.
3. Song, J.C., Liu, D.Y., Wang, E.D., etc. Cause and Mechanism of Mine's Fault-Type Earthquake and Its Forecast. Mining Engineering, 2007, 5(3). 16-18.
4. Beipoao Mining Bureau. Investigation Report on Mine Seismicity Damage in Taiji Mining Area, 1986.

UNUSUAL FRACTURING ABOVE INTERMEDIATE- TO DEEP-LEVEL BUSHVELD PLATINUM WORKINGS

BRYAN-PHILIP WATSON, ALEX MILEV and DAVE ROBERTS

Council for Scientific and Industrial Research

Johannesburg, 2006, South Africa

Severe fracturing is occurring at some distance above the hangingwalls of some excavations. These conditions could affect the long-term sustainability of the South African platinum industry if current horizontal to vertical stress ratios persist to deeper levels. The fracturing is different to that experienced in the South African gold mines, probably owing to the higher horizontal stresses in the shallow-dipping Bushveld strata and the ductile nature of the darker platinum rocks. The severity of the problem appears to be related to the proportion of plagioclase, i.e. lighter coloured rocks. As the immediate hangingwall of the Merensky Reef is usually pyroxenite, which grades upwards into anorthosite, fracturing sometimes occurs in the upper strata whilst the immediate hangingwall remains unfractured. This work was designed to determine if the observed discontinuities were fractures that resulted from mining and, if so what the mechanism of formation was. Our investigations included instrumentation that could monitor the seismicity associated with the fracturing and that could detect the position and persistency of the planes that were formed. Evidence of prominent, persistent shallow-dipping parting planes at heights of between 1.4 m to 2.4 m above the excavation was provided by a ground penetrating radar survey, borehole core and borehole camera surveys. This set of discontinuities extended over at least an area of 20 m x 20 m. The seismicity measured during excavation suggested that these discontinuities were fractures that developed as a result of mining. The micro-seismic network suggested that the fracturing above the excavation occurred near or at the face and little influence of other mining or external seismicity was detected. Stress measurements conducted at a separate site showed high horizontal stress in some anorthositic rocks - so called 'stress channelling'.

1 Introduction

The Bushveld Complex is a large layered igneous intrusion which spans about 350 km from east to west. This remarkable geological phenomenon is situated north of the city of Pretoria in the northern part of South Africa (Figure 1), and hosts not only the majority of the world's known platinum group metal resources but also contains nickel and gold. There are also vast quantities of chromium and vanadium in seams parallel to the platinum ore bodies, some hundreds of metres in the footwall and hangingwall respectively. The platinum group metals are concentrated in two dipping planar ore bodies known as the Merensky Reef, a mineralised pegmatoidal pyroxenite 0.7 m to 1.4 m thick, and, underlying this, the UG2 Reef, comprising one or more chromitite seams of similar thickness. The strata generally dip toward the centre of the complex at 8° to 20°. The k ratio varies from about 0.8 to over 2.5 and locally can cause severe strata control problems. The depth of mining ranges from outcrop to 2300 m. In-stope chain pillars oriented either on strike for breast mining (Figure 2) or on dip for up or down dip mining are generally used to prevent backbreaks (stope collapses involving large volumes of rock). At deeper levels these pillars are required to fail in a stable manner soon after being cut (crush pillars). The residual strength of the pillars provides the required support resistance to prevent backbreaks and keep the stope hangingwall stable.

Severe fracturing occurs at some distance above the hangingwalls of some Merensky excavations, producing parting planes and causing unstable hangingwall conditions. The fracturing is different to that experienced in the gold mines, probably owing to the higher horizontal stresses in the anorthosites and the ductile nature of the darker platinum rocks. The severity of the problem appears to be related to the proportion of plagioclase, i.e. lighter coloured 'anorthositic' rocks. Thus fracturing sometimes occurs in the upper anorthositic strata whilst the immediate pyroxenite hangingwall remains unfractured. In this study, borehole camera observations, borehole core inspections, joint surveys, fracture mapping and Ground Penetrating Radar (GPR) were used to classify a stope hangingwall and determine the extent of the fracturing at an instrumentation site. Geophones were installed to determine whether the small events often heard in the stopes were caused by the fracturing.

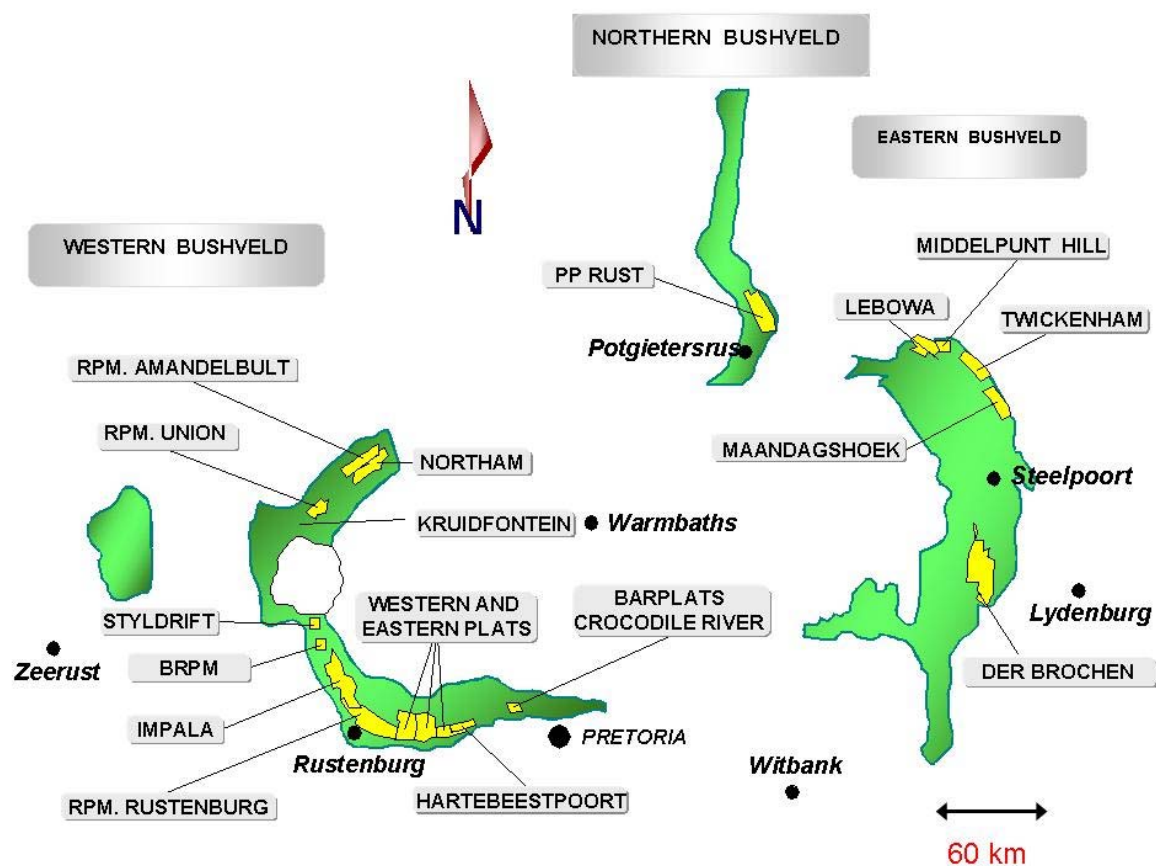


Figure 1 The extent of the Bushveld platinum exposure.

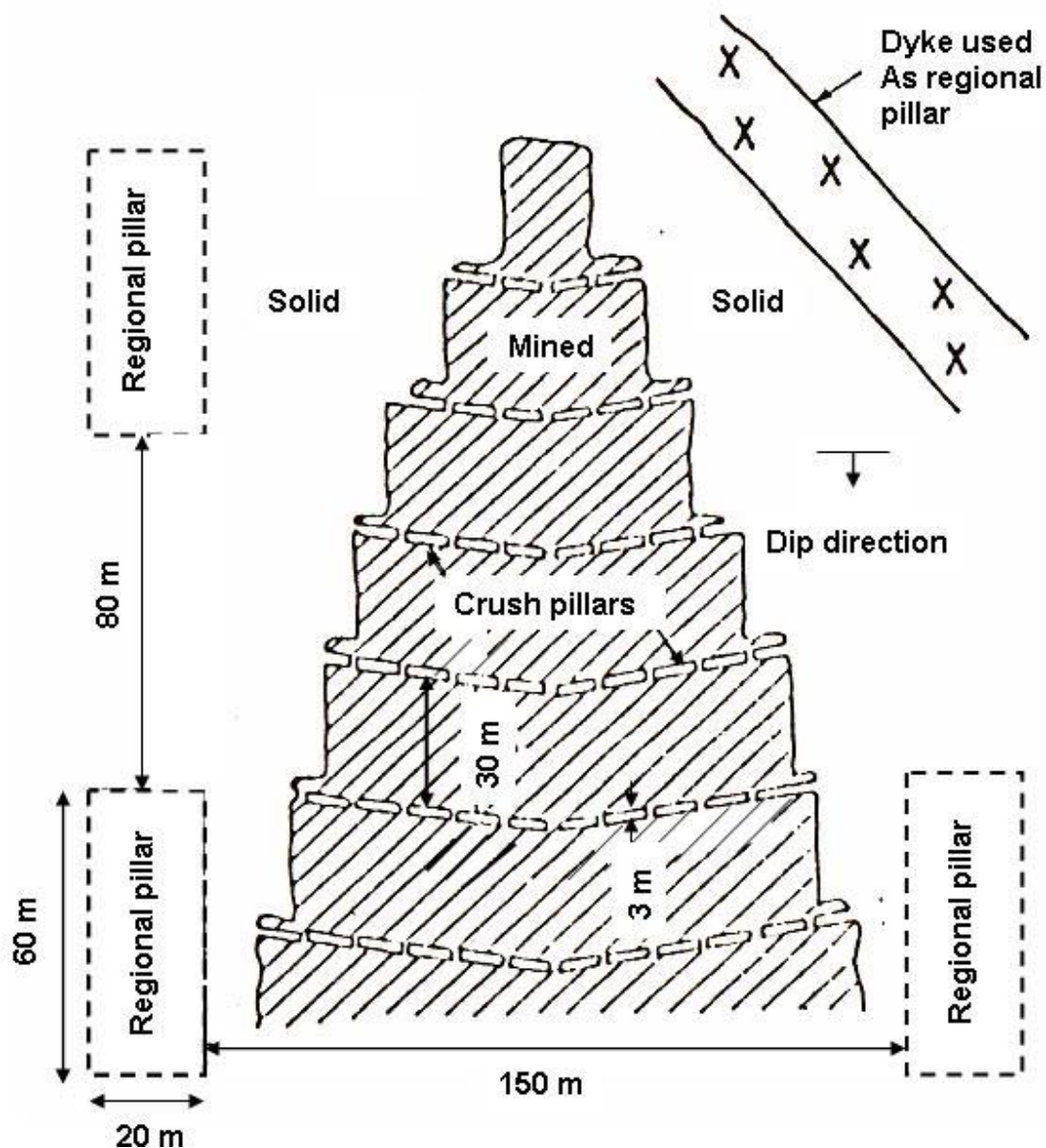


Figure 2 Plan view of a typical stope on one of the planar platinum ore bodies [1].

2 Site Description

An instrumentation site was established at Impala Platinum, at a depth of 1100 m below surface. Very little mining had taken place around the panel (Figure 3). A 5 m long vertical borehole was drilled into the hangingwall from the Advanced Strike Gully (ASG) and a geophone installed. A borehole camera survey was conducted in this borehole and the core was geologically logged and inspected to determine fracture densities above the stope. A joint survey was conducted along Traverse A; the results are plotted in Figure 3. Since the joint survey was conducted before the final face position (between 0 m and 45 m in the figure), the

discontinuities in the region of Traverse C are not shown except for the shallow-dipping dome joints (Set D) observed in the ASG at the bottom of the panel.

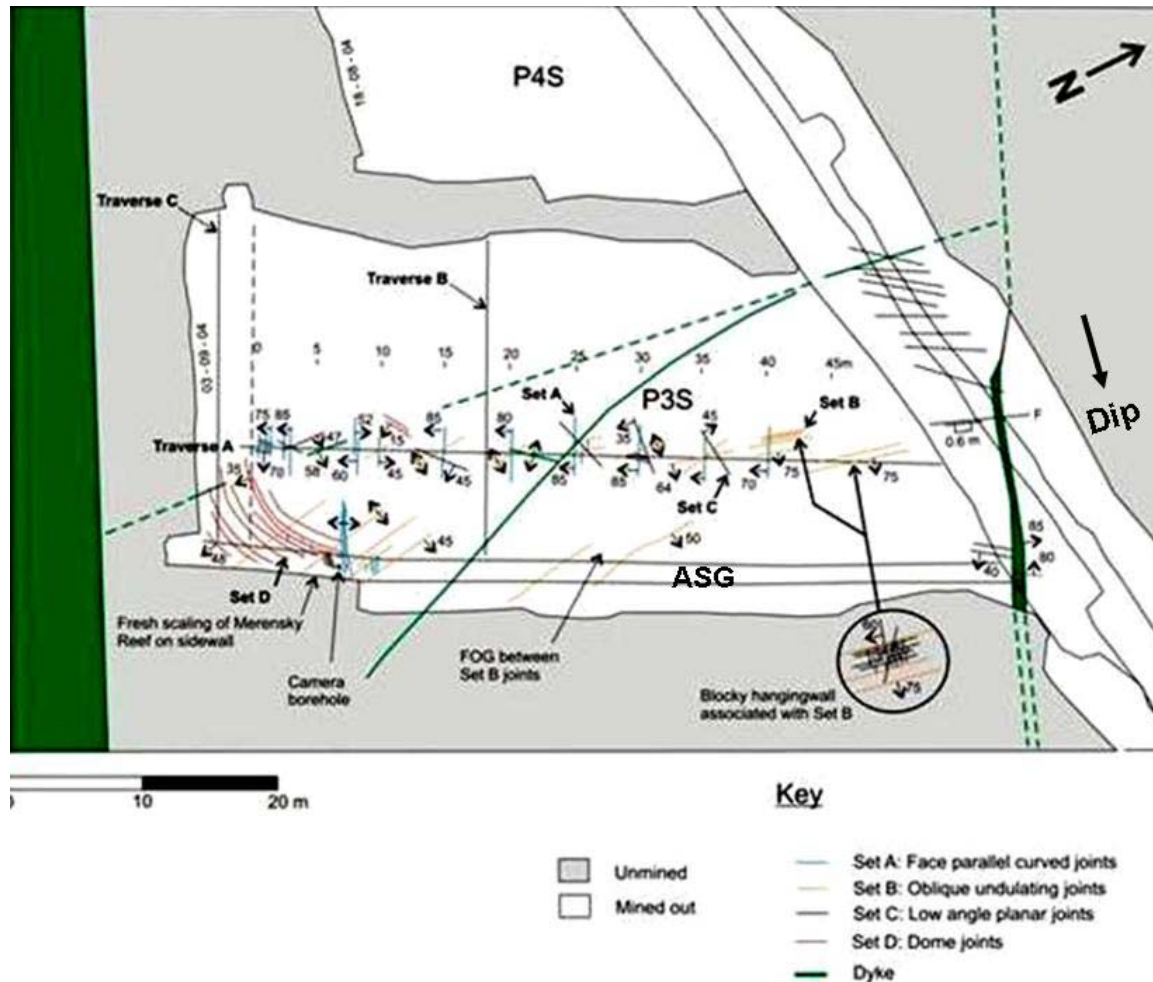


Figure 3 Stope sheet showing the instrumentation site. Traverses A, B and C show the hangingwall Ground Penetrating Radar scan lines.

The Reef dips at 9° towards the East. A major NW-SE dyke trend and a minor N-S to NNE-SSW structural trend in the form of small dykes and faults occurs in the area. The average panel stoping width was 1.4 m with a face length of 27 m and maximum strike span of 70 m. Four joint sets (Set A - D) were identified and the traces of these discontinuities on the hangingwall are shown in Figure 3.

Figure 4 depicts a stratigraphic column of the lithologies immediately above the Merensky Reef stope. The immediate footwall and hangingwall of the Reef is mottled anorthosite and pyroxenite respectively. There was a typical gradational change between rock types above the instrumented stope with the nearest sharp contact between rock types occurring at about 12 m above the stope.

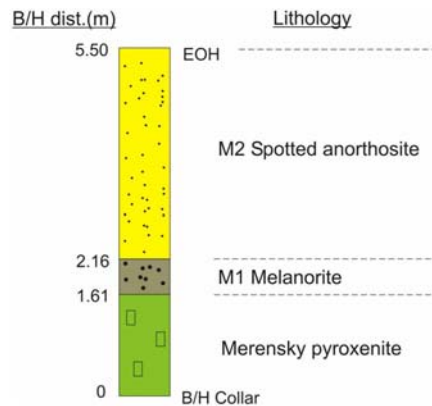


Figure 4 Stratigraphic column for the immediate stope hangingwall, based on the core from the borehole camera hole.

Stresses were not measured at the site. However, in another project on the same mine, measurements conducted in nearby footwall anorthosites showed a horizontal to vertical stress ratio (k -ratio) of 1.3, or a reasonably low horizontal stress of about 40 MPa. As no measurements were conducted in the anorthosites above the hangingwall, the stress condition in these anorthosites is unknown. However, measurements above the hangingwall at another Bushveld mine (Figure 5) showed that very high horizontal stresses are sometimes uniquely resident in the anorthosites, but not in the other lithologies - so called 'stress channelling'. The open horizontal plane at about 10 m above this stope may be a fracture that developed during mining. The mechanism for the development of this fracture could be a form of extension fracturing [3] that occurred when the vertical confinement was relieved during mining.

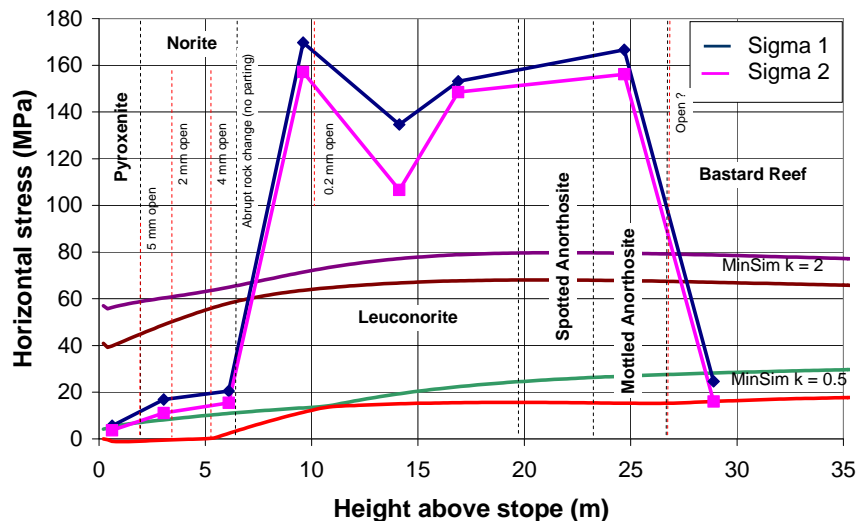


Figure 5 Horizontal stress measured above the centre of a Merensky stope compared to elastic models with k -ratios of 0.5 and 2.0. The black dashed lines show the approximate boundaries of the rock types and the red dashed lines show open discontinuities of fractures. The discontinuity at 10 m above the stope may be a fracture plane that developed during mining.

3 Borehole Camera Survey and Borehole Core Inspection

The borehole was located 9.7 m from the face and 1.7 m ahead of the siding (Figure 3) at the time of the investigation. The borehole camera survey revealed only one open discontinuity between heights of 1.2 m and 1.4 m. The borehole core (Figure 6) also indicated solid rock conditions above the stope with one possible fracture plane at 1.6 m above the collar. The slightly higher position of this plane in the core is attributed to errors due to drilling cracks in the core and the uneven collar used as a reference in the camera survey.



Figure 6 Borehole core and a possible fracture position at 1.6 m above the stope.

5 Ground Penetrating Radar Survey

Three traverses were undertaken in the dip and strike directions (Figure 3). The strike traverse line (Traverse A) extended along the mid-panel area between 5 m and 30 m of the stopped face position. Dip traverses were surveyed in a down-dip direction at distances of 18 m (Traverse B) and 3 m (Traverse C) from the face position. Figure 7 shows the interpreted radargram results.

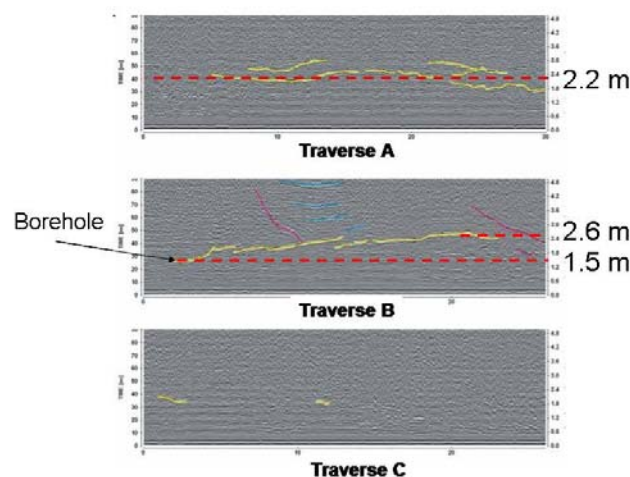


Figure 7 Interpreted GPR radargrams. The main near horizontal anomaly is shown by a yellow line. Steep lines (pink) are interpreted as near vertical joints (e.g. Set A or Set B). The anomaly indicated by blue lines could be associated with minor dyke structures occurring in this area.

Traverse 'A' shows a distinct horizontal anomaly occurring at about 2.2 m above the hangingwall (Figure 7). The feature, indicated by yellow lines, appears irregular and undulating with possible splays (which could be processing artefacts). The feature is also detected in Traverse B where it is shown to dip at a shallow angle to the hangingwall and also appears to flatten in the up-dip area. The distance between the hangingwall and the structure is 1.4 m and 2.4 m in the down-dip and up-dip sides of the panel respectively. Clear dislocations of the feature in Traverse B could represent minor fault displacements or en-echelon shear planes, indicative of high horizontal stresses. Traverses A and B both show evidence of a prominent shallow-dipping parting plane striking parallel to reef that is persistent for at least 20 m in both dip and strike directions. The anomaly could represent a low-angle joint (set C) or dome joint (set D). However, these joint sets are closely spaced and if the anomaly does represent these features, other similarly orientated features should be shown in the radargrams. The appearance of this feature may be explained in three ways [6]:

The feature is a low-angle joint that contains abundant infill or is slightly open (air gap) compared to similarly orientated joints;

A well developed fracture plane or fracture zone; and

A lithological contact reflecting the different rock properties of neighbouring rock types.

The absence (or limited presence) of the detected feature in the Traverse C radargram suggests either that the face area is highly disturbed, possibly by fracturing, or that fracturing has not occurred in this area [6]. The latter is unlikely as both the underground observations (Set D joints in Figure 3) and the seismic system suggest the former. A similar radargram pattern is observed in the first 10 m of Traverse A. As the survey started about 5 m from the face, the results suggest that the disturbed face area actually extends about 15 m from the face.

The relative change in height of the horizontal anomaly determined in Traverse B, from 1.4 m to 2.4 m over a 20 m distance, may mean that the feature consists of many smaller features. The data shows that the feature dips at about 10° to the hangingwall and flattens out at around 2.4 m above the stope.

6 Seismic Monitoring

6.1 Instrumentation and Monitoring Configuration

The Ground Motion Monitor (GMM) used in this study (Figure 8) consisted of eight uniaxial geophones. The GMM is a battery-powered stand-alone device capable of storing 512 waveforms, recorded on each of eight channels. For this work, the system was modified to increase the sampling rate and expand the frequency band towards the higher frequencies. This increased the quality of registration of the high-frequency microseismic events associated with hangingwall fracturing. Seven geophones were installed in or on the hangingwall and one geophone on the footwall (Figure 9). To improve the vertical resolution of the recording configuration, one of the hangingwall geophones was installed in a vertical borehole at a height of 4.3 m above the stope.

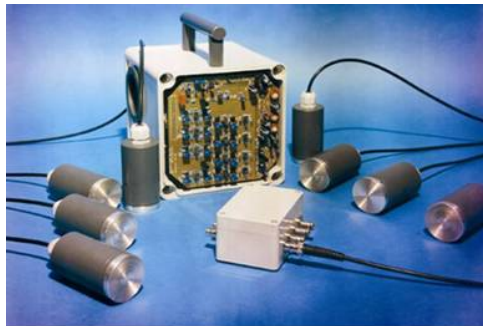


Figure 8 Ground Motion Monitor used in this study.

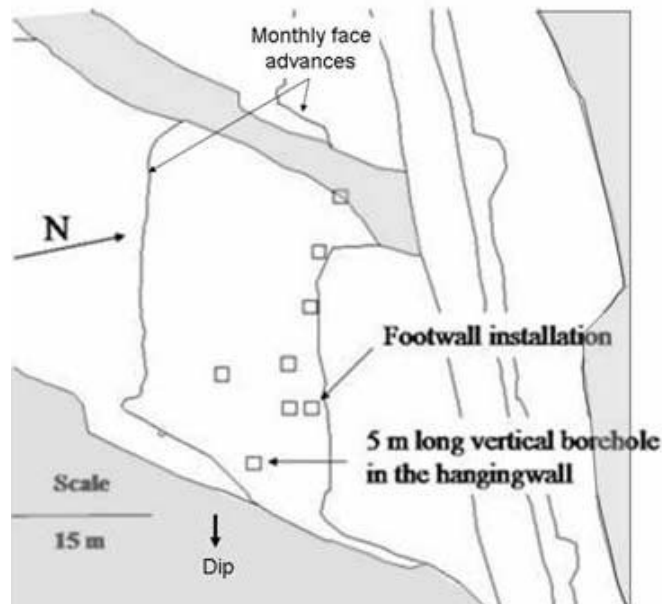


Figure 9 Stope sheet showing the geophone layout at the instrumentation site (Figure 3). The squares represent the locations of the geophones. The grey shows the unmined and pillar areas.

The site was monitored for about two months, which included periods of active mining and no mining in the panel. During the monitoring period a total number of 1618 seismic events were recorded by the system. This included near-field and far-field seismic events, blasts and noise triggers. The mine seismic network was not used in the assessment as at the time of the investigation, only a single geophone, located far from the site, was available.

6.2 Data Analysis

The first step in the seismic analysis was to determine the location of the seismic events. This involved digitising the mine plan, surveying the positions of geophones and organising the database in an appropriate format. The seismic processing software [7] was used to locate the seismic events and analyse their temporal and spatial distribution.

Knowledge of the wave propagation velocity between the event and the geophone is critical in the event location process. However, the variations in seismic velocities are not well known and could be a source of significant location error. Locations of the seismic events were first evaluated using P- and S- velocities of $V_p=6600$ m/s and $V_s=3900$ m/s. These values are commonly used by mine seismic networks in the region, but represent the velocities of propagation in the solid rock in which the mine-network geophones are normally installed. In this project, the geophones and the seismic sources of interest were located in the immediate hangingwall where the rock mass was significantly more fractured and the location identification was therefore relatively poor. Better velocity approximations were determined by carrying out a number of calibration blasts at the site. The P-wave velocity was measured and the S-wave velocity was calculated from the ratio $V_s=V_p/1.732$, and adjusted to compensate for the higher horizontal stresses (the k-ratio was assumed to be 1.47). The velocities used in the evaluations were 5600 m/s and 3400 m/s for the P-wave and S-wave, respectively.

6.3 Seismic Results

Figure 10 shows the seismic events located in this panel. The results were grouped for the period of active mining (10a) and no mining (10b) in the panel.

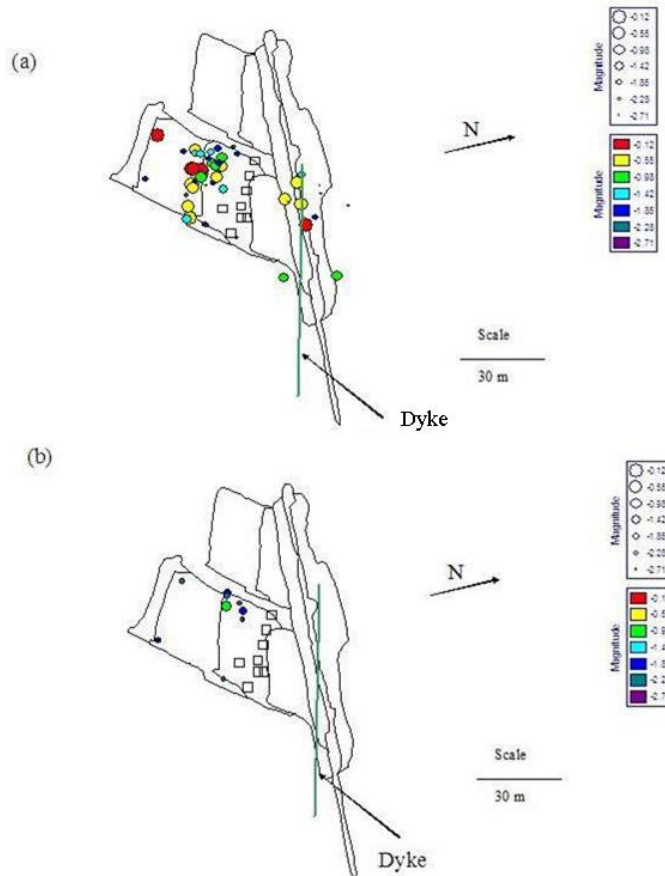


Figure 10 Location of the seismic events - plan view: a) seismic events during the period of active mining in the panel; b) seismic events during the period of non-mining in the panel.

It is clear from Figure 10 that most of the seismic events occurred during the active mining of the panel. Only a few seismic events were induced from mining elsewhere or from other sources of seismicity. The majority of the seismic events located in the face area and are associated with fracturing during blasting. However, a few strong seismic events located around a dyke positioned on the north side of the panel.

A section view of the seismic events, shown in Figure 11, indicates that the seismic events located mainly in the hangingwall. The majority of these events located within 2 m to 2.5 m of the stope hangingwall, however some events located up to 5 m above the stope. The average height of the recorded events appears to have increased towards the up-dip side of the panel.

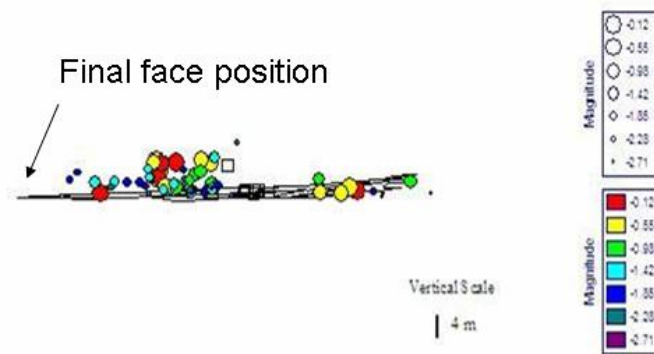


Figure 11 Location of seismic events – section view.

A good correlation was found between the depth and size of the seismic events and the lithology of the hangingwall. The first 2.2 m of the hangingwall is made up of pyroxenites and melanorites which correlate with a high number of small seismic events occurring in a low stress environment. Stronger and probably less fractured spotted anorthosites are located above 2.2 m, coinciding with the stronger seismic events located higher in the hangingwall. However, there are two vertical geological structures running through the cluster of the stronger seismic events which could be related to some of these events.

The Peak Particle Velocity (PPV) is a widely used parameter in the mining industry to characterise dynamic loading of excavations. A number of studies carried out in gold mines have shown strong variations of the PPVs in relation to:

The distance from the source [8];

The hangingwall and footwall behaviour [9]; and

The site effect measured on the surface of excavations [10, 11].

The distributions of PPVs recorded at this site during the period of active mining and period of non-mining were compared in order to distinguish the level of loading during each period (Figure 12). The figure indicates clearly that the PPVs were four to six times higher during the period of active mining than when no mining occurred in the panel. From this it can be concluded that very few of the recorded events resulted from external stimuli such as other seismic activity or mining outside of the panel.

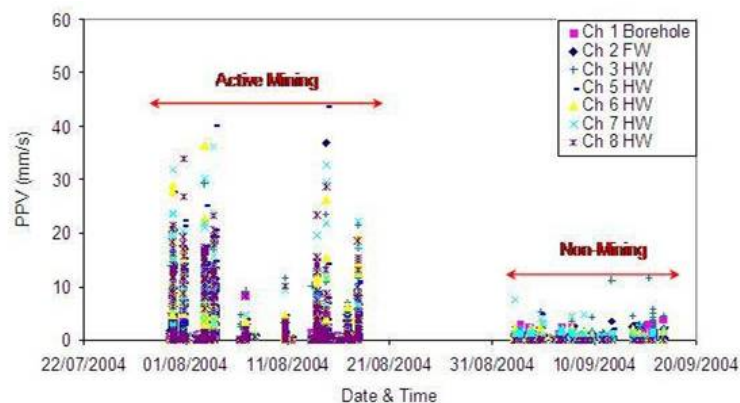


Figure 12 Peak particle velocities recorded during the monitoring period: a) PPVs recorded during active mining in the panel; b) PPVs recorded while there was no mining in the panel.

The site effect is defined as a difference between PPVs measured in the solid rock and the skin of the excavation. To evaluate this effect the PPVs measured in the solid rock were compared to the PPVs measured on the skin of the hangingwall (Figure 13). Again the figure clearly shows that the site effect during the period of active mining is much higher than the site effect generated by outside seismic activities (during the period of no mining in the panel).

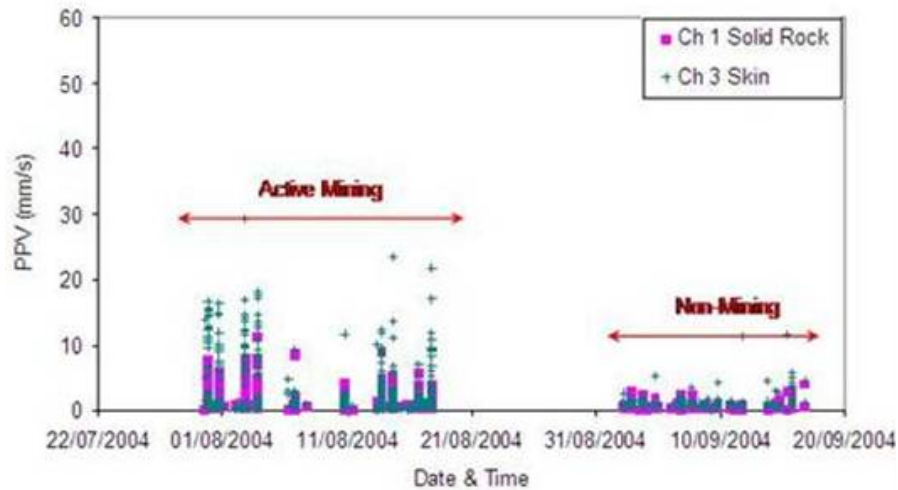


Figure 13 Peak particle velocities recorded in the solid rock above the hangingwall and in the skin of the hangingwall: a) during active mining; b) during non-mining at this panel.

Figure 14 shows the PPVs recorded in the hangingwall and footwall. During the period of active mining, the PPVs recorded in the hangingwall were generally much higher than those in the footwall. However, during the period of no mining in the panel, the PPVs were similar in the hangingwall and footwall. These results indicate that, during the active mining period, dynamic loading was concentrated in the hangingwall. When mining in the panel ceased, the rate at which damage occurred in the hangingwall appears to have reduced accordingly.

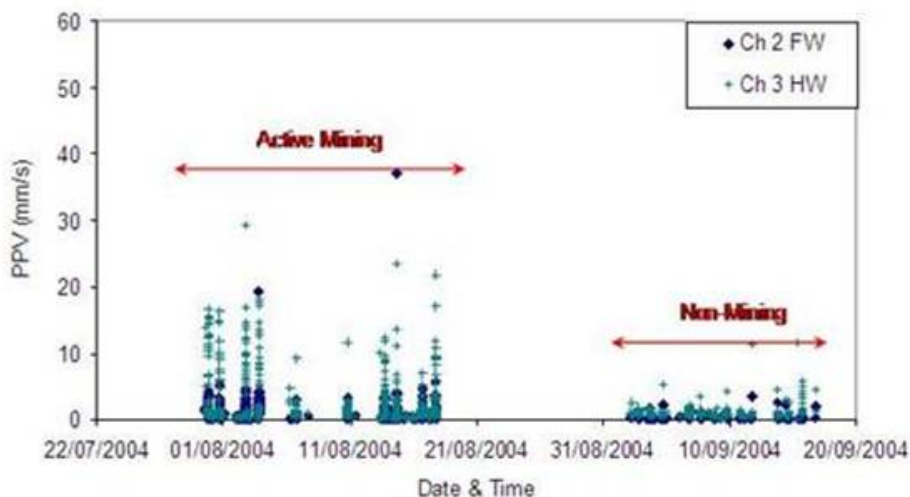


Figure 14 Peak particle velocities recorded in the hangingwall and the footwall: a) during active mining; b) during non-mining at this panel.

7 Conditions under which the Fracture Problem Occurs

14 panels associated with the hangingwall fracture problem were investigated to determine under what conditions the fracturing is likely to occur. Interestingly, the panels were all relatively deep, mostly below 1100 m, and were often associated with lead-lag and remnant mining problems. This suggests that the fracture problems are associated with abnormally high stress conditions. Stopes adjacent to a large pothole had to be abandoned. Stress measurements conducted in a pothole [12] showed that high horizontal stresses can be associated with some pothole structures.

Most of the observed fracturing occurred in anorthositic rocks and these lighter rocks, with a higher percentage plagioclase, appear to be more susceptible to fracturing than are the darker rocks. In some cases fracturing was observed at the approximate position of a change in rock type, as was apparently the case at the instrumentation site.

The investigated panels mostly had relatively small minor spans, indicating that this form of fracturing occurs even in limited spans and that stability is probably more dependent on good mining practice and stope orientation than on span.

8 Discussion of Instrumentation Results and Observations

All of these results suggest that at the instrumentation site a parting plane developed between 1.6 m and 2.4 m above the hangingwall. The borehole core shows that these heights coincide with the lithological changes from pyroxenite to melanorite, and melanorite to spotted anorthosite, respectively.

The seismic events were generally located in the hangingwall of the panel. Most of the events, especially in the low and intermediate range, were located close to the excavation surface in the pyroxenite and melanorite belts ranging in thickness between 1.6 m and 2.4 m. The stronger seismic events were located higher in the spotted anorthosites. Most of the seismic events were located around the face and were generated during or shortly after the blasting. A good correlation was found between the site lithology, the rock properties, GPR surveys and the physics behind the seismic events. The mechanism of the fracturing is suspected to be a form of extension fracturing [3] due to the reduction of the vertical confining stress during mining. This fracturing may also have been assisted by the stress conditions around the face and abutments.

GPR Traverse B, performed in the dip direction (Figure 15), indicates that the observed parting increased in height above the stope towards the top of the stope. This plane could correspond to a change in lithology thickness, or the plane of weakness could have migrated up from 1.6 m (top of pyroxenite) at the gully to 2.4 m (approximately the top of the melanorite) towards the up-dip end of the panel. This would explain the location of small seismic events at greater height in this portion of the panel.

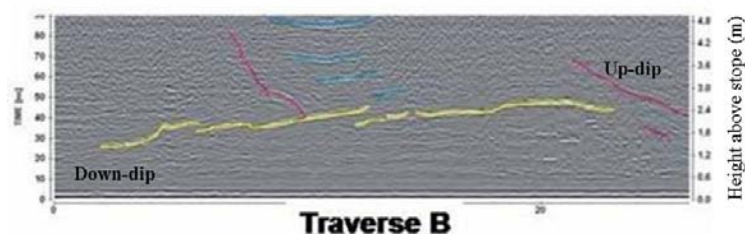


Figure 15 Radargram results of the GPR scan line in the reef dip direction.

The peak particle velocities measured during active mining of the panel were found to be four to six times higher than the PPVs measured during the period of no mining in the panel. The site effect was also found to be much higher during the active mining period. In addition, during the active mining period most of the dynamic loading was concentrated in the hangingwall. However, during the period when no mining was taking place in the panel, the hangingwall and the footwall were equally loaded by outside seismic activities. The differences in seismicity between the periods of mining and no mining show that damage to the hangingwall was due to seismicity induced by mining in the panel. Remote blasting and seismic events had little effect on hangingwall damage.

The panels identified with the fracture problem all suggested high stress conditions. As the fracturing phenomenon has only been observed at deeper levels and associated with features associated with high horizontal stress, the mechanism appears to be stress related. This implies that deeper level mining will evoke more fracturing if the k ratios remain the same.

10 Conclusions

The research showed that the source of at least some of the small events (often heard in the stopes) is the fracturing of the hangingwall. Rock tests conducted by the CSIR suggest that the lighter coloured anorthositic rocks are more brittle than the pyroxenites. Observations suggest that horizontal fracturing develops preferentially in the more brittle material. The seismic network also showed that the larger seismic events occurred in the anorthosites. Historical studies conducted on stopes where fracturing was observed, suggest that the horizontal stress levels were relatively high and the fracturing is suspected to be the result of a form of extension fracturing [3] that occurs when the vertical confinement is reduced due to mining. This condition may be exacerbated by the stress condition at the face and abutments.

The results of the investigation suggest that the fracture problem could worsen with depth if the current k ratios persist to deeper levels. These conditions could affect the long-term sustainability of the platinum industry.

Acknowledgements

Individual mines and their staff have accommodated extensive data collection, which often interfered with production demands. Their contribution is therefore highly appreciated.

This work was sponsored by PLATMINE, and permission for publication is gratefully acknowledged.

References

1. Özbay, M.U. and Roberts, M.K.C. Yield Pillars in Stope Support. Proc. Rock Mechanics in South Africa, (Sangorn, 1988).
2. Watson, B.P. The Feasibility of Using Rock Mass Ratings for the Design of Panel Spans and Support in the Shallow to Intermediate Depth Bushveld Platinum Mines, MSc project, Dept. of Mining Engineering, University of Witwatersrand, Johannesburg, (South Africa, 2003).
3. Stacey, T.R. A Simple Extension Strain Criterion for Fracture of Brittle Rock. Int. J. Rock Mechanics mining Science and Geomechanics, 1981,18. 469-474.
4. Watson, B.P., Kuijpers, J.S., Henry, G., Palmer, C.E. and Ryder, J.A. Nonlinear Rock Behaviour and Its Implications on Deeper Level Platinum Mining. Proc. Platinum in Transformation. Third int. Platinum SAIMM conf. Sun City, (South Africa, 2008).
5. Watson, B.P. Rock Behaviour of the Bushveld Merensky Reef and the Design of Crush Pillars. PhD Dissertation to be Submitted to the Dept. of Mining Engineering, University of Witwatersrand, Johannesburg, (South Africa, 2009).

1. Schoor, V. and Pers, M. comm., 2005.
2. AURA. Software for Routine and Scientific Processing of Seismic Data, CSIR Mining Technology, Johannesburg, (South Africa, 2003).
3. Hagan, T.O., Milev, A.M., Spottiswoode, S.M., Vakalisa, B. and Reddy, N. Improvement of Worker Safety Through the Investigation of the Site Response to Rockbursts, SIMRAC Final Project Report GAP 530, Pretoria: Department of Minerals and Energy, 1998.
4. Durrheim, R.J., Milev, A. M., Spottiswoode, S.M. and Vakalisa, B. Improvement of Worker Safety through the Investigation of the Site Response to Rockbursts, SIMRAC Final Project Report GAP 201, Pretoria: Department of Minerals and Energy, 1997.
5. Milev, A. M., Spottiswoode, S. M. and Stewart, R. D. Dynamic Response of the Rock Surrounding Deep Level Mining Excavations. Proc. 9th ISRM, (Paris, 1999).
6. Milev, A.M., Spottiswoode, S.M., Noble, B.R., Linzer, L.M., Van Zyl, M., Daehnke, A. and Acheampong, E. The Meaningful Use of Peak Particle Velocities at Excavation Surfaces for the Optimisation of the Rockburst Criteria for Tunnels and Stopes, SIMRAC Final Project Report GAP 709, Pretoria: Department of Minerals and Energy, 2002.
7. Watson, B.P., Roberts, M.K.C., Jager, A.J., Naidoo, K., Handley, R., Milev, A.M., Roberts, D.P., Sellers, E.J. and Kanagalingam, Y. Understanding the Mechanical Properties of the Anorthosite Suite of Rocks. PlatMine Final Project Report, Johannesburg. RSA, 2005.

SEISMIC MANAGEMENT AND SEISMIC HAZARD QUANTIFICATION AT KANOWNA BELLE MINE

RICHARD-P VARDEN

*Senior Geotechnical Engineer, Kanowna Belle Mine, Barrick Gold Corporation
Kalgoorlie, 6430, Western Australia*

Kanowna Belle Gold Mine is a seismically active mine with stoping below 1000m. Control of seismicity is critical to the future of the mine, both in terms of safety and economics. To achieve this a number of control systems have been put in place so as to manage seismicity on a mine wide scale down to day to development headings. This seismic management has been achieved through hazard quantification. Seismic hazard involves the study of the mines seismicity in conjunction with geological, Geotechnical settings and the layout and stoping method. The results of this work is the stoping sequence, planning implications, support system and other tertiary control systems.

1 Introduction

1.1 Overview of Kanowna Belle Mine – Location, Geological Setting and Mining Method

The Kanowna Belle Gold Mine is located 18 km NE of Kalgoorlie and 2 km west of the historic gold mining centre of Kanowna, Western Australia.

The Kanowna Belle deposit is hosted by sedimentary volcanoclastic and conglomeratic rocks, which are separated into hangingwall and footwall sequences by a major, steeply SSE dipping zone of structural disruption. The orebody strikes East West, varies from 5 – 50 m in width with an average dip of 65°. The strike length is 500 m with a down-plunge extent greater than 1400 m.

The main structural feature of the deposit is the Fitzroy fault, varying width and dip – a undulating feature dipping on average 65° and is gouge filled in some areas, but mainly a zone of highly broken rock. The fault forms the footwall in A,B and C block and the hanging wall of the ore zone in D and E block and this is encompassed by a footwall and hanging wall shear zone, which can be up to 30 m wide. Three felsic units occur in the footwall, which terminate at the Fitzroy fault. A number of splay structures off the fault exists. These are sub-parallel to the fault and occur either side of the fault. They are substantial in length and down dip strike. Figure 1 shows a plan view of the generalised geology for Kanowna Belle. [1]

The mine has been split into five mining blocks, A block – mined out, B – partly mined, C – currently mining almost complete, D – currently mining, E – developing. The mining method is long-hole open stoping, with 30 m sublevels. Sequencing is centre out bottom up with paste fill.

The rockmass has an intact rock strength measured between 90 to 140 MPa. Up to 4 joint sets are present throughout the mine with local areas (stopes) having 2 to 3 joint sets. In general the rock mass can be described to be fair to very good, with the exception of the Fitzroy fault being very poor, [2].

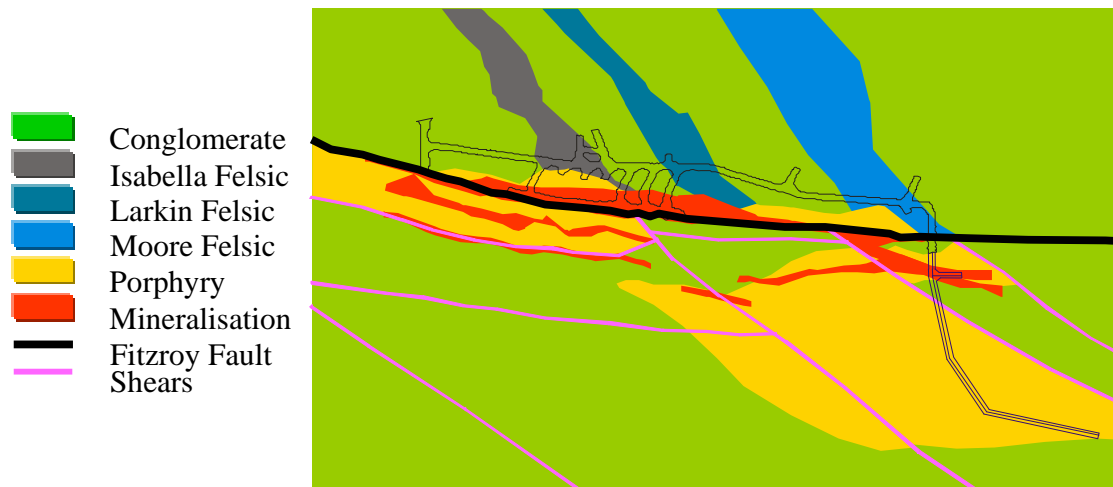


Figure 1 Generalised geology of Kanowna Belle

The major principal stress at 1000 m is 75 MPa and is horizontal (124/06). In general walls are more affected by stress than the backs. This due to the high horizontal stress acting on the walls, whereas the backs, with an arched profile, are in compression and have been stable in observed seismic events.

2 Seismicity at Kanowna Belle

Seismicity at Kanowna Belle is mainly associated with structures. The position of major structures and lithological contacts are known and seismicity clusters located consistently along these structures. Seismicity associated with structures is considered to be greater than -0.5 local, (ISS) magnitude. Number of events typically recorded in a month is around 1000, of these 20 – 50 can be greater than -0.5 magnitude.



Figure 2 A 2.0 local magnitude seismic event during development of an ore drive

The failure mechanism is typically fault-slip. The ratio of S-wave Energy to P-wave Energy of the seismic event indicates shear mechanism of the structures present. Floor heave is a common characteristic of large events at Kanowna Belle, along with bulking of the sidewalls and is possibly linked to re-adjustment of structural blocks at critical equilibrium along lines of weakness where the development/stope openings provides freedom of movement. Where support fails there is often evidence of ejection from the sidewalls. In most incidences there is little to no damage to backs of the drive, this is shown in figure 2. An explanation for this is that due to the high horizontal stress and orientation of structures being almost parallel results in low strength to resist shearing.

The Fitzroy fault the dominant structure of the mine, which is gouge filled, has been modelled to have high shear strength, probably due to asperities, but slips relatively easily which does not necessarily result in significant seismicity. The Fitzroy fault is approximately 30° from the principle stress direction. It is considered that the movement of the Fitzroy fault then initiates other structures to move, and as these are near parallel to the stress field the result is more significant with seismicity sometimes resulting in damage.

2.1 History of Damaging Events

Monitoring started in May 2000, first significant damaging event occurred on the 1st April 2002, a 0.1 local magnitude event, in development 9440 HW drive. The majority of seismicity has occurred in D block, below a depth of 740 m, where the Fitzroy fault now locates on the hanging wall of the ore zone and general ground condition have become worse due to a larger number of cross cutting structures.

Seismicity in E block, below 1000 m, has been mainly confined to the western end of the footwall drive and truck loop. There is a larger concentration of active cross cutting structures intersecting the footwall and truck loop. Stopping activities in E block has only recently begun and has had a low seismic reaction so far. E block below 1000 m has only just begun stoping and few events have occurred, the most active location being the 9330 level and truck loop, this level is influenced by the crown level below D block and has been subjected to change in stress distribution, stope firings and backfill water opening joints. Additionally the 9330 has a large amount of cross cutting structures. The most active area of the mine, D block from the 9590 to 9500 levels has been influenced by a number major seismically active structures intersecting the Fitzroy fault in an area approximately 60 m by 90 m down dip.

During development approximately 21 significant events have occurred, greater than local magnitude 1. Of these 15 caused damage and of these 9 were during development. During stoping 23 significant events have occurred with 9 causing damage in accesses. All the events had the potential to injure personnel, only 1 minor injury occurred and only 1 machine damage. This injury was to a long hole driller who was stepping off his rig when an event caused floor heave to occur. Events that caused failure within stopes have not been included.

2.2 The Seismic System

The system is an ISS system and consists of: 45 sensors, these are connected to 16 boxes, an assortment of MS, QS and GS boxes. Sensors are spaced at approximately 150 m to create a reasonable sensitive array.

Accelerometers, (triaxial and Uniaxial), are the most common sensor so as to be able to detect a large magnitude range, especially less than 1, the triaxial geophones allow a balance in locating larger events and when events are situated close to accelerometers. Due to this mix the array density is reasonable dense. The majority of sensors are located on the footwall side of the orebody, but where access, such as exploration drill

drives, sensor are placed on the hanging wall side. A seismic controller located underground, this collects the data and sends it to surface. This system, allows data to be collected even if communications are down between underground and surface, data is sent at a later date or can be down loaded. This system also allows for two backs ups, one underground the other on surface.

Processing is done on site by the Geotechnical department every morning with JMTS. Additional analysis is then done using JDi – analysis software provided by ISS and MSRAP, software provided by the Australian Centre for Geomechanics to interpret the data. MSRAP has been recently acquired by the company and is mainly used for reporting and is being developed for hazard assessment. JDi is the main interpretation package used on site.

3 Seismic Management Systems

This section details the systems used at Kanowna Belle to manage seismicity. The management of seismicity relies on a combination of control systems and analytical techniques. No one system can be used to control seismicity.

3.1 Mine Design

Mine design is the first means to control seismicity, but to do this the hazard has to be identified. Mine design incorporates data collection, seismic hazard identification, development layout and stope sequence and design.

3.1.1 Seismic Hazard Identification

Seismic hazard identification consists of ranking the seismic risk against a set of criteria, these include:

- Structural interpretation: data is from diamond drill geological interpretation, underground mapping and seismic activity/clustering. The mine has recently purchased Adamtech, a 3D photogrammetry system. This is allowing structural data collection when incycle shotcreting is being used, where standard mapping practices are not possible.
- Rockmass quality: data if collected from diamond drilling and entered in to a rockmass database to create a rockmass model with RQD, Fracture frequency and other properties to be analysed in three dimensions.
- Active seismic clusters: in combination with known structures, structures can be extended where no interpretation exists, new structures can be interoperated. The spatial and temporal distribution is studied to determine a structures behaviour over time and its reaction to development and stope blasts, figure 3 shows an example of seismicity occurring on structures.
- Stress analysis: stress and stress-change analysis, (dS1; dS2; dS3 – instability), sequence modelling in Map3D and Abacus.
- Historic seismic displacement contours: displacement contouring is used to determine the extent of risk based on historic behaviour. Seismic displacement contours is based on the distribution and magnitude of past events.
- Occurrence of large seismic events: these are important to study as they generally indicate the behaviour of a structure that is likely to be high risk,
- Extraction and development geometry: actual verses planned mine extraction layout.

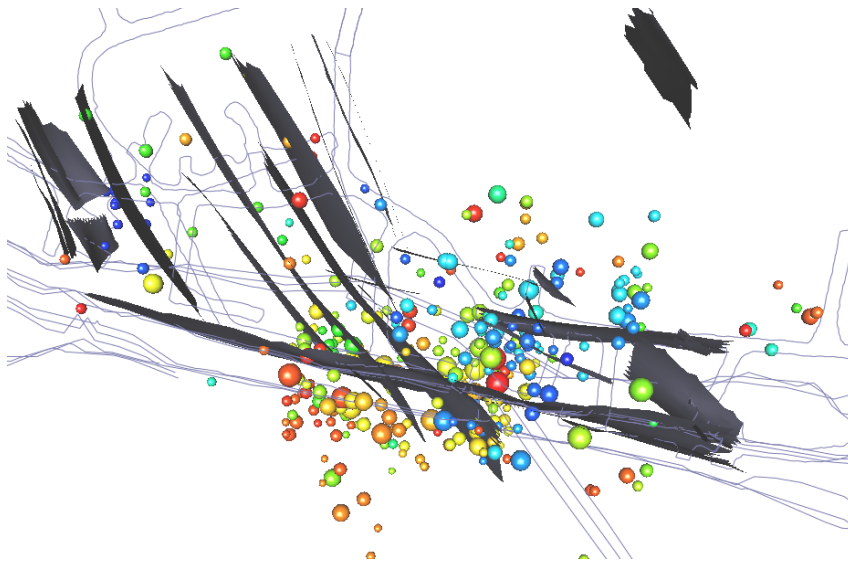


Figure 3 Plan view of a level showing structure and seismic activity aligning

3.1.2 Risk Ranking

The seismic hazard identification leads on to risk ranking of development and stopes. The ranking is based on the following definitions of risk:

Low seismic hazard: rockmass response to mining and stress change results in a high probability that events exists of less than -0.5 local magnitude within the time of the planned development and or stope extraction. Historically majority of events less than -0.5 local magnitude and can not associate events with structures. No damage or deterioration is expected in this area.

Moderate seismic hazard: rockmass response to mining and stress change results in a 40-60 % probability that events exists of greater than -0.5 local magnitude within the time of the planned development and or stope extraction. There is a low response in the area, no mapped structures, but possible structure exists. Low level of damage and or deterioration is expected.

Medium seismic hazard: rockmass response to mining and stress change results in a 60-80 % probability that events exists of greater than 0.5 local magnitude within the time of the planned development and or stope extraction. Structures exist, but have a low level of seismicity associated with them, no significant events greater than 1+ local magnitude have occurred. Some medium level of damage and or deterioration may occur.

High seismic hazard: rockmass response to mining and stress change results in a 80 %+ probability that events exists of greater than 1.5 local magnitude within the time of the planned development and or stope extraction. Active structures are known to exists with a history of events greater than magnitude 1 exists. Extensive rehabilitation has occurred and or is likely to be required from damage and deterioration.

Extreme seismic risk: Extensive damage and events greater than magnitude 2 have occurred in the past and extensive rockmass deterioration exists. Structures are highly active and have a large response to development/stoping. It is highly likely mining and further stope extraction will not be feasible in the future.

3.1.3 Development Layout

Based on the seismic hazard identification a number of rules and learning's have been developed, these include:

- Stand-off ore drives from the Fitzroy by at least 5 m – this reduces the risk of a seismic event during development and reduces potential damage to draw points and stope accesses.
- Developing from the west to the east has a higher risk of seismicity than from east to west. This is due to the structure and stress orientation being similar.
- Minimise development in poor quality rock and seismic prone areas.
- Where possible development to intersect structures perpendicularly.
- Footwall drive to be placed 20 m minimum from planned stope footwall.
- Apply dynamic support to active/high risk structures
- Avoid structural intersections in openings
- Minimise intersection size, i.e. avoid where possible four-way intersections.

3.1.4 Stope Designs

Each stope has a specific stope design. This design is geotechnical assessed and recommendations made relating to seismic risk rating a dilution risk rating. Expected exclusion zone are given and backfill requirements given. A number of design rules for stopes have been developed, these include:

- Inter-level spacing 30 m
- D block maximum strike width 20 m, for E block 15 m
- D block A panel (up against Fitzroy fault), maximum HW dip exposure 40 m
- D block B/C panels maximum stope height 60 m
- E block HW dip exposure maximum distance is 75 m – with the 15 m strike length, double and possible triple lifts will be allowable due to the reduced dilution risk.
- Wall design no undercut of hanging wall, east or west walls by stoping or sub-parallel development

3.1.5 Sequencing

The mining sequence is geotechnically controlled. A number of rules have been developed and once set can not be changed unless a geotechnical study shows otherwise, the base design rules include:

- D and E block bottom up extraction centre out.
- Where possible develop east-west.
- Design continuous retreat extraction and avoid pillars where possible. Where it is necessary to place pillars a study will be made on the minimum pillar strike width.
- Avoid double stope abutments along strike.
- Avoid double dip hanging wall exposures in D block due to 20 m strike lengths.

- Maximum of 1 A-panel stope lead/lag along strike.
- Maximum 2 filled vertical stope abutments along dip.
- 100 % sequential pastefill.
- Minimise delay to paste filling of stope, stopes must be paste filled.

3.2 Support Systems

The second line of defence in controlling seismicity is the use of support systems. This needs to be viewed as control on a local scale and may require maintenance over the life of a particular area. Kanowna Belle has developed a number of support systems for varying ground conditions and seismic risk. In-cycle fibrecrete is used in all E block development and as required in other areas above E block. Friction bolts in combination with mesh and fibrecrete are the most common systems used for support of low to medium seismic risk. For high seismic risk areas dynamic support systems have been developed. The Garford bolt in conjunction with high strength fibrecrete and mesh is used in high seismic risk areas and has been extensively described in papers [3] [4]. Mesh placed over the fibrecrete is an important part of the system. During a significant seismic event the fibrecrete between bolts maybe ejected in small, mesh controls this ejection.

The concept of how support is managed at Kanowna Belle is by an analysis of specific areas where support is not placed on a blanket approach. Support systems can be “switched on switched-off” as required depending on the environment and seismic monitoring. Development is coded into seismic risk and relevant Ground Support Instructions (GSI) is issued.

3.3 Exclusion Zones

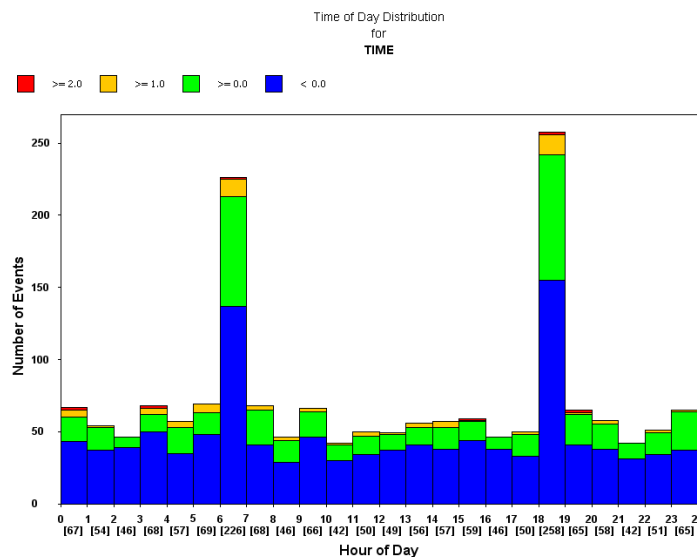


Figure 4. Time of day distribution of seismicity for Kanowna Belle

Exclusion zones is the third means of controlling dilution and protecting personnel. They are set based upon the seismic risk and history of the area. Exclusion times vary from 1 hour to 24 hours, with the most common time

being 3 hours. Figure 4 shows a time of day distribution for seismicity at Kanowna Belle. The graph shows that the majority of events occur after blasting, 6 am and 6 pm, but there is a consistent amount of events occurring throughout the day with the chance of large events occurring outside blasting times. Large events have occurred days to weeks after a major stress change in that area.

3.4 Reporting

All underground personnel report ground movement occurrences, (includes noise, cracks opening up, falls of ground, support damage, water inflow), on a Ground Observation form. This form allows Geotechnical engineers to investigate any ground movement or ground noise. A valuable tool that backs up seismic reports and damage. Also if the seismic system is down or sensor not working additional information can be given first hand by personnel in the area.

7 Conclusions

In conclusion Kanowna Belle has developed a multi-tiered system to manage seismicity. Based on the identification and quantification of seismicity, the systems developed aim to design out high risk areas first, then use support methods to target specific high risk areas. Final control systems offer the least effective system, as seismicity can not be predicted and has been shown may occur outside exclusion zone, but exclusion zones and support are systems that the workforce can identify with and gain an understanding and respect for seismicity. Kanowna Belle future is to stope below 1000 m, the systems developed and lessons learnt will be critical to the success in mining in an increasing high risk environment.

Acknowledgements

The author would like to acknowledge Barrick Kanowna for the support in being able to write this paper, Ronald Lachenicht for previous work as Geotechnical Superintendent and mentor, John Player of WASM who developed the system to test dynamic support and who was greatly involved with the implementation of the Garford bolt.

References

1. Beckett, T.S. Fahey, G.J. Sage, P.W. and Wilson, G.M. Kanowna Belle Gold Deposits in Geology of Australian and Papua New Guinean Mineral Deposits. Eds, 1998.
2. Berkman, D.A. and Mackenzie, D.H. The Australian Institute of Mining and Metallurgy: Melbourne. Hoek, E., Kaiser, P.K., Bawden, W.F., Support of Underground Excavations in Hard Rock, (Balkema, Rotterdam, 1997).
3. Varden, R., Lachenicht, R., Player, J., Thompson, A. and Villaescusa, E. Development and Implementation of the Garford Dynamic Bolt at Kanowna Belle Mine. The AusIMM 10th Underground Operators Conference, (Launceston, Tasmania, 2008).
4. Varden, R. Implementation of the Garford Dynamic bolt at Kanowna Belle Mine. The 7th International Symposium on Rockburst and Seismicity in Mines, (Dalian, China. 2009).

ROCK MASS STRENGTH AND SEISMICITY DURING CAVING PROPAGATION AT THE EL TENIENTE MINE, CHILE

ANDRES BRZOVIC

Superintendence Geology, CODELCO CHILE El Teniente Division

Millan 1040, Rancagua, Chile

Rock masses of primary copper ore at the El Teniente mine have been described as very competent and massive during caving operations. Underground mining operations have been accompanied with intense induced seismicity, and severe seismic failures have been experienced in past years during caving propagation. Major factors causing seismicity have been analysed through back analysis studies undertaken at the Esmeralda mine sector during caving initiation and propagation. These studies included, rock structure characterization, data analysis of the recorded seismicity and the production records, and numerical modelling to assess the state of the stress in three different mine sectors. Mining parameters such as the extraction rate that influence caving propagation, were found to be similar between the studied sectors, however, the recorded seismicity of completely caved rock masses of similar volumes were found to be very different from each other. The numerical model results indicated that the stress path in a rock type from one particular sector during caving propagation moved in a direction where severe seismicity should be expected, however the recorded seismicity was benign compared to the observed seismicity in other studied sectors. This rock mass response is only possible for a rock mass with low strength, which can be described through the application of a novel definition of weak discontinuities. The results agree with the concept that the low rock mass strength correlates with the abundance of weak discontinuities, and therefore these rock mass features that to be considered in any kind of seismic risk analysis at the mine site.

1 Introduction

Mining activities, such as block caving, disturb the near stress field within the rock mass surrounding the excavations (cave). This may result in stress levels exceeding the rock mass strength. If this is the case, rock failure may occur and the potential energy accumulated in the rock mass may be released (unloaded) gradually or suddenly. The rock failure may occur through the intact rock material (fracturing) or through a pre-existing discontinuity (slip). A mining induced seismic event corresponds to the radiated energy during a sudden rock mass failure. In general, the characteristic of the induced seismic event will depend of the strength of the rock mass, the state of stress, the size of the source of the seismic radiation, and on the rate at which the rock mass is deformed during rock mass failure [1].

The El Teniente mine is the largest underground mine in the world located in central Chile. The mine has been operating since 1906 and is currently mining of around 140,000 tonnes per day (tpd) using block caving methods. Rock masses of primary copper ore at the El Teniente mine have been described as very competent and massive during caving operation. This is because caving performance has been typified by larger than expected fragmentation, and the rock mass has exhibited brittle, often violent failure under a high stress conditions [2,3,4]. Severe seismic failures have compromised the safety of underground operators and caused delay in mine development and production. It is currently believed that induced seismicity during caving operation *'has more relation to the rock mass characteristics (competence) rather than other factors'* [5]. In fact, a massive hydraulic fracturing experiment has been undertaken within particular El Teniente mine sectors to facilitate caving propagation. This is expected to result in a more controlled dissipation of energy (seismicity) as the rock mass strength properties will have been modified [5].

Rock mass strength has been historically assessed through the application of rock mass classification schemes. For a jointed rock, its strength can be correlated to the degree of rock mass fracturing. The “competent” and “massive” rock mass of the primary copper ore at the El Teniente mine is a rock with almost no joints (open *discontinuities* according to the International Society of Rock Mechanics [6]). However, there is a high frequency network of small scale veins (cemented-healed joints) coupled with widely spaced faults. Recently studies have found an empirical criterion to define *weak discontinuities* from such rock masses [7]. These weak discontinuities represent the weak path where the competent rock mass can fail during the fragmentation process. It is believed that the rock mass strength of the primary copper ore can be correlated with the abundance of these weak discontinuities, and therefore, these are important factors in the seismic response during caving propagation.

A back analysis study was undertaken at the Esmeralda mine sector within the El Teniente mine to investigate the importance of these weak discontinuities relating to the rock mass strength and the induced seismicity. The main studies included; new rock structure characterization and structural data analysis, data analysis of the recorded seismicity and the production records, and numerical modelling to assess the state of the stress prior and during caving propagation. This paper presents the result of this study and discusses its implication on seismic risk assessment to the new mine level project which will be located around 320m deeper than the existing Esmeralda undercut level within the ore body.

2 The El Teniente Overview

The El Teniente mine is a Codelco-Chile underground copper mine. It is located in the Andes Mountains in the central zone of Chile, about 70 km South-Southeast from the capital city, Santiago (Figure 1). Since 1906 more than 1100 million tons of ore have been mined using block caving methods. Panel and pre-undercut caving methods, variations of the conventional block caving, were introduced in 1982 and 1994 respectively to exploit primary copper ore. Taking advantage of gravity, block caving recovers the disassembled ore in regular ‘block’ areas. At the same time panel caving develops a continuous front cave, which sometimes can be 600m long [5]. Pre-undercut caving mainly differs from panel caving, called conventional according to [8], because the undercut level (ucl) is developed ahead of all development below the undercut levels (Figure 2).

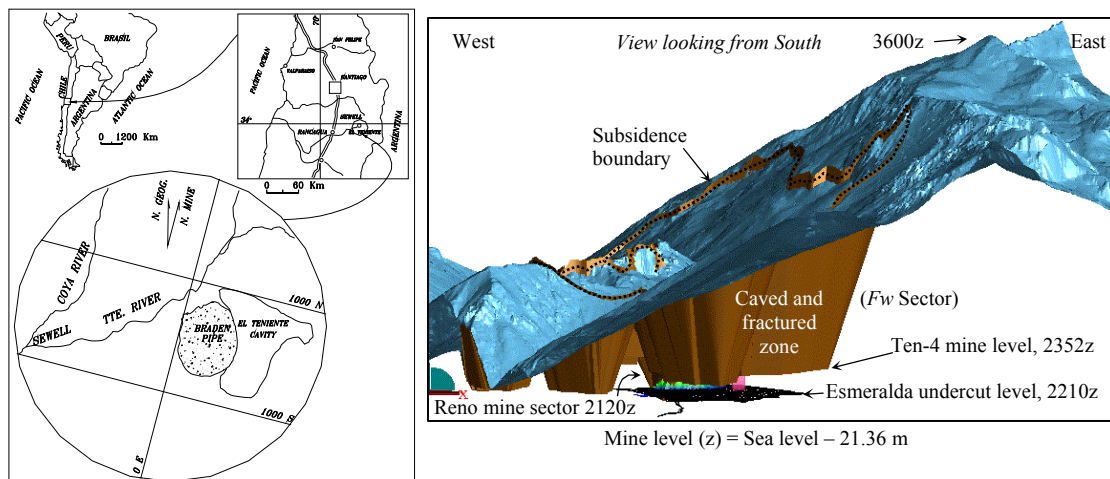


Figure 1 Location of the El Teniente mine and isometric view showing the highly variable topography of the andes mountains.

El Teniente is the largest known copper-molybdenum deposit in the world; main rock types include Mafic (gabbros, diabases and other called *Cmet*) and Felsic (dacite and tonalite-diorite porphyries) intrusives, and

hydrothermal breccias of the Miocene era [9]. Two main structure types are observed within the primary copper ore; a system of large-scale faults and a stockwork having a high frequency of small-scale vein features [7]. Veins are mainly cemented with quartz, sulphides and anhydrite. The stockwork veins containing the original mineralogy are healed. Different vein types have been identified, and these define alterations zones according to their local abundance.

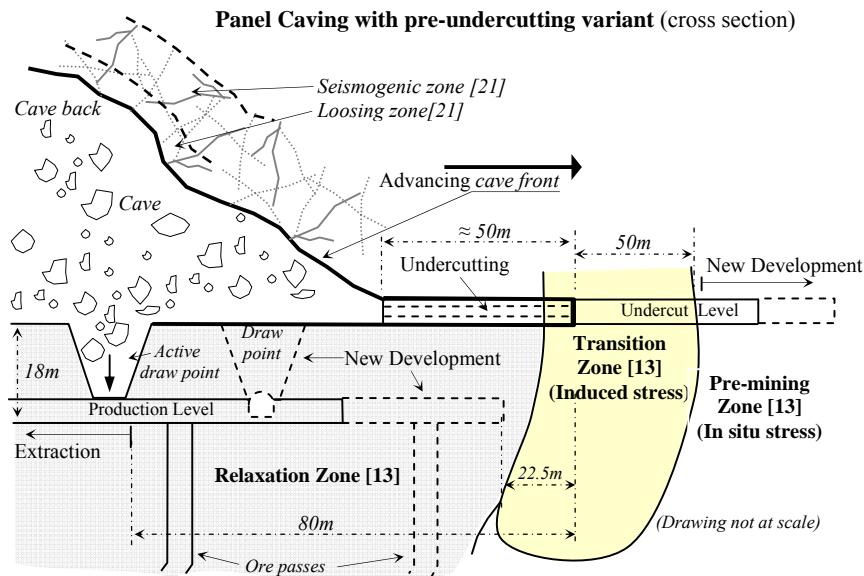


Figure 2 Pre-undercut caving method variant applied at the Esmeralda mine sector (modified from [4]).

These geological features agree with its observed “competent” and “massive” behaviour. However, caving has been achieved in such rock masses with a small hydraulic radius of around 25m at both the Esmeralda mine sector [8] and Reno mine sector (former Ten Sub-6) during its experimental operation [4]. These two caving experiences seem to be contrary to the description of a competent and massive rock mass considering that rock masses of secondary ore, which are heavily fractured, have achieved caving with a hydraulic radius of 22m. Intact rock properties based on hundreds of laboratory test and rating of main rock mass classification system used in current mine planning for main rock types are presented in Table 1.

Table 1. Intact rock properties and rock mass quality rating per main rock types at the El Teniente mine

Rock type	Intact rock properties				Rock mass rating		
	Density (tonnes/m ³)	E (GPa)	ν	UCS (MPa)	IRMR	Q'	GSI
Braden breccias	2.61	21	0.19	70	—	—	—
Dacite	2.63	30	0.18	90	59–66	22–32	75–95
Diorite	2.77	45	0.21	140	64	19	75–90
Cmet	2.77	56	0.20	115	53–59	19–22	70–85

Notes: E; Young’s modulus, ν ; Poisson’s ratio, IRMR [10], Q' (without J_w/SRF quotient) adapted from [11], and the geological strength index (GSI) [12].

2.1 The Esmeralda Mine Sector

The Esmeralda mine sector introduced the pre-undercutting caving method at the El Teniente mine. This mine sector included a production plan of 350Mtons of ore with 1% of Cu and a life span of over 35 years. The

undercutting was initiated in October 1996, and caving initiation started one year later triggered by ore drawing at the production level. The breakthrough to upper mine level was estimated to occur between April and May 1999, when the hydraulic radius reached a value of 25m. The effective mined area, defined by active draw points or *Active Footprint*, at this time was 16,800m² [13]. This mine sector is located in the central part of the El Teniente ore body, at the Eastern side of the Braden Pipe. Caving initiation was located only 100 meters below the old Teniente 4 South mine level to reduce the seismic risk level (see Figure 1).

Main geological features within the area of interest are; two main rock types, *Cmet* and diorite porphyry (just diorite here); two hydrothermal alteration zones, late (*LH*) and principal (*PH*); one mayor fault system named Fault B [14]. The hydrothermal alteration zones coincide with the principal orientation reference at the mine such as the hangingwall (*Hw*) and the footwall (*Fw*) sectors (Figure 3). Evidence of seismicity at the Esmeralda mine sector started after the undercutting initiation [3]. Until 2005 more than 150,000 events have been processed by the mine wide microseismic system monitoring in that mine sector. Seismicity due to blasting has not been included in this number.

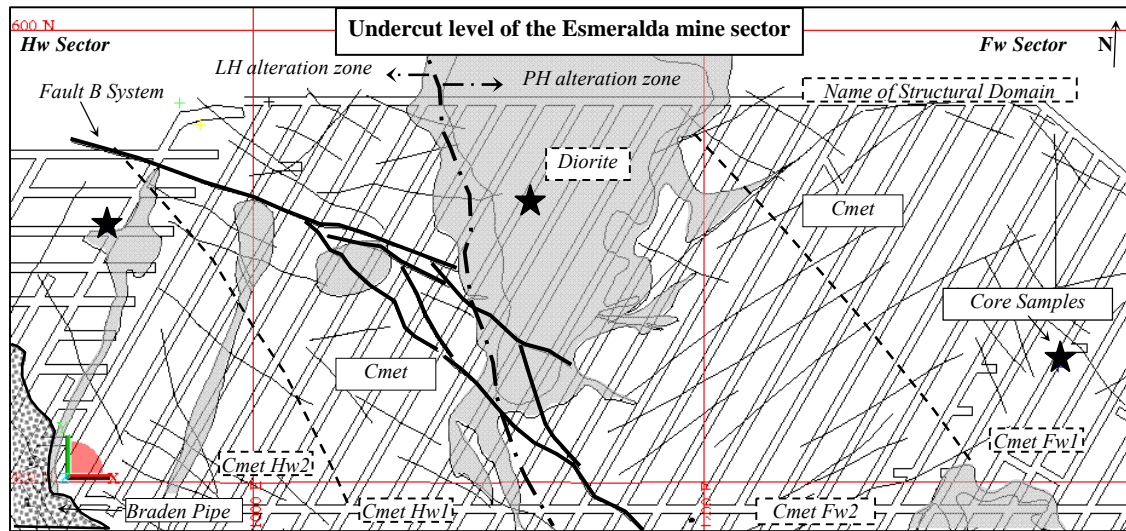


Figure 3 Main geological features and structural domain definition (within dashed lines) at the Esmeralda mine sector (adapted from [14]).

3 Back Analysis Studies

3.1 Rock Structure Characterization

The characterisation of rock structure was undertaken mainly considering two mapping scales; data collected from drive mapping to account for large scale structures, and large diameter oriented core logging to account for small scale structures. Drive mapping and oriented core logging used a truncation bias length ≥ 4.0 and 0.1 meters long respectively. Different structural domains (Figure 3) of this mine sector were characterised using the same methodology, which is described in detail in [7]. Only three large diameter oriented cores were available for data collection within this mine sector (denoted by black stars in Figure 3), and only horizontal sampling directions were used during drive mapping, then orientation bias in the structural analysis is expected.

To evaluate the impact of orientation bias, additional structural data were reviewed. These included old data collected using scanlines placed in three semi-orthogonal sampling directions in mine drives of the mine sector, and new fault data collected using three 100m long, small diameter oriented core, drilled in three orthogonal sampling directions [15].

Similar to what has been found in other mine sectors, veins comprise at least three semi-orthogonal set orientations each having high frequency [7], whereas up to two sets of widely spaced sub-vertical faults having spacing in excess of 5m have been found (Figure 4, 5 and Table 2). Figure 4 shows the principal orientations of veins that were collected using scanlines placed in *Cmet* rock type from the *Fw* sector. Sub-vertical fault orientations observed in Figure 4 are in agreement with the strike-slip faults' characteristics described at the mine scale [16] and with the fact that no sub-horizontal faults were observed in the small diameter sub-vertical oriented cores located below the *Fw* sector in the area of study [15].

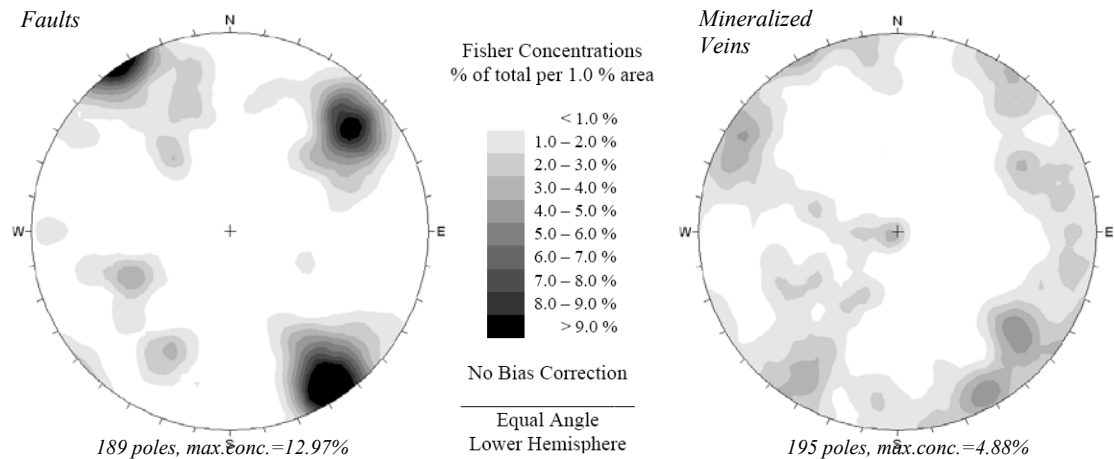


Figure 4 Stereographic projection of faults and mineralized veins recognized at the Esmeralda mine sector

The structural analysis of veins presented in Table 2 and Figure 5 considered the novel definition of weak discontinuities [7], i.e., only weak veins were included to the spacing determinations. Figure 5 shows the result of a stochastic simulation of the rock structure base on data collected using large diameter oriented core. In this case, only thicker weak veins (thickness $\geq 2\text{mm}$) were included in the simulation [17,18]. The software program used, assumed a Fisher distribution for orientation, negative exponential distribution for spacing and infinite trace length for discontinuity size.

Table 2. Normal set spacing of weak veins and faults observed in mine drives (drive mapping) per structural domain [17,18].

Discontinuity type	Dip/Dipdir**	Mean of the normal set spacing (m)				
		<i>Cmet Hw2</i>	<i>Cmet Hw1</i>	<i>Diorite</i>	<i>Cmet Fw2</i>	<i>Cmet Fw1</i>
Weak Veins	90/316	7.4*	5.2	5.8	3.2	5.3
	80/232	8.6†	9.3		9.5	5.3
	75/029	5.8	7.6	6.0		8.1
	49/191		9.9‡	9.0		6.8†
Faults	89/143		7.2‡	5.5‡	6.7†	8.0
	86/035	8.7*	8.8	5.2†		8.8

Notes: **, approximate orientation. The spacing values were obtained from less than 40(†), 20(*), and 10 (‡) spacing data, respectively.

Figure 5 shows the in situ block size distributions defined by weak veins, which also indicates the abundance of weak veins ("fracturing") per unit type. There is more abundance of weak discontinuities in rock from *Cmet Fw* than other rock types and sector. Therefore, data suggest that rock masses of primary copper ore at the El Teniente mine consist of an assemblage of blocks mainly bounded by veins of different strength and widely spaced sub-vertical fault contacts. This rock mass concept agrees with which has been observed in caved rock blocks from production level draw points [7], i.e., rock mass disassembly during caving and fragmentation progress occurred through all these weak discontinuities (faults and weak veins).

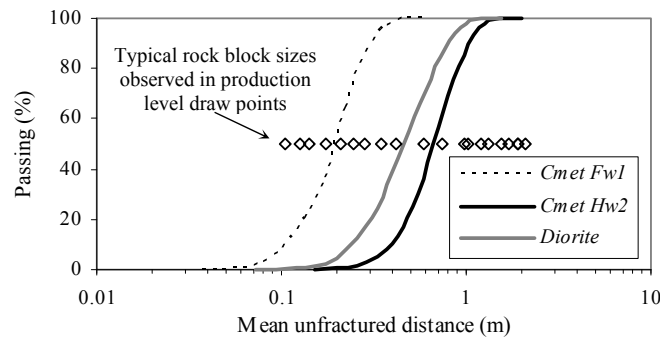


Figure 5 In situ rock block distributions per unit type based on large diameter oriented core data.

Weak veins can be correlated with the late alteration stages during ore formation, which are more related to the diorite intrusions. Therefore, and based on geological model interpretation, it is expected to find more abundance of weaker veins within *Cmet* rock type surrounding diorite intrusions and less abundance of weaker veins far away from them, and close to the breccia Braden (*Hw* sector).

3.2 Mine Production and Control of the Induced Seismicity

Various rules, based on mining activities, have been established to control induced seismicity at the El Teniente mine [2,3,4,19]. Mining parameters such as the undercutting advance rate (increment of the hydraulic radius) and the extraction rates (draw) modify the size and geometry of the cave, which control induced stresses that cause induced seismicity. Therefore, management the induced seismicity can be based on controlling the rate of these mining parameters, as used at the Esmeralda mine sector [4,8].

One of the main concepts gained through Esmeralda's experience is the "30% of the column height extraction" (applied only to primary copper ore). It has been observed, particularly in this mine sector during caving propagation (1998-9), that for 1 meter high of ore extraction at the production level draw points, the broken rock mass in the caveback grew up to 3 meter high, therefore the caveback may breakthrough (reach the top of extracted rock column) after the ore extraction reach 30% of the column height. It is expected that most of the induced seismicity occurs before the ore extraction reaches this 30% of the primary ore column height, therefore, extraction rate is only constrained to this column height [4,8].

Three similar rock volumes within Esmeralda mine sector were studied through the present back analysis. These represent three rock/unit types; *Cmet Hw(1)*, *Diorite*, and *Cmet Fw(1-2)* as shown Figure 6 (grey colour areas). Figure 6 also shows the area delimited by the 30% of the column high extraction by year (extraction front), including when breakthrough occurred. Most of the areas of *Cmet Hw* and *Diorite* unit types were extracted before Dec-1999, and *Cmet Fw* before Dec-2001. The same figure includes the undercutting area affecting these studied sectors. Again, most of the areas of the column base of *Cmet Hw* and *Diorite* unit types were completely cut before Dec-1998, and *Cmet Fw* before Dec-1999. The extraction rates in these three studied volumes in terms of cumulative tonnes extracted per month is shown in Figure 7. As it could be expected, due to the draw strategies, the three sectors were practically exploited at the same extraction rate.

3.3 Mine Seismicity

The characteristics of the seismic monitoring system used to record the seismicity at the El Teniente mine and particularly to the Esmeralda mine sector has been described in *RaMiS5* [3]. It is necessary to mention that some seismic error location ($\approx 40\text{m}$?) may be expected, as the velocity model used at the mine site does not

considered the void produced by caving. In other words, the velocity model assumes straight ray path whereas seismic wave travel around the cave. Moment tensor estimates using the inversion procedure with the JMTS-ISS software package at the mine site are less affected by error location according to the assessment undertaken by ISS Limited [20].

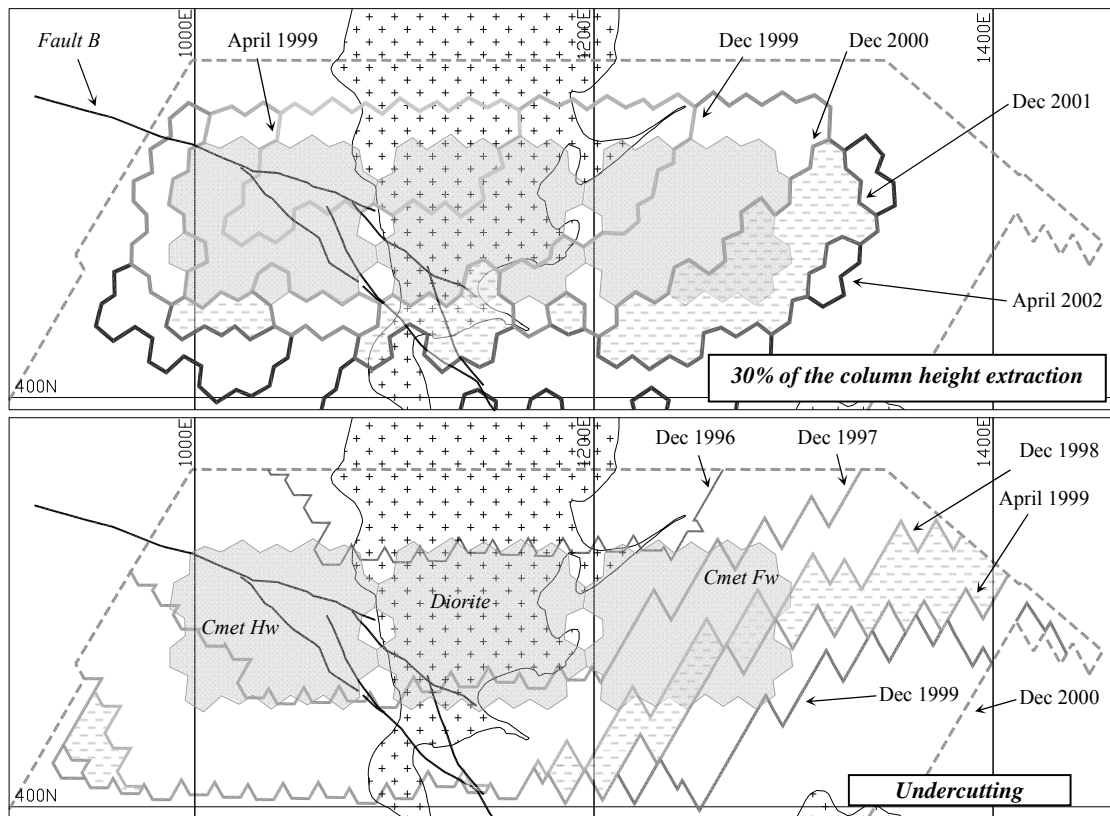


Figure 6 Studied areas at the Esmeralda mine sector showing the extraction front (30% of primary ore column height) and the undercutting by years.

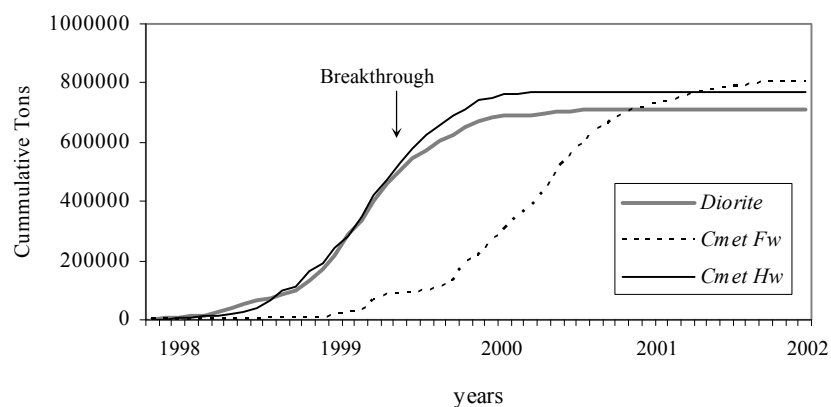


Figure 7 Cumulative production (tonnes) for different mine sector considering up to 30% of primary ore column high.

The whole seismicity recorded within the three studied rock volumes between 1996 and 2003 is presented in Figure 8. Each volume encompasses its own area shown in Figure 6, and its column height goes from 2210m(z) to 2250m(z). Three important increments of seismic intensity are shown this figure; the first one was during caving initiation, the second one correlated when the caveback reached (breakthrough) the broken rock located in the Ten-4 upper level (see also Figure 1), and the last one was during 2001. During breakthrough, undercutting had taken place in most of the area including the three studied sectors. The remaining induced seismicity occurred after breakthrough, which maybe interpreted to correlate to both the advancing cave and extraction front. The last increase of seismic activity which occurred during 2001 and beginning of 2002 is discussed later. Nevertheless, it is considered that this seismicity is related to the continue movement of extraction front outside of studied sectors (see Figure 6).

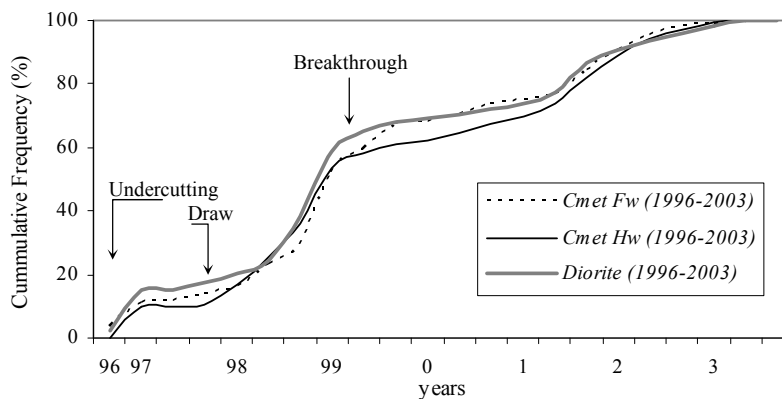


Figure 8 Proportion of the cumulative seismicity recorded in Esmeralda mine sector per each location.

Since the rock mass encompassed in each of the studied volume was completely caved (failed), it could be expected, that the whole seismicity recorded was the result of two main factors; the rock mass strength (rock structure features) and the stated of stress (stress path) during caving propagation [1]. It has been shown that the extraction rate was similar in each sector (Figure 7), i.e., the average mining activities were undertaken in a similar fashion.

The seismicity recorded within each sector of *Cmet* rock type, and the Gutenberg -Richter curve for each studied rock volume are illustrated in Figure 9. The Gutenberg -Richter curves show that the system sensitivity (Mw_{min}) is the same in each of the studied sector within Esmeralda mine sector. This plot also shows that *Cmet* rock masses of the *Fw* sector have recorded considerably fewer seismic events and lower local magnitude than other unit types. It seems to be that *Cmet* rock masses of the *Fw* sector tend to fail more in an aseismic way.

The apparent volume of the recorded seismicity throughout caving propagation within each rock volume is shown in Figure 10. A first jump in the cumulative apparent volume correlates with the breakthrough (early 1999), which is also very different between units types. This agrees with the large number of events observed in diorite and *Cmet Hw* units types. A possible interpretation is that the major stiffness of these two rock types (inferred from Figure 5) led to store more potential energy, which is released through more large seismic events. The second clear jump in this figure occurred during early 2001 in rock masses of *Cmet Fw* sector, and during middle 2001 in diorite and *Cmet Hw* units types. Although, this is not longer interpreted here, this agrees with Figure 8. However, it is very clear from Figure 10, that considerably less apparent volume was observed in the *Cmet Fw* unit when the complete rock mass was caved.

A special data collection for the present back analysis was designed to obtain moment tensor estimates using the inversion procedure with the JMTS-ISS software package at the mine site. Seismic events contained

within a selected rock volume of 50m length x 80m width x 60m high located at north of Esmeralda cave and completely encompassed by diorite rock type were studied. Only seismic events occurring between February and April 1999 were analysed. This mine section can be represented as a seismogenic zone [21] located very close to the caveback during caving propagation prior breakthrough [detailed in 17]. In terms of calculation, estimates included re-picking of S and P wave arrivals, rejecting waveform data with either unclear arrival phases or large gaps, and selecting data where wave forms from at least 8 sensors were available were used to obtain stable focal plane solutions in each case [22].

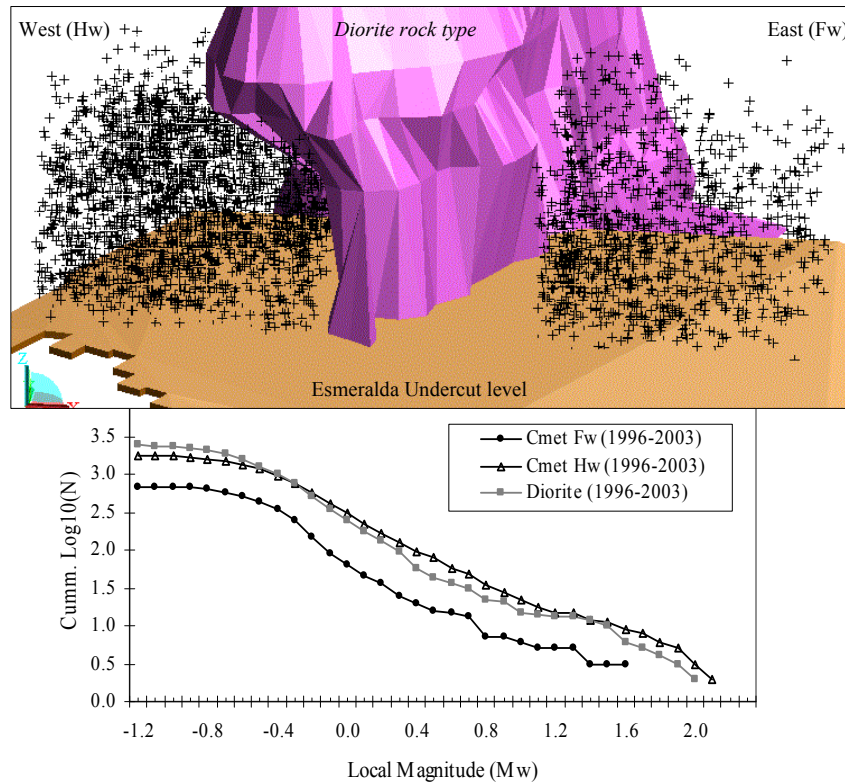


Figure 9 Isometric view of Esmeralda mine sector showing the recorded seismicity within *Cmet* rock type (above). Gutenberg-Richter curve for each studied unit type (below).

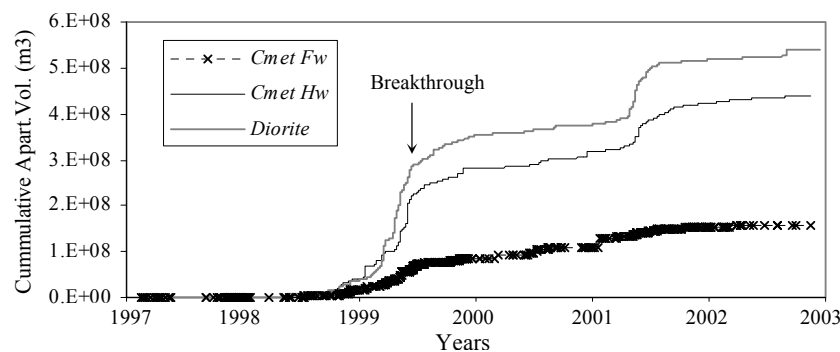


Figure 10 Cumulative apparent volume recorded per each mine sector studied.

Only 67 seismic events having lower location residual ($R \leq 20$) were studied. Based on the direction of the motion given by the slip vector in fault plane, around half of these seismic events can be considered to have inverse-strike slip mechanism (upper side of the fault moves in upward direction). The other half can be considered to have normal -strike slip mechanism. If the calculation and assumptions involved in these results can be considered correct, the damage orientation that occurred for small mine section during a short time (3 months) do not follow a unique and clear trend.

In addition, the 134 pairs of focal plane solutions obtained were compared against fault orientation data from the same area (Figure 11). Assuming that sampling bias against sub-horizontal discontinuities is not significant (as discussed earlier), this information can be used to assess whether every pair of plane solutions is likely to be a fault or another discontinuity such as weak veins. The stereographic projection shows that mostly steeply-dipping faults collected in mine drives are present in this structural domain (Figure 11a). If most of the seismic events occurred due to slip on pre-existing discontinuities as found by [7], therefore, for orientations where no faults have been identified, slipping is likely to correspond to weak veins as shown Figure 11b. In this figure, squares represent the cases where either one or both plane solutions are assigned as being a fault, with the black asterisks represent the case when the second plane solution is assessed as being a vein (with less probability to fail due its harder infill). Finally, black dots represent the case where neither of both plane solutions can be assigned as being a fault, i.e., these solutions can be assigned as being weak veins. This interpretation is plausible since veins observed within the rock mass have been found comprising at least 3 semi-orthogonal directions. The results of this analysis infers that rock masses of primary copper ore offer multiple options to accommodate strain caused by stress redistribution. However, it seems that the more abundant the options (i.e., more fault and weak veins), the less likely potential energy will be stored in the rock mass, and therefore be available to be released as seismic events.

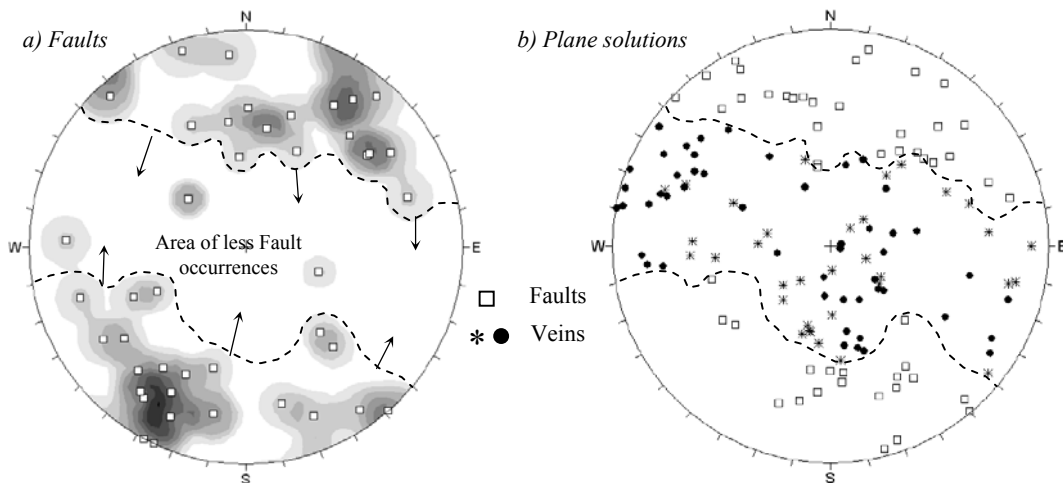


Figure 11 Fault orientations and focal plane solutions observed within *Diorite* structural domain

3.4 Numerical Modeling

One of the purposes to model the Esmeralda caving process from initiation to breakthrough was to assess the state of stress in the rock mass surrounding excavations. The modelling package used for this work was Abaqus Explicit. The entire mine history was simulate in more than 80 mine steps, from prior 1917 to recently past in 2002. 13 mine steps were used between 1998 and 1999. Mohr-Coulomb yield criteria were used to best match the yield criteria developed in previous analyses at the mine. The constitutive model in both cases is a strain softening, dilatants material model [17,18]

Only three rock types were included in the model; breccia Braden, Diorite and *Cmet*, in the model *Cmet* is assumed as being similar mine wide. The model did not include any mine drives of any mine level, only cave geometries were included. The model calibration was only based on a methodology that correlates the dissipated plastic energy (Joule/m³) and an observed seismic event probability [described in 23]. In terms of the state of stress in the rock mass, the results of this particular model agrees with the state of the stress currently used by mining planning at the mine site [24].

Several points in the model, as shown in Figure 12 were used to assess the state of the stress in the rock mass during caving propagation. These points represent different location and heights within the three volumes studied. The back analysis results are presented in Figure 13.

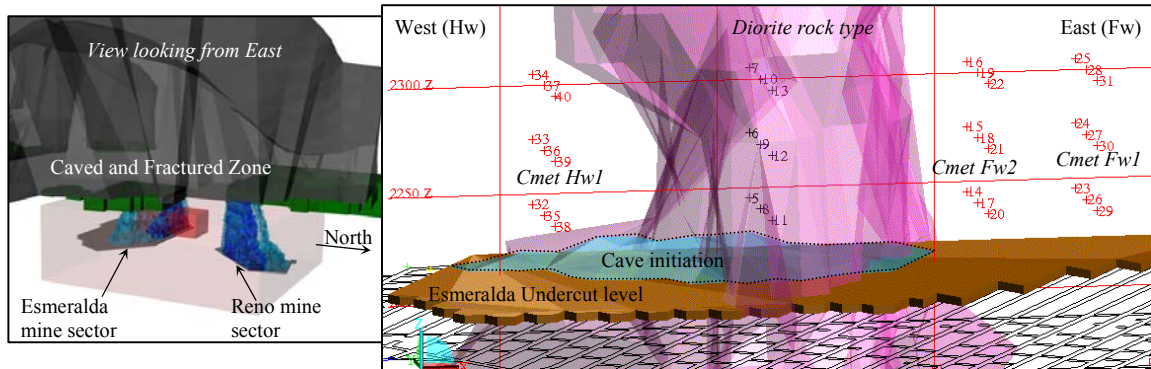


Figure 12 Isometric view of the geometric model for simulation (left) and point locations within the model for stress path analysis per structural domain (right).

The initial state of stress at each structural domain within the three volume studied is shown as circles in Figure 13. It shows that higher initial stress level predominates at the *Fw* sector, which agrees with the major overburden observed in this place (see Figure 1). The stress level before the rock mass reaches the peak strength move (black arrow in this figure) toward the confinement reduction in the *Hw* sector (diorite and *Cmet Hw2*), whereas at the *Fw* sector (*Cmet Fw1-2*) it moves not only toward the confinement reduction, but also toward high confining pressure levels. Increasing σ_1 at constant high σ_3 level may result in high stress release, i.e., a large seismic event may occurs.

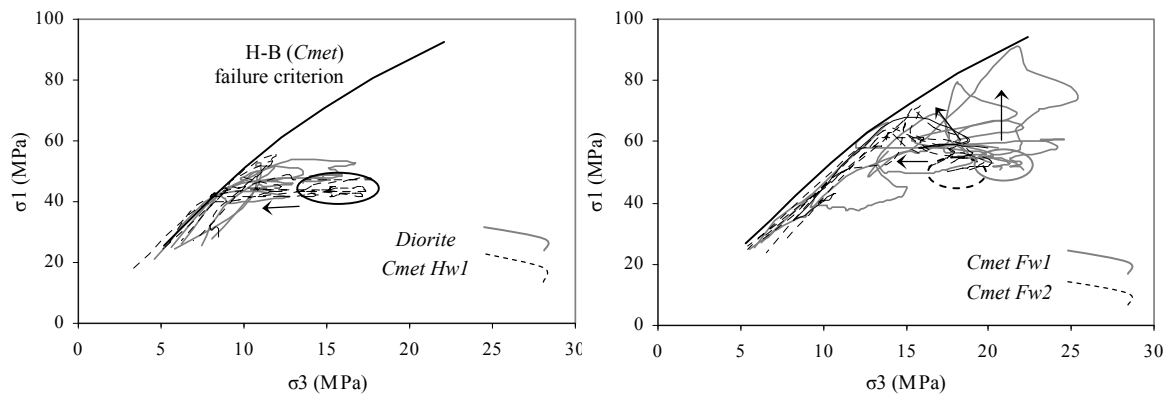


Figure 13 Stress paths (lines and arrows) at different structural domains as the result of cave geometries during caving propagation at the Esmeralda mine sector. Small circles indicate initial state of stresses.

4 Discussion

The present work attempts to demonstrate the relationship between rock mass strength and seismicity at the El Teniente mine, which is undertaken through the back analysis studies of the Esmeralda caving experience occurred between 1997 and 2002.

The back analysis studies relating to the rock mass characterization indicates that the rock structure in the Esmeralda mine differ between sectors and rock types. There is one major fault system (fault B), which is only present in the *Cmet Hw1* unit type. Considering to the large scale observations in *Cmet* rock type, there is more appreciable differences between nearby structural domains (*Hw1- Hw2* or *Fw1- Fw2*) than between major *Hw* or *Fw* sectors. For example, there is more faulting (and large scale weak veins as well) in *Cmet Fw1* than in *Cmet Fw2*, but it looks the same between *Cmet Hw1* and *Cmet Fw1* (Table 2). Considering the small scale observation, the differences are substantially clearer between rock/unit types when the infill strength of discontinuities is taken into account (Figure 5). It is important to note that existing rock mass classification systems fail to discriminate differences between sectors/units as shown Table 1.

It has been shown that the three sectors studied were mined out at a very similar rate, consequently, this factor can be disregarded as an important contribution to explain the differences on the recorded seismicity between them. However, it is also necessary to mention that the relationships between drawing and cave propagation (caveback grows up 3m for 1m of draw) has been well validated only in rock masses of *Cmet Hw1* structural domain [25], and major fault B could have been played a relevant role in that process. This rule is considered relevant to cave propagation in upward direction, however no rules have been established with regard to advancing front direction (see Figure 2). In addition, although drawing is necessary for caving propagation (i.e., allowing space for the broken rock), it is not guaranteed that caving will propagate after drawing (e.g. air-gaps), other factors regarding to the rock structure and state of stress need to be considered in this phenomenon. It is very clear that more research is needed to understand this important mine parameter used widely in mining planning.

The recorded seismicity was completely different between the studied unit types, particularity between *Cmet* rock masses from *Hw* and *Fw* sector. These observed differences (seismic intensity and magnitude) have been also observed through several years in this mine sector (2002-2007), but under different cave geometries [26], which confirm that the features of the rock structure are a relevant factor in the seismicity at the El Teniente mine.

The cave geometry is one of the key factors that control induced stress. The relationships between drawing and cave propagation have been used to build the cave geometry in the model. Assuming that a rock mass with more abundant weak discontinuities has less strength, the cave should have propagated faster in *Cmet* rock masses of *Fw* sector. If this is the case, the cave geometry could have been different to what was used in model for the *Fw* sector. Although, this has not been properly evaluated (run a different cave geometry in the model), this seems to be less relevant in the model result because the general geometry and shape of the cave will change only slightly.

The model results shown in Figure 13 indicate that the stress path in *Cmet* rock masses of *Fw* sector goes in a direction where a severe seismicity should be expected in comparison to the rock masses of the *Hw* sectors. Since all mine sectors were stimulated by draw in a similar way, only the rock mass strength appears to be the most important factor that explain such differences in the recorded seismic intensity (as also stated [5]). Considering the features of rock structure at different scales, this back analysis strongly suggests that not only large scale faults, but also the small scale weaker veins accommodate strain when the rock mass is loaded, and therefore all these structures play a major role is the seismicity at the El Teniente mine. It can also be inferred that when there is a less abundance of small scale weak veins (usually in the *Hw* sector of Esmeralda and Reno

mine sector), the rock mass not only tends to store more potential energy (allowing major seismic event to occurs), but also constrains caving propagation.

In this respect, the third increase in seismic activity shown in Figure 8, together with the second one (apparent volume) in Figure 10, maybe correlated with the advancing extraction front under a constrained caving propagation. In other words, more column height extraction would be needed for a rock mass with less abundance of weak discontinuities to the caveback to reach the top of the extracted ore column.

Therefore, this back analysis strongly suggests that any seismic risk analysis undertaken at the mine site should incorporate a proper geotechnical characterization that accounts for the occurrence of the large scale faults and of the small scale network of weak veins.

5 Conclusions

Major factors causing seismicity have been analysed through the back analysis studies of the Esmeralda caving experience between 1997 and 2002. These studies included; rock structure characterization, data analysis of the recorded seismicity and the production records, and numerical modelling to assess the state of the stress during caving propagation.

The structural data collected at different mapping scales suggest that rock masses of primary copper ore at the El Teniente mine consist of an assemblage of blocks mainly bounded by veins of different strength and widely spaced sub-vertical fault contacts. Geotechnical units can be clearly distinguished by the application of a novel definition of weak discontinuities, which are not included in traditional rock mass classification systems. Data also suggest that under certain stress conditions, the rock mass fails along both the large scale faults and the small scale weak veins.

Mining parameters such as the extraction rate, which help caving propagation, were found to be similar between three studied sectors. However, the recorded seismicity was found very different between the same three studied sectors.

The stress paths followed by the rock masses within the three sectors studied during caving propagation were obtained through the numerical model. The model results indicated that the stress path in rock masses of *Fw* sector generally proceeded in a direction where severe seismicity should be expected, however the recorded seismicity was benign compared to the other studied sectors. This rock mass response is only possible for a rock mass with low strength. These results agree with the concept that the rock mass strength correlates with the abundance of weak discontinuities; therefore these particular rock structure features are an important factor to understand and to predict the seismic response during caving propagation at the El Teniente mine.

Acknowledgements

The author wish to acknowledge the financial support and permission to publish this paper by the Western Australia School of Mines (WASM) and the Teniente Division (CODELCO). Special thank to Professor Ernesto Villaescusa for his encouragement to continue this research to PhD degree.

References

1. Mendecki, A.J. Seismic Monitoring in Mines. London, Chapman & Hall, 1997.
2. Dunlop, R. and Gaete, S. Controlling Induced Seismicity at the El Teniente Mine: the Sub-6 case history. In Gibowicz, S.J. Lasoki, S., eds. Proceeding of *RaSiM4* conference, (Krakow, 1997).
3. Dunlop, R. and Gaete, S. Induced Seismicity at the El Teniente Mine: the Esmeralda Sector Case History. In Van Aswegen, G., Durrheim, R.J., Ortlepp, W., eds. Proceeding of *RaSiM5* conference, (Johannesburg, 2001).
4. Rojas, E., Cavieres, P., Dunlop, R. and Gaete, S. Control of Induced Seismicity at El Teniente Mine, Codelco Chile. In Chitombo, G., ed. Proceeding *Massmin 2000*, AusIMM, (Brisbane, 2000).

5. Araneda, O. and Sougarret, A. Keynotes Address: Lessons Learned in Cave Mining, El Teniente 1997-2007. In Stacy, T.R. ed. Proceeding *Cave Mining* conference, SAIMM, (Cape Town 2007).
6. Brown, E.T. Rock Characterization Testing and Monitoring, Suggested Methods. London, ISRM, 1981.
7. Brzovic, A. and Villaescusa, E. Rock Mass Characterization and Assessment of Block-Forming Geological Discontinuities during Caving of Primary Copper Ore at the El Teniente mine, Chile. *Int. J. Rock Mech. Min. Sci. and Geomech., Abstr.*, 2007, 44(4). 565-583.
8. Rojas, E., Molina, R. Bonani, A. and Constanzo, H. The Pre-Undercut Caving Method at El Teniente Mine, Codelco Chile. In Chitombo, G., ed. Proceeding *Massmin 2000*, AusIMM, (Brisbane, 2000).
9. Skewes, M.A., Arevalo, A., Floody R., Zuniga, P. and Stern, C.R. The El Teniente Megabreccia Deposit, the World'S Largest Deposit, Super Porphyry Copper & Gold Deposit – a Global Perspective. In Porter, T.M. ed. PCG Publishing, (Adelaide 2005).
10. Laubscher, D. and Jakubec, J. The MRMR Rock Mass Classification System for Jointed Rock Masses. In Hustrulid W.A., Bullock R., ed. Proceeding *Underground Mining Methods: Engineering Fundamental and International Case Studies*. SME, (Colorado 2001).
11. Barton, N., Lien, R. and Lunde, J. Engineering Classification of Rock Masses for the Design of Tunnel Support. *Rock Mech*, 1974, 6(4).189-236.
12. Hoek, E., Kaiser, P.,K. and Dawden, W.F. Support of Underground Excavations in Hard Rock, 1995.
13. Rojas, E., Molina, R. and Cavieres, P. The Pre-Undercut Caving in El Teniente Mine, Chile. In Hustrulid W.A., Bullock R., ed. Proceeding *Underground Mining Methods: Engineering fundamental and International Case Studies*. SME, (Colorado 2001).
14. Seguel, J. Antecedentes Geologicosy Geotecnicos Alnorte XC-3 ucl Esmeralda. The El Teniente Division, Internal Report SGL-I-050.
15. New Mine Level Project. Data Base of the Oriented Core Logging (triada). The El Teniente Division.
16. Garrido, I., Riveros, M., Cladouhos, T., Espineira, D. And Allmendinger, R. Modelo Geologico Estructural Yacimiento El Teniente. Proceeding *VII Congreso Geologico Chileno*, SGC, 1994, 2. 1553-1558.
17. Brzovic, A. Characterization of Primary Copper Ore for Caving at the El Teniente Mine, Chile, PhD thesis (under examination). Western Australia School of Mines, 2008.
18. Dunlop, R. and Gaete, S. An Estimation of the Induced Seismicity Related to a Caving Method. In Van Aswegen, G., Durrheim, R.J., Ortlepp, W., eds. Proceeding of *RaSiM5* Conference, S.Afr.Inst.Min&Met, (Johannesburg, 2001).
19. ISS. Seismological back analysis of large events at Reservas Norte, El Teniente. ISS International Limited, The El Teniente Division, 223.
20. Duplancic, P. and Brady, B.H. Characterization of Caving Mechanics Through Analysis of Seismicity and Rock Stress. In Vouille, G., Berest, P., eds. Proceeding 5th Int. Congress on Rock Mechanics, (Paris, 1999).
21. Brzovic, A., Villaescusa, E. and Beck, D. Rock Mass Disassembly during Caving Propagation at the El Teniente Mine, Chile. In Schunnesson, H., Nordlund, E., eds. Proceedings *Mass Mining 2008*. University of Lulea, (Lulea 2008).
22. Belmonte, A. Excel Data Base with Moment Tensor Estimates from Esmeralda Mine Sector. The El Teniente Division.
23. Beck, D., Reusch, F., Arndt, I., Thin, I., Stone, C., Heap, M. and Tyler, D. Numerical Modelling of Seismogenic Development during Caving Initiation, Propagation and Breakthrough. In Hadjigeorgiou, J., Grenon, M., eds. *Deep and High Stress Mining*. Laval University, (Quebec 2006).
24. Pardo, C. Comparison between Map3D and Abaqus Numerical Models in Pillar Norte Mine Project, Personal Communication. 2007.
25. Parraguez, R., Campos, M. Informe Hundibilidad Mine Esmeralda, Fase II. The El Teniente Division, Internal Report DERK DI-CT-SP-029.
26. Parraguez, R. and Zepeda, R. Analisis de aplicacion de pre-acondicionamiento sector Fw Mina Esmeralda 2007. The El Teniente Division, internal report SGM-I-018, 2007.

ON DYNAMIC GROUND SUPPORT IN BURST-PRONE ROCK MASSES

CHARLIE-CHUNLIN LI

The Norwegian University of Science and Technology (NTNU)

Norway

Deep mines face increasing ground control issues when the mining gets deeper with time. Ground support systems have to provide a satisfactory containment to the fractured rock in deep mines. The concept of ductile, or energy-absorbing, ground support has been adopted by many practitioners of ground support. The paper focuses on discussions of the philosophy of dynamic ground support for burst-prone rock masses. It includes components of a dynamic support system and ways how to dissipate the burst energy. Existing energy rock bolts are also given a brief introduction in the paper.

1 Introduction

Many deep mines in the world face more and more serious rock burst problem with increasing in depth. For instance, a rock burst event with a magnitude of 3.8 hit seven levels of the Kidd Creek mine, Canada [1]. Inspections done in the mine after the event showed that the rebar-bolted areas suffered serious damages, while the areas supported with energy bolts (cone bolts) survived very well the event. This example clearly indicates that conventional stiff ground support elements are not suitable for deep mines. Many mine engineers have adopted the philosophy that ground support for burst-prone rock conditions should be energy absorbing. Conventionally, one pays a lot attention to the strength of support elements. One prefers to use high strength support elements in convention ground support design. In burst-prone conditions, the issue is no longer how much a support element can carry rather than how much energy it can absorb. Support design for burst-prone rock conditions should be based on energy absorption. The main objective of this paper is to discuss the philosophy of ground support in burst-prone rock masses. In addition, existing energy-absorbing rock bolts will be also given a short introduction.

2 Strength Support and Energy-Absorbing Support

A typical element for strength support is the so call rebar bolt. Fully grouted rebar bolts may be the most commonly used support element in both civil and mining engineering. It is widely adopted because of its high load-bearing capacity. The shortcoming of rebar is its high stiffness, that is, it accommodates a small deformation prior to failure. Rebar is a satisfactory support element when it is used to support a dead weight, for instance a loosen rock block. In high stress rock masses, however, rock bolts have to be more ductile than rebar in order to avoid premature failure of the bolt. Split set and Swellex are two types of ductile rock bolts that have been used to deal with squeezing rock problems for a long time. They are good in ductility, but their load-bearing capacities are smaller than rebar. In securing burst-prone rocks, the desired support elements should not only be able to accommodate large rock deformations (i.e. ductile), but also to carry a high load. Such a type of element is called energy-absorbing support element. Taking rock bolt as an example, the load-bearing capacity of the ideal energy-absorbing rock bolt should be as high as rebar and at the same time it should be able to

accommodate large deformations prior to failure. In other words, it should be able absorb a large amount of energy. Referring to Figure 1, three types of support elements are defined from energy-absorbing point of view:

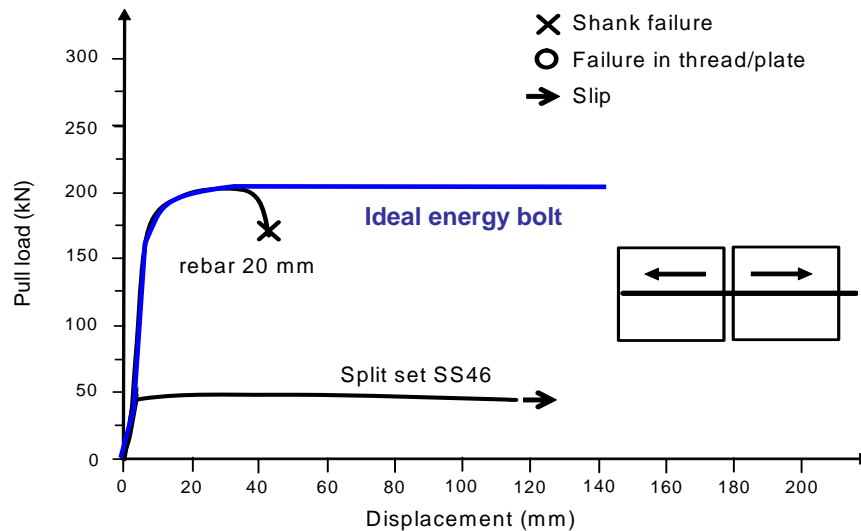


Figure 1 Stiff bolt (rebar), ductile bolt (Split set) and energy-absorbing bolt.

- A *stiff support element* has a high load-bearing capacity, but it deforms little prior to failure. Rebar is an example of stiff rock bolt.
- A *ductile support element* is able to accommodate a large rock deformation, but its load-bearing capacity is limited. Split set belongs to this category.
- An *energy-absorbing support element* has a high load-bearing capacity, and at the same time it is able to accommodate a large rock deformation.

3 Philosophy of Dynamic Ground Support

Fault-slip rock bursts may release a huge amount of strain energy that would cause damages to underground infrastructures. When a burst event occurs, the strain waves propagate outward radially from the epicentre of the event, Figure 2. The waves hit the free surfaces of underground openings and are reflected back. This incidence-reflection process would bring about tensile fractures in the near field of the opening if the magnitude of the burst event is large enough. Without competent rock support, the fractured rock would be thrown into the opening. This type of wall/roof collapse has been observed in many deep mines. Figure 3 shows an example of such collapse in a deep hard rock mine.

When subjected to dynamic loading, the philosophy of ground support is not anymore to balance the dynamic force rather than to help the rock to dissipate the dynamic energy. The dynamic force is not a constant but a function of the stiffness of the support system. If the support system is stiff, the dynamic force applied to the system would be very large. In this case, a stiff support system would be easily destroyed under the dynamic loading. A soft or ductile support system would yield at a certain dynamic force and deform together with the rock mass to dissipate the dynamic energy. The purpose of the ground support is not to provide a support load rather than to absorb a certain amount of energy in burst-loading conditions. Thus, ductility is necessary for a dynamic support system.

A dynamic ground support system is composed of surface support elements and holding elements that are installed within the rock mass, Figure 2. The task of the surface support elements is to provide a good

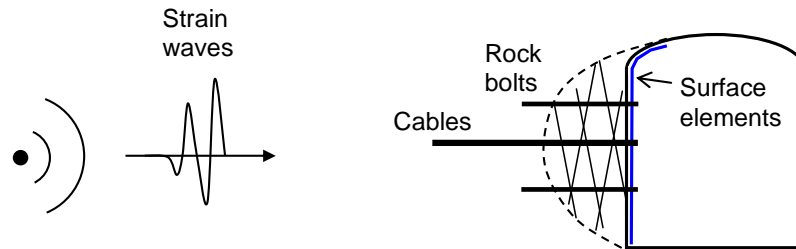


Figure 2 A sketch illustrating burst waves support elements in a dynamic support system.



Figure 3 Roof collapse following a powerful seismic event in a deep mine.

containment to the surface so that the surface rock does not disintegrate when it becomes damaged by the rock burst. Therefore, a full coverage of the surface is necessary to achieve a satisfactory surface containment. The surface support should be ductile enough to accommodate large rock dilations. Wire mesh and fibre or mesh reinforced shotcrete are two kinds of surface support elements that have been used in many burst-prone mines. Ductile thin liners with a full surface coverage may be an even better solution for surface support in the future. The holding support elements have two roles in the support system. The first role of a holding element is to limit the rock dilation through a certain amount of elongation of the holding element self. The second role is to hang up the surface support elements so that the load on the surface elements is transferred into the rock mass through the holding element. Rock bolts in a length of 2 – 3 m are the most commonly used holding elements in mines today. Long cable bolts (4 - 6 m long) are added as a second layer holding elements in some mines where large rock bursts are expected that may cause extensive damages to mine openings.

All the support elements, particularly the holding elements (i.e. bolts and cables), in a dynamic support system must be energy absorbent. The energy absorption capacity of any dynamic support system is limited no matter what types of support elements are used in the system. When designing a dynamic support system, one must bear in mind that it is not the support system that absorbs all the burst energy. The support system is

aiming to contain the deforming surface and limit the rock dilation. A well contained and dilation-limited volume of rock would absorb a large amount of energy through rock fragmentation. More fragmented the rock is, more energy is dissipated. Figure 4 shows two examples how the burst energy was dissipated through rock



(a) Contained damage in the roof [2]



(b) Finely shattered rock contained by mesh [3]

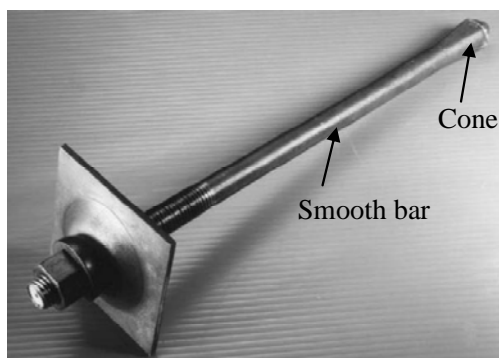
Figure 4 Two examples illustrating dissipation of the burst energy through rock fragmentation behind surface-containing meshes.

4 Energy-Absorbing Rock Bolts

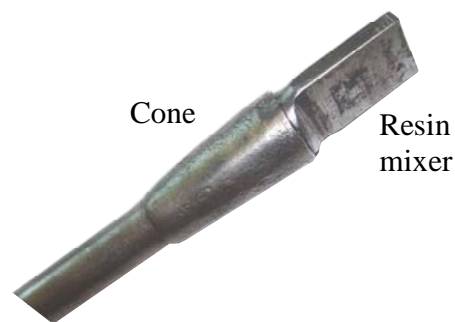
Energy-absorbing rock bolts are the most important elements in a dynamic support system. A few of such rock bolts will be briefly introduced in this section.

2.1 The Cone Bolt

The cone bolt was invented in South Africa in the 1990s [4]. It may be the first energy rock bolt designed to combat rockburst problems. The original cone bolt was designed for cement grout. A cone bolt consists of a smooth steel bar with a flattened conical flaring forged on to one end, see Figure 5a. The smooth bar is coated with a thin layer of wax so that it will be easily de-bonded from the grout under pull loading. The cone bolt was modified later for resin grout in Canada [3]. The modified cone bolt (MCB) is similar to the cement cone bolt. The difference is that MCB is added a blade at its far end for resin mixing, see Figure 5b.



(a) Cement cone bolt



(b) Resin cone bolt

Figure 5 The cone bolt

Cone bolts are fully grouted in boreholes with either cement grout or resin. The bolt is designed so that the deformation of the dilating rock is transferred to the bolt via the face plate, thus pulling the conical end through the grout; thereby doing work and absorbing energy from the rock. The working mechanism of the bolt demands that the strength of the grout must be precisely as designed in order to get the designed performance. The reality is that it is not easy to control the strength of the grout so that the designed performance of the bolt is not guaranteed. The cone bolt is two-point anchored so that there is a risk that the bolt loses its reinforcement function in case that the face plate loses contact with the rock. It has been found in the field that the quality of resin hardening can not be guaranteed for MCB because the end blade of MCB can not properly mix the resin sometimes [5].

2.2 Durabar

Durabar is an element evolved from the cone bolt. The anchor of Durabar is a crinkled section of the smooth bar plus a smooth tail at the far end, see Figure 6. When the face plate is loaded, the anchor slips along a waved profile under pull loading. The maximum displacement is equal to the length of the tail that is about 0.6 m. Similarly to the cone bolt, Durabar is also a two-point anchored tendon.

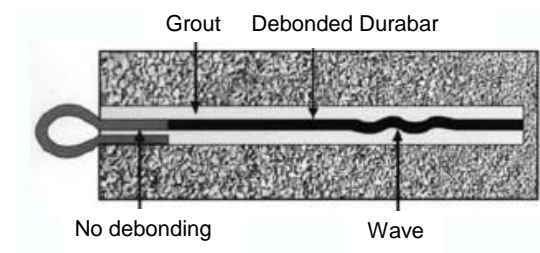


Figure 6 Durabar.

2.3 Hybrid Bolt

The hybrid bolt is composed of two bolt elements: a rebar resin-grouted in a Split set, see Figure 7. Installation of the hybrid bolt is conducted in three steps:

- Step 1: Push in a Split set into the borehole and set epoxy cartridges (fast and low settings) in the tune of the Split set.
- Step 2: Spin a rebar in the Split set.
- Step 3: Tight up the nut to apply a pre-load to the rebar.

Pullout tests show that the ultimate pull load of the hybrid bolt is up to 160 kN and its displacement capacity is similar to Split set.

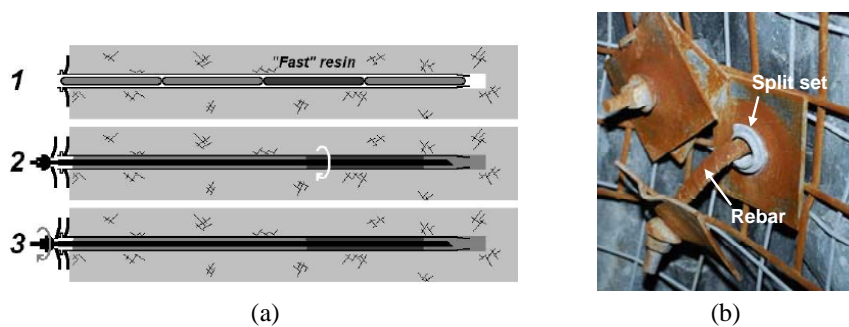


Figure 7 The hybrid bolt. (a) the process of installation, (b) a hybrid bolt in situ. [6]

2.4 Garfold Solid Bolt

Garford dynamic bolt consists of a steel solid bar, an anchor and a coarse threaded steel sleeve at the end, see Figure 8. The bolt is designed for use of resin grout. The threaded sleeve is a mixer of resin substances. This bolt is characterised by its engineered anchor which allows the bolt to stretch for a large amount when the rock dilates. The anchor is a thick wall steel cylinder which is pressed to the solid steel bar at the position of 350 mm from the far end of the bar. The diameter of the solid bar is reduced from its original size to a smaller one in the position of the anchor. When the rock dilates between the anchor and the face plate, the solid bar is pulled through the hole of the anchor so that an extruding process occurs. The extruding force remains at an approximately constant level when the bar is stretched. The bolt can accommodate an elongation of 390 mm prior to failure, see Figure9.

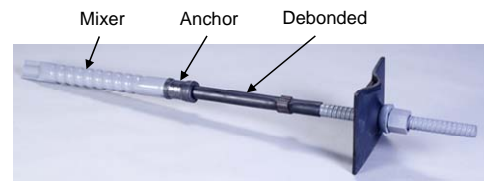


Figure 8 Garford dynamic solid bolt

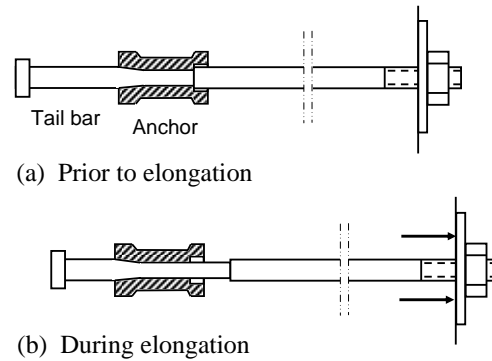


Figure 9 Loading process of the Garford bolt.

2.5 Roofex

Roofex is a new ductile rock bolt developed by Atlas Copco. It consists of an anchoring unit and a smooth bar, see Figure 10. The anchor is firmly fixed using resin or cement grout in the borehole. The smooth bar slips through the anchor, generating a constant frictional resistance of about 90 kN. This yield load is designed slightly lower than the yield load of the bar material.

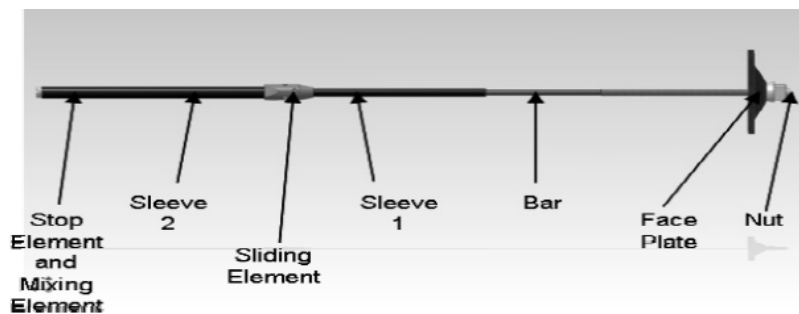


Figure 10 Roofex rock bolt [7].

2.6 D-bolt

The D bolt is made of a smooth steel bar that has a number of integrated anchors evenly or unevenly spaced along the length of the bar, Figure 11. In the current design, the anchors are stronger than the shank of the bolt. The purpose for this design is to mobilise both the strength and the elongation capacity of the shank when the bolt is subjected to loading. The shank, rather than the anchors, is designed to yield, ultimately failing under extreme loading conditions. The anchors can have different shapes. The anchor shown in Figure 11 is called the paddle-anchor. In the case of using polyester resin grout, D bolts use the anchor paddles to mix resin.

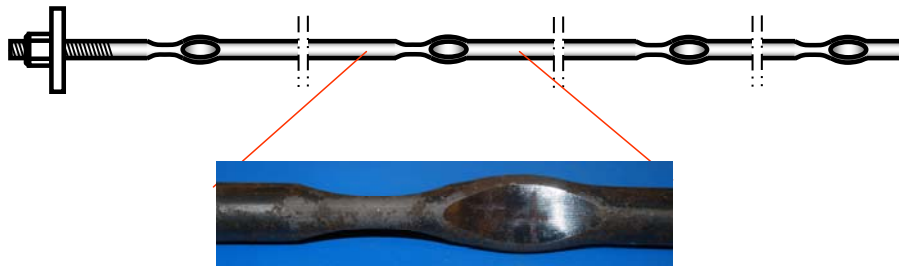


Figure 11 A sketch of the D-bolt.

After grouted in a borehole, D-bolt is firmly anchored to the rock at the anchor positions. Rock dilation will load the bolt shank at the anchors and the de-bonded smooth shank sections between the anchors are stretched and freely elongate under loading. The shank yields when the load is large enough. After that, the load in the bolt will slightly increase with further elongations until failure of the shank at its ultimate strain limit of 15% - 20% for the steel material. The elongation capacity of a section between two adjacent anchors is proportionally related to the length of the section. For instance, a 0.65 m long section can elongate more than 0.1 m prior to failure, see Figure 12. The total elongation of a D-bolt is the sum of the elongations in all the sections. Since most of the elongation of the shank occurs at a load level close to the ultimate strength of the shank, the D bolt can absorb a great amount of energy.

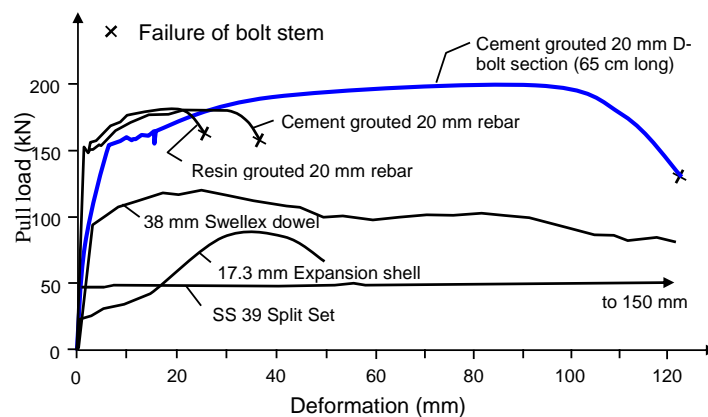


Figure 12 Pullout test result of a 65 cm long section of D-bolt. The results of the other types of bolts are redrawn from Dahle and Larsen [8] for Swellex and from Stillborg [9] for expansion shell, split set and rebars.

5 Concluding Remarks

A certain amount of burst energy has to be absorbed by the support system when a rock burst event occurs. The task of the support system is to provide a satisfactory containment to the rock in the near field of the opening so that the burst energy is dissipated by the rock itself through a process of fracture and fragmentation. A dynamic support system may be composed of three layers: a surface support layer, a short bolt layer and a long cable layer. The surface support layer provides a surface containment to avoid rock disintegration at the surface. The short bolt layer limits rock dilation. Rock fracture, fragmentation and friction occur in the dilation-limited volume so that a large amount of the burst energy is dissipated in this process. The cable layer limits the movement of the bolt-reinforced rock party and absorbs an extra amount of deformation energy

Practices in many deep mines, for instance in Canada, have proven that energy-absorbing rock bolts perform very well when they are subjected to rock bursts. Most of the existing energy bolts are two-point anchored in boreholes. It is quite often observed the face plates of the two-point anchored energy bolts are heavily loaded and even lose their anchoring functions. Loss of one of the anchoring points will lead to a complete loss of the reinforcement for this type of bolt. Resin mixing is another problem for two-point anchor bolts when resin is used as grout. The D bolt is a multi-anchor energy bolt. It may provide a more reliable anchoring mechanism. Another characteristic of the D bolt is the cross section of its anchors is similar to the bolt shank so that that it is easy to push it into the borehole.

References

1. Counter, D. Personal Communication. 2009.
2. Li, T., Singh, U. and Coxon, J. A Case Study of Management of High Stress and Seismicity at Junction Mine. Challenges in Deep and High Stress Mining. (edited by Potvin, Hadjigeorgiou, J. and Y., Stacey, D.), Australian Centre for Geomechanics, 2007, 617-28.
3. Simser, B. Geotechnical Review of the July 29th, 2001 West Ore Zone Mass Blast and the performance of the Brunswick/NTC rockburst support system. Technical report, 2001,46.
4. Jager, A.J. Two New Support Units for the Control of Rockburst Damage. Proc. Int. Symp. on Rock Support, Sudbury, Canada, 1992, 621-31.
5. Simser, B. The Weakest Link: Ground Support Observations at Some Canadian Shield Hard Rock Mines. Deep Mining 07 – Proceeding of the 4th International Seminar on Deep and High Stress Mining, (Pether, Australia, 2007).
6. Mercier-Langevin, F. and Turcotte, P. Evolution of Ground Support Practices at Agnico-Eagle's LaRonde Division – Innovative Solutions to High-Stress Yielding Ground, 2007.
7. Charette, F. and Plouffe, M. Roofex Results of Laboratory Testing of a New Concept of Yieldable Tendon. Deep Mining 07 – Proceeding of the 4th International Seminar on Deep and High Stress Mining, (Pether, Australia, 2007).
8. Dahle, H. and Larsen, T. Full-Scale Pull and Shear Tests of 5 Types of Rock Bolts. SINTEF report, Report no. SBF55 F06033. 2006, 8.
9. Stillborg, B. Professional Users Handbook for Rock Bolting. Trans Tech Publications, 1994.

CONTROLLING SEISMIC HAZARD IN UCHUCCHACUA MINE

DAVID-REGALADO PALOMINO and RICARDO-RIVERA BEGAZO

Geotechnical Company of Mines Buenaventura S.A.A -Uchucchacua Mine

Avenue Carlos Villarán # 790-Lima, 13- Perú

Uchucchacua's deposit is located in the western slope of the Andes and department of Lima - Peru belongs to Oyón's province. From 1953 year up to have taken place 19Millions onz. of mineral of silver with systems of exploitation cut and fill ascendant and sub level stopping, nowadays one comes exploiting 3200 TMS with 16 onz of Ag / TM of head. The seismicity comes to be the result " High concentrations of stress, product of a natural state of stress of great magnitude, those that can associate to a great rock covering, to tectonic stress or residual stress that act or they are present in the rock and that, as product of the mining exploitation, they can be increased in significant form and to concentrate on specific places of the mine. Presence of rocks generally of high resistance and high modules of elasticity that to the subjected being to efforts of great magnitude, they are not deformed but rather they accumulate energy, the one that once overcome the values of maximum resistance of the rock, it is liberated in violent form and for the existence witnesses mainly of persistent failures sub vertical that allow the displacement of the rock.

1 Introduction

Uchucchacua mines in the last two years it shows us that most of the seismicity is been of a mined induced, high stress and vertical sub systems of flaws that generate slips. The events generally take place among 10 at hundred of meters far from the one mined as the result of the biggest disposition of flaws, seismically active, slip areas and also after the explosions of great volume.

In some case they are events of small to medium and in few cases of great magnitude and these they are happened after some minutes, hours, days of or weeks after having carried out the production explosions.

2 Regional and Local Geology of the Deposit

Uchucchacua's deposit is related to a geological principal Structure of them covers head plants. The opposing rocks are of intermediate acidity. The principal geoestructuras are of the system NE-SW and they tense sound of the System EW - NW-SE Uchucchacua is a deposit hydrothermal Epigenetic of the type of landfill of fractures, which also were channels of traffic and emplacement put somatically of solutions ore that finally formed bodies of ore. The economic commercial mineralization belongs basically to Ag, since by-product extracts Zn and Pb to itself. The structures are located in calcareous rocks of the top cretaceous in the formation Jumasha and associated with they find bodies of irregular and discontinuous emplacement.

2.1 Folding

The presence of the tectonic Andean one in our deposit metallic has created systems of principal folding where the mined one is exposed to susceptible zones to the occurrence of the rockburst[4] see (Figure2)

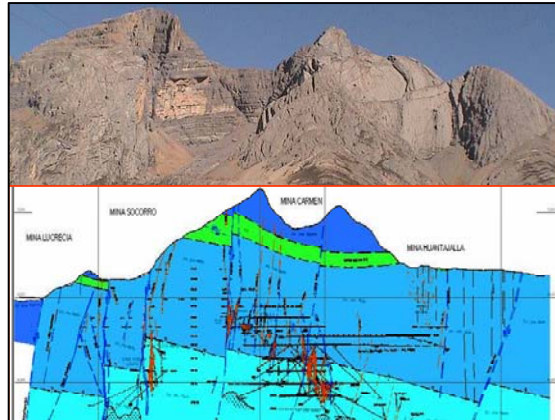


Figure 2. Folding deposit Uchucchacua mine

2.2 Characteristics Petromineralógicas

Composed principally by two litologic one is the limestone fragile one and of high resistance another ore of Proustite, Argentite, Pirargirita, Native Silver, Esfalerita, and Marmatita of under metallic content Pyrite, Alabandita, Rodocrosita, Calcite, Pirrotita in different combinations forming a rocky hard structure and of high compressive resistance.

3 Mined of the Deposit Uchucchacua

The mining activity in Uchucchacua comes treating mineral from the year 1975 with more than 3 decades of progressive production of 350 TM/day and nowadays 2008 with 3000 TM/day, it is the fourth mine in the world silver producer with 11 million oz. during año2008, this mine uses two shaft and two main ramps of accesses to the bodies of mineral production for the extraction service, transport of materials and of personal. Along the years the methods of exploitation have been in the use since they are shrink, court and predominant of fill in the irregular bodies of dimensions different with the rooms and pillars and level of the subordinate one that stop in the regular bodies of big dimensions. Nowadays in Uchucchacua mine we have near 30 bodies of exploitation in the different levels and sectors of mined Carmen, Socorro and Huantajalla, being the sector Carmen the exploited more and with major rocky coverage in the current level 3990 (depth 1000m), loudly fault and rock of high resistance.

The principal areas of production in Uchucchacua mine are:

- Carmen, bodies Rosario, Rita, Alison, Ruby, Rosary, with production of 30,000TM-
- Socorro, bodies in faults Socorro floor, Magaly, Gina, Leslie, with a production of 40,000TM for month.
- Huantajalla, bodies in faults Edith, Iris, Karina, 4A, 3A, with a production of 20,000 TM for month.

Nowadays the decrease of reserves of ore in the top nivels taking this one to us to a strategic planning of increasing reserves in the levels of deepening it is 3990 say under the levels in Carmen and Socorro mines continuing the systems of ramps and shaft where the mined one will be exploited by the system of cut and fill ascendant in small bodies from 4 to 8 meters of width by 30 to 40meters of length, by equipments of manual perforation (jackleg and stopper) by perforation in stopping and scoop of 2.2 yd³ of capacity, and in bodies of big dimensions from 10 to 20 m of width by 40 to 80 meters of length by equipment jumbo electro hydraulic in stopping.

4 Characterization of the Rocky and Tensile Clump of Stress

The principal domains litológicos are the limestone of formation jumasha and the mineralization in different compositions where there were realized laboratory tests of equipment controlled Cervo MTC-815[1] to determine the rock indexes if they are ó not capable to burst. In addition we find other domains of minor importance since they are the intruder daciticos and andesitic and sulphurs with major presence of zinc.

Table 1. Average rock properties domains

DIAMETER 48mm					DIAMETER 48mm				The rock is susceptible to the explosion ?
Witnees N°	Mine	Depth	Type Litologia	Level mmm	Uniaxial compressive strength σ_{cr} Mpa	Elasticity modulus E Gpa	Poisson's V	Elastic index of potential Energy PES kj/m3	
(26-1)	Carmen	880	Limestone	4120	279.59	100.66	0.28	388.28	very susceptible
(27-1)	Carmen	640	Limestone	4360	246.99	95.88	0.38	318.15	veru susceptible
(28-1)	Huantajalla	640	Limestone	4360	136.59	77.98	0.49	119.64	considerably
(29-1)	Huantajalla	640	Limestone	4360	186.8	83.08	0.23	212.27	very susceptible
(30-2)	Huantajalla	640	Limestone	4360	240.8	77.4	0.18	374.60	very susceptible
(30-3)	Huantajalla	640	Limestone	4360	250.63	73.08	0.14	429.80	very susceptible
(32-1)	Carmen	880	Ore	4120	163.5	54.8	0.4	244.93	very susceptible
(34-1)	Socorro	760	Ore	4240	162.5	68.8	0.2	192.10	considerably
(35-1)	Socorro	760	Ore	4240	84.7	64	0.2	56.12	susceptible
(36-1)	Socorro	760	Ore	4240	129.5	69.4	0.2	120.91	considerably
(37-1)	Socorro	760	Ore	4240	82.7	52.6	0.2	65.00	susceptible
(38-1)	Socorro	760	Ore	4240	102.7	62.5	0.4	84.36	susceptible
(39-1)	Socorro	760	Ore	4240	125.9	50.4	0.2	157.05	considerably

Elastic index of potential energy PES

$$PES = 500 R_c^2 / E \text{ [KJ/m}^3\text{]}$$

Density of limestone 2.70kg/m³

Density of ore 3.2 kg/m³

Realizing a structural analysis after systematic cuts and mapped there are had identified the major regional and principal failures apart from a set of structures tense them important of mineralization, which they go of NE-SW and of NW-SE-EW con the influence of the anticline of cachipampa and fracturamientos in 3 stages of fractures. The maximum stress principal is of NE 35° to 45°SW.

Apart of the indirect method the tensile one of stress would be of:

- Principal major stress is sub horizontally for (folding anticlines' and synclinals, failure) approximately major of 48Mpa.
- Principal intermediate stress approximately equal to 48 Mpa.
- Principal minor stress approximately minor of 48 Mpa.[2]

5 History of Seismicity

From the year 1991 evidences of events were had as rearrangement of the hill ó blows of mountain from the year 2003 the first incident was experienced by rockburst by bodily injuries to a depth of 2400pies (800m) in a front of advance in 12 I pierce sale a rockburst with 1.5 Mw (moment magnitude) of approximate intensity; the year 2004 other events of 1.5 Mw to depth 2700 feet (900m) without bodily injuries; the year 2005 another event of great magnitude approximately 2.0 Mw. With bodily injuries to depth of 2100pies (700m) two persons in perforation in embossment with stopper there was the rockburst of the box roof not registered for not possessing in this moment seismic system but for the evidences of the damages(Figure 3,4); in addition the year

2006 realizes the first seismic study in a network of 4 seismographs in surface covering 16 square kilometers of area of monitoring where the seismic registered events were for effect of mined induced and activation of some important faults.

Then to beginnings of the 2007 the seismic system was installed with the technology of ESG of Canada, at the present time one has registered but of 3000 events



Figure 3 Depth 700 meters



Figure 4. Depth 800 meters

6 Management of High Stress and Seismicity in Uchucchacua Mine

6.1 Seismic Monitoring

To beginnings of 2007 the system installed 24 geophones uniaxials of 15 Hz (G-15) omnidireccionals. The seismic events of magnitude -1 have a typical frequency closely of 400 hertz's, where as the events of the magnitude -2 near 800 hertz's. The reliable identification of the frequency needs a limit of the frequency of the equal recording at least two times to the frequency. This way, it hopes that the aforesaid acquisition of information allows the identification of seismic events with magnitude so down as approximately -1.5. To assure this level of the sensibility, nevertheless, distances between sensors it needs to be supported generally in the range from 100 to 150 m The response of frequency of these geophones will allow the recording event with magnitude up to (even) near 3. Even if the geophones nearest to a seismic big event shorten, this one will not affect the location of the event, which will continue being provided 6 geophones with every Paladin (recorders) a resolution offers 24-bit with the dynamic effective range of the DB 115 in the sampling rates of up to 10 kilocycles. To transmit all the constant registered information, a high tariff of the transmission of information is needed of Paladin to the PC of the acquisition, and of here to the PC of process in surface this can be reached using the modems DSL.

6.2 Model of Stress

The method of mined and sequences the numerical modelamiento is a part of a planning to short and medium term to determine the sequence of mined and to analyze the behavior of the state tensional of stress in every stage of mined the software used in uchucchacua mine is the Phases2 v6.0 package for rocky elastic environment in two dimensions and structural analysis with software Dips v3.0, Unwedgev5.1 and Cpillar for calculation of stability the pillar, example see model the stopped 990 Carmen mine depth 1,000 meters (Figure 5).

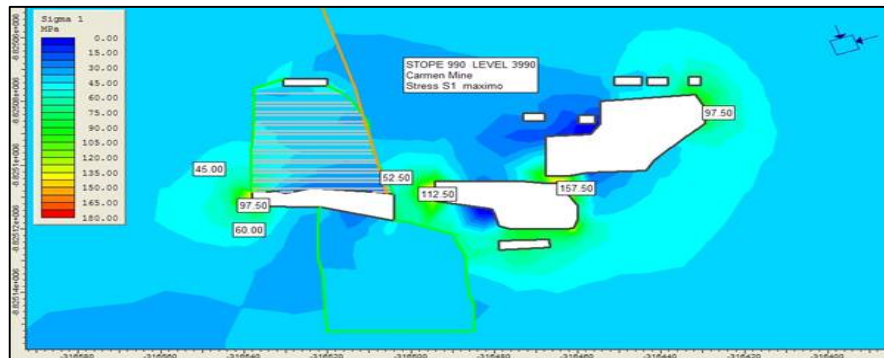


Figure 5 Modelamiento stopped 990 Carmen mine

6.3 Project of Seismic Risk

Uchucchacua mine comes operating on for 35 years with a seismic history product of induced stress and a structural system that generates seismic activity apart from has a rock of elastic behavior of stress deformation that they overcome them 100Mpa of compressive resistance and bigger than 40 Gpa of module of elasticity, the system of seismic monitoring was exposed in the section 6.1 where there is controlled the seismic damage related to the production.

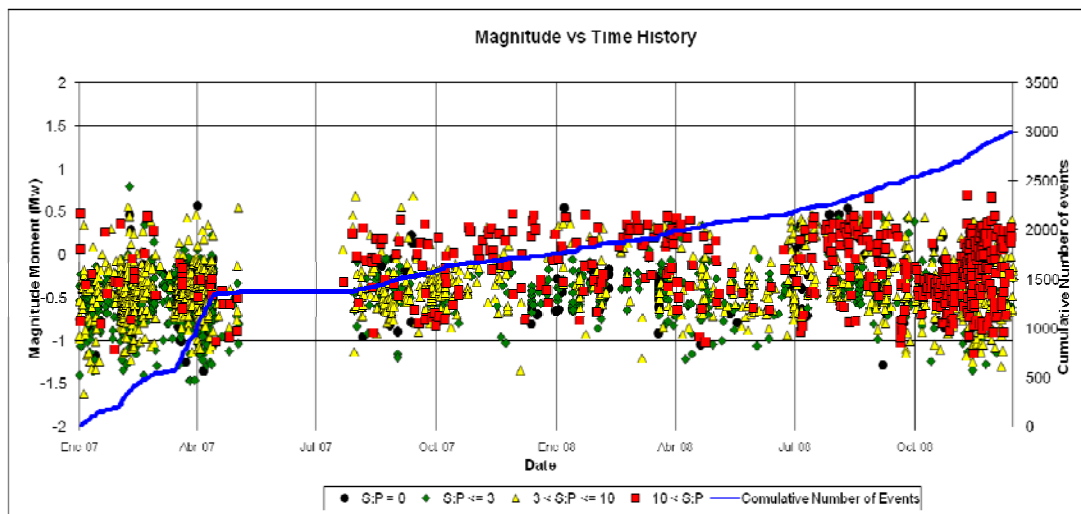


Figure 6 Monitoring seismic 2007and 2008 with 3053 events

The present graphic (Figure 6) it shows that the seismicity is presented in a range of $(-1.50Mw \text{ to } +0.8 Mw)$; admass show that in the last months of the 2008 year an increase of events exists. The relationship S/P (wave energy S vs. energy waves P) found among $(3 < S/P \leq 10)$ increase, being at the moment the concentration average of events with a relationship $S/P = 10$.

This means that the events seismic product of the production (induced seismicity) this in increase and it is producing bigger fracturamiento in the rock mass.

6.4 General Concepts of the Seismic in Uchucchacua Activity:

The events experienced in mine resulted from turning uncontrolled rock, which paralysed the operation of the mining work; seismic events are within the types:

a. Events on the level of production that is associated with high pillars, bridges of mineral for the high indices de production occasional seismic events during their development stress.

b. Deep events this also occurs in the mine where the rock massif experiencing a minor influence stress induced by the mining. Los events are the result of unstable fractures located around the stopped of exploitation and/or a combined release energy tectonics and induced the cup of production (by mining).

c. A typical effect of the cause of rockburst is the effect called (scissors) shear when two faults are intersection and at the centre is an ore body that to be exploited at each stage stress main horizontal maximum it acts perpendicular to the failure creating deformation stress on the walls and with rockburst effect.

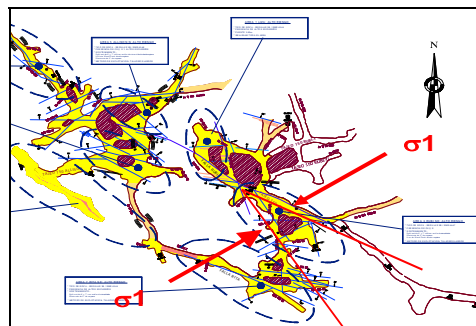


Figure 11 .Effect scissors between two faults and stress maxims Control of seismic parameters:

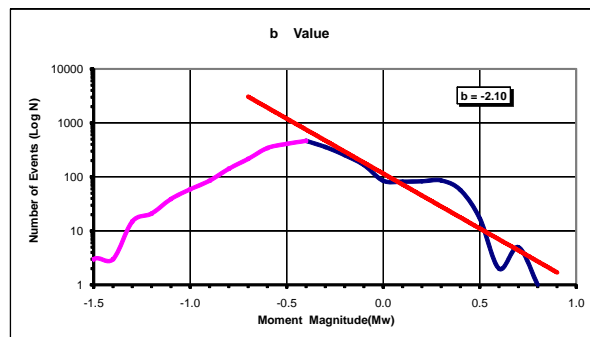


Figure 12 Moment Magnitude vs. Number Events

According to sample the graph the direct “b” it indicates that one can wait seismic events close or similar to +1.0 Mw, also sample a deflexion of the curve that means that the biggest quantity in events according to seismic record is of -0.4 Mw.

As “b” = -2.10 represent the slope of the direct product of the relationship magnitude moment (Mw) with the time, if this slope increases the damage increases to have events (rockburst) of more intensities, contrary case if the slope diminishes the damage it diminishes.[3]

6.5 Strategic Development of the Support and Improvement of Support

Leaving of the seismic parameters for the fortification plans like they are magnitude moment (Mw), liberation energy (E) that have caused us rockbursts, we consider the values but high according to our statistics, for the design and support elements like it is shown:

- PPV (m/s) = 0.34(speed chops particle)
- MW = + 0.8 (Moment magnitude)
- E = 7 E 04 Joules (liberated energy)

In the different levels of exploitation was located the zones of seismic source (Figure 7) and partner to the monitoring seismic mike established as a standard to reinforce the labors planned inside the zones of risk with spikes and / or super split set with mesh and a cap of shotcrete of 5cm with hybrid fiber (polypropylene and ferry) .Energy needed by the systems of fortification considering the eventual generation of a seismic event.

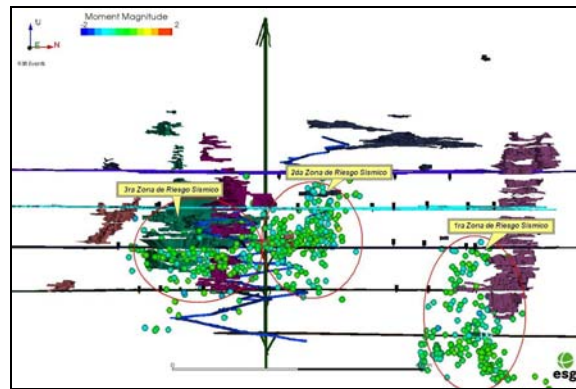


Figure 7 Zone's Seismic Source Carmen mine 2008

6.6 Zones of Seismic Source

On the basis of the information of the monitoring seismic mike, the areas of risk are had sectorizado in the maps Carmen observes the behavior of the events in the last levels of the Mine, these being grouped in 3 zones of seismic source on the basis of the number of events and accumulated intensity that understand:

First zone they understand them Rosita prays body Rosary, Rosemary. It 2nd zone located between 2 important faults, the fault Raquel-Margot and 3rd zone of seismic risk that Ruby and Veronica appreciates this one in the failures.(Figure 7)

6.7 Reinforcement Design

Implementing measures as increasing stiffness of sustaining the mining system in areas identified with potential damage rockburst with the zoneamiento of the seismic monitoring, in the design of work is recommending apply the following equal:

Energy of design=Energy Liberate/Area*FS

Example of calculation of design of support for the level 3990 Carmen mines with:

0.8 Mw. (Magnitude moment) and with liberated energy 7. E+04Joules

Shotcrete with hybrid fiber 530 Joules/m2 of energy of absorption

Bolt of 1.80m of 22mm of diameter with energy of absorption of 2200 Joules/m².

Area affected by the rockburst 20m²

FS (safety factor needed) = 1.4

ED=70000/20*1.4 = 4900 Jules/m² (necessary) Maintenance: 2 (bolt) +1m² (shotcrete)

ED (Energy design) = (4400 +530) = 4930 Joules/m²

The suitable maintenance to absorb the energy liberated with a FS =1.4

According Ortlepp & Stacey (1995) in base experiences and laboratory [5] rehearsals settle down that not more than 80 mm of the total longitude of the fortification system (based on fasteners and/or cables), they act indeed in the calculation of the maximum elongation when they are subjected at a certain load level. This maximum elongation that reaches near 15% in the case of the fasteners of anchorage of the helical bolt type with steel A44-28H is dear until reaching its fallamiento limit for break to the pure traction. Then, the maximum elongation to the pure traction that could experience the fortification system based on helical bolts is near 12 to 15 mm (=80mm * 0,15). therefore, the energy absorbed average is obtained starting from the total displacement and of the maximum resistance of the steel according to the following thing:

Energía capaz de absorber un perno de 22 mm de diámetro (calidad A44-28H) = 2200 Joules

7 Conclusions

On having studied our rock if it is capable to burst it put in alert his zones with rocky environment capable of exploding if we were generating the conditions structural and mined induced. The communication with the operation of mine is constant to give the call of alert if certain zone presents a potential high place of risk evacuating to the personnel and the labor is paralyzed up to his geotechnical evaluation. After has experienced a series of accidents and losses in the productive process with these measures of control our mining unit; from the year 2006 in forward it has be minimizing and controlled this hazard. Hazard Map helps identifying seismically active faults (shear zones). It will determine what each risk zone this formed turn with 2 sources seismic and sustaining and direction of future tasks have to be related to the location of these sources. The relation energy accumulation event and blast this shows us that the seismic events are a response to the shooting, these events occur immediately after hours and even after several deals of made the shot. Risk associated with fault slip events is mitigated (managed) by strategic & timely placement of enhanced support.

8. References

1. Krzyszton, D., Carvajal A., Regalado D. Susceptibility of Rocks Bumps. The Results of Simple Investigation in a Stress-Testing Machine. Fundacja Nauta I traduce Gore reinforcement design nicze country Polonia, 2007,102.
2. Abel, J. Estimate of the State Tensional In-Situ Starting from the Methodology to Locations with Systems of Failures as Uchucchacua, 1979.
3. O'Diana, M., R. Lazo, and R. Rivera. Evaluation of the Seismic Risk in the South of Peru (14°–19°S). Institute Geophysics of the University San Agustín, 2005, 29.6.
4. Regalado D., Carbajal A. Thesis Magister of Engineering in Mineral Resources. University The Serena, Chile, 2007.
5. Ortlepp and Stacey Experiences and Laboratory the Energy Absorbed Average for the Fortification System, 1995.

ANALYSIS OF TREMORS EFFECT ON THE STABILITY OF EXCAVATION AND SUPPORT SYSTEM IN UNDERGROUND COAL MINING

YI-XIN ZHAO, YAO-DONG JIANG and JIE ZHU

*State Key Lab of Coal Resources and Safe Mining, School of Mechanics, Architecture and Civil Engineering,
China University of Mining and Technology
Beijing, 100083, P.R. China*

The effect of progressive mining is one of the main factors that exert a significant influence in coal bumps. This research aims at analyzing the impact on roadway stability caused by the dynamic loading of mining tremors and the support system responses in underground coal mining. A mechanical model was described to analyze the mechanism of coal bumps induced by tremors in underground mining. The FLAC2D code was applied to analyze the tremor impact on deep excavations and responses of different kinds of support system. And the ANSYS software was adopted to simulate the structural responses of two kinds of U-style steel support system under the bumps condition in Zhaogezhuang mine. The results indicate that the tremors underground can not only cause the stress redistribution near the excavations, but also induce the decrease of frictional force in the interfaces of coal seam and surrounding rocks. Moreover, the U-style steel yieldable support system with circular shape was proved to be more efficient to offer superior protection in bursting region.

1 Introduction

Underground coal bumps is a catastrophic mine failure resulting from sudden releases of strain energy [1]. With enormous amounts of released energy, coal bumps may cast several tons of coal mass into openings horizontally, which can result in the destruction and collapse of roadways, damage of facilities or even death and injury to the miners. In the mining process, there are several kinds of factors can induce coal bumps, such as blasting tremors, periodic roof movements, earthquake seismicity and etc. The tremors caused by progressive mining are one of the main factors causing roadway instability or coal bumps in Chinese coal mines. Statistics indicate that more than fifty percent of coal mines, which apply the method of blasting, have potential coal bumps hazards in China [2]. However the contribution of underground tremors to coal bumps has not been fully understood. A better understanding of tremor effects on coal bumps can provide the effective insight for proper design of support system in coal bumps prone region.

This paper study the effect of blasting tremor on coal bumps and the responses of yieldable support systems during the dynamic impact. FLAC3.3 code has been applied in numerical modelling. The main emphasis is placed on selecting a better yieldable support system to mitigate mining tremors influencing the roadway stability in the Zhaogezhuang mine. In addition, ANSYS is adopted to evaluate the structural responses of two kinds of yieldable support system affected by tremors by calculating the self frequency and vibration mode.

2 Mechanism of Coal Bumps Induced by Tremors

2.1 Analysis of Tremor Effects on Bumps

Tremors associated with blasting or bumps can not only influence the stress distribution, but also cause unstable crack propagation in the coal seam and surrounding rock; which will accelerate the deteriorated process of rock

and coal mass. Moreover, dynamic impact can also cause decreasing of normal stress and increasing of shear stress to the interfaces between coal seams and adjacent overlying or underlying rock layers, which may convert the sticking friction into a sliding friction on the interfaces [3, 4].

On the other hand, perturbations in the original lithostatic stress field caused by the excavation can, therefore, result in coal/joint failure on the seam horizons [5-7]. Thus, the coal seam can be divided into three zones: pressure relief zone A, maximum static equilibrium zone B and primitive overburden pressure zone C as shown in figure 1a. The tremors effects can increase the width of zone A and induce the instability of zone B. Moreover, because the coal mass consists of the solid grain, the condensed liquid and the gaseous substance, the rarefaction shock wave can propagate in this medium, crush the skeleton of the porous medium and accelerate the failure process of coal mass. The stored energy released by the shock wave can induce breakdown of the medium and impart kinetic energy to the coal mass at zone A and portion of zone B. Figure 1b and figure 1c present gateroads failure caused by coal bumps, triggered by mining tremors in Tangshan mine, Hebei province.



Figure 1 Scheme of damage regions in coal seam and gateroads after coal bumps in Tangshan mine. (a) Scheme of damage regions. A- pressure relief zone B- maximum static equilibrium zone C- primitive overburden pressure zone. (b) , (c) Gateroads after coal bumps.

2.2 Modelling of Shock Wave Propagation in Coal Seam

Consider the one-dimensional problem of a plane wave propagating in the direction of the x-axis. Denoting the stress component by p , the density of the medium by ρ , its velocity with respect to the x-axis by u and the time t , we obtain the equations for the conservation of mass and conservation of momentum of the medium, without viscous friction, in the form [8].

$$\frac{\partial \rho}{\partial t} + \frac{\partial \rho u}{\partial x} = 0 \quad (1a)$$

$$\frac{\partial u}{\partial t} + u \frac{\partial u}{\partial x} + \frac{1}{\rho} \frac{\partial p}{\partial x} = 0 \quad (1b)$$

Equation (1a) can be written in the form:

$$\frac{\partial p}{\partial t} + u \frac{\partial p}{\partial x} + \rho c^2 \frac{\partial u}{\partial x} = 0 \quad (1c)$$

where $c^2 = dp/d\rho$. The initial boundary conditions are

$$t = 0 \quad x > 0 \quad u(x, 0) = 0 \quad p(x, 0) = p_0 \quad (2)$$

$$t > 0 \quad x = 0 \quad p(0, t) = p_0(t) \quad (3)$$

where p_0 and $p_0(t)$ can be measured. Thus, according to the above equations from equation (1b) to equation (3), we can obtain $t > 0$, $p = \rho c x / t + p_0(t)$ and $t = 0$, $p = p_0$.

In the condition of $dp_0(t)/dt < 0$ and there are two assumed different time t_1 and t_2 ($t_2 > t_1 > 0$), the stress difference at the point of x_0 ($x_0 > 0$), which is in the direction of shock wave propagation, can be

$$\Delta p = p(t_1) - p(t_2) = \frac{t_2 - t_1}{t_2 t_1} \rho c x_0 + p_0(t_1) - p_0(t_2) \quad (4)$$

If $\Delta p > \sigma_t$ (σ_t is the tensile strength of coal), the coal will be broken. Until the energy of rarefaction shock wave decreases to some value, the fractures will not propagate periodically.

3 Modelling Analysis of Mining Tremor Impact on Roadway Stability

3.1 Modelling of Shock Wave in the Coal Seam

Numerical modelling using FLAC2D code has been carried out for Zhaogezhuang coal mine in order to investigate stability of roadway in No.9 coal seam on 14th level. Numerical models were developed for analyzing the effects of mining tremor on coal bumps and responses of two kinds of yieldable support system during dynamic impact. The geometry of the two-dimensional simulation model is shown in figure 2.

The roadway size is 4m×3.5m. The original lithostatic stress of 27 Mpa is imposed on the top boundary of the mechanical model. The tectonic stress is 30 Mpa loaded on the left and right boundaries horizontally. The nonreflecting boundaries and a dynamic load applying a 10 Hz Ricker impulse are both used. The velocity of horizontal wave is 1m/sec [9].

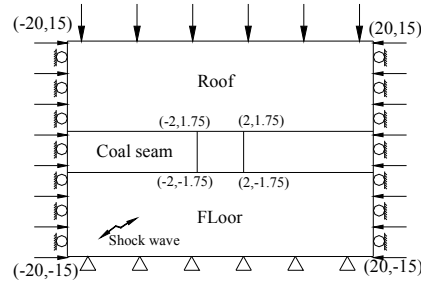


Figure 2 Schematic view of numerical model

3.2 Geo-Material Properties

In current numerical modelling, the Strain-Soft constitutive model has been adopted. For all cases, the mechanical properties for coal seam and both the roof and floor rock are presented in table 1.

Table 1. Mechanical parameters of rock masses and coal

Position	Rock property	Bulk density, N/m ³	Young's modulus, MPa	Passion's ratio	Fraction angle, Deg	Cohesion MPa
Roof	Grayish-white grit stone	2.7×10^4	30×10^3	0.25	31	1.5
Coal seam	Massive	2.5×10^4	7.7×10^3	0.3	29	1.0
Floor	Dark gray sandstone	2.5×10^4	26×10^3	0.28	30	1.0

3.3 Properties of Support System

Bolting support and yieldable U-steel support have been installed respectively and observed based on the magnitude of displacements and plastic region. Full length bolting was applied with bolt length 2.5m and average interval spaces of bolts 740mm. The strength of bolting is 80kN with yield strength of bolt 180kN. The density of bolt is 7000kg/m³ and young's modulus is 200 GPa.

3.4 Analysis of the Results

The simulation results indicate that the plastic region around the excavation could be expanded and some tensile failures occurred during the dynamic impact as shown in figure 3a and figure 3b.

The bolting support system can reduce the stress concentration adjacent to the excavation during the dynamic impact. The plastic region and occurrence of tensile failures decreases and the convergence of the excavation reduces a lot. Compared with bolting, U-style steel yieldable support is more suitable to control the plastic

region expansion, reduce the tensile failures and mitigate the convergence of excavation as shown in figure 3. Both of these two support systems are yieldable systems, which can absorb the released energy of surrounding rock. Simulation results demonstrate that the U-style steel yielding support system is safety and efficient to offer superior protection in Zhaogezhuang coal mine, see figure 4 and table 2

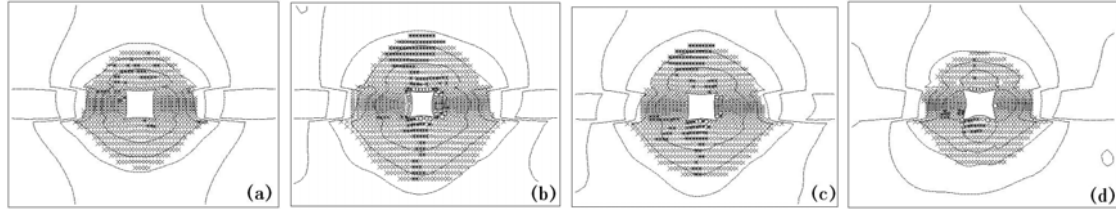


Figure 3 Distribution of plastic region and mini-principle stress around excavation in different conditions. (a) Before dynamic impact, no support (b) After dynamic impact, no support; (c) After dynamic impact, bolting support (d) After dynamic impact, U-steel support

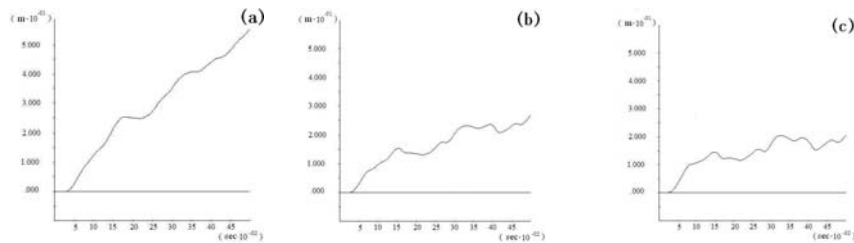


Figure 4 Deformation of the sidewall during dynamic impact. (a) No support, (b) Bolting support, (c) Yieldable U-style support

Table 2. Convergence of roadway in different support conditions after seismic

num	Support method	Vertical Convergence/mm	Vertical convergence ratio/%	Side wall convergence/mm	Side wall convergence ratio/%
1	No support	460	100	1100	100
2	Roof, sidewall and floor bolting	320	69.6	490	44.5
3	Yieldable U-style support	330	71.7	330	30

4 Structural Mode Analysis of two Types of Yieldable U-Style Support Systems

The aim of simulating the modes of yieldable U-style support system is detection of behaviour of steel support systems during the course of dynamic response provoked by blasting or bumps. Earlier investigations proved that the failure features of arch shaped U-style support system under dynamic loading condition were associated with the preloaded, constraints, cross section area and etc. And the critical amount of energy, causing permanent strain and large deformation of steel support, is also calculated for arch shaped support under the impulse loading conditions [10]. However, seldom attentions were paid to the self vibration features of different support systems. In underground mining conditions, the frequency of tremors triggered by blasting, coal bumps or rockbursts ranges from few hertz to hundreds of hertz. So the calculation of self vibration features of different steel support systems in the low frequency range is very important in the support design progress.

4.1 Numerical Modelling and Computation Result

The computer modelling is conducted to simulate the responses of two shapes of yieldable support system. The basic dimensions of cross-sections of two shapes of roadway are indicated in figure 5a and figure 5b. The profile of support is rolled U-type steel section, i.e applied section U29 (weight 29kg/m). The ANSYS program was applied to calculate natural frequencies and vibration modes of two shapes of support system. The profile of sliding clamp joint is presented in figure 5c. And the overlapping length is 0.48m. The FEM models of the support system are created by shell elements. First ten orders of vibration mode of two support systems are calculated and the features of self vibration and dynamic responses are also analyzed.

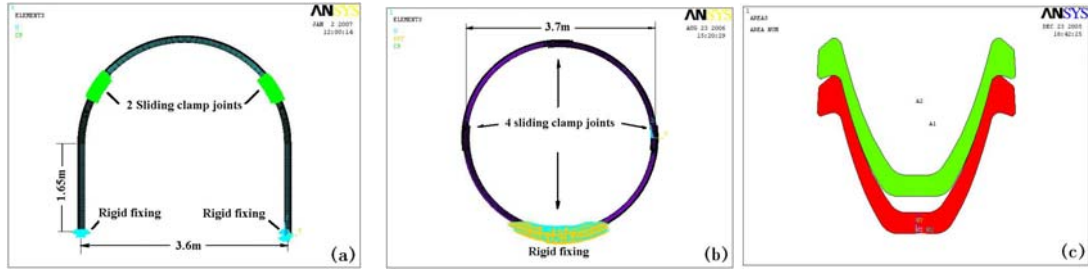


Figure 5 Boundary conditions of different shapes of support system.
(a) Arch shaped, (b) Circle shaped, (c) Scheme of the interface of two U-type steel parts at sliding clamp joint.

Figure 6 presents the structural vibration models of arch shaped support system. The results indicate that the higher of self frequency, the more complexity of vibration models and more permanent strain caused. The failure is mainly concentrated at the sliding clamp joints in the modes of first order and second order. And the damages are at the side parts of system in the modes of third order and fourth order. The torsion shear began to occur in the modes of fifth order and sixth order. Large deformation of the system appears as the modes reach the seventh order. The several plastic joints appeared in the system at the tenth order mode.

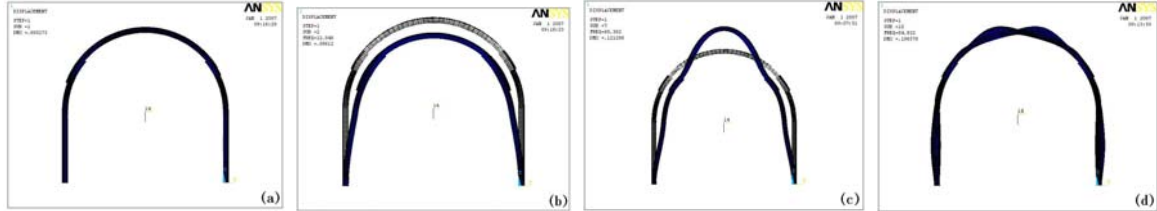


Figure 6 Different structural vibration models of arch shaped support.
(a) First order structural mode; (b) Second order mode; (c) Seventh order mode; and (d) Tenth order mode.

Figure 7 presents the structural vibration models of circle shaped support system. The results indicate that the sliding joints are damaged at first and second modes. With the increasing of self frequency, the larger plastic deformation of support system appears. However, the deformation of support is very small at any modes. From the third mode to the seventh mode, the local materials in supporting structure would be unstable. With the increasing of the mode order, the amplitude of deformation decreases and the corresponding natural frequency rises. From the eighth mode to the tenth mode, the several plastic joints appear and system becomes unstable.

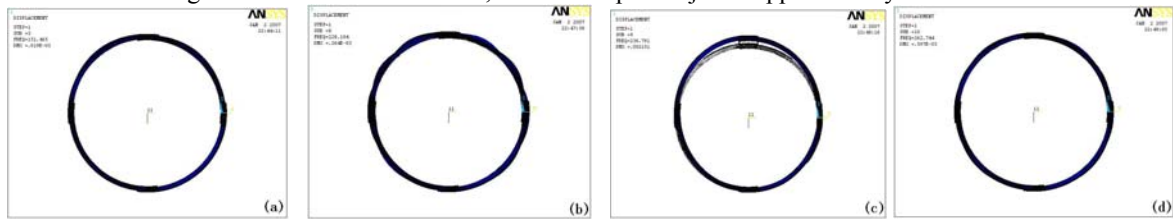


Figure 7 Different structural vibration models of circle shaped support.
(a) 3rd order structural mode; (b) 8th order mode; (c) 9th order mode; and (d) 10th order mode.

4.2 Analysis Of Results

The results of mode analysis are obtained as follows:

- (1) Impact resistance and mechanical performance of circular shaped support is better than the arched support on the conditions of the dynamic load effects. The support resonance is avoided, because the natural frequency of circular shaped support is far away from the bump's frequency region (0-50Hz), see table 3.
- (2) The circular yieldable support shows better performance in surrounding-rock control and self-deformation.

- (3) The impact resistance of arch shaped support is not as good as the circular support, but it is easy to construct and cost small. And the arched support with the thickened mudsill can avoid the floor heave and resist certain dynamic load.

Table 3. Self frequency of two shapes of support systems (Unit: Hz)

	1 st order	2 nd order	3 rd order	4 th order	5 th order	6 th order	7 th order	8 th order	9 th order	10 th order
Arch	0.000	12.048	13.394	16.427	16.740	41.721	60.362	63.697	66.591	84.832
Circle	0.032	0.033	151.46	159.99	179.25	189.44	215.06	228.18	236.78	262.74

7 Conclusions

This paper presents a discussion of the mechanism of tremor induced excavation instability. The study indicates that the tremors can not only cause the stress redistribution, but also decrease the frictional force between the coal seam and surrounding rock.

Simulation results show that the plastic region expands, tensile failure occurs, the state of stress deteriorates in the surrounding rock and coal seam during the dynamic impact. Moreover, two kinds of yieldable support system investigated can both reduce the stress concentration adjacent to excavations and control the convergence of openings. But compared with the bolting system, the U-style steel yieldable support system was proved to be safety and efficient to offer superior protection in the bursting region in the Zhaogezhuang mine.

However, the circular shaped support system was proved to be easier to avoid resonance than the arched support in tremor influenced conditions. The natural frequency of the circular support was far from the bump's frequency range. In addition, circular shaped support systems can provide better ground control and reduce the concentration of ground pressure adjacent to the excavations.

Acknowledgements

The research is financially supported by the National Natural Science Foundation of China under grant No. 50704034, the Major State Basic Research Development Program Fund under grant No. 2006CB202203 and the State Scientific Support Fund under grant No. 2006BAK03B06. These supports are gratefully acknowledged.

References

1. Grouch, S.L. and Fairhurst, C. Mechanics of Coal Mine Bumps. AIME Transactions, 1974, 256. 317-322.
2. Zhao, B.J and Teng, X.J. Coal Bumps and Its Control. China Coal Industry Publishing House, 1995.
3. Burgert, W. and Lippmann, H. Models of Translatory Rock Bursting in Coal. International Journal of Rock Mechanics Mining Science & Geomechanics Abstract, 1981, 18. 285-294.
4. Maleki, H., Zahl, E.G. and Dunford, J.P. A Hybrid Statistical-Analytical Method for Assessing Violent Failure in U.S Coal Mines. DHHS (NIOSH) Publication, 1995, (99-114). 139-144
5. Salamon, M.D.G. Energy Considerations in rock Mechanics Fundamental Results. Int J S Afr. Inst. Min. Metall, 1984, 84. 237-246.
6. Lippmann, H. Mechanics of "Bumps" in Coal Mines: a Discussion of Violent Deformations in the Sides of Roadways in Coal Seams, 1987, 40(8).1033-1043.
7. Bräuner, G. Ground Pressure and Coal Bumps. China Coal Industry Publishing House, 1985.
8. Litwiniszyn, J. A Model for the Initiation of Coal-Gas Outbursts. International Journal of Rock Mechanics Mining Science & Geomechanics Abstract, 1985, 20(1). 39-46.
9. Pilecki, Z. Dynamic Analysis of Mining Tremor Impact on Excavation in Coal Mine. In: Proceedings of the International FLAC Symposium on Numerical Modeling in Geomechanics. Rotterdam, (Balkema, 1999).
10. Horyl, P. and Snuparek, R. Modelling of Effects of Rockbursts on Steel Arch Roadway Support Underground. In: Proceedings of Sixth International Symposium on Rockburst and Seismicity in Mines, (Australia, 2005).

DEVELOPMENT WORKING SUPPORT METHOD AND PRACTICE IN THE HIGH GROUND PRESSURE MINE

WEN-JIE WANG

College of Resources and Environmental Engineering, Wuhan University of Science and Technology

Wuha, 430081, P.R. China

Hubei Key Laboratory for Efficient Utilization and Agglomeration of Metallurgic Resources, WUST

Wuhan 430081, P.R. China

With the increase in underground mining depth and the ground pressure redistribution because of mining, the problem of development working failure is more serious because of the high ground pressure. It is the key to keep those development workings in stable condition, so it is very necessarily to take effective support method. Based on the theoretical analysis and the in-situ test, it is found that the depressurized mining and support can be taken to keep the development stability in the high stress area. According to the mining operation of ore deposit, the ground pressure surrounding the stope tunnel can be reduced by the depressurized mining technology, thus the tunnel destroy degree can be reduced and the stability capability of rock mass can be increased. Besides, the relations between depressurized mining and the support are analyzed. It indicates that the support can coordinate the tunnel deformation, but can not control the tunnel distortion. Therefore, the support form and the parameters can be choiced based on the stress reduction degree after mined by depressurized mining method. Based on this study, the method is successfully applied in the mine, and the results show that the depressurized mining and support can keep the tunnel in stable condition.

1 Introduction

In underground mining, the safety due to ground pressure distribution is a serious problem. The slope stress is a continuous redistribution due to mining, which immediately influences the stability of stope. Especially with regards to weak rock, the slope failure is very serious because of the ground pressure redistribution. With the increase in mining depth, more and more underground mines are facing this problem. If the ground pressure of the weak surrounding rock mass is very high, the ore may be lost permanently due to the damaged development tunnels which are inaccessible due to safety reasons. It is the key to keep those developments working in stable condition to guarantee safe production and to effectively convey the support method.

In regards to the ore body's high ground presses mining characteristics, many researchers and mining engineers have obtained remarkable results through explorations and practice of different research methods for

many years. Their results include many ground pressure distribution rules and stress control methods. These methods can be summarized as three types: supporting[1-3], filling, and depressurized mining[4-5]. Furthermore, many researchers have directed the tunnel support through estimating the parameters of rock mass deformation and strength based on the different standards for engineering classification of rock masses[6-7]. However, the three main factors that affect development stability are ground pressures, rock mass strength, and the support method. Therefore, it is the key to keep the development workings stable to decrease ground pressures, increase the rock mass strength and choose the reasonable support method.

2 The Principle of Depressurized Support

The depressurized support refers to keep the tunnel in stable with depressurized mining and support method. The depressurized mining refers to using the stress transfer principle to release ground pressure by some project measures, so the tunnel will be stable. The depressurized mining technology is mainly divided into the vertical depressurized and the horizontal depressurized craft. The vertical depressurized means part or completely transfer the vertical pressure to around area. The rock mass lower the pressure arch only bear its weight, so the ore can be mined easily because of the ground pressure decreased. The horizontal depressurized means isolation the horizontal stress, forms the area of horizontal stress reduced, so the hazard will be reduced[5]. Now, the depressurized methods mainly include three methods. The first method is formation slot, joint-cutting, drill hole or blasting loosely in the tunnel. The second method is development the special-purpose depressurized tunnel nearby the protected tunnel. The third method is reduced the pressure by mining or the tunnel be arranged in the low stress area [8]. The three depressurized methods may be called the peripheral depressurized, the tunnel depressurized and the mining depressurized.

The Depressurized mining method is not reduce the stress of stoping region by mining, but changes the stress distribution characteristic and the rule by the first sublevel mining, so the new distribution characteristic of high stress region and low stress region may be formed. Based on the rock mass stress redistribution rule and characteristic, the under level project can be arranged in the low stress region to ensure the stability through the reasonable design parameters choice and the stope structural arrangement. So, the depressurized mining mainly includes two aspects. One is depressurizing of ground pressures, which means to form low stress scope under the sublevel by the depressurized sublevel mining; Another is mining, which includes the depressurized sublevel mining and the under sublevel mining, but it is the successful key that the reasonable stope structure arrange and the stope design parameters choice.

Therefore, the principle of depressurized support is that the ore be mined with depressurized mining method firstly, then the development be supported with some effect method.

3 The Analysis of Relation between Depressurized and Support

In order to study the relations between depressurized and support and the influence of depressurized support on development stability. According to the conditions of depressurized mining and no depressurized, the paper not only analyze the mechanics of rock-bolt support but also analyze the relation of depressurized mining and supporting parameters based on different numerical analysis models. Which provides the theory evidence for the rock-bolt support parameters selection. The numerical analysis projects is shown in table1.

Table1 The rock-bolt support numerical analysis projects

	No support			Support		
Depressurized	0.6m×0.6m	0.8m×0.8m	0.6m×0.6m	0.8m×0.8m	0.6m×0.6m	0.8m×0.8m
No depressurized	0.6m×0.6m	0.8m×0.8m	0.6m×0.6m	0.8m×0.8m	0.6m×0.6m	0.8m×0.8m

The maximal falling displacement, the monitor maximal displacement and the maximal rock-bolt axial strength are shown in table 2. The table 2 data shown that the difference of tunnel convergence quantity which supported with different rock-bolt parameters is very small in the same stress condition. Which shown that the rock-bolt supporting method can not control the tunnel distortion. So the function of rock-bolt support can not control the tunnel distortion, the function main be corresponding the distortion.

Table 2. The contrast of different projects numerical calculate results

Results	Not depressurized				Depressurized			
	0.6*0.6	0.8*0.8	1.0*1.0	No support	0.6*0.6	0.8*0.8	1.0*1.0	No support
Maximal displacement (mm)	3.780	4.150	4.180	4.120	2.480	2.710	2.730	2.740
Arch crown monitor(mm)	3.120	3.231	3.290	3.701	2.073	2.155	2.195	2.469
Arch corner monitor (mm)	2.376	2.335	2.518	2.695	1.586	1.556	1.691	1.800
Bilateral monitor (mm)	1.214	1.238	1.319	1.397	0.785	0.808	0.871	0.923
Maximal axial strength (MPa)	3.564	3.785	4.779	-	2.605	2.725	3.540	-

The anchor support cannot effectively control tunnel distortion, but it is very obvious to improve the arch roof stress condition, as in figure 1 and figure 2. In the same stress condition, the vertical stress reduced scope and degree are maximal in the roof if the tunnel do not support with rock-bolt. After supported the tunnel with different anchor support parameters, the vertical stress reduced scope and degree of arch roof have reduced obviously. Moreover, the support parameters are more smaller that the change of stress are more smaller. Which show that the tunnel roof anchor parameters are smaller and the rock-bolt is more denser, its roof stress variation is smaller. Obviously, the rock-bolt support can improve the rock mass stress condition of tunnel roof.

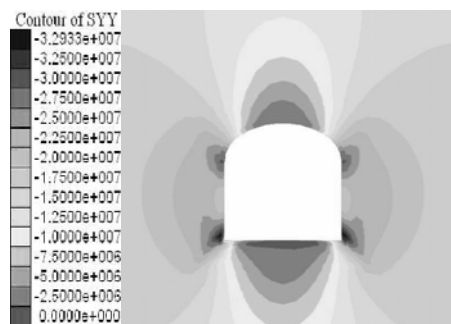


Figure1 Distribution of vertical stress without support

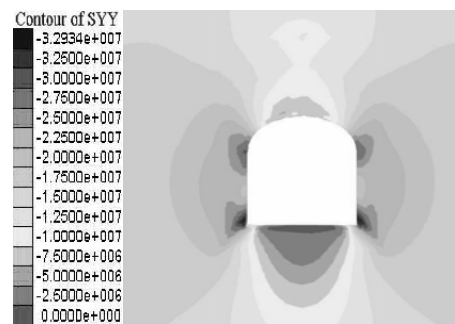


Figure2 Distribution of vertical stress with rock-bolts support

The data of 3 are change rate of maximal roof falling displacement, the measuring point displacement and the rock-bolt maximum axial strength in the condition of no support and the same support parameters. In the conditions of release pressure 30%, the rate of displacement change is basically between 33%~35% and the rate

of maximum rock-bolt axial strength change is between 25%~28%. So, the depressurized degree affect the tunnel distortion extent and the rock-bolt supporting effect. therefore, the depressurized degree is more higher and more advantageous to the tunnel stability. Comparing the change rate of same support parameters in the different ground presses condition and the change rate of different support parameters in the same ground presses condition, the rate of tunnel distortion and the plastic area size caused by depressurized are bigger than the rate of caused by changed supporting parameters. Which show that the method of depressurized mining is better than the method of changing support parameters regarding the tunnel stable under certain conditions.

Table3. The analyse results change rate contrast of rock-bolt support

Changing rate(%)	Support parameters			
	0.6*0.6	0.8*0.8	1.0*1.0	No support
Maximal roof falling displacement	34.39	34.69	34.69	33.50
Arch crown monitor	33.56	33.30	33.28	33.29
Arch corner monitor	33.25	33.36	32.84	33.21
Bilateral monitor	35.34	34.73	33.97	33.93
Maximal axial strength	26.91	28.01	25.93	-

The numerical analysis result shown that the rock-bolt support does not control tunnel distortion size but coordinate the tunnel distortion. The support can improve the stress condition of tunnel arch crown rock mass, thus the tunnel can be kept in stable because of the rock mass self-stabilization. Therefore, the numerical analysis result indicated that the depressurized mining has the important influence to the maintenance tunnel stability, but the support function cannot be neglected. The depressurized and support should be considered together to keep the high stress tunnel in stability.

4 Project Test

The Chambishi copper mine, located at the northern Chambishi basin of Zambia, is main a metamorphosed sedimentary ore deposit. The ore dip angle is small and the ore body thickness is also small. The average thickness of ore body is 10m. The joint fissures of ore body and rock mass are developed, so the stability of stope is very bad. The activity of ground presses is frequent, and the drift often fails because of stress redistribution, which affect the production badly. The spot investigation result shows that the main ground pressed of Chambishi copper mine is the vertical stress, and it act on the ore and rock mass centralized. So the tunnel and stope often fail because of high stress. Therefore, the copper mine test the sublevel depressurized caving method.

According to the Chambishi copper mine rock-bolt support numerical analysis result, it can be take that reducing the support intensity in the depressurized mining section, namely increasing the rock-bolt support parameters and reducing the rock-bolt number. But in the area of not mined by depressurized method, the reverse measures can be adopted to maintenance the tunnel stable.

Moreover, the numerical analysis result indicated that the rock-bolt axial strength and destroyed scope are biggest in the arch crown region. So, the small rock-bolt support parameters can be used to increase the arch

crown support intensity. But the big rock-bolt support parameters can be used in the other area. According to the principle, the Chambishi copper mine rock-bolt parameters are arch crown 0.8m~1.0m and other area 1.0m~1.2m, the rock-bolt array pitch is 1.0m~1.2m after depressurized mining. Regarding the rock mass very cracked area, the arch crown support parameter is 0.6m~0.8m. the outside arch crown area support parameter is 0.8m~1.0m and the rock-bolt array pitch also is 0.8m~1.0m.

After depressurized and supported, the tunnel destroyed phenomenon is obvious reduction, and has made good mining effect. The data of table 4 and table 5 are 529m level three panel 6# development tunnel monitor convergence record, together 11 row of monitoring points. The tunnel is developed by development and support together construction technology, supported by 0.8m×0.8m rock-bolt parameters.

The monitor data indicated that after Chambishi copper mine mined by depressurized mining and rock-bolt support, only the tunnel distortion of 5th row and 9th row position is big, other position distortion is small. Using the depressurized and support technology, the ground pressure is controlled effectively, the breakage of development also decreased, the ore recovery ratio effective increased.

Table 4. The roof vertical displacement data of convergence monitoring(unit:mm)

Date	Monitoring points										
	1	2	3	4	5	6	7	8	9	10	11
06-10-6	0.00	0.00	0.00	0.00	0.00	0.00	0.00	0.00	0.00	0.00	0.00
06-10-10	2.09	-2.25	2.16	-5.80	-45.76	-0.10	0.73	-0.15	32.37	-0.07	5.68
06-10-25	3.35	-2.62	-56.76	-7.46	-45.74	-3.87	20.10	1.36	33.16	-2.45	5.19
06-11-3	1.16	-5.53	0.05	-7.15	-46.36	-4.05	3.72	-0.45	12.26	-6.10	1.07
06-11-17	7.89	-1.27	2.99	-8.10		-6.34	13.96	2.91	11.54		0.68

Table 5. The rorizon displacement data of convergence monitoring(unit:mm)

Date	Monitoring points										
	1	2	3	4	5	6	7	8	9	10	11
06-10-6	0.00	0.00	0.00	0.00	0.00	0.00	0.00	0.00	0.00	0.00	0.00
06-10-10	-3.03	-1.10	-0.01	-1.14	88.42	-0.82	1.39	-0.04	-0.44	0.46	-5.73
06-10-25	-0.75	-0.55	-0.69	-1.11	85.40	-1.62	-33.63	-2.52	-2.56	-1.34	-7.05
06-11-3	-3.09	-0.89	-2.13	-1.30	84.53	-4.41	-1.96	-2.42	5.28	-2.16	-7.12
06-11-17	-2.94	-0.60	-0.39	10.72		-1.03	-4.81	-1.33	8.71		-10.98

5 Conclusions

The theoretical and numerical analysis indicated that the tunnels at high stress area may reduce the ground pressure by depressurized method, and can be kept stable through the supporting method and parameters. However, the depressurized degree affects the tunnel distortion size. The numerical analysis of the rock-bolt support system shows that the support may coordinate the tunnel distortion, but cannot control the tunnel

distortion. The testing results in the Chambishi copper mine show that the method is feasible to stabilize the high ground stress development.

Acknowledgement

The financial support provided by the National Natural Science Foundation of China (Grant No. 50804036)

References

1. He, T.J. Soft-Rock Drifts Supported by Releasing Pressure With Guided Roadway. *Journal of Huainan Institute of Technology*, 1999, 19(1). 27-30.
2. Yang, X.A., Huang, H.W. and Liu, B.W. Study on the Deformation and Support of Weak Rock Mass Roadway in the Jinchuan Nickel Mine. *J.Xiangtan min. inst.*, 2000, 15(3).12-16.
3. Zhu, J.M., Gao, Q. and Lin, X.P. Study on the Once Reinforced Enhanced Support Techniques for Stope Drift in the High-Stress Fractured Ore Body and Its Application. *Journal of Engineering Geology*, 2002,10(4). 400-403.
4. Feng, S.H. and Huang, B.X. The Principle and Testing of Releasing Rock Stress Support of the Soft Rock Tunnel Filled with Substance Behind It. *China Mining Magazine*, 1994, 3(5).42-45.
5. Xie, S.J. Depressurized Mining. *Mine Technology*, 1992, (2).19-21.
6. Carranza-Torres, C. and Fairhurst, C. The Elasto-Plastic Response of Underground Excavations in Rock Masses that Satisfy the Hoek-Brown Failure Criterion. *Int. J. Rock Mech. and Min. Sci.*, 1999, 36(6). 777-809.
7. Hoek, E. Reliability of Hoek-Brown Estimates of Rock Mass Properties and their Impact on Design, *Int. J. Rock Mech. and Min. Sci.*, 1998, 35(1). 63-68.
8. Hou, C.J. Development Way of Underground Pressure and Technique of Preparation Workings, *Ground Pressure and Strata Control*, 1995, 3(4). 105-108.

LABORATORY SIMULATION OF MICROSEISMICITY OBSERVED AT SOUTHERN LONGWALL COLLIERY, AUSTRALIA

XUN LUO and JIM BOLAND

CSIRO Exploration and Mining, Australia,

PETER HATHERLY

The University of Sydney, Australia

MANABU UTAGAWA

2National Institute of Advanced Industrial Science and technology, Japan

In underground longwall coal mining, the caving process is closely associated with rock failure induced by the abutment stress near the longwall face. Knowledge of the relationship between the characteristics of the rock failure and the abutment stress should lead to improved understanding of longwall geomechanics and mining hazards around the face. A study on the relationship between rock failure processes under uniaxial loading stresses was carried out in laboratory on Helidon sandstone samples. Twelve single component mini acoustic sensors and four strain gauges were placed on the surface of the samples to measure the acoustic emissions and strain changes associated with sample stressing. The laboratory results were then compared with weak seismic events observed at LW704 of Southern Colliery in order to interpret roof fracturing under periodic abutment stress. This paper presents the results from the laboratory tests and the comparison.

1 Introduction

In underground longwall coal mining, dynamic loading and unloading processes occur in the roof and floor rock layers with the advance of the working face. The abutment stress near the longwall face induces rock failures and controls the roof caving processes. Knowledge of the relationship between the characteristics of the rock failure and the abutment stress should lead to improved understanding of longwall geomechanics and mining hazards around the face.

The longwall loading process can be estimated using numerical modelling on three dimensional models. This has been widely used in longwall panel design, strata control planning and mining machinery selection. The stress changes during mining can be validated using measurements of stress at selected locations [1, 2]. The stress changes in coal and rock mass can change seismic properties. Novozhilov and Dobrynin [3] firstly used seismic method to detect rock stress changes in a coal mine for the prediction of coal outbursts. Seismic tomography using the coal cutter as the source has been used for roof stress condition mapping [4, 5]. Microseismic events observed in a coal mine were found to be closely correlated with abutment stress [6]. A periodic roof loading pattern was observed in a longwall coal panel from cluster locations of microseismic events [7]. Kelly et al. used microseismic monitoring for longwall stress estimation [8]. However, the relationship between rock failures due to periodic loading stress and associated the microseismic events has not been well explored.

In this paper, we investigate this relationship through a study of the total seismicity occurring in a longwall panel at Southern Colliery, Australia. This style of analysis has similarities to acoustic emission experiments

undertaken on rock samples undergoing destructive testing. For comparison, a study of the acoustic emissions associated with testing the strength of a sample of Helidon sandstone was also conducted.

2 Determination of cyclic fracturing progress – A case study at Southern Colliery

A microseismic monitoring was carried out at Southern Colliery to investigate the fracture characteristics of the heavy roof in longwall panel 704 (LW704), associated with mining [9]. The microseismic system comprised 20 triaxial geophones installed in 4 boreholes, A, B, C, and D (Figure 1). Borehole C is located right in the centre of the panel. For the five triaxial geophones in borehole C, the bottom geophone is installed in the immediate roof of the coal seam being mined and the top geophone is 110 m above the seam. Five sections of the roof rock near the borehole were divided for the analysis (Figure 2). With the longwall face approached, each of the rock blocks should experience variable loading process and that should have correlation with rock fracturing process.

The analysis of in-situ rock failure under the abutment stress was carried out through determining the number of seismic events occurring in the vicinity of borehole C. Each event was considered to be the result of a rock fracture and the total seismic activity occurring in the vicinity of the borehole provides an indication of the extent and timing of the rock failure induced by abutment stresses leading to ultimate rock failure through caving.

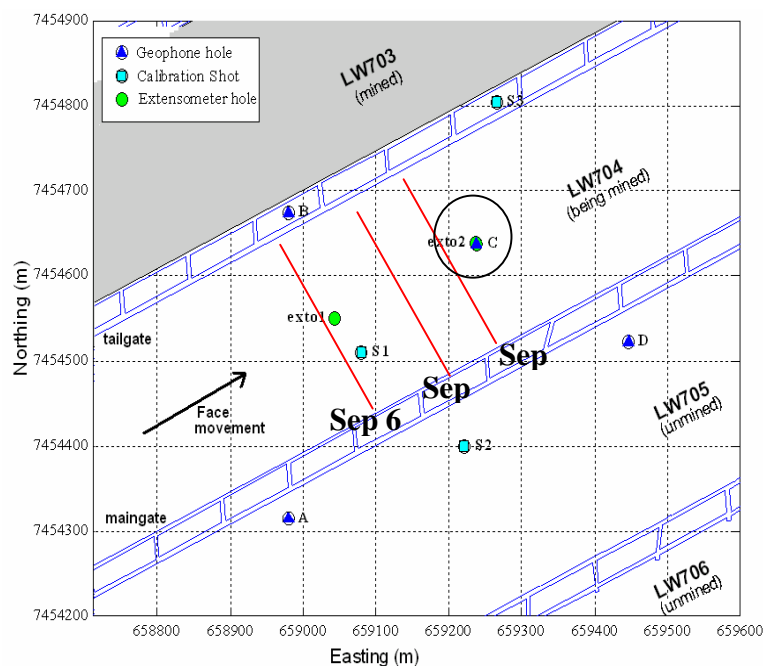


Figure 1. Plan view showing the location of borehole C at LW704 of Southern Colliery. The arrow indicates the progress direction of the working face. The longwall face positions on Sep 6, 22 and 29, 2000 are marked. The radius of the circle centred at borehole C is 50 m. The seismic events in this analysed are located within this region.

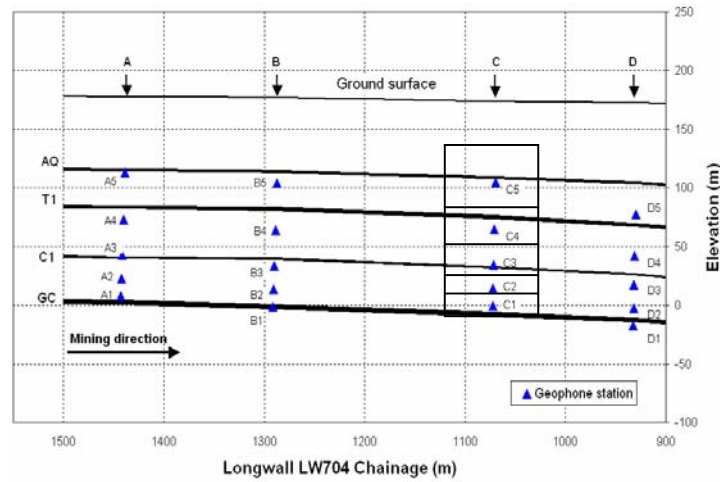


Figure 2. Cross section showing the locations of the geophone in borehole C, viewed side on to the longwall panel and the regions into which the weak events were assigned. The roof rocks near borehole C are divided into 5 regions with diameter of 100 m and thickness varies between 20-50 m depending on the spacing of the geophones.

In this microseismic experiment, many small seismic events were detected. These events are so weak so that they were only recorded by 1-3 geophones in single borehole. Because the weak events were only detected at one borehole, it was not possible to locate them on the basis of the travel times to the different boreholes and so only the hypocentral distances of the events from the borehole could be estimated on the basis of the time difference between the P- and S-wave arrivals (S-P times). It was found that the majority of the weak events had S-P times less than 15 ms. This suggests that the events were within 50 m of the borehole (assuming P-wave velocity $V_p=3.8$ km/s and S-wave velocity $V_s=1.9$ km/s). Many of the events actually occurred closer than this to the borehole because their P- and S-waves could not be separated.

The elevations of the events could also be estimated. If an event was recorded by only one geophone, it was considered to be at the elevation of that geophone. If it was recorded by several geophones, the geophone with the highest amplitude and earliest arrival time was considered to be closest to the event. Through this approach, the location errors should be less than half of the spacing between two adjacent geophones.

There were more than 10,000 weak events recorded by the geophones in borehole C. In Figure 3, the number of the events recorded per hour and assigned to the vicinity of each geophone is plotted against the longwall face position for the period September 1 to October 9, 1999. On September 1, the face was about 240 m from the borehole and on October 9 it was 25 m past the borehole. Unfortunately the microseismic system was not operating between October 2-4 and no events were recorded during this critical period. After the passing of the longwall face on October 6, and with the exception of the top geophone, all of the geophones ceased to function.

As seen in Figure 3, the amount of seismicity generally increased with the approach of the longwall face and with most occurring at the bottom geophone, C1 and least occurring at the top, geophone C5. The activity started when the face was about 200 m away from the borehole and all geophones recorded a similar pattern of activity which can be correlated with mine production. When there was no production, the seismicity was significantly reduced.

To enable the seismicity to be studied independently of the periods with no production, the number of events per shift in which there was production was determined for each geophone. As an example, Figure 4 shows the seismicity assigned to geophone C1.

Once the amount of seismicity exceeds about 50 events per shift, there is some degree of cyclicity evident in the data. There are local peaks (or troughs) occurring at about 14 m intervals. This may be associated with cyclic loading. In particular it is interesting to note that there were weighting events at the face on September 25 and 28, at the time the seismicity was at a local maximum and just prior to a lull in the amount of activity. It is also interesting to speculate as to when the front abutment passed by the borehole - on September 27 when there was a local maximum in the microseismic activity or in October when there is a peak in the microseismic activity just prior to the final caving and destruction of the geophones.

Examination of representative seismograms allows this proposition to be partially tested. Early seismograms (September 6) show both the P-and S-wave motions that are to be expected from failures involving a shear component of motion. Such seismograms continued through September 22 and up to at least October 4. However at later dates, events showing less distinct shear components increasingly start to. The decrease in the presence of the shear waves is presumable due to the change in the type of individual failures in the rock mass as its overall failure progresses. Certainly by the time the face had passed the borehole on October 6, the shear components of the seismic events had ceased and the activity was more representative of tensile failure.

On the basis of this general type of behaviour in the waveforms and when the peak of the seismicity occurred, it is considered more likely that the stress abutment was close to the longwall face and that the earlier local peaks in the seismicity are due to the cyclic caving and weighting behaviour experienced under the sandstone roof.

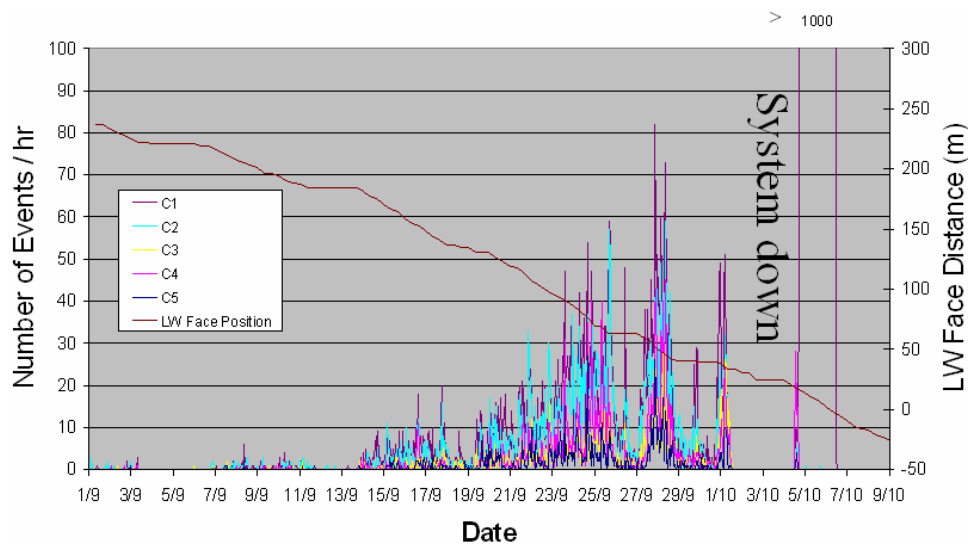


Figure 3. Hourly seismicity in the vicinity of each geophone between 1 Sep and 9 Oct. The distance of the longwall face to the borehole is also shown. Unfortunately the microseismic system here was not operating between 2-4 Oct. With the passing of the longwall face on 7 Oct, all geophones except the top geophone were destroyed by caving.

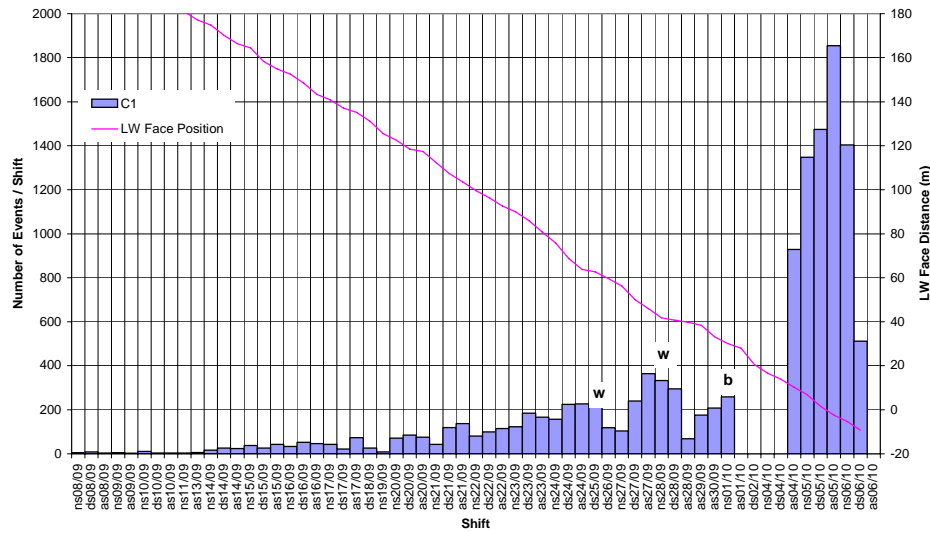


Figure 4. Seismicity at geophone C1 during shifts when production occurred. Weightings (w) occurred on dayshift 25/09 and nightshift 28/09. There was a blockage (b) on night shift 01/10 just as the seismic system was temporarily not available.

3 Acoustic emissions of sandstone under cyclic loading – A laboratory test

As part of this project it was intended to undertake acoustic emission tests on rock samples in a laboratory experiment intended to simulate the stress environment experienced under longwall mining. The results obtained under these controlled conditions could then be compared with the microseismic results obtained in longwall situations.

Two cylindrical samples of Helidon sandstone were cored from a block obtained from a dimension stone quarry. It is a clean, quartz-rich sandstone (~ 50% quartz), typical of the sandstones found in Australian coalfields. The samples had identical dimensions with a length of 58.82 mm and a diameter of 28.62 mm (Figure 5). Its UCS is typically about 40 MPa. The testing of the two samples was performed at the National Institute of Advanced Industrial Science and Technology, Japan. Initially it was intended to conduct the tests using a triaxial cell to provide confinement but unfortunately this equipment was not available at the time the experiment was undertaken. Uniaxial stress conditions could only be tested.

For the experiment, 12 single component mini acoustic sensors were placed on the surface of the samples at three levels. The sampling rate for the recording system measuring the acoustic emissions was 0.1 microseconds (10 MHz) per channel and all trigger information and acoustic waveforms were stored on a hard disk for later analysis. In conjunction with the acoustic monitoring, four strain gauges were placed on the samples to detect the changes in the strain with stress. One opposing pair was oriented in a radial direction and the other was oriented in the axial direction.

In the testing, satisfactory failure conditions were only achieved for one of the samples. The loading on this sample is shown in Figure 6 and was designed to simulate a periodic longwall caving situation. Prior to the shear failure at 41 MPa, there were three loading peaks at 22, 30 and 38 MPa followed by stress drops of between 8 and 12 MPa. The acoustic emissions recorded by sensors 1 and 2, are shown in Figure 7. Figure 8 shows the stress-strain curves recorded at the four strain gauges.

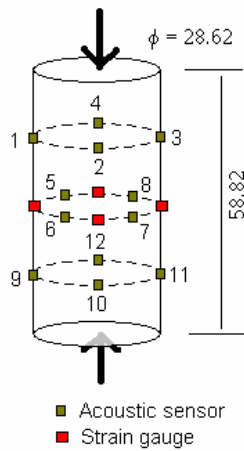


Figure 5. The arrangement for the 12 acoustic sensors and 4 strain gauges used for the acoustic emission experiments on samples of Helidon sandstone. An uniaxial loading force was applied in the directions of the arrows.

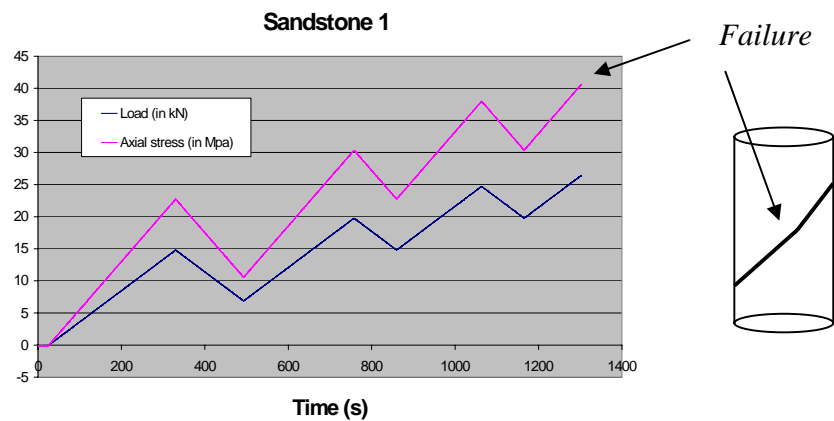


Figure 6. Stress, load and eventual fracture of the Helidon sandstone sample.

As shown by these figures, the occurrence of the acoustic emissions is directly related to the applied load. The emissions increase during the loading periods and decrease during the unloading. They start at a load of about 10 kN (15 MPa stress and 700 microstrain) and from the moment the load comes off on each cycle, there is an immediate decrease in the emissions. When the load comes back on, the acoustic emissions again start to build up, even though the initial loads are less than the previous peak. It also interesting to note that the peak in the emissions prior to the final failure occurred at an intermediate load of 20 kN (31 MPa and a strain of 1400 microstrain). Failure occurred at 26 kN (41 MPa and 1900 microstrain).

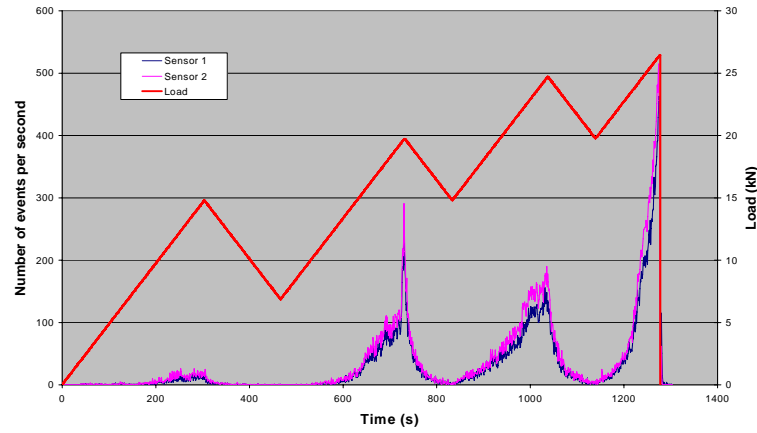


Figure 7. Axial load and associated acoustic emissions recorded at sensors 1 and 2.

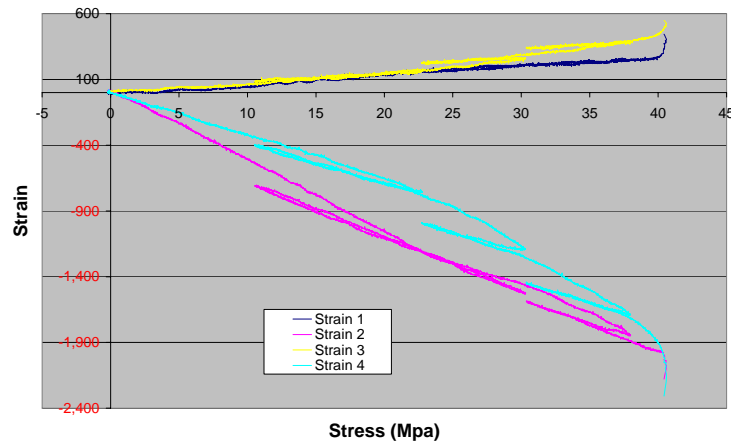


Figure 8. Stress-strain curves recorded by the strain gauges. The strains are microstrains with gauges 2 and 4 being the axial strains and 1 and 3 radial.

Given that only single component sensors could be used, identification of S-waves on the recorded waveforms proved to be difficult. As a general rule, a pattern whereby strong acoustic events were followed by groups of smaller events was observed. Events from typical strong and weak events recorded during a loading period are shown in Figure 9 and Figure 10. These waveforms are all normalised to the same nominal amplitude.

During the unloading periods, the number of the acoustic events decreased and they were generally weaker compared to those during the loading period. Unexpectedly, several strong events occurred during the unloading stages. An example of one of these is shown in Figure 11.

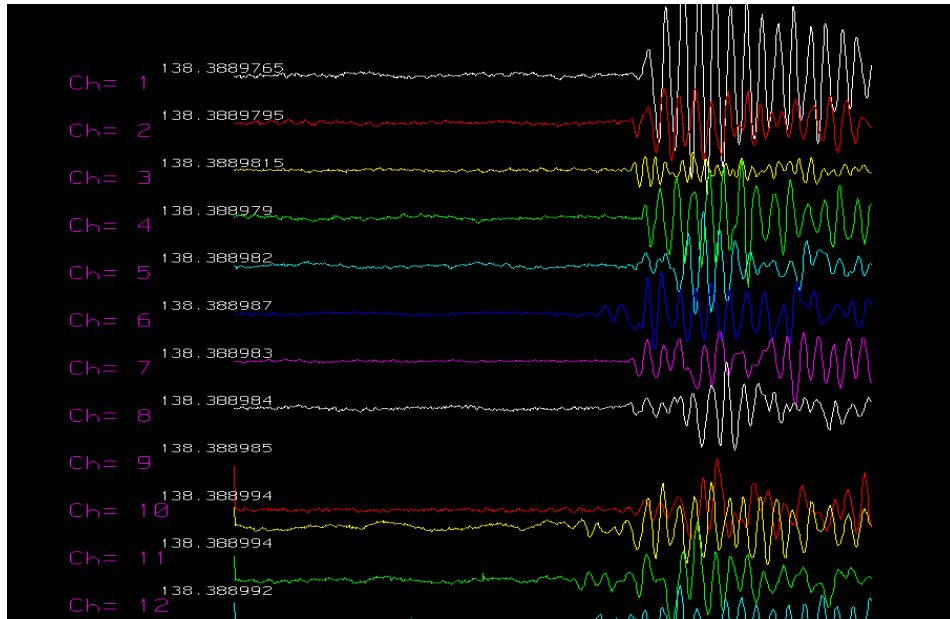


Figure 9. Acoustic waveforms from a strong event recorded during a loading period. The waveforms are normalised to the one nominal value.

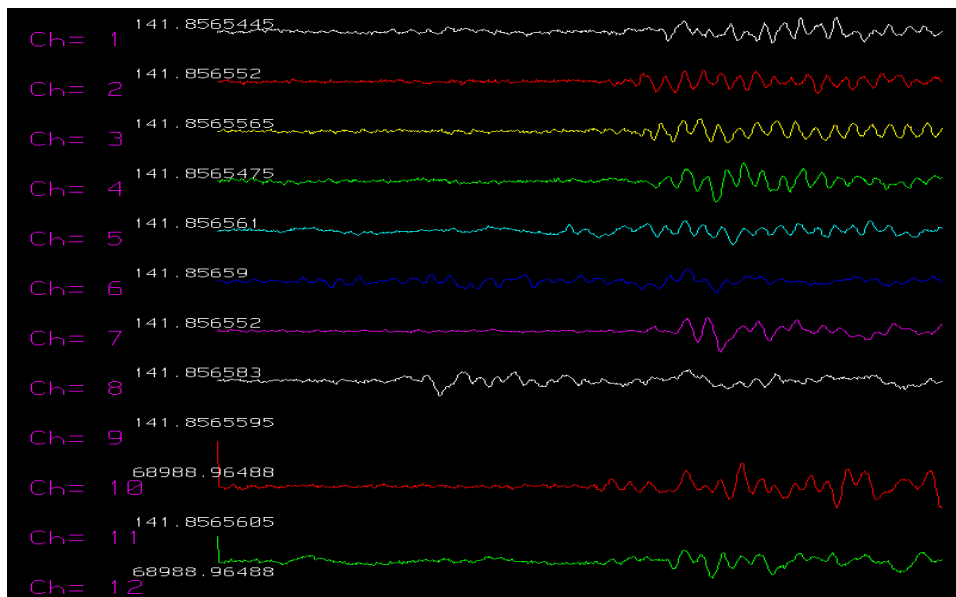


Figure 1. Normalised acoustic waveforms of a weaker event after the strong event, Figure 15.

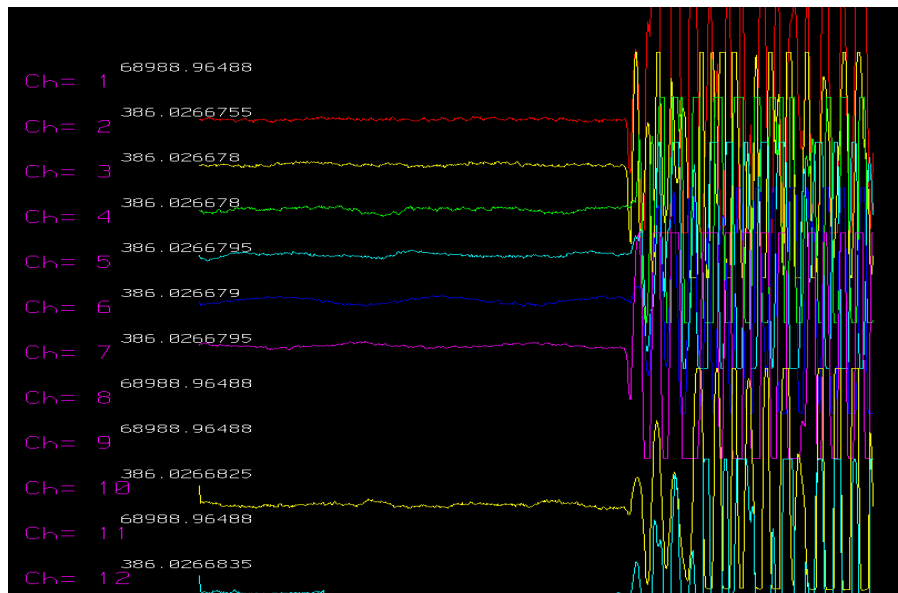


Figure 11. An example of a strong event observed during an unloading period. The waveforms are normalised against the same value as the previous waveforms.

4 Discussions

The pattern in the seismicity observed in the vicinity of the single geophone hole C in LW704 shows much similarity with the pattern of the acoustic emissions observed from the testing of the sample of Helidon sandstone. The activity started at levels of stress well below the strength of the rocks concerned and there was a sense of cyclicity in the results that can be related to pauses and decreases in the build up of stress. In the case of LW704 this arises through pauses in production and weighing cycles. Prior to both weighing events in LW704 immediately before the geophone hole, peaks in the microseismicity occurred.

From the acoustic emission study, it was observed that the acoustic emissions started at about 35% of the UCS and 0.07% strain. These figures are indicative of the values that might be required for the onset of microseismicity. Further acoustic emission studies using a range of rock types and loading conditions, preferable under triaxial conditions, is clearly an area worthy of further investigation.

References

1. Seymour, J.B., Tesarik, D.R., McKibbin, R.W. and Jones, F.M. Monitoring Mining-Induced Stress Changes with the Biaxial Stressmeter, in Proc. 5th Intern. Symp. on Field Measurements in Geomechanics, Dec. 1-3, 1999, Singapore, C.F. Leung, S.A. Tan, and K.K. Phoon, eds., Rotterdam: Balkema, pp. 55-60.
2. Zahl, E. G., Dunford, J.P., Tesarik, D.R., Larson, M.K., and Chen, J. 2001, Development of Stress Measurements and Instrument Placement Techniques for Longwall Coal, in Proc. 38th U.S. Rock Mechanics Symposium, July 7-10, 2001, Washington, D.C., D. Ellsworth, J.P. Tinucci and K.A. Heasley, eds., Rotterdam: Balkema, pp. 327-335.
3. Novozhilov, Yu. L. and Dobrynin, V. I. Measurement of stress in a coal mass by the seismic method, Journal of Mining Science, 1969, 5(2). 98-101.
4. Westman, E. C., Haramy, K. Y. and Rock, A. D. "Seismic tomography for longwall stress analysis, Rock Mechanics," in Proc. 2nd Rock Mechanics Symp., Montreal, Quebec, pp. 397-403, June 19-21, 1996.

5. Luo, X., King, A. and Van, de Werken M., 2009, Tomographic imaging of rock conditions ahead of mining using the shearer as a seismic source – A feasibility study, IEEE Trans. Geoscience and Remote Sensing, TGRS - 2008 – 00498.R1 (In printing).
6. Hatherly, P., Luo, X., McKanvanagh, B., Dixon, R., Devey, D., 1995, Seismic monitoring for mapping longwall caving at Gordonstone Mine, in Proc. Bowen Basin Symp. 1995, Geological Society of Australia, Mackay Qld, 1-3, October 1995, pp 117-126.
7. Luo, X. and Hatherly, P. 1998, Understanding of high gas emissions at Appin Colliery through microseismic monitoring, in Proc. Int. Mining Tech.' 98 Symp. (eds. D. Zhu, S. Jiang and R. Wang), Chingqing, China, Oct 14-16, 1998, pp74-79.
8. Kelly, M. and Luo, X.. S. Craig, 2002, Integrating tools for longwall geomechanics assessment, Intern. J. Rock Mechanics and Mining Sciences. 39, 661-676.
9. Guo, H., Luo, X., Zhou, B, Poulsen, BA, Kelly, M, Craig, S, Adhikary, D, LeBlanc Smith, G, Caris, C, Yago, J, A King, A, Ross, J and Coulthard, M., 2000. Southern Colliery LW704 Geotechnical Study, CSIRO Exploration and Mining Report 759.

EFFECT OF STRESS WAVES ON THE DANGER OF ROCK BURST

AI-HONG LU, XIAN-BIAO MAO and HAI-SHUN LIU

*State Key Laboratory for Geomechanics & Deep Underground Engineering, China University of Mining &
Technology, Xuzhou, Jiangsu, 221008, P.R. China*

*School of Sciences, China University of Mining & Technology
Xuzhou, Jiangsu, 221008, P.R. China*

The energy accumulation and its position are two main factors used for judging rock burst occurring. An energy density criterion to distinguish the danger of rock burst was proposed based on this assumption. The process of the energy accumulation and the effect of the intensity of stress wave p_{\max} on the energy accumulation was simulated and analyzed by employing ANSYS/LS-DYNA, and the characteristic and the position of the energy accumulation was obtained. Research results show that the stress wave is an important factor in energy accumulation in rocks near excavation boundary and it can result in rock burst; moreover, its intensity, p_{\max} , determines the value of the maximal energy density $(U_d)_{\max}$ and the distance between the position and the surrounding roadway, namely, the value of energy density factor k . The study results are useful to the study of rock burst mechanism and the forecast of rock burst.

1 Introduction

Rock burst is a typical dynamic disaster in mining which has been increasing continually and has been become a serious threat to safe mining. This disaster is a complex dynamic instability accompanied by lots of coal powder outburst. A series of theories [1-5] were put forth in a series based on the systemic studies on the mechanism of origination of the rock burst and its prevention. However, there is not an accepted theory of the mechanism and formation of rock burst because it is a type of complicated dynamic instability. Therefore, it is of urgent importance to study the forming mechanism of the dynamic hazard of such as rock burst.

The stress wave may be triggered by driving blasting, roof breaking, working face weighting, and seismic waves in the mining process; thus external disturbances are often introduced for the occurrence of the rock burst. Although many studies [6-13] have been performed on the influence of dynamic disturbance on rock burst, the energy accumulation and its characteristics still need further research because of the complexity and uncertainty of stress waves. Further relative research may contribute to the understanding of the rock burst mechanism and the prevention of rock burst induced by stress.

The stability of the surrounding rock mass and energy accumulation characteristics were investigated by simplifying the driving blasting, dynamic disturbance (roof breaking, working face weighting, etc.) as stress

waves, and the effects of stress waves on the danger of rock burst was analyzed.

2 Energy Density Criterion of Rock Burst

Rock burst is a dynamic phenomenon by nature; part of the rock body is destroyed quickly and releases a great deal of transformative energy. The intensity of the rock burst lies on the dispersion between the accumulation energy and the energy consumed by the wall rock ruptured. The more that energy is accumulated, the less that energy is consumed, and the more likely a violent rock burst is likely to happen.

The rock burst is nearly correlative with the local energy accumulation of rock mass. Whether the accumulative energy releases relies on two factors: one is the degree of the local energy accumulation, it can be token by energy density U_d ; and the other is the position of the energy accumulation, it can be obtained by the vertical distance between the position of the maximum energy density $(U_d)_{\max}$ and the boundary on the roadway side. Obviously, the bigger the value of $(U_d)_{\max}$ is, the higher degree the energy accumulation is. If the position is near the boundary of the roadway side and the stress of the wall rock is close to the strength of the rock mass, the rock burst can occur easily. Similarly the closer the distance between the position of the maximum energy density $(U_d)_{\max}$ and the boundary of the roadway side, the less energy consumed, so rock burst is easy to occur. Thus a combined quantity of maximum energy density $(U_d)_{\max}$ and the distance d between the position of the maximum energy density $(U_d)_{\max}$ and the boundary of the roadway side is applied to weigh the fatalness of rock burst in roadway wall rock. Obviously, it is reasonable and feasible. Let

$$k = \frac{(U_d)_{\max}}{d} \quad (1)$$

From formula (1), it can be seen that when the value of $(U_d)_{\max}$ is big and the distance d is small, the value of k is bigger, the fatalness of rock burst is bigger; contrarily, when the value of $(U_d)_{\max}$ is small and the distance d is big, the value of k is smaller, the fatalness of rock burst is smaller. Obviously, the value of k reflects the degree of energy accumulation and its position; we name k as energy density factor. When k exceeds a certain value, rock burst occurs. The criterion is denoted as k^* , here, k^* is the critical energy density factor. So the condition whether rock burst occurs can be written as:

$$k \geq k^* \quad (2)$$

Critical energy density factor k^* is related to the rock features and structure of wall rock, so its value must be determined by experiment, practical measurement and mass rock burst data and so on. And energy density factor of wall rock can be obtained by numerical simulation.

3 Numerical Simulation Model and Scheme

3.1 Numerical Simulation Model

The rock burst occurs nearly correlative to the depth of the roadway. So the influence of the upper terrane must be taken into account. In the paper the implicit function of LS-DYNA is applied to analyze the action of the upper terrane on the roadway structure before analyzing the action of the stress wave. Then, the result is added on the structure as an initial stress; finally, the explicit function of the LS-DYNA software is applied to analyze the action of the stress wave on the structure. According to the request of the implicit analysis, the numerical simulation model of static analysis, as shown in Fig.1 (a). horizontal chain poles restriction are set on the both sides of the model to simulate the boundless boundaries; the constrained boundary is set on the bottom of the model; and the top of the model is added the even distributing load q to simulate the upper terrane's action, and the value of the q is determined by the formula below.

$$q = \gamma H \quad (3)$$

where γ is the average density of the upper terrane's rock mass ($\gamma = 2 \times 10^4 \text{ N/m}^3$); H is the depth of roadway.

When analyzing the stress and energy accumulation of the roadway wall rock, due to the request of the explicit analysis, the non-reflect boundaries are set on the both sides of the model to eliminate the effect of the boundary on the stress wave spread; the constrained boundary is set on the bottom of the model; and the freedom boundary is set on the top of the model; Then a disturbed stress wave $p(t)$ is added on certain scope of the middle part of the left side of the model. The disturbed stress wave $p(t)$ is shown in Fig.2, to simulate the disturbed load aroused by the driving exploder of the roadway nearby or the ground pressure of coal face of stope. Finite element girding of roadway's surrounding rock is shown in Fig.1 (b). The mechanical parameters of the roadway's roof, floor and the coal seam are listed in Table 1.

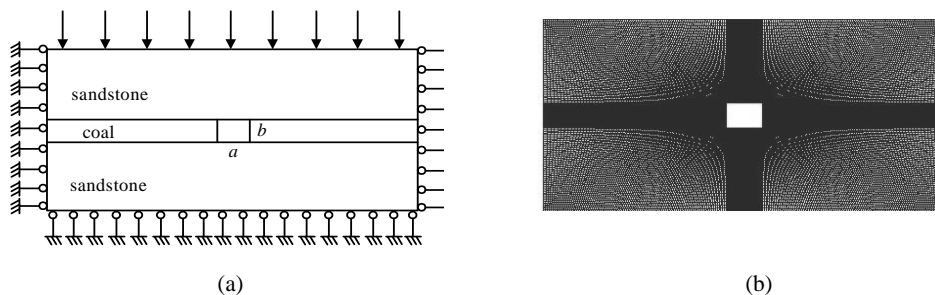


Figure 1 Numerical simulation model of roadway's surrounding rock and its finite element girding

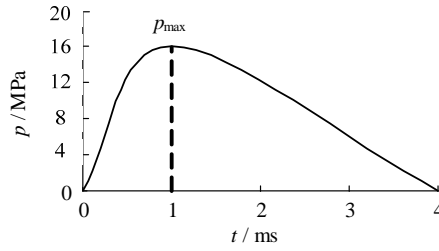


Figure 2 The stress disturbance loading curve

Table 1 Mechanical parameters of roadway's surrounding rock

lithology	thickness h/m	Elastic modulus E/GPa	Poisson's ratio μ	Compressive strength σ_c/MPa	Bon strength c/MPa	Internalfrictional angle $\varphi/^\circ$
sandstone	11	15	0.30	20	2.5	41
coal	3	5	0.35	5	1.5	30
sandstone	11	15	0.30	20	2.5	41

3.2 Numerical Simulation Scheme

According to the some related blasting regulations[14], Peak stress of blast load can be calculated by formula (4) based on blast hole position and actual parameters of position of the blast hole and powdered charge. It is concluded from calculation that Peak stress of blast load is ranged from 5MPa~20MPa.

$$p_{\max} = \frac{139.97}{Z} + \frac{844.81}{Z^2} + \frac{2.154}{Z^3} - 0.8034 \quad (4)$$

where, $Z = R/Q^{1/3}$ is scaled distance, R is the distance between blast hole and the acting surface of blast load, Q is powdered charge of the blast hole. The formula was obtained by statistical analysis of present blast load.

Considering the action characters of stress wave, this paper mainly analyzes the influence of time (t) and the intensity of stress wave p_{\max} . According Peak Stress of blast load, take Peak Stress of blast load $p_{\max} = 5\text{MPa}$ 、 10MPa 、 15MPa 、 20MPa 、 20MPa four cases to analyze.

4 Energy Accumulation Features of Roadways Surrounding Rock

4.1 Variation of Energy Accumulation Features with Time

On account of the static analysis is the foundation of the dynamic analysis, the numerical system considers the initial stress-strain state as zero strain energy, so the value of the numeric is the strain energy increment. When $H=600\text{m}$, $p_{\max}=10\text{MPa}$, time t is 0ms、0.4ms、0.8ms、0.12ms、0.16ms、2.0ms respectively, the roadway wall rock energy density distribution plot is shown in fig.3 and the corresponding $(U_d)_{\max}$ 、the distance d between its position and the surrounding roadway and the energy density factor k are listed in Table 2.

Table 2 Variation of $(U_d)_{\max}$, d with time t

t / ms	0.4	0.8	1.2	1.6	2.0
$(U_d)_{\max} / \text{J} \cdot \text{m}^{-3}$	1.186×10^6	1.469×10^6	1.553×10^6	1.406×10^6	1.496×10^6
d / m	0.11	0.12	0.40	0.31	0.10

From Fig.3 and Table 2, it can be seen that : (1) With the stress wave spreading, the value of the maximum energy density and its position is changing , that illuminates the energy density of wall rock is distributed over again for the action of the stress wave, some area energy accumulated and some area reduced; (2) The position of the maximum energy density $(U_d)_{\max}$, firstly lies on the top of the roadway side, and the value is little; with the stress wave spreading the position of $(U_d)_{\max}$ moves to the below and inside of the roadway side, and the value of the $(U_d)_{\max}$ is increasing.

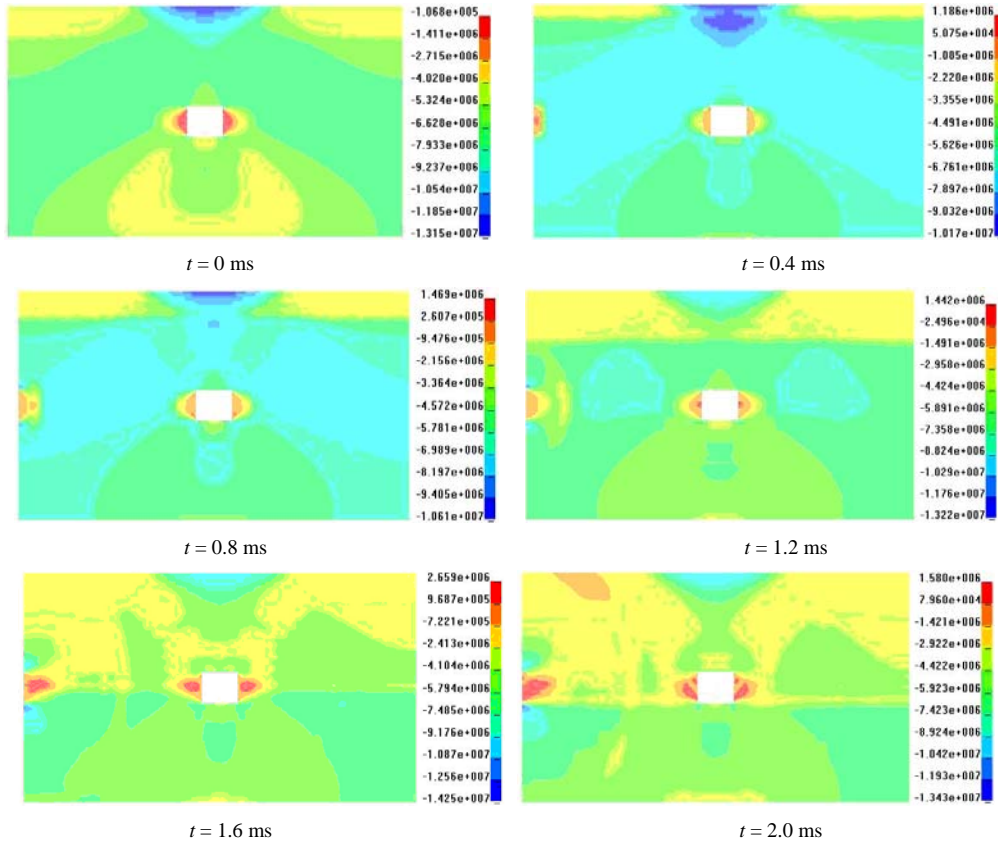


Figure 3 The energy density distribution of roadways surrounding rock changed with time

4.2 Variation of Energy Accumulation Features with Intensity of Stress Wave

Set $t = 2.5 \text{ ms}$ when analyzing the effect of the intensity of stress wave p_{\max} on energy accumulation of the wall rock. From simulation the roadway wall rock energy density distribution plots of different p_{\max} are shown in Fig.4, the right is blown-up plot of the local of the roadway wall rock. The $(U_d)_{\max}$ and the distance d between its position and the surrounding roadway vs. p_{\max} are listed in Table 3. The rule of the maximum energy density $(U_d)_{\max}$ vs. intensity of stress wave p_{\max} is shown in Fig.5. The rule of the distance d vs. intensity of stress wave p_{\max} is shown in Fig.6.

Table 3 Variation of $(U_d)_{\max}$, d , k with intensity of stress wave p_{\max}

p_{\max}/MPa	5	10	15	20
$\langle U_d \rangle_{\max} / \text{J.m}^{-3}$	2.007×10^6	2.717×10^6	3.409×10^6	3.981×10^6
d / m	1.45	1.25	1.15	0.8
$k / \text{J.m}^{-4}$	1.384×10^6	2.714×10^6	2.964×10^6	4.976×10^6

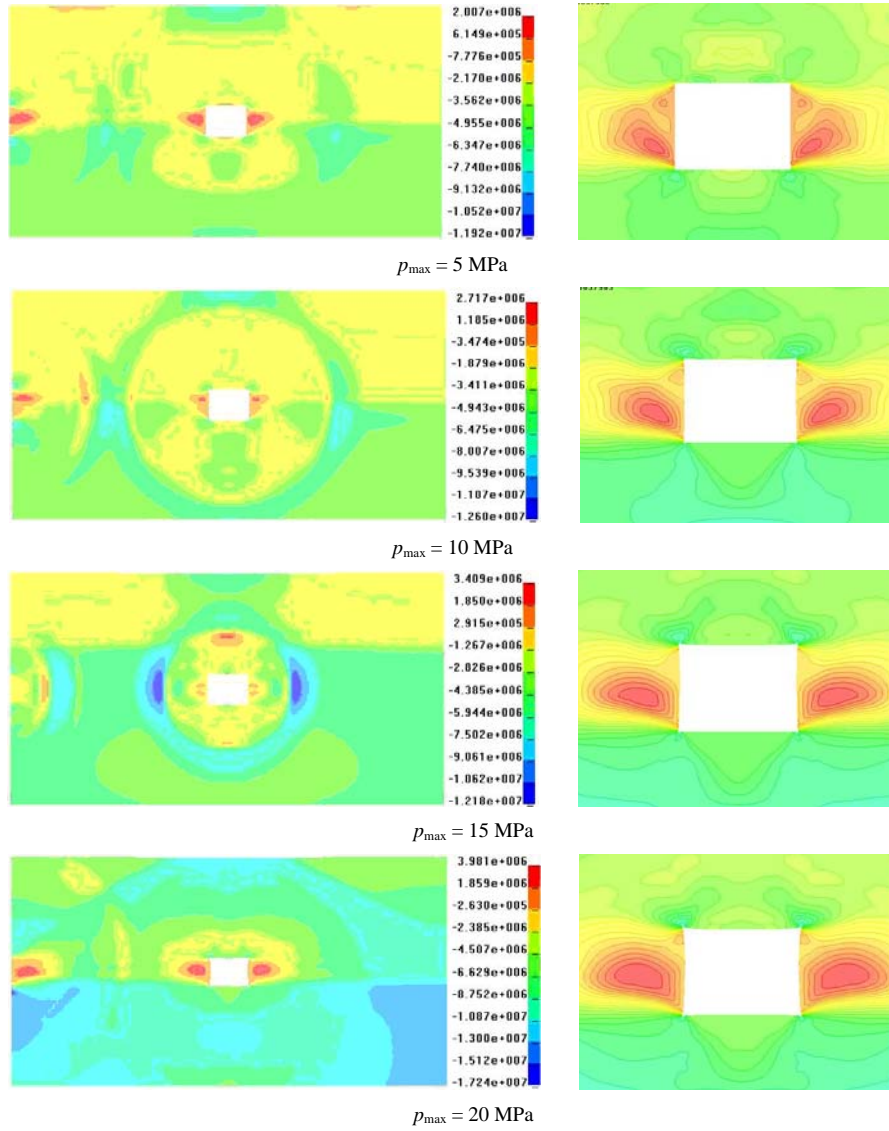


Figure 4 Variation of the energy density distribution of roadways surrounding rock with p_{\max}

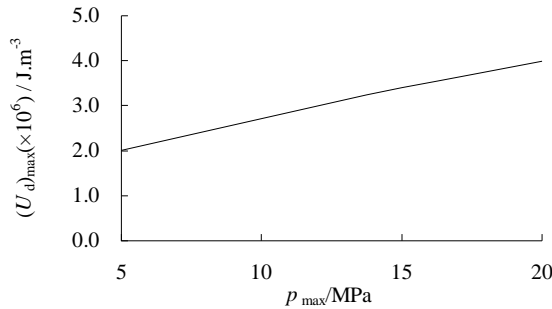


Figure 5 Variation of $(U_d)_{\max}$ with p_{\max}

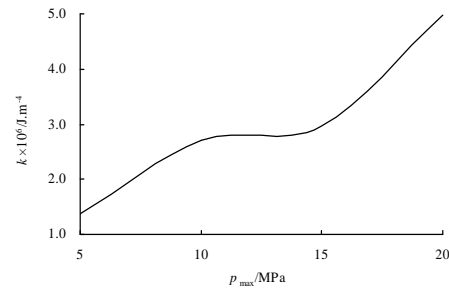


Figure 6 Variation of k with p_{\max}

5 Conclusions

The process of the energy accumulation and the character of the energy accumulation were simulated and studied by employing LS-DYNA software. The effects of the intensity of stress waves and the time of the energy accumulation were investigated. It is of important significance to research the mechanism of inducing rock burst.

Research results show that maximum energy density increases and the distance decreases with the increase of the intensity of stress waves. The value of energy density generally increase and the risk of the rock burst is increased significantly. The results of the study have an important significance to understand the mechanism of inducing rock burst and the forecasting of rock burst.

Acknowledgements

This work was supported by National Natural Science foundation of China (50874104), and National Basic Research Program of China (2007CB209400) .

References

1. Morrisonr, G.K. Theory and the Practical Problem of Rock Bursts. Engineering and Mining Journal, 1948, 149(3). 66-72.
2. Brady, B.T. Anomalous Seismicity Prior to Rock Bursts; Implications for Earthquake Prediction. Pure and Applied Geophysics, 1977, 115(1/2). 357-374.
3. Mueller, W. Numerical Simulation of Rock Bursts. Mining Science & Technology, 1991, 12(1). 27-42.
4. Casten, U. and Fajklewicz, Z. Induced Gravity Anomalies and Rock-Burst Risk in Coal Mines: a Case History. Geophysical Prospecting, 1993, 41(1): 1-13.
5. Zhao, B.J. and Ten, X.J. The Rockburst and Its Prevention and Treatment. Beijing: Beijing Coal Industry Publishing House, 1995.
6. Wang, X.N. and Huang, R.Q. Analysis of the Influence of the Dynamic Disturbance on Rock Burst. Mountain Research, 1998, 16(3): 188-192.
7. Mansurov, V.A. Prediction of Rock Bursts by Analysis of Induced Seismicity Data. International Journal of Rock Mechanics and Mining Sciences, 2001, 38(6). 893-901.
8. Qi, C.Z. and Qian, Q.H. Physical Mechanism of Dependence of Material Strength on Strain Rate for

- Rock-Like Material. Chinese Journal of Rock Mechanics and Engineering, 2003, 22(2): 177-181.
9. Dyskin, A.V. and Germanovich, L.N. Model of Rock Burst Caused by Cracks Growing Near Free Surface. In: Younged. Rockburst and Seismicity in Mines Rotterdam: A A Balkema, 1993, 169-174.
 10. Germanovich, L.N., Dyskm, A.V., Tsyrunikov, N.M., et al. A Model of the Deformation and Fracture of Brittle Materials with Cracks under Uniaxial Compression. Mechanics of solids, 1993, 28(1). 116-128.
 11. Myer, L.R. and Kemeny, J.M. Extensile Cracking in Porous Rock under Different Copressive Stress. Appl Mech Rve, 1992, 45(8). 263-280.
 12. Zhang, X.C. A Study on Mechanism of Rock Burst in Coal Mines. Wuhan: Department of Mechanics, Huazhong University of Science and Technology, 1999.
 13. Lu, A.H. Study on Dynamic Mechanism of Rock Burst Induced by Stress Wave. Xuzhou: College of Science, China University of Mining and Technology, 2005.
 14. Hsn, Y.L. and Hong, Hao. Reliability Analysis of Reinforced Concrete Slabs under Explosive Loading. Structural Safety, 2001, 23. 157-168.

IS MINE EARTHQUAKE PREDICTION POSSIBLE?

STEVE SPOTTISWOODE

24 Mail Str, Florida Park 1709.

Johannesburg, South Africa

Short-term prediction of large earthquakes and mine seismic events has been an elusive goal for many years. Some South African deep-level gold mines use a system of hazard estimation that varies from day to day and that is meant to provide warnings of increased likelihood of impending large events. In essence, this is an attempt at predicting the incidence of large events. In this study, I look for any consistent changes in the rate or type of seismicity before large events (Magnitude M greater than 2.5) in two mines. The only consistent change is a small increase in the rate of seismicity soon before large events. The same increased rate is also observed before small events (M between 0.0 and 1.0). As small events are numerous and rarely pose significant hazard, consistent short-term prediction of large events does not seem to be possible. I therefore recommend that the daily issuing of seismic hazard assessments be scrapped.

1 Introduction

Daily hazard estimation is provided on many South African deep-level gold mines, particularly by the most popular seismic service providers, Integrated Seismic Systems International (ISSI) (van Aswegen, 2003, 2005 & 2007). Van Aswegen's 2007 report stated that:

"The principles of the timeous detection of rockmass instabilities have been described in detail elsewhere (Mendecki, 1997). The applications to short term seismic hazard assessment procedures, as referred to below, have essentially not change since 1995. Success rates vary. In some cases the seismic rockmass response to mining is too fast or too slow for the methods to be useful on a daily basis. Since lives could be at stake, however, we have no choice but to a) keep doing the best we can and b) research methods to improve the success rates."

The implications of seismicity and resulting rockburst damage are so severe that van Aswegen (2007) can justifiably claim that:

"In seismically hazardous mines, the management of the seismic risk is the first priority of the rock engineers."

Attempts at short-term seismic hazard assessments are driven by optimism for the success of such assessments. Despite numerous cautious statements that seismic prediction is not currently viable, some overly optimistic statements have been made. Creamer (2009) reported a National union of Mineworkers (NUM) spokesman as saying:

"NUM urged the implementation of best practice and better use of equipment that warned of impending seismic danger so that people could be removed from dangerous areas."

The recent South African Presidential Mine Health and Safety Audit that was prepared by the Department of Minerals and Energy (DME) (DME, 2009, p15) takes a somewhat curious view about the predictability of large seismic events."

“This (seismic) information is often only made available by mines after injuries and deaths and cannot be relied on because it always indicates that there were no major warning (sic) before the main incidents that injure and claims lives.”

The DME appears to be saying that mine seismic data or its interpretation is unreliable because it does not show warnings.

Extreme pressure has been brought to bear on seismologists to provide predictions on time scales of hours. Van Aswegen (2007) reports on a meeting that was held to discuss needs for seismic research:

“...a local production manager put it bluntly: they want to know where, when and how large the next potentially damaging tremor will be.”

van Aswegen (2003 & 2005) has found that daily hazard assessments routinely issued on mines perform better than random, in other words, large events more often follow when warnings are issued than if warnings were issued randomly. Unfortunately, these assessments are based on long-term average behaviour (seismicity rate) as well as on day-to-day variations in seismicity in areas of high and low seismicity rates. As van Aswegen did not report on the relative contributions of short- and long-term effects on daily hazard assessments nor did he separate the data from active and quiet area, it is impossible to judge from his reports whether his successes reflected daily or long-term variations in hazard.

In contrast, the standard approach for earthquakes is one of **forecasting** the probability of a possibly damaging event (e.g. Michael, 1995). This currently based partly on long-term seismicity rates and partly on aftershock behaviour. The USGS (2009) currently operates an earthquake forecast map for California that is updated hourly. Long-term rates are based on 50 years of earthquake recordings.

Jordan (2009) makes a clear distinction between forecasting and prediction:

Forecasting can apply at all times and places and describes a low probability of occurrence; and

Prediction refers to short-term warnings with high probability (and hopefully a high probability of success)

Forecasting is eminently suitable for South African gold mine seismicity as the rate of seismicity is fairly constant over time and is in many cases proportional to the volume of elastic convergence (e.g. McGarr and Wiebols, 1977) or, equivalently, the elastic strain energy released (Spottiswoode et al, 2008).

2 Theoretical Basis to ISSI Short-Term Hazard Assessment

The central thesis of Mendecki's 1997 theory is the hypothesis of “seismic flow of rock” as proposed by Kagan (1992) and others. In a *tour de force* study of earthquake physics, Ben-Zion (2008) reassessed the theory of turbulence of solids “The existence of these power law distributions led Kagan [1994] to suggest that seismicity and faults are associated with “turbulence of solid.” This analogy may be appropriate over very large space and time scales (e.g., the entire lithosphere and 10^8 – 10^9 years), for which the solid motion in the lithosphere produces sufficient “mixing” and reorganization of the tectonic plates and the faults they contain. Over shorter space-time scales, however, and especially the scales relevant for seismic hazard assessment (e.g., 10^2 – 10^3 km and 10^2 – 10^4 years), geological domains and faults can be considered to be statistically frozen, and the turbulence analogy is not appropriate.”

Only a few years after Kagan's 1992 & 1994 papers, he co-authored a paper with the title “Earthquakes Cannot Be Predicted (Geller et al 1997). An editorial summary of this paper is provided in the link in the reference and reads:

“Can the time, location, and magnitude of future earthquakes be predicted reliably and accurately? In their Perspective, Geller et al.'s answer is “no.” Citing recent results from the physics of nonlinear systems “chaos theory,” they argue that any small earthquake has some chance of cascading into a large event.

According to research cited by the authors, whether or not this happens depends on unmeasurably fine details of conditions in Earth's interior. Earthquakes are therefore inherently unpredictable. Geller et al. suggest that controversy over prediction lingers because prediction claims are not stated as objectively testable scientific hypotheses, and due to overly optimistic reports in the mass media.”

These doubts about the predictability of earthquakes extend to other regions of brittle shear failure, such as deep gold mine seismicity. According to Ben-Zion (2008, p13), exceptions to the brittle shear are oceanic faults and the presence of certain rock types and minerals such as serpentines and talc that may produce locally creeping fault segments. What is at stake at deep South Africa gold mines is whether similar conditions exist in these mines. Certain ductility such as that which occurs below the thin oceanic crust is out of the question, but perhaps some faults in SA gold mines creep?

Ironically, although there is now some doubt about the relevance of the “seismic flow of rock” theory of Mendecki (1997) and applied by van Aswegen (2003, 2005 & 2007) in the brittle environment of deep Witwatersrand mines, it was van Aswegen himself who recently presented further evidence of the brittle nature of dynamic failure in these mines (van Aswegen, 2008).

3 Hypothesis

The analysis presented here is aimed at testing the truth of two statements:

1. The event rate or event type changes before large events; and
2. The event rate or event type does not change in a similar manner before the more numerous small events.

If the answer to both of these questions is “yes”, then useful prediction is possible. If the answer to either question is “no”, then useful prediction is not possible:

1. If the event rate or event type does not change before large events, then prediction is not possible at all; and
2. If the event rate or event type changes in the same way before numerous small events, then too many false alarms (false positives) would be issued to be useful.

I will test the seismicity prior to large and small events over time scales of minutes to two weeks.

Large events are considered to be those with Magnitude (M) greater than 2.5 ($M > 2.5$), while small events were defined as M between 0.0 and 1.0 ($0 < M < 1$).

4 Case Study

As there are still no complete theories that quantify the seismic response to mining, we need to work on case studies to develop theories or models. In a recent case study from large data sets from two mines, Spottiswoode et al (2008) found that, over a time scale of months, seismicity is proportional to strain energy changes associated with mining. The same data is used here to see if there are any consistent changes in the amount or character of seismicity in the days and hours prior to large and small events. Data came from mining of the Carbon Leader Reef, labelled “CLR” here and mining on the Ventersdorp Contact Reef (VCR). Some statistics of the two mining situations is listed in Table 1.

Kgarume et al (2009) studied aftershocks of mine events using the custom-built OMORI program. For this report, I extended OMORI to analyse foreshocks from the two data sets studied by Spottiswoode et al (2008).

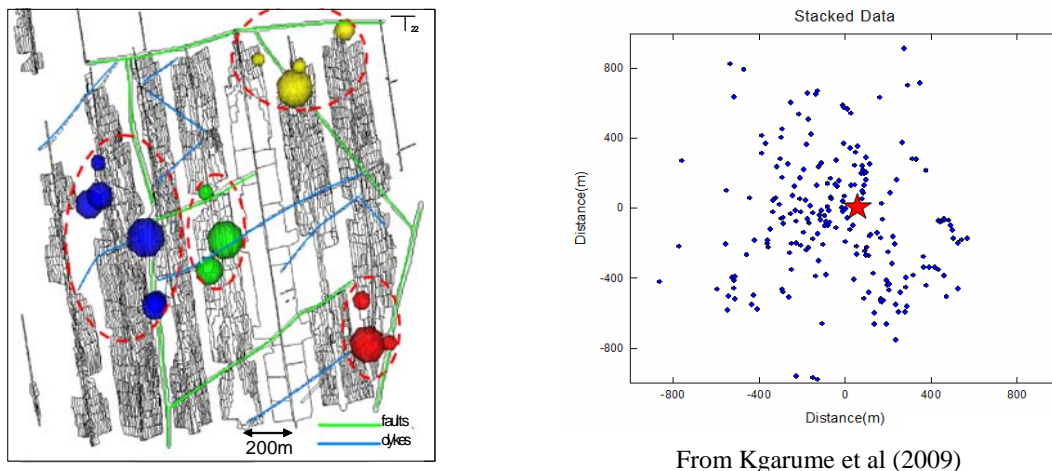
Table 1. Some Parameters for the two case studies

Parameter	VCR mine	CLR mine
Area mined	543 636 m ²	1 057 896 m ²
Duration of seismic data	4.2 years	9 years
Average depth below surface	3300 m	3100 m
Total number of events	16626	39966
Number 0.0<M<1.0	6425	~24000
Number M<2.5	48	187

As applied here, the custom-built program OMORI uses the following steps to write output files containing average seismicity rates before and after events that can be defined as main shocks:

1. Read a catalogue of seismic events;
2. Identify main shocks based on their Magnitudes;
3. Stack all events with Magnitude greater than -1.0 ($M > -1.0$) within 14 days and 200m in plan of the main shocks by time difference according to their occurrence and properties; and
 - a. Cumulate the number of events earlier and later than the main shocks; and
 - b. Smooth the event property data.

Stacking of events is explained graphically in Figure 1.



From Kgarume et al (2009)

Figure 1 Diagram to illustrate spatial stacking of main shocks

Daily hazard assessments should be at their most successful if large seismic events are preceded by significant changes in seismicity that do not also precede small events. To see whether large events are, on average, preceded by changes in seismicity, main shocks are “stacked” at time zero and distance zero. (Main shocks are normally larger events, but small events are also considered separately as main shocks in this study.) Events before and after main shocks within a radius of 200 m in plan were chosen after discussions with Mendecki et al (2009). Earlier work using data within a radius of 100 m gave similar results.

The stacking method applied here is aimed at giving the best possible chance of finding consistent precursory behaviour, if such behaviour exists.

5 Analysis and Results

5.1 The Rate of Seismicity

The average time-of-week occurrence is calculated over the two weeks before and one week following main shocks. The overall seismicity rate over the 14 days before and 7 days after the stacked main shocks is constant to the first order (Figure 1). There are several deviations from a constant rate of seismicity:

1. The increased rate of seismicity immediately following the main shocks can be attributed to aftershocks (Kgarume et al, 2009);
2. A ripple with peaks at multiples of 24 hours occurs because events, both large and small, take place preferentially soon after the daily face blasts (Figure 4);
3. An increased rate of seismicity over a few hours prior to large and small events; and
4. More aftershocks occur after large event than after small events.

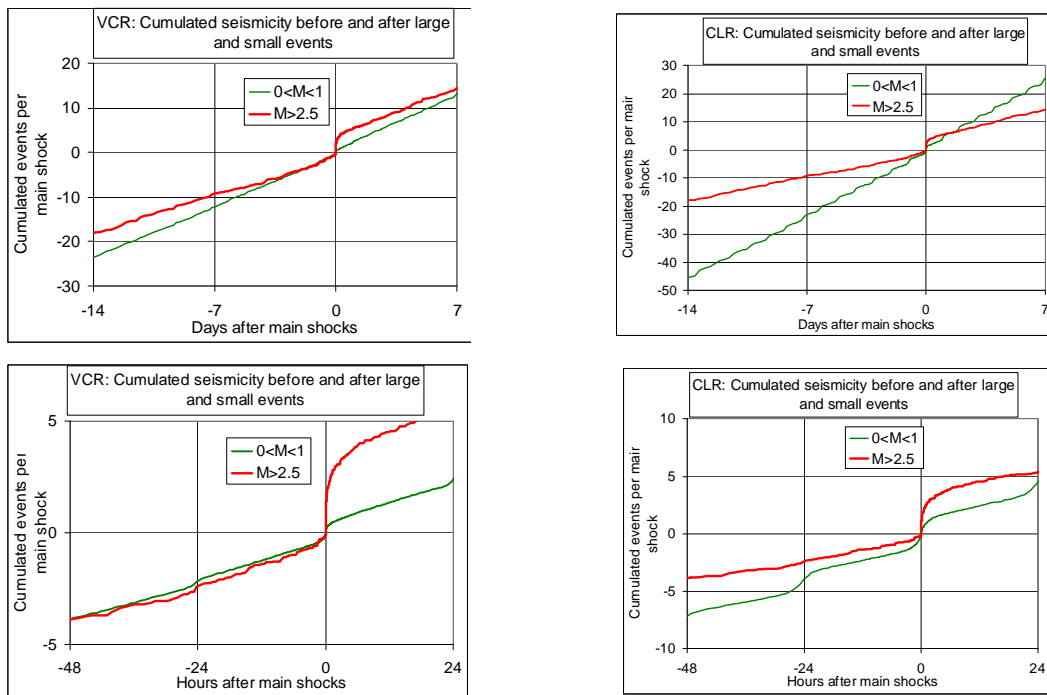


Figure 2 Cumulated number of seismic events within 200m before and after big and small events.

The average rate of seismicity before large is compared to the rate before small events in Figure 3. The lack of significant and accelerated curvature before the main shocks (indicated with the red diamonds) occur shows that there is no consistent change in the event rate before large events that does not also occur before small events.

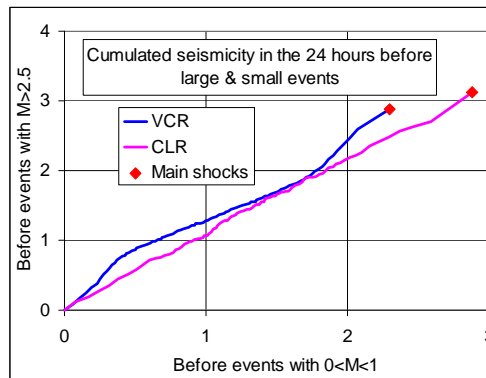


Figure 3 Comparison between the cumulated seismicity in the 24 hours before large and small events, averaged over number of main shocks

The non-linear shape of the graph for VCR data in Figure 3 is probably a complex function of factors relating to variations in time of day statistics shown in Figure 4 and Figure 6 and the different rate of precursory seismicity shown in Figure 2. The accelerated rate of seismicity in the afternoon is directly related to the daily production blast.

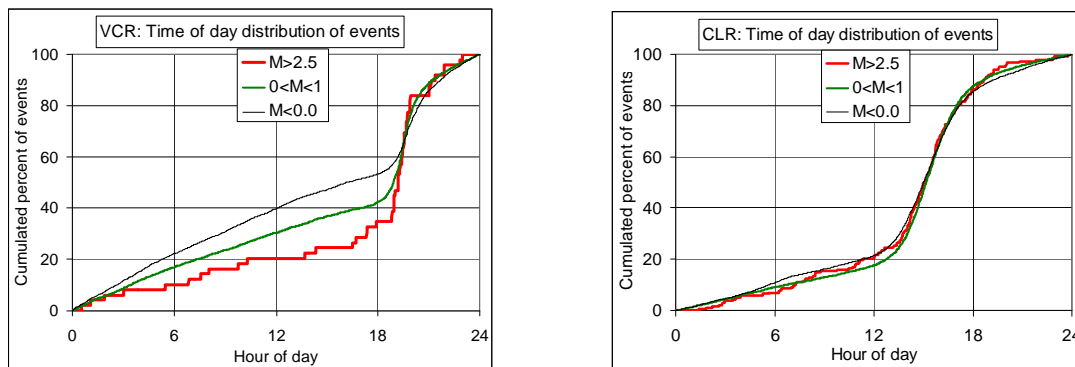


Figure 4 Distribution of seismicity by time of day

A weekly cycle also influences the rate of seismicity, causing minima at multiples of seven days before and after main shocks (Figure 5). The overall seismicity rate on the CLR following large events, once aftershocks have occurred, is less than the seismicity rate before large events.

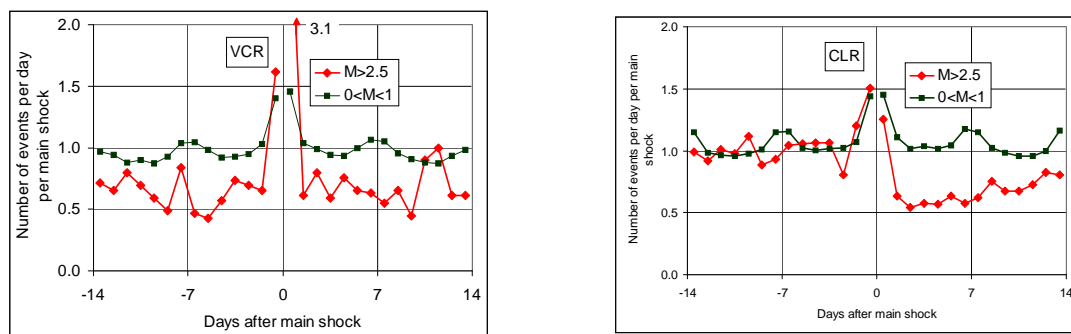


Figure 5 Average daily seismicity rate

Comparison between the statistical behaviour of large events is facilitated by the lines of constant (negative) slope ("b" value) of 1.0.

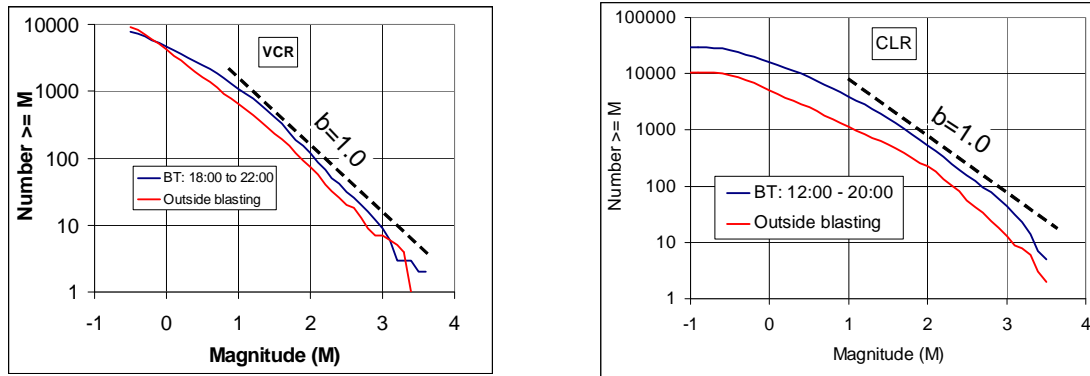
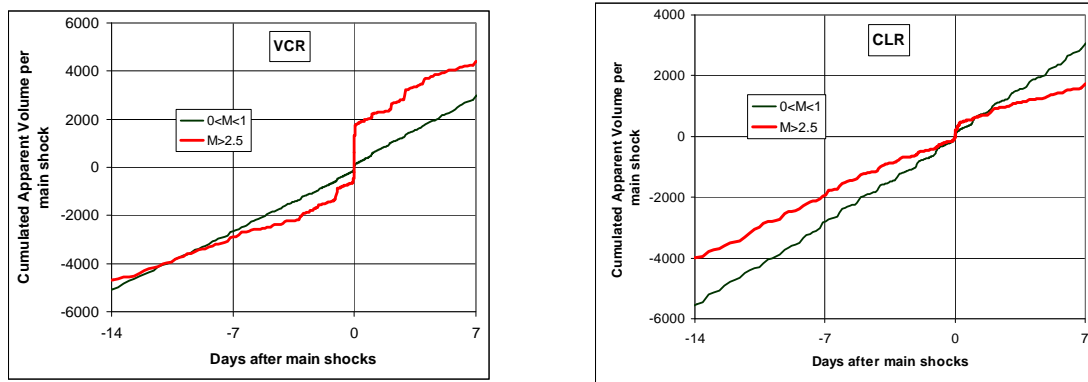


Figure 6 Magnitude-frequency distribution

The analysis for the cumulated incidence of seismicity is repeated here for cumulated Apparent Volume as this parameter has been used routinely on mines (van Aswegen, 2005) (Figure 7). Figure 7 is similar to Figure 2 in many ways, although differing in several aspects:

1. The moment rate immediately after the main shocks is relatively higher for Apparent Volume (Figure 7) than for number of events (Figure 2).
2. Both data sets show a more pronounced 24-hour ripple, compatible with the large number of events at blasting time, especially for VCR mining.
3. The VCR data is less smooth than the CLR data. This can be attributed to a greater contribution of the few $M > 3$ events towards the total seismic moment, as suggested by the slow roll-off at high magnitudes of the curves for CLR data.
4. VCR data in particular shows more rapid increase in the rate of apparent volume soon before the time of the main shocks than was the case for cumulated number of events in Figure 2. The rapid increase in Figure 7 is likely to be a more accurate representation of real seismicity as many small aftershocks within approximately the first 30 seconds are probably lost (Kgarume et al (2009).



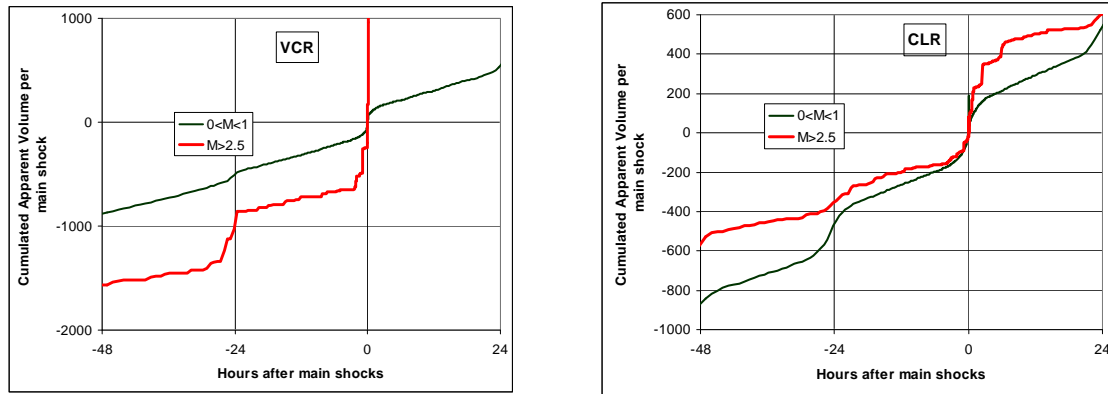


Figure 7 Cumulated apparent volume for events within 200m before and after big and small events.

In contrast to **Figure 3**, **Figure 8** does show some accelerated increase in the apparent volume before large events during VCR mining that was not shown for seismicity rate (**Figure 3**). As seen by the markers (“+”) that are used in **Figure 3** to show 15-minute intervals, two large events were preceded by large foreshocks within the previous one hour.

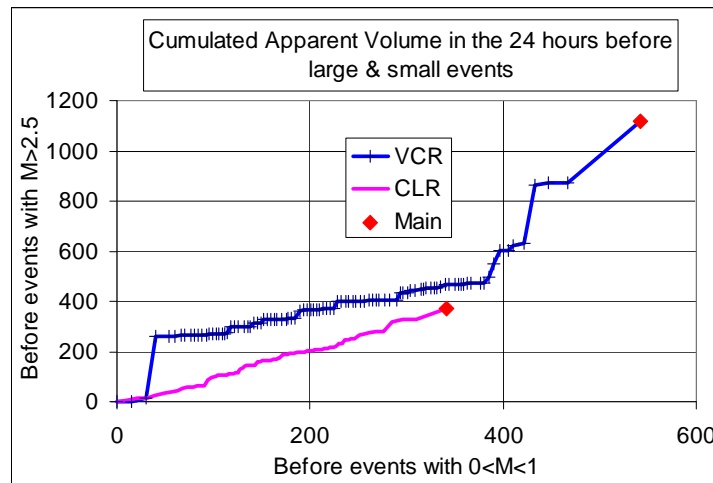


Figure 8 Comparison between the cumulated apparent volume in the 24 hours before large and small events, averaged over number of main shocks

The analysis so far in this report has involved the **average** behaviour of seismicity before and after main shocks. Seismicity rates in the day prior to individual events are shown in **Figure 9**. As was shown in previous Figures, the seismicity during the day before main shocks is, on average, higher than the rate over the previous 13 days, this number chosen as two weeks less one day. As many more small events were chosen as main shocks, average values of the number of foreshocks in the previous day were calculated for each average value over the previous 13 days. With only a few circled exceptions, the values for large events lay equally above and below the average values for the small events.

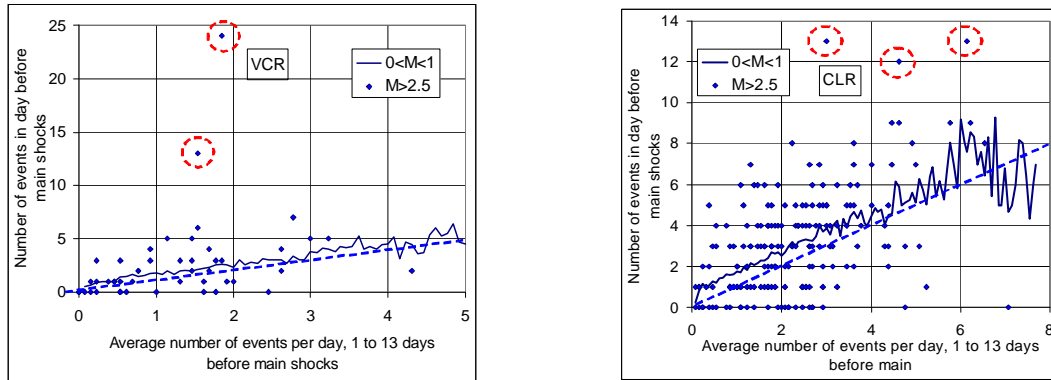


Figure 9 Seismicity rate in the 24 hours prior to main shocks as a function of the average rate in the previous 13 days. Solid symbols are used for precursory activity prior to large events while the “noisy” graph is the average rate for events before small main shocks. The five most active periods are circled.

Further detail is provided in **Figure 10** for the five “anomalous” events identified in **Figure 9**. All five events show what appear to be mainshock-aftershock sequences occurring in the day before the chosen main shock. None of the events were preceded by an accelerated rate of seismicity leading up to the main shock

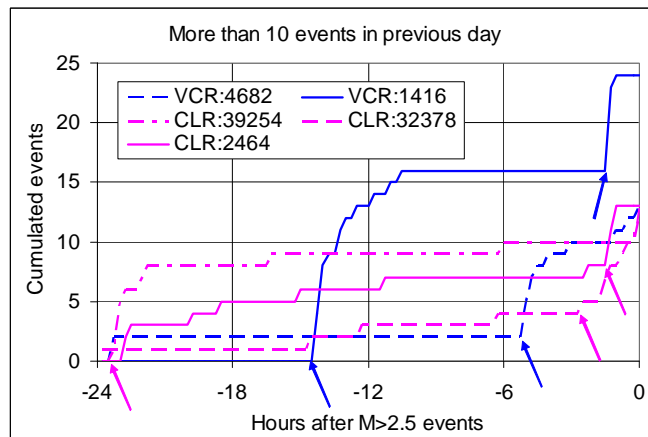


Figure 10 Cumulated seismicity in the 24 hours prior to the five events with most foreshocks. Arrows indicate the start of mainshock-aftershock sequences.

5.2 Type of Seismicity

Figure 10 and **Figure 11** shows smoothed values of four parameters of foreshocks and aftershocks that I analysed. They are analogous to some of the parameters used by ISSI for their seismic rating system. I considered:

1. P/S_{Mo}, or the ratio of seismic moment estimated from P waves to that from S waves;
2. Magn, or the magnitude;
3. D_{xy}, or the distance between the main shock and the prior and following events within 200m of main shocks, expressed as a fraction of 200m; and
4. EI, or Energy Index (Mendecki and van Aswegen, 2001).

Seismic moment ratio is our preferred way of considering the proportion of volume change compared to shear slip in the seismic source. We prefer this to the energy ratios sometimes used by ISSI and interpreted as “pops” and “slips” as moment ratios are not sensitive to source complexity or source slip velocity.

D_{xy} is used for looking for any changes in the clustering of fore shocks shortly before main shocks.

The energy index was geometrically averaged, i.e. logarithmic values were averaged and then anti-logged for plotting.

The dominant feature in the time histories shown in **Figure 10** and **Figure 11** is random variations about the mean for all parameters over time scales of hours to days. The more dense variations in the plots for foreshocks and aftershocks of small main shocks compared to the plots for large main shocks is a result of the larger number of events considered. The mean values are similar for large and for small main shocks. Noticeable exceptions from the random variations are:

1. P/S_{Mo} decreases slightly during the 20 hours before CLR main shocks. This decline is well within the range observed over the previous 13 days.
2. The average magnitude has a maximum immediately after the main shock as well as at multiples of 24 hours before and after the main shocks. This observation is related to the blasting cycle.

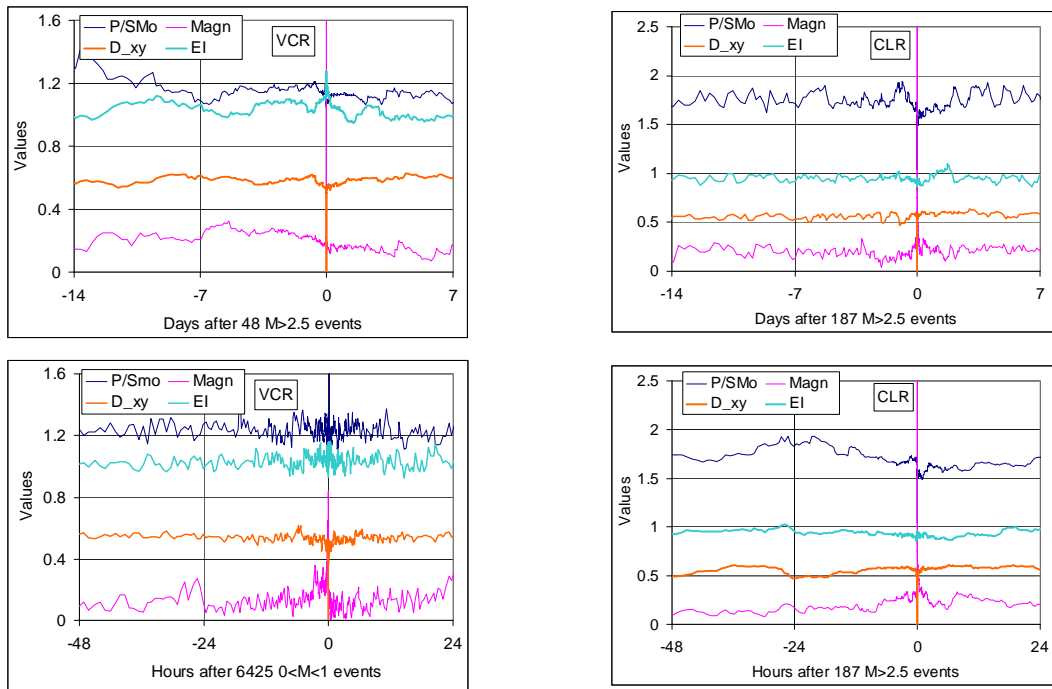


Figure 11 Cumulated seismicity over 14 days before and 7 days after M>2.5 events: (left) CLR & (right) VCR

Data from both mines show peak values in the average Magnitude at multiples of 24 hours. This is more pronounced in the case of VCR and can be explained by a higher proportion of all events taking place within the blast windows and by an increase in the proportion of events with higher Magnitudes during this time period (**Figure 4** and **Figure 6**).

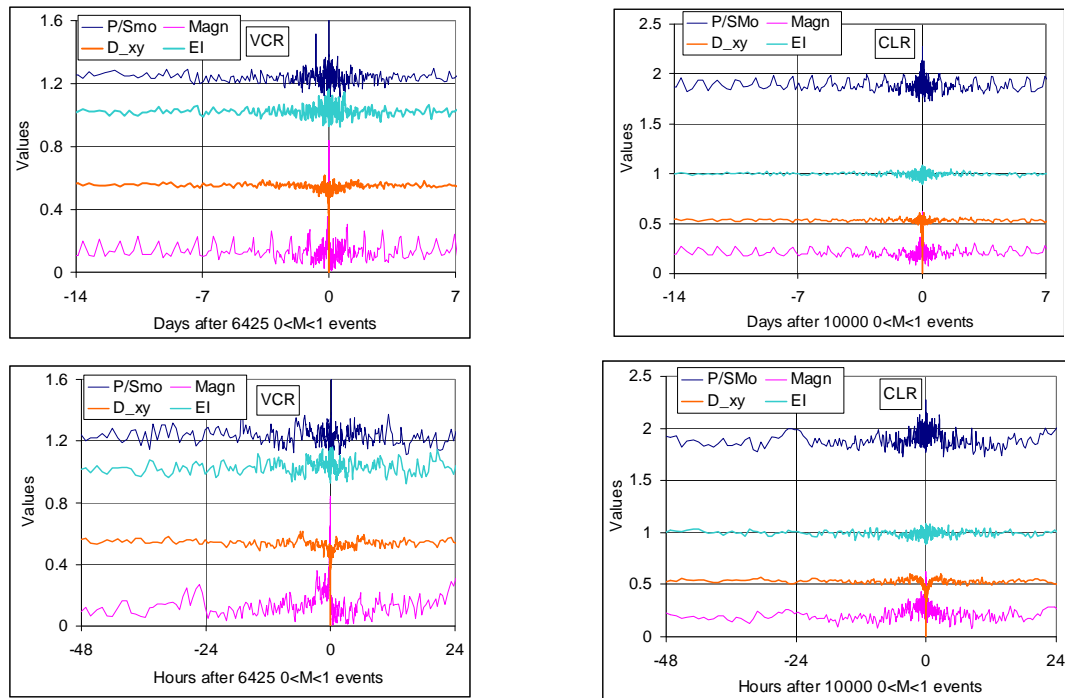


Figure 12 As for Figure 10 with small events being considered as “main shocks”

Other than the larger number of points presented in Figure 12, it is so similar to Figure 11 that no case can be made for the use of any of the four parameters as a useful precursor to large events.

6 Conclusions and Discussion

Are large events in South African deep mines predictable in the short term? It is clear from the analysis in the previous section that any short-term precursors to large events in the two data sets are also precursors to small events. This appears to be in direct contradiction to the work of van Aswegen (2003, p130) who reported results that were considerably better than random. Van Aswegen’s positive results could possibly be explained by the use of factors other than day-to-day variations in seismicity, such as hazard magnitude or the mine’s panel-rating system, as well as by combining results from area of high and low rate of seismicity.

Issuing of routine daily hazard assessments for South African gold mines based on daily changes in seismicity does not provide a clear indication of the potential of large events in particular. I suggest that they be scrapped and that hazard assessments be presented in three forms, namely:

1. an immediate response to large events on account of possible damage and aftershocks;
2. a monthly assessment based on overall seismicity rate, with due account taken of expected changes in mining rate and stress conditions; and
3. long-term planning.

7 Acknowledgments

This work was partially supported by the CSIR and by Harmony Gold Mining Company Limited. I was motivated to prepare this paper after discussions with Martin Pretorius, Gerrie van Aswegen, Gerhard

Hoffmann and Ray Durrheim. I was also encouraged by discussions with Rock Engineers and Seismologists when this work was first presented at the ISSI conference on 4th May 2009.

References

1. Ben-Zion, Y. Collective Behavior of Earthquakes and Faults: Continuum-Discrete Transitions, Progressive Evolutionary Changes, and Different Dynamic Regimes, *Rev. Geophys.*, 46, RG4006, doi:10.1029/2008RG000260, 2008.
2. Creamer, M. Mine Deaths Worsening, Section 28 Artisans in Many Accidents, in <http://www.miningweekly.com/article/mine-safety-slumps-as-more-die---num-2009-03-17>, 2009
3. DME. Presidential Mine Health And Safety Audit Department of Minerals And Energy, 2009.
4. Geller, R.J., Jackson D. D., Kagan, Y. Y. and Mulargia, F. Earthquakes Cannot Be Predicted. *Science*, 1997, 275(5306). 1616-1620.
5. Jordan, T.H. Earthquake Prediction: The Unsolved Problem, Keynote Lecture at the General Assembly of the International Association of Seismology and Physics of the Earth's Interior (IASPEI), (Cape Town, South Africa. 2009).
6. Kagan, Y. Y. Observational Evidence for Earthquakes as a Nonlinear Dynamic Process. *Physica D*, 1994,77.160-192.
7. Kgarume, T.E., Spottiswoode, S.M. and Durrheim, R.J. Statistical Properties of Mine Tremor Aftershocks, Submitted to PAGEOPH SPECIAL ISSUE: INDUCED SEISMICITY, 2009.
8. McGarr, A. and Wiebols, G.A. Influence of Mine Geometry and closure volume on Seismicity in deep level mine. *Int. J. Rock Mech. Min. Sci., & Geomech. Abstr.*, 1977, 14.139-145.
9. Mendecki, A.J. Seismology for Rockbursts Prevention, Control and Prediction. GAP017, SIMRAC, 1997,1-309.
10. Mendecki, A.J. and Van Aswegen, G. Seismic Monitoring in Mines: Selected Terms and Definitions. In: Van Aswegen, G., Durrheim, R.J. and Ortlepp, W.D. (Eds.) *Rockbursts and Seismicity in Mines – RaSiM5*, South African Institute of Mining and Metallurgy, Johannesburg, (South Africa,2001).
11. Mendecki, A. Persistence of Seismic Rockmass Response to Mining. *Proceedings of the Sixth International Symposium on Rockbursts & Seismicity in Mines*, Y. Potvin & M. Hudyma (eds), (Australian Centre for Geomechanics, 2005).
12. Mendecki, A. Forecasting Seismic Hazard in Mines, in *SHIRMS 2008 – Y. Potvin, J. Carter, A. Dyskin, R. Jeffrey* (eds) Australian Centre for Geomechanics, (Perth, 2008).
13. Mendecki et al. Discussions at ISSI seminar, Stellenbosch, (South Africa, 2009).
14. Michael, A., Reasenberg, P., Stauffer, P.H., and Hendley, J.W. Quake Forecasting- an Emerging Capability, U.S. Geological Survey Fact Sheet-242-95. <http://quake.usgs.gov/prepare/factsheets/QuakeForecasts/>, 1995.
15. Spottiswoode, S.M., Linzer, L.M. and Majiet, S. Energy and Stiffness of Mine Models and Seismicity. in *SHIRMS 2008 – Y. Potvin, J. Carter, A. Dyskin, R. Jeffrey* (eds), Australian Centre for Geomechanics, (Perth, 2008).
16. USGS. 24-Hour Aftershock Forecast Map. <http://earthquake.usgs.gov/eqcenter/step//>, 2009.
17. Van Aswegen, G. Towards Best Practice for Routine Seismic Hazard Assessment in Mines. 30th International Conference of Safety in Mines Research Institutes, South African Institute of Mining and Metallurgy, (Johannesburg, South Africa, 2003).
18. Van Aswegen, G. Routine Seismic Hazard Assessment in South African Mines. 6th Intl Symposium on Rockbursts and Seismicity in mines, (Perth, Australia, 2005).
19. Van Aswegen, G. Routine Seismic Hazard Assessment for Some S.A. Mines. Unpublished ISSI Document, Western Levels, September, 2007.
20. Van Aswegen, G. Ortlepp Shears – Dynamic Brittle Shears of South African Gold Mines, in *SHIRMS 2008 – Y. Potvin, J. Carter, A. Dyskin, R. Jeffrey* (eds) Australian Centre for Geomechanics, (Perth, 2008).

NUMERICAL SIMULATION FOR ACOUSTIC EMISSION AND SOURCE LOCATION OF ROCK UNDER TRIAXIAL COMPRESSION

FENG-SHAN HAN and JU-YING YANG

Centre for Material Failure Modelling Research, Dalian University

Dalian, 116622, P.R. China

Numerical simulation for Acoustic emission (AE) and source location are carried out on the rock specimen granite under triaxial compression using the rock failure process analysis code RFPA^{2D}. RFPA^{2D} is used to determine the fracture process of rock. Moreover, AE source location can be found using RFPA^{2D}. Numerical simulation shows that there is some microseism precursory before main shock; tension stress is the source of rock failure. Using the space distribution characteristics of AE and information which is produced by tension stress, instability failure can be predicted. Through analysis, it is founded that the previous stage of a microseism event is mainly induced by compression stress, and in the middle and later stage there exists many microseism events which are induced by tension stress. This is useful in practical engineering.

1 Introduction

Brittle deformation in rock is accompanied by the formation of micro cracks that emit elastic energy, partly in the form of acoustic emissions (AE). The AE technique is an indirect method used to study the fracture mechanisms and laws governing fracture initiation at the onset of inelastic deformation. Important features in AE study include location of the event hypocenter.

The study on AE rock began in the 1940's for the prediction of rock bursts in mines, and since then, many researchers [1-6] have investigated and observed AE parameters according to increasing stress, and they have identified the fracture of rock or investigated the relation between AE and deformation of rock.

In this study, numerical simulation for AE is used as a means of investigations, and AE source location is performed taking into consideration the characteristics of deformation and fracturing of rock under triaxial compression.

2 Numerical Models

2.1. Basic Principle of RFPA^{2D}

In RFPA^{2D}, the solid or material is assumed to be composed of many elements with the same size, and the mechanical properties of these elements are assumed to conform to a given Weibull distribution as defined in the following function:

$$f(u) = \frac{m}{u_0} \left(\frac{u}{u_0} \right)^{m-1} \exp \left[- \left(\frac{u}{u_0} \right)^m \right] \quad (1)$$

Where u is the parameter of the element (such as strength or elastic modulus); the scale parameter of u_0 is related to the average of the element parameters, and the shape parameter m defines the shape of the distribution function. We call this parameter m , the homogeneity index. According to the definition, a larger m implies a more homogeneous material. In general, we assumed that the young's modulus and strength of

macroscopic elements with the same homogeneity index. The microscopic elements are assumed to be isotropic and homogeneous.

2.2. Numerical Model

The rock specimen used in the test was granites [1], the diameter of specimen is 54mm and the height of the specimen is 108mm. Mechanical parameters used in our numerical simulation are shown in Table 1. In order to consider the influence of heterogeneity, we assume the homogeneity index parameter m is 2. The numerical model size is 54mm×108mm, and the model is divided into a 200×100 grid, the numerical model for our numerical simulation is shown in Fig.1. The model adopts plane stress analysis, displacement control loading, 0.01mm/step. Also, the confining pressure σ_3 is 4.9MPa.

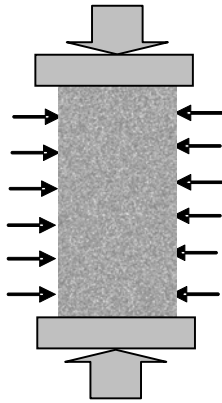


Figure 1 Physical model

Table 1 Mechanical parameters for numerical simulation

Mechanical Parameters	Values
Homogeneous Degree M	2
Elastic Modulus Mean Value E /Gpa	56.1
Compressive Strength Mean Value σ_0 /Mpa	640
Poisson ' S Ratio M	0.24
Bulk Specific Gravity ρ / N/Mm ²	2.67×10^{-4}
Confining Pressure σ_3 /Mpa	4.9

2.3. Progressive Failure of Granite Specimen

Progressive failure of granite specimen for numerical simulation are shown in Fig.2

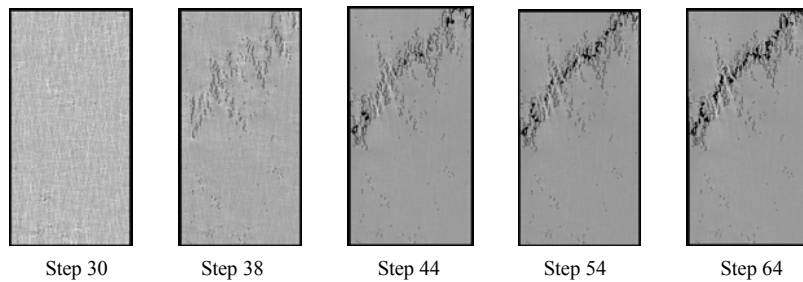


Figure 2 Progressive failure of granite specimen at confining pressure 4.9Mpa for numerical simulation

3 AE rock Specimen under Triaxil Compression

AE area and Damage situation for differential step of granite specimen at confining pressure 4.9Mpa for numerical simulation are shown in Fig.3. Y load and steps curve is shown in Fig.4. AE count and load steps Is shown in Fig.5.

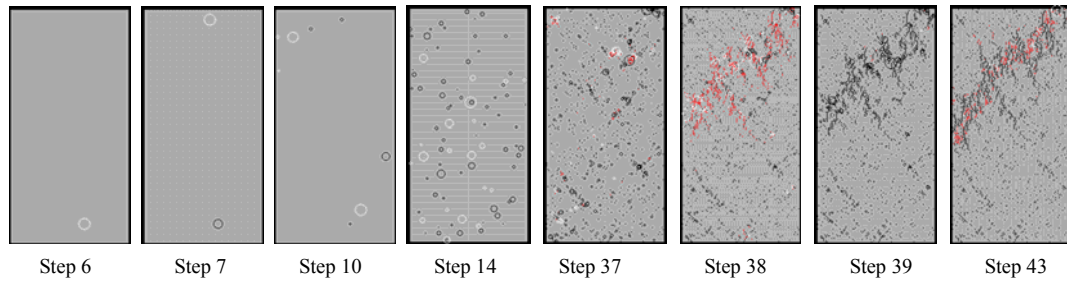


Figure 3 AE area and Damage situation for different step

As can be seen in Fig 4 and Fig 5, the microseism activity of sample is of stage character. In linear elastic stage, MS event is mainly produced by crack closing, sometimes there is rarely or even no microseism activity. In the expansion, a lot of microseism activities are produced. The main shock happens after stress peak, at this time macroscopic crack of rock has formed, and finally the rock loses bearing capacity. Figure 3 is the numerical simulation result of microseism activity space distribution. AE area for different step. In Fig.3, each circle represents a microseism position, the red circle shows that the microseism event is produced by the tension stress; the white circle shows that the microseism event is produced by the compression stress.

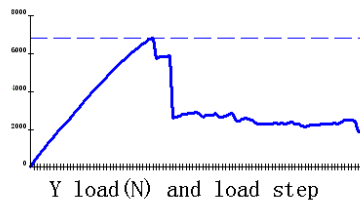


Figure 4 Y load and steps curve

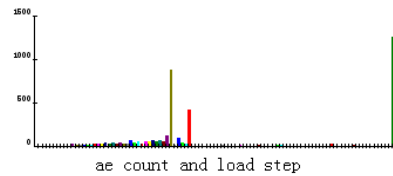


Figure .5 Microseism count and load steps

4 Conclusions

Numerical simulation for Acoustic Emission (AE) and source location are carried out on granite rock specimens under triaxial compression by rock failure process analysis code RFPA^{2D}. In this study, numerical simulation for AE is used as a means of investigation, and AE source location is performed taking into consideration the characteristics of deformation and fracture of rock under triaxial compression.

Using the space distribution characteristics of AE, information which is produced by tension stress, the instability failure can be predicted. Through analysis, the simulation samples microseism activity space distribution characteristics, we can find that in the previous stage of microseism event, it is mainly induced by compression stress, in this time macroscopic failure doesn't occur in the sample, in the middle and later stage there exist many microseism events which are induced by tension stress. This is useful in practical engineering.

Acknowledgements

This research is supported by the "973 Program of National Basic Research Program of China" (2007CB209404) and Open Research Foundation of China Institute of Water Resources and Hydropower Research and Doctoral Research Foundation of Dalian University (No.0302221).

References

1. Heo, J.S., Lee, C.I. and Jeon, S. Measurement of Acoustic Emission Behavior and Source Location Considering Anisotropy of Rock under Triaxial compression. *Key Engineering Materials*, 2004, 270-273. 1574-1579.
2. Chang, S.H. and Lee, C.I. Estimation of Cracking and Damage Mechanisms in Rock under Triaxial Compression by moment tensor analysis of Acoustic Emission. *International Journal of Rock Mechanism and Mining Sciences*, 2004, 41. 1069-1086.
3. Eberhardt, E., Stead, D. and Stimpson, B. Quantifying Progressive Prepeak Brittle Fracture Damage in rock during Uniaxial Compression. *International Journal of Rock Mechanism and Mining Sciences*, 1999, 36(3). 361-380.
4. Butt, S.D. and Calder, P.N. Experimental Procedures to Measure Volumetrically Changes and Microseismic Activity during Triaxial Compression Tests. *International Journal of Rock Mechanism and Mining Sciences*, 1998, 35(2). 249-254.
5. Carvalho, F.C.S., Shah, K.R. and Labuz, J.F. Source Mode of Acoustic Emission Using Displacement Discontinuities. *International Journal of Rock Mechanism and Mining Sciences*, 1998, 35(4-5). 86.
6. Lajtai, E.Z., Carter, B.J. and Ayari, M.L. Criteria for Brittle Fracture in Compression. *Eng Fracture Mech*, 1990, 37(1).59-74.

NUMERICAL SIMULATION OF UNLOADING VELOCITY INFLUENCING STABILITY OF SOLID FLUID SURROUNDING ROCK

AN-NAN JIANG

Institute of Highway and Bridge, Dalian Maritime University

Dalian, 116026, P.R. China

AN-NAN JIANG, CHUN-AN TANG and ZHENG-ZHAO LIANG

School of Civil and Hydraulic Engineering, Dalian University of Technology

Dalian, 116024, P.R. China

The rock mass of underground engineering excavation is a dynamic effect problem, especially in geological zones with solid-fluid interaction in high stress fields. The dynamic excavation should induce the coupling adjustment of both solid framework stress fields and pore pressures of liquids. It is difficult to get these analytical computing results with laboratory testing. This paper contains numerical simulations for solid-fluid surrounding rocks in dynamics unloading conditions using the Lagrange soft code-FLAC. The time course regulations of tangential stress, radial stress, and pore water pressure with dynamic unloading have been found, and the pore water pressure's effect on stress disturbance of unloading has been summarized. While using the dynamic effect according to three different unloading velocities, the paper simulates and compares the stress and pore pressure time course lines of character points respectively while creating the distribution contour maps of pore pressure and plastic zones. The simulation result states that unloading velocity has a significant effect on solid-fluid rock. The faster the unloading velocity, the larger the degree of rock destruction will occur.

1 Introduction

The stability of rock mass of underground engineering depends on the unloading effect of excavation; this unloading effect relies on the engineering excavation style and produces a series of new physical phenomena. Now, researchers use conventional methods to deal with a lot of excavation engineering problems, which is not consistent with the true engineering. Therefore, considering excavation problems from unloading effects, debating the unloading effect mechanism according to different construction styles is the basement to solve the excavation problem[1-2].

The rock mass unloading mechanical properties were studied by scholars both abroad and home, and they reached many results^[3-7]. Notably, general unloading mechanics adopts a quasi-stationary method, but in fact unloading is a dynamics process, which should produce stress waves acting on surrounding rock. Literature [8] studied the dynamic unloading effect of blast excavation and simply analyzed it by elastic wave control equations.

Generally, water is inevitable in general underground engineering, because of excavation in high stress geological body that contains water and then unloading induces inner stress field and pore pressure changing and interaction, companied with plastic strain and rock failure, which brings difficulties in analytical method. Limited by size and unloading velocity, there are difficulties in lab test. Along with the development of computing technique, numerical simulation becomes a powerful tool of science research and engineering computation.

2 Numerical Simulation of Surrounding Rock with Fluid-Solid Coupling

While excavate tunnel from rock mass with original stress field in a short time, the constraint stress losing just like applying a stress on surrounding rock surface, ie unloading stress. The stress acts from surface to inner of

rock, until it balances (Figure 1). Especially in the environment of high stress and high pore pressure. Because of the time of unloading is shorter, the fluid-solid interaction is complex, on one hand, the solid matrix produces displacement, the hole enlarging or reducing, thus inducing the change of pore pressure. On the hand, the changed pore pressure affects the effect stress and deform of solid matrix.

For simplicity, according to un-drainage condition, the construction of tunnel in high stress saturated rock mass is simulated (suppose the pore water without dissipation in excavation process). There are 40 MPa initial stress in every directions before excavation, the pore pressure is 3.5 MPa. The Young's modulus is 60GPa, Passion ratio is 0.25, the cohesion is 15MPa ,the tension strength is 2MPa, friction angle is 30° . Based on Mohr-Coulomb criterion that the shear flow rule is non-associated and the tensile flow rule is associated, considering the strain soft constitutive model, ie the cohesion, friction and tension strengths weaken after plastic yielding. The numerical model is shown in figure 2.

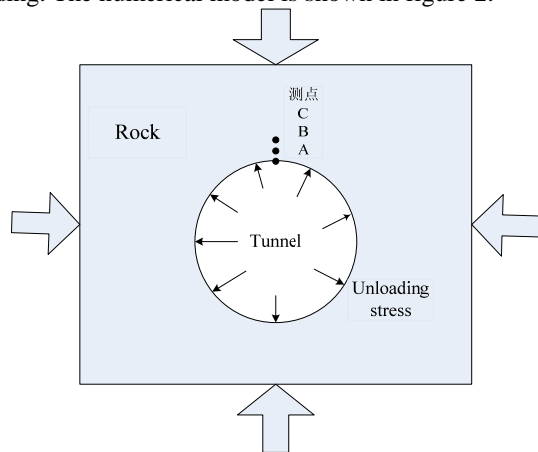


Figure 1 The tunnel unloading sketch

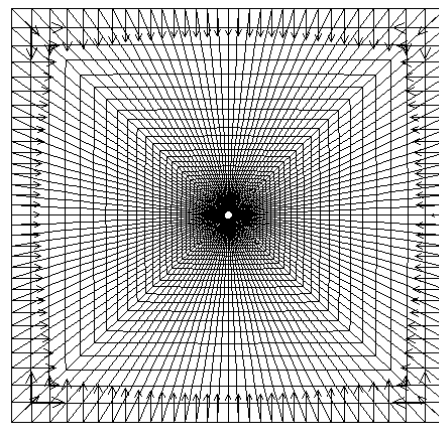


Figure 2 The grid of tunnel simulation

The boundaries are set by command of “APPLY”, the initial stress field and initial pore pressure are set by “INI” command. The change of stress and pore water pressure is monitored by “Hist” command. For convenience, the time step of FLAC is used as time unit. Figure 3 is the change of pore water pressure of monitoring points A,B,C in surrounding rock(A,B,C points are arranged as Figure 1, the corresponding grid points corresponding the vertical grid j of 1, 4 and 8).

It is shown that at the 20th time step after unloading, the pore water pressure of each point goes down to the lowest value, then in succeeding time steps it goes up, about at 200th time step it reaches quiet. The pore water pressure of Point A is lower than others because it is mostly approaches the open face, its pore water pressure range of variation is maximal and waves in ascent stage. For B and C, along to the inner rock, the pore water pressure range decreases, the time of reaching lowest point is longer and pore water pressure increasing after stabilization. The closer it is to free surface, the more serious the pore water pressure is disturbed by unloading.

Figure 4 and Figure 5 are respectively the radial stress and tangential stress of point A induced by unloading, the unloading time is still 20 time steps. It is shown in Figure, the radial stress and tangential stress all suffered an oscillatory process and then converged to steady state value, there are dynamic effect in the progress. According to conventional method, the steady value is the quasi-static value, witch is expressed by a straight line in coordinate system.

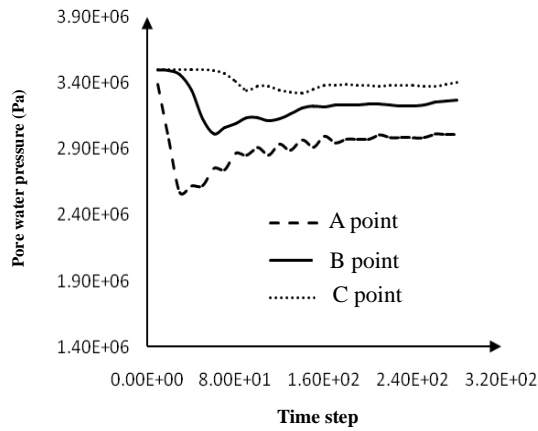


Figure 3 The change of pore water pressure while unloading

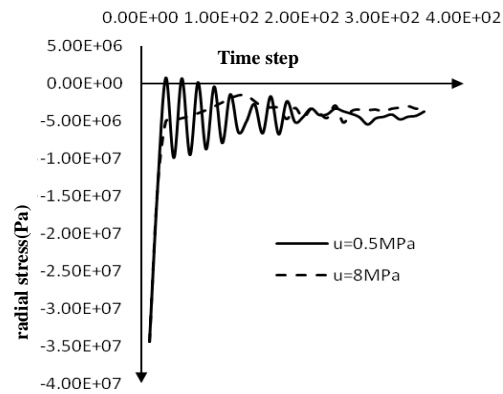


Figure 4 Disturbance of radial stress at point A by unloading

Contrast is also given in the figure that different initial pore water pressure will bring radial and tangential stress change. Judging from radial stress, when initial pore water pressure is comparatively small (0.5MPa), after unloading, stress oscillation frequency is fast, amplitude is large, rate of convergence to steady-state value is tardiness. When initial pore water pressure is comparatively large (8MPa), after unloading, stress oscillation is un conspicuous, astringing to steady-state value rather quickly, and the radial stress instance is similar. It is shown that different initial pore water pressure results in different stress variation course, higher initial pore water pressure is likely to results in stress dynamic effect reduction. So far as concerns initial pore-water pressure and stress dynamic variation relation, which still require more concretion analyses by incorporating more test. As compressive stress being intended to be negative in FLAC, along with surrounding rock radial compressive stress reducing, it is unloading, whereas circumferential compressive force increase exhibit loading, which accord to traditional analytic theory. Contrasting the two figures, radial stress reacted to disturbance much more strongly, and tangential stress reacted comparatively inconspicuous.

3 Numerical Simulation for Unloading Velocity Impacting on Fluid-Solid Surrounding Rock

Unloading velocity was defined as that in definite time how much load takes off, practically, it reflects how many time is needed to disburden combination of loads entirely. Surrounding rock unloading velocity in practical engineering made great difference according to different excavation mode, for underground engineering has a variety of excavation constructions, such as full-face digging、step excavation、branch excavation and TBM excavation and so on. For example, locale demolish high-speed photography material shows that, in the rock broken process of full-face blast, the time of exploded rock mass broken away from matrices and chuck is only several milliseconds to a few hundred milliseconds, which approaches to instant unloading. Whereas, step excavation is a inching off-loading process, the process will achieve its end when excavation shell is dug out. The difference of such unloading velocity would evidently bring different effects to fluid-solid surrounding rock.

In the following, we carry out surrounding rock excavation simulation by still using numerical model above, and then look into stability of fluid-solid coupling surrounding rock according to three different conditions, who are of different unloading velocity as following, speed rate 1 correspond with instant unloading which drops to zero, speed rate 2 is time step 500 of unloading process, speed rate 3 is time step 1200 of unloading process.

3.1 Unloading Velocity Affecting the Stress

In Figure 5, it is minor principal stress time interval variety curve under different unloading speed rate, in the condition of velocity 1, mutation is evident at the unloading beginning, and minor principal stress comes

through a variety of high frequency oscillation, and then keeps steady around quasi-static value. While both velocity 2 and 3 transit rather smoothly to around steady-state value, severalty with different slope ratio, mutation is not obvious at the end of unloading.

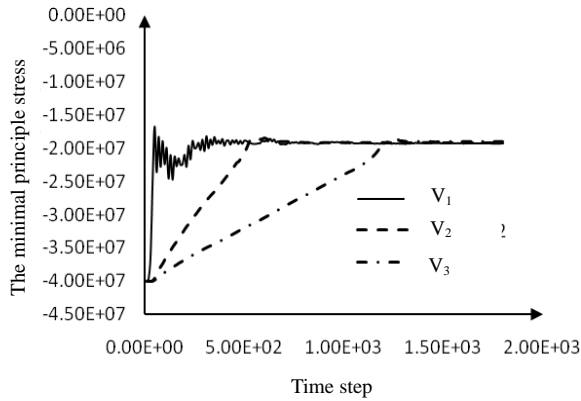


Figure 5 Change of minimum principal stress of A while unloading

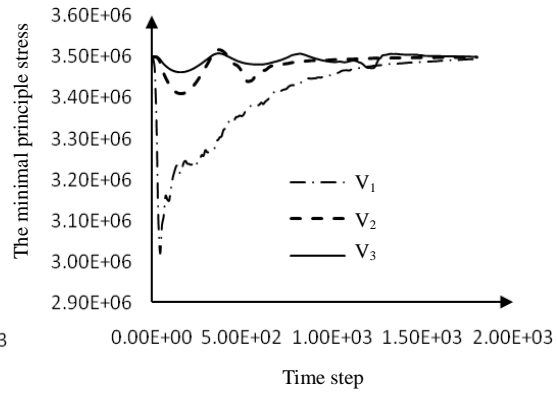


Figure 6 The change of pore pressure of B point

3.2 The Unloading Velocity Influence Pore Water Pressure

The pore water pressure is an important physical quantity which affects system dynamics behavior of surrounding rock with fluid-solid coupling, Figure 6 gives out time interval variety outcome of point B under different unloading speed rate. As it is shown from the figure, pore water pressure varies in a complicated way under different unloading velocity. According to three velocity conditions, shape of deformation curve are different, as instant unloading (speed rate 1), pore water pressure drops suddenly, and then moves up slowly. For unloading velocity 2 and 3, extent of range of pore water pressure decreases, but wave phenomena appears. Which shows that unloading velocity goes higher, extent of pore water pressure depression goes larger. By taking un-drained condition into account, for the above three conditions, it tends to be a little smaller than original pore water pressure value.

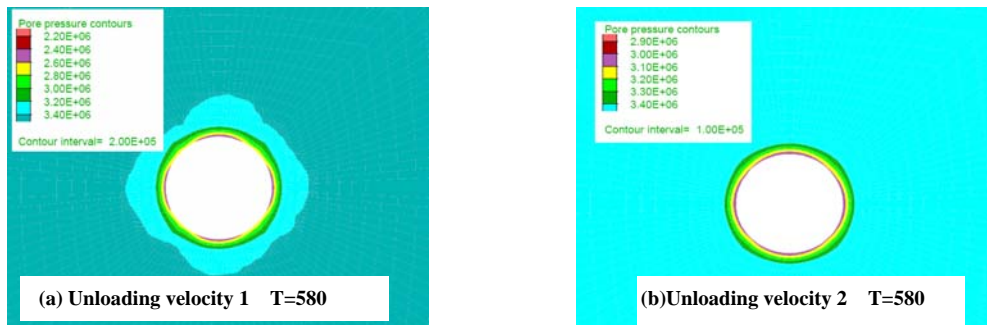


Figure 7 The pore pressure contour corresponding to different unloading velocity

Figure 7 is pore water pressure contour of surrounding rock unloading velocity 1 and 2, and corresponding to time step $T = 58$. Higher the unloading speed rate is, larger depression extent of the pore water pressure will be, so that discreteness of pore water would exist for a much longer time. While the unloading velocity is lower, pore water pressure depression extent of surrounding rock will be smaller, which is in a position to get steady-state value much more quickly, and so pore water pressure of surrounding rock would get orderliness distribution more quickly.

By analysing figure 6 and figure 7 synthetically, for surrounding rock with fluid-solid coupling system,

the stress and pore water pressure both vary dynamically along with time, until arriving at steady-state equilibrium. The pore water pressure brings disadvantageous influence to the shear strength of surrounding rock. The faster the unloading is, the larger discreteness of the variety of stress and pore water pressure will be, the time to arrive at steady state will be longer, which evidently go far from quasi-static. Especially before arriving at steady state, pore water pressure is varying dynamically.

3.3 Unloading Velocity Affecting Plastic Zone

Plastic zone is an important gist to analyze stability and failure mechanism of surrounding rock system. As unloading effect, stress and pore water pressure all went through a process of dynamic variation, difference of validity principal stress also takes dynamic variation correspondingly, strength and property of rock will also deteriorate (characteristic of such deteriorate is expressed in the strain softening model of this simulation), as a result it will give different effects to the finally plastic zone. FLAC distinguishes plastic zone through checking unitary plastic state in each time step. In a single time step, compute stress increment based on total strain increment at first, and check stress according to yield criteria. In the event that respective stress violate yield criteria, plastic yield would take place, according to plastic flow criteria, stress would ensure they are on yield surface. The activity yielding element has major role in the failure mechanism of surround rock. Figure 8 is the currently plastic zone of $T = 2200$ under three unloading velocities. We can see from the figure, unloading velocity affects surrounding rock plastic zone obviously, plastic zone of surrounding rock increases along with the increase of unloading velocity.

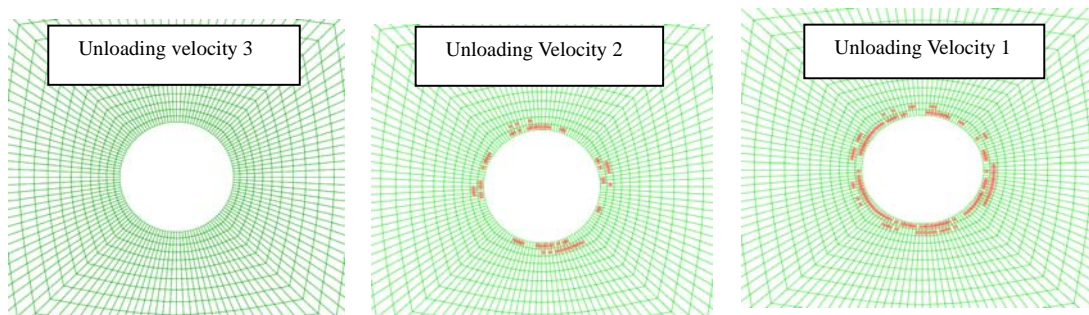


Fig 8 The plastic zones corresponding to different unloading velocity when $T=2200$

4 Conclusions

Unloading after underground engineering excavation would produce unloading stress waves and bring about surrounding rock dynamic effects. Traditional quasi-static theory is a type of sublimite model; however, it is unable to describe such a dynamic effect. We carry out preliminary numerical modelling study about effects of dynamic unloading and different unloading velocities of surrounding rock with fluid-solid coupling, and obtain the following conclusions:

Numerical simulation shows that: radial stress in surrounding rock has a stronger disturbance than tangential stress after excavation, radial stress appears as unloading, tangential stress behaves as loading, and that after oscillation the two tend to a quasi-static value. Pore water pressure itself fluctuates with time course, high pore water pressure would weaken stressful dynamic disturbance, which states that unloading brings about dynamic fluid-solid coupling effect.

Unloading velocity affects rock mass stress and pore water pressure of surrounding rock obviously. Unloading velocity is higher, disturbance extent of the stress and pore water pressure would be larger, the higher the frequency is, the time it take to get steady would be longer. Analyzing from distribution of pore water pressure, when unloading velocity is faster, discrete-time of pore water pressure distribution in surrounding rock would take more time.

Unloading velocity affects the final surrounding rock plastic zone; the plastic region went over larger when

unloading velocity went over higher. The other reason is that dynamic unloading induces the surrounding rock damage more seriously, thus the rock property becomes weaker. So, for fluid-solid surrounding rock, the higher the unloading velocity is, the easier the system destabilization is. On the contrary, the surrounding rock stability is better.

For the complexity of the problem, the work of this paper is primary, and the true tunnel excavation is in draining condition and accompanied with cracks propagation. Future research is needed to consider the draining condition and the crack propagation to study the surrounding rock failure process.

Acknowledgments

The authors would like to deeply appreciate the Project supported by the State Program of National Natural Science of China (Grant No. 50508007, 2007CB209404) and Chinese postdoctoral fund (20070420205).

References

1. Wu, G.. Current Status and Prospects of Research on Mechanism for Unloading Failure of Engineering Rock Mass, *Journal of Engineering Geology*, 2001, 9(2). 174-181.
2. Deng, G.Z. and Zhu, W.S. Criterion of Entropy Catastrophe of Stability of Surrounding Rock, *Journal of Xi'an University of Science & Technology*, 1997, 17(4). 358-361.
3. Zhou, X.P., Ha, Q.L. and Zhang, Y.X. Analysis of Location of Deformation and Complete Stress-Strain Relation For Mesoscopic Heteroscopic Heterogenous Brittle Rock Materials When Axial Stress keeps Constant While Lateral Confinement is Reduced. *Chinese Journal of Rock Mechanics and Engineering*, 2005, 24(18). 3236-3244.
4. Swanson, S.R., et al. An Observation of Loading Path Independence of Fracture Rock. *Int. J. Rock Mech. Min. Sci.*, 1971, 8(3). 277-281.
5. Miklowitz, J. Plane Stress Unloading Waves Emanating from a Suddenly Punched Hole in a Stretched Elastic Plate. *Journal of Applied Mechanics*, 1960, 27(4). 165-171.
6. Cai, M. Influence of Stress Path on Tunnel Excavation Response-Numerical Tool Selection and Modelling Strategy. *Tunnelling and Underground Space Technology*, 2008, 23. 618-628.
7. Ruistuen, H. and Teufel, L.W. Analysis of the Influence of Stress Path on Compressibility of Weakly Cemented Sandstones Using Laboratory Experiments and Discrete Particle Models. In: Aubertin, M. et al. (Eds.), *Proceedings of Second North American Rock Mech. Symposium*, 1996, 1525-1531.
8. Yan, P., Lu, W.B. and Xu, H.T. Primary Study to Damage Mechanism of Initial Stress Dynamic Unloading When Excavating Under High Geostress Condition, *Explosion and Shock Waves*, 2007, 27(3). 283-288.

ASSESSMENT OF BLASTING SEISMIC EFFECT ON STRUCTURE BASED ON WAVELET PACKET ANALYSIS

GUO-SHENG ZHONG

*The College of Resource & Environment Engineering, Jiangxi University of Science and Technology
Ganzhou, 341000, P.R. China*

LI-PING AO

*Jiangxi University of Science and Technology
Ganzhou, 341000, P.R. China*

According to the multi-resolution decomposition of wavelet packet transform, the wavelet packet frequency band energy has been deduced on different bands of blasting vibration signal. It can reflect the total influence of all of the three key elements (the intensity, frequency and duration of vibration) of blasting vibration. Considering the dynamic response of structures, the influence of the inherent characteristics of the controlled structures to blasting vibration dynamic response has been discussed, and the frequency band response coefficients for the controlled structures by blasting vibration have been obtained. First, a multi-factors blasting vibration safety criterion is established, called response energy criterion. The criterion can reflect the total influence of the intensity, frequency and duration of vibration and the characteristics (natural frequency and damping ratio) of dynamic response from the controlled structures themselves, and the feasibility and reliability of the criterion are validated by the instances.

1 Introduction

When we assess the blasting safety, we should first establish the safety criterion, which reflects factors impacting blasting seism. Practice shows that in many cases, a single particle velocity as the only indicator to measure blasting seismic intensity does not accurately reflect the structure's actual breakage [1, 2]. This is because seismic wave frequency and duration of vibration, and other factors were not considered. Research shows that [3, 4], damage to the structures caused by blasting vibration is a result from a variety of factors, such as: the intensity, frequency and duration of vibration and the characteristics of dynamic response of the controlled structures themselves. However, the current safety standards have not considered blasting vibration time and the controlled structure's inherent properties (natural frequency and damping ratio), inevitably, there are some defects and shortcomings. As soon as possible, to advance new safety criteria to reflect the comprehensive factors of blasting vibration should be put on the agenda [5, 6].

This paper uses the wavelet packet to analyze the blasting vibration signal. From the wavelet packet energy spectrum and the structure of the dynamic response, a new safety criterion has been set up, which can reflect the total influence of the intensity, frequency and duration of vibration and the characteristics of dynamic response of the controlled structures themselves. It has important theoretical and practical value to assess accurately and rationally blasting seismic effects by the criterion. The feasibility and reliability of the criterion are validated by blasting vibration live data.

2 Wavelet Packet Energy Spectrum Analysis of Blasting Vibration

2.1 Wavelet Packet Analysis of Blasting Vibration

Decomposition level is determined by the signal itself and adopted blasting vibration data acquisition instruments. The instrument used in our test is the IDTS 3850 blasting vibration recorder manufactured by Chengdu VIDTS Dynamic Instrument Co.Ltd, which has a minimum operating frequency of 1Hz. Main vibration frequency of blasting variation is generally below 200Hz, so according to the sampling theorem [7], the signal sampling frequency is set to 2000Hz, then its Nyquist frequency is 1000Hz. As a result, according to wavelet packet analysis's algorithm using binary-scale transformation, the signal can be decomposed into the 7 level, corresponding to the lowest band 0~7.8125Hz. Frequency bands of reconstruction signal at all levels of decomposed blasting vibration signal by wavelet packet as shown in Table 1.

Table 1. The range for frequency band of reconstructed signal of blasting vibration signal by wavelet packet analysis /Hz

level	$S_{i,0}$	$S_{i,1}$	$S_{i,2}$...	$S_{i,j-1}$	$S_{i,j}$
1	0~500					500~1000
2	0~250	250~500	500~750			750~1000
3	0~125	125~250	250~375	...	750~875	875~1000
4	0~62.5	62.5~125	125~187.5	...	875~937.5	937.5~1000
5	0~31.25	31.25~62.5	62.5~93.75	...	937.5~968.75	968.75~1000
6	0~15.625	15.625~31.25	31.25~46.875	...	968.75~984.375	984.375~1000
7	0~7.8125	7.8125~15.625	15.625~23.4375	...	984.375~992.1875	992.1875~1000

There $S_{i,j}$ denotes reconstruction signal at i th level, j th wavelet packet decomposition coefficients. $i = 1, 2, \dots, 7$; $j = 0, 1, 2, \dots, 2^i - 1$.

2.2 Principle of blasting vibration signal's wavelet packet energy spectrum analysis

When we decomposes signal $s(t)$ using wavelet packet into i level, we can obtain 2^i sub-band, that is, $s(t)$ can be denoted as following:

$$s(t) = \sum_{j=0}^{2^i-1} f_{i,j}(t_j) = f_{i,0}(t_0) + f_{i,1}(t_1) + \dots + f_{i,2^i-1}(t_{2^i-1}), \quad j = 0, 1, 2, \dots, 2^i - 1 \quad (1)$$

Where, $f_{i,j}(t_j)$ is reconstruction signal at node (i, j) . If lowest and maximal frequency of $s(t)$ are 0 and ω_m , then frequency width at i th level is $\omega_m / 2^i$.

According to Parseval theorem [8] in spectrum analysis, we can obtain wavelet packet energy spectrum of signal $s(t)$:

$$E_{i,j}(t_j) = \int_T |f_{i,j}(t_j)|^2 dt = \sum_{k=1}^m |x_{j,k}|^2 \quad (2)$$

Where $x_{j,k}$ ($j = 0, 1, 2, \dots, 2^i - 1$; $k = 1, 2, \dots, m$; m denotes Discrete sampling points of blasting seism) is discrete point amplitude of reconstructed signal $f_{i,j}(t_j)$. $E_{i,j}(t_j)$ is frequency band energy when signal decomposed to i level, j node.

Total energy of $s(t)$ gotten by equation (2):

$$E = \sum_{j=0}^{2^i-1} E_{i,j}(t_j) \quad (3)$$

Ratio that each band's energy accounts for of total energy as:

$$P_{i,j} = \frac{E_{i,j}(t_j)}{E} \times 100\% \quad (4)$$

By equation (1) - (2), we can see that blasting vibration signals decomposed by the wavelet packet into different frequency components, which can reflect the influence of blasting vibration frequency, and the band energy while at the same time reflect blasting vibration intensity and duration. As a result, the wavelet packet band energy obtained on this basis is able to reflect the influence of three elements of blasting vibration (vibration intensity, frequency and duration).

3 Criterion Of Security Response Energy of Blasting Seism

3.1 Analysis of Construction Response to Blasting Seism

Blasting seism waves could be seen synthesis by a series of sine waves, that is:

$$A(t) = \sum_{i=1}^n A_i \sin(\omega_i t + \varphi_i) \quad (5)$$

Where A_i , ω_i and φ_i denote amplitude, frequency and initial phase of i th sine wave respectively.

In order to simplify the calculation, the structure of the system is usually assumed to be a single degree of freedom system, according to the principle of balance of power get [9]:

$$\ddot{x} + 2\xi\omega_0\dot{x} + \omega_0^2 x = \frac{F_i}{m} \sin \omega_i t \quad (6)$$

Where $\omega_0 = \sqrt{k/m}$ and $\xi_0 = c/2m\omega_0$ are natural frequency and damping ratio of structure.

We can see from the structural dynamics theory [9], under blasting seism loading component $F_i \sin \omega_i t$ force, magnified factor, which is maximum displacement of construction compare to corresponding displacement, is:

$$\beta = \frac{1}{\sqrt{(1 - \omega^2/\omega_0^2)^2 + 4\xi_0^2 \cdot (\omega^2/\omega_0^2)}} \quad (7)$$

Where ω is inspirit frequency of blasting seism; ω_0 and ξ_0 are natural and damping ratio of structure.

This shows that the magnification factor β , structure's response coefficient to blasting vibration, is a physical quantity of non-dimensional. Equation (7) tells us that response factor of controlled structure is closely related to its own natural frequency and damping ratio. When the blasting vibration incentive frequency is closer to natural frequency as well as the damping ratio of construction smaller, the greater the vibration response factor, that is, the greater the vibration response; On the other hand, less vibration. As a result, according to structure's vibration response coefficient, we can obtain frequency band response coefficient.

3.2 Determining the Frequency Band Response Coefficient of Structure

Assumption that incentive frequency is ω , natural frequency and damping ratio of structure are ω_0 and ξ_0 , respectively, according to the equation (7), the frequency band response coefficient of structure by wavelet packet analysis is as follows:

$$\varepsilon_{i,j} = \frac{1}{\omega_m/2^i} \int_{\omega_{i,j-1}}^{\omega_{i,j}} \frac{1}{\sqrt{(1 - \omega^2/\omega_0^2)^2 + 4\xi_0^2 \omega^2/\omega_0^2}} d\omega \quad (8)$$

where $\varepsilon_{i,j}$ is response coefficient when blasting seism decomposed by wavelet packet to i level and j node; $\omega_{i,j}$ and $\omega_{i,j-1}$ are respectively upper and lower limit of frequency.

3.3 Criterion of Response Energy

An important factor that surface vibration caused by explosion damage to the building is vibration energy. Since the blasting vibration is a broadband signal of non-stationary random signals, we using wavelet packet technology analysis seism speed signal into time and frequency domain and calculate the energy spectrum of the wavelet packet, and then according to different frequency impact on structure differently, wavelet packet energy multiplied by the corresponding the band's response factor and cumulative them can get response energy (expressed by E_R), called criterion of response energy. That is, response energy E_R is:

$$E_R = \sum_{j=0}^{2^l-1} E_{i,j}(t_j) \cdot \varepsilon_{i,j} \quad (9)$$

where $E_{i,j}(t_j)$, $\varepsilon_{i,j}$ denote band energy and response coefficient of seism signal component at i th level, j th node.

As the wavelet packet band energy is able to reflect the intensity, frequency and duration of blasting seism. The frequency band response coefficient can reflect the response level of structure's inherent properties (natural frequency and damping ratio). As a result, criterion of response energy established on this basis that will be able to consider seismic intensity, frequency and duration, as well as dynamic response characteristics of structure, accurately and comprehensively describe the response degree.

4 Examples in Engineering

4.1 Test of Blasting Seism

In order to validate veracity and practicability of energy response criterion of blasting seism, authors tested it at a metal mine. Authors specially select a same type structure as test object. Before blasting, the structures are intact. We choose particle vibration speed at perpendicularity direction as measurements. Results of this test are displayed in figure 1 and table 2.

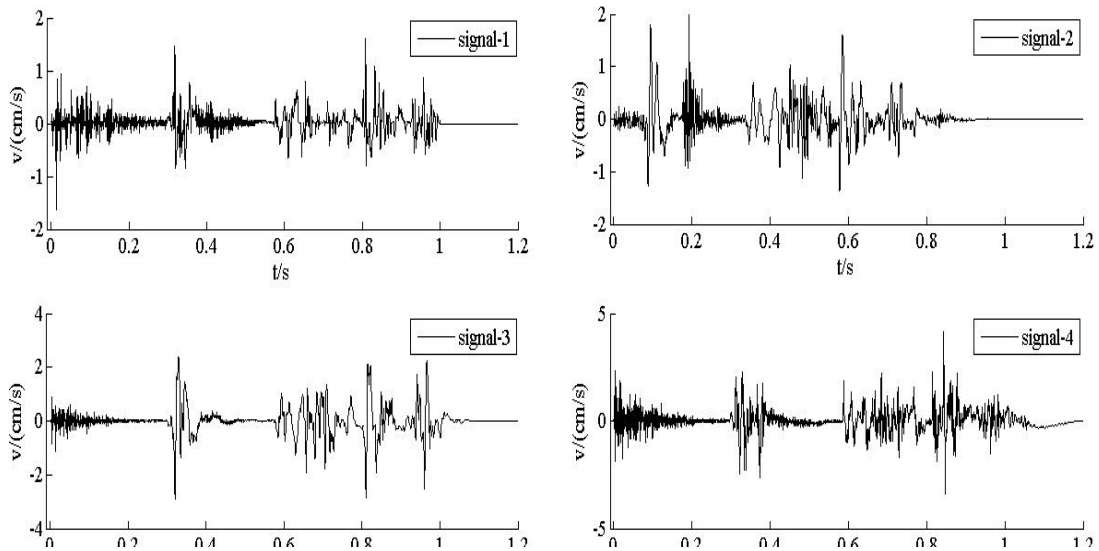


Figure 1 The velocity history curves of blasting vibration monitoring.

Table 2. The result of blasting vibration monitoring

number	construction	structure	PPV/(cm/s)	Main frequency/Hz	Status after blasting
1	house A	brick & stone	1.6392	6.8359	small chinks
2	house B	brick & stone	1.988	21.4844	no destruction
3	house C	brick & stone	2.8948	30.2734	no destruction
4	public house	brick & stone	4.1504	47.8516	no destruction

4.2 Evaluating Safety Response Energy Criterion of Blasting Vibration

(1) Wavelet packet energy spectrum analysis:

In this analysis method, how to choose wavelet basis is an important problem because different basis analysis the same signal is able to bring different outcome [10]. Studies indicated that db7 and sym8 are compactly supported, smooth and symmetrical similarly [11]. They are best wavelet basis to analysis non-stationary random signals. We analyze blasting vibration signals 1 into 7 level wavelet packet decomposing with sym8, shown in figure 2. According to the equations (1) to (4), the wavelet packet energy spectrum, band energy and its distribution are available; see Figure 2 and Table 3 below.

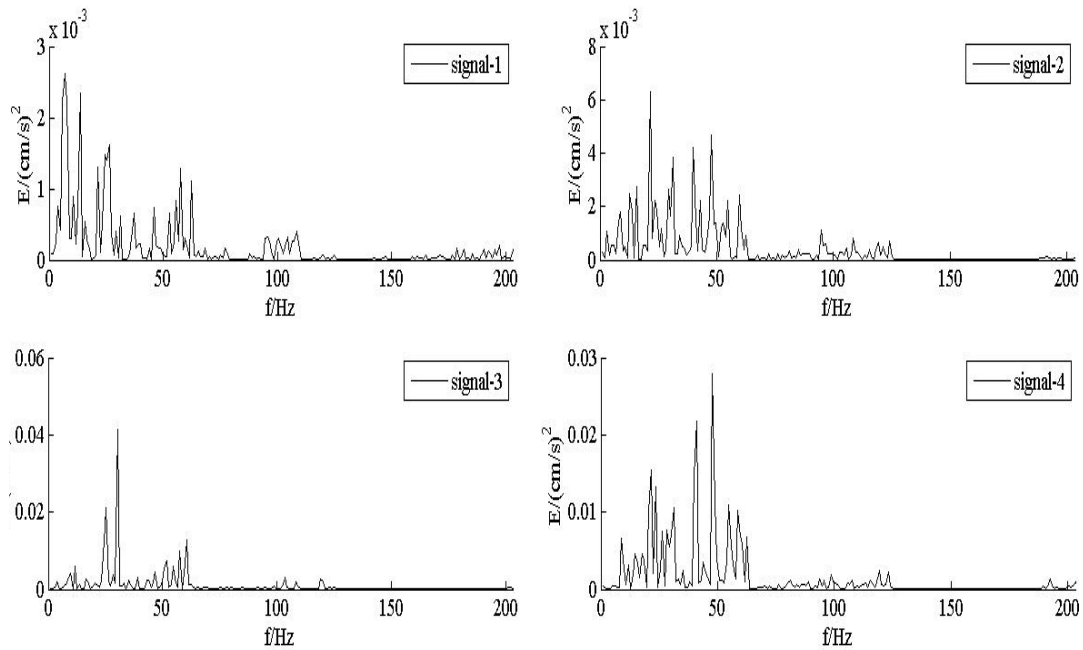


Figure 2 The wavelet packet energy spectrum for blasting vibration signal.

The following conclusions could be obtained by blasting vibration signals wavelet packet energy spectrum analysis: We can see from figure 2 and table 3 that four signals in 0~203.125Hz account for 95.3044%,

95.6787%, 96.1285% and 97.3513% of total energy respectively. The energy of blasting vibration distribute is concentrated in 0~200Hz, so the energy larger than 200Hz was ignored.

Table 3. The wavelet packet frequency band energy and distribution for blasting vibration signal

Frequency band /Hz	singal-1		singal-2		singal-3		singal-4	
	$E/(\text{cm/s})^2$	$P/\%$	$E/(\text{cm/s})^2$	$P/\%$	$E/(\text{cm/s})^2$	$P/\%$	$E/(\text{cm/s})^2$	$P/\%$
0~7.8125	0.0086471	21.197	0.0043853	4.9068	0.0055592	2.3904	0.0019808	0.61129
7.8125~15.625	0.00536	13.14	0.0098769	11.051	0.014891	6.4031	0.02314	7.1412
15.625~23.4375	0.002476	6.0698	0.0108	12.084	0.010857	4.6686	0.051063	15.758
23.4375~31.25	0.0059694	14.633	0.012328	13.794	0.084446	36.312	0.04159	12.835
31.25~39.0625	0.0014752	3.6164	0.0032754	3.6649	0.0095638	4.1124	0.0073848	2.279
39.0625~46.875	0.00143	3.5054	0.011345	12.694	0.012182	5.2383	0.045932	14.175
46.875~54.6875	0.0014872	3.6456	0.013258	14.835	0.023856	10.258	0.060725	18.74
54.6875~62.5	0.0041362	10.139	0.0051814	5.7976	0.032017	13.767	0.041324	12.753
62.5~70.3125	0.0005638	1.3821	0.00044796	0.50123	0.0024172	1.0394	0.0014631	0.45152
70.3125~78.125	0.00046083	1.1297	0.00083128	0.93014	0.0018913	0.81326	0.0015606	0.48162
78.125~85.9375	7.5791e-005	0.18579	0.0013258	1.4835	0.0015877	0.68269	0.0047236	1.4577
85.9375~93.75	0.00025544	0.62618	0.0011181	1.2511	0.0011673	0.50196	0.0044929	1.3865
93.75~101.5625	0.0017429	4.2725	0.0031731	3.5505	0.0025757	1.1075	0.006311	1.9476
...
203.125~1000	0.0019155	4.6956	0.003862	4.3213	0.0090037	3.8715	0.0085829	2.6487
Σ	0.040793	100	0.089372	100	0.23256	100	0.32404	100

(2) Calculation of response energy

We may acquire dynamic response parameters of these 4 structures by impulse method and vibration analysis, shown in table 4. According to equations (8) and (9), we can acquire frequency band response coefficient and response energy of these 4 structures, shown in table 5.

Table 4. Parameters of dynamic response property for the controlled structures

construction	structure	floor	Natural frequency ω_0 /Hz	Damping ratio ξ_0
house A	brick & stone	1	6.6	0.041
house B	brick & stone	1	5.6	0.044
house C	brick & stone	2	4.5	0.043
public house	brick & stone	1	5.2	0.045

Table 5. The frequency response coefficient and response energy for the controlled structures

Frequency band /Hz	house A		house B		house C		public house	
	$E_{7,j}/(\text{cm/s})^2$	$\varepsilon_{7,j}$	$E_{7,j}/(\text{cm/s})^2$	$\varepsilon_{7,j}$	$E_{7,j}/(\text{cm/s})^2$	$\varepsilon_{7,j}$	$E_{7,j}/(\text{cm/s})^2$	$\varepsilon_{7,j}$
0~7.8125	0.0086471	2.8309	0.0043853	2.5893	0.0055592	2.234	0.0019808	2.4544
7.8125~15.625	0.00536	0.65934	0.0098769	0.37581	0.014891	0.20714	0.02314	0.30334
15.625~23.4375	0.002476	0.1361	0.0108	0.094152	0.010857	0.058721	0.051063	0.080078
23.4375~31.25	0.0059694	0.063338	0.012328	0.044782	0.084446	0.028454	0.04159	0.03837
31.25~39.0625	0.0014752	0.037024	0.0032754	0.026377	0.0095638	0.016872	0.0073848	0.02266
39.0625~46.875	0.00143	0.024374	0.011345	0.017427	0.012182	0.011184	0.045932	0.01499
46.875~54.6875	0.0014872	0.017288	0.013258	0.012386	0.023856	0.0079626	0.060725	0.010661

54.6875~62.5	0.0041362	0.012909	0.0051814	0.0092602	0.032017	0.00596	0.041324	0.0079743
62.5~70.3125	0.0005638	0.010012	0.00044796	0.0071875	0.0024172	0.0046294	0.0014631	0.0061912
70.3125~78.125	0.00046083	0.0079933	0.00083128	0.0057417	0.0018913	0.0037	0.0015606	0.0049468
78.125~85.9375	7.5791e-005	0.0065304	0.0013258	0.0046928	0.0015877	0.0030253	0.0047236	0.0040438
85.9375~93.75	0.00025544	0.0054361	0.0011181	0.0039076	0.0011673	0.0025198	0.0044929	0.0033675
93.75~101.5625	0.0017429	0.0045959	0.0031731	0.0033045	0.0025757	0.0021313	0.006311	0.002848
...
203.125~1000	0.00054886	0.0011909	0.00028505	0.00085707	0.0014466	0.00055326	0.0024375	0.00073892
$E_R / (\text{cm/s})^2$	0.028928		0.017179		0.019283		0.019507	

(3) Analyzing the criterion of blast vibration response energy

In table 5, largest response energy (0.028928) of house A great larger than those of house B (0.019507), house C (0.019283), and public house (0.019507). Considering that 4 buildings are all masonry structure, where response energy only of house A is larger than that of masonry destroy threshold, the results also is the case. So results from method in this paper are completely consistent with the actual monitoring results.

5 Conclusions

In this paper, based on wavelet packet energy spectrum analysis and dynamics response characteristics, we set up a safety criterion — response energy criterion, which takes intensity, frequency and duration into account. It is validated by engineering and several conclusions are also drawn:

1) Response energy criterion reflects intensity, frequency and duration of blasting vibration, as well as dynamic response characters, so it can depicts the influences more accurately and more comprehensively. However, for the destruction threshold of various types of building, a large number of blasting vibration data measured is to be determined.

2) Establishment of safety response energy criterion of blasting vibration needs a large number of various sectors' efforts. This paper has done research work for construction of a complete and scientific safety criterion and has laid a theoretical and technical basis.

References

1. Yang, S.Q., Liao, X.K. and Liu, B.C. Default of the Judging Standard of Blasting Vibration Safety Ababstract. Explosion and Shock Waves, 2001, 21 (3). 223-228.
2. Wang, X.G., Yu, Y.L. On Several Problems of Safety Criterion for Blasting Vibration. Engineering Blasting, 2001, 7 (2). 88-92.
3. Li, Z.K., Wang, A.M. and Li, S.C.. Analysis for a Triggered Collapse in Construction of an Underground Powerhouse. Chinese Journal of Geotechnical Engineering, 1997, 19 (5). 74-79.
4. Zhong, G.S., Xu, G.Y. and Xiong, Z.M. Application Research of the Energy Analysis Method for Blasting Seismic Signals Based on Wavelet Transform. Explosion and Shock Waves, 2006, 26 (3). 222-227.
5. Li, H.N., Wang B.Q. and Lin, G.. Studies on Some Problems on Explosion Earthquake Responses. Explosion and Shock Waves, 1996, 16 (1). 61-67.
6. Chen, M., Lu, W.B., Yi, C.P., et al. Research on Safety Standard for Rock Anchor Beam Under Blasting Vibration in Large Underground Powerhouse. Chinese Journal of Rock Mechanics and Engineering, 2006, 25 (3). 499-504.
7. Zou Y.P. and Li X.. Signal Transform and Processing. Huazhong University of Science and Technology Press, 1993.

8. Zhou, D.L. and Shao, G.Y. Modern Testing Technology and Signal Analysis. China University of Mining and Technology Press, 2005.
9. Yu, Z.D.. Basic Structural Dynamics. Tongji University Press, 1987.
10. Hu, C.H.hang-hua, Zhang, J.B., Xia, J., et al. System Analysis and Design Based on Matlab — Wavelet Analysis. Xi'an: XIDIAN University Press, 1999.
11. Zhong, G.S. and Fang, Y.G. Safety Criterion of Blasting Vibration for Structure Based on Wavelet Packet Analysis. Chinese Journal of Geotechnical Engineering, 2009, 32 (2). 223-228.

PANORAMIC INSPECT AND EVALUATON ON BLAST EFFECTING OF INDUCTION CAVING IN HARD ROCK ROOF

JIAN-HUA HU

*State Key Laboratory of Geomechanics and Geotechnical Engineering, Institute of Rock and Soil Mechanics,
Chinese Academy of Sciences, Wuhan, 430071, P.R. China*

*School of Resources and Safety Engineering, Central South University, Key Laboratory of Deep Mining &
Disaster Control in Hunan Province, Changsha, 410083, P.R. China*

KE-PENG ZHOU

*School of Resources and Safety Engineering, Central South University
Changsha, 410083, P.R. China*

XIAN-WEI LUO

*Tongkeng Mine, Liuzhou China Tin Group Company Ltd
Liuzhou, 545000, P.R. China*

Abstract: Technology of induction caving roof is based on the successive mining, and it is said that the zone of fracturing is controlled through the pre-splitting blast and induce fracture was developed by the forced blast. With the development and expansion of the cracks, the rock mass would have been instability and caving in the roof. But, due to the process of the induction caving roof by the blast in the underground mine, the effects were invisible to the pre-splitting blast and the force blast. It is difficult to evaluate the effect of blast. Using the borehole camera system, the technique of front view and digital panoramic were used to inspect the effect of blast. The shape of the hole was detected before blast, and the blast effect was inspected after the blast. Especially, after blasting, the cracks character is described by the digital panoramic borehole camera. The photographs were analyzed by the viewing them digitally. The results of the digital panoramic borehole camera show: (1) To pre-splitting blast, the pre-splitting cracks were formed after the blast. Its width is up to 20~40 mm, and the half wall of hole could be seen in the bottom of the hole. (2) Large amounts of secondary cracks were formed in the rock mass of the roof. The crack form is an "X", and the original cracks were expanded. The mass shapes of blast was right, the rock stacked by the natural angle of slope. It is an advantage to induction caving roof to the large cracks and ruptured structural rock mass.

1 Introduction

To the induction caving roof based on the successive mining, it is a course of the artificial disturbance and control is used to induction caving in hard roof[1-4]. Its idea is following. First, the state is analyzed to the energy accumulation and the stress concentration during the successive mining in the hard roof. Second, the process of the cracks evaluation is induced by the artificial disturbance, such as blasting caving in the part. Third, the condition of the natural caving is formed to handle roof in order to safety. Today, the technology of

induction caving roof include the blasting induction and hydraulic fracturing. To the blasting caving roof, it is difficult visible and inspect to the effecting of the blast[5]. For example, how do inspect to the form of the pre-splitting crack. In order to inspect the effecting of the blast induction caving roof, the technology is introduced that the digital panoramic borehole camera. It is effective to video and inspect to the concealed works of the pre-splitting crack and the induced cracks.

The development stages include the borehole picture camera (BPC), the borehole video camera (BVC) and the digital borehole optical tomography (DBOT). It is a quickly developing technology to engineering application. The two kinds of technologies are the main technologies international to the digital borehole optical tomography. One is the digital optical picture television (OPTV and OBI-40), and the other is the digital panoramic borehole camera system. To the digital panoramic borehole camera system, it change the inspect method of the traditional sidewall observation. The technologies make up for the disadvantages of the traditional borehole picture camera by developing to panoramic technology, quickly inspect and low cost. The technologies are widely applied in the geotechnical engineering, mining engineering, civil engineering, hydraulic engineering and glacier and frost soil engineering.[8-11]

In the paper, it is applied to evaluate the induce-blasting effect to the digital panoramic borehole camera system. The quality and the form of the blast-hole are judged by the results of the vision. And the blasting induce-fractures are fine described in the light of the digital panoramic borehole camera results.

2 Engineering Background

Tongkeng Tin Mine is a lager-scale underground mine, and it is one of the main mine in China Tin Group Corporation. The 92th ore body has been became the main mining ore body at present. It is a layer structure and net vein impregnation deposit-body. The possible ore are more than the 35 million ton. It lied below the 91th ore body, there are close joined. And its integrality is damaged due to the mining activities in the 91th ore body, the direct roof is the cementing or non-cementing filling body in the emptied areas, in the part distract zone, the roof is the emptied areas evenly, so that the incipient dangerous zone are formed in the mining filed. At present, the mine method is induction caving roof based on the successive mining had been tested in the T112-T115 mine segment of 92th ore body. In order to study the effect of the induce-fracture, the digital panoramic borehole camera system is used to inspect the induce-cracks in the borehole.

3 Parameters of Induce Blast

To the induction caving roof based on the successive mining, it is important to improve the resources recycle ratio and guarantee the safety in the mining process. The key technologies are induce blast structures and detonation modes in the induction caving roof[12]. It is used to control the distance between the mining and goaf. And the caving body could be formed the characteriatics.

3.1 Borehole Diameter

These factors should be considered to design the borehole diameter such as the existing engineers and the work safety. According to the roof thickness, the drill equipments and mining site, and the principle to reduce the borehole quantity[13], the borehole diameter is confirmed 165 mm.

3.2 Blast Parameter of Forced Caving Roof

To the forced caving roof, the first request is meet the characteristics thickness. So the length of the load detonators is up to 20m. The scope of distance between two rows is from 3.80 to 4.95 in the light of the borehole diameter. In fact, the value of the distance between two rows is 4.00m[13]. The borehole spacing was made up to 4.00m in the middle two rows borehole. Because the lumpiness haven't request to the rock in the caving roof. To the periphery-hole, the hole-bottom spacing is up from 12m to 18m, the pop hole space is 0.465m. The tilt angle is 60° in the high side and 70-72° in the low side of the roof. The explosive is the emulsified ammonium nitrate-fuel oil agent. The length is 0.6-0.8m, weight is 12.5kg to the single explosive tube. In order to avoid flapping top when the process of the induction caving roof, the method was used to add strengthen explosive charge in the bottom. To the forced caving roof, the boreholes form was sector.

3.3 Pre-Splitting Blast Parameter

When the pre-splitting blast borehole diameter more than 60mm, the borehole distance scope is from 1.32 to 1.98m, take 1.4m. The explosive charge is emulsified ammonium nitrate-fuel oil agent. Its diameter is 90mm, the length is 0.8m, and the weight is 5.85kg. To the charge structure, the method was used to the air interval charge. The interval distance was 2.0m. The depth of the pre-splitting borehole was controlled to 25m. In order to assure the pre-splitting perforation, the strengthen-explosive charge or the 2-3m successive charge should be used in the pre-splitting bottom. The detonator segment was same between the east and west pre-splitting borehole.

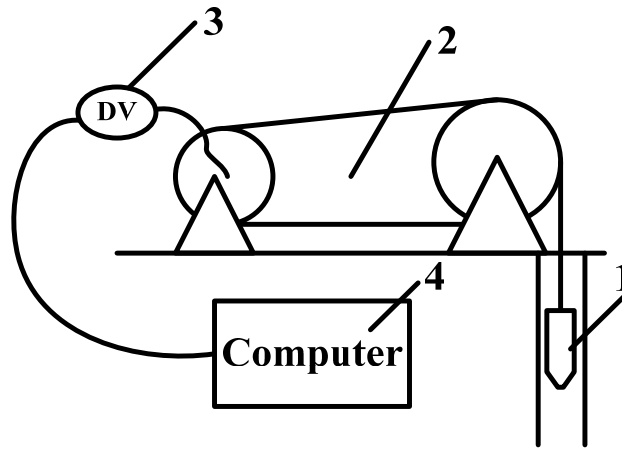
3.4 Detonation Mode

The studied results of the induction caving roof mode showed it is advantage to induction caving and work safety. That is the hole-by-hole microsecond delay firing, which the first is pre-splitting blasting and the second is forced blasting, the caving space is formed in once time [14]. At the same time, think of the safety, the detonating method was selected the nonelectric squib in the pre-splitting and the forced caving blast ^[15]

4 Visual Inspect

4.1 Inspect System

Borehole camera system made in the Institute of Rock and Soil Mechanics, The Chinese Academy of Science, its name is digital panoramic borehole camera system. It is a kind of integration application technology of electronic technology, video technology, digital technology and computer technology[16]. It could solve the visual and digital collected to the engineering geology datum in the borehole. The system frames are formed include to the hardware and software, seen Figure 3.



1.digital panoramic borehole camera probe; 2.winch(depth pulse); 3.digital camera; 4. computer

Figure 1 System chart of borehole camera

4.2 Inspect the Borehole Form

Before blasting, the method was used to inspect the borehole from and quality which was the forward looking of the digital panoramic borehole camera probe. Furthermore the deformation and penetration of borehole were inspect in the light of the forward looking results. The results were seen in Figure 2.

The inspect results show the following. (1) In the west pre-splitting chamber, the borehole shape was changed from the round shape to ellipse shape because of the ground pressure action. That was the ground pressure reflex was significantly in the west chamber (seen in Figure 2.a) . It would influence the direction of the pre-splitting crack. (2) The original cracks were developed as the mining space effects (seen in Figure 2.b). And these cracks would be reduced the blasting energy effects. The explosive charge should be avoided to set the cracks site. (3) The roof rock mass were penetrated by borehole in the 90% of the borehole (seen in Figure 2.c). To other boreholes, it was difficult to endure the weight of the explosive as the bottom was thin (seen in Figure 2.d).The methods of handling the borehole were following. First, to deformation, the propose was put forward to the adding the borehole by the deformation borehole. Second, the sites of the cracks were precisely oriented and the charge was dislocation charge to avoid the blast energy reduce. Third, the explosive charges were bounded by the iron wire or rope.

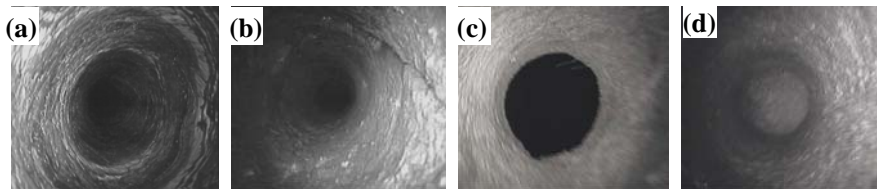


Figure 2 Inspecting shape picture of holes

4.3 Inspect

After blast, to the induction blasted muck-pile, its shape angle is the natural-rest-angle of rock mass under roof. From the shape, the average thickness is up to 16 m, the middle is higher than the two ends from the direction of empty width. In the mining course, the disaster phenomenon haven't be found such as segmentation falling, specially lager scale falling of roof. It is advantage to safety mining.

In the induction caving roof test of Tongkeng Mine, the cracks were inspected by the digital panoramic borehole camera system. In order to contract between the blast and non-blast to the cracks growth effect, the X55, X37 and X23 were inspected in the west prespplting blast hole. The B19, B16 and B12 were inspected in the forced caving hole. The D55, D35 and D23 were inspected in the east prespplting hole. The inspect holes characters seen Table 1.

Table 1 Reality and original depths of bole

measuring point	original depth	measuring depth	remakes
X23	53.5	11	It is 6 m distance to caving empty zone
X37	43.6	21	
X55	50	26	Non-mining and blast, the measuring depth is up to 525m lever.
B12	29.6	11	It is 10 m distance to caving empty zone
B16	37	20	
B19	36	26	non-blast
D23	25	12	It is 10 m distance to caving empty zone
D25	25	15	
D37	20	15	non-blast

Note: The first blast induction caving have been carried out. In the table, the "X" is the west presplitting hole, the "D" is the east presplitting hole, the "B" is the forced caving hole.

During the process of induction caving roof, cracks are frequently encountered in a rock mass. After induction caving roof, the inspect results show that the cracks have two form through the cracks parameters from the hole. The first is the original cracks. The second is the secondary cracks. From the cracks structure, the cracks obliquity is main steep obliquity. At the same time, the secondary cracks are cracks group around the original cracks. From the width of cracks, the original cracks are 5mm, and the secondary cracks are growth by the induce fracture.

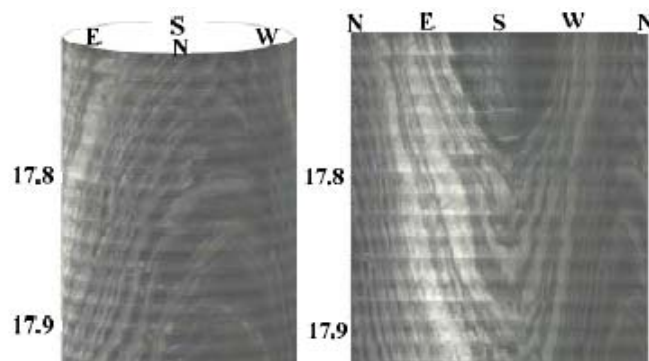


Figure 3 Detect picture of primary cracks in roof

Inspect find that the rock mass is the haricot limestone. In the non-mining roof, the original cracks is less than the empty roof, the cavabilities is uncavable. So, the rock mass stability of roof is middle. To the small scale exposure area, it is difficult to natural caving in the roof. The hole pictures of roof seen Figure 3.

The pre-splitting slit have been found between two pre-splitting holes. The slit width is up to 20~40 mm. The slit is continuum and vertical along the hole wall. And influence the free face, the slit width become capacious in the bottom of the hole. Addition to, the half hole wall have been found in the bottom of the pre-splitting hole. It prove that the caving zone have been controlled by the pre-splitting slit in the roof, seen in Figure 4 a and b.

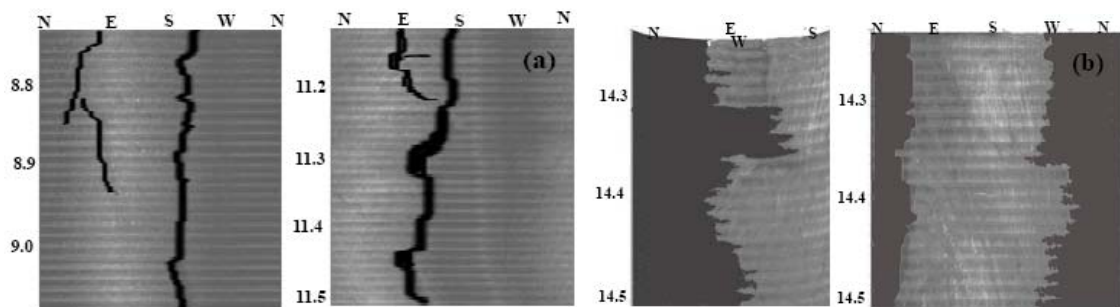


Figure 4 visualization picture of presplitting blast bores

In the rock mass of roof, the cracks were numerous developed by induction caving. Seen Figure 5 a and b. From the cracks shape, there are two typical characters. One is the steep obliquity, one is “X” type of cracks. And the original cracks were enlarged after induction caving.

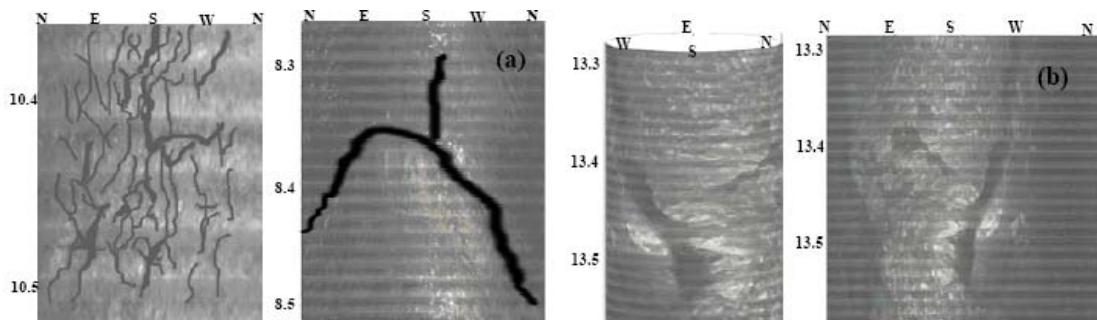


Figure 5 Visualization picture of induce cracks in the caving blast bores

Statistic results show that the length of crack obey the the normal distribution. The mean length of cracks are 50~60 mm in the sight of borehole camera. By the induction caving engineering, the frequency of cracks is up to 15~20 strips/ m. Especially the cataclastic texture of the part rock were found in the hole. To the cataclastic texture, it is advantage to induce-caving roof.

5 Conclusions

In the paper, the induced fractures were inspected through the forward looking and panoramic by the digital panoramic borehole camera system. Also, the visual results are clear and digital. The results propose the base data to blasting in the induction caving roof. So it is very useful to evaluate the induce blast effects.

Through the induction caving roof, the induce cracks had been large scale developed in the roof. The shapes of induce cracks is steep obliquity and “X” type. The width of pre-splitting cracks is up to 20-40mm. The half borehole was exist in the pre-splitting borehole bottom. The length of crack obey the the normal distribution. The mean length of cracks are 50~60 mm in the sight of borehole camera. The results show that the hard rock mass roof was induced caved by the induce cracks.

Acknowledgements

The authors wish to acknowledge the collaborative funding supported by the Open Research Fund of State Key Laboratory of Geomechanics and Geotechnical Engineering, Institute of Rock and Soil Mechanics, Chinese Academy of Sciences, under grant NO. Z110703. And supported by National Key Technology R&D Program in the 11th five year plan period(2006BAB02B04-1-1).

References

1. Hu, J.H., Zhou, K.P., Li X.B., Yang, N.G., et al. Numerical Analysis of Application for Induction Caving Roof. *Journal of Central South University of Technology*, 2005, 12(Supp 1). 146-149.
2. Hu, J.H., Zhou, K.P., Li, X.B., Yang, N.G., et al. Numerical Analysis and Applying to Induction Caving Roof. *Ground Pressure and Strata Control*, 2005, 22(3). 68-70.
3. Zhou, K.P., Su, J.H., Gu, D.S., Shi, X.Z., et al. The Nonlinear Forecasting Method of the Least Security Coping Thickness When Mining under Complex Filling Body. *Journal of Central South University of Technology: Science and Technology*, 2005, 36(6). 1094-1099.
4. Hu, J.H., Zhou, K.P., Gu, D.S. and Su, J.H. Analysis the Time-Varying Character of Induction Caving Roof Based Continuous Mining. *Mining Technology*, 2006, 6(3). 157-160.
5. Mu, Z.L., Dou, L.M., Zhang, G.W., Zhang, S.B., et. al. Study of Prevention Methods of Rock Burst Disaster Caused by Hard Rock Roof. *Journal of China University of Mining & Technology*, 2006, 35(6). 737-741.
6. Wang, C.Y. and Lawk, T. Review of Borehole Camera Technology. *Chinese Journal of Rock Mechanics and Engineering*, 2005, 24(15). 3440-3448.
7. Wang, C.Y., Ge, X.R. and Bai, S.W. Study of the Digital Panoramic Borehole Camera System. *Chinese Journal of Rock Mechanics and Engineering*, 2002, 21(3). 398-403.
8. Bennecke, W. The Identification of Basalt Flow Features from Borehole Television Logs. *International Journal of Rock Mechanics and Mining Sciences and Geomechanics Abstracts*, 1994, 31(5): 371-383.
9. Chen, Y.Q., Takashi, N., Michinao, T., et al. A Fluorescent Approach to the Identification of Grout Injected into Fissures and Pore Spaces. *Engineering Geology*, 2000, 56(3/4): 395-401.
10. Zhang, G.Y., Zhang, H.X. and Yue, G.Z. Observation and Analysis of Fissures in Overburden Strata Induced by Coal Mining. *Rock and Soil Mechanics*, 2003, 24(Supp.). 414-417.
11. He, M., Gan, G.Q. and Tang, W.J. Application of Water Television System to Water Conservancy Engineering. *Chinese Journal of Rock Mechanics and Engineering*, 2001, 20(Supp.). 1842-1844.

12. Hu J.H., Su, J.H., Zhou, K.P., Zhang, S.C., et.al. Time-varying numerical analysis of the mode in the induction caving roof. *Rock and Soil Mechanics*, 2008, 29(4). 887-891.
13. Zhang, C.L., Li, X.P., Mi, J. and Wang, Y.L. Numerical Analysis and Parameters Option Based on Damage in Smooth Blasting. *Journal of Wuhan University of Technology*, 2006, 28 (7). 86-89.
15. Hu, J.H., Su, J.H., Zhou, K.P., Zhang, S.C. and Gu, D.S. Evaluation and Time-varying Mechanical Numerical Analysis to Induction Caving Roof. *Proceeding in Mining Science and Safety Technology* 2007, Parts A: 48-54.
16. Gong, J. An Example of Wide-space Millisecond Multiple-row Holes Blasting. *Blasting*, 2001, 18(2). 37-38.

RESEARCH ON ROCKBURST PREDICTION WITH EXTENICS EVALUATION BASED ON ROUGH SET

SHENG-WU QIN, JIAN-PING CHEN and QING WANG

*College of Construction Engineering, Jilin University
Changchun, 130026, P.R. China*

DAO-HONG QIU

*Research Center of Geotechnical and Structural Engineering, Shandong University
Jinan, 2500616, P.R. China*

Rockburst is one of the main engineering geological hazards at high geostress zones, and the prediction of the possibility and classification of rockburst are important issues in many underground engineering practices. The evaluation results of rockburst differ according to the criteria. The extenics evaluation can be used to handle contradictory problems. However, the evaluation results are influenced by the weight coefficient. In this paper, a rockburst prediction method with extenics evaluation is proposed. Weight coefficient of extenics evaluation is determined by the rough set theory. Determination of the weight coefficient is translated into the estimation significance of attributes among rough sets. Based on the analysis of the main causes of rockburst, the compressive strength, tensile strength, the angle between the preferred structural plane and the maximum principal stress, elastic energy index of rock, and the maximum tangential stress of the tunnel wall are chosen as the criterion indexes for rockburst prediction, and then the decision table about rockburst prediction is established. By analyzing the significance of the conditional attribute set for the decision attributes, the weight coefficient of the extenics evaluation model is determined by rough set. Finally, the model is applied to predict the rockburst gradation of the Kuocangshan tunnel. The practical example demonstrates that the proposed method overcomes the subjectivity of traditional determination of the weighting coefficient. The prediction results indicate that the proposed method is effective and reliable in the prediction of rockburst.

1 Introduction

Rockburst is a dynamic instability phenomenon of surrounding rock mass in high geostress, caused by the violent release of strain energy stored in rock mass. Rockburst occurs during excavation of underground space in the form of stripe rock slices, rock falls or throwing of rock fragments, sometimes accompanied by crack noise. It occurs suddenly and intensely usually causing catastrophic destruction and damage to equipment, injuries and fatal accidents, construction and production delays, and a higher cost of construction. It is an emergency issue which needs to be solved in deep mining engineering and rock engineering, and more and more attention is given to rockburst along with the development of underground space excavation.

At present, the studies on rockburst primarily focus on the phenomenon, regularity and mechanism, as well as the cause of formation, the critical conditions and preventive methods. After studying numerous cases, many scholars have suggested many theories and various prediction methods [1-5]. In this research, various criteria are proposed, such as: Hoek's criterion [1], Kidybinski's elastic energy index [2], and Russenes's criterion [3]. To one project, the evaluation results may be different according to different criteria. Therefore, it is very necessary to find a rockburst prediction method to solve the disaccords among different criteria.

Extenics can change the contradiction issue into a compatibility issue [6], and the key problem of extenics evaluation is to determine the weight coefficient. There is usually subjectivity in determination the coefficient among current forecasting methods of extenics [7-8], which often affects the accuracy and the reliability of evaluation results. Rough set theory is a mathematical method to handle inexact, imprecise knowledge. The attribute reduction operation of rough sets can find useful attribute data and delete redundant attributes. By analyzing the supporting degree and the significance of the conditional attribute to the decision attribute, the weight coefficient can be calculated [9-10]. In this article, rockburst extenics prediction of a new tunnel in the Zhejiang Province is carried out using the weight coefficient calculated base on rough set theory.

2 Attribute Significance of Rough Set Theory

Rough set theory (RS) is a powerful mathematical tool introduced by Pawlak [11-13] to deal with inexact, uncertain or vague information, and has attracted attention of many researchers to contribute to its development and application[14].

Rough set theory is based on the concept of an upper and a lower approximator of a set. Assuming an information system $K = (U, R)$ is given, and for a given subset $X \subseteq U$ and a equivalence relation $R \in K$, the R-lower approximation $\underline{R}X$ of set X in R and the R-upper approximation $\bar{R}X$ of set X in R are defined as: $\underline{R}X = \{x \in U \mid [x]_R \subseteq X\}$, $\bar{R}X = \{x \in U \mid [x]_R \cap X \neq \Phi\}$. Thus $bn_R(X) = \bar{R}X - \underline{R}X$ is called as R-boundary region of X, and $pos_R(X) = \underline{R}X$ is called as R-positive region of X.

Attribute reduction is one of the most important parts, which can remove the redundancy and incompatibility attributes, so that we can obtain the key information and make the decision rule.

A decision information system is defined as $S = (U, A, V, f)$, where U is a finite set of object, A is a finite set of attributes, V is the value domain of A , and $f: U \times A \rightarrow V$ is an information function. An information system is seen as a decision table assuming that $A = C \cup D, C \cap D = \Phi$, C is the condition attribute set and D is the decision attribute set.

Given a decision table, the dependence between C and D is defined as:

$$k = \gamma_C(D) = |pos_C(D)| / |U| \quad (1)$$

It is said the decision attribute set D depends on the condition attributes with the degree k . When $k=1$, D depends on C completely. When $0 < k < 1$, D depends on C partially. When $k=0$, D is independent with C completely.

The attribute significance of subset is defined as:

$$\sigma_{CD}(C_i) = \frac{\gamma_C(D) - \gamma_{C-C_i}(D)}{\gamma_C(D)} = 1 - \frac{\gamma_{C-C_i}(D)}{\gamma_C(D)} \quad (2)$$

Where

$$\gamma_{C-C_i}(D) = \frac{1}{|U|} \sum_{i=1}^m |pos_{C-C_i}(Y_i)| \quad (3)$$

The attribute significance indicates the important degree of attribute in information table. The bigger the significance of attribute is, the higher its position is in the decision information table, otherwise, the lower its position is. So the weighting coefficient α_i of evaluation index C_i can be expressed as follow:

$$\alpha_i = \frac{\sigma_{CD}(C_i)}{\sum_{i=1}^n \sigma_{CD}(C_i)} \quad (i=1, 2, \dots, n) \quad (4)$$

3 Extenics evaluation

Extenics theory is proposed by CAI (1983)[15] and its object is the contradiction problem. Extenics theory describes an object in three elements: name, character and character value. The name of an object is defined as N , the character C , and the character value V . Therefore, the matter element is defined as $R = (N, c, v)$. According to the divergence, extension, correlation and conjugation, a matter-element can be expanded to solve the contradiction. This is what we call extenics. Detailed steps are shown as follows.

(1) Define classical field

$$R_j = (N_j, C_j, V_j) = \begin{bmatrix} N_j & c_1 & V_{j1} \\ & c_2 & V_{j2} \\ & \dots & \dots \\ & c_n & V_{jn} \end{bmatrix} = \begin{bmatrix} N_j & c_1 & \langle a_{j1}, b_{j1} \rangle \\ & c_2 & \langle a_{j2}, b_{j2} \rangle \\ & \dots & \dots \\ & c_n & \langle a_{jn}, b_{jn} \rangle \end{bmatrix} \quad (5)$$

where N_j refer to rockburst gradation; c_i ($i = 1, 2, \dots, n$) here refer just to the evaluation indexes, which affect the gradation N_j ; V is a value scale of N_j about character c_i , which is scale of every evaluation gradation about character c_i .

(2) The segment field is defined as follows:

$$R_p = (P, C, V_p) = \begin{bmatrix} P & c_1 & V_{p1} \\ & c_2 & V_{p2} \\ & \dots & \dots \\ & c_n & V_{pn} \end{bmatrix} = \begin{bmatrix} P & c_1 & \langle a_{p1}, b_{p1} \rangle \\ & c_2 & \langle a_{p2}, b_{p2} \rangle \\ & \dots & \dots \\ & c_n & \langle a_{pn}, b_{pn} \rangle \end{bmatrix} \quad (6)$$

where P refers to the whole gradation about the evaluation of an object; V_{pn} is the value scale of P about c_i , that is, P 's segment field.

(3) The matter-element to be evaluated is defined as follows:

$$R = (p, c, v_i) = \begin{bmatrix} p & c_1 & v_1 \\ & c_2 & v_2 \\ & \dots & \dots \\ & c_n & v_n \end{bmatrix} \quad (7)$$

For the evaluation object p , the database or analysis result of a matter-element thus obtained is called the matter-element to be evaluated. In the formula mentioned above, v_i ($i = 1, 2, \dots, n$) refer to the value of object p about evaluation indexes c_i .

(4) Determination of weight coefficient

Weight coefficient reflects the importance degree of evaluation indexes and plays an important role in the evaluation result. In this article weight coefficient is determined through attribute reduction based on rough set theory above mentioned.

(5) Dependent function of evaluation index

The dependent function about matter-element analysis for the evaluation index is defined as follows:

$$K_{0j}(v_i) = \begin{cases} \frac{\rho(v_i, V_{0ji})}{\rho(v_i, V_{pi}) - \rho(v_i, V_{0ji})} & \rho(v_i, V_{pi}) - \rho(v_i, V_{0ji}) \neq 0 \\ -\rho(v_i, V_{0ji}) - 1 & \rho(v_i, V_{pi}) - \rho(v_i, V_{0ji}) = 0 \end{cases} \quad (8)$$

$$\text{Where } \rho(v_i, V_{0ji}) = \left| v_i - \frac{a_{0ji} + b_{0ji}}{2} \right| - \frac{b_{0ji} - a_{0ji}}{2} \quad \rho(v_i, V_{pi}) = \left| v_i - \frac{a_{pi} + b_{pi}}{2} \right| - \frac{b_{pi} - a_{pi}}{2}$$

(6) Calculation of evaluated object's dependent degree

$$K_{0j}(p) = \sum_{i=1}^m \alpha_i K_{0j}(v_i) \quad (9)$$

where α_i refers to weight coefficient. The determination of the weight coefficient is made based on rough set theory.

(7) Assessment of evaluating gradation

$$K_{j\max}(p) = \max_{j \in \{1,2,3,\dots,m\}} K_{0j}(p) \quad (10)$$

The gradation number j , which is the maximum element of K vector, is regarded as the degree of evaluated matter-element.

$$\text{Let } \bar{K}_{0j}(p) = \frac{K_{0j}(p) - \min_j K_{0j}(p)}{\max_j K_{0j}(p) - \min_j K_{0j}(p)} \quad j^* = \frac{\sum_{j=1}^m j \cdot \bar{K}_{0j}(p)}{\sum_{j=1}^m \bar{K}_{0j}(p)} \text{ is called as eigenvalue.}$$

4 Calculation Process

Firstly, we choose the main factors of rockburst, by researching the rockburst origin and mechanics. These factors should be obtained easily and can be compared with each other in different cases. Then, using a series of investigation of underground rock projects at home and abroad, compose a rockburst sample set. Because RS theory only deals with quantitative data, continuous condition attributes should be discretized. Then adopt RS theory to deal with quantitative data to obtain the evaluating index significance and weighting coefficient. At last, make weighting coefficient determined by RS theory as the weighting coefficient of extenics evaluations, and go to rockburst prediction. The process of rockburst prediction method with extenics evaluation based on rough set is shown in Figure1.

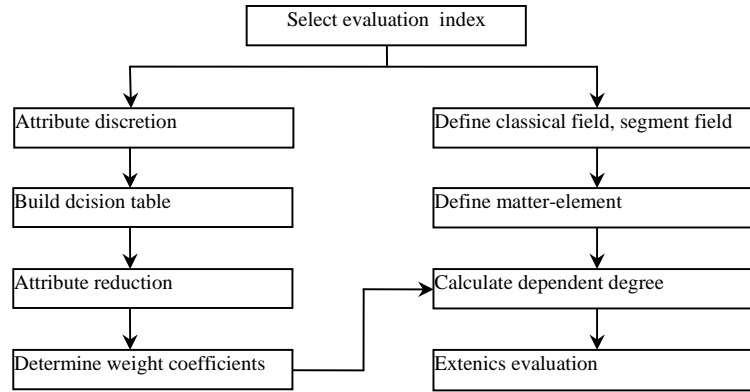


Figure 1 Flow chart of extenics prediction based on rough set theory.

4.1 Identification of the Indexes of Criterion

The indexes of criterion should reflect the main factors of rockburst--the properties and stress of surrounding rock. At the same time, they should be obtained easily and can be compared with each other in different cases. In this paper, compressive strength σ_c , tensile strength σ_t , the angle between preferred structural plane and the maximum principal stress β , elastic energy index W_{et} and the maximum tangential stress σ_θ are chosen as the

criterion indexes. Compressive rock strength, tensile strength, the angle between preferred structural plane and the maximum principal stress, and the elastic energy index can reflect the properties of surrounding rock. Tangential stress can reflect the virgin geostatic stress condition, the influence of the shape, and dimension of the underground space on rockburst.

4.2 Continuous Attribute Discretization

Rough set theory only can be used to deal with discretization attribute, however the influence factors of rockburst usually are real values. So we should take discretization measure to real attribute values when we calculate the weighting coefficient of evaluation indexes. In the geotechnical engineering, through many engineering experiences and research on the single index of rockburst factors, it is discovered that the rockburst level changes with the change of influencing factors, and the change is regular[5]. So in this paper, real values are discretized according to the gradation of each evaluating index to rockburst level, as table 1:

Table 1. Discrete interval of condition attributes

NO.	σ_c /MPa	σ_c/σ_t	β	W_{et}	σ_θ/σ_c	Rockburst gradation
1	<80	>40	30~40	<2.0	<0.3	No rockburst
2	80~120	40~26.7	20~30	2.0~3.5	0.3~0.5	Light rockburst
3	120~180	26.7~14.5	10~20	3.5~5.0	0.5~0.7	Medium rockburst
4	>180	<14.5	0~10	>5.0	>0.7	Violent rockburst

4.3 Weight Coefficient Calculation Based on RS

The calculation process of weighting coefficient is as follows:

Step 1. According to formula (1), obtain the dependence $\gamma_C(D)$ of the decision attribute to all conditional attributes. Step 2. According to formula (3), for each evaluation index C_i , calculate the dependence $\gamma_{C-C_i}(D)$ of the decision attribute to the conditional attributes $C-C_i$. Step 3. According to formula (2), calculate the significance $\sigma_{CD}(C_i)$ of each evaluation index C_i . Step 4. Get the weighting coefficient of evaluation index C_i by formula (4)

4.4 Determination of Classical Field and Segment Field

According to table 1, Normalization processing is made, and classical field and segment field are determined as follow.

$$\begin{aligned}
 R_{01} &= \begin{bmatrix} I_1 & C_1 & \langle 0.00, 0.33 \rangle \\ & C_2 & \langle 0.00, 0.67 \rangle \\ & C_3 & \langle 0.80, 1.00 \rangle \\ & C_4 & \langle 0.00, 0.30 \rangle \\ & C_5 & \langle 0.00, 0.20 \rangle \end{bmatrix} & R_{02} &= \begin{bmatrix} I_2 & C_1 & \langle 0.33, 0.50 \rangle \\ & C_2 & \langle 0.67, 0.78 \rangle \\ & C_3 & \langle 0.53, 0.80 \rangle \\ & C_4 & \langle 0.30, 0.50 \rangle \\ & C_5 & \langle 0.20, 0.50 \rangle \end{bmatrix} & R_{03} &= \begin{bmatrix} I_3 & C_1 & \langle 0.50, 0.67 \rangle \\ & C_2 & \langle 0.78, 0.89 \rangle \\ & C_3 & \langle 0.29, 0.53 \rangle \\ & C_4 & \langle 0.50, 0.70 \rangle \\ & C_5 & \langle 0.35, 0.50 \rangle \end{bmatrix} & R_{04} &= \begin{bmatrix} I_4 & C_1 & \langle 0.67, 1.00 \rangle \\ & C_2 & \langle 0.89, 1.00 \rangle \\ & C_3 & \langle 0.00, 0.29 \rangle \\ & C_4 & \langle 0.70, 1.00 \rangle \\ & C_5 & \langle 0.50, 1.00 \rangle \end{bmatrix} \\
 R_p &= \begin{bmatrix} P & C_1 & \langle 0.00, 1.00 \rangle \\ & C_2 & \langle 0.00, 1.00 \rangle \\ & C_3 & \langle 0.00, 1.00 \rangle \\ & C_4 & \langle 0.00, 1.00 \rangle \\ & C_5 & \langle 0.00, 1.00 \rangle \end{bmatrix}
 \end{aligned}$$

4.5 Extenics Evaluation

According to formula (8) (9), we can calculate the evaluated object's dependent degree. Then through searching the maximum element of K vector according to formula (10), we can determine the evaluation gradation and obtain the eigenvalue further more.

5 Application Example

Kuocangshan tunnel is a new expressway, which is located in low mountains and hill district in Zhejiang Province. The length is 4147 m and maximum embedded depth is 504.0m. The rock mass of this tunnel mostly is Jurassic tuff. Due to the great difference of engineering geological condition along the tunnel, it is divided into five engineering segments to analyze rockburst.

To build the decision table, eighteen representative engineering examples are adopted. Table 2 shows the engineering original data[5]. Then according to table 1, discretize each index and calculate weight coefficient. The weight coefficient is shown as table 3.

Table 2. The engineering original data

No.	Project	σ_c /MPa	σ_c / σ_t	β	W_{et}	σ_θ / σ_c	Rockburst gradation
1	Tianshenqiao II hydropower station	88.7	24.0	21	6.6	0.3	Medium rockburst
2	Ertan hydropower station	220	29.7	28	7.3	0.41	Light rockburst
3	Longyangxia hydropower station	178	31.2	33	7.4	0.106	No rockburst
4	Lubuge hydropower station	150	27.8	22	7.8	0.227	No rockburst
5	Yuzhixi hydropower station	170	14.8	34	9.0	0.53	Medium rockburst
6	Taopingyi hydropower station	165	17.5	18	9.0	0.38	Light rockburst
7	Liji Xia hydropower station	115	23.0	36	5.7	0.096	No rockburst
8	Pubugou hydropower project	123	24.6	30	5.0	0.36	Medium rockburst
9	Jinping II hydropower project	120	18.5	28	3.8	0.82	Medium rockburst
10	Laxiwa hydropower project	176	24.1	24	9.3	0.315	Medium rockburst
11	Norway Sima hydropower station	180	21.7	9	5.0	0.27	Medium rockburst
12	Norway Heggura road tunnel	175	24.1	21	5.0	0.37	Medium rockburst
13	Norway Sewage tunnel	180	21.7	32	5.0	0.42	Medium rockburst
14	Sweden Forsmark nuclear power station	130	21.7	19	5.0	0.38	Medium rockburst
15	Sweden Vistas tunnel	180	26.7	27	5.5	0.44	Light rockburst
16	USSR Rasvumchorr mine	180	21.7	24	5.0	0.317	Medium rockburst
17	Japan kankoshi road tunnel	236	22.1	31	5.0	0.377	Medium rockburst
18	Italy Raib Zinc sulfate lead mine	140	17.5	18	5.5	0.774	Violent rockburst

Table 3 Weighting coefficient of the indexes

Evaluating index	σ_c /MPa	σ_c / σ_t	β	W_{et}	σ_θ / σ_c
Index dependence	0.667	0.778	0.778	0.778	0.556
Index significance	0.222	0.111	0.111	0.111	0.333
Index weighting coefficient	0.25	0.125	0.125	0.125	0.375

To proof the correctness of this method, extenics evaluations of these eighteen engineering examples are carried out according to the method which adopts rough set theory to determine weighting coefficient. In the evaluation results of the eighteen examples, only the example one and thirteen are different from the practical situation, and the evaluation gradation is light rockburst, so the rate of correctness is 89%.

According to the weighting coefficient determined by RS theory, the Kuocangshan tunnel adopts this method to predict rockburst. Evaluating indexes of each tunnel segment are shown in table 4. The prediction results of each tunnel segment and practical excavation situation are shown in table 5.

Table 4. Value of evaluating indexes of each tunnel segment

Highway kilometer	σ_c /MPa	σ_c / σ_t	β	W_{et}	σ_θ / σ_c
k155+200~k156+178	124	29.4	17	2.04	0.112
k156+203~k157+573	161	31.4	19	2.19	0.139
k157+573~k58+078	153	28.1	25	2.11	0.151
k157+078~k159+250	142	27.9	33	2.26	0.155

From table 5, the prediction result is accordant with practical excavation situation, which indicates that it is an effective method to predict rockburst with extenics evaluation using weighting coefficient determined by rough set.

Table 5. The extenics evaluation results and practical situation

Highway kilometer	Prediction gradation	Eigenvalue	Practical situation
k155+200~k156+178	No rockburst	1.4495	No rockburst
k156+203~k157+573	Light rockburst	1.5462	Light rockburst
k157+573~k58+078	Light rockburst	1.6464	Light rockburst
k157+078~k159+250	Light rockburst	1.6345	Excavation partly

6 Conclusions

Rockburst prediction is a complex non-linear problem. According to different criteria, the evaluation results may be different. As an effective method to solve the contradiction problem, extenics can transform paradoxical problems into compatibility problems. However, the key issue of extenics prediction is the selection of the weight coefficient. This paper presents a rockburst extenics prediction method based on the rough set theory to determine the index weighting coefficient. Through analyzing dependence of rockburst gradation to evaluate the index, obtain the significance of each evaluating index, and then calculate the weighting coefficient of each evaluating index in extenics evaluation. This method can avoid subjectivity of the traditional method to determine the weight coefficient, and make the extenics evaluation method more objective and accurate. Practical example indicates that the method can be effectively used in the field of rockburst prediction, which has a vast prospect in predicting rockburst and also has some referential significance in the other evaluations.

Acknowledgements

The authors wish to acknowledge the collaborative funding support from National Natural Science Foundation of P. R. China, Grant No.:40472136; Scientific Research Foundation for the Returned Overseas Chinese Scholar, State Education Ministry, Grant No.: 120413133; 985 project of Jilin University, Grant No.: 105213200500007; Graduate innovation fund of Jilin University, Grant No.:20080240.

References

1. Hoek, E. and Brown, E.T. Underground Exavation in Rock. London: Institute of Mining and Metallurgy, 1980.
2. Kidybinski, A. Bursting Liability Indices of Coal. Int. J. Rock Mech. Min. Sci. & Geomech. Abstr., 1981, 18(4). 295-304.

3. Russenes, B.F. Analysis of Rock Spalling for Tunnels in Steep Valley Sides (in Norwegian). In: M.Sc. thesis, Norwegian Institute of Technology, Dept. of Geology, 1974, 1- 247.
4. Linkov, A.M. Rockbursts and the Instability of Rock Masses. *Int J Rock Mech Min Sci & Geomech Abstr*, 1996, 33(7). 727-732.
5. Wang, Y.H., Li, W.D., Li, Q.G., et al. Method Of Fuzzy Comprehensive Evaluations For Rockburst Prediction. *Chinese Journal of Rock Mechanics and Engineering*, 1998, 17(5). 493-501.
6. Yang, C.Y. and Cai, W. Study on Extension Engineering. *Engineering Science*, 2000, 2(12). 90-96.
7. Yang, Y.C. and Zhu, J. A Matter-Element Model and its Application to Classified Prediction of Rockburst. *Practice and Theory of System Engineering*, 2001, 8. 125-129.
8. Yang Y.C. and Zhu, J. A New Model for Classified Prediction of Rockburst and its Application. *Journal of China Coal Society*, 2000, 25(2). 169-172.
9. Zhao, X.Q., Cao, X.Y., etc. Study of the Method for Determining Weighting Coefficient of Coal Ash Slagging Fuzzy Combination Forecast Based on Rough Set Theory. *Journal of China Coal Society*, 2004, 29(2). 222-225.
10. Song, X.X. Rough Sets Theory and Its Application. *Journal of Xianyang Normal University*, 2005, 20(2). 29-31.
11. Pawlak, Z. Rough sets. *International Journal of Computer and Information Sciences* 11 (1982) 341-356.
12. Pawlak, Z. *Rough Sets: Theoretical Aspects of Reasoning About Data*, Kluwer Academic Publishers, Dordrecht, 1991.
13. Pawlak, Z. Rough Sets and Intelligent Data Analysis. *Information Science*, 2002, 11(147). 1-12.
14. Liu, J., Hu, Q. and Yu, D. A weighted rough set based method developed for class imbalance learning. *Information Sciences*, 2008, 178(4). 1235-1256.
15. Cai, W. *Extension Engineering Method*. Beijing: Science Press, 1997, 1-10.

APPLICATION OF ELECTROMAGNETIC RADIATION TECHNOLOGY IN ROCK BURST PREDICTION IN COAL MINES

EN-YUAN WANG, XIAO-FEI LIU, XUE-QIU HE and LI LING

School of Safety Engineering, China University of Mining and Technology

Xuzhou, 221008, Jiangsu, P.R. China;

State Key Laboratory of Coal Resources and Mine Safety

Xuzhou, 221008, Jiangsu, P.R. China

This paper is a review of research on the rock burst prediction by the electromagnetic radiation (EMR) technology and equipment. It is universally acknowledged that EMR signals are accompanying all stages of the deformation and fracture of rock or coal samples, so we can monitor the change of EMR signals to predict rock burst which is the result of the deformation and fracture of rocks or coals. Based on the EMR experiments of coal or rock, the effect and the generation mechanism of EMR signals are analyzed, the EMR monitors of KBD5 and KBD7 types are invented and applied in the rock burst prediction of coal mines in China. Similar to earthquake, there are obvious EMR precursors before rock burst in coal mines and EMR value increases suddenly or gradually, or with rapid EMR fluctuations. Besides, EMR can evaluate the effects of rock burst control measures as the destressing blasting and water injection. After these rock burst control measures, the EMR intensity value in the monitoring area decreases. In addition, EMR technology can be used to monitor the roof movement and forecast the periodic roof pressure on the working face which possibly causes rock burst. EMR technology is widely applied in some coal mines which have rock burst problems.

1 Introduction

In recent years, China's demand for coal resources has increased with the rapid economic development leading to the rapid growth of the mining of coalmines in the country. Many of these coalmines are deep mines. With the increase of the mining depth, compared to shallow mining, rock burst in deep mining, which is influenced by complex geological factors and mining factors, has become more serious. Rock burst occurrence frequency has increased, its degree of destruction intensified, and its manifestation is obviously different. Prediction and control of rock burst with gas has become a difficult problem of mines in deep mining.

Recently, the finite element numerical simulation, stress measurement in mining fields, electromagnetic radiation (EMR) monitoring technology, acoustic emission (AE) monitoring technology, and micro-seismic monitoring and location technology, have been widely and successfully applied in the prediction of rock burst.

Numerous experiments have demonstrated that the fracture of coal or rock could produce EMR signals and acoustic emission signals. The research on the EMR of coal-rock fracture provides a new way to monitor and predict rock burst. EMR research results have shown that the EMR technology is an effective geophysical method to monitor and predict rock burst. Frid.V^[1,2] studied EMR signals in coal-rock during the formation of rock burst to predict roof fall by monitoring high frequency EMR signals and low frequency acoustic signals. The Research Mining Institute of Siberian Branch of the Russian Academy of Science developed the И Э М И -1 EMR Instrument which was introduced to predict the fracture of rock mass in the Muchengjian Mine in China^[3]. Since the 1990s, the EMR research team at the China University of Mining and Technology has studied rock burst prediction through EMR technology in the field. Such as, the generation mechanism^[4-6], characteristics^[7-9], rules^[11], and transmission characteristics in coal-rock seam of EMR signals, the principles

and methods of EMR prediction^[4,11], and the EMR monitoring equipment^[12,13] including KBD5 and KBD7 which are used to forecast rock burst, coal and gas outburst and other dynamic disasters. The predictions show that the rock burst prediction by EMR has an clear advantage in the technology and that EMR is a promising method of forecasting dynamical rockcoal disasters.

2 The EMR Characteristics and Mechanism of Impact Coal-Rock

The essential of coal-rock dynamic disasters is the result of evolution of the deformation and the fracture of the loaded coal-rock. The EMR is a physical phenomenon that electromagnetism energy emitted from deformation and fracture of loaded coal-rock, and is closely related to the load state and the process of the deformation and fracture of coal-rock.

2.1 EMR Characteristics of Impact Coal-Rock

The EMR experimental results of coal or rock samples under different loading modes show that there were EMR signals in the process of the deformation and fracture of coal-rock under uniaxial compression, shearing, creep, and triaxial compression, and the greater the load, the stronger the EMR signals. EMR signals increase obviously before the main fracture^[4,14-15].

The impact energy index can reflect the risk of the impact coal-rock. There is a very good linear relationship between the EMR index (including EMR energy index and EMR pulse index) and the impact energy index, as in Figure 1. So we can also use the EMR index to reflect the risk of the impact coal-rock.

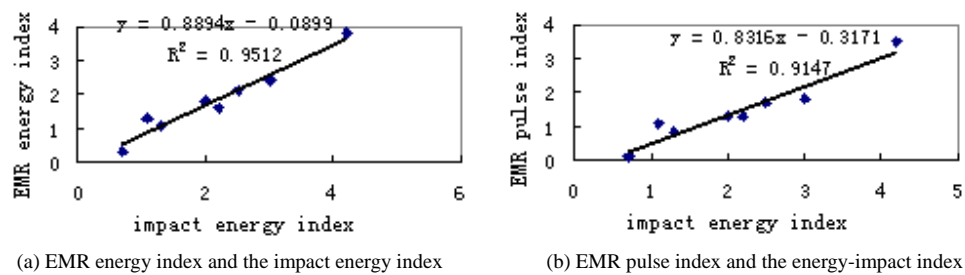


Figure 1 The curves of EMR index and the impact energy index

2.2 The EMR Mechanism of Loaded Coal-Rock

The coal-rock mass is a non-homogeneous material containing the massive micro-fracture defects. The sources of EMR signals generated in the process of the deformation and fracture of loaded coal-rock are the free charges or the separated charges that produced by the mechanisms of the piezoelectric effect, the friction effect, the fracture, the polarization, the thermionic emission, the electromagnetic field, the electric potential and so on.

The research shows that the main mechanisms of EMR signals are the stress-induced charge polarization and the variable motion of the charged particles. The non-uniform deformations of coal-rock induced by the stress produce the charged particle group in different parts of coal-rock body, and EMR signals are produced when the charged particle group moves. Or the deformation and fracture of coal-rock leads to the redistribution of charges and electric fields between the interfaces of the internal units, and the electric dipole group is formed by this redistribution. And the change of the electric quantity and the moment of the electric dipoles produce the EMR signals. The larger the load, the larger the deformation and fracture, and the stronger the EMR signals. The EMR can show the degree of the deformation and fracture of the loaded coal-rock.

The EMR monitoring results in the mining field prove that there is a coupling relationship between the stress of coal-rock on working face and the EMR signals, and the greater the stress of coal-rock, the stronger the

EMR intensity. Especially the EMR signals of the region influenced by abutment pressure on the working face and in the tunnel are obviously stronger than these of the region influenced by non-abutment pressure.

3 EMR Monitoring Equipment and Early Warning Technology

The EMR equipments for predicting rock bursts are the KBD5 and the KBD7 electromagnetic radiation monitor (as in Figure 2), invented and developed by China University of Mining and Technology. The testing method of KBD5 and KBD7 is non-contact and directional. The receiving frequency of the KBD5 or KBD7 antenna is 0-500 kHz and the effective testing distance is 7-22 m.

EMR methods for predicting rock burst are dynamic and combined with a critical value method. In general,, based on the EMR forecasting criterion, the EMR value which is 1.5 times the normal EMR value, is selected as the initial critical EMR value in the monitoring area. After a period of testing and given the EMR value before the incidence of a rock burst, the initial critical EMR value is modified by fuzzy mathematics. But this modified EMR value still needs to be verified further. In the end, a critical EMR value can be confirmed. During the test process, if the EMR value of the monitoring area exceeds the critical EMR value and the EMR value appears as a special time trend (the trend is explained in section 4) over several shifts or days, then a rock burst will occur in this monitoring area. Therefore, effective measures can be implemented to eliminate or depress the danger of a rock burst.



(a) KBD5 EMR monitor



(b) KBD7 EMR monitor

Figure 2 Two types of EMR monitors

4 The Application of EMR Monitoring and Predicting Rock Bursts

The EMR monitoring and predicting rock burst technology has been applied in some coalmines with the danger of rock burst widely and successively, such as Sanhejian coalmine in Jiangsu province, Huafeng coalmine and Dongtan coalmine in Shandong province, Qianqiu coalmine and Yuejin coalmine in Henan province, Yanbei coalmine in Gansu province, and Laohutai coalmine and Wulong coalmine in Liaoning province^[16-17].

4.1 EMR Prediction of Rock Bursts

Figure 3 shows that on Jan.12, 2006 there was a rock burst with Magnitude=2.4 at the head entry of the No.237 gob-surrounded coal face. It had the same EMR precursor monitored by the KBD5 monitor, showing two rapid EMR fluctuations and the EMR peak value was larger than the critical value (30 mV). When there were EMR precursors of rock bursts in the monitoring area, emergency measures such as destressing blasting and water injection were used to reduce or eliminate the extent of potential destruction of rock bursts in time. An example is shown in Figure 3. When the EMR precursor before Jan.19 was shown, the excavation of the No.237 working face was stopped for two days. As effective distress measures were taken, the potential rock burst on Jan.19 was eliminated and did not re-occur^[17].

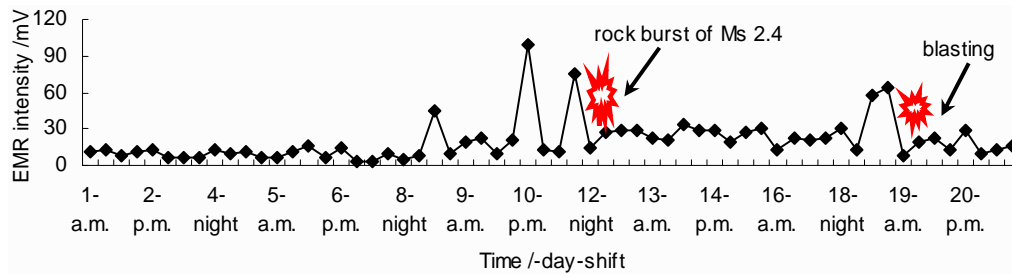


Figure 3 EMR precursor before rock burst on No.237 working face in Nanshan coalmine

Figure 4 shows that three rock bursts happened during August 2007 on No.3223 working face in Wulong coalmine, occurring at 17:23 on Aug.5, 4:20 on Aug.15, and 12:04 on Aug.20. Before the occurrence of rock bursts, there was obvious EMR precursor monitored by the KBD7 monitor.

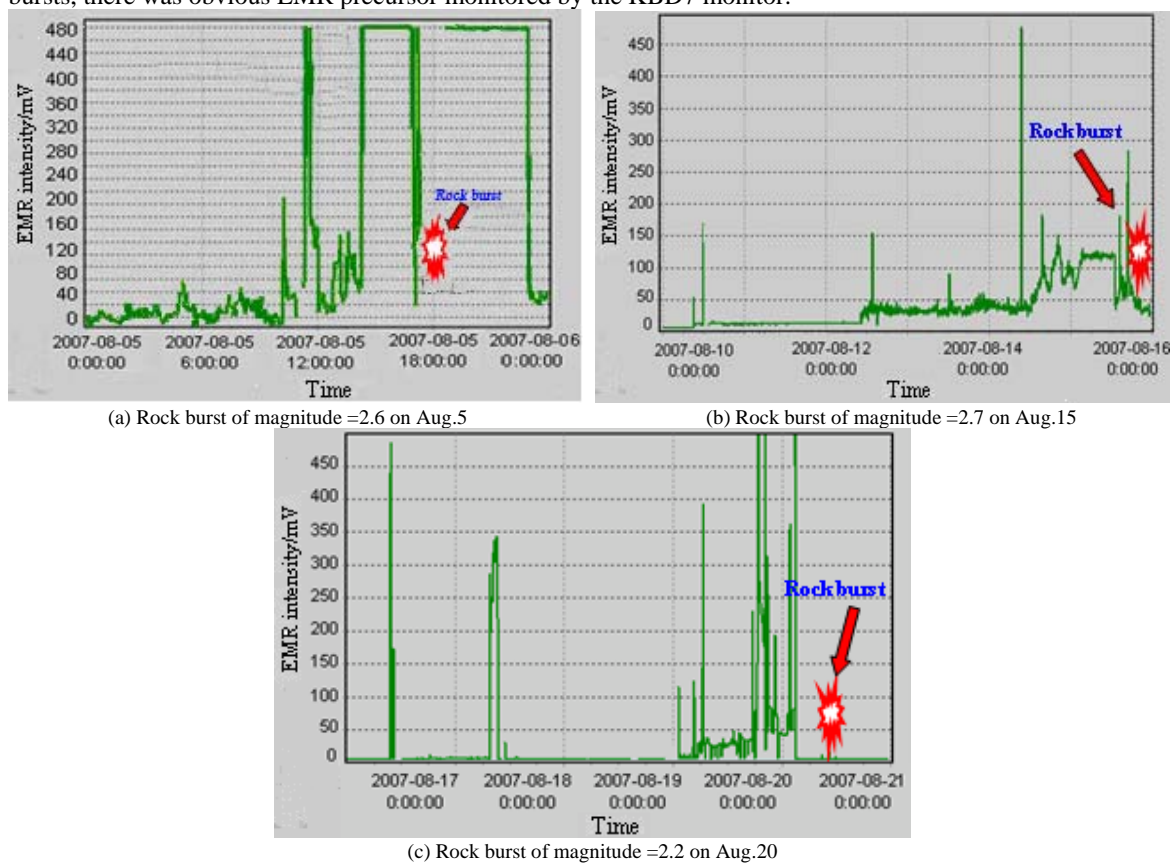


Figure 4 EMR precursor before rock bursts on No.3223 working face in Wulong coalmine

4.2 Effectiveness Evaluation of Rock Burst Control by EMR

The effective method of rock burst control is to change the stress condition of coal-rock on coal face, destroy the structure of the surrounded coal-rock, reduce the accumulation of the elastic energy in coal-rock, and even induce rock burst under the non-personnel existing condition necessarily, and includes the destressing blasting and water injection.

Figure 5 shows that the EMR intensity value exceeded the critical value on No.9202 working face of Sanhejian coalmine, and a rock burst would occur later. So a destressing blasting was used in the dangerous fields of No.9202 working face, and after the destressing blasting, the EMR intensity value decreased to less than the critical value.

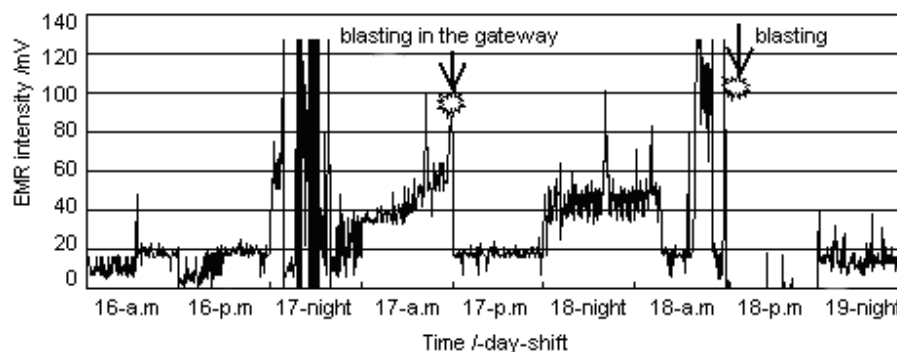


Figure 5 EMR change before and after using destressing blasting on No.9202 working face in Sanhejian coalmine

Figure 6 shows that there was an obvious change of the EMR intensity value after rock burst control measures used on the No.250205 working face. Before destressing blasting and water injection, the EMR intensity value of the working face was quite high when there was a rock burst danger. After destressing blasting, the EMR intensity value decreased to a certain degree. After water injection, the EMR intensity value decreased within the field of water injection.

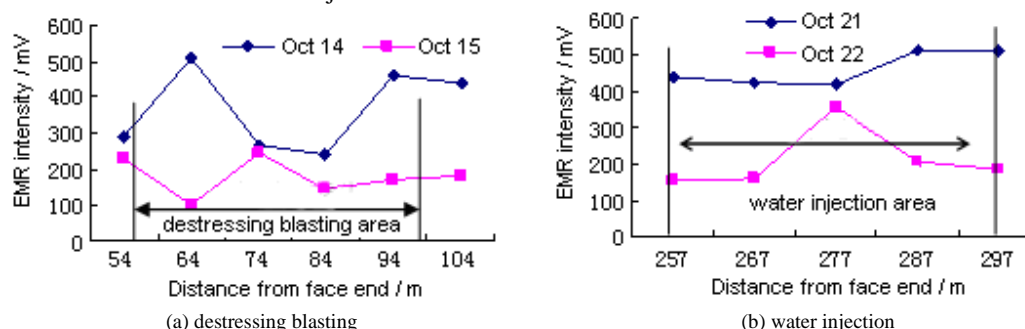


Figure 6 EMR change before and after using destressing blasting and water injection on No.250205 working face in in Yanbei coalmine

5 Prospect on the Development of Rock Burst Prediction by the EMR

In the past 30 years, the research on the EMR effect of rock fracture in theory and in application has been developed rapidly. The development and the application of the digital technique and computer technology in recent years have greatly impelled the development of the evaluation and the prediction technology of rock burst and other coal-rock dynamic disasters. As earthquake prediction, the research on rock burst prediction by EMR technology had been made certain progress, however, compared with the request of the practical application on the scene, it has a certain gap. Although, there are some aspects of the EMR technology of rock burst prediction that needs to be further developed in the future; such as, the EMR nonlinear characteristic of rock burst, the EMR precursor rule of rock burst, and the EMR early-warning mechanism of rock burst prediction etc.,

Acknowledgements

The authors wish to acknowledge the funding supports from the project 40874070 supported by National Natural Science Foundation of China, the project 2006AA06Z119 supported by the National High Technology Research and Development Program of China, Project 2005CB221505 supported by the National Basic Research Program of China, the project 2007BAK29B01 supported by National Key Technology R&D Program of China, and the program for New Century Excellent Talents in University.

References

1. Frid, V. Electromagnetic Radiation Method for Rock and Gas Outburst Forecast. *Journal of Applied Geophysics*, 1997, 38(1-2). 97-104.
2. Frid, V. and Vozoff, K. Electromagnetic Radiation Induced by Mining Rock Failure. *International Journal of Coal Geology*, 2005, 64(1-2). 57-65.
3. Yang, Y., Pan, Y.S. and Li, G.Z. Research on Monitoring Dangerous Area of Rock Bursting with Portable Electromagnetic Emission Instrument. *Coal Mining Technology*, 2007, 12(2). 62-64,72.
4. He, X.Q., Wang, E.Y., et al. *Electromagnetic Dynamics of Coal or Rock Rheology*. Science Press, 2003.
5. He, X.Q. and Liu, M.J. *Rheological Dynamics of Coal or Rock Containing Gas*. China University of Mining and Technology Press, 1995.
6. Wang, E.Y. *Study on the Effect and Application of Fracture Electromagnetic Radiation &Acoustic Emission of Coal or Rock Containing Gas*. China University of Mining and Technology Press, 1997
7. He, X.Q., Wang, E.Y. and Liu, Z.T. The General Charastics of Electromagnetic Radiation during Coal Fracture and Its Application in Outburst Prediction. In: *Proceedings of the 8th U.S. Mine Ventilation Symposium*, Rolla, Missouri, June 11-17, 1999, 81-84.
8. Wang, E.Y., He, X.Q., Liu, Z.T., et al. Study on Electromagnetic Emission Characteristics of Loaded Rock and Its Application. *Chinese Journal of Rock Mechanics and Engineering*, 2002, 21(10). 1473-1477.
9. Wang, E.Y. and H, X.Q. Research on EMR in Deformation and Fracture of Coal or Rock. *Journal of Geophysics*, 2000, 43(1). 131-137.
10. Wang, E.Y., He, X.Q., Liu, Z.T., et al. Principle of EMR in Deformation and Fracture of Coal or Rock and Its Application. *Journal of China Safety Science*, 2000, 10(2). 35-39.
11. Wang, E.Y., He, X.Q., Liu, Z.T., et al. Principle of Predicting Coal and Gas Outburst with Electromagnetic Radiation. *Journal of China University of Mining and Technology*, 2000, 29(3). 225-229.
12. Wang, E.Y., He, X.Q. and Liu, Z.T. Electromagnetic radiation detector of coal or rock dynamic disasters and its application. *China Safety Science Journal*, 2003, 28(4). 366-369.
13. Wang, E.Y., He, X.Q. and Liu, Z.T. The Progress of Coal and Rock EMR Characteristic & Application Study. *Progress in Natural Science*, 2006, 16(5). 532-536.
14. Zhu, Y.Q., Luo, X.L., Guo, Z.Q., et al. Theoretical Investigation of Electromagnetic Radiation Induced by Rock Fracture. *Chinese J.Geophys*, 1991, 34(5). 595-601.
15. Guo, Z.Q., You, H.J., Li, G., et al. The Model of Compressed Atoms and Electron Emission of Rock Fracture. *Chinese Journal of Geophys*, 1989, 32(2). 173-177.
16. Wang, E.Y., He, X.Q. and Dou, L.M. *Forecasting Rock Burst with the Non-Contact Method of Electromagnetic Radiation*. Progress in Safety Science and Technology. Tai'an, Science Press, 2002, 111-116.
17. Wang, E.Y., Liu, X.F., Zhan, E.L., et al., Study of Electromagnetic Characteristics of Stress Distribution and Sudden Changes in the Mining of Gob- Surrounded Coal Face. *Journal of China University of Mining & Technology*, 2008, 18(1). 1-5.

APPLICATION OF REMOTE SENSING IN THE INFORMATION ACQUISITION OF EARTHQUAKE DISASTERS

GUO-YAN WANG

Liaoning Technical University

Fuxin, 123000, P.R. China

Qingdao Technological University

Qingdao, 266033, P.R. China

MING-WU DOU

Ocean University of China

Qingdao, 266003, P.R. China

AI-XIA DOU

Institute of Earthquake Science, China Earthquake Administration

Beijing, 100036, P.R. China

CHENG-YI CHEN

Qingdao Technological University

Qingdao, 266033, P.R. China

YONG-ZHAN PAN

Henan University of Science and Technology

Luoyang, 471003, P.R. China

Social public security is threatened seriously by earthquake disasters. Information acquisition ability and accuracy of disaster evaluation is improved by using space observation technology such as satellite remote sensing data obtained from visible light, infrared, and radar imaging. The reliable data can be provided for emergency rescue effort. In recent years, spatial resolution and spectral resolution of remote sensing image are being improved constantly. The technological progress provides a solid foundation for application of remote sensing in disaster evaluation and mitigation. In this paper, the function of remote sensing data sources in the information acquisition of earthquake disaster is analyzed. Research status and prospect of the key technology of extraction of earthquake disaster information according to multi-scale remote sensing image are introduced.

1 Introduction

The distribution of destructive earthquakes is very extensive where strong earthquakes are active, Disaster situational information can be acquired precisely and monitor secondary disasters, such as post-earthquakes, can be dynamically modelled based on modern space observation technology. Such as, aerial remote sensing and high-resolution satellite remote sensing, which is not limited by time and region and is not effected by earthquake damage.

Remote sensing technology is used to extract information about disaster situations post-earthquake in developed countries such as America and Japan. It can acquire remote sensing images of disaster areas in time and evaluate earthquake loss after earthquakes occurred; such as, the Osaka-Kobe earthquake in Japan in 1995, the Turkey earthquake in 1999, the Indonesia earthquake tsunami in 2004, and the Pakistan earthquake in 2005. In China, information on disaster situations is acquired successively in the meizoseismal area of destructive earthquakes, such as the Xingtai earthquake in 1966, the Haicheng earthquake in 1975, the Tangshan earthquake in 1976, the Datong earthquake in 1989, the Jiashi earthquake in 2003, the Wenchuan earthquake in 2008 and so on based on satellites or aerial remote sensing. Large image data from satellites and aerial remote sensing has played an positive role in emergency rescue, disaster evaluation, secondary disaster monitoring, restoration, and reconstruction after earthquakes [1,2,3].

2 Introduction of Remote Sensing Data Sources on Earthquake Disaster

With development of remote sensing technology, remote sensing data sources become more and more abundant and resolution becomes higher and higher which are used for earthquake emergency rescue and disaster investigation. Geological disaster induced by earthquake such as landslide, barrier lake and so on can be recognized based on moderate resolution images. Every building and its damage can be recognized by using of high resolution images.

At present, high resolution remote sensing satellites on-orbit operation used for acquiring the information on earthquake disaster conclude Ikonos, Quickbird and OrbView-3 in America, EROS in Israel, SPOT in France, KOMPSAT-2 in Korea, TES in India, COSMO-SkyMed in Italy, RADARSAT in Canada, ZY-2 in China etc. Remote sensing satellites with resolution of 0.4m will be launched in the next two years by many countries such as America, France and so on. Two mapping satellites will be launched in china from 2008 to 2009. In addition, resolution of ZY-3 in china will arrive to 2m and DuYan dragon satellite will be launched from Taiwan of China. Aerial remote sensing and unmanned airplane remote sensing become the major modes for acquiring remote sensing images after earthquake except on-orbit or high resolution satellites to be launched in near future.

3 Extraction of Earthquake Damage Information Based on Remote Sensing

Information extraction methods include three. The first is artificial visual interpretation. Based on the original image or image for enhancement processing, type of ground objects and degree of earthquake damage can be identified directly by investigation experts with the previous experiences of earthquake damage information extraction according to the interpretation marks of earthquake damage. The method has a relatively higher precision, but less efficient. The second is the computer automatically extraction. Type of ground objects and degree of earthquake damage can be identified automatically by using of supervised classification, unsupervised classification and object-oriented classification on the basis of image for enhancement processing. The method has a relatively higher speed, but less accuracy. The third is human-computer interaction extraction. The recognition method of man-machine combination is computer aided artificial identification consideration to accuracy and efficiency.

3.1 Earthquake Damage Extraction Detection According to Images Changes Before and after Earthquake

Change detection method might identify earthquake damage by obtaining change information of landmark and comparing the two phases of remote sensing data. Both high resolution optical and radar images can be used in changes detection Identify, such as buildings damage, landslides, barrier lake and so on. Change detection methods can be divided into two. One is qualitative method. The scope and relative strength of the earthquake damage can be analyzed more or less by enhancing process, such as the false colour composite image before and after earthquake and directly expressing the interested damage information. It can compare gray value,

texture and enhanced features between two images by using of change detection. Quantitative detection methods determine the differences of gray by difference ratio or more complex approach such as the relevance of computing [4,5].

3.2 Extraction of Earthquake Damage Post-Earthquake from a Single Image

Earthquake damage can be recognized by using of integrated pattern recognition on based of features enhancement and features combination enhancement for the single-temporal images post-earthquake. Damage features of ground objects induced by earthquake can be obtained on based of texture enhancement and features combination. Features enhancement methods are developed from neighbourhood statistics, the co-occurrence matrix, morphology on basis of pixel to texture features and regional structure [5,6,7]. Extraction of earthquake damage is essentially division or classification of images with enhancement features.

Damage classification includes two methods. One is per-pixel classification. The method is applied generally in classification, including supervised classification and unsupervised classification. The other is object-oriented damage classification which is emphatically introduced as followed.

Target object as analysis unit is taken for object-oriented damage recognition not adopting single pixel. Adjacent pixels with the same characteristics in an image are combined with image object by multi-scale image segmentation. Objects classification is achieved according to the information such as hue, shape, scale, texture and so on which is reflected by many factors, for example spectrum heterogeneity, density heterogeneity and smoothness heterogeneity, including object adjacent relation on basis of multi-scale image segmentation. Object-oriented classification accuracy is higher than per-pixel classification accuracy. Moreover, the former eliminates salt and pepper effect of images. It provides theory foundation and new method for recognition damage characteristics from remote sensing images.

4 Quantitative Evaluation Based on Remote Sensing Images

Earthquake damage is evaluated quantitatively on basis of remote sensing image processing and the extraction of earthquake damage post-earthquake. The extraction results can not be directly applied to earthquake damage evaluation on the ground. It is necessary to evaluate the damage according to the criteria of classification and grading for earthquake damage and quantitative evaluation model [2,3,8].

4.1 The Criteria of Classification and Grading for Building Damage Induced by Earthquake

Damage grade is divided according to general and partial characteristics of building images post-earthquake, especially geometry information and hue information of images such as integral Building, roof structure and so on. Building damage is divided into three grades that is collapse, partial collapse and not collapse based on remote sensing investigation of earthquake damage.

The criteria of classification and grading of earthquake damage is basis for visual interpretation and automatic recognition. The criteria of classification and grading and the marks of earthquake intensity for fast evaluation from remote sensing images are established by Mr Wei etc [1] based on intensity table of China earthquake (1980). The main characteristics of damage from aerial remote sensing images are established by Mr Ding etc [9]. Corresponding relation between the ratio of collapsing houses and damage index is set up by Mr. Wang etc based on historical investigation about earthquake damage from remote sensing [2,3].

4.2 Quantificational Evaluation Model on Earthquake Damage

Ground evaluation model can not be directly applied to assess the results of earthquake damage recognition. Relation model between remote sensing evaluation and ground evaluation is set up and damage index as the parameter of quantificational evaluation is put forward by Mr Wang ect [2,3,8]. In the model, the damage

intensity of earthquake is determined by recognition damage results from different ways on the basis of damage index, thus loss of earthquake damage is evaluated. Relation model played an important role in evaluation earthquake damage for Wenchuan earthquake of 12 May 2008 in China.

5 Conclusions

It is possible to investigate the situation of earthquake damage in the lab through the use of high resolution satellites and aerial remote sensing. Visual interpretation technology of earthquake damage has been successfully applied many times. Studies on automatic recognition of earthquake damage have made great progress. Criteria for classification and gradation of earthquake damage have become increasingly better based on the analysis of earthquake cases. Study on quantificational evaluation has also made primary progress. With the further development of science and technology, remote sensing will continue to play an important role in the field of earthquake preparedness and disaster reduction.

Acknowledgements

The authors thanks for Basic Scientific Research Foundation of Institute of Earthquake Science China Earthquake Administration, "Research of earthquake damage information extraction from multi high-resolution remote sensing images(0207690230)".

References

1. Wei, C.J., Zhu, B.Q. and Zhang, Z. Quick Investigation of Seism Disaster Using Remote Sensing Technology. Science Publishing House in Beijing, 1993, 35-39.
2. Wang, X.Q., Jiang, M., Zhang, D.C., et al. Aviation Image Damage Automatic Identification Preliminary Study. Yuhang publishing house, 1997, 152-156.
3. Wang, X.Q., Wang, L., Ding, X., et al. SiChuan Wenchuan Earthquake Emergency Remote Sensing Studies to Assess Earthquake Damage. Earthquake defense technology, 2008, 3(3). 13-16.
4. Dou, A.X., Zhang, J.F. and Tian, Y.F. Retrieve Seismic Damages from Remote Sensing Images by Change Detection Algorithm, IGARSS2003, Toulouse, French.
5. Zhang, J.F., Xie, L.L., Tao, X.X., etc. Change Detection of Remote Sensing Image for Earthquake-Damaged Buildings and Its Application in Seismic Disaster Assessment. Journal of Natural of Disasters, 2002, 11(2). 59-64.
6. Liu, J.H., Shan, X.J. and Yi, J.Y. Automatic Recognition of Damaged Buildings Caused by Earthquake Based on the Statistic Features of Region Structure. Eearthbreak, 2004, 26(6). 623-633.
7. Liu, J.H., Yang, J.F., Qin, X.W., et al. Imagery Region Analyzing Method of Urban Building's Earthquake Damage: A Comparative Study with Point Characteristics-Based Criterion Approaches. Journal of Natural Disasters, 2004, 13(5). 149-156.
8. Wang, D.L., Wang, X.Q., Dou, A.A., et al. Primary Study on the Quantitative Relationship between the Typical Building Structures in Western China. Earthquake, 2007, 27(3). 44-48.
9. Ding, J. and Wang, D. Aerial Remote Sensing Image Interpretation of Seismic Damage on the Structure and Geometry Characteristics of the Model to Obtain. Disaster Science, 1997, 12(1). 1-6.

MICROSEISM MONITORING RESEARCH ON HEIGHT OF “TWO REGIONS” OF OVERBURDEN STRATA IN COAL FACE

QING-ZHAO WANG and SHENG JIANG

Luxi Mining Co., Ltd of Shandong Lineng Group

Jining, 272100, P.R. China

YONG-JIE YANG, YANG-QIANG ZHANG and DE-CHAO WANG

Key Laboratory of Disaster Prevention and Control, Shandong University of Science and Technology

Qingdao, 266510, P.R. China

Coal face mining causes the failure of overlying strata and forms the caving and crack zones that means “two regions”. The reliability of the height of “two regions” is the key factor to determine the upper limit of safety mining. In the forming process of caving zone and fracturing zone of overburden strata of coal face, due to the releasing of strain energy, the corresponding wake seismic waves (microseismic waves) will be induced at the same time. Three dimensional monolithic observation can be realized by microseism monitoring technology. In this paper, the microseismic events are monitored which are caused by the fracturing of the overburden strata in 3up107 coal face extraction of Luxi Coal Mine. The close relation between evolution of microseism and fracturing of the overburden strata is proved by the location of the monitored microseismic events. Through the microseism monitoring analysis of “two regions” height in 3up107 coal face of Luxi Coal Mine , for the uppermost 10 percent of microseismic events of the overburden strata, the distances are relatively large and the energy is relatively small. Moreover, the induced cracks can not form effective water flowing connectivity. In the other hand, the position under the uppermost 10 percent microseismic events of the overburden strata is determined as the fractured zone upper limit. Accordingly, the height of “two regions” is determined as 38 meter, which is almost the same as 36.2m identified by the popularly accepted measuring method of “two ends injection water instrument”. As a result, microseism monitoring technology is proved to be available in determining the fracturing height of overburden strata of coal face. It provides one new technical method to measure the height of “two regions” of overburden strata of coal face.

1 Introduction

Underwater coal-mining technology is a safety working technology for situations where water exists on the surface of the earth or overburden strata of coal seam. Reliable security evaluation of underwater coal-mining technology is very important to improve the mining limit, achieve underground safety and rational mining, increase the rate of coal recovery and protect surface and underground water resource.

The key factor to determining the safe working upper limit is the height of fracturing of overburden strata of coal seam, found by extraction (caving zone and fracturing zone means “two regions”). Generally, the “two regions” height [2] is determined by exploration boring and well logging technology and the present engineering analogy method. There are many defects if we adopt the drilling method to determine the “two regions” height: first the surveillance result is limited by the location of borehole, the result only represents one point data in the space, so it can not reflect the entire situation of overburden strata, and the limitation is

relatively big. Second, one borehole only represents one instant point at one time, but the formation of “two regions” height is always a dynamic process, so the surveying result may be different at different time. Third, the drilling method is always difficult to determine the height of the caving zone, because when it is close to the caving zone, the drilling construction is difficult. When we adopt empirical formula or engineering analogy method to determine the “two regions” height, the result reliability can not be guaranteed, because the specific geology and mining technology condition are different.

Microseism monitoring is a new monitoring method[3], which is similar to earthquake, with the forming of caving zone and crack zone of the overburden strata of coal face, the seismic waves whose intensities are relatively small will be produced, it means microseism. Using microseism monitoring technology we can trace, record, analyze, disposal much microseism information. Through synthesis analysis of the microseismic events location, the height of fracturing of overburden strata of coal face can be determined. The microseism information can be traced, noted, analyzed and disposed by microseism monitoring technology. With microseism positioning and comprehensive analysis, we could know the height of fracturing of overburden strata of coal face. Microseism monitoring technology can not only realize dynamic monitoring but also realize three dimensional space integral monitoring [4], so more reliable results to conduct mine mining and also safety and rational working can be achieved.

2 Geological Condition of Coal Face and Design of Microseism Monitoring System

To study the height of fracturing of overburden strata of coal face, the microseism monitoring work about overburden strata motion is carried on in 3up107 fully mechanized coal face of Luxi Coal Mine. The dip length of 3up107 working face is 135m, strike length is 860m, shear height is 2.5m. From interconnection, along strike in the 260m arrange two sides are solid coal. The last length is about 600m, one side is solid coal, the other side is mined goaf of 3up105 working face. 3up107 working face immediate roof is mudstone, thickness range is from 0.2 to 6.8m; the main roof is lutite, thickness range is from 3.5 to 9.4m; the immediate floor is mudstone, thickness range is from 0.7 to 2.5m. Microseism monitoring adopts space monitoring system which is composed of vertical drilling and seam sensor. The aperture of the two vertical drilling is 98mm, while the height is 60m and the hole spacing is 100m. The three-component sensors are installed in each of the two vertical drillings, every sensor is poled by oil sleeper beam. Two strings seam sensors are installed at track gate and haulage gate of the coal face, every string has five sensors, and the space between which is about 50m. Seam sensors are consolidated by cement. Figure 1 shows the design of underground microseism surveillance system.

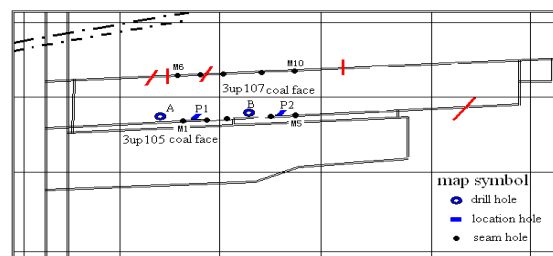


Figure 1 The design schematic plan for the surveillance system

3 Results of Microseism Monitoring and Determination of Height of Fracturing Zone of Overburden Strata of Coal Face

3.1 Microseism Monitoring Results Analysis of Fracturing of Overburden Strata of Coal Face

According to the theory of linear equation location [5], the space location result of microseismic events of overburden strata of coal face is obtained as Figure 2 after inputting the parameters of coordinate and time-difference parameter of microseism monitoring. * represents the position of the microseismic events, the relative coordinate type is adopted. Figure 3 and Figure 4 show the monitored microseismic events' position projected under the horizontal and vertical plane respectively.

To be explained, according to the geological data, the elliptic area in Figure 3 is a fault fracturing area, mining causes the fault activation which would induce microseismic events, so it can not reflect the fracturing of overburden strata induced by extracting.

From the monitoring results we can acquire that microseismic events occurred in immediate roof are relatively dispersive, the periodicity is not obvious. This is because the immediate roof is relative crushing and breaking down after rupture, so the energy of the microseismic events is relatively small and the periodicity is not obvious in immediate roof.

The feature of microseism of the main roof fracturing is that microseismic events are tend to assemble in space, most of the events occur near the main roof breaking line ahead of the rib; micro seismic events are relatively concentrated in the time, that is to say the frequency of the big events is relatively high when main roof fractures, and shows that the periodicity of big events frequency is relatively obvious and the energy of the micro seismic events is universally high. So the position that the events with high energy is relatively concentrated in the time and space can be determined as the position that main roof fractures.

The feature of microseismic events that occurred in crack zone above the main roof is also relatively dispersal in the time and space and the energy is relatively small, which is similar with the feature occurred in immediate roof.

3.2 Determination of Height of Fracturing Zone of Overburden Strata of Coal Face

From Figure 2 and Figure 4 ,it can be acquired that the monitored microseismic events can involve 60m above the working face at most. However, generally speaking, single microseismic event can not conclude that the rock mass has fractured. The rock fractures can not form water flowing fractured zone until the fractures passing through. The energy, quantity and frequency of microseismic events reflect the level of rock mass fractures and their connecting to some extent. From this monitoring result, we can see that the supreme microseismic events of the overburden strata of which the distances are relatively large and the energy is relatively small, the induced cracks can not form effective water flowing connectivity, Those microseismic events are about 10 percent of all the events. So the position under the uppermost 10 percent microseismic events of the overburden strata is determined as the fractured zone upper limit. According to this, the height of the fractured zone of the coal face is determined as 38m. To be explained, there is an inherent relationship between the height of the fractured zone and the overburden strata and its structure. When we adopt microseism

monitoring analysis, the density and energy of microseismic events as the height of fractured zone should be analyzed based on the specific geological and technological condition, this need to be deeply researched.

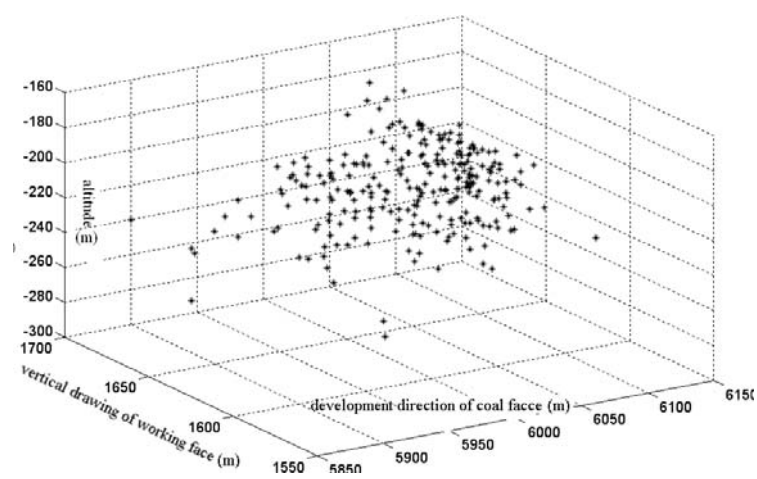


Figure 2 3D position of MS events

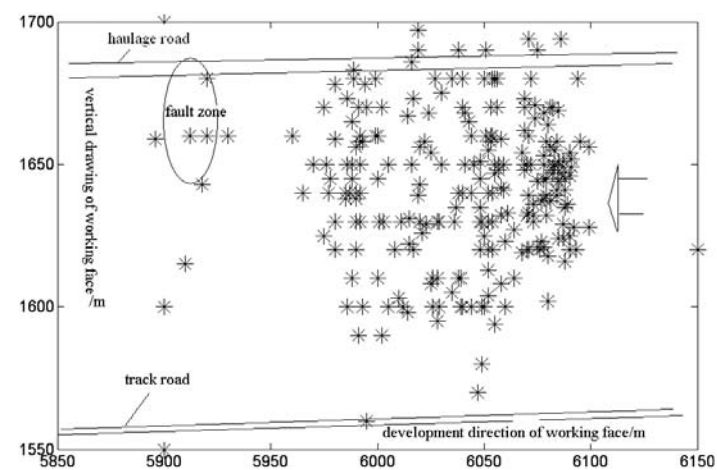


Figure 3 The monitored MS events' position projected under the horizontal plane of the coal face

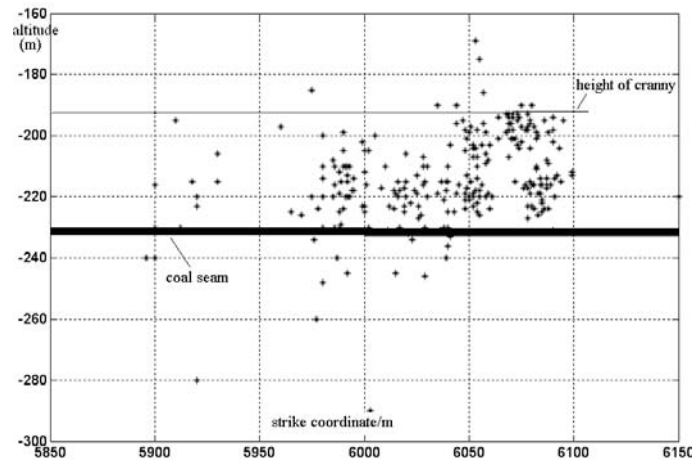


Figure 4 The monitored MS events' position projected under the vertical plane of the coal face

4 Field Measurement Analysis on Height of Fracturing of Overburden Strata of Coal Face

To determine the “two regions” height of 3up107 working face in Luxi Coal Mine furthermore and analyze the reliability of the microseism monitoring result, “two ends injection water instrument” which is thought to be more reliable at present is carried on sublevel injection observation of overburden strata after extraction. We get that the observation section is along seam strike, drill hole is directed above the mined area, plus angle is 45° . The technical parameter of observation is that hole pressure is 0.45-0.50Mpa, injection pressure is 0.1Mpa, observation depth is 70m. Figure 5 shows a picture that the result of height of fractured zone which is observed by two ends injection water method. We can acquire that there is no leakage water upper 36.2m of drill hole. It indicates that the height of the fractured zone is 36.2m.

The height of the fracturing zone of overburden strata of 3up107 working face in Luxi Coal Mine is acquired as 38m by adopting microseism monitoring method, and the result is 36.2m measured by the method of “two ends injection water instrument”. The conclusion about the two methods is generally consistent. It indicates that adopting microseism to monitor the height of the fracturing zone of overburden strata of coal face is available. Height of fractured zone by field measurement is slightly smaller than the result by microseism monitoring analysis, the reason may be the rock mass fractures near the fracturing zone upper limit are not entirely through connection.

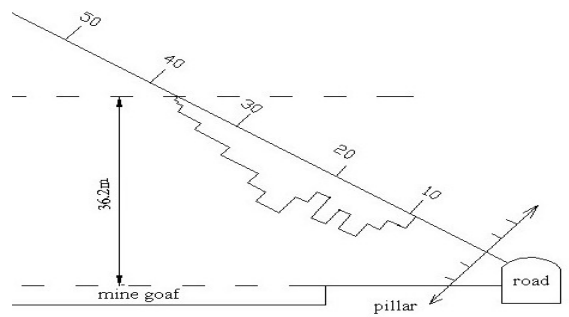


Figure 5 Picture of the result of height of field measuring by “two ends injection water method”

5 Conclusions

(1) Height of the fracturing zone of overburden strata of coal seam is caused by mining and is the key factor to determining safest working upper limit. It has a very important meaning for underwater coal-mining to achieve safety and rational working. It also increases coal resources recovery rate to determine the height of fracturing of overburden strata scientifically and reasonably.

(2) Three dimensional monolithic observation can be understood by microseism monitoring technology. Through synthetic analysis, which consists of tracing and location of microseismic events induced in the process of caving and crack zone formation, the height of the fracturing zone of overburden strata of coal faces can be determined.

(3) Through the microseism monitoring analysis of “two regions” height in 3up107 coalface of Luxi Coal Mine, the uppermost 10 percent of microseismic events of the overburden strata of which the distance is relatively large and the energy is relatively small, the induced cracks can not form effective water flowing connectivity, the position under the uppermost 10 percent microseismic events of the overburden strata is determined as the fractured zone upper limit. According to this, the height of “two regions” is determined as 38 m, which is almost the same as 36.2m identified by field measurement method. Microseism monitoring technology is proved to be available in determining the fracturing height of overburden strata of coal face.

Reference

1. Wang, Y.L. and Jia, W.Y. Analysis and Application of “Two Zone” Height in Deep Seam Mining. *Coal Science and Technology*, 2003, 31(3). 31-33.
2. Kang, J.R. and Wang, J.Z. The Mechanical Model of the Overburden Rock under Mining and the Broken Condition Analysis. *Journal of China Coal Society*, 2002, 1. 23-24.
3. Jiang, F.X., Xun, L. and Yang, S.H. Study on Microseism Monitoring for Spatial Structure of Overlying Strata and Mining Pressure Field in Longwall Face. *Chinese Journal of Geotechnical Engineering*, 2003, 25(1). 23-25.
4. Xun, L., Jiang, F.X. The New Development of Rock Rupture Microseism Monitor in Dealing with Mine Disaster. *The Research Paper Corpus of the fourth Chinese Science Association Youth Academic Conference*. BeiJing: Chinese Science and Technology Publisher, 2001, 194-195.
5. Pang, H.D., Jiang, F.X. and Zhang, X.M. Parameter Variation of Rock Mass Acoustic Emission Revealed by Mathematical Experiment. *Journal of disaster prevention and mitigation engineering*, 2004, 24(2). 158-161.

STUDY ON ACOUSTIC EMISSION FORECAST OF COMPRESSIVE RUPTURE OF ROCK SAMPLE

YONG-JIE YANG, DE-CHAO WANG and YANG-QIANG ZHANG

*Key Laboratory of Mine Disaster Prevention and Control, Shandong University of Science and Technology,
Qingdao, 266510, P.R. China*

YONG-JIE YANG, YU-SHOU LI and GANG ZHOU

*State Key Laboratory for GeoMechanics and Deep Underground Engineering, China University of Mining &
Technology, Xuzhou 221008, P.R. China*

Process of compressive deformation and breakage of rock is certain to be accompanied by occurrence of acoustic emission (AE), and the information of acoustic emission contains plenty of gradual damage precursory information of rock. Study on acoustic emission prediction of compressive rupture of rock has significant meaning by using microseism(acoustic emission) monitoring technology to prevent mine disasters such as roof falling, roof and floor water bursting, rock burst induced by rock breakage. The acoustic emission experimental results under uniaxial compression of sandstone samples indicate that the compressive deformation and damage evolution process of rock can be well expressed by AE characteristics. In addition, wavelet analysis is an important tool of signal processing, and it aims to accurate analysis, diagnosis and forecast of signal information. Wavelet analysis is particularly suitable to process unstable signal. AE signal of rock compressive rupture is a kind of typical unstable signal with time. According to the discrete data series of AE parameters with time obtained from the experimental tests on sandstone samples, and through wavelet coefficient decomposition of AE energy rate and calculation, Lipschitz indexes negative α on different scales are obtained. Further analysis indicates that the time when α first becomes negative on different scales can accurately forecast the rock breakage, which agrees with the experimental result. It is of significant meaning for early predicting of the breakage of rock strata.

1 Introduction

The application of wavelet analysis combines well with its theoretical research. Currently, signal processing is an important part of science and technology work, and it aims to accurate analysis, diagnosis and forecast of signal information. Many applications of wavelet analysis can be regarded as signal processing. For a signal that is stable with time, an ideal processing tool is Fourier analysis. But, most of the signals in practical application are unstable, while wavelet analysis is the particularly applicable tool for unstable signal.

During mining underground, mine disasters, such as roof falling, water inrush, rock burst and coal-gas outburst, are not isolated, but occur with much precursor information. Microseism is one of the important precursors of rock failure and instability [1]. Small sizes of rock samples in labs are micro-object which contain a certain amount of grain, cement, cavity, and fracture sets. AE signal is the released energy when the elements of aggregate occur relative displacement, and its scale is relatively small. Rock samples contain aggregate with much fracture, fault and defect, microseismic signal is also the released energy, but its scale is relatively large. Though the size and microseismic wave energy of rock samples and rock mass are different, the theory is similar. Experimental research of acoustic emission in lab and study on acoustic emission prediction of rock are

of significant meaning for using microseism (acoustic emission) monitoring technology to prevent mine disasters such as roof falling, roof and floor water bursting, rock burst etc.

AE signal parameter with time of rock compressive rupture is one kind of typical unstable discrete signal with time. Based on the experimented discrete data series of AE energy rates with time of sandstone sample, AE prediction analysis is carried out on rock compressive fracture with discrete wavelet processing method.

2 Experiment Equipments and Method

815.03 Electro hydraulic servo-controlled rock pressure testing system imported from USA by Shandong University of Science and Technology was adopted as loading system in this uniaxial compression acoustic emission test. Displacement controlling mode was adopted during the loading process with a loading velocity of 0.1mm/s. Loading wouldn't stop until the sample came into a stage of residual deformation, and the entire loading time was 120 seconds.

The type of AE instrument is AE-400B, and the probe is single component geophone, central resonant frequency is 120 KHz, optical preamplifier gain is 40 db, main amplifier gain is 40db, threshold voltage is adjusted as 1.0 v, and the interval of AE events is set as 3 ms. The AE signal picked by probe through preamplifier and main amplifier is treated into AE parameters (ringing count, ringing counting rate, energy accumulation, energy rate, etc).

The sandstone was taken from the roof of No.3 coal seam of Xinhe Colliery. The rock blocks were immediately sealed and transported to laboratory after acquired from underground. According to test specifications of rock mechanics, samples were machined into cylindrical standard specimens with diameter of 50mm and height of 100mm.

Before experiment, the acoustic emission sensor is coupled on the specimen. Ensuring coupling effect, a layer of grease was wiped on the contact region of probe and specimen, and the probe should be fixed by using adhesive tape. In addition, the acoustic emission detector should be as far as possible from the specimen top and bottom ends in order to decrease end effect.

3 Results Analysis on Rock Compressive Rupture Acoustic Emission Test

Using former method, acoustic emission test was carried out with sandstone sample of Xinhe No.3 coal roof under uniaxial compression, the results was shown as Figure 1

There are many acoustic emission parameters [2], AE rate and energy rate are chosen to analyze the AE characteristics of sample under compression in this paper. AE rate is the ringing counts in unit time, and is also called ringing count rate CNT (N/S). AE rate reflects the frequency of AE, AE signal range as well, so it is concerned with AE energy. AE energy count rate ENE is the energy summation of the whole events in unit time, it is in direct proportion to the square of amplitude of events. It reflects the intensity of AE, for short, energy rate ENE (mV).



Figure 1 Test results of acoustic emission under uniaxial compressive condition of sandstone sample of Xinhe No.3 coal roof

From the AE test results of uniaxial compression on rock sample, the compression failure evolvement of rock sample can be simplified to the following 5 stages as Figure 2

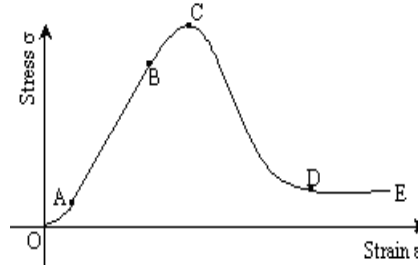


Figure 2 Evolution process of deformation and failure under uniaxial compressive test of rock samples

(1) Stage OA—densification stage. Rock interior generally contains defects, such as pores, fractures, beddings and joints, they are densified to close under loadings. Shown on the stress and strain curve, stage OA presented as upward concave, and strain rate is greater than stress rate. Rough wall surface in rock sample will appear deformation and fracture when the pores and fractures are densified under loading. So the acoustic emission is caused, but the frequency and energy of it are both relatively low.

(2) Stage AB—apparent linear elastic deformation stage. This stage is similarly linear elastic and stress-strain curve appears linear continuous. Because the stress is relatively small, and it can not produce relatively large scale fractures, the number of AE events is little, and the energy rate is low.

(3) Stage BC—accelerating non-elastic deformation stage. After linear elastic deformation stage, rock sample appears some new fractures whose number is much more and size is larger, which making loading capacity of rock decrease. Rock interior accumulates enough elastic energy, in process of energy release, deformation begins accelerate, loading increases relatively slow. Rock internal emerges amount of microcrack confluence, transfixion and at last the rock failures and is instable. In this stage, the number of AE events rapidly increase and the energy rates rapidly enlarge.

(4) Stage CD—fracture and development stage. After rock becoming unstable failure, the stress decreases gradually, the deformation increases, and the fracture has been encryption and transfixion. In this time the number of AE events become smaller and the energy rate becomes lower than the stage BC. Continue loading, rock sample is in the process of residual crushing deformation. The AE rate and energy rate are both further decrease.

(5) Stage DE—plastic flow stage. Rock sample reaches loosen and crush residual strength at last with the continue development of plastic deformation. AE events disappear gradually in this stage.

Obviously, the process of compressive deformation of rock sample closely relates [3] with the evolvement process of primary fracture pressure consolidation, new fracture emergence, extension, transfixion in rock interior. The information of acoustic emission contains plenty of gradual damage precursory information [4] of rock, AE prediction method of compressive rupture can be found through the process of rock AE signal.

4 Discrete Wavelet Analysis on Compression Rupture Prediction of Rock

4.1 Wavelet analysis method

The meaning of wavelet transform[5] is that a function of named basic wavelet (also named mother wavelet) $\phi(t)$ shifts b and then make inner product with needed analysis signal $X(t)$ in different scale a :

$$WT_z(a, b) = \frac{1}{\sqrt{a}} \int_{-\infty}^{+\infty} x(t) \phi^*\left(\frac{t-b}{a}\right) dt, a > 0 \quad (1)$$

Here, a and b are dilation and translation factors respectively, they are continuous variety.

Due to the data series obtained by experiment are discrete, a and b should choose the forms of discretion for application convenience. Let $a = a_0^j$ and $b = ba_0^j b_0$, make discrete sample. When $a_0 = 2$, dyadic orthogonal wavelet can be obtained:

$$\psi_{j,k}(t) = 2^{-j/2} \psi(2^{-j}t - k) \quad (2)$$

In practice, the discrete coefficient at every size can be easily obtained by MATLAB, and this discrete coefficient is of significant meaning for the prediction of rock rupture.

4.2 Discrete Wavelet Processing of AE Parameters

AE energy count rate is analyzed, and main steps contain: ① checking and processing data series with MATLAB; ② transferring wavelet toolbox in MATLAB; ③ analyzing parameters; ④ displaying discrete coefficient.

According to the experiment result of No.3 coal roof sandstone of Xinhe Colliery, Figure 3 shows the extraction of wavelet coefficient of AE energy rate at different scale by wavelet toolbox in MATLAB. At different scales, the maximum of coefficient is corresponding with rupture, while sudden change can basically post the law of rock rupture. Using the variation of discrete coefficient before rupture of rock, the rupture of rock can be predicted. For safety, the time that AE energy rate produce coefficient mutation earliest is adopted as prediction time of rock rupture at different scales.

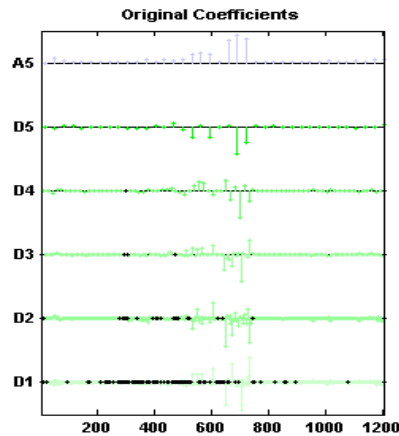


Figure 3 Discrete wavelet coefficients of AE energy rate of sandstone sample

4.3 AE Prediction Index on Compression Rupture of Rock Sample

Using the singularity of function, the regularity of the function can be obtained [5]. If there is discontinuity some where or some order derivative is discontinuous, it means this function is of singularity here. The partial variation of function can be measured by Lipschitz exponent α [6], and the bigger is Lipschitz exponent α , the smoother is the function, and the mutation degree at the mutation point can be estimated. If $0 < \alpha < 1$, it means the mutation of this point is between polygonal function and step function; $\alpha=0$ is corresponding with step mutation point; if $-1 < \alpha < 0$, it means the mutation at this point is between δ function and step function. The α of mutation signal is different from that of normal signal in size. Using singular signal detecting method, make singular signal detecting on graph at every scale in figure (b) of Figure 1. Using the law that the maximum of wavelet transform coefficient changes with scale, the first negative α of AE energy rate at different scale can be made out showing as table 1. Because α will change notably before rock rupture, the first negative α is adopted as beginning time predicted. Adopting the earliest time at different scale as final predicting time, and it is well coincident with the experiment result.

Table 1 The first minus α and its corresponding time of AE energy rate under different scales

Scale	D5	D4	D3	D2	D1	Predict rupture time	Actual rupture time
Time/s	311	315	355	372	381	311	313
A-negative	-0.81	-0.82	-0.25	-0.17	-0.42		

Annotation: time unit is 1/10s

It indicates that the final predicting rupture time is the result of the comparison of coefficient at different scales, but not lying on some one scale coefficient. For safety, the earliest time is adopted as the predicted result. The meaning of site application is to provide as early as possible time for preventing life and wealth from disaster. It is of significant meaning for rupture prediction of coal, and it will have wide application foreground.

5 Main Conclusions

(1) The process of compressive deformation of rock samples closely relates with the evolvement process of primary fracture pressure consolidation, new fractures emergence, extension, and transfixion in rock interior. The information of acoustic emission contains plenty of gradual damage precursory information of rock. It is significant to study acoustic emission prediction of rock by using microseism monitoring technology to prevent mine disasters such as the outburst of coal and gas, rock burst, etc.

(2) Wavelet analysis is an important tool of signal processing, and it is especially suitable to process unstable signals. AE signal of rock compression is one kind of typical unstable signal with time, and discrete wavelet analysis is more suitable for it.

(3) According to the experimented discrete date series, through decomposition of wavelet coefficient and calculation, negative α of Lipschitz exponent of energy rate at different scales can be obtained. Further analysis indicates that the time when α first becomes negative on different scales we can accurately forecast the rock breakage, which is connected with the experiment result. This is of significant meaning for early predicting of the breakage of rock strata.

Acknowledgements

Supported by Open Foundation Subject of State Key Laboratory For Geomechanics & Deep Underground Engineering (SKLGDUE08002X) and Mining Safety Engineering and Environment Protection Key Laboratory of Shandong Province (MDPC0803)

References

1. Jiang, F.X. and Xun, L. Application of Microseismic Monitoring Technology of Strata Fracturing in Underground Coal Mine. Chinese Journal of Geotechnical Engineering, 2002, 24 (2). 147.
2. Tao, J.A., Zhang, K.L. and Zheng, J.F. Research of Parameter of Acoustic Emission under Rock Failure. Chinese Journal of Rock Mechanics and Engineering, 1996, 15. 452-455.
3. Yang, Y.J., Song, Y. and Chen, S.J. Experimental Study on Triaxial Compression Strength and Deformation Characteristic. Journal of China Coal Society, 2006, 31(2). 150-153.
4. Wang, E.Y., He, X.Q., Liu, Z.T., et al. Study on Frequency Spectrum Characteristics of Acoustic Emission in Coal or Rock Deformation and Fracture. Journal of China Coal Society, 2004, 29 (3). 289-292.
5. Yang, F.S. Engineering Analysis and Application of Wavelet. Beijing: Publisher of Science, 2000, 42-68.
6. Dong, X.Z., He, J.L. and Ge, Y.Z. Dyadic Wavelet Transform and Signal Singularity Detection. Relay, 1999, 27(3). 65-68.

A DEPLOYMENT OF BROADBAND SEISMIC STATIONS IN TWO DEEP GOLD MINES, SOUTH AFRICA

A. MCGARR, M. BOETTCHER, J. B. FLETCHER and M. JOHNSTON

U.S. Geological Survey

MS 977, 345 Middlefield Rd., Menlo Park, CA, 94025, USA

R. DURRHEIM, S. SPOTTISWOODE, and A. MILEV

CSIR

POB 91230, Johannesburg, South Africa

In-mine seismic networks throughout the TauTona and Mponeng gold mines provide precise locations and seismic source parameters of earthquakes. They also support small-scale experimental projects, including NELSAM (Natural Earthquake Laboratory in South African Mines), which is intended to record, at close hand, seismic rupture of a geologic fault that traverses the project region near the deepest part of TauTona. To resolve some questions regarding the in-mine and NELSAM networks, we deployed four portable broadband seismic stations at deep sites within TauTona and Mponeng for one week during September 2007 and recorded ground acceleration. Moderately large earthquakes within our temporary network were recorded with sufficiently high signal-to-noise that we were able to integrate the acceleration to ground velocity and displacement, from which moment tensors could be determined. We resolved the questions concerning the NELSAM and in-mine networks by using these moment tensors to calculate synthetic seismograms at various network recording sites for comparison with the ground motion recorded at the same locations. We also used the peak velocity of the S wave pulse, corrected for attenuation with distance, to estimate the maximum slip within the rupture zone of an earthquake. We then combined the maximum slip and seismic moment with results from laboratory friction experiments to estimate maximum slip rates within the same high-slip patches of the rupture zone. For the four largest earthquakes recorded within our network, all with magnitudes near 2, these inferred maximum slips range from 4 to 27 mm and the corresponding maximum slip rates range from 1 to 6 m/s. These results, in conjunction with information from previous ground motion studies, indicate that underground support should be capable of withstanding peak ground velocities of at least 5 m/s.

1 Introduction

The NELSAM project is an international effort intended to investigate earthquake rupture in the near-field. The main study area of the NELSAM project is focused on a region several hundred meters in extent near the deepest portion of the TauTona mine, about 80 km west of Johannesburg, and is instrumented with borehole accelerometers, geophones and other instrumentation. Because the NELSAM project [16] relies on the in-mine seismic network [14] to provide precise hypocenters and seismic source parameters at low magnitude thresholds, it is important to have confidence in this information. To address some questions concerning both the NELSAM and in-mine networks, including system response, transducer orientation, and component polarity, we deployed four broadband field stations, on loan from IRIS/PASSCAL, at depths ranging from 2000 to 3600 m over a region approximately 4 km in extent within the TauTona and Mponeng gold mines (Figure 1).

During this deployment, 18-25 September 2007, we recorded ground acceleration at 200 samples per second. Each field system, consisting of a Reftek* recorder, an Episensor* accelerometer, and a 12-volt battery, was installed in an alcove with the accelerometer glued to the base surface. T066 and T120 (Figure 1a) were located near the vertical shafts that provide access to TauTona and T118 was located in the NELSAM experimental area near the bottom of TauTona (Figure 1). M116 was located in an alcove used by a Japanese-German-South African project [15] near the deepest part of Mponeng. As seen in the cross section (Figure 1b),

T066 was at a depth of 2 km and the other three broadband stations were at depths near 3.6 km. For scale, the horizontal distance between T066 and M116 is about 4 km.

During our deployment, four nearby earthquakes of magnitude 2, designated events 3 to 6, were recorded by the IRIS/PASSCAL stations and their locations are shown in Figure 1. In addition, we also consider an

*Use of trade names is for descriptive purposes only and does not imply endorsement by the U.S Government.

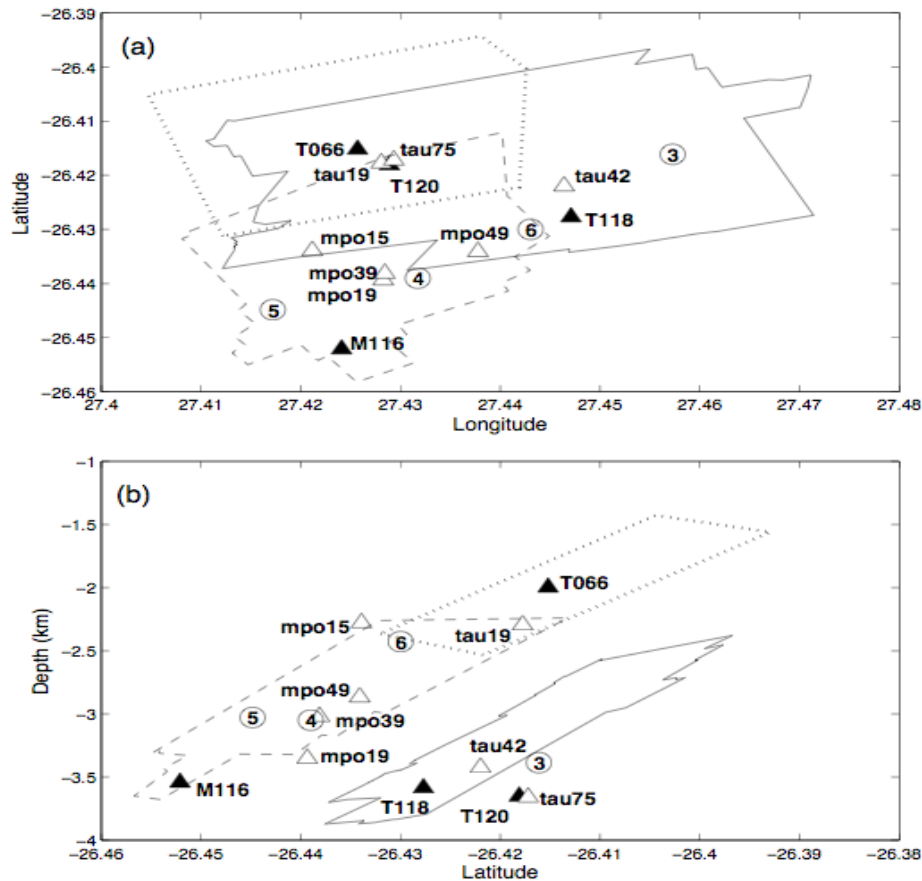


Figure 1. (a) Map and (b) cross section (looking west) views of IRIS/PASSCAL network (filled triangles) and selected stations of the in-mine network (empty triangles). The solid line shows the Carbon Leader Reef within TauTona whereas the dotted and dashed lines outline the shallower Venterdorp Contact Reef within TauTona and Mponeng, respectively. In-mine stations mpo19, tau19, etc., also provided important seismic data for this study.

earthquake of magnitude 2.2, designated 12/12 2004, that occurred in December 2004. This earthquake, which pre-dated our field deployment, was analyzed using the in-mine network ground motion data as corrected by Boettcher et al. (manuscript in preparation). Event 12/12 2004, is of special interest because it was associated with rupture within the ancient Pretorius fault zone, where slip ranging up to 25 mm was measured by Reches et al. [16] quite close to station T118 (Figure 1).

2 IRIS/PASSCAL Seismic Data

To illustrate the data used in our analysis, we show ground velocity and displacement (Figure 2), from event 3 (Table 1, Figure 1), recorded at T118, located 1.65 km northeast of T118. The ground motions for events 3 to 6 were corrected for intrinsic and scattering attenuation using $Q=200$ [4, 17]. These ground motion data were

used here to determine two parameters, $R\bar{v}$ and M_0 , where R is hypocentral distance, \bar{v} is the peak amplitude of the vectorially- summed shear-wave ground velocities [7], and M_0 is the seismic moment. These parameters, in turn, yield estimates of the maximum slip and slip rate within the rupture zone of an earthquake, as will be seen.

Complete seismic moment tensors (six components) have been determined by Boettcher et al. (manuscript in preparation) using updated versions of a technique described by McGarr [8, 9]. This entails measuring ground displacement (e.g., right-hand column of Figure 2) at selected points for comparison with similar measurements made on synthetic seismograms calculated for each moment tensor component. As seen in Figure 2 (right-hand column), the body-wave pulses for P and S are quite clear and simple and we also see the near-field components including the ramps between the P and S pulses, especially evident on the radial and vertical components. The near-field components are quite useful for constraining the moment tensor [8].

As described in more detail by Boettcher et al. (manuscript in preparation), our approach for addressing uncertainties concerning the in-mine network was first to determine moment tensors for events 3-6, the four largest earthquakes that were located within or adjacent to our IRIS/PASSCAL network, and then to calculate synthetic seismograms from the moment tensor solutions at the in-mine station locations for comparison with the seismograms actually recorded.

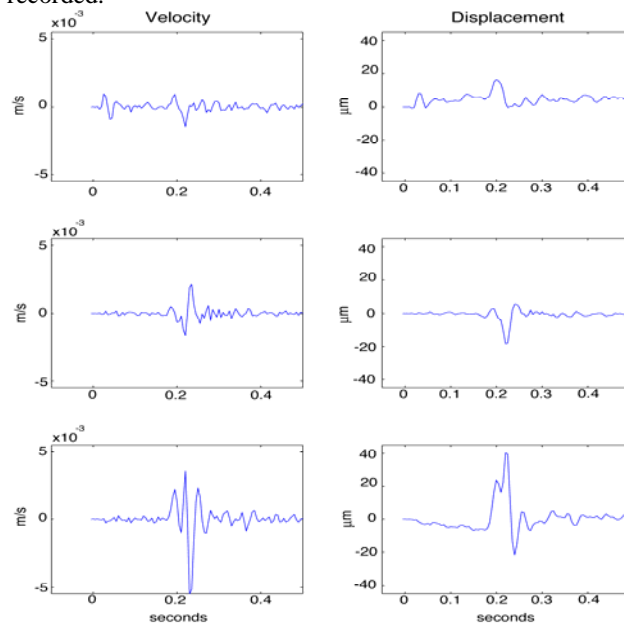


Figure 2. Ground velocity and displacement for event 3 recorded at T118. From top to bottom, the traces are radial (horizontal), transverse, and vertical.

3 Event 12/12 2004

The analysis of this interesting earthquake required first checking polarities and orientations of the seven in-mine stations shown in Figure 1. Then, the records of velocity at these stations for event 12/12 2004 were integrated to obtain ground displacement from which a moment tensor was determined (Boettcher et al., manuscript in preparation). As is the case for many mining-induced earthquakes, this moment tensor is a combination of deviatoric (shear-faulting) and implosive deformation, associated with nearby stope collapse [8]. Ground velocity from event 12/12 2004, recorded at tau19, is shown in the left-hand column of Figure 3 where we see fairly simple body-wave pulses. The ground displacement and the synthetic seismograms of displacement from the moment-tensor solution, are shown in the right-hand column. The fit at this station is good in that the synthetics replicate most of the main features of the ground displacement. The moment tensor, based on ground displacement recorded at the seven in-mine stations shown in Figure 1, was well constrained.

Similarly, the ground motion parameter R_v was measured from the S-wave velocity pulses at these in-mine stations including those shown in the left column of Figure 3 for tau19.

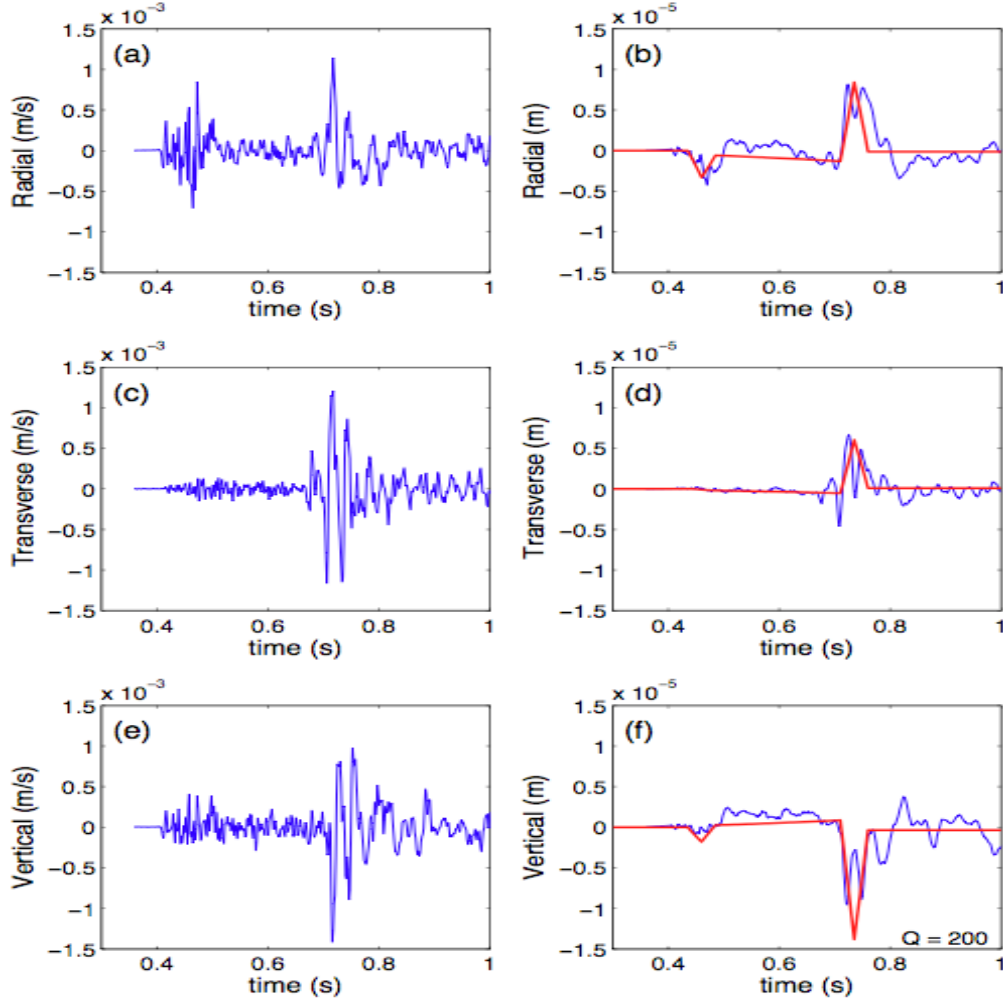


Figure 3 Ground velocity in the left-hand column and displacement in the right-hand column as recorded at in-mine station tau19 with synthetic displacements (red) calculated from the moment tensor solution for event 12/12 2004.

In the next section we apply a technique for relating the maximum slip D_{\max} within the rupture zone of an earthquake to the peak velocity parameter R_v . In the case of 12/12 2004, the maximum slip measured in the Pretorius fault zone of 25 mm will be compared with that inferred from the median peak velocity parameter for this earthquake.

4 D_{\max} and R_v

McGarr [7] developed a simple relationship between the peak velocity parameter R_v and the maximum slip within the rupture zone of an earthquake D_{\max} , $R_v = 0.124\beta D_{\max}$, where β is the shear wave speed. More recently, McGarr et al. [13] updated this relation to be more consistent with the observed spectral character of ground motion, as well as the most commonly-used radiation factor, to obtain

$$R_v = 0.087\beta D_{\max} \quad (1)$$

and found that D_{\max} estimated using equation (1) is consistent with D_{\max} measured directly within fault zones exhumed underground. To demonstrate this, we consider the data listed in Table 1 and illustrated in Figure 4. Table 1 has been adapted from Table 1 of McGarr et al. [13] and augmented by adding parameters reported by McGarr [10] for four earthquakes for which both the seismic moments and the peak velocity parameters have been reported. These four earthquakes were selected from a larger set reported in [10] on the basis that they were large enough and located sufficiently far from the stopes that effects of anelastic and scattering attenuation are unlikely to have affected the peak velocity amplitudes significantly; it was not feasible to apply a correction for the effects of Q to these older data.

There are two earthquakes listed in Table 1 for which both R_y and D_{\max} are listed. For event 1040939, D_{\max} estimated using equation (1) is 0.23 m, which agrees well with the maximum slip of 0.2 m measured underground shortly after this earthquake [1]. R_y for event 12/12 2004 yielded a maximum slip of 16 mm,

Table 1. Peak velocity parameters, maximum slips, and maximum slip rates

Event	M_0 , N-m [#]	R_y , m ² /s	D_{\max} , mm	D_{\max} , m/s	Reference
Event 3	4.4×10^{12}	8.54	27.3*	6.3	McGarr et al. [13]
Event 4	1.8×10^{12}	3.05	9.7*	2.0	McGarr et al. [13]
Event 5	5.4×10^{11}	1.35	4.3*	1.1	McGarr et al. [13]
Event 6	4.0×10^{12}	3.06	9.8*	1.4	McGarr et al. [13]
1040939	4.7×10^{15}	72.5	230* 200 ^{##}	4.7	McGarr [7]
12/12 2004	2.3×10^{12}	4.98**	15.9* 25 ^{##}	3.8	Reches et al. [16]
1989Brand	7.9×10^{15}	-	370 ^{##}	-	Dor et al. [3]
1982Welk	1.8×10^{16}	-	410 ^{##}	-	Dor et al. [3]
1992Welk	1.26×10^{16}	-	150 ^{##}	-	Dor et al. [3]
1999Welk	5.0×10^{16}	-	440 ^{##}	-	Dor et al. [3]
Wessel. Ft.	$1. \times 10^{16}$	-	500 ^{##}	-	Brummer and Rorke [1]
1986 2Shaft	1.26×10^{16}	-	200 ^{##}	-	Brummer and Rorke [1]
3141709	1.5×10^{12}	3.24	10.3*	2.5	McGarr [10]
3231839	4.06×10^{12}	9.0	28.7*	7.0	McGarr [10]
3241529	4.18×10^{12}	11.1	35.4*	9.5	McGarr [10]
0331352	2.1×10^{12}	4.44	14.2*	3.4	McGarr [10]
Adjusted lab	4.4×10^{10}	5.2	-	5.2	Lockner and Okubo [5]

[#] Seismic moment tensors for events 3 to 6 and 12/12 2004 were determined by Boettcher et al. (in preparation). The deviatoric components of these solutions are listed here. (See also [8].)

*Estimated using equation (1).

** From McGarr et al. [13].

^{##} Underground measurements of slip.

from equation (1) whereas the maximum slip measured in the rupture zone, as noted before, was 25 mm [16].

All of the maximum slip data listed in Table 1, either measured directly or inferred using equation (1), are plotted in Figure 4. These results are distributed about the line $D_{\max} = 10^{-5.83} M_0^{1/3}$, which is the regression fit to a much larger set of maximum slip data for earthquakes with magnitudes as high as 7.9 [11]. Also shown in Figure 4 is the maximum slip of 5.24 mm for a laboratory stick-slip event and adjusted, as will be described in the next section, to be on the regression line just mentioned. This stick-slip event is event 9 from the study of Lockner and Okubo [5] and is the median result from 15 experiments.

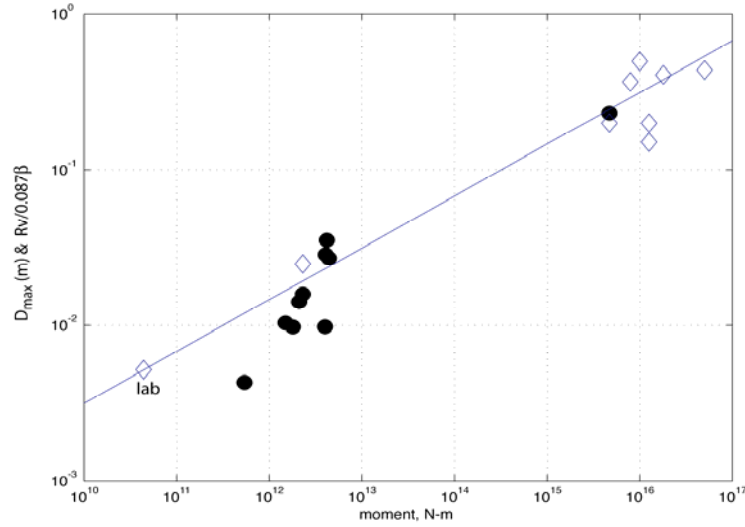


Figure 4. Maximum slips within the rupture zones of the mining-induced earthquakes and laboratory stick-slip event 9 (adjusted) listed in Table 1. The diamonds represent maximum slips measured within the rupture zone and the filled circles represent those inferred using equation (1). The equation $D_{\max}=10^{-5.83}M_0^{1/3}$, from [11], is represented by the solid line.

5 Maximum Slip Rate

Following McGarr et al. [13], we start by considering the experiment that yielded the lab result in Figure 4, stick-slip event 9 reported by Lockner and Okubo [5]. For this experiment, the slip is 93×10^{-6} m. The lab set-up has an unloading stiffness of 3.3 MPa/mm and so to match this experimental stiffness to a more realistic earthquake fault, we replace the laboratory fault, which is 2 m long and 0.4 m wide, by a buried circular shear crack of radius $r=10.4$ m [19, 12]. Thus, our laboratory earthquake, adjusted for stiffness, has a seismic moment $M_0=G\pi r^2 D_{\max}=7.9 \times 10^8$ N-m and the same final slip, 93 microns; for the granite sample, the modulus of rigidity is $G=2.5 \times 10^4$ MPa [5].

The rise time T for the slip, in one of these laboratory events, to increase from zero to its final value is always close to 2 ms; T is controlled by the stiffness and mass of the laboratory system. McGarr et al. [13] represented the slip rate of the lab events as an isosceles triangle with a base $T=2$ ms and height equal to the maximum slip rate. Thus, for any laboratory experiment, we assume

$$\dot{D}_{\max} = \frac{2D}{T} \quad (2)$$

where D is the final slip and $T=2$ ms. (Laboratory slip is represented as D , instead of D_{\max} , because it is homogeneous over the fault surface, in contrast to the maximum slip in an earthquake rupture zone.)

In Figure 4, we have adjusted event 9, the laboratory earthquake to be on the regression line $D_{\max}=10^{-5.83}M_0^{1/3}$ [11] by maintaining the same stiffness and increasing the slip from 93×10^{-6} m to 5.2×10^{-3} m and the seismic moment from 7.9×10^8 N-m to 4.4×10^{10} N-m. Because we have maintained the same stiffness during this adjustment, T remains close to 2 ms and so the maximum slip rate, from equation (2), is 5.2 m/s. Any point on the line passing through the laboratory result in Figure 4 represents an earthquake with the same maximum slip rate [13].

To estimate \dot{D}_{\max} for any of the earthquakes represented in Figure 4, we note that each point in this figure can be used to determine C in the following function

$$\dot{D}_{\max} = CM_0^{1/3} \quad (3)$$

Once the regression line, equation (3), is determined for a given earthquake, we can adjust laboratory event 9 by increasing its slip until it plots on the line. This procedure yields the adjusted slip, which then can be converted to the maximum slip rate using equation (2); these results are listed in Table 1 and plotted in Figure 5, where we see that the maximum slip rate is independent of earthquake magnitude or moment.

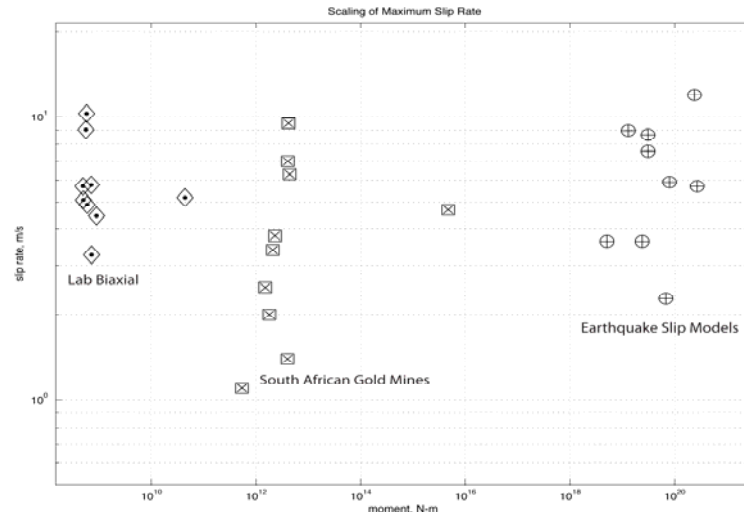


Figure 5. Maximum slip rate as a function of seismic moment for laboratory stick-slip events, mining induced earthquakes, and from slip models developed for major earthquakes [12]. The lab slip rates near the left edge were reported by Lockner et al. [6] and were adjusted to seismogenic loading stresses as described by McGarr and Fletcher [12]; the lab slip rate further to the right, event 9, is the median adjusted result of 15 experiments from Lockner and Okubo [5]. Of the mining-induced earthquakes listed in Table 1, only those with D_{\max} estimated from R_y are represented here because estimates of this parameter from exhumed fault zones are much more uncertain. Adapted from Figure 6 of McGarr and Fletcher [12].

6 Conclusions

Peak ground velocities adjacent to mining-induced ruptures correlate well with underground damage inasmuch as the stope support is often designed to be able to withstand a specified rate of stope closure without failing [18]. To a good approximation, the peak ground velocity next to a slipping fault is half the maximum slip rate. Thus, our results (Table 1, Figure 5) indicate that underground support in the vicinity of mining-induced earthquakes should be capable of withstanding at least 5 m/s without failing. This maximum ground velocity is independent of earthquake moment or magnitude, but the region that might be subjected to this maximum velocity increases with magnitude. Interestingly, the maximum slip rates of the mining-induced earthquakes cover much the same range as was found for major tectonic earthquakes (Figure 5).

Maximum slip is another important predictor of underground damage. For instance, if a rupture with a maximum slip of 0.2 m, or more, intersects a vertical shaft, then the resulting misalignment might put the shaft out of operation. In contrast to near-fault peak velocity, which is independent of magnitude, the maximum slip (Figure 4) scales robustly as the cube root of the seismic moment. Thus, maximum slip due to small magnitude earthquakes is generally of little consequence whereas for events of magnitude of 3 and greater, the maximum slip may be an important factor in the resulting damage.

Acknowledgements

We are grateful to IRIS/PASSCAL for the loan of the broadband systems that were key to the success of this project. Tony Ward, Sylvester Morema and Gilbert Morema, all with Seismogen, Lourens Scheepers, Frans Rheeder, and George Kgigori, all with Tautona Gold Mine, and Jonas Machake of the CSIR provided valuable

support, especially underground, for this challenging project. Justin Rubinstein and Nick Beeler provided insightful reviews that helped to improve this report.

References

1. Brummer, R.K. and Rorke, A.J. Case Studies of Large Rockbursts in South African Gold Mines. in Rockbursts and Seismicity in Mines, C. Fairhurst (Editor) Balkema, (Rotterdam, 1990).
2. Dieterich, J.H. Potential for Geophysical Experiments in Large-Scale Tests, *Geophys. Res. Lett.* 1981, 8. 653-656.
3. Dor, O., Reches, Z. and Van Aswegen, G. Fault Zones Associated with the Matjhabeng Earthquake, 1999, South Africa, in Rockbursts and Seismicity in Mines, van Aswegen, G., Durrheim, R. J., and Ortlepp, W.D. (Editors), South African Institute of Mining and Metallurgy, (Johannesburg, 2001).
4. Hemp, D.A. and Goldbach, O.D. The Effect of Backfill on Ground Motion in a Stope During Seismic Events, Rockbursts and Seismicity in Mines, R. P. Young (Editor), Balkema, Rotterdam, 1993.
5. Lockner, D.A. and Okubo, P.G. Measurements of Frictional Heating in Granite, *J. Geophys. Res.* 1983, 88. 4313-4320.
6. Lockner, D.A., Okubo, P.G. and Dieterich, J.H. Containment of Stick-Slip Failures on a Simulated Fault by Pore Fluid Injection, *Geophys. Res. Lett.* 1982, 9. 801-804.
7. McGarr, A. Observations Constraining Near-Source Ground Motion Estimated from Locally Recorded Seismograms, *J. Geophys. Res.* ,1991, 96(16), 495-16,508.
8. McGarr, A. An Implosive Component in the Seismic Moment Tensor of a Mining-Induced Tremor, *Geophys. Res. Lett.* ,1992, 19. 1579-1582.
9. McGarr, A. Moment Tensors of Ten Witwatersrand Tremors. *Pure Appl. Geophys.*,1992, 139. 781-800.
10. McGarr, A. Factors Influencing the Strong Ground Motion from Mining-Induced Tremors, in Rockbursts and Seismicity in Mines 93, Young, R. P. (Editor), (Balkema, Rotterdam, 1993).
11. McGarr, A. and Fletcher, J.B. Maximum Slip in Earthquake Fault Zones, Apparent Stress, and Stick-Slip Friction, *Bull. Seism. Soc. Am.* 2003,93. 2355-2362.
12. McGarr, A. and Fletcher, J.B. Near-Fault Peak Ground Velocity from Earthquake and Laboratory Data, *Bull. Seism. Soc. Am.* 2007, 97. 1502-1510.
13. McGarr, A. et al. Broadband Records of Earthquakes in Deep Gold Mines and a Comparison with Results from SAFOD, California, submitted to *Bull. Seismol. Soc. Am.* ,2009.
14. Mendecki, A.J. *Seismic Monitoring in Mines*, Chapman & Hall, London, 1997.
15. Ogasawara, H. Research Group for Semi-Controlled Earthquake-Generation Experiments South African Deep Gold Mines. Review of Semi-Controlled Earthquake-Generation Experiments in South African Deep Gold Mines (1992-2001), in *Seismogenic Process Monitoring*, H. Ogasawara, Yanagidani, T. and Ando, M. (Editors), Balkema, (Tokyo, 2002).
16. Reches, Z. et al. Building a Natural Earthquake Laboratory at Focal Depth (DAFSAM-NELSAM Project, South Africa), *Scientific Drilling*, doi:10.2204/iodp.sd. 3. 06. 2006, 30-33.
17. Spottiswoode, S.M. Seismic Attenuation in Deep-Level Mines, Rockbursts and Seismicity in Mines, Young, R.P. (Editor), Balkema, Rotterdam, 1993.
18. Wagner, H. Support Requirements for Rockburst Conditions, Rockbursts and Seismicity in Mines, Gay, N. C. and Wainwright, E. H. (Editors), South African Institute of Mining and Metallurgy, (Johannesburg, 1984).
19. Walsh, J.B. Stiffness in Faulting and Friction Experiments, *J. Geophys. Res.* 1971,76, 8597-8598.

APPLICATION OF ROCK FAILURE SIMILARITY CONCEPT FOR SEISMIC HAZARD ASSESSMENT

VICTOR I. GERMAN

Strata Control Centre, Kazakhmys Co. Ltd

Zhezkazgan, 100600, Republic of Kazakhstan

Research Department, Siberian Aerospace State University

Krasnoyarsk, 660014, Russia

Physical concepts of strong seismic event forecasting based on laboratory experiments and earthquake seismology investigations are considered. High concentration of events, seismic gaps and seismicity migration can be used as forerunners of strong seismic events. A parameter, which characterises the possibility of weak events interacting and forming a strong seismic event is introduced. The case study of strong event with radiated energy $10^{7.1}$ J which was forecasted in real time mode by analysing only seismic data is considered.

1 Introduction

Rockbursts and collapses forecasting is an old and complicated problem, which is in many mines To solve this problem it is productive to use idea about self-similarity of the seismic/failure process in the earth's crust/rocks on different scales from micro-level to strong earthquakes [2, 4, 9-11], which is very popular now. It reveals the possibility to estimate seismic hazard in mines with application of methods which are designed in seismology as well as using of regularities determined in laboratory experiments.

2 Physical Principals of Seismic Hazard Estimation

The basis for strong seismic events forecasting (they can correspond to collapses, rockbursts etc) is rock failure physical concepts, which were established as a result of laboratory experiments and earthquake seismology investigations [5, 6, 8, 9, 16]:

Failure is a process, which is developed in space and time on different scale levels.

There is a similarity of failure process on different scale levels.

Each strong seismic event corresponds to large scale failure of rock mass prepared by smaller events.

An experimental studies of the rock failure process on the microscopic and macroscopic levels showed that this process may be subdivided in two main stages [4, 5, 14]. It allows to develop a two-stage model of rock fracture [4].

According to this model, the accumulation of non-interacting cracks (or rock's flaws or defects) I rank at specific locations in the rock volume due to inhomogeneities and stress fields is considered as the first stage of the failure process (see Figure 1a). Further, as the process of failure develops in time, concentration of cracks in some location reach the critical threshold level that leads to a nucleation of a failure process (Figure 1b) and interaction of cracks with joining and propagation (Figure 1c). As a result, flaws/cracks of the next scale level ($I + 1$ rank) are generated. This is the second stage of the failure process. Then cracks of $I + 1$ rank will form

cracks $I + 2$ rank and so on. The transition between stages in considered volume occur when the concentration parameter

$$K = \frac{D_{av}}{L_{av}} = \frac{(V/N)^{1/3}}{\sum L_i / N} \quad (1)$$

(ratio of average distance between cracks estimation D_{av} to its average size L_{av} , V is considered volume of rock and N is number of cracks in it) will be less a critical value κ_* . For rock fracture $\kappa_* = 2.5 \dots 10$ [4, 12, 15].

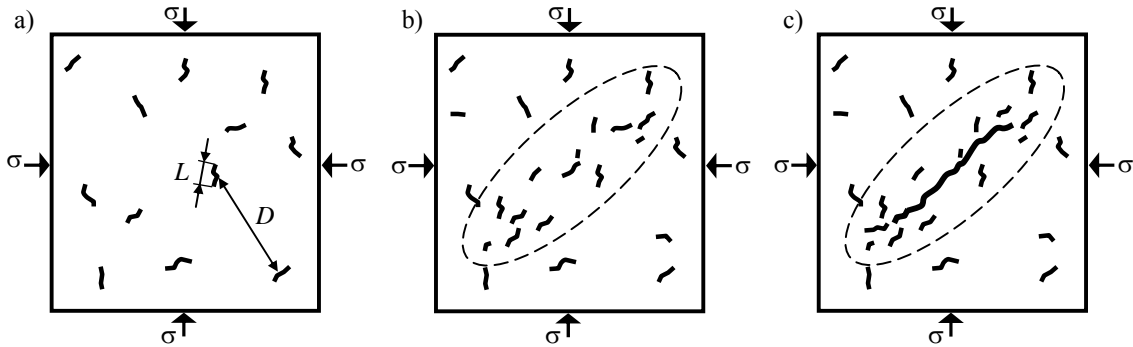


Figure 1 A two-stage model of rock fracture: a) the first stage – accumulation of non-interacting cracks, b,c) the second stage – formation of area with high concentration of cracks (b) and development of fracture, caused by interaction of these cracks (c)

According to the two stage model there is a common physical mechanism of failure process on different scale levels. It leads to similarity of rock failure process on different levels. As a result the basic statements of the two stage model of solid fracture, which originally was based on laboratory experiments with different materials (metals, polymer and so on), are valid for specimen fracture as well as for seismic event preparation [1, 9, 12, 15]. Moreover the two stage model is very similar with avalanche-unstable fissuring model, which is well known in seismology [7], and concentration parameter is used for earthquakes forecasting [12, 15].

Additional important forerunners of strong seismic events are “seismic gaps” of the first and second type (areas with anomaly low seismic activity) and migration of seismicity [8]. They are actively used in seismology. The seismic gap of the first type is an inactive area, which is surrounded by areas with strong seismic events (with collapses). In this case it can be a barrier between active areas and be under high stress. The failure of this area can leads to strong seismic events occurrence accompanied by joining of adjacent active areas.

Redistribution of stress caused by collapse or failure development can be a reason of seismic event migration with collapse of the correspondent area. Determination of such trends can allow to forecast the place of future collapse.

Seismic gap of the second type is area with temporary lack of events. It is necessary to accumulate energy for final failure of this area. Often such area is delineated by active areas which form a “circular structure”, which shows contour of the future collapse.

3 Modified Concentration Criterion of Solids Fracture Used in Zhezkazgan Mines

The concentration criterion of solids fracture [4] is used as a basic principal to forecast collapses. It is based on the analysis of spatial distribution of seismic events and takes into account the scale of each event.

On Zhezkazgan mines the modified concentration criterion is used [2]. The rule of dangerous areas delineation can be easily demonstrated graphically (see Figure 2). Let's associate each event with a sphere

having diameter equal $L \cdot \kappa_*$ (κ_* is a constant), roughly it corresponds to area of event influence. An intersection of these areas for some events means that potentially they can interact with each other with joining and formation event of the next scale level. The group of such events should be considered as potentially high dangerous. They can be a cause for strong seismic event arising. To estimate hazard of cracks joining the dimensionless parameter κ was introduced [2], it is ratio of distance between centers of cracks (between hypocenters of corresponded events) to their average lengths. This parameter is calculated for each pair of seismic events with indexes i and j :

$$\kappa = 2 \sqrt{(X_i - X_j)^2 + (Y_i - Y_j)^2 + (Z_i - Z_j)^2} / (L_i + L_j), \quad (2)$$

where X, Y, Z – are coordinates of registered seismic events, caused by crack occurrence with linear size L , which is calculated from radiated energy E :

$$\log_{10} L(m) = 1/3 \cdot \log_{10} E(J) - 0.3. \quad (3)$$

Decreasing of parameter κ (increasing of cracks/defects concentration) down to threshold value κ_* leads to occurrence of crack of the next scale level, which can initiate collapse. The theoretical value for κ_* is 3 [4], but for real conditions $\kappa_* \approx 5 \dots 10$.

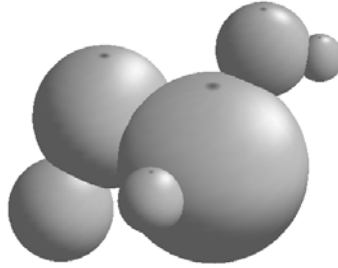


Figure 2 Formation of a dangerous area from areas of influence of seismic events

To delineate areas with high hazard of collapses seismic events for previous years are back analyzed. For calculation of the parameter κ events with radiated energy $E > E_{max}$ are considered as events with $E = E_{max}$. It allows to avoid excessive decreasing of the join parameter κ in the area of strong seismic event. As a rule $E_{max} \approx 100 E_{min} \dots 1000 E_{min}$ [2]. Chains of events with $\kappa \leq \kappa_*$ united to areas corresponded to high dangerous of collapses. Analysis of seismic activity in Zhezkazgan mines allows to establish that zones with $\kappa_* = 8$ corresponds to potentially dangerous areas and with $\kappa_* = 5$ – to critical (unstable) ones or to destroyed ones. Thus for Zhezkazgan mines, which its grey sandstones and red rocks (fine grained sandstones, siltstones and claystones) the threshold value of join parameter is $\kappa_* \approx 5 \dots 8$.

Each strong seismic event is prepared by smaller events, their radiated energy can be down 3 decimal order less energy of the corresponded strong event [2]. Therefore to forecast strong events with radiated energy E the seismic network should reliably register all event with radiated energy more then $E/1000$.

Moreover analysis of expression (2) shows that to guarantee that error of parameter κ determination will not exceed 50% it is necessary: to determine coordinates X, Y, Z with error which does not exceed double size of the crack L (it is about 10 m for weak events); to determine radiated seismic energy E , which is used for calculation of L , with error, which does not exceed 300%.

The seismic monitoring systems currently used in Zhezkazgan mine allows to determine these parameters with such precision not in all cases. It reduces the effectiveness of the parameter κ application. This problem should be solved after installation of additional sensors and final attenuation of a new seismic system (ISS

International Ltd), which was installed in 2007. Earlier the SDSC seismic system produced by Elgeo Ltd (Kazakhstan) was operated [3].

4 Case Study

Lets consider a forecasting of one of the strongest event, registered on Zhezkazgan mines. It occurs at 17th November 2005 and has radiated energy $10^{7.1}$ J. The forecasting was realized in real time mode, and only seismic monitoring information was used.

The room-and-pillar method is used in Zhezkazgan copper mines. Typical depth of mining is -300...-140 m. After many decades of mining the overall extraction volume has reached a value of about 180 million m³, which is supported by tens of thousands of rib and inter cavern pillars. Progressive increasing of number of destroyed pillars, increasing of number of collapses correspond to worsening of geomechanical conditions. It is caused by increasing of number of excavated beds and decreasing of supporting massif area. Since 1990-s qualitative changes of geomechanical conditions have taken place: some local unstable areas with destroyed pillars have started to unite and form extensive unstable regions and collapses. These processes were accompanied by strong seismic events and air blows in excavations.

The room-and-pillar method for 7 overlapped mined levels was used in considered area. This area is characterized by big number of unstable and caving rooms. This leads to formation of two collapses with significant movements of surface (solid contours on Figures 3, 4). The left/west collapse has started to form from 1979 and then it was significantly developed in 2000, 2003 and 2005. Each development was accompanied by increasing of seismic activity. The right collapse was formed in 1992. Contours of the collapses at the beginning of 2005 are shown on Figures 3 and 4 by gray solid line, further developments are shown by gray dotted lines with date indication.

The forecasted event occur between these collapses, when distance between them reach value comparable with linear size of the forecasted strong event. The area between these collapses can be considered as a seismic gap of the first type.

The spatial-temporal and energy/scale distribution of seismicity registered prior to the strong event occurrence is shown on Figure 3. Only reliably registered events with radiated energy more then $E_{\min} = 10^{2.6}$ J are shown. Analysis of Figure 3 demonstrates that the initial moment for preparation of this strong event was 14.03.2005 when another strong event with radiated energy $10^{6.1}$ J occurs. During next five days some new seismic events were registered. Each this event is shown on Figure 3 as circles with crosses in the center. Two of these events were between two collapses, where seismic events were not registered before (Figure 3). One and half week later seismicity moved to east with activation of west part of left collapse and occurrence of additional events between collapses. These events are shown on Figure 3 as filled circles. Note that seismic activity between collapses in this moment had circle shape without events in the center (on Figure 3 a dash-dot contour corresponds to this area). The forecasted event occurred in this area later. It was considered as a gap area of second type. Moreover the left and the right of this gap area two areas with high value of parameter κ were formed. They correspond to dotted contours on Figure 3, $\kappa_* = 5$, $E_{\max} = 100 \cdot E_{\min} = 10^{4.6}$ J. Thus the following conclusion was made up: the formation of seismic gap of the first type between two collapses is finished. As a result the forecast of high danger in this area has been done and mining has been stopped, the collapse occurs at 17th November 2005.

The forecasted event is shown on Figure 4 as the circle with maximum diameter. At the same figure all registered events before and after it are shown. The active stage of the collapse correspondent to the strong event lasts about one week. As a result four rooms was fallen, significant movements of surface was occur, it leads to uniting of the nearest collapses. The movement areas involve a road and a heating main to shaft 65.

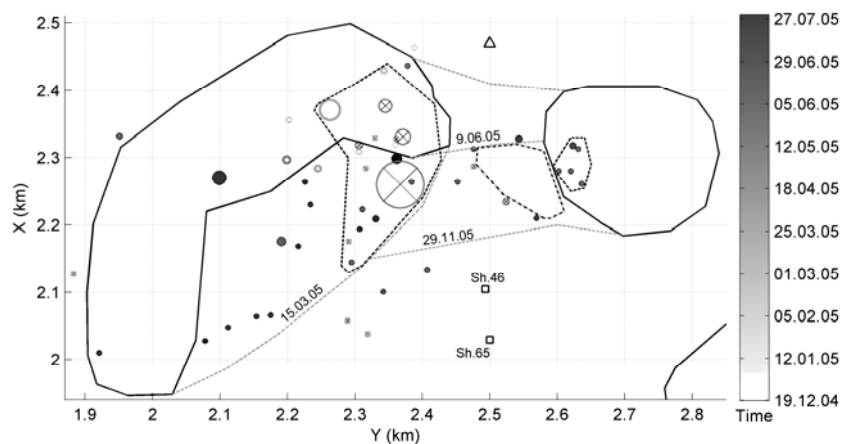


Figure 3 Seismicity prior to the forecasted event occurrence

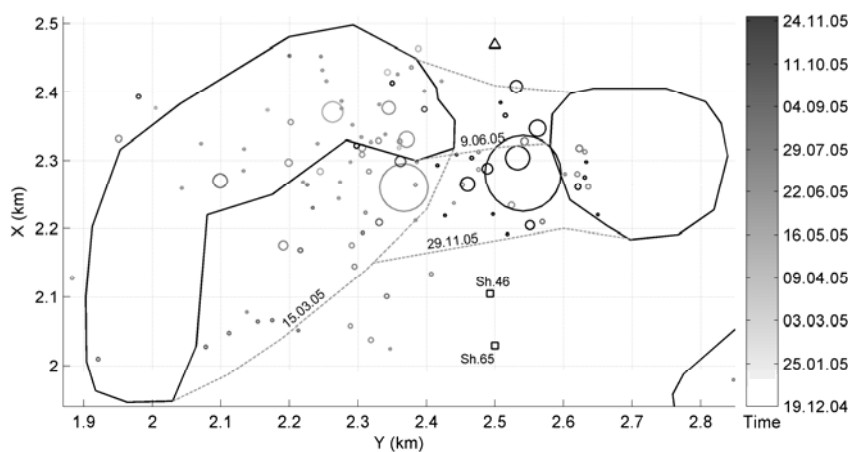


Figure 4 The forecasted strong event and seismic activity before and after it

5 Conclusions

Application of rock similarity concept allows effectively estimate seismic hazard in mines with using of methods which are designed in seismology as well as of regularities determined in laboratory experiments with application. Practice of seismic monitoring in Zhezkazgan mines (Kazakhstan) shows that most part of collapses can be forecasted month before it occurrence.

References

1. Anikolenko, V.A. and Mansurov, V.A. Invariant Kinetic Approach to the Description of a Rock Fracture Process and Induced Seismic Events. *Pure Appl. Geophys.*, 1996, 147(2).
2. German, V.I. and Mansurov, V.A. Induced Seismicity Monitoring and Procedure of Rock-Burst Focus Localization. *Journal of Mining Science*, 2002, 38(4). 336-343.

3. German, V.I., Mansurov, V.A. and Boiko, P.A. Seismic Monitoring in Zhezkazgan Mines: Case Study of an Strong Seismic Event Forecasting Deep Mining 07: Fourth international seminar on deep and high stress mining. Australian Centre for Geomechanics. (Perth,Australia, 2007).
4. Kuksenko, V. S., Tomilin, N. G., Damaskinskaya, E. and Lockner, D. A. A Two-Stage Model of Fracture of Rocks. *Pure and Applied Geophysics*, 1996,146 (2). 253-263.
5. Lockner, D.A., Byerlee, J.D., Kuksenko, V., Ponomarev, A. and Sidorin, A. Observations of quasistatic fault growth from acoustic emissions. In *Fault Mechanics and Transport Properties of Rock*. B. Evans and T.F. Wong (editors) Academic Press, London, 1992, 3-31.
6. Mansurov, V.A. Laboratory Experiments: Their Role in the Problem of Rock Burst Prediction. *Comprehensive Rock Engineering*, London, Pergamon Press, 1993.
7. Miachkin, V. I., Brace, W. F., Sobolev G. A., Dieterich J.H. Two Models for Earthquake Forerunners, *Pure Appl. Geophys.* , 1975,113. 169-181.
8. Mogi, K. *Earthquake Prediction*. Academic Press, (Tokyo,1985).
9. Ponomarev, A.V., Zavyalov, A.D., Smirnov, V.B., Lockner, D.A. Physical Modeling of the Formation and Evolution of Seismically Active Fault Zones. *Tectonophysics*, 1997, 277. 57-81.
10. Rykunov, L.S., Smirnov, V. B., Starovoit, Yu.O. and Chubarova, O.S.: Self-Similarity of Seismic Emission in Time, *Doklady AN USSR*, 1987, 297(6). 1337-1341.
11. Sadovsky, M. A., Bolkhovitinov, L. G. and Pisarenko, V. F. *Deformation of Geophysical Medium and Seismic Process*, Nauka, Moscow, 1987,1-100.
12. Sobolev, G.A. and Zavialov, A.D. A Concentration Criterion for Seismically Active Faults. In "Earthquakes Prediction - an International Review", Maurice Ewing Series 4, New-York, 1981, 377-380.
13. Ulomov, V. I. Focal Zones of Earthquakes Modeled in Terms of the Lattice Regularization, *Izvestiya, Physics of the Solid Earth*, 1998, 9. 717-733.
14. Yanagidani, I.T., Ehara, S., Nishizawa, O., Kusunose, K. and Terada, M. Localization of Dilatancy in Ohshima Granite under Constant Uniaxial Stress. *J. Geophys. Res.* 1985, 90(138). 6840-6858.
15. Zavyalov, A.D. and Habermann, R.E. Application of the Concentration Parameter of Seismoactive Faults to Southern California. *Pure and Applied Geophys.* 1997, 149. 129-146.
16. Zhurkov, S.N. Kinetic Concept of the Strength of Solids. *Int. Journal of Fracture Mechanics*, 1965,1. 311-323.

MICRO SEISMIC MONITORING OF A BLOCK CAVE: LOGISTICS AND PERFORMANCE MEASUREMENT.

SIMON MORRIS

Golder Associates (NZ), Auckland Office

SAMI TALU

Northparkes Mines, Rio Tinto,

DAVID ALLISON

Golder Associates, Maidenhead office, UK

Micro seismic monitoring is the only established way to continuously and remotely monitor cave back progress in block cave mining. A seismic monitoring system represents a substantial capital investment. To maximise the return on this investment, it is important to have a clear understanding of how the system is going to be implemented and managed. A plan for this management should be in place before commissioning of the system.

The return on investment in a seismic monitoring system can be framed by information on the performance of the cave and assessment of potentially damaging or harmful rock mass response to mining.

This paper addresses the requirements of a system design, and the requirements of the subsequent management of the commissioning process. This includes aspects such as hardware redundancy and the experience of project managers. Following this, attention should be paid to the ongoing management of the seismic system. While advances in automatic processing have been made, a careful gap analysis needs to be performed to determine whether the results of automatic processing is at a sufficiently high confidence level to be used in day to day cave management. This paper discusses the results of a study of automatic processing and points out factors and potential pitfalls to be considered when assessing the locations of seismic events.

Effective continuous seismic monitoring requires considerable commitments in terms of maintenance and human resources. This paper highlights and quantifies these commitments.

1 Introduction

Block caving as a mass mining method has been in existence for over a century. It's main economic benefit is the ability to access deeper sections of low grade ore bodies. Block caving has been used in kimberlite (and more recently lamprolite eg Argyle) and porphyry and skarn type deposits for their favourable geometries and geological environments. Limitations to block caving are based on geotechnical conditions of the rockmass (eg. Cavability). There are limitations are determined in the feasibility studies in terms of economic recovery and operational safety (Chen 2000). A block cave program requires a large upfront investment and effective monitoring of the caving process is essential to maximise both safety and return on investment.

Seismic monitoring is the only established way to continuously and remotely monitor a block cave. The overall cost of a seismic monitoring system can be substantial where the hardware and software, labour and communications infrastructure are all accounted for.

The management of a seismic system is a key element in the design of the seismic system, and should be set in place before the commissioning of the system.

2 Investment

2.1 Hardware and Software

The large upfront cost of the hardware and software alone is considerable. Depending on the density and extent of the seismic system, thousands of meters of cable, several units of instruments and support hardware will be acquired. The easiest way to reduce the cost of an installation is to keep external labour to a minimum, which means that careful planning into the installation needs to take place. Accounting for lead times decreases the amount of stand-down time for contractors and consultants.

The investment also extends to the software that runs the seismic system. There are different methods of Run Time Engine, which can be placed on Linux or Windows platforms. Both systems can have technical implications further down the track, and should be identified by local IT and support staff.

2.2 Communications and Cabling

Thousands of meters of copper and Fibre Optic cables will be purchased that will carry power to sensors and data along the lines. These cables act as the lifeblood and nervous system of a Seismic Monitoring System. Arrangements to avoid areas of potential extra damage (beyond simple aging of the cables) should be sought to improve overall performance of the seismic system.

2.3 Holes and Installation of Sensors.

There is consideration to the time costs in the planning of a seismic system. The location of sensors in their optimum arrangement may result in holes having to be drilled around site. Cost savings at the expense of the use of existing holes can result in a drop in sensitivity of the seismic system. Also, checks and test of equipment done on site will reduce the potential risk of loss of a hole when sensors have been finally installed.

3 Requirements of a Seismic System Design

A seismic monitoring system is designed to detect seismicity. Seismicity is a result of changes in stress in a rock mass. It can indicate the cave back progress and response to drawing of the muck pile. Management of this asset is important to maximise return on investment of infrastructure.

The seismic monitoring system design can be broken into two basic parts or concepts. The first and most identifiable is the physical system, including the sensor arrangement design, hardware and software. The second is the management system, including the installation commissioning and monitoring of the system. Experience has shown that of no matter how good the hardware is, optimum performance and availability requires active system management and preventative maintenance.

4 Considerations to Seismic System Design

4.1 Physical Components of a Seismic System.

The basic outline of a seismic system is simply sensors attached to a seismometer, which in turn transmits seismic data to a central point for analysis.

Hardware includes seismometers, cables, communications infrastructure (copper/fibre-optic hard lines and radio); power provisions are critical. These considerations are important in the way the system will function, and continual operability of the seismic system.

4.2 Sensor Location.

Sensor locations are fundamental of the seismic system design, as there are optimum geometries and layouts to consider (Courier, et al. 2009). These play a large role in the overall sensitivity of the system to seismicity and

location accuracy. The desired outputs of the system and area of interest must be clearly established a before geometric design is performed.

4.3 Communications Infrastructure.

In all instances, timing is a critical signal for communications. It is an essential element to micro seismic location models and parameters.

Radio has been established in the past as a method of communications, but until recently has been limited due to exceptional high cost. Surface seismometers linked by radio had to have a individual pair, with one radio at the central database point namely the appointed office building, and another out at the seismometer. The use of TCP/IP protocols has lead to cheaper and more accessible radio instrumentation to be used, at a price for data security measurements. However, TCP/IP protocols don't carry timing, so timing on surface can be achieved through adaptation of GPS signals.

Underground communications currently still requires hard line support. This is achieved through either copper cables or Fibre Optic communication protocols. This can has exposure to aging effects (ie. Damage and corrosion). Experience shows that a system can operate for around 5-6 years before aging of the hardware becomes an issue with reliability of communications. The ability to swap out the communications components easily should be noted in the design.

4.4 Power

Power supply is an important aspect to the design. Power availability dictates availability for underground locations of seismometers. Surface mounted seismometers can have power provided by solar or wind generation, but these sources can be limited in extreme environmental conditions. Batteries should also be used for

4.5 Suppliers and Seismometers.

The choice of a hardware and software supplier should be made with respect to the availability (around the clock) for technical support, including the time it takes mobilise someone to site. The availability of the supplier to site can have profound effects on the overall operation of the seismic system. Ensuring required remote access is a primary concern to clients and contractors alike. Restrictive access to the seismic monitoring system can lead to large down times for the system, ultimately decreasing the recoverability of cost for a seismic system.

4.6 Redundancies

Redundancies for the seismic system are designed to prevent catastrophic failure to sections and the seismic system overall. Redundancies in the system will also include obtaining extra sensors, seismometers and RTEs. Having stock of extra critical components to a seismic system is useful due to aging and strengthens preventative maintenance.

Redundancies also come out of reconsideration of areas of the block cave which may have become under review due to a decline in caving and production. If extensions to caves and fracturing programs come into light, extra components being readily available mean that lead times for equipment become less significant.

The redundancies extend to having a duplicate run time engine: One would be used to operate the run time engine; with the other as a duplicate but to also be used for remote access, process data and produce information sets for analysis and backup data. This ensures that due to disk failure, computer malfunction and ageing can be compensated for. These machines should be stored in separate locations on site to prevent a single catastrophic loss in a building.

Uninterrupted Power Sources (UPS), and batteries should also be sought for all equipment requiring power (Seismometers, RTE, GPS, Radio). Power outages are fairly common place in mining environments, both on surface and underground. The use of these products can reduce the amount of time a seismic system may be down due to power failure. The UPS units can also come with configurations to prevent power surges.

Maintenance and support personnel are also important. During installation, to have onsite staff gaining familiarity with operating and maintaining the seismic monitoring system will have large benefits down the track of the project. The dependency and significance of incident for suppliers by an operation can also be reduced with suitably trained onsite staff.

5 Logistics of a Seismic System:

Effective cave propagation management is the reason for a seismic system installation. The effective management of the installation is the first step to management of the seismic system. Encouraging client participation should be regarded as good practice, as it results in efficient maintenance of the system in the long term. It also means that issues, in particular, around mine activities in terms of inductions, site access, etc, are overcome because of client involvement.

5.1 Management Method of the Seismic System

The management system is also part of the seismic system design. It requires careful thought into the logistics, the ongoing maintenance, data processing, production and distribution of outputs. Good management systems will involve contractor-client relationship handling, technical assistance and serviceability.

A program of installation should be presented as this will quickly identify potential hang-ups on staff movements and requirements, remote access, site access and product delivery. Remote access is one of the first steps to be established and can involve a lot of paper work from several different departments, not mention the configuration and testing. Significant lead times can be accounted for, and manipulated to ensure and synchronous arrival of stock to site.

Testing of equipment onsite is another aspect to management. Equipment must be ensured in working order before final installation. Oversight of this can be costly in terms of downtime for the system, and use of resources. For example, not inspecting and ensuring the integrity of a sensor cable risks the sensor becoming useless when grout has been inserted

5.2 Installation Management

Installation of the system is best achieved with a solid management system set in place before the installation starts. A well discussed management system before the installation will ensure that there is a minimum of pitfalls with supplier (parts and run time engine) to owner relationships and speed at which equipment can be emplaced on site.

The management of the seismic system as the second part of the seismic system design, includes the assembly time and commitments by supplier staff and client staff. Mine environments are more effectively overcome when access and delivery is assisted by the client or representative. The speed is greatly increased with support and drive comes from both the suppliers and the client. This is important to realise that the seismic systems are the property of the client. Therefore direct maintenance and support should be encouraged to be upheld by the client.

It's not always the case, as often with staff movements between suppliers and clients, intellectual property as a concept of the equipment and relationship often go with the staff. The management system should address procedures either lacking or existing within either party.

6 Intellectual Experience of Managers: Client and Consultant

Various reasons affect the seismicity of a block cave. Production changes can account for seismicity a major proportion of the time. Large drawing of ore, leading to cave propagation will no doubt have an effect on seismicity. But so can system performance. An increase in the system sensitivity can increase the amount of seismicity seen in analysis, as a faulty sensor or seismometer can reduce the amount of seismicity seen in analysis. Recording the system performances is just as valuable to the understanding seismic response, as production.

And in this respect, the management of software is also critical. Changes in processing software can have consequences of a different local magnitude calculation, which will affect historical comparisons. For example, a catalogue of 700,000 events over the life of a block cave requires a lot of time intervention for reprocessing, even by batch mode.

Part of active seismic monitoring requires the continual production of data and deliverables of analysis. Adequate coverage through up-to-date seismic data processing is a significant contribution for seismic hazard management. Assurances through auto-processing techniques can not always accurately convey seismic data. There is a lot of reliance on data handling from the monitoring software, whether it be that the data is handled at the seismometer or the central run time engine itself, not until manual interaction with the system can results be accurately displayed.

Typically, seismic events occur in the rock mass monitored, and the seismic energy transmitted as seismic waves manipulate the sensor. The movement within the sensor is recorded by the seismometer, and is recorded into an Events Database. Analysis of a database shows that within this dataset, cultural and electrical noise, blasts, and single seismic events are presented. The quality of the waveforms is an important aspect in determining into exactly what category the data pertains to.

Human pattern recognition is (currently) better equipped in determining whether seismic data is noise, blasts or seismic events. Automatic processing can mix up actual seismic events for noise, and noise for actual seismic events.

7 Case Study of Automatic Processing Compared to Manual Processing.

7.1 Introduction

A small case study is presented here, from Northparkes Mines, where daily manual processing was conducted at the time of data collection, due to high activity. Several sets of seismic data were extracted before manual processing had occurred on the events. As a result the data sets were over a few hours at a time, in between periods of manual processing. The total number of automatically processed events was 611 seismic events. A comparison of manual and automatically accepted events was conducted by Trifu et al. (2007) using data from Ridgeway Mine gathered by an ESG system, during undercutting sequence in 2002. Trifu et al (2007) however did not directly compare the two approaches.

In the context of this analysis, at the time of collection of this data set, Northparkes was a block cave, and had a more modern ISS system than compared to 2002. This example is not a comparison between the two system datasets.

7.2 Method

The comparison of accepted events between data sets; let A be events from automatic processing and B be the events accepted from manual processing. A summary is presented in Table 1. Statistical analyses of actual differences were carried out between the automatic and manual locations and respective magnitudes. Active

cave management employs location accuracy less than 15 m due to issues such as cave back location and tracking.

Accepted events under manual processing had specific guidelines involving maximum location errors and criteria for event parameters given magnitudes. Events were distributed in magnitude bins.

Distributions of location errors for these events were constructed for given accepted events.

Table 1: Summary of comparison of automatically and manually accepted events

Condition of events	Number of events
Accepted by automatic processing.	266
Accepted by manual processing.	197
Overlap in accepted events.	174

7.3 Results.

The differences in manual locations and magnitudes can be seen in Figure 1, summarised in .There is some bias seen in location towards a north-easterly direction, there is probably bias also in magnitude bins. There also appears to be slight overestimation of magnitude in the automatically processed events in comparison. Normal distribution of the differences was not tested.

Table 2: Differences in location and local magnitude estimates: Automatic processing less manual processing

Quantity	Mean Difference (m)	Standard Deviation (m)
Easting	9.4	43.7
Northing	46.3	125.4
RL	1.4	139.8
Local Magnitude	0.1	0.2

The distribution of location errors were constructed for the events accepted by both processing methodologies (automatic and manual), and for events that were accepted by each methodologies (automatic and manual). Uncertainties came to be as large as 100m for automatically accepted events.

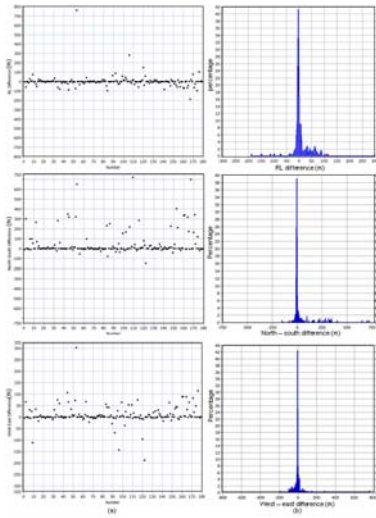


Figure 1: Comparison between automatically processed and manually processed seismic event locations (a) and distributions of differences in 5m bins (b) - ISS system, Northparkes Mines.

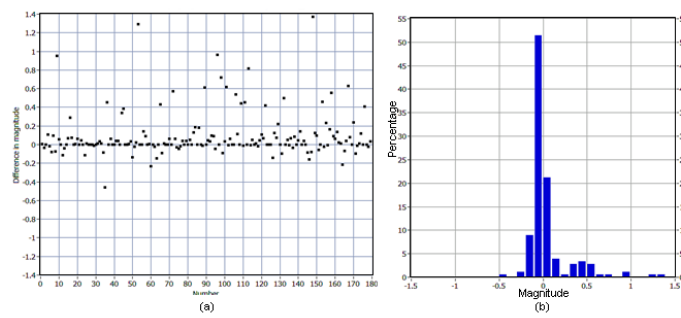


Figure 2: Comparison between automatically processed and manually processed seismic local magnitudes (a) and distributions of differences in calculated magnitude in magnitude 0.1 bins (b) - ISS system, Northparkes Mines.

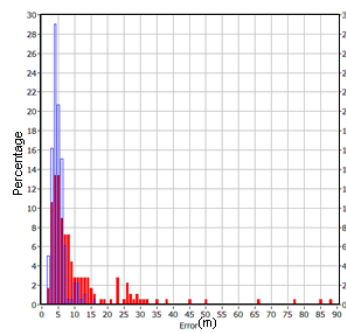


Figure 3: Event location for automatically processed (solid red) and manually processed seismic events (blue) for events accepted by both methodologies.

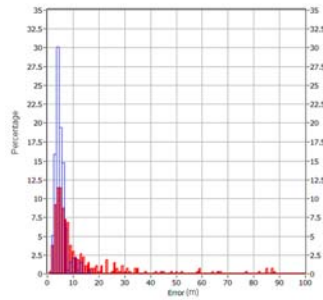


Figure 4: Event location error for all automatically processed (red) and all manually processed seismic events (blue).

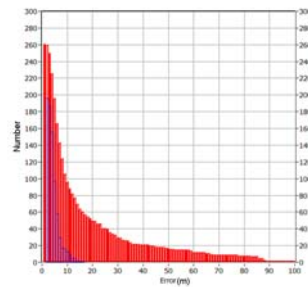


Figure 5: Cumulative event location error for all automatically processed (red) and all manually processed seismic events (blue).

8 Conclusions

Micro seismic monitoring is the only established way to continuously and remotely monitor cave back progress in block cave mining. Effective continuous seismic monitoring requires considerable commitments in terms of maintenance and human resources.

To maximise the return on the investment of a seismic monitoring system, it is important to have a clear understanding of the system that has been implemented and how it is managed. A plan for this management should be in place before commissioning of the system.

The requirements of a system design and the requirements of the subsequent management of the commissioning process include aspects such as hardware redundancy and the experience of project managers. Following this, attention should be paid to the ongoing management of the seismic system. While advances in automatic processing have been made, a careful gap analysis needs to be performed to determine whether the results of automatic processing is at a sufficiently high confidence level to be used in day to day cave management.

References

1. Chen, D. Meeting Geotechnical Challenges – A Key to Success for Block Caving Mines. In proceedings of MasssMin 2000 (Brisbane, 2000).
2. Currier, N., Talu, S., van As, A. and Allison, D. Uses and Pitfalls of Microseismic Monitoring at Northparkes Mines, yet to be published, 2009.
3. Trifu, C.I., Shumila, V. and Burgio, N. Characterisation of the Caving Front at Ridgeway Mine, New South Wales, Based on Geomechanical Data and Detailed Microseismic Analysis. In Eds. Polvin, Y. and Hadjigeorgiou, J. and Stacey, T.R. Challenges in Deep and High Stress Mining, 2007.

SEISMIC MONITORING OF LARGE-SCALE KARST PROCESSES IN A POTASH MINE

DMITRIY A. MALOVICHKO, RUSLAN A. DYAGILEV, DENIS Y. SHULAKOV, PAVEL G. BUTYRIN

Mining Institute, Ural branch of the Russian academy of sciences

Perm 614007, Russia

SERGEY V. GLEBOV

JSC Uralkali

Berezniki, Perm region, 618426, Russia

In October 2006 a serious accident happened in Berezniki-1 mine of the world's second largest Verkhnekamskoye potash deposit. The integrity of the waterproof stratum which separates mine workings from aquifers was broken and an uncontrolled flooding of the mine had begun. The accident resulted in the appearance of several potential problems associated with karst processes in the rock mass above the mine, i.e. hazardous subsidence of the earth's surface and formation of a sinkhole. The exact position of the water inflow zone was unknown due the inaccessibility of the excavations within the problematic part of the mine. This aggravated the situation seriously. The applied complex of geophysical and geotechnical methods made it possible to localize the inflow zone, to estimate the size of the expected sinkhole and to monitor its development in time. Seismic monitoring played an essential role in these investigations. This paper summarizes the details of the seismological observations in Berezniki-1 mine and the main results thereof.

1 Introduction

1.1 Features of Mining in the Verkhnekamskoye Potash Deposit

The Verkhnekamskoye potash deposit is situated in the northern part of Perm region (Russia) and comprises of seven minefields six of which were in development in 2006. Productive layers in sylvinite and carnallite zones (figure 1) are 140-420 m below the earth's surface. The room-and-pillar mining method is used in all mines.

The main requirement for safe mining in the Verkhnekamskoye deposit is the keeping of integrity of the waterproof stratum. This stratum consists of salt-clay rocks which are laid above the productive layers (figure 1) and prevent them against solving by weakly mineralized water or brines from the upper horizons. Penetration of the brines through the waterproof stratum may cause unavoidable mine flooding and forming of a karst depression or sinkhole on the surface.

Such situation had already taken place in the Verkhnekamskoye deposit previously - in Berezniki-3 mine in 1986 (figure 2).

1.2 An Emergency Situation in Berezniki-1 Mine in 2006

On 18 October 2006 a loss of integrity of the waterproof stratum and penetration of brines from upper layers to the mining excavations were identified according to indirect indicators (dynamics and chemical composition of brines in mine) in the western part of Berezniki-1 mine (figure 3). This area was mined out in the sixties-

seventies and most of the excavations there were partially backfilled or collapsed which restricted the access to the area. For this reason the place of brines inflow was unknown within the area of 800x1000 m size (see ‘Initial position of brine inflow zone’ in figure 3). The problem of localizing the inflow zone was solved promptly by applying a complex of surface geophysical and geotechnical methods (including seismological observations). As the result, a 400x500 m so-called risk zone was contoured (figure 3).

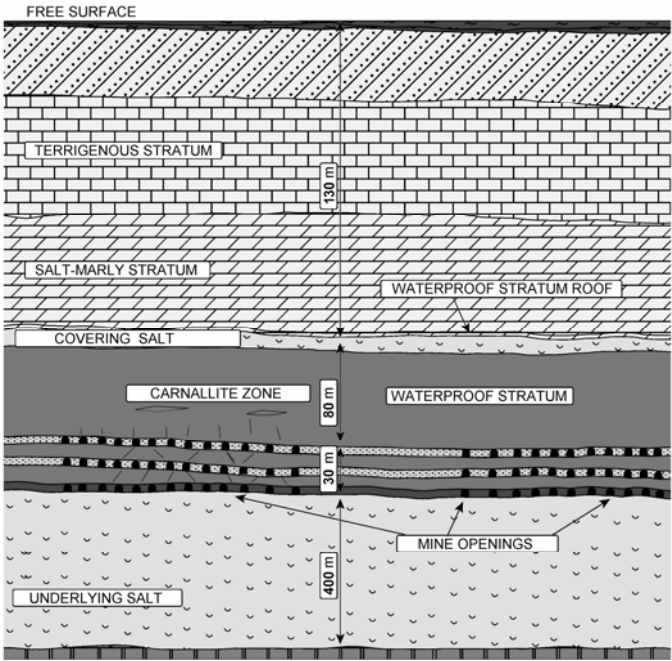


Figure 1 Schematic geological section of the Verkhnekamskoye deposit

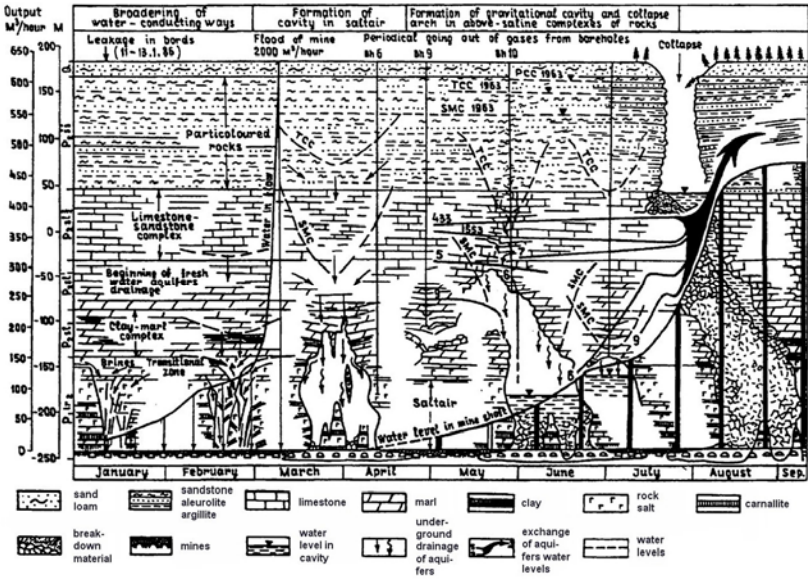


Figure 2 Evolution of karts processes in Berezniki-3 mine in 1986 [1]

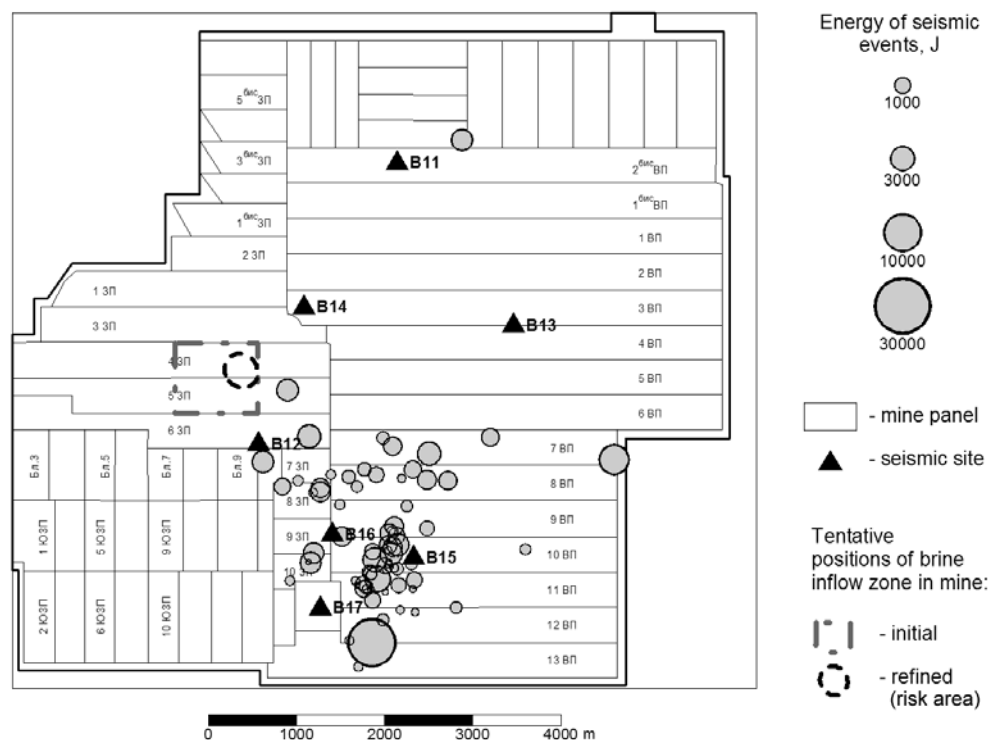


Figure 3 Plan view of Berezniki-1 mine with position of the risk area. Regional seismic network and seismic activity observed in 2006 are shown also

A federal railway which is the only mean of freight transportation for several large industrial enterprises in the towns of Berezniki and Solikamsk happen to pass through the risk zone. An alternative (reserve) railroad was quickly built just outside the boundary of the risk zone in the beginning of 2007. Nevertheless, the task of controlling any possible karst processes within the risk zone remains high on the agenda. As the result a set of geotechnical techniques (active surface seismic surveys, borehole and surface hydrodynamical and hydrochemical observations, land-surveying) was applied in the monitoring mode within the risk area and its surroundings.

From October 2006 to July 2007 the karst processes had no visible manifestations. However, the several techniques pointed to significant variations of the controlled characteristics and properties (i.e. gradual decrease of seismic wave velocity for different horizons within the risk area, anomalous subsidence (with rates up to 270 mm/month) in the eastern part of the risk zone, formation of local areas with high concentration of methane in soils).

At 3 PM of 28 July 2007 a sinkhole had appeared on the earth's surface 150 m to south-west from the center of the risk zone. The initial size of the sinkhole was 55 x 80 m (figure 4a). A huge gas and rock blowout had happened next morning (figure 4b).

During the following several months the sinkhole had actively grown mostly in the northern and north-eastern directions toward the federal railway (figure 5). The growth decelerated significantly during the winter months, but nevertheless the eastern slope of the sinkhole reached the old federal railway in December. During February and April 2008, a short-time increase in the rate of the sinkhole expansion was noted in the eastern and southeastern directions.

At the end of 2008 the flooding of Berezniki-1 mine was completed and the growth of the sinkhole virtually stopped. Its size had stabilized at approximately 440x320 m.

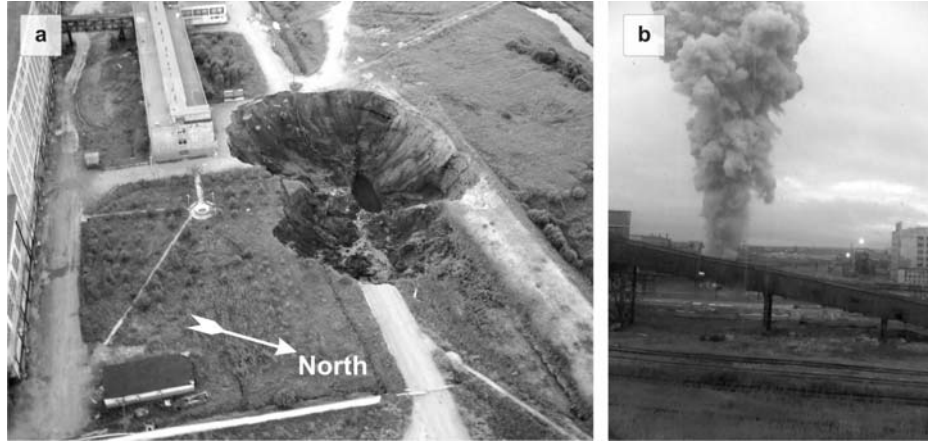


Figure 4 A sinkhole appearance at 28 July 2007 (a) and gas blowout at 29 July 2007 (b)

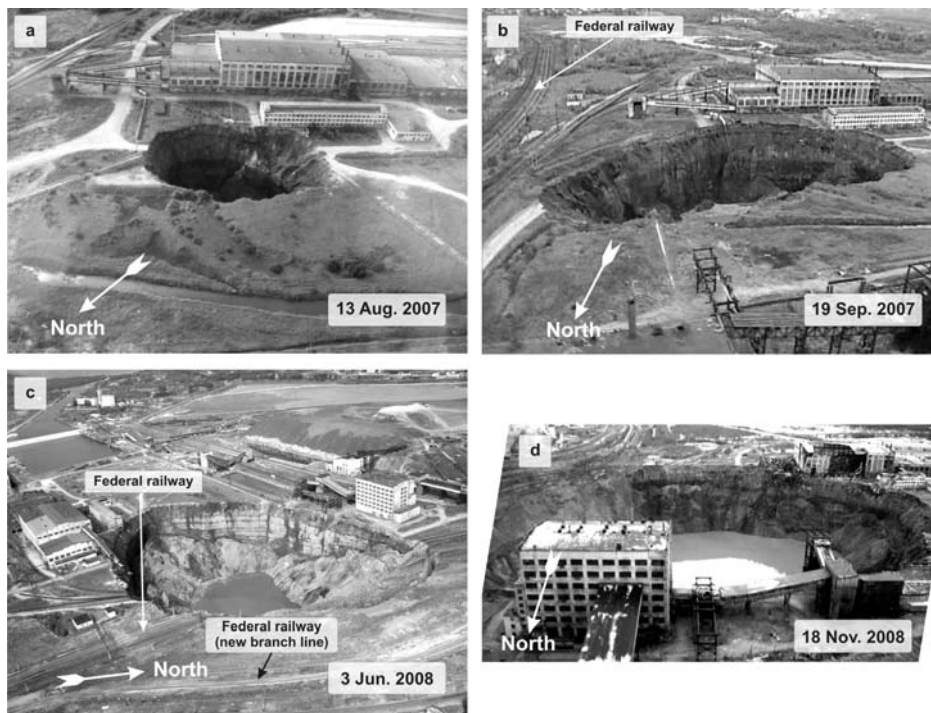


Figure 5 Evolution of the sinkhole

2. Seismic Monitoring Systems in Berezniki-1 Mine

2.1 Regional Seismic Network

A regional seismic network was in operation in Berezniki-1 mine since 1998. The network consisted of 6 underground and 1 surface vertical geophones installed 1-2 km apart from each other (figure 3). The network

allowed to reliably detect all events with seismic energy above 1000 J within the whole area of the mine (about 50 km²) (table 1).

Table 1. Characteristics of the regional and the local seismic networks used in Berezniki-1 mine

Characteristics	Regional network	Local network
Controlled area, km ²	50	0.5
Average distance between sensors, m	1000-2000	150
Minimal seismic energy of events, J	1000	10
Frequency range, Hz	0.5-100	10-1000

The system registered several dozens of events per year. The largest ones had seismic energy below 10⁵ J. The analysis of the source mechanisms showed that most of the events could be associated with rock falls from roof of the excavations. More detailed information and main results of the routine seismic monitoring in the mines of the Verkhnekamskoye potash deposit could be found in [2].

The regional seismic network of Berezniki-1 mine has been functional until 28 October 2006, when the mine-wide power supply system was switched off and the access to the mine was restricted.

It was the termination of the regional monitoring and the need of more detailed seismic information which initiated the organization of local seismic monitoring in the risk zone.

2.2 Temporary and Permanent Local Networks

The first variant of local seismic system was based on temporary arrays: 1 central triaxial sensor and 3 uniaxial ones installed in a circle of 100-200 m radius. This system may monitor an area several hundred meters in diameter. Arrays of this kind are also known as SNS (Seismic Navigation System) [5]. They provide much better sensitivity than the regional networks (table 1). Initially such temporal SNS-s were installed underground for limited periods of time (several days) in several areas of the mine.

After restricting access to the mine and closing down of the regional network the only possible way to obtain information about seismic activity was by commissioning the SNS on the earth's surface. Monitoring with it was organized in short time. The first SNS (on the western boundary of the risk zone) started operation on 29 October, the second one (inside the risk zone) – on 2 November 2006.

In spite of their advantages, the use of the temporal SNS-s was not optimal. On the one hand, surface sites were under influence of intensive seismic and electrical noise due to heavy traffic and numerous mechanisms operating near the risk zone. On the other hand, the installed system didn't allow acquiring and processing the data in real time or close to it. To overcome these obstacles a permanent local seismic network based on ISSI hardware and software was promptly installed. The network included 8 vertical geophones deployed in boreholes at the depths of 10 and 50 m and 6 geophones installed on the surface (4 vertical and 2 triaxial) (figure 6). The signals from the sensors were processed by data acquisition units. The information from these units was transmitted in a real time to a central site situated 1.5 km away from the risk zone. Continuous quality control over the performance of the new system was maintained remotely from the central site and the delay in data transmission never exceeded 1.5 min. The network was commissioned in January 2007.

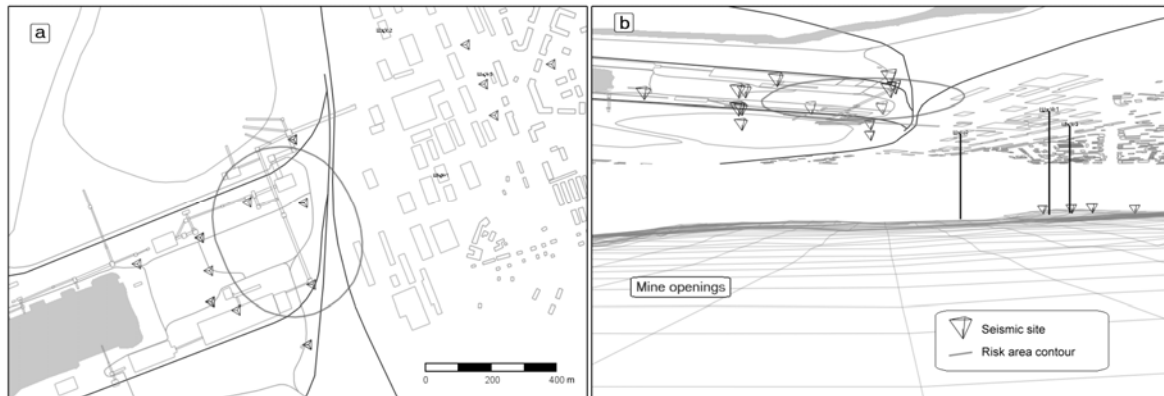


Figure 6 Permanent local seismic network near the risk zone (a – plan view, b – cross-section view).

In August 2007 four more sensors (3 vertical and 1 triaxial) were installed underground at the depth of 300 m in 800 m to northeast from the risk zone (figure 6).

3. Results of the Seismic Monitoring

3.1 Results from the Regional Monitoring

The level of seismic activity in Berezniki-1 mine was low both in 2006 and in the previous years. In 2006 most of the seismic events were concentrated in the southern part of the mine (figure 3). There was not a single event registered within 500 m from the risk zone in the course of regional monitoring. Therefore, we may assume that the failure of the waterproof stratum progressed gradually without the radiation of intensive seismic waves. It is possible to assume that only small events (below the sensitivity threshold of the regional network, that is of seismic energy less than 1000 J) could occur.

3.2 Seismic Data Obtained by the Local Systems and Their Processing

Several factors hampered the local seismic monitoring in the risk zone:

- 1) Intensive background seismic noise. Various mechanisms and equipment operating in the vicinity of the risk zone induced stationary seismic wavefield which screened the weak impulsive seismic signals from the karst accompanied processes. Furthermore artificial surface impacts (due to demounting of buildings, etc.) generated impulsive seismic signals which were quite similar to and thus difficult to distinguish from the signals initiated inside the rock mass under monitoring.
- 2) Non-optimal layout of the sites. The network covered the risk area in horizontal plane rather well. But due to safety reasons (to exclude interlayer flows of brines and groundwater) the maximum allowed depth of the sensor's boreholes was limited by 50 m. As the result, the extent of the system in vertical direction was much smaller than in horizontal plane. Only installation of four additional sensors in mining excavations in August 2007 improved the vertical resolution of the system (figure 6)
- 3) Significant heterogeneity of the rock mass. Results of the active seismic surveys show considerable gradient of P waves velocities in vertical direction – from 1500 m/s near the earth surface up to 4200 m/s in the salt rocks at the depth 300 m. This strongly distorts seismic waves as they propagate through the rock mass and complicates registered signals. Besides, the sinkhole appeared in the later stages of

the monitoring and manifested itself as an essential 3D heterogeneity which produced additional difficulties for the processing of the seismic data.

From October 2006 till May 2008 the monitoring systems had registered more than 10 000 seismic events which could be associated with karst processes in the risk zone. It was efficient to divide those seismic events in two groups:

- 1) Events of the 1st type distinguished by clear arrivals of P waves and relatively high frequency content (30-60 Hz) (figure 7a). The arrivals of S wave are hardly identifiable event for tri-axial sensors. We associate this kind of events with fracturing at the level of mining openings or in the consolidated part of the overlying rock mass.
- 2) Events of the 2nd type characterized by low frequency (5-20 Hz) long-duration (several seconds) signals without clear arrivals (figure 7b). We associate this sort of events with fracturing in the soft part of the rock mass (slopes of the sinkhole, near-surface layers) or rockfalls from roof and walls of karst cave(s). A not karst- or mining-related origin of these events is not excluded in some cases, i.e. they may be caused by failures in foundations of surface buildings due to their extensive deformation.

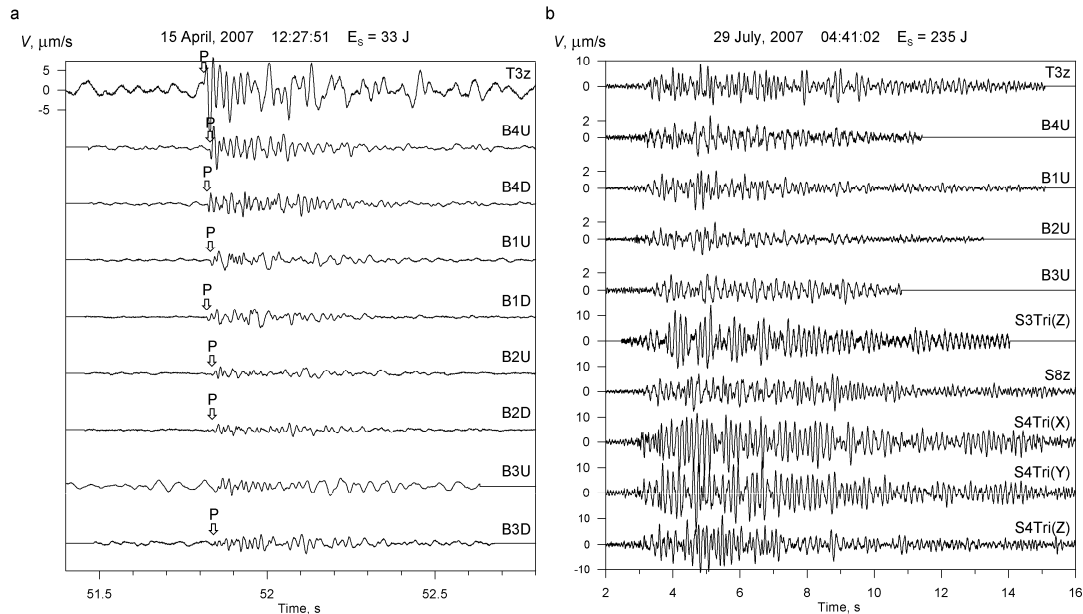


Figure 7 Examples of registered in the risk zone seismic events of the 1st (a) and 2nd (b) type

The described classification of the events is not strict – sometimes events possessing the features of both types were observed.

The major problem during the first months of monitoring in the risk zone was obtaining reliable locations of the events' sources. Neither the algorithms used in routine regional monitoring in mines of the Verkhnekamskoye deposit nor the ISS standard location techniques provided acceptable estimates of coordinates of the sources (especially for events of the 2nd type). Special location algorithms were implemented to overcome these difficulties.

To locate events with clear P-wave arrivals a Nelder-Mead simplex algorithm initially developed and applied in seismic monitoring in potash mines of Canada [3] was adapted for our specific needs. The original

Nelder-Mead simplex algorithm is applicable to arbitrary medium models, but for the risk area a model in the form of horizontal layered half-space was chosen. Our modification of the basic variant of the algorithm consists in adding the capability to take into account variations for both wave arrivals and velocities of layers in the model. It is supposed, that all variations are normally distributed. As the result of Monte Carlo simulations, possible deviations of the velocities and the arrivals were transformed into deviations of source position and origin time.

Figure 8 shows results of location for the 1st type event whose waveforms were displayed in figure 7a. It could be seen that the variations of the arrivals and velocities of the model have resulted in ellipsoidal cloud of possible source positions. As the spatial distribution of sites used in the location is close to horizontal, the vertical location error is 3 times worse than horizontal one.

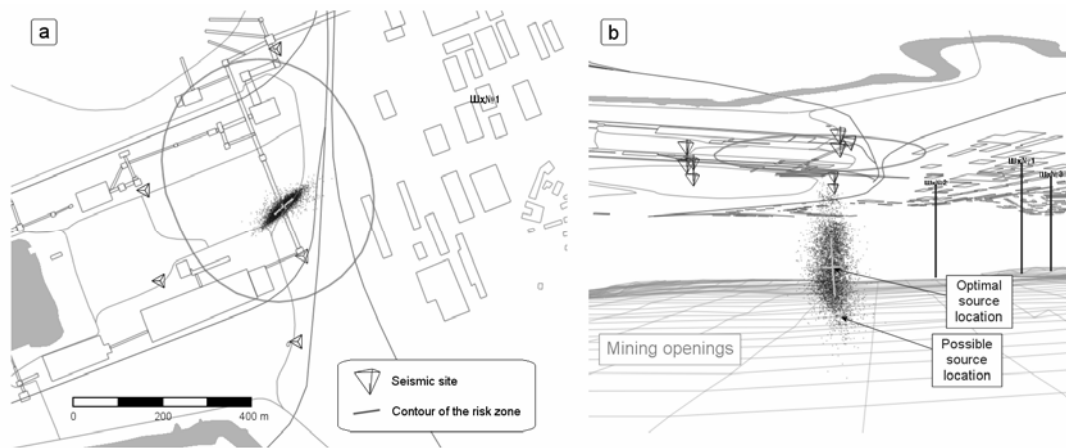


Figure 8 Result of location of the 1st type event: plan view (a), cross-sectional view (b)

For events of the 2nd type a so-called *Correlation* location algorithm was developed. Analysis of the waveforms of this type of events has revealed that the low frequency waves (3-8 Hz) are correlated between different sites. The relatively long wavelength of such waves (300-600 m) results in a weak dependence of their kinematic and dynamic properties from lateral heterogeneities of the rockmass. These features make it possible to test any point of space as a potential source position of the event by the following steps:

- 1) Introduction of phase shifts into waveforms of every site according to their position relative to the tested point
- 2) Calculation of a cross-semblance coefficient R of all phase shifted waveforms in low frequency range (3-8 Hz).

The probable position(s) of the source could be found from the maximum of R over a spatial grid. Example of application of the *Correlation* algorithm for the event shown in figure 7b is presented in figure 9. The global maximum of R at 100 m east from site S8z indicates the epicenter of the event.

The *Correlation* algorithm provides only horizontal coordinates of the source because the low frequency part of the waveforms is generally formed by surface waves and their phase characteristics don't contain information about depth of the source.

In the course of the monitoring in the risk zone a gradual decrease in the location accuracy of the *Correlation* algorithm was observed. At some stage the growing sinkhole (figure 5b-d) started to essentially

disturb even waves with wavelengths 300-600 m. This worsened the semblance of the low frequency part of the waveforms. In order to overcome this obstacle not only the phases but also the amplitudes of low frequency waves were utilized in the calculation of the cross-semblance coefficient R . Similar location approaches are used in volcano seismology [4].

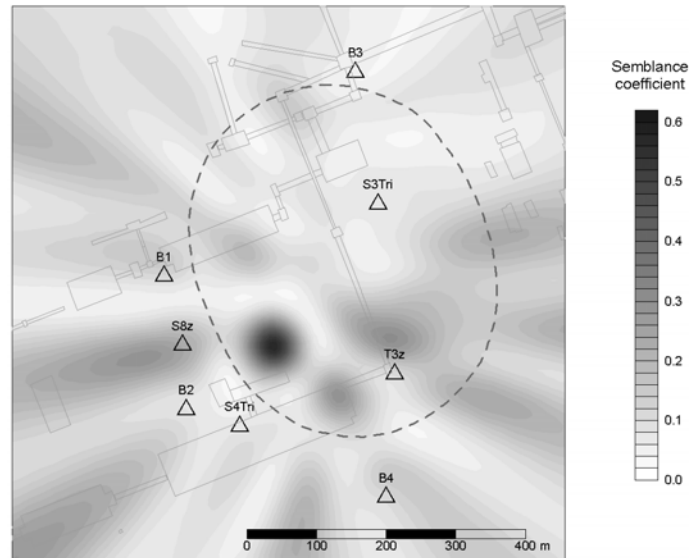


Figure 9 Location of events shown at figure 7b with correlative algorithm

3.3 Results of Observations with Local Temporary Seismic Systems

On October 2006 only 3 of the registered seismic events were reliably located. Their epicenters with location error bars estimated using the *Nelder-Mead simplex* algorithm are shown in figure 10. The depth of the sources was in the 150-300 m range. Therefore, they were associated with fracturing in a consolidated rock mass above of the mining excavations.

These results were obtained within a 10 days period after discovering the loss of integrity of the waterproof stratum in the mine. The positions of the sources were in general agreement with the anomalous rock mass properties (velocities of P waves) and rock mass behavior (intensive subsidence) as revealed by other techniques. This made it possible to localize the area of the waterproof stratum desintegration and to identify the zone of expected karst processes (the risk zone).

3.4 Results from the Observations with the Local Permanent Network

Until the appearance of the sinkhole, the level of seismic activity in the risk zone was low: on average just several events mainly of the 2nd type occurred daily. For most of them it was difficult to identify arrivals of seismic waves and to apply *Nelder-Mead simplex* algorithm. The *Correlation* algorithm generally didn't produce stable results too. At the end only 14 events were reliably located (figure 11). The location error for the rest of the events was too large (more than 100 m in a horizontal direction).

Most of located events were of the 1st type. Their sources were generally within the risk zone, close to its western part. The depth of the sources was more than 140 m.

Three events had been ascribed to the 2nd type and one to the mixed type. Two events had occurred out of the risk zone and one of them, which had happened 13 June 2007 at 18:16:23 had its source on the earth's surface. So the later event was associated with foundation destruction of a building.

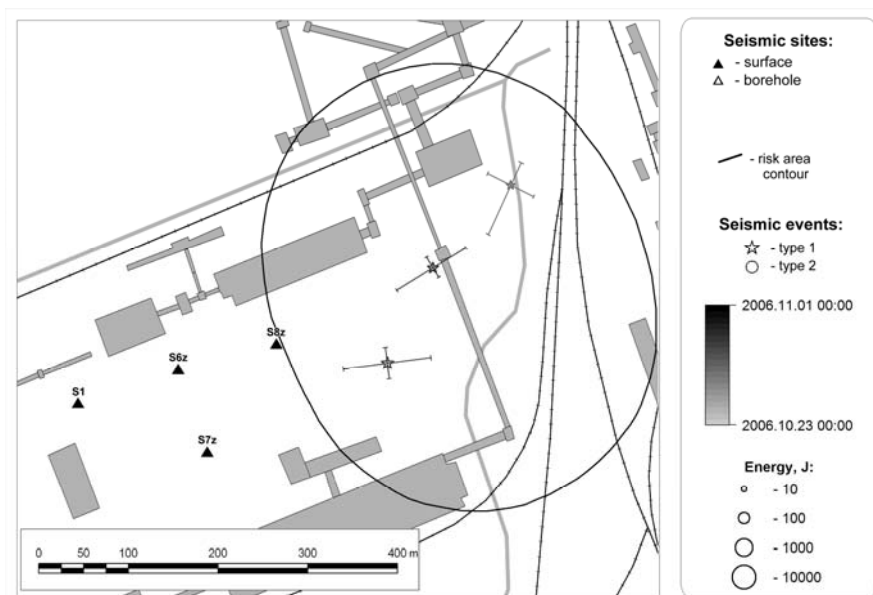


Figure 10 Result of location of seismic events occurred during 10 days of monitoring in October 2006

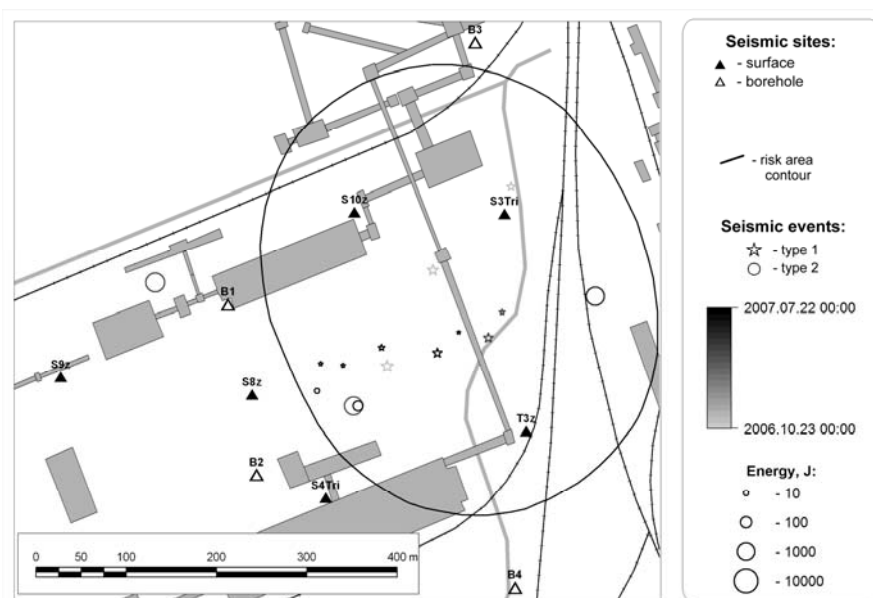


Figure 11 Result of location of seismic events in the risk zone occurred before 22 July 2007

Anomalous seismic activities have been detected during the two weeks before the formation of the sinkhole. The anomalies took the form of swarms of events of the 2nd type with huge rate (100 and more events per hour) and overall duration up to several hours (figure 12). Initially it was assumed that all these events are associated with fracturing in near-surface layers (having depth less then 100 m) or with structural damage of foundations of buildings situated in the risk zone. The post processing of the events using *Correlation* algorithm made it possible to determine their locations more precisely. All of them had occurred in the south-western part of the risk zone (figure 13) where the sinkhole was formed initially.

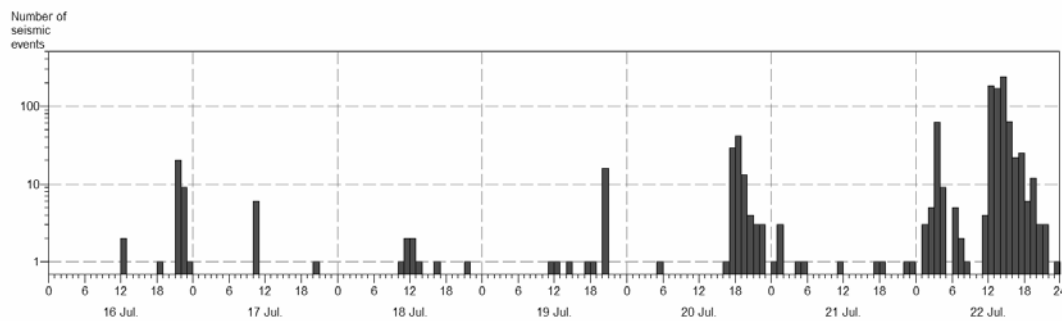


Figure 12 Time history of seismic activity in the risk zone from 16 to 22 July 2007

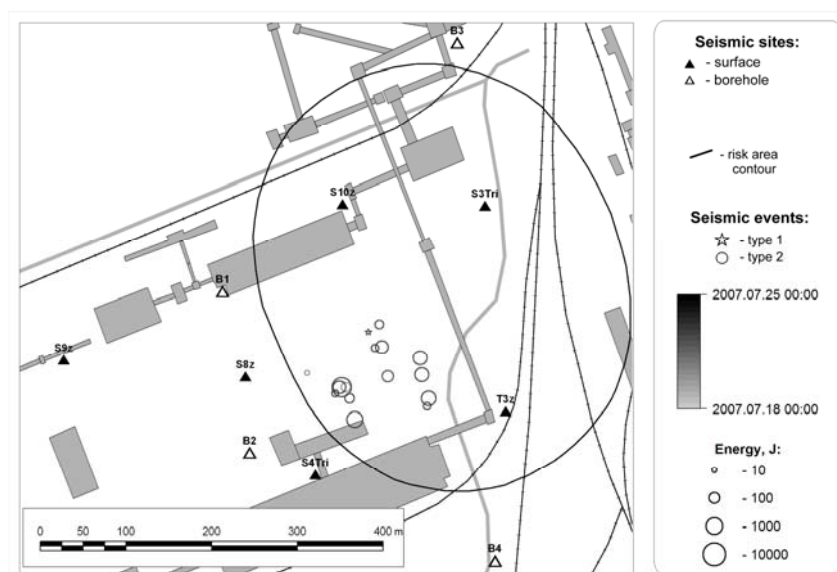


Figure 13 Seismic activity in the risk zone from 16 to 22 July 2007

During the 5 days before the appearance of the sinkhole the rate of the seismic activity was low (figure 14). At 2 PM of 28 July the seismicity increased sharply (figure 14). Most of events in this swarm were of the 2nd type. At 3:30 PM the sinkhole was visually discovered (figure 4a). Next day (29 July) the seismic activity had risen again and this burst was accompanied by a blowout of gas and rocks from the sinkhole (figure 4b).

Therefore at this stage it had become obvious that bursts of seismicity (especially events of the 2nd type) preceded by a period from several minutes to hours the onset of the sinkhole development. This fact has forced

us to switch over to around-the-clock monitoring to ensure an immediate response to any bursts of seismic activity in the risk area. Triggering of 10 events on eight sensors within 10 minutes was set up as an alarm criterion. When this criterion was met the emergency services of the mine and railway station (which manage train operations in the vicinity of the risk area) were notified.

The alarm criterion was met 10 times in August and September 2007 and every time the duration of the alarm condition was less than 8 hours. Almost every alarm was followed by an acceleration of the sinkhole growth sometimes accompanied by blowout or emission of gas.

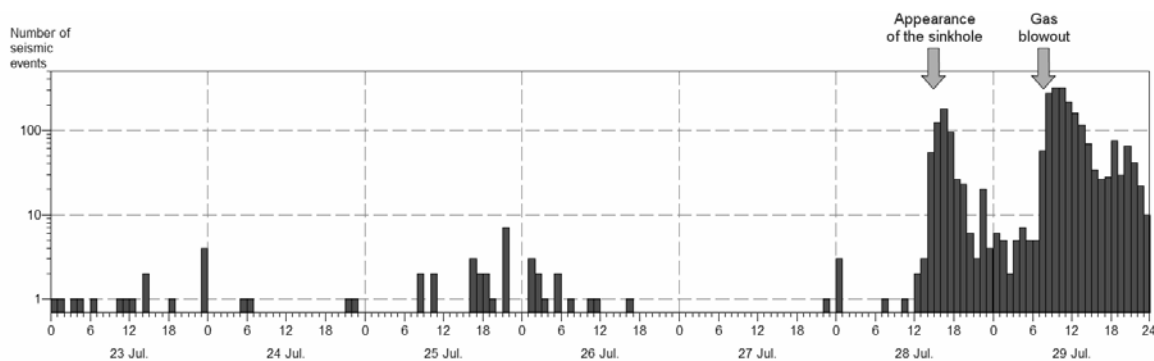


Figure 14 Time history of seismic activity in the risk zone from 23 to 29 July 2007

Both the intensity and the frequency of the seismic activity bursts decreased in September 2007. From October 2007 till the end of 2008 the alarm criterion was never met. In total, the level of seismic activity in the risk zone gradually decreased. In the first half of 2008 the average rate of seismicity was 20-40 events per day (i.e. 10 times lower than in August and September of 2007). In the end of 2008 the rate was several events per day.

The event location results revealed a space-time correlation of seismicity and direction of the sinkhole growth. More than once the sinkhole 'responded' to the grouping of seismic sources in clusters by a directional expansion. For instance, in the beginning of August 2007, the events were clustered near the eastern slope of the sinkhole. And in the following weeks this was followed by an accelerated growth of the sinkhole eastward (figure 15-16). Then the sources migrated eastward and again the sinkhole followed them.

Analysis of several samples of such space-time correlations has revealed that the time delay between the clustering of seismicity and the directional sinkhole growth can be from several days to 2 weeks.

4 Conclusion

The presented results of both regional and local seismic monitoring in Berezniki-1 mine make it possible to draw several general conclusions concerning a matter of seismological investigation of karst processes in potash mines of the Verkhnekamskoye deposit.

First of all, the loss of integrity of the waterproof stratum may develop aseismically.

The regional seismic network was in operation in Berezniki-1 mine approximately 8 years before the emergency situation in October 2006. The network provided sensitivity of 1000 J over the whole mine and it didn't fix any events within the distance of 500 m from the future risk zone. These facts allow us to conclude

that the disintegration in the waterproof stratum went quasi-statically, without dynamic processes of more than 1000 J radiated seismic energy.

Secondly, the seismic activity which accompanies karst cave(s) development processes and the formation and growth of sinkhole(s) could vary in scales greatly.

During the ‘pre-sinkhole’ stage of local monitoring in the risk zone (October 2006 – July 2007) the level of seismicity was extremely low. Only 14 events were recorded with waveforms of sufficiently good quality for the purpose of location. Nevertheless, even such limited piece of information was valuable. The spatial distribution of the sources indicated the area of probable appearance of a sinkhole. Dramatic bursts of seismicity were observed two weeks before appearance of the sinkhole. Several tens or even hundreds events were registered per hour at that time.

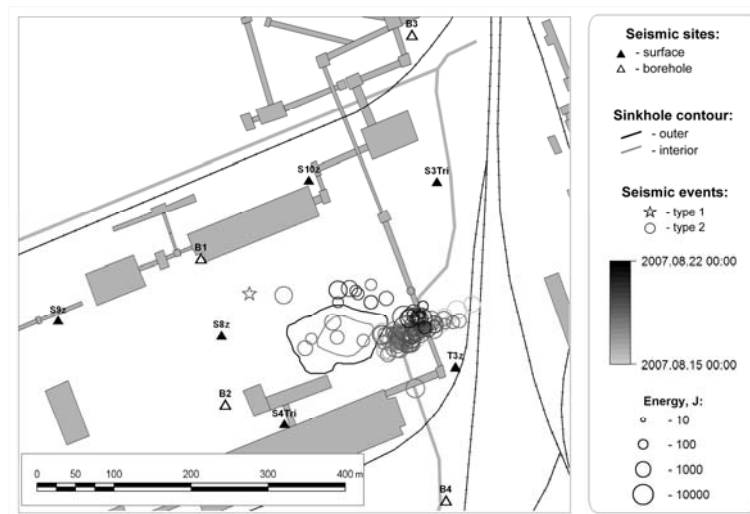


Figure 15 Seismic activity in the risk zone from 15 to 22 August 2007

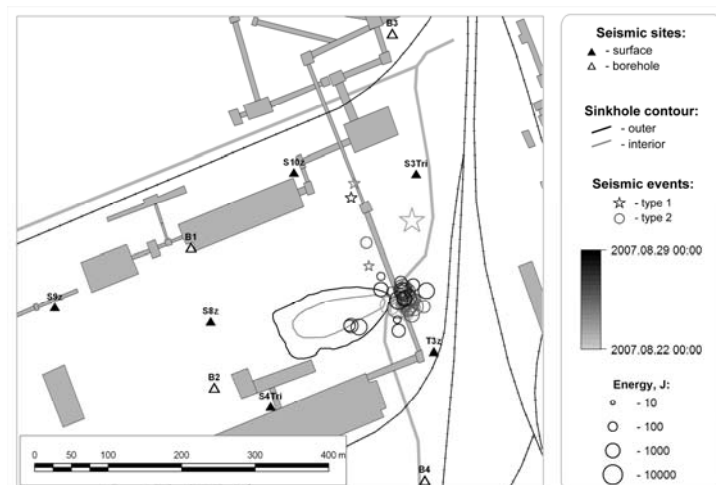


Figure 16 Seismic activity in the risk zone from 22 to 29 August 2007

The seismicity had clearly pronounced intermittent character during the 'sinkhole' stage. Periods of relative quiescence (several events per hour) alternated with intervals of bursts of seismicity (several hundreds of events per hour). The seismic activity correlated both in time and in space with the visible development in and around the sinkhole, viz. collapses of its slopes, blowouts and emissions of gases.

Finally, the complexity of seismic source processes and rock mass properties require improvements in standard techniques of seismic data processing.

Both extension in time of some source processes (collapses of rocks from the floor or wall of karst caves) and heterogeneity of the rock mass (significant gradient of velocities in vertical direction) result in complication of observed seismic signals. Only P wave arrivals could be identified for some seismic events (i.e. events of the 1st type). Other events (so called 2nd type events) don't have distinguishable arrivals at all. The algorithm which utilizes ray tracing in layered half space and takes into account inaccuracy of both arrival of seismic waves and parameters of velocity model may be efficient for location of events of the 1st type. The algorithm of location based on amplitude and phase characteristics of low frequency surface waves could be useful to cope with events of the 2nd type.

The acquired experience of seismic monitoring of karst processes in Berezniki-1 mine is of considerable practical value. According to numerical modeling of solution processes in the mine an intensive dissolving of carnallite pillars is expected in several areas, one of which is within the populated part of Berezniki town. An intensive deformation of the undermined strata was predicted for these areas which may result in hazardous subsidence of the earth's surface. A variety of geotechnical methods was employed in the monitoring of rock mass deformation and for identifying potential karst processes within the new risk zones. During the summer of 2008 a seismic monitoring system based on 12 tri-axial borehole sites was commissioned in one of the most hazardous zones. The practical skills obtained during monitoring of the old risk zone are applied now when processing and interpreting seismic monitoring data of new system.

Acknowledgements

The authors would like to thank co-workers Alexander Zverev, Alexander Peresypkin, Alexander Saharniy, Evgeniy Chepurov, Inga Golubeva, Yury Baranov, Elena Tallerman, Roman Maltsev and Denis Touzhikov for help in carrying out of the seismic monitoring in Berezniki-1 mine. We wish to acknowledge the support of leading specialists of JSC "Uralkali" (Alexander I. Shumacher and Nikolay V. Kuznetsov) in solving technical problems accompanying the monitoring. In particular we wish to thank Dr. Assen Ilchev from ISS International Ltd. for his help in improvement of the text of the paper.

References

1. Andreichuk, V., Eraso, A. and Domínguez, M.C. A Large Sinkhole in the Verchnekamsky Potash Basin in the Urals, *Mine Water and the Environment*, 2000, 19 (1). 2-18.
2. Malovichko, A.A., Sabirov, R.H. and Akhmetov, B.S. Ten Years of Seismic Monitoring in Mines of the Verkhnekamskoye Potash Deposit. in *Proc. of the 6th International Symposium on Rockburst and seismicity in mines*, (Australia 2005).
3. Prugger, A.F. and Gendzwill, D.J. Microearthquake Location: A Nonlinear Approach that Makes Use of a Simplex Stepping Procedure. *Bul. Seismol. Soc. Am.*, 1988, 78. 799-815.
4. Wassermann, J. *Volcano Seismology. The IASPEI New Manual of Seismological Observatory Practice*, V. 1, ed. P. Bormann, 2002.
5. Wust-Bloch, G.H. and Joswig, M. Pre-collapse Identification of Sinkholes in Unconsolidated Media at Dead Sea Area by 'Nanoseismic Monitoring' (Graphical Jackknife Location of Weak Sources by Few, Low-SNR records). *Geophys. J. Int.*, 2006, 167. 1220-1232.

MECHANISM OF THE SELF-SIMILARITY OF THE GUTENBURG – RICHTER RELATION: A KM-SCALE IN-SITU OBSERVATIONAL INVESTIGATION

TIE LI and SHUANG-HU CHEN

*School of Civil and Environment Engineering, University of Science and Technology Beijing
Beijing 100083, P.R. China*

In this paper, the mechanism of the self-similarity of the Gutenberg – Richter relation is studied through a km-scale in-situ experimental investigation. The study is completed by using the complete mine seismic monitoring data from a coal mine over a period of 38 years, in combination with field in-situ stress measurement and mine operation data. It is found that the magnitude – frequency or Gutenberg – Richter relation at the mine site exhibits a “two-peak” curved distribution characteristic, which can be explained by the combination of mining-induced seismicities that are directly and indirectly correlated to mining activities. Overall, the self-similarity of the Gutenberg – Richter relation is satisfied. The linearization trend at the high magnitude end is considered to be proportionally influenced by the in-situ stress. An in-situ stress controlled pace-time sequence of the dynamic response of rocks is introduced to explain the linearization trend at the high magnitude end and the mechanism of the accuracy in predicting large possible seismic events. In addition, it is confirmed that the b value is an indicator of the rock fracturing sequence and the change of its mechanical behavior. Finally, the application of the approach to rockburst risk assessment and evaluation of the rock mass behavior after mining is also discussed.

1 Introduction

Gutenberg and Richter (1941) have found the following log-log relationship between magnitude and frequency by studying seismic activity characteristics ^[1] ((1) is normally known as the G-R law):

$$\lg N = a - bm \quad (1)$$

Where m is the magnitude; $N (\geq m)$ is the frequency has a magnitude that is greater than or equal to m ; $N (=m)$ is frequency that the magnitude is equal to m ; constant a is the level of seismic activity; constant b is the property relation of the numbers of seismic events.

Afterward a great deal similar research work, such as laboratory, earthquake and mining-induced seismicity (and/or rock burst), indicates that “G-R” relation has universality ^[2-4]. While it was found that the magnitude–frequency is a not strict logarithm linear relation but a curve with downward bends at the two ends in most cases. After speculating, the deviation at the low magnitude end may stem from incomplete information; the deviation at the high magnitude end indicates that the missing magnitudes will possibly be replenished in the future. Therefore, any earthquake deviating from this relationship and shortage is likely to be filled in the future. Specifically, there is an obvious significance in predicting the largest seismic event that has not yet occurred When $N = 1$, $m = a / b$ in (1) ^[5-8]. However, the space-time scale of predicting possible seismic events in the future still is most relied upon through judgment on experience for the greater part, and its mechanism is unclear.

Our job is to study the reason for the nonlinear relationship in G-R, the space-time scale of prediction and mechanism of the accuracy in predicting large possible seismic events; as well as their application in Mine Safety through a km-scale rocks fracturing in-situ experimental investigation, based on the complete mine seismic monitoring data from a coal mine over a period of 38 years.

2 Research Background and Seismic Monitoring

In this paper, the surface projection area of the coalfield is about 10 km². The main mining coal is located in the south wing of the North-dipping syncline fold, and the total seam thickness is 0.6~110.5m. The mine uses the downlink subsection-slice mining method, mining segment high is 50m, the largest depth is at the -830m level (910 m below surface).

At the mine site, the first mining-induced rockburst happened when the mining depth was about -225m level (300 m below surface, the elevation of the ground surface is +80m). From the mining depth was -430m level, the modern microseism equipments had been used for continuous monitoring of mining-induced seismicity at the mine site since 1968. A single observation that was 3~4km apart from main mining area was laid in earlier period, the analog short-period seismographs, such as VKG, 573, DD-1,768 and so on, were also used. Digital equipments, JC-V100 and V104, were added in June 2000, these sampling rates are 50sps and 100sps, and the frequency ranges corresponding to that are 0~20Hz and 0~60Hz, respectively. Six sub-networks constituted a seismic network. Two kinds of equipments' working cycle was 1 s, the sensors had a frequency range of 1~20 Hz.

In order to ensure the completeness and comparability of mine seismic monitoring data, we asked specific people using the unified method to re-determine and recheck all the seismic events that were recorded on paper. The result showed that the lowest limit magnitude of the seismic events that could be monitored was $M_L = -0.9$, because the amplification of monitoring equipments was different at different time, the limit of the lowest monitoring ability was $M_L = -0.3$ at all period of time. Although the system factors of the loss of low magnitude events have already been excluded basically, the mine microseism data $M_L < 0$ has been left in analysis to reduce the possibility of accidental loss of that.

2 The General Characteristics of G-R Relation

The statistical function relation of frequency N (n) and magnitude M (M_L) has been deduced by studying a total of 93,773 mine seismic events ($M_L \geq 0$) that have been recorded over the last 38 years (from 1969 to 2006), initial magnitude $M_0 = 0$, magnitude increment $\Delta M = 0.1$ (Fig.1: $M_0 = 0$).

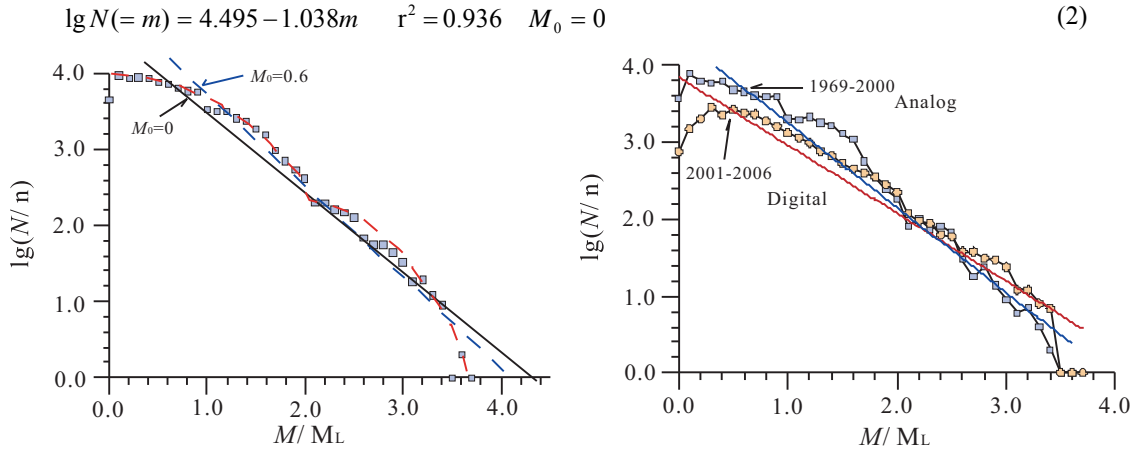


Figure 1 Magnitude-frequency relation of mining-induced seismicity from 1969 to 2006

Figure 2 Comparison of the mining-induced seismicity recorded by different monitoring equipments

Thus, we have known the G-R relation at the mine site for three aspects:

First, it is found that the mine seismic G-R relation shows a “two-peak” curved distribution characteristic. The statistic tendency for year by year is similar with it (Fig is omitted), and the magnitude of inflection point in two “the peak” approximately is about $M_L 2.0$. In order to explain the distribution characteristic has nothing to do with monitoring equipments, the monitoring result of analog equipment is used from 1969 to 2000, the digital equipment's monitoring data is used in 2001 ~ 2006 (Fig. 2), and two kinds of equipments are both used to contrast over the period from June 2000 to May 2001, the difference of data has not been discovered.

The statistics shows, with different time scale, because of the downward trend at the low magnitude end, causing the slope of the straight line (value b) becomes smaller, the result seems exaggerated in predicting the loss seismic events. After statistical selection, mine seismic monitoring data at the low magnitude end was discarded, initial magnitude $M_0=0.6$, magnitude increment $\Delta M = 0.1$ (Fig.1: $M_0 = 0.6$), which May be appropriate to reduce the exaggerated possibility and improve the quality of fitting. By means of statistics fitting to the mine seismic monitoring data over a period of 38 years, we obtained the equation:

$$\lg N(=m) = 4.895 - 1.194m \quad r^2 = 0.963 \quad M_0 = 0.6 \quad (3)$$

Second, the downward trend at the high magnitude end of the natural earthquakes indicates the loss seismic magnitudes have the possibility to complement from now on. If the mining activities are no longer carried on towards the position that is beneficial to induce the release of strong energy, the frequency of small energy release events will reduce, but still unceasingly accumulate, which causes the curving no longer tending straight but further increasing the curvature. If we just use statistics rule to forecast the largest loss seismic magnitude in the future without considering the mining activities and the geological environment, the future danger of mine microseism will be exaggerated. Thus, only noting statistical significance of G-R relation cannot reflect the modulating action of future mining activities for the G-R the relation.

Third, we are not clear what kind of time window should be used and how long the loss seismic magnitude should be forecasted in the future, so it is the question of time scale and its mechanism. Before we used many kinds of time scale to attempt and compare with actual extreme magnitude, when $r^2 = 0.65$, the average absolute deviation is 0.3, the relevance is the best. The choice of time scale and the position that seismic events will happen in the future belong to the experience to judge, its mechanism is not clear^[9].

3 Characteristics of G-R Relation in Pace-time Sequence Controlled by In-situ Stress

The pace-time sequence that the natural earthquakes and mining-induced seismicities comply with has been one of important scientific questions to explore in this field. We attempt establish one kind of pace-time sequence based on constitutive relation, and we take mining actions of the same in-situ stress magnitude and the dynamic response of rocks (mine microseism) as the same pace-time set, which is called "an in-situ stress controlled pace-time set of the dynamic response of rocks", and the mine microseism actions are explored in pace-time set based on the in-situ stress magnitude.

A systematic study on the stress field of the mine site indicates that, stress boundary conditions of the mining area is basic in stability, the buried depth of rocks at the mine site can be used as the measure of average in-situ stress magnitude^[10]. The results of situ stress measurement with stress relief method at the mine site show that maximum and minimum principal stress close to the level direction, the medium principal stress closes to the vertical direction^[11]. There is a linear relationship between the principal stress and the buried depth of rocks, the relationship between the maximum principal stress σ_1 (MPa) and the buried depth H (m) as follows:

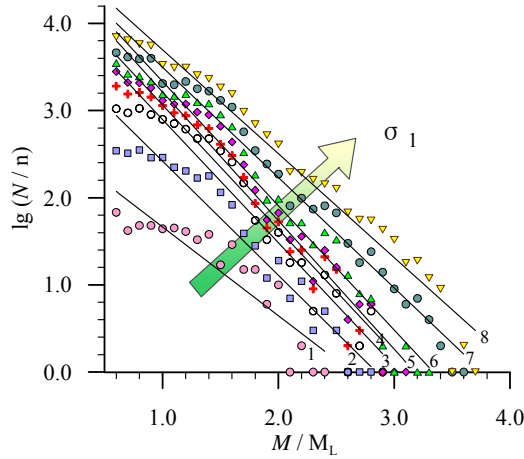
$$\sigma_1 = 0.0305 + 0.0408H \quad (4)$$

There is a total of 8 pace-time sets of the in-situ stress magnitude (Table1) according to the complete mine seismic monitoring data (-430 m ~ -830 m at the level).

We have the G – R relationship spectrum based on the in-situ stress magnitude (Fig.3: $M_0 = 0.6$), with mine seismic events that happen around smaller than or equal to the in-situ stress magnitude.

Table1 Zoning of rockburst according to in-situ stress magnitude

Mining stage	1	2	3	4	5	6	7	8
Depth (m)	510	585	620	660	710	760	860	910
σ_1 (MPa)	20.84	23.90	25.33	26.96	29.00	31.04	35.12	37.16



The figure marked the straight line correspond to the in-situ stress magnitude in table 1

Figure 3 G – R relationship spectrum based on σ_1

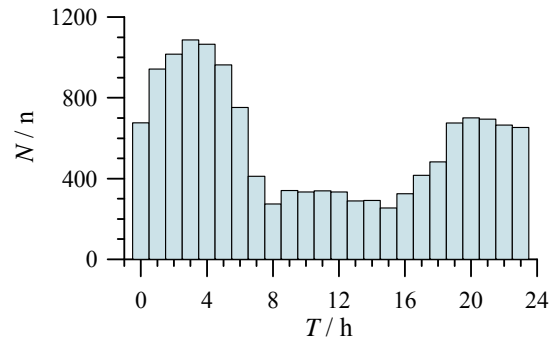


Figure 4 Distribution of accumulated seismic events for $0 \leq M_L \leq 1.5$

According to the G-R relationship spectrum of figure 3, we obtain the largest loss seismic magnitude, which is examined by the extreme seismic magnitude that occurs actually in a high stress intensity, the correlation coefficient $r^2 = 0.895$, the average absolute deviation is 0.1, to be find the accuracy of prediction is improved significantly.

With the regression method, we obtain the relationship(the formula (5)) between the maximum principal stress σ_1 (MPa) and the largest loss seismic magnitude for the future based on the G-R relationship spectrum of figure 3, which reflects the external energy release is considered to be proportionally influenced by the in-situ stress.

$$M = 5.534 \cdot \lg \sigma_1 - 4.915 \quad r^2 = 0.91 \quad (5)$$

The practice proves the accuracy in predicting extreme seismic magnitude with the self-similarity of G-R is high in "the in-situ stress controlled pace-time sequence". Its essence is, under the condition of mining intensity remain unchanged, using mine microseism that happen at lower stress to predict next extreme seismic events that will happen during the mining at the stress intensity increased by stress gradient, rather than a certain period of time designated by experience. The space site that the extreme seismic events happen is closely related to the high-stress zone. The in-situ stress controls the evolutionary trend of the G-R relation and the accuracy in predicting large possible seismic events under mining intensity remain unchanged.

4 Mechanism Discussion

(1) The “two-peak” curved distribution is the result of the combination of two mining-induced seismicities.

From 1969 to 1985, the mine takes mining operation system of three consecutive eight-hour, which has stronger comparability. Above the complete mine seismic frequency over a period of 17 years has been put into at 24-hour time axis, and its distribution of accumulated frequency shows that, at 24 hours, distribution of $0 \leq M_L \leq 1.5$ mine seismic activities is uneven, and there are three significant differences stages (Fig. 4). There is very strong correlation between such cycle regularity and the mining activities: 8:00 ~ 15:59 of every day recovering the coal wall of 6m wide that is left after bursting mining by the front of two teams, the microseismicity of the mine is the lowest as without blasting and initial disturbance to the original coal body; 16:00 ~ 23:59 after goaf filling of front two teams with two hours, then starting to blast at the original coal body, and mine seismic frequency begins to increase; 0:00 ~ 7:59 continuing blasting at the original coal body, and mining seismic frequency reaches the peak of the day. At the same time, $M_L > 1.5$ the high-magnitude mining-induced seismicities are not directly related to the mining activities (Fig. 5). There is a combination of mining-induced seismicities that are directly and indirectly correlated to mining activities among all mine seismic events^[12].

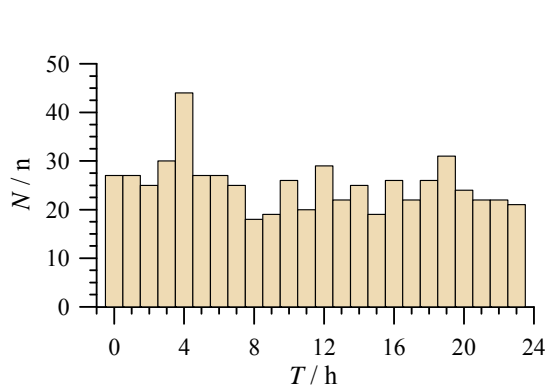


Figure 5 Distribution of accumulated seismic events for $M_L > 1.5$

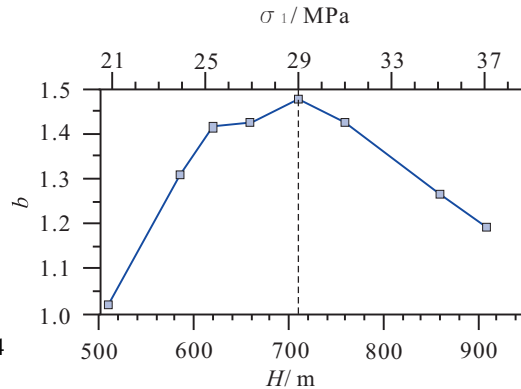


Figure 6 Distribution of b value

(2) The reason for nonlinearity of G-R relation

Figure 1 and figure 3 show the apparent non-linear characteristics of G-R relation, the non-linear characteristics at the low magnitude end of G-R relation. If there are the problems of inadequate monitoring capability in the early result of single observation, but the latter digital monitoring networks can exclude the factors of the leakage of monitoring data. We can speculate that, there may be “frequency band saturation” of micro-fracture observation in the frequency band of monitoring system.

At the high magnitude end, if the mining activities continue to next high stress intensity according to gradient increment of in-situ stress, the large loss seismic events tend to be filled, and the curve of G-R will tend to linearization. If the mining activities turn to the less than or equal to the in-situ stress intensity of exploitation in the past, the nonlinear of G-R relation at the high magnitude end will tend to maintain, the large loss mining microseism will no longer happen. Even if the intensity of exploitation increases, the number of small and medium-sized mining microseism will only increase, the loss extreme mining microseism will not occur. The linear approach of G-R relation at the high magnitude end is mainly influenced by the in-situ stress.

(3) In-situ stress controlled trend of development and evolution of the G-R relation

The G-R relationship spectrum based on in-situ stress magnitude in Figure 3 shows that, with the increase of the in-situ stress magnitude, the fitting straight lines move to the high magnitude end successively, although the slopes of the straight lines (b value) do not exactly correspond, they do not intersect at the first quadrant. The intercepts at y-axis (a value, the mining seismicities) and at x-axis (the loss magnitudes) increase with the in-situ stress monotonously. The G-R relation, as well as the mining seismicities and the loss seismic magnitude are considered to be proportionally influenced by the in-situ stress; the in-situ stress magnitude controls the trend of development and evolution of the G-R relation. The space position that the extreme mining microseism happens in the future, is closely related to high-stress zone. The pace-time scale of prediction in G-R relation conforms to an in-situ stress controlled pace-time sequence in this paper, and the mechanism is explained from the constitutive relation.

(4) The b value is an indicator of the rock fracturing sequence and its change

Figure 6 shows that the eight stages of the in-situ stress from weak to strong at the mine site, the b value at the upper 710m depth ($\sigma_1 = 29\text{MPa}$) increases monotonously, decreases monotonously at the upper 710m depth, the depth of 710m is the inflection point of maximum. The above phenomenon conforms to physical explanation of the literature [2, 3].

According to the self-similarity analysis of rock breaking, the literature [13] deduces that the structure of fracture has the fractal dimension characteristics; the b value is the half of fractal dimension d , the distribution between the frequency and magnitude is a self-similar system; the d value can be determined by b value. According to literature [14], the study of acoustic emission experiment shows that, the change of b value is directly related to stress conditions, the b value increases in the beginning of pressure, and drops at the stage of subcritical crack growth, and decreases sharply at the stage of rupture nucleation, which reflects the evolution of rock failure from disorder to order. The numerical simulation of literature [15] also obtains the same cognizance. There are many similar studies, they are confirmed that the b value is an indicator of the rock fracturing sequence and its evolution.

The evolution of the b value indicates that, the disorder of rock fracture is stronger at low confining pressure, and rock failure gradually turns to the order at high confining pressure. The 710 m depth is the critical depth that the rock fracturing sequence of the mine happens to change substantively.

Coincidentally, the initial critical depth of the interactional-type disaster between rockburst and gas energy, the rocks' apparent constitutive relation of a km-scale established based on the maximum principle stress and relative Benioff strain, and mining dynamics numerical experiments displayed fault dynamics and stress field property happen to change substantively, happen to change substantively, the critical depth is concentrated at about 700m depth^[10]. They meet by chance seems it's not accidental, they may together prove that the mechanical behavior of rocks at the depth of 700m happens to change substantively from the linear to non-linear. The survey reveals that various dynamic disasters at the mine site are abnormal at this depth and conventional measures for reducing and control dynamic disasters are failed. From those we infer that the depth of about 700m, the maximum principal stress is about 29MPa, may be the critical depth of "Deep Mining" that is widely discussed currently. The ratio (σ_1/σ_c) for the maximum principal stress of this depth with the uniaxial compressive strength of the coal body and the oil shales of main roof, as well as the hornblende gneiss of main floor, are 3.6, 0.6 and 0.2 respectively. It is likely the coal body reaches the critical parameter $\sigma_1/\sigma_c=3.6$ and that plays a leading role, the rocks of roof and floor are caused by the domino effect after the destruction and instability of the coal body.

5 Engineering Applications

(1) Rockburst risk assessment

Using the G-R prediction method based on in-situ stress controlled pace-time sequence in quarter 3, we may judge the general trend of mine microseism risk under various stress magnitude with the formula (5). If mining continues under the condition that the mining depth is -880m level and the largest principal stress magnitude is about 39MPa, possible future magnitude of the extreme will be $M_L = 3.9$. But when the tectonic stress strengthens or the partial abutment pressure concentrates in the region, the comparative magnitude mine microseism will possibly happen, so long as the maximum principal stress of the mining site achieves about 39MPa, and may not reach the depth of - 880m level. After a next high stress magnitude environment's extreme magnitude occurs, the formula (5) need to be re-calculated with the recent data, and revised unceasingly. If the mining depth was no longer deep from now on, the extreme magnitude that corresponds with each in-situ stress magnitude environment will happen according to formula (5).

(2) Judging the change of rock mass mechanical behavior

Using the method of calculating b value based on the "in-situ stress controlled pace-time sequence of the dynamic response of rocks" in 4(4), in combination with other dynamic response index of rocks after mining, which expected to become a way of evaluating the rock mass behavior's evolution and variation after mining, and provide the scientific criteria to take appropriate measures of underground pressure's mitigation and control for the mining engineering at the right moment.

6 Conclusion and Discussion

(1) The mechanism of the self-similarity of the Gutenberg - Richter relation is studied by a km-scale in-situ experimental investigation. G-R relation at the mine site shows a "two-peak" curved distribution characteristic, which can be explained by the combination of mining-induced seismicity that is directly and indirectly correlated to mining activities. Overall, the self-similarity of the Gutenberg-Richter relation is satisfied. The linearization trend at the high magnitude end is considered to be proportionally influenced by the in-situ stress.

(2) "An in-situ stress controlled pace-time sequence of the dynamic response of rocks", which is introduced by the in-situ stress and the mining activities that correspond with it, as well as the dynamic response of rocks (mine microseism); reflects the fracturing sequence of rocks based on the constitutive relation.

(3) The G-R relation, as well as the mine seismicity and the seismic magnitude missing are considered to be proportionally influenced by the in-situ stress. The in-situ stress controls the evolutionary trend of the G-R relation and the accuracy in predicting large possible seismic events, and the mechanism is explained from the constitutive relation. Whether the missing magnitude of the G - R relation at the high magnitude end can be filled, it is not decided by the time system of humans, but by the in-situ stress controlled time system; which conforms to the Kaiser Effect of rock with a memory. This realization also has significance for the G - R relation to the application in natural earthquakes.

(4) There is a good application for the approach of rockburst risk assessment after mining and evaluation of the rocks behavior. If the mode of action and intensity of stress field surrounding the mining area can be measured and considered to the local stress field of mine, as well as disproportion for the local tectonic stress and support pressure of the mine, the result of prediction will be more accurate and is expected to have universal significance.

References

1. Gutenberg, B. and Richter, C.F. Seismicity of the Earth. Geol. Soc. Am. Spec. Pap., 1941, 34 (1). 1-33.
2. Mogi, K. Study of the Elastic Shock Caused by the Fracture of Heterogeneous Materials and the Relation to Earthquake Phenomena. Bull. Earthq. Res. Inst., 1962, 40. 125-173.
3. Scholz, C.H. The Frequency-magnitude relation of. Microfracturing in Rock and Its Relation to Earthquakes. Bull. Seism. Soc. Am., 1968, 58. 399-415.

4. Gibowicz, S.J. and Kijko, A. An Introduction to Mining Seismology. San Diego: Academic Press, 1994.
5. Uzu, T. Estimation of Parameters for the Earthquake Magnitude Distribution with the Consideration of the Maximum Earthquake Magnitude. *Earthquake*, 1978, 1. 367-382.
6. Bender, B. Effects of Observational Errors in Relating Magnitude Scales and Fitting the Gutenberg-Richter Parameter β . *Bull Seism Soc Amer.*, 1987, 77 (4). 1400-1428.
7. Okuda, S., Ouchi, T. and Terashima. Deviation of Magnitude Frequency Distribution of Earthquakes from the Gutenberg-Richter Law: Detection of Precursory Anomalies Prior to Large Earthquakes. *Phys. Earth. Planet. Inter.*, 1992, 73 (3-4). 229-238.
8. Lu, Y.Z., Li, S.L., Deng, Z.H., et al. A GIS Based Earthquake Analysis and Prediction System. Chengdu: Chengdu Map Press, 2002.
9. Li, Tie., Ji, L.W., Zuo, Y., et al. Study on the Seismological Method to Forecast Stronger Mine Tremor. *Seismological Research of Northeast China*, 2003, 19 (3). 53-59.
10. Li, T. Study on the Mechanism of Mining-induced Seismicity and Its Safety Control. Beijing: University of science & technology Beijing, 2007, 35-94.
11. Cai, M.F., Ji, H.G. and Wang, J.A. Study of the Time-space-strength Relation for Mining Seismicity at Laohutai Coal Mine and Its Prediction. *International Journal of Rock Mechanics & Mining Sciences*, 2005, 42 (1). 145-151.
12. Li, T., Cai, M.F. and Cai, M. A Discussion on the Classification of Mining-induced Seismicity. *Chinese Journal of Rock Mechanics and Engineering*, 2006, 25 (Supp.2). 3679-3686.
13. Chen, Y. and Chen, L. *Fractal Geometry*. Beijing: Seismology Press, 2005.
14. Lei, X.L., Takashi, S. and Osamu, Nishizawa. Three-stage Fracturing Model for Granitic Rocks under Triaxial Compression-role of Microcrack Density and Stress Rate on Fault Formation. *Seismology and Geology*, 2004, 26 (3). 436-449.
15. Chen, Z.H., Tham, L.G. and Yeung, M.R. Numerical Simulation of Damage and Failure of Rocks under Different Confining Pressures. *Chinese Journal of Geotechnical Engineering*, 2001, 23 (5). 576-80.

EFFECT OF SENSOR ARRAY GEOMETRY ON MICROSEISMIC SOURCE LOCATION ALGORITHMS

BING-RUI CHEN, XIA-TING FENG

*State Key Laboratory of Geomechanics and Geotechnical Engineering, Institute of Rock and Soil Mechanics, the
Chinese Academy of Sciences, Wuhan 430071, P.R. China*

The algorithms of source location can be classified into four classes in terms of required solved parameters theoretically: firstly, velocity structure is given, and locations of microseismic sources and time of microseismic occurrence are identified on basis of arrival time recorded; secondly, given locations of microseismic sources, velocity structure and time of microseismic occurrence are solved in terms of arrival time; thirdly, velocity structure and locations of microseismic sources are inversed based on the time difference of sensor-pairs; lastly, velocity structure, locations of microseismic sources and time of microseismic occurrence are recognized together based on arrival time. The effect of sensor array geometry on the four algorithms of source location is studied systematically. Studies show that velocity of convergence is faster and precision of convergence is higher in ranges of sensor array than out of sensor array for the first algorithm; if only sensors can receive microseismic signals, the solution is unique and sensor locations are unlimited theoretically for the second conditions; the same association characteristics are found for the last two algorithms by theoretical analysis and the necessary condition that the association occurs, is $\Delta L_k / V = \Delta W_k$. So to improve precision of source location, the different algorithms should adopt different strategy for acquiring good sensor array geometry.

1 Introduction

Many studies, such as assessment of excavation damaged [1], quantification of rock mass damage and zone [2], source location algorithm [3,4], optimization of sensor array geometry [5,6] and prediction of rockburst [7], are carried out based on acoustic emission/microseismic (AE/MS) signals. It is generally accepted that not only microseismic signals reception is affected, but also velocity and precision of convergence and location result for different algorithms of source location are influenced at different degrees by sensor array geometry. So it is very important for these studies based on AE/MS signals to select an appropriate sensor array in space. If sensor array geometry is better, a great of useful microseismic signals can be monitored and source location can be solved quickly and precisely vice versa.

The algorithms of source location can be classified into 4 classes in terms of required solved parameters: firstly, velocity structure is given, and locations of microseismic sources and time of microseismic occurrence are identified on basis of arrival time recorded; secondly, given locations of microseismic sources, velocity structure and time of microseismic occurrence are solved in terms of arrival time; thirdly, velocity structure and locations of microseismic sources are inversed based on the time difference of sensor-pairs; lastly, velocity structure, locations of microseismic sources and time of microseismic occurrence are recognized together based on arrival time. Ge M.[3-5] studied deeply effect of sensor array geometry on the first source location algorithms, including all kinds of non-iterative methods and iterative methods and thought that velocity of convergence is faster and precision of convergence is higher in ranges of sensor array than out of sensor array, that if the sensors are placed in an arch, the location accuracy will be best in the foci area and decrease as sources move away. In fact, as velocity structure is given for this algorithm, if sum of distance is little enough from microseismic source location to all sensor locations, the precision of source location is high enough. Effect

of sensor array geometry on the later three other algorithms is studied rarely. The empirical method or semi empirical method is overwhelming for them. It is different that different schemes of sensor placement which are designed by different engineers receive signals, sensors' capability for monitoring microseismic signals can't be utilized completely sometimes, it is difficult that a good sensor array is formed and prediction of shock bump is affected greatly. So it is very necessary to study deeply performance and characteristic of the four source location algorithms and analyze effect of sensor array geometry on them.

2 Source Location Theory

Arrival time monitored is main information used for identifying source location. Generally, sum of squares of residues between monitoring arrival time and calculating arrival time is regard as the goal for recognizing hypocenter parameters. The formula for calculating arrival time of the NO. K sensor can be described as formula (1),

$$t_k = t + \frac{\sqrt{(x_k - x)^2 + (y_k - y)^2 + (z_k - z)^2}}{V} \quad (1)$$

Where, t is time of microseismic occurrence, (x_k, y_k, z_k) is coordinates of the NO. K sensor, (x, y, z) is location of microseismic source, V is equivalent to velocity of elastic wave in different medium.

So the arrival time difference of sensor-pairs (the NO. $K+1$ sensor and NO. K sensor) can be calculated by formula (2),

$$\Delta t_k = t_{k+1} - t_k = \frac{L_{k+1} - L_k}{V} = \frac{\Delta L_k}{V} \quad (2)$$

In which, L_{k+1} and L_k is the distance from the NO. $K+1$ sensor and the NO. K sensor to microseismic source respectively.

The goal function is illuminated as formula (3) based on residual sum of squares of calculated and monitored difference of arrival time between two neighbor sensors,

$$Q = \sum_{k=1}^n [\Delta W_k - \frac{\Delta L_k}{V}]^2 \quad (3)$$

Here, ΔW_k is difference of monitoring arrival time of the NO. $K+1$ sensor and the NO. K sensor; If K is equal to n , ΔW_k is equal to $W_1 - W_n$, n is number of sensors.

The goal function is as following based on sum of squares of residues between monitoring arrival time and calculating arrival time,

$$Q = \sum_{k=1}^n [W_k - t_k]^2 \quad (4)$$

In which, W_k is monitoring time, t_k is calculating time coming from formula (1), n is number of sensors.

If V and (x, y, z) are given in advance, then t can be solve by formula (4) as following,

$$t = \frac{\sum_{k=1}^n (w_k - \frac{L_k}{V})}{n} \quad (4)$$

3 Four Source Location Algorithms

As the goal is different and surrounding conditions is different, sometimes the velocity structure is known, sometimes microseismic location is clear, sometimes time of microseismic occurrence can be obtained and sometimes all variables can't be tested. So the different algorithms must be adopted under different conditions. The algorithms of source location can be classified into 4 classes in terms of required solved parameters as following:

1) Firstly, velocity structure is given in advance by testing in lab or *in situ*, and locations of microseismic sources and time of microseismic occurrence are identified on basis of arrival time recorded. This algorithm is pop in field of microseismic monitoring and location. If velocity structure is provided correctly, accuracy of source location is high and velocity of source location is fast vice versa. In fact, as rock material is a complex geological medium including a great deal of microcrack, joint and faults, its velocity is variables in different direction and in different zone. It is difficult to ascertain propagation velocity of elastic wave accurately so that accuracy of source location is very high impossibly.

2) Secondly, given locations of microseismic sources, velocity structure and time of microseismic occurrence are solved in terms of arrival time. The algorithm is often used for testing wave velocity of material.

3) Thirdly, velocity structure and locations of microseismic sources are inversed based on the time difference of sensor-pairs, then time of microseismic occurrence is solve by formula (5).

4) Lastly, velocity structure, locations of microseismic sources and time of microseismic occurrence are recognized together based on arrival time.

4 Effect of Sensor Array Geometry on Different Source Location Algorithms

Suppose that there is a cuboid consisting of homogeneous rock material, coordinates of its 8 pop-points are A(0,0,0), B(1000,0,0), C(1000,1000,0), D(0,1000,0), E(0,0,1000), F(1000,0,1000), G(1000,1000,1000) and H(0,1000,1000) respectively, 8 sensors are placed in each pop-point of the cuboid, propagation velocity of elastic wave is 5.7 m/ms in this medium, there live five microseismic sources which are O(500,500,500), P(0,500,500), Q(323.2,500,676.8), R(300,900,550) and S(600, 1700,2400) respectively in/near the cuboid and all length unit is meter, as shown in figure 1.

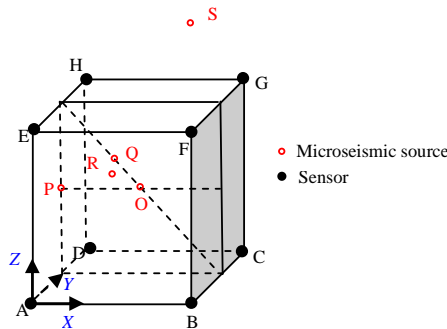


Figure 1 Distribution of Sensors and microseismic sources

4.1 The First Class Source Location Algorithm

Suppose that velocity is 5.7m/ms and arrival time can be acquired accurately, identifying locations of microseismic sources and time of microseismic occurrence, which is acquired by an improved version of PSO described in literature [8], is shown as table 1. The conclusion that locations of microseismic sources and time of microseismic occurrence are identified quickly and precisely, can be drawn from table 1. In fact, as complex

of rock material, propagation velocity of elastic wave is different in different direction and in different zone. In addition, mining art also affects propagation velocity of elastic wave, so it is difficult to obtain the velocity structure that elastic wave propagates in rock material correctly. If there is a very little error between real velocity and given velocity, the decrease of location accuracy is very great, especially in z -direction generally.

Table 1 Location accuracy and velocity of the first class source location algorithm

Microseism source		Location			Occurrence time/ms	Iteration times	Tolerance
		x/m	y/m	z/m			
O	Real	500.0	500.0	500.0	100.0	---	---
	Calculated	500.0	500.0	500.0	100.0	88	3.3e-022
P	Real	0.0	500.0	500.0	100.0	---	---
	Calculated	0.0	500.0	500.0	100.0	55	6.0e-011
Q	Real	323.2	500.0	676.8	100.0	---	---
	Calculated	323.2	500.0	676.8	100.0	65	6.7e-011
R	Real	300.0	900.0	550.0	100.0	---	---
	Calculated	300.0	900.0	550.0	100.0	69	8.1e-011
S	Real	600.0	1700.0	2400.0	100.0	---	---
	Calculated	600.0	1700.0	2400.0	100.0	14038	1.0e-09

Note: “---” means that this item doesn’t lie.

Suppose velocity is regarded as 5.757 m/ms, that is there is a 0.01 error from real velocity, location result for microseismic source Q、R、S as indicated in table 2. Effect of velocity structure on microseismic sources in different zone is different and velocity of convergence is faster and precision of convergence is higher in ranges of sensor array(for microseismic sources R and Q) than out of sensor array(for microseismic source S). If the sensors are placed in an arch, the location accuracy will be best in the foci area and decrease as sources move away. In fact, we find that as velocity structure is given for this algorithm, if sum of distance is little enough from microseismic source location to all sensor locations, the precision of source location is high enough. So monitor object had better lie in range good sensor array.

Table 2 Location result of the first class source location algorithm as velocity = 5.757m/ms

	Microseism source R				Microseism source Q				Microseism source S			
	Occurrence time /ms	x/m	y/m	z/m	Occurrence time /ms	x/m	y/m	z/m	Occurrence time /ms	x/m	y/m	z/m
Real	100.0	300.0	900.0	550.0	100.0	323.2	500.0	676.8	100.0	600.0	1700.0	2400.0
Calculated	101.3	297.9	904.6	550.5	101.5	321.4	500	678.6	81.9	606.6	1774.4	2511.4
Absolute error	1.3	2.1	4.6	0.5	1.5	1.8	0	1.8	18.1	6.6	74.4	111.4
Relative error /%	1.3	0.7	0.5	0.08	1.5	0.6	0	0.3	18.1	1.1	4.4	4.6

4.2 The Second Class Source Location Algorithm

For this algorithm, the source position is known in advance. From formula (1) and (4), we can see t and velocity can be solved, only if signal is accepted by the two sensors. The solution is unique and sensor locations are unlimited theoretically when sensor can receive microseismic signals. The relation of microseismic occurrence time and location accuracy is illustrated as figure 2. The algorithm is often used for testing wave velocity of material.

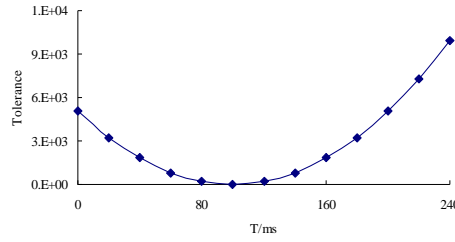


Figure 2 Relation of microseismic occurrence time and location accuracy

4.3 The Third and Fourth Class Source Location Algorithm

The formula (3) regarded as goal function, velocity structure and locations of microseismic sources are inversed based on the time difference of sensor-pairs firstly, then time of microseismic occurrence is solve by formula (5) in the third source location algorithm. While, the formula (4) is goal function in the fourth source location algorithm, velocity structure, time of microseismic occurrence and locations of microseismic sources are recognized together based on arrival time. They both have 3 variables requiring to be solved, only order in which the variables are solved is different. So they are same in essence.

Only if ΔL_k and V meet the following relations, Q is equal to zero forever, as deducted from formula (3).

$$\frac{\Delta L_k}{V} = \Delta W_k, \quad k = 1, 2, L, n \quad (6)$$

So this implies that x 、 y 、 z coordinates and velocity is associated with each other. But a great deal of numerical calculation shows formula (6) is necessary condition for association of V and $(x$ 、 y 、 $z)$ coordinate.

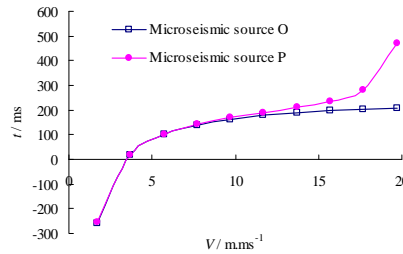


Figure 3 Association of velocity and time of microseismic occurrence for two special location

In particular, when k is equal to $1, 2, \dots, n$, ΔL_k and ΔW_k are both zero, that is the distance is same from microseismic source to all sensors and monitored arrival time for all sensor is the same. If V is zero, then Q is equal to zero forever. The microseismic source O is used as an example for illustrating it. Suppose V is increase by 2.0m/ms interval from 1.7m/ms to 19.7m/ms, all microseismic positions can converge to real point (500 m, 500 m, 500 m) and Q is equal to zero in formula (3). But time of microseismic occurrence can't converge to real value, it has its law with increase of velocity, as shown figure 3.

Suppose signal of microseismic source P is monitored by 8 sensors. In order to study association of coordinates and velocity, velocity increases from 1.7m/ms to 19.7m/ms by 2.0m/ms interval. When Q is equal to zero in formula (3), y and z coordinates of microseismic source P both converge to real value, while x coordinate shows its evolution law with increase of velocity, as indicated in figure 4 and the relation of velocity and time is shown as figure 3. Location position for microseismic source P is different point on the PO line. So we can draw that when microseismic source lies on the intersecting line of plane of symmetry of sensors, the coordinate value

along the intersecting line is associated with velocity and occurrence time and position of source location is uncertain. These conclusion can be used to other intersecting line of plane of symmetry of sensors.

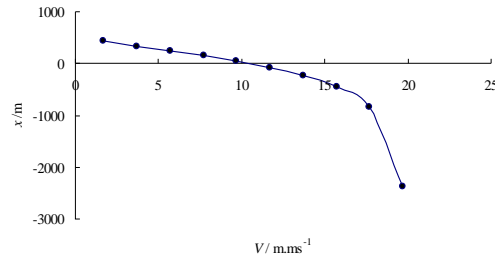


Figure 4 Association of velocity and x coordinate of microseismic source P

5 Conclusions

For the first source location algorithm, velocity of convergence is faster and precision of convergence is higher in ranges of sensor array than out of sensor array; for the second, The solution is unique and sensor locations are unlimited theoretically; for the third and the fourth, the same association characteristics are found and the necessary condition which the association occurs is $\Delta L_k / V = \Delta W_k$. So it had better that microseismic source is in range of sensor array geometry and the necessary condition is satisfied simultaneously.

Acknowledgements

Financial supports from the Hi-Tech Research and Development Program of China (863Program) under Grant No. 2006AA06Z117, National Natural Science Foundation of China under Grant No.50539090 and the Knowledge Innovation Program of the Chinese Academy of Sciences under Grant No. 0711031Q01 are gratefully acknowledged.

References

1. Cai, M. and Kaiser, P.K., Assessment of Excavation Damaged Zone Using a Micromechanics Model. Tunnelling and Underground Space Technology, 2005, 20 (4). 301-310.
2. Cai, M., Kaiser, P.K. and Martin, C.D. Quantification of Rock Mass Damage in Underground Excavations from Microseismic Event Monitoring. International Journal of Rock Mechanics & Mining Sciences, 2001, 38 (8). 1135-1145.
3. Ge, M. Analysis of Source Location Part I: Overview and Non-Iterative. J. Acoustic Emission, 2003, 21. 14-28.
4. Ge, M. Analysis of Source Location Algorithms Part II: Iterative Methods. J. Acoustic Emission, 2003, 21. 29-51.
5. Ge, M. Optimization of Transducer Array Geometry for Acoustic Emission/Microseismic Source Location. PhD thesis. Department of Mineral Engineering, Pennsylvania State University, 1988.
6. Tang, L., Yang, C. and Pan, C. Optimization of Microseismic Monitoring Network for Large-Scale Deep Well Mining. Chinese Journal of Rock Mechanics and Engineering, 2006, 25 (10). 2036-2042.
7. Li, S., Yin, X. and Zheng, W. Research on Multi-channel Microseismic Monitoring System and Its Application to Fankou Lead—zinc Mine. Chinese Journal of Rock Mechanics and Engineering, 2005, 24 (12). 2048-2053.
8. Chen, B. R. and Feng, X. T. Particle Swarm Optimization with Contracted Ranges of Both Search Space and Velocity. Journal of Northeastern University (Natural Science), 2005, 26 (5). 488-491.

STUDY ON FAULT MODELING METHOD BASED ON TIN AND GEOLOGY MAPS OF MINE

XIU-QIANG HAO

China ENFI Engineering Corporation, Beijing, 100038, P.R. China

ZHONG-XUE LI, MA BIN and YI-QING ZHAO

*State Key Laboratory of High-efficient Mining and Safety Metal Mines of Ministry of Education, University of
Science and Technology Beijing, Beijing, 100083, P.R. China*

Based on the characteristics of geology map of mine, this paper studied the fault model construction with fault curves on series of geology maps. Firstly, under AutoCAD environment, reference points of fault curves on geology maps of mine are read and these points and their coordinates are saved into database according to some rules. Secondly, based on the reference points saved in database and given constraints, building triangulation network for fault with Delaunay Triangulation Algorithm. At last, the TIN of fault will be constructed after the operations of cutting, geometrical coherence and topologic coherence. Based on the data from one gold mine of China, this model was validated and the function of 3D display of faults was also realized. It provided supports for deposit development, mining preparation and the selection of mining methods.

1 Introduction

Some complicated geological structures exist in underground ore deposit, for example, some fractures, faults and caves have a large influence on the development and cut of ore deposits and the selection of mining methods. It is necessary to know the distribution of geological structures and their influence zone in ore deposit before beginning development and mining. Also, it is the key factor to carrying out efficient mining activities and reducing the mining cost. Fault is a kind of fracture structure in the rock which has obviously relative displacement, and it is the most important and common kind of geological structure [1]. The research of 3D data models and 3D displays of faults is the important part of the research of 3D visualization for mines.

At present, the focuses of domestic and overseas research to 3D data models of fault are the following 5 aspects:

(1) Taking the fault as the stratum unit border during the stratum modeling, thus the stratum model which contains faults can be expressed correctly [2][3].

(2) Based on section data, which cut across the fault and other data, constructing a mathematical model of the fault with the methods of Chevron construction[4-6], inclined shear construction[7] and the fault-bend fold

theory[8], thus the computer simulation of faults can be realized.

(3) Fault surface generation technologies based on contour lines[9].

(4) Simulation with one or several planes [10][11]. Taking known azimuth and obliquity of fault surface as a precondition, this method constructs the plane equation for fault surface with two broken dots (the fall between the two broken dots can't be approximately perpendicular to the horizontal) on fault surface, and simulating the fault with one or several planes based on the known data.

(5) Based on the conception of "one surface with three layers", the fault surface is divided into the obverse layer, the inverse layer and the middle layer, and the fault surface can be expressed with the data structure based on volume, surface, ring, edge and node [12].

The fault model constructed with the methods mentioned above can simulate the 3D shape of the fault existing in stratum, and it can express the relationship between faults and the stratum appropriately. However, it can't simulate the spatial relationship for all kinds of spatial modeling objects in geological and mining engineering, for example, the relations among orebody, tunnels and faults. And it's difficult to simulate the fault with complicated shapes [13] with these methods. Some methods mentioned above indirectly realize the visualization of faults with the 3D simulation of stratum unit and the fault model hasn't been really constructed.

Geology maps are familiar in mining engineering and most of them are drawn with AutoCAD. These geology maps correspond with the levels and sublevels of the mine. In these geology maps, the faults are expressed as some curves. These curves contain some spatial and geometrical information of faults. In some cases, the fault can be treated as a surface in Euclidean space without thickness[14]. If these curves in geology maps of different level or sublevel of mine are linked according to some spatial rules, the 3D spatial model of faults can be formed. Based on this theory, this paper brings forward a method to construct 3D spatial model for fault with geology maps of mine.

2 The Theory of Fault Modeling Based on Geology Maps

The geology maps of mine contain curves which were formed by the intersection of geology plane and faults. One fault can forms several curves in different geology plane, as figure 1 and figure 2 showed. These curves are constituted by a series of reference points. The fault surface can be formed by the means of linking these reference points of adjacent curves formed by one fault in different geology maps.

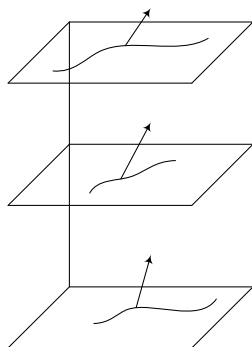


Figure 1 Fault curves on geology map

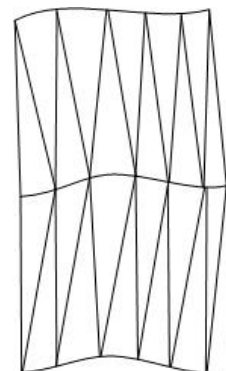


Figure 2 Fault surface with the linking of fault curves on each layer

3 Fault Drawing Method Based on TIN

According to the characteristics of fault curves in geology map, the shape of fault in Euclidean space can be expressed by TIN (Triangulated Irregular Network). The method which carried out Delaunay Triangulation Algorithm based on the reference points constituting the fault curves in the geological map is an efficient way to construct TIN for faults.

3.1 The definition of Triangulation Algorithm

For a set V of points in 2D real number field, edge e was constituted by the points in points set as the endpoint and e was contained in a set E . Then one triangulation $T=(V,E)$ of set V is a plane G , and this plane fulfills the following conditions:

- (1) Except the endpoints, there are no other points in the edges of plane G ;
- (2) There are no intersectant edges;
- (3) All the surfaces in plane G are triangle surface and the set of all triangle surfaces is the convex hull of set V .

3.2 Definition of Delaunay Triangulation Algorithm

(1) Delaunay edge: suppose one edge e (point a , point b are endpoints) in set E , if e fulfill the following conditions, edge e can be called Delaunay edge: If a circle passing through point a and point b doesn't contain any other points in set V in its interior, then the segment connecting the two points is an edge of a Delaunay triangulation of the given points.

(2) Delaunay triangulation: if one triangulation T of set V merely contains Delaunay edges, this triangulation can be called Delaunay triangulation.

3.3 Rules in Delaunay Triangulation Algorithm

There two important rules must be fulfilled:

- (1) Delaunay triangulation network is uniquely and a circle circumscribing any Delaunay triangle does not contain any other input points in its interior, as figure 3 shows;
- (2) In the plane, the Delaunay triangulation maximizes the minimum angle. Compared to any other triangulation of the points, the smallest angle in the Delaunay triangulation is at least as large as the smallest angle in any other, as figure 4 shows. However, the Delaunay triangulation does not necessarily minimize the maximum angle.

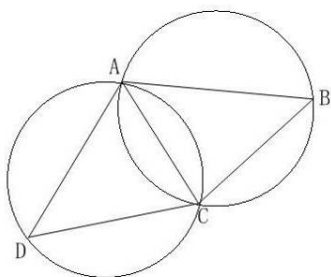


Figure 3 Circumcircle of Delaunay Triangulation

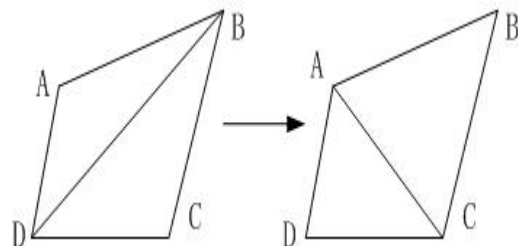


Figure 4 Quadrangle constructed by adjacent Delaunay Triangulations

3.4 The construction of TIN model of faults based on geology map

The azimuth of faults can be expressed by fault curves in geology map, and other factors can be learned from the fault curves made by the same faults in several geology maps. The relations of faults and geology plane are also expressed by fault curves and the intersectional relations among several faults on same stratum can be get directly from geology maps.

The modeling objects of fault based on TIN can be divided into the followings:

- (1)Point: contained in fault curves formed by fault and geology plane;
- (2)Edge of Triangulated triangle: formed by linking the corresponding points in adjacent geological plane;
- (3)Triangulated Triangle: formed by linking one point in one geology plane with other two points in adjacent geology plane or linking two points in one geology plane with one point in adjacent geology plane;
- (4)Fault surface: formed by several triangles among which two triangles are connected by one common edge.

3.5 Constraint of realizing Delaunay Triangulation Algorithm for reference points of fault curves

The reference points in several fault curves formed by one fault with several geology planes are point-sets in 3D field. The Topologic inconsistency will appear if the Delaunay triangulation is carried out without setting constraints during the course of constructing 3D model for faults with geology map of mine. As figure 5 shows, the part of broken line shouldn't be triangulated. So, some constraints must be set before carrying out d Delaunay Triangulation Algorithm.

Constructing 3D TIN model of faults based on the triangulation of reference points in fault curves must follow the rules of Delaunay Triangulation Algorithm and some constraints also need to be fulfilled as followings:

- (1)Constraints for geology plane: all geology planes are parallel in 3D field;
- (2)Constraints for fault curves: the fault curves formed by one fault with different geology plane are disconnected;
- (3)Constraints for reference points in fault curve: the reference points in same fault curve of the same geology plane formed by one fault can't be triangulated.

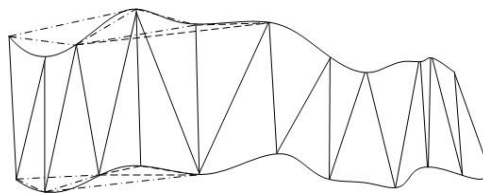


Figure5. Topologic inconsistency caused by the absence of constraints setting

3.6 The algorithmic flow of constructing TIN for fault

Generally speaking, a series of reference points provided by geology maps express the fault structural characteristics and the spatial shape indirectly. Aimed at constructing 3D model of faults, some mathematical models must be built based on these reference points and some mathematical transform and some discrete

operations must be carried out. Based on the constraints mentioned above, this paper constructs the fault TIN through the following process, as figure 6 shows:

(1)Data collection: the purpose of data collection is dispersing the fault curves and the method is reading the coordinates of reference points from geology map of each level and sublevel. The value of x coordinate and the y coordinate can be read directly, the value of z coordinate is equal to the elevation of the geology map;

(2)Data save: save the coordinate values of reference points to database according to some rules sorted by the name of faults;

(3)Data interpolation: If some reference points in fault curve are sparse, some skinny triangles will appear. To ensure the reliability of the shape simulation of faults, linear interpolation operations to reference points must be carried out;

(4)Carrying out Delaunay Triangulation: forming Delaunay triangles with linking one reference point(or two reference points) on one geology map with two reference points(or one reference point) following the rules of Delaunay Triangulation Algorithm, circulate this operation until the triangulation is finished;

(5)The treatments of cutting, geometrical coherence and topologic coherence to triangulated triangle network of fault, and then the TIN of fault have been constructed.

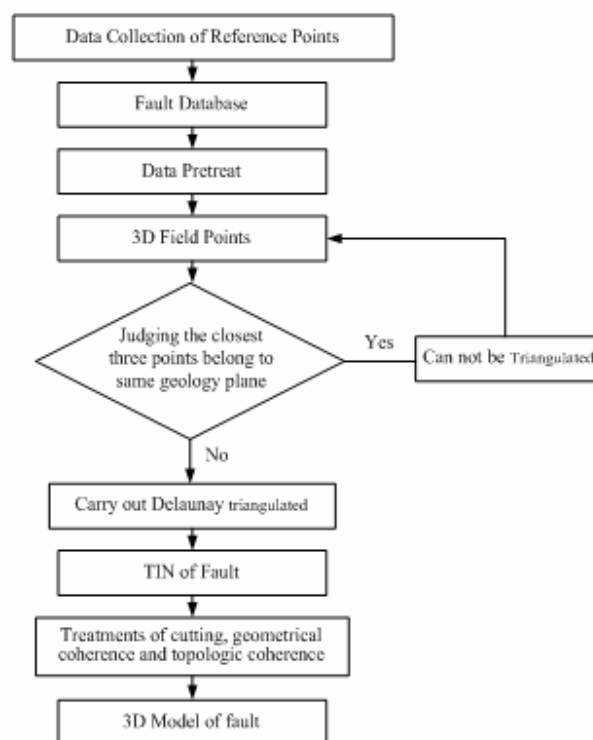


Figure 6 Fault TIN algorithmic flow chart based on geological layout plan of mine

4 Instance Validating

As one subsystem of B/S mode based 3D visualization system for mine developed by author, with Java language and combined with JOGL, taking Netbeans as development tool, the fault modeling and 3D display functions have been realized based on the geology maps from one gold mine of China. There are 5 big faults distributing in geology maps of -210~-380 level. The distribution of faults in -300 level was showed as an example. These 5 faults are taken as modeling and 3D display objects.

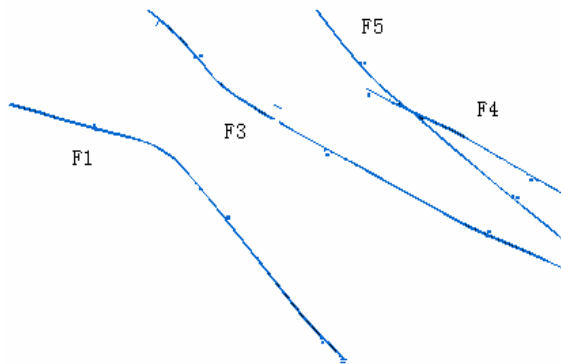


Figure 7 Fault layout plan of one gold mine -300m section

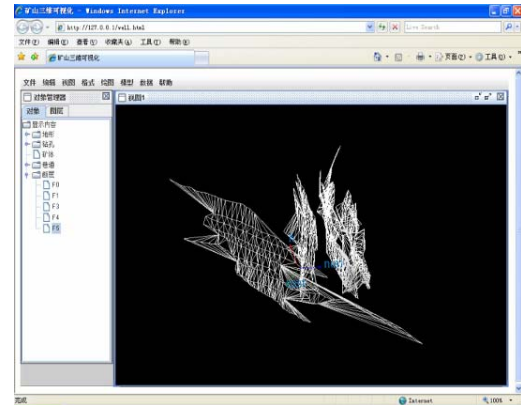


Figure 8 Combinational display of fault line-frame

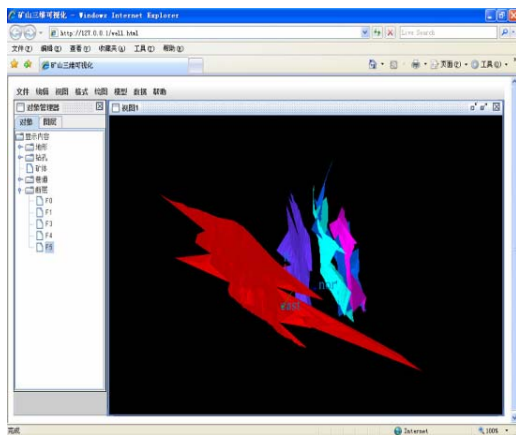


Figure 9 Combinational display of fault surface

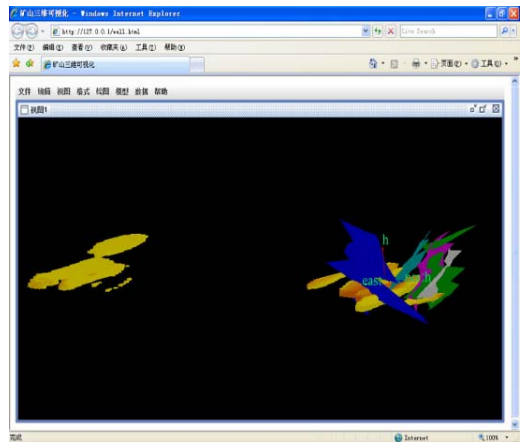


Figure 10 Integrated display of orebody and faults

There two 3D display modes for faults: line-frame and surface. The line-frame model is the TIN of faults formed by Delaunay triangulation based on reference points on fault curves. Under this mode, the spatial shape and relations of reference points and fault curves can be showed properly. The coherence of spatial Topologic relation and geometrical relation of the triangulated Delaunay triangle can also be checked based on line-frame model of fault. The surface model of fault can be formed through some operations based on line-frame model. The surface display mode aimed at discovering the spatial shape and the distribution of faults. The results of line-frame display mode and surface display mode are showed in figure 8 and figure 9. To develop the

application of fault 3D display, the display mode can also be divided into single fault display, fault combinational display and integrated display of faults and other objects in geological and mining engineering. The combinational display mode can show the relations among these 5 faults and each fault is dyed with different colors. The integrated display mode realized the function of displaying faults and orebody in one window. Under this mode, the relations of faults and orebody can be discovered thus provide evidences for mine design and the selection of mining method. The result of integrated display is showed in figure 10.

5 Conclusions

According to the characteristics of the geology map, this paper brings forward a 3D modeling method for faults with fault curves expressed by geology maps. Compared with other modeling methods of faults, it can reduce the calculation of spatial topologic relations for the objects existing in geology and mining engineering during the construction of fault model, thus the fault modeling flow can be simplified. After the setting of constraints for Delaunay triangulation and the operations of cutting, geometrical coherence and topologic coherence, the formed fault model can show the 3D shape, the distribution, the relations of the faults and the relations of faults and orebodies properly.

Acknowledgements

This work was financially supported by Natural Science Foundation of P. R. China (No.50604003) and “the Eleventh Five-year Plan” National Key Technology R&D Program (2006BAK04B04).

References

1. Shi, Y. and Yang, P. A New 3D Modeling. Technique of Fault Structure. 2006, 4 (2). 53-55.
2. Sirakov, N.M. and Muge, F.H. A System for Reconstructing and Visualizing Three-Dimensional Objects. Computers & Geosciences, 2001, 27 (1). 59-69.
3. Chen, X.X., Wu, L.X. and Che, D.F. 3D Modeling Method of Geological Bodies Including Faults Based on Borehole Data. Coal Geology & Exploration, 2005, 33 (05). 5-8.
4. Verrall, P. Structural Interpretation with Application to North Sea Problem. JAPPEC 3, 1981.
5. Gibbs, A.D. Balanced Cross-Section Construction from Seismic Sections in Areas of Extensional Tectonics. Journal of Structural Geology, 1983, 5 (2). 153-160.
6. Gibbs, A.D. Structural Evolution of Extensional Basin Margins. Journal of the Geological Society, 1984, 141 (44). 609-620.
7. White, N.J., Jackson, J.A. and McKenzie, D.P. The Relationship between The Geometry of Normal Faults and that of the Sedimentary Layers in their Hanging Walls. Journal of Structural Geology, 1986, 8 (8). 897-909.
8. Marrett, R. and Bentham, P.A. Geometric Analysis of Hybrid Fault Propagation/Detachment Folds. Journal of Structural Geology, 1997, 19 (3-4). 243-248.
9. Renard, P. and Courrioux, G. Three-dimensional Geometric Modeling of a Faulted Domain: the Soultz Horst eExample (Alsace, France). Computers & Geosciences, 1994, 20 (9). 1379-1390.

10. Wu, Q. and Xu, H. An Approach to Computer Modeling and Visualization of Geological Faults in 3D. *Computer & Geosciences*, 2003, 29 (4). 503-509.
11. Wu, Q. and Xu, H. Technique for 3D Fault Simulation in Virtual Mine System. *Journal of Liaoning Technical University*, 2005, 24 (03). 316-319.
12. Li, Q.Y. and Chang, Y.Q. Concept of "One Surface with Three Layers" in 3D GIS Topologic Relation and Its Extension in 2D. *Acta Geodaetica et Cartographica Sinica*, 2002, 31 (04). 350-356.
13. Wang, R.H. Study on 3D data Model for Geological Objects of Mine, Thesis of Master's Degree. Chengdu: Southwest Jiaotong University, 2003.
14. Hou, W.S., Wu, X.C., Liu, X.G., et al. 3D Complex Fault Modeling with Wire Frame Model. *Rock and Soil Mechanics*, 2007, 28 (7). 169-172.

STUDY OF THE DISTRIBUTION OF IN-SITU STRESS AND ROCKBURST FORECAST FROM AKEHE TO MAKEHE OF SOUTH-TO-NORTH WATER TRANSFER WEST ROUTE PROJECT

SI-WEI WANG

*North China Institute of water conservancy and hydroelectric power, 2 Zhengzhou University
Zhengzhou, 450011, P.R. China*

HAI-NING LIU

*North China Institute of water conservancy and hydroelectric power
Zhengzhou, 450011, P.R. China*

ZHONH-FU WANG

*North China Institute of water conservancy and hydroelectric power
Zhengzhou, 450011, P.R. China*

The tectonic activities are much stronger in areas of South-to-North Water Transfer West Route project with complicated engineering geological conditions. It is most important to study in-situ stress for the project design. In terms of the measurement values of in-situ stress, the model, which describes the relationship between in-situ stress and the depth, can be set up, and regression equation can be obtained. Uniform experimental design was adopted, with only two infinite drill measurements being taken on in-situ stress; all possible factors considered, the most optimal regression equation can be reached in terms of the least variance. According to the characteristics of high in-situ stress, comparisons have been made between engineering rock grading and the Russenes method, Hoek method, and the optimal method for rock burst and assessment have been presented.

1 Introduction

The South-to-North Water Transfer West Route project is the most important infrastructure to relieve the drought of Northern China. The engineering site lies in the north east of the Qinghai-Tibet Plateau, in which new tectonic activities are very strong, and engineering geological conditions are complicated. In-situ stress is one of the important problems of engineering geologies, and is crucial to engineering design. The Makehe river to Akehe river section, one portion of the South-to-North Water Transfer West Route project, belongs to Maerqu~Akehe in engineering geology^[1]. There is sandstone with slate interbeds on the engineering site, with block texture, the angle between the tunnel route and tectonic route is 50°~60°; and the tunnel crosses a regional active fault. There are two drill holes for measurement of in-situ stress in the passage of Makehe~Akehe, which measures the distribution of the in-situ stress in the depth of 200m~500m. To study the engineering geological conditions and rockburst, the distribution of in-situ stress will be studied by regression analysis, through uniform experimental design to search for the most optimal equation. According to characteristics of high in-situ stress, comparisons have been done between engineering rock mass grading and the Russenes method, Hoek method and the optimal method for rock burst and assessment have been presented.

2 Analysis of Measurement of In-situ Stress

The maximum horizontal principle stress is 12.0MPa~25.82MPa, which changes dramatically, and it came from the route drill hole XLZK14 and XLZK15, and the minimum horizontal principal stress is 8.0MPa~15.82MPa, which is mainly 9.0MPa~11.3MPa, and it changes little; and the vertical principal stress lies in 5MPa~11.12MPa, which change least^[1]. The three principal stresses increase with rock depth. The vertical principal stress is proportional to overlying rock thickness; the maximum horizontal stress and minimum horizontal one are proportional to overlying rock depths at drill hole XLZK15, however, the maximum horizontal stress and minimum horizontal one are not proportional to thickness at drill hole XLZK14. Poor integrity, and low strength rocks have been discovered by drill hole, as illustrated in figure 1. It shows the maximum principal stress and the minimum one of in-situ stress are high in the integrity, high strength site, vice versa.

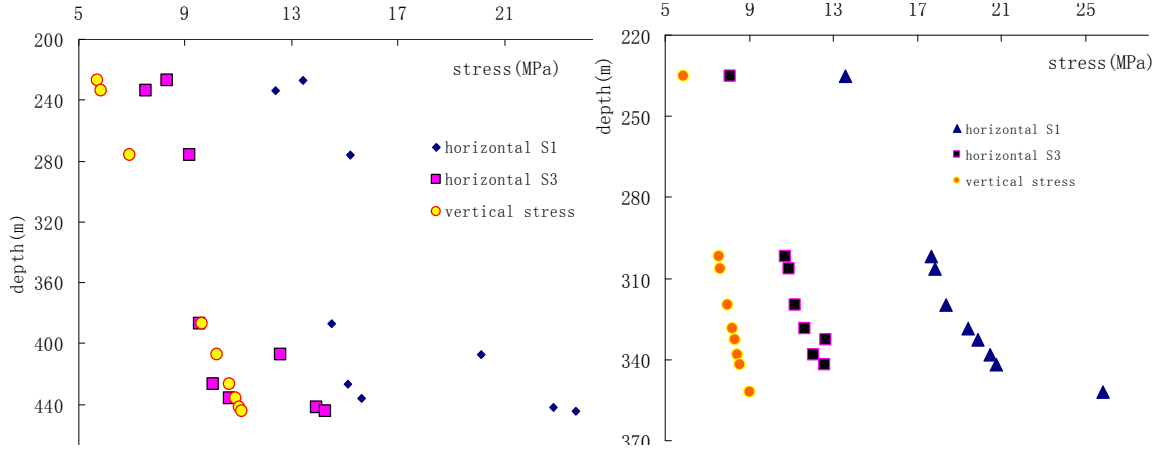


Figure 1(a) distribution of in-situ at drill hole XLZK14

Figure 1(b) distribution of in-situ at drill hole XLZK15

3 Uniform Experiment Analysis

Uniform experiment design is brought out by Wang yuan and Fang Kaitai in 1978. There are x factors, and there are n levels each factor, and only n time experiment will be selected. So it can reduce experiment times, and control all possible experiment^[2]. In-situ stress field have been studied in literature^[3~7], and good results have been gotten.

There are 10 route drill holes and 5 dam site drill holes for measurement in-situ stress of south to north water transfer west route project. The regression equation can be gotten between the maximum and minimum horizontal stress and rock depths, $\sigma_1 = 0.0306x + 6.3804$, given in figure 2^[1]. In term of statistical analysis of measurement of in-situ stresses, they are proportional to rock overlying depths in engineering site, and ratio with depths resembles like vertical stress one. So the distribution of in-situ stress is assumed to be linear in the engineering site.

$$\left. \begin{aligned} S_1 &= A_1 h + B_1 \\ S_2 &= A_2 h + B_2 \\ S_3 &= A_3 h \end{aligned} \right\} \quad (1)$$

Where, A1,A2,A3,B1,B2-constant, h-elevation difference from the earth crust to calculation point, S1,S2,S3-the horizontal maximum, minimum horizontal stress and vertical one.

According to data of two drill holes, regression equation needed to be modified, through uniform experiment design, and made upper limit and lower one of model parameters A1, A2, A3,B1, B2, and fixed ten levels, given in Table1. Refer to uniform design schedule table, and get to 10 sample, given in Table 2.

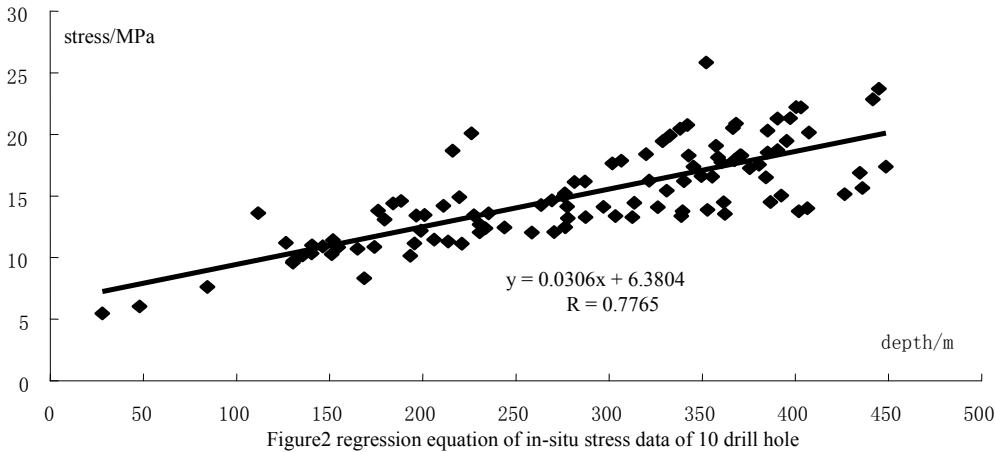


Table 1 level of sample

level	A1	B1	A2	B2	A3
1	0.027	6.20	0.025	0.10	0.024
2	0.028	6.25	0.026	0.15	0.024
3	0.029	6.30	0.027	0.20	0.024
4	0.030	6.35	0.028	0.25	0.024
5	0.031	6.40	0.029	0.30	0.024
6	0.032	6.45	0.030	0.35	0.025
7	0.033	6.50	0.031	0.40	0.025
8	0.034	6.55	0.032	0.45	0.025
9	0.035	6.60	0.033	0.50	0.025
10	0.036	6.65	0.034	0.55	0.025

Table 2 uniform design scheme

level	A1	B1	A2	B2	A3
1	0.027	6.30	0.028	0.30	0.025
2	0.028	6.45	0.032	0.55	0.025
3	0.029	6.60	0.025	0.25	0.024
4	0.030	6.20	0.029	0.50	0.024
5	0.031	6.35	0.033	0.20	0.024
6	0.032	6.50	0.026	0.45	0.025
7	0.033	6.65	0.030	0.15	0.025
8	0.034	6.25	0.034	0.40	0.025
9	0.035	6.40	0.027	0.10	0.024
10	0.036	6.55	0.031	0.35	0.024

Standard deviation of each item is calculated by the following equation,

$$C = \frac{1}{n} \sum_{i=1}^3 \sum_{j=1}^n (S_{ij} - \hat{S}_{ij})^2 \quad (2)$$

Where, S_{ij} , \hat{S}_{ij} -measurement value and calculation value; n-measurement times each drill hole. So result of calculation can be gotten, the result of XLZK14 is given in table3, and the result of XLZK15 is given in table 4.

Table3 calculation of XLZK14

level	A1	B1	A2	B2	A3	deviation
1	0.027	6.30	0.028	0.30	0.0253	11.099
2	0.028	6.45	0.032	0.55	0.0251	13.243
3	0.029	6.60	0.025	0.25	0.0249	11.756
4	0.030	6.20	0.029	0.50	0.0247	10.475
5	0.031	6.35	0.033	0.20	0.0245	13.709
6	0.032	6.50	0.026	0.45	0.0254	11.952
7	0.033	6.65	0.030	0.15	0.0252	13.407
8	0.034	6.25	0.034	0.40	0.0250	18.245
9	0.035	6.40	0.027	0.10	0.0248	15.386
10	0.036	6.55	0.031	0.35	0.0246	18.792

Table4 calculation of XLZK15

level	A1	B1	A2	B2	A3	deviation
1	0.027	6.30	0.028	0.30	0.025	33.097
2	0.028	6.45	0.032	0.55	0.025	23.387
3	0.029	6.60	0.025	0.25	0.024	31.707
4	0.030	6.20	0.029	0.50	0.024	23.468
5	0.031	6.35	0.033	0.20	0.024	17.039
6	0.032	6.50	0.026	0.45	0.025	9.655
7	0.033	6.65	0.030	0.15	0.025	15.106
8	0.034	6.25	0.034	0.40	0.025	11.208
9	0.035	6.40	0.027	0.10	0.024	18.644
10	0.036	6.55	0.031	0.35	0.024	9.877

Contrast between measurement value and calculation one was being listed in table 5

Table5 Contrast between measurement value and calculation one of XLZK14、XLZK15

Number and depth		S1	S2	S3
XLZK14/ 227.40	measurement	13.42	8.33	5.69
	calculation	13.78	6.36	5.77
XLZK14/ 444.87	measurement	23.71	14.28	11.1
	calculation	20.74	12.07	11.3
XLZK15/ 301.79	measurement	17.64	10.71	7.55
	calculation	16.16	8.30	7.67
XLZK15/ 341.96	measurement	20.76	12.60	8.55
	calculation	17.47	9.34	8.69

According to measurement values of XLZK14 and XLZK15, standard deviation at NO.6 is least, so distribution of principle stress confirm the law:

$$\left. \begin{aligned} S_1 &= 0.032h + 6.50 \\ S_2 &= 0.026h + 0.45 \\ S_3 &= 0.0254h \end{aligned} \right\} \quad (3)$$

4 Rockburst Forecast

Rockburst is a common geological hazard in high stress engineering site. There are several method of analysis of ruockburst, eg. strength theory, stiffness theory, energy theory and failure theory ect. Rock burst have been assessed by engineering rock mass rating method, Russenes method and Hoek method.

4.1 Russenes method

In Russenes method, rockburst intensity figure are set up in term of relation between maximum tangential stress σ_θ and point load strength Is. Is should be changed in uniaxial compressive strength Rc, and rockburst would be assessed by rockburst intensity figure. The rule is:

$$\begin{aligned} \sigma_\theta / R_c &< 0.20 && \text{no rock burst} \\ 0.20 \leq \sigma_\theta / R_c &< 0.30 && \text{weak rockburst} \\ 0.30 \leq \sigma_\theta / R_c &< 0.55 && \text{mediate rockburst} \\ \sigma_\theta / R_c &\geq 0.55 && \text{strong rockburst} \end{aligned}$$

4.2 Hoek method

$$\frac{\sigma_\theta}{R_c} = \begin{cases} 0.34 & \text{slight sidewall failure} \\ 0.42 & \text{serious sidewall failur} \\ 0.56 & \text{reinforcement supported} \\ 0.70 & \text{serious rockburst} \end{cases} \quad (4)$$

Tunnels which will be caved are assumed to be circle, according to measurement value of in-situ stress near the tunnel elevation and compressive strength value of rock mass in the route(Rc=70MPa), so stress values at NE 73° in the axial direction of tunnel see table 6, and result of rockburst can be gotten by four kinds of method, see table 7. And σ_L , σ_θ , σ_{\max} can be calculated by the equation:

$$\sigma_L = \frac{\sigma_H + \sigma_h}{2} - \frac{\sigma_H - \sigma_h}{2} \cos 2\alpha, \sigma_\theta = \frac{\sigma_H + \sigma_h}{2} + \frac{\sigma_H - \sigma_h}{2} \cos 2\alpha, \sigma_{\max} = 3\sigma_\theta \sigma_y.$$

where σ_H , σ_h –the maximum and minimum measurement of in-situ stress, α -angle between σ_H and tunnel axial direction, σ_y - selfweight stress.

Table6 basic data for forecasting rockburst

tunnel axial direction		XLZK14	XLZK15
	Classification of rock mass	sandstone	sandstone
	Maximum depth	441m	291m

	Uniaxial compressive strength R_c	70MPa	70MPa
NE730	Axial stress σ_L	15.21MPa	11.30MPa
	Maximum tangential stress σ_θ	21.60MPa	17.05MPa
	Maximum in-situ stress σ_{\max}	53.77MPa	43.54MPa

Table 7 result of rockburst

	Tunnel axial direction	Rock mass rating	Russenes method	Hoek method
XLZK14	NE73 ⁰	3.06<4 rockburst	0.77>0.55 Strong rockburst	0.77>0.7 Serious rockburst
XLZK15	NE73 ⁰	3.97<4 rockburst	0.62>0.55 Strong rockburst	0.62>0.7 Serious rockburst

5 Conclusions

1. The regression equation can be obtained by uniform experimental design from Akehe to Makehe with two drill holes; according to the regression equation of in-situ distribution by all measurement of drill hole in South-to-North Water Transfer west route project. It shows in-situ stress increases with overlying rock depths.

$$\left. \begin{aligned} S_1 &= 0.032 h + 6.50 \\ S_2 &= 0.026 h + 0.45 \\ S_3 &= 0.0254 h \end{aligned} \right\}$$

2. In this route, there is rockburst, sometimes strong ones by the Rock mass rating method, Russenes method and Hoek method.
3. Distribution of in-situ stress is complicated, which is influenced by much geological conditions; therefore a lot of attention should be given in engineering design.

References

1. Wu, H. Research Institute of Rock and Soil Mechanics, China Academy of Sciences. Experimental study report on geostress of west route project stage 1 for south - to -north water transfer II, 2004. 3.
2. Hu, B., Feng, X.T., Huang, X.H., et al. Regression Analysis of Initial Geostress Field for Left Bank High Slope Region at Longtan Hydropower Station. Chinese Journal of Rock Mechanics and Engineering, 2005, 22 (24). 4055-4064.
3. Tang, H., Shi, G., Ge, X.R., et al. Application of Uniform Design to Displacement Back Analysis in Underground Engineering. Chinese Journal of Rock Mechanics and Engineering, 2006, 10 (25). 2017-2022.
4. Shu, J.Q., Ren, X.H., Zhang, J.X., et al. Regress Analysis on 3-D Initial Geostress Field in Tunnel Region. Hongshui River, 2006, 1 (25). 46 - 49.
5. Liu, Y.Q., Luo, C.W., Li, H.B., et al. Study on In-situ Stress Measurements and Characteristics of In-situ Stress Field in West Route of South -to -north Water Transfer Project. Chinese Journal of Rock Mechanics and Engineering, 2005, 20 (24), 3620-3624.
6. Wang, S.W., Liu, H.D. and Gao, D.Y. Study on Analysis of In-situ Stress between Ahehe and Makehe of South to North Water Transfer West Route Project. Underground Space and Engineering, 2007, 3 (6). 1073-1076.

STUDY ON THE CONSTRUCTION AND FIELD MONITORING OF SPECIAL SECTIONS OF SHALLOW-BURIED METRO TUNNEL

WEN WAN and ZHI CHEN

*Hunan Provincial Key Laboratory of Safe Mining Techniques of Coal Mines in Hunan university of science and
technology, Xiangtan 411201, China*

Abstract: In the temporary Channel Construction of Daping Subway Station in the first metro line of Chongqing, the methods of supporting roof with I-steel and broking rock with FengGao to knock down the existing Shallow-buried and soft-rock tunnel are adopted. Step by step circular excavation with some core soils left and artificial non-blasting excavation methods are adopted in the new construction of the tunnel. It is seen from field monitoring that the surface settling curve follows certain pattern, and the settlement is generally larger at places near the tunnel's middle line. In weak and soft stratum, it is important to control the subsidence which is caused by the excavation of face and the second half cross section of the tunnel. When the right construction methods are used, the deformation of ground surface can be controlled, and reference is provided to similar projects in the future.

1 Foreword

With the newly built urban subways in our country; gradually, shallow-buried and mining methods have become more widely used in the construction of subway tunnels because of the economic and flexible nature of construction. When the stratum material is excavated at the shallow depth, the stratigraphy stress field adjusts with the cavity formation to the depths of the invading stratigraphic replacement. This is described by the moving of stratum material macroscopically and will spread to the surface due to construction, and land subsidence will come into being. Excessive ground settlement and stratigraphic replacement will endanger of the integrity of ground-level structures, and the safety of construction^[1,2]. Study on surface the deformation caused by excavation of the tunnel with shallow-buried mining methods is essential. Therefore, because of the characteristics of the new tunnel with the existing intersection to the Channel Construction of Daping Subway Station, shallow-buried rock with poor conditions makes research a necessity. The "New Austrian Tunneling Method" has three requirements for construction: monitoring and measurement of the deformation, stability and mechanical status of the support structure, judgment of support parameters, and the feasibility of construction methods^[3].

In this paper, monitoring results of two key cross-sections (k0 +36, k0 +50) were selected as the focus of analysis. The laws of deformation of ground surface are observed, while the methods of supporting roof with I-steel and breaking rock with FengGao to knock down the existing shallow-buried and soft-rock tunnel are adopted. The methods of circular excavation are carried out step by step, while some core soils are left and artificial non-blasting excavation is adopted in the new construction tunnel. The deformation of the ground surface can be controlled through synthesizing the period supports and protections measures of pouring the

thick liquid into rock with ductile in advance. This reference is provided for similar projects in the future.

2 Introduction to the Project

The entrance of the original light rail station on the 2nd line is used for the temporary Channel Construction of the Daping Subway Station. The temporary Channel Construction is 185.44 meters long constructed along the eastern Daping primary school and is used to carry ballast or transport materials and equipment. The tunnel vault is covered by 4-6 m depth of soil for the junction of entrance road, and 1-7m of loose soil for the surface, and with mudstone and sandstone underlying. There is poor groundwater, humid rock, and about 0.5m soil of grade IV vault which prone to collapse. The bedrock has two groups of fissures with block structure, and its saturated compressive strength of sandy mudstone is 6.4Mpa. It's a kind of shallow-buried tunnel with integrated rockmass and grade IV wall rock.

There is a drainage box culvert whose bottom 2.06m away from the vault in K0 +028; on the left side of the tunnel in K0 +033.02 is the 10th residence Lane 1 in Daping Center Street. The tunnel shortest distances from the northwest corner of the residence line 1.33m, in K0 +030 the same on the left there are two DN100 aslant tunnels with cast iron pipes which provide water, Pipelines elevation should be confirmed by drugging ditch at the scene. There is the new secondary lining region made by two DN300 aslant branch holes with concrete drainage pipes whose bottom 2.5m away from the vault approximately on the right side of the tunnel. The characteristics of this tunnel is its small cross-section, shallow buried depth, and 33.75m² (4.5m × 7.5m) of the average cross-section excavation. Poor stability of surrounding rock, hard and tight construction are also its characteristics. The plane map of intersection paragraph is shown in Figure.1.

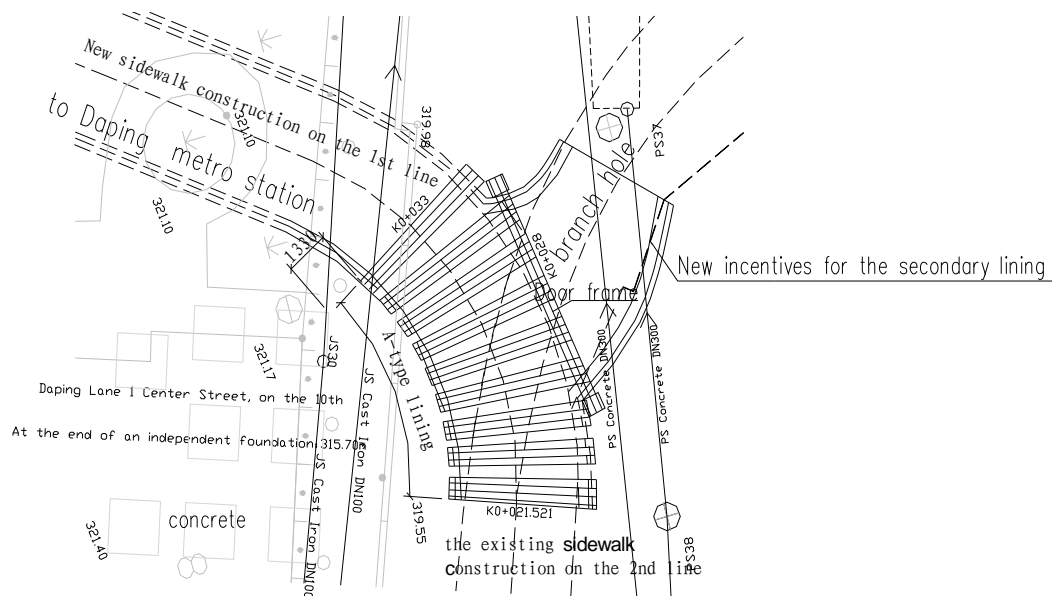


Figure 1 The plane map of intersection paragraph

The method of shallow tunneling is adopted in the temporary Channel Construction of Daping Subway Station. The Channel Construction of the 2nd line is used in k0 +0.00 ~ k0 +021.52 completely. With the

method of enlarged excavation in k0+021.52~ k0+031.707, it must be done after the removal of existing sidewalk construction on the 2nd line of the secondary lining. The methods of supporting roof with I-steel and broking rock with FengGao to knock down the existing tunnel are adopted. It must be controlled in 0.4m for per circle footage. The k0+031.707~k0+185.44 is a part of new construction tunnel , the methods of circular excavation step by step while some core soils are left and artificial non-blasting excavation are adopted in the k0+031.707~k0+082.00. The per circle footage of k0+031.707~k0+082.00 should be controlled in 1.2m. The methods of fully-cross-section excavation and technique of controlling earthquake、noise and blast are adopted in the rest construction of k0+031.707~k0+185.44 whose per circle footage should be controlled in 1.5m. The principles of " advanced pipe 、strict Grouting、 short excavation、 strong support、 early into a ring、 diligent measurement、 close lining followed" must be followed in the methods of circular excavation step by step while some core soils are left, and in ensuring the quality and safety of construction for premise.

3 Monitoring Results and Analysis

Monitoring is one of the three requirements for construction of "New Austrian Tunneling Method" .Rule of rock deformation , stability and mechanical status of the support structure will be mastered through measuring. and also the support parameters and construction methods will be judged that it is reasonably or not. The following measuring items are mainly adopted in this paragraph of the tunnel at the process of construction: Observation of geological and support situation , Convergence of surrounding displacement, settlement of vault and ground surface etc.The measurement points' arrangement of inside convergence and ground surface settlement are shown in Figure 2.

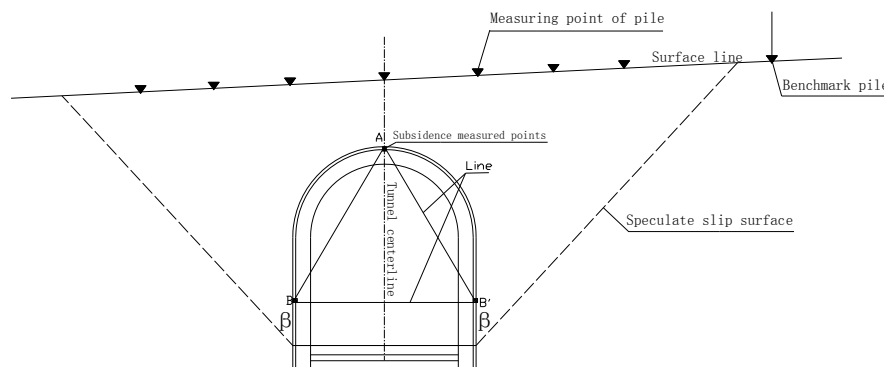


Figure 2 The measurement points' arrangement of inside convergence and ground surface settlement

3.1 Vault Settlement

According to the geological conditions and engineering requirements, two monitoring sections were placed in the entrance of shallow-buried tunnel ,they are k0+28 and k0+36 Separately. One of them k0 +28 is placed on steel beams which Locate at the door frame of the existing tunnel. The other section K0 +36 laid at the entrance of the new tunnel , these two sections are placed at the junction department of the existing tunnel and the new

tunnel which has a certain degree of representativeness. Curve of Vault settlement-time relation are shown in Figure 3 and Figure 4.

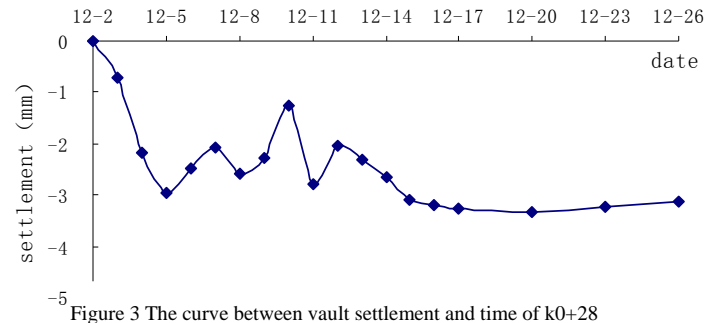


Figure 3 The curve between vault settlement and time of k0+28

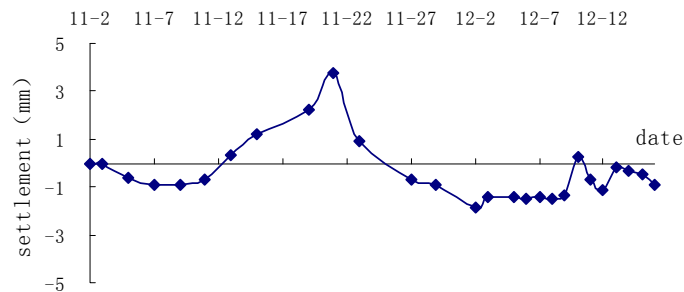


Figure 4 The curve between vault settlement and time of k0+36

We can see from Figure 3, the maximum value of vault's subsidence volume in the cross section k0+28 appears on December 2, 2007, is about 1.83mm, afterward the adjacent formation tends to be in stability. vault settlement appeared obvious rebound situation on November 22, and the biggest value of bounce achieves 3.78mm, it is precisely at this time of the construction process from the existing tunnel to the new tunnel with step method. The steel beam which led to the door frame appeared in the short-term rebound situation, because of blasting and soil beside the door frame was excavated. It is clearly that this cross-section vault settlement gradually stabilize at after one month from the whole curve. In the temporary Channel Construction of the 2nd light rail, the settlement of vault can be controlled while these methods of grouting reinforcing surface soil, digging the existing tunnel with artificial excavation and supporting roof with I-steel are used.

We can see from Figure 4, the maximum value of vault settlement in the cross section k0+36 appeared about December 20, 2007, is about 3.33 mm, The total subsidence quantity is 3.14mm, afterward the adjacent formation tends to be in Stability. It is clear that vault settlement reached 3mm less than a week from the whole curve, it is noted that rock has a faster rate to be stability. But it appears repeated fluctuations between some situation, because of effects of blasting, the short-term rebound effect of unloading appears at the surrounding rock.

3.2 Ground surface settlement

The entrance of the temporary Channel Construction of Daping Subway Station is shallow-buried, the greatest

depth does not exceed 10m, there are intensive pipeline underground and many buildings on the surface of ground. Two cross-sections are placed at which near the 10th Housing of Lane 1 Center Street in Daping. There are 7 measuring points each Section, section mileage is k0+36 and k0+50 separately. When measured piles are emplaced, attention that test piles should be arranged every 3 ~ 5m, and keep them in the same section, the benchmark pile should be located outside the whole sphere of influence of the tunnel, at the same time attention should be paid for each Measurement of pile's protection. Cross-sections' time history curves of every pile's total settlement and two sections' time history curves of middle pile's settlement are shown in respectively Figure 5 and Figure 6 below.

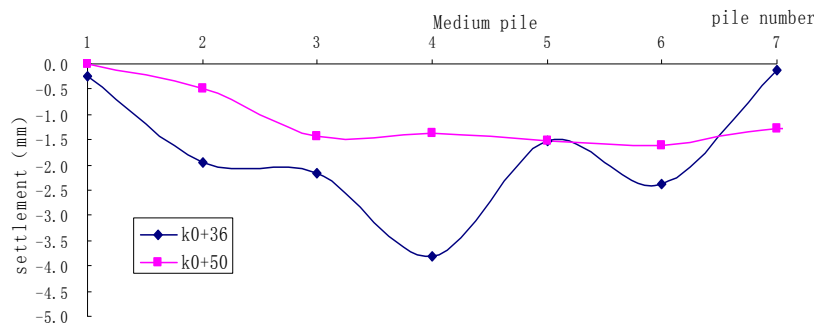


Figure .5 Two sections' time history curves of every pile's total settlement

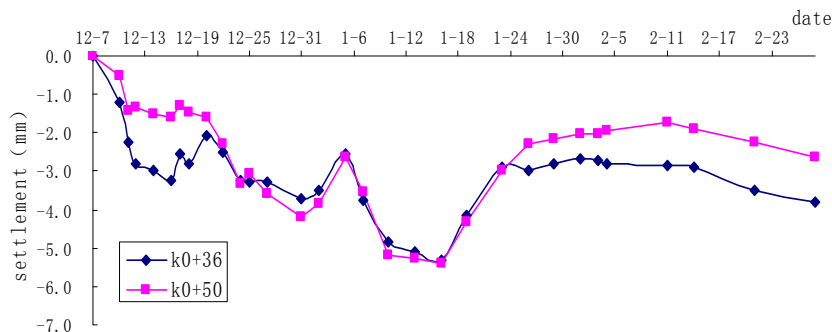


Figure 6 Two sections' time history curves of middle pile's settlement

From Figure 5 it is clear that the general trend of two sections' surface subsidence are or less the same, the shape like a funnel, both of which occurred in the largest settlement on the 4th test pile location, that is, the tunnel centerline location, the final settlement of k0+36 is 3.82mm, and the final settlement of k0+50 is 2.63mm, don't exceed regulatory requirements (surface subsidence should be controlled at less than 30mm). The main impact of regional of tunnel excavation is about 18m far away from the tunnel's axis, which has a larger sphere of influence. Area of subsidence trough of cross-sections k0+36 and k0 +50 accounted for the total area of subsidence trough are approximately 90.6% and 85.7%.

In weak and soft stratum, it is key to control the subsidence which is caused by the excavation of face and

the second half cross section of the tunnel. At this stage, the value of subsidence and sedimentation rate of measuring piles of tunnel's axis are a little larger. The amount of surface subsidence of k0 +36 and k0 +50 are 2.89mm 1.95mm respectively, while working face and the second half of the cross-section passing through and accounted for 36.1% and 54.2% of the total surface settlement.

It can be seen From Figure 6, on January 16, 2008, the largest value of surface subsidence of cross-section k0 +36 reached to 5.33mm, the largest value of surface subsidence of cross-section k0 +50 reached to 5.41mm. With the passage of time and working face moving forward, the settlement of two cross-sections' measuring points have been basically stable in time.

4 Conclusion

(1) For the characteristics of shallow-depth and poor conditions to the rock, the new tunnel with the existing intersection to special sections of the Channel Construction of Daping Subway Station, methods of a supporting roof with I-steel and breaking rock with FengGao to knock down the existing tunnel are adopted. The methods of circular excavation are performed step by step while some core soils are left and artificial non-blasting excavation is adopted in the new construction tunnel. Synthesizing the period supports with protections measures of pouring the thick liquid into rock with ductile in advance and I-steel arch centering, the surface and building's subsidence are effectively controlled. The security and time of construction are guaranteed, the good economic efficiency and the social efficiency are obtained, and will provide the reference for the similar projects.

(2) It is obtained from monitoring the results of the surface settling curve, generally the closer the distance of tunnel's middle line, the bigger subsidence quantity is. In weak and soft stratum, it is important to control the subsidence which is caused by the excavation of the face and the second half cross section of the tunnel.

References

1. Fan, W.X. Control and Analysis of Settlement to the Shallow-buried and Subsurface Metro Tunnel. Municipal Technical. 2006, 24 (6). 398-402.
2. Zhang, B. Study on Control Measures to Surface Subsidence Caused by Construction of Shallow-Buried Tunnel. Geotechnical Engineering and Technology. 2007, 21 (5). 265-268.
3. Zhang, Y., et al. Construction and Field Monitoring of Shimen'ao Tunnel of Beijing-Zhuhai Expressway. Research of Highway and Transportation, 2001, 18 (1). 47-50.
4. Huang, N.Q. Study on Construction Technology of Shallow Soft Rock of Large-span Metro Tunnel. Construction Technology, 2006, 35 (11). 75-77.
5. Xia, C.C., et al. Study on Field Monitoring of Large section of Highway Tunnel with Small Spacing. Journal of Rock Mechanics and Engineering, 2007, 26 (1). 44-50.
6. Jing, H.W., et al. Research on Stability of Surrounding Rock and Control Technology of Buried Roadway. Rock and Soil Mechanics, 2005, 26 (6). 877-880.
7. Zhang, X.N. Analysis of Finite Element and Ground Surface Settlement to Tunnel of Expressway. Hunan Communication Science and Technology, 2006, 32 (3). 154-156.

CHARACTERISTICS AND MECHANISMS OF ROCKBURST IN A DEEP MINE IN CHINA

AI-XIANG WU¹, CHUN-LAI WANG¹, XIAO-HUI LIU¹, XUE-WEN JI², XIANG LI², QING-WEN
YAN², XUE-GUI HUANG², XIAO-BING HOU²

*1 School of Civil & Environment Engineering, University of Science & Technology Beijing
Beijing, 100083, P.R. China*

2 Yunnan chihong Zn & Ge Co. LTD. , Qujing, 654212, P. R. China

The Huize Lead & Zinc mine is a deep km mine in Yunan chihong Zn & Ge Co.,LTD. in China with mining of the eighth orebody. The basic problems of this deep hard rock mine were high underground stress and development of the fault structure. After summarizing the geological conditions of this mine, the characteristics of rockburst such as rock core disk and rock formation spalling were described and the basic rules of rockburst were elucidated by the field investigation. The rockburst types and intensity classifications were progressed to the surrounding rock of eighth orebody, and the medium to intense rockburst trend was defined for 1451m to 1261m levels in the eighth orebody. The influencing factors of rockburst including the initial rock stress, geological structure and mining depth were considered for analysis for causes and mechanisms of rockburst in this mine.

1 Introduction

Rockburst is a geological disaster of dynamic instability in the hard and brittle rock mass, which was located a state of high underground stress in the excavation of underground works. It produces changes in the surrounding rock stress and abrupt release of the elastic strain energy stored in the rockmass; producing the bursting, loosening, shooting, and throwing phenomena of rock blocks. This elastic strain energy of deformation stored in the accumulated rockmass and generated over a long time due to the movement of the earth's crust. Presently, with the increasing depth of mines in the world, there are many deep underground engineering sites where the surrounding rock are under high in-site stress and the threat of rockburst to underground safety mining tends is greatly increasingly. The problem of rockburst in deep hard rock has not been solved completely, although scholars at home and abroad have made tremendous progress in the occurrence, mechanism and monitoring of rockburst. Rockburst is a very complicated phenomenon of dynamic equilibrium loss and these difficult problems in rockburst need to be urgently solved [1-7].

The eighth orebody of the Huize Lead & Zinc mine is a rare, rich large-sized multimetal orebody in Yunan chihong Zn & Ge Co., LTD. in China. The characteristics of the orebody are tremendous geological reserves, high ore grade, and rare multimetals; such as germanium, silver, and cadmium. The geological conditions of the orebody are complicated, including the presence of water, deepness, fragmentary and difficult together, which hasn't precedent in China. The distance is only 900 meters from Niulaijiang River, causing the accident of mine water invasion in case that the rocklayer was broken by mine activity. The depth of orebody is 1280 meters from the ground in the mine, which is one of deepest metal mines in China and is under high in-site stress because of the deep mine and Yunnan-Kweichow Plateau. Rockburst occurred locally in the mine, the threat of rockburst to mining safety production tends to be greatly increasing.

2 Geology of the Study Area

The mining area is located at the southwestern edge of the Yangtze metaplatform, and at the northeastern end of the thrust structure zone of the Kuangshanchang—Jinniuchang anticline on the eastern edge of the northeastern fold beam in Yunnan (Figure 1). The developing northeastern folds, faults, along-faults and near-faults in the mine area are favorable to spatial distribution of mineral deposits. The structure of mine area was patterned toward the northeast-southwest direction, which was characterized firstly by schuppen structure, and secondly by the northwestern-southeastern structure.

The geology of this study mine was described as in Ref. [1]. Briefly, the strata is divided from upper to lower, i.e. (1) Mapping formation of upper Carboniferous(C3m):purple and grayish purple argillaceous striped breccia limestone with purple mud stone; (2) Weining formation of middle Carboniferous(C2w):grey middle-thick layer-like limestone with oolitic limestone; (3) Baizuo formation of lower Carboniferous(C1b):grayish white, ecru and pinkish red middle-coarse-grained dolomite with light grey limestone; (4) Datang formation of lower Carboniferous(C1d):grey crypto-crystal limestone, a layer of 0.3 - 3.5m brown black fine siltstone and purple mud stone on bottom; (5) Third member of Zaige formation of upper Devonian(D3zg3):grey crypto-crystal limestone and yellowish white, pinkish red middle-grained dolomite. Qilinchang orebody occurred in the middle-lower of Baizuo formation of lower Carboniferous, whose strike was $N12^{\circ} - 25^{\circ}E$, dip direction was SE and dip angle was $54^{\circ} - 65^{\circ}$.

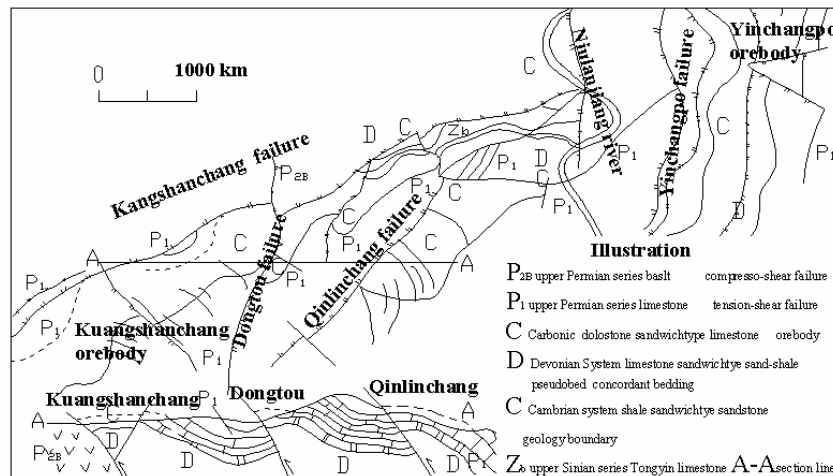


Figure 1 Geological structure of mining area in Huize Lead-Zinc Mine

3 Characteristics of Rockburst

3.1 The Phenomenon of Rock Core Disking

The rock core from geology exploration bore is the most basal information to find out the characteristic of rockmass mechanics. Rock core disking is the phenomenon that the rock core is broken into 'disk' in the process of drilling, marks the production of brittle rupture and different unloading drilling, indicates obviously the state of high in-site stress, and are caused by the multiple mechanisms of tension, relaxation and stress release. Early in 1960s, this phenomenon is seen in the igneous rock area, but it can be seen in the hard

metamorphic rock and sedimentary rock too [8-9]. Thereafter, the rock core diskling phenomenon was found in the construction of water power stations at Ertan, Lubuge and Laxiwa, including in Jinchuang mining area in China.

At the eighth orebody in Huize lead-zinc mine, the different extent of rock core diskling phenomenon in all strata was observed in the process of drilling exploration of engineering geology. By analyzing the site drilling data, the rock core diskling phenomena are characterized by (1) Wide distribution but small size. The diskling phenomenon was found in most holes along the strike of orebody. There are generally two or three locations in a boring; every rock diskling is about 20 cm, which means the diskling was not serious; (2) Thin thickness. It is about 0.5 - 2cm, 0.2 - 0.3cm for the thinnest and about 1cm in general; (3) One type of rock cores are unbroken into disk. On the surface of this rock core, there was some ring zones which were clear and obvious and were composed of staggered fine tooth-like fissures with about 0.5mm (max). This type of rock cores can be separated into disk along fissures, and then recovered to its original. (4) Two types in morphology: one was irregular, the other was flat and smooth, whose surfaces were fresh and without any disseminated mark.

Rock disk produced in drilling and rock-core disked morphology are shown in Figure 2.



Figure 2 Rock core disk produced in boring

3.2 Phenomenon of Schistose Scaling on Sidewalls in Tunnel



Figure 3 Schistose scaling on sidewalls in tunnel

The depth of the eighth orebody excavated is more than 1 000 m. There are different degree phenomenon of schistose scaling on sidewalls in across vein and main haulage way at 1391m and 1331m levels (Figure 3), the phenomena of scaling are characterized by: (1) The scaling generally occurred in the ‘shoulder ’wall of tunnel. (2) The phenomenon of schistose scaling in hanging wall is less severe than footwall. (3) The phenomenon of schistose scaling in surrounding rock of the deep tunnel is less severe than shallow. (4) Schistose scaling is plate like sliver, the thickness is 0.5 - 20cm, the direction of schistose scaling is toward the vertical axes of tunnel, and spreading along the tunnel axes, the length is from several meters to dozens.

4. Types and Intensity Classification of Rockburst

The prediction and control of rockburst is based on the types and intensity classification of rockburst. The classification basis is the characteristics of the elastic strain energy storing and release, or the pattern of stress activity. At present; it hasn’t been acquired consensus in study fields. Based on the results of investigation on site, types and intensity classification of rockburst were studied and analyzed for grasp the basis on occurring rockburst in the eighth orebody, so as to adopt a measure of rockburst prevention. Firstly, rockburst was defined as a break loosening type according to an extent of rock fracture; Secondly, it was defined as small size (0.5 - 10m long) and large size (10 - 20m long) according to rockburst range; Thirdly, based on the failure pattern of rockmass where rockburst occurred, it was defined as a schistose scaling type. Lastly, according to the genesis of high in-situ stress and the direction of maximal principal stress in rockmass where rockburst occurred, it was defined as a hybrid stress type.

The study status is summed up at home and abroad [10-11]. The intensity classifications of rockburst were divided into slight, medium, intense and severe, as shown in Table 1.

The method of stress was taken from Barton to distinguish α and β in Norway, which is one of most simple methods [12]:

$$\left. \begin{aligned} \alpha &= R_c / \sigma_1 \\ \beta &= R_t / \sigma_1 \end{aligned} \right\} \quad (1)$$

Where R_c is uniaxial compressive strength (MPa), R_t is uniaxial tensile strength (MPa), σ_1 is the maximum principal stress (MPa).

The distinguished method:

$$\left. \begin{array}{lll} 10 < \alpha & \beta > 0.66 & \text{No rockburst} \\ 5 < \alpha \leq 10 & 0.33 < \beta \leq 0.66 & \text{Slight rockburst} \\ 2.5 < \alpha \leq 5 & 0.16 < \beta \leq 0.33 & \text{Medium rockburst} \\ \alpha \leq 2.5 & \beta \leq 0.16 & \text{Intense rockburst} \end{array} \right\} \quad (2)$$

Based on results obtained from tests and calculation, parameters of the eight orebody related to rockburst are shown in Table 2.

Table 1 Rockburst intensity classification

Rockburst intensity classification	Slight rockburst	Medium rockburst	Intense rockburst	Severe rockburst
Main basis	<p>The surface of wall rock has the phenomena of burst stratum disjunctum and stripping, collateral rupturing sound.</p> <p>Rockburst occurred fragmentary and disconnected, engineering was weak influence.</p>	<p>The surface of wall rock has the severe phenomena of burst stratum disjunctum and stripping, collateral shooting and clear bursting sound, duration period of time, depth of rockburst reaches to 1m.</p> <p>Medium rockburst has a certain extent influence to engineering.</p>	<p>Intense burst ejected from wall rock like ‘shoot’. Rockburst has continuity and develop depth of wall rock, and depth of rockburst reaches to 2m. Intense rockburst has a largely extent influence to engineering.</p>	<p>Severe rockburst can cause severe burst ejecting even throwing destroys; collateral tremendous bursting sound, rockburst occurs abruptly.</p> <p>Rockburst has continuity and develop depth of wall rock; Severe rockburst has a severe extent influence to engineering, even destruct it.</p>

Table2 rock mechanics parameters and rockburst proneness indexes of the eighth orebody rockmass

	Indexes	Rock characters				Remarks
		C3m	C2w	C1b	C1d	
rock mechanics parameters	$R_c(\text{MPa})$	56	74	53	65	
	$R_t(\text{MPa})$	3	2.7	1.7	2.7	
	R_c / σ_1	2.33	3.08	2.21	2.705	
1451m Level	R_t / σ_1	0.125	0.112	0.707	0.112	800m depth
	Rockburst proneness	Intense rockburst	Medium rockburst	Intense rockburst	Medium rockburst	
	R_c / σ_1	1.78	2.35	1.68	2.06	
1261m Level	R_t / σ_1	0.095	0.086	0.054	0.086	1060m depth
	Rockburst proneness	Intense rockburst	Intense rockburst	Intense rockburst	Intense rockburst	

Note: Rock mechanics parameters were obtained on MTS from laboratory.

The previous results have shown that there is possibility of rockburst indeed in strata, under the action of in-situ stress, in the mining area. This is the in-situ condition making rockburst occur.

5 Occurance and Mechanisms of Rockburst

5.1 Occurance of Rockburst

It was known that there are many factors influencing the rockburst occurring, such as rock brittleness, rock strength, water ratio of rock, depth of engineering, geological structure, size and direction of in-situ stress field, etc. By analyzing, the following were thought of as the main factors on rockburst occurring in the eighth orebody.

5.1.1 Effects of Geological Structure, Rockmass Structure, Rock Property on Rockburst

Generally, under horizontal in-situ stress, the brittle and compact rockmass are easy to be ruptured into rock block, which obtain the stress to some extent to make rockbursts release abruptly. In usual case, rock whose uniaxial compressive strength (R_c) is > 60 MPa tends to rockburst. Direct roof of the eighth orebody is C_1b rock strata, and floor is C_1d rock strata, every rock is hard and intact, is tested that uniaxial compress stress is about 60MPa, and RQD is in exceed of 70 percent. Rock spalling was found in the ‘shoulder’ sidewall of tunnel under the condition of high in-site stress.

5.1.2 Effect of In-Situ Stress Field on Rockburst

The elastic strain energy is stored in rock under in-site stress. Engineering was excavated under high stress, whose stress in rockmass can reach 2~3 times higher than initial in-site stress. The maximal in-site stress in 1391m and 1261m levels were obtained in tests, is 25.5MPa and 31.5MPa, respectively. Method of stress was used to distinguish the high stress zone, $R_c / \sigma_1 = 2 \sim 2.6$ was considered as great stress zone where intense rockburst frequently occurred. The results showed that the eight orebody had the proneness from the medium rockburst to intense rockburst.

5.1.3 Effect of Depth on Rockburst

About the source location, rockburst occurred at the depth deeper than 700 m, and it can be found at shallow and medium depth in high stress field. For example, rockburst occurred at 200~400m in coals in Europe, 180~400m in metal mine in Russia, and at 150m in Kolar mine in India [13-15]. In this mine, the depth of engineering is 1 060m at 1 261m level in the eighth orebody, which indicated the intense rockburst proneness.

5.2 Mechanisms of Rockburst

With the excavating of the tunnel, rockmass of the tunnel locates under the state of uniaxial or low confining pressure, which occurred spalling at ‘shoulder’ by horizontal in-site stress. According to the results of uniaxial compression test of rock, it can be known that the fracture of rock specimen in the state of brittle failure was divided into two patterns: One is tensile crack, which is characterized by the parallel of crack plane to the acting direction of main stress; the other is the inclined shearing plane. Their failure characteristics were corresponding to those of both split-loosening type and tensile-shear shooting type rockburst.

In the mining area, the site investigation showed that the tensile crack was the main failure mode for the rockmass of hanging wall under the condition of in-situ stress level. The failure characteristic of rockburst was a brittle and unstable split failure, which occurred under the condition of higher stress level. Obviously, the brittle failure of host rock was a deciding factor for the characteristics of rockburst failure. The results can be used as an important geological basis to predict and prevent rockburst in the process of drift excavating in the mining area.

6 Conclusions

According to the experimental results combined with the geological investigations on site, the medium

rockburst or intense rockburst proneness exists at the levels of mining at 1331m and 1391m. The stress concentration at rock wall increases with the mining activity around engineering. Therefore, in mining design, the mining method, stopping sequence and stopping structural parameters should be considered adequately to avoid the high stress concentration and prevent a large-size rockburst. The conclusions provide the genesis and mechanisms of rockburst in deep hard mines, and offer a basis for large scale rockburst prevention.

Acknowledgments

We thank the financial support from the Key Technology P&D Program supporting project of the National ‘Eleventh Five-Year-Plan’ of China (No.2006BAB02A01).

References

1. Tang, S.H. and Chen, J. The Law and Mechanism of Rockburst Occurring in Huize Lead—Zinc Mine. in Fifth International Conference on Case Histories in Geotechnical Engineering, (New York, 2004).
2. Dou, X.H., Yuan, Y. and Zhang, C.X. Geological Disasters of Metal Mines and Trend in Their Research. *Met. Mine*, 2006, 6. 1-4.
3. Xu, L.S., Wang, L.S. and Li, T.F. Present Situation of Rockburst Research at Home and Abroad. *J of Yangtze River Scientific Research Institute* 1999, 19 (4). 4:24-27.
4. Li, G.Y., Li, J.L., Zhao, X.J., et al. Forecasting and prevention Technology of Rockburst in Deep Tunnel. *J. of Henan Polytechnic University*, 2006, 25 (4). 266-269.
5. Wang, C.L., Xu, B.G. and Li, S.L. Sound Wave Measurement of Rock Mass for Fankou Deep Orebody. *Chinese Mining Technology*, 2003, 23 (1) .41-42.
6. Xiong, Z.Q. and He, H.J. Approach to Controlling Measurements of Rockburst in Deep Tunnel with Hard Wall rock. *IM&P*, 2006; 35 (9):25-27.
7. Xu, L.S. and Wang, L.S., Study on the Mechanism of Rockburst. *J. of Chongqing University (Natural Science Edition)*, 2001, 30 (2):115-117.
8. Tang, S.H., Wu, Z.J. and Chen, X.H. Approach to Occurrence and Mechanism of Rockburst in Deep Underground Mines. *Chinese Journal of Rock Mech Eng*, 2003, 22 (3). 1 250-1 254.
9. Guo, R., Pan, C.L. and Yu, R.C. Theory and Technology of Orebody Mine in Rockburst Proneness Hard Rock. Metallurgical Industry Press, 2003.
10. Xu, L.S., Wang, L.S. and Li, Y.L. Study on Mechanism and Judgment of Rockburst. *Rock and Soil Mechanics*, 2002, 30 (3): 300-303.
11. Xu, D.J., Zhang, G. and Li, T.J. Study on Stress State of Rockburst. *Chinese Journal of Rock Mech Eng* 2000, 43 (2). 169-172.
12. Barton, N.A.Q. System Case Record of Cavern Design in Faulted Rock. In *Proc. Symposium on Tunneling in Difficult Conditions*, (Turino, 1994).
13. Shivakumar, K., Rao, M.V.M.S., Srinivasan, C., et al. Multifractal Analysis of the Spatial Distribution of Area Rockburst at Kolar Gold Mines. *Int. J. Rock Mech. Min. Sci.&Geomech. Abstr*, 1996, 33 (2).167-172.
14. Srinivasan, C., Arora, S.K. and Benady, S. Precursory Monitoring of Impending Rockbursts in Kolar Gold Mines from Microseismic Emissions at Deeper Levels. *Int. J. Rock Mech. Min Sci*, 1999, 36 (7). 941-948.

15. Arora, S.K., Willy, Y.A., Srinivasan, C., et al. Local Seismicity Due to Rockbursts and Near-field Attenuation of Ground Motion in the Kolar Gold Mining Region, India. *Int. J. Rock Mech. Min Sci*, 2001, 38 (5). 711-719.

SAFECOMINE INTRINSICALLY SAFE SYSTEM FOR MONITORING OF HAZARDS IN MINES RELATED TO DISTURBANCE OF THE STRATA AND ENVIRONMENT EQUILIBRIUM

ZBIGNIEW ISAKOW

*Department of Geophysical Systems, Research and Development Centre for Electrical Engineering and
Automation in Mining – EMAG, Katowice, Poland*

A structure and operating of SAFECOMINE - intrinsically safe system for monitoring of risk in mines, related to disturbance of the strata and environment equilibrium have been described. The system has a modular structure and consists of several cooperating sub-systems: seismo-acoustic ARES-5/E, seismic ARAMIS M/E, GEOTOMO/E and seismic at surface ARP 2000 P/E. The sub-systems record current physical parameters (velocity and acceleration) of spatial vibration field of the strata. The excitation of spatial vibration field can be resulted by the group of natural events connected with fracture of the strata, like: bumps accompanied by vibrations as well as by subsidence on surface. The information recorded by the measurement network consisted of sub-systems placed on the area of one or more mines can be integrated in time by the use of time markers generated by GPS clock. The system controls risk on the area of mine with special attention to longwalls. By the use of seismic, seismo-acoustic and small diameter borehole-drilling methods the system allows for comprehensive assessment of rock bumps risk in areas of workings. The system allows for determination of the stress concentration area in front of the longwall by the use of attenuation-tomography methods, where the shearer is used as a source of imaging wave. Passive tomography and natural seismic events are the second method used by the system for determination of the stress concentration area in front of the longwall. The parts of the system operating in the areas hazarding by methane explosion are intrinsically safe and can be supplied remotely from the surface. Such solution allows the system to keep its metrological functions at any conditions, independently of the underground power-net state. Several dozen of sub-systems from SAFECOMINE were implemented in many Polish mines, some in China and Russia and few in Ukraine.

1 Introduction

Intrinsically safe seismic and seismo-acoustic systems developed and produced by EMAG Centre are widely used in the Polish coal and copper mines.

In the South-African and Australian gold, diamond, and copper mines, as well as in many other locations, the ISSI Ltd of South Africa [5] and Hyperion Seismic Monitoring System designed by Engineering Seismology Group Canada INC are being utilized. Chen, Gray, and Hudyma [1] used the hyperion system to monitor mining seismicity and research the rock mass response to gold mining under high stress conditions. These systems have good technical parameters and great dynamics, but do not fulfil the intrinsic safety demands of long transmission lines or they don't allow central supply from the surface.

The author was a leader of the Eureka project E!3355 - SAFECOMINE [4]. The project was designed to develop and apply the new system in order to monitor and predict seismic and environmental hazards in underground and open pit mines.

The EMAG R&D Centre for Electrical Engineering and Automation in Mining in Poland and the Institute for Complex Managing of Natural Resources at the Russian Science Academy of Moscow were partners in the Eureka project. In reference to the agreement on co-operation, this project was supported by the ISSI International Ltd of Stellenbosh in South Africa and Tuzla University of Bosnia and Herzegovina.

The SAFECOMINE system consists of many subsystems. Systems described in this article: ARES-5/E, ARAMIS M/E, GEOTOMO/E and ARP 2000P/E are SAFECOMINE subsystems.

2 Rock-bump hazards monitoring systems

2.1 Seismo-acoustic method control

The seismo-acoustic system ARES-5/E (Fig.1) has been developed to assess rock-bump hazards in mines, in accordance with the principles included in the seismo-acoustic method for hazards assessment which is in force in Polish mines. A basic task of the system is to process, by means of SP 5.28/E geophone probes (mounted on anchors in walls of advanced galleries), the velocity of mechanical strata vibrations, and then, after amplification and filtration in N/TSA-5.28/E transmitters, the transfer of the measured signals to the Geophysical Centre on the surface by means of a telecommunications cable network and receiving circuits of the OA 5/E surface station. Digital processing of obtained signals and their computer interpretation is performed at the surface part of the system.

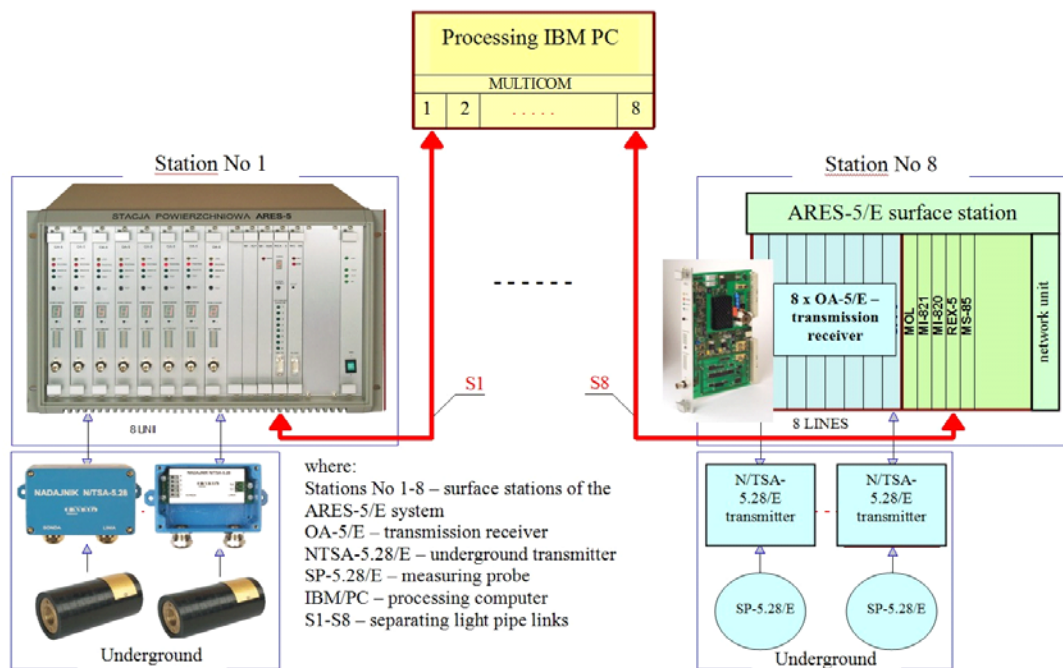


Figure 1 Structure of seismo-acoustic system ARES-5/E.

The ARES-5/E system, including a full set of equipment for one surface station, consists of underground equipment (SP-5.28/E type measuring probe, N/TSA-5.28/E underground transmitter) and surface equipment (surface station of the ARES-5/E system, speaker for replay of measuring probe signals, optical fibre separating link S, personal computer with a monitor and printer, used both as a processing unit and surface terminal).

In the ARES-5/E system, there are available up to 8 cassettes connected to one PC including the ARES_OCENA software. Thus, the maximum number of measuring channels in the system is 64 items. The software being applied perceives the ARES-5/E cassette modules as one 64-channel module, so the data

recorded by particular geophones can be configured, grouped and presented on the monitor screen according to a user's request. Frequency of data sampling - the system parameter (default 1 minute) - may be modified, along with the interval of refreshing other current values of calculated indexes (average values, deviations). Hour and shift data are calculated on the basis of minute data. On the screen, both minute, hour and shift data recorded in different ARES channels can be observed at the same time. The screen consists of windows including graphs. The user can group the graphs, e.g. place in one window all graphs presenting the data recorded by geophones from hazardous workings and in another one the graphs of geophones ordered by names of workings, etc. The recorded screen configuration can be saved for future retrieving. Switching between screens (windows) is quick and user-friendly.

The user may select and determine a way of data presentation. The example of a printout of a seismo-acoustic activity diagram, performed for the selected time interval including marked bumps of minimum energy, has been presented in Figure 2.

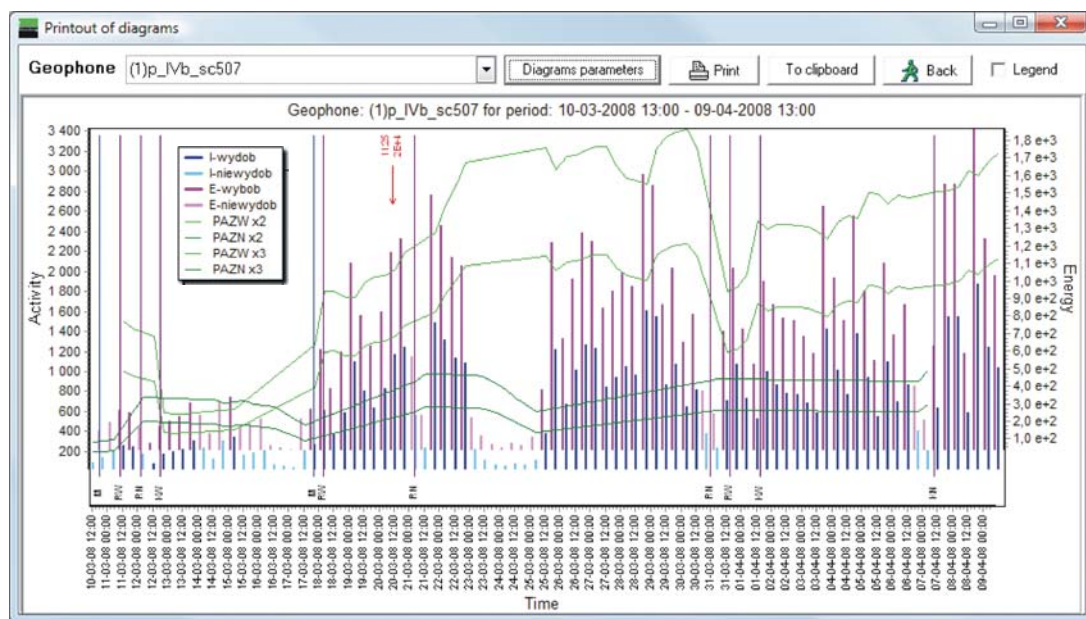


Figure 2 Printout of a seismo-acoustic activity diagram for the selected time interval

Interpretation process is based on:

- observation (measurements) of seismo-acoustic activity,
- observation (measurements) of quantity representing summarized pulse energy in a chosen period (i.e. energy intensity),
- mining, geological and exploitation data influencing the interpretation process.

PAZW average shift activity for working shifts (mining)

PAZN average shift activity for non-working shifts (non-mining)

I – Wydob average shift energy intensity for working shifts (mining)

I – Niewyd average shift energy intensity for non-working shifts (non-mining)

2.2 Microseismic method control

The ARAMIS M/E seismic system, together with the digital DTSS transmission module, permits tremor location, determining the energy of tremors occurring in the mine as well as seismic hazard estimation. Designed in the EMAG Centre, the DTSS intrinsically safe seismic transmission module provides the mains supply of underground transmitters from the surface, signal digitalisation at the seismic sensor site and transmission to the surface. A high level of registration dynamics of 110 dB, 0 150 Hz frequency band and interference-resistant transmission provide correct, saturation-free registration of low energy (10^2 J), as well as high energy signals, and identification of their characteristic phases. According to the extent of the mining area, the system is based on seismometers or, optionally, on low frequency geophones. The equipment is intrinsically safe and centrally powered from the surface. Digital data transmission allows triaxial transmitting (X, Y, Z) of the ground velocity movements by a single teletransmission line. Signal sampling is performed by (24 bit) Sigma Delta converters, providing high dynamics of conversion and recording. The system also allows continuous, on-line registration of seismic signals with the help of a recording server. The standard software provides registration of a single signal component per channel. An optional 3-component DTSS system requires a non-standard software version allowing using triaxial seismic sensors (seismometers or geophones).

A schematic diagram of the ARAMIS M/E system with DTSS digital transmission module is shown in Figure 3.



Figure 3 Schematic diagram of ARAMIS M/E

The ARAMIS M/E system consists of: ARAMIS M/E processing server comprising the ARAMIS_WIN software (location and energy determination) and the HESTIA software (seismic hazard evaluation), ARAMIS M/E recording server with the ARAMIS_REJ software and one (standard) or two (optional) digital DTSS transmission modules.

Each SP/DTSS surface transmission station is fitted with: OCGA digital receivers, ST/DTSS transmission control module with a GPS timer, mains switching module and a supply unit with a safety transformer.

The surface station functions together with SN/DTSS underground transmitting stations, each one fitted with: SPI-70 seismometer and NSGA seismic transmitter.

Optionally, NSGA seismic transmitters can be connected to: GVu geophones (mounted vertically on a bolt in the roof), GVD geophones (mounted vertically on a bolt in the floor), GH geophones (mounted horizontally on a bolt), SPI-70 seismometers in a CS/DTSS box (working along the Z-axis, or X,Y axes) and a geophone probe SG3 (mounted on anchor at a roof or a floor or in boreholes to be made in a roof or a floor).

In a standard version, the ARAMIS M/E seismic system is fitted with the ARAMIS_WIN software. It enables monitoring of seismic events in underground mines and performs the following functions:

- collecting records from the register in a continuous automatic mode with an instant preliminary processing (indicating characteristic phases of the signal, source location and energy determination),
- seismogram presentation,
- archiving records in ordered catalogues,
- opening signals stored in archives,
- convenient presentation of archive seismograms:
 - smooth amplitude magnification,
 - different modes of amplitude scaling,
 - expanding and shortening of the time axis; smooth and rough movement along the time axis, fast time window selecting,
- approval of settings in the operator's mode (correction of marker positioning with respect to characteristic signal phases, location and energy evaluation),
- presentation of an event location on a schematic mining map (with location in the operator's mode),
- hard copying of the seismogram,
- entering and modifying sensors description,
- programming seismic recording transmitters,
- selecting program options,
- selecting data for processing (location and energy),
- interaction with other programs:
 - ARP 2000 software used with the ARP 2000P/E system (linking the surface recorded data for better location of seismic events),
 - ARES_OCENA software used with the ARES-5/E system (linking recorded data for better location of seismoakustic events),

- ARAMIS_WIN/E software used with the ARAMIS M/E system (linking recorded data in adjacent mines for better location of seismic events),
- HESTIA software (transmitting the event data to the global database and supplying other data, e.g. names of workings or areas, etc.),

The HESTIA program functions are as follows (Hestia reports – Fig.4):

- automatic data collection (results of seismo-acoustic evaluation by ARES_OCENA and shift deviation values) from the systems other than ARAMIS M/E used in Polish mines (e.g. the seismo-acoustic system ARES-5/E),
- automatic data collection (date, co-ordinates, energy of seismic events) from the ARAMIS M/E system,
- recording small-diameter drillings results,
- automatic seismic hazard assessment by means of the summary and complex methods,
- automatic seismic hazard assessment by means of the seismology method and small-diameter drillings. Optionally, by means of the seismo-acoustic method, provided that there is an ARES system in use in the mine,
- printing reports: daily report on seismic hazards, reports on seismic activity (huge configuration possibility),
- entering details of the mine structure (names of seams, areas, workings co-ordinates, shift advance, etc.) and parameters for hazard estimation (e.g. critical drillings yield value with small-diameter drilling).

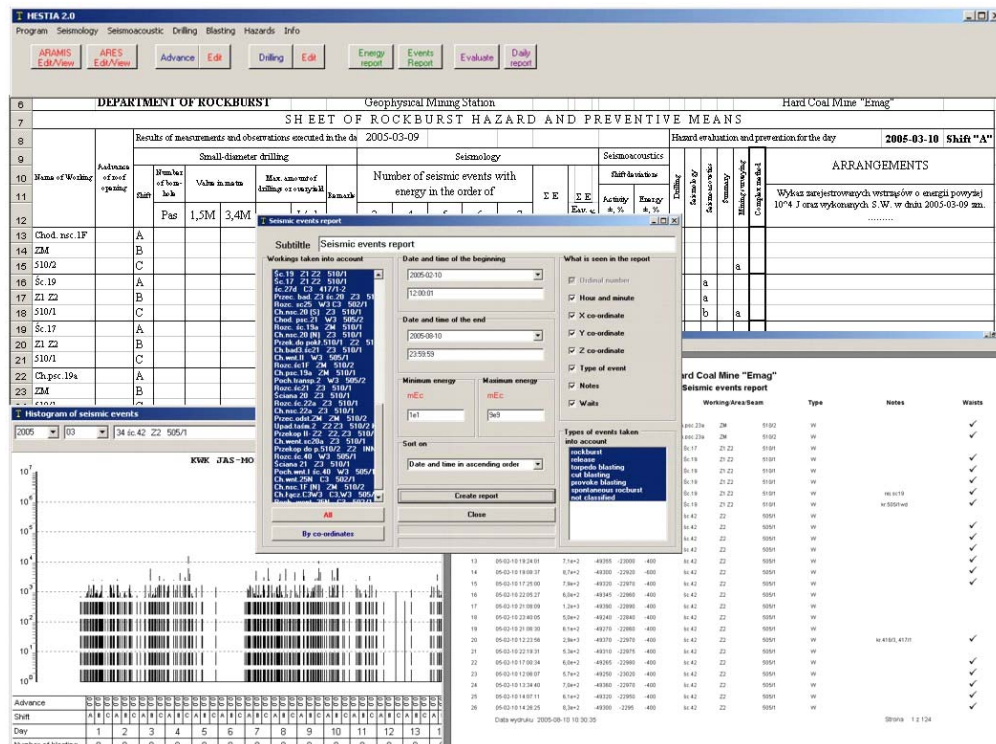


Figure 4 HESTIA reports.

2.3 Geotomography method control

The new Polish intrinsically safe system GEOTOMO/E, developed at the EMAG under direction of the author has been designed for monitoring relative-stress changes that occur in the coal roof and seam in front of a longwall. Rock-mass imaging is achieved by seismic waves generated by the cutting head of a cutter-loader. This enables the detection of zones where stress is concentrated and the identification of their occurrences and the hazards they may induce. A seismic signal generated by the cutting head of a cutter-loader, the position of which is monitored in the course of penetrating the imaged area, is recorded by a properly configured network of sensors mounted in advanced galleries to provide optimal conditions for signal identification.

Signals detected by sensors installed in the coal roof and seam, after A/D conversion, are transmitted to the GEOTOMO/E seismic device, constructed especially for this purpose, that interfaces with the system that monitors the coal getting process (a system that provides information on the cutter-loader position) (Fig.5). The system has been made on the basis of the equipment of the ARAMIS M/E system and geophones GVu and GHa including appropriate software (Figure.6).

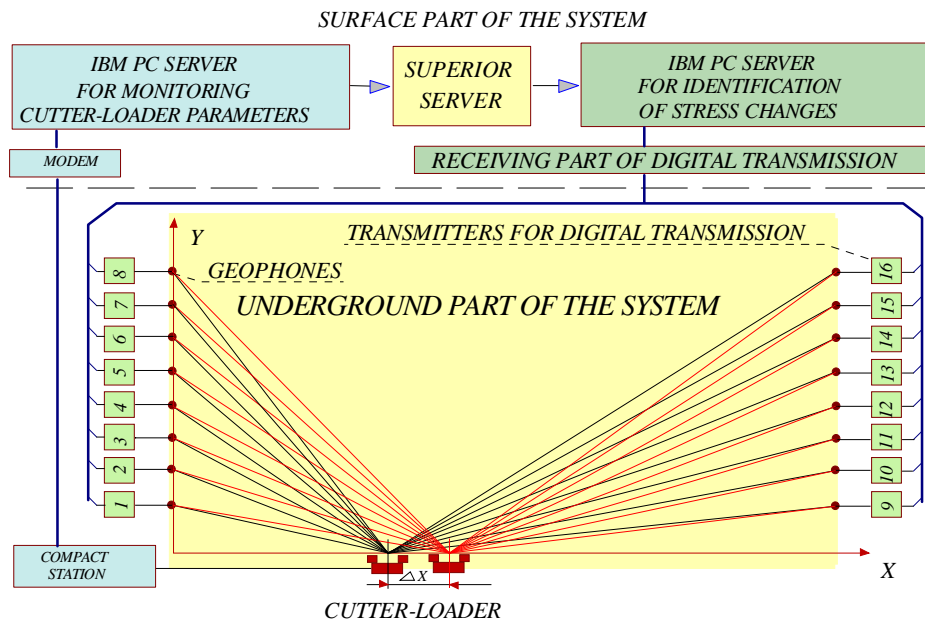


Figure 5 Structure of the interconnected systems for monitoring relative changes in stress and the coal getting process. (This figure is an example of sensors in the array scheme for coal-seam geo-tomography; a scheme for coal-roof geo-tomography is not shown.)

The digital transmission of data ensures a high-quality recording and enables a reduction both of the device-specific noise and noise generated by the telecommunication network. The interpretation of the recorded signal is based on algorithms verified in the analysis of continuous seismic monitoring results in the course of geological drilling. These algorithms are based principally on examination of the energy of the registered signals.

The method presented here enables the description of the distribution of coefficients for the elastic-wave attenuation in rock on the basis of registered decreases in average amplitudes of vibrations generated by the cutting head of the operating longwall cutter-loader. For the purpose of determining the attenuation coefficients

in the elementary cells, into which the monitored regions of the coal bed and roof in front of the longwall have been divided, the inversion algorithm [2, 3] was applied, based on matrix decomposition together with the method of solution regularisation in cases of high-level random noises.

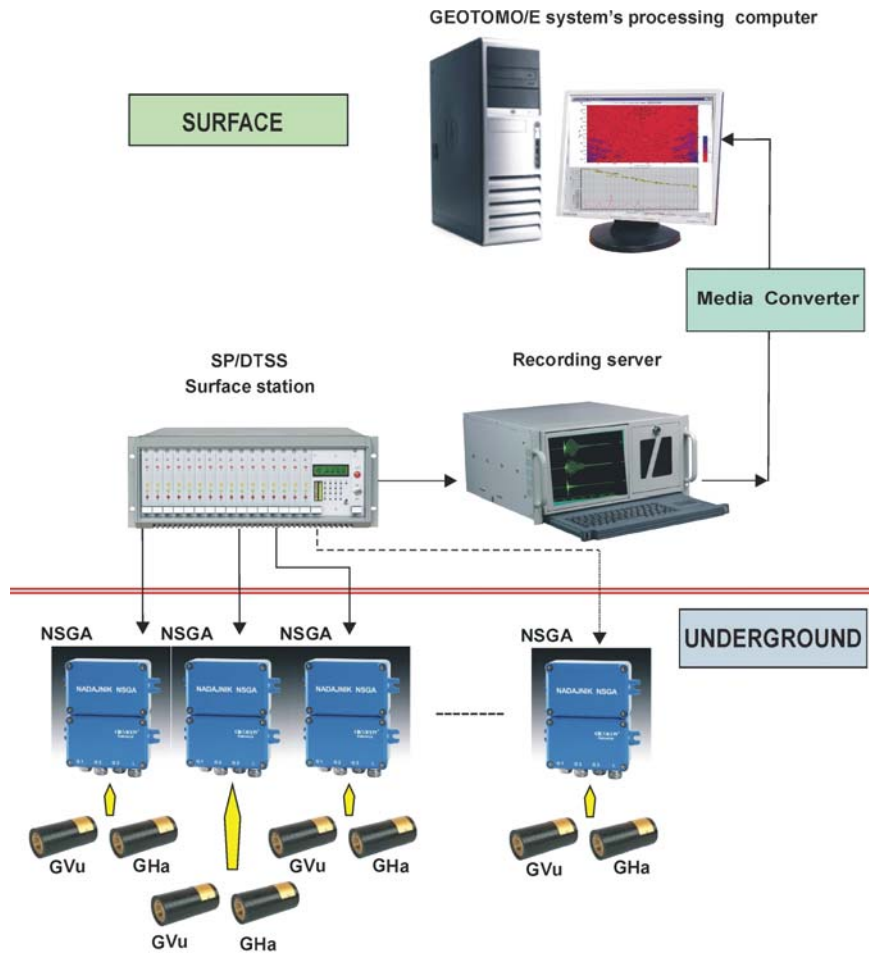


Figure 6 Structure of the GEOTOMO/E system for monitoring relative changes in stress in front of a longwall.

The standard GEOTOMO/E system for monitoring relative changes in stress consists of the following: GVu-type geophones, GHa-type geophones, NSGA underground transmitters, SP/DTSS surface station with digital OCGA receivers and ST transmission control module, recording server, separating network connector with the Media Converter, and the GEOTOMO/E system's processing computer.

The supply of the system's underground component is made centrally from the surface with the appropriate intrinsically safe voltage. Such supply ensures proper operation of the geophones and transmitters, unaffected by the incidental breakdowns in local supply network on the longwall or in close-to-longwall roads.

The intrinsically safe underground part of the system consists of seismic geophone GHa sensors installed horizontally in the seam on anchors adapted specifically for that purpose, and seismic geophones of the GVu

type installed vertically on anchors in the roof. Sensors are compatible with seismic NSGA transmitters. Each of the 16 seismic transmitters is compatible with 1 GHa sensor and 1 GVu sensor.

Sets of GHa/GVu sensors, together with an NSGA transmitter, are installed in both of the advanced galleries, symmetrically against the longwall front in 20-m intervals. Measurement points are established in 20m intervals, which, on the one hand are appropriate for coverage of the measured area, and on the other hand are sufficient when taking into account the limit of propagation of the seismic signal generated by the working element of a cutter-loader.

NSGA seismic transmitters serve as programmable “intelligent” underground-measurement concentrators that facilitate control of amplification and filtration of signals, switching of amplification between measurement channels in accord with the commands given from the surface, A/D conversion with dynamics not less than 100 dB, and digital transmission of data to the surface.

A sample result of operation of the system is shown in the Figure 7.

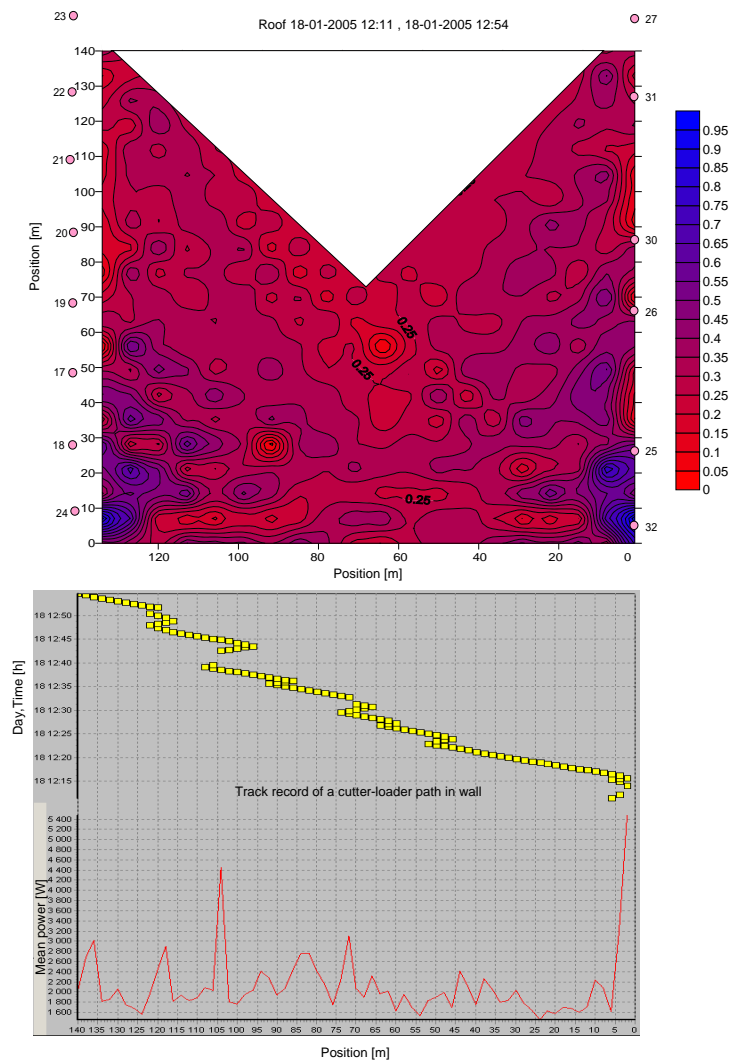


Figure. 7 Map of attenuation in a coal roof on 18 January 2005 as a result of cutting of wall no. 306 with a cutter-loader within the period of 12:11 to 12:54 hour, set against the track record of a cutter-loader operating path.

The information obtained, presented in the form of attenuation distribution changes (being approximately inversely proportional to stress changes) in front of the getting cutter-loader, enables optimisation of the performance of powered supports as well as selection of the most appropriate parameters of their operation, (supportiveness). Such information also improves the work safety in the mine workings. The results of measurements can be compared with other data, such as the value of active power consumption of a longwall cutter-loader during cutting. Thus, data can be obtained for calculating the relationships between control of sufficient support, relative-stress distribution within the longwall during cutting, and the energy expenditure necessary for completion of such an operation.

Analysis of the results obtained revealed a notable correlation of zones where the effects of stress changes (rock falls, outbursts) were manifested with the zones identified in the course of operation of the system monitoring the attenuation changes (approximately inversely proportional to the relative changes in stress). Such a coincidence is not accidental and positively verifies the operating system with regard to its accuracy in determining tensed or tightened zones (marked with various shades of red) as well as de-stressed and yield zones (marked with various shades of blue).

Verification tests for the performance correctness of the system for monitoring relative changes of stress in a coal seam and roof in front of a longwall, carried out in operating conditions, have proved the system's efficient performance has been considered most promising. The results obtained are stable and indicate a trend of occurring changes. Also it has been proved that the formation of dangerous stress waves in front of a longwall causes rock falls and side outbursts of coal. Diversification of stress is greater in the roof than in the coal seam, although the stress distributions are of similar character.

3 Monitoring of Hazards to the Surface by Means of Vibrations Caused by Mining Tremors

ARP 2000P/E is a digital telemetric system designed for recording and analysing low frequency vibrations of ground and buildings situated in hazardous areas with tremor occurrence as the results of mining, tectonic or traffic origin. Modular structure of the system facilitates creation of distributed measuring networks. Transfer of measured data is made by means of wireless GSM network.

The system is based on two kinds of sensors: one, two and three component acceleration probes or electrodynamic gauges – seismometers. Data concentrators assure very precise time base synchronization by means of satellite clock GPS.

Software applied in monitoring centre works under control of operating system Windows. It provides remote data collecting from data concentrators, storing and frequency analysis. Optionally specialized software for automatic assessment of harmful tremor influence including different standards is available.

ARP 2000P/E consists of two parts (Fig.8): a station and an object. Elements of the station part, situated in the surface hazard control centre, are: a computer of PC class fitted with GSM (Global System for Mobile Communications) modem for bi-directional, digital wireless communication with object concentrators, and software for archive, presentation and initial processing of recorded data. Elements of the object part are concentrators of measured data. Each concentrator is fitted with a telephone modem and GPS receiver. Optionally a portable computer – laptop may be used for transferring data from concentrators.

The parts of the system are:

- telephone modem GSM (dual band GSM modem 900/1800) of FALCOM – model Twist,
- GPS receiver with integrated antenna of GARMIN - model GPS35-LVS with “one second impulse” output for precise time measuring,

- one component seismometric sensor (SPI-70) named “transmitting station SN/ARP” or three component acceleration sensor type CZP3X (option),
- local measured data concentrator LKP-ARP type.



Figure 8 Shows ARP 2000P/E system structure with one component acceleration probes.

System assures vibration detection of mining seismic or traffic origin, synchronized recording of signals from one, two or three component sensors (of acceleration or seismometers) displaced in unlimited wide-spread area, digital wireless transmission of recorded data to the centre, where data are archived, and processed. The result of data processing is the assessment of harmful vibrations influence on surface objects in relation to legal standards.

Taking into account only telemetric functions, system provides:

- recording of ground vibrations by either three component electrodynamic (velocity) or optionally acceleration sensors, for frequency range from 0,5 – 100 Hz in many local concentrators distributed in wide-spread area,
- very precise time base synchronization by GPS in local concentrators and other recording devices located in neighbouring objects,
- recording of seismic events with great dynamics of measured signal variations; 90 dB is guaranteed by converting circuits nearby sensors and recording circuits of local concentrators,
- convenient measured signal to noise ratio,
- digital transmission to local concentrator via one pair telecommunication cable and digitally formed signal to RS-485 standard,
- possibility of bus communication of maximum four sensors connected to common trunk,
- detecting of significant seismic events in measuring concentrators, buffering records in SRAM memory and initial processing of recorded data,
- reliable, bi-directional, digital, wireless transmission via GSM between local concentrators and host computer,
- buffered, remotely controlled power supply of local concentrators.

4 Summary

In the years 2004-2006 within EUREKA!3353 project, EMAG realized SAFECOMINE system for monitoring and forecasting of risk related to disturbance of the strata and environment equilibrium designated for the underground and open-cut plants of natural resources in mining. The effect of carried out and verified in lab and field trials results have been implemented as prototype versions of the system.

Seismic ARAMIS M/E and seismo-acoustic ARES-5/E systems, in performance designated for Russian market, obtained positive opinion of certifying unit in Moscow SERITUM and on the basis of certificates issued by Russian Federation Mining Authorities have been approved to apply in Russian mines. Seismic system ARAMIS M/E collaborating with system for monitoring of surface hazards ARP2000P/E has been approved to apply in Chinese mines. All elaborated systems of SAFECOMINE system have been broadly implemented, also in Polish mining plants.

In 2004-2008 new installations of EUREKA!3353 systems were performed:

- Seismic systems ARAMIS M/E in Hua Feng, Tiger (Lahutai) Mine in People's Republic of China, KUZBAS Union – Piervomaiskaia Mine (Russian Federation), Zasiadko Mine (Ukraine), in JAS-MOS, Marcel, Rudułowcy-Anna, Zofiówka, Jankowice, Sośnica –Makoszowy, Piast and Bielszowice coal mines in Poland;
- Seismo-acoustic systems ARES-5/E in KUZBAS Union – Piervomaiskaia Mine (Russian Federation), Zasiadko Mine (Ukraine), in Huating, Yambei, Huafeng Mine in People's Republic of China in Knurów, Kazimierz –Juliusz, Rydułowcy-Anna, JAS-MOS, Staszic, Piekary, Piast, Marcel, Zofiówka, Wesola and Jankowice coal mines in Poland;
- Seismic systems for recording of vibrations at surface ARP2000P/E installed in Hua Feng Mine in People's Republic of China, in Wesola, Knurów, Staszic, Zofiówka, JAS-MOS, Kazimierz-Juliusz, Piast, Jankowice coal mines and several in KGHM Polska Miedź O/ZG Rudna copper mine;
- Intrinsically safe GEOTOMO/E system was installed and tested in the “Bielszowice” hard coal mine.

The research and development works currently conducted on the systems aim at a program integration of the measuring networks of the systems being in use in order to gain new opportunities of explanation of events by compression of measuring points within especially hazardous areas (e.g. a longwall) and by diversification of their placement in the space (in particular vertical). This will allow more accurate location and a broad use of a passive tomography to determine the points of stress concentration.

References

1. Chen, D., Gray, L. and Hudyma, M.R. Understanding mine seismicity – A way to reduce mining hazards at Barrick's Darlot Gold Mine. Proc.of the 6th Symposium on Rockburst and Seismicity in Mines, (ed. Potvin Y. and Hudyma M.) ACG, Perth, Australia, 2005, 269-274.
2. Golub, G.H., and Reinsch, C., Singular Value Decomposition and the Least Squares Solutions. Numer. Math., 1970, 14, 403–420.
3. Isakow, Z., Initial Experience on Operation of a System for the Continuous Monitoring of Stress Changes in Front of a Longwall. Mechanization and Automation in Mining Industry, 2003, 1/385, 32–53
4. Isakow, Z. System for Monitoring risks in Mining Connected with Disturbance of the Strata and Environment Equilibrium. Project Eureka number E!3355 –SAFECOMINE., 2006, Final Report.
5. Lynch, R. A., Wuite, R., Smith, B.S. and Cichowicz, A. Microseismic Monitoring of Open Pit Slopes. in Proc.of the 6th Symposium on Rockburst and Seismicity in Mines, (Australia, 2005).

SCALING LAWS AND THEIR IMPLICATIONS FOR RE-ENTRY PROTOCOL DEVELOPMENT

JAVIER-A. VALLEJOS and STEPHEN-D. MCKINNON

Department of Mining Engineering, Queen's University

Kingston ON K7L3N6, Canada

The statistical properties of empirical scaling relations, such as the modified Omori's law $n(t)=K(c+t)^{-p}$ for the temporal decay of aftershocks following a main event and Båth's law Δm for the magnitude of the largest aftershock are examined for mining-induced aftershock sequences in a number of mines in Ontario, Canada. We focus our attention on significant statistical correlations of seismic parameters for re-entry protocol development after blasts and large events. The Omori's law parameters along with their error assessment are estimated using the maximum likelihood method and considering only the time interval that satisfy power-law behaviour ($c=0$). The sites analysed presented normally distributed p values, ranging from 0.4 to 1.6. The parameter K can be satisfactorily expressed as $K=\kappa N_{1 \text{ hour}}$, where κ is well represented by a log-normally distributed variable with parameters μ and σ , and $N_{1 \text{ hour}}$ is the measured number of events occurring during the first hour after the main event. We found that μ and σ are in a well constrained range with mean values of 0.334 ± 0.060 and 0.146 ± 0.043 , respectively. Using Monte Carlo simulation, isoprobability curves are derived for estimating a re-entry time after a main event. Båth's law was evaluated for seismic moment magnitude. The results are more scattered due to the limitations of microseismic monitoring systems to appropriately quantify large magnitude events. However, normally distributed values of Δm were found at the three sites, with a mean value of 1.25 ± 0.31 . Mining-induced aftershock sequences present similar scaling properties to earthquakes. The practical implications of these statistics for re-entry protocol development one hour after a main event are: (1) a probabilistic re-entry time can be estimated; (2) the most probable largest aftershock for a specific time window can be estimated.

1 Introduction

Prediction of the time and location of seismic events, whether they are crustal-scale earthquakes or mining induced events, remains an unsolved problem. It has been recognized for some time now that seismicity in the earth's crust is a complex dynamical problem exhibiting many elements of chaotic behaviour, implying that prediction will not be possible [2, 9]. Despite our limited understanding of the mechanisms involved, certain characteristics of aftershocks have been recognized that enable useful decisions on tasks such as re-entry to be made.

Aftershock characteristics of crustal-scale seismic events have been studied extensively with the objective of understanding the basic physics of the process and for application to hazard assessment. Aftershock statistics are attributed to a number of causes. Stress change induced by the main event clearly has some influence, either in terms of static stress change [4, 21] or dynamic stress change [7, 12]. Other mechanisms have also been proposed including stress corrosion [6], and damage mechanics [19]. Despite the natural variability associated with aftershock sequences, most results are expressed in terms of scaling laws. These laws are statistical fits of functions to observable patterns of aftershock sequences, and regardless of whether they explain the underlying physics the patterns that they fit are valuable in terms of applications such as the development of re-entry protocols. Two such scaling laws are

- 1) The modified Omori's law [18, 22, 23] describes temporal decay rate of aftershocks after a main event. Statistical evidence for the validity of the modified Omori's law (MOL) applied to mining-induced

seismicity and preliminary guidelines on how to use it for re-entry protocol development have been proposed [24, 25]. In this study, we use aftershock statistics of the MOL in connection with Monte Carlo simulations to establish probabilistic re-entry times.

- 2) Båth's law [3] states that the difference in magnitude between the main event and the largest aftershock is a constant, independent of the main event magnitude. In this paper we redefine Båth's law based on the temporal characteristics of the aftershock sequences. This result will be useful in selecting values for parameters such as the magnitude of re-entry resetting events.

The primary purpose of this paper is to study the statistical properties of mining-induced aftershock sequences. To accomplish this, we have applied the two scaling relations to 172 mining-induced aftershock sequences from three different mine sites in Ontario, Canada, namely: Copper Cliff North, Kidd Creek and Macassa. Additional results from another four mine sites are provided.

2 Data and Methods

Details of the sites analyzed, the methodology employed for identifying aftershock sequences and processing the data, have been published elsewhere [24, 25].

3 Omori's Law

The temporal decay rate of aftershocks is described by the modified Omori's law [18, 22]:

$$n(t) = \frac{K}{(c+t)^p} \quad (1)$$

where $n(t)$ is the rate of occurrence of aftershocks, t is the elapsed time since the main event, c is a time offset constant, p is a parameter that determines the speed of decay and K is an activity parameter.

3.1. Estimation of the Decay Parameters

The parameters K , c , p and their uncertainties ΔK , Δc , Δp are estimated by the method of maximum likelihood [17]. If the occurrence times t_i ($i=1, \dots, N$) of the individual events are available in a target time interval $[T_A, T_B]$, the following log-likelihood function becomes available:

$$\ln L(K, c, p, T_A, T_B) = N \ln K - p \sum_{i=1}^N \ln(t_i + c) - KA(c, p, T_A, T_B) \quad (2)$$

where

$$A(c, p, T_A, T_B) = \begin{cases} \ln(T_B + c) - \ln(T_A + c) & \text{for } p = 1 \\ \left[(T_B + c)^{1-p} - (T_A + c)^{1-p} \right] / (1-p) & \text{for } p \neq 1 \end{cases} \quad (3)$$

As a goodness of fit the Anderson-Darling statistic W^2 [1] is used:

$$W^2 = -N + \sum_{i=1}^N (2i-1) [\ln(u_i) + \ln(1-u_{N+1-i})] \quad (4)$$

where u_i is the cumulative density function after time t_i , which for a MOL process is given by:

$$u_i = \begin{cases} \frac{\ln(t_i + c) - \ln(T_A + c)}{\ln(T_B + c) - \ln(T_A + c)} & p = 1 \\ \frac{(t_i + c)^{1-p} - (T_A + c)^{1-p}}{(T_B + c)^{1-p} - (T_A + c)^{1-p}} & p \neq 1 \end{cases} \quad (5)$$

$W^2=0$ indicates a perfect fit. We will assume that sequences with $W^2 \leq 1.0$ conform to a MOL [15, 16].

From the above equations the following steps are used to estimate the MOL parameters:

- 1) Specify a target time interval $[T_A, T_B]$.
- 2) Maximize the log likelihood function.
- 3) Test if the proposed decay relation adequately describes the aftershock sequence ($W^2 \leq 1.0$).

There are numerous time intervals that satisfy $W^2 \leq 1.0$ for a given aftershock sequence. We adopt the method proposed in [24] which attempts to estimate the maximum time interval $[T_S, T_E]$ that follows power-law behaviour ($W^2 \leq 1.0$, $c=0$). Figure 1 illustrates the estimated power-law time interval, with the corresponding MOL parameters, for a blast related aftershock sequence.

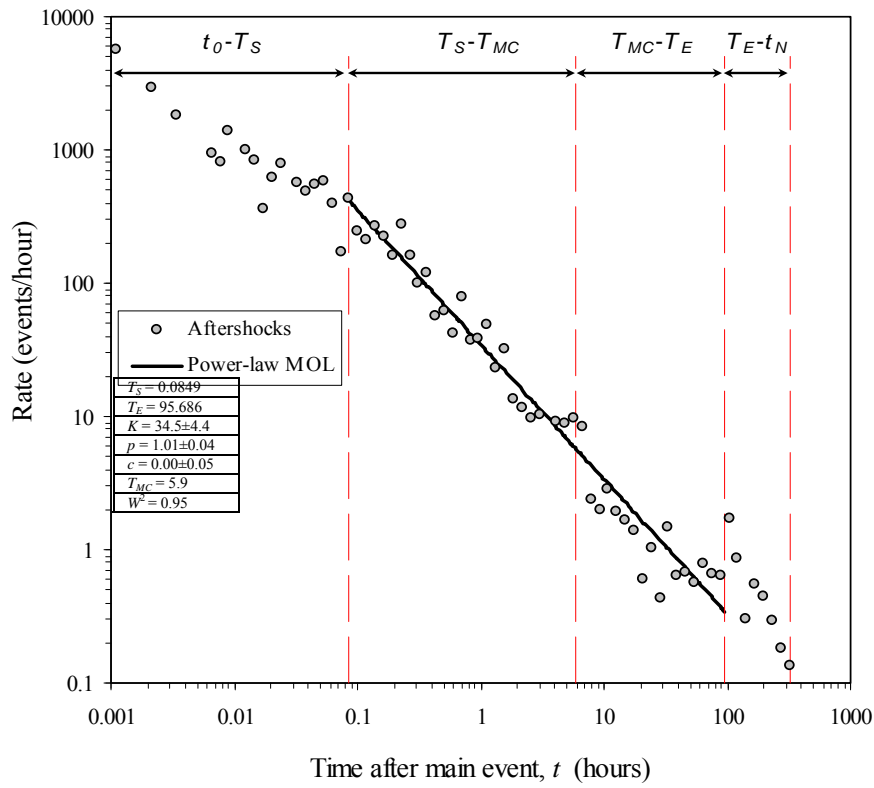


Figure 1 Different stages for a blast related aftershock sequence

At least four different stages can be identified from figure 1.

- 1) t_0-T_S : Initial noisy stage before the beginning of the power-law decay. Several factors may affect the decay during this stage, such as; overlapping of seismic records that make it difficult to identify and locate the many event [11], a complex process which the Omori equation is not able to adequately describe, or the sequence may actually begin gradually and build to a higher rate before the onset of smooth decay [10].
- 2) T_S-T_{MC} : Once the power-law decay starts, there is a characteristic point corresponding to the maximum curvature, given by:

$$T_{MC} = \left[Kp \sqrt{\frac{2p+1}{p+2}} \right]^{\frac{1}{p+1}} - c \quad (6)$$

This point defines the transition from high to low event change rate [24]. This can be demonstrated by replacing Eq. (6) in the first derivative of Eq. (1):

$$\dot{n}(T_{MC}) = \frac{dn(T_{MC})}{dt} = -\sqrt{\frac{p+2}{2p+1}} \quad (7)$$

For the typical range of p values found in mining-induced aftershock sequences, between 0.4 to 1.6, $\dot{n}(T_{MC})$ can range from 1.15 to 0.93. The implication is that after T_{MC} the change in event rate starts to decrease at a speed of approximately less than one.

- 3) T_{MC} - T_E : After T_{MC} the power-law decay can continue until a time where the data starts to deviate from a single MOL ($W^2 > 1.0$).
- 4) T_E - t_N : T_E defines the end of the power-law regime and a transition to a different process [24], while t_N is the last event identified by the (temporal) clustering algorithm. In figure 1, T_E is coincident with the start of a secondary aftershock sequence.

In the following sections we present statistics for the estimated parameters K and p , and for the start T_S and end T_E times of power-law decay.

3.2. Start T_S and End T_E Times of Power-Law Decay

Figure 2 provides the population distribution of the estimated start and end time of power-law decay for seven different mine sites. In general, the decay of mining-induced aftershock sequences starts during the first hour after the main event (figure 2(a)). On the other hand, the end time of the power-law process may commence over 100 hours after the mainshock, but median values range between 14 to 22 hours, which is driven by the mining process (figure 2(b)). The Macassa site presented the largest 95% percentile as a consequence of the large average time between large blasts.

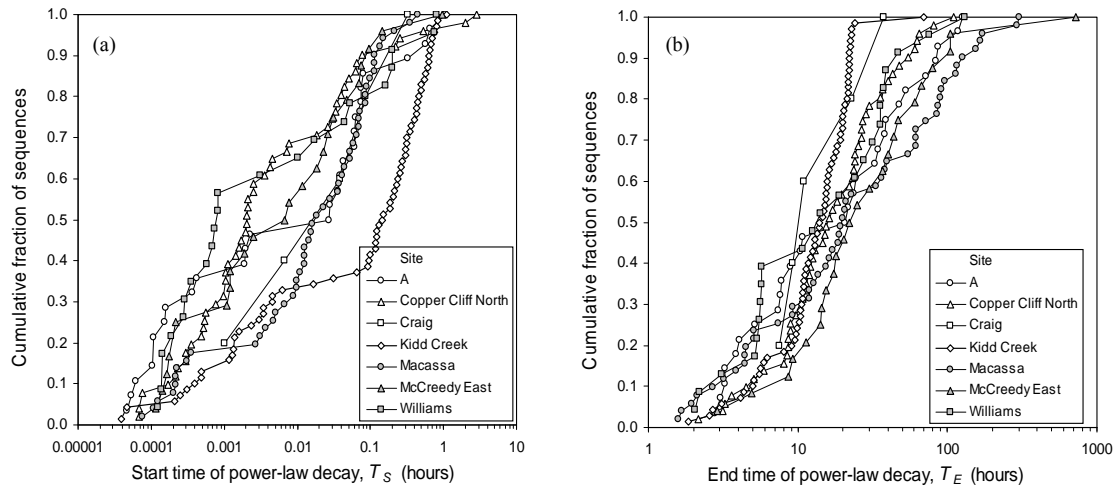


Figure 2 Start and end times of power-law decay for seven different mine sites

3.3. p and K Values

Figure 3(a) presents the distribution of p values estimated for the power-law time interval at the three sites of interest. Each distribution seems to represent site specific conditions, with higher mean p values for the Kidd Creek and Macassa sites. In the crustal scale literature, this variability has been related to the properties of the fault system and surrounding lithosphere [13, 14], but it is still not possible to draw conclusions about the significant factors that affect the p value in aftershock sequences.

Theoretical and empirical correlations between the parameter K and the number of events measured during the first hour after the main event $N_{1 \text{ hour}}$ were proposed [24]. K can be adequately expressed by:

$$K = \kappa N_{1 \text{ hour}} \quad (8)$$

where κ is a site specific parameter obtained by a least squares fit between K and $N_{1 \text{ hour}}$. By excluding cases with $\kappa > 1$ and $T_S > 1$, the coefficient κ presented a surprisingly narrow range, between 0.25 and 0.50, with an average of 0.35 ± 0.07 , for seven different mine sites in Ontario [25]. In order to incorporate the previously excluded cases in the analysis we test if there is any significant distribution for representing the complete population of $\kappa = K/N_{1 \text{ hour}}$. We found no significant statistical departure from a two parameter log-normal distribution, as shown in figure 3(b). Table 2 presents the maximum likelihood estimates of the log-normal parameters, μ and σ , with their corresponding Chi-square significance levels for seven different sites in Ontario. The two parameters that best describe these distributions are in a well constrained range.

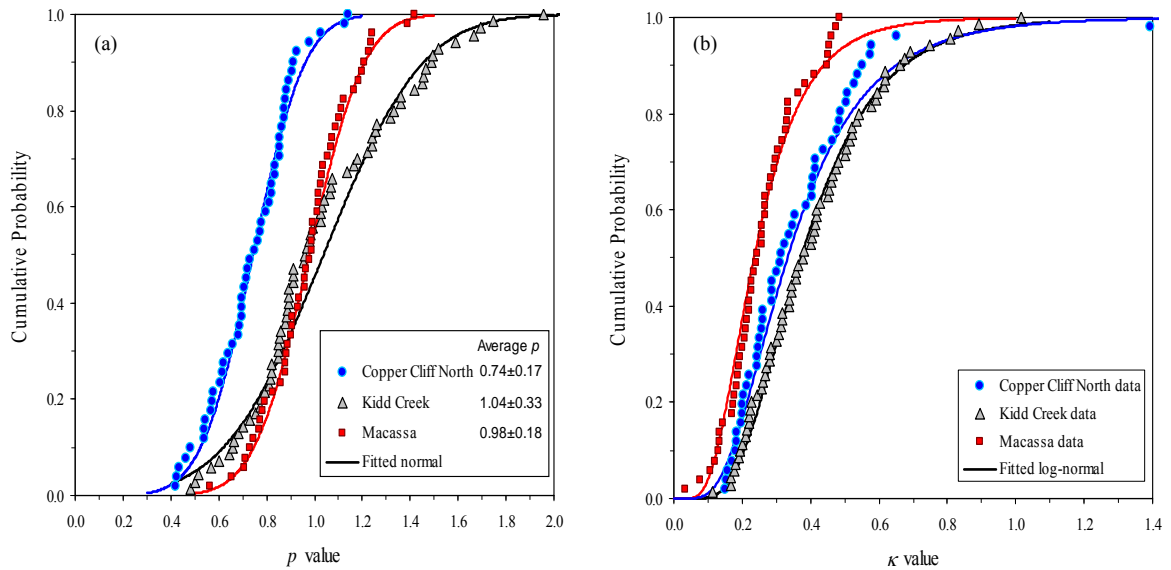


Figure 3 Population of p and κ for the three sites under study with their corresponding fitted distributions

Table 2. Estimated parameters and significance levels for a log-normal distribution representing the complete population of κ

Site	min κ	max κ	μ	σ	Chi-Square significance level
A	0.159	0.953	0.306	0.124	0.320
Copper Cliff North	0.149	2.189	0.382	0.214	0.764
Craig	0.131	0.401	0.289	0.123	0.655
Kidd Creek	0.115	1.015	0.414	0.202	1.000
Macassa	0.034	0.483	0.264	0.137	0.801
McCreedy East	0.142	0.545	0.290	0.104	0.965
Williams	0.232	0.761	0.394	0.121	0.952
min =	0.034	0.401	0.264	0.104	0.320
max =	0.232	2.189	0.414	0.214	1.000
mean =	0.137	0.907	0.334	0.146	0.779
S.D. =	0.059	0.612	0.060	0.043	0.238

3.4. Probabilistic Re-Entry Protocol

The well-defined distributions presented by the seismicity parameters p and κ , can be incorporated into a Monte Carlo simulation to derive probability distributions of re-entry times. By replacing Eq. (8) in (6), for a power-law process ($c=0$), we obtain an expression for the time of maximum curvature as a function of the variables κ and p , and the input N_1 hour. Isoprobability plots for T_{MC} as a function of N_1 hour are obtained for the three sites under study, as shown in figure 4. These plots are interpreted directly as the probability that T_{MC} is lower than a certain time t for a given N_1 hour. As a reference the least squares fit between T_{MC} and N_1 hour are also indicated in figure 4.

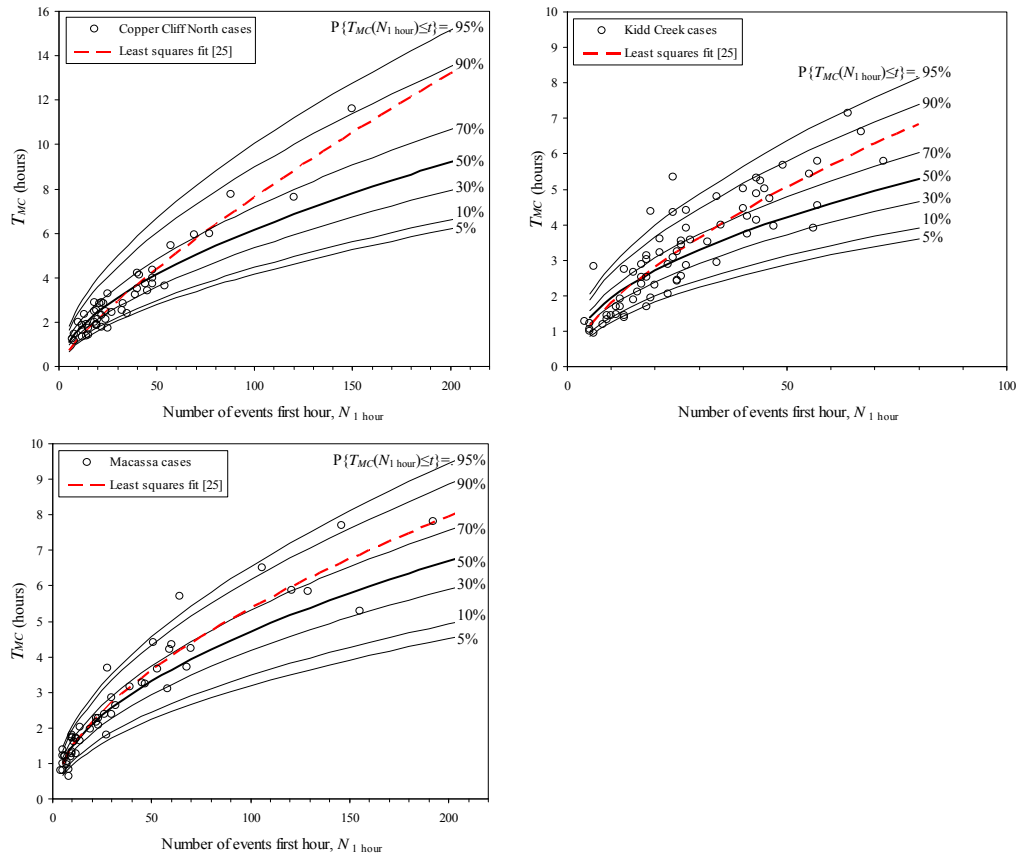


Figure 4 Isoprobability plots for T_{MC} as a function of N_1 hour for the sites under study

Current re-entry practices are based on the requirement for the monitored parameter to return to a previously defined background/normal level of seismicity for a specified time window, which is known as the background time window. Based on a survey on current re-entry practice [25], mines typically use a background time window of 2 hours, although this is a relatively arbitrary choice. Given the inherent variability of the event decay rate displayed in figure 4, we propose a background time window as the difference in T_{MC} for the 95% and 50% probabilities:

$$\Delta T_{BW} = T_{MC_{95\%}} - T_{MC_{50\%}} \quad (9)$$

4 Båth's Law

This scaling relation states that the difference in magnitude between the main event and its largest aftershock is approximately constant, independent of the magnitude of the main event [3]. That is:

$$\Delta m = m_{ME} - m_{LA} \approx \text{const} \quad (10)$$

where m_{ME} and m_{LA} are the magnitude of the main event and largest aftershock, respectively. The scaling associated with Båth's law implies that the stress transfer responsible for the occurrence of aftershocks is a self-similar process [20]. For crustal earthquakes this difference is typically taken to be $\Delta m \approx 1.2$. Many studies have confirmed Båth's law, however Δm seems to differ from sequence to sequence, with large fluctuations between 0.0 and 3.0 [5, 8, 22]. In terms of re-entry protocol development, large magnitude aftershocks could occur during the background time window. Båth's law provides a potential method to estimate the magnitude of the largest aftershock.

From a preliminary analysis of mining-induced aftershock sequences, it was determined that the majority of the larger aftershocks have a tendency to occur close to the first event in the sequence. In addition, for some sequences, the largest magnitude event was not always associated with the initiation of the sequence. These considerations limited the direct applicability of Båth's law to mining-induced seismicity. In order to be useful for re-entry purposes, Båth's law should consider the main event as the largest magnitude induced at the beginning of the sequence and the largest aftershock at a latter stage in connection with the aftershock decay rate. We considered the following adjustments:

- 1) The main event was defined as the largest magnitude event occurring during the first hour after the event that initiated the sequence. This selection was based on the fact that 98% of the sequences analysed presented T_S less than 1 hour (see Section 3.2). It is also necessary to have the first hour of data for estimating T_{MC} .
- 2) The largest aftershock needs to be defined for a time period of interest after the first hour. A natural choice is the time period after the aftershock rate has significantly decreased. This is well represented by the maximum curvature point. A possibility is the time period $T_{MC} - T_E$ (see figure 1). However, some sequences presented T_E higher than 24 hours. For re-entry purposes it is impractical to have an estimate of the magnitude of the largest aftershock one day after the main event. It was decided that the most practical time period for developing statistics for the largest aftershock was immediately after T_{MC} but before the background time window ends, i.e., during ΔT_{BW} . This is the period of greatest interest, should there be a large aftershock event.

With these two considerations we rewrite Båth's law as:

$$\Delta m = \max\{m_{1\text{hour}}\} - m_{LA}^{\Delta T_{BW}} \quad (11)$$

To demonstrate the practical application of this modified form of Båth's law we evaluated Eq. (11) using the seismic moment magnitude scale. The magnitude of the main event of the aftershock sequences ($\max\{m_{1\text{hour}}\}$) ranged between -0.8 to 1.4, -0.8 to 0.7 and -0.9 to 0.8, for the Copper Cliff North, Kidd Creek and

Macassa sites, respectively. Figure 5 presents the population distribution of the modified Δm values estimated for the three sites under consideration. Despite the fact that actual microseismic monitoring systems have limitations for appropriately quantifying large magnitude events, Δm presents the same average range of crustal earthquakes, with mean values of 1.16 ± 0.62 , 1.51 ± 0.58 and 1.09 ± 0.34 for the Copper Cliff North, Kidd Creek and Macassa sites, respectively. In terms of the Δm probability distribution, by using the Anderson-Darling test the hypothesis that Δm is normally distributed at the three mines cannot be rejected for a significance level of at least 10%.

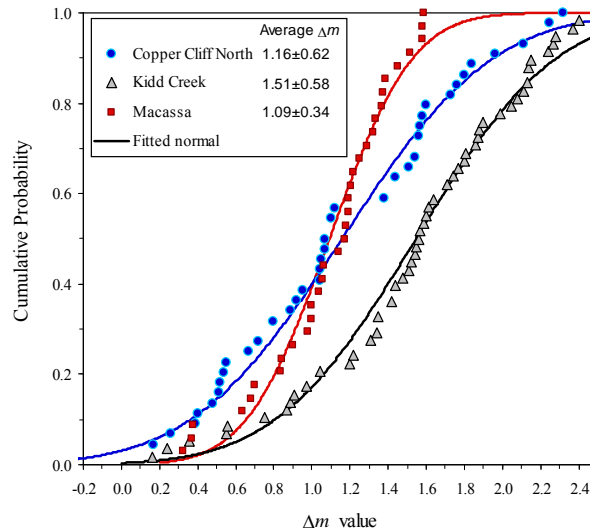


Figure 5 Sample population of Δm for the three sites under study and the best fitted normal distributions

5 Conclusions

Aftershock sequences are complex in nature; nevertheless they present common statistical properties of different systems, from crustal earthquakes to mining-induced microseismic events. These statistics are valuable in terms of application for re-entry protocol development. In this paper we have analyzed the decay characteristics of aftershock sequences to determine the applicability of two scaling laws to mining-induced seismicity. The modified Omori's law for the temporal decay of aftershocks after a main event and Båth's law for the magnitude of the largest aftershock. The seismicity parameters of these two scaling laws are site specific, however, they presented particularly narrow ranges for different mine sites in Ontario. The irregularity in the rate decay of mining-induced aftershocks sequences motivates incorporation of a background time window or "factor of safety" to be used before re-entering the area.

The practical implications of these findings for developing a real time re-entry protocol are as follows:

- (1) Following the principal event and after recording the number of seismic events during the first hour $N_{1 \text{ hour}}$, we can estimate the value of the value of T_{MC} for a particular curve of isoprobability. The 50% curve is recommended. As an alternative the isoprobability curves can be used to calculate the probability that T_{MC} is less or equal than t for a given $N_{1 \text{ hour}}$.
- (2) An appropriate background time window can be defined based on the natural variability of aftershock sequences and the level of induced seismicity during the first hour $N_{1 \text{ hour}}$.
- (3) Given the maximum magnitude event recorded during the first hour and the fact that Δm is normally distributed we can estimate the probability of occurrence of a seismic event larger than a certain magnitude

during the proposed background time window. It can also be used directly to estimate the most probable largest aftershock magnitude.

Acknowledgements

This project was identified and supported by the MASHA Ground Control Committee (Mines and Aggregates Safety and Health Association) and funded by WSIB (Workplace Safety and Insurance Board). The authors wish to acknowledge the permission of the mines to publish this work. The first author acknowledges partial support from the Department of Mining Engineering of the University of Chile for his Ph.D. studies

References

1. Anderson, T.W. and Darling, D.A. A Test of Goodness of Fit. *Journal of the American Statistical Association*, 1952, 49 (268). 765-769.
2. Bak, P. and Tang, C. Earthquakes as a Self-organized Critical Phenomenon. *Journal of Geophysical Research*, 1989, 94 (B11). 15635-15637.
3. Båth, M. Lateral Inhomogeneities in the Upper Mantle. *Tectonophysics*, 1965, 2 (6). 488-514.
4. Casarotti, E., Piersanti, A., Lucente, F.P. and Boschi, E. Global Postseismic Stress Diffusion and Fault Interaction at Long Distances. *Earth and Planetary Science Letters*, 2001, 191 (1-2). 75-84.
5. Console, R., Lombardi, A.M., Murru, M. and Rhoades, D. Båth's Law and the Self-similarity of Earthquakes. *Journal of Geophysical Research*, 2003, 108 (B2). 2128.
6. Das, S. and Scholz, C.H. Theory of Time-Dependent Rupture in the Earth. *Journal of Geophysical Research*, 1981, 86 (B7). 6039-6051.
7. Felzer, K.R. and Brodsky, E.E. Decay of Aftershocks Density with Distance Indicates Triggering by Dynamic Stress. *Nature*, 2006, 441 (04799). 735-738.
8. Felzer, K.R., Becker, T.W., Abercrombie, R.E., Ekström, G. and Rice, J.R. Triggering of the 1999 MW 7.1 Hector Mine earthquake by aftershocks of the 1992 MW 7.3 Landers Earthquake. *Journal of Geophysical Research*, 2002, 107 (B9). 2190.
9. Grasso, S.D. Testing of Self-organized Criticality by Induced Seismicity. *Journal of Geophysical Research*, 103 (B12). 1998, 29,965-29,988.
10. Gross, S.J. and Kisslinger, C. Test of Models of Aftershock Rate Decay. *Bulletin Seismological Society of America*, 1994, 84 (5). 1571-1579.
11. Kagan, Y.Y. Short-Term Properties of Earthquakes Catalogs and Models of Earthquake Source. *Bulletin of the Seismological Society of America*, 2004, 94 (4). 1207-1228.
12. Kilb, D., Gomberg, J. and Bodin, P. Triggering of Earthquake Aftershocks by Dynamic Stresses. *Nature*, 2000, 408. 570-574.
13. Kisslinger, C. Aftershocks and Fault Zone Properties. *Advances in Geophysics*, 1996, 38. 1-36.
14. Mogi, K. Earthquakes and Fractures. *Tectonophysics*, 1967, 5 (1). 35-55.
15. Nyffenegger, P. and Frohlich, C. Recommendations for Determining p Values for Aftershocks Sequences and Catalogs. *Bulletin of the Seismological Society of America*, 1998, 88 (5). 1144-1154.
16. Nyffenegger, P. and Frohlich, C. Aftershock Occurrence Rate Decay Properties for Intermediate and Deep Earthquakes Sequences. *Geophysical Research Letters*, 2000, 27 (8). 1215-1218.
17. Ogata, Y. Estimation of the Parameters in the Modified Omori Formula for the Aftershock Frequencies by the Maximum Likelihood Procedure. *Journal of Physics of the Earth*, 1983, 31 (2). 115-124.
18. Omori, F. On the After-shocks of Earthquakes. *Journal of the College of Science, Imperial University Tokyo*, 1894, 7. 111-200.
19. Shcherbakov, R. and Turcotte, D.L. A Damage Mechanics Model for Aftershocks. *Pure and Applied Geophysics*, 2004, 161 (11-12). 2379-2391.
20. Shcherbakov, R. and Turcotte, D.L. A Modified Form of Båth's Law. *Bulletin of the Seismological Society of America*, 2004, 94 (5). 1968-1975.
21. Stein, R.S. The Role of Stress Transfer in Earthquake Occurrence. *Nature*, 1999, 402 (6762). 605-609.
22. Utsu, T. A statistical study of the occurrences of aftershocks. *Geophysical Magazine*, 1961, 30. 521-605.

23. Utsu, T., Ogata, Y. and Matsu'ura, R. The Centenary of the Omori Formula for a Decay Law of Aftershock Activity. *Journal of Geophysical Research*, 1995, 43 (1). 1-33.
24. Vallejos, J.A. and McKinnon, S.M. Omori's Law Applied to Mining-Induced Seismicity and Re-entry Protocol Development. submitted to *Pure and Applied Geophysics: Special Issue Induced Seismicity*. 1995, (30).521-605.
25. Vallejos, J.A. and McKinnon, S.M. Re-entry Protocols for Seismically Active Mines using Statistical Analysis of Aftershock Sequences. *Rock Engineering in Difficult Conditions*. Paper 4028. in *Proceedings of the 20th Canadian Rock Mechanics Symposium*, (Toronto, 2009).

IN-SITU STRESS MEASUREMENT AND ITS DISTRIBUTION LAW IN THE TANGKOU DEEP MINE

JIAN-JUN WEI , HOU-QUAN ZHANG

*State Key Laboratory for Geomechanics and Deep Underground Engineering, School of Architecture and Civil
Engineering, China University of Mining and Technology
Xuzhou, 221008, China*

JIAN-JUN WEI

*Department of Civil Engineering, Xuzhou Institute of Architectural Technology
Xuzhou, 221116, China*

There are three mine shafts over a thousand meter deep at Tangkou mine. At present, drifts at the mine site are strongly deformed and severely damaged by deep mining. In order to study the stress state in deep mining and design effective rock support for coal roadways, in-situ stress measurement was carried out in the middle coal roadway at the -1030m level. In this measurement, the technique of improved hollow inclusion cells was adopted which can accomplish complete temperature compensation. From the measurement, three-dimensional stresses at three measuring points were obtained, and a distribution model of in-situ stress was established. The in-situ stress distribution law of Tangkou Mine was analyzed. The measurement results show that at the depth of 1000m, the maximum principal stress is about 30 MPa, and the stress field is mostly self-weight induced. In local fields, the stress states are governed by the horizontal stress induced by geological structures.

1 Introduction

The Tangkou coal mine is located in the northwest of the Jining, Shandong Province. It's the first super-vertical shaft mine of 1000 m depth, with a production capacity designed for 3.0Mt/a. There are 3 vertical shafts with a kilometer depth in industrial plaza. The underground rock mass is siltstone or mudstone of the Permian's shihezhi group, and the performance is gray-black, easy-broken and has vertical fracture growth. Due to the high in-situ stress and softness of the rock, the roadways completed previously have been damaged heavily. Hence, the excavations and the support of the shafts and roadways have become very difficult.

In-situ stress is the fundamental cause for the deformation of roadways and mining faces, which impacts the stability of the surrounding rocks directly. The distribution detection of in-situ stress is the basic premise for the safety and stability analysis of roadways and the design of the support structure [1,2]. In order to understand the distribution of deep field stress, the research project of stress measurement and soft roadway support in deep mine was carried out by the research group of China University of Mining and Technology.

2 Measurement Method and Measuring Points

2.1 Measurement Method

The current in-situ stress measurement methods used commonly at home and abroad are the hydraulic fracturing method and overcoring method [3]. The overcoring method is divided into the piezomagnetic

overcoring method and the hollow inclusion relieved stress method. Hydraulic fracturing method is mainly used in deep stress measurement and piezomagnetic overcoring method is mainly applied in the plane stress and superficial measurement [4]. The hollow inclusion triaxial stress relief method has the advantage of higher accuracy, easy installation, and high efficiency. Therefore, the method is generally used in mines, tunnels and other underground engineering purposes, and applied in the in-situ stress measurement of Tangkou mining [5,6].

The YH3B-4 type hollow inclusion triaxial strain gauge was used in the field stress measurement. The sensor consisted of 9 cells embedded in epoxy resin tube and 3 rosette cells separated by 120 ° and felted around the epoxy resin tube. Each cell is embedded in the cylinder wall by the epoxy resin layer about 0.5mm thickness. The compensation strain cell is affixed to the rear of strain gauges.

The measurement principle based on that the wall of hole is plastered with elastic ring layer in the three-dimensional stress rock mass which is postulated as the elastic body. When the rock is drilled cutting, the deformation energy of rock will release and the elastic restoring distortion is used for the field stress calculation. Surrounding rock stress-strain relationship as follows:

$$E\varepsilon_{ij} = \left\{ K_1(\sigma_x + \sigma_y) - 2(1 - \mu^2)k_2[(\sigma_x - \sigma_y)\cos 2\theta_i + 2\tau_{xy}\sin 2\theta_i] \right\} \sin^2 \varphi_{ij} + [\sigma_z - \mu(\sigma_x + \sigma_y)] \cos^2 \varphi_{ij} + 2(1 + \mu)k_3(\tau_{yz}\cos \theta_i - \tau_{zx}\sin \theta_i) \sin 2\varphi_{ij} \quad (1)$$

where ε_{ij} is the strain value measured of j cell in the i strain rosette; θ_i is the polar angle of i strain rosette; φ_{ij} is the angle of j cell in the i strain rosette; K is strain cell correction factor determined by the inside radius of strain gauge, the radius of strain cell and bore hole, rock character, the Young's modulus and Poisson's ratio of epoxy resin, the general take of 0.8 ~ 1.3.

2.2 Measuring Points Layout

The principle of the measuring points' layout is:

- (1) The points should generally be far away from the fault and avoid the rock fracture zone.
- (2) The location should be far away from the opening boundaries as big mine cavity.
- (3) The location should avoid the stress concentration zone such as the bend, fork, corner and the top of the tunnel and cavity.
- (4) The points should layout around three or more levels.

Combined with the principles and the actual production conditions, three measurement locations are chosen in the mine (Figure 1). 1# and 3# measuring stations are located at the return airway crosscut, the roof rocks of three up coal seam. 2# measuring stations is located at the west auxiliary transport crosscut, the floor rocks of three up coal seam.

(1) Measuring point 1: the 1# measuring point lied in the return airway crosscut that is 71.5m far away from the bottom of wind well. The lithologic character of packsand in the measuring station under the ground about 1030m is fine-grained and stable. The elevation of borehole is 6° and the azimuth is 12°. The direction of drill and crosscut is nearly perpendicular. Three measurement sections were carried out the release curves and calibration curves show that the strain cell is in good condition and the measured data are reliable.

(2) Measuring point 2: the 2# measuring point is located at the top of the west auxiliary transport crosscut roadway that is 702m far away from the fifth intersection. The borehole under the ground about 1028m with the azimuth 193° and elevation 16°. The rack mass in the area is gray, tight and integral.

(3) Measuring point 3: the 3# measuring point is located at the return airway crosscut that is 560.5m far away from the bottom of wind well. The azimuth of borehole is 11° and elevation is 14° . The drilling hole at -1028m level and there rock mass is integral and stable.

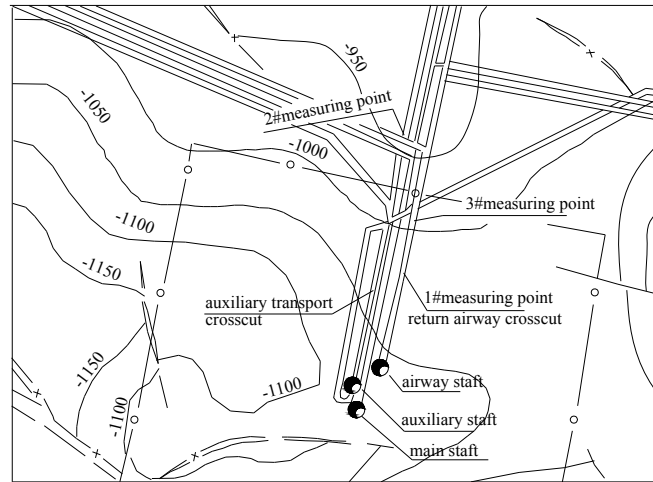


Figure 1 Schematic location map of ground stress observation points

3 Field Stress Measurement

3.1 The Stress Relief Test

The measuring hole was drilled by special tools. During the stress relief process, the distortion data was recorded by the KDJY-2 portable static resistance strain surveying instrument that produced by China University of Mining and Technology, and the stress curve was drawn synchronously. The strain value was collected every 10~20mm according to lithology and the relieving speed, and the strain change of the non-stress-affected zone, stress elastically release zone and strain stabilization zone was clear at a glance. The relieved depth was generally 420~500 mm and the time was controlled to limit in 40~50 minutes in the stress relieved measurement.

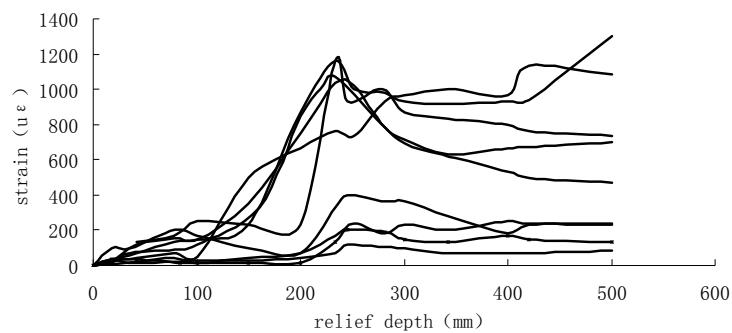


Figure 2 Curves of in - situ stress relief process for 1# point

The most important aspect is to ensure the pasting quality between the measuring cells and the wall of hole. The wall of drill hole required to be clean, smooth and integrative, and the diameter is strictly controlled. Only if strain cell stuck on rock wall firmly, the strain data can reflect the elastic recovery characteristics of rock accurately. From the stress relieved curves, the work status of strain cell can be checked and the reliability of measured data can be determined.

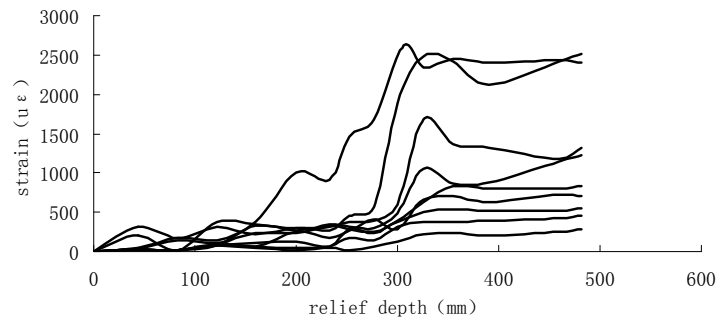


Figure 3 Curves of in - situ stress relief process for 2# point

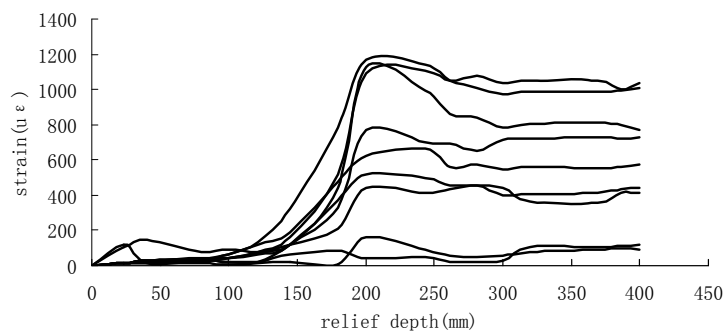


Figure 4 Curves of in - situ stress relief process for 3# point

3.2 Measuring Result

(1) Stress Relieved Test Results

The stress relieved test was carried out individually in the three stations, and the stress relieved curves and calibration curves were obtained. The vast majority of those have typical variety regulation which indicates the work status of strain cell in the gauge is normal. For more than six unknown stress components in the strain observed values, the method of least squares is applied to gain the best target [7].

The varieties of strain response along the relieving process are portrayed in Figures 2~4. These strain data are in general smaller before the drill depth meet the measurement section (strain gauge location) in which some cells obtain negative values. These can be interpreted as the result of stress transfer for trepanning, equal to "excavation effect." Measurement sections are a vital demarcation boundary in the curves. When the drill depth is close to that, parts of curves change toward contrary direction and the maximum is obtained in the position that drill head passes that. After the drill depth exceed the section a certain distance, the strain is gradually stabilized and the final stable value is the basis for field stress calculation. However, the strain value tend to

decrease in the curves after the relieved depth exceeds measurement sections, mainly because the joint and crack in the rock haven't become cracked in the drill head pass moment [8].

The joint and crack opened gradually with the increase of drill depth and the deformation that the self-sensed gradually decreased for the rock's ability to drive strain gauge wear off. Therefore, appropriate strain data used for field stress calculation are consistent with the strain values that drill depth is just over measurement section. Those are drawn as the signs of obvious decline in the curves.

(2) Cores Calibration Test Results

The mechanical parameters of the rock specimens in each measuring point were determined by MTS815 electro hydraulic servo system. The test results are given in table 1.

Table 1 Elasticity constant of the rocks

Measuring point	Location of point	lithology	elastic modulus [GPa]	Poisson's ratio	Uniaxial compressive strength [MPa]
1#	-1030m	sandstone	16.9	0.21	45.23
2#	-1028m	sandstone	20.27	0.25	31.65
3#	-1030m	sandstone	36.6	0.17	153.76

(3) The Field Stress Calculation Result of Measuring Point

Combine the relative stable strain value of measuring point with the elastic modulus and Poisson's ratio of rocks, the three-dimensional field stress results are obtained.

Table 2 Results of crustal stress measurement in mining area

Measuring point	σ_1				σ_2				σ_3			
	value	X	Y	Z	value	X	Y	Z	value	X	Y	Z
1#	31.107	55.91	34.09	90.16	15.03	45.22	118.35	58.16	10.12	115.82	72.68	31.84
2#	27.91	79.24	44.24	129.2	19.9	74.16	54.656	39.76	13.35	19.31	108.4	95.58
3#	36.09	74.20	70.80	25.27	6.371	66.04	35.635	114.7	2.948	29.268	118.7	95.03

4 Main Features Analysis of Field Stress

The test results are given in table 2 and the main features of field stress in the mining area are induced as follows:

(1) The difference between the maximum principal stress and minimum principal stress is too large. That of 1# measuring point is 20.99 and 2# measuring point is 14.56 MPa, 3 # measuring point is 33.14 MPa.

(2) The angle of maximum principal stress with the vertical direction of 1# and 2# measuring points are 34° and 41° separately. The ratios of maximum principal stress to vertical stress component are 1.21 and 1.51. These indicate that the area is controlled by the vertical stress, and the area is self-weight stress field.

(3) There are about 400 meters distance between the 3# and 1# measuring points. The angle between the maximum principal stress with the vertical direction is about 70°, and the horizontal stress σ_x is 30.65MPa that is more than the vertical one 8.79MPa. The ratio of maximum principal stress to vertical stress component is 4.1, which indicate that the area is affected by tectonic stress and controlled by the horizontal stress. On the mine development map, the area lies at the axis of the synclinal and was influenced by the renovation movement of Neocathaysian tectonic system.

(4) Compared with other parts of china, the level of horizontal stress in the mine is slightly larger than the average level of other areas.

(5) The field stress is inhomogeneous and the value and direction of main stress in the three points are rather larger difference. The causation conjectured is the combined action of the Mesozoic east-west structure and Neocathaysian tectonic system.

5 Conclusion

The field stress at 1 km underground in the Tangkou mine has prominently horizontal stress tectonic stress characteristics. The regional structural features and the stress field have a strong impact on coal and rock stresses. Due the effect of horizontal stress in the coal mine, the rock on the roof and floor of the tunnel was destroyed through shear and followed by dislocation formation and bottom rock expansion. As a result, the deformation of the surrounding rock is too large to self-stabilize.

The absolute value of stress shows that the stress is higher, but the mining area isn't characterized as a high-stress region. The difference of the maximum and minimum principal stress is greater. This may be the cause of the serious driving force and rock burst on 3 up coal beds and roof strata.

The result of rock test displays that the sandstone in the 1#, 2# measuring zone has characteristics of lower strength, joint development, and water softening; however, the 3# measuring zone is the opposite. This may be one of the reasons of the non-uniform stress field. In addition, because of the small amount of experimental data, the conclusion of this article is preliminary and further analysis is needed in the future with the collection of more data.

Acknowledgements

This study was supported by NSFC (Nos:50804046, 50774082 and 50490273) , Scientific Research Fund for youths of CUMT (No: 0B080240) and Scientific Research Fund of Jiangsu Construction Bureau(No: JS2007ZD18).

References

1. Wang, L.J., Pan, L.Z. and Liao, C.T. Geostress Measurements and Their Application to Engineering. Geological House, 1991.
2. Liu, Y.F. and Luo, C.W. Geostress and Engineering Construction. Hubei Science and Technology Press, 2000.
3. Jing, F., Liang, H.C. and Bian, Z.H., Geostress Measurement Methods Overview. Hydraulic work college Journal, 2008, 29(2). 71-76.
4. Dong, C., Wang, L.J. and Yang, X.C. Stress Measurement of Anqing Copper Mine. Geomechanics Journal, 2001, 7(3): 259-264.
5. Li, H.M., Zhou, Y. and Su, C.D. Measurement and Characteristics Analysis of In-situ Stresses of Yanbei Coal Mine. Chinese Rock Mechanics and Engineering Journal, 2004, 23(23). 3938-3942.
6. Wu, M.L., Li, G.J. and Liao, C.T. Measurements of In-situ Stress in The Pushihe Hydropower Station in Liaoning Province. Geomechanics Journal, 2006, 12(2). 191-196.
7. Cai, M.F. Principle and Techniques of In-situ Stress Measurement. Science Press, 2000.
8. Cai, M.F., Qiao, L. and Yu, B. Results And Analysis of In-situ Stress Measurement at Deep Position of NO.2 Mining Area of Jinchuan Nickel Mine. Chinese Rock Mechanics and Engineering Journal, 1999, 18(4). 414-418

STUDY ON MINING-INDUCED MICROSEISMIC ACTIVITY AND ITS MONITORING METHOD IN THE HONGTOUSHAN COPPER MINE

XING-DONG ZHAO, WU-KUN ZHAO, YUAN-HUI LI and JIAN-PO LIU

*School of Resources & Civil Engineering, box 265, Northeastern University
Shenyang, 110004, P.R. China*

Mining-induced seismicity is directly related to the interaction of mine excavations and geological structures with regional and local stress fields. In this paper, the ground pressure characteristics and hazards of deep ore bodies, especially rockburst etc, at the Hongtoushan copper mine in China are summarized briefly. The velocity of P- and S-waves in the rockmass were measured by using wave analyzing instruments. In order to obtain the activity rule of ground pressure, a six-channel microseismic monitoring system called Hyperion (including the 3-monodirectional and one tridirectional sensors) was established and employed to monitor the rockburst activity in the Hongtoushan copper mine. The microseismic monitoring technique is a good tool to detect the activity rule of ground pressure for deep bedding ore bodies, and it can monitor the occurring time and position of rockburst events in the stope continuously and in-real-time. By using a Simplex location algorithm, the microseismic event can be determined by AE sensors from first arrival times. Source location errors are tested by artificial blasts. The monitoring results show a locating error which is less than 5-10 meters within the sensors array and the perfect source locating performance of the system. The monitoring data can be transmitted far distances, and the source location figure is presented for analyzing the activity law of ground pressure (including the rockburst etc.). The monitoring results have been contributed to the prediction of the occurrence deposition of rockburst to guarantee safe production in Hongtoushan copper mine.

1 Introduction

The research on rockburst has become a hotspot and difficult problem for rock mechanical workers. According to incomplete statistics [1~3], there were more than 110 mines reporting the occurrence of rockburst. Especially in South Africa and Australia, serious rockburst disaster in these two countries accounted for more than 30% of all of rockburst in mines. In China, typical rockburst typically occurs in the Laohutai coal mine, Hongtoushan copper mine and Dongguashan copper mine [10] etc. Rockburst does not only causes surrounding rock to rapidly deformed and be destroyed, throws rock, exhibits intense noise, causes vibration and air shock waves, but also is a serious threat to personnel and surrounding cities. It is one of project-induced disasters in deep mining, and is also a major problem which constrained the development of technology in deep mining.

Presently, the microseismic monitoring system has become a good tool to detect rockburst effectively. Internationally[4~9], there are 19 different band mine microseism monitoring stations which apply earthquake monitoring stations in South Africa. The microseismic monitoring system is also used to detect the disaster of rockburst in deep mining in Canada, Poland, Australia, etc. In our country [11~15], there has been some progress in detecting the disaster of rockburst since introducing the microseism monitoring system used in the Polish mines to monitor rockburst, from the 20th century over the past 50 years. Since 1985, the Taozhuang coal mine installed the SKA-3 type sound system and the SYLOK type microseism system which were introduced from Poland for monitoring mining-induced earthquakes [11]. The Fankou Lead-Zinc mine introduced the microseism monitoring system which was produced by ESG of Canada to monitor its rockburst[12]; The Dongguoshan copper mine applied ISS of South Africa to monitor its rockburst[13]; Jiangfuxing cooperated with the Huafeng coal mine to monitor rockburst and roof caving[14]; Northeastern

University cooperated with Hongtoushan copper mine [15], by using microseism monitoring system of Canadian ESG company to set up specifically microseism monitoring system for monitoring the dynamic evolution process of rockburst.

The mining microseismic monitoring technique is on rock mass deformation and the launch of elastic waves by itself after destruction to monitor the stability of engineering rock technique. Each microseismic signal contains changes in a rock about the internal state of abundant information, for signals received which are treated, analysed, and can be used as the basis for stability evaluation of rock. In this paper, as to the frequent situation of deep pressure activity in the Hongtoushan copper mine, by establishment of mining microseismic monitoring system, monitoring deep pressure activity laws continuously and in-real-time on the Hongtoushan copper mine, researching on the laws of deep rock pressure activities.

2 The Situation Of Deep Ground Pressure Activities In The Hongtoushan Copper Mine

The Hongtoushan copper mining have been near forty years of mining history since 1958, and the exploitation of the depth has reached 1,300 meters, and is the biggest mining depth of the nonferrous metal mine in China. With the increasing depth of mining, types of ground pressure occurred in a larger change, from the static ground pressure controlled by the shallow geological structure, and gradually developed into the dynamic ground pressure mainly with rock block ejection, burst or even the phenomenon of a large transient caving rock bodies.

According to the test of rock stress in the mine and field observations over the past few years, as well as the different forms of the characteristics of the ground pressure of top and bottom, comprehensive analysis of thinking[16]: The ground stress field of the Hongtoushan copper mine takes -347m for the boundary, the upper part is the static ground pressure phenomenon affected mainly by geological structure, the lower part is the ground pressure phenomenon affected mainly by the stress condition and a combination of dynamic ground pressure, but the phenomenon more obvious with the bigger mining depth. Nearly 10 years, the frequency and intensity of deep ground pressure gradually increased in the Hongtoushan (Figure.1). There are both loose ground pressure controlled by structure in the mid-shallow part, and weak rockburst type ground pressure phenomenon controlled by stress with rock-chip ejection, rock powder escaped in the deep ground pressure phenomenon [1].

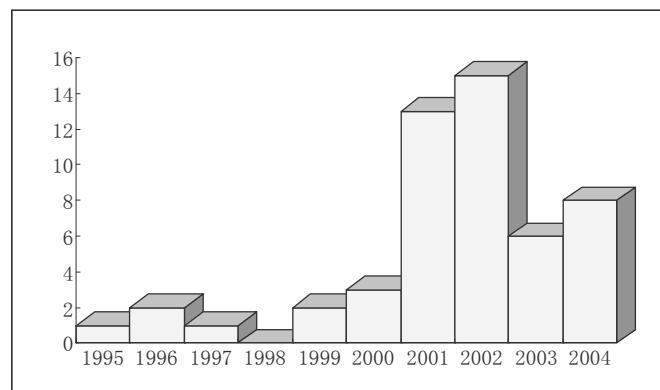


Figure 1 the frequency of rockburst in Hongtoushan copper mine from 1995 to 2004

3 The Establishment of Mine Microseism Monitoring System

After site investigation, making sure that set up the microseismic monitoring system in the -767m level 13th stope footwall rock, mainly because: during the construction of route in the level of 9-1, the more serious ejection and caving phenomenon happened to roadway wall, the impact degree relatively strong and the damage range relatively large; In the level 13th stope is going on mining activities, disturbing ore and rock around relatively large; The -767m level is about 1200m away from the surface, and the biggest(smallest) principal stress reaches to 109.7(31.3) MPa, a larger possibility to happen medium to strong rockburst tendency. Monitoring points layout see Figure 2. The Hongtoushan microseismic monitoring system is composed of three parts in general, the remote control room, surface stations, underground monitoring room, and sensor (Fig 3). Microseismic signals collected by the sensors and preamplified meanwhile, and spread through the signal cable to the microseismic monitor at underground monitoring room for data analysis and treatment, meanwhile analysis results will be sent to the surface through the cable stations, so as to achieve real-time microseismic monitoring and data transmission purpose.

4 Microseism Monitoring Data Analysis

The Hongtoushan copper mine adopt the working system of three classes in turn daily, namely: the first class (am 8:00~16:00), the second class (16:00~24:00), the third class (0:00~8:00). And the blasting work mainly concentrates in between pm 15:00 and 23:00. The figure 4 showed 24-hour complete microseismic monitoring data, and we can see from the figure, the vibration monitored by the microseismic monitoring system concentrate in about pm 15:00, but in other time the information about rock damage of microseismic activity are very few. It explained that this observation system already obtained a very good time result about the vibration caused by blasting operation.

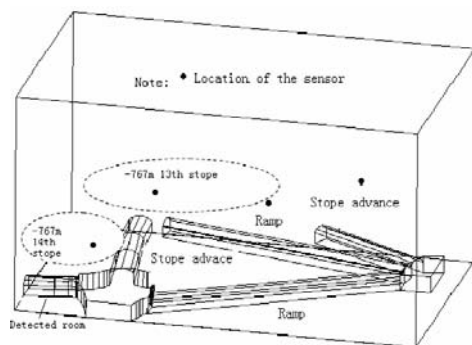


Figure.2 the monitoring result of the explosion event

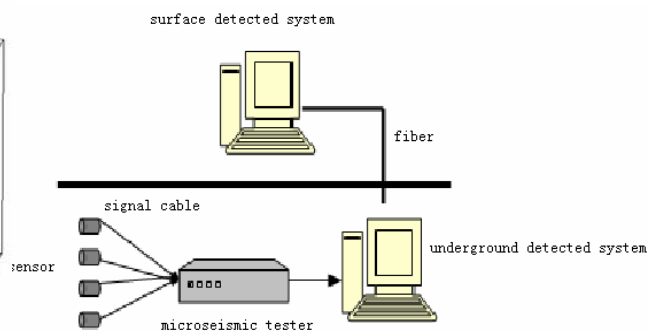


Figure.3 the microseism monitoring system

For understanding the monitoring system to microseismic event's space location precision, we have carried on the actual test to the system, to compare the error between hypocenter location of actual blasting and the result of source localization the monitor system analysis obtained. The test method is producing vibration source by artificial blasts, Determining the space position coordinate of the seismic center on the spot, obtaining the localization coordinate of the blasting seismic centre according to the analysis and calculation of microseismic system's monitoring results, comparing the two then obtain this monitoring system to position error of vibration source.

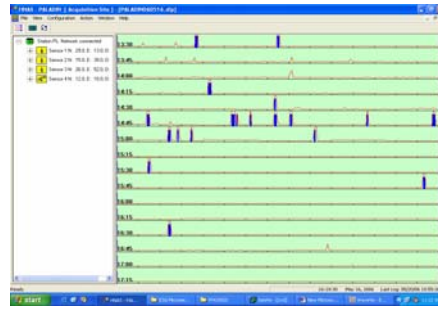


Figure. 4 the monitoring result of the explosion event

The artificial fixed-point blasting place chooses the end of ramp upper the underground microseismic monitor room (Fig.5), because there is developing roadway to ore body, preparing for ore removal, easy to blast and not affecting the mine production schedule. Before blasting, determines and records the space coordinates position of blasting on the spot, the staff are monitoring indoor the monitor room, gain oscillogram of vibration source (Fig.6), and then obtain the space position coordinate of vibration source through the software real-time analysis.

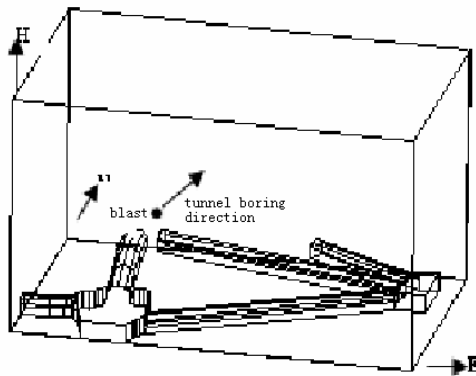


Figure.5 the position of the explosion event

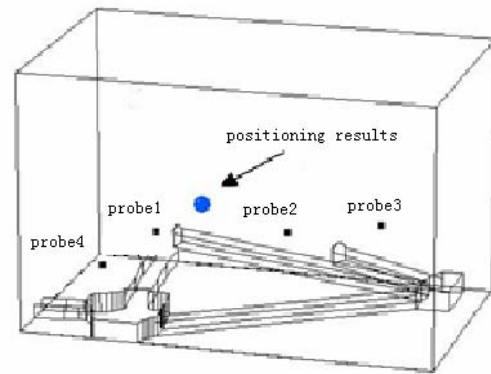


Figure.6 the monitoring results of the explosion event

The layout of Sensor is basis of location to micro source, and all information of microseismic monitoring came from the sensor, and it determines the initial positioning error on the impact of the final results. Well emplaced sensor array allows the impact of the initial error to minimize, in contrast the initial error can achieve maximum, so the sensor layout is an important part of automatically sound source positioning technology[8]. The layout of sensors takes the following aspects into account:

- (1) Combined with the positioning algorithm, the positioning parameter of sensor must make calculation process convergence;
- (2)The monitoring range must be within the range of the permit of the microseismic monitoring system;
- (3)In the process of the layout of sensors, sensors and signal cables should be avoided whatever possible interference with other signals, such as electrical signals, mechanical vibration and so on.

Through contrastive analysis between spaces coordinates position of vibration source through the software real-time analysis and actual blasting position (Table 3), both's error is in the error range of microseism monitor permits, thus proves the accuracy of localization result.

Table 3 the analysis on the man-made explosion locate result

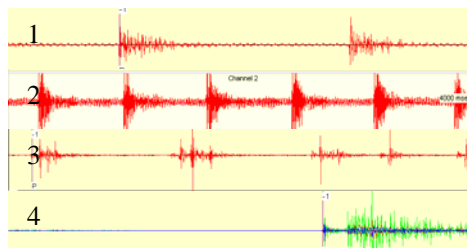
Position coordinates	Actual coordinates/m	Monitoring coordinates /m	Error /m
N	25.5	25.195	0.305
E	34.7	31.226	3.474
H	14	15.345	1.345

5 Discusses

The scene test result indicated the Hongtoushan microseismic monitoring system for ground pressure of deep bedding ore bodies to the vibration blasting work produces has achieved a good monitor result, and has provided a precious experience for the monitor to the activity law of ground pressure for future. But we discovered the microseismic monitoring system also has many problems after the data analysis:(1)The sensors are few;(2)The scene monitor needs a long time accumulation experience. (3)This microseism monitor's localization has supposed the rock mass is a homogeneous material, and has not considered its anisotropic characteristic and elastic wave's weakness as well as reflection, refraction and so on factors.

5.1 Signal Recognition Methods of Microseismic Model

On the monitoring process to deep mining's rockburst event by applying microseismic monitoring system, we faced with this kind of very thorny question that how to distinguish the complex signals gathered. The signals microseismic monitoring system gathered include the microseismic signal which the rock mass fracturing sends out, as well as containing the rock drilling signal, kinds of blasting signal, high-voltage interference signal and so on. Because of each kind of signal's disturbance, it is very difficult to recognize the microseismic signals which the rock mass fracturing produce. To each kind of signal's disturbance in this article, we used wavelet analysis method, analyzed the frequency and amplitude of each kind of wave gathered and removed each kind of unwanted signal, through the establishment of pattern recognition mathematical model (Figure 7) (this model mainly includes data acquisition, signal processing, extraction information characteristics of microseismic signals through application neural network artificial intelligence, classification and data-output). Through application the pattern recognition's method to microseismic monitoring system localization result, removed the above several kind of unwanted signal's influence on the microseism monitor information finally, its result contrast see Figure 8.



(1)Burst signal; (2)Rock drill signal; (3) Power signal; (4) Microseismic signal

Figure. 7 the different signal waveforms

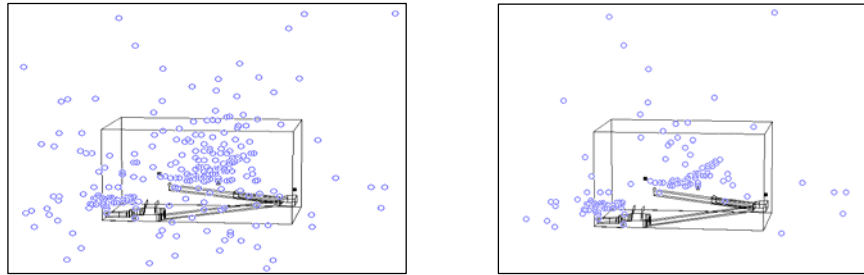


Figure.8 Curves of elastic modulus before and after being Prestressed

5.2 Microseismic Event Energy Release rate Analysis

Through data analysis, we discovered microseismic event energy release rate mainly concentrated in two scopes obviously (take $1E+09$ as boundary) (Figure 9). Initially determines these two obviously different scopes represent two kinds of microseismic signals; one kind of microseismic signal is mining activities as the ore rock vibration and so on, this kind of signal is caused by the blasting explosive energy or the mechanical shock, big energy, concentrating on the upper region; another kind of signal is a energy release caused by the generating crack and expansion ground-stress change produces in rock mass, little energy, concentrating on the lower region.

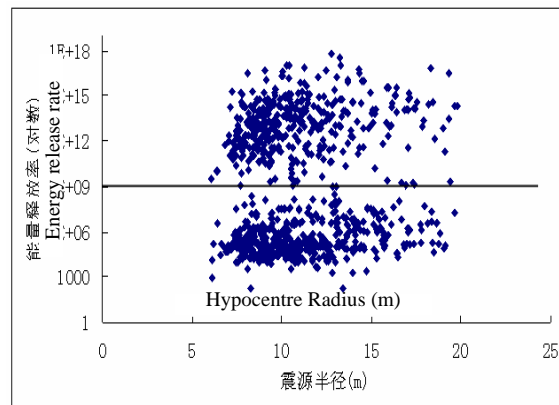


Figure.9 Regional distribution of energy release rate of microseism

6 Conclusions

By measuring depth portion's geostatic stress of the Hongtoushan copper mine by the method of exterior's distortion, we can find that the geostatic stress of the Hongtoushan copper mine is becoming bigger and bigger along with the depth of working. Through measurement of rock's characteristics of anti-concussion we can find that rocks of this mine have medium to intense and above rockburst tendentiousness. Construction of three dimensional geological models of the Hongtoushan Copper mine in the - 767 level 13 stopes, disposes the sensor, establishes mine microseism monitoring system, carries on continuous monitoring to depth portion geostatic pressure, catches information of microseism which causes by geostatic pressure activity, and realizes

microseism's source localization. Analysing microseism monitoring information's unwanted signal, energy liberation rate and continuous monitoring data; we can draw following conclusion:

(1) Regarding the excrescent massive microseism monitor data, we can eliminate unwanted signal's (demolition, rock drilling, power electricity and so on) disturbance to microseism monitoring result using the method of neural network pattern recognition, to effectively show the microseism monitor localization result;

(2) Carries on energy liberation rate analysis to microseism monitoring data, we can differentiate microseism energy liberation size effectively, then analyze production reasons of different microseism events;

(3) Carries on time's nonlinear analysis to continuous monitoring microseism event,s estimates rockburst's probability by setting the number of microseism events in unit of time, this is of vital practical importance to the development of power disaster's forecast research in mines.

In brief, rockburst tendentiousness analysis of deep mining and microseism monitoring system's establishment, as well as the effective analysis of microseism monitoring data's in the Hongtoushan copper mine, can supply information to choose safe and highly effective mining or support methods. This will play a positive role in the disaster-prevention and disaster-reduction in the safe in production of the Hongtoushan copper mine's depth portion ore deposit mining. Also it will simultaneously provide a model to similar mine's microseism monitor information's processing.

Acknowledgement

The work was funded By Education Bureau High School Doctoral Subject Special Fund in the People's Republic of China (20070145121).

References

1. Graham, G. Seismological Bulletins (produced quarterly). Council for Geoscience, Pretoria, 2006.
2. Durrheim, R. J., Anderson, R. L., Cichowicz, A., et al. The Risks to Miners, Mines, and the Public Posed by Large Seismic Events in the Gold Mining Districts of South Africa. in Proceedings of the Third International Seminar on Deep and High Stress Mining, (Canada, 2006).
3. Aswegen, G.V. Routine Seismic Hazard Assessment in Some South African Mines. in Rockbursts and Seismicity in Mines, RaSim 6. (Australia, 2005).
4. Cichowicz, A. Automatic Processing and Relocation Methods. Controlling Seismic Risk. in Sixth International Symposium on Rockburst and Seismicity in Mines Proceedings, (Australian, 2005).
5. Hedley, D.G.F. and Udd, J.E. The Canada-Ontario-industry Rockburst Project. Pageoph, 1989, 129 (3-4). 661-672.
6. Blake, W., Leighton, F. and Duvall, W.I. Microseismic Techniques for Monitoring the Behavior of Rock Structures. BuMines, 1974.
7. Williams, T.J., Wideman, C.J. and ScottD, F. Case History of a Slip- type Rockburst. Pure and Applied Geophysics, 1992,139(2).627-637.
8. Wilhams, D.J., Arabasz, W.J. Mining-related and Tectonic Seismicity in the East Mountain Area Wasatch, Utah, U.S.A. Pageoph, 1989, 129 (3-4). 345-368.
9. Gibowicz, S.J. Seismicity Induced by Mining. Advances in geophysics, 1990, 32. 1-74.
10. Qi, Q.X., Chen, S.B., Wang, H.X., et al. Study on the Relations among Coal Bump, Rockburst and Mining Tremor with Numerical Simulation. Chinese Journal of Rock Mechanics and Engineering, 1996, 22 (11). 1852-1858
11. Taozhuang Coal Mine et al. The Investigation and Analysis on the Tectonic Stress in the Taozhuang Coal Mine. Inner reference, 1989.
12. Li, S.L, Yin, X.G., Zheng W.D., et al. Research of Multi-Channel Microseismic Monitoring System and Its Application to Fankou Lean-Zinc Mine. Chinese Journal of rock Mechanics and Engineering, 2005, 24 (12). 2048-2053.

13. Zhang, Y.P. Rock-mass Acoustic Emission and Micro-Seismic Monitoring and Localizing Technology and Its Application. *Engineering Blasting*, 2003, 8 (1).58-61.
14. Jang, F.X., Xun, L. and Yang, S.H. Study on Micro Seismic Monitoring for Spatial Structure of Overlying Strata and Mining Pressure Field in Longwall Face. *Chinese Journal of Geotechnical Engineering*, 2003, 25 (1). 23–25.
15. Zhao, X.D., Shi,C.Y., Li, Y.H., et al. Microseismic Monitoring System Establishment and Its Application Study in Hongtoushan Copper Mine. *Northeastern University (natural Science)*, 2008, 29 (3). 399~402.
16. Research Report of Exploitation Technique in Hongtoushan Copper Deep Orebody Mine. Northeastern University, 1996

IN-SITU PULL TESTING OF A YIELDABLE ROCK BOLT, ROOFEX

UGUR OZBAY

*Department of Mining Engineering, Colorado school of Mines
Salzburg, Austria*

ERICH NEUGEBAUER

*Atlas Copco
Salzburg, Austria*

A recently introduced yielding rock bolt, trade name Roofex, appears to have the required energy absorbing component of a dynamic support system. According to the manufacturer's specification, the Roofex bolts can yield 300 mm (or more) displacement while holding 80 kN pull load. In order to assess the performance of this support unit in situ, particularly in coal ribs, a series of in situ pull tests performed in one hard rock and two coal mines. The results show that, under conventional pull test loading conditions, Roofex yielding bolts perform very close to their claimed specifications, thus showing a potential for their use as the main energy absorbing component of a dynamic support system. Further studies are required to confirm the in situ performance of these bolts under dynamic loading conditions.

1 Introduction

One of the manifestations of the dynamically induced failures in deep coal mines is the violent ejection of rock material from the sidewalls. A possible protection against such failures is the use of a specifically designed dynamic support system comprised of reinforcement units with sufficient capacity to absorb the kinetic energy of the dynamic failure and a skin support that can adequately contain the disintegrated coal. A recently introduced yielding rock bolt, trade name Roofex, appears to have the required energy absorbing component of a dynamic support system (Plouffe et al, 2008). However, the ability of these bolts adequately anchoring in coal needed to be confirmed for the application of these bolts to violent coal rib failures. This paper describes and presents the results from a series of in situ pull tests conducted on the Roofex bolts in a hard rock mine and two coal mines with the objective of assessing their anchorage performance at the acclaimed yield load and displacement.

2 Roofex Yielding Rock Bolt

The Roofex bolts, patented by Atlas Copco, are manufactured in different lengths and configurations. The particular bolt that this study focused on is the 1.8 m long, 12.5 mm diameter high strength stainless steel tendons with a yield load capacity of 80 kN and yield displacement range of 300 mm. Variations of this bolt with lower yield loads of 20, 30, and 40 kN were also tested. The maximum capacity of these bolts is 100 kN.

The yielding action of the bolt is provided through the "energy absorber" unit. This unit is a 30 mm outer diameter, 65 mm long hollow cylinder, truncated on one end. The unit is slid over the tendon and friction fixed at 300 mm from the bolt's end as seen in Figure 1. Having a larger diameter than the steel tendon, the energy absorber anchors against the resin as the rock face moves, pushing out the bolt's plate, which in turn induces pull loads on the tendon. The tendon is disconnected from the resin by being encased in stainless steel tubes.

The frictional movement of the tendon through the energy absorber unit is controlled by a set of carbide pins placed within the energy absorber. These pins can be adjusted to halt tendon sliding through the energy absorber until a set yield load (e.g. 80 kN) is reached. When the pull load attains the yield load, the tendon starts deforming and sliding through the energy absorber as controlled by the frictional resistance affected by the carbide pins. Figure 2 shows a yielded end of a Roofex tendon cold-rolled into a hexagonal shape as the result of having been pulled through the energy absorber.

In the coal mine tests, the bolts were installed in 35 mm diameter 1.8 m long holes drilled by an automated bolter. The resin used was a 1.5 m long Minova Lokset cartridge with a set time of 35 seconds. The mixing/stop element at the bolt end provided the penetration and mixing of the resin. The collar end of the bolt is threaded for a dome nut placement behind a domed shape plate. In the hard rock mine, installation was done using a jackleg drill.

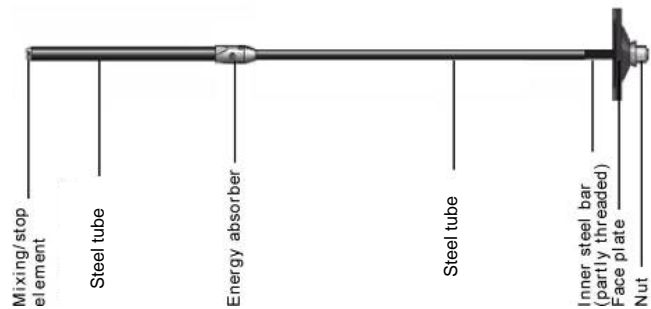


Figure 1 Components of a Roofex rock bolt (Atlas Copco, 2008).



Figure 2 End of a yielded Roofex bolt. The initially round steel tendon has been cold rolled into a hexagonal shape as it was pulled through the energy absorber

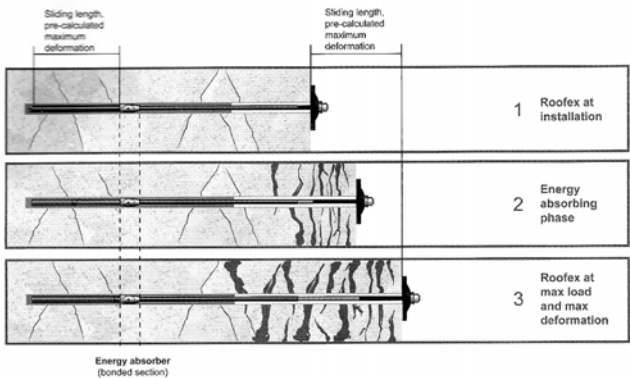


Figure 3 Yielding stages of a Roofex bolt (Atlas Copco, 2008).

Figure 3 is a drawing from Atlas Copco showing the Roofex bolt performance at three different stages of loading. The dark gray color in the borehole indicates the extent of the resin column. The first stage shown is after installation prior to any loading. The second stage shows “energy absorbing phase” when the bolt is pulled through the energy absorber’s grip while the remainder of the steel tendon moves freely inside the steel tubes that protects it from being in contact with the resin. The third stage shows the rock bolt after the maximum displacement has been achieved. Note that the energy absorber remains anchored in the same position in the borehole.

3 In-Situ Pull Tests

The in situ pull tests were performed at three different mines. Initial tests were performed at the Edgar Mine, which is the Colorado School of Mines experimental mine, mainly to familiarize the research team with the Roofex bolts and the specially designed pull test equipment. The main series of the pull tests were performed at two coal mines (Harvey and Ozbay, 2009).

A total of 24 pull tests were performed in three mines, 5 at the Edgar mine, 11 at Coal Mine A, and 8 at Coal Mine B. The testing was performed with an Enerpac electric ram equipped with a 250 mm stroke mounted on a custom made tripod. The pull load applied was 40 mm/min. The ram was connected to a computer which recorded the loads and displacements in real time. Figure 4 shows the tripod and ram in position prior a test at Edgar mine.



Figure 4 Tripod and ram pull test assembly at Edgar Mine.

As tests progressed, the following pull test parameters were identified as important and methods for their determination were established:

Bolt load: The pull load applied on the bolt was measured by the pressure sensor within the Enerpac hydraulic pump during the testing period and recorded on the portable computer.

Bolt displacement: The displacement induced on the bolt was monitored by a linear variable differential transformer fixed on the pull tester. The displacement data was recorded on a portable computer, which also allowed generation of real time plots of load-displacement performance of the bolts.

Borehole depth: This is the distance measured from the borehole collar to the back of the hole, measured using the drill steel and a tape meter.

Resin length: This measurement refers to the length of the bolt encased in resin. It assumes that the resin reaches the back of the hole. The resin length is the distance from the back of the hole to the front of the resin column in the hole.

Free length: This is the distance from the collar to the start of resin block in the borehole. It was measured before and after the test to establish if the resin was pulled out during the test.

Active resin column: This is an estimation of the resin length in front of the energy absorber. It was calculated by subtracting from the length of hole i) manually measured distance from the outside edge of the pull test nut to the borehole collar, ii) distance from the collar-side edge of the energy absorber to the back of the borehole (assumed to be constant at 380 mm), and iii) the free length as described above.

Rib deflection: The outward displacement of the collar area was measured using a laser range finder mounted to a tripod. Measurements were taken approximately every 30 seconds during the pull test to determine if the coal was being pulled out of the rib as a result of the testing.

3.1 Edgar Mine Hard Rock Tests

The Edgar Mine, located in Idaho Springs, Colorado, USA is the experimental mine of the Colorado School of Mines used for research and training. The first series of pull tests was performed in this mine as a way to become familiar with the mechanics of the rock bolt and the testing procedure prior to performing testing in two operational coal mines.

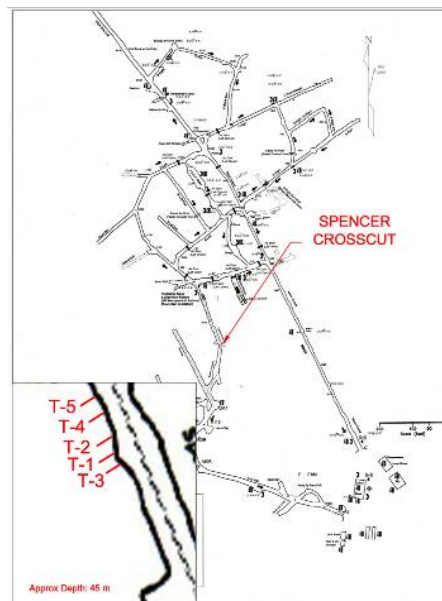


Figure 5 Edgar Mine test site and bolt locations

The drifts at the Edgar mine are typical horseshoe shaped openings mostly developed in the Precambrian Idaho Springs Formation, which consists of pegmatitic granite and gneiss with occasional igneous intrusions. The installation and testing was performed in the Spencer Crosscut under approximately 45 m of cover. Figure

5 shows an overview of the mine and the rock bolt locations in the insert. At the test location, the uniaxial compressive strength of the rock is about 150 MPa and the Rock Mass Rating ranges from 65 to 75.

The five 80 kN yield load rock bolts tested were 1.5 m long, with available yield displacement of 300 mm. A Gardner-Denver jackleg drill was used to drill 35 mm diameter holes to install the bolts. The bolts were secured with Lokset Medium Set resin provided by Minova USA.

Table 1 Edgar Mine installation parameters.

Test Id	Hole Depth (mm)	Resined Length (mm)	Free Length (mm)	Resin Spin Time (sec)	Active Resin Column (mm)
T-1	1500	1195	305	20	740
T-2	1498	1168	330	8	715
T-3	1500	1227	273	15	772
T-4	1500	1005	495	13	550
T-5	1486	1213	273	13	772

Table 1 shows the parameters that were measured during installation and testing. For the calculation of active resin column, the distance from the outside edge of the pull test nut to the borehole is assumed to be constant at 75 mm.

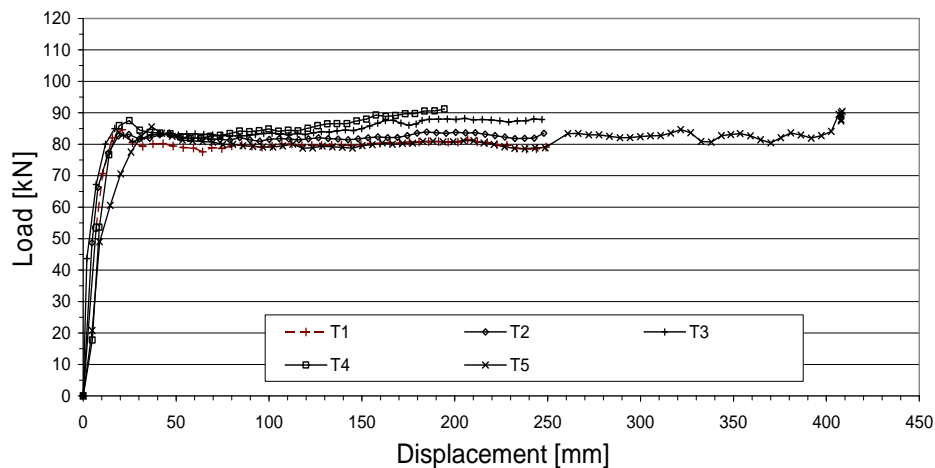


Figure 6 Edgar Mine pull test load - displacement plots.

Figure 6 shows the load - displacement plots developed from the pull test results. The graphs show that the bolts began to yield at loads of approximately 85 to 90 kN. Tests T-1, T-2, and T-3 were pulled one stroke of the ram (250 mm). During test T-5 the ram was pulled one stroke, then reset and pulled again. This test was stopped at 410 mm of displacement. Because the bolts only had an available displacement of 300 mm, the additional displacement must have occurred at another location. It is postulated that the steel was stretched, the bolt was pulled through the grout, or the grout was pulled out of the borehole at the back of the hole.

3.2 Coal Mine Tests

The second round of pull testing was performed at the Coal Mine A, which is a longwall operation at depths of about 220 m. The testing took place in the ribs of coal pillars located in a development section. Figure 7 shows an overview and detail (see insert) of the test location.

Eleven pull tests were performed at this location. All bolts were 1.8 m in length with available displacements of 300 mm. Five 80 kN, two 20 kN, two 30 kN, and two 40 kN yield load bolts were tested. The bolts were installed in 35 mm diameter boreholes by a Fletcher bolter and secured with Lokset Fast Set resin provided by Minova USA.

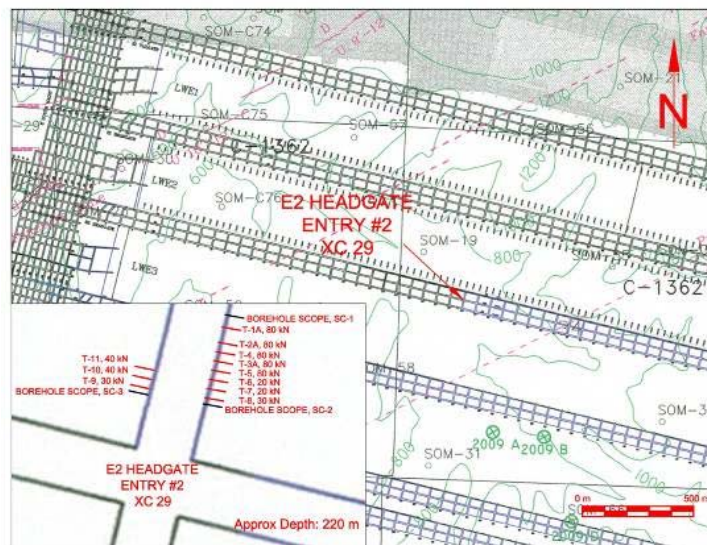


Figure 7 Coal Mine A test location.

Table 2 shows the experiment parameters measured during installation and testing. The hole lengths were slightly above the specifications within 2 percent. Also, the recorded magnitude of the rib deflection is too small to be concerned about. The resined lengths vary significantly possibly as a function of degree of fracturing around the hole.

Table 2. Coal Mine A Mine installation and test measurements.

Test Id	Design Yield Load (kN)	Hole Depth (mm)	Resined Length (mm)	Change in Free Length (mm)	Estimated Active Resin Column (mm)	Measured Rib Deflection (mm)
T-1A	80	1829	1639	--	1155	0
T-2A	80	1829	1613	0	1129	-2
T-3A	80	1829	1480	6	996	1
T-4	80	1816	1626	0	1155	2
T-5	80	1842	1690	0	1192	-1
T-6	20	1829	1699	0	1215	0
T-7	20	1816	1660	-3	1189	1
T-8	30	1829	1324	-10	840	1
T-9	30	1829	1635	-3	1151	0
T-10	40	1816	1530	19	1059	-2
T-11	40	1829	1569	--	1085	0

Figure 8 shows the load - displacement plots developed from the pull tests records. All of the bolts were pulled one stroke of the ram, i.e. 250 mm. Tests T-1A, T-2A, T-3A, T-4, and T-5 were performed on 80 kN bolts. The graphs show that these bolts start yielding around 80 to 88 kN pull force. The bolt loads during yielding within a bandwidth of 5 kN.

There does not seem to be an obvious relationship between the load variation and the measured parameters in Table 2. The largest measurement variations in this table occur with the parameters related to resin, however these are not necessarily consistent with the load variations. Typical example is the T-3 test that has largest load variation yet the least resin length coverage. An explanation could be that the intensity of loading by the energy absorber reduces along the resin length and becomes insignificant at a certain distance away from the energy absorber. If this postulation is true, it can be suggested that the resin length required to keep the energy absorber engaged without pulling out the resin or coal was more than sufficient in all the tests. The load variations were then most likely caused by the geological and geometrical variations around the borehole as well as the changes in pull directions as the tripod was being forced into the coal rib.

The smaller yielding capacity bolts show yielding at larger loads than their nominal values and slight load increase toward the end of their yield limit. The 20, 30, and 40 kN yield capacity bolts end up being loaded about 10 to 30 percent more than the design yield loads, respectively. It is believed that the cause for larger yield loads is related to the adjustment of the carbide pins. Otherwise, the overall steadiness of the yielding behaviour accords with the expected performance.

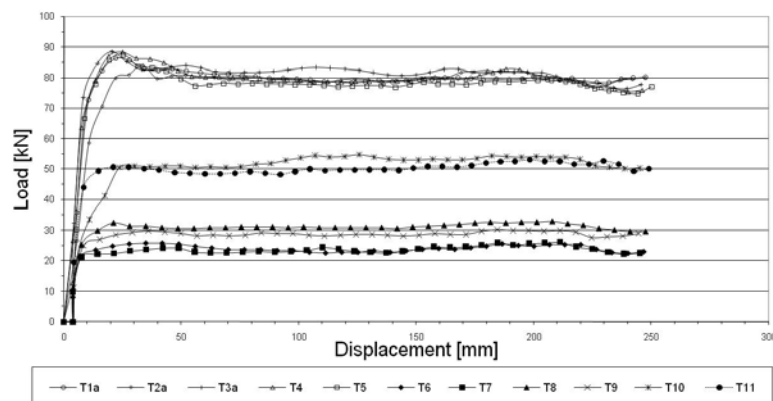


Figure 8 Coal Mine A Mine pull test load vs. displacement graphs.

3.3 Coal Mine B Tests

The third and last round of pull testing was performed at the Coal Mine B, also a longwall operation, but deeper. The tests took place in the ribs of both sides of a crosscut. The depth at this location is approximately 670 m, which caused spalling of ribs during development. Figure 9 shows the details of the test site.

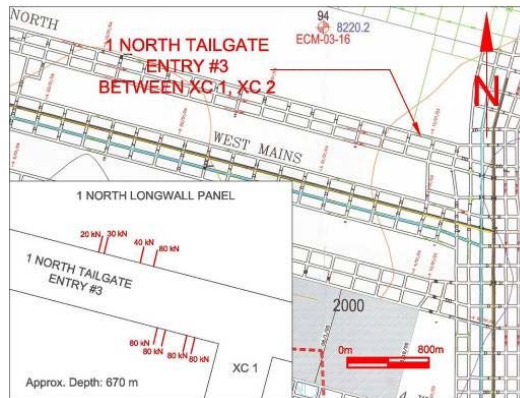


Figure 9 Coal Mine B test location.

Eight pull tests were performed at this site. Of these, five were performed on 80 kN, and one of each of the 40, 30 and 20 kN yield load bolts. As with the previous test site, the bolts were installed in 35 mm diameter boreholes drilled with a Fletcher bolter and secured with Lokset Fast Set resin provided by Minova.

Table 3 shows the parameters measured during installation and testing, and Figure 10 shows the load - displacement plots developed from the pull test results. As with the previous site, the bolts were pulled one stroke of the ram, 250 mm. Tests T-1, T-1R (repeat), T-2, T-3, T-4 and T-5 were 80 kN yield load bolts.

Table 3. Coal Mine B installation and test measurements.

Test Id	Design Yield Load (kN)	Hole Depth (mm)	Resined Length (mm)	Change in Free Length (mm)	Estimated Active Resin Column (mm)	Measured Rib Deflection (mm)
T-1	80	1943	1435	--	837	1
Retest	80	1829	1423	--	939	--
T-2	80	1854	1416	0	906	-2
T-3	80	1842	1556	0	1059	0
T-4	80	1778	1226	0	793	0
T-5	80	1854	1295	0	786	0
T-6	40	1854	1422	0	913	-1
T-7	30	1854	1568	6	1059	1
T-8	20	1854	1568	6	1059	1

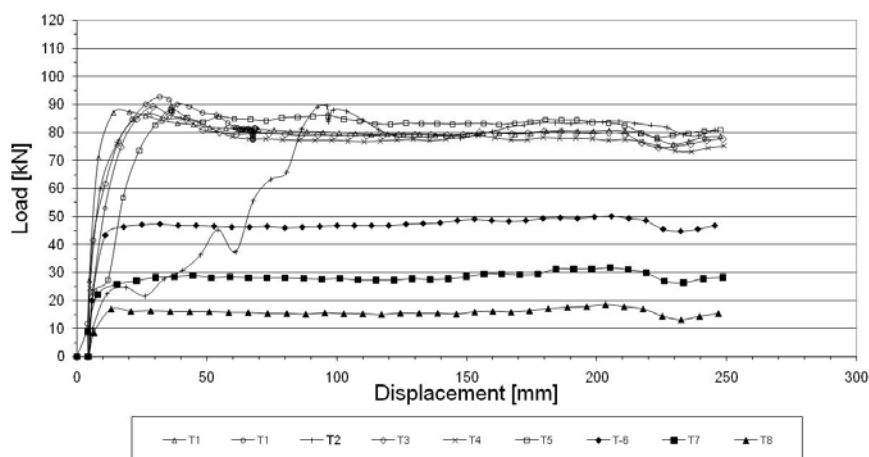


Figure 10 Coal Mine B pull test load - displacement graphs.

The load – displacement plots of the results from the Coal Mine B are presented in Figure 10. The fractured rib surface at the location of T-2 made the bolt installation difficult, resulting in a 150 mm gap between the plate and the coal rib. The irregularities before reaching the yield load in the load – displacement plot for this test, and on a smaller scale for T5 too, are caused by the settling of the tripod during the initial stage of loading at this location.

Otherwise, the plots in Figure 10 are similar to those obtained from the previous coal mine site, although the yield load of the 80 kN bolts are slightly more at this site. It is difficult to explain load increase on these bolts based on the available data other than knowing that the coal being reasonably fractured at this site due to mining depth.

The tests T-6, T-7 and T-8 were performed on bolts with yield loads of 40 kN, 30 kN, and 20 kN, respectively. The graphs of these tests indicate that yielding began at approximately 47 kN, 25 kN, and 18 kN, respectively. Overall, the bolts in this series plot a very similar load - displacement curves to those obtained in the Coal Mine A site tests.

4 Discussion of the Pull Test Results

Overall, the in situ tests results performed in three mines showed performance characteristics of the 80 kN yield load - 300 mm displacement Roofex bolts remained close to their design specifications. An important objective of the study was to find out whether the yielding mechanism of the Roofex bolts could engage coal without pulling the resin or the coal through the borehole. The results of the 80 kN yield load pull tests show that these bolts performed in coal as good as they did in the hard rock.

In general, the load - displacement plots of the 80 kN bolts show reasonably uniform performance with less deviation from the design values in the shallow coal mine compared to the deeper one. The occasional load peaks in the deeper mine case is believed to be, at least partially, due to the increased rib fracturing, which can potentially cause squeezing on the bolts.

The results from the 20 kN, 30 kN, and 40 kN yield load bolts show similar overall load - displacement behavior in both coal mine sites. They also show fairly levelled yielding behavior. The yield loads show up to 30 percent larger than the design load with these bolts. This is believed to be caused by the inaccuracies in the settings of the carbide bits rather than an inherent bolt or coal seam condition property.

The rib surface deflection measurements showed surface displacements of -2 to +2 mm around the hole. The negative deflection is due to coal flaking off at the measurement point. By taking into account the ± 1.5 mm accuracy of the laser range finder, the maximum deflection during pull testing may range from 0.5 to 3.5 mm, which is small enough to be considered inconsequential.

To determine if and how much the resin body had been pulled out of the borehole, the free length of the bolt from the resin end to the borehole collar was measured before and after a pull test. Of the 19 tests, the free length for 13 tests remained unchanged implying no resin movement at the point of measurement. Three tests show small shortening by 3, 4, and 10 mm and three tests show lengthening by 6, 7, and 19 mm. The shortening magnitudes are too small to be taken as these being translational movement of the resin body by the pull load affected on the energy absorber. The causes for lengthening is difficult to interpret from the test data, however, considering the fact that five of the six free length measurements took place at the smaller yielding load bolts, it may be postulated that these measurements could be caused due to inconsistencies between the before and after measurement locations. It is most likely that, during the tests, the resin body did not experience any significant translational pull out through the borehole during the pull before and after yielding.

It should be noted that all the interpretations and opinions presented in this report are based on the monitored and measured data. Further verifications of the findings would require additional efforts, such as overcoring of the tested bolts for visual observations.

5 Conclusions

The in situ tests showed performance characteristics of the 80 kN yield load - 300 mm displacement Roofex bolts remained close to their design specifications. All the bolts tested were able to secure anchorage in coal and yield over 250 mm displacement under slow (40 mm/min) loading conditions. The results also show that the bolts performed without pulling the resin body out of the borehole and without pulling the coal out of the rib.

It is important to note that pull testing do not necessarily replicate the loading conditions that exist in practice. Further studies of the performance of these bolts in actual mining conditions, including under dynamic loading ones, are necessary for a more complete assessment of the effectiveness of these bolts in mitigating dynamic rib failures. Nevertheless, the encouraging performance shown through the pull test study should be seen as a step forward towards building an effective dynamic support system, inclusive of adequate skin support.

Acknowledgements

This experimental information presented in this paper was obtained during a contract project supported by NIOSH, Spokane Research Laboratory, Spokane, WA. The authors would like to thank the managements of the two coal mining companies as well as the Atlas Copco and Minova USA for their support and assistance in making these research findings possible.

References

1. Plouffe, M., Anderson, T. and Judge, K. Dynamic Testing of Roof Tendons (Roofex). <http://www.roofexrockbolt.com/kampanj/index.html>, 2008.
2. Harvey, S. and Ozbay, U. In-situ Testing of Roofex Yielding Rock Bolts. A Report Submitted to NIOSH, Spokane Research Laboratory, Spokane, (WA, 2009).
3. Atlas Copco. Atlas Copco Rock Reinforcement Products, Rock Reinforcement Catalogue, Roofex™ Rock Bolts and Monitor Bolts. Atlas Copco Craelius AB, Marsta, (Sweden, 2008).

EVENT MECHANISM ANALYSIS FOR SEISMICITY INDUCED BY A CONTROLLED COLLAPSE IN FIELD II AT OCNELE MARI, ROMANIA

VLADIMIR SHUMILA and CEZAR-IOAN TRIFU

Engineering Seismology Group Canada Inc.

Kingston, Ontario K7K 7G3, Canada

The monitoring of a controlled collapse with an array of 36 uniaxial geophones provides stable and reliable point source event mechanism solutions based on automatic moment tensor inversion using time domain estimates of low frequency amplitudes with first polarities attached. Uniaxial recordings with 10% random noise allow for only marginally lower quality solutions compared to inversions based on triaxial recordings. Detailed analysis of failure mechanism components is carried out on 912 solutions with conditional number $CN < 100$ and a correlation coefficient $r^2 > 0.5$. The largest pure shear (DC) components characterize the events surrounding the cavern ceiling, which exhibit normal and strike-slip failures. The majority of mechanism solutions include up to 30% explosive failure components, which correspond to roof caving under gravitational collapsing. The largest vertical deformation rate relates closely to the cavern roof and floor, as well as the rest of the salt formation, whereas the horizontal deformation rate is most prominent in areas of detected collapses.

1 Introduction

Twenty-two years of salt exploitation through dissolution in Field II at Ocnele Mari (Romania) has led to the elimination of inter-chamber pillars of six of the fifteen wells, containing 5.5 million m³ of compressed brine uphill an inhabited area. A major collapse in March 1991 was followed by a second in September 2001, when a part of the roof sunk leaving a crater of 200 m diameter, and a third in July 2004, which increased the earlier sinkhole and the hazard of a catastrophic spill. To resolve this problem, a controlled collapse was designed and implemented during the second half of 2005 [1]. This included the opening of the cavern roof through a rock fragmentation process accelerated by the pumping of the brine out, while sterile was introduced to maintain the overall hydraulic pressure in check.

A subsurface seismic array was installed around the cavern to continuously monitor an area of about 1 km² to ensure the safety of the workforce and equipment employed, as well as provide information as to how the collapse proceeded. The array comprised of 36 uniaxial, omni-directional 15 Hz geophones sensors installed in 12 boreholes down to 360 m deep, three sensors per borehole. Data were recorded at the top of each hole with a sampling frequency of 2 kHz and transmitted continuously via radio Ethernet to a control centre. A total of 2392 seismic events with Mw from -2.6 and 0.2 were recorded between July 2005 and March 2006. Location errors (in a vectorial sense) fit closely a normal distribution with an average of 18 m, while the frequency magnitude distribution outlined a b-value of 1.5.

The monitoring results have been presented in [2]. Using a collapsing technique that provides higher accuracy relative event locations, they showed that the distribution of seismicity is composed of several spatially tight clusters. Most seismicity was related to the fragmentation and falling of the main cavern roof, whereas lesser active clusters correspond to the roof fracturing of smaller size, nearby caverns. Seismicity located deeper in the main cavern was caused by subsequent debris. The b-value changed over time from 0.5 to 1, and then to 1.5. This indicates that the fracture process initiated as a linear fracture pattern ($D = 2b = 1$).

Three months later roof fragmentation was well developed and shear fractures dominated ($D = 2$), while towards the end of the reported period fractures occurred within the entire volume ($D = 3$). Analysis of the off-spring seismicity outlined a super-critical process.

The present study attempts to investigate the mechanisms of the seismic events induced during the controlled collapse. Event mechanism solutions are obtained through the seismic moment tensor inversion of the uniaxial geophone recordings. First, the reliability of such inversions is analyzed for the sensor array employed. Then, spatial distribution of different failure components is examined. Based on the derived mechanism solutions, an estimate of the seismic deformation field is finally obtained.

2 Stability and Reliability of Seismic Moment Tensor Inversions

The use of uniaxial recordings maintains the linear dependence of the low frequency far-field displacements, with first polarities included, on the six unknown components of the symmetrical seismic moment tensor which describes a point seismic source [3]. As such, evaluation of the event mechanism consists in the determination of the seismic moment tensor through the linear inversion of the above displacements. Worth noting, low frequency displacements can be calculated in the time domain, which allows for an automated, on-line estimate of source mechanisms [4]. Before discussion the inversion results obtained for the recorded seismicity, the stability and reliability of the seismic moment tensor inversions is analyzed for the array geometry and sensor characteristics employed at Ocele Mari. The sensor array geometry is shown in Figure 1.

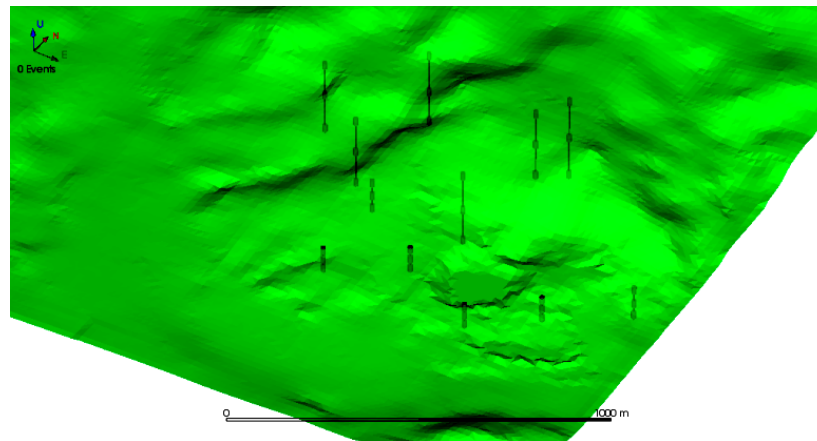


Figure 1 Seismic array configuration at Ocele Mari. The sinkhole occurred in 2001 is also evident.

A measure of the stability of seismic moment tensor inversion is given by the Conditional Number (CN) [5]. This is defined as the ratio between the largest and smallest eigen values of the data matrix to be inverted [4]. It is equal to one for a perfectly invertible matrix and approaches infinity for a very ill-conditioned matrix. CN can be interpreted as a data noise amplifier that defines the upper bound of the model parameter errors. Since it depends only on the source location and array geometry, expected CNs are calculated and displayed in Figure 2. The most stable inversions ($CN < 10$) are expected for the sources located below 200 m elevation. In the close proximity to the major cavern ceiling the anticipated inversion CN is around 15 and increases towards surface (Figure 2b). In immediate vicinity of most sensor wells CN reaches the highest values and these zones should be considered as ‘blind spots’ for inversions. Overall, the CN results suggest that reasonably stable moment tensor inversions are expected for the installed sensor array.

To further analyze the stability and reliability of moment tensor inversions, data were randomly perturbed using a Monte-Carlo approach to simulate increased noise levels. Additionally, tests have been carried out to evaluate the effect of using triaxial recordings, as compared with actual uniaxial recordings, from a potential array of sensors installed in identical locations. Figure 3 summarizes the results obtained for three arbitrarily chosen seismic events located in the vicinity of the major cavern ceiling. Based on actual event mechanism solutions, theoretical low frequency amplitude levels with first motion polarities were calculated for the P-, SV-, and SH-waves. These data were then perturbed by 10% Gaussian noise in the amplitude domain and randomly altering 10% of first polarities.

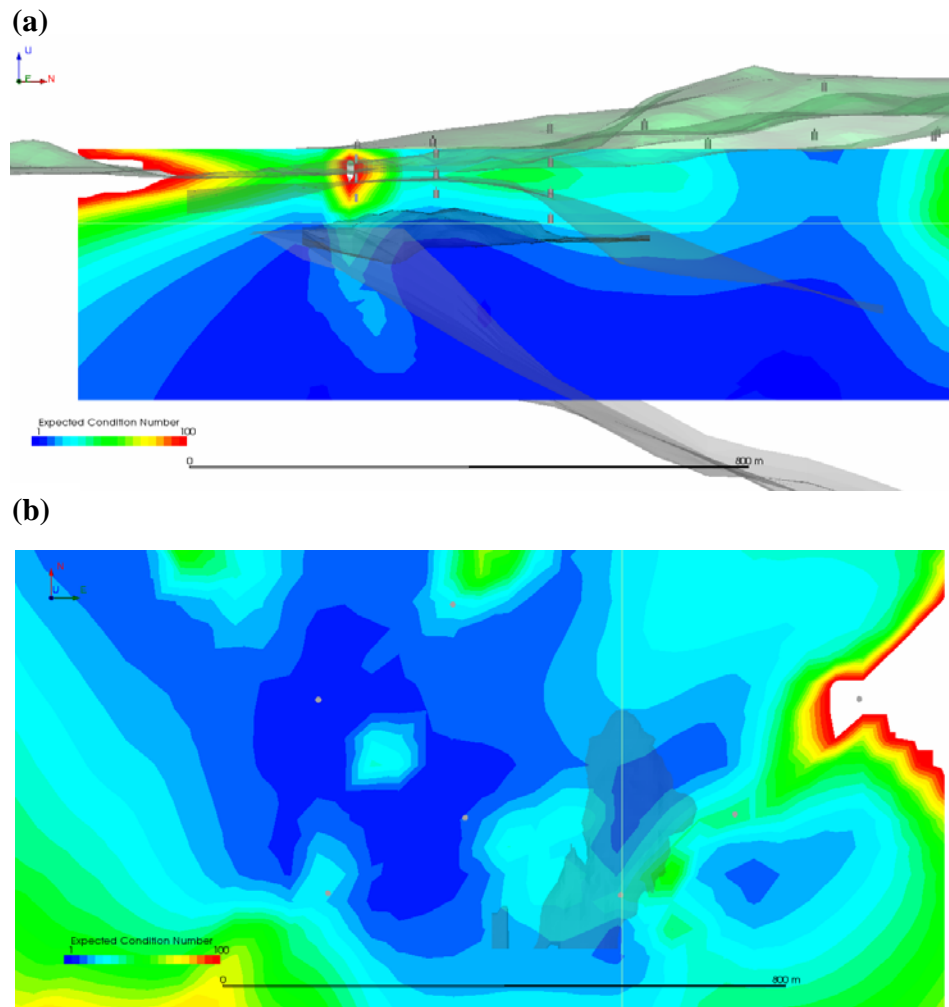


Figure 2 Distribution of expected CN for seismic moment tensor inversions: (a) south-north vertical cross-section looking east and (b) north-east plane at 200 m elevation looking down. Horizontal and vertical thin light lines show the positions of the respective projections. Semitransparent surfaces in (a) represent - from top to bottom - the topography, salt layer upper boundary, major cavern ceiling, and salt layer lower limit. Gray cylinders in (a) denote uniaxial geophone locations, whereas gray circles in (b) the positions of vertical boreholes. Semi-transparent surface crossed by the vertical line in (b) is the part of the major cavern that lies above 200 m elevation.

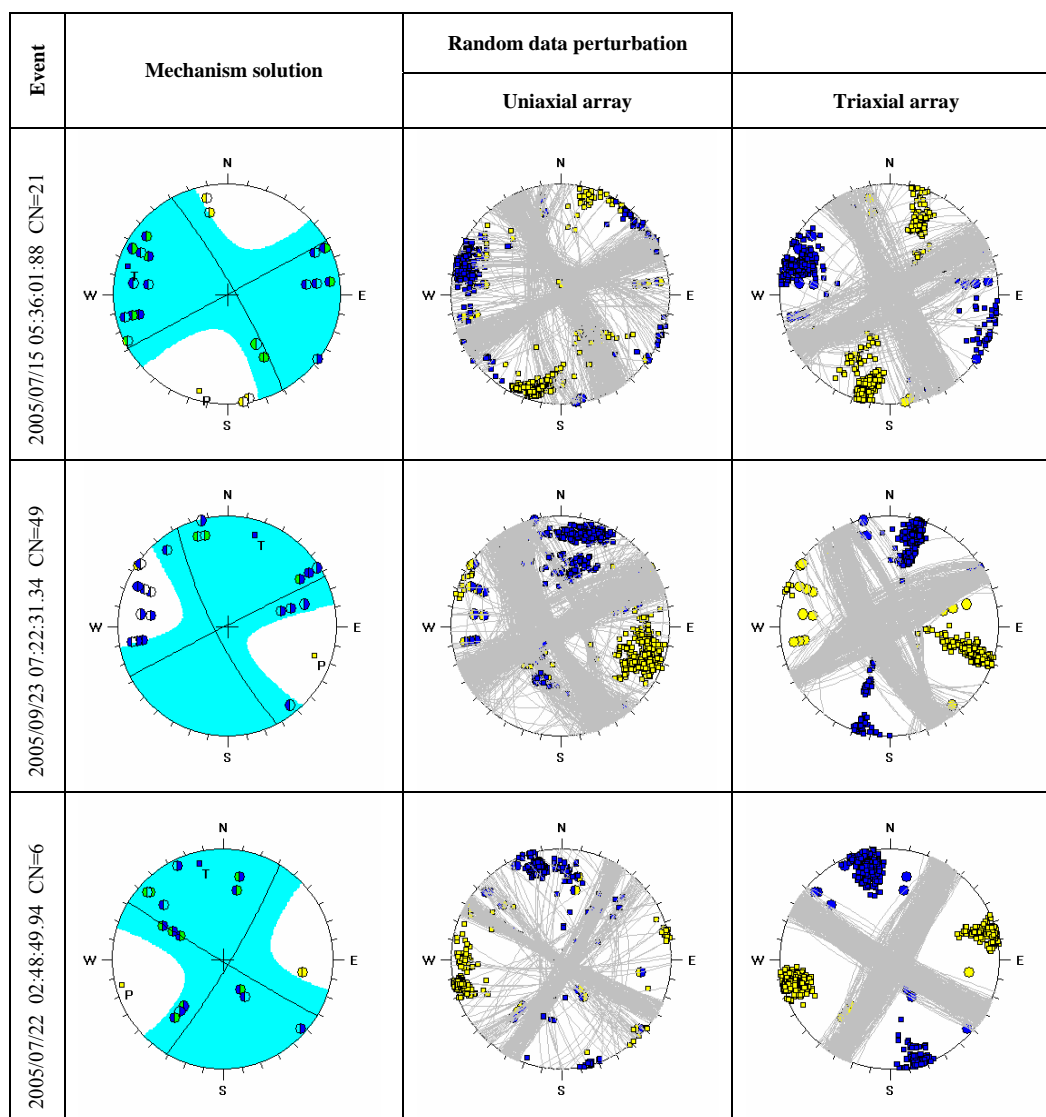


Figure 3 Stability of moment tensor inversions (column 1) under 10% random perturbations for the installed uniaxial seismic array (column 2) and a hypothetical triaxial seismic array (column 3) with similar sensor locations.

For each particular moment tensor solution shown in column 1, 500 major double-couple (DC) solutions [6] obtained through random perturbations are displayed superimposed in columns 2 and 3 using a lower hemisphere equal angle projection [7]. These results indicate that the use of uniaxial recordings provided by the geophone array installed at Ocele Mari offer both stable and reliable seismic moment inversions. Interestingly, the use of triaxial recordings would only lead to slightly more stable solutions.

A total of 2159 events were recorded and located between July 7 and December 31, 2005. Seismic activity included three outburst episodes associated with two minor collapses in October and November, and the major cavern collapse at the end of December. Automatic seismic moment tensor solutions have been obtained for

1518 events. The distributions of Condition Numbers (CN) and multiple correlation coefficients (r^2) for this dataset are shown in Figure 4.

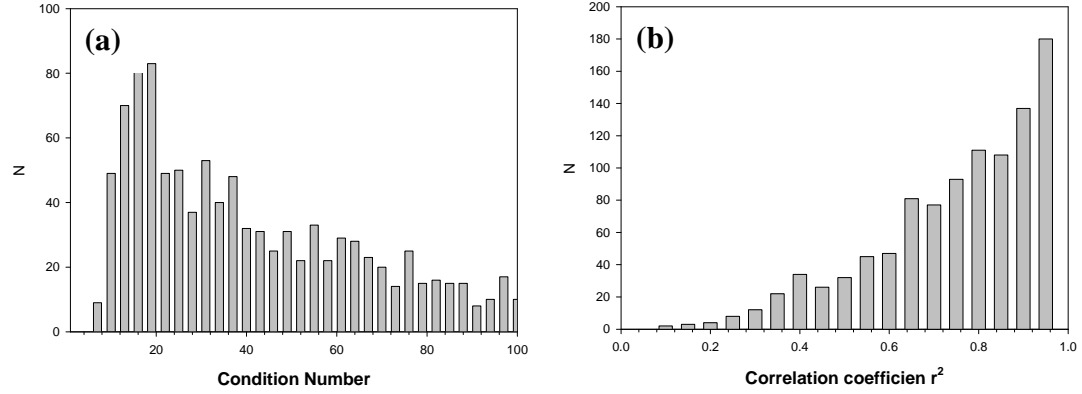


Figure 4 Condition number (a) and multiple correlation coefficient (b) distributions for automatic event mechanism solutions.

Average CN estimates for real moment tensor inversions are calculated over the same three-dimensional grid employed to analyze the expected CN values for the array (Figure 2). Space distributions of average CNs are presented in Figure 5. In general, real CN values are in agreement with expected ones. Slightly higher levels of real estimates in some areas are easily explained by the extrapolation of observed CNs to no-data grid points.

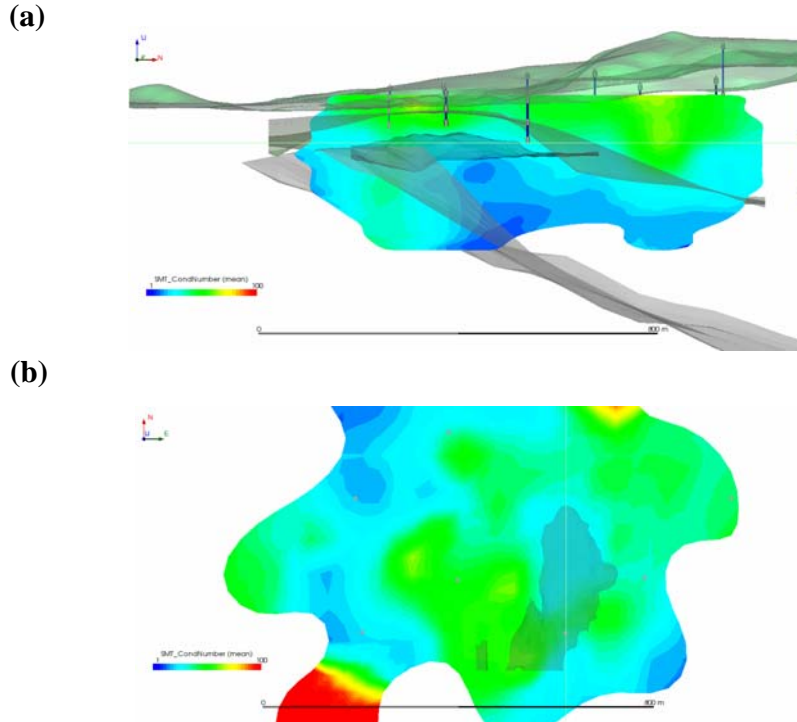


Figure 5 Distribution of average CN for actual moment tensor data inversions: (a) south-north vertical cross-section looking east and (b) north-east plane at 200 m elevation looking down. Horizontal and vertical thin light lines show the positions of respective projections (see Figure 2 for legend).

3 Analysis of Event Mechanisms

Due to previous massive collapses occurred in 1993, 2001 and 2004, the salt deposit is expected to contain highly fractured volumes with a heterogeneous local stress distribution. The collapsing of a fractured rockmass is compatible to the presence of both shear and non-shear fracture components. Consequently, it is anticipated that the seismicity generated by the controlled roof collapse will exhibit a large variety of seismic source mechanisms. After filtering out the events with $CN > 100$ and $r^2 < 0.5$, a dataset of 912 solutions is available for further analysis.

Traditional two-dimensional mapping of event mechanisms involves equal area or equal angle projections on upper or lower hemisphere. This type of representation is adequate for tectonic seismicity with relatively limited number of solutions and predominantly DC type mechanisms. In case of induced seismicity, however, source distribution is essentially three-dimensional. To represent as much information as possible, each moment tensor solution will be shown as a three-dimensional sphere with nodal planes defined by the major DC component.

A red-green-blue (RGB) three-dimensional color space offers a convenient equivalent for the coloring of the tensional quadrants based on the fact that the absolute values of the decomposition coefficients into isotropic, compensated linear vector dipole (CLVD), and double-couple (DC) failure components vary between 0 and 1 and their sum is equal to one [8]. Since present monitoring seismic arrays can provide online mechanism solutions for thousands of events, the visualization of this amount of information is not trivial. Figure 6 shows the spatial distribution of the derived mechanism solutions.

To further emphasize the relationship between the underlying geological structures and spatial distribution of seismic sources, Figure 7 displays the event mechanisms in a north-east plane view. It is worth noting that source locations exhibit strong correlation with structural elements on site, particularly with the sinkholes caused by previous collapses.

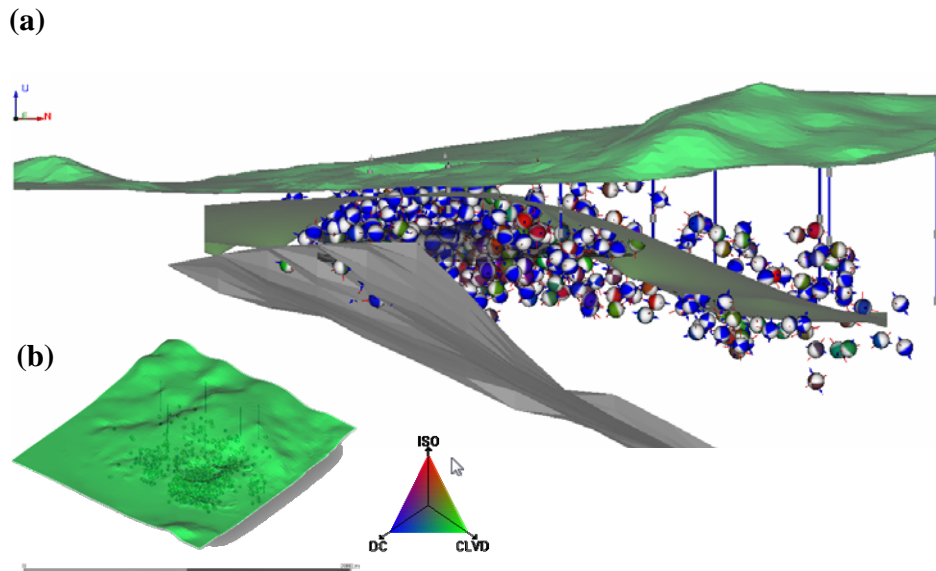


Figure 6 (a) Cross-section looking east projection of the mechanism solutions. Vertical lines represent the boreholes in which the sensors were deployed (gray cylinders). (b) Aerial view looking north-west of the monitoring area is shown to illustrate the relationship between source locations and topography.

Tension (T) and pressure (P) axes are presented in Figure 8 for major DC components of the mechanism solutions. Spatial distribution exhibits the ‘broken glass’ pattern, a reflection of the local stress distribution in the highly fragmented upper part of the salt dome. Note the quasi-circular and radial orientation of the T- and P-axes, respectively, adjacent to the sinkhole.

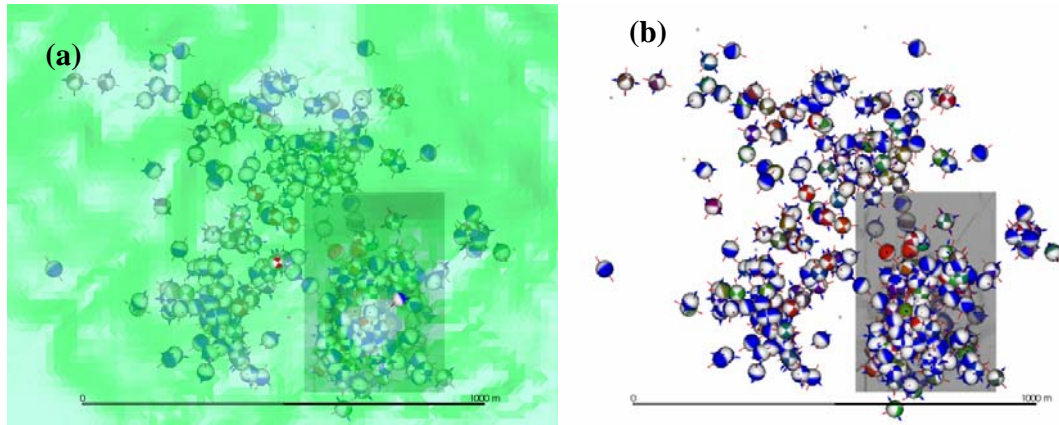


Figure 7 Plane view (north-east looking down) distribution of even mechanism solutions (a) with and (b) without underlying landscape. The darker rectangle indicates the location of the cavern collapsed in 2001.

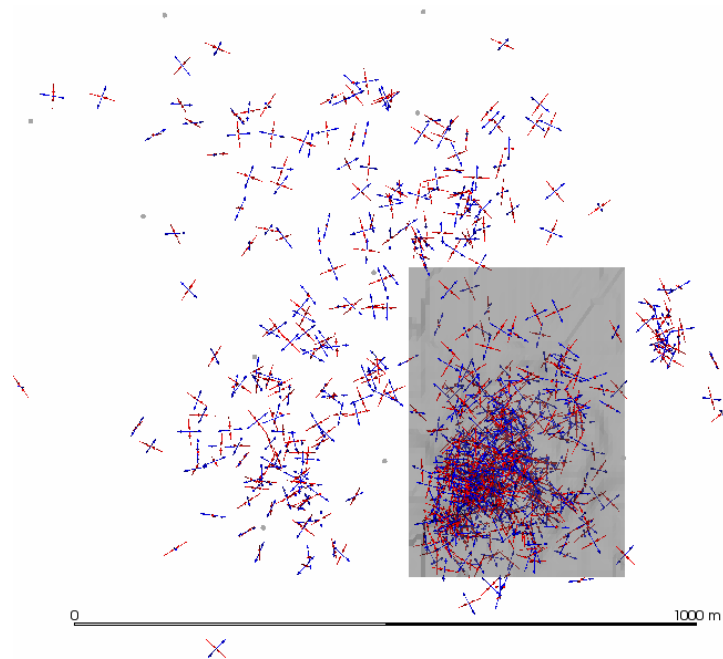


Figure 8 Distribution of the T (blue) and P (red) axes for the analyzed mechanism solutions.

A summary of the geometry of the shear faulting components and of mechanism distributions are presented in Figure 9 on the faulting [9] and source type [10] diagrams. Faulting type diagram (Figure 9a) shows that the data set predominantly contains normal and strike-slip events. The mechanism type diagram (Figure 9b) also

includes the location error ellipsoid (purple area) in t-k coordinates, calculated using a linear error propagation approach. Subvertical grid line (k) measures volumetric changes and remains constant along subhorizontal grid line (t) which characterizes departure from pure DC mechanism. Both coordinates range from -1 to +1. The following notations are used: \pm Crack for opening (+) or closing (-) tensile fault; \pm Dipole for force dipoles directed outward (+) or inward (-); \pm CLVD for compensated linear vector dipole with sign determined by the direction of dominated dipole forces. As expected, the dataset reveals a variety of source mechanism types. Most events lay in the region containing the nodal planes of the P-wave radiation. This is the latitudinal strip between \pm Dipole marks. Also, note that majority solutions are in the area where tensile components of failure (slip vector out of faulting plane) are allowed.

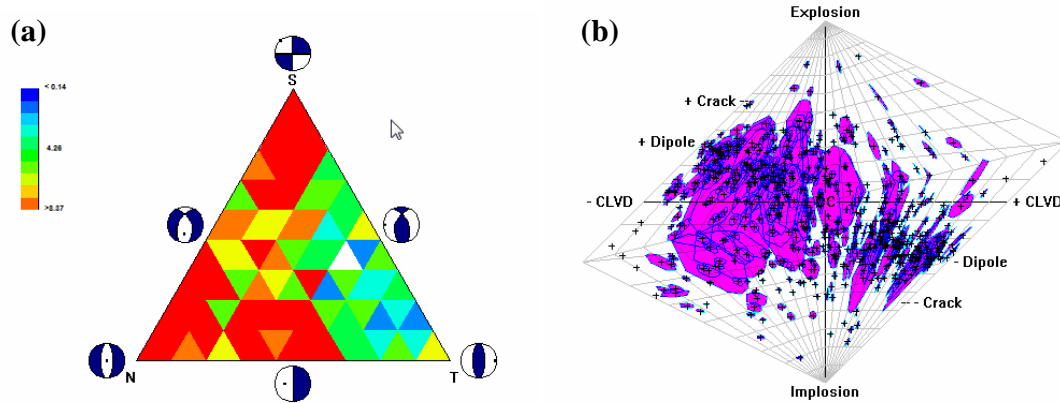


Figure 9 (a) Faulting and (b) mechanism type diagrams of the obtained mechanism solutions.

Evaluating the failure components is important for the understanding of the stress re-distribution and geomechanical processes taking place on site. Although Figure 9 provides an insight into the seismicity generation in the area of the controlled collapse, it does not contain information on the spatial distribution of the failure components. To obtain this, average parameter estimate is calculated over the closest events at each grid mapping by employing a nearest neighborhood approach with restriction on the search radius.

Spatial distribution of the isotropic failure component evaluated through the decomposition of the moment tensor solution is presented in Figure 10. Scale is from -10 to 100%. Negative and positive values indicate implosional (contraction) and explosional (expansion) volumetric changes, respectively. As expected for the geomechanical processes which took place in the area under investigation, only a small part of the study volume was subjected to seismic events with implosional components of failure. It can be speculated that such events occurred either on the floor of the cavern under gravitational forces, or in places where the inter-chamber pillars were destroyed by dissolution processes. The results indicate that vast majority of the mechanism solutions include up to 30% explosional failure components, which correspond to roof caving under gravitational collapsing.

DC components indicating pure-shear failure are shown in Figure 11. The largest such components correspond to events surrounding the cavern ceiling. Above and below this area the percentage of the DC component decreases. Note that low values that occur towards the map boundary are caused by very sparse sampling.

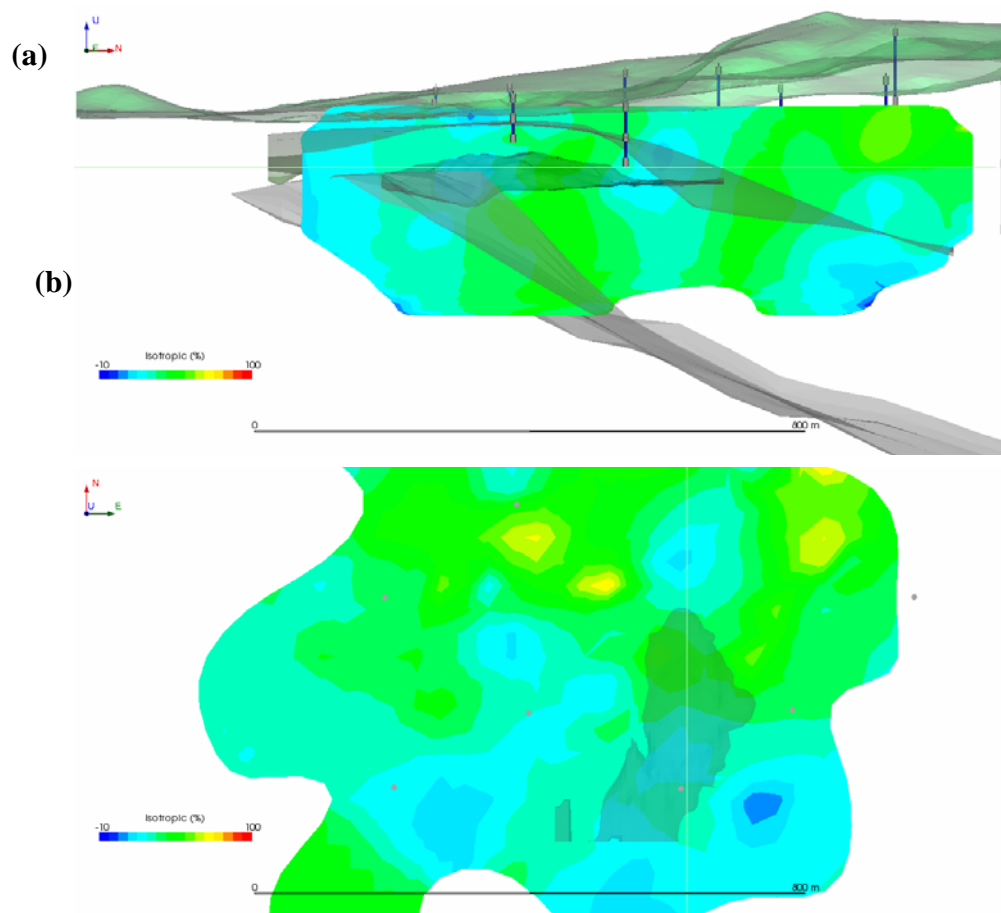
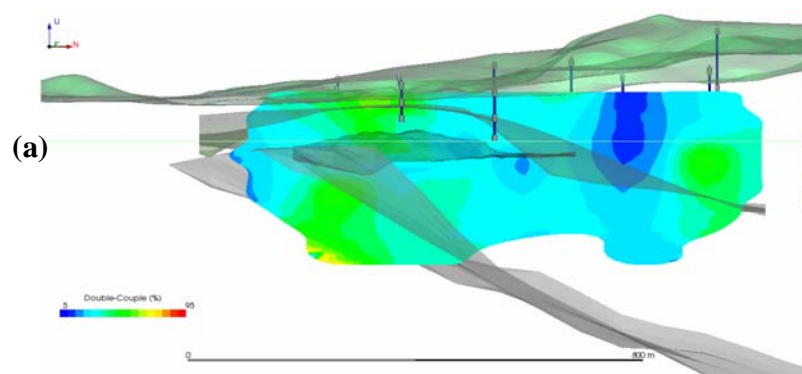


Figure 10 Isotropic failure component in (a) south-north vertical cross-section looking east and (b) north-east plane at 200 m elevation looking down. The horizontal and vertical thin light lines show the positions of the respective projections (see Figure 2 for legend).



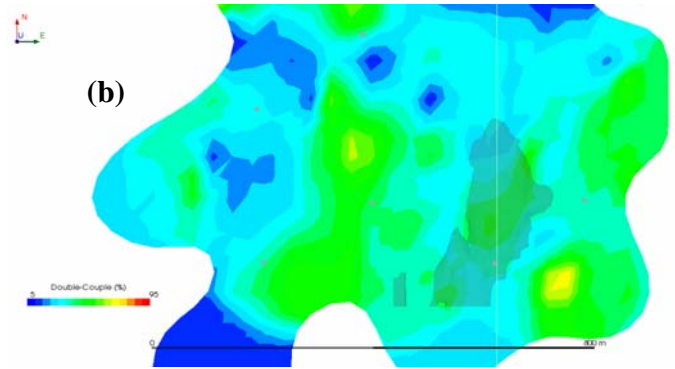


Figure 11 Pure-shear (DC) failure component in (a) south-north vertical cross-section looking east and (b) north-east plane at 200 m elevation looking down. The horizontal and vertical thin light lines show the positions of the respective projections (see Figure 2 for legend).

Distribution of the CLVD components is displayed in Figure 12. Such a failure component could correspond to a rotation of the plane of slip, or off-plane shear. Low percentage CLVD components dominate the mechanism solutions for the vast majority of the monitoring volume. The pronounced zones with high percentage of CLVD are noticed at the periphery of this volume and correspond to poor data sampling.

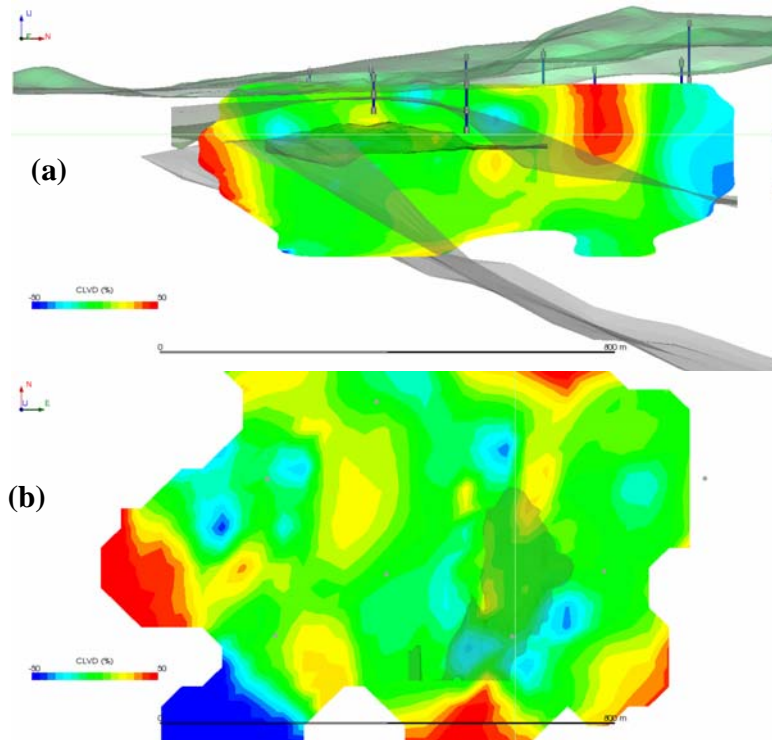


Figure 12 CLVD failure component in (a) south-north vertical cross-section looking east and (b) north-east plane at 200 m elevation looking down. The horizontal and vertical thin light lines show the positions of the respective projections (see Figure 2 for legend).

A generalization of the pure-shear point source model was proposed by [8] in which the slip vector could be out of the faulting plane by an angle α called tensile angle. A positive angle indicates a tensional seismic

source, whereas a negative value denotes a compressive source. Pure shear sources will have $\alpha = 0^\circ$, while 90° and -90° correspond to pure tensile and pure compressive sources, respectively. Tensile angle is estimated from the coefficients of the moment tensor decomposition and its spatial distribution is presented in Figure 13. Discarding extreme values at the boundary of the study volume, it is apparent that regions characterized by tensile / compressional values correlate well with pre-existing geological structures.

4 Seismic Deformation Field

When source locations are distributed over an entire volume rather than over limited number of failure planes, the integrated seismicity can be treated as a flow within the rock mass [11]. A formalization of this approach [12] shows that the integrated effect of N seismic sources that occurred in the elementary volume ΔV during the time interval Δt causes a deformation described by the following strain rate tensor

$$\dot{\epsilon}_{ik} = \frac{\sum_{n=1}^N M_{ik}^n}{2\mu\Delta V\Delta t} \quad (1)$$

where M_{ik}^n are the components of second rank symmetric moment tensor for the n -th event in ΔV , μ is the shear modulus, and i, k are indexes denoting the axes of the coordinate system. Standard approach for strain rate mapping was based on sparse regional seismicity, in which case it was necessary to account for missing small earthquakes. This was done by separating moment tensor geometry (failure components) and size (scalar seismic moment M_0). M_0 was then integrated using a recurrence law over the entire expected energy range in the volume of interest [12].

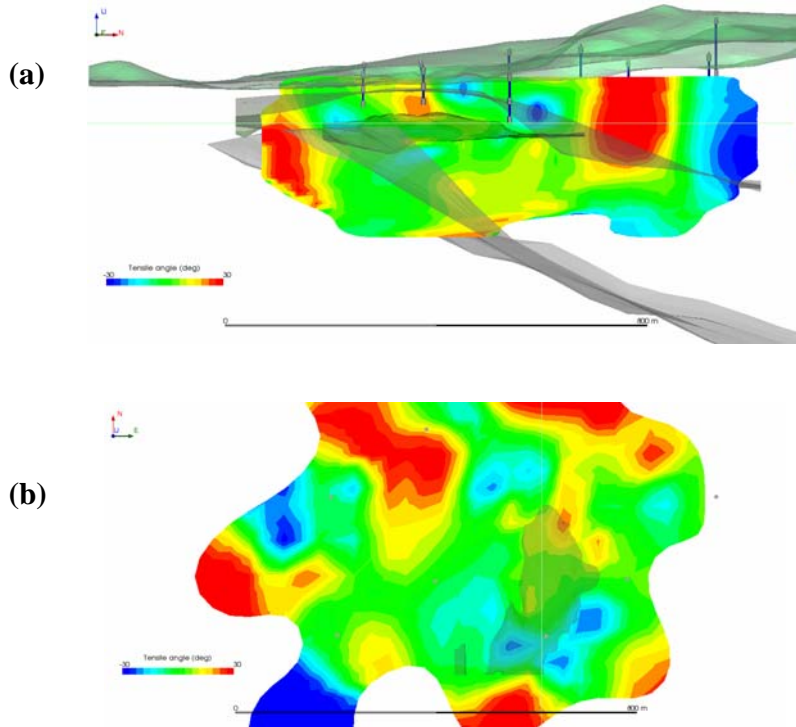


Figure 13 Tensile angle ($^\circ$) in (a) south-north vertical cross-section looking east and (b) north-east plane at 200 m elevation looking down. The horizontal and vertical thin light lines show the positions of the respective projections (see Figure 2 for legend).

In the current study statistics are very rich. As such, there is no need to use a recurrence law for seismicity extrapolation. Instead, equation (1) can be applied directly. Evaluation of strain rate tensor components is performed over a rectangular three-dimensional grid with 20 m steps in both northing and easting coordinates, and 10 m step in elevation. At each grid point the volume comprising a predefined number of events is used as elementary volume ΔV . Time interval between the first and last event occurrence in ΔV is considered as elementary time interval Δt in equation (1). Figure 14 displays the vertical component of the strain rate tensor ($\dot{\epsilon}_{zz}$).

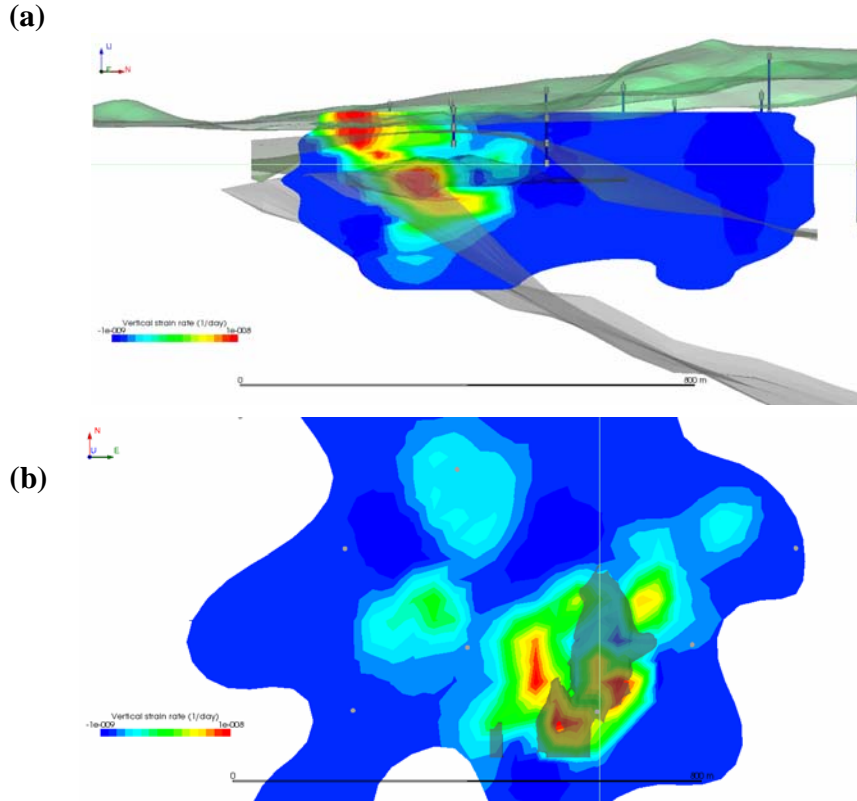
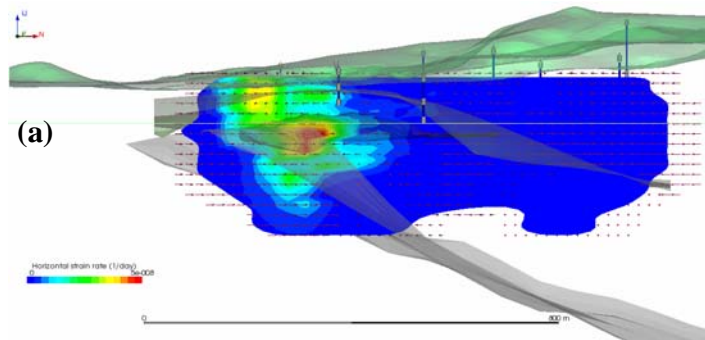


Figure 14 Vertical component of the strain rate (day^{-1}) in (a) south-north vertical cross-section looking east and (b) north-east plane at 200 m elevation looking down. The horizontal and vertical thin light lines show the positions of the respective projections (see Figure 2 for legend).



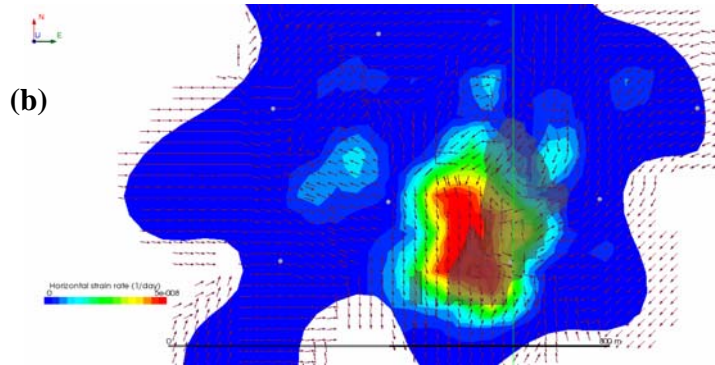


Figure 15 Horizontal component of the strain rate (day^{-1}) in (a) south-north vertical cross-section looking east and (b) north-east plane at 200 m elevation looking down. The horizontal and vertical thin light lines show the positions of the respective projections (see Figure 2 for legend).

The highest vertical deformation rate tends to be related to pre-existing geological structures, such as the cavern roof and floor, as well as the rest of the salt formation. Horizontal component of the strain rate tensor is defined as $\bar{u} = \{\dot{\epsilon}_{xx}, \dot{\epsilon}_{yy}\}$ and shown in Figure 15. The vector magnitude corresponds to the colour code, while its direction is represented by the unit arrow. Note that vertical cross-section is looking at the projection of unit direction. As expected, the horizontal deformation rate is most prominent in the areas of detected collapses.

5 Discussion and Conclusions

The goal of this study was to analyze the mechanisms of seismic events recorded during the controlled collapse of a large salt dissolution cavern in Field II at Ocele Mari. Since the monitoring was carried out with a staggered array of 36 uniaxial geophones, assessing the feasibility of carrying out moment tensor inversions on uniaxial recordings was important. Based on results obtained on simulated (theoretical) data with 10% random noise, it has been concluded that the uniaxial geophone array installed on site allows for stable and reliable event mechanism inversions. It has also been shown that the use of triaxial recordings obtained at similar sensor locations would have only marginally contributed to increase the stability and reliability of event solutions.

A total of 1518 event mechanism solutions have been obtained for the seismicity occurred from July and December 2005 (2159 events with magnitudes between -2.6 and 0.2). Eliminating the solutions characterized by a conditional number $CN > 100$ and a multiple correlation coefficient $r^2 < 0.5$, a dataset of 912 solutions was retained for detailed analysis. The analysis of spatial distribution of various failure components of the moment tensor solutions reveals interesting correlations with pre-existing geological and man-made structures on site. The tension (T) and pressure (P) axes for the major DC components exhibit a quasi-circular and radial orientation adjacent to the major sinkhole, respectively. The largest pure shear (DC) components characterize the events surrounding the cavern ceiling, which appear to exhibit normal and strike-slip failures.

The analysis of the isotropic failure component outlines that only a small part of the study volume was subjected to seismic events with implosional sources, associated with roof fragments hitting the cavern floor under gravitational forces, or the dissolution of inter-chamber pillars. Worth noting, the majority of the mechanism solutions include up to 30% explosional failure components, which correspond to roof caving under gravitational collapsing. Low percentage CLVD failure components, perhaps indicative of shear occurring off the plane of slip, dominate the mechanism solutions within the monitoring volume. The presence of the CLVD failure and tensile shear faulting [8] need further investigations. Meanwhile, the presence of high fluid pressure

on site satisfies the main physically condition for permissible tensile faulting. Also, salt dissolution processes can produce failure components departing from pure-shear.

Moment tensor solutions are further employed to evaluate the strain rate tensor components over a rectangular three-dimensional grid with 20 m steps in both northing and easting coordinates, and 10 m step in elevation. The highest vertical deformation rate relates closely to the cavern roof and floor, as well as the rest of the salt formation, whereas the horizontal deformation rate is most prominent in areas of detected collapses.

The present study proves that automatic event mechanism evaluation reflects expected trends for controlled salt mine collapsing. Further studies should analyze the evolution of the mechanism solutions over time, since this has the potential to offer indicative elements for detecting the initiation of the above processes and thus contribute to the assessment of the progress and control of this engineering activity. Such an analysis will obviously benefit from information on the geotechnical measurements carried out on site during the controlled collapse, such as surface crack orientation and size, rate of water inflow, brine pressure, etc.

References

1. Zamfirescu, F., Mocuta, M., Constantinescu, T., Nita, C. and Danchiv, A. The Main Causes and Processes of Instability Evolution at Field II of Ocnele Mari – Romania. Solution Mining Research Institute Spring Meeting, (Basel, 2007).
2. Trifu, C.I. and Shumila, V. Microseismic Monitoring of a Controlled Collapse at Ocnele Mari, Romania, Proc. 42th US Rock Mechanics Symposium, American Rock Mechanics Association, (San Francisco, 2008).
3. Trifu, C.I. and Shumila, V. The Use of Uniaxial Recordings in Moment Tensor Inversions for induced Seismic Sources, *Tectonophysics*, 2002,(356). 171-180.
4. Trifu, C.I., Angus, D. and Shumila, V. A Fast Evaluation of the Seismic Moment Tensor for Induced Seismicity, *Bull. Seismol. Soc. Am.* , 2000, (90). 1521-1527.
5. Dufumier, H. and Rivera, L. On Resolution of the Isotropic Component in Moment Tensor, *Geophys. J. Int.* , 1997, (131). 595-606.
6. Jost, M.L. and Herrmann, R.B. A Student'S Guide to and Review of Moment Tensors, *Seism. Res. Lett.* , 1989,(60). 37-57.
7. Aki, K. and Richards, P.G. *Quantitative Seismology: Theory and Methods*, W.H. Freeman, (San Francisco, 1980).
8. Vavrycuk, V. Inversion for Parameters of Tensile Earthquake, *J. Geophys. Res.* , 2001, (106). 16339-16355.
9. Frohlich, C. Display and Quantitative Assessment of Distributions of Earthquake Focal Mechanisms. *Geophys. J. Int.* , 2001, (144). 300-308.
10. Hudson, J.A., Pearce, R.G. and Rogers, R.M. Source Type Plot for Inversion of the Moment Tensor, *J. Geophys. Res.* , 1989, (94). 765-774.
11. Riznichenko, Y.V. Seismic rock flow, in *Dynamics of the Earth Crust*, (Nauka, Moskow, 1965).
12. Kostrov, B.V. and Das, S. *Principles of Earthquake Source Mechanics*, Cambridge University Press, 1988.

USE OF MICROSEISMIC MONITORING FOR ROCKBURST MANAGEMENT AT VALE INCO MINES

CEZAR-I. TRIFU

*Engineering Seismology Group
Kingston, Ontario K7K 7G3, Canada*

FIDELIS-T. SUORINENI

*MIRARCO, Laurentian University
Sudbury, Ontario P3E 2C6, Canada*

Seismic systems provide characterization of mine seismicity and represent a monitoring tool for the management of seismic hazard and rockbursting. Seismic data is employed at all Vale Inco mines in the Sudbury Basin to evaluate and perform mine development activities by optimized stope sequencing, destress blasting and ground support. It is also used for the calibration of numerical models and the identification of major seismically active geological structures for strategic placement of secondary or enhanced support. Seismic monitoring is essential in the assessment and mitigation of seismic hazard and risk, thus minimizing the exposure of equipment and personnel through the use of re-entry protocols.

1 Introduction

The impact of rockbursts on mine operations can be enormous. Economic losses, safety of personnel and destroyed equipment have severe constraints on operations in mines with high seismicity. Minimizing the impact of seismic activity on mining operations may take one of several forms of proactive measures such as tele-remote mining, increased ground support or reinforcement, introduction of new enhanced support systems, and minimizing worker and equipment exposure by use of seismic monitoring systems. Each of these measures requires strategic planning, systematic implementation and a good understanding of the mine seismicity and the mechanism of major seismic events. In recent years an integrated approach using all the proactive measures indicated above has been found more beneficial than the use of any particular element.

Current technology cannot predict when rockburst will occur, and the best we can achieve today is to identify areas of high rockburst potential using numerical models and/or experience. Microseismic monitoring systems have become an integral part of most hard rock deep mines in an effort to characterize mining induced seismicity for a quantitative evaluation of the seismic hazard. These systems have a considerable impact on the mitigation of the seismic risk by minimizing the exposure of personnel and equipment to seismic hazards remains. Full waveform Hyperion and Paladin systems, developed and distributed by the Engineering Seismology Group (ESG), are very popular in both the Canadian mines and worldwide.

This paper describes the practical application of seismic systems for the management of seismicity at Vale Inco mines in the Sudbury Basin. Geology and mining activities, including sequencing play major roles in triggering seismicity. Both regional and local mine geology with reference to structural geology play dominant roles in rockbursts occurrence. Because stress changes cannot be avoided in mining, they must be managed through optimum sequencing to minimize their impact. The geology and mining sequences at Vale Inco mines

are first presented briefly in the following sections, with a special emphasis on Creighton Mine. Then, the use of the seismic data for the calibration of numerical modelling results and identification of major seismically active geological structures for the strategic placement of enhanced support system are overviewed.

2 Geology

2.1 Regional Geology

The copper-nickel sulphide deposits in Sudbury are part of the Sudbury Igneous Complex (SIC), which forms an elliptical ring separated into the North and South Ranges, which differ with respect to the thickness of the norite and gabbro units, the character of the footwall rock and metamorphic history. The separation between these ranges occurs across a series of ductile shears at the southwestern and southeastern corners of the SIC (Figure 1). The discontinuous sublayer unit of the complex is the usual host for the ore and comprises a series of mafic to ultramafic inclusions of varying size and frequency in a matrix of norite and sulphides. Orebodies generally have a high-grade footwall with a gradational lower-grade hanging wall.

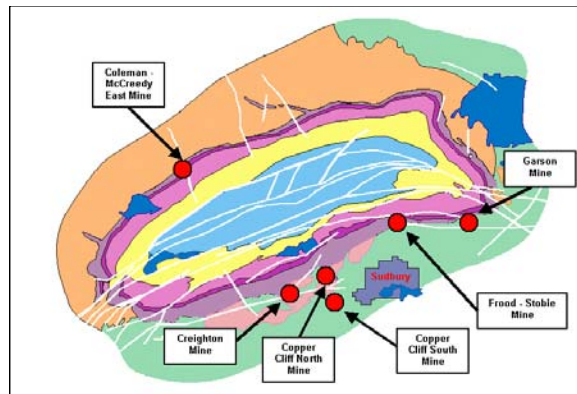


Figure 1 Location of Vale Inco mines in the Sudbury Basin.

The rocks of the SIC are affected by five major fault sets, as follows [1]: (1) A major, south-dipping, curvilinear, reverse fault set trending ENE-NW, exiting the basin at its SW and SE corners. These faults are part of the Penokean Orogeny that occurred between 1870 and 1700 Ma. (2) A set of steeply dipping NNW trending faults cuts the North Range and crosscuts the mineral deposits at Coleman Mine, with a mostly sinistral displacement of up to 1000 m on the Fecunis Lake Fault. (3) Another set of faults cuts at a shallow angle on the East side of the basin. These faults have a sinistral displacement of up to 700 m. (4) The Murray system consists of E-W trending, steeply-dipping faults that cut the South Range and have right lateral displacement. (5) A late-stage set of faults and fractures formed by the current tectonic stress field, infilled with low-temperature sulphides and carbonate minerals. These structures exhibit low microseismicity and are sometimes associated with poor ground conditions.

Two major dyke swarms are apparent: (a) A system of quartz diabase dykes striking E-W along the southern margin of the basin, varying in thickness from a few inches to several tens of meters, commonly referred to as “trap” dykes. The quartz diabase dykes cross-cut several mineral deposits at Creighton Mine. (b) A system of olivine diabase dykes, commonly referred to as the “Sudbury Swarm” that strike NW-SW and are steeply dipping, dated at about 1235 Ma. Note that this system is offset by fault sets 2 to 4 above.

2.2 Local Geology

Most orebodies at Vale Inco mines are commonly intersected by different geological structures or dykes, which affect the overall mining induced stress and rock mass behaviour. To exemplify this, we will discuss in detail the situation of Creighton Mine, located within the Creighton embayment, on the outer rim of the South Range of the SIC (Figure 1). This embayment includes two smaller satellite embayments to the west called Gertrude and Gertrude West. Creighton Fault, which strikes N70°E and dips 85°N, truncates a small, near-surface portion of the Creighton embayment at its southern margin.

Four main geological units have been identified in the mine: (1) Basal norite, towards the base of the main SIC, overlying the embayment, which contains a small percentage of inclusions and disseminated sulphides. (2) Sublayer norite, the common ore host, consisting of sulphide inclusions of varying composition, size and frequency of occurrence. (3) A short, variably mineralized, quartz diorite offset dyke. Mineralization is spatially associated with the dyke, but the dyke itself is usually barren. (4) Footwall rocks comprising Creighton granite that intrudes lower Huronian metavolcanics and metasediments.

Mineralization is contained within a NW plunging embayment of norite into the footwall and is controlled by two troughs or indentations (Figure 2). The majority of orebodies are located along one of these troughs (Creighton 400 trough), plunging towards NW and following the general geometry of the main Creighton embayment, while the remainder are located along a near orthogonal trough (Gertrude 402 trough) plunging NE at 40 degrees.

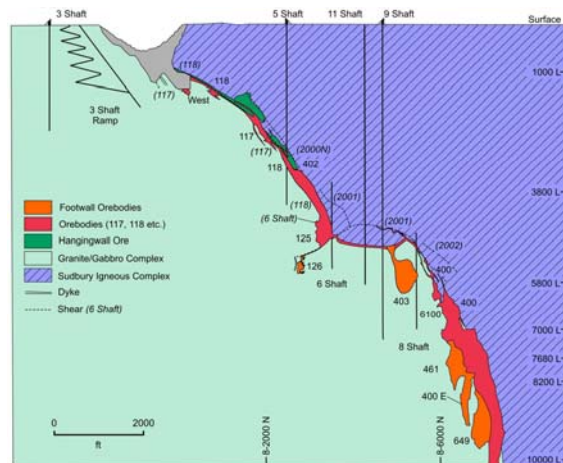


Figure 2 Composite geology section of Creighton Mine [2].

At depth, the Creighton main orebody strikes roughly E-W and dips steeply to the north. Along strike, the bulk of the remaining orebody extends about 150 m with an average thickness of 100 m. At a depth of 2295 m (7530 ft) the ore zone extends about 250 m E-W with an average thickness of 50 m. In addition, there are several ore zones located in the hangingwall and footwall of the main orebody at depth. Creighton Mine comprises 15 orebodies of which the majority of the higher grade mineralization in the Main, West, 117, 118, 128, 125, 126, and 401 orebodies has been depleted. Remaining reserves and resources are concentrated in the 3 Shaft remnants, Deep 400, Up-dip 402, 403 remnants and the recently discovered 649 orebody [1].

2.3 Characteristic of Major Rock Units

The mining zone at Creighton can be characterized as footwall granite-gabbro domain, massive sulphide ore zone domain and hangingwall norite domain (Figure 2). Other ore zones, such as the 461 orebody, are embedded in the footwall granite-gabbro domain.

Structural analyses identified mostly two subvertical joint sets and one low angle to flat lying joint set in the footwall domain. The joint set orientation in the hanging wall norite domain is different with three high angle to subvertical joint sets and a low angle joint set. There are four joint sets in the ore domain with three subvertical joint sets and one low angle to flat lying joint set. Table 1 summarizes the intact rock properties from all three rock domains.

Table 1 Average geomechanical properties of major units at Creighton Mine.

Domain	Density [Kg/m ³]	UCS [MPa]	Young Modulus [GPa]	Poisson ratio [v]
Granite	2600	240	60	0.26
Norite	2850	190	78	0.28
Ore	3600	130	68	0.25

Systematic logging and mapping have been carried out over the last few years to identify major joint sets and structures. Core logging data is processed by external consultants using procedures developed internally by Vale Inco. The derived results are regularly employed to identify the distribution of rock mass quality and location of major structures for design purposes (e.g., stope design, support design, location of major infrastructure).

The pre-mining far-field stress regime used in the Sudbury Basin is derived from far-field stress measurements taken in the mid to late 1980s. In the absence of more recent measurements, the stress tensor used for numerical modelling at all Vale Inco mines is derived from these measurements and field observations. In general, the major principal stress is horizontal and trending E-W. The minor principal stress is vertical (Table 2). With mining going deeper it is appropriate to update the mine far field stress tensor. A number of in-situ stress measurements using acoustic emissions were tried in the last years with inconclusive results. More work is needed in this area since this method is inexpensive and relatively fast.

Table 2 Stress tensor used for the numerical modelling (Z is depth in meters).

Stress	Magnitude [Kg/m ³]	Trend [°]	Plunge [°]
σ_1	$10.9 + 0.0407 Z$	270	0
σ_2	$8.7 + 0.0326 Z$	0	0
σ_3	$0.029 Z$	90	90

3 Mining Activities

Vale Inco mines have been in operation for over 100 years in the Sudbury Basin. At most mines exploitation started with open pits and underground mining at shadow depths. In 1940s for example, mining was very labour intensive, with small access and timber support. The 1960s signal early mechanization and introduction to mechanical bolts as mining extends to 900 m depth. Mechanized mining with remote equipment became available and operations reached 1800 m depth. Rebars, cables, mesh wire and shotcrete were introduced. The widespread use of the above support systems, through mechanized bolters, allowed the mining to extend to 2200 m depth a decade later. Meanwhile, mine design was introduced in the 1990s, including standard

distressing, blast scheduling and numerical modelling, allowing for pillar less sequence and mining through fill. In the 2000s mining reached 2400 m depth, new support was developed, such as the cone bolts, zero gauge straps and shotcrete arches. New mining techniques have been implemented such as the pillar less center out mining sequence, the development sequence and orientation, and the mining rate control.

Over the years, various mining methods were employed to extract the ore from these Vale Inco mines, including shrinkage, sub level caving, block caving, cut-and-fill, vertical crater retreat and slot-and-slash mining. Slot-and-slash is the principle mining method used at all mines, with the exception of Coleman and Stobie Mines, which are using the cut-and-fill and sub-level caving, respectively. Backfill of mine stopes uses mainly mill tailings mixed with water and cement in the sand fill plants and delivered through a series of boreholes and 4-inch sand fill lines to the mined stopes. Garson Mine mainly employs a paste fill system, whereas Copper Cliff North Mine uses a combination of sand fill and cemented rockfill.

Presently, mining activities take place between 300 and 2400 m below surface. Most operating shafts reach down to 1200 m, while the deepest shaft is Creighton's Number 9 shaft with access to the 2135 m level (7000 ft). Below this depth, Creighton has adopted an incremental strategy to reach the ore below shaft's bottom via a haulage ramp system.

4 Monitoring of Mine Seismicity

Historically, the first documented seismic events and rockbursts were observed at Creighton Mine in the 1930s, predominantly in crown and sill pillars at a depth of 700 m (2300 ft). Over time, seismicity began to occur in single development headings (i.e., strain bursts) at a depth of 1200 m (4000 ft) and in sill accesses following production blasts at a depth of 2000 m (6600 ft). Most rockbursts in sill accesses occurred due to the day to day mining activity and have typically been the result of sill and crown pillar mining (pillar bursts), whereas most strain bursts have been associated with geological structures.

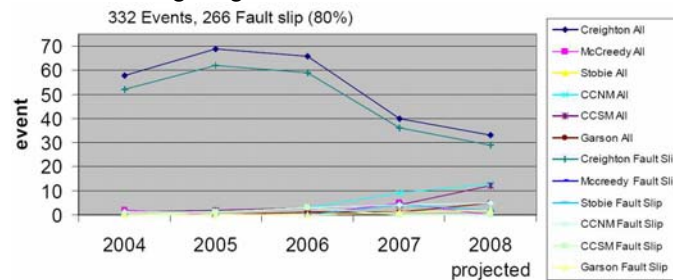


Figure 3 Number of seismic events with magnitude ≥ 2 .

Figure 3 presents the number of seismic events with magnitude larger than 2 occurred during each of the last five years [3] at each of the six Vale Inco mines in Sudbury. Worth noting, 266 seismic events or 80% of the total 332 large events were generated by fault slips and only 20% were caused by pillar bursts. If the large magnitude seismicity at Creighton Mine was known, the increase in the large magnitude events at the rest of the mines indicates a new trend, most likely associated with the development of their mining operations, particularly increase depths and extraction rates.

The rock mechanics group at Vale Inco initiated a systematic approach for the management of seismicity and rock bursts by investing in a number of initiatives depending on the situation. These initiatives include: (a) Use of detailed numerical modelling for the understanding of rock mass behaviour. (b) Testing and implementation of a number of burst prone support systems at various mines. (c) Implementation of stope de-stressing in high stress areas (e.g., 461 orebody at Creighton Mine). (d) Adapt development procedures and support systems to particular ground such as in proximity to major dykes, faults and shears. (e) Increase use of

microseismic systems and expansion of the seismic sensor array coverage within individual mines. (f) Use of 3D Virtual Reality Laboratory (VRL) for better understanding of mine seismicity. This has resulted in the development of a hazard map procedure used to identify areas of high hazard and risk [4].

Associated with the long history of mining in Sudbury are stress-induced and structurally generated seismic activities, as well as the evolution of seismic monitoring systems. The first microseismic system in the Sudbury Basin was a 16-channel MP250 manufactured by Electrolab (Spokane, WA). installed in 1980 at Creighton Mine, later expanded to monitor increased seismicity at depth. Similar systems were subsequently installed at Copper Cliff North, Stobie, Levack and Crean Hill Mines.

Table 3 Seismic monitoring systems at Vale Inco mines.

Mine	Development Max. Depth (m / ft)	Production Max. Depth (m / ft)	Micro- seismic System	No. Channels	No. Tri- axials	Strong Motion System	No. Sensor s	Re-entry Protocol
Creighton	3420 / 7940	2380 / 7810	Hyperion	104	11	Paladin	4	Seismic Work
Coleman	1660 / 5440	1550 / 5080	Hyperion	96	9	Paladin	3	Event Rate
Copper Cliff North	1525 / 5000	1280 / 4200	Hyperion /Paladin	100	7	Paladin	1	Seismic Work
Copper Cliff South	1525 / 5000	1320 / 4330	Paladin	60	6	Paladin	1	Seismic Work
Frood Stobie	1200 / 3930	1100 / 3600	MP250	32	0	Paladin	0	Event Rate
Garson	1555 / 5100	1525 / 5000	Hyperion	32	0	Paladin	1	Event Rate

The original MP250 system installed at Creighton Mine was converted in 1988 into a 12-bit full waveform system developed by Queen's University as part of the Canadian Rockburst Research Program. This system employed the accelerometer array already in operation underground, but improved first arrival picking and with them both event location and magnitude estimates. In 1999, the seismic system was replaced by a 16-bit Hyperion system developed by the Engineering Seismology Group (ESG, Kingston, ON). This is a central acquisition system with trigger based recording. Hyperion microseismic systems were installed and regularly expanded at Garson, Coleman, Copper Cliff North, Copper Cliff South and Creighton Mines. The sensor array consists typically of uniaxial accelerometers with a sensitivity of 30 V/g and a frequency range of 50 to 5000 Hz, and triaxial accelerometers with sensitivities of 0.3 and 0.5 V/g, and a frequency range of 3 to 8000 Hz.

Although microseismic systems can locate any seismic event within the mine, the magnitude estimates are limited to events between -2 and 1. For larger magnitude events all sensors of these arrays will clip. Consequently, in order to correctly estimate the magnitude of larger events, mines operate one or more triaxial 4.5 Hz geophones recorded by a 24-bit Paladin system, also developed by ESG (Table 3). Paladin is a distributed acquisition system with continuous and trigger based recording, designed to replace the older Hyperion architecture [5]. Over time, it will replace the older systems as needed.

5 Management of Seismicity and Rockbursting

Elevated stresses in mines can cause both strain bursts around rockmass openings and structurally-induced seismicity along structures. The latter can result when elevated stresses lead to the destruction of rockbridges in discrete geological planes of weakness, fault slip or fracture propagation(Figure 4). Contrary to conventional representation, most geological structures such as faults are not continuous but contain intact rockbridges either

linearly or in an en-echelon format. Destruction of intact rock can occur in major discrete or stepped continuous geological structures [6].

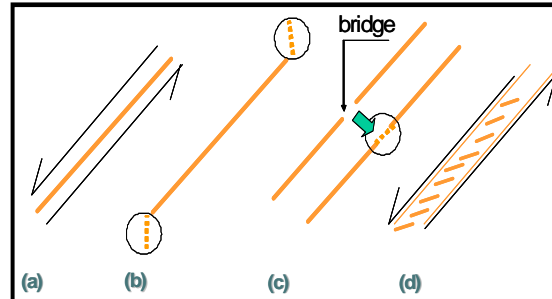


Figure 4 Conceptual rockburst mechanisms: (a) slip along continuous fault, (b) fracture propagation, (c) damage of rockbridges co-linear with faults, and (d) damage of en-echelon rockbridges in apparently continuous discrete fault.

Seismic monitoring systems identify, locate and quantify mine seismicity, allowing for a better understanding of the rockbursting mechanism. As such, they contribute to the management and mitigation of seismic hazards, for improved worker safety and enhanced mining productivity. In the following, various aspects of this management are discussed, such as mining development strategy and ground support, use of seismicity for the calibration of numerical models, and the evaluation of restricted access and re-entry protocol.

5.1 Mine Development Strategy and Ground Support

Rockmass damage is typically tied to high stresses and the presence of geological structures, sometimes quite remote from mining activity. Stress-induced seismicity in intact rock around excavations (strain bursts) is well managed for development activities through optimized stope sequencing, destress blasting and good ground support practices. The deepest mining in the region is carried out at Creighton Mine, where top sills are developed below a depth of 2135 m (7000 ft) underneath or within previously mined and backfilled zones. The ground is supported with a first layer of shotcrete, followed by a layer of split set bolts and screen, and finished with a second layer of shotcrete. The development is done in short, 1.8 m (6 ft) rounds.

Ground support system is continuously improved based on trials and analyses of the ground response and stress levels, confirmed through the monitoring of increased mine seismicity. A combination of cone bolts with zero-gauge straps or shotcrete arches is employed for enhanced support, proven very effective in burst-prone conditions and around seismically active geological structures, especially when installed during development or at the early stage of mining. With the exception of development in damaged ground (under sandfill), all deep development follows a strict perimeter and destress blasting to reduce the number of strain bursts in the development headings [1].

5.2 Calibration of Numerical Modelling

Numerical modelling is an integral part of both short and long term mine planning. Modelling software includes three-dimensional elastic packages (Examine-3D, MAP3D) and finite element codes (3DEC, FLAC-3D). MAP3D has been used at Vale Inco since the 1990s. Being easy and quick to use it became a valuable tool for the Ground Control Engineer to employ in mine planning and stope sequencing. The mine's stope model can be easily expanded to include new mining areas and the results can be rapidly compared against years of empirical data.

Figure 5 shows the numerical modelling results across the crown pillar between the 3000 and 3050 levels at

Copper Cliff North Mine after mining of the 94531 stope between the 3050 and 3200 levels (left). These results outline a high stress zone defined by the major principal stress greater than 100 MPa contour. Seismic data is often used as a calibration tool to adjust the parameters of the numerical model until a good correlation is obtained between the areas of high stress and burst potential and occurred seismicity. Seismic data in the crown pillar after the actual mining of the stope is shown on the right side of Figure 4. The strong correlation between the high stress region and recorded microseismicity is apparent, which gives confidence in the use of such a numerical model for the stress and rockburst management.

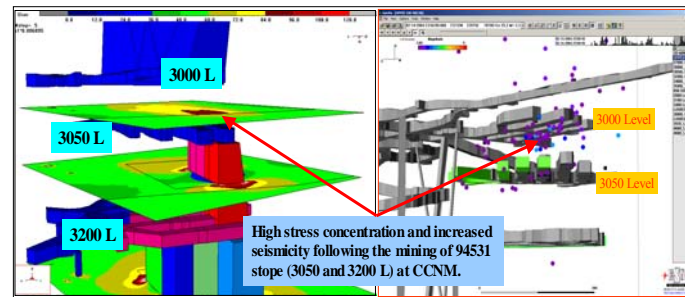


Figure 5 Modelling results (left) show strong correlation with seismic data (right) at Copper Cliff North Mine.

5.3 Seismic Active Structures and Hazard Assessment

Not all geological structures are directly observed and mapped. Moreover, it is the occurrence of seismicity that characterizes if a geological structure is active. Both the individual characteristics and number of geological structures or seismically active planes (SAP) with rockburst potential is critical for a reliable evaluation of the seismic hazard to mining operations. Microseismicity related to these structures is also evidence of rockmass degradation from elevated stresses as each microseismic (MS) event indicates rock fracturing. Rockbursts also generate dynamic stress waves that cause damage to the rockmass, extent of which depends on the peak particle velocity (ppv) level. Individual hazard maps can be generated for each of these three factors, MS, SAPs and ppv, as well as for combined factors. An example of a combined seismic hazard map is shown in Figure 6 [7].

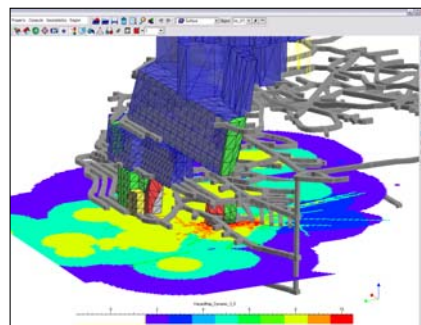


Figure 6 Composite hazard map at Creighton Mine based on MS rockmass degradation, presence of and number of SAPs and ppv, assuming the occurrence of a magnitude 3.0 seismic event (color scale from 1 to 10).

Hazard maps can be used for (i) support selection and tracking of rockmass condition for excavation support rehabilitation, and (ii) future mine development planning by locating infrastructure away from hazardous areas, if practical, or by installing stronger support in these areas if they cannot be avoided. Hazard

maps need to be continuously calibrated against underground observations to include existing rockmass conditions and support effects at the time of bursting. More work is required for automated generation of hazard maps for daily, routine application at mines [8].

5.4 Re-entry Protocol

Since 1980s, mine seismic systems have been used to monitor the seismic activity by providing the time, location and magnitude of the occurred events. At first, mine management would close down an entire level or a number of levels after a large event and would wait until the seismicity decayed to background noise in the affected area. Then, technical and operating staff would visit the affected areas to assess if any damage occurred and what type of reconditioning is required. With the increased performance of the monitoring systems, locations and magnitudes of significant events became more accurate. Such information is essential to guarantee that workforce is safely routed and not sent in the harm's way and to allow for restrictions to be defined to smaller and more-specific areas, rather than entire levels.

Number of events per hour has guided the management on when and where to remove personnel. At times, seismic events occur in the vicinity of underground excavations, in which case access to some areas is temporarily restricted. When the seismicity decreases to background levels, these areas are deemed safe and investigation personnel are permitted to re-enter in order to assess for damage and stability issues. Information is rigorously communicated to the affected crews and mining personnel with details on (i) seismic intensity (i.e., number of events per hour), (ii) location and magnitude of the seismic event, (iii) any restricted access and damage.

In the last few years, Creighton Mine, followed by other Vale Inco mines, particularly Copper Cliff North and South Mines, developed a process for evacuating areas affected by major seismic events or excessive seismicity. Re-entry to these areas follows an assessment approach based on the energy or seismic moment release, developed and calibrated from historical data in partnership with ESG (i.e., Seiswatch). This tool plays an important role in identifying and isolating areas at risk for the safety of workers. The rest of the mines are using event rates for the re-entry protocol and are at the development stage of procedures similar to those in use at Creighton, Copper Cliff North and South Mines.

Figure 7 depicts a typical response curve for the seismic moment (Seismic Work) parameter. The red line indicates the data for seismic events following a large burst, the red dashed line indicates the regression for the past 4 hours of data, the purple line indicates the curve for a 'typical' large event, and the blue line indicates the slope derived during 'normal' or background seismicity. Three main phases are shown: the initial steep slope indicates a period of instability after the event, followed by a transition period, and the return to stable conditions.

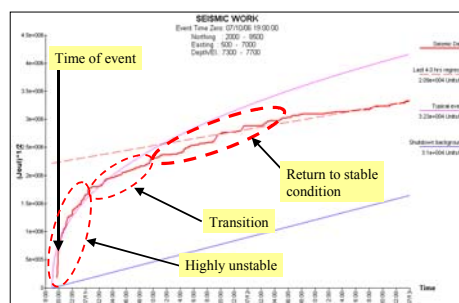


Figure 7 Seismic Work as a function of time.

6 Conclusions

The presence of mining activities in the context of regional and local geology invariably leads to stress redistribution. Rockmass response to this stress redistribution manifests as mine seismicity. The response can sometimes take the form of rockbursts, which can have a considerable impact on mining operations, including potential loss of resources, damage to equipment and even loss of life. Seismic monitoring systems allow for a quantitative characterization of seismicity, thus providing the means for the management of seismic hazard and rockbursting. Worth noting, all Vale Inco mines in the Sudbury Basin operate such seismic monitoring systems.

Seismic data is routinely evaluated for mine development activities through optimized stope sequencing, destress blasting and ground support. Support practice is continuously improved based on trials and analyses of the ground response and stress levels, confirmed through the monitoring of seismicity. Seismic data is also used for the calibration of numerical models. Thus, model parameters are adjusted until a good correlation is obtained between observed seismicity and expected fracture modelling results. It is through calibrated models that potential locations of future rockbursts are estimated. Furthermore, seismic monitoring allows the identification of major seismically active geological structures for strategic placement of secondary or enhanced support.

In view of published scientific results to date, this study cautions against the application of seismic monitoring for rockburst prediction purposes, as this can be misleading and with disastrous consequences. Instead, it underlines the use of the seismic technology as a monitoring tool, which can be employed effectively in the assessment and mitigation of seismic hazard, similar to its use by civil engineers in establishing design requirements and building codes. By minimizing the exposure of equipment and personnel to seismic hazards, through the use of re-entry protocols, seismic systems have also a considerable impact on the mitigation of seismic risk.

Acknowledgments

The authors would like to thank Farid Malek (Vale Inco Ltd.) for his inspirational discussions that led to the present study, as well as for his suggestions throughout a critical review of the manuscript.

References

1. Malek, F., Suorineni, F.T. and Vasak, P. Geomechanics Strategies for Rockburst Management at Vale Inco Creighton Mine, *ROCKENG09: Proceedings of the 3rd Canada-US Rock Mechanics Symposium*, (Toronto, Ontario, 2009).
2. Malek, F., Trifu, C.I., Suorineni, F.T., Espley, S. and Yao, M. Management of High Stress and Seismicity at Vale Inco Creighton Mine, *Proceedings of American Rock Mechanics Association General Assembly*, (San Francisco, California, 2008).
3. Thibodeau, D. Fault Slip Event Issue, *CEMI Fault Slip Workshop*, (Toronto, Ontario, 2009).
4. Kaiser, P.K., Vasak, P., Suorineni F.T. and Thibodeau, D. New Dimensions in Seismic Data Interpretation with 3-D Virtual Reality Visualization for Burst-Prone Mines, in *Controlling Seismic Risk*, (Perth, Australia, 2005).
5. Alexander, J. and Trifu, C.I. Monitoring Mine Seismicity in Canada, in *Controlling Seismic Risk*, (Perth, Australia, 2005).
6. Vasak, P, Suorineni, F.T. and Verma, A. Identification of Seismically Active Structures for Hazard Assessment at Creighton Mine, *Report to INCO Technology Centre*, 2004.
7. Vasak, P. Creighton hazard map project, *Internal Report to Vale Inco Creighton Mine*, 2008.
8. Trifu, C.I. and Shumila, V. Seismic Hazard Assessment in Mines Using a Marked Spatio-Temporal Point Process Model, in *Controlling Seismic Risk*, (Perth, Australia, 2005).

POTENCY TENSORS FOR SIMPLE AND EXTENDED SOURCES IN THE TIME DOMAIN

ERNEST C. LÖTTER

ISS International Limited

P.O. Box 12063, Die Boord, 7613, South Africa

Assuming a homogeneous medium and a point source, we perform full-waveform potency tensor inversion in the time domain by linearisation. This method takes into account near-, intermediate- and far-field terms of the wavefield, and can also be used to invert for simple extended sources. The method is tested on synthetic examples where the source mechanism and directivity effects are prescribed and can be qualitatively compared with inversion results.

1. Overview

Various seismological problems from the context of routine seismic monitoring require determination of reliable focal mechanisms of seismic events. In deep gold mines, normal faulting is usually expected. This expectation can be compared with an obtained second-order potency (or moment) tensor solution, which carries the necessary geometrical information to show a volumetric component of the mechanism, as well as two possible fault planes and associated slip vectors.

In the most routine case, such potency tensor solutions can be obtained in the frequency domain by taking into account the low-frequency plateaus of the spectra of recorded waveforms, as well as the polarity of first motion for both P- and S-wave components. This allows the determination of the six independent components of the potency tensor for a point source, but assumes a simple impulsive source time function. Therefore, the more detailed complexity of the source cannot be discerned in this way.

It is well known (see [1]) that displacement at a point \mathbf{x} at time t (relative to the point source at the origin and at time 0) can be expressed as the convolution of the time-dependent potency tensor components with the Green's function for an infinite homogeneous isotropic medium as

$$\begin{aligned} u(\mathbf{x}, t) &= P_{pq}(\mathbf{x}) * G_{npq} \\ &= \frac{1}{r^4} \left(\frac{(15Y_n Y_p Y_q - 3Y_n \partial_{pq} - 3Y_p \partial_{nq} - 3Y_q \partial_{np})\beta^2}{4\pi} \right) \int_{-\frac{r}{\beta}}^{\frac{r}{\alpha}} \tau P_{pq}(\tau - \tau) d\tau \\ &\quad + \frac{1}{r^4} \left(\frac{(6Y_n Y_p Y_q - Y_n \partial_{pq} - Y_p \partial_{nq} - Y_q \partial_{np})\beta^2}{4\pi\alpha^2} \right) P_{pq} \left(t - \frac{r}{\alpha} \right) \\ &\quad - \frac{1}{r^4} \left(\frac{(6Y_n Y_p Y_q - Y_n \partial_{pq} - Y_p \partial_{nq} - 2Y_q \partial_{np})}{4\pi} \right) P_{pq} \left(t - \frac{r}{\beta} \right) \\ &\quad + \frac{1}{r} \left(\frac{Y_n Y_p Y_q \beta^2}{4\pi\alpha^2} \right) P'_{pq} \left(t - \frac{r}{\alpha} \right) \\ &\quad - \frac{1}{r} \left(\frac{(Y_n Y_p - \partial_{np})\beta^2}{4\pi\beta} \right) P'_{pq} \left(t - \frac{r}{\beta} \right) \end{aligned}$$

with P-wave velocity α , S-wave velocity β , Kronecker delta δ_{ij} , hypocentral distance r and direction cosines Y_i . As we will consider seismograms containing both velocity (geophone) and acceleration (accelerometer)

traces, and the right-hand side of the Green's function convolution expresses displacement, we take the second time derivative of both sides to rather have $u(x, t) = P_{pq}''(t) * G_{np,q}$, which can be expressed in terms proportional to the time-dependent functions $P_{pq}''(t)$ and $P_{pq}'''(t)$ instead of $P_{pq}(t)$ and $P_{pq}'(t)$ as near-, intermediate- and far-field terms.

Specifically, if we simplified the original expression for displacement using a suitable time-independent factorisation as

$$u(x, t) = NF \int_{r/\alpha}^{r/\beta} \tau P_{pq}(t - \tau) d\tau \\ + IF_P P_{pq}(t - \frac{r}{\alpha}) + IF_S P_{pq}(t - \frac{r}{\beta}) \\ + FF_P P_{pq}'(t - \frac{r}{\alpha}) + FF_S P_{pq}'(t - \frac{r}{\beta})$$

where NF , IF and FF respectively represent the near, intermediate and far-field terms, one would express velocity as

$$v(x, t) = NF \frac{d}{dt} \int_{r/\alpha}^{r/\beta} \tau P_{pq}(t - \tau) d\tau \\ + IF_P P_{pq}'(t - \frac{r}{\alpha}) + IF_S P_{pq}'(t - \frac{r}{\beta}) \\ + FF_P P_{pq}''(t - \frac{r}{\alpha}) + FF_S P_{pq}''(t - \frac{r}{\beta})$$

and acceleration as

$$\ddot{u}(x, t) = NF \frac{d^2}{dt^2} \int_{r/\alpha}^{r/\beta} \tau P_{pq}(t - \tau) d\tau \\ + IF_P P_{pq}''(t - \frac{r}{\alpha}) + IF_S P_{pq}''(t - \frac{r}{\beta}) \\ + FF_P P_{pq}'''(t - \frac{r}{\alpha}) + FF_S P_{pq}'''(t - \frac{r}{\beta})$$

In the following sections, these expressions for velocity and acceleration will be utilised for geophone and accelerometer records respectively.

2. Source Description

To describe a time-dependent source time function $P_{ij}(t)$ for $t_0 < t < t_0 + t_{dur}$, we assume its third derivative to be piecewise linear, so that we can write

$$P_{ij}'''(t_0 + k\Delta t) \equiv x_{ijk}$$

for each $1 \leq i, j \leq 3$ and $k = 1, 2, 3, \dots, \lfloor \frac{t_{dur}}{\Delta t} \rfloor$ where we assume that $x_{ij0} = 0$, corresponding to $P_{ij}'''(t_0) = 0$ and $k = \lfloor \frac{t_{dur}}{\Delta t} \rfloor$ corresponds to the end of the finite duration of the event, where Δt is a chosen

resolution for the source time functions, and the x_{ijk} are the $6k$ unknown parameters uniquely determining the discretised source time function for this point source.

The assumption of piecewise linearity allows us to derive explicit equations for the lower-order derivatives of $P(t)$ as linear combinations of these $6k$ unknown parameters. For example, we trivially have that

$$P''_{ij}(t_0 + k\Delta t) \equiv x_{ijk}$$

and we can derive that

$$P'_{ij}(t_0 + k\Delta t) \equiv (\Delta t) \left(\sum_{l=0}^{k-1} x_{ijl} + \frac{1}{2} x_{ijk} \right)$$

and

$$P_{ij}(t_0 + k\Delta t) \equiv (\Delta t)^2 \left(\sum_{l=0}^{k-1} \left(\frac{1}{2} x_{ijl} + \frac{1}{6} x_{ij(l+1)} \right) + \frac{1}{2} \sum_{m=0}^{k-1} x_{ijm} + x_{ij(k+1)} \right)$$

and by employing the chain rule, similar higher-order expressions are derived for $P(t)$ and $P^{(-1)}(t) = \int_{t_0}^{t_0+k\Delta t} P(t) dt$. The last case, being rather unwieldy, is only necessary if the near-field terms are to be used in the inversion. Similarly, due to the linearity, the interpolated points in time which do not correspond to integer multiples of k in the expressions above can themselves also be expressed as a linear combination of the x_{ijk} .

These assumptions imply that $P''_{ij}(t)$ is piecewise linear (with corners defined for points corresponding to integer k), $P'_{ij}(t_0 + k\Delta t)$ is piecewise quadratic, $P'_{ij}(t_0 + k\Delta t)$ is piecewise cubic (splines) and $P_{ij}(t_0 + k\Delta t)$ piecewise quartic.

Assuming that the third derivative of time-dependent potency is piecewise linear then means that the coefficients of the terms in the simplified expressions for $u(x, t)$, $v(x, t)$ and $\phi(x, t)$ can all be written as linear combinations of the $6k$ entries in x_{ijk} . Therefore, at each point in time $t_0 + \frac{t}{k} < t < t_0 + \frac{t}{k} + \Delta t$ on a acceleration or velocity), the observed value can be written as a linear combination of the unknown x_{ijk} .

3. Point Sources

To describe the complexity of our (asynchronous) point source, we write its time-dependent second-order potency tensor as the symmetric matrix

$$P_{ij}(t) = \begin{bmatrix} P_{xx}(t) & P_{xy}(t) & P_{xz}(t) \\ P_{xy}(t) & P_{yy}(t) & P_{yz}(t) \\ P_{xz}(t) & P_{yz}(t) & P_{zz}(t) \end{bmatrix}$$

where the coefficients are assumed to be identically zero at all time before a reference time (origin time) t_0 .

Therefore $|P'_{ij}(t)| = 0$ for all $t \leq t_0$. As only a finite amount of slip on the fault is modelled (the event has a finite duration), we have that the time derivative

$$P'_{ij}(t) = \begin{bmatrix} P'_{xx}(t) & P'_{xy}(t) & P'_{xz}(t) \\ P'_{xy}(t) & P'_{yy}(t) & P'_{yz}(t) \\ P'_{xz}(t) & P'_{yz}(t) & P'_{zz}(t) \end{bmatrix}$$

will also be identically zero a certain period of time after initiation of slip, that is $|P'_{ij}(t)| = 0$ for all $t > t_0 + t_{dur}$. The quantity $|P'_{ij}(t)| = 0$ can therefore only be non-zero for $t \in [t_0, t_{dur}]$.

In terms of the previous section, it is therefore clear that the values of each of these components at a fixed time t can be expressed as a linear combination of the x_{ijk} which define the 6 asynchronous source time functions describing the source. In turn, the symbolic equations for $v(x, t)$ and $a(x, t)$ imply that observed velocity and accelerometer traces can be written, sample by sample, as linear combinations of these shared, unknown x_{ijk} . Moreover, as we have written the Green's function convolutions as a linear combination of derivatives of $P_{ij}(t)$ (for example $P'_{ij}(t - \frac{r}{a})$ for the P-wave component of the velocity intermediate field wavefield) which are independent of the material properties α , β and ρ , hypocentral distance and direction cosines being linear combinations of the x_{ijk} multiplied with a factor (for example IF_P) containing possibly geometry and medium-dependent factors, the same will hold for all samples on traces recorded at different stations, even with possibly different average medium properties between them and the known hypocenter.

Therefore, as the velocity or acceleration representations of $v(x, t)$ and $a(x, t)$ directly yield samples of synthetic seismograms at each point in time t , it implies that synthetic seismograms (on synthetic sensors with perfectly flat instrument response at low frequencies) can be generated as a linear combination of the x_{ijk} s, where these coefficients depend on the relative position and material properties between the source and respective recording stations.

Inversion

Given a known hypocenter, a conservative (not too late) estimate for t_0 , a conservative (not too short) estimate for t_{dur} , a combination of response- and instrument-corrected acceleration and geophone traces from stations with known locations, as well as phase arrival times on the seismograms, we now have the makings of an over-determined inverse problem.

As each observed sample on a seismogram can be written as a linear combination of the x_{ijk} s, we can add a linear equation to our system for each such sample. Assuming that there are N such observed samples (over all seismograms and their components), the linear system can be written as $Ax = b$ where

- A is a $N \times 6k$ matrix, where row m consists of the $6k$ coefficients expressing the m th element of b (observed sample) as a linear combination of the x_{ijk} .

- \mathbf{x} is a $6k \times 1$ vector consisting of the elements $[x_{111}, x_{112}, \dots, x_{11k}, x_{121}, \dots, x_{12k}, \dots, x_{331}, \dots, x_{33k}]$
- \mathbf{b} is a $N \times 1$ vector consisting of the seismogram samples, corresponding to rows of \mathbf{A} . Note that \mathbf{b} may contain multiple components of multiple seismograms, which could have different numbers of samples.

Given the configuration above, the resolution for the source time function via the parameter Δt is bounded below by $\frac{t_{dur}}{N}$, where N is the total amount of used samples. However, as the linear system stands, not all physical constraints are set on this system. For each $1 \leq i, j \leq 3$, we need that each of $P'_{ij}(t)$, $P''_{ij}(t)$ and $P'''_{ij}(t)$ must be identically zero for all $t > t_0 + t_{dur}$. For the third derivative, this condition is already met by only allowing a bounded number of non-zero x_{ijk} for each ij . For the first and second derivatives, these constraints are required due to the far-field terms in the Green's functions for respectively geophones and involving them and the event having finite duration.

These last two constraints are added to the set of equations by adding two weighted rows to \mathbf{A} which represent these constraints, thereby forming a new $(N + 12) \times 6k$ matrix \mathbf{A}' , and an $(N + 12) \times 1$ vector \mathbf{b}' .

By employing Singular Value Decomposition for such a constrained over-determined system, it is possible to solve the above system in a weighted least squares sense. To rather solve using the L1 norm, numerical optimization techniques using a genetic algorithm could be used with the L2 norm solution (obtained using SVD) as initial estimate.

Systems of equations involving hundreds of unknowns ($k \approx 100$) and thousands of used data points ($N \approx 10000$) can be solved in tens of seconds on modern computers, making the method practical for interactive use. Some overhead is added while computing the contents of rows of \mathbf{A}' involving near-field terms, however they have no ill effect during the inversion step, as it is linearised (and superimposed) on the intermediate and far field effects. In any case, it is recommended to not add the near field terms for sensors more than a few wave lengths away from the source, as the extra computational cost will not lead to improved accuracy.

We produce a synthetic example by placing 20 triaxial sensors in random positions of within a few hundred meters from the origin. We then prescribe a simple Haskell source rupturing northwards (in the negative x-direction) over a distance of 10 meters, and prescribe the strike-slip focal mechanism to be a simple shear motion that can be described by a potency tensor having only the P_{xy} components being non-zero, and positive. Synthetic waveforms are then generated at the sensors using kinematic forward modelling. Our method is tested using the simple pulse recorded at the sensors, and attempts to accurately resolve the focal mechanism at the source. For t_0 , we use the calculated origin time (from locating the event objectively using body wave arrival times), and t_{dur} is chosen to be 1.5 times the reciprocal of predominant period.

Solving for the x_{ijk} leads to the source time function shown in Figure 1.

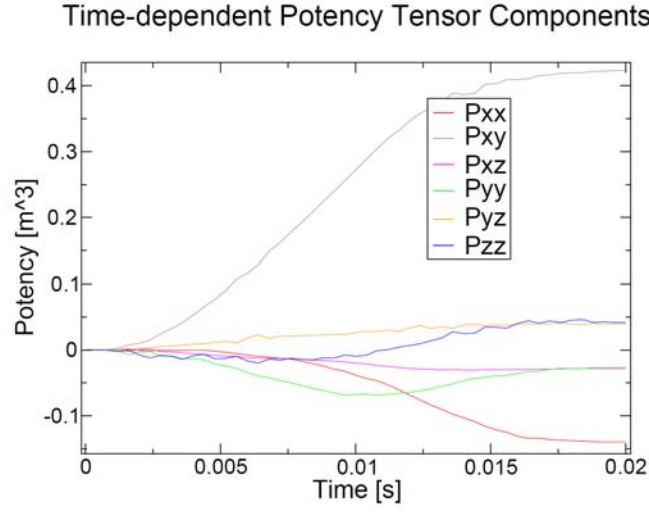


Figure 1: Six independent potency tensor components for a source. This was obtained for a synthetic (Haskell model source) 20-station event with a focal mechanism chosen so that $P_{xy}(\infty)$ should be positive, but all other components of the time-dependent potency tensor should be zero. While they are not identically zero in this case, it is clear that the xy component of the potency tensor is indeed the dominant component and is successfully resolved using this method.

Given the six independent components of the potency tensor, we can compare the prescribed and the obtained focal mechanisms. This comparison is done in Figure 2, from where generally good agreement can be seen, with the fault and auxiliary planes being within a few degrees of each other, and the obtained focal mechanism gaining a small isotropic (implosive) component of about 0.2%, in comparison with the assumed model that had no isotropic component.

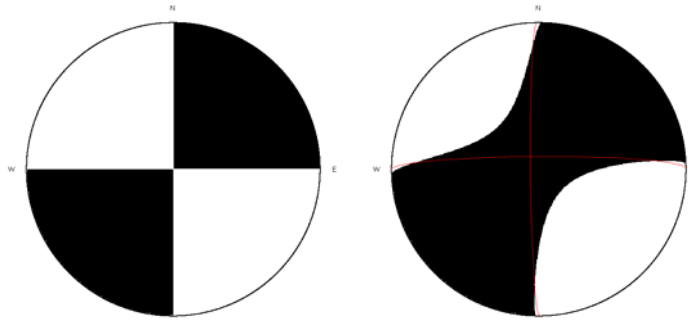


Figure 2: On the left, the original pure-shear source which was used to kinematically model the observed waveforms. On the right, the obtained lower hemisphere projected focal mechanism (with fault and auxiliary planes highlighted in red), as derived from the final values as seen in Figure 1. While the actual fault has a strike of 0 degrees, dip of 90 degrees and rake angle of 0 degrees, our inversion leads to a strike of 179 degrees, a dip of 87 degrees and a rake of -5 degrees, and a negligible isotropic component of about 0.2%.

Once we have solved for the \mathbf{x}_{GR} , the point source is completely determined, and it is possible to generate synthetic waveforms, which can be compared with the observed waveforms. This is particularly simple under our assumptions of piecewise linearity of the source time functions, as generating all synthetic samples for seismograms used in the inversion can be obtained by using the corresponding entries in the vector $\mathbf{x} = \mathbf{A}^t \mathbf{x}_i$. As we have originally solved $\mathbf{A}^t \mathbf{x} = \mathbf{b}^t$ using either the L1 or L2 norm (where \mathbf{b}^t contains the observed samples and weights), we expect $\|\mathbf{s} - \mathbf{b}^t\|$ to be small. Figure 3 shows the observed and synthetic seismograms (3 components) for one of the stations used in the above example.

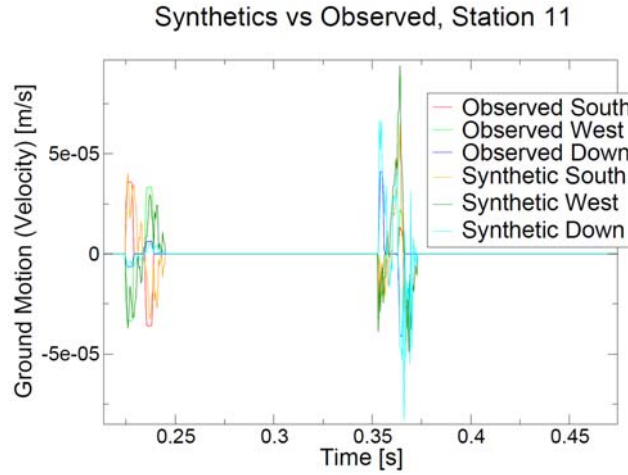


Figure 3: Comparison of observed and synthetic seismograms for station 11 of the example point source inversion considered in this section. The observed seismograms are those kinematically modelled from our initial assumptions of the Haskell source. The synthetics are those obtained from our time-dependent point source approximation.

4. Extended Sources

As seismic sources are often complex, with different possible rupture scenarios and varying directivity effects, the point source assumption of the previous section is often too restrictive and unrealistic. As an alternative, we approximate the extended source by a set of independent point sources, each with their own initiation time and duration. These point sources are not independent from the dynamical rupture point of view, as they jointly represent where the majority of energy is radiated. However, we will consider them and their source time functions as independent during inversion.

Suppose our extended source is modelled by n point sources. If we had performed the point source procedure of the previous section on the i th of these n point sources, it would have involved approximating a solution of the system $\mathbf{A}_i \mathbf{x} = \mathbf{b}$, where \mathbf{b} is the set of observed samples from seismograms only (no weights), \mathbf{A}_i is the $N \times 6k_i$ matrix for the i th point source (excluding weights) and \mathbf{x}_i is a $6k_i \times 1$ vector consisting of the elements

$$[x_{(i)111}, x_{(i)112}, \dots, x_{(i)11k_i}, x_{(i)121}, \dots, x_{(i)12k_i}, \dots, x_{(i)331}, \dots, x_{(i)33k_i}]$$

which is analogous to the point source case, where k_i is the number of data points we choose to use in the source time function of the i th point source. To satisfy the $2 \times 6 \times n = 12n$ weighting constraints that ensure

that the final first and second derivatives are equal to zero at $t = t_0 + t_{dur}$, the necessary $12n$ respectively rows and entries are added

By superposition, we can construct a single linear system that will simultaneously act as a Green's function for all n point sources. This is done by mimicking the original $Ax = b$ by writing

$$Ax = [A_{(1)} \ A_{(2)} \ A_{(3)} \ \dots \ A_{(n)}] \begin{bmatrix} x_{(1)} \\ x_{(2)} \\ x_{(3)} \\ \vdots \\ x_{(n)} \end{bmatrix} = b$$

where A is a $N \times 6(k_1 + k_2 + \dots + k_n)$ matrix, and x a $6(k_1 + k_2 + \dots + k_n) \times 1$ vector, which still uses the original input data vector b , but now has $6(k_1 + k_2 + \dots + k_n)$ unknowns.

As with the simple point source case, this linear system can be solved in a weighted least squares sense after the $2 \times 6 \times n$ weighting equations (that ensure that the final first and second derivatives of $P_{ij}(t)$ are equal to zero at $t = t_0 + t_{dur}$ for each subsource) were added to the system, which results in the system $A'x = b'$ with $12n$ rows and entries added to the matrix A and vector b respectively.

The multi point source case also requires that individual initiation (origin) times $t_{(i)0}$ and durations $t_{(i)dur}$ are set for each point source. Such values can be estimated once a selection of a small, adequate set of point sources have been made to represent the extended source. Otherwise, these point source locations can be estimated by locating the subevents using their indirect P- and S-wave arrivals at sensors, and making these point source subevents parts of our extended source.

We again consider the synthetic example from the previous section, but now choose to model it as an extended source, consisting of two simple point sources, the first, representing the initiation point of the extended source at (0,0,0) and a second at (-10,0,0), representing the northernmost part of the extended source. Although slip at the second source is only expected some time after the first, we choose $t_{(1)0} = t_{(2)0}$ and $t_{(1)dur} = t_{(2)dur}$ to make it easier to compare the source time functions on a similar time scale, and allow the inversion more freedom to distribute nonzero potency rate between the two point sources' respective $6k_1$ unknowns of $x_{(1)jk}$ and $6k_2$ unknowns of $x_{(2)jk}$. In our example, we choose $k_1 = k_2 = 50$. However, as essentially all sensors are in the far field, the effect of modelling the source as two simultaneous point sources does allow for a better fit with observations, but increases the condition number due to the near-ambiguous interplay possible between the two point sources.

Performing the inversion leads to the potency time dependencies shown in Figure 4, whereas simply summing the time-dependent potencies over the subsource leads to a single time dependency as shown in Figure 5. The representation in Figure 5 is, due to the sensors being in the far field, comparable with that of Figure 1.

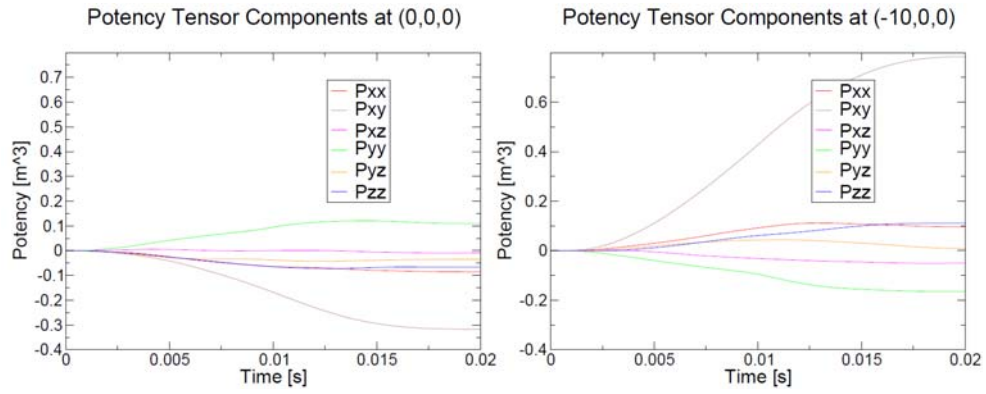


Figure 4: Time-dependent potency tensors for the point sources at respectively (0,0,0) and (-10,0,0).

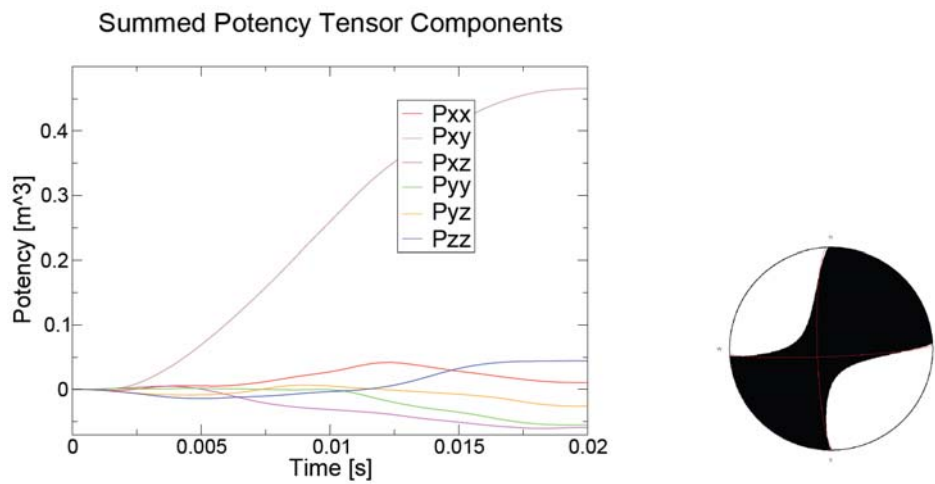


Figure 5: On the left, stacked potency curves (representing the source time function) for the extended source modelled as two point sources, as sum of those from Figure 4. This compares well with the results for the single point source inversion in Figure 1. On the right, the final potency tensor beach ball representation for this inversion, having a strike angle of 178 degrees, dip angle of 82 degrees and rake angle of 4 degrees. This compares well with the original strike-slip fault as shown in Figure 2 (left), and has a small isotropic component of 0.3%.

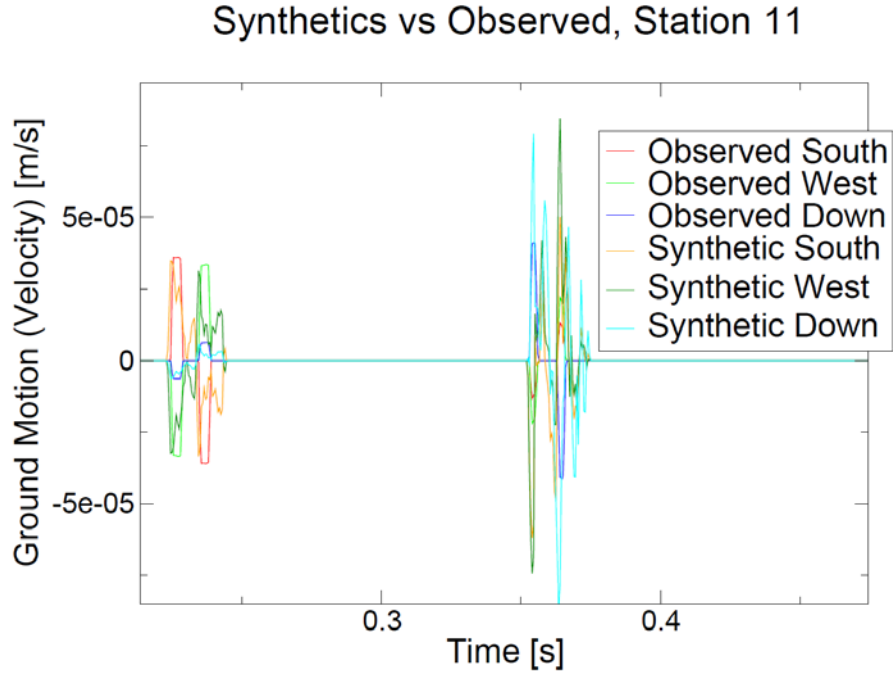


Figure 6: Comparison of observed and synthetic seismograms for station 11 of the example extended source inversion considered in this section. The observed seismograms are those kinematically modelled from our initial assumptions of the Haskell source. The synthetics are those obtained from our time-dependent two-point source approximation, and can be compared with those for the simple point source in Figure 6.

5. Real Data

In order to test our method on real data, we consider a small magnitude -0.9 event recorded at a European mine, for which 16 stations (a mixture of uniaxial and triaxial sensors) triggered and recorded seismograms. After careful reprocessing of the event, we use 13 viable components of seismograms from these, and we invert for a singular point source, with $k = 250$ and $t_{dur} = 250$ ms. Finding a least squares solution to the weighted linear system with SVD leads to considering a system of 4492 equations in $1500 = 6k$ unknowns. This system is solved in about 5 minutes on a single-core 2.4GHz CPU.

To compare observed seismograms with synthetics generated from our inverted source model, we show these comparisons in Figures 7 and 8.

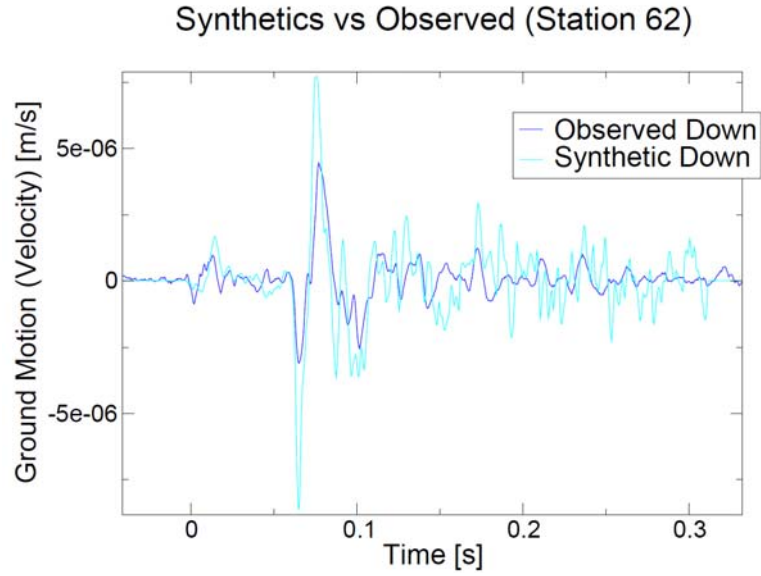


Figure 7: Observed and synthetic component for the uniaxial station 62, for the magnitude -0.9 event.

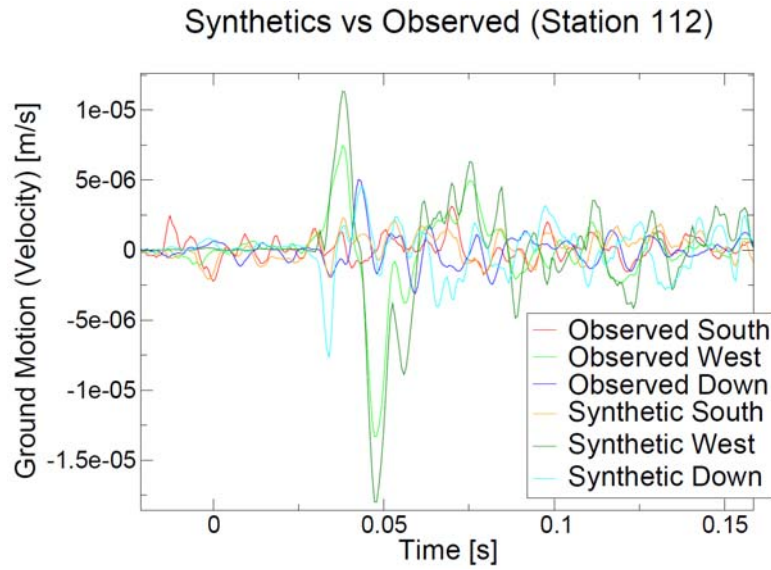


Figure 8: Observed and synthetic component for the triaxial station 112, for the magnitude -0.9 event.

6. Conclusions

Linearised time-domain inversion of the potency tensor for synthetic sources is shown to be able to resolve the focal mechanism and some source complexity very accurately. Moreover, for extended sources involving possibly many point sources (with inter-point source distances comparable to the wavelength of the dominant

frequency for the S-wave) this could provide a methodology for obtaining a simple estimate of the rupture scenario at the source, given near-field observations and a sufficiently homogeneous medium.

With careful manual processing of real mine events, it is possible to find high-resolution representations of the source time functions of these events. Although this yields point source approximations that yield synthetics matching well with the observed seismograms, the uniqueness of the solutions (especially if we are using near-field terms when inverting for an event with little or no stations in the near field) is in doubt, due to large condition numbers for the system in these cases.

Acknowledgements

A special acknowledgement is made to Dr. Dmitriy Malovichko (ISS International Limited) for his help in creating the synthetic Haskell model examples which was amongst others things, used to test the inversion procedure described herein on synthetic data.

References

1. Aki, K. and Richards, P. G. Quantitative Seismology, Second Edition, University Science Books, Sausalito, CA. 2002.
2. Backus, G. E. and Mulcahy, M. Moment Tensors and Other Phenomenological Descriptions of Seismic Sources I - Continuous Displacements. Geophys. J. R. astr. Soc., 1976, 46. 341-362
3. Backus, G. E. and Mulcahy, M. Moment Tensors and Other Phenomenological Descriptions of Seismic Sources II - Discontinuous Displacements. Geophys. J. R. astr. Soc., 1976, 46. 301-330
4. Frohlich, C. Earthquakes with Non-double-couple Mechanisms, Science, 1984, 264. 804-809.
5. Mendecki, A. J. Seismic Monitoring in Mines. Chapman and Hall, London, 1977
6. Sileny, J., Panza, G. F. and Campus, P. Waveform Inversion for Point Source Moment Tensor Retrieval with Variable Hypocentral Depth and Structural Model. Geophys. J. Int., 1992, 109. 259-274.

CODA WAVE INTERFEROMETRY IN MINES

RICHARD-A LYNCH

*ISS International Limited, P O Box 12063
Stellenbosch, 7613, Republic of South Africa*

The suitability of the coda wave interferometry technique for seismogram data recorded routinely in mines is examined. Synthetic data is used to show that for typical mine scales, the presence of tunnels and excavations is enough to cause a long coda, and that analysis of these codas can reveal small changes in seismic wave velocities. The technique is then applied to recorded seismic data from a mining-induced doublet and from a pair of development end blasts. Velocity variations as small as 0.06% were detected using coda wave interferometry. Changes in the source location are also estimated from the subtle differences of the codas.

1 Introduction

Large seismic events and rockbursts cause significant injuries or even loss of life to underground miners around the world, as well as serious damage to tunnels and excavations. Routine mine-wide seismic monitoring has been a standard technique for many years now. Modern monitoring systems produce vast amounts of quality seismogram data, and the time, location and source parameters such as radiated energy and inelastic deformation of each micro-seismic event may be estimated [1].

It is obviously desirable to be able to forewarn of large seismic events in mines, and there have been some scattered successes on the road towards this goal. In some cases, mainly heterogeneous low-stress mines, simple seismic activity works well [2,3]. In Russia and other countries of the former Soviet Union, spatial and temporal information together with source dimension has been used with some success [4,5]. In deeper, highly stressed mines more sophisticated uses of seismic source parameters have been demonstrated [6,7]. These latter techniques are routinely used in evaluation of seismic hazard for over 150 working areas in deep South African mines on a daily basis [8]. Nevertheless, a significant proportion of large ($m > 2.0$) seismic events are still unexpected.

A recent experiment on the San Andreas fault [9] showed that highly sensitive measurements of S-wave velocity could indicate precursory behaviour prior to some seismic events. The event sizes in that experiment (m1.0 and m3.0) are considered large by mining standards. Of further interest to mine seismologists, the precursory time windows were 2.5 hours before the m1.0, and 10.6 hours before the m3.0. The key to this experiment was regular high-precision travel time measurements, able to detect subtle ($\sim 0.03\%$) changes in S-wave velocity. This experiment is currently being attempted in a deep South African gold mine [10].

The new technique of coda wave interferometry [11] has been used to detect small seismic wave velocity variations. In one laboratory experiment, temperature-induced variations of the order of $0.1\% \pm 0.02\%$ were detected [12]. In another small-scale experiment, a pressure cell was used to change the local stress in a shallow mine [13]. The corresponding seismic velocity change detected by coda wave analysis was of the order $0.25\% \pm 0.02\%$.

In principal, coda wave interferometry could be a useful technique for mine seismology. However, it is not clear if a typical mining geometry would generate sufficiently developed coda waves. This point is addressed using dynamic seismic wavefield modelling in Section 2.

Coda wave interferometry requires identical, broad-band, seismic sources in order for the corresponding seismograms to be compared. In the published studies, air-cannon, piezo-electric and hammer-blow sources have been used. This work examines whether two types of common mine seismic sources – development end blasts and naturally-occurring fractures – would be suitable for use with coda wave interferometry, and if so, what the resulting resolution would be. Section 3 contains the results of this investigation.

2 Seismic Dynamic Modelling – Synthetic Data

A 3-D finite difference seismic wavefield modelling code was used to construct synthetic seismograms for some simple cases. The standard Ricker wavelet was used as a source time function. The source and sensor were placed 200 m apart in a homogeneous mass rock with P-wave velocity of 6060 m/s and S-wave velocity of 3500 m/s. The tunnel infrastructure and stopes (mining excavations) from a small (300 m × 500 m × 500 m) mine in Finland was then incorporated into the model. The seismic velocities within the tunnels and stopes were that of air with $v_P = 330$ m/s and $v_S = 0$ m/s. The synthetic seismograms with and without these tunnels and stopes are shown in Figure 1.

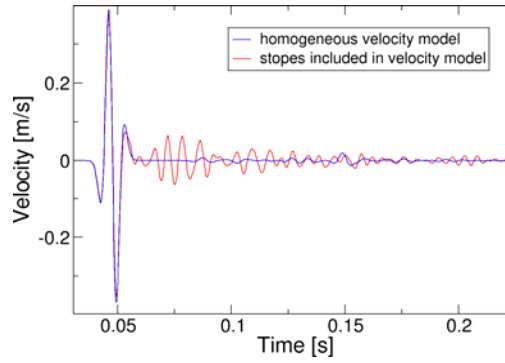


Figure 1: Synthetic seismograms computed for the case of homogeneous velocity model (blue) and same velocity model with only mining tunnels and stopes incorporated (red). Evidently merely the presence of tunnels causes a significant coda to develop.

If the seismic wave velocity of the medium is perturbed, then the arrival times of the wavelets will be changed, although the path each wavelet follows to arrive at the sensor will remain unchanged. Thus the arrival times of the coda waves, which travel for longer through the medium, will be perturbed more than the direct

wave arrival times. It is easy to show that $\frac{\delta v}{v} = -\frac{\delta t}{t}$, where δt is the time shift between parts of the seismogram that arrive a time t after the direct pulse, and $\frac{\delta v}{v}$ is the relative change in seismic wave velocities. For a rigorous derivation of this, see the 11th reference. It has been shown [12] that coda wave interferometry measures an effective velocity shift sensitive to mainly the S-wave velocity - for a Poissonian solid ($v_P = \sqrt{3} v_S$):

$$\frac{\delta v}{v} = 0.09 \frac{\delta v_P}{v_P} + 0.91 \frac{\delta v_S}{v_S} \dots \quad (1)$$

The increasing time shift of the coda can be seen by increasing the S-wave velocity by 1%, and comparing the original and perturbed synthetic seismograms – Figure 2.

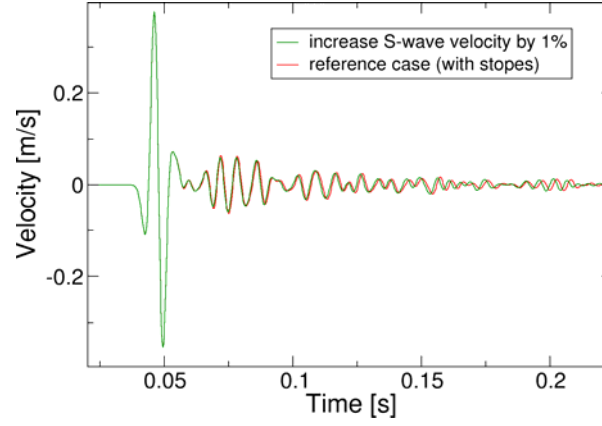


Figure 2 Synthetic seismograms obtained with the homogeneous medium in which tunnels and stopes have been inserted, for the reference case (red) and the perturbed case in which S-wave velocity has been increased by 1% (green). Note how the perturbed coda waves are increasing advanced with time since the direct wave arrival. This phenomenon may be used to estimate the velocity shift.

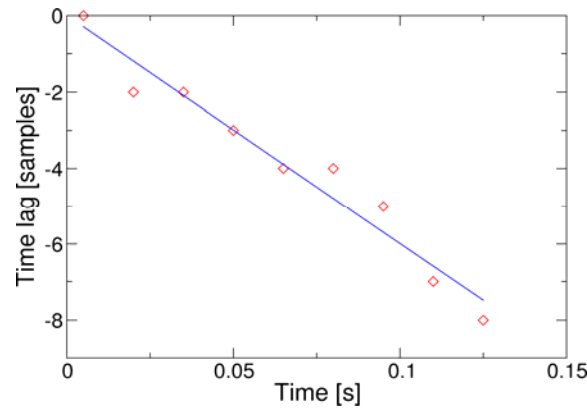


Figure 3: Plot of observed time shifts for each coda wave segment waves, as a function of the central time of the segment, relative to the time of the direct pulse arrival. The linear fit has gradient of -0.90% with standard error of 0.03%.

The time shift δt may be measured from the seismogram data using the cross-correlation function:

$$R^{(t,t_w)}(t_s) = \frac{\int_{t-t_w}^{t+t_w} u(t') \tilde{u}(t' + t_s) dt'}{\sqrt{\int_{t-t_w}^{t+t_w} u^2(t') dt' \int_{t-t_w}^{t+t_w} \tilde{u}^2(t') dt'}} \quad (2)$$

where t is the centre time of the window of length t_w , with $u(t)$ and $\tilde{u}(t)$ being the original and perturbed seismograms, respectively. The time shift δt is then the value of t_s for which $R(t_s)$ is maximal.

The value of t_w for each non-overlapping window with increasing centre time is plotted in Figure 3. The gradient of a linear fit to this data is thus our estimate for the velocity shift. In this case, we estimate the velocity shift is +0.90%, with standard error 0.07%. This is the same as the expected value of +0.91% from equation (1), as we have increased only v_s by 1%.

This simulation implies that coda wave interferometry should work on data recorded by a typical mine micro-seismic monitoring system.

3 Seismograms Recorded by Mine-wide Seismic Monitoring System

On the 14th March 2009, a local magnitude m1.2 seismic event was recorded at TauTona gold mine in South Africa. While this size event is recorded at this mine nearly every day, it is remarkable because a highly similar seismic event was recorded at this mine 10 days later, on 24th March. Figure 4 presents the recorded seismograms at one of the sensors. Even the late codas are quite similar. While such fracture doublets are common in crustal tectonics [14] there have been no published examples of mining induced fracture doublets.

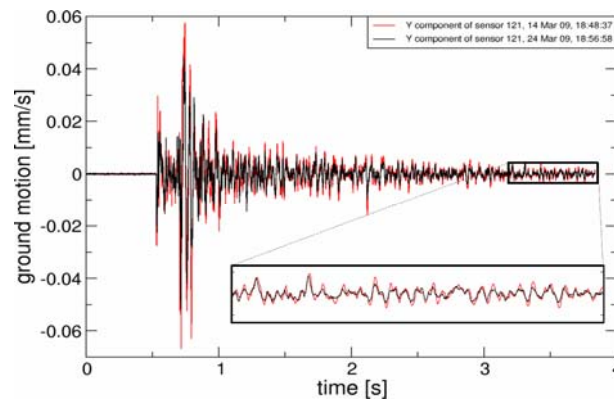


Figure 4: Seismograms recorded 10 days apart by the Y-component of a sensor in a deep South African gold mine. The seismograms have been overlaid such that the S-wave arrivals are co-incident. Even the late coda waves are quite similar (inset).

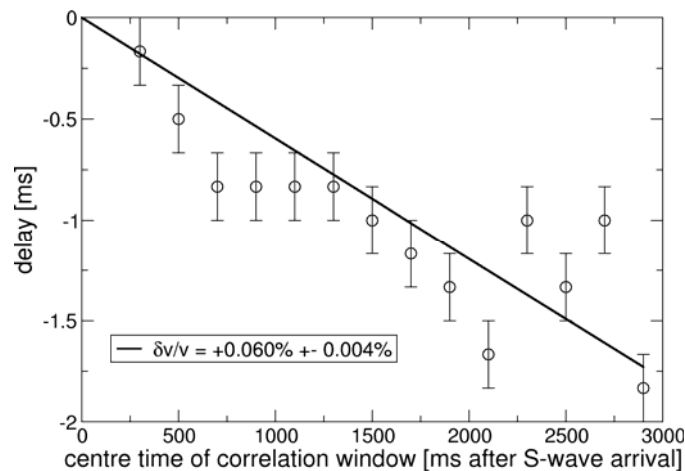


Figure 5: Plot of delay time vs time after the S-wave arrival, for the seismograms recorded at one of the sensors on the 14th and 24th March 2009. A consistent decrease in delay time is observed, indicating a seismic velocity increase of 0.06% in this 10-day period.

The seismograms were divided into windows. For each pair of windows, the time shift corresponding to the maximal cross-correlation $R(\delta t)$ was found. This plot and the fit is presented in Figure 5. The data reflects an underlying velocity shift of +0.060% over this 10-day period, with a standard deviation of 0.004%.

This kind of analysis represents only part of the information coda wave interferometry can provide. It has been shown [11] that the value of the maximal cross-correlation $R(\delta t)$ also provides information. The quantity σ_T^2 is defined by:

$$\sigma_T^2 = \frac{2}{\bar{\omega}^2} [1 - R(\delta t)]$$

where

$$\bar{\omega}^2 = \frac{\int \dot{u}^2(t') dt'}{\int u^2(t') dt'}$$

and can thus be calculated from the recorded data. If σ_T^2 is non-zero, and does not increase with time, then it is related to a change in source position r in a Poissonian solid by [15]:

$$\sigma_T^2 = \frac{0.329}{v_s^2} r^2 \quad \dots \quad (3)$$

The plot of σ_T^2 as a function of time for our data is given in Figure 6. The values of σ_T^2 are approximately constant in time, with average value of $1.8 \pm 0.7 \times 10^{-6} \text{ s}^2$. By equation (3), this would imply a source separation of $8 \pm 3 \text{ m}$, which seems plausible.

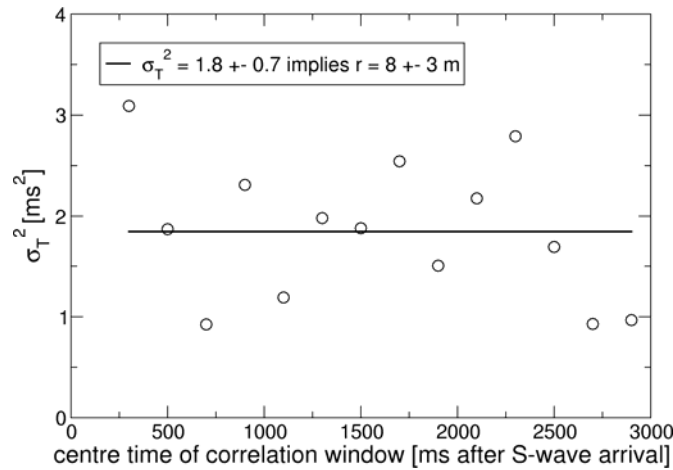


Figure 6: Plot of σ_T^2 as a function of time. The relation is approximately constant, with non-zero offset, and thus a source separation of $8 \pm 3 \text{ m}$ is indicated, using equation (2) with $v_s = 3500 \text{ m/s}$.

A search in the seismic event database collected for this mine in the first four months of 2009 (29,000 events) for very similar pairs of seismograms yields about 1,000 pairs. The time-of-day distribution of these pairs is presented in Figure 7. A large portion of the similar seismograms have development end (tunnel) blasts as sources. At this mine, development shots are separated in time from each other by a few seconds, and so clear seismograms are typically recorded. Each day, the same amount of explosive is used, separated in space by the daily tunnel advance: 1-2 m. Thus near-identical seismograms are not unexpected for these blasts.

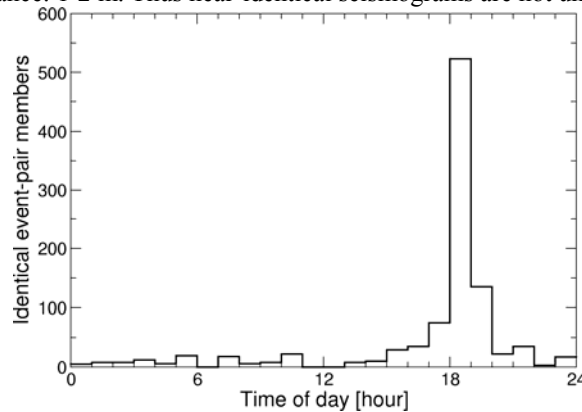


Figure 7: The time-of-day distribution for highly similar pairs of seismograms found in first 4 month's of seismic data recorded in a deep South African gold mine in 2009. The peak around blasting time (18h00-19h00) is due partially to the fact that most of the micro-seismicity is recorded at this time, but mainly due to the relatively high proportion of similar seismograms recorded for development-end blasts.

One such pair of seismograms of development-end blasting is shown in Figure 8. The seismograms feature a strongly developed P-wave arrival, as one would expect from a blast. Our coda wave analysis uses the S-wave arrival and following coda. In this case, the coda is rather short (300 ms) and so only a few windows can be analysed.

The plots of δt and σ_T^2 with time are shown in Figure 9. The linear increase of the time shift (delay) with time indicates a small velocity decrease (0.09% with standard deviation 0.02%) in the 24-hour period between seismic events. The non-zero and constant travel time variance implies a source separation of 1.2 ± 0.2 m, which is consistent with daily tunnel advance.

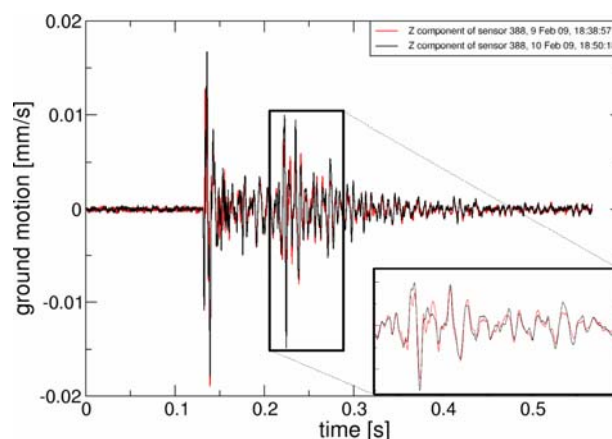


Figure 8: Seismograms recorded during development end blasting on subsequent days in February 2009. The S-wave arrivals (inset) are highly similar, with correlation coefficient 0.93.

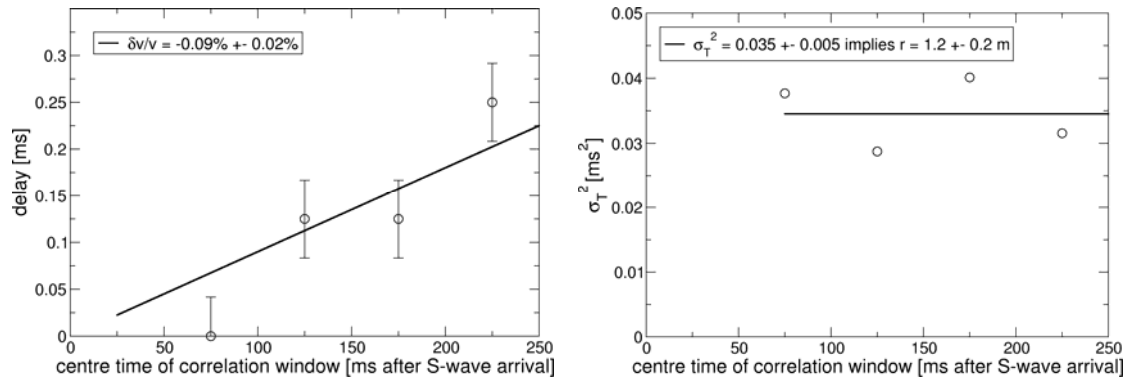


Figure 9: Plots of δt (top) and σ_T^2 (bottom) with time for the pair of blast seismograms recorded on 9 and 10 February 2009. In this 24 hour period, the seismic wave velocity in the region decreased by 0.09%, with standard deviation 0.02%. A source separation of $1.2 \pm 0.2 \text{ m}$ is indicated, which is consistent with a day's tunnel advance.

4 Conclusions

Coda wave interferometry, when applied to identical seismic sources recorded in a typical mining environment, provides additional information above the standard location and source parameters routinely extracted from the data. The in-situ, averaged seismic wave velocities can be carefully monitored with this technique, and small shifts of the order of 0.1% or less can be detected. The technique makes use of the fact that the complicated wave codas are deterministically generated, and thus identical seismic sources would result in identical seismograms, including the codas.

The identical seismic sources used in this work are “natural”, in the sense that the sources are not explicitly controlled for this purpose, and fall into two categories: mining-induced fractures of the rock mass surrounding underground excavations, and blasting of single shots separated in time from one another by at least a second or so. The identical fracture sources are only a few percent of all recorded mine micro-seismicity, which is consistent with the quickly changing stress conditions of underground mining. In mature tectonic fault systems, with practically constant loading, identical earthquakes (doublets) form a considerable proportion of recorded seismicity [16].

The majority of highly similar pairs of seismograms found during this study are caused by explosive sources. In particular, shots used in the development of tunnel ends on subsequent days tend to generate near-identical seismograms, as the amount of explosive and manner of detonation is unchanged over this time scale. The shots on subsequent days would be spatially separated by the amount of tunnel advance, typically 1-2 m, and this too can be estimated by the coda wave interferometry technique.

The use of “natural” mining seismic sources with coda wave interferometry has the attraction that this input data is already available in the 200+ mines around the world with passive micro-seismic monitoring systems. Of course, the disadvantage of this input data is that a measurement of seismic wave velocity cannot be induced on demand: we must wait for a seismic doublet to occur before information can be obtained by this technique.

This study has shown how coda wave interferometry could be routinely implemented with mine seismic data. Detection of seismic velocity variations of 0.1% or smaller is possible, although the benefit of this additional information for routine mining operations remains to be established.

Acknowledgements

This work was supported by the ISS International Self-Funded Research Program, 2009 and AngloGold-Ashanti. The author gratefully acknowledges assistance with the seismic dynamic modeling provided by Mr Paul Joubert of ISSI, as well as assistance with data mining provided by Dr Ernest Lötter of ISSI.

References

1. Mendecki, A. J. Seismic Monitoring in Mines. Chapman & Hall, 1997.
2. Edwards, J. Seismic Monitoring for Windblast Prediction, in Mine Seismicity and Rockburst Risk Management in U/G mines, (Perth, 1998).
3. Iannacchione, A. T., Bajpayee, T. S. and Edwards, J. L. Forecasting Roof Falls with Monitoring Technologies: A Look at the Moonee Colliery Experience. in Proc 24th Int Conf Ground Control in Mining, (Morgantown, University of West Virginia, 2005).
4. Malovichko, A. and Dyagilev, R. Technique for Predicting Seismic Hazard Zones in Mines. in Proceedings of the 5th International Symposium on Rockbursts and Seismicity in Mines, Johannesburg, (South Africa, 2001).
5. Mansurov, V.A. Prediction of Rockbursts by Analysis of Induced Seismicity Data. Int. J. of Rock Mech. & Mining Sci., 2001,(38). 893–901.
6. Mendecki, A. J., Van Aswegen, G. and Mountfort, P. A guide to Routine Seismic Monitoring in Mines, in A Handbook on Rock Engineering Practice for Tabular Hard Rock Mines, The Safety in Mines Research Advisory Committee, Johannesburg, 1999.
7. Lynch, R. and Mendecki, A. J. High-Resolution Seismic Monitoring in Mines. in Proceedings of the 5th International Symposium on Rockbursts and Seismicity in Mines, Johannesburg, (South Africa, 2001).
8. Van Aswegen, G. Routine Seismic Hazard Assessment in Some South African Mines. in Proceedings of the 6th International Symposium on Rockbursts and Seismicity in Mines, Perth, Australia, (Australian Centre of Geomechanics, 2005).
9. Niu, F., Silver, P. G., Daley, T. M., Cheng, X. and Majer, E. L. Preseismic Velocity Changes Observed from Active Source Monitoring at the Parkfield SAFOD Drill Site. Nature, 2008,(454). 204-208.
10. ISS International, Self-Funded Research Program 2009. Internal note, 2009.
11. Snieder, R. The Theory of Coda Wave Interferometry. Pure and Applied Geophys., 2006, 163(2-3). 455-473.
12. Snieder, R. Coda Wave Interferometry and the Equilibration of Energy in Elastic Media. Phys. Rev. E, 2002, (66). 046615–1,8.
13. Grêt, A., Snieder, R. and Özbay, U. Monitoring In situ Stress Changes in a Mining Environment with Coda Wave Interferometry. Geophys. J. Int., 2006, (167).504-508.
14. Richards, P.G., Waldhauser, F., Schaff, D. and Kim, W. The Applicability of Modern Methods of Earthquake Location. Pure appl. Geophys., 2006, (163). 351-372.
15. Snieder, R. and Vrijlandt, M. Constraining Relative Source Locations with Coda Wave Interferometry: Theory and Application to Earthquake Doublets in the Hayward Fault. California, J. Geophys. Res., 2005, 110, B04301, 10.1029/ 2004JB003317.
16. Ben-Zion, Y. Personal Communication, 2009.

THE EVALUATION OF FAILURE PROBABILITY OF DEEP HARD-ROCK MINING ENGINEERING

JIAN DENG, DE-SHENG GU and HUAI-SHENG PENG

School of Resources and Safety Engineering, Central South University

Changsha 410083, China

Stability of engineering structures continues to be an intensive research topic in mining engineering. How to effectively calculate the failure probability of complex engineering structures in deep metal mine is still problematic. This paper attempts to put forward a new probabilistic analysis method for failure probability evaluation of deep hard rock mining engineering, which combines radial basis function network, first order second moment method with numerical analysis method. In this new approach, radial basis function network is used to approximate the implicit performance function and its partial derivatives of rock engineering. Then statistical moments can be obtained and reliability index and/or probability of failure are calculated. The proposed method is illustrated by a practical example, which deals with reliability analysis of a pillar structure in an underground mine. It can be readily extended to other areas with implicit or complex performance functions such as structural engineering and slope engineering.

1 Introduction

In the last three decades, theory and practice of probabilistic analysis or reliability analysis in rock and soil engineering have been widely recognized and rapidly developed [1]. In deep hard rock mining engineering, stability of stope, shaft or pillar has relations with many factors such as in-situ stresses, secondary stresses and engineering activities which in turn caused the performance functions of the engineering structure in probabilistic analysis very complicated or even implicit. Implicit performance functions are often encountered when numerical methods such as finite element methods are adopted for the mechanical analysis of a structural system. As a result, it's difficult to calculate the performance function's gradients analytically.

A few approaches have been proposed to cope with the issues with implicit performance functions: Rational polynomial technique [2], Point-estimate methods, Monte Carlo simulation, and response surface methods [3]. Artificial neural network algorithms have been rapidly developed for a universal function approximator [4,5]. Neural networks are capable of learning from training examples and finding meaningful solutions without the need to specify the relationship among variables. A multilayer perceptrons (MLP) network was developed as an approximate performance function. Another neural network—radial basis function network (RBFN) attracts more and more attentions recently, which have been rapidly developed for universal function approximator [6]. RBFN is a computational mechanism that is able to acquire, represent, and compute a mapping from multivariate space of information to another, given a set of data representing that mapping. In this paper, RBFN is used to approximate the performance function and its partial derivatives of deep hard rock mining engineering. Then, statistical moments can be obtained and reliability index and/or probability of failure are calculated. This new method is illustrated by a practical example, which deals with reliability analysis of a pillar structure in an underground mine.

2 Calculation of failure probability

In probabilistic analysis, the first step in evaluation the failure probability or reliability is to decide on specific performance criteria and the relevant load and resistance parameters, called the basic variables X_i , and the function relationships among them corresponding to each performance criterion. Mathematically, this relationship or the performance function or the limit state function of deep rock engineering may be established as follows,

$$Z = g(X_1, X_2, \dots, X_n) = F(X_1, X_2, \dots, X_n) - 1 \quad (1)$$

where $X_i (i = 1, 2, \dots, n)$ is the pre-selected random variables in reliability analysis, $g(X_1, X_2, \dots, X_n)$ is the performance function, $Z > 0$ indicates stable, $Z < 0$ stands for failure, and $Z = 0$ for boundary between stable and un-stable. $F(X_1, X_2, \dots, X_n)$ is factor of safety.

A Taylor series expansion of the performance function about the mean value gives

$$Z = g(\mu_x) + \sum_{i=1}^n \frac{\partial g}{\partial X_i} (X_i - \mu_{x_i}) + \frac{1}{2} \sum_{i=1}^n \sum_{j=1}^n \frac{\partial^2 g}{\partial X_i \partial X_j} (X_i - \mu_{x_i})(X_j - \mu_{x_j}) + \dots \quad (2)$$

where the derivatives are evaluated at the mean values of the random soil variables (X_1, X_2, \dots, X_n) , and μ_{x_i} is the mean value of X_i .

The mean and variance of performance function using first order approximation can be obtained

$$\mu_Z = g(\mu_{x_1}, \mu_{x_2}, \dots, \mu_{x_n}) \quad (3)$$

and

$$\sigma_Z^2 = \sum_{i=1}^n \sum_{j=1}^n \frac{\partial g}{\partial X_i} \frac{\partial g}{\partial X_j} \text{cov}(X_i, X_j) \quad (4)$$

where $\text{cov}(X_i, X_j)$ is the covariance of X_i and X_j , μ_Z is the mean value of the performance function Z , and σ_Z^2 is the variance value of Z (σ_Z is the standard deviation of Z). If the random variables are uncorrelated, the variance is simply

$$\sigma_Z^2 = \sum_{i=1}^n \left(\frac{\partial g}{\partial X_i} \right)^2 \text{Var}(X_i) \quad (5)$$

where $\text{Var}(X_i)$ is the variance of random variable X_i . According to Eq.(1), we obtain

$$\mu_Z = \mu_F - 1; \sigma_Z = \sigma_F \quad (6)$$

where μ_F and σ_F are the mean value and the standard deviation of the safety factor F , respectively. Consequently, the reliability index in deep rock engineering was evaluated as follows based on the concept of the FOSM method.

$$\beta = \frac{\mu_Z}{\sigma_Z} = \frac{\mu_F - 1}{\sigma_F} \quad (7)$$

where β is the reliability index in stability analysis. The probability of failure (failure probability) in terms of the reliability index can be obtained as

$$p_f = \Phi(-\beta) = 1 - \Phi(\beta) \quad (8)$$

Where p_f is the failure probability.

The key step of Eq.(7) is calculation of the statistical moments of the safety factor, *i.e.*, the mean value (μ_F) and the standard deviation (σ_F) of F . Calculation of μ_F and σ_F needs the values of safety factor and the corresponding first order partial derivatives according to Eq.(4). Such calculations can be performed efficiently when the performance function $g(X)$ can be expressed as an explicit form or simple analytical form in terms of the basic variables X . When the performance functions are implicit, however, such calculations require additional effort and can be time-consuming. Such implicit performance functions are normally encountered when physical experiments or numerical analysis such as finite element methods has to be adopted for the mechanical analysis of deep rock engineering. It has been recognized that RBFN can be used to approximate nearly any function and its partial derivatives [6]. In this paper, RBFN is used to approximate the performance function and its partial derivatives of deep rock engineering.

3 Radial basis function networks

Consider a set of n labeled pairs $\{x^{(i)}, y^{(i)}\}_{i=1}^n$, which represent samples of a multivariate implicit performance function. The input variables (independent variables) are represented by x , $x = [x_1, x_2, \dots, x_p]^T$. The output variables (dependent variables) are represented by y . n is the number of samples, p is the dimension of input variables, *i.e.* the number of input neurons of radial basis function network. RBFN can be regarded as a mapping from p dimension space to one dimension space $f: R^p \rightarrow R^1$, which is composed of radial basis functions $\{g^{(i)}\}_{i=1}^m$ and weights $\{w^{(i)}\}_{i=1}^m$, $m \leq n$.

The response characteristics of the i th hidden unit are given by:

$$g^{(i)}(r) = \phi^{(i)}(\|x - c^{(i)}\|) \quad i = 1, \dots, m \quad (9)$$

where $\phi^{(i)}(r)$ is called radial basis function; $r = \|x - c^{(i)}\|$ denotes the Euclidean distance, and

$$r = \sqrt{(x - c^{(i)}) \cdot (x - c^{(i)})} = \sqrt{\sum_{j=1}^n [x_j - c_j^{(i)}]^2}; \quad c^{(i)} \text{ is the centroid of the radial basis function that can be}$$

chosen from among the data points. m is the number of radial basis functions, *i.e.* the number of hidden units. The most commonly-used radial basis function is Gaussians, which can be described as

$$\phi^{(i)}(r) = \phi^{(i)}(\|x - c^{(i)}\|) = \exp\left(-\frac{r^2}{a^{(i)2}}\right) \quad (10)$$

where $a^{(i)}$ is the width of the i th radial basis function. The output of the RBFN network is the linear combination of outputs of hidden units, which is given by:

$$F(x) = \sum_{i=1}^m w^{(i)} g^{(i)}(x) \quad (11)$$

The safety factor $F(x)$ is approximated in terms of radial basis functions as indicated in Eq.(11). The partial derivatives of safety factor are calculated by the differential rule.

$$F_j(x) = \frac{\partial F(x)}{\partial x_j} = \sum_{i=1}^m w^{(i)} h^{(i)}(x) = \sum_{i=1}^m w^{(i)} \frac{\partial \phi^{(i)}(x)}{\partial x_j} \quad (12)$$

and

$$\frac{\partial \phi^{(i)}(x)}{\partial x_j} = \frac{-2(x_j - c_j^{(i)})}{a^{(i)2}} \exp\left(-\frac{r^2}{a^{(i)2}}\right) \quad (13)$$

4 Algorithm and Example

4.1 Algorithm

A new probabilistic analysis method for deep hard rock engineering is proposed, which combines radial basis function network, first order second moment method with numerical analysis method. The flowchart of this methodology is shown in Figure 1. Radial basis function network is used to approximate the performance function and its partial derivatives of deep rock engineering. Then statistical moments can be obtained and reliability index and/or probability of failure are calculated by using first order second moment method. This new method is illustrated by a practical example, which deals with reliability analysis of a pillar structure in an underground mine.

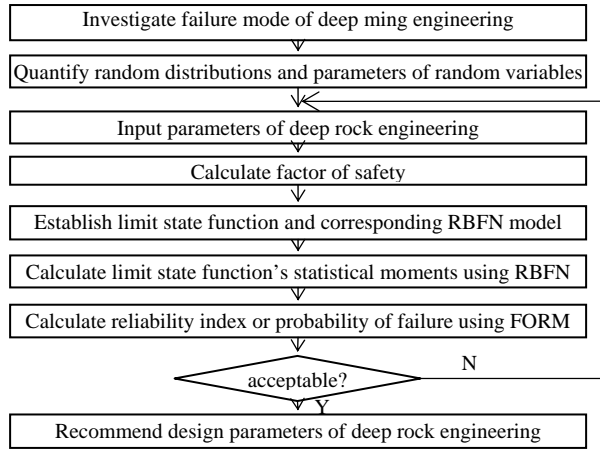


Figure 1 Reliability analysis of deep rock engineering

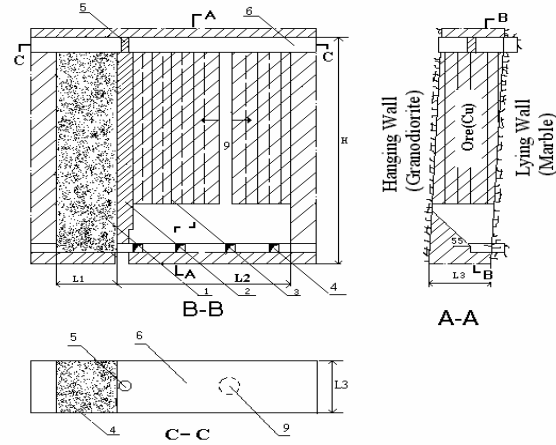


Figure 2 Outline of the underground mining method.

Note: 1—sub-stope A (backfilling); 2—temporary ore wall; 3—sub-stope B; 4—basement structure; 5—ore pillar; 6—drilling room; 9—blasting cut borehole; L1—length of sub-stope A; L2—length of sub-stope B; L3—width of ore body; and H—height of level. The figure B-B is the longitudinal section of the stope along the strike of the ore-body; (A-A) dip cross-section of the stope; (C-C) plan of the drilling room

4.2 An Example

Figure 2 shows the detailed layout of the mining method. The stope is divided into sub-stope A and sub-stope B. Sub-stope A is 15m long along the ore longitudinal direction. Sub-stope B is 35m. A temporary ore wall, which is 5m wide, is needed between substopes A and B to support an ore pillar. Ore rock in substope A is extracted at

first. Ore blocks in sub-stope A are directly drawn down to the drift. Once ore rock in sub-stope A is completely extracted, ore tailings mixed with Poland cement will be used to backfill the open space of sub-stope A. Until sub-stope A is completely backfilled, mining activities will commence in sub-stope B. The temporary ore wall would function as a barrier to prevent backfilling materials in sub-stope A from collapsing into sub-stope B during excavation of sub-stope B. Blasted ore blocks in sub-stope B are drawn via a vibrating machine. This vibrating machine requires sub-stope B to be 35m long. Sub-stope B will be backfilled once its ore is completely extracted. The mining operations will commence and are repeated for next stope.

Method of extraction is drilling and blasting. Those mining works are carried out in drilling room, top section of stope. A special drilling machine is used to drill holes in stope below drilling room. This drilling machine requires the drilling room to be 3.8m high. The drilling room therefore occupies an open space of 20m wide, 55m long and 3.8m high. The roof area is equal to 1100m². The drilling room roof, composed of in situ ore rock, could collapse if it is improperly designed and constructed. For safety and economy, the excavation for drilling room space would leave one cylindrical ore pillar of 3.8m high in the central area of temporary ore wall in drilling room. The pillar becomes an intact part of the roof and bottom ores. The pillar should be an intact ore block and have no discontinuities such as joints and fractures. The pillar functions as a column structure to support roof strata and to reduce ground subsidence. The cylindrical pillar diameter should be neither too small to support roof loading nor too large to impede drilling and other work and to reduce mining productivity. Accordingly, the ore pillar becomes the most critical structure for successful mining operations. Structural analysis and design of the pillar are to determine the best location and the optimal diameter.

Based on the computation of pillar strength and stress analysis, the pillar safety factor is

$$F_s = \sqrt{s\sigma_c^2} (0.778 + 0.222 \frac{w}{h}) / \sigma \quad (14)$$

where s is material parameters depending on the properties of the rock and the extent of joints or fractures, σ_c is the uniaxial compressive strength (UCS) of intact rock, w and h are the pillar width and height, σ is the pillar average vertical stress, which is obtained by 3-dimensional finite element analysis. Table 3 lists statistical values of the basic random variables for ore properties. The corresponding pillar performance function is

$$Z = g(X_1, X_2, \dots, X_n) = F(E, \gamma, \mu, \sigma_c) - 1 \quad (15)$$

Table 3 Probabilistic parameters of ore rock

Variables	Type of distribution	Mean	Standard deviation	Coefficient of variation
Elastic modulus E (Mpa)	Normal	63000	15750	0.25
Density γ (MN/m ³)	Normal	0.0328	0.00328	0.10
Poisson's ratio μ	Normal	0.23	0.0345	0.15
UCS, σ_c (Mpa)	Normal	53.0	7.95	0.15

Table 4 Comparison of pillar reliability index (β) and failure probability (p_f)

Coefficient of variation of UCS	0.10		0.15		0.20		0.25	
Reliability index	β	p_f (%)	β	p_f (%)	β	p_f (%)	β	p_f (%)
This paper's method	3.40	0.033	2.48	0.657	1.89	2.938	1.58	5.705
Reference[7]	3.43	0.030	2.51	0.604	1.94	2.619	1.52	6.425

The performance function is implicit in terms of the basic random variables. A radial basis function network is established to model the implicit performance function. Four variables listed in table 3 are designed as the input variables, and the performance function as the output variable. The validation set is generated randomly. All the performance function values in the training set and validation set were computed by a three-dimensional finite element program. The predicted ones of the RBFN are in agreement with the calculated values of performance function. It shows that the network establishes a mapping approximate to the performance function and its partial derivatives. Pillar's reliability index under different coefficient of variation computed by using the proposed method are listed in Table 4. For comparison, the results of reference [7] are also listed. It shows that both results are in agreement. It can be concluded that the proposed method is correct and can be used in probabilistic analysis of rock engineering.

5 Conclusion

This paper presents a new probabilistic analysis method for deep hard rock engineering, which combines the radial basis function network, first order second moment method with numerical analysis method. Radial basis function network is used to approximate the performance function and its partial derivatives of deep rock engineering. Then statistical moments can be obtained and reliability index and/or probability of failure are calculated. This new method is illustrated by a practical example, which deals with reliability analysis of a pillar structure in an underground mine. In the proposed RBFN based approaches, it is not necessary to know the underlying relationship or to suppose a relationship between the input variables and the output, unlike the response surface method. The RBFN is a universal approximator and can be used to approximate linear or non-linear, implicit or explicit performance functions. The proposed method can be extended to other areas with implicit or complex performance functions such as slope engineering. For detailed algorithm and more examples, please refer to [6].

Acknowledgements

Supports from NSFC (Nos 50574098 and 50404010), Hunan NSF (05jj10010), program for NCET-07-0860 in universities, SRFDP-200805330029, and SRF for ROCS, SEM were acknowledged by the authors.

References

1. Quek, S.T. and Leung, C.F. Reliability-based Stability Analysis of Rock Excavations. *International Journal of Rock Mechanics and Mining Sciences*, 1995, 32 (6). 617-620.
2. Chowdhury, R.N. and Xu, D.W. Rational Polynomial Technique in Slope-reliability Analysis. *Journal of Geotechnical Engineering Division, ASCE*, 1993, 119 (12).1910-1928.
3. Haldar, A., and Mahadevan, S. *Reliability Assessment Using Stochastic Finite Element Analysis*. New York: John Wiley & Sons, Inc. 2000
4. Deng, J., Gu, D.S., Li, X.B. and Yue, Z.Q. Structural Reliability Analysis for Implicit Performance Function Using artificial Neural Network. *Structural Safety*, 2005, 25 (1). 25-48.
5. Li, X. Simultaneous Approximations of Multivariate Functions and Derivatives by Neural Networks with one Hidden layer. *Neurocomputing*, 1996, 12. 327-343.
6. Deng, J. Structural Reliability Analysis for Implicit Performance Function Using Radial Basis Function. *International Journal of Solids and Structures*, 2006, 43 (11-12). 3255-3291.
7. Deng, J., Yue, Z.Q., Tham, L.G. and Zhu, H.H. Pillar Design by Combining Finite Elements, Neural Networks and Reliability. *International Journal of Rock Mechanics and Mining Sciences*, 2003, 40 (4).585-599.

FORECASTING OF ROCK BURST BASED ON ANT COLONY CLUSTERING ALGORITHM

WEI GAO

*State Key Laboratory of Geomechanics and Geotechnical Engineering, Institute of Rock and Soil Mechanics, CAS
Wuhan, 430071, P.R. China*

For the rock burst is the big disaster in deep underground engineering, it is very important to study the forecasting of rock burst. For the influence factors of rock burst are numerous and their relationship is very complicated, it can not be solved by traditional methods, so generally based on engineering analogy and geology analysis, the clustering methods are used widely. For the complicated environment influence of rock burst, this clustering problem is a very complicated fuzzy and random optimization problem, and can not be solved by traditional methods very well. So, here the new bionics clustering optimization method-Ant Colony Clustering Algorithm which is proposed recently has been introduced into rock burst forecasting field for the first time. Based on this new bionics clustering method, one new method for forecasting of rock burst is proposed. Based on analyzing the data of rock burst samples, from the engineering analogy thinking by ant colony clustering algorithm, the rock burst can be forecasted. Two real engineering examples are used to verify calculating effect of the new algorithm. The engineering application can prove that, this new algorithm can automatically sort the rock burst samples, and the validity is very high, so it is a very practical method for rock burst forecasting, and should be popularized in real practice.

1 Introduction

From analysis of the rock burst statistic data in the world, we can see that, rock burst has been occurred in many underground fields, and is one big disaster in deep underground engineering of the world [1]. The final goal of rock burst study is to forecast it and to control it as soon as possible. For the forecasting of rock burst is a very important work, there have been proposed a lot of traditional methods on rock burst forecasting [1-2]. But for the complicated nonlinear relationship between the rock burst and its influence factors, so there are a lot of shortcomings in the traditional methods.

For the rock burst is a very complex opening giant system, it is influenced by many factors, in these influence factors, some are certain and quantitative, while the others are random, qualitative and fuzzy. So, to solve this problem, the engineering analogy and geology analysis is a more suitable method. Now, there have been existed many methods based on engineering analogy [3-5]. The key thinking of engineering analogy method is cluster. In the traditional clustering method, some clustering parameters, such as category number, initial cluster center, et al, should be determined by some engineering experience. And then the samples are trained according to the principles of distance minimum, until the square sum of distance between the samples and cluster centers is reached the minimum. Generally, the computing results of traditional method are depended on the clustering parameters. But the suitable clustering parameters can not be determined easily when the number of engineering samples is very large. And while, the argument and objective function are all discrete variables in rock burst forecasting problems, so there are many local minimax solutions. To solve this problem, the traditional method is not valid. In order to solve this problem very well, some profound studies are necessary.

Ant colony clustering algorithm is a new bionics optimization algorithm, and can solve many complicated optimization problems, which can not be solved very well by traditional methods. So, to solve the hard problem of rock burst forecasting, this new algorithm is introduced and while one new method to forecast the rock burst is proposed.

2 Ant Colony Clustering Algorithm

The idea of ant colony clustering algorithm is inspired by the behaviour of ant colonies in clustering their corpses and sorting their larvae. The first studies related to this domain is the work of Deneubourg, et al [6], who have proposed a basic model that allowed ants to randomly move, pick up and drop objects according to the number of similar surrounding objects so as to cluster them. This basic model has been applied in robot field successfully. Based on the basic model, some other scholars [7-8] have proposed many other modified algorithms, and obtained some useful achievements. Although the studies on the ant colony clustering algorithm are deficient, the preliminary study has proved its rationality and affectivity.

In order to describe the algorithm very well, the basic principle of the ant colony clustering algorithm is introduced here firstly.

Firstly, the data objects have been randomly projected onto one plane. Then each ant chooses an object at random, and picks up or moves or drops down the object according to picking-up or dropping probability with respect to the similarity of the current object within a local region. Finally, clusters are collected from the plane.

The process of the ant colony clustering algorithm is described by the pseudo-code as follows.

1) Initialization: initialize the number of ants: N , the entire number of iteration: M , side length of local region: s , and other parameters;

2) Project the data objects on a plane, i.e. give a pair of coordinates (x, y) to each object randomly;

3) Each ant that is currently unloaded chooses an object at random;

4) To each ant, one randomly selected moving speed is given;

5) For $i=1, 2, \dots, M$

For $j=1, 2, \dots, N$

The average similarity of all objects is calculated.

If the ant is unloaded, compute picking-up probability P_p . If P_p is greater than a random probability and one object is not picked up by the other ants simultaneously, then the ant picks up this object, marks itself as loaded, and moves this object to a new position; else the ant does not pick up this object and re-selects another object randomly.

If the ant is loaded, compute dropping probability P_d . If P_d is greater than a random probability, then the ant drops the object, marks itself as unloaded, and re-selects a new object randomly; else the ant continues moving the object to a new position.

End

End

6) For $i=1, 2, \dots, n$ // for all objects

If an object is isolated, that is the number of its neighbour is less than a given constant, then label it as an outlier;

Else give this object a cluster labelling number, and recursively label the same number to those objects who is the neighbours of this object within local region.

End

The operations of the algorithm are described detailed as follows.

1. The average similarity function

We assume that an ant is located at site r at time t , and finds an object o_i at that site. The average similarity density of object o_i with the other objects o_j present in its neighbourhood $f(o_i)$ is given by follow equation.

$$f(o_i) = \max\{0, \frac{1}{s^2} \sum_{o_j \in \text{Neigh}_{s \times s}(r)} [1 - \frac{d(o_i, o_j)}{\alpha(1 + (v-1)/v_{\max})}]\} \quad (1)$$

where, α defines a parameter to adjust the similarity between objects. The parameter v defines the speed of the ants, and v_{\max} is the maximum speed. $\text{Neigh}_{s \times s}(r)$ denotes a square of $s \times s$ sites surrounding site r . $d(o_i, o_j)$ is the distance between two objects o_i and o_j in the space of attributes. Here the Euclidean distance or Cosine distance is used. The Euclidean distance can be described as follows.

$$d(o_i, o_j) = \sqrt{\sum_{k=1}^m (o_{ik} - o_{jk})^2} \quad (2)$$

where, m defines the number of attributes.

The Cosine distance can be described as follows.

$$d(o_i, o_j) = 1 - \text{sim}(o_i, o_j) \quad (3)$$

where, $\text{sim}(o_i, o_j)$ reflects the similarity metric between two objects. It measures the cosine of the angle between two vectors (their dot product divided by their magnitudes), which can be described as follows.

$$\text{sim}(o_i, o_j) = \frac{\sum_{k=1}^m (o_{ik} \bullet o_{jk})}{\sqrt{\sum_{k=1}^m (o_{ik})^2 \bullet \sum_{k=1}^m (o_{jk})^2}} \quad (4)$$

As the objects become more similar, the Cosine similarity $\text{sim}(o_i, o_j)$ approaches 1 and their Cosine distance approaches 0.

From formula (1), we note that the parameter α affects the number of clusters and the speed of algorithm convergence. Otherwise, the speed v affects the cluster scale and the tendency of an ant to pick up or drop an object. Here, to study simply, the follow definition of speed v is used.

v is an uniformly random: the speed of each ant is distributed randomly in $[1, v_{\max}]$.

2. The probability conversion function

The probability conversion function is one function of $f(o_i)$, and its purpose is to convert the average similarity $f(o_i)$ into the picking-up and dropping probabilities. The approach that the average similarity $f(o_i)$ converts into the picking-up and dropping probabilities are based on: the smaller the similarity of a data object is (i. e. there are not many objects that belong to the same cluster in its neighbourhood), the higher the picking-up probability is and the lower the dropping probability is; on the other hand, the larger the similarity is, the lower the picking-up probability is (i. e. objects are unlikely to be removed from dense clusters) and the higher

the dropping probability is. According to this principle, the sigmoid function is used as probability conversion function here.

The picking-up probability for a randomly moving ant that is currently not carrying an object to pick up an object is given by follow equation.

$$P_p = 1 - \text{Sigmoid}(f(o_i)) \quad (5)$$

As the same method, the dropping probability for a randomly moving loaded ant to deposit an object is given by follow equation.

$$P_d = \text{Sigmoid}(f(o_i)) \quad (6)$$

The sigmoid function has a natural exponential form as follow.

$$\text{Sigmoid}(x) = \frac{1 - e^{-cx}}{1 + e^{-cx}} \quad (7)$$

where, c is a slope constant and can speed up the algorithm convergence as it is increased.

It must to be pointed out that, during clustering procedure, there might be some objects (also called outliers) with high dissimilarity to all other data element. The outliers block ants dropping down them and slow down the algorithm convergence. Here we choose larger parameter c to help ant to drop the outliers at the later stage of the algorithm.

Otherwise, the number of ants also affects the performance and convergence speed of algorithm. So, in real application, the suitable number of ants should be selected by trial or engineering experience.

3 Engineering Examples

Lot of researches prove that the rock burst is depended on two kinds of influence factors, such as internal cause and external cause. The main influence factor is rock character, which is the sufficient condition of rock burst, while the high initial stress is the necessary condition [1].

In this example, according to the previous studies, the four indexes are considered as the main factors of rock burst, which are uniaxial compressive strength σ_c , tensile strength σ_t , maximum tangential stress σ_θ and impact index Wet , which describes the storage capability of elastic strain energy. In order to describe the status of rock burst, the rock burst is divided into four rates, which are strong rock burst, moderate rock burst, weak rock burst and no rock burst. In computation, the rock burst rate is denoted by 1, 2, 3 and 4. From the reference [4], the engineering examples are showed as follow Table 1.

Table 1 Engineering examples of rock burst

Engineering examples	influence factors				Real situation
	σ_c /MPa	σ_t /MPa	σ_θ /MPa	Wet	
Tunnel of Tianshegqiao Power Station	88.7	3.7	30.0	6.6	moderate rock burst
N. 2 Tunnel of Ertan Power Station	220.0	7.4	90.0	7.3	weak rock burst
Underground Space of Taipinxi Power Station	165.0	9.4	62.6	9.0	weak rock burst
Underground Plant of Laxiwa Power Station	176.0	7.3	55.4	9.3	moderate rock burst
Diversion Tunnel of Jinping Power Station	120.0	6.5	98.6	3.8	moderate rock burst
Underground Plant of Longyangxia Power Station	178.0	5.7	18.8	7.3	no rock burst

Underground Plant of Lijiaxia Power Station	115.0	5.0	11.0	5.7	no rock burst
Underground Plant of Sima Power Station in Norway	180.0	8.3	48.75	5.0	strong rock burst sometimes
Sewage Tunnel in Norway	180.0	8.3	75.0	5.0	moderate rock burst
Cooling Water Tunnel of Forsmark Nuclear Power Station in Sweden	130.0	6.0	50.0	5.0	moderate rock burst
Vietas Tunnel in Sweden	180.0	6.7	80.0	5.5	weak rock burst
Kanetsu Tunnel in Japan	236.0	8.3	89.0	5.0	moderate rock burst
Roadway of Raibl Mine in Italy	140.0	8.0	108.4	5.5	strong rock burst
Diversion Tunnel of Yuzixi Power Station	170.0	11.3	90.0	9.0	strong rock burst
Underground Space of Pubuxi Power Station	123.0	6.0	43.4	5.0	weak rock burst
Underground Space of Lubuge Power Station	150.0	5.4	34.0	7.8	no rock burst
Heggura Highway Tunnel in Norway	175.0	7.3	62.5	5.0	moderate rock burst
Roadway of Rasvumchorr Mine in Former Soviet Union	180.0	8.3	57.0	5.0	moderate rock burst

The parameters of ant colony clustering algorithm are selected as follows, $N = 20, M = 2000, s = 3, \alpha = 1.5, v_{\max} = 0.85, c = 3$. According to those parameters, the results of engineering examples are as follow Table 2. To comprise, the results by neural networks in reference [4] are also showed in Table 2.

Table 2 Results of engineering examples

Engineering examples	Results in reference [4]	Results of new algorithm	Real situation of rock burst
Tunnel of Tianshegqiao Power Station	moderate	moderate	moderate rock burst
No. 2 Tunnel of Ertan Power Station	weak	weak	weak rock burst
Underground Space of Taipinxi Power Station	moderate	weak	weak rock burst
Underground Plant of Laxiwa Power Station	moderate	moderate	moderate rock burst
Diversion Tunnel of Jinping Power Station	moderate	moderate	moderate rock burst
Underground Plant of Longyangxia Power Station	no	no	no rock burst
Underground Plant of Lijiaxia Power Station	no	weak	no rock burst
Underground Plant of Sima Power Station in Norway	moderate	strong	strong rock burst sometimes
Sewage Tunnel in Norway	moderate	moderate	moderate rock burst
Cooling Water Tunnel of Forsmark Nuclear Power Station in Sweden	moderate	moderate	moderate rock burst
Vietas Tunnel in Sweden	no	weak	weak rock burst
Kanetsu Tunnel in Japan	moderate	moderate	moderate rock burst
Roadway of Raibl Mine in Italy	moderate	strong	strong rock burst
Diversion Tunnel of Yuzixi Power Station	moderate	strong	strong rock burst

Underground Space of Pubuxi Power Station	moderate	moderate	weak rock burst
Underground Space of Lubuge Power Station	no	no	no rock burst
Heggura Highway Tunnel in Norway	moderate	moderate	moderate rock burst
Roadway of Rasvumchorr Mine in Former Soviet Union	moderate	moderate	moderate rock burst

From the Table 2, we can see that, the results of our new algorithm are almost the same as those of neural networks and the real situation. But the judgement error of our new algorithm is less, or the accuracy is higher.

4 Conclusions and Future Work

For its computing complex, to forecast rock burst, the engineering analogy is a more suitable method. But for the influence factors of rock burst are numerous and their relationship is very complicated, in engineering analogy method, the clustering idea is used widely. Because the real environment influence of rock burst is very complicated, the clustering problem is a very complicated fuzzy and random optimization problem, and can not be solved by traditional methods very well. To solve this problem very well, the new bionics clustering optimization method-Ant Colony Clustering Algorithm which is proposed recently is used for the first time. Based on this new bionics clustering method, one new method for study forecasting of rock burst is proposed. At last, the real engineering examples are used to verify the calculating effect of the new algorithm. And the results show that, it is a very practical method for rock burst forecasting, and should be popularized.

For our work here is the preliminary application of ant colony clustering algorithm in geotechnical engineering field, there are lot of aspects, which must be researched profoundly, and then this is our next work.

Acknowledgements

The author wish to acknowledge the collaborative funding support from the National Natural Science Foundations of China under grant no. 40638040 and 40872187.

References

1. Board, M. and Fairhurst, C. Rockbursts Prediction and Control. The Institution of Mining and Metallurgy, 1983.
2. Jiang, T. Study on Method of Rockburst Prediction and Its Prevention in Deep and Long Tunnel. North China Institute of Water Conservancy and Hydroelectric Power, 1998.
3. Yang, T. and Li, G.W. Study on Rockburst Prediction Method Based on the Prior Knowledge. Chinese Journal of Rock Mechanics and Engineering, 2000, 19(4). 429-431.
4. Chen, H.J., Li, N.H. Nie, D.X., et al. A model for prediction of rockburst by artificial neural network. Chinese Journal of Geotechnical Engineering, 2002, 24(2). 229-232.
5. Feng, X.T. and Zhao, H.B. Prediction of Rockburst Using Support Vector Machine. Journal of Northeastern University (Natural Science), 2002, 23 (1). 57-59.
6. Deneubourg, J.L., Goss, S. Franks, N., et al. The dynamics of collective sorting: robot-like ant and ant-like robot. in Meyer, J. A. and Wilson, S. W. eds. Proceedings first conference on simulation of adaptive behavior: from animals to animats. MIT Press, 1991, 356-365.
7. Lumer, E. and Faieta, B. Diversity and adaptation in populations of clustering ants. in Proc. third international conference on simulation of adaptive behavior: from animals to animats. MIT Press , 1994, 499-508.
8. Ramos, V. and Merelo, J.J. Self-organized stigmergic document maps: environment as a mechanism for context learning. in Alba, E., Herrera, F. and Merelo, J. J., et al. eds. AEB'2002 -1st Spanish conference on evolutionary and bio-inspired algorithms. Mérida, 2002, 284-293.

PREDICATION OF ROCKBURST BASED ON GAUSSIAN PROCESSES WITH THE COMBINATORIAL KERNEL FUNCTION

JIA-QI GUO, CHUN-SHENG QIAO, CHONG XU

*School of Civil Engineering, Beijing Jiaotong University
Beijing, 100044, P.R. China*

LI-CHAO CHENG

*School of Energy Resource, Hebei university of Engineering
Handan, 056038, P.R. China*

Rockburst is a kind of dynamic phenomenon for the surrounding rock mass in deep underground works. At present, it is still difficult to understand the mechanism of rockburst and carry out effective predication of rockburst. The Gaussian process is a completely new machine developed rapidly in recent years. Compared with ANN and SVM, this method has some advantages for example: easy programming, self-adaptive acquisition of hyperparameters, flexible non-parameters inference, prediction with probability interpretation and so on. Based on the analysis of main factors of rockburst, the Gaussian process with the combinatorial kernel function obtained by combination of squared exponential and rational quadratic covariance function is implemented by learning machine routine in Matlab for overcoming poor predictive precision and network generalization ability of single kernel function. Then the automatic relevant determination is introduced into combinatorial Gaussian kernel function in the programme and GP regression model with regard to hyperparameters was established. Meanwhile, the correlation and characteristics selection about inputs and prediction for testing samples on the basis of the net are completed respectively. The predicted results show that it is feasible and valid to use the GP regression model for predicating rockburst. Compared with RBF neural network and SVM, the prediction precision of GPR with the kernel function is relatively better.

1 Introduction

Rockburst is caused by the violent release of strain energy stored in a surrounding rock mass of underground space in high geostatic stress. Because it occurs suddenly and intensely, rockburst usually causes injury including death to workers, damage to equipment, even substantial disruption and economic loss of underground space excavation. Since the first record of rockburst at a tin mine in England in 1738 [1], rockburst has occurred in many countries' coal mine. In China, the disaster has become more and more frequently in recent years. There exists a complicated nonlinear relationship between rockburst causes and it, so, its prediction is always a difficult point in safety of coal mine.

Up to now, many theories have been proposed, such as strength theory, stiffness theory, energy theory, burst trend theory, catastrophic theory, chaotic theory, fractal theory, etc. Also, a lot of methods to monitor rock burst have been established [2], such as drilled chip measurement, AE technique, seismological method, etc. We find that those theories have only studied rockburst by mechanical method or mathematic method, and cannot be used well in real engineering. While those monitor methods are all only to collect data about rock burst simply and not to analyze data by theory. Rockburst is a very complicated dynamic system, and the only information which we can get is the field data about its exterior behaviour, so the most suitable method to model the rockburst should analyze the field data well. From this viewpoint, some methods to analyze the field data have been proposed. But through analysis of those methods, we can find that those methods have some

disadvantages [3~6]. Gaussian process is a completely new machine learning way developed rapidly in recent years. It embodies characteristics of programming easily, self-adaptive acquisition of hyperparameters, flexible non-parameters inference and prediction with probability interpretation than ANN and SVM. In this study, Gaussian process is introduced to predict the occurrence and intensity of rockburst.

2 Gaussian Process and Its Algorithm

Gaussian processes are a nonparametric Bayesian regression technique [7]. It has ability to obtain state of the art good model, when only a small set of training data is available infer hyperparameters directly from the training data and give a probabilistic measure of the uncertainty of the model prediction [8].

Given a dataset $D = \{X_i, y_i\}_{i=1}^n$, in the present work, $X_i = [x_i^{(H)} x_i^{(I)} x_i^{(On)} x_i^{(Off)}]^T$, and we assume here $y_i = y_i^{(MRR)}$. For multiple responses regression, refers to [9]. In the probabilistic view, the dataset could be regarded as a sampling from the conditional distribution $p(y|x)$ under the assumption that the observations y are independent and identically distributed. This relation can be decomposed into a systematic and a random component.

$$y = f + \varepsilon \quad (1)$$

That is, the observation y assumed to contain the latent functions $f: X \rightarrow R$ and additive Gaussian noise $p(\varepsilon) = N(0, \sigma_n^2)$. Note that the GP treats the latent function values f_i as random variables, indexed by the corresponding input X_i .

In order to make inference about f , GPR assumes a zero-mean Gaussian prior over f in function space, and the covariance given by covariance matrix $K(x, x')$ [7]. Therefore the noisy observations are

$$p(y|x_1, x_2, \dots, x_n) = N(0, K(x, x') + \sigma_n^2 I) \quad (2)$$

The entries of $K(x, x'): X \times X \rightarrow R$ are given by covariance function, which we used most commonly here is squared-exponential function(K_{SE}) with automatic relevance determination (ARD) or rational quadratic covariance function(K_{RQ}) with ARD:

$$K_{SE}(X_i, X_j) = \sigma_f^2 \exp(-\frac{1}{2}(X_i - X_j)^T M^{-2}(X_i - X_j)) \quad (3)$$

$$K_{RQ}(X_i, X_j) = \sigma_f^2 (I + \frac{1}{2\alpha}(X_i - X_j)^T M^{-2}(X_i - X_j))^{-\alpha} \quad (4)$$

where σ_f^2 is the signal variance, usually initialized to 1. The matrix $M = \text{diag}(\ell)$, where $\ell = [\ell_1, \ell_2, \ell_3]^T$ is scaling factors, Note that having a scaling factors for each input dimension allows the model to adjust the influence of the respective input variables. The hyperparameters of GPR are defined by $\theta = [\sigma_f^2, \ell, \sigma_n^2]$ which are inferred in the training process.

2.1 Predicting with Gaussian processes

This Given a unseen X_* , GPR predicts the distribution of the latent function f_* by computing the posterior distribution which is evaluated to Gaussian distribution,

$$p(f_*|y) \sim N(\hat{f}_*, \text{cov}(f_*)) \quad (5)$$

With the mean and the variance given by

$$f_* = K(X, X_*)^T [K(X, X) + \sigma_n^2 I]^{-1} y \quad (6)$$

$$\text{cov}(f_*) = K(X_*, X_*) - K(X, X_*)[K(X, X) + \sigma_n^2 I]^{-1} K(X_*, X) \quad (7)$$

The predictive output (6) can be expressed as a linear combination of N kernel functions:

$$\hat{f}_* = \sum_{i=1}^n \alpha_i K(X_i, X_*) \quad (8)$$

Where

$$\alpha = (K(X, X) + \sigma_n^2 I)^{-1} y \quad (9)$$

2.2 Training a Gaussian processes

A well GP model comprises encoding appropriate prior of application over covariance function and optimal setting of hyperparameters θ . Markov chain Monte Carlo methods can be adopted here to approximate effectively the integral. However these methods might be prohibitively expensive to use in practice. Alternatively, we consider model selection by determining an optimal setting for θ . Advantage of the probabilistic GP framework is optimization of hyperparameters θ directly inferred from the training data by minimizing negative log marginal likelihood:

$$L(\theta) = -\log p(y|X, \theta) = \frac{1}{2} y^T (K(X, X) + \sigma_n^2 I)^{-1} y + \frac{1}{2} \log |K(X, X) + \sigma_n^2 I| \quad (10)$$

The first term involving y controls the data fitting, and the second term controls the complexity of model. The optimization of (7) uses approximate conjugate gradients with the partial derivatives of (7) with respect to hyperparameters:

$$\frac{\partial L(\theta)}{\partial \theta_j} = -\frac{1}{2} \text{tr}((\alpha \alpha^T - K^{-1}) \frac{\partial K}{\partial \theta_j}) \quad (11)$$

where K denotes $K(X, X) + \sigma_n^2 I$.

3 Predication Model of Rockburst Based on GPR

3.1 Design of Combinatorial Kernel Function

The most commonly used kernel function for GPR is squared-exponential function(K_{SE}) or rational quadratic covariance function(K_{RQ}). On the basis of statistics, these traditional kernel functions are modified to form a new kernel function. Assume that $f_1(x), f_2(x), \dots, f_n(x)$ are independent Gaussian random processes,

therefore, the random processes($f(x) = \sum_{i=1}^n f_i(x)$) is also a Gaussian processes. The combinatorial kernel function is formed as follows:

$$K = K_{SE} + K_{RQ} \quad (12)$$

The Gaussian processes regression with the combinatorial kernel function by use of Eq.12 is expressed as:

$$\hat{f}_* = \sum_{i=1}^n \alpha_i K(X_i, X_*) \quad (13)$$

Where K is the combinatorial kernel function, $\alpha = (K(X, X) + \sigma_n^2 I)^{-1} y$

3.2 Main Factors of Rockburst

There are many diverse and complicated factors that induce rockburst in coal mine, so, the selected factors in regression model should be representative and independent, meantime, these factors should be accessible. According to the causes and some actual rockburst examples in coal mine, nine indexes are chosen as the

influential factors of rockburst in coal mine [10]. The influential factors and its quantitative classification are listed in table 1.

Table1. Influential factors and its quantitative classification

Influential factors	Criteria of quantitative classification
Mining depth	Recorded as the actual depth minus 200m
Thickness of coal seam	The actual thickness of coal seam
Angle of coal seam	The actual angle of coal seam
Structure	Recorded as 1,2,3,4 by simple, general, relatively complicated, complicated
Unloading	Recorded as 1,2,3,4 by good, relatively good, general, bad
Roof control	Recorded as 1,2,3,4 by reasonable, relatively reasonable , general, unreasonable
Mining speed	Recorded as 1,2,3,4 by reasonable, relatively reasonable , general, unreasonable
Coal pillar	Recorded as 0,1 by coal pillar, no coal pillar
Blasting tremor	Recorded as 1,2,3,4 by weak tremor, general tremor, relatively strong tremor, strong tremor

3.3 The Classification of predicating Result

The output vector-rockburst degree is recorded as 1, 2, 3, 4 by no rockburst, weak rockburst, moderate rockburst, strong rockburst. When the predicting results approximate sufficiently all levels of classification, it is considered that the corresponding level rockburst will happen.

3.4 Algorithm Realization

The former 20 data are used for training computation, and the last 5 are used for testing computation in table 2.

Table 2. The set of learning samples

Number	Depth /m	Thickness /m	Angle /°	Structure	Unload	Roof control	Mining speed	Coal pillar	Blasting tremor	Rock burst
1	0.5389	0.1333	0.4359	0.5	0.5	1	0.75	0	0.5	2
2	0.8428	0.4333	0.6154	0.75	0.75	0.75	1	1	0.75	3
3	1	0.5	0.7051	1	0.75	0.75	0.5	1	1	4
4	0.7252	0.6667	0.6667	1	1	1	0.5	1	1	4
5	0.5496	0.5	1	0.5	0.25	0.5	0.5	0	0.75	3
6	0.4428	0.2	0.5128	0.25	1	0.5	0.25	0	0.5	2
7	0.4366	0.2167	0.9359	1	1	0.75	0.5	1	1	4
8	0.3695	0.5	0.3205	0.25	0.25	0.25	0.25	0	0.25	1
9	0.4046	0.2	0.3846	0.5	1	0.75	0.5	1	0.75	3
10	0.455	1	0.8589	1	1	1	1	0	1	4
11	0.5496	0.35	0.5641	0.25	0.25	0.25	0.75	0	0.25	1
12	0.4428	0.2333	0.3462	0.25	0.5	0.5	0.25	0	0.5	2
13	0.3817	0.2	0.8333	1	0.75	0.75	0.75	1	1	4
14	0.1741	0.4167	0.7692	1	1	1	0.5	1	1	4
15	0.5695	0.2833	0.3077	0.25	0.25	0.5	0.5	0	0.25	1
16	0.4763	0.5	0.4487	0.75	1	0.5	0.25	1	0.75	3
17	0.4351	0.1833	0.6026	1	1	0.75	0.5	1	1	4
18	0.5847	0.2667	0.4487	0.75	0.25	0.25	0.75	1	0.5	2
19	0.5038	0.25	0.4487	0.25	0.25	0.25	0.5	0	0.25	1
20	0.1634	0.2667	0.7948	1	1	1	1	1	1	4
21	0.8137	0.46667	0.6666	0.75	0.5	0.5	0.75	0	0.75	3
22	0.3345	0.5	0.6645	1	0.75	0.75	1	1	1	4
23	0.5038	0.21667	0.3718	0.25	0.25	0.25	0.25	0	0.25	1
24	0.4274	0.23333	0.4487	0.25	1	0.5	0.75	1	0.5	2
25	0.5648	0.25	0.8333	0.5	0.5	0.75	0.75	0	0.75	3

On the Matlab platform, the GPR network model, which takes account of three kernel functions: the squared-exponential function, the rational quadratic covariance function, the combinatorial kernel function, is trained by the training data and testing data. In order to quantitatively assess the predicting precision of GPR, three functions are defined as fellows:

(1) average relative error (*are*)

$$are = \frac{1}{n} \sum_{i=1}^n |y_i^* - y_i| \times 100 / y_i \quad (14)$$

(2) mean square error (*mse*)

$$mse = \sqrt{\frac{\sum_{i=1}^n (y_i^* - y_i)^2}{n}} \quad (15)$$

(3) maximum relative error (*mre*)

$$mre = \max(|y_i^* - y_i| \times 100 / y_i) \quad (16)$$

Where y_i^* is the predicting value, y_i is the actual value.

3.5 Analysis of Predicting Result

Compared with the predicting result of ANN with RBF and SVM model in table 3, GPR with the kernel function in this paper is a relatively better regression model.

Table 3. The results of testing samples prediction

Number	Sample value	GPR			ANN		SVM	
		Kernel function			Kernel function		Kernel function	
		SE	RQ	SE + RQ	RBF		RBF	Linear
21	3	3.147	3.056	3.039	3.054		2.936	2.757
22	4	4.005	4.101	3.959	3.978		3.982	4.021
23	1	1.032	1.042	0.967	1.038		0.977	0.978
24	2	1.998	2.052	1.969	1.982		2.018	1.948
25	3	2.938	2.895	2.914	2.902		2.881	3.054

The analysis of error precision can be seen in the table 4. Either from *are*, *mse*, or *mre*, GPR with the combinatorial kernel function is better than GPR with SE or RQ and obviously improve the predicting precision and generalization capability of GPR with single kernel function, therefore, the choice of kernel function has an important influence on the predicting results of GPR.

Table 4. The error analysis

Error	GPR			ANN		SVM	
	Kernel function			Kernel function		Kernel function	
	SE	RQ	SE + RQ	RBF		RBF	Linear
<i>are</i>	2.078	2.938	2.008	2.063		1.957	3.045
<i>mse</i>	0.073	0.076	0.050	0.054		0.063	0.115
<i>mre</i>	4.900	4.200	3.300	3.800		3.967	8.1

The data in table 4 indicate that SVM and ANN with RBF also achieve a good predicting results, but the predicting results of SVM with linear function is worst. Compared with ANN with RBF, the prediction precision of GPR with the combinatorial kernel function is much better on all the aspects of *are*, *mse*, *mre*. The prediction precision of GP is slightly less 0.051 about *are* than that of SVR with RBF, but much

better on the aspects of *mse*, *mre*. What is more, from probability meaning, GPR embodies the characteristics of programming easily, prediction with probability interpretation than ANN and SVM.

The hyperparameters in table 5 reflect correlation between the nature of inputs and the nature of outputs. After sorting, two kernel functions have the basically same correlation rule that unload, blasting tremor, structure are close in relevance to rockburst, but thickness of coal seam have minor relevance to rockburst.

Table 5. The optimal hyperparameters based on the combinatorial function

	ℓ_1	ℓ_2	ℓ_3	ℓ_4	ℓ_5	ℓ_6	ℓ_7	ℓ_8	ℓ_9
SE	84.796	72.774	14.092	1.294	1.304	3.694	38.217	2.945	3.009
RQ	13.218	16.621	16.446	0.027	0.644	13.013	10.800	10.966	14.425

Note that: because the dimension of input factor is ten, the number of hyperparameter is ten

4 Conclusions

Based on the combinatorial kernel function, we have put forward a new GPR model for rockburst prediction. The predicting results show that this method can model the complicated nonlinear problem very well. The comparison between GPR with the combinatorial kernel function and the traditional method, such as ANN and SVM, demonstrates that the prediction precision of GPR is relatively better and the dispersion degree between the predicting value and actual value is smaller. By the automatic relevant determination hyperparameters, the correlation between the nature of inputs and the nature of outputs is analysed.

References

1. Zhang, G. and Zheng, Y.X. Study of the theory of rockburst and it's application. in Proceedings of the Third National Conference on Rock Dynamics. (Wuhan, 1992).
2. Tian, M. G. and Liu, T. C. Mining Pressure and Its Control. Mining Industry Press, 1992.
3. Feng, X.T. Introduction of intelligent Rock Mechanics. Science Press, 2000.
4. Yang, X.Y., Wu, F.Q. and Su, S.G. Expert system of fuzzy information for classification of surrounding rock mass in highway tunnel. Chinese Journal of Rock Mechanics and Engineering, 2005, 25(1):100-105.
5. Zhou, H.Q. and Chen, Z.H. Expert system knowledge of intelligent choice of supporting type for deep excavation in Xiamen. Chinese Journal of Rock Mechanics and Engineering, 2004, 23(5): 867-870.
6. Feng, X., Zhu, L.M. and Wang, L.Z. Modified grey system forecasting model and its application for analyzing information of landside monitory. Chinese Journal of Rock Mechanics and Engineering, 2001, 24(22): 4100-4155.
7. Rasmussen, C.E. and Williams, C.K.I. Gaussian Processes for Machine Learning. The MIT Press, 2006.
8. Quinonero-Candela, J. Learning with uncertainty-Gaussian processes and relevance vector machines. PhD thesis, Technical University of Denmark, Lyngby, Denmark, 2001.
9. Yuan, J., Wang, K. and Yu, T. Reliable multi-objective optimization of high-speed WEDM process based on Gaussian process regression. International Journal of Machine Tools and Manufacture, 1999, 48(1): 47-60.
10. Pei, L. and Yang, Z. R. Prediction of rockburst base on RBF neural network. Coal technology, 2000, 27(3): 137-139.

STUDY ON OVERLYING STRATA STRUCTURE DEFORMATION AND ROCKBURST PREDICTABILITY IN DEEP MINES

WEI-JIA GUO, JIN-XIAO LIU and XI-KUN CHANG

*Key Laboratory of Mine Disaster Prevention and Control, Shandong University of Science and Technology
Qingdao, 266510, P.R. China*

Through the observation of overlying strata structure deformation, ground movement, room test and numerical calculation analysis, it is found that large-scale separation interspace in bending strip upside crack strip is caused by un-consistency of overlying strata subsidence movement in deep mines. Different characters of movement and deformation of overlying strata and ground are made of periodic caving of separation interspace with work face mining. Conglomerate layer movement is the main mechanism of rockburst according to field observation. Rockburst changes periodically as conglomerate layer moves periodically. Practice indicates that the method for forecasting and predicting rockburst using the information of overlying strata structure deformation and ground movement observation is feasible and can be used in mines with similar geological conditions.

1 Introduction

Overlying strata movement and deformation due to underground mining are complicated physical mechanics phenomenon. It is affirmed that the structure combination and its mechanics character (parameters of deformation and intensity) are main influencing factors. That is, structure, occurrence, thickness and rigidity of overlying strata and alluvium are the main parameters expressing the movement process and displaying deformation due to underground mining [1-4].

Table 1 Representative cases of devastating rockburst

Serial number	Time	Place	Induced factor	Destroying instance	Remark
1	96.4.27	Top gate 1407	Blasting	Destroyed coal wall 50m,damaged entry 100m, production stopp 3 days, GBH 10 persons, flesh wound 1 person, shake level 2.9	Due to concentration stress of coal pillar in top level and overlying conglomerate layer movement
2	96.6.11	Top end 2407	Blasting	Destroyed coal wall 5m,shake level 1.7	Due to huge deep conglomerate layer movement
3	96.6.17	2407 work face	Blasting	Destroyed coal wall 10m,mangle 10 supports,floor heave 300mm,shake level 2.0	Due to huge deep conglomerate layer movement
4	01.11.3	Work face 3407,mini ng 83m	Blasting	13 persons flesh wound, bottom road 50m was jammed entirely from lower exit,8~35m of two sides of entry moved severely,mangle 53 supports and beyond 40 roof beams	Movement of separation in overlying conglomerate layer due to excessive mining activities for the reasons of work face 3405、3406、3407、2408 being excavated

Strata, ground movement, and deformation, which are the comprehensive response of structure stress, conceal abundant information. They can be the effective physical prediction qualities if some quantitative marks can be distinguished from the information above [5]. The generation mechanism of roof rockburst and characteristics of overlying strata separation are discussed on the basis of movement and deformation

characteristics of strata and ground due to underground mining of huge thick conglomerate layers. Premonitory information of dangerous impact is concealed before the generation of rockburst.

The tertiary conglomerate layer, which has a good integrality (integrality parameter of rock mass $k=0.89$) and large intensity (elastic modulus $E=4.92 \times 10^4 \text{ MPa}$, $f=5.9$), is 500~650m in thickness on -750m level of part of the mine. On the bottom of the conglomerate strata about at 50m is red sandy mudstone (simply named red layer) and at about 20m is mottle soft mudstone ($E=1.34 \sim 0.92 \times 10^4 \text{ MPa}$, $f=1.4$). Permo-carboniferous strata below these layers primarily includes middle white minute sandstone with a compressive strength of 50~70MPa.

The fourth coal mining seam has a strong impact tendency leads to rockburst with a quake-degree of about 2.6 and generally 570m of critical mining depth. The strata pressure is becoming bigger and bigger with increasing exploitation depth where the constitution stress is about 1.7~2.0 times the deadweight stress at the -750m level, and horizontal structure stress attained is 46.8~55MPa. Representative cases of devastating rockburst are shown in Table 1.

2 Overlying Strata Structure Deformation and Ground Movement

2.1 Separation Movement of Overlying Strata

Separation is brought by un-consistency of overlying strata subsidence movement due to underground mining. It is determined by the overlying strata lithology which has big contrast such as hard rock(conglomerate) upper and soft rock(red layer) down. weakness plane is undrew when additional stress of strata movement exceed cementation intensity of bedding joint. Rock mass was simply transformed to complex layer linear-elastic medium and separation height could be expressed as follows[6,7]:

$$\Delta v = \frac{2}{\pi} \int_0^{\infty} [v_n(\xi, 0) - v_{n-1}(\xi, h_{n-1})] \cos \xi x d\xi \quad (0 \leq x \leq b)$$

Where, Δv separation height of strata,

Separation space volume can be showed by deflection difference value between lower stratum and upper stratum in a certain mining area ,that is:

$$V = \int_a^b \int_c^d (w(x, y)_d - w(x, y)_a) dx dy$$

Where, $w(x, y)_d$ is deflection of lower stratum, $w(x, y)_a$ is deflection of upper stratum

2.1.1 Drilling Geophysical Observation of Overlying Strata Structure Deformation Movement

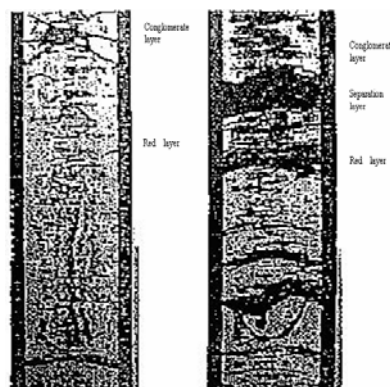


Figure 1 Photograph of bore with technology of exceeding sound

The detection of overlying strata structure deformation is done through electrical resistivity, drilling electromagnetic waves, radioactive detecting shaft and sound wave method. The electrical resistivity, the sound wave speed, and gamma curve change obviously between tertiary conglomerate layer and red layer, which shows that larger separation crack has generated. Figure 1 is the hole wall photo with the equipment hole ultrasonic wave imaging, the layered shadow between conglomerate layer and red layer is the separation crack.

2.1.2 Experiment in Room and Numerical Calculation

Simulation research in reason is offered on the basis of bore full wave measure and rock mechanics experiment which indicates that physical mechanics characters of overlying strata are basically definite, especially single lithology and good stability of interface between conglomerate rock layer and red layer.

(1) Similar material simulation showed clear caving, rupture, periodic separation and bending of roof in mining process, especially visible separation space at interface between conglomerate layer and red layer with the working face advancing. Separation growth curve observed from experiments between conglomerate layer and red layer is showed at figure 2.

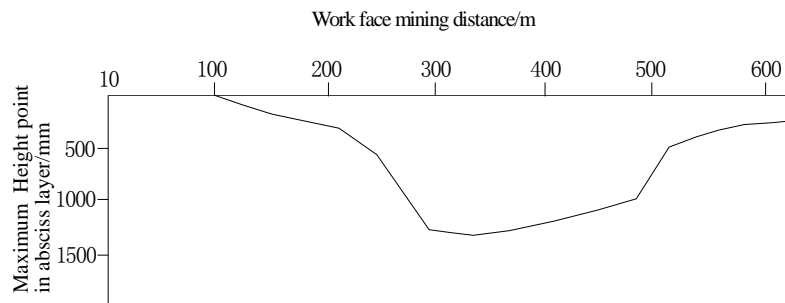


Figure 2 Growth curve of separation terrane

(2) Numerical simulation for separation movement of overlying strata is calculated by use of having manufactured three dimension semi-analytical numerical calculation method and visco-elasticity finite element. Figure 3 is the overlying strata subsidence graph in the strike, polygonal line appears in the interface between conglomerate layer and red layer where the distance between overlying strata subsidence contour line and coal seam is 120m. It shows the un-consistency of overlying strata subsidence movement. The size of separation crack can be judged. Partial results of dynamic simulation are shown in table 2.

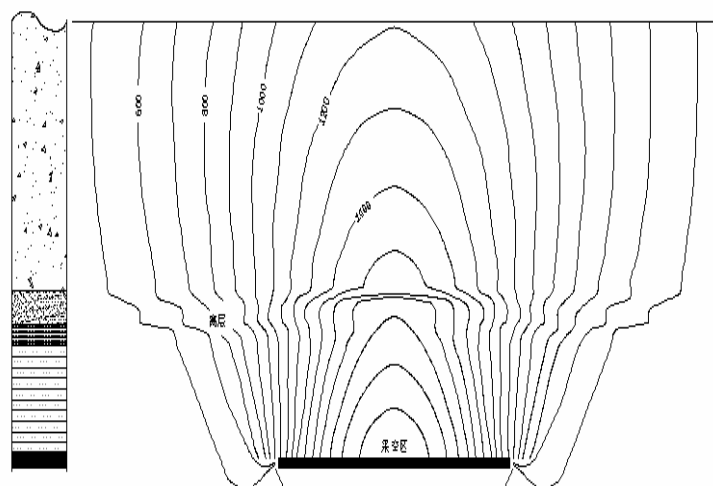


Figure 3 Overlying strata subsidence contour line graph

Tab.2 Partial dynamic simulation result

Bed	Stabilization time of conglomerate layer (d)	Stabilization time of coal-strata (d)	Maximum subsidence value of bottom interface of conglomerate layer (mm)	Maximum subsidence value of top interface of red layer (mm)	Maximum stability height of separation (mm)	Maximum dynamic height of separation (mm)	Maximum continuance time of separation (d)
1 st	420	150	1087	1610	523	1310	95
3 rd	600	210	3224	4872	1647	2910	115

2.2 Ground Movement and Deformation Characteristic

In order to evaluate movement law of strata and ground correctly, reliable warranty that plentiful observation data accumulated and ground movement parameter and subsidence character upon geological mining condition acquired are offered from 10 years continuous observation of ground movement and deformation.

(1) Obvious convergence and delayed phenomenon displayed in the course of ground movement and deformation and subsidence speed varies largely.

(2) Rebound drove up at outskirts of subsidence basin due to deep hard conglomerate layer which had good integrity and large strength.

(3) Bigger speckle and crack appeared in stretch region on the dip heading direction of ground basin.

The subsidence value in principal section is calculated and the analysis of ground movement and deformation is done under the condition of full mining according to the observing results on top of mined-out area. The biggest subsidence speed empirical formula of coal mining is as followed by analysis:

$$V_{\max} = 6.266 \times \frac{c \times m \times D \times \cos \alpha}{H_0}, (\text{mm} / \text{d})$$

Where, m-mining thickness, D-the dip length of working face, α -the dip angle of coal seam, H_0 -average mining depth, c-advance speed of working face.

Figure 4 shows that the subsidence speed of point 23 in the line of ground dip main section changed with the working face advancing and it also reflects concentration and sluggishness phenomenon of overlying strata movement.

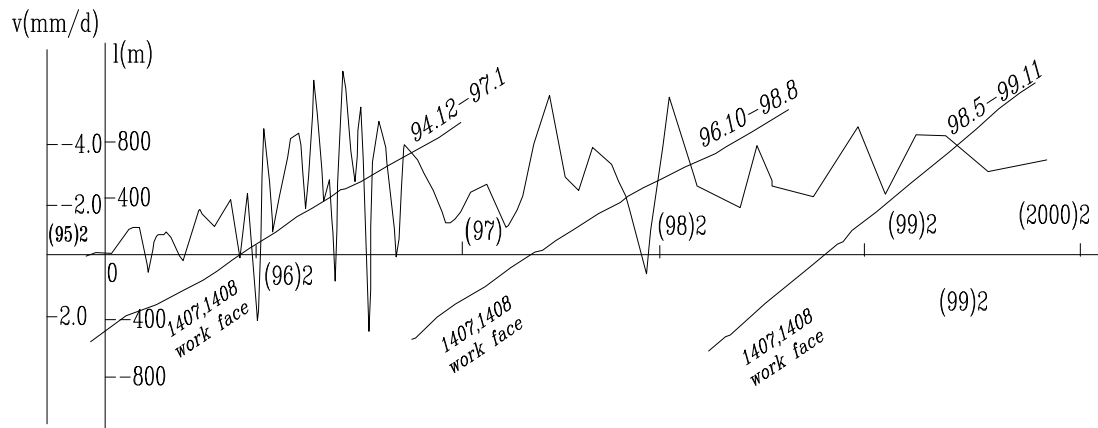


Figure 4 Curve of subsidence speed along with work face mining at point 23

3 Overlying Strata Structure Deformation and Rockburst Predictability

Ground and overlying strata structure deformation movement reflects the process that the crack of conglomerate bottom developed, grew and destabilized. Separation crack within bending strip upside crack strip generated (between thick and hard conglomerate and red layer).and its range develops continuously as work face mining (maximum growth height about 2.1m, 230m wide). Large numbers of elasticity energy garnered in conglomerate mass being induced by rock mass deadweight, which acted on the surrounding rock of mined out area, and high-pressure stress concentration strip appeared. Separation rock mass equilibrium conditions are destroyed when it develops sufficiently. And bottom Stratum of conglomerate breaks suddenly with strong rockburst when length of separation crack is bigger than utmost span.

3.1 Relations between Rockburst and Huge Thick Conglomerate Layer Structure Deformation

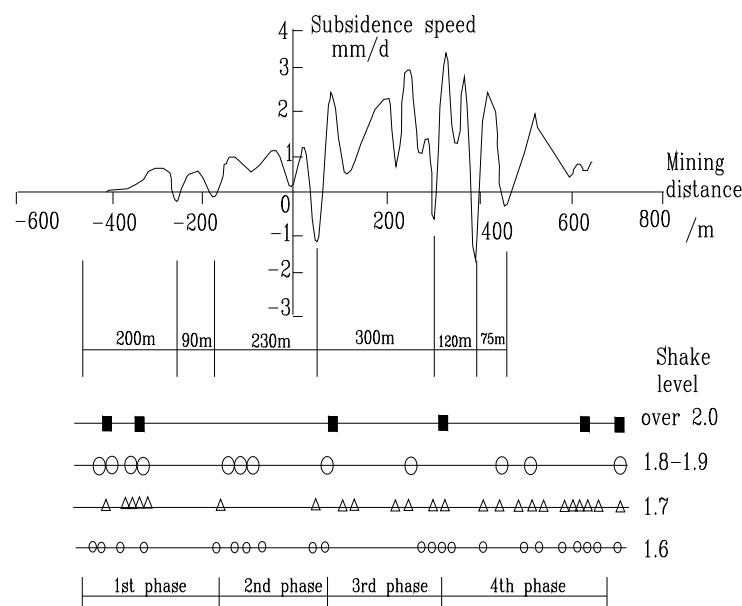


Figure 5 Relation chart among mining distance, subsidence speed and rock burst

Stage diversification characters of conglomerate movement that intensity vary from weak to strong and frequency degree changes from low to high could be reflected objectively by ground subsidence speed movement tendency, it can be seen from Figure 5.

Ground subsidence speed varies acutely and rockburst occurring frequency is higher at the same place. Sometimes it arises before or after the speed several days, commonly about 70% more feasible within 10 days. Especially rebound places of which ground subsidence goes with bigish rockburst which rebound more big goes with more big rockburst are more danger. Statistic indicates that the ratio of strong shock over 2 degree takes place about 50%.

3.2 Relation between Conglomerate Movement and RockBurst

3.2.1 Relation between Phase Characters of Conglomerate Movement and RockBurst

Data of ground subsidence observation indicated subsidence speed increased markedly about every 250m~300m distance of mining after short time strong ground rebound which prefigured its increasing movement intensity. One period of movement of conglomerate layer comprised four stages: elementary movement phase, stable movement phase, marked movement phase and acute movement phase.

The changing trend of ground subsidence speed reflects objectively conglomerate phase characters, namely the strength becomes from weak to strong and the frequency becomes from low to high.

3.2.2 Rockburst Law in Conglomerate Movement Phase

Much more rockburst converged at initial mining stage in conglomerate movement phase, stable movement phase fastened on the beginning and the end, marked movement phase took place at former and after time of ground subsidence speed curve, and acute movement phase happened more frequently due to rebound continually or chop subsidence speed. Occurring intensity and frequency for rockburst were determined by mining distance and influenced subsidence speed simultaneously. Conglomerate layer came into staggered movement about every 300m as work face mining generally. Namely the mining distance determined the strength and frequency of rockburst and it influenced the change of subsidence speed at the same.

Rockburst with biggish shake level above 2.0 almost occurred at the end of each stage besides at the origination time of elementary stage. Conglomerate layer moved quickly when the wave stage of ground subsidence speed curve appeared as work face mining distance about 60~90m at stable movement phase. The peak of ground subsidence speed curve came forth when mining 40~80m at working face at conglomerate layer marked movement stage. The subsidence speed increased obviously and the conglomerate layer activity speeded up. More changing of ground subsidence speed curve appeared when mining 50~60m at conglomerate layer acute movement phase and the more violent subsidence movement of conglomerate layer appeared. Table 3 shows the subsidence curve changing condition in every conglomerate movement stage and Table 4 shows rockburst occurring law in very conglomerate movement stage.

Tab.3 Subsidence curve changing condition in every conglomerate movement stage

Name	Number of the curve wave crest	Number of the curve trough
Elementary movement phase	2	3
Stable movement phase	3	4
Marked movement phase	4	5
Acute movement phase	5	6

Tab.4 Rockburst occurring law in very conglomerate movement stage

Name	Occurring law for rock burst
Elementary movement phase	Everage shake level 1.74 and 15 times within 100m of mining origination distance at this stage.
Stable movement phase	Everage shake level 1.69 account for 61% within 100m of mining origination distance and everage shake level 1.7 account for 39% ,15 times within 30m of mining end distance at this stage.
Marked movement phase	Everage shake level 1.7 account for 41% within 100m of mining origination distance and everage shake level 1.8 account for 59% ,12 times within 120m of of mining end distance at this stage.
Acute movement phase	Everage shake level 1.69 account for 53% of mining origination distance and everage shake level 1.69 account for 47% ,20 times within 100m of mining end distance at this stage.

3.3 Relations between Rockburst Energy Release and Work Face Mining Distance

Direct reason of periodic movement of conglomerate layer is that the interspace in middle of overlying conglomerate layer and red layer develops, grows and caves periodically with work face mining. Energy release of roof had obvious orderliness and periodicity in the process of entire work face mining. Its quantity increases gradually along with accretion of mining distance from smaller beginning number and to maximum at a certain distance and then decreased gradually.

Periodic roof energy release reflects periodicity of conglomerate layer and ground subsidence movement with work face mining. So forecasting and analysis of rockburst can be done based on instance of movement and deformation of strata and ground.

The appearance of energy release area is inevitable when working face promotes some distance in general case, it should be prevented and controlled at this area. The energy release of rockburst decreases when the working face almost is finished in eneral case.

4 Rockburst Occuring Predictability by Strata Movement Observation

A mass of rockburst were forecasted successfully and good result was obtained with the rockburst predictability index ground rebound phenomenon and subsidence speed variation in Huafeng mine since 1999 based on the recognition that overlying strata structure deformation and ground movement observation can forecast rockburst. For instance, movement rebound of ground subsidence was found on 7 December 2004, it become enhancing 1.5~2mm with original subsidence 3~5mm. Rockburst with shake level 2.4 took place on 16 December 2004, the loss was reduced to minimum because of forecasting and prediction beforehand.

5 Conclusion

It has been confirmed that the movement of the thick and hard conglomerate layer is the main source of force through microseismic monitoring, room test research, and observation of rock movement. Large scale rockburst activity appears in every violent conglomerate structure movement; therefore the appearance of rockburst has periodicity. The frequency of rockburst is high at the violent changing positions of ground subsidence speed. The rebound of ground subsidence speed changes in response and the shake level is large. The appearance of the energy release area is inevitable when the working face promotes some distance in the general case, and should be prevented and controlled at this area. The energy release of rockburst decreases when the working face almost finished.

Experience shows that it is feasible for the rockburst to be predicted with the relative information of overlying strata structure deformation and ground movement under the conditions of huge thick conglomerate layers in the Huafeng mines.

Acknowledgements

Supported by: National Natural Science Foundation of China [50874070] and Natural Science Foundation of Shandong[Y2008F01]

References

1. Zhang, Z. P., Zhang, S.Q., Guan, J., et al. Hazard Estimation between Rock Burst and Mine Micro-shake. *Journal of Chinese Earth-quake*, 1988, 4 (2).123-124.
2. Li, Y.J., Liu, L.M. Lan, C.Y,et al. Research on Forecasting Mine Shake by Using Deformation of Underground Strata in Mine. *Journal of Chinese Mining*, 2005, 14(10).66-68.
3. Guo, W.J. Liu, L.M. Guo B.Z,et al. Research on Prevention and Control Measure and Mining Hazard of

- Huge Thick Cover Rock. Journal of the Chinese Journal of Geological and Hazard Control, 1994, 5(2).37-42.
4. Guo, W.J., Shen, G.H. Yan, Q.G., et al. Research on Measures and Movement Deformation of Overlying Strata in Huafeng Colliery. Journal of Shandong Mining Institute, 1995, 14 (4).359-364.
 5. Song, W.Y, Pan, Y.S, Su, R.H,et al. Chaos Mathematics Model and Forecasting and Prediction for Rock Burst. Journal of China Coal Society, 2001, 26 (1).26-30.
 6. Guo, W.J. Liu, L.M, Shen G.H.,et al. Research of Bed-separated Feature and Method on Ensuring Position of Bed-Separated Characteristics for Overlying Strata in Mining. Journal of China Coal Society, 1995, 20 (1).39-44.
 7. Guo, W.J. Resolution Characteristics of Development for Subsidence Bed separation of Overlying Strata. Journal of China Coal Society, 2000,25.49-53.

OPTIMAL MODEL OF ROCKBURST PREDICTION BASED ON THE FUZZY NEURAL NETWORK

KAI-QING LI

*School of Civil and Environmental Engineering, University of Science and Technology Beijing
Beijing 100083, P.R. China*

FU-LIAN HE

*College of Resources & Safety Engineering, China University of Mining & Technology (Beijing)
Beijing 100083, P.R. China*

SHENG-RONG XIE, SHOU-BAO ZHANG, HONG-QIANG HAN & YONG-JUN HE

*School of Civil and Environmental Engineering, University of Science and Technology Beijing
Beijing 100083, P.R. China*

The rockburst is one of the major disasters in coal mine. Because of the shortage of traditional methods to forecast rockburst, the method based on combining the fuzzy theory with artificial neural networks using MATLAB program is applied to predict rockburst with model optimization. The fuzzy neural network is also an information processing system combining the artificial neural network with the fuzzy theory, which can learn from incomplete and inaccurate data with strong noise, and has a very strong ability of error-tolerance. Meanwhile, by using the field rockburst monitoring data of Yaoqiao Coal Mine, the rockburst fuzzy neural network model is optimized. It is seen that the method is feasible and the result is satisfactory.

1 Introduction

With the ever-increasing depths of coal mines in recent years, rock mass instabilities are proving to be a prominent safety hazard in underground coal mines. They are many type of underground rock mass instabilities. The best known among these is rockburst phenomena that can have severe consequences; such as damage to underground operations, equipment, and a long delay of the mining operation. Most of all, the occurrence of rockburst can cause injuries and even fatalities. Rockburst not only brings about accidents such as casualties, equipment destruction, roadway destruction, and collapse; but also results in other mining disasters. Such as gas explosions and coal dust explosions^[1], which threaten personal security and normal mining production. Through theory analysis and indicative engineering experience, rockburst always occurs on the roof in the coal seam.

Many factors influence the stability of coal seam roofs, the relationships of dynamic, nonlinear and interacting forces. They relate to engineering geology, mechanics of rock masses, coal mining and so on. Therefore, it is necessary to adopt a combined rockburst forecasting system for the different factors related to rockburst and it must be effective for the prediction of coal seam roof stability. It is possibly useful to apply artificial neural network for a general model building, however, it is harder to apply artificial neural network for a complicated building model. Based on the complexity that influenced factors and the fuzziness that impacted parameters, it is a feasible method to combine the artificial neural network with fuzzy logic [2-4]. In this paper,

the fuzzy neural network is implemented by using the normal fuzzy neural network (NFNN). It is against the influence of the man-induced factor, by rebuilding and optimization of the structure of the fuzzy neural network.

2 Analyse influenced on Rockburst

2.1 Geologic structure of coal mine on rockburst

2.1.1 The exploitation depth

With the depth of exploit increases, it is easier and easier that the possibility of the rockburst occurs, and elastic energy resilience in coal and rock is bigger and bigger. It is a basic condition that depth of exploit is result in rockburst. As a matter of fact, though the experience that exploitation of coal mine in home and abroad.

2.1.2 The physics mechanics property of coal and rock

For a specific coal mine, it is very important of the physics mechanics property of coal and rock seam, and it is also an intrinsic influencing factor for the occurrence of the rockburst. The factors include that the rockburst tendentiousness, the thickness, the strength, the elastic brittleness, the pitch angle of coal seam and so on.

2.2 Exploitation condition of coal mine on rockburst

As mentioned above, it has a significant effect for geologic structure of coal mine on rockburst. At the meantime, because it is different that the coal cutting method, the excavating subsequence, the size of coal wedge and so on, it is also different for the occurrence of rockburst of coal seam.

3 Principle of Fuzzy Neural Network

The fuzzy neural network (FNN) is a new branch of intelligence science and has developed rapidly since the 1980s. The FNN is a combination method between the artificial neural network and the fuzzy theory, which is also an information processing system. It includes on numerous simple processing elements connected together in response to certain rules and is able to respond dynamically to an outside stimulus and process information. Like the human brain, it can adapt itself to the outside environment and has a very strong learning ability^[5-6]. In an FNN, knowledge is not stored in some memories, but distributed in the whole system according to the fuzzy rules.

3.1 Principle of Normal Fuzzy Neural Network

In this paper, fuzzy neural network is implemented by using normal fuzzy neural network (NFNN).As the form below, a typical format of fuzzy rule base is still the sum of several fuzzy If-then rules.

Rule j : if x_1 is F_1^j , \dots , x_n is F_n^j , thus

$$y = \beta^j \quad (1)$$

Where: F_i^j and β^j are separately fuzzy sets on $U_i \subset R$ and $V \subset R$. $x = (x_1, x_2, \dots, x_n)^T \in U_1 \times \dots \times U_n$, and $y \in V$ are separately the input and the output of fuzzy logic system. The fuzzy logic system simplified represent as the output fuzzy sets of every fuzzy rule, though setting a fuzzy monodrome. So β^j is the fuzzy monodrome of the j th rule conclusion^[7].

Suppose m as the number if fuzzy If-then rule, as $j = 1, 2, \dots, m$ in the equation (1). The numeric output of fuzzy logic system, which is constitute of the centre average anti-fuzzy controller, the arithmetic product reasoning rules, and the monodrome fuzzy generator, has the form as

$$y = \frac{\sum_{j=1}^m \beta^j (\prod_{i=1}^n \mu_{F_i^j}(x_i))}{\sum_{j=1}^m \prod_{i=1}^n \mu_{F_i^j}(x_i)} \quad (2)$$

Where: $\mu_{F_i^j}$ is the membership function of fuzzy sets F_i^j , which is represented as Gaussian function.

3.2 Establishment of Fuzzy Neural Network for Rockburst

There are four layers in NFNN as shown in Fig.1. The first layer is input layer, which is membership function of the Gaussian function. The second layer is normalization layer, which normalises the input layer. The third layer is regulation layer, which connects first the component (normalization nod) with the conclusion (output nod), by some fuzzy logic rules. The fourth layer is output layer. All regulation nodes all connect with the output nod by the conclusion connection line [8-10].

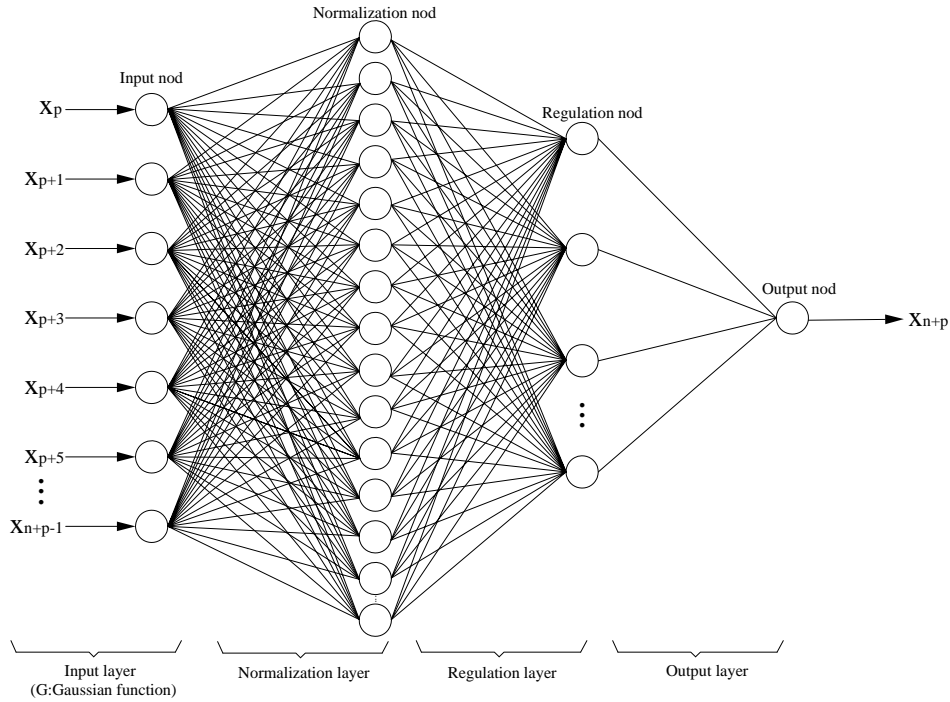


Figure 1 Structure of NFNN

Suppose a measured series $\{x_i\} = (x_1, x_2, \dots, x_n)$ on rockburst influencing factors. Modelling the rockburst influencing factors series is to establish relationship between the influencing factors and the rockburst strength.

According to the cross-country field data, combining the field data of Yaoqiao Coal Mine, It was accepted with NFNN in this paper. The number of the input layer nodes is 7, and the number of the output layer nodes is 4. The training sample data set as shown in Table 1 is used to train the normal neural network. For the requirement

of NFNN, it is necessary to quantify the qualitative description in the training sample data. The quantified method is shown as shown in Table 1.

Table 1. Training Samples

Code number	Depth	Coal seam thickness	Coal seam inclination	Roof characters		Exploitation method		Coal wedge		Earth-sound
				Mudstone	sand rock	long	short	yes	no	
1	-540	2.6	8	0	1	1	0	1	0	10.03
2	-545	4.3	6	0	1	1	0	1	0	10.12
3	-550	2.8	12	0	1	1	0	0	1	11.35
4	-560	3.5	9	0	1	1	0	1	0	11.59
5	-570	4.5	14	0	1	1	0	0	1	11.61
...

4 Simulation Analysis

The rockburst fuzzy neural network model is used for the # 7249 coal mining face of Yaoqiao Coal Mine. Using MATLAB 7.0, the model was designed, which was the modularization structure. The relation and function of these modules were shown as in Fig.2.

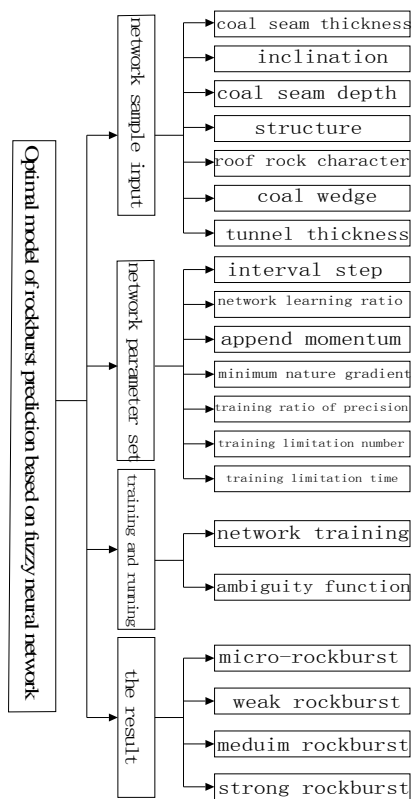
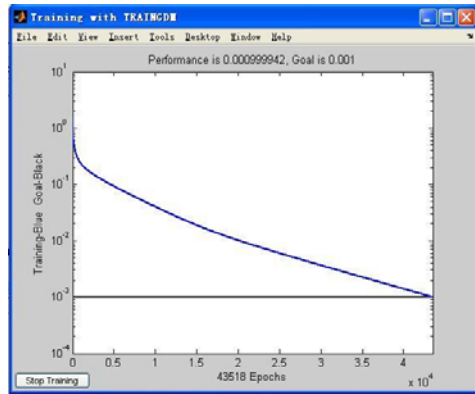
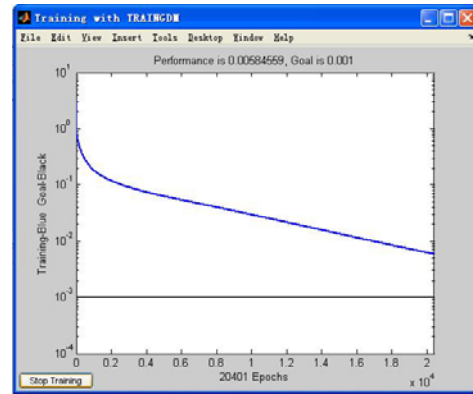


Figure 2 Modularization Structure of NFNN



(a)



(b)

Figure 3 Progress chart of NFNN

In the simulation progress, the number of input layer nodes is 7, which corresponding to the influencing factors on rockburst. In the training progress, the progress chart of NFNN was shown as in Fig.3 (a), (b). In command windows of MATLAB, the data variation in NFNN training progress can be shown, which include the current step number, the performance gradient, and the sum of square. As we can as shown in Fig.3, after 43518 times training, the error square sum of the practical output data and the expectancy output data is $0.000999942 < 0.2$. It is indicated that the network has been optical.

5 Conclusions

Based on the special performance of the rockburst origin, the normal fuzzy neural network (NFNN) model is put forth and can be used for predicting rockburst. This model integrates the artificial neural network with the fuzzy theory, and the multi-information couple can be solved. Meanwhile, the high-performance information extraction may be obtained. The practice application indicates that the prediction result and the practice result are a coincidence, which is an effect method for the prediction of rockburst. Through the simulation analysis, it proved that NFNN applied for the prediction of rockburst is true. However, in the rockburst history record of the Yaoqiao Coal Mine, the qualitative description is more than the quantitative description, which results in the limitation of fuzzy neural network. Therefore, to increase the prediction accuracy, more research on the influencing factors and samples on rockburst needs to be done.

Acknowledgements

Work is supported by the Scientific Research Foundation for the Returned Overseas Chinese Scholars under grant No. 2007-1108, and the Teaching and Research Award Fund for Outstanding Young Teachers in Higher Education Institutions of State Education Ministry, People's Republic of China. The authors sincerely wish to thank the technicians of Yaoqiao coal mine for their contributions to the practice work in this paper.

References

1. Qian, M.G., and Shi, P.W. Mine Pressure and Control. China Coal Industrial Press, 2003.
2. Dou, L.M., and He, X.Q. Theory and Technology of Rock Burst Prevention. China University of Mining & Technology Press, 2001.
3. Berkam, R.C., and Trubatch, S.L. Fuzzy systems Design. IEEE Neural Networks Council, 1997.

4. Alekasander, L., and Morton, H. An introduction to neural computing. Chapman & Hall, 1990.
5. AKsoy, H., and Eranglu, M. Rockfall source rule-based fuzzy system. Hazards Earth Syst Sci, 2006, (6). 941-954.
6. Gao, W., and Feng, X.T. Non-linear dynamic modelling of rockburst based on evolutionary neural network. Rock and Soil mechanics, 2003, 24 (S), 48-53.
7. Li, W.X. Fuzzy models of analysis for rock mass displacements due to underground mining in mountain areas. Math Pract Theory, 2003, 33 (2), 26-30.
8. Li, X.C., Sun, Y., and Tao, X.Y. Application of neural network in evaluating sustainable development for mining areas. China Univ Min Tech, 2001, 30 (4), 392-395.
9. Hemminger, A.L., Yoh-Han, P. Detection and classification of underwater acoustic transients using NN. IEEE Trans NN, 1994, 5 (5), 712-718.
10. Guo, Y.S., Meng, Z.P., Yang, R.Z., et al. Seismic attributions analysis and its application in predicting thickness of coal. China Univ Min Tech, 2004, 33 (5), 557-562

HAZARD SEISMIC NUCLEATION AND PREDICTION OF ROCK BURST AT DONGGAUSHAN COPPER MINE

LI-ZHONG TANG and CHANG-LIANG PAN

*School of Resources and Safety Engineering, Central South University
Changsha, 410083, P. R. China*

LING-HUI WANG

*Dongguashan Copper Mine, Tongling Nonferrous Metals Group Holdings Co.,Ltd.
Tonglin, 244031, P. R. China*

FENG DAI

*Department of Civil Engineering, University of Toronto
Toronto, M4Y 1R5, Canada*

Studies of the rock burst prediction are carried out on the basis of the data from Dongguashan Copper Mine, the deepest metal mine in China. The seismic responses to mining at this mine are investigated through the analyses of spatial-time distribution of hypocenters, apparent stress, and displacement of seismic events. Based on the results and the theory of asperity in seismic source mechanism, a conceptual model of assessment of hazard seismic nucleation is proposed. A mine seismic stiffness method for rockburst prediction is discussed in the framework of the unstable failure theories. In addition, after the analyses of rock failure cases at Dongguashan Mine, the rate of change in the ratio of stiffness of rock in nucleation area to its surrounding area is defined as a criterion for rockburst prediction.

1 Introduction

Dongguashan Mine, near the Tongling City in Anhui province, China, is a large deep-level hard rock copper mine, having started production in the fourth quarter of 2005. For safe and sustainable production, a rockburst monitoring system was built before production. Currently, the main objective is to identify areas with potential rockburst hazards and make medium-term prediction of rockbursts during mining activities, and as a result, to be used as the base of the rockburst control.

The rockburst event has a nucleation phase. It is thus important for rockburst prediction to investigate the variation of seismicity in time and space. It has been demonstrated that there is good correlation between the heterogeneity of seismicity and the properties of rock mass. This heterogeneity of seismicity bears important information for rockburst nucleation for mining engineering structure under the mining condition [1, 2, 3, 4]. Many attempts have been made to quantify the mechanisms of rockbursts using seismic parameters and rock mechanics methods. Some seismological based theories and methods for rockburst prediction have been proposed. Among these methods, mine stiffness theory that was studied preliminarily using data from some mines in South Africa, is attractive and thus will be used here [5-7].

This paper will discuss the model of seismic nucleation based on theories of seismic heterogeneity. Using the in-situ micro-seismic data from Dongguashan Mine, the rockburst prediction is made using the criterion based on the mine stiffness theory.

2 Geologic and Mining Conditions

Dongguashan copper deposit is at 1000m beneath the surface and it is controlled by an anticline. The strike of the deposit is NE350°-400° and the dip along the strike is about 10° northeast. The two wings of the ore-body dip northwest and southeast respectively. The average dip angle is about 20°. Its horizontal projection length is 1820 m and its horizontal projection width varies from 204 m to 882m. The average thickness of the ore-body is about 40 m. The ore body is mainly composed of cupriferous skarn, with direct roof rock mainly marble and siltstone and quartz diorite floor. There are few large faults and dense joints in the ore body. The maximum in-situ stress is 30~35 MPa, approximately parallel to the strike direction of the ore body; the minimum in-situ stress is 9~16 MPa, approximately vertical. The ore and its major surrounding rocks are very hard and thus are prone to rockburst during mining operation[8, 9].

The ore body is divided into panels along its strike, with the length of each panel being equal to the horizontal width of ore-body and width being 100 m. Panel barrier pillars of 18m in width are kept temporarily between the two neighboring panels. The stopes are arranged along the long axis of panels. Each stope is of 78 m or 82 m in length and 18 m in width. The stope is mined and backfilled with cemented tailings afterwards, this is followed by the excavation and backfill of the pillars.

3 Seismic Monitoring System

The Dongguashan rockburst monitoring system is composed of a seismic monitoring system and a conventional stress and deformation monitoring system. The seismic monitoring system is ISS system by Integrated Seismic System International(South Africa). The system was tuned and optimized for the geologic and mining conditions of Dongguashan Mine[10]. It has 24 channels and 16 sensors. All signals are transmitted by copper twist cables to the monitoring control centre underground, and then transmitted by an optical cable to the monitoring center on the ground surface as well as the safety and production management offices of the mine. Currently, the area of monitoring is the first stage mining area that has four panels, which include area between the #52 exploration line and the #60 exploration line and the surrounding rock mass. The monitoring area will be extended the entire mine.

4 Seismic Response to Mining

4.1 Spatial-time Distribution of Hypocenters

In spatial volume and time period, seismic events are plotted in 3D with coordinates of hypocenters of events (Figure 1). The change of the spatial aggregations can be analyzed by comparing the spatial distribution of events during different time periods. For example, it can be seen in Figure 1 that there are nine areas of aggregated events in the first stage mining area. The area 1, 2, 3, 4 and 8 are induced by the driving of draw shafts, the area 5, 6 by development of drifts, and the area 7 by the extracting of a stope. However, the mechanism in area 9 is believed to be the slip of one pre-existing fault, activated by blasting. Analyzing the data from the first stage of mining area from September 1, 2005 to August 30, 2008 reveals that the events induced by driving of draw shafts and development of drifts are located near these mining sites, and they are sensitive to these activities. On the other hand, the extracting of a stope can induce seismicity in larger area.

4.2 Apparent Stress and Displacement of Seismic Events

A series of nephograms of displacement, u , and contour maps of apparent stress logarithm, $\log(\sigma_A)$, at different levels in the different time periods were plotted for Dongguashan Mine. Figure 2 shows the apparent stress contour and displacement nephogram of -760m level, during the same time period as in Figure 1. Areas of stress concentration and deformation are clearly showed in Figure 2.

It is seen that some concentration of stress and deformation are not located at the aggregation areas of events. For example, development of single drift usually does not cause obvious stress concentration and deformation, despite of the aggregations of events occurring in these areas. Also important are cases where the stress is not positively related to the deformation. It is manifest from the discordance between area of seismic apparent stress concentration and of deformation. Because seismic apparent stress and displacement are independently calculated in seismology [4], relative rate of change between the seismic apparent stress and deformation at the same space reflects the mechanical property of rock mass.

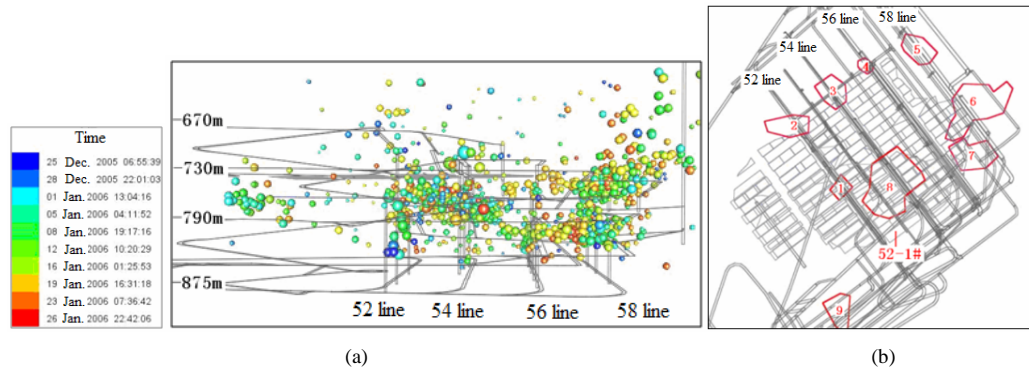


Figure 1 (a) Scenograph of seismic events and (b) delineation of horizontal projection of areas of aggregated events in the first stage mining area (2005-12~2006-1)

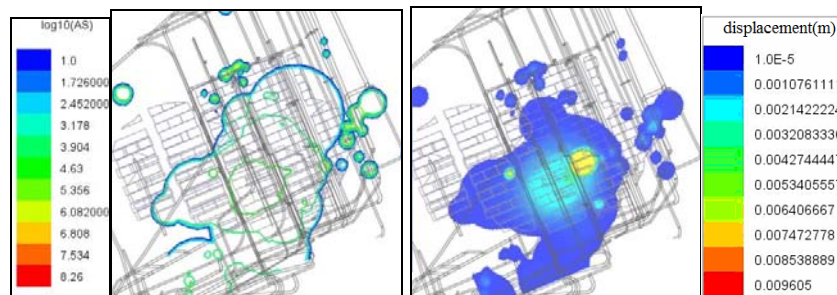


Figure 2 Apparent stress contour map and displacement nephogram on -760m level (2005-12~2006-1)

4.3 Conceptual Model and the Criterion of Hazard Seismic Nucleation

Because there are no obvious large scale geological discontinuity in this mine, the dominant factor that controls the heterogeneity of rock mass is the mining engineering structure and mining activities. Panel barrier pillars and temporary pillars are formed between hanging wall and foot wall with mining. These pillars restrain relative deformation of the walls, which can be roughly considered as compression-shear. In the framework of the theory of asperity in seismic source mechanism [1, 11], these pillars can be considered as asperities where

seismic nucleation may occur. Therefore, we can develop a conceptual model of seismic nucleation at Dongguashan Mine, as shown in Figure 3, in which the areas enclosed by red dashed curve are considered approximately the potential areas of the seismic nucleation.

It is seen in Figure 4, in which rectangles are stopes designed, that concentration of stress and deformation are located in panel barrier pillars and their surrounding rock. These areas worked as asperities on faults. This fact demonstrates that the conceptual asperity model can be used for analyzing areas of hazard seismic nucleation. However, due to interaction between mining activities, aggregation of events and distribution of stress and deformation are very complicated to be included in the conceptual model.

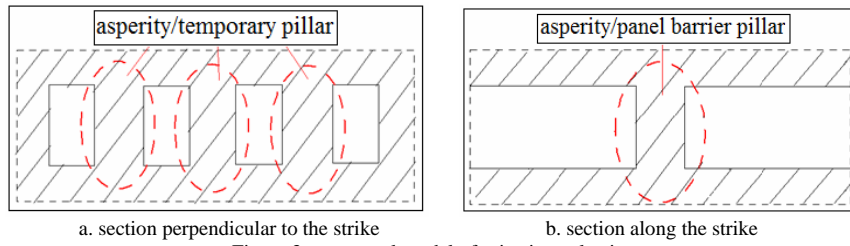


Figure 3 conceptual model of seismic nucleation

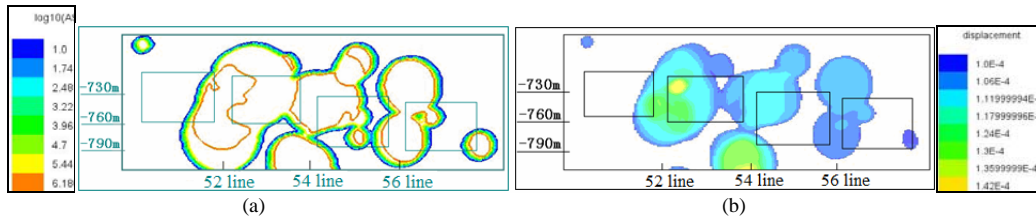


Figure 4 (a) The apparent stress and (b) the displacement on the section of initial mining area along strike of 52-6# stope (Jun.1~Jul. 30, 2006)

5 Mine Seismic Stiffness Method of Rockburst Prediction

5.1 Measure of Parameters of Unstable Failure

According to the mine stiffness theory, the rock burst may occurs if the stiffness of rocks in the seismic nucleation area is larger than that of rock mass outside the nucleation area. Because there are many events in a nucleation area, ΔV , during some time period, Δt , we can take advantage of a fitting method to determine the average stiffness of this area in a given time period. The scatter diagram of $\log E$ and $\log M$ of events can be drawn and a relation of E-M is given below in Equation (1) from fitting [6]:

$$\log E = c + d \log M \quad (1)$$

Where c and d are fitting constant, with given ΔV and Δt . The slope, d , shows the stiffness of nucleation area. d increases with the increase of stiffness [6].

The surrounding rock mass outside the nucleation area should be considered as mine loading system, whose stiffness is named mine stiffness. In the seismic prediction, b value in the G-R relation has been studied extensively. The G-R relation is:

$$\log N(\geq m) = a - bm \quad (2)$$

It has been demonstrated that b value is affected by the stiffness of loading system. The b value decreases with the decrease of mine stiffness [12, 13].

5.2 Criterion of Rockburst Prediction

We analyzed the properties of b and d parameters using the data recorded at Gongguashan Mine to predict rockburst using seismic stiffness. A typical case is shown in this paper. From Sept. to Oct. 2006, a few rock failures occurred in surrounding rocks of drifts under the panel barrier pillar along #54 exploratory line. Figure 5 is the distribution of the stress and displacement on the vertical section along midline of this panel barrier pillar. The area where rock failure occurs is recognized as the seismic nucleation area, where the concentration of stress and deformation is identified. Some rocks outside the nucleation area are selected as the load system rock. For nucleation area, we plot the scatter diagram of $\log E$ and $\log M$ to determine c and d ; for load system rock, we plot the frequency of events vs magnitude of events to determine a and b . The time period for analysis is from April, 2006 to April, 2007. Every two months is used as the time interval for analysis and the parameters b and d are determined for every time interval, and shown in Figure 6.

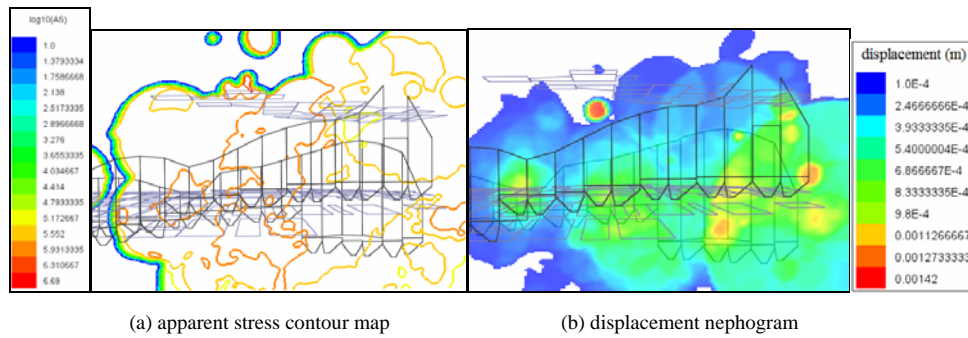


Figure 5 Stress and displacement in panel barrier pillar along 54 exploratory line

Theoretically, we can make rock burst prediction by comparing relative change between d and b (Figure 6). However, it is difficult to identify sizable changes from this Figure. Furthermore, we cannot get the absolute values of stiffness. To solve this problem, we proposed the change of the ratio of d in nucleation area to b in loading system to measure the change of the relative stiffness of both areas, and further to determine the possibility of rock burst. The ratio of d to b is defined as S below:

$$S = d / b \quad (3)$$

The curve of S with time period is shown in figure 7. The change of S reflects the relative change of the stiffness of nucleation area to that of load system area. Therefore, we defined the dS/dt as a rock burst prediction criterion in mine, i.e. increase of possibility of rock burst if $dS/dt > 0$, decrease of possibility of rock burst if $dS/dt < 0$.

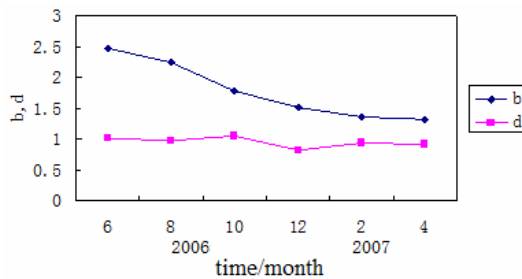


Figure 6 The b in loading system area and d in nucleation area

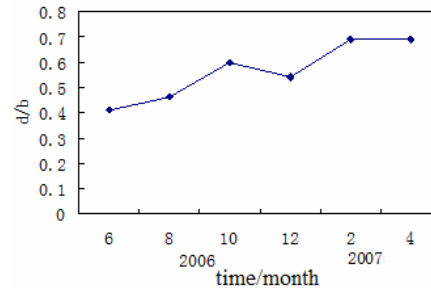


Figure 7 The ratio of the stiffness of load system area to that of nucleation area

6 Conclusion

1. By the analysis of spatial-time distribution of hypocenters, apparent stress, and displacement of seismic events, the characteristics of space-time-intensity of mining-induced seismicity and the seismic response to mining are studied with the data of seismicity in Dongguashan Mine. The relationships between seismicity and size and property of excavation are discussed. A conceptual model of hazard seismic nucleation are proposed for Dongguashan Mine according to the conditions of this mine, which provides a method for the locating areas of hazardous seismicity and rockburst in the mine.

2. A mine seismic stiffness method of rockburst prediction is proposed on the basis of mine stiffness theory and the analysis of rock failure cases in Dongguashan Mine. The variable rate of ratio of stiffness of rock mass in nucleation area to its surrounding rock's is used as a criterion of rockburst prediction.

3. The studies in this paper are preliminary research. With accumulation of data recorded and extension of scale of mining in the mine, further investigation on these results will be developed through analyses of more cases of rock bursts and rock failures in this mine.

Reference

1. Aki, K. Asperities, barriers, characteristic earthquakes and strong motion prediction. *J. Geophys. Res.*, 1984, 89, 5867-5872.
2. Tang, C., Fu Y. and Zhao, W. Numerical Simulation Of growth of Seismic source simulation. *Journal of earthquake*, 1997, 19 (4). 377-346.
3. Lei, X., Masuda K. Nishizawa, O. et al. Detailed Analysis of Acoustic Emission Activity during Catastrophic Fracture of Faults in Rock. *Journal of structural geology*, 2004, (26). 247-258.
4. Mendecki, A.J. *Seismic Monitoring in Mines*. London. Chapman & Hall, 1997.
5. Cook, N.G. W., Hoek E. Pretorius J P G, et al. *Rock Mechanics Applied to Rockbursts*. J. S. Afr. Inst. Min. Metall., 1966, 66, 436-528.
6. Amidzic D. Energy-moment Relation and Its Application. In: *Controlling Seismic Risk - Proceedings of Sixth International Symposium on Rockburst and Seismicity in Mines*, (Nedlands. Australian, 2005).
7. van Aswegen, G. Routine seismic hazard assessment in some South African mines. In: *Controlling seismic risk - Proceedings of sixth international symposium on rockburst and seismicity in mines* (Edited by Potvin Y, Hudyma M). Nedlands. Australian Centre for Geomechanics, 2005.435-444.
8. Tang . L., Pan. C. and Xie, X. Analysis and prediction of rock burst dangerous areas in Dongguashan Copper Mine under deep well mining. *J. CENT. SOUTH UNIV. TECHNOL.*, 33(4),2002.335-338
9. Tang, L., Pan, C. and Xie ,X. Study on rockburst control in deep seated hard ore deposit, *Chinese Journal ofRock Mechanics and Engineering*, 22(7), 2003,1067-1071
10. Tang Lizhong, Yang C.X., and Pan Changliang. Optimization of stations of seismic monitoring at a large deep mine. *Chinese Journal ofRock Mechanics and Engineering*, 25(10), 2006.2036-2042.
11. Kanamori, H. and Stewart, G. S. Seismological aspects of the Guatemala earthquake of February 4, 1976. *J. Geophys. Res.* 1978(83). 3427-3434.
12. Funk, C., van Aswegen, G. and Brown, B. Visualisation of seismicity. In: *Proceedings of the 4th international symposium on rockbursts and seismicity in mines* (Edited by Gibowicz S J). Rotterdam. A. A. Balkema, 1997.81-87.
13. Brink, A.V.Z. Application of a microseismic system at Western Deep Levels. In: *Proceedings of second international symposium on rockburst and seismicity in mines* (Edited by Fairhurst C). Rotterdam. A. A. Balkema, 1990.355-361.

WEIGHT FACTOR ANALYSIS AND RISK PREDICTION FOR THE MINING-INDUCED SEISMICITY USING NEURAL NETWORK

ZI-QING YUAN

*Beijing General Research Institute of Mining & Metallurgy
Beijing, 100044, P.R. China*

XIAO-CONG YANG

*Beijing General Research Institute of Mining & Metallurgy
Beijing, 100044, P.R. China*

XUE-SONG CHEN

*China Minmetals Non-Ferrous Metals Co.Ltd.
Beijing, 100044, P.R. China*

Based on monitored seismic data of Dong Guashan copper mine, with the geologic factors, exploiting factors and local natural earthquake considered, this paper applies a trained neural network to analyse the seismic factors weight and estimate the probable accumulative seismic energy released in next month, at last, predicts the risk of large seismic events in this month. The conclusion shows: For Dong Guashan copper mine, the seismic risk has a strong correlation with the blasting, prone of rock-burst, released energy of pre-month and the local natural earthquake, the factors weight are 27%, 17%, 24% and 11%, respectively. And it also has a weak correlation with the depth of mining, geologic factors and empty stope structure. There is a relativity of 78% between the predicted and the monitored energy.

1 Mining and Geology Situation of Dong Guashan Copper Mine

1.1 Mining Situation

Dong Guashan copper mine is one of the primary sources of copper in china and primarily uses the open stopping backfill methods. The depth of extraction has reached to about 1000 meters. This mine, from the starting of excavation has shown occurrences of the phenomenon of rock-burst [1]. Currently, 10 thousands tones of material are mined per day and more than 3 million tones per year are being mined using largely open stope backfill methods and remnant mining near unconsolidated backfill.

1.2 Geology Situation

This mine is controlled by layers. The major ore-body comparatively look like a saddle, with a thicknesses of 30 to 50 meters being small compared to their dip and strike dimensions. The ore-body contains pyrites, magnetite, serpentinite and so on. The angles of strike and dip are respectively 35 and 30 to 35 degrees. The faults of mines are very simple, and there are little joints. The rock mass of mine is very hard and stable. But the rocks have serious prone of rock-burst. The sequence of rock-burst prone is: diorite>siltstone>quartz sandstone>pomegranate silicon>silicon>marble.

2 Seismic Analysis

2.1 Introduction for SeismicSystem

In 2005, a 24-channel micro-seismic monitoring system is installed in Dong Guashan copper mine. The hardware contains geophones, QS (Quake Seismometer), seismic controllers, computers, cables and so on. Each QS has 3 uni-axial and 1 tri-axial geophones that were installed in the hanging-wall and footwall of the mine (Figure 1). The software contains RTS (run time system), JMTS, JDI. The depth of installation is from -670 to -875 meters, and the location error is about 10 meters. From installation of micro-seismic system, more than 10 thousands seismic events have been recorded in mine and vary in local magnitude from -2.6 to +1.8 (approximately).

2.2 Seismic Sources in Mine

Spatial cluster analysis of the Dong Guashan copper mine micro-seismic data show 7 concentrated seismic source regions (Figure 2), witch almost happened in the districts of mining, crossways and weak rocks. It's especially affected by mining. By initiatively analyzing, the occurrence of seismic activity is generally believed that the seismic activity can be related to the depth of mining, blasting, empty stope structure, prone of rock-burst and ratio of rock layers intensity etc.

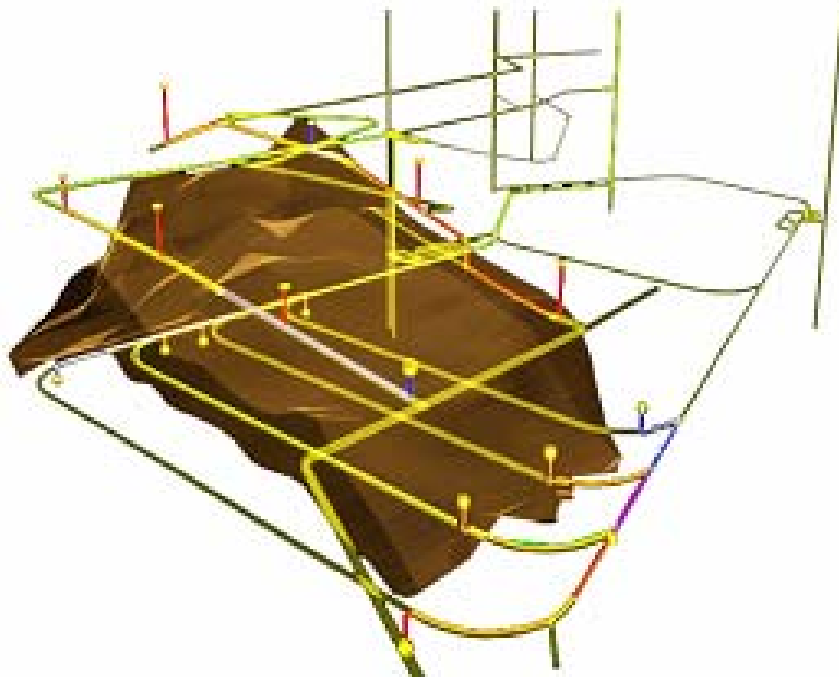


Figure 1. Geophones locations of micro-seismic monitoring system at Dong Guashan copper mine

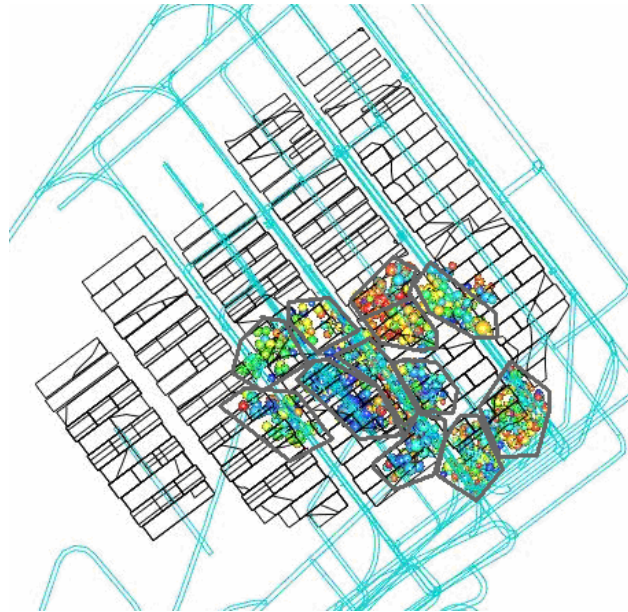


Figure 2. Concentrated seismic source regions at Dong Guanshan mine. There are 7 concentrated seismic source regions which almost happened in the districts of mining, crossways and weak rocks. It's especially affected by mining.

2.3 Seismic Factor Weight and Risk Prediction

Though, mining is one of the most important factor for seismic activity, there are also many other important influential factors. Naturally, each factor weight vary from different conditions. So, it's very useful to know each factor weight for controlling the seismic hazard of a mine.

In risk assessment and prediction, a reliable methodology or system is desirable to estimate seismic risk. Ideally seismic risk assessment and prediction is done in the mine planning stage, prior to the start of mining, so that when a new stope or mining block is being designed, the seismic risk associated with extracting that block is estimated. This would help to assess the seismic risk to worker safety [2].

For seismic risk prediction, many authors choose the magnitude, seismic energy or other parameters as a assess standard, and get some useful conclusions [3, 4]. However, the almost chose seismic energy as a assess parameter, because witch is mostly related and obvious to the seismic risk. About the storage and release of seismic energy, there are not clear and unambiguous relationships between these factors and seismic risk. As mentioned above, seismic risk is generally dependent on the depth of mining, blasting, empty stope volume, prone of rock-burst, ratio of rock layers intensity and local natural earthquake. It's not easy to exactly forecast the seismic risk using usual methods. The use of neural networks has been proved as a means of predicting approximate seismic risk and weighting all of these complex seismic factors.

3 Neural Networks

3.1 Choice of the BP Network's Structure

The BP (back-propagation) network is most usually used by people. It's a network with error back-propagation, and also are a very useful tool for problems such as pattern recognition, function approximation and data classification. According some articles [5], BP network of three layers can almost accomplish a mapped of N to

M. So author chooses a three-layer's BP network (Figure 3) composed of input layer, hidden layer and output layer, and synchronously confirmed 15 hidden layer's nodes by optimizing configuration (Figure 4).

3.2 Data Grouping

In this problem, the input data for the BP network were derived from the mine micro-seismic records and the history of stope extraction. For easily analysis and extraction situation, author arbitrarily decides that the data would be grouped in consecutive one-month periods, starting from Nov 01, 2005, to Dec 31, 2006 (Table 1).

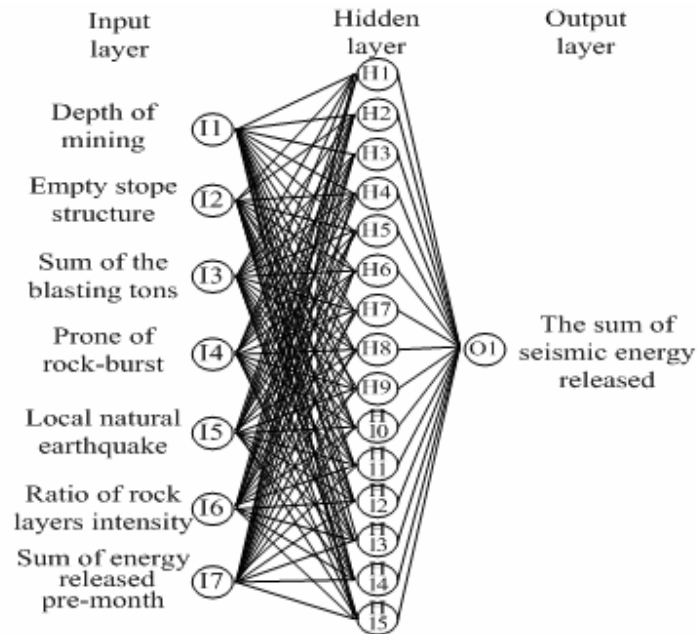


Figure 3. The optimal neural network topology for estimating seismic risk

3.3 Input Data for the Network

The input data must represent the factors of mainly inducing seismic events. For seismic events of this mine, the induced factors, according the analysis, are consisting of geological, mining, natural earthquake and seismic history parameters related to each of the 7 seismic concentrated source regions over 14 consecutive one-month time periods.

Each of the seismic concentrated sources is described by factors following:

- ◆ *The depth of mining pre month, which is directly related to the depth of seismic source below surface, and is one of the most important factor for seismic activity.*
- ◆ *The empty stope structure per month, which is related to the stress level distribution and change of rock mass due to mining, and is represented by empty stope volume.*
- ◆ *The sum of the blasting tons every month, which is also directly related to the seismic intensity, and is other most important factor for seismic activity.*
- ◆ *The prone of rock-burst, which is seriously related to the seismic activity of rock mass, and is represented by index of elastic deformation energy.*

- ◆ The local natural earthquake, which is monitored by local mine's seismic station net, and is represented by the sum of all event's magnitude ($M_L > 1$) in this article.
- ◆ Ratio of rock layers intensity, which shows the ratio of two different touched rock layers intensity, and is represented by uni-axial compressive intensity, and
- ◆ The sum of energy released previous month— \log_{10} (accumulative energy), considering the continuity of happened seismic events in time

The Table 1 shows the unitary input data for every seismic factor.

Table1. The unitary input data table for neural network

Factors No	Depth of mining	Empty stope structure	Blasting tons	Prone of rock-burst	Natural earthquake	Ratio of rock layers intensity	Energy released pre-month
1	0.93726	0.24214	0.22907	1.0000	0.5873	0.241	0.71349
2	0.95134	0.27971	0.23572	1.0000	0.5555	0.241	0.72462
3	0.96159	0.29540	0.21483	1.0000	0.5396	0.241	0.82893
4	0.97695	0.29710	0.13265	1.0000	0.6031	0.241	1.00000
5	0.96543	0.62401	0.49132	1.0000	0.5396	0.241	0.86092
6	0.97311	0.42927	0.30123	1.0000	0.5714	0.241	0.76773
7	0.98848	0.58784	0.42278	0.6784	0.8412	0.241	0.79277
8	0.97183	0.56381	0.43517	1.0000	0.5396	0.241	0.99305
9	0.96415	0.78191	0.66904	1.0000	0.5079	0.241	0.76634
10	1.00000	0.81859	0.75765	0.6816	0.5873	0.241	0.76912
11	0.99872	0.75372	0.68533	0.6816	0.6190	0.241	0.81919
12	0.99104	0.73817	0.62849	0.6816	1.0000	0.241	0.76495
13	0.97567	0.76676	0.68873	1.0000	0.6825	0.241	0.87204
14	0.98848	1.00000	1.00000	0.6816	0.6031	0.241	0.74409

3.4 Output Data for the Network

The output data of the neural network is the accumulative seismic energy— \log_{10} (accumulative energy) (Table 3) , which in this network is defined as the sum of released energy for all of the recorded seismic events in a month period. The sum of seismic energy released is chosen to present seismic risk as it is related to the largest event that this month will happen. Besides, the output data contain the weight coefficient between every neural node, for example, weight between the input and hidden layer nodes, and also between the hidden and output layer nodes (Table 2) . Furthermore, the output data also contain testing error curve and training error curve (Figure 5, Figure 6).

4 Conclusions

In this article, 7 seismic factor's clusters in 14 different time periods result in 98 data exemplars, previous half of which are trained, and back tested. It's found that a hidden layer with 15 nodes is an optimal configuration (Figure 4). The trained neural network reaches the goal in 264 epochs (Figure 5).

The neural network just gets the weight coefficient between every neural node, but can't get the weight of input factor to output factor, i.e. the seismic factor weight. Given this reason, author has to deal with the weight coefficient between every neural node by numerically computing [6, 7], and at last got the seismic factor weight table (Table4), in which shows that the seismic risk has a strong correlation with the blasting, prone of rock-burst, released energy of pre-month and the local natural earthquake, the factor's weights are respectively 27%, 17%, 24%, 11%, and also has a weak correlation with the depth of mining, geologic factors and empty stope structure.

Table2. The weight coefficient table between every neural node

Hidden nodes	Input nodes							Output nodes
	1	2	3	4	5	6	7	
1	-2.59	1.76	-0.13	2.06	-0.25	-1.17	1.24	-0.37
2	0.46	2.77	0.79	-0.56	0.9	-0.83	2.47	-0.56
3	-0.9	0.78	-1.48	2.05	-1.93	-0.94	2.14	-0.1
4	2.14	-1.7	1.98	-1.98	-1.13	-0.59	-0.15	-0.35
5	-0.84	-1.17	2.47	2.03	0.57	0.04	2.15	-0.83
6	1.37	0.97	0.8	2.2	-2.42	1.72	-0.45	0.36
7	-2.54	0.11	-2.62	-0.32	0.65	-1.14	1.5	0.41
8	-0.75	-2.27	1.57	0.59	-1.36	-2.01	1.65	-0.09
9	-0.18	-2.55	0.43	2.37	0.22	-0.53	-2.13	-0.4
10	-0.8	-2.66	2.33	1.64	0.26	-0.37	-1.15	0.66
11	0.36	-0.55	-2.44	-1.52	-0.22	-2.9	-1.15	-0.42
12	1.31	-0.4	-0.98	-1.88	0.56	1.92	-1.15	0.98
13	-1.88	2.09	-0.58	-1.51	2.17	1.16	-1.15	-0.41
14	2.81	0.71	-2.25	0.03	-1.02	-1.46	-1.15	0.27
15	1.97	-1.33	2.59	-0.7	-0.75	-1.85	-1.15	0.21

Table3. The comparative table of the monitored and predicted energy

Log ₁₀ (Monitored energy)	5.51	5.53	5.89	5.50	6.27	5.35	5.75
Log ₁₀ (Predicted energy)	5.13	6.02	5.84	5.61	6.05	5.78	5.55

Table4. The seismic factor weight table

Factors No	1	2	3	4	5	6	7
Weight	0.05	0.07	0.27	0.17	0.11	0.09	0.24

Table3 shows that the predicted energy basically is in accordance with the monitored. There is a slight under-predicting of large energy released, and a slight over-estimating of small energy released, this generally is in accordance with other scholars[2]. Furthermore, from the Figure 6, which shows there is a relativity of 78% between the predicted and the monitored energy. All of these express the neural network is an effective way to predict the seismic risk.

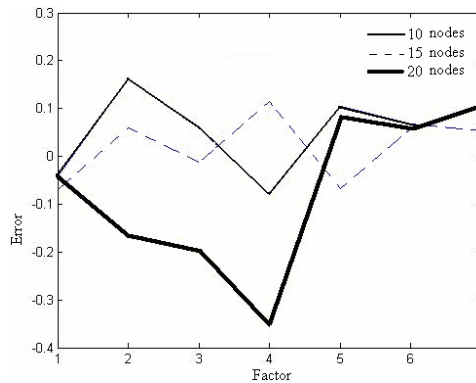


Figure 4. The training error curve of different hidden layer's nodes, which shows hidden layer with 15 nodes is the optimal configuration

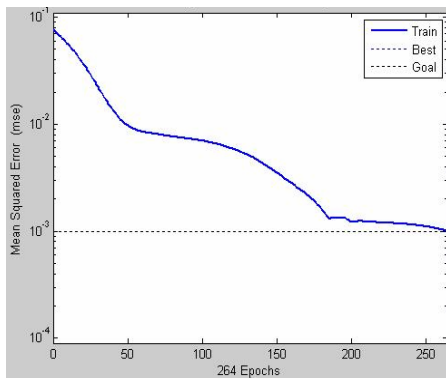


Figure 5. The training error curve with 15 hidden layer's nodes

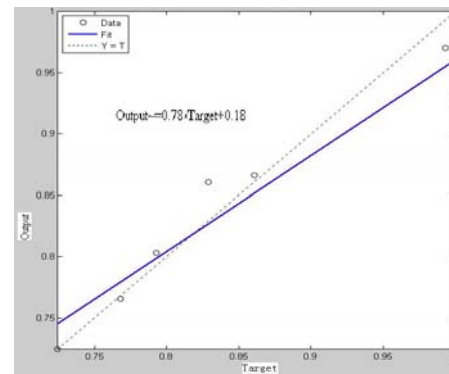


Figure 6. The testing error curve, in which the Target represents the monitored seismic energy released, and the Output represents the predicted seismic energy released

5 Discussion and Future Work

In this paper we have trained a neural network to analyse every seismic factors weight and predict the probable accumulative seismic energy released in next month. We have got basically satisfactory result in the mass, which indicates that the neural network is a quick and effective way to analyse the factor weight and predict the seismic risk. However, there are obviously two shortages in choosing the input data. Firstly, that the effect of local natural earthquake is represented by the sum of all event's magnitude ($M_L > 1$) is not serious and precise. Secondly, it's arbitrarily that the seismic data is grouped in consecutive one-month periods. Besides, in this paper, there are also two significant assumptions. One is only production blasting is considered in this analysis, the other is there is no interaction between seismic event clusters, but other mines have reported significant interaction between seismic source [2, 8, 9]. Therefore, in the future work, we should work on how to scientifically estimate the effect of natural earthquake and how to measure the seismic data in time.

Acknowledgements

The authors wish to acknowledge the support from Dong Guashan copper mine, Prof LI – ZHONG TANG and senior engineer CHENG-XIANG YANG etc for their contributions to this paper.

References

1. Zhu, F.C., Pan, C.L., Cao, P., and Jia, M.T. Analysis of Rock-burst Mechanism of Dong Guashan Deposit. Metal Mine, 2002, 38 (2). 20-21.
2. Hudyma, M.R. and Mikula. P.A. Quantifying Seismic Hazard Using Neural Networks. Rock-bursts and Seismicity in Mines-RaSiM 5. South African Institute of Mining and Metallurgy, 2001, 551-555.
3. Sharma, Mukat L., Arora and Manoj K. Prediction of Seismicity Cycles in the Himalayas Using Artificial Neural Network. 2005, 53(3). 299-309.
4. Mansurov, V. A. Prediction of Rock-bursts by Analysis of Induced Seismicity Data. International Journal of Rock Mechanics and Mining Sciences, 38(6), September, 2001, Application of Geophysics to Rock Engineering, 893-901.
5. Hecht and Nielson. R. Neural Computing. Addison-Wesley Press. 1990.
6. Ma, Y.J., Li, J.Y., and Zhang ,Z.T. Factors Weight Measurement and Analysis of Agricultural Mechanization Level Affect with BP Neural Network. Manufacturing Information of China. 35(5), 2006, 74-77.
7. Sun, H.J. and Wang, X.H.. Determination of the Weight of Evaluation Indexes with Artificial Neural Network Method. Journal of Shandong University of Science and Technology (Natural Science). 20(3), Sep. 2001, 84-86.
8. Kijko,A. and Funk,C.W. Space-time Interaction Amongst Clusters of Mining Induded Seismicity. Pure and Applied Geophysics, 147(2), 1996.
9. Hudyma, M.R. Seismicity at Brunswick Mining. Proceedings of 10e Colloque en Controle de Terrain, Val D'Or, Quebec, 1995.

PRACTICE OF SEISMIC HAZARD ASSESSMENT AND RISKS MANAGING IN ZHEZKAZGAN COPPER MINES (KAZAKHSTAN)

VLADIMIR A. MANSUROV

*“Kazakhmys Co” LTD,
Zhezkazgan, 100600, Republic of Kazakhstan*

The major collapse which happened at Annenskiy Mine, “Kazakhmys Co” Ltd at September 2006 is considered. Some inadequate design in conjunction deviation from design led to roof collapse occurred at September 2006. The collapse involved over 1 million cubic meters of rock and resulted in up to two meters of subsidence, along with fissuring, at ground surface level. The area of ground affected by subsidence at the ground surface is approximately 733,000m².

Monitoring of failure processes at Annenskiy Mine allowed avoid human victims and proceeds excavation work with the most efficiency till the last moment before the collapse.

The analysis of cause of this collapse shows that the main reasons of the collapse are

- rejection of low levels stowing;
- disparity of design principles to rock mechanics features of the Annenskiy Mine.

Shown limitation of the room and pillar mining methods for mining of the inclined seams (angle more than 20 degree) for the depth more than 300 meters.

Induced seismicity is the best tool for detection and control stability of underground openings

1 Strata of Zhezkazgan mine fields

Zhezkazgan copper mine fields include East, West, Field, South Mines and Annenskiy Mine. The Annenskiy Mine is the newest mine (opened in 1990) within the Zhezkazgan District and forms one of a group of five underground mines in the district that remains operational. In terms of area of influence, the older East Mine and younger Annenskiy Mine overlap. The junction between the two mines has been reported at the +90 meter level. Ore bodies located above the +90m level are currently mined through the East Mine, while lower levels are taken by the Annenskiy Mine.

The rocks of the ore body region consist of an apparently undifferentiated, alternating sequence of grey fine to coarse sandstones and red fine grained sandstones and siltstones. Both sandstone types vary between about 5 and 30m thick and are present in roughly equal proportions across the Zhezkazgan region as a whole. However in the mining sequence at the Annenskiy Mine, the fine grained, red sandstones are dominant. A copper mineralisation is exclusively confined to the grey fine to coarse sandstone layers. In addition to the two prevailing red and grey sandstone rock types, the ore body zone includes occasional thin (1 to 2m thick) layers of argillite and conglomerate. The Zhezkazgan ore body region as a whole is located between two major tectonic structures including the north to south running Zhezkazgan Syncline and the north-east to south-west trending Kingirskaya Anticline. These structures were formed about 280 million years ago. For the most part, the strata within the Zhezkazgan mining areas of East, South, West and Field mines are sub-horizontal. However, at Annenskiy Mine, the strata are inclined at angles of up to 35° from the horizontal, as they dip towards a local synclinal structure. Faulting is present throughout the Zhezkazgan region. Many faults are

orientated approximately north to south or parallel to other tectonic structures. Locally to the ore bodies within the Annenskiy Mine area, faults are known to exist.

According with data of the table 1, the ore body and grey sandstone units can be classified as ‘Very Strong’ (uniaxial compressive strength, UCS, between 120 and 245 MPa) using British Standard BS5930:1991 classification. However, the red sandstone, and particularly the red siltstones are much weaker, the latter having a UCS of between 30 and 60 MPa, albeit it still classifies as ‘Medium Strong to Strong’.

Table 1 shows the results of averaged geotechnical tests for the most critical rock material properties

Table 1. Typical Geotechnical Properties Of Strata at Annenskiy Mine

Formation	Uniaxial Compressive Strength MPa	Tensile Strength MPa	Cohesion MPa	Angle of Friction o	Young's Modulus GPa	Poisson's Ratio
Copper Ore	120 - 140	10 - 18	25 - 30	35	22 - 45	0.20 – 0.22
Copper/Lead Ore	160 - 240	10 - 18	30 - 34	35	50 - 65	0.18 – 0.21
Grey Barren sandstone	160 - 245	8 - 11	25 - 34	35	45 - 65	0.18 – 0.21
Red Sandstone	80 – 120	2 - 4	20 – 25	35	39 – 42	0.20 – 0.22
Red Siltstone	30 - 60	2 - 4	18 - 20	35	32 - 40	0.22 – 0.25

While uniaxial compressive strength is a useful indicator of rock strength, when it comes to assessing the strength of a mining rock pillar, rock mass properties are critical. For the most part, rock mass strength is dependent on fracture spacing, orientation, surface coating and other properties. Rock mass strength can be assessed using accepted evaluation methods that have been developed in western countries. During the site visit samples and exposures of the grey and red sandstones/siltstones were observed in outcrop, both underground and within surface open pits. From these inspections, it appeared that the red sandstone is particularly prone to weathering. In a dry condition, weathering takes the form of fissile fractures parallel and perpendicular to bedding planes resulting in a relatively low rock mass strength compared with the ‘fresh’ rock material strength demonstrated by the UCS results shown above. Therefore, for the most part, the rock mass condition of the red sandstone can be assessed qualitatively as ‘Poor’. In contrast, the grey sandstone does not appear to weather so readily, and depending on the natural jointing condition at any particular location, it’s rock mass condition can be assessed qualitatively as ‘Good’. Little geotechnical information is available relating to the relatively thin argillite and conglomerate layers. But these layers are not of significance with respect to mine stability.

2 Design Principles at Zhezkazgan

All of the underground mines within the Zhezkazgan District operate using the ‘room and pillar’ mining method. The principle of this method relies on the partial extraction of ore, leaving pillars of ore to support the roof and prevent roof collapse. The room and pillar mining method is suited to flat lying or shallow dipping and relatively thick ore bodies where total extraction is inhibited by the need to restrict the magnitude of subsidence at the ground surface. The prevention of surface subsidence in room and pillar mines is controlled by ensuring that the remaining ‘pillars’ have sufficient rock mass strength to carry the extra load imposed by the removal of ore from the rooms between the pillars. The mining design principles are understood to have been developed on the basis of research and investigations undertaken over many years both at the four original mines at Zhezkazgan (Field, East, South and West) and at the Annenskiy Mine. These mine design principles cover many different mining scenarios.

3 Safety Monitoring Systems

The Geotechnical Survey of the Kazakhmys Corporation is operating by three teams of technicians to operate underground stability monitoring systems. In practice two systems operate from above ground and one below ground. The first system comprises geodetic surveying of the ground surface to monitor mining induced subsidence; the second above ground system records micro-seismic events associated with rock movements and shearing caused by room and pillar roof instability. The third, underground, system involves teams of technicians to inspect for areas of instability within new development and historic room and pillar mining areas.

All of these systems played an important role in predicting and allowing the management of the major collapse / subsidence that occurred in September 2006.

3.1 Visual Inspection Team

The team comprises trained technicians who inspect both operational development and mining areas and historical non-operation room and pillar mined areas. The team gives advice to production personnel with regard to the roof conditions and supplementary support requirements. This advice takes the form of the roof rock characterization system described in section 2.4. In addition to the above, the visual inspection team carries out regular inspections of all existing pillars within the mines to record their condition and monitor time dependant deterioration. The results of these inspections are recorded on mine plans using a three tier classification system. The mechanics of this classification system is based on a visual assessment of loss of cross-sectional area. Categories are understood to be defined as follows:

- Class 1 loss of up to 10% of cross section;
- Class 2 loss of between 10% and 30% of cross section;
- Class 3 loss of more than 30% of cross section.

Pillar conditions are shown by hand annotation to mine survey drawings with reference to a notation that is indicated in Figure 2. The system of pillar condition assessment in principle provides a valuable database on time dependant behavior of support pillars.

3.2 Surface Geodetic Surveying

A large number of surface geodetic survey monitoring stations have been established across

the Zhezkazgan mining region. This has allowed the establishment of 30 or more traverse lines across the district. Surveying is carried out using modern total station equipment, which is apparently being well maintained and serviced by a local manufacturers' representative. However, measurements to each survey line take one day to complete and process and so each line is only surveyed 3 or 4 times per year.

It was clear that the surveying data had accurately predicted the eventual locations of fractures which were to develop as a result of the ground surface subsidence caused by the collapse of 2006. Using this information, local infrastructure, including pipelines, railways and roads were reinforced, so as to accommodate the eventual subsidence.

3.3 Geophysical Seismic Monitoring

An array of 20 surface mounted seismic 3D geophones has been established across the Zhezkazgan region. A seismic data is constantly transmitting by radio telemetry to a 'Mother Station' located at the approximate centre of the district. Here the data are recorded by a team of technicians 24 hours per day.

The array can detect events in frequency range 1-200Hz that include the sliding of rock masses within the various ore bodies and host rocks. These events are part of normal progressive stress redistribution arising from

mining operations. The distribution of the surface stations and the processing software that has been developed at the mine enables technicians to triangulate (by signal travel time) the location of any significant seismic event.

The current system appears robust and data provided by Kazakhmys Corporation, showed that the September 2006 was preceded by seismic event data that gave adequate forewarning (2-3 months) and enabled management of men and equipment in the affected areas to be re-deployed well in advance of the collapse. However, the system presently does not have the sensitivity to record the higher frequency seismic events which accompany individual pillar distress.

It is necessary to use of placing seismic monitoring geophones underground, in specific development or mining areas.

4 September 2006 Collapse

4.1 Events Leading to Collapse

The Annenskiy Mine began mining at the deepest levels – seam designation ANN 2-I-II. This seam was mined out over a period of about 3 years between 1997 and 1999.

Mining was carried out using the massive pillar method, with massive pillars of up to 50m diameter being used. The calculations indicated that the extraction ration in this seam is about 70%. Mining in the ANN 2-I-II level took place on a number of fronts. In particular, early development occurred from the Eastern, and deepest area. Mining activity progressed satisfactorily until the position of the massive pillar Mu-8 was established (Drawing S00870/SK1-Figure 1).

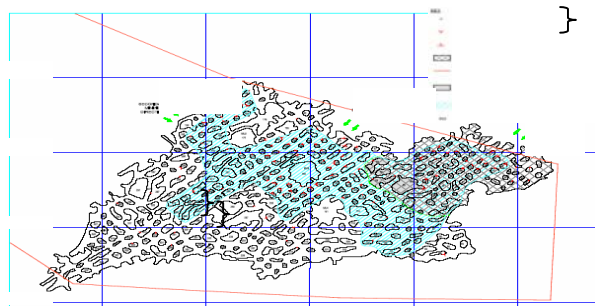


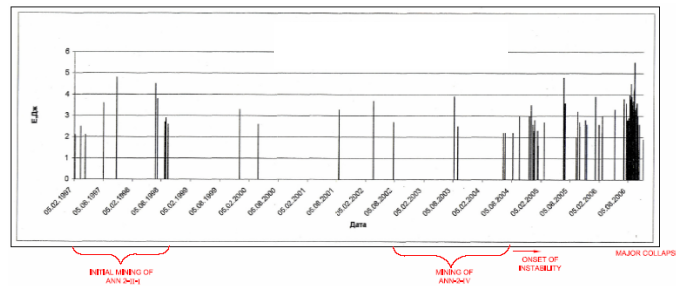
Figure 1 Mining level 2-II-I

At this point it was found that the design pillar contained high grade ore. Proposals were made to modify the position of the pillar.

During this period, some distress was noted in the inter chamber pillars. As a result, mining in this area, around Mu8, was terminated and continued from other directions. Ultimately the situation is stabilized.

Apart from the minor modifications and stability issues noted above, it is understood that mining progressed in the ANN 2-I-II seam without major incident. A record of instability is indicated by the frequency of seismic events occurring in the district as shown on Drawing OS00870/SK2-Figure2.

Following the extraction of ore at the ANN 2-I-II level, mining then took place at the uppermost (shallowest) levels between 1997 and 2002. During this phase no deterioration of the pillars occurred at the ANN 2-I-II level from visual inspection. This is confirmed by the general low level of micro seismic events during this period.



FFigure 2 Frequency of Micro-Seismic events in the vicinity of the ANN-2-I-II seam at Annenskyi Mine

During 2002 to 2004 mining took place in the ANN 2-IV seam. This seam is located just 15 to 20m above the ANN 2-I-II seam. The mining layout is shown on Drawing OS00870SK3-Figure 3.

Visual inspections of the pillars in the ANN 2-I-II seam began to record increasing levels of distress from this time. These visual observations of distance were matched by an increasing frequency of seismic events in the rock around this seam – see Drawing OS00870/SK2.

From the beginning of 2006, the frequency of seismic events began to accelerate. At the same time geodetic surveying indicated the development of a zone of ground surface subsidence and the formation of surface fractures. In recognition of the impending roof/pillar collapse, men and equipment were withdrawn from the ANN 2-I-II and ANN 2-IV mined levels.

From August 2006, micro seismic events were occurring hourly up to the eventual collapse on 16 September 2006. Roof collapse at the lower ore levels was accompanied by subsidence of up to 2m at ground surface. Cracking is present at the edge of the subsidence zone.

The areas of ground affected by the roof/pillar collapse at the ANN 2-I-II and ANN 2 IV levels are:

- ANN 2-I-II - 126,000 m²
- ANN 2-IV – 126,000 m²

The area of ground affected by subsidence at the ground surface is approximately 733,000m².

4.2 Implications of Collapse

The implication of the collapse will be as follows:

- Annual ore production for 2006 will be slightly reduced.
- Reserves of copper ore contained within remnant pillars within the ANN 2-I-II level will be extracted by secondary mining methods.
- Reserves of copper ore contained within remnant pillars within the ANN 2-IV level have been lost.
- It has been recognized that the removal of ore contained within remnant pillars at the ANN 2-I-II level will be slower and less efficient than had previously been planned.
-

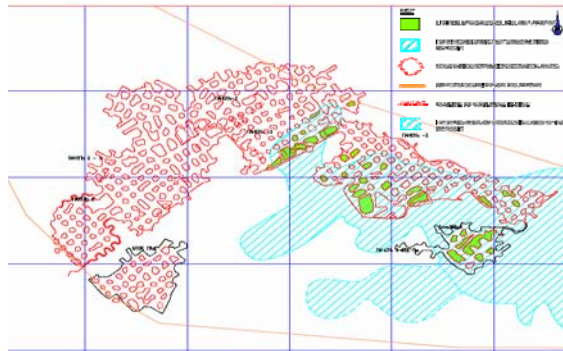


Figure 3 Mining level 2-IV

5 Possible causes of the collapse

One of the principle objectives of this study has been to arrive at a conclusion regarding the cause of the September 2006 roof collapse and subsidence. These preliminary conclusions are based on the initial findings from the site visit along with simplified calculations.

The potential causes of collapse can be summarized as follows and are discussed below.

- Deviation from design;
- Interaction effects;
- Effects of groundwater;
- Inadequate design

5.1 Deviation from Design

With respect to deviation from design, two issues are raised here. Firstly, was the design prepared in accordance with the design methodologies set out in the standards and norms prepared by the various State mining institutes. Secondly, was a correctly prepared mine plan, designed in accordance with the recommendations of the various standards and norms, followed during mine development.

Where it has been possible to check actual mine layouts with design pillar layouts approved by the mining institutes, the designs appear to have been adhered to. Where departures from layouts have been made, it is understood that the mining institutes have approved them.

Notwithstanding this, minor variations were noted, usually relating to the shape of pillars which are often elliptical in practice compared with circular pillars which form part of the design. Of greater concern has been the observation that some pillars that are shown to have been present in the ANN 2-IV seam are not supported by pillars in the underlying ANN 2-I-II seam. Where these have been observed, they have been highlighted on Drawing OS00870/SK3.

It has not been possible to replicate the design process for the seams most clearly associated with the collapse. It cannot be confirmed therefore at this stage that the design does indeed comply with the specified design procedures. For the time being an assessment of design has been based on a review of extraction ratios. These show a range between about 68 and 83% with the lower extraction ratios associated with the lower seams.

5.2 Interaction Effects

The design methodologies apparently take into consideration interaction effects between seams. However, this appears to be limited to methods of ensuring that pillars located in upper seams are positioned above pillars in lower seams. This is to ensure the conformity of stress through pillars at different depths. However, as noted above this does not always appear to have been the case.

It was also apparent that consideration could also be given to the effects of stress concentration generated within unmined areas at the margins of the room and pillar workings. It was stated that these stress concentrations could amount to up to between 2 and 2.5 times the overburden stress at a distance of 2 to 10 times the seam thickness in advance of the mined area. In practice this magnitude would depend on the extraction ratio within the mined area. It was stated that consideration of this was taken by leaving enlarged pillars beneath these peripheral mining areas. The general principle of this is illustrated in Figure 4.

However, it is not clear how this is accommodated in practice. Furthermore, while this design methodology works for the cases where the sequence of mining begins at the shallowest depth going deeper, it does not work for the reverse situation, where the stress caused by mining in a shallower seam passes over pillars of standard size during mining. In other words, when mining was taking place in the ANN 2-IV seam, above the worked out ANN 2-I-II, then the pillars in the ANN 2-I-II seam can become overstressed depending on the position of the mining. It is believed that this dynamic condition is not catered for by the mining design procedures. Indeed this type of analysis is not amenable to static calculation.

5.3 Effects of Groundwater

A moderate inflow of water into the mine is there. The effects of this water on mine stability due to swelling of red siltstones are clear. It correlates with velocity of subsidence during spring time.

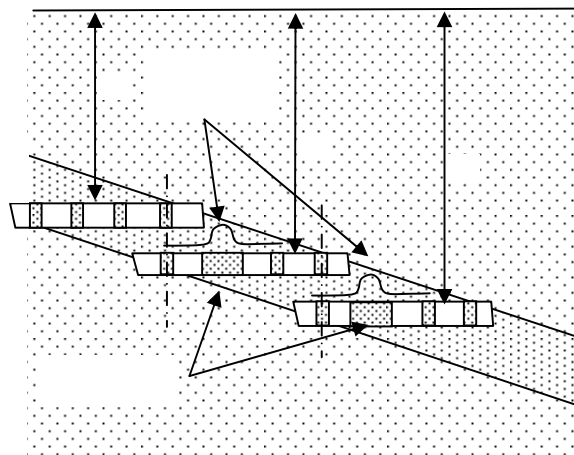


Figure 4 Theoretical Interaction between Mining Levels

5.4 Inadequate Design

Given that an unplanned collapse / subsidence has occurred then this leads to an inevitable conclusion that there has been some sort of inadequacy of design or construction or both.

Unless it can be demonstrated that the mined layout of the ANN 2-I-II and ANN2-IV seams departed more than in minor terms from the approved mining plan, then the collapse can only be accounted for by some form of unexpected ground behavior. On the basis of a brief review of the mining plans and survey drawings, it appears that there has been no radical departure from the approved mining layout. However, this can only be ruled out as a significant cause after further careful checking. If deviation from design is ruled out as a significant cause of the collapse / subsidence then it must be concluded that it has occurred as a result of some form of design inadequacy.

The various possibilities of design inadequacy are discussed below.

The procedure of mine layout design is set out in a series of manuals and design guidelines prepared and approved by mining and research institutes in Kazakhstan and the former Soviet Union. These procedures seem to lead to an empirical design approach based apparently on scientific based calculation and research. Unlike western design methods, the approach does not arrive at a factor of safety that can be independently assessed. From an assessment of the design using western methodologies, factor of safeties more than 2 are indicated for flat lying, shallow depth mining areas, reducing to between 1.1 and 1.8 in inclined seams at the depths of the ANN 2-I-II seam, which was the location of the major collapse.

Under different circumstances, such factors of safety might be considered appropriate. However, where this section of mine is overlain by the other seams to be worked in the future, they could be considered inadequate. It should be noted that the assessment of factor of safety does not take into consideration time dependent effects of rock pillar strength, the relatively low level of rock tensile strength compared with compressive strength and the effects of stress concentration caused by natural geostatic stress and interaction effects resulting from multiple seam mining.

6 Conclusions

The investigation of the cause(s) of the major roof collapse/subsidence, number of uncertainties has arisen with regard to the design methodologies used at the Annenskiy Mine and in the implementation of the design.

Back analyses of the mining layout used for the lowest seams at Annenskiy mine have been carried out to assess extraction ratios and pillar strengths (the latter using Kazakh methods). These analyses have suggested that at depths of around 450m in inclined seams, the factor of safety of pillars was less than might be hoped for.

The effects of local variations in rock pillar strength either due to geological or geometrical factors could result in local overstressing of some pillars.

The calculations carried out so far have not considered the effects of additional stresses being applied to pillars in ANN 2-I-II as a result of the mining of the ANN-2-IV seam.

The barrier/rib and inter cavern room and pillar mining method has been developed throughout the world as a method of limiting the extent of major roof collapse. In effect, the rib/barrier pillars are designed to halt 'domino effects' of inter chamber pillar collapse. It is not clear how the massive pillar mining method achieves a similar objective, when in theory, strings of inter cavern pillars could fail allowing a domino effect to migrate through a mining area.

Some deviations from design methodologies have been identified. Notably, these include the formation of pillars located within ANN 2-IV seam do not appear to be supported in the underlying ANN 2-I-II seam. This situation can result in punching failure of pillars in the upper seam into the lower seam.

Forecasting of this collapse was successfully done in time in accordance with developed technique by monitoring of the induced micro seismic events space & time distribution.

THE MESHLESS MANIFOLD METHOD FOR 2D CRACK PROBLEM

WEN-SHENG YU

Jiangxi Center Traffic Engineering Consultation and Supervision

Nanchang, 330008, P.R.China

SHU-CHEN LI, SHU-CAI LI

Geotechnical and Structural Engineering Research Center

Shandong University, Jinan, P.R.China

The meshless manifold method based on circle covers consists of the partition of unity method and the finite cover approximation theory. The method provides a unified framework for solving both continuous and discontinuous problems. In the method based on circle covers, two cover systems are employed. The mathematical covers system provides the nodes for forming finite covers of the solution domain and the partition of unity functions. The physical covers system describes geometry of the domain and the discontinuous surfaces in the domain. The shape functions in the method are derived by the partition of unity and the finite covers approximation theory. The approximation functions and the equations of the coupling method are developed in detail in the paper. The validity and accuracy of the meshless manifold method are illustrated by numerical examples.

1 Introduction

In meshless methods the discretization is purely nodal, and the finite element concept of connectivity between elements is not introduced. The shape functions are constructed on a given nodal arrangement in the solving domain. Basing an analysis on nodes or particles, demonstrates flexibility in modeling complex discontinuities [1,2]. It also avoids the distortion of mesh when extreme large deformation is encountered [3], and provides an efficient means for addressing high gradient problems such as that occurred in strain localization [4]. The advantage of meshless methods by Belytschko [5, 6] is that it is possible to model arbitrary growth of cracks without remeshings and adaptive refinement at the crack tip is easily accomplished. With adequate refinement, stress intensity factors can be computed accurately. The disadvantage of the method is that test functions have nearly been constructed by the original visibility criterion [7] which is empirical method to model cracks leads to interior discontinuities in the displacements, especially arbitrary cracks.

To overcome shortcomings of discontinuities in the meshless method, the meshless method based on circle covers is developed in the paper. The method is based on the partition of unity method and the finite cover approximation theory in the mathematical manifold. The basic idea of the method is derived from the numerical manifold method [8] which is extended to meshless method by circle covers in this paper. Two cover systems

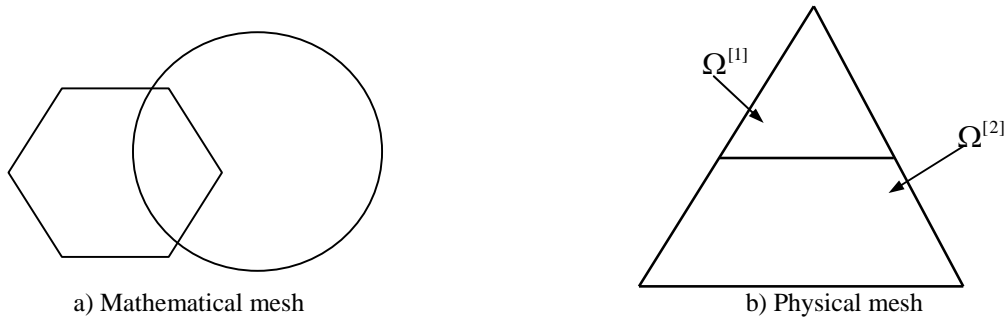
are employed in the meshless manifold method. The circle mathematical cover system provides the nodes for forming finite covers of the solution domain and the partition of unity functions; and the physical cover system describes geometry of the domain of the problem and the discontinuous surfaces in the domain. The shape functions in this method are formed by the partition of unity and the finite covers approximation theory, hence the shape functions are not affected by discontinuity of a domain.

2 A Brief Review of Finite Covers in Manifold Method

Following the formulation of the manifold method proposed by Shi [8], we present how the use of meshless finite covers instead of finite element covers is effective for modeling discontinuities and its growth in strain and displacement.

2.1 Mathematical and physical covers

Based on finite cover systems, the newly developed “manifold method” has the potential to meet more engineering requirements. With reference to the schematic presented in Figure 1, we provide the definitions of domains and covers. A domain where mathematical functions independent of physics are introduced is called a mathematical domain, whereas a domain where physical quantities are defined is referred to as a physical domain. The mathematical domain can be constructed as a union of a finite number of patches, which can be overlapped either partially or totally. These patches are called mathematical covers which are chosen by engineers and may consist of finite overlapping covers which occupy the whole material volume. If the joints or block boundary divide a mathematical cover to two or more completely disconnected domains, those domains are defined as physical covers. Therefore, physical covers are subdivision of mathematical covers by discontinuities. The manifold method is more suitable to compute large deformations, moving boundaries of both continuums and jointed or blocky materials. The above concept of cover systems is illustrated in the example shown in Figure 1. The circle and the hexagon mesh are arbitrarily selected as the mathematical mesh, as shown in Figure 1a. Figure 1b shows the structure containing a crack that defines the physical mesh. The common region of the mathematical cover M_I and the physical mesh $\Omega^{[\alpha]}$ forms the physical covers, and is denoted by $P_I^{[\alpha]}$ in Figure 1.



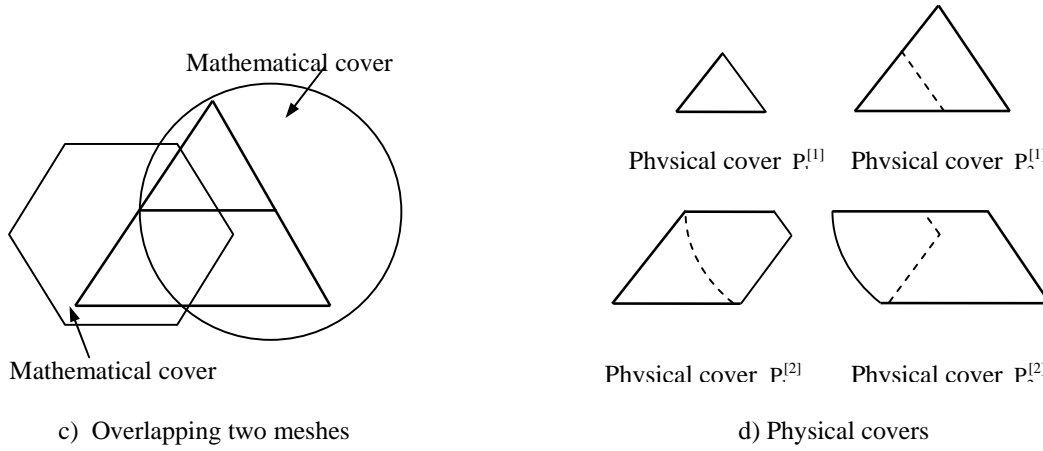


Figure 1 Mathematical and physical covers

2.2 Approximation based on finite covers

In the following, the approximation properties facilitated in the meshless manifold method is presented assuming the one-dimensional version of the problem see [9] in detail.

Then the displacement $u(x) \in H^1(\Omega)$ is approximated as

$$u(x) \approx u^h(x) = \sum_{l=1}^{N_M} \sum_{i=1}^{n_i} \phi_l(x) u_l^{[\alpha]}(x) \quad \text{on } \Omega \quad (1)$$

where n_l is the number of physical covers associated with mathematical cover M_l and $u_l^{[\alpha]}(x)$ is cover displacement functions corresponding to the physical cover $P_l^{[\alpha]}$.

3 Research Approach Cover Functions and Weight Functions

In this section, the construction of the basis functions and test functions are described and some properties of these functions are reviewed in the meshless manifold method. One key idea used in the construction of the meshless manifold method is that of a finite cover approximation theory in manifold method and the partition of unity function. The finite cover approximation theory formed the sub-covers which constructed the approximation function by the partition of unity.

We used the basic idea of the approximation based on finite covers in the section 2.2, for a continuous domain, the numbers of physical covers equal to one of the mathematical covers. The shape functions are the partition of unity functions of the local covers by Equation (1), the approximation function, $u^h(x)$, can be expressed as

$$u^h(x) = \sum_{i=1}^{N_M} \phi_i(x) \cdot u_i \quad (2)$$

where $\phi_i(x)$ is the partition of unity function of the local cover M_i , u_i is the value of the function at node i .

The same above process, for a discontinuous domain of two-dimensional problem, one cover is divided into two sub-covers at a discontinuity. The partition for sub-covers is also separated so that there is one partition associated with each sub-cover. To facilitate a sub-cover partition, let sub-cover \overline{M}_i^j be the j th sub-cover of M_i . The partition of unity function for \overline{M}_i^j , denoted as $\phi_i^j(x)$, is given by

$$\phi_i^j(x) = \phi_i(x) \cdot \delta_i^j(x) \quad (3)$$

where $\phi_i(x)$ is the partition of unity function for cover i , and

$$\delta_i^j(x) = 1 \quad x \in \overline{\Omega}_i^j \quad (4)$$

$$\delta_i^j(x) = 0 \quad x \notin \overline{\Omega}_i^j \quad (5)$$

With the introduction of sub-covers, i.e. more than one covers subordinated to one node, the meshless method based on circle covers can model a discontinuous function over a disjoint local cover by the finite cover technology. Since each of the sub-cover has an independent cover with its own partition of unity function, a discontinuous approximation function is obtained by

$$u^j(x) = a_1 \phi_1^1(x) + a_2 \phi_1^2(x) \quad (6)$$

where, a_1 and a_2 are the nodal values associated with P_i^1 and P_i^2 , respectively. Hence, to the discontinuous domain, $u^h(x)$ by the Eq. (1) can be expressed as

$$u^h(x) = \sum_{l=1}^{N_M} \sum_{i=1}^{n_l} \phi_l(x) \delta_l^j(x) u_l^{[\alpha]}(x) \quad \text{on } \Omega \quad (7)$$

Given a cover $\mathfrak{R}_N = \{M_I, I = 1, \dots, N\}$ we can then define a partition of unity and local approximation functions by using Shepard functions or Moving least square as $\phi_i(x)$, and local approximation spaces V_i^m on the cover M_i .

4 The Discrete Equation of the Meshless Method

Consider a two-dimensional domain Ω bounded by S . The equation of equilibrium is

$$\sigma_{ij,j} + f_i = 0, \quad \text{in } \Omega \quad (8)$$

where σ_{ij} is the stress tensor, f_i is the body force. The boundary conditions are

$$\sigma_{ij} n_j = \bar{t}_i, \quad \text{on } S_\sigma \quad (9)$$

$$u_i = \bar{u}_i, \quad \text{on } S_u \quad (10)$$

where \bar{u}_i and \bar{t}_i denote the prescribed displacements and tractions, respectively, n_j is the unit outward normal to S , and S_σ and S_u are complementary parts of S where essential and nature boundary conditions are prescribed.

The variational (or weak) form for Equation (8) can be written as

$$\int_{\Omega} \nabla \delta u : \sigma(u) d\Omega - \int_{\Omega} \delta u \cdot f d\Omega - \int_S \delta u \cdot \bar{T} dS - \delta W_u(u) = 0 \quad (11)$$

where ∇ is the symmetric gradient operator. The term $\delta W_u(u)$ is required for enforcing the essential boundary conditions in a meshless manifold method.

For linear elasticity, the strain-displacement equation and the stress-strain law are

$$\varepsilon = \frac{1}{2}(\nabla u + (\nabla u)^T) \quad (12)$$

$$\sigma = D : \varepsilon \quad (13)$$

which can be used to write the weak form in Eq. (11) in terms of the displacements u . The discrete form can be obtained by Eq. (7) as approximations for u and δu . This leads to the system of equations

$$Ku = F \quad (14)$$

where

$$K_{IJ} = \int_{\Omega} B_I^T \cdot D \cdot B_J d\Omega \quad (15)$$

$$F_I = \int_{s_{\sigma}} \phi_I^T \bar{t}_I dS + \int_{\Omega} \phi_I^T f_I d\Omega \quad (16)$$

$$B_I = \begin{bmatrix} (\phi_I \delta_I^j)_{,x} & 0 & (\phi_I \delta_I^j)_{,y} \\ 0 & (\phi_I \delta_I^j)_{,y} & (\phi_I \delta_I^j)_{,x} \end{bmatrix}^T \quad (17)$$

in which E and ν are Young's modulus and Poisson's ratio, respectively.

5 Numerical Examples

In this section, a classical problem will be solved an edge crack problem in fracture mechanics using the meshless manifold method to model discontinuous problems. A rectangular plate with an edge crack is shown in Figure 2. The plate is loaded in tension at the top with $\sigma = 0.2GPa$ and essential boundary conditions are applied at the bottom of the plate. The following parameters are used in the numerical simulations:

$L = 52mm$, $D = 20mm$, $a = 12mm$; Elastic modulus $E = 76GPa$; Poisson's ratio $\mu = 0.286$; Plane strain state of deformation is assumed.

The closed form solution for the crack is obtained by using the well-known near tip field in a domain about the crack tip and prescribing the displacements along the boundary of this field. The computed mode I stress intensity factors are compared with a finite geometry corrected value $K_I = C\sigma\sqrt{a\pi}$ where the correction is given by Ewalds and Wanhill [10].

Linear and quadratic bases with Gaussian weight function and a cover diameter of $d_{\max} = 4.0mm$ are used in the numerical simulations. For linear and quadratic bases, a node system with 1722 regular nodes is used to form the local covers.

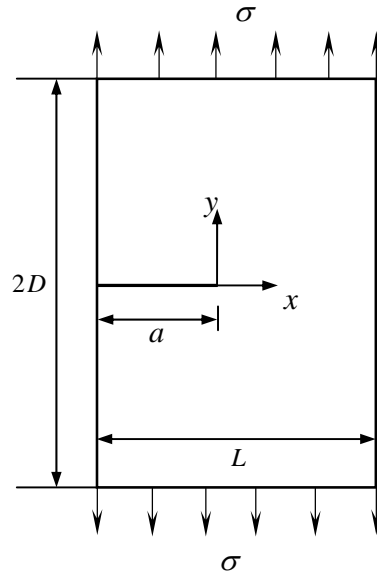


Figure 2 An edge crack model

The stress intensity factor K_I is normalized by $\sigma\sqrt{a\pi}$ and the normalized K_I value by the linear and the quadratic basis functions are calculated to be 1.32 and 1.40, respectively. The analytical solution is $C = 1.44$. The errors for linear and quadratic bases are 8.3% and 2.7%, respectively. It clearly indicated that the quadratic of basis function results in a higher accuracy of solution at the same number of node.

The stress field in front of the crack tip is shown in Figure 3. It can be seen from the figures that the numerical solutions agree well with the exact solution. It can also be seen that the singularity at the crack tip is better modeled by the nonlinear (quadratic) bases method.

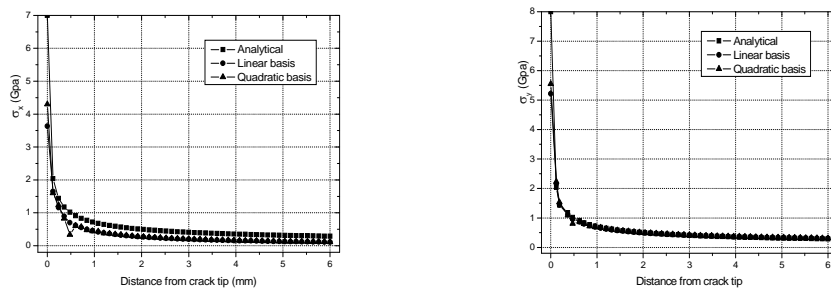


Figure 3 Stresses σ_y and Stresses σ_x ahead of the crack tip for the edge crack problem

6 Conclusions

The meshless manifold method has been presented in this paper. The proposed method is based on the mathematics of partition of unity and finite cover approximation theory for the discontinuous problems in the solving domain. It constitutes a new class of meshless methods.

When problems of cracks are solved with the method, each node in the affected domain is separated into two or more nodes. All nodes that are not affected by the crack remain unchanged. As a result, arbitrary cracks can be treated easily.

The meshless manifold method is given a kind of the mathematical method to treat discontinuity in solving domain. The method mainly used the finite covers approximation theory to model cracks that lead to interior discontinuity of displacement. Consequently, the method overcomes the shortcomings of the empirical methods that include three methods of the visibility criterion.

References

1. Belytschko, T., Krongauz, Y., Organ, D., etc. Meshless methods. an overview and recent developments. *Comput. Methods. Appl. Mech. Engrg.*, 1996, 139(1-4).3-47.
2. Oden, J.T. and Duarte, C.A.M. Solution of singular problems using h-p clouds, in. J.R. Whiteman (Ed.), *The Mathematics of Finite Elements and Applications*, John Wiley & Sons, NY. 1997.
3. Chen, J.S. Pan, C. Roque, M.O.L. and Wang, H-P. A Lagrangian reproducing kernel particle method for metal forming analysis. *Comput. Mech.*, 1998, 22(3.).289-307.
4. S. Li, W.K. Liu, Numerical simulations of strain localization in inelastic solids using mesh-free methods. *Int. J. Numer. Meth. Engrg.*, 2000, 48(9.).1285-1309.
5. T. Belytschko, Y. Y. Lu and L. Gu, Crack Propagation by Element Free Galerkin Method, *Engineering Fracture Mechanics*, 1995, 51(2.).295-315.
6. Belytschko etc. Fracture and crack growth by element-free Galerkin methods. *Modeling Simulations in Materials Science and Engineering*, 1994, 2.519-534.
7. T. Belytschko, Fleming M. Smoothing, enrichment and contact in the element-free Galerkin method. *Computer and Structures*, 1999, 71(2).173-195.
8. Shi, G.H. Modeling rock joints and blocks by manifold method. *Proceedings of the 33rd US Rock Mechanics Symposium*. 1992.
9. Li, S.C., Li S.C. and Cheng, Y.M.. Enriched meshless manifold method for two-dimensional crack modeling. *Theoretical and Applied Fracture Mechanics*, 2005, 44(3).234-248.
10. Ewalds, H. and Wanhill, R. *Fracture Mechanics*. Edward Arnold. New York. 1989.

RESEARCH ON PREDICTION OF INSTABILITY FAILURE FOR GASSY COAL BASED ON MICROSEISM

DONG DUAN

*School of Resources and Civil Engineering, Northeastern University
Shenyang, 110004, P.R China*

CHUN-AN TANG

*School of Civil and Hydraulic Engineering, Dalian University of Technology
Dalian, 116024, P.R China*

XIAO-JING FENG

*Shenyang Branch of China Coal Research Institute
Shenyang, 110016, P.R China*

LIE-XIAN TANG

Dalian Mechsoft Co., Ltd., Dalian, 116622, P.R China

In this paper, according to the rock failure damage theories and the gas-solid coupling method, RFPA^{2D}—GasFlow soft code is used to investigate the distribution characteristics of microseism for gassy coal in failure process. Herein, the distribution characteristics of microseism in time and space prediction potential failure danger area are considered. Simulation results show that there is some microseism precursory before the main shock, which is calculated based on the characteristics of microseism in time. The characteristics of microseism precursory made by tension stress in space can be used to divide potential failure danger areas. It is found that the potential failure danger area is consistent with crack initiatory zones by contrasted potential failure danger area to crack development process. Therefore, the development of cracks can be prevented through taken precautions and cure measures to prevent potential failure danger area; consequently preventing the occurrence of mine disasters.

1 Introduction

As many coal and rock materials withstand the load, they can induce the phenomenon of energy accumulation and sudden release. Namely as the material is under external stress, local elasticity capability centralization phenomenon will come into being in its interior, and when energy accumulates to some marginal value, it will cause the production and the expansion of microcracks, the elastic wave or stress wave the production and the expansion of microcrack release and will spread quickly. This kind of elastic wave or the stress wave release process, which is relative to the large rock mass because high frequency weakens quickly. The examined signal

frequency is low, usually in the range of 20~200Hz, but the energy is high, called microseism (MS), relative to the small rock sample and the examined wave frequency is usually higher than 200Hz. Also the energy is very low, and it is called acoustic emission(AE), their characters are the same in many aspects and also doesn't have very explicit boundaries.

The essence of gas outburst is also the coal failure. MS is the important precursory information which the gas outburst occurs, studying the microcrack characteristics of failure process of gassy coal guides the application of microseism monitoring technology in gas outburst monitoring and forecast and so on. In former research of AE or MS, very few experiments looked at gassy coal which caused research to lack accurate results and reliability when are applied to coal mines and especially when applied to gas outburst monitoring. Based on this, and on the basis of consideration of coal physical mechanics nature and heterogeneity this article does some numerical experimentation research on the MS characteristics of failure process of gassy coal, and provides the theory basis for the application of microseism monitoring technology in coal mines.

In RFPA^{2D}-GasFlow code, we consider that microseism in coal and rock distortion and failure process and the formation of micro-failure (damage) inside are directly correlative. We can anticipate that there exists some necessary connection between microseism and the damage of coal and rock. As an intuitionistic estimation, if we ignore how high the energy of microseism is, and assume that each material mesoscopic unit failure has contribution to microseism, well then we can draw a conclusion involuntary that in numerical simulation calculation there exist a direct proportion connection between unit damage quantity and microseism of rock. Based on this thought, we can study microseism rule of coal and rock failure process through calculating the quantity of damage unit. In RFPA2D-GasFlow code, we use the damage unit number to represent MS counts, thus it is possible to use simple model simulate the microseism distributing rule of coal material.

2 Solid-gas Coupling Mathematical Model

Solid-gas coupling model of gassy coal which this article applies mainly includes three parts: seepage equation of gas flowing in coal, coal deformation equation and coupling equation of the coal damage under disturbing stress and breathability coefficient evolvement. These equations may be expressed as:

$$\alpha_p \nabla^2 P = \frac{\partial P}{\partial t} \quad (1)$$

$$(\kappa + G)u_{j,j} + Gu_{i,jj} + f_i + (\alpha p)_{,i} = 0 \quad (i, j = 1, 2, 3) \quad (2)$$

In the formula: $\alpha_p = 4\lambda A^{-1} P^{0.75}$, λ is breathability coefficient tensor, A is coal gas content coefficient, P is square of coal gas pressure, κ is the lame constants, G is shear modulus, u is coal distortion displacement, f is coal volume force component, α is pore pressure coefficient, p is pore pressure.

When the stress state or strain state of coal mesoscopic unit meets some appointed damage threshold, the unit begins damaging. We can know through the experiment, the damage will causes the coal sample breathability coefficient to increase suddenly, in the condition of uniaxial compression and uniaxial tension, the breathability coefficient of coal mesoscopic unit—the change of damage parameter D may be described by (3) and (4).

$$\lambda = \begin{cases} \lambda_0 e^{-\beta(\sigma_1 - \alpha p)} & D = 0 \\ \xi \lambda_0 e^{-\beta(\sigma_1 - \alpha p)} & D > 0 \end{cases} \quad \text{uniaxial compression} \quad (3)$$

$$\lambda = \begin{cases} \lambda_0 e^{-\beta(\sigma_3 - \alpha p)} & D = 0 \\ \xi \lambda_0 e^{-\beta(\sigma_3 - \alpha p)} & 0 < D < 1 \\ \xi' \lambda_0 e^{-\beta(\sigma_3 - p)} & D = 1 \end{cases} \quad \text{uniaxial tension} \quad (4)$$

In the formulas: λ_0 is initial breathability coefficient, σ_1 and σ_3 are maximum principal stress and minimum principal stress respectively, β is the coupling coefficient, ξ and ξ' are increasing coefficient of breathability coefficient when the coal unit is damaged and destroyed respectively.

(1) ~ (4) are solid-gas coupling mathematical model of gassy coal failure process which considers coal and rock distortion and damage and gas seepage.

3 Numerical Simulations

For the research of failure process of gassy coal, in the former research, the heterogeneity character of coal weren't considered, in RFPA^{2D}-GasFlow code, which this article adopts, has considered the heterogeneity character of coal sufficiently. Elastic modulus of unit, uniaxial compressive strength, poisson 's ratio, gas content coefficient, permeability coefficient etc. distribute according to Weibull distribution, as can be seen in formula (5), among them ϕ represents the Weibull distribution function, α is mechanical property coefficient of coal medium(strength, elastic modulus etc.) unit, α_0 is average value of unit mechanical property, m is coefficient of homogeneity which is used to describe sample homogeneity. The coal sample is more homogeneous whose coefficient of homogeneity is higher.

$$\phi(\alpha) = \frac{m}{\alpha_0} \cdot \left\{ \frac{\alpha}{\alpha_0} \right\}^{m-1} \cdot e^{-\left\{ \frac{\alpha}{\alpha_0} \right\}^m} \quad (5)$$

3.1 Numerical Models

In order to consider the influence of heterogeneity, we assume the m is 1.5. In order to reduce the influence which the randomness acts on the result, each numerical model is calculated for 10 times. The model size is 100mm×50mm, and the model is divided into 200×100 grid, numerical model can be seen from Figure 1. The physical and mechanical parameters and seepage parameters of numerical model can be seen in table1. The model adopts plane stress analysis, displacement control loading, 0.005mm is loaded in each step. In the actual mine, coal seams all bear some confining pressure effect, in order to make the research more actual, we assume the confining pressure is 6MPa. The surrounding of sample is airproof that is the gas flow is 0.

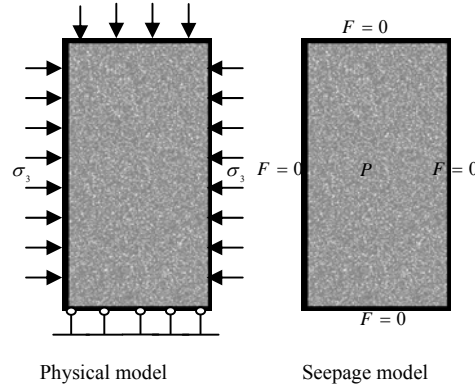


Figure 1 Numerical model

Table 1 Mechanical and seepage parameters of numerical model

mechanical parameters	values
homogeneous degree m	1.5
elastic modulus mean value E . [GPa]	30
compressive strength mean value σ_c . [MPa]	200
poisson 's ratio μ	0.3
breathability coefficient [m ² /MPa ² ·d]	0.5
gas content coefficient A	10
pore pressure coefficient α	0.5
coupling coefficient β	0.2

3.2 Numerical Results

As can be seen in Figure 2, the microseism activity of sample is of stage character, in the pressure consolidation and linear elastic stage of coal, MS event is mainly produced by crack closing, sometimes there is rarely or even no microseism activity. In the expansion, transfixion and forming macroscopic failure stage of crack, a lot of microseism activities are produced. Combine Figure 2 and Figure 3, we can know that the main shock happens after stress peak, at this time macroscopic crack of coal has formed, and the coal loses bearing capacity. There is a lot of microseism precursor information before main shock happening, the microseism precursor information is more abundant when the main shock is drawing near, when the microseism precursor is formed in coal, its damage degree is low, the damage is local and the bearing capacity doesn't reach stress peak. It is clear that using macroscopic precursor accurately to predict can avoid the occurring of instability failure effectively. In the nether content the process which uses time and space distribution characteristics of microseism precursor to predict instability failure accurately will be introduced detailed.

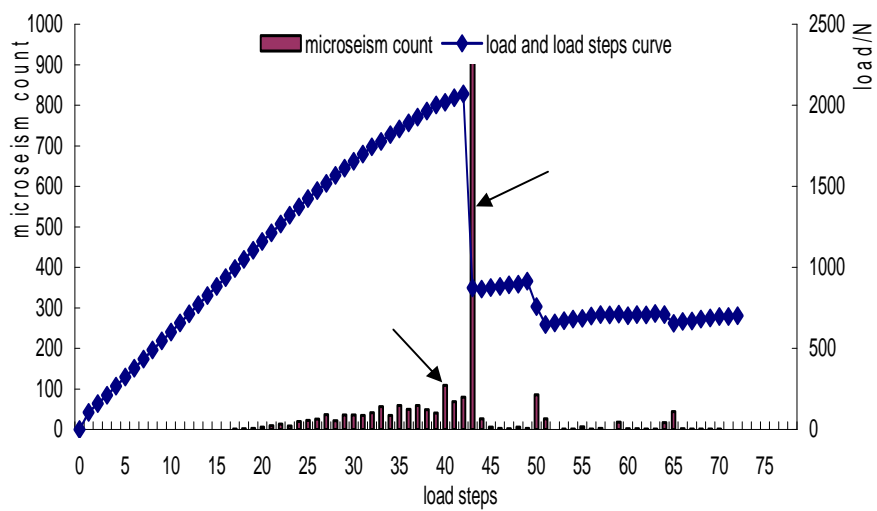


Figure 2 Microseism count, load and load steps curve

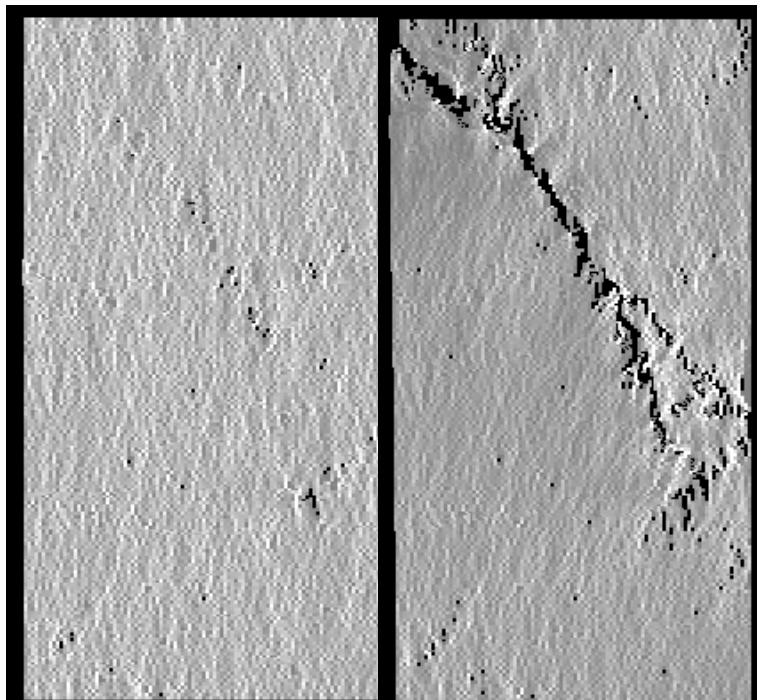


Figure 3 Damage situation when microseism precursor and main shock are corresponding

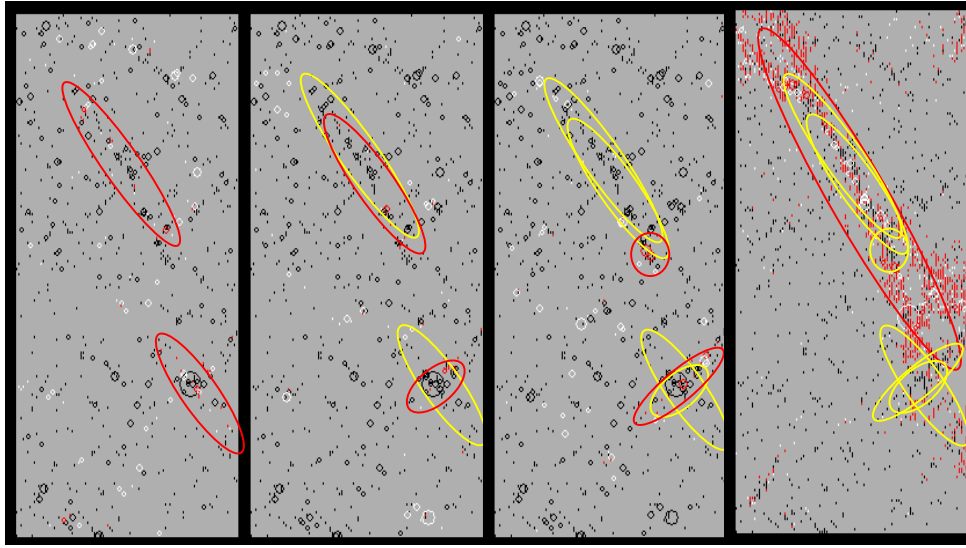


Figure 4 Dividing process of potential damage danger area

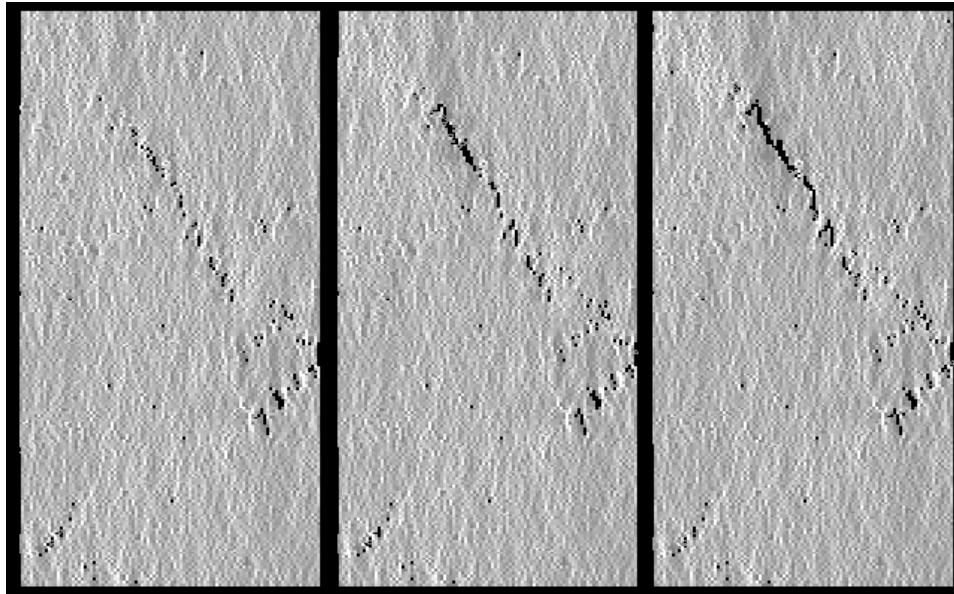


Figure 5 Process of crack initiation

Figure 4 is the numerical simulation result of microseismic activity space distribution. In the figure each circle represents a microseismic position, the red circle shows that the microseismic event is produced by the tension stress effect, the white circle shows that the microseismic event is produced by the compression stress effect, the circle diameter represents the energy which the microseismic releases.

As can be seen in Figure 2, the main shock is produced in the 43rd step, obvious microseismic precursor is produced in the 40th step, so we can use microseismic precursor information which is before the main shock namely the 40th~42th step microseismic precursor information to predict coal potential damage danger area.

Through all the simulation samples microseism activity space distribution characteristics, we can find that in the previous stage of microseism event, it is mainly induced by compression stress, in this time macroscopic failure doesn't occur in the sample, in the middle and later stage there exist many microseism events which are induced by tension stress. When the main shock occurs, the microseism events in the failure area are mainly produced by tension stress. At the same time, according to the compression resistance and non-tension resistance character of coal, we can consider that the space distribution of microseism event which is produced by tension stress has high consistency with the sample potential damage danger area. Based on this idea, its division result can be showed in Figure 4. The red ellipse expresses the potential damage danger area divided based on current step microseism event which is produced by the tension stress, the yellow ellipse expresses the potential damage danger area divided based on pre-current step microseism event which is produced by the tension stress. Through the 43rd step (main shock) division result, we can find that the potential damage danger area which is divided by using microseism precursor information is mainly contained in main failure area or surrounding. It is clear that division result of potential damage danger area is more accurately. Figure 5 is process of crack initiation, comparing Figure 4 with Figure 5, we can find that potential damage danger area which is obtained by predicting is the area where crack initiation occurs, so if we adopt protection measures to potential danger area, the occurring of instability failure can be prevented.

4 Conclusions

Using the time and space distribution characteristics of microseism precursor information, we can predict the position of potential damage danger areas accurately. Use of the distribution characteristics of microseism information in time, can give advance warning. Using the space distribution characteristics of microseism information, which is produced by tension stress to divide the potential damage danger area, can reduce interference of other microseism information and raise the accuracy of potential damage danger area dividing. When using the microseism precursor to predict instability failure, failure shape of macroscopic crack when the main shock occurring can't be predicted completely, but the position and area of crack initiation can be predicted accurately. This is of important practical significance for practical engineering applications. If effective protection measures can be adapted to the position of crack initiation, the expansion of cracks can be inhibited the disasters can be prevented.

Acknowledgements

This research is supported by the NSFC (Grant No. 40638040, 10672028 and 50504003) and FCCRI (Grant No.2008QN45). The authors are grateful for these supports.

References

1. Martin, M.W., Koerner, R.M. and Jrlord, A.E. Acoustic Emission Behavior of Concrete Laboratory Specimens. *Journal of the American Concrete Institute*, 1976, 73-7.367-371.
2. Hsu, N.N, Simmons, J.A, and Hardy, S.C. An Approach to Acoustic Emission Signal Analysis. *Material Evaluation*, 1977, 35. 100-106.

3. Maji, A K. and Sahu, R. Acoustic Emissions From Reinforced Concrete. *Experimental Mechanics*, 1994, 34. 379-388.
4. J.Coughlin and R.Kranz. New Approaches to Studying Rock Burst-associated Seismicity in Mines. *Rock Mechanics as a Multidisciplinary Science*, 1991, 491-500.
5. Peter Styles. Implications of Harmonic-tremor Precursory Events for The Mechanism of Coal and Gas Outbursts. *Rockbursts and Seismicity in Mines*, 1993, 415-421.
6. Zhao, X.D., Li, Y.H., Yuan, R.F. etal. Study on Crack Dynamic Propagation Process of Rock Samples Based on Acoustic Emission Location. *Chinese Journal of Rock Mechanics and Engineering*, 2007, 26(5).944-950.
7. Zhao, X.D., Li, Y.H., Liu J.P., etal. Study on Rock Failure Process Based on Acoustic Emission and Its Location Technique. *Chinese Journal of Rock Mechanics and Engineering*, 2008, 27(5).990-996..
8. Zhao, X.D., Liu, J.P., Li, Y.H., etal. Experimental Verification of rock Locating Technique with Acoustic Emission . *Chinese Journal of Geotechnical Engineering*, 2008, 30(10).1472-1476.
9. Zang, Y.P. Rock-mass Acoustic Emission and Micro-seismic Monitoring and Localizing Technology and Its Application . *Engineering Blasting*, 2002, 8(1).58-61.

STUDY ON ROCKBURST PREDICTION AND STABILITY EVALUATION FOR LARGE CAVERN GROUP UNDER HIGH GEOSTRESS CONDITIONS

GUO-SHAO SU, XING-YI FU and LIU-BIN YAN

School of Civil and Architecture Engineering, Guangxi University

Nanning, 530004, P.R. China

XIA-TING FENG and QUAN JIANG

*State Key laboratory of Geomechanics and Engineering, Institute of Rock and Soli Mechanics, Chinese Academy
of Science, Wuhan, 430071, P.R. China*

Rockburst hazard has become a headache problem for safe excavation of the large caverns groups under high geostress conditions. In this paper, based on elasto-brittle-plastic constitutive model, a novel rockburst index, namely Local Energy Release Rate (LERR), is proposed. By using the new index, the intension of rockburst, the position and extent of brittle failure zone can be predicted quantitatively during rockmass excavations under high geostress conditions. Furthermore, a new comprehensive stability evaluative index including LERR rockburst index, damage degree index, rockfall risk index, failure status index, displacement index, is proposed for the stability comprehensive evaluation of surrounding rock masses under high geostress conditions. Analytic hierarchy process method based on experience of expert group is applied to achieve the comprehensive index. Finally, the comprehensive index is applied in stability analysis and risk prediction for the excavating and supporting process of the large underground cavern groups of Shuangjiangkou Hydropower Station. The research results have been accepted as the important guidance for rational design and safe construction of the project.

1 Introduction

In line with the realization of the great development strategy of the Western China, a great number of large hydropower stations in plans or under construction to meet the need of the west-east electricity transfer project. To accommodate new underground hydropower plants, many super-large underground cavern groups are designed for most of these hydropower stations. Rockburst hazard has become a frustrating problem for the safe excavation of the large caverns groups under high geostress environments in western China. Therefore, it is very necessary to study rockburst prediction and safety evaluation for large underground caverns under high geostress conditions.

A reasonable index is needed to appraise potential failure of the surrounding rocks of the large cavern group in brittle rocks in high stress conditions, catching intrinsic essence of brittle rock masses in high stress conditions. Cook et al. [1] proposed an index, called the energy release rate (ERR), to study rockburst problems in South African gold mines. It indicated that frequency of rock burst occurrence and its intensity are related to loss and the energy release rate induced by underground mining. After that, more efforts were put towards the energy index study to analyze the conditions of rock burst occurrence by using numerical analysis. Several indexes have been proposed, such as the elastic energy index, impact energy index, energy dissipation index, effective energy release rate, etc. [2-3]. However, it shall be pointed out that some indexes reflect the dynamic stress effect generated instantaneously during the excavation of rock masses based on analysis of linear elastic theory which considers rock mass as a linear elastic body without influence of geological structures. Failure of

rock mass and its induced stress re-distribution are not considered in these indexes. These indexes are useful to judge the possibility of rock burst occurrence, but it is not easy to estimate whether the location and depth of rock burst occurrence in rock masses. Therefore, a new index is needed for the point of energy release to estimate the possibility, intensity and location of rockburst occurrence.

Aiming at the unique mechanics behavior of hard rock mass under high geostress conditions, a novel index for rockburst prediction and new integrated safety indexes for the stability evaluation of surrounding rock mass of large caverns are proposed.

2 A New Index to Predict Rockburst

Unstable and failure of brittle rocks occur due to sudden release of energy with high intensity in rocks under high stress conditions when stress in surrounding rock is larger than its strength. Rock bursts at most of caverns and tunnels under high rock stress conditions in China are revealed in strain-type. It refers to strength of rock masses decrease suddenly when the stress state is converted from three dimensions to two dimensions due to excavation of underground projects and elastic strain energy stored in rock mass excess its maximum capability of energy storage. It results sudden release of high intensity of energy stored in rock mass. The released energy is not only to induce continuous failure of rock mass but also to generate dynamic energy for the crashed rocks. It is still difficult to understand clearly of release and dissipation rules of energy stored at brittle rock mass after peak load under high stress conditions. However, it is generally known that more release of elastic energy in local rock mass and larger possibility of rockburst occurrence and larger rock failure extent and dynamic energy.

In order to quantitatively analyze intensity of strain-type rockburst, a new index, local energy release rate, $LERR$, is proposed. That means, during excavation of caverns, sudden release of energy stored in rock mass per volume when strain energy centralized in local area of surrounding rocks is larger than its limit capacity. The index is an approximate representation of energy released of rock mass per volume at brittle failure and can be considered as a quantitative index of rock bursts risk assessment. The index can be calculated using numerical analysis to trace entire change process of elastic energy intensity of rock masses using elastic-brittle-plastic model. It records the difference of energy stored at rock mass before and after brittle failure, i.e., local energy release rate of the elements. It ignores small energy release of the elements generated due to non-brittle failure. The formula can be written by:

$$LERR_i = U_{i \max} - U_{i \min} \quad (1)$$

In which, $LERR_i$ is local energy release rate of the i^{th} element. $U_{i \max}$ and $U_{i \min}$ are peak and lowest value of elastic strain energy intensity before and after brittle failure occurrence at the i^{th} element respectively. V_i is volume of the i^{th} element.

$$U_{i \max} = [\sigma_1^2 + \sigma_2^2 + \sigma_3^2 - 2\nu(\sigma_1\sigma_2 + \sigma_2\sigma_3 + \sigma_1\sigma_3)]/2E \quad (2)$$

$$U_{i \min} = [\sigma_1'^2 + \sigma_2'^2 + \sigma_3'^2 - 2\nu(\sigma_1'\sigma_2' + \sigma_2'\sigma_3' + \sigma_1'\sigma_3')]/2E \quad (3)$$

where, $\sigma_1, \sigma_2, \sigma_3$ are three principal stresses corresponding to peak strain energy of the element. $\sigma_1', \sigma_2', \sigma_3'$ are three principal stresses corresponding to the lowest strain energy of the element. ν is Poisson's ratio and E is Young's modulus.

Calculation of the local energy release rate is carried out by tracing dynamic evolutionary process of energy in the elements revealing elastic-brittle-plastic behaviour, such as, concentration, release, transfer and dissipation of energy. It considers influence of stress path and its change induced by excavation on energy

concentration and release process. Therefore, the index can directly reflect the conditions that different limited energy storage capacity of rock mass with different stress status in rock mass. When carry out the LERR using numerical method, we suggest adopting cohesion weakening and frictional strengthening (CWFS) constitutive model, an elasto-brittle-plastic constitutive model for hard and brittle rock mass [4-5].

2.1 Case Study

A circular tunnel is 46 m in length, 3.5 m in diameter and 420 m in depth in Canada [6]. The measured rock stress are $\sigma_1=60\text{MPa}$, $\sigma_2=45\text{MPa}$ and $\sigma_3=11\text{MPa}$. Mechanical parameters of Lac du Bonnet granite are listed in Table 1. The tunnel had occurrence of brittle failure during excavation (Figure 1(a)). If self-gravity of scrap rock blocks on floor of the circular tunnel were ignored, distribution of failure zone at floor and top of tunnel is symmetrical.

Figure 1(b) shows that the location of brittle failure area analyzed from the LERR index is good in agreement with the actual one.

Table 1 Mechanical parameters of Lac du Bonnet granite

Peak value of cohesion [MPa]	Residual cohesion [MPa]	Initial friction angle [°]	Peak value of friction [°]	Tensile strength [MPa]	Young' modulus [MPa]	Possion's ratio	Shear-extension angle [°]
50	15	0	48	10	60	0.25	30

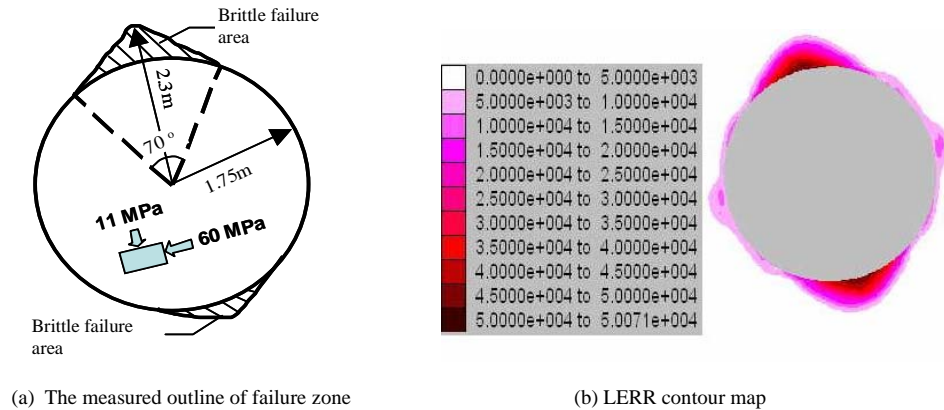


Figure 1. Rockburst prediction for Mine-by tunnel

3 A Comprehensive Evaluative Index

A new comprehensive stability evaluative index based on LERR (rockburst index), Failure Approach index [7] (damage degree index), potential energy of failure zone (rockfall risk index), failure zone and displacement is proposed for stability analysis at underground caverns under high geostress condition in order to overcome the limitation of tradition stability evaluative index on predicting multi failure mode of surrounding rocks of caverns under high geostress condition.

Analytic Hierarchy Process (AHP) method [8] according to the different viewpoint and experience from expert group is applied to build the comprehensive evaluative index.

3.1 Case study

The same case as section 2.1 is studied. Firstly, we invite expert group to mark the importance of different index. According to AHP principle, the judgement matrix of the understratum index is shown in Figure 2, where, a_1 is

LERR, a_2 is failure approach index, a_3 is potential energy of failure zone, a_4 is failure zone and a_5 is displacement. In judgement matrix, $[a_{ij}, b_{ij}]$ indicate interval estimation of comparing between i^{th} index and j^{th} index according to the i^{th} expert. Then, using AHP method, we can obtain the reasonable weighing of each index as shown in Table 3. Moreover, nondimensionalization are carried out for each index. The value of each index is mapped to the bound $[1, 100]$. Finally, the comprehensive index is obtained by comprehensive weighted score. In comprehensive index, 1 represent minimum degree of stability, and 100 represent maximum degree of stability.

	a_1	a_2	a_3	a_4	a_5
a_1	[1,1]	[1,3]	[3,5]	[3,5]	[1,3]
a_2	[1/3,1]	[1,1]	[3,5]	[3,5]	[1,3]
a_3	[1/5,1/3]	[1/5,1/3]	[1,1]	[1,3]	[3,5]
a_4	[1/5,1/3]	[1/5,1/3]	[1/3,1]	[1,1]	[3,5]
a_5	[1/3,1]	[1/3,1]	[1/5,1/3]	[1/5,3]	[1,1]

Figure.2 The judgement matrix of the understratum index of AHP method

Table 2 The weighing of different index

Index	a_1	a_2	a_3	a_4	a_5
Weighing	0.3350	0.2754	0.1307	0.1168	0.1421

Contour map of different index and comprehensive index for Mine-by tunnel is shown in Figure 3. According to comprehensive index, we can straightforwardly and concisely predict the degree of stability of surrounding rock mass of the tunnel without multi-index analysis. In addition, it is more important that the comprehensive index can provide more reasonable evaluation index for stability analysis of surrounding rock mass under multi failure mode condition.

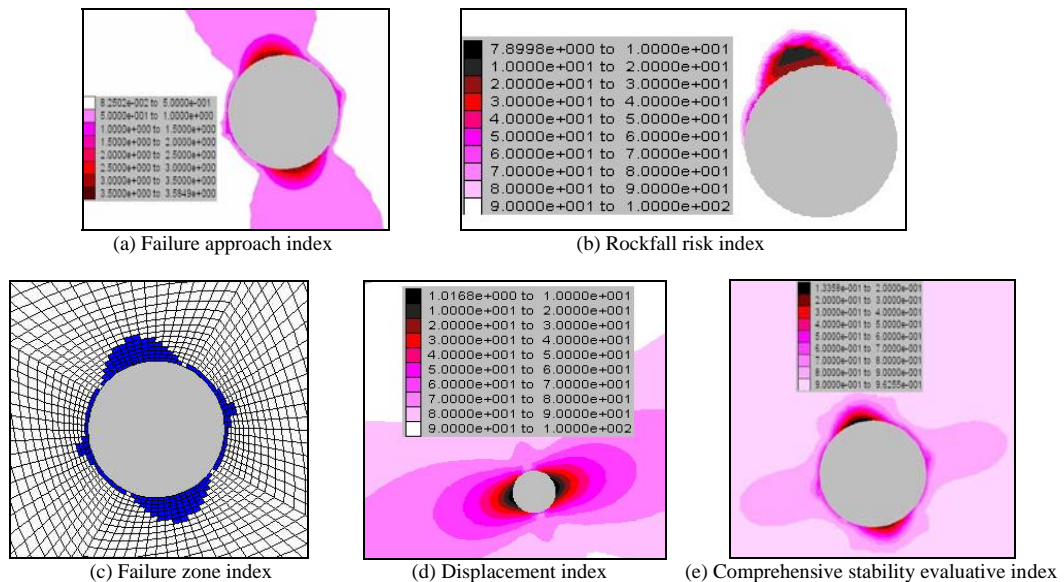


Figure 3. Contour map of different index and comprehensive stability evaluative index of Mine-by tunnel.

4 Application Study

Shuangjiangkou hydropower station locates in the Sichuan Province, Western of China. Its underground hydraulic powerhouse, consists of main powerhouse, auxiliary powerhouse, main transformation cavern, surge chamber and tailwater tunnel (Figure 4). The size of main powerhouse is 116.6×18×25.2 meters in length, width and height. The main transformation cavern, excavation size of 141.6×20×34.7 meters is at downstream side of and parallel to the main powerhouse and connected to the main powerhouse through the busbar channel. Excavation scheme of underground powerhouses is shown in Figure 4(b). We use the numerical method to simulate the overall excavating and supporting process of the cavern groups.

It is granite in the area of the underground powerhouse. Granite is high in strength, hard and compact. The underground powerhouse cavern groups are located in high stress field. The three dimensional geo-stress measurements indicate that the maximal principle stress is 28-32 MPa. Mechanical parameters of rock mass are shown in Table 3.

Some results are shown in Figure 5.

Table 3 Mechanical parameters of granite

Peak value of cohesion [MPa]	Residual cohesion [MPa]	Initial friction angle [°]	Peak value of friction [°]	Tensile strength [MPa]	Young' modulus [GPa]	Possion's ratio
1.8	0.2	0	55	1.0	15	0.2

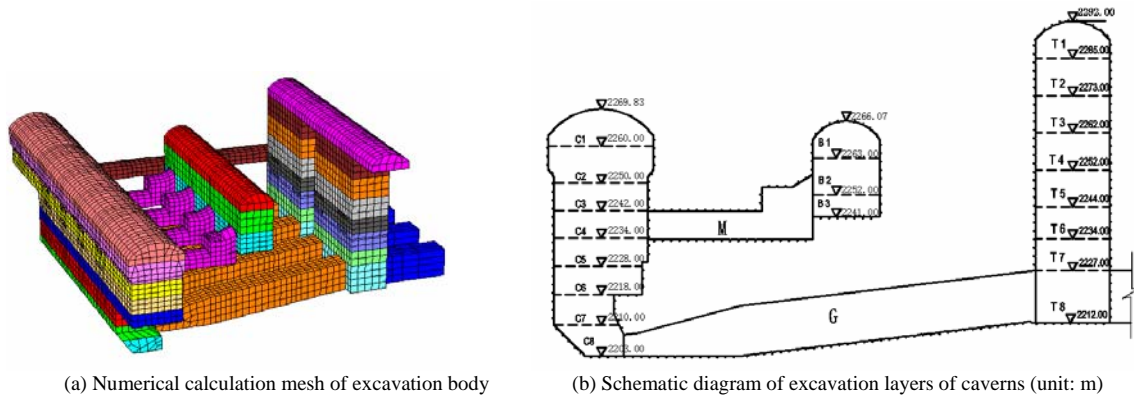


Figure 4. Numerical calculation mesh and excavation scheme of underground powerhouses

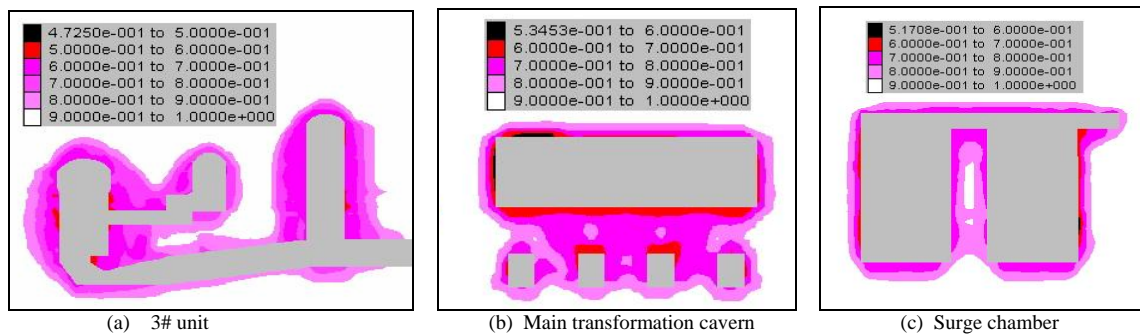


Figure 5. Contour maps of the comprehensive stability evaluative index at various cross-sections of powerhouses

The results indicate that comprehensive stability index is rather low at upstream sidewall and downstream sidewall of main powerhouse, roof of main powerhouse, left sidewall of main powerhouse, upstream sidewall and downstream sidewall of surge chamber, left sidewall and right sidewall of surge chamber, roof of tailwater tunnel of 2[#] and 3[#] unit, and intersections of different caverns. So, the part mentioned above must strengthen the support in order to keep stability of surrounding rock mass. The degree of strength can be determined by different value of comprehensive stability index at different position of surrounding rock mass.

The comprehensive index not only can provide more reasonable appraise index for stability analysis surrounding rock mass under multi failure mode condition, but also can offer great convenience especially for constructors and proprietors without necessary professional knowledge of rock mechanics and rock engineering. The results had been adopted as important guidance for rational design and safe construction of the project.

5 Conclusions and Future Work

The stability evaluation of large cavern groups in brittle rocks under high geostress condition is a complicated and unsolved problem. In this paper, a rockburst index, LERR, is proposed based on numerical analysis using a nonlinear elastic-brittle-plastic model to predict the risk of rockburst occurrence. Furthermore, a new comprehensive stability evaluative index including the LERR index, damage degree index, rockfall risk index, failure degree index and displacement index of the surrounding rock mass is proposed using the AHP method for the stability analysis of surrounding rock mass under high geostress conditions. The results of the study indicate that the feasibility of the LERR index and the comprehensive stability evaluative index can overcome the limitations of the traditional stability evaluative index on predicting multi failure modes of the surrounding rock mass of large caverns under high geostress conditions. This can give more a reasonable evaluation index and offer great help, especially for decision makers, without necessary professional knowledge of rock mechanics to make strategic decisions for reasonable design and safe construction. Future work will be focused on improving the comprehensive stability evaluative index through the consideration of a more evaluative index, such as safety index of support structure.

Acknowledgements

This work is supported by National Natural Science Foundation of China under Grant No. 50809017 and Postdoctor Foundation of China under Grant No. 20080440812.

References

1. Cook, N.G.W., Hoek, E., Pretorius, J.P.G., et al. Rock mechanics applied to the study of rockbursts. *Journal of the South African Institute of Mining and Metallurgy*, 1966, 66(10). 436-528.
2. Kaiser, P.K., Tannant, D.D., McCreath, D.R. *Canadian Rockburst Support Handbook*. Geomechanics Research Centre, 1996.
3. Xie, H.P., Peng, R.D., Ju, Y., et al. Study On Energy analysis of rock failure. *Chinese Journal of Rock Mechanics and Engineering*, 2005, 24(15). 2603-2608.
4. Hajiabdolmajid, V., Kaiser P.K. and Martin, C.D. Modelling brittle failure of rock, *International Journal of Rock Mechanics & Mining Sciences*, 2002, 39. 731-741.
5. Su, G.S. and Feng, X.T. Parameter identification of constitutive model for hard rock under high situ stress condition using particle swarm optimization algorithm. *Chinese Journal of Rock Mechanics and Engineering*, 2005, 24(17). 3030-3034.
6. Hajiabdolmajid, V. and Kaiser, P.K. Brittleness of rock and stability assessment in hard rock tunnelling. *Tunnelling and Underground Space Technology*, 2003, 18. 35-48.
7. Zhang, C.Q., Zhou, H. and Feng, X.T. Stability Assessment of Rockmass Engineering Based on Failure Approach Index. *Rock and Soil Mechanics*, 2007, 28 (5). 888-894.
8. Xu, S.B. *Principium of the Analytic Hierarchy process*. Tianjin University Press, 1988.

EXPERIENCE OF LOCALIZATION AND PREVENTION OF ROCK BURSTS IN UNDERGROUND IRON-ORE MINING IN GORNAYA SHORIA

ANDREY EREMENKO, VICTOR SERYAKOV and VITALY EREMENKO

Institute of Mining, Siberian Branch, Russian Academy of Sciences

54 Krasny Prospect, Novosibirsk 630091, Russia

GARRY MONINGER, VLADIMIR FILLIPOV and IRINA GROMOVA

EVRAZRUDA Joint-Stock Company

Novokuznetsk, Russia

Based on the analysis of geotechnical and geomechanical conditions of mining closely occurring ore bodies, it has been decided to choose the optimum variant of stoping and to carry out confined blasting in stress concentration areas with the aim of preventing rockbursting. Efficiency of the solutions has been shown.

1 Introduction

High tectonic stresses feature iron ore mining in Siberia. Large-scale blasting in this seismically active area generates critical stresses, and elastic strain energy releases in the form of shocks and rock bursts. All mines are under continuous geomechanical control that involves geoelectric prospecting, horizontal and vertical benchmarking, driving relieve slots. This allows detecting areas of potential hazard and selecting the related precautions.

Large depths where ore bodies occur set rigid conditions for mining. Stopping is carried out from the centre of an ore body towards its periphery, by longwalling with confined blasting. Stopping schedule and geometry of a stope and mined-out space are chosen so that to eliminate ultimate stress zone formation, minimize open mined-out space, minimize fissuring of the rock mass in front of stopping, optimize the width of stopes and other dimensions of technological elements.

The most complex and nonstandard geomechanical conditions are in the area where neighbouring ore body districts are mined. Sometimes stopping fronts are advanced towards one the other, to a diminishing pillar between the mining districts. This requires new engineering solutions on prevention of probable rockburst hazard.

2. Case study

2.1 Description of the deposit

We analyzed some approaches to solving the indicated above problem in terms of Sheregesh iron-ore deposit. It occurs in the seismically active Altai-Sayan folded zone where tectonic movements of the earth crust are currently observed. Depth of mining ranges from 300 to 600 m. Ore and host rocks are characterized by brittle fracture and can accumulate high elastic strain energy. Balmstones and spalling are observed at 300 m depth, while sudden rockbursting, shocks and microshocks are met deeper. Ore-bearing zone has sublatitudinal strike

and is more than 2 km long. Host rocks are skarns, albitophyre, porphyrites, syenites, marmorized limestones and granites. Lenticular ore bodies have steep dip and are 2 to 100 m thick [2].

The ore-bearing zone is broken down into seven mining districts. Mining covers six levels (from +525 to +115 m), production mining has reached the depth of 470 m and development mining is carried out at -600 m (refer to Figure 1). Ore production totals 2 to 4.5 Mt per annum.

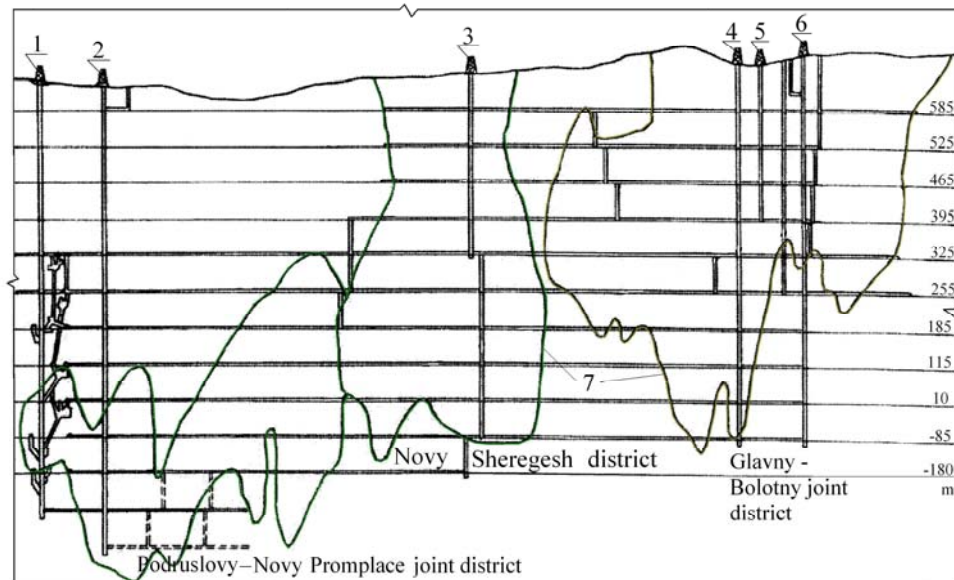


Figure 1. Sheregesh deposit, mining districts, longitudinal section

2.2 Mining advance and stress state

Under stoping in district Glavny, strong microshocks (energy class 6.3 and 9.4) took place at level +325÷+255 m. Failure zones, floor quelling, rail hoisting were observed in mine workings. Based on that, this part of the ore body and host rocks was referred to rockburst-hazardous.

The discussed area lies below +325 m, at the junction of districts Glavny and Bolotny, where mining is carried out in the conditions of the highest geomechanical complexity. In one of these districts, stoping advances from the junction point, whereas it is head towards the junction point in the other district. Thus, a pillar is formed between the districts. At a certain span in the junction area, overburden pressure zones in the mined-out spaces overlap.

Figure 2 illustrates ore extraction in districts Glavny and Bolotny. Blocks No. 8 to 10 are extracted in district Bolotny, and blocks No. 17 to 24 are mined out in district Glavny, where ore removal is carried out from block No. 16. Stopping advance entails the increased rock pressure around stopes and higher stress concentration in the periphery of the rock mass. In the zone where district Glavny and Bolotny are located, σ_2 is 1.4-1.7 γH and σ_3 is -2.8 to -3.0 γH (γ is overlying rock weight, H is depth below surface), and average mining depth at level 255-325 m is 410 to 430 m. Taking this into account, we have that $\sigma_2 \sim 20$ MPa and $\sigma_3 \sim 40$ MPa (σ_1 equals γH) in the intact rock mass. Stresses in the concentration zones can exceed initial values several times and reach the ultimate rock strength [1]. When stoping reaches the margin blocks in district Glavny, a rock pillar will be formed between these blocks and blocks No. 8-10 in district Bolotny, this pillar will undergo the ultimate stress state.

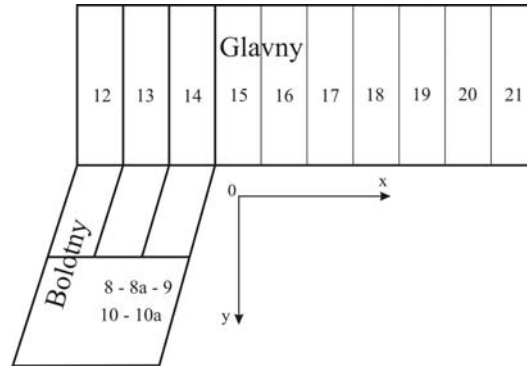


Figure 2. Districts Glavny and Bolotny, stoping blocks

2.3 Selection of mining scheme

Admissible mining schemes were chosen based on the evaluation of rock stresses in the area of stoping by using the finite element method and algorithms for sequence mined-out space forming [4]. Since stresses are predominantly affected by the horizontal tectonic forces, we considered a 2D model of deformation of the rock mass near mined-out space; the calculation scheme was based on the plan of level 255 m.

Axes H and Y are directed so that σ_x and σ_y match σ_2 and σ_3 , respectively. Initial stress state was set as follows: $\sigma_x = -36$ MPa, $\sigma_y = -20$ MPa. Dimension of the calculation domain was chosen such that mined-out spaces have no influence on the initial stress state of the rock mass near the calculation domain boundaries. It is supposed that brittle host rocks and ore behave elastically under deformation.

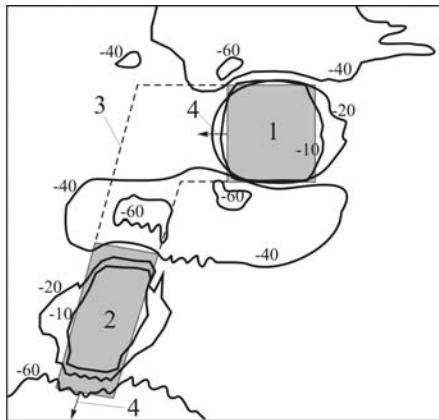


Figure 3. Distribution of principal compression stress at level 255-325 m: 1 and 2 — mined-out spaces in districts Glavny and Bolotny, respectively; 3 — ore pillar boundary. 4 — stoping advance; -10 - -60 — stress values, MPa

Based on the experimental studies at the Sheregesh deposit [3], we accepted $E=90000$ and 75000 MPa, $\nu=0.29$ and 0.25 for the ore and host rocks, respectively. Caved rocks are modelled by a material with $E=18000$ MPa and $\nu=0.45$. The stress state analysis was focused on the stress distribution in the pillar between districts Glavny and Bolotny, and in the area of the current stoping block. Figure 3 describes the stress state character in the mentioned areas. Here, isolines of σ_3 are shown for the situation when depletion is completed in blocks N. 17-21 in district Glavny and in blocks No. 8-10 in district Bolotny.

The highest concentration of σ_3 is observed in the pillar between the mined-out spaces. The calculation of

stresses for the ongoing stoping in district Glavny (blocks No. 16 and 15, Figure 2) showed that the compression stresses increase in the intact part of the ore body between the discussed mining districts, while stresses in the centre of the block prepared for stoping are insignificant. This is a consequence of the chosen stoping direction in district Glavny so that to match the maximum compression stress direction: the lager is mined-out space, the lower are stresses σ_2 and σ_3 in the area of the current stoping block.

2.4 Blasting

The revealed features of stress distribution allow recommending a variant of ore breaking by vertical concentrated charges. Based on the experience of using vertical concentrated charges at other deposits, it is possible to control explosion energy when mining with block caving by the joint application of multi-row beam contiguous charges and vertical concentrated charges. The advantage of this scheme is a joint effect of the charges of both types on lowering the dynamic action on the surrounding rock mass and on the rock fragmentation quality [1]. The developed blasting scheme for level 255-325 m in district Glavny and the arrangement of beam contiguous and vertical concentrated charges is demonstrated in Figure 4.

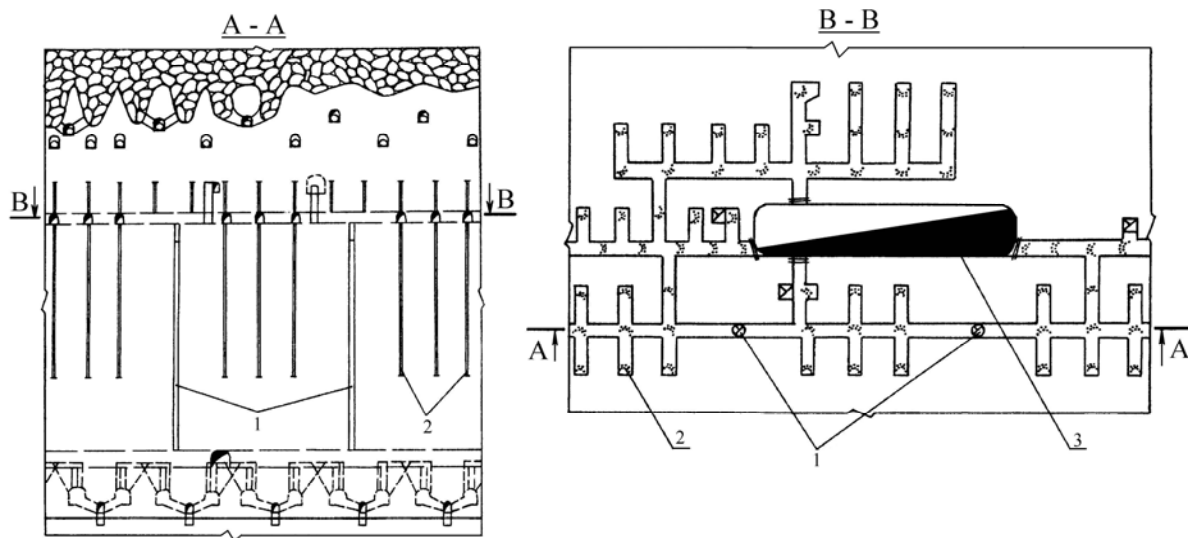


Figure 4. Blasting in district Glavny, level 255-325 m: 1 – vertical concentrated charges; 2 – beam contiguous charges; 3 – compensatory chamber

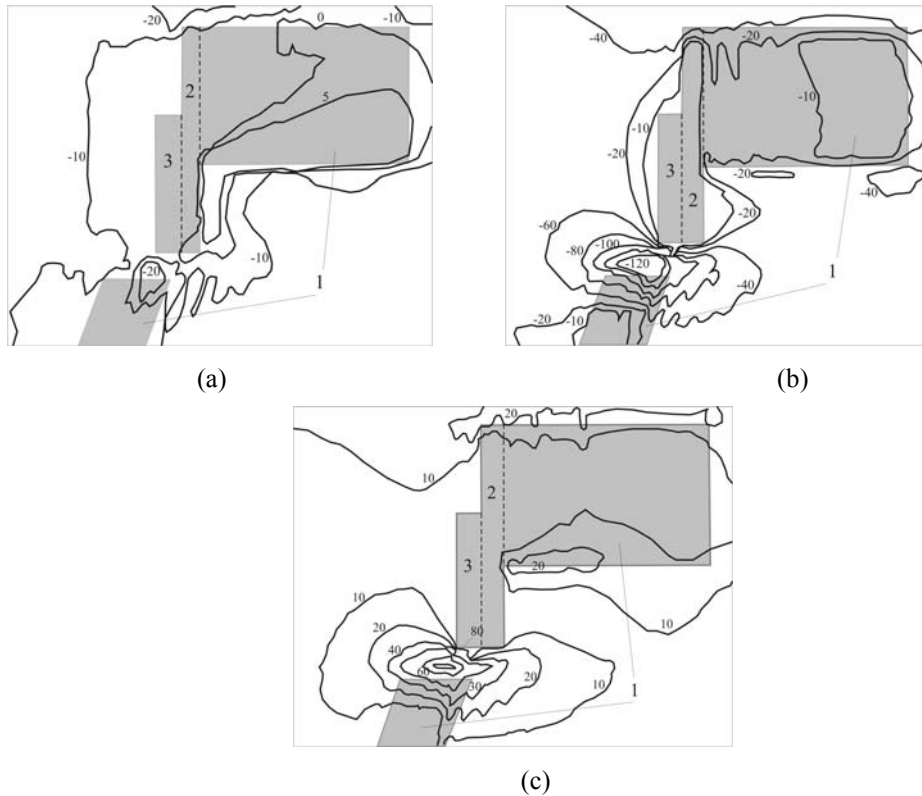
First the beam contiguous charges are blasted. This generates free surfaces around the vertical concentrated charges, which improves rock fragmentation and decreases effect of the vertical concentrated charge blasting on the surrounding rock mass.

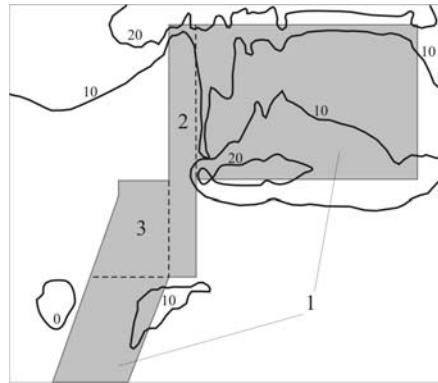
With using this scheme, blocks No. 21 to 15 in district Glavny were extracted. Due to the higher compression stresses in the area of blocks No. 14 to 12 in the ore pillar formed between districts Glavny and Bolotny, block No. 14 extraction was split into three stages. Stage I caving decreased the compression stresses in the non-caved part of block No. 14. Stages II and III stoping resulted in no high dynamic events. But diminishing of the ore pillar, caused by block No. 14 depletion, generated even higher compression stresses in the pillar.

After depleting block No. 14, stoping may follow two alternative ways: (I) breaking in block No. 13, then breaking in block No. 12; (II) breaking in a part of blocks No. 14 and 12 near the caved rocks, then breaking in the remaining part of blocks No. 13 and 12. To choose the optimum variant, we evaluated the stress state in

either. Figure 5 illustrates geomechanical situation for variant I. It is seen that after breaking in block No. 13, the compression and shear stresses grow near the ore pillar, whereas σ_2 is -220 MPa, that is nearly by 50% higher. Figure 6 describes stress distribution for variant II. We see that the ore body and host rocks in the area of stoping (a) and development working (b) are free from the high normal and shear stresses.

Based on the calculation results, the stopping variant II was chosen for the extraction of the ore pillar at level 255-325 m. Alongside with that, in order to prevent from rock pressure manifestation and to decrease the stress state in the area of the ore pillar, it was decided to make a fan of relief blastholes between caved rocks in districts Glavny and Bolotny. The blastholes were drilled in ventilation drift at level +255 m. The relief blastholes were blasted all at once, explosive weight was 9970 kg.





(c)

Figure 6. Distribution of stresses σ_1 (a), σ_2 (b) and τ_{\max} (c) after the first stage breaking in blocks No. 13 and 12 (MPa); 1 — mined-out space; 2 — block No. 14; 3 — extracted ore pillar (part of blocks No. 12 and 13) between Glavny and Bolotny districts

After the relief blasting, no blast-generated shocks had been recorded for three months. The first stage depletion of blocks No. 13 and 12 unloaded the ore pillar, and the follow-up development mining in the remaining part of these blocks was conducted under undisturbed geomechanical conditions.

Later mining in the vicinity of the ore pillar proved the validity of the accepted engineering solutions. Analyzing consequences of a strong dynamic event (energy class 8.7) occurred in the host rocks near the ore pillar showed that the blast-formed cavity prevented from the rock pressure zone migration into the area of actual stoping and from the mine working damage.

3. Conclusion

When mining is carried out at great depths, where compression stresses are higher, and mining and blasting activities cause various-extensive dynamic events, it is possible to improve mining safety by pre-evaluating the stress state via numerical modelling and, based on the latter, scheduling the stoping and designing the technological elements.

References

1. Ermak, G., Control of the Shattering Effect Produced by Combined Charges on Large-Scale Ore Caving (Novosibirsk, 2001).
2. Kurlenya, M., Eremenko, A., and Shrepp, B., Geomechanical Problems of Iron-Ore Mining in Siberia. Nauka (Novosibirsk, 2001).
3. Recommendations on Safe Mining at Rockburst-Hazardous Deposits in Gornaya Shoria. VostNIGRI (Novokuznetsk, 1991).
4. Seryakov, V., Influence of mining schedule on stress redistribution in a rock mass. in Proceedings of International Geodynamics and Stress State of the Earth's Interior Conference (Novosibirsk, 1999).

RESEARCH OF GROUND VIBRATION IN DEMOLISHING BUILDINGS BY BLASTING

ZE-PEI XU and XI-BING LI

School of Resources and Safety, Central South University, Changsha, 410083, P.R. China

CONG-SHI WU and TONG-HUA LING

*School of Civil Engineering and Architecture, Changsha University of Science and Technology
Changsha, 410004, P.R. China*

Based on the resemblance between the course of the building colliding with earth in blast demolition and the course of bullet penetrating a target, the model of colliding is set up with the theory of bullet intruding a target, and the differential equation deduced by the Cylindrical Cavity-Expansion Theory (CCET). The vertical and horizontal displacement of the site at the time of the quake is calculated with the colliding theory. Onward, when the colliding force to earth is compared to the hemi-sine pulse load, the quaked velocity of the load can be derived. It proves that the theory and the method of using the CCET on a collision course is suitable and has a preferably applied foreground.

1 Introduction

Presently, during the rebuilding and expansion of buildings in the city, old buildings are generally demolished by blasting. However, the collapse of the demolished building will induce ground vibration. Many project examples indicate that the ground vibrations can endanger nearby buildings and other construction. The research of earthquake and blasting vibration is carried out in some extent, but the ground vibration in demolishing building by blasting [1,2] is very rare. With the increase of demolishing building by blasting in the city, the danger of ground vibration is being paid more and more attention [3]. Therefore, the qualitative and academic research is pressing required to make the demolition more scientific and exact.

2 To Set up the Model of Collision

Because the course of the demolished building colliding with earth is very complex, the normal theory cannot be used in the research. On the basis of the resemblance between the course of the blasted building colliding with earth and the course of a bullet penetrating target [4], the Cylindrical Cavity-Expansion Theory (CCET) is used in studying the collision course. Due to the fact that the mass of the demolished building is excessively heavier than that of bullet, and the collision velocity of the demolished building is excessively smaller than that of the bullet, and the CCET must be modified to solve the practical problem of ground vibration in demolishing buildings by blasting.

Considering the CCET and the characteristic of collision in blasting demolishing building [5,6,7,8], the model of collision is set up, as in figure 1. R is radius of the section that the building penetrated the horizontal level, r is radius of the range that the ground moves at the time t , and r^* is radius of the wave array level. On the supposition that:

(a) The collapsed building by blasting falls freely and collides ground. (b) The demolished building is global rigid and dispersed mass, and the ground is symmetrical, seriate and isotropy semi-infinite elastic body [9,10,11]. (c) The building collides with the ground vertically, and it always contacts the ground during the penetrating course, even it is not off the ground at the end of it. (d) As the target, the particles of ground move

horizontally in the ground level, that is to say, the particles of the ground move vertically to the colliding direction during the penetrating course. For the above supposition, the process of colliding ground of the demolished building can be regarded as in one dimension, so the stress, the displacement, the velocity and the acceleration of ground can be calculated with the theory of elasticity space.

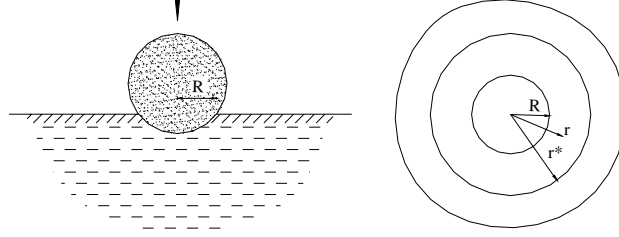


Figure1 The model of colliding

3 The Application of Cylindrical Cavity-Expansion Theory

Due to freely falling, the demolished building collides with ground with the velocity V_0 , at zero time ($t=0$). And then a cave is produced in the earth, which is like Ball-crown shape. Radial displacement of the cave wall is $u(0,t)=R(t)$, at a time t , as in figure 2.

$$R(t) = \sqrt{2Az - z^2} \quad (z < A) \quad (1)$$

In the equation (1): A is the radius of the global body of demolished building, and z is the depth caved by colliding that is less than the radius. The colliding course is completed instantaneously.

With the CCET it is deduced that:

$$F_z = 2\pi\{\rho_0 B_1 \frac{(A-z)^2 \dot{z}^2}{2} + \rho_0 B_2 [\frac{(A-z)^2 \dot{z}^2}{6} + \frac{A\ddot{z} - z\ddot{z} - \dot{z}^2}{3} (2Az - z^2)] + B_3 \frac{2Az - z^2}{2}\} \quad (2)$$

In the equation (2): F_z is vertical stress quantity during colliding, as in figure3. ρ_0 is primary instantaneous density of ground element.

$$B_1 = [\eta^* + (1-\eta^*)\xi^2]^{-\frac{\nu}{2}} - \frac{[\eta^* + (1-\eta^*)\xi^2]^{-\frac{\nu}{2}} - [\eta^* + (1-\eta^*)\xi^2]^{-1}}{(2-\nu)(1-\eta^*)} \eta^*$$

$$B_2 = \frac{[\eta^* + (1-\eta^*)\xi^2]^{-\frac{\nu}{2}} - 1}{\nu(1-\eta^*)}, \quad B_3 = \frac{\tau_0}{\lambda} \{[\eta^* + (1-\eta^*)\xi^2]^{-\frac{\nu}{2}} - 1\}, \quad \xi = \frac{r}{r^*}, \quad \nu \neq 0, \nu \neq 2, \eta^* = 1 - \rho_0/\rho^*$$

Where the quantities of wave front are distinguished from others with ‘*’.

With the Second Newton’s Law, the movement equation of fallen building is:

$$m\ddot{z} = F_z - mg \quad (3)$$

Put equation (2) into (3), and equation (3) becomes:

$$m\ddot{z} = 2\pi\{\rho_0 B_1 \frac{(A-z)^2 \dot{z}^2}{2} + \rho_0 B_2 [\frac{(A-z)^2 \dot{z}^2}{6} + \frac{A\ddot{z} - z\ddot{z} - \dot{z}^2}{3} (2Az - z^2)] + B_3 \frac{2Az - z^2}{2}\} - mg \quad (4)$$

Equation (4) is not general differential equation, and its primarily condition is:

$$t=0, \quad V = \dot{z} = V_0, \quad z=0 \quad (5)$$

With the numerical solution, the maximal colliding force F_{max} can be obtained.

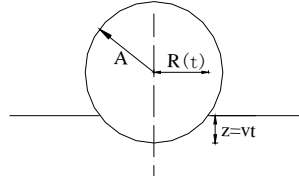


Figure2 The ball-crown cave

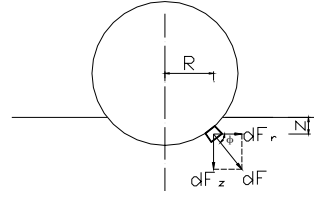


Figure3 The colliding stress in geometry

4 The Ground Vibration due to Colliding

At a time t and on the surface of semi-infinite elastic earth, there is a uniform load $q(t)$ acting on the area whose radius is r_0 . At a point M out of the area, the vertical displacement is w and the horizontal one is u . The w and u can be obtained by integrating the results that the central force acts on the surface semi-infinite elastic body with the symmetry semi-infinite theory, as in figure 4. That is:

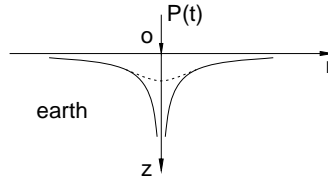


Figure 4 The result of central force acting on the surface of semi-infinite elastic body

$$w = \frac{(1 - \mu^2)P(t)}{\pi E r} \quad (6)$$

$$u = -\frac{(1 + \mu)(1 - 2\mu)P(t)}{2\pi E r} \quad (7)$$

In equation (6) and (7): $P(t)$ is central force at a time t . r is the distance between the point M and the acting point of force. E is modulus of elasticity. μ is Poisson's ratio.

From equation (6) and (7), when $r \rightarrow 0$, w and u will be infinite, that is to say, equation (6) and (7) is not adapted to the acting point of central force, and the result is applicable on the place out of the area around acting point of central force. The actual displacement in the area is shown with dashed, as in figure 4. The uniform load $q(t)$ acting on the surface of semi-infinite elastic earth, as in figure 5, is discussed as follows. In the coordinate plane that is vertical to z axis, two radials which corner $d\phi$ are made from point M , and two arcs whose radii are respectively l and $l+dl$ are made around point M . The two radials and the two arcs make up an element whose area is dA , $dA = ldl d\phi$. The resultant force of the uniform load acting on dA is;

$$dp(t) = q(t)dA = q(t)l d\ell d\phi \quad (8)$$

If the resultant force acting on dA is regarded as the central force $dp(t)$, the vertical displacement $dw(t)$ and the horizontal one $du(t)$ under the central force $dp(t)$ are:

$$dw(t) = \frac{1 - \mu^2}{\pi E} \cdot \frac{dp(t)}{\ell} \quad (9)$$

$$du(t) = -\frac{(1 + \mu)(1 - 2\mu)}{2\pi E} \cdot \frac{dp(t)}{\ell} \quad (10)$$

Equation (8) is put into the above equations, then

$$dw(t) = \frac{1-\mu^2}{\pi E} q(t) d\ell d\varphi \quad (11)$$

$$du(t) = -\frac{(1+\mu)(1-2\mu)}{2\pi E} q(t) d\ell d\varphi \quad (12)$$

Equation (11) and equation (12) show that the displacement is linear with its load. With superposition principle, the two equations is integrated on the circle A, then

$$w = \int_A dw = \frac{1 - \mu^2}{\pi E} q(t) \iint_A d\ell d\varphi = 2 \frac{1 - \mu^2}{\pi E} q(t) \int_0^\varphi d\varphi \int_{nm} d\ell \quad (13)$$

$$u = \int_A du = -\frac{(1+\mu)(1-2\mu)}{2\pi E} q(t) \iint_A d\ell d\varphi = -\frac{(1+\mu)(1-2\mu)}{\pi E} q(t) \int_0^\varphi d\varphi \int_{nm} d\ell \quad (14)$$

The corner by r axis and the tangent of the circle through the point M is supposed to ϕ . It is known that the maximal ϕ is ϕ , and integral length of dl is \overline{nm} . So, with $r_0 \sin \theta = r \sin \phi$, Equation (11) and (12) are integrated sequentially, then

$$w = \frac{4(1-\mu^2)}{\pi E} q(t) r \left(\int_0^{\frac{\pi}{2}} \left(\sqrt{1 - \left(\frac{r_0}{r}\right)^2 \sin^2 \theta} \right) d\theta - \frac{r^2 - r_0^2}{r^2} \int_0^{\frac{\pi}{2}} \left(\sqrt{1 - \left(\frac{r_0}{r}\right)^2 \sin^2 \theta} \right)^{-1} d\theta \right) \quad (15)$$

$$u = -\frac{2(1+\mu)(1-2\mu)}{\pi E} q(t) r \left(\int_0^{\frac{\pi}{2}} \left(\sqrt{1 - \left(\frac{r_0}{r}\right)^2 \sin^2 \theta} \right) d\theta - \frac{r^2 - r_0^2}{r^2} \int_0^{\frac{\pi}{2}} \left(\sqrt{1 - \left(\frac{r_0}{r}\right)^2 \sin^2 \theta} \right)^{-1} d\theta \right) \quad (16)$$

Equation (15) and (16) show the vertical and horizontal displacement of the point M produced by the circular uniform load. The integral in the equations is the standard form of ellipse integral. If r_o/r is known, the integral value is obtained from mathematics manual. Equation (15) and (16) show that the maximal displacement due to colliding is in direct proportion to the colliding force and the vertical displacement is more than the horizontal one.

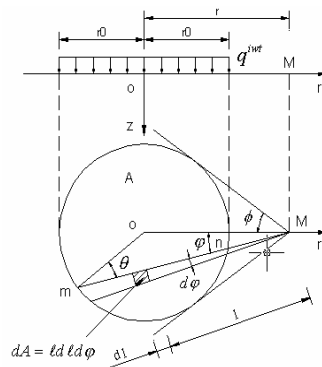


Figure 5 The solution under uniform load

5 Colliding Example and Discussion

The following example verifies the above theory. A clinical building in Hunan Children Hospital was demolished on Aug. 20, 2002. Author monitored the ground vibration on the site. With the primary value of equation (5), the equation (4) was solved and the curve between velocity and time (v-t) was obtained which was shown in figure 6. At the beginning of colliding between blasting demolishing building and ground, as the

complex of its course, the v-t curve was not like figure 6. The maximal colliding force F_{max} was obtained from a_{max} , and then the uniform load $q(t)$ was obtained from the circular area acted on by force. In deriving $q(t)$, the circular area was approximately calculated by using half of radius of dispersed mass, as the penetrated depth was tiny.

$$q(t) = \frac{F_{max}}{\frac{1}{4}\pi A^2} = 3.34 \times 10^5 \text{ KN/m}^2$$

$q(t)=3.34 \times 10^5 \text{ KN/m}^2$, $\mu=0.25$, $E=2 \times 10^9 \text{ Pa}$, etc. were put into equation (15) and (16), the curves of $w(r)$ and $u(r)$ were obtained, as in figure 7. The vertical maximal displacement was larger than the horizontal at the same site, but it attenuated more rapidly with distance increasing.

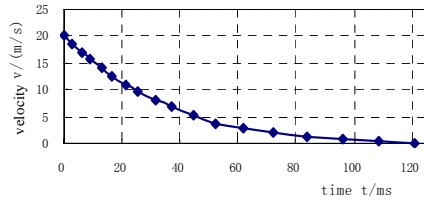


Figure 6 The v-t curve

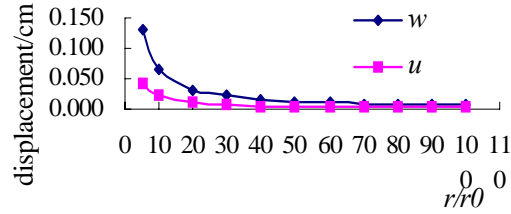


Figure 7 The displacement-r/r0 curve

The colliding load from a freely falling body can be supposed to be semi-sine pulse [12,13], which is shown in figure 8. For example, when $r/r_0=50$, the pulse of displacement was obtained from equation (15) and (16), then the velocity pulse was obtained by differentiating with respect to the displacement pulse as in figure 9.

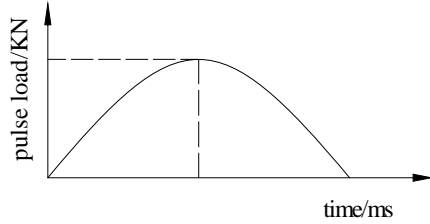


Figure 8 The wave of colliding pulse

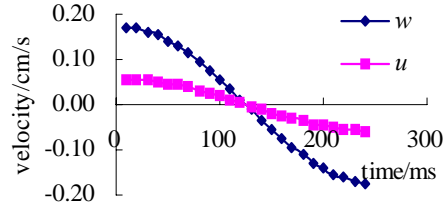


Figure 9 The wave of velocity pulse

The velocity ground of points concerned was calculated. All the monitored values and the calculated values were plotted on a chart, the vertical values in figure 10 and the horizontal in figure 11.

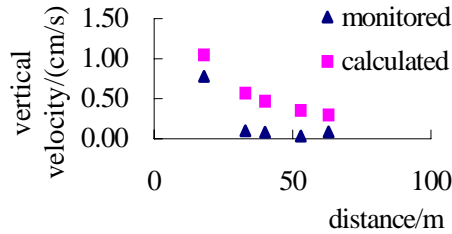


Figure 10 The chart of vertical testing and calculated values

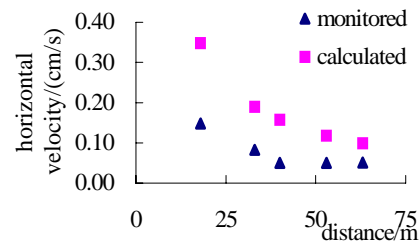


Figure 11 The chart of horizontal testing and calculated values

The monitored and calculated values had the same variation law with distance, but there was a difference in some extent between the monitored value and the calculated one, the monitored value is smaller than the calculated. The reason for this is the error in observation, which induced by different soil condition under the monitor, by the located angle of the monitor and by noise in recorded signal, etc. Another reason is the error in calculation; for instance, the radius of dispersed mass with CCET is not always accurate.

6 Conclusion

The conclusion can be summarized: (a) On the basis of the resemblance between the course of a demolished building colliding into earth and the course of a bullet penetrating target, the analysis results of ground vibration approximates practical engineering. It shows that the theory and the method of using the CCET on collision courses are suitable and has preferably applied foreground. (b) By using the CCET and supposing that the colliding force is a semi-sine pulse load, it is obtained that the peak particle velocity induced by blasting demolishing building decreases gradually with increasing distance from the collision center. (c) There is a difference to some extent between the monitored value and the calculated one, but their variation with distance is alike.

Acknowledgements

It is a project supported by Natural Science Foundation of China(50678028). The authors would like to thank the authorities concerned.

References

1. He, J., Yu, Y.L. and Li, T.H. Current Situation of Demolishing Urban Structures with Controlled Blasting at Home and Abroad. *Engineering Blasting*, 1999, 5(3): 76-81.
2. Williams, G.T. The explosives demolition of tall building. *Proceedings of the third international RILEM symposium*. 1993.
3. Feng, S.Y. and Gu, Y.C. Security: The Permanent Topic of Blasting -A Review of Important Demolition Blasting Projects in 2001. *Blasting*, 2002, 3(1): 1-4.
4. Yang, G.T. *Soil Dynamics*. Beijing: Construction Material Industry Press of China, 2000.
5. Zhang, S.Z. *Blasting and Impact Dynamics*. Beijing: Enginery Industry Press, 1993.
6. Yin, F.L., Wang, M.Y. and Qian, Q.H. An Engineering Computing Model for Penetration Depth of Profectile Normal Into Target. *Explosion and Shock Waves*, 1997, 17(4): 333-339.
7. Heuze, F.E. An overview of projectile ion into geological materials-with emphasis on rocks. *Int J rock Mech Min Sci & Geoech Abstr*, 1999, 27(1): 1-14.
8. Lu, Z.H., Qian, L.X. and Jin, J.M. Theoretical analysis for arbitray Nosed Projectile Penetrating into Goological Materials. *Explosion and Shock Waves*, 2003, 7(4): 325-330.
9. Forrestal, M.J. and Luke, V.K. Dynamic spherical cavity-expansion in a compressible elastic-plastic solid. *Journal of Applied Mechanics*, 1998, 55: 275-279.
10. Jin, F.N., Zhang, L.P. and Xia, Z.G., et al. Engineering Method for Calculating the Penetration Depth into Rocks. *Journal of PLA University of Science and Technology*, 2003, 4(2): 41-44.
11. Luke V.K. and Forrestal, M.J. Penetration into semi-infinite reinforced-concrete targets with spherical and ogiveal nose projectiles. *Int J Impact Engineering*, 1999, 16(4): 291-216.
12. Wang, J.K. and Ding, L.Z. *Elastic Solid Mechanics*. Beijing: Railway Press of China, 1990.
13. Yang, S.Y. *Base of Rock Blasting dynamics*. Beijing: Charcoal Industry Press, 1993.

INVESTIGATION ON THE INFLUENCE OF FAULT ON THE DAMAGE BEHAVIOR OF UNDERGROUND OPENING

LIAN-CHONG LI, GEN LI, TIAN-HUI MA and ZHENG-ZHAO LIANG

Center for Rock Instability and Seismicity Research, Dalian University of Technology

Dalian, 116024, P.R. China

Both the far-field stress ratio and local geological structures play an important role in the stability of underground openings. Numerical tests are conducted to investigate the effects of the stress ratio and different dip angles of faults and the stability of underground openings. The damage of rock mass surrounding the opening is aligned to the minimum horizontal stress. Extensile cracking is a basic mechanism of breakout initiation, followed by a progressive detachment of rock flakes bounded by cracks, leading to V-shape cross-sections. Although the existing of faults induces the asymmetry of the failure mode, the high tectonic stress will dominate the stability of the openings. These results have referential and guiding significance to the site selection and layout, and help with the construction of deep underground openings of the same kind.

1 Introduction

Fractured rock masses are often encountered during underground excavation. Many failures of underground openings during excavation and in operation closely relate to geo-structural changes such as folding, jointing, and the faulting process. The rock masses easily slide along structural planes or detach, flex and break because of the low shear strength and tensile strength of these discontinuities, as well as the looseness of rock mass due to the unloading by excavation. Under some conditions, these discontinuities may lead to big disasters for underground opening construction.

A general way to investigate the deformation and failure characteristics of the underground opening is to carry out model tests and numerical analysis. Goodman et al. examined the behavior of the deformation of tunnels in jointed rock mass using the scaled model test [1,2]. Yeung and Leong carried out a parametric study using two-dimensional, discontinuous, deformation analysis (DDA) to study the effects of the attribute of joints in a rock mass on the stability of a tunnel excavated in the rock mass [3]. Jeon et al. performed scaled model tests to investigate the effect of a fault and grouting on the stability of a tunnel [4]. Hao and Azzam (2005) investigated the influence of some parameters of a fault on tunnel stability by numerical method (UDEC) [5]. Jiang et al. (2006) developed a multiple system for analyzing the feature of geometrical distribution of rock joints, and discussed the relationship between deformational behavior and fractal dimension and orientation of joint sets based on fractal analysis and numerical simulation of underground opening in the jointed rock masses [6]. In the investigation on the stability of underground openings, the in-situ rock stress (stress ratio, K) is one of the most sensitive input data to the results of analysis. It is not only the magnitude, but also the orientation of the stresses that are needed for the design of underground openings [7-10].

Although the influences of rock joints and the stress state to the stability of underground structures have been studied, both analytically and experimentally, the failure mechanism of underground excavations under complex geological conditions is still far from being complete and satisfactory. A strong understanding of this is required, and deemed important for a desirable support design and safe excavation. The main objective of the study presented herein is to investigate the influence of different dip angles of fault zones and the effect of the

in-situ stresses on the stability of tunnels excavated in rock mass. Meanwhile, the progressive failure process of deep underground opening in rock mass is presented.

2 Numerical Model

To better understand the damage behavior of rock mass surrounding underground opening, a numerical code, RFPA^{2D}, based on damage mechanics, statistical theory and FEM, is employed to conduct numerical investigation. In RFPA^{2D}, the material properties of each element are different from each other and are specified according to Weibull distribution, which makes it capable to simulate the nonlinear behavior of distortion and failure of rock mass. The modified Mohr–Coulomb criterion with tension cut-off is adopted in this code, thus characteristics of the brittle-plastic rock can be simulated. The most unique feature of this code, which makes it totally different from other kind of numerical code is that it can simulate the whole fracturing process of initiation, propagation and coalescence of fractures around excavation with no need to give assumptions on where and how fractures and failure will occur [11-13].

In the following simulations, four numerical models are considered (see Figure1). There are no faults in the first model; in the other three models, there is a fault with a dip angle of 0°, 45°, and 90°, respectively. These four models have a common dimension of 27×27 m. The diameter of circular tunnel is 3m. We assume that the tunnel is quite deep so that the influence of the Earth's surface will be disregarded. The depth will be taken into account in the analysis by the value of the primary stress state at that particular depth. The pressure in vertical direction is denoted with σ_v , while that in horizontal direction is σ_h . Then the lateral pressure coefficient is defined as $k = \sigma_h / \sigma_v$. The Parameters of rock mass and fault zone are showed in Table 1.

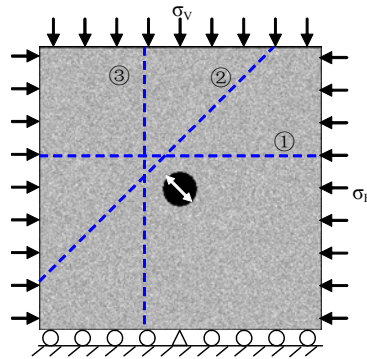


Figure 1 Sketch of model for numerical test

Table 1. The parameters employed in numerical simulation

Type of material	Young's modulus (GPa)	Compression strength (MP)	Tension strength (MP)	internal friction angle (°)	Poisson's ratio
Faults	3	4	0.2	20	0.40
Surrounding rock mass	30	42	4.2	35	0.25

3 Simulation Results and Discussion

Under far-field stress conditions above certain thresholds, excavation induced diametrically opposed failure zones that can be described as V-shaped breakouts, wide at the opening wall and relatively short in depth. These breakouts resemble those observed in previous studies in carbonate and crystalline rocks, and in the medium porosity Berea sandstone [14]. Figure 2 depicts three photographs showing opening cross-sections under different σ_h and σ_v . The figures demonstrate the breakout dependence on the state of far-field stress. In Figure 2

the breakout depth is denoted with L and the breakout angular span is denoted with θ . It is shown that the V-shaped breakouts are consistently aligned with σ_{H_2} and are deeper and wider at the opening wall as σ_H increased. The breakout length and angular span variation with the far-field stress are independent of each other. Knowledge of these will lead to a potential ability to estimate both horizontal principal stress and the failure mechanism of underground opening.

For other cases with faults, the breakout mode of opening depends on both the far-field stress conditions and the configuration of faults in rock mass. Figure 3, 4 and 5 are the corresponding numerical results.

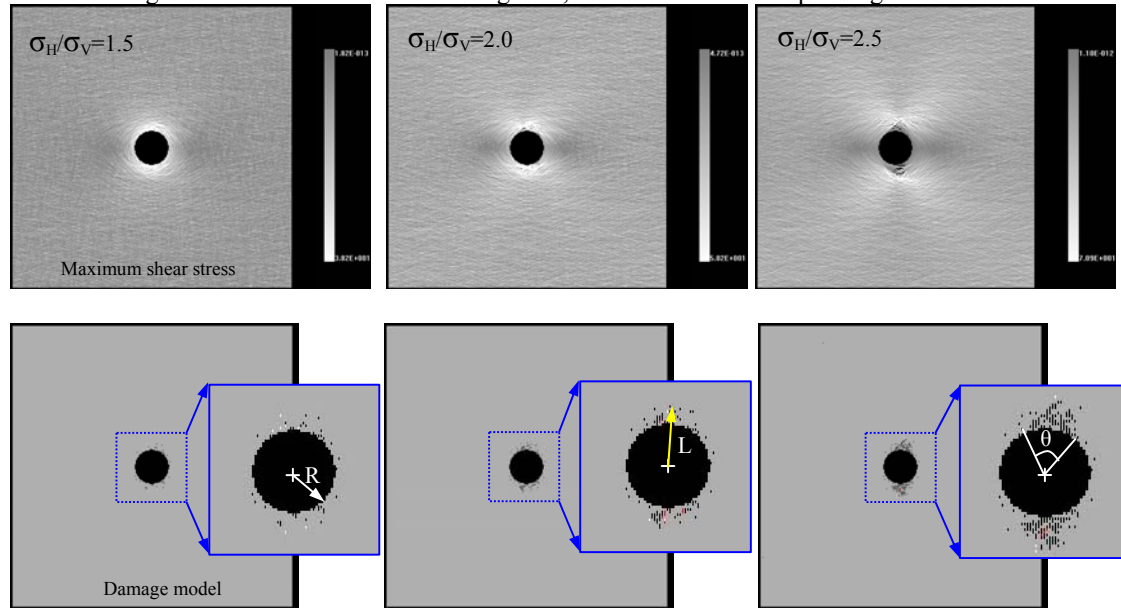


Figure 2 Failure mode of underground opening surrounded by intact rock mass.

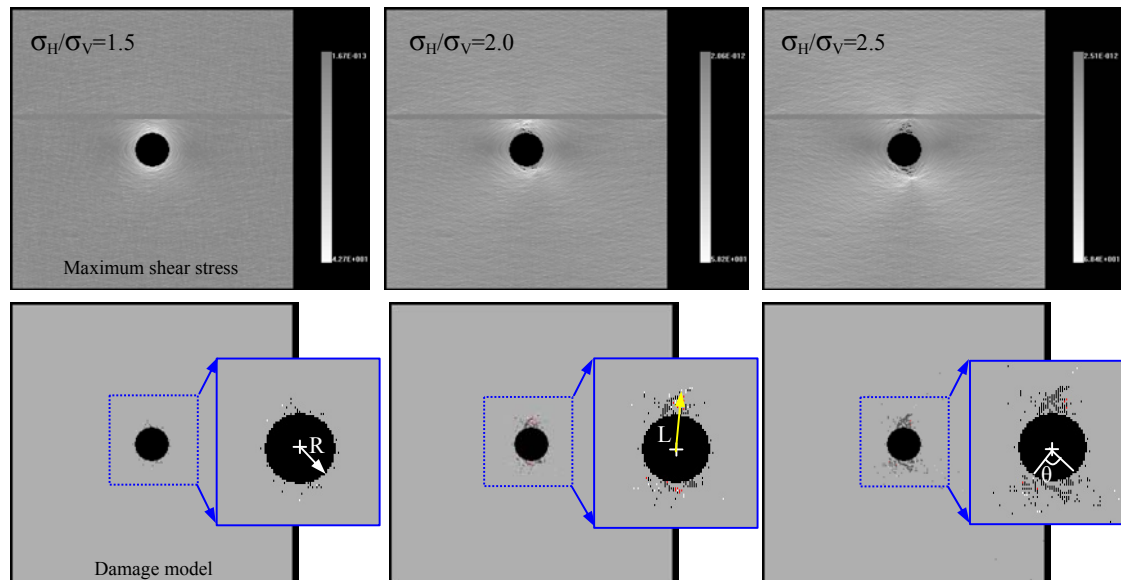


Figure 3 Failure mode of surrounding rock mass containing a fault with a dip angle 0° .

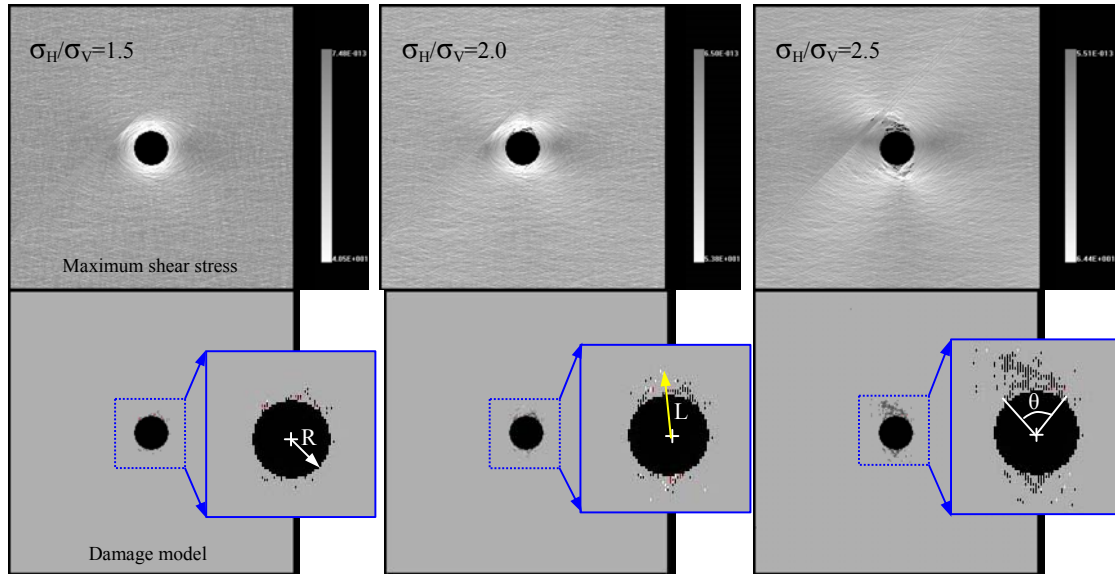


Figure 4 Failure mode of surrounding rock mass containing a fault with a dip angle 45°.

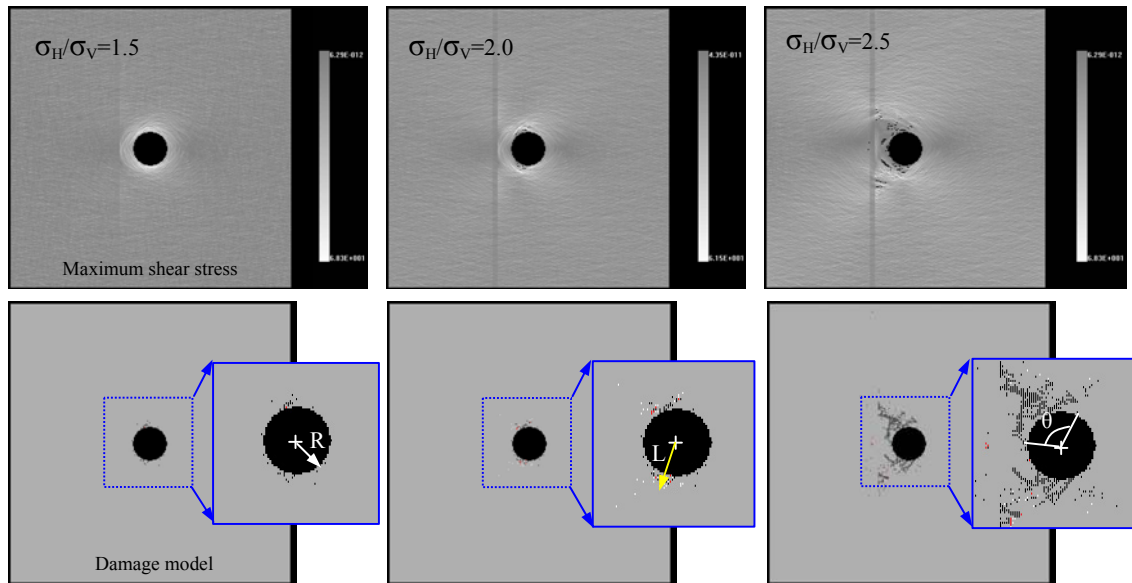


Figure 5 Failure mode of surrounding rock mass containing a fault with a dip angle 90°.

From this figure we can see that for intact rock mass, the stress distribution around the opening is symmetric; but for the cases with faults, with the increasing of the dip angle, the asymmetry of stress around opening increases gradually, which causes the asymmetry of the failure mode. In the case where the fault is perpendicular to the direction of maximum principal stress, the effect of fault on the failure mode of opening is the most remarkable, in which the breakout depth and the breakout angular span are all larger than those in other cases.

With the relatively lower lateral pressure coefficient k , the failure mode for the four cases is similar. Figure 6 is the final breakout mode with the condition of $\sigma_H/\sigma_V = 2.5$. It is shown that although faults and other

structural planes have obviously effect on the failure mode of underground openings, the high tectonic stress will have dominate effect on the failure of tunnel.

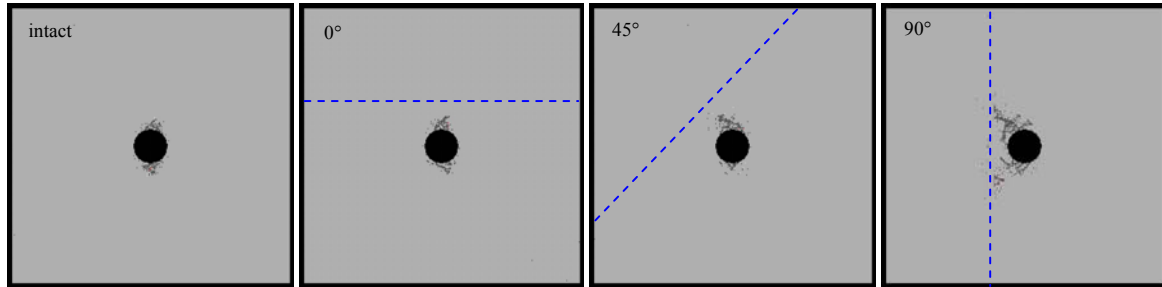


Figure 6 Numerical results of the four cases with the condition of $\sigma_H/\sigma_V=2.5$.

Plotting the normalized breakout length (with respect to borehole radius) as a function of the far-field stress ratio reveals a clear correlation (Figure 7). The rates of increase tend to rise with the magnitudes of the applied σ_H and σ_V . This stress-dependent breakout depth agrees in principal with that in granite and different limestones[14]. A significant increase in the angular span with higher σ_H is also observed (Figure 8). Hence, the damage span at the opening wall is also correlatable to the state of far-field stress. This result is of great interest because the extent of breakout angular span can be determined from borehole logging with considerably higher accuracy than breakout length[15].

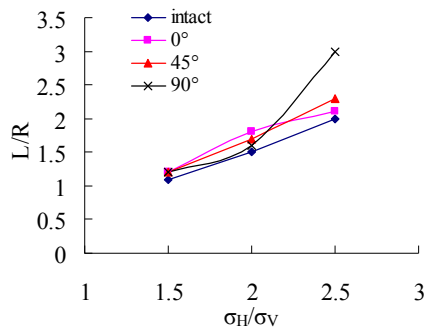


Figure 7 Normalized breakout length (L/R) as a function of the far-field principal stress ratio (σ_H/σ_V)

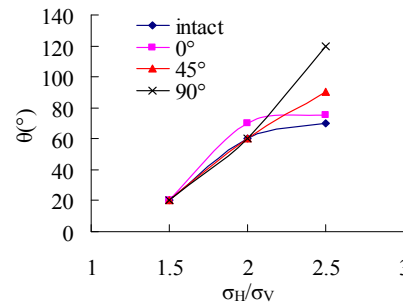


Figure 8 Breakout angular span (θ) as a function of the far-field principal stress ratio (σ_H/σ_V)

4 Conclusions

In this study, numerical tests are conducted to investigate the effect of the stress ratio and different dip angles of faults on the stability of underground opening. Numerical analysis indicates that both the dip angle and lateral pressure coefficient have significant impact on the stability of the opening. Based on the simulations, the following conclusions are drawn:

The major breakout mechanism of initiation of micro-cracks is the tensile rupture along surfaces, parallel to the opening wall. After micro-crack development, the coalescence of micro-cracks and the macroscopic spalling are followed. In the final stage there is a progressive detachment of rock flakes bounded by cracks, leading to V-shape cross-sections. In general, the breakouts are aligned to the minimum horizontal stress. The breakout depth and angular span increase linearly within the value of the maximum horizontal stress for fixed values of the vertical and minimum horizontal stress.

The existing of faults changes the failure mode of opening. The failure mode is due to the asymmetry of stress around opening caused by faults. However, with the relatively lower lateral pressure coefficient k , the

failure mode for the cases with faults is similar. So, although faults and other local geological structural planes have an obvious effect on the failure mode of underground openings, the high tectonics have a dominated effect on the failure of the openings.

Acknowledgements

The authors wish to acknowledge the funding support from the China National Natural Science Foundation (Grant No. 50820125405 and No. 40638040) and the National Basic Research Program of China (Grant No. 2007CB209404).

References

1. Goodman, R.E., Heuze, H.E and Bureau, G.J. On modelling techniques for the study of tunnels in jointed rock. Fourteenth Symposium on Rock Mechanics, 1972, 441-479.
2. Goodman, R.E., Methods of Geological Engineering in Discontinuous Rocks. West Publishing Co., 1976.
3. Yeung, M.R., Leong, L.L., Effects of joint attributes on tunnel stability. International Journal of Rock Mechanics and Mining Science, 1997, 34, 3-4.
4. Jeon, S., Kim, J., Seo, Y., Hong, C., Effect of a fault and weak plane on the stability of a tunnel in rock – a scaled model test and numerical analysis. International Journal of Rock Mechanics and Mining Science, 2004, 41 (1). 658-663.
5. Hao, Y.H., Azzam, R., The plastic zones and displacements around underground openings in rock masses containing a fault. Tunnelling and Underground Space Technology, 2005, 20, 49-61.
6. Jiang, Y., Tanabashi, Y., Li, B., Xiao, J., Influence of geometrical distribution of rock joints on deformational behavior of underground opening. Tunnelling and Underground Space Technology, 2006, 21 (5). 485-491.
7. Hoek, E. & Brown, E.T. Underground excavation in rock. Institution of Mining and Metallurgy, 1980.
8. Zhu, W.C., Liu, J., Tang, C.A., Zhao, X.D., Brady, B.H., Simulation of progressive fracturing processes around underground excavations under biaxial compression. Tunnelling and Underground Space Technology, 2005, 20 (3). 231-247.
9. H. Lee & B.C. Haimson. Borehole breakouts and in-situ stress in sandstones[C]. In-situ Rock Stress, Ming Lu , Charlie C.Li, Halvor Kjørholt, & Halgeir Dahle (eds), Taylor & Francis Group, London, 2006, 201-207
10. Jia, W.C., Tang, C.A. Numerical study on failure mechanism of tunnel in jointed rock mass. Tunnelling and Underground Space Technology, 2007, 22 (8). 562-571.
11. Tang, C.A., Numerical simulation of rock failure and associated seismicity. International Journal of Rock Mechanics and Mining Science, 1997, 34 (2). 249-262.
12. Zhu, W.C., Tang, C.A., Micromechanical model for simulating the fracture process of rock. Rock Mechanics and Rock Engineering, 2004, 37 (1). 25-56.
13. Tang, C.A., Li, L.C., Li, C.W., et al., RFPA strength reduction method for stability analysis of geotechnical engineering. Chinese Journal of Rock Mechanics and Engineering, 2006, 25 (8). 1522-1530.
14. Song, I., Borehole breakouts and core diskings in Westerly granite: mechanisms of formation and relationship to in situ stress, Ph.D. thesis, University of Wisconsin, 1998.
15. Barton, C.A., Development of in situ stress measurement techniques for deep drill holes. Ph.D. Dissertation, Stanford University, Palo Alto, 1988.

STUDY ON APPLICATION OF GPRS REMOTE WIRELESS TRANSMISSION TECHNOLOGY IN MICROSEISMIC MONITORING SYSTEM

CHAO LIU and CHUN-AN TANG

*Center for Rock Instability & Seismicity, Research School of Civil and Hydraulic Engineering,
Dalian University of Technology, Dalian, P. R. China, 116024*

GUO-FENG YU

*National Engineering Research Center for Coal Mine Gas Controlling,
Huainan Mining(Group) Co., Ltd, Huainan, P. R. China, 232001*

GPRS is suitable for wireless transmission systems because of its flexibility, extensibility, convenience, low cost and high speeds in communication network establishments. Field monitoring data for the microseismic monitoring system project are real-time and continuous. Qualified microseismic analysis technique personnel and large-scale computer equipment is also lacking in sites. Monitoring data should be transmitted to the computer center server. GPRS remote wireless transmission technology is used widely for microseismic monitoring system projects. The function and characteristics of GPRS in the microseismic data transporting are explained, its realization forms is summarized, and the advantages and disadvantages of every form are analyzed. This further explains how GPRS has an important market future and application. These results show that microseismic monitoring information is transmitted in time to the computer server by GPRS to realize scientific management and analysis. This greatly accelerates the analysis and judgement efficiency.

1 Introduction

Field monitoring systems are invaluable tools in civil and mine engineering practice. In the construction phase of engineering projects, field monitoring can provide key indicators about the safety of the construction site and its surroundings. Once the construction is completed, the project enters the maintenance phase, and field monitoring provides vital information that helps assess the service condition of structures [1-4]. Therefore, field monitoring has become an integral part of large-scale civil engineering project. With the growing demand for real-time and remote applications over wireless networks, increasing attention is paid to the GPRS networks[5-7]. Microseismic monitoring projects and contents are continuously increasing every year. The conflict between qualified microseismic analysis technique personnel and computer equipments and so much project sites has gradually been visualized. Because the projects on sites are very dispersed, someone has to attend and run them. Still, many problems exist.[8-11] Some examples are: information blockade, big error, no time, not professional, expensive, etc. Then the form can't adapt to monitoring automatization and informatization requirements in the technology and economy. As wireless technologies emerge and improve, the boundary of their applications blur. Wireless technologies, which were once intended for specific applications, can now provide comparable services for monitoring. The technology based on GPRS service provides a new solution for remote wireless transferring data acquisitions. In this paper, the principle, features and structure of GPRS are presented in detail, and a viable operation case is introduced. In contrast to previous applications, the technology is applied to combine with microseismic monitoring systems for realizing remote wireless transmission in China and abroad.

2 GPRS Technology

The GPRS(General Packet Radio Service) is a service enabling mobile access to the Internet. In contrast to circuit-switched mobile communications, GPRS uses packet-switching, which results ineffective use of radio bandwidth. This has made GPRS a system affordable to a mass market.

2.1 Basic Principle

Over the past decade, Internet use has exploded with people gaining rich information from the World Wide Web. Meanwhile, technology has made wireless devices smaller, less expensive and more powerful. Wireless networks have become increasingly popular for accessing the Internet, because they enhance mobility. People can connect to the Internet and remain on-line while roaming[12]. GPRS technology, based on the GSM system, can supply high mobility and 'always on' connectivity for mobile users. So the technology can make wireless communication and internet connect closely. The GPRS and GSM system have the same wireless modulation standard, frequency band, emergent structure, frequency-hopping and TDMA frame structure. GPRS data terminal supports TCP/IP, PPP and clear data transmission, allowing each user occupy multiple channels. At the same time, every channel can also share by many users. GPRS bandwidth can reach theoretically 171.2 kb/s[13]. It could communicate with the internet and other public data networks. As a transition technology (2.5G) from GSM to the third generation mobile communication, GPRS has remarkable advantages in many aspects[14].

2.2 Character and Structure

GPRS is one of GSM Phase2+ standard realization contents and can provide fast data transmission speed. In theory, this service is ten times faster than the current Circuit Switched Data services on GSM networks. It involves overlaying a packet based air interface on the existing circuit switched GSM network, providing end-to-end, wide area wireless IP connection. GPRS uses fully shared wireless channels and provides faster and long-distance connection for data terminals by IP over PPP. Compared to SMS, it uses TCP/IP to communicate avoiding data package lost, bidirectionally communicating quickly and real-time among many monitoring projects. In addition, GPRS networks constantly experience congestion due to the limited resource architecture. An appropriate pricing scheme could help resolve the allocation of scarce resources to users, as well as generate additional revenue for network. Due to using public network, just need install GPRS equipment, so it is very cheap to operate and maintain on daily.

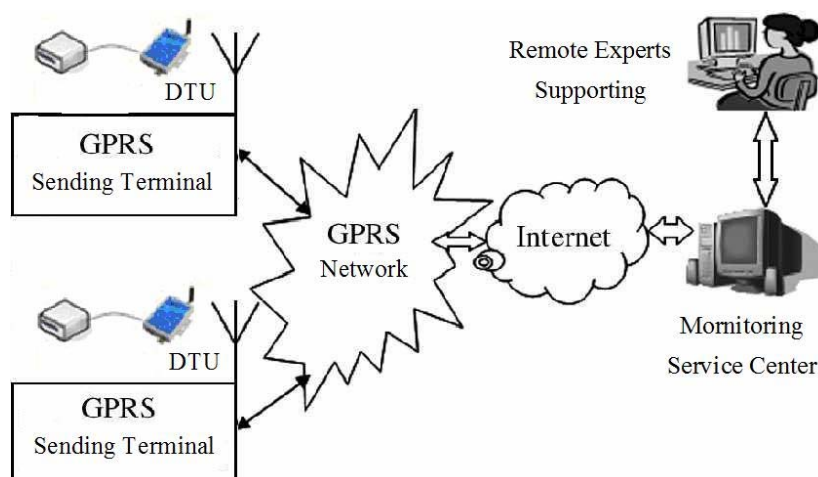


Figure 1 Monitoring dispatch system structure

A fixed IP or domain name must be supplied as GPRS is data blocks communication network based on IP address, so each monitoring project can access service center to establish communication by means of IP or domain name. Field monitoring computer should connect with GPRS sending terminal by copper date wire, then computer will process, package and send monitoring site date to GPRS network relying on transmitting terminal (MMS-View). Subsequently, the network interface module can decode and transfer date format for sending to monitoring service center by GPRS. Finally, qualified microseismic analysis technique personnel or remote microseismic experts can analyze and read seriously the useful monitoring sites date by internet, as shown in Figure 1.

2.3 GPRS Equipment

There are five fittings in the GPRS sending terminal, including GPRS MODEM, copper date wire, power wire, antenna and mobile card, as shown in Figure 2.

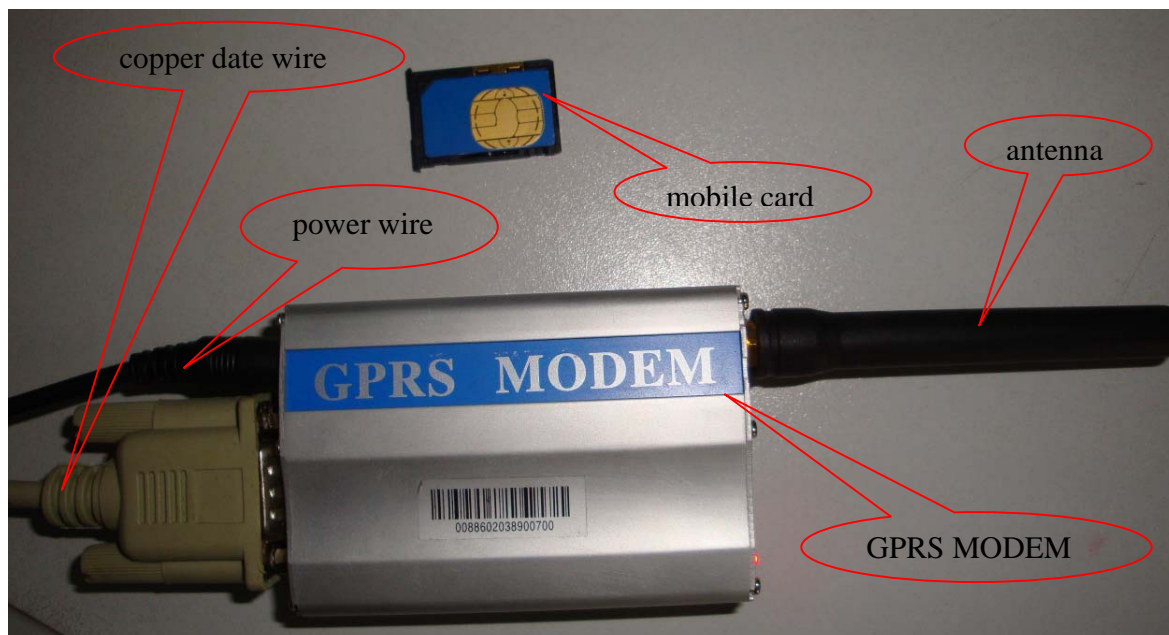


Figure 2 GPRS equipment

3 A Case Study

It is generally accepted that most solids emit low-level seismic signals when they are stressed or deformed. In the geotechnical field, this phenomenon is generally referred to as acoustic emission/microseismic (AE/MS) activities [15]. When rock fractures, it produces AE/MS signals transmit through the rock as elastic waves. The application of the AE/MS system, which monitors self-generated acoustic signals occurring within the ground, has now rapidly increased for monitoring of the stability of underground structures such as mines, tunnels, natural gas, and petroleum storage caverns, as well as surface structures such as foundations, rock, and soil slopes.

Regarding monitoring projects on site, a microseismic monitoring system case of Xinzhuangzi coal mine at Huainan is introduced and studied deeply. The aim of system focus on the acoustic emission of coal and rock mass at mining area. In order to monitor the stability of the coal and rock mass, predict possible gas outburst zone, divide dangerous area, minimize the hazardous ground conditions, and provide safer working conditions for the miners, Huainan Mining (Group) Co., Ltd installed an microseismic system, which had 30-channel

uniaxial geophones connected to a HNAS data acquisition system. The system started to monitor AE/MS activity at the mine on March,6,2009,as shown in Figure 3.

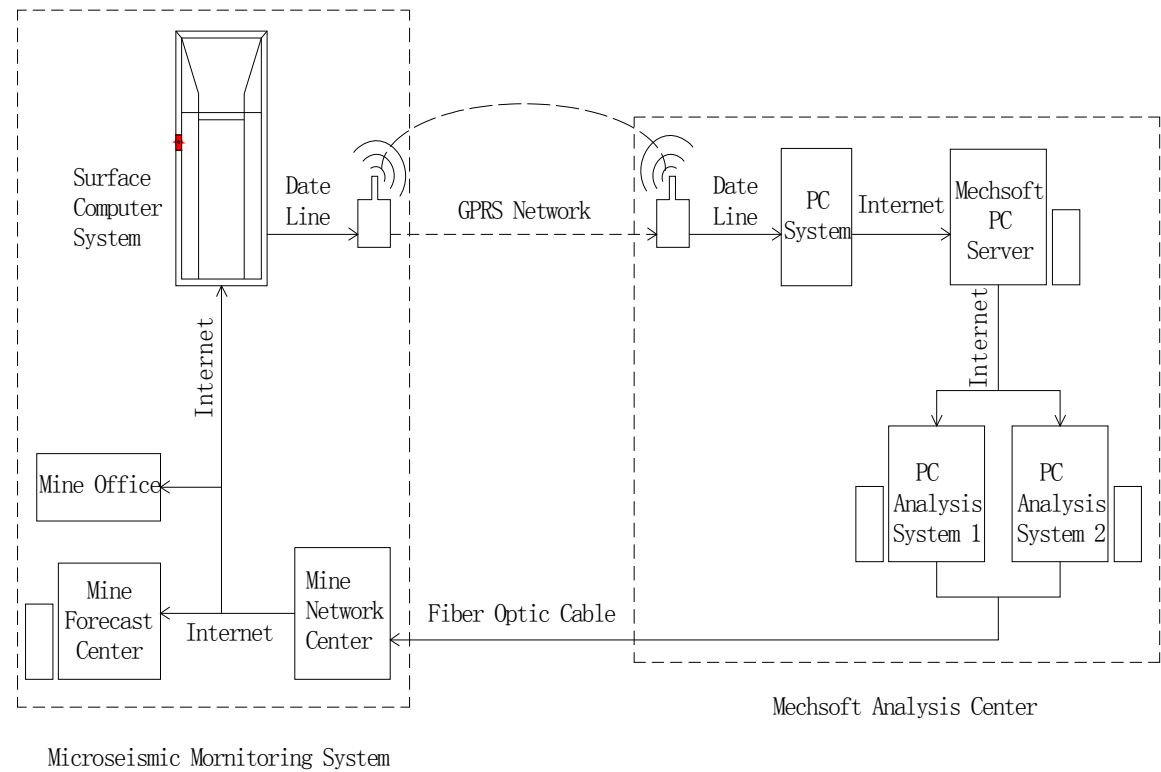


Figure 3 Topological diagram of Xin Zhuangzi mine microseismic monitoring system

3.1 Sending and Receiving

As described above, the surface computer can control monitoring data and transmit database file(seismic.mdb) to GPRS network by sending terminal(MMS-View), as shown in Figure 4. As a result, sending terminal can find automatically database file and transmit it real-time by itself to wireless network. While the system can adapt to conform to many kinds of fault management problems, supporting off-line and online service. The main advantage of the concept is real-time, so long as can generate database file at time, network will emit it in time, and increasing based on original sets of date. Additionally, the operators need no special knowledge about communication network, just making the monitoring system run normally every day. In fact, users can receive database file(seismic.mdb) from monitoring service center by GPRS remote wireless transmission network, as shown in Figure 5. Replace is corresponding to Recent Date, which means that system date is transmitting real-time;

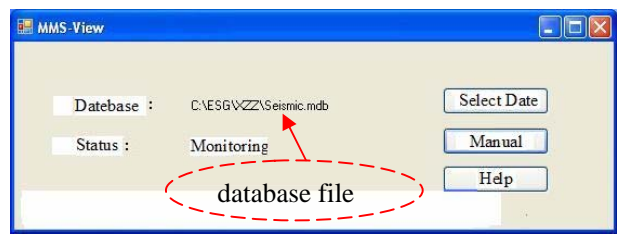


Figure 4 Sending terminal(MMS-View)

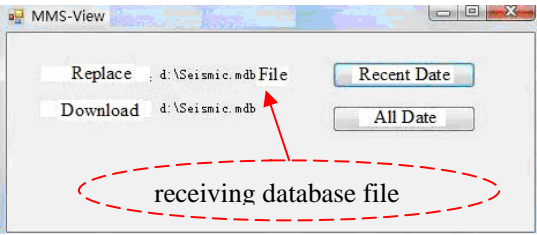
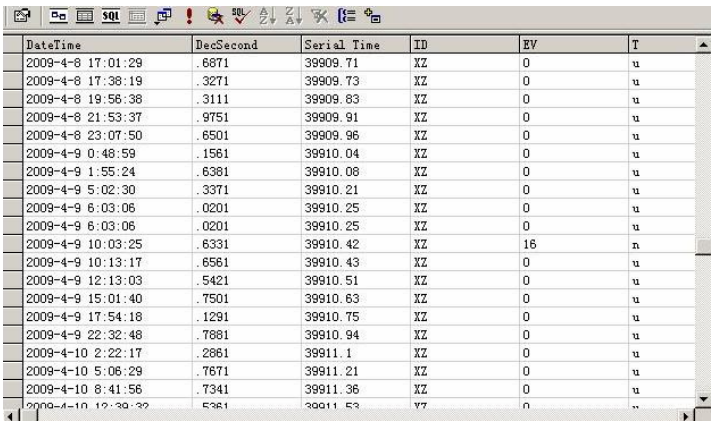


Figure 5 Receiving terminal(MMS-View)

at the same time,Download is corresponding to All Date,which means that system date has transmitted in the past,and the database file(All Date)will be added based on Recent Date.

3.2 Results Analysis

Since there is a monitoring date going on in the wireless network due to sending and receiving terminal,we have performed sensitivity analyses which can help and rock mechanics experts and mining managers to make decisions scientifically. The operator find the system easy to use,obtaining the database file(seismic.mdb) which shows the date property of receiving including important events location time,number, three-dimensional coordinates,frequency,moment magnitude and energy,as shown in Figure 6.



DateTime	DecSecond	Serial Time	ID	EV	T
2009-4-8 17:01:29	.6871	39909.71	XZ	0	u
2009-4-8 17:38:19	.3271	39909.73	XZ	0	u
2009-4-8 19:58:38	.3111	39909.83	XZ	0	u
2009-4-8 21:53:37	.9751	39909.91	XZ	0	u
2009-4-8 23:07:50	.6501	39909.96	XZ	0	u
2009-4-9 0:48:59	.1561	39910.04	XZ	0	u
2009-4-9 1:55:24	.6381	39910.08	XZ	0	u
2009-4-9 5:02:30	.3371	39910.21	XZ	0	u
2009-4-9 6:03:06	.0201	39910.25	XZ	0	u
2009-4-9 6:03:06	.0201	39910.25	XZ	0	u
2009-4-9 10:03:25	.6331	39910.42	XZ	16	n
2009-4-9 10:13:17	.6561	39910.43	XZ	0	u
2009-4-9 12:13:03	.5421	39910.51	XZ	0	u
2009-4-9 15:01:40	.7501	39910.63	XZ	0	u
2009-4-9 17:54:18	.1291	39910.75	XZ	0	u
2009-4-9 22:32:48	.7881	39910.94	XZ	0	u
2009-4-10 2:22:17	.2861	39911.1	XZ	0	u
2009-4-10 5:06:29	.7671	39911.21	XZ	0	u
2009-4-10 8:41:56	.7341	39911.36	XZ	0	u
2009-4-10 12:30:32	.5361	39911.53	Y7	0	u

Figure 6 Date property of receiving

In the end, when the database file is received successfully,it is convenient extraordinary for users to run and apply by MMS-View coming from Mechsoft.Generally speaking,professional analyst,as well as mining managers can open the database and analyze the three-dimensional microseismic events location,finding and forecasting microseismic activities rule at any time and everywhere,as shown in Figure 7,just need access to monitoring service center.

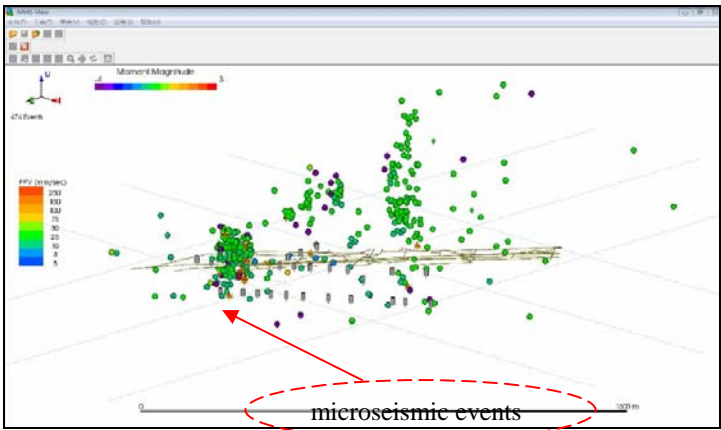


Figure 7 3-D microseismic events location

4 Conclusion

In this paper ,the comprehensive performance study of the GPRS technology and applied case is presented. This method, combining with GPRS network and microseismic monitoring system, is a new management system for

processing data on site. The monitoring system described in this paper is a modular and flexible system in both hardware and software. It permits freely users accessing to service center and studying project's dynamic disaster changes, promoting obviously monitoring of data to be managed scientifically and reliably. We hope that we will soon establish a more stable and general approach method for monitoring.

Acknowledgement

This material is based upon work partially supported by the National Science Foundation,40638040 and International Important Cooperation Project, 50820125405. Any the opinions, findings, and conclusions or recommendations expressed in this material are those of the author(s) and do not necessarily reflect the views of the projects,Furthermore,the work is supported vigorously by Dalian Mechsoft Co.,Ltd (MMS-View software).

References

1. P. Thomson, J.M. Casas, J.M. Arbelaez. and J. Caicedo, Real-time Health Monitoring of Civil Infrastructure Systems in Colombia, Health Monitoring and Management of Civil Infrastructure Systems, Newport Beach, CA, USA, 2001, pp. 113-121.
2. K.-Y. Wong, Instrumentation and Health Monitoring of Cable-supported Bridges, Structural Control and Health Monitoring 11 (2004) 91-124.
3. J. Brownjohn, S.C. Tjin, G.H. Tan, B.-L. and Tan, S. Chakraborty, A Structural Health Monitoring Paradigm for Civil Infrastructure, 1st FIG International Symposium on Engineering Surveys for Construction Works and Structural Engineering, Nottingham,United Kingdom, 2006.
4. H. Li, J. Ou, X. Zhao, W. Zhou, H.Li, Z.Zhou, Y.Yang, Structural Health Monitoring System for Shandong Binzhou Yellow River Highway Bridge, Computer-Aided Civil and Infrastructure Engineering 21 (2006) 306-317.
5. Min Xie, Martin Haenggi, Towards an End-to-end Delay Analysis of Wireless Multihop Networks,in- Ad Hoc Networks 7 (2009) 849-861.
6. Yan X.P., Cheng L.H. Q. Fu,et al,Design of Distance-data Acquisition System Based on GPRS. Microcomputer Information, 2008, 24(1-2).115-116.(in Chinese)
7. Sha Liu, Rahul Srivastava, Can Emre Koksalt,et al,A hidden Markov Model Based Scheme for Energy Efficient DataTransmission in Sensor Networks,in- Ad Hoc Networks 7 (2009) 973-986.
8. Pan Zhengrong, Teng Shangwei, Yin Xiaopei,et al,Design and Realization of Remote On-line Monitoring System of Oil Extractor in Oil Field Based on GPRS.Control and Instruments in Chemical Industry, 2008, 35 (1).75-77. (in Chinese)
9. Saravut Yaiparaj, Fotios Harmantzis, Vinoth Gunasekaran, On the Economics of GPRS Networks with Wi-Fi Integration,European Journal of Operational Research 187 (2008). 1459-1475.
10. Pietari Pulkkinen, Mikko Laurikkala, Aino Ropponen,et al, Quality Management in GPRS Networks with Fuzzy Case-based Reasoning, Knowledge-Based Systems 21 (2008). 421-428.
11. Tang Huiqiang, XU Fang, Automtic Monitoring System of Flood Regimen Based on GPRS. Instrument Technique and Sensor, 2008,22(1).74-76.(in Chinese)
12. RongHong Jan,WenYueh Chiu, An Approach for Seamless Handoff Among Mobile WLAN/GPRS Integrated Networks,in-Computer Communications 29 (2005). 32-41.
13. Qingshan She, Hongye Su,Lida Dong, Design of Wireless Environment Monitoring Terminal Based on CDMA/GPRS/RAD IO.Control and Instruments in Chemical Industry,2006,33 (3).39-43. (in Chinese)
14. GU Qinghua, LU Caiwu, LI Faben,et al, Monitoring Dispatch In formation System of Trucks and Shovels in an Open Pit Based on GIS/GPS/GPRS,in- Journal of Univercity Mining & Technol 18 (2008) 0288-0292.
15. Hongliang Wang, Maochen Ge, Acoustic Emission/Microseismic Source Location Analysis for a Limestone Mine Exhibiting High Horizontal Stresses,in- International Journal of Rock Mechanics & Mining Sciences 45 (2008) 720-728.

NUMERICAL MODELING OF MODE I CRACK PROPAGATION IN ROCKS WITH MESHLESS METHOD

CHENG FAN and JU-YING YANG

Center for Material Failure Modeling Research, Dalian University

Dalian, 116622, P.R. China

It is difficult to simulate crack propagation in rock and implement essential boundary conditions using the traditional meshless method. Kriging interpolation procedure is used instead of the least squared procedure to construct a function which has the property of the Kronecker δ function and the essential boundary conditions so that it can be easily imposed. The proposed method can effectively simulate singular stress fields near the crack tip and discontinuous problems such as crack growth. The problem with mode I crack in rock is analysed, and the path of crack growth is simulated by the proposed method. The results show that the numerical results are in agreement with the experimental results.

1 Introduction

The actual deformation and failure process of geo-materials and geo-structures is a rather complex progressive evolution, involving initial elastic deformation, crack propagation, large-scale displacement and even movement of a discrete system. A numerical method with capabilities in dealing with both continuous and discontinuous deformation problems as well as crack growth simulations is potentially required. A large number of meshless methods have been developed in past decades, such as FEM, BEM, MM [1], EFGM [2], FCEFM [3], Enriched meshless manifold method [4], PIM [5], and so on.

The meshless method is suitable to simulate the propagation of cracks owing to the connection of nodes. Also, the process of the construction of the approximation function and the nodes can be added in or subtracted as needed. In this paper, a new formulation of element-free methods is developed based on Kriging interpolation technology. The shape function has the Kronecker delta function property which is not satisfied in the conventional element-free method and the essential boundary conditions are easy to be imposed. The fundamental theory of this procedure is illustrated and mathematical formulations are given. Then numerical examples are analyzed by the proposed procedure.

2 The meshless method based on kriging interpolation technology

Consider an arbitrary point \mathbf{x} in the computational field Ω , $\mathbf{x}_1, \mathbf{x}_2 \cdots \mathbf{x}_n$ are given a set of nodes with function values $\mathbf{u}_1, \mathbf{u}_2 \cdots \mathbf{u}_n$, where n is the total number of nodes in Ω . The approximation of $\mathbf{u}(\mathbf{x})$ is defined as $\mathbf{u}^h(\mathbf{x})$, The Kriging interpolation method assumes a combination of linear regression plus departure [6],

$$\mathbf{u}^h(\mathbf{x}) = \sum_{j=1}^m p_j(\mathbf{x}) \mathbf{a}_j + \mathbf{z}(\mathbf{x}) = \mathbf{P}^T \mathbf{a} + \mathbf{z}(\mathbf{x}) \quad (1)$$

Where $p_j(\mathbf{x})$ is the base function of monomials with regard to space coordinate $\mathbf{x}^T = [x \ y \ z]$, \mathbf{a} is the coefficient for the $p_j(\mathbf{x})$ corresponding to the arbitrary point \mathbf{x} , $\mathbf{z}(\mathbf{x})$ is assumed to be a stochastic process whose mean, variance and covariance are zero, σ^2 and non-zero respectively. The equation (1) is used to interpolation based on the sampling nodes. The covariance matrix with regard to $\mathbf{z}(\mathbf{x})$ is defined by the following equation

$$\text{Cov}\{\mathbf{z}(\mathbf{x}_i), \mathbf{z}(\mathbf{x}_j)\} = \sigma^2 \mathbf{R}[\mathbf{R}(\mathbf{x}_i, \mathbf{x}_j)] \quad (2)$$

Where $\mathbf{R}[\mathbf{R}(\mathbf{x}_i, \mathbf{x}_j)]$ is the correlation matrix with unit one on the diagonal. $\mathbf{R}(\mathbf{x}_i, \mathbf{x}_j)$ is the correlation function of arbitrary two given point \mathbf{x}_i and \mathbf{x}_j , here Gaussian function $\mathbf{R}(\mathbf{x}_i, \mathbf{x}_j) = \exp(-\theta r_{ij}^2)$ is usually used as correlation function, $\theta \geq 0$ is the model parameter and r_{ij} is the correlation distance between \mathbf{x}_i and \mathbf{x}_j . r_{ij} is defined as $r_{ij} = \|\mathbf{x}_i - \mathbf{x}_j\|$. The correlation vector $\mathbf{r}(\mathbf{x})$ of arbitrary \mathbf{x} and the known n sampling nodes and vector \mathbf{U}_s which collects the values of field variables at the n nodes which contains the arbitrary point \mathbf{x} are defined respectively

$$\mathbf{r}^T(\mathbf{x}) = [\mathbf{R}(\mathbf{x}, \mathbf{x}_1), \quad \dots, \quad \mathbf{R}(\mathbf{x}, \mathbf{x}_n)]^T \quad (3)$$

$$\mathbf{U}_s = [\mathbf{u}(\mathbf{x}_1), \quad \dots \quad \mathbf{u}(\mathbf{x}_n)]^T \quad (4)$$

In above equation, vector \mathbf{U}_s can be expressed as the following form by using equation (1)

$$\mathbf{U}_s = \mathbf{P}_m \mathbf{a} + \mathbf{Z} \quad (5)$$

Where \mathbf{P}_m and \mathbf{Z} are $n \times m$ moment matrix based on the known nodes and $n \times 1$ error matrix respectively

$$\mathbf{P}_m = \begin{bmatrix} \mathbf{p}(\mathbf{x}_1) \\ \mathbf{p}(\mathbf{x}_2) \\ \vdots \\ \mathbf{p}(\mathbf{x}_n) \end{bmatrix} = \begin{bmatrix} p_1(\mathbf{x}_1) & p_2(\mathbf{x}_1) & \dots & p_m(\mathbf{x}_1) \\ p_1(\mathbf{x}_2) & p_2(\mathbf{x}_2) & \dots & p_m(\mathbf{x}_2) \\ \vdots & \vdots & \vdots & \vdots \\ p_1(\mathbf{x}_n) & p_2(\mathbf{x}_n) & \dots & p_m(\mathbf{x}_n) \end{bmatrix} \quad (6)$$

$$\mathbf{Z} = [z_1 \quad z_2 \quad \dots \quad z_n]^T \quad (7)$$

The field function $\mathbf{u}(\mathbf{x})$ can be estimated by linear predictor

$$\hat{\mathbf{u}}(\mathbf{x}) = \mathbf{c}^T(\mathbf{x}) \mathbf{U}_s = [\mathbf{c}_1(\mathbf{x}), \dots, \mathbf{c}_n(\mathbf{x})] \begin{Bmatrix} u_1 \\ \vdots \\ u_n \end{Bmatrix} \quad (8)$$

The error function between equation (1) and equation (8) is

$$\hat{\mathbf{u}}(\mathbf{x}) - \mathbf{u}^h(\mathbf{x}) = \mathbf{c}^T \mathbf{U}_s - \mathbf{u}^h(\mathbf{x}) = \mathbf{c}^T \mathbf{Z} - \mathbf{z} + (\mathbf{P}_m^T \mathbf{c} - \mathbf{p}(\mathbf{x}))^T \mathbf{a} \quad (9)$$

The mean squared error (MSE) of equation (8) and the constraint condition for best unbiased predictor are the following respectively

$$\text{MSE}[\hat{u}(\mathbf{x}) - u^h(\mathbf{x})] = E[\mathbf{c}^T(\mathbf{x})\mathbf{U}_s - u(\mathbf{x})]^2, \quad (10)$$

$$\mathbf{P}_m^T \mathbf{c} - \mathbf{p}(\mathbf{x}) = 0 \quad (11)$$

Equation (10) is converted into unconditional minimum problem with constrain condition equation (11) based on Lagrange multiplier method. The interpolation function under best linear unbiased estimate conditions can be obtained by adopting functional analysis

$$\mathbf{u}^h(\mathbf{x}) = \mathbf{p}^T(\mathbf{x}) \left[\left(\mathbf{P}_m^T(\mathbf{x}) \mathbf{R}_Q^{-1} \mathbf{P}_m \right)^{-1} \mathbf{P}_m^T \mathbf{R}_Q^{-1} \mathbf{U}_s \right] + \mathbf{r}^T(\mathbf{x}) \mathbf{R}_Q^{-1} \left(\mathbf{U}_s - \mathbf{P}_m \left[\left(\mathbf{P}_m^T(\mathbf{x}) \mathbf{R}_Q^{-1} \mathbf{P}_m \right)^{-1} \mathbf{P}_m^T \mathbf{R}_Q^{-1} \mathbf{U}_s \right] \right) \quad (12)$$

Where \mathbf{R}_Q is a $n \times n$ matrix

$$\mathbf{R}_Q = \begin{bmatrix} 1 & R(\mathbf{x}_1, \mathbf{x}_2) & \cdots & R(\mathbf{x}_1, \mathbf{x}_n) \\ R(\mathbf{x}_2, \mathbf{x}_1) & 1 & \cdots & R(\mathbf{x}_2, \mathbf{x}_n) \\ \vdots & \vdots & \ddots & \vdots \\ R(\mathbf{x}_n, \mathbf{x}_1) & \cdots & R(\mathbf{x}_n, \mathbf{x}_{n-1}) & 1 \end{bmatrix} \quad (13)$$

Equation (12) can be expressed as equation (14)

$$\begin{aligned} \mathbf{u}^h(\mathbf{x}) &= \left[\mathbf{p}^T(\mathbf{x}) \left(\mathbf{P}_m^T \mathbf{R}_Q^{-1} \mathbf{P}_m \right) \mathbf{P}_m^T \mathbf{R}_Q^{-1} + \mathbf{r}^T(\mathbf{x}) \mathbf{R}_Q^{-1} (\mathbf{I} - \mathbf{P}_m \mathbf{S}_{\bar{a}}) \right] \mathbf{U}_s = \left[\mathbf{p}^T(\mathbf{x}) \mathbf{S}_{\bar{a}} + \mathbf{r}^T(\mathbf{x}) \mathbf{S}_{\bar{b}} \right] \mathbf{U}_s \\ &= \boldsymbol{\Phi}(\mathbf{x}) \mathbf{U}_s = \sum_i^n \phi_i(\mathbf{x}) \mathbf{u}_i \end{aligned} \quad (14)$$

Where $\boldsymbol{\Phi}(\mathbf{x})$ is matrix of shape function and $\phi_i(\mathbf{x})$ is the shape function.

3 Numerical example

Huang [7] has studied the failure forms of mode I crack in concrete with Test Device shown in figure 1. Here consider the same problem with the proposed method. The computational model is shown as figure 2, the discretization involves 31×31 regular distributed nodes and 36 additional nodes around the crack tip. For numerical analysis, values of crack length $a=75\text{mm}$, material parameters are $E=80\text{GPa}$, $\mu=0.3$ and the fracture toughness $K=0.5\text{MPa} \cdot \text{m}^{1/2}$. This problem is simplified into plane strain condition in the process of calculation. 30×30 background cells is adopted and 4×4 Gauss integration scheme is employed over each background cell.

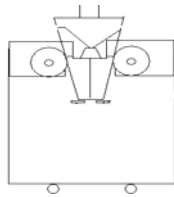


Figure 1 Model of wedgy splitting

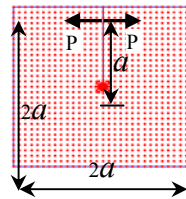


Figure 2 Computational model

Displacement-controlled load is imposed on the rock specimen and the load for each step is $5\text{e-}5\text{mm}$. The computational result of crack propagation at different step is illustrated in figure 3. Figure 4 shows the stress intensity factor curve at different step, it can be seen from it that K_{II} is almost equal zero at all steps, so this is

one typical fracture of model I . For comparison between test and numerical result, figure 5 and figure 6 are numerical and experimental results respectively, Both results are very consistent.

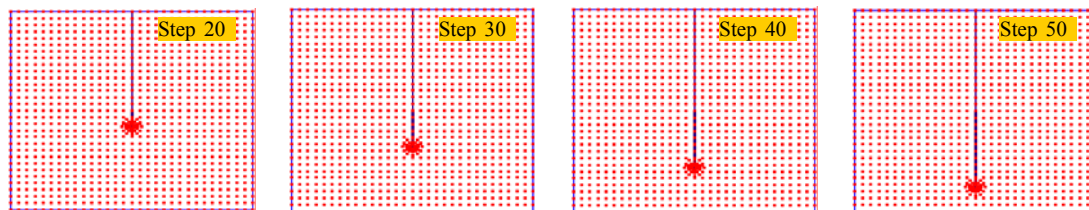


Figure 3 The computed results of different steps

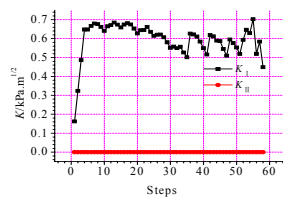


Figure 4 The curve of SIF

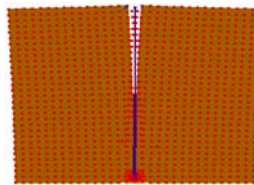


Figure 5 The result of simulation (500 times)



Figure 6 The result of test [7]

4 Conclusion

A new type of meshless method based on the Kriging interpolation technology has been proposed in this paper. The most important feature of the presented method is that the shape function possesses the Kronecker delta property which make the essential boundary condition can be easily enforced as the conventional finite element method and crack problems can be treat better. The numerical result shows that the presented method is effective and has excellent accuracy.

Acknowledgement

The authors are very thanks for sustain from Natural Science Fund of China (No.10672028).

References

1. Shi, G.H., Manifold method. Proceedings of the first international forum on Discontinuous Deformation Analysis(DDA) and Simulations of Discontinuous Media, Berkeley, California, USA, 1996, 52-204.
2. Belytschko, T., Liu, Y. and Gu, L., Element free Galerkin methods. International Journal for Numerical Methods in Engineering, 1994, 37, 229-256.
3. Luan, M.T., Yang, X.H., Tian, R. and Yang, Q. Numerical analysis on progressive fracture behavior by using element-free method based on finite covers. International Journal of Computational Methods, 2005, 2(4). 1-11.
4. Li, S.C., Cheng, Y.M. and Li, S.C., Enriched meshless method, Chinese Journal of Rock Mechanics and Engineering, 2005, 24(12). 2065-2073.
5. Liu, G.R. and Gu, Y.T., A point interpolation method for two-dimensional solid. International Journal for Numerical Methods in Engineering, 2001, 50. 937-951.
6. Gu, L., Moving Kriging Interpolation and Element-free Galerkin Method, International Journal for Numerical Method in Engineering, 2003, 56. 1-11.
7. Huang, Z.Q., Study on Induced Joints and Fracture Property of Layer Surface in RCC with Test and Numerical Modeling. Dalian: Dalian University of Technology, 2006.

NUMERICAL SIMULATION ON INFLUENCE OF CONFINING PRESSURE ON DYNAMIC FAILURE PROCESS OF ROADWAY CONTAINING DISCONTINUOUS INTERLAYER

YU-JUN ZUO

Research Center for Numerical Test of Material Failure, Dalian University, Dalian, 116622, P.R.China

CHUN-AN TANG

Civil & Hydraulic Engineering School, Dalian University of Technology, Dalian, 116024, P.R.China

SHU-CAI LI

Geotechnical and Structural Engineering Research Center, Shandong University, Jinan, 250061, P.R.China

Based on mesoscopic damage mechanics, numerical code RFPA2D was developed to simulate the failure process of rock roadways containing a discontinuous interlayer under a dynamic disturbance. This paper discusses the dynamic failure behavior of rock roadways containing discontinuities under different confining pressures. The results show that the discontinuous interlayer in roadways can hinder the stress wave propagation, and spallation failure of roadways may be inhibited by a discontinuous interlayer. The stability state of roadways is different when the rock roadway is on the condition of different confining pressures. For example, the stability of rock roadways under the same dynamic disturbance are enhanced when confining pressures of roadways are lower. The roadway is closer to or in the critical state of stability when the confining pressure of the roadway is higher, and fewer disturbances may cause large scale expansion fractures instantaneously, leading to the roadway losing stability. Meanwhile, with much strain energy releasing fast, i.e., when the confining pressure of roadway is higher, losing stability is more likely to occur under the same dynamic disturbances.

1 Introduction

There are different scales of structures left in rock mass as a result of the stress field of geological structure movement [1]. In underground engineering, even if intact and hard rock is selected as the surrounding rock of a main roadway, there may be a discontinuous interlayer at the local place in the rock mass. The influences of big and small faults or joint crannies on stability of surrounding rock of roadway are obvious, and their behaviors are complicated [1]. The structure is stable under usual conditions, but rock mass may be damaged and stability of surrounding rock is difficult to control when it is faced with exterior disturbance, such as explosive stress waves. Therefore, it is of realistic significance to study the failure process of the roadway with soft interlayer or discontinuous interlayer under dynamic disturbances.

For demand of production security, researchers commonly study the stability of surrounding rock mass when roadway with soft interlayer or discontinuous interlayer is affected by gravity of rock mass above roadway, and stability of roadway under dynamic disturbance is often studied[2]. However, there is less literature on study of failure process analysis of roadway with soft interlayer or discontinuous interlayer under dynamic disturbance.

The newly developed dynamic rock failure process analysis system RFPA2D [3-6] was used in literature [7] to simulate the dynamic failure process of roadway containing discontinuous interlayer, and dynamic failure

behavior of rock roadway was analyzed under consideration of heterogeneity of mechanical properties of material which consists of element at mesoscopic scale. The results indicated that attenuation of stress wave is obvious because of discontinuity in surrounding rock of roadway, and the influence of discontinuity on stability and failure of roadway is great, for example, smaller discontinuous interlayer can weaken the surrounding rock of roadway, the larger discontinuous interlayer can effectively restrain the spallation of roadway.

2 Brief description of RFPA2D

Rock Failure Process Analysis (RFPA2D) Code (dynamic edition) is a programme used to analyze the progressive fragmentation of solids under impact loads. A salient feature of RFPA2D code is that heterogeneity of rock has been incorporated by assuming Weibull distribution of material parameters, such as the element modulus and strength parameters. Because of this spatial heterogeneity, the overall stress-strain response of the model is highly nonlinear. The rock sample is assumed to be composed of many mesoscopic elements and these mesoscopic elements is formed based on elastic damage mechanics. When the element is under compression or tension, and then when the failure criteria is satisfied, the element failure occurs, and modulus or damages is reduced. Thus, continuum medium mechanics is considered to be appropriate to describe the discontinuous interlayer process resulting from such loading.

In addition, the elements above which material is composed of are used in finite element analysis model. The equilibrium equations governing the linear dynamic response of a system of finite elements can be expressed in the following form:

$$M\ddot{U} + C\dot{U} + KU = R \quad (1)$$

where M , C and K are the mass, damping, and stiffness matrices; R is the vector of externally applied loads; and U , \dot{U} and \ddot{U} are the displacement, velocity, and acceleration vectors of the finite elements.

By using finite element method to analyze stress, the stress distribution and strain distribution of analyzed object are obtained. Then the failure criterion of a Mohr-Coulomb type of condition with a tensile cut-off, in which strength parameters are functions of the strain rate, is used to determine whether the failure of element occurs. After the failure element is dealt with according to constitutive law of elastic damage mechanics, the next step is continued to analyze the element until the complete analysis process is finished, i.e. the complicated failure process of specimen at macrostructure scale is studied with simple constitutive law of element at mesoscopic scale under consideration of heterogeneity of mechanical properties of material. The assignment to parameters of material mechanical properties and constitutive law of element were introduced in detail in literatures [8]. In the meantime, stiffness degradation (processing separation of element) and stiffness reconstruction (processing contact of element) are adopted to deal with fractured element, so that continuum mechanics method is used to deal with the problems of physical discontinuity.

In addition, dynamic rock failure process analysis system RFPA^{2D} can be used to analyze the energy of failed element. For the ideal elastic and brittle material, cumulative value of released energy of failed element EN can be expressed as follows[9]:

$$EN = \sum \frac{1}{2C_f} \sigma_{cf}^2 \cdot v_f = \frac{v_e}{2} \sum \frac{\sigma_{cf}^2}{C_f} \quad (3)$$

Where v_e is the single element volume, v_f is the volume of the individual failed element, C_f is the elastic modulus for the element, σ_{cf} is the peak strength of the failed element.

In dynamic analysis, the finite element is analyzed using step of time under inputting a stress wave and reasonable step length of time. More detail on dynamic RFPA code is referred to literatures [3-6].

3 Numerical simulation and analysis

3.1 Numerical model

Certain roadway which is not reinforced is used as the calculation example to analyze the roadway section failure. Here the horizontal geo-stress σ_h of roadway is higher, and the vertical geo-stress is so small that the influence of vertical geo-stress on the deformation of roadway structure is ignored. The model of roadway is shown in Figure 1, which is 100m×100m in dimension in practical scale, whose shape of roadway section is horse's hoof, thereinto the rectangle part is 15m×15 m in dimension, and the round crown height is 3 m; besides, there is a discontinuous interlayer above roadway roof, and angle between interlayer and horizontal direction is 30°. The values of mechanical parameters for rock roadway are shown in Table 1.

Using the dynamic rock failure process analysis system RFPA2D, the failure process of aforementioned roadway is analyzed. In numerical simulation, the numerical sample model is used to represent the practical model. The numerical sample model which is 50mm×50mm in dimension is composed of 100×100 elements that are 0.5mm×0.5mm in dimension. The width of discontinuous interlayer is 2 elements (1mm). The bottom boundary and right boundary of model are fixed, and the model in the horizontal direction and vertical direction can be compressed and tensile. The dynamic loading in Figure 1 is an impact stress wave loaded from surface. In general, the impact stress wave is assumed to be a pulse load in order to simplify the numeration in dynamic analysis. Here only influence of spherical impact stress wave on failure process of roadway is analyzed, and the pulse load is assumed to be trapezoidal wave wave, whose duration is 1.5 μ s, peak value is 220MPa, as shown in Figure 2. The material is assumed to be heterogeneous, and the mechanical properties of these elements are assumed to conform to a given Weibull distribution, and the Weibull distribution parameters is listed in Table 2. The macro mechanical parameters of sample composed of elements listed in Table 2 corresponds approximately to the rock mechanical parameters shown in Table 1.

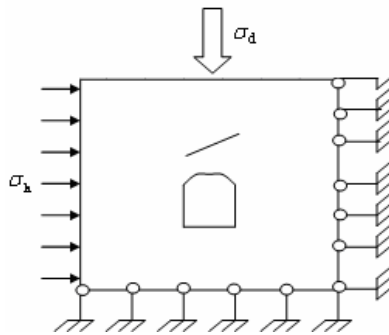


Figure 1. Model for calculation

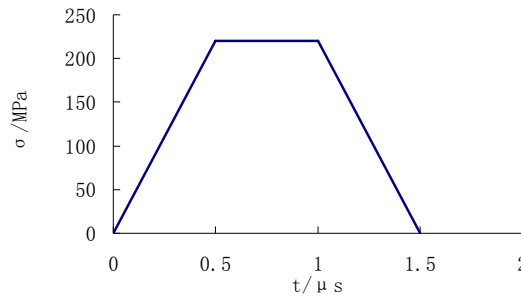


Figure 2 loading waveform

Table 1. Values of mechanical parameters for rock

parameters	value
specific gravity /kg.m-3	2500
Young's modulus /GPa	25
Poisson's ratio	0.25
tensile strength /MPa	5.00
compressive strength /MPa	50
internal frictional angle /°	35

Table 2 Weibull distribution parameters of rock material

parameters	value	parameters	value
mean of Young's modulus /GPa	30	homogeneity index	3.0
mean of uniaxial compressive strength /MPa	200	homogeneity index	3.0
Poisson's ratio	0.25	homogeneity index	100
specific gravity /kg.m-3	2500	homogeneity index	100
residual strength coefficient /MPa	0.1	compressive-tensile strength ratio	10
residual Poisson's ratio	1.1	internal frictional angle /°	35
maximum tensile strain	5	maximum compressive strain	100

The aforementioned model is simplified as plane strain problem to be solved, and only the propagation process before stress wave reaches the numeration boundary is considered. In numerical simulation, the step length of time is 0.1 μ s.

In order to analyze influence of confining pressure on dynamic failure process of rock roadway containing discontinuous interlayer, confining pressure is set to be 0 MPa, 5 MPa, 10MPa. During numerical simulation of roadway, horizontal confining pressure is loaded by static stress, according to 1MPa / step, until it reaches the assigned value; dynamic load is loaded after the static loading is finished, and the following loading steps refers to dynamic loading steps.

3.2 Numerical simulation of failure process of roadway under spherical impact stress

3.2.1 Confining pressure of roadway is ignored

Calculation model is shown in Figure 1. Due to limitation of page, only the fracture processes for the shear stress field of the time steps are used, as shown in Figure 3. In the following figures of stress distributions, the gray degree denotes corresponding magnitude of element shear stress, i.e., the brighter the point, the greater the shear stress of the element; and the black points indicate failure of elements. The bright half circularity in Figure 3 denotes the wavefront of the spherical impact stress wave, which propagate from top of sample to bottom. Seen from shear stress field, there is a black hole at the place of wave origination of the spherical impact stress wave, denoting the failed elements here. The stress wave after the black hole is largely attenuated, and then there is few failed elements at region where stress propagates, i.e., there is small area of black dot in shear stress figure. Stress wave is interdicted at one face of discontinuous interlayer when stress reaches discontinuous interlayer, as shown in figure of No.30 loading step, and then stress wave goes around and reaches another face of discontinuous interlayer from one face, as shown in figure of No.35, No.45 and No.55 loading step, resultantly one gap appears on wavefront. Because the stress wave diffraction occurs at discontinuous interlayer, the stress wave speed becomes slow. Moreover, when stress wave reaches discontinuous interlayer, the spherical impact stress wave reflects, and spallation failure can be seen at face of discontinuous interlayer near wave origination, and in shear stress distribution figure it is seen that black dots distribute along the direction of discontinuous interlayer, as shown in figure of No.45, No.55 and No.100 loading step. From final failure result, the spallation failure of roadway roof in Figure 3 is not obvious because of stress wave attenuation. According to the results in literature [7], it is because more stress wave energy is consumed when stress wave propagates in rock mass with discontinuous interlayer, spallation failure in roadway with discontinuous interlayer is restrained.

From aforementioned analysis, the stress wave propagation phenomenon can be simulated realistically by using numerical code RFPA2D (dynamic edition).

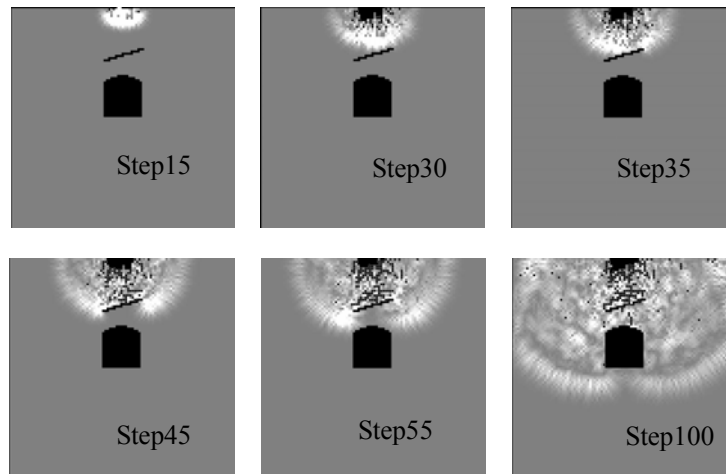


Figure 3 Maximal shear stress distribution figure of failure process of roadway containing discontinuity under spherical wave (confining pressure is 0)

3.2.3 There is horizontal confining pressure

When the confining pressure is 5MPa, the maximal shear stress distribution figure of the failure process of roadway under the same spherical stress wave is shown in Figure 4. The law of stress wave propagation in Figure 4 is mostly the same as that in Figure 3. Compared with Figure 3, there is a smaller black hole at the place of wave origination of the spherical impact stress wave, denoting less failed elements here; when stress wave reaches discontinuous interlayer, the spherical impact stress wave reflects, there is not the spallation phenomenon show in Figure 3. These phenomenon indicate that amount of failed element in surrounding rock of roadway can be reduced by confining pressure. Compared with the results in literature [7], the influence of confining pressure on stress wave speed is not clear. Besides, there is not spallation failure of roadway roof, and the roof is more intact than that in Figure 3, it indicating that discontinuous interlayers and confining pressure effect can effectively restrain the spallation of roadway.

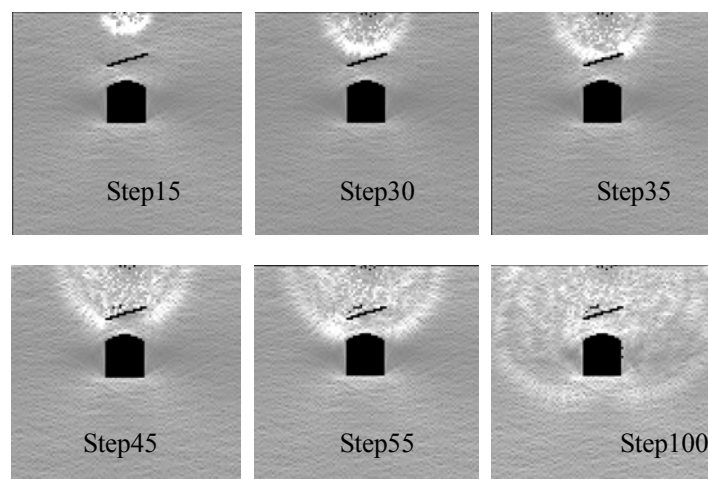


Figure 4 Maximal shear stress distribution figure of failure process of roadway containing discontinuity under spherical wave (confining pressure is 5MPa)

When the confining pressure is 10MPa, the maximal shear stress distribution figure of the failure process of roadway under the same spherical stress wave is shown in Figure 5. The law of stress wave propagation in Figure 5 is mostly the same as that in Figure 3 and Figure 4. Compared with Figure 4, the larger confining pressure causes obvious bending deformation of roadway wall and obvious stress concentration in the bottom corner of roadway; change of the black hole at the place of wave origination is not obvious; when stress wave reaches discontinuous interlayer and roadway roof, the spherical impact stress wave reflects, however, there is no spallation phenomenon occurrence shown in Figure 3. When the stress wave propagation reaches No. 101 loading step, roadway model abruptly becomes black, denoting that roadway loses stability.

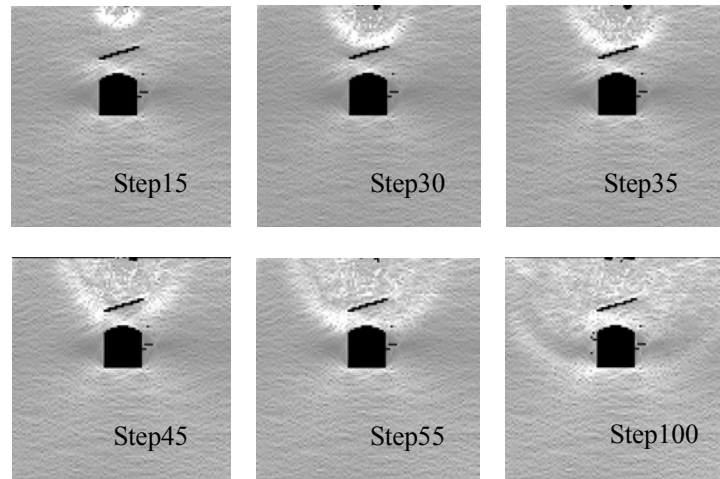


Figure 5 Maximal shear stress distribution figure of failure process of roadway containing discontinuity under spherical wave (confining pressure is 10MPa)

In order to analyze further the failure mechanism of roadway under different confining pressure subjected to disturbances, the figure for cumulative failed element counts vs. loading step under three different state of confining pressure is given in Figure 6. From Figure 6, when the confining pressure is lower (for example, confining pressure is 5MPa), with confining pressure increasing, cumulative failed element counts in rock specimen decrease at the same loading step. It is shown that failure of specimen under the same dynamic disturbance is difficult to occur at the same loading step. This is mainly because that the increasing confining pressure leads to increase of rock strength. When the stress wave propagates to discontinuous interlayer, from loading step No.35 to No.45, cumulative failed element counts vs. loading step curve flattens out, indicating that after stress wave propagates to discontinuous interlayer, it becomes weaken, and failed element counts in specimen decreases. When the confining pressure is higher (for example, confining pressure is 10MPa), with confining pressure increasing, cumulative failed element counts in rock specimen increase slowly at the same loading step. When the stress wave propagates to about $7 \mu s$ (No.70 loading step), instead cumulative failed element counts at the same loading step become greater than that without confining pressure; when the stress wave propagates to about $10.1 \mu s$ (No.101 loading step), cumulative failed element counts at the same loading step increase abruptly, and corresponding specimen subjected to disturbance is broken, indicating that roadway loses stability.

In the meantime, the figure for cumulative release energy of failed element vs. loading step under three different state of confining pressure is given in Figure 7. Likewise, when the confining pressure is lower (for example, confining pressure is 5MPa), with confining pressure increasing, cumulative release energy of failed element in rock specimen decrease at the same loading step. When the stress wave propagates to discontinuous interlayer, from loading step No.35 to No.45, cumulative release energy of failed element vs. loading step curve

flattens out. When the confining pressure is higher (for example, confining pressure is 10MPa), with confining pressure increasing, cumulative release energy of failed element in rock specimen increase slowly at the same loading step. When the stress wave propagates to about $7 \mu s$ (No.70 loading step), instead cumulative release energy of failed element at the same loading step become greater than that without confining pressure; when the stress wave propagates to about $10.1 \mu s$ (No.101 loading step), cumulative release energy of failed element at the same loading step increase abruptly, and it also indicated that corresponding roadway subjected to disturbance loses stability. The results gained here is the same as that in figure 6.

In addition, from Figure 6 and Figure 7, during stress wave propagates, cumulative failed element counts in specimen under confining pressure is increasing; but the failed element in shear stress distribution figure shown in Figure 4 and Figure 5 doesn't appear, it is because failed element becomes re-closed under confining pressure, and this phenomenon is expressed using stiffness reconstruction (processing contact rigidity) in rock failure analysis system.

As mentioned above, when the confining pressure of roadway is lower, the stability of roadway structure under the same disturbance is enhanced; when the confining pressure is higher, roadway structure under the same disturbances is more likely to lose stability. Actually, the stability of roadway structure under different condition of confining pressure is not the same. According to literature [10], when the geological mass is close to the critical state of stability due to evolution, geological disaster can be induced by tiny disturbance. In this paper, when confining pressure is 5MPa, roadway structure is so far from critical state of stability that external certain disturbance can't cause instability of roadway, but only local fragmentation caused by stress wave; when confining pressure is 10MPa, roadway structure is close to critical state of stability, then the exterior certain disturbance can cause instability of roadway, in the meantime, with much strain energy releasing fast.

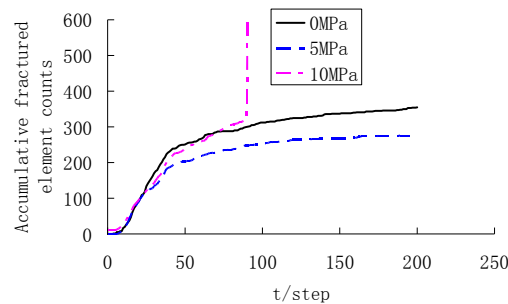


Figure 6 Cumulative counts of failed element in specimen vs. loading step under different confining pressure

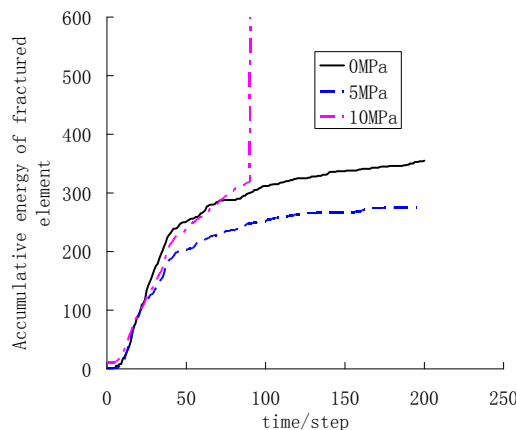


Figure 7 Cumulative release energy of failed element in specimen vs. loading step under different confining pressure

4 Conclusions

Based on mesoscopic damage mechanics, numerical code RFPA2D is developed to simulate the failure process of a rock roadway containing a discontinuous interlayer under a dynamic disturbance, and the stress wave propagation process is re-built realistically, and the following conclusions are drawn:

Discontinuous interlayers in roadways can hinder the stress wave propagation, and spallation failure of roadway may be inhibited by the discontinuous interlayer.

The stability state of a roadway is different when the rock roadway is on the condition of different confining pressure. For example, the stability of rock roadway under the same dynamic disturbance is enhanced when confining pressure of roadway is lower; the roadway is more close to or in the critical state of stability when the confining pressure of roadway is higher, and the less disturbance may cause fractures expansion instantaneously and cosmically, leading to the roadway losing stability, in the meantime, with much strain energy releasing fast, i.e., when the confining pressure of roadway is higher, losing stability is more likely to occur under the same dynamic disturbances.

Acknowledgements

The study presented in this paper was funded by the National Natural Science Foundation of China (50874020, 40638040, 50674025, 50874024) and 973 Program (No.2007CB209407), Liaoning Province Education Office Colleges and Universities Research plan (200802515)

References

1. Duan, Q.W., He, M.C. and Zhang S.G. Numerical Simulation of Deformation Character of Surroundings in Complicated Situations. *Coal Science Technology*, 2002, 30(6). 55-58.
2. Xue, Y.D., Zhang, S.P. and Kang, T.H. Numerical Analysis of Dynamic Response of Rock Bolts in Mining Roadways. *Chinese Journal of Rock Mechanics and Engineering*, 2003, 22(11). 1903-1906.
3. Zhu, W.C., Tang, C.A. Numerical Simulation of Brazilian Disk Rock Failure under Static and Dynamic Loading. *International Journal of Rock Mechanics and Mining Sciences*, 2006, 43 (2). 236-252.
4. Tang, C.A., Liu, H. and Lee P.K.K. Numerical Tests on Micro-Macro Relationship of Rock Failure under Uniaxial Compression, Part I: Effect of Heterogeneity. *International Journal of Rock Mechanics and Mining Sciences*, 2000, 37(4). 555-569.
5. Chau, K.T., Zhu, W.C., Tang, C.A. and Wu, S.Z. Numerical Simulations of Failure of Brittle Solids under Dynamic Impact Using A New Computer Program_DIFAR. *Key Engineering Materials*, 2004 , (261-263). 239-244
6. Zhu, W.C., Tang, C.A., Huang, Z.P. and Pang, M.Z. Numerical Simulation on Splitting Failure Mode of Rock under Static and Dynamic Loadings. *Chinese Journal of Rock Mechanics and Engineering*, 2005, 24(1). 1-7.
7. Zuo, Y.J., Tang, C.A. and Li, S.C. Numerical Analysis on Failure Process of Rock Tunnel with Discontinuity under Dynamic Disturbance. *Chinese Journal of Underground Space and Engineering*, 2008, 4(4). 595-599.
8. Zhu, W.C. and Tang, C.A.. Numerical Simulation on Shear Fracture Process of Concrete Using Mesoscopic Mechanical Model. *Constructions and Building Materials*, 2002, 16(8). 453-463.
9. Tang, C.A. and Kaiser, P.K. Numerical Simulation of Cumulative Damage and Seismic Energy Release During Brittle Rock Failure-Part I : Fundamentals. *International Journal of Rock Mechanics and Mining Sciences*, 1998, 35(2). 113-121
10. Xu, Q., Huang, R.Q., Wang, L.G. Mechanism Analysis on Geological Hazards Triggered By External Disturbance. *Chinese Journal of Rock Mechanics and Engineering*, 2002, 21(2). 280-284.

NUMERICAL ANALYSIS OF STABILITY OF ROCK MASS IN SHIRENGOU IRON MINE, TANGSHAN CITY, FROM OPEN-PIT TO UNDERGROUND MINING

TIAN-HUI MA, CHUN-AN TANG, LIAN-CHONG LI and YONG-BIN ZHANG

Center for Rock Instability and Seismicity Research, Dalian University of Technology

Dalian, 116024, P.R. China

This paper examines the stability of the rock mass during the transition from open pit to underground mining of the Shirengou Iron Mine. This was analysed using 2D Realistic Failure Process Analysis system (RFPA2D). In order to get a reasonable thickness of the barrier pillars, the process of failure for rock mass was modeled, and the deformation and stress changes induced by open excavation were predicted. Eventually, optional mining schemes and measures to control the spalling and caving of rock masses were proposed. These results enable the operators to make the most efficient use of resources both for ground support and excavations, as well as to address safety issues, which are of top priority.

1 Background

Mining involves extraction of non-renewable resources that play a dominant role in economic development of some regions in China. Recently, many mines in our country are facing the transition from open-pit to underground mining, such as Shirengou Iron Mine, Banshigou Iron Mine and Tongguanshan Iron Mine [1-5].

Since its opening in 1975, the Shirengou Iron Mine has produced more than 30 million tons. Nearly all of the ore production has been from open-pit mining. However, as two pits deepen, it is planned to convert to underground mining. The south open-pit has been selected as a trial underground mine for the purposes of testing mining methods and to provide access to the lower elevations of the first mineral vein (called M1).

2 General Geology

Shirengou Iron mine is the primary ore supplier of the TangGang mining industry company, and its open-pit mining is going to end. Mining area is divided into a south working section and a north working section taking the 16th line as the dividing line. At present, the south mining area is already over, and it has become the dump. It will be adopted with the segmented, open-stope method with reserve top pillar and forward mining then back stoping. There is a well-developed monoclonal structure in the south area, and it has a great influence on orebody. In the design area, there are many dangerous faults. They are F5, F8, F18, F20, F21, Fa, F19, F11, F1. They make the rock mass fragmentize and the mechanic parameters decrease. The 16th line to the 28th line, about 1440m long area, is focused on in this paper. In the area, most are M2 ore bodies, others are M1 ore bodies. Most of them are magnetite, others are hematite and the rock mass is plagioclase gneiss.

This paper gives an introduction to the engineering geological characteristics. From the typical case, the mechanism of surrounding rock movement and pillar deformation and failure caused by mining is analysed. This is of great significance to the design of mine

3 Models and Mining Scheme

The model for Shirengou Iron we considered includes backfill, surrounding rock mass, ore bodies and faults. At the direction of the length, from the 16th line to the 28th line, the model is 1200 meters and it is 685 meters at the direction of the width. At the direction of the height, from the top of backfill to -200m, it is 140 meters.

The FEM code, 2D Realistic Failure Process Analysis system (RFPA2D), is used to simulate the process of pillars failure and deformation of rock mass for the cavern during caving.

The numerical code, RFPA2D, is widely applied to simulate failure processes of materials, such as concrete, ceramics, fibrous materials and rocks. It based on a stress analysis method and a material failure constitutive law, can be taken as a tool in numerical modeling analysis to enhance our understanding of the failure mechanisms of materials. On the other details please consult the reference [6-10].

From the typical case, we choose six sections along the line of mineral vein. They are 16, 20, 22, 24, 25 and 28 section individually. For the 2D model, it is 350m wide and 220m high. In the model, bilateral border and bottom border are fixed at the direction of perpendicular borders and upper part is free. Self-weights for all materials are only considered and about 18m high ores are caved each step as designed. In our research, Mohr-Coulomb criterion is used to be the damage threshold and different bi-layered models are not pre-assigned fractures. Weibull distribution is used to define the heterogeneity of the bi-layered material and the associated parameters are listed in Table 1.

Table 1 Mechanical property of different rock materials

Materials' Name	Density [g/cm ³]	Compressive Strength [MPa]	Cohesion [MPa]	Internal Friction Angle [°]	Elastic Modulus [GPa]	Poisson Ratio
M1 mineral vein	3.00	10.00	2.20	38.00	48.00	0.21
M2 mineral vein	3.00	13.00	2.40	38.00	48.00	0.21
Rock Mass	2.71	9.00	1.50	36.00	43.10	0.22
Backfill	2.00	0.20	0.01	32.00	1.00	0.32
Fault	2.00	0.80	0.22	31.00	2.00	0.30

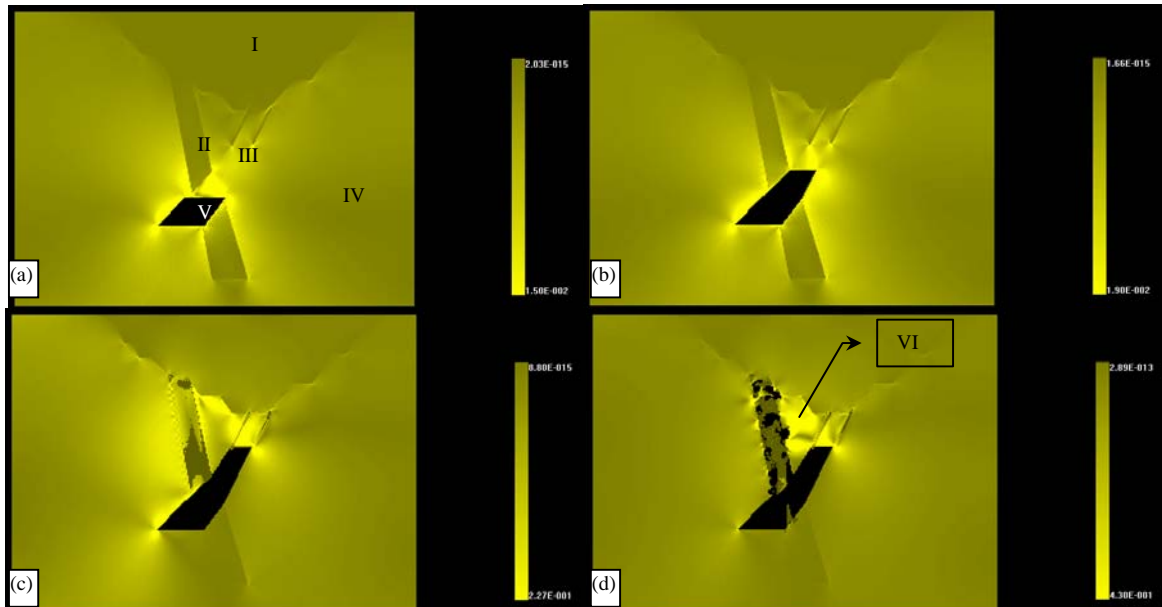


Figure . 1 Distribution of shear stress and damage for the 25th section at -4m level. (Light location has higher stress; I-backfill; II-fault; III-ore body; IV-surrounding rock mass; V-caved zone; VI-failure zone; (a) the first step; (b) the second step; (c) the third step; (d) the fourth step.)

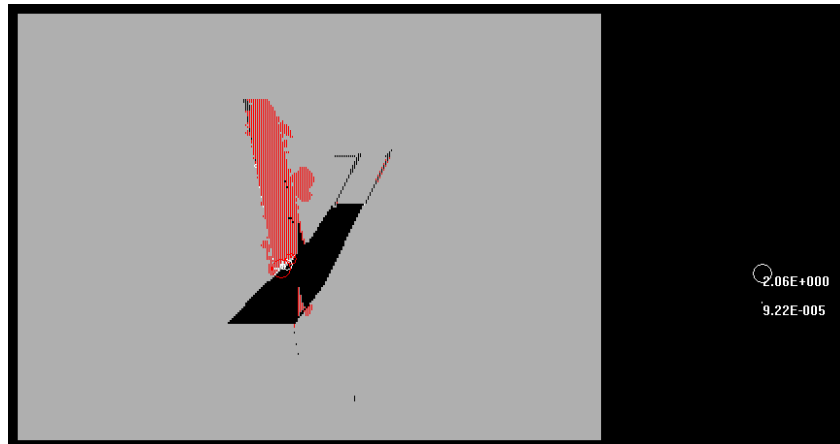


Figure 2 Distribution of acoustic emission for the 25th section at -4m level

4 Numerical Simulation Results and Discussion

For studying the stability of surrounding rock mass during excavating, a few across sections were chosen to take as the research subjects on the assumption that the top pillars are designed at 0m, -4m or -6m. Because of the limit of the article length, the dangerous 25th section setting top pillar at -4m was taken as an typical example to illustrate. The numerical models are designed to excavate four steps and 14m high ore body is excavated for each step.

The distribution of shear stress and damage for the 25th section at -4m level simulated by RFPA2D are showed in Figure .1. Light location has higher stress and it is the potential damage zone. In the first step and the second step, the excavating did not affect the stability of the faults and the surrounding rock mass. In the third step, there are many failure zones at the interface of the faults and the backfill and the interface of the faults and the excavated zone. After finished the fourth step, all the fault zones have been damaged completely. Enclosed triangle zone by the faults, the backfill and the ore body has light higher stress and its displacement reached the maximum. Under the weights of the top backfill, it will collapse at any moment. At this time, Figure .2 illustrated the acoustic emission zone. It indicates there are much energy release and many micro-fractures in this area.

5 Conclusions

The simulation results show that top pillars are more effective than the pillars interval stope rooms for surrounding rock mass stability. If the pillar interval rooms are not taken into account, the top surrounding rock mass is stable for all sections. However, we can not be sure that some pillars, for example 19, 20 and 25 section, are stable in three years.

So the top pillars are designed at -6m level, and 8m wide interval pillars are reserved. The top pillars and surrounding rock mass for all the sections will be stable for a long time. The conclusions are based on two following preconditions:

First, when the mining operation reaches the faults F8 and F18, the mining programs need to change, and safer pillars must be reserved near the faults.

Second, only 19, 20 and 25 sections are not stable at -4m level as the size of the interval pillars changed, but the others are stable at this height.

Acknowledgements

This paper is funded by and the Chinese Postdoctoral Science Foundation (No. 20070421048) and the National Key Basic Research Science Foundation (No. 2007CB209400), the Chinese National Natural Science Foundation (No. 40638040, 10672028, 10872046, 50674025).

References

1. Wang, Y. The Confirmation Method on the Safety Thickness of Boundary Pillar on the Mined-out Areas. Express Information of Mining Industry , 2002 , 1. 17-18.
2. Cai, M.F., He, M.C. and Liu, D.Y., Rock Mechanics and Engineering. Science Press, Beijing, 2002.
3. Hoek, E. and Brown, E.T., Empirical Strength Criterion of Rock Masses. Journal of Geotechnical Engineering Division American Society of Civil Engineering , 1980 ,106. 1013- 1035.
4. Deere, D.U., Technical Description of Cores for Engineering Purposes. Rock Mech. Eng. Geot. , 1963, 1. 1-22.
5. Bieniawski, Z.T. Determining Rock Mass Deformability. Rock Mech. Min. Sci., 1978, 15. 237-247.
6. Tang, C.A. Numerical Simulation of Rock Failure and Associated Seismicity. Rock Mech. Min. Sci., 1997, 34. 249-262.
7. Kaiser, P.K. and Tang, C.A., Numerical Simulation of Damage Cumulation and Seismic Energy Release during Brittle Rock Failure —Part II: Pillar Collapse. Rock Mech. Min. Sci. , 1998, 35. 123-134.
8. Tang, C.A. and Kaiser, P.K. Numerical Simulation of Cumulative Damage and Seismic Energy Release during Brittle Rock Failure —Part I: Fundamentals. Rock Mech. Min. Sci., 1998, 35. 113-121.
9. Tang, C.A., Xu, X.H., Kou, S.Q., et al, Numerical Investigation of Particle Breakage as Applied to Mechanical Crushing —Part I: Single-particle Breakage. Rock Mech. Min. Sci., 2001, 38. 1147-1162.
10. Tang, C.A., Wang, S.H. and Fu, Y.F., Numerical Test on the Process of Rock Failure. Science Press, Beijing, 2003.

NUCLEATION AND GROWTH OF CRACKS FROM TWO SURFACE FLAWS UNDER UNIAXIAL COMPRESSION

SHI-BIN TANG^{1,2}, ROBINA HC WONG¹ and CHUN-AN TANG²

¹ *Department of Civil and Structural engineering, The Hong Kong Polytechnic University, Hong Kong, China*

² *Center for Rock Instability and Seismicity Research, Dalian University of Technology, Dalian, 116024, China*

Development of cracks from a 3-D surface flaw is significantly different from the 2-D sample. This is because the sliding of the surface flaw is controlled by the cracking mechanism at the interior flaw fronts. Studying the crack growth mechanisms of 3-D surface flaw is worthwhile, especially the coalescence mechanisms from multiple surface flaws. This paper investigates crack nucleation, propagation, and coalescence from two surface flaws using the numerical tool known as Realistic Failure Process Analysis (RFPA). By studying crack development on the surface and cutting sections of the samples, the crack growth process and crack growth mechanisms are better understood. Numerical results indicate that both heterogeneity features and loading directions significantly effect mechanical behaviour. Petal cracks (Mode III cracks) play an important role in the crack growth process from 3-D surface flaws because substantial petal crack growth is required for further propagation of wing cracks and anti-wing cracks. .

1 Introduction

The length scale of fractures or flaws found in natural rocks ranges from micrometers (cracks) in rock samples to thousands of kilometres (fault) in the earth's crust. The crack growth and coalescence processes from those pre-existing flaws play an important role in the stability of rock engineering projects, such as slopes and tunnels. In the past several decades, investigations on the crack initiation, propagation and coalescence from single 2-D pre-existing flaws under uniaxial compression indicated that tensile cracks initiate and propagate first from the flaw tips, named as wing crack [1]. But for multiple 2-D pre-existing flaws, the interaction between the flaws is a sensitive factor influencing the crack growth pattern. In order to fully understand the mechanisms of crack coalescence in rock masses containing multiple flaws, Wong et al [2] investigated the patterns of crack coalescence and strength of a sandstone-like material containing two parallel inclined frictional 2-D flaws under uniaxial compression. Zhou et al [3] studied the stress state of two Griffith cracks subjected to uniform tension, and found that the fracture criterion is unified at both the macroscopic and microscopic scales. Tang et al [4] and Sagong et al [5] also reported the coalescence of three or multiple flaws in a rock-like material subjected to uniaxial compression. However, most of these researches focused on the crack growth from a 2-D pre-existing flaw. In nature, most pre-existing flaws are three-dimensional (3-D). Few of the studies refer to the crack growth from 3-D pre-existing flaw, in particular to the crack growth from surface flaw, i.e. the depth of the flaw extends to a certain depth of the crust. Wong et al [6-10] investigated the crack growth from a 3-D surface flaw (Fig. 1a) under uniaxial and biaxial compression with different observation tools such as multiple channel digital strain gauge (MCDSG), video camera, digital speckle correlation method (DSCM) and acoustic emission (AE). The results indicated that a type of crack occurred at the opposite side of the wing crack, named the anti-wing crack. It was also reported that two types of anti-wing cracks development were found (see Figs 1b and 1c). One type of anti-wing crack was formed by the growth of petal cracks extending from the interior of the sample to the surface, while the other type of the crack was formed by the growth of tensile cracks from the sample surface extending into the interior of the rock. Both types of anti-wing crack are the mixed mode pattern of tensile and compressive crack. Furthermore, the growth behaviour of wing crack and anti-wing crack can be

explained by the result of strain record. The result of studies by Wong et al. [6-10] provides more knowledge and understanding on the crack development of the 3-D surface flaw.

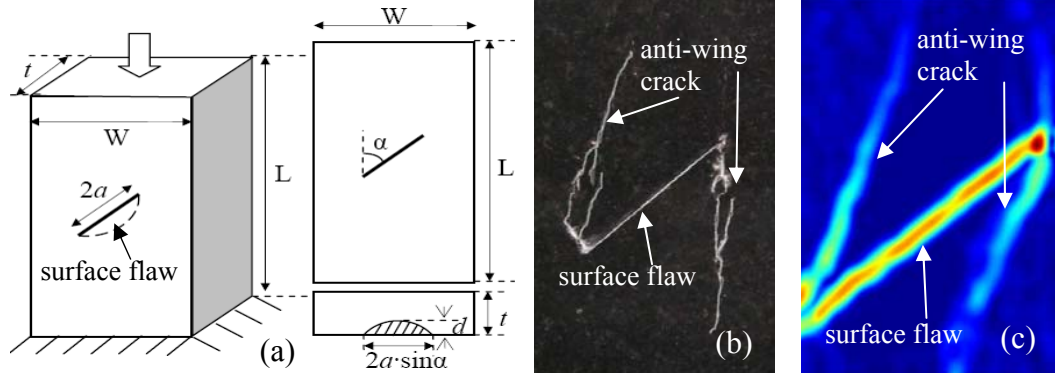


Figure 1 (a) Sketch of model with a single surface flaw [6]; (b) experimental obtained crack pattern of the sample; (c) DSCM obtained maximum shear strain around the flaw area [10-11].

However in nature, rock mass containing numbers of pre-existing surface flaw. The interaction between existing flaws plays an important role in its mechanical behaviour, which is more prone to result in failure of rock mass. Thus, it is important to investigate crack initiation, propagation and coalescence processes from multiple surface flaws under uniaxial or biaxial compression. Generally speaking, the experimental approach provides an intuitional understanding of the fundamental nature of rock failure in samples containing multiple flaws. However, it is difficult to observe the crack development inside the samples. Dyskin pointed out that the details of the development of the essentially 3-D crack feature could only be modelled numerically [11-12]. The numerical investigation provides a thorough understanding of the failure mechanism and coalescence modes in rock containing multi-flaws. Thus in this paper, the Realistic Failure Process Analysis (RFPA) 3D code is used to investigate crack initiation, propagation and coalescence from two surface flaws subjected to uniaxial compression.

2 Brief introduction of RFPA^{3D} code

The heterogeneity of rock is regard as the source of nonlinear mechanical behaviour of rock. Failures in heterogeneous material not only occurred at the high-stress site, but also start at the weaker locations due to the presence of micro-cracks and grain boundaries [13-14]. Thus, in order to reflect the heterogeneity of rock material, the rock sample is discretized to many cubical elements with the same size, and Weibull distribution function is adopted to characterize the elements' failure strength as defined in the following probability distribution function

$$f(\omega) = \frac{m}{\omega_0} \left(\frac{\omega}{\omega_0} \right)^{m-1} \exp \left[- \left(\frac{\omega}{\omega_0} \right)^m \right] \quad (1)$$

where ω is the mechanical property of rock, such as strength, Young's modulus or Poisson's ratio, etc. ω_0 is defined as the mean value of the element parameter, m is defined as the homogeneity index of material. The lower homogeneity index value represents more heterogeneous of the material, and vice-versa. When the mechanical properties of more elements distribute in a narrow range around parameter ω_0 , it indicates that a higher homogeneity sample is generated. According to the definition of Weibull distribution, it should be note that the value of parameter m must be greater than 1.

In RFPA^{3D} code, the stress and displacement fields are calculated as the finite element method (FEM), and the mesoscopic damage mechanics is employed to simulate the crack initiation, propagation and coalescence. At the beginning of loading, the elements are elastic deformation, and elastic properties are defined by Young's modulus E_0 and Poisson's ratio ν . The stress-strain curve of each element is linear elastic until the given damage threshold is attained. In RFPA^{3D} model, maximum tensile stress criterion and the Mohr-Coulomb criterion are used as the tensile and shear damage criterion, respectively. Firstly, the tensile criterion will check whether the element is damaged in tensile mode or not under the current stress state. If the element is not damaged in tensile mode, then Mohr-Coulomb criterion is used to judge whether the element damage occurs in shear modes.

According to Lemaitre damage mechanics, the damage in the model is simulated as the reduction of material elastic properties, i.e. the Young's modulus of the damaged material E can be estimated by reducing the Young's modulus of the initially undamaged solid E_0 as

$$\sigma = E_0 \varepsilon (1 - D) \quad (2)$$

where σ and E_0 are the stress and initial Young's modulus of element, respectively. D is the damage variable.

In RFPA^{3D} code, the failure of an element could occur in either a shear or tensile mode. If the failure occurs, the stress and deformation distribution throughout the sample are then adjusted instantaneously to reach a new equilibrium state without further loading. At locations where the stress is increased after stress redistribution, it may exceed the critical value and further failures will occur. This process is repeated until no new elements failure, and further external displacement or stress loading is then applied. As a result of stress redistribution, a single element failure may induce an avalanche of additional failures in the neighbouring elements. Fractures will grow, interact, and coalesce, which then results in nonlinear deformation behaviour of rock and the formation of macroscopic fractures and cracks.

3 Modelling Strategy

The numerical sample for studying the crack growth mechanism of rock-like material with two pre-existing surface flaw is shown in Fig.2.

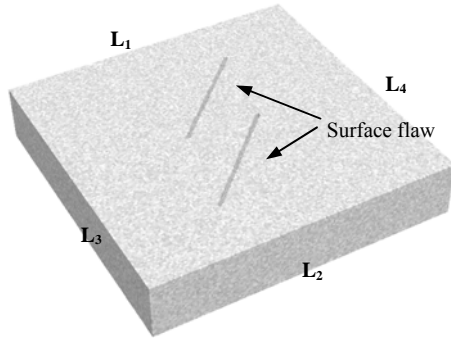


Figure 2 Sketch of numerical model

Table 1. Mechanical parameters of numerical sample

Parameter name	Value
Homogeneity index, m	3
Compressive strength, σ_{c0} (MPa)	300
Tensile strength, σ_{t0} (MPa)	15
Young's modulus, E_0 (MPa)	50,000
Poisson's ratio, ν	0.25
Friction angle, $\alpha(^{\circ})$	30

The model has a common dimension of 160mm×160mm×30mm. In the finite element method, smaller element size indicates more accuracy of the calculation results. However, due to the capacity limitation of computer, the sample is discretized into a mesh that consists of 160×160×30 (768,000) cubic elements. The depths of the surface flaws are 6mm, i.e. $d/t=0.2$. The length of the flaw is 70mm, and inclining angle α is 45°. In order to investigate the different crack growth behaviour from the surface flaw under different loading direction, the numerical sample is subjected to a constant rate of 0.002mm/step displacement loading in two directions respectively. One is loading on L_1 lateral and fixed on L_2 lateral (Fig. 2); but the other is loading on L_3 lateral and fixed on L_4 lateral. Table 1 shows the mechanical properties of numerical sample.

4 Modelling results

Figure 3 shows the numerical simulated crack growth and coalescence from two pre-existing flaw as L_1 lateral subjected to displacement loading. With the increasing of external loading, tensile stresses accumulate around the flaw tips, resulting in failures at the flaw tips. Due to the effect of heterogeneity on mechanical behaviour of the sample, some weak elements at the flaw tips meeting to their tensile failure criteria at first and damage occurred. With more and more failures accumulate at the flaw tips, wing crack would formed at two flaw tips (see Fig. 3 Step 140), which similar to that of cracks growth in 2-D sample with a single pre-existing flaw. The increasing of loading lead to wing cracks further propagation. As loading increase to Step 150 (Fig. 3), wing crack 1 and wing crack 2 at the centre of specimen coalesce with two pre-existing flaws. It can be observed from those figures that the heterogeneity consideration in the samples result in unsmooth crack path and the wing cracks of the two pre-existing surface flaw are not symmetrical, which are recognized to be realistic for real disordered materials.

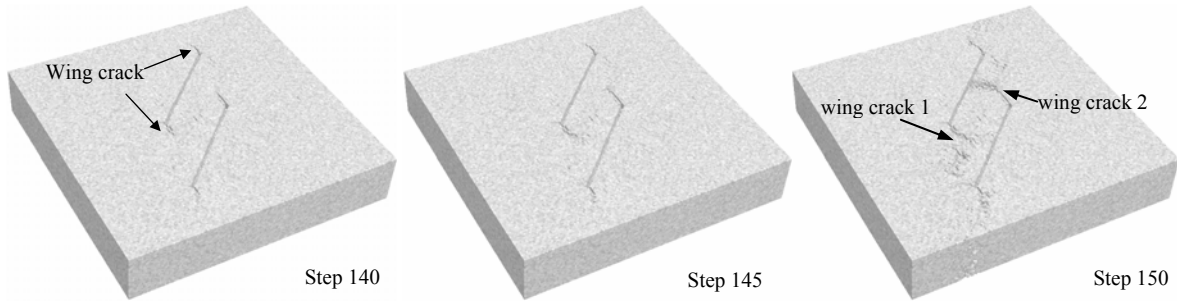


Figure 3 Wing crack growth and coalescence from two pre-existing flaw as L_1 lateral subjected to displacement loading

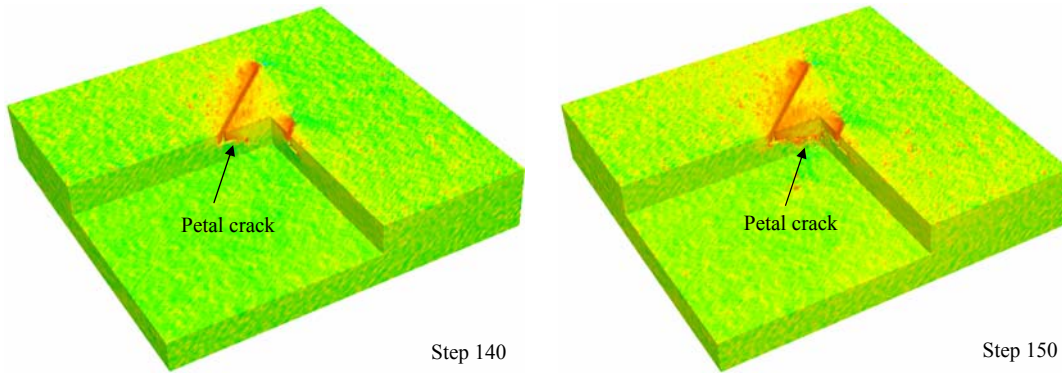


Figure 4 Cracks development inside the specimen as L_1 lateral subjected to displacement loading

It is believed that high stress concentrated around the pre-existing flaw and tensile stress occurred at the flaw tips, either 2-D or 3-D. However, the flaw slide freely in 2-D except for the tips where tensile stress induced wing cracks following a curvilinear path and eventually aligns with the loading direction. However, for the surface flaw, part of the flaw embeds into the sample while other part exposes on the free surface which indicate that the flaw plane near the free surface can slides freely while the deformation of embed part is restricted by the intact portion in the sample. The geometrical feature of surface flaw indicates that it not only subjected to tensile stress at the flaw tips, but also undergoes mode III stress along the contour of the flaw. Different from crack growth from 2-D flaw, crack development from surface flaw not only result in wing cracks at the flaw tips due to tensile stress, but also lead to petal cracks along the contour of the flaw due to mode III

stresses (see Fig. 4). Petal cracks play an important role in the crack growth process from 3-D surface flaw and would result in the middle part between the two pre-existing flaws from the sample, i.e. rockburst.

However, cracks initiation and growth from two surface flaws subjected to loading on L_3 lateral are significantly different from that of specimen subjected to loading on L_1 lateral. It can be seen from Fig. 5 (step 140) that wing cracks initiated at the tips of the flaws. However, with the loading increased, wing cracks did not develop further. But at the center between the two flaws, cracks initiated roughly parallel to the loading direction. With further loading increased, cracks propagated and coalesced with the tips of two pre-existing surface flaws (Fig. 5 step 145). This phenomenon is similar to the crack development from single 3-D surface flaw [6-10] which was named as anti-wing crack. Figure 6 shows the sections of the sample to present the development of the petal cracks and the anti-wing crack. It can be seen that petal cracks initiated and propagated towards the neighbouring flaw. It was observed that when the petal crack coalesced with the neighbouring flaw, the sample failure. The different crack growth behaviour between specimens loading on L_1 and L_3 laterals indicate that loading direction is one of the factors effect on mechanical behaviour of specimens with existing flaws. That's to say, it is important to consider the loading direction for rock engineering as anglicising its mechanical behaviours.

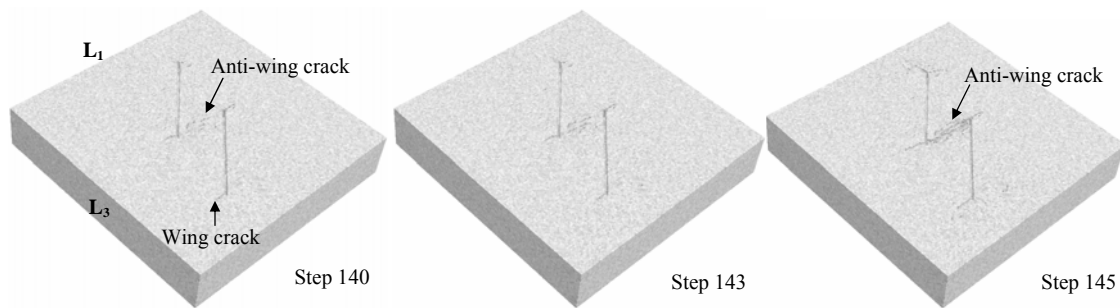


Figure 5 Crack growth and coalescence from two pre-existing flaw as L_3 lateral subjected to displacement loading

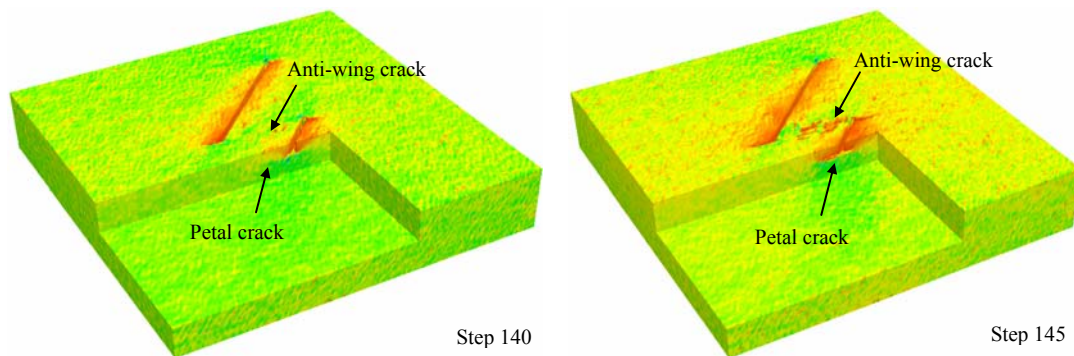


Figure 6 Cracks development inside the specimen as L_3 lateral subjected to displacement loading

5 Conclusions

This paper presents our numerical tests designed to simulate crack initiation, propagation and coalescence from two pre-existing surface flaws contained in samples, resembling brittle rocks under a uniaxial compressive stress field. After examining the simulated results, the following conclusions can be drawn:

(1) There are three types of cracks initiated from surface flaws: wing cracks, petal cracks and anti-wing cracks. Wing cracks initiate at an angle with the pre-existing flaw while anti-wing cracks initiate away from the flaw tip and at the opposite direction of the wing crack. Petal cracks are initiated at the contour of the flaw and

propagate along the flaw plane and parallel to the sample surface. Wing and anti-wing cracks are caused by tensile stress, but mode III stresses are the source of petal cracks formation.

(2) The heterogeneity consideration in the samples result in unsmooth crack path and the wing cracks of the two pre-existing surface flaw are not symmetrical, which are recognized to be realistic for real disordered materials.

(3) Loading direction significantly influence the crack development from surface flaw. The existing of micro- or macro-cracks in real rock and heterogeneity feature may be one of the sources of anisotropic behaviour of heterogeneity rock sample.

Acknowledgements

This project was financially supported by the Hong Kong Polytechnic University to RHC Wong (PolyU5285/05E and G-YF88), National Basic Research Program of China (973 Program, Grant No. 2007CB209404), and the National Natural Science Foundation of China (10672028).

References

1. Horii, H. and Nemat-Nasser, S. 1986, Brittle failure in Compression: splitting and brittle-ductile transition. *Philosophical Transactions of the Royal Society of London, Series A*, 319,337-374.
2. Wong, R.H.C. and Chau, K.T. 1999, Crack coalescence in a rock-like material containing two cracks. *Int. J. Rock Mech. Sci.* 35(2): 147-164.
3. Zhou, Z.G., Zhang, X.W. and Bai, Y.Y. 1999, Investigation of two Griffith cracks subject to uniform tension by using the non-local theory. *International Journal of Engineering Science*, 37: 1709-1722.
4. Tang, C.A., Lin P., Wong, R.H.C. and Chau, K.T. Analysis of crack coalescence in rock-like materials containing three flaws - Part II: Numerical approach. *Int. J. of Rock Mech. & Min. Sci.*, 2001, 38, 925-939.
5. Sagong, M. and Bobet, A. 2002, Coalescence of multiple flaws in a rock-model material in uniaxial compression. *Int. J. of Rock Mech. & Min. Sci.*, 39 (2), 229-241.
6. Wong, R.H.C., Guo, Y.S.H., Chau, K.T., Zhu, W.S. and Li, S.C. 2006, Anti-wing crack growth from surface flaw in real rock under uniaxial compression. *The 16th European Conference of Fract. (ECF16)*, 825, Alexandroupolis, Greece.
7. Wong, R.H.C., Guo, Y.S.H. Chau, K.T., Zhu, W.S. and Li, S.C. 2006, The fracture mechanism of 3-D surface flaw with strain and acoustic emission measurement under axial compression. *Asian Pacific Conference on Fract. & strength*, 336, Sanya, Hainan Island, China.
8. Wong, R.H.C., Li, T.C. Chau, K.T., Li, S.C. and Zhu, W.S. 2007, Crack growth study of a 3-D surface fracture under compressions using strain and acoustic emission measurements. *1st Canada-U.S. Rock Mech. Symposium*, 565-573.
9. Wong R.H.C., Guo Y.S.H., Liu L.Q., Liu P.X. and Ma S.P. 2008, Nucleation and growth of anti-wing crack from tips of strike-slip flaw. *42nd U.S. Rock Mech. Symposium and 2nd U.S.-Canada Rock Mech.*, San Francisco.
10. Liu Liqiang, Liu PeiXun, Wong H.C., Ma ShaoPeng, Guo YanShuang, 2008, Experimental investigation of Three-dimensional propagation process from surface faults, *Science in China Series D: Earth Sciences*, 38(7), 833-841.
11. Germanovich, L.N. and Dyskin, A.V. 2000, Fracture mechanisms and instability of openings in compression. *Int. J. Rock Mech. Min. Sci.*, 37:263-84.
12. Dyskin A.V. 1964, A 3-D model of wing crack growth and interaction. *Engng. Fract. Mech.* 1999; 63:81-110.
13. Fairhurst C. On the validity of the Brazilian test for brittle materials. *Int J Rock Mech Min Sci* 1: 535-546.
14. Tang C.A., Tham, L.G., Wang, S.H., Liu, H. and Li, W.H. 2007, A numerical study of the influence of heterogeneity on the strength characterization of rock under uniaxial tension. *Mech. Mater.*, 39:326-339.

NUMERICAL SIMULATION OF ZONAL DISINTEGRATION OF ROCKS AROUND UNDERGROUND WORKING AT GREAT DEPTH

YONG-BIN ZHANG, ZHENG-ZHAO LIANG, TIAN-HUI MA and LIAN-CHONG LI

Center for Rock Instability and Seismicity Research, Dalian University of Technology

Dalian, 116024, China

YU-JUN ZUO

Research Center for Numerical Tests on Material Failure; Dalian University

Dalian 116622, China

With the economy developing rapidly, rock engineering is becoming increasingly important. Zonal disintegration has an important effect on rock engineering construction. In this paper, the fracture evolution of zonal disintegration around two holes is represented using the numerical code RFPA3D-Parallel. The numerical results indicate that zonal disintegration of rock mass around a deep tunnel maybe found using high ground stresses parallel with the tunnel axis. The distance between tunnels has influence on the fractures of zonal disintegration. Zonal fracturing is not continuous; the spacing distances between adjacent fractures are approximately equal to the radius of the hole.

1 Introduction

With the rapid development of the economy, the depth of underground rock engineering construction and the exploration of mining resources has stepped much deeper than ever before. Thus, more experts and engineers in the rock mechanical field have showed interest in the problems of rock mechanics and rock engineering at larger depths.

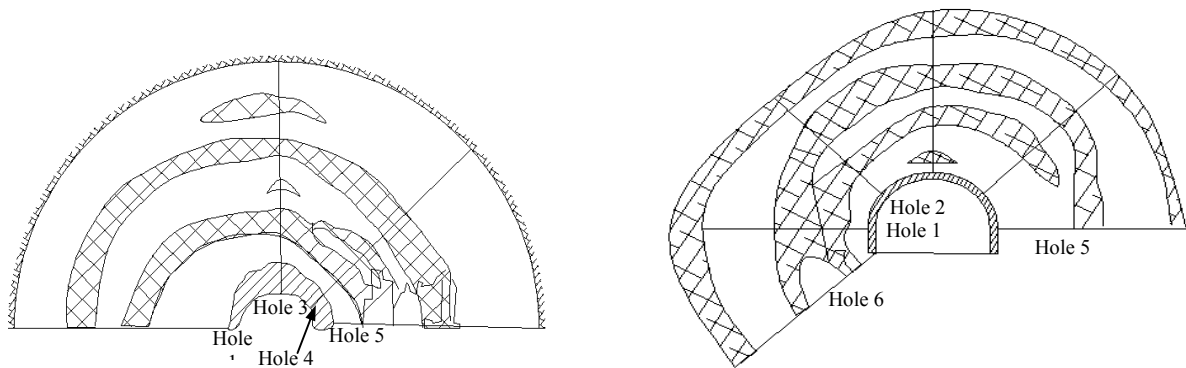


Figure.1 Zonal disintegration in MaЯK mine of Russia[6]

In general, elastic-plastic theory is employed to study the stress and strain states of rock mass around underground workings based on continuum mechanics [1-5]. According to this, the areas around underground working are classified into the failure zone, the nonlinear deformation zone (plastic zone) and the undisturbed

zone (original state zone). However, Russian academician Shemyakin and Kurlenya observed that the alternated regions of fractured and relatively intact rock mass distributed around or in front of the working stope at great depth in Russia mines in the late 1980s [6](see Figure 1). They also represented the phenomenon through simulation in equivalent materials [7]. They defined the phenomenon as zonal disintegrations. In-situ field investigations [8, 9] also proved the Zonal disintegration phenomenon around underground mines or tunnels at large depth.

The occurrence of zonal disintegration phenomenon can not be interpreted with the classical continuum model of traditional rock mechanics. And it has important effect on rock engineering. Research of zonal disintegration is becoming important as deep coal and ore deposits are being opened up, deep mines being planned and constructed, and system for mining at great depths being created. So many researchers show much interest on this phenomenon. They have put forward a lot of explanations about its formation mechanism through in-situ observation and measurement tests, laboratory equivalent material model experiments and various theoretical studies. E.I. Shemyakin et al. [6-7] carried out experimental tests in their laboratory with similar material and research on engineering practical application of zonal disintegration.. Their study showed that rock mechanical property, rock structure, tunnel shape and support pattern have influence on zonal disintegration. And that the stress changes around tunnel not the blasting caused zonal disintegration around deep tunnel. Based on this, they studied the mechanism of zonal disintegration phenomenon theoretically [10]. A.M. Kozel[11] and G.G. Mirzaev [12]considered the dynamic process such as blasting or sudden formation of the working space due to excavation, seismic wave as the mechanism of zonal disintegration phenomenon. V.N.Reva[13] analyzed the stability of surrounding rock on the condition of appearing zonal disintegration using the energy approach. Qian Qihu [14] connected high initial earth stress and unloading face by tunnel excavation to the mechanism of zonal disintegration. Wang Mingyang et al. [15] discussed the mechanism of zonal disintegration on his developed static-mechanics model and definition of “deep rock engineering” based on zonal disintegration. Pan Yishan et al. [16] studied the phenomenon from the view of rock mass creep instability. Li Shucan et al.[17] have monitored zonal disintegration of surrounding rock mass in deep mine roadways and put forward prediction model of zonal disintegration.

Although there are various theories such mentioned above, the consistent conclusion on its mechanism has not been made. Gu Jincai et al [18] indicated that loading direction must be taken into account in studying the mechanism of zonal disintegration. They carried out three-dimensional loading tests and represented the zonal disintegration phenomenon in experimental tests in which the first main principle stress is parallel to the axial line of the model hole. This results show that the larger compresses stress in the tunnel axial direction is the key reason of zonal disintegration. Based on this, we take the direction influence of principle stress into account and investigate zonal disintegration around parallel tunnels using a newly developed numerical code named RFPA3D-Parallel(Parallel Three-dimensional Rock Failure Process Analysis) running on Lenovo 1800 cluster at Research Center for Numerical Tests on Material Failure of Dalian University. The numerical test represents the fracturing process of zonal disintegration, helping to understanding the phenomenon.

2 Numerical Model

2.1 RFPA3D-Parallel

RFPA3D-Parallel is the parallel code developed from the original RFPA3D code by introducing the message-passing interface (MPI) library. The RFPA3D code is based on the theory of elastic-damage mechanics and FEM (finite element method). In RFPA3D, an elastic-brittle constitutive law with certain residual strength is used to describe the mechanical behavior of elements. The parallel version is developed with Fortran and C++. Parallel preconditioned iterative solver is adopted. The package RFPA3D-Parallel is a process-safe, high-performance, robust, memory efficient and easy to use numerical tool for solving large scale rock-like material

failure process on multi-processors system. More details about RFPA3D-Parallel are expatiated in [19-20]. The Lenovo 1800 cluster we used in this paper consists of 32 nodes and each node composes dual Intel Xeon 2.8 GHz processors and 2 GB DDR2 main memories, 73GB hard disk drive. Myrinet 2000network system is utilized for parallel computing. The Linux (Redhat 9, Kernel 2.4.20-8smp) system is used for operating system. MPICH (version 1.2.5) is adopted for message passing library. In this work, the numerical experiments were executed on this cluster system.

2.2 Numerical Model

The numerical model containing two parallel holes is shown in Figure.2. This model geometry is $80 \times 180 \times 180$ mm and the radius of hole is 8mm, the distance between the two centers is 32mm. The model is discretized into $80 \times 180 \times 180 = 2,592,000$ 8-nodal brick elements. The homogeneity index m is 5. The mean Young's modulus, compressive strength and Poisson's ratio of the model are 40GPa, 60MPa, and 0.25, respectively. We choose the maximum tensile stress criterion and the Mohr-Coulomb criterion, respectively, as the damage thresholds. The model with two holes is subjected to loading parallel with the direction of hole axial and the other boundaries are fixed. When displacement loading Δu parallel with the hole axial line increases, stress concentration will be produced around tunnel and model will damage for homogeneity. The loading speed 0.005mm/step is used for loading condition.

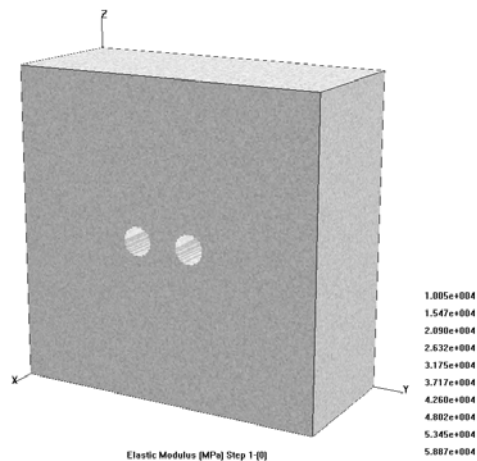


Figure 2 Numerical model with two parallel holes

3 Numerical Results

Figure.3 shows the numerical results that demonstrate the model fracturing complete process of zonal disintegration. The model is under a quasi-static, slowly increasing axial strain. At first, some fractures initiation and fractures nucleate at a small number of points around two holes when the strain is small (Figure 3a). With the strain increasing, fractures grow spirally, joint each other and develop around the two holes respectively (Figure 3b). Then they form two half circle fractures around the two holes (Figure 3c-d). We found that the two fractures are not the same. The left fracture is larger then the right. This is maybe homogeneous influence. Defects (model elements with lower strength) around the left hole presumably are right there and serve as nucleation sites. At the same time, the other fractures develop (Figure 3d). One grows from the lower part of the two holes, and the other grows at the right part of the model. When the loading is continually increasing, the two circle fractures joint together by some small fractures (Figure 3e). The bottom fracture stops

growth and the right fracture forms a bigger half circle. At the top of the two hole, a new fracture begins to develop. The new fracture delops around the two holes and at the end, it forms a ring fractures (Figure 3f).

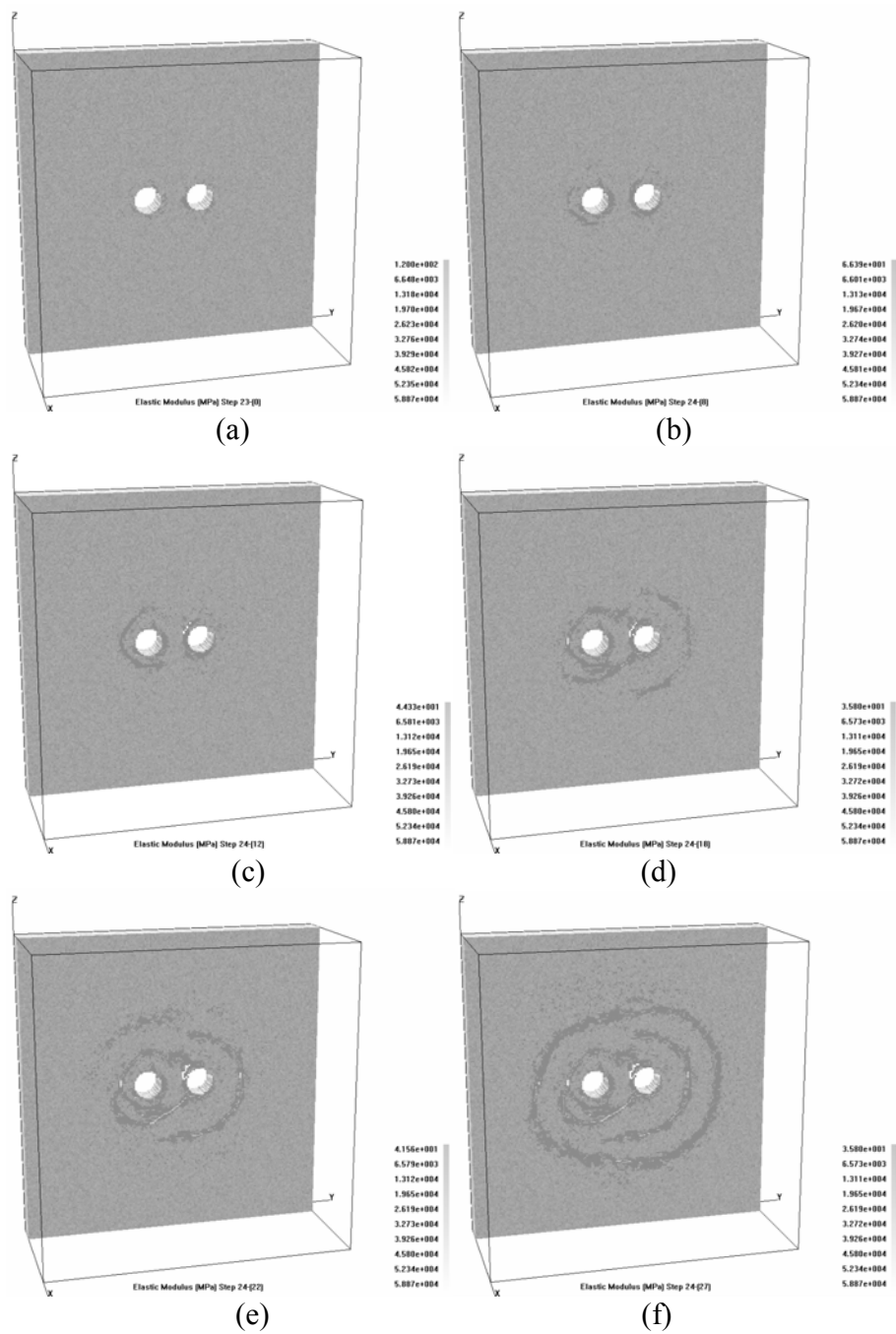


Figure 3 The process zonal disintegration (numerical results)

From the results, we can found that, the spacing distances between adjacent fractures are approximate equal to the radius of the hole. In the whole process of zonal disintegration, zonal fracturing is not continuous. When the first ring fracture is developing, the second begins. If the distance of the two circles is small enough, maybe the first ring fracture is only one that grows around the two holes. If the distance of the two circles is large enough, there are maybe several ring fractures growing around each hole.

4 Conclusion

In this paper, the fracture evolution of zonal disintegration around two holes is represented using the numerical code of RFPA3D-Parallel system. The numerical results indicate that zonal disintegration of rock mass around deep tunnels may be found with high ground stress parallel with tunnel axial. The distance between tunnels has influence on the fractures of zonal disintegration and zonal fracturing is not continuous. The spacing distances between adjacent fractures are approximately equal to the radius of the hole.

Acknowledgements

The authors wish to acknowledge the collaborative funding supports from National Natural Science Foundation of China (No.50809012, 10672028, 40638040 and 50778046) and National Basic Research Program of China “973 Program” (No.2007CB209400). In particular we wish to thank Research Center for Numerical Tests on Material Failure of Dalian University providing the parallel computation environment.

References

1. Qian, Q.H. Key Science Problems for Deep underground Space Excavation in the 230th Xiangshan Science Conferences, (Beijing, 2004).
2. Tan, T.K. Mechanical Problems of Long Term Stability for underground Laneway. Chinese Journal of Rock Mechanics and Engineering, 1982, 1 (1). 1-20.
3. Tao, Z.Y Theory and Practice of Rock Mechanics. China Water Conservancy Press, 1981.
4. Sadovsky, M.A. Natural of Lumpiness of Rock. Dokl.AN SSSR, 1979, 2 (4). 437-43.
5. Kurlenya, M.V., Oparin, V.N. and Yeryomenko, A.A. On the Ratio of the Linear Dimensions of Rock Blocks to the Magnitudes of Crack Opening in the Structural Hierarchy of a Mass. Fiz.-Tekh.Probl. Razrab. Polezn. Iskop, 1993, 4 (2). 6-33.
6. Shemyakin, E.I., Fisenko, G.L., Kurlenya, M.V., et al. Zonal Disintegration of Rocks around Underground Workings, Part I: Data of in situ Observations. Journal of Mining Science, 1986, 22 (3). 157-168.
7. Shemyakin, E.I., Fisenko, G.L., Kurlenya, M.V., et al. Zonal Disintegration of Rocks around Underground Workings. Part II: Rock Fracture Simulated in Equivalent Materials. Journal of Mining Science, 1986, 22 (4). 223-232.
8. He, Y.N. Analysis of Loose Zone around the Roadway in Soft Rock. Journal of China Coal Society, 1991, 16 (2). 63-69.
9. He, M.C. Soft Rock Tunnel Support in Chinese Mines: Theory and Practice. China Coal Industry Publishing House, 1996.
10. Shemyakin, E.I., Fisenko, G.L., Kurlenya, M.V., et al. Zonal Disintegration of Rocks around Underground Workings, Part III: Theoretical Concepts. Journal of Mining Science, 1987, 1 (23). 1-6.
11. Kozel, A.M., Borisovets, V.A and Repko, A.A. Pressure and Support of Vertical Shaft. Nedra, Moscow, 1976.
12. Mirzae, G.G., Protosenya, A.G., Dgorodnikov, Y.N., et al. Support of Systems of Deep Mines. Nedra Moscow, 1984.
13. Reva, V.N. Stability Criteria of Underground Workings under Zonal Disintegration of Rocks. Journal of Mining Science, 2002, 1 (38). 31-34.
14. Qian, Q.H. The Current Development of Nonlinear Rock Mechanics: the Mechanics Problems of Deep Rock Mass in Proceedings of the 8th National Conference on Rock Mechanics and Engineering, (Beijing, 2004).

15. Wang, M.Y., Song, H. Zheng, D.L., et al. On Mechanism of Zonal Disintegration within Rock Mass around Deep Tunnel and Definition of “Deep Rock Engineering”. Chinese Journal of Rock Mechanics and Engineering, 2006, 9 (25). 1771-1776.
16. Li, Y.J., Pan, Y.S., Li, Z.H, et al. Analysis of Mechanism of Zonal Disintegration of Rocks. Chinese Journal of Geotechnical Engineering, 2006, 9 (28). 1124-1128.
17. Li, S.C., Wang H.P., Qian, Q.H., et al. In-situ Monitoring Research on Zonal Disintegration of Surrounding Rock Mass in Deep Mine Roadways. Chinese Journal of Rock mechanics and engineering, 2008, 8 (27). 1545-1553.
18. Gu, J.C.,Gu, L.Y., Chen, A.M., et al. Model Test Study on Mechanism of Layered Fracture within Surrounding Rock of Tunnels in Deep Stratum. Chinese Journal of Rock Mechanics and Engineering, 2008, 3 (27). 433-438.
19. Zhang, Y.B., Tang, C.A., Liang, Z.Z., Ma, T.H. and Zhang, H. Parallel Computing of Stress Analysis with Rock Failure Process Analysis Code (RFPA). Chinese Journal of Rock Mechanics & Engineering, 2006, 3 (25). 479-483.
20. Zhang, Y.B., Tang, C.A., Liang, Z.Z.and Xu, T. Research on Parallel Computational Method of Rock Failure Process Analysis System. Chinese Journal of Rock Mechanics and Engineering, 2006, 9 (25). 1795-1801.

NUMERICAL ANALYSIS OF SURROUNDING ROCK STABILITY ON THE INFLUENCE OF DIFFERENT GEOMETRY

NU-WEN XU, CHUN-AN TANG and ZHENG-ZHAO LIANG

Centre for Rock Instability and Seismicity Research, Dalian University of Technology

Dalian, 116024, P.R. China

As underground development continues at great depths, the dangers of surrounding rock instability will inevitably increase in mining and tunnel engineering. Predicting the deformation of tunnels effectively and making sure surrounding rocks are safe are problems civil engineers constantly encounter. This paper investigates how the geometry of tunnels influences the stability of surrounding rocks. A numerical program called RFPA-2D is used to simulate the tunnel failure process at various geometries in deep mining rock masses. The numerical model can be used not only to produce fracturing patterns similar to those reported in previous studies, but also to predict fracturing patterns under a variety of loading conditions. Numerical results indicate that both the width to height ratio of pillar and tunnel shapes have a significant influence on the failure points of pillars and tunnels. The simulated results reproduce the failure process of surrounding rock at different geometries, and they are helpful in construction and support design. This paper suggests that RFPA can be applied to model the surrounding rock failure behavior in complicated rock masses.

1 Introduction

Stability is the most concerned matter in the underground construction of pillars and tunnels, and many factors affect the stability of pillars and tunnels, such as rock or rock reinforcement mechanical properties, tunnel geometry and stress environment. Because the demand for mineral resources is extremely high and the mining activities are progressing deeper and deeper, an increase trend of pillar and tunnel instability hazards in China may be anticipated for the near future. Many investigations on the effect of tunnel geometry and stress environment on rock, either experiment or numerical, have been reported in the previous researches [1, 2].

Numerical simulation has become one of the most important methods to take into account of crack initiation, propagation, coalescence and stress distribution in tunnels and provide an increased insight into stability of pillars and roadways in subterranean engineering. In light of the heterogeneity of rock, by introducing the constitutive model based on damage mechanics and statistical theory and using the RFPA^{2D}, Zhang [3] discussed the influence of the horizontal in-situ stresses on the distributions of plastic zones. He also analyzed the deformation and nonlinear gradual failure characteristics of circular roadway in deep rock mass as well as the displacement and the stress variation of the key positions in the periphery of the roadway. With respect to rib pillar collapse, Wang [4] illustrated how failure modes and related seismicity changes as the host rock strength was reduced, and shear deformations were permitted to alter the stress field near or inside the pillars. Jia [5] used RFPA to simulate failure mechanism of tunnels in jointed rock mass, and the numerical analysis indicated that both the dip angle of joints and the lateral pressure coefficient had significant impacts on the failure mode and displacement characters of the tunnel. Jiang [1] made some investigation on roadway failure in the Kailuan mining group and modelled the process of laneway deformation and failure under various high stress states by FLAC2D. Investigations mentioned above do not consider the effect of different geometry on the stability of pillars and laneways.

By the means of RFPA-2D program, this paper reproduce the failure process of surrounding rock at different geometry, and considers the effect of width to height ratio on the instability of pillars and tunnels. The aim of this paper is to throw some light on the previous design and later support of chain pillars and tunnels with special reference to their stability.

2 Numerical Model Description of Tunnel

The development of computational methods has enabled applied mathematicians, engineers and scientists to make significant progress in the solution of previously intractable problems. Numerical simulation is currently the most commonly used method in the solution of important coupled problems in rock mechanics and engineering. Rock or rock reinforcement is an obviously heterogeneity material and how to characterize this type of feature is important for the engineering. To consider the heterogeneity of rock or rock reinforcement at the mesoscale level, In RFPA-2D code [6, 7], the solid of structure is assumed to be composed of many mesoscopic elements with the same size, and the mechanical properties of these elements are assumed to conform to a given distribution law, such as uniform distribution, normal distribution and Weibull distribution [8]. Hereby, Weibull distribution is employed to define the material properties, and it can be described as following:

$$f(u) = \frac{m}{u_0} \cdot \left(\frac{u}{u_0} \right)^{m-1} \cdot e^{-\left(\frac{u}{u_0} \right)^m} \quad (1)$$

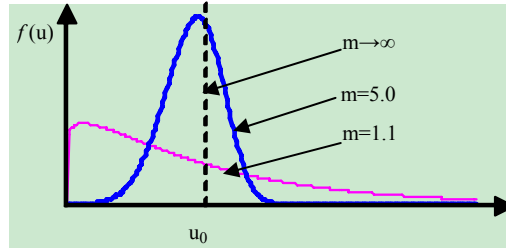


Figure 1 Curve of different homogeneity index

Where u is the mechanical or thermal parameter of the element, such as strength, elastic modulus, thermal conductivity and coefficient of thermal expansion, etc; the scale parameter u_0 is related to the average of the element parameters and the parameter m defines the shape of the distribution function. In RFPA-2D code, m is defined as the homogeneity index of the material. It can be seen from the properties of the Weibull distribution (Figure 1), a larger value of m implies a more heterogeneous material and vice versa. For higher values of the homogeneity index, the strengths of more elements are concentrated closer to u_0 . In the definition of the Weibull distribution, the value of the parameter m must be larger than 1.0. The computationally produced heterogeneous medium is analogous to a real specimen tested in the laboratory, so in this investigation it is referred to as a numerical specimen. The mesoscopic elements themselves are isotropic and homogeneous. The elements in the specimen must be sufficiently small to reflect the heterogeneous mechanical properties of materials at the meso-scale and still provide conditions under which a current computer can perform the analysis efficiently [9].

For the damage evolution, we employ the damage mechanics to describe the failure behaviour. And on the basis of Lemaitre damage model, damage behaviour can be defined as following:

$$E = (1 - \omega)E_0 \quad (2)$$

where ω represents the damage variable, and E and E_0 are the elastic modulus of the damaged and the undamaged material, respectively. In the current method, the element as well as its damage is assumed isotropic, so the E , E_0 and ω are all scalar.

3 Different Geometry Induced Tunnel and Pillar Damage

In the following simulations, the specific geometries and loading conditions for the models are shown in Figure 2 and Figure 3. In this study, when considering various widths to height ratio of the pillar, the specimens undergo a plane strain compression that is imposed by the relative motion of the upper and a lower rigid plate at a constant rate of 0.05mm/step, with the left and right boundaries fixed in the x-displacement. Otherwise, plane strain axisymmetric analyses were conducted for “deep” underground openings in homogeneous and isotropic rock mass subjected to hydrostatic in situ stress, with a constant rate of 2.5MPa/step and the initial stress is 12.5MPa. The ratio of uniaxial compressive strength to tensile strength of all elements is fixed at 10 with the bottom boundary fixed in the y-displacement. A Mohr-Coulomb material is applied in these models. Each numerical model is divided to 62,500 elements (250×250), with a common dimension of 250mm×250mm. The parameters of the model are listed in Tab. 1.

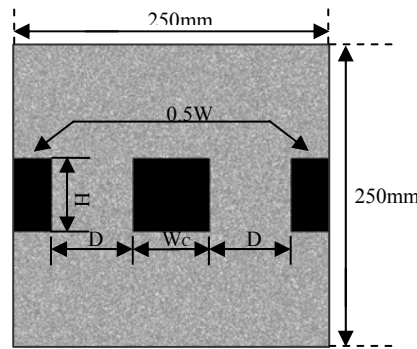


Figure 2 Numerical model

Table 1. Mechanical Properties of the model	
Parameter name	Value
Homogeneity index m	2
Young's modulus E [GPa]	51.7
Possion's ratio ν	0.25
Tensile strength [MPa]	15
Compressive strength [MPa]	302.3
Density [kg/m ³]	2400

4 Simulation Results and Discussion

4.1. Effect of width to height ration on the stability of tunnel

Figure 4 shows the failure process of each model. In this Figure, the failure patterns at four typical loading steps are shown. We can see that the width to height ratio has a distinct effect on the failure mode of tunnel. The stress Figure s implicated that pressure induced by tunnel excavation had been taken on by the sidewalls of laneway, which made pressure stress and shear stress during tunnels concentrated, whereas the tensile stress accumulated at the roof of tunnel. When the width to height ratio was small, e.g. $\lambda = 0.75$, there would mainly be one inclined shear crack. On the contrary, if the ratio was relatively great, e.g. $\lambda = 1, 1.25$, the failure patterns of tunnel and pillar changed obviously, and shear failure was the main mode on both sidewalls of tunnel. With the increment of loading steps, there would also be shear crack generated in the middle of pillars, but the failure mode would be substituted by tensile failure gradually. X shape shear cracks can be found in pillars with the increase of λ . Since values of Young's modulus and rock strength in the numerical models are realized according to a Weibull distribution in which the distribution parameters represent the level of heterogeneity of the medium, the failure modes of pillars show different fracturing patterns.

The Figure above summarizes the relationship between the failure mode and width to height ratio. It is clearly seen that the distributions of failure patterns around underground cavern is strongly dependent on the ratio of width to height.

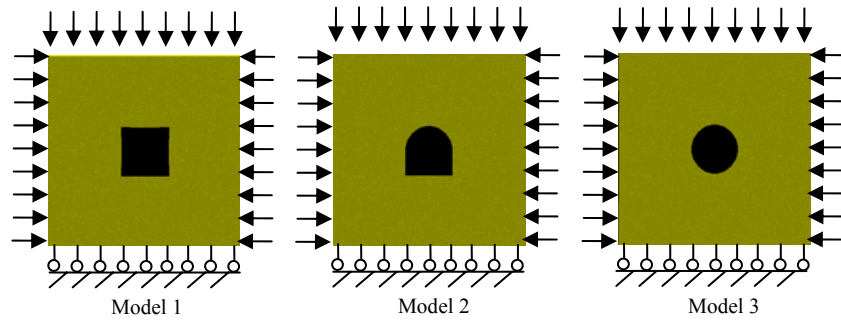


Figure 3 FEM models with different geometry (The brightness of rock mass in the figures expresses the mechanical parameters such as elastic modulus and compression strength of rock mass, the brighter the color, the bigger the value of strength parameters).

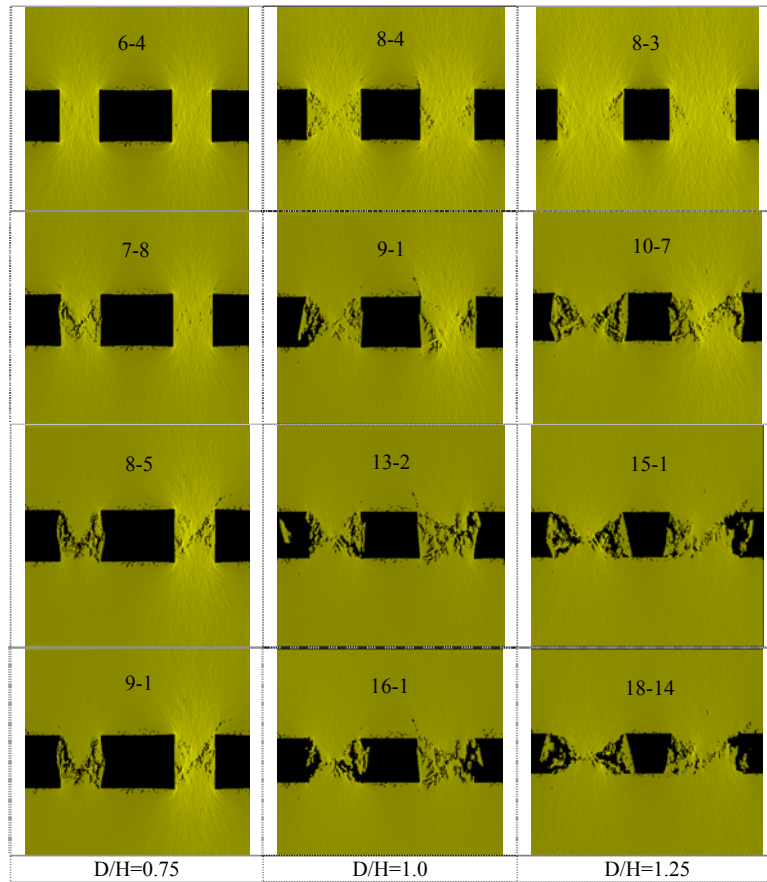


Figure 4 Failure process of numerical model and the induced stress redistribution (In these Figure s, the gray levels represent the magnitude of the value, the lighter of the gray, the higher of value. The black points represent failure elements. Cracks can be seen when the failure elements accumulated.)

4.2. Effect of various geometry on failure mode of tunnel

Progressive fracturing processes of numerical models after excavation and the induced shear stress redistribution are presented in Figure 5(a), (b), (c). All the simulation results are obtained by RFPA^{2D} under hydrostatic pressure. With the increment of loading steps, the curve of damage element along a variety of

tunnels and its related failure steps have been shown in the following Figure s. From these Figure s we can see that tunnel geometry has a significant influence on the failure mode of tunnel.

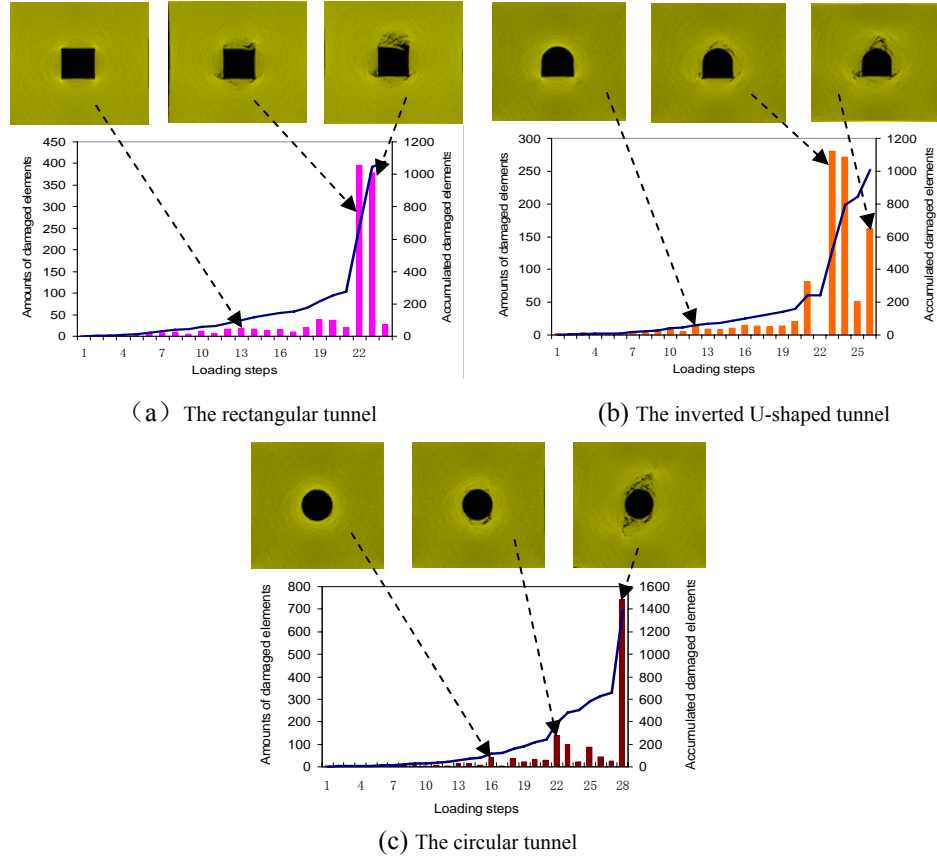


Figure 5 Damage element curve of different geometry tunnels under loading steps

For model 1, the results of modelling the rectangular opening are illustrated in Figure 5(a). Cracks initiate at the roof and floor of tunnel. With the increment of loading, more cracks appear and extend at the roof along the direction of maximum principle stress until failure of the whole tunnel. Figure 5 shows that amounts of damaged elements increase with the increment of steps, and the maximum amount of damaged elements will occur at the 22nd step, which agrees with the stress distribution very well.

For model 2, the results of modelling the inverted U-shaped opening are illustrated in Figure 5(b). Several shear fractures are formed in the roof and floor of the tunnel and on remote crack is observed. With the loading increasing, crack extends upward and the roof breaks into tunnel. Meanwhile, cracks at both two sidewalls extend along the bottom of sidewall and eventually rock mass at two sidewalls spall into tunnel. The maximum amount of damaged elements will happen at the 23rd, which correspond closely to the shear stress redistribution.

For model 3, the results of modelling the circular tunnel are shown in Figure 5(c). The maximum shear stress distribution is shown in this Figure, where the brightness indicates the magnitude of maximum shear stress. At Step 16, shear damage of several elements are observed firstly in the downward-right sidewall. Subsequently, more elements in the roof and floor of the tunnel undergo damage in tensile mode, which eventually leads to the formation of primary crack in the floor and roof. Furthermore, during the final stage of progressive fracturing, the maximum amount of damaged elements occurs at the 28th step, and the primary cracks propagate and extend along 45° angle from the horizontal line.

For the rectangular, inverted U-shaped and circular tunnels, one or more cracks can be observed when the confining pressure is relatively low. This suggests that it is necessary to reinforce the roof and floor of tunnel. However, different geometry of tunnel has different simulation results under hydrostatic pressure. From the three Figure s above, we can see the maximum amount of damaged elements will occur at the 22nd step in rectangular tunnel, the 23rd step in inverted U-shaped tunnel and the 28th step in circular tunnel, which implies circular tunnel is the most stable opening. The preceding numerical simulation results and the interpretation of different geometry effect on pillar instability play a major role in previous design and later support of tunnels.

5 Conclusion

In this study, the numerical software package RFPA^{2D} is applied to simulate complete progressive failures of various tunnels. The approach turns out to be a realistic and reliable procedure to simulate the process of pillar instability. The following conclusions can be drawn from numerical tests results.

(1) The width to height ratio of pillars has significant impacts on the failure mode of pillars and tunnels. With the increment of ratio, the failure mode will be substituted by tensile crack gradually from shear crack and X shape shear cracks can be found in the pillars.

(2) The initiation, propagation and coalescence of cracks around tunnels with different cross-sections under a hydrostatic pressure are clearly expressed in RFPA simulations, and the curve of damaged elements amount implicates inverted U-shaped and circular tunnel will be more suitable for engineering need than a rectangular tunnel.

Acknowledgements

Financial supports provided by the National Natural Science Foundation of China (Grant No. 50804006, 40638040) and by National Basic Research Program of China (973 Program, Grant No. 2007CB209400) are gratefully acknowledged.

References

1. Jiang, Y.D., Liu, W.G., Zhao, Y.X., et al. Study on surrounding rock stability of deep mining in Kailuan mining group. *Chinese Journal of Rock Mechanics and Engineering*, 2005, 24(11). 857-862.
2. Gabriel, S.E. and Anthony, T.I. Investigation of pillar-roof contact failure in northern Appalachian stone mine workings.
3. Zhang, Z., Tang, C.A., Yu, Q.L., et al. Numerical simulation on influence coefficient of lateral pressure on broken zone of circular aperture, 2009, 30(2). 413-418.
4. Wang, S.Y., Tang, C.A., Xu, T., etc. Numerical Simulation on Acoustic Emission During Pillar Rockburst. *The Chinese Journal of Nonferrous Metals*, 2003, 13(3). 556-561.
5. Jia, P. and Tang, C.A. Numerical study on failure mechanism of tunnel in jointed rock mass. *Tunnelling and Underground Space Technology*, 2008(23). 500-507.
6. Tang, C.A. Numerical simulation of progressive rock failure and associated seismicity. *International Journal of Rock Mechanics and Mining Sciences*, 1997, 34. 249-261.
7. Tang, C.A., Liu, H., Lee, P.K.K., et al. Numerical studies of the influence of microstructure on rock failure in uniaxial compression—Part I: Effects of heterogeneity. *Int. J. Rock Mech. Min. Sci*, 2000, 37. 555-569.
8. Weibull, W., A statistical distribution function of wide application. *Journal of Applied Mechanics*, 1951, 18. 293-297.
9. Zhu, W.C. and Tang, C.A. Micromechanical model for simulating the fracture process of rock. *Rock Mechanics and Rock Engineering*, 2004, 37(1). 25-56.

THE DYNAMIC PROCESS ANALYSIS OF STRATUM MOVEMENT INCLINED SEAM MINING

FENG-HAI MA and YU DING

Geotechnical & Structural Engineering Institute of Liaoning Province, Dalian University, Dalian 116622, China

The overburden strata movement and surface subsidence are a complicated dynamic process. In the process of stratum movement and deformation, the rock mass has the property of rheology. At the same time, strata have the different deformations in time-space processes for the laminar combinatorial structure of the rock. Based on the theory of thin plate flexure and rheology, the time and space process of the strata movement and surface subsidence are studied. The related formulas are derived to calculate the surface subsidence and time coefficient, which also provides a new method to predict dynamic process of surface subsidence.

1 Introduction

The mined-out region is caused by the exploitation of the mine. At the same time, the movement deformation and destruction of strata results to the destruction of the nearby rock natural stress condition. Strata and surface's deformation is a dynamic process, which relates to many factors such as the size of mined-out region and the speed of exploitation. Thus, studies on the movement principles of mined-out region's strata will have a profound effect on predicting the scale of surface subsidence, protecting architectures, fundamental facility and underground water resources.

Mine exploitation is the reason for the strata movement and destruction and people put an increasing emphasis on the problems that follow. By the 1950s, studies on strata and surface movement had developed rapidly [1, 2]. The theory of layered media, the theory of drop rand, the theory of key layer, the theory of injuring mechanics, etc. were put forth successively. In the meantime, research were carried out on strata movement and surface subsidence by applying the method of analogy material model, the method of finite element, the method of boundary element, the method of discrete element, and so on with rich achievements being made. However, effective methods were not discovered pertaining to space-time processes and the time coefficient of strata movement [3, 4]. In this thesis, based on the theory of thin plate flexure and rheology, the time-space process of the strata movement and surface subsidence are studied. The related formulas are derived to calculate the surface subsidence and time coefficient. A visual procedure simulating dynamic process of surface subsidence is developed in the light of powerful mathematical calculations and graphic functions of the MATLAB software. Dynamic processes of surface subsidence in a mine are predicted, results of the prediction

coincide with long-term practical observation data of mines. It also provides a new method to predict dynamic process of surface subsidence.

2 Mechanical Model of Strata Movement

2.1. Strata Movement Mechanical Model

As the forming of mined-out region, the stress balance between the overburden strata and the underplate strata is destroyed. Strata will break-down and crush if the stress exceeds the rock's strength limit. Rock's tensile strength is far smaller than its shearing strength and compression strength. Maximum tensile stress is the main reason for rock breaking. Rock strata is brittle material so that its deflection is far less than the mining depth of coal-seam. And the rock strata's thickness is mostly larger than the mining depth of coal-seam. As a conclusion, rock strata's deflection is far smaller than its thickness, which is in coincidence with the precondition of the theory of minor deflection in thin plate flexuring. Therefore, it's reasonable to choose thin plate mechanical pattern as a mechanical model of strata movement.

Suppose thin plate's deflection is $W(x,y,z)$. When compression P is put in the Z (longitude) direction, premised on isotropic medium, the equilibrium differential equation of thin plate is as follows

$$D \cdot \nabla^4 W(x, y, z) = P(x, y) \quad (1)$$

where, ∇^4 is differential double-arithmetic operators, D is bending rigidity of thin plate, $P(x,y)$ is longitudinal force and

$$\nabla^4 = \frac{\partial^4}{\partial x^4} + 2 \frac{\partial^4}{\partial x^2 \partial y^2} + \frac{\partial^4}{\partial y^4}, D = \frac{Eh^3}{12(1-\mu^2)} \quad (2)$$

Where, E is elastic modulus, μ is poisson ratio and h is the thickness of single layer thin plate.

2.2. Differential Equation of Strata Movement

Based on the equilibrium differential equation of thin plate, each layer of strata is composed of composite strata. From the model established in figure 1 and its coordinate system, equation (1) is its equation. For strata's any layer from the surface

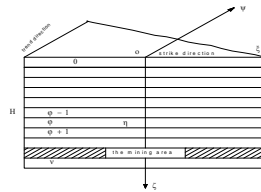


Figure 1 Spatial laminar model

$$\frac{h^2}{12(1-\mu^2)} \cdot \nabla^4 W + \frac{\partial^2 W}{\partial Z^2} = 0 \quad (3)$$

if $\lambda^2 = \frac{h^2}{12(1-\mu^2)}$ then

$$\lambda^2 \cdot \nabla^4 W + \frac{\partial^2 W}{\partial Z^2} = 0 \quad (4)$$

Equation (4) is the basic differential equation of stratum movement.

2.3. The Equation of Continuous Exploiting Strata Movement

The key to the random exploiting can be derived from the iteration of mining step-distance of first pressure, As for the key to mining step-distance of first pressure, it can be obtained from the Dirac delta function, problems with definite solution are as follows:

$$\left. \begin{aligned} \lambda^2 \cdot \nabla^4 W_e + \frac{\partial^2 W_e}{\partial Z^2} &= 0 \\ W_{e|z=0} &= \delta(x, y) \end{aligned} \right\} \quad (5)$$

where $\delta(x, y)$ is Dirac delta function. It stands for concentrated disturb per unit, the Fourier transform coefficient is 1.

Double Fourier integral transform turns $W_e(x, y, z)$ to (x, y) by the method of frequency spectrum analysis. Solve the constant differential equation, as follows:

$$\begin{aligned} W_e(x, y, z) &= \frac{1}{8\pi^2} \int_{-\infty}^{+\infty} \int_{-\infty}^{+\infty} \tilde{W}(x, y, z) \cdot \exp[-i(\zeta x + \eta y)] d\zeta d\eta \\ &= \frac{1}{8\pi^2} \int_{-\infty}^{+\infty} \exp[-\lambda(\zeta^2 + \eta^2)z] \cdot \exp[-i(\zeta x + \eta y)] d\zeta d\eta \end{aligned} \quad (6)$$

Finally surface subsidence caused by mining step-distance of first pressure can be calculated from the following formula:

$$W_e(x, y, z) = \frac{1}{8\pi\lambda z} \cdot \exp\left(-\frac{x^2 + y^2}{4\pi z}\right) \quad (7)$$

According to the principle of iteration, assuming the volume of mining coal is V , the surface subsidence can be calculated from the following equation:

$$W(x, y, z) = \iiint_V W_e[(x - x_0), (y - y_0), (z - z_0)] dx_0 dy_0 dz_0 \quad (8)$$

Assuming the thickness of mining exploiting is m , the surface subsidence can be calculated from equation (8):

$$W(x, y) = \frac{m}{8\pi\lambda H} \iint_S \exp\left[-\frac{1}{4\lambda H} \cdot [(x - x_0)^2 + (y - y_0)^2]\right] dx_0 dy_0 \quad (9)$$

Considering practical situation, the derivation of the formula of surface subsidence and stress can be established on condition that surface has subsidence but no stress. So calculation must follow the principle of image exploiting. Then surface subsidence can be calculated from the following formula:

$$\begin{aligned}
w(x, y) &= w_a(x, y) + w_m(x, y) \\
&= \frac{m}{8\pi\lambda z_1} \iint_s \exp\left\{-\frac{1}{4\lambda z_1}[(x-x_0)^2 + (y-y_0)^2]\right\} dx_0 dy_0 - \frac{m}{8\pi\lambda z_2} \iint_s \exp\left\{-\frac{1}{4\lambda z_2}[(x-x_0)^2 + (y-y_0)^2]\right\} dx_0 dy_0 \\
&= \frac{m}{R^2} \iint_s \exp\left\{-\frac{\pi}{R^2}[(x-x_0)^2 + (y-y_0)^2]\right\} dx_0 dy_0
\end{aligned} \tag{10}$$

where $R^2 = 4\pi\lambda H$. It is a parameter related to strata mechanical properties, which can be fixed according to practical situation.

3 Dynamic Process of Strata Movement

3.1. Time Coefficient of Rock Mass Movement

Stratum movement is obviously related to time, which can be testified from a large amount of practical observation data. It reveals that overburden strata has the property of rheology. For rock mass of medium on weak degree or hardness, its property of rheology can be expressed approximately by the model of Kelvin and a flexible component connected in series. As is seen from figure 2, its constitutional equation is as follows:

$$\sigma = k_1 \cdot \left(\varepsilon - \frac{\sigma}{k_2}\right) + \eta \cdot \left(\dot{\varepsilon} - \frac{\dot{\sigma}}{k_2}\right) \tag{11}$$

The overburden rock mass on ore mass can be simplified as an upper cantilever board on the visco-elasticity foundation. Formula can be established on the longitudinal strain and curvature of plate as follows:

$$\varepsilon = \frac{y}{k} = y \frac{\partial^2 w}{\partial x^2} \tag{12}$$

Where y is longitudinal coordinate, which is the same with vertical direction. w is deflection of plate. In equation (8), calculation of first-order derivative for time factor is as follows:

$$\dot{\varepsilon} = y \frac{\partial^2 \dot{w}}{\partial x^2} \tag{13}$$

Putting equations (12) and (13) into equation (11), the result is :

$$K_2 y \frac{\partial^2 \dot{w}}{\partial x^2} + \frac{k_1 k_2}{\eta} y \frac{\partial^2 w}{\partial x^2} = \dot{\sigma} + \frac{k_1 + k_2}{\eta} \sigma \tag{14}$$

Deflection of overburden rock mass on ore mass can be derived from the following formula by putting equation (14) into equation (7):

$$w_1(x, t) = w_0 \frac{\beta}{\alpha + \beta} e^{-\alpha x} \cdot \cos \alpha x \cdot (1 - e^{-pt}) \tag{15}$$

Deflection of overburden rock mass on mined-out region:

$$w_2(x, t) = w_0 [1 - e^{\beta x} \frac{\alpha}{\alpha + \beta} \cos \beta x] \cdot [1 - e^{-pt}] \tag{16}$$

Time coefficient of surface subsidence can be calculated from the following formula by using equations (15) and (16):

$$f = 1 - e^{-pt} \quad (17)$$

Equation (17) can reflect the rheology property of rock mass affected by mine exploiting if the rock mass is pretty intact and the properties of each vertical layer are the same.

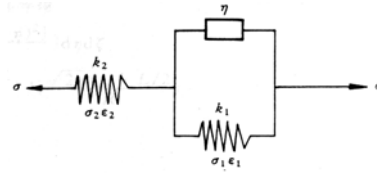


Figure 2 Rheology model of rock mass

3.2. Dynamic Process of Overburden Rock Mass Movement.

Mining of coal layer underground is at a definite rate of advance. After the mining, subsidence of overburden rock mass is a time-space process and studies on time-space dynamic process of strata's moving play a very important role in protecting architectures. Using horizontal coal-layer mining on longwall face as a starting point, longwall system in strike direction is applied to mining method and working face is advanced along strike direction. Based on the actual production process, it can be considered that the length of working face in strike direction increases as time increases, whereas the length in trend direction remains constant during mining. Assuming L is the length in trend direction, then:

$$\begin{aligned} w(x, y) &= \int_{-L/2}^{L/2} \int_{-L/2}^{L/2} \frac{m}{R^2} \cdot \exp\left[-\frac{\pi[(x-\xi)^2 + (y-\eta)^2]}{R^2}\right] d\eta d\xi \\ &= \frac{m}{R^2} \int_{-L/2}^{L/2} \exp\left[-\frac{\pi(x-\xi)^2}{R^2}\right] \left[\left(-\frac{R}{\sqrt{2\pi}}\right) \cdot \frac{\sqrt{\pi}}{2} \left[\phi\left(\frac{\sqrt{2\pi}(y-L/2)}{R}\right) - \phi\left(\frac{\sqrt{2\pi}(y+L/2)}{R}\right) \right] \right] d\xi \end{aligned} \quad (18)$$

where $\phi(x) = \frac{2}{\sqrt{\pi}} \int_0^x \exp(-\frac{t^2}{2}) dt$ is probability integral.

If $M(y) = \phi\left(\frac{\sqrt{2\pi}(y+L/2)}{R}\right) - \phi\left(\frac{\sqrt{2\pi}(y-L/2)}{R}\right)$, then

$$W(x, y) = \frac{m}{2\sqrt{2}R} M(y) \cdot \int_{-L/2}^{L/2} \exp\left[-\frac{\pi(x-\xi)^2}{R^2}\right] d\xi \quad (19)$$

If time factor isn't taken into account, surface subsidence is:

$$W(x, y) = \frac{m}{2\sqrt{2}R} M(y) \cdot \int_{-L/v}^{a/v} \exp\left[-\frac{\pi(x-v\tau)^2}{R^2}\right] \cdot v d\tau = \frac{1}{8} m M(y) \cdot \left[\phi\left(\frac{\sqrt{2\pi}(x+L)}{R}\right) - \phi\left(\frac{\sqrt{2\pi}(x-a)}{R}\right) \right] \quad (20)$$

If time factor is taken into account, it is

$$W(x, y, t) = \frac{m}{2\sqrt{2}R} \cdot M(y) \cdot \int_{-l/v}^{a/v} \exp\left[-\frac{\pi(x-v\tau)^2}{R^2}\right] \cdot v d\tau - \frac{m}{2\sqrt{2}R} \cdot M(y) \cdot \int_{-l/v}^{a/v} \exp\left[-\frac{\pi(x-v\tau)^2}{R^2}\right] \cdot \exp[-p(t-\tau)] \cdot v d\tau \quad (21)$$

$$= W(x, y) - W'(x, y, t)$$

It can be seen that the subsidence calculated when considering time factor is equal to the final subsidence $W(x, y)$ subtracts the delayed subsidence $W'(x, y, t)$. Where l , a -advancing size of working face both coordinate axis left and right sides.

V is the advancing rate of working face in strike direction and its unit is meter per month

$$W'(x, y, t) = \frac{m}{2\sqrt{2}R} M(y) \int_{-l/v}^{a/v} \exp\left[-\frac{\pi(x-v\tau)^2}{R^2}\right] \cdot \{\exp[-p(t-\tau)] \cdot v\} d\tau \quad (22)$$

$$= \frac{m}{8} M(y) \exp\left[-pt + \frac{p}{v}\left(x + \frac{pR^2}{4\pi v}\right)\right] \cdot \left[\Phi\left(\frac{\sqrt{2\pi}\left(\alpha - x - \frac{pR^2}{2\pi v}\right)}{R}\right) - \Phi\left(\frac{\sqrt{2\pi}\left(-L - x + \frac{pR^2}{2\pi v}\right)}{R}\right)\right]$$

If $l \rightarrow \infty, \alpha = 0$, then

$$W(x, y, t) = W(x, y) - W'(x, y, t) \quad (23)$$

$$= \frac{m}{8} M(y) \left[1 - \Phi\left(\frac{\sqrt{2\pi}x}{R}\right)\right] - \frac{m}{8} M(y) \cdot \exp\left[-pt + \frac{p}{v}\left(x + \frac{pR^2}{4\pi v}\right)\right] \cdot \left[1 - \Phi\left(\frac{\sqrt{2\pi}\left(x + \frac{pR^2}{2\pi v}\right)}{R}\right)\right]$$

Surface final subsidence basic can be calculated when $l \rightarrow \infty$, equations (23) is the space-time dynamic variation equation of semi-infinite mining strata movement. Both the form of surface subsidence basic and the space between each layer are different as time goes by.

4 Conclusions

- 1) The overburden stratum movement is a complicated dynamic process. In the process of stratum movement and deformation, rock mass has the property of rheology. At the same time, strata have different deformation characteristics in time-space processes for the laminar combinatorial structure of rock.
- 2) Based on the theory of thin plate flexure and rheology, the time-space process of the stratum movement and surface subsidence have been studied in the paper. The related formulas are derived to calculate the surface subsidence and time coefficient. The calculation data derived by the theory coincides with the practical observation data.

Reference

1. Ma, F.H., Wang, Y.J. and Fan, X.L. Rheology theory of continuous medium and its application in the dynamic of strata subsidence. The Chinese Journal of Nonferrous Metals, 1996, 6(4). 7-12.
2. Kang, J.R. and Wang, J.Z. The mechanical model of the overburden rock under mining and the broken conditions analysis. The Journal of Coal, 2002, 27(1). 16-20.
3. Li, R.H. and Zhang, P.G. Mastering Matlab general coach and guidance. Xi'an: Xi'an University Press, 1998.

NUMERICAL SIMULATION OF ROCK BREAKING MECHANISM BY DISC CUTTER

YUE YU, CHUN-AN TANG and ZHENG-ZHAO LIANG

Center for Rock Instability and Seismicity Research, Dalian University of Technology

Dalian, 116024, P.R. China

PENG-CHENG SU and LI-YING DENG

North heavy industry group Limited Company

Shenyang, 110004, P.R. China

In this study, the rock breaking mechanism by disc cutter was investigated by using numerical method-RFPA 2D. Rock fracture process induced by a single indenter, double indenters and three indenters were simulated respectively. There were about four stages, powder body appeared, the formation of the powder nuclear body, the initiation and propagation of cracks, and broken blocks occurred respectively. And we carried out the disc cutter spacing optimization study when the multi-indenters function in rock; which would provide useful information for the design of Full Face Rock Tunnel Boring Machine and the arrangement of the indenters.

1 Introduction

Domestic and foreign engineering have been paying more and more attention to Full Face Rock Tunnel Boring Machine, because of the quicker speed of construction, the higher quality of construction, the good operating personnel working conditions, the security of construction and so on. But the rock breaking mechanism by discs or indenters has not yet unified. During the past few decades, the rock fragmentation by mechanical tools has been extensively investigated by analytical, experimental and numerical methods. Poul and Sikasskie thought that the rock was destroyed by the shearing force. But there are some phenomena which are difficulty to be explained, such as the leap phenomena in rock breaking, rock chips with non-sliding friction trace and so on. Some people thought that the rock was destroyed by the tensile stress. Maurer (1966), as well as Cheatham and Gnirk (1966) reviewed the early studies and concluded that as the indenter was applied to the rock, both tensile and shear stresses were produced in the rock near the indenter and as a result either tensile or shear failures could occur. [1] So, this article studied the Rock breaking mechanism by disc cutter with the method of numerical simulation.

2 Model Building

As we know, the rock is very complex material with heterogeneous microstructure or texture, microcracks and weak interfaces. So we should take the heterogeneity into consideration. Here, the Weibull statistical distribution was used to characterize the rock heterogeneity. The density of Weibull distribution function can be expressed as Eq. 1:

$$f(\sigma_c) = \frac{m}{\sigma_0} \left(\frac{\sigma_c}{\sigma_0} \right)^{m-1} \exp \left(- \frac{\sigma_c}{\sigma_0} \right)^m \quad (1)$$

Where: σ_c is rock microstructure nature parameter (such as strength, elasticity coefficient, and Poisson's ratio and so on; σ_0 is the mathematical expectation value; m is the shape parameter describing distribution function, The physical meaning of m can reflect the rock 's homogeneity, with the shape parameter m increasing, the more homogeneity of rock; $f(\sigma_c)$ is mechanical properties of rock microstructure σ_c , statistical distribution density. Obviously, the shape parameter m reflects the numerical model material structure's homogeneity. The shape parameter m is defined as the homogeneous index of the rock [6], with the shape parameter m increasing, the more homogeneity of rock.

In this numerical simulation, $m=3$, the material is taken from the geologic report of Qinghai Project. Concrete parameters are shown in Table 1.

Table 1. Parameters of material from Qinghai Project

Material	Density (g/cm ³)	Rock compressive strength (MPa)	Friction angle ϕ ($^{\circ}$)	Modulus of elasticity (103MPa)	Poisson's ratio μ
Pulpy sandstone	2.61	33~52	33.8	9.2~10	0.30
Granite	2.75	93.6	33.4	15~20	0.19

In this paper, the configuration of the computational model is schematically shown in Figure 1. The dimension of the model is 200 mm×400 mm, for the single indenter with 80,000 elements and 200 mm×500 mm, for the double indenter and three indenters with 100,000 elements, respectively. The compressive strength of pulpy sandstone is 150 MPa. $\phi=33.8^{\circ}$, $\mu=0.3$, modulus of elasticity is 20GPa; the compressive strength of granite is 300 MPa. $\phi=33.4^{\circ}$, $\mu=0.19$, and modulus of elasticity is 30GPa. A displacement increment (0.005 mm/step) is applied on the indenters and a confining pressure (20 MPa) acts on both the lateral sides of the constructed rock specimen.

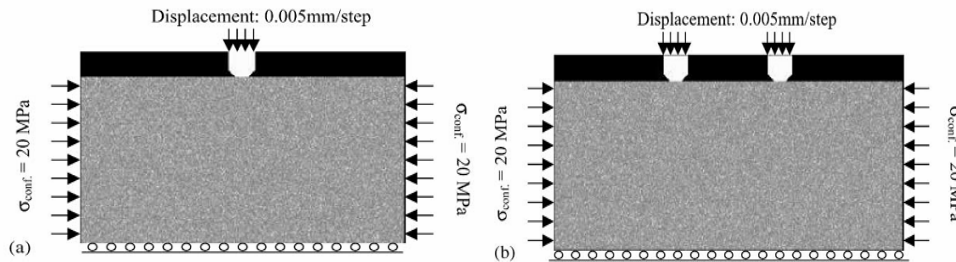


Figure 1 Numerical simulation models

3 Results for the Rock Fragmentation Process Induced by a Single Indenter

High compressive stress concentration was found around the indenters when they acted on the model, with dazzlingly bright area as shown in Figure 2(a). It represents large strain zone. The large strain zone will expand, with the loading displacement increasing, as shown in Figure 2(b). The rock failed beneath the indenter because of high compressive stress. The indenter was pressed in the rock and powder body appeared produced by compressive stress. Also, there would be some powder body produced by shearing strength inside the rock. With the loading displacement increasing, the powder body was crushed into the powder nuclear body. It was interesting to find that the laboratory phenomenon was similar with the phenomena which had been observed in

laboratory tests in 1981. The powder nuclear body with high energy and large density could store energy during loading and emit energy finally. Through the glass material indenter-experiment, it was interesting to find that the radial cracks initiated from the powder nuclear body [1].

As shown in Figure 2(c), the black parts just were the initiation of the radial cracks. With the loading displacement increasing, the stress of indenter was passed to the undestroyed rock through the powder nuclear body, as shown in Figure 2(d). Tensile stress was found in the rock around the powder nuclear body, and the cracks propagated from the black parts, forming radial cracks. The radial cracks could not endlessly develop vertically because of deep compressive stress. Some radial cracks expanded rapidly to free surface with the help of the wedge of rock powders [2, 3]. These cracks could be named the side cracks, as shown in Figure 2(e). With the loading displacement increasing further, broken blocks occurred, as shown in Figure 2(f). But we amazingly found that the side cracks did not propagate symmetrically because of the rock heterogeneity.

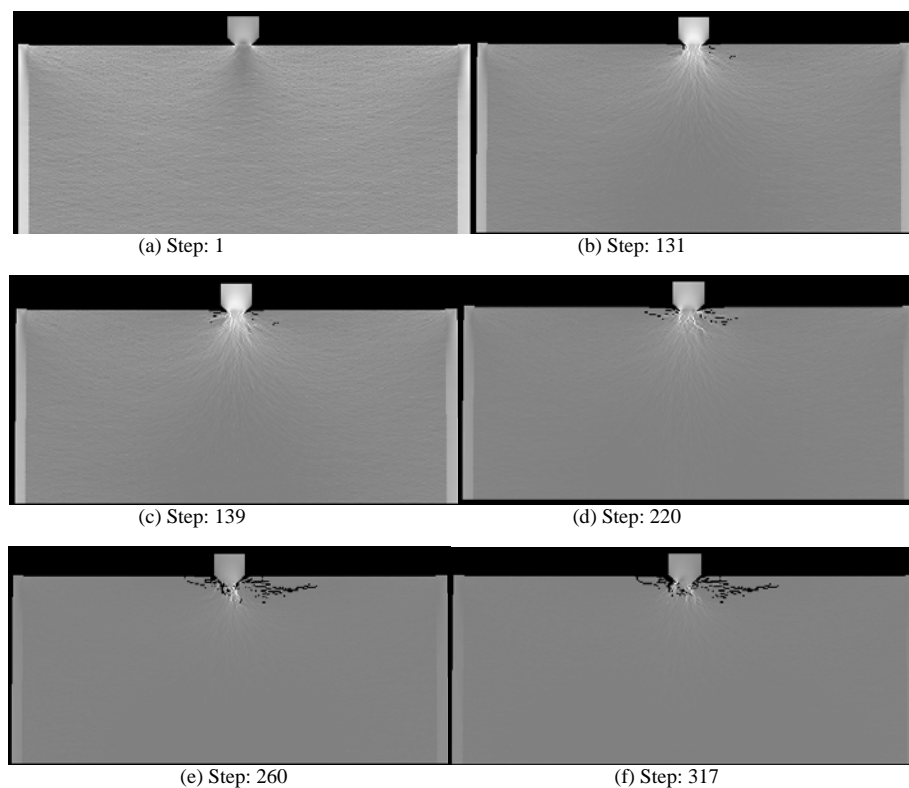


Figure 2 Results for pulpy sandstone fragmentation process induced by single indenter.

In the process of numerical modelling, the powder nuclear body had an important effect on researching the rock breaking mechanism by disc cutters, such as energy storage, medium transmission, crack propagation, and rock chips formation.

4 Results for the Rock Fragmentation Process Induced by Multiple Indenters

In fact, there was the interaction and coalescence of multiple button-bits when tunnel boring machines acted on rocks. Numerically simulated results for the rock fragmentation process induced by double indenters were shown in Figure 3. When double indenters acted on the specimen, the rock beneath each indenter was extruded

with dazzlingly bright area (stress concentration area) as shown in Figure 3(a). It was the same as a single indenter at the beginning of fracture process. There was a large strain zone beneath each indenter. The rock was crushed into powders, then the powder nuclear body appeared and initial crack propagated, as shown in Figure 3(b) and Figure 3(c). But there was interaction between the neighbouring indenters. We named the phenomenon as synergism between the indenters. The cracks propagated relatively in a curvilinear path, as shown in Figure 3(d) and Figure 3 (e) with further loading displacement. Finally, the cracks coalesced as shown in Figure 3(f), forming largest rock chips. When it was three indenters, the fragmentation processes were the same as double indenters as shown in Figure5 (d). It only needed more loading displacement and penetration.

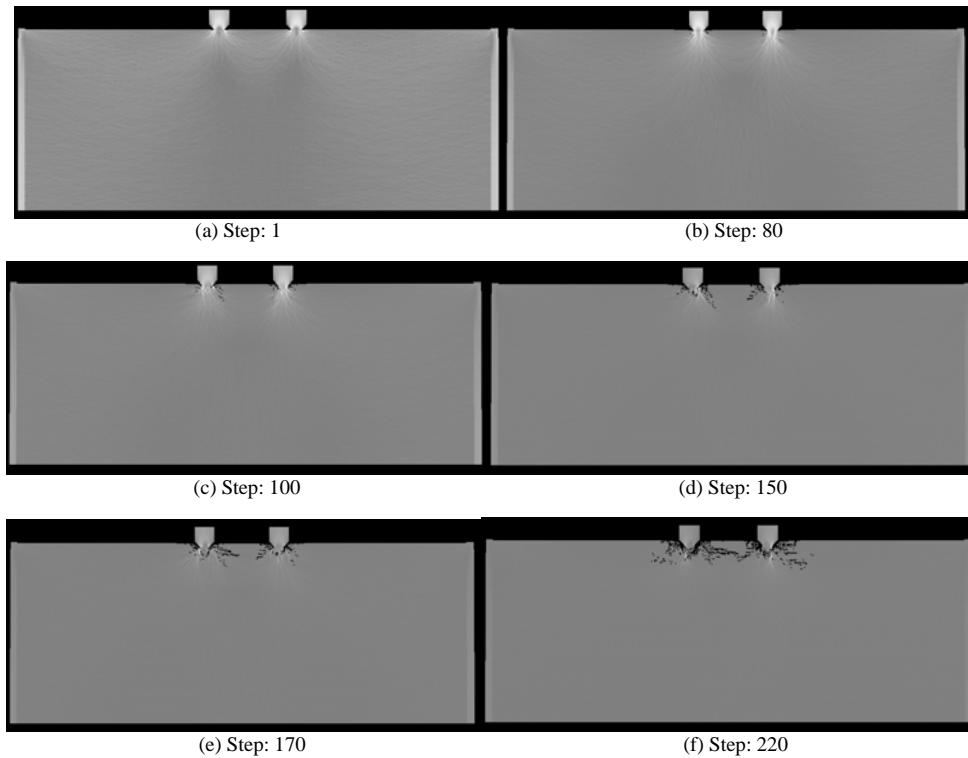


Figure 3 Result for pulpy sandstone fragmentation process induced by double indenters.

5 The Optimization of Joint Spacing

The conception of disc cutter spacing optimization was proposed by RadP.F, and he considered that the optimization increases with the load increases [4]. Different disc cutter spacing produced different fragmentation shape, and the deeper penetration needed larger disc cutter spacing and more load. But if the cutter spacing was too large, the side crack would not coalesce. Therefore the reasonable cutter spacing determination had the practical significance for the actual project. RadP.F suggested that we should use specific energy to discuss the optimization. The specific energy could be defined as how much energy needed when crushing each volume of rocks. It was found that most of energy was consumed on the formation of rock chips, and the smaller energy was consumed by the formation of powder body. When the cutter space was most optimized, the specific energy was the smallest and it could achieve the best fragmentation effect. Because the simulation was two dimensional, we used energy needed when crushing each area (not volume) rock to describe the optimization. The efficiency of the indenters to break up rocks was analyzed by cutter spacing optimization. The coalescence step, penetration depth, fracture area and loading energy of Pulpy sandstone and Granite

obtained from RFPA2D by double indenters were showed in Table 2. The coalescence step, penetration depth, fracture area and loading energy of Pulpy sandstone and Granite by three indenters were showed in Table 3.

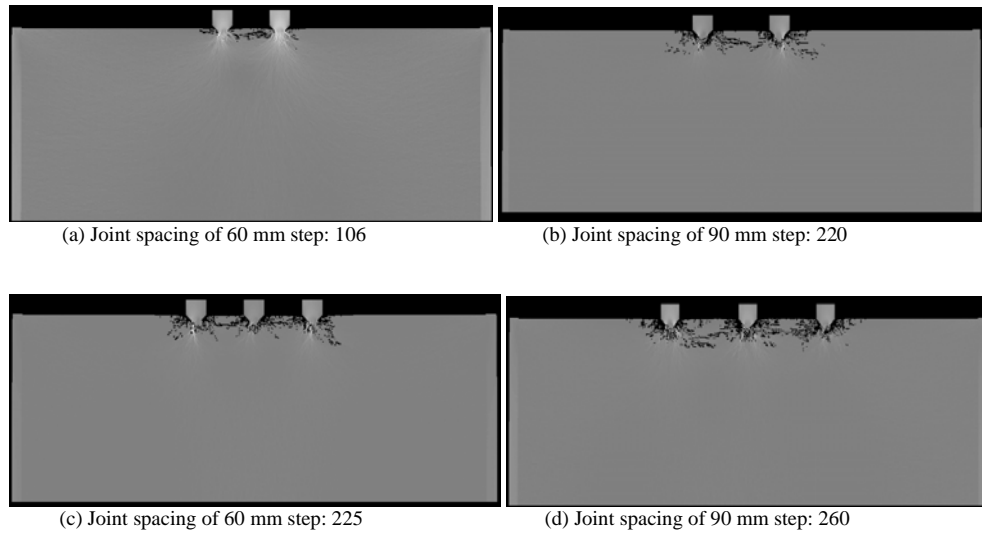


Figure 4 Results for pulpy sandstone fragmentation process with different joint spacing

Table 2. The data of double indenters

Material	Cutter spacing(mm)	Coalescence step	H: penetration depth (mm)	A: fracture area(cm ²)	W: loading energy (J)	W/A
Pulpy sandstone	60	190	11	6.6	4.728	0.7164
	70	190	11	7.7	4.831	0.6274
	80	220	12	9.6	5.7995	0.6041
	90	220	13	11.7	5.853	0.5001
	100	350	18	18.0	10.580	0.5878
Granite	60	364	14	8.4	13.090	1.558
	70	350	13	9.1	12.288	1.3504
	80	390	17	13.6	14.744	1.0841
	90	448	15	13.5	17.624	1.3055

Table 3. The data of three indenters

Material	Cutter spacing(mm)	Coalescence step	Left penetration depth (mm)	Right penetration depth (mm)	A: fracture area(cm ²)	W: loading energy (J)	W/A
Pulpy sandstone	60	220	11	10	12.6	7.960	0.632
	70	255	13	10	16.1	9.911	0.616
	80	255	15	15	24.0	10.026	0.418
	90	255	18	14	29.8	9.866	0.331
	100	342	20	19	39.0	14.885	0.382
Granite	60	345	15	12	16.2	17.537	1.083
	70	395	15	17	22.4	20.607	0.920
	80	460	21	20	32.8	24.916	0.759
	90	530	22	21	38.7	29.787	0.770

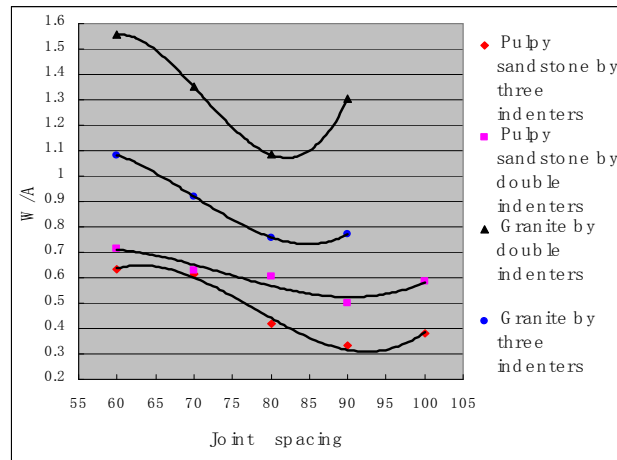


Figure 5 The cutter spacing optimization by multiple indenters

6 Conclusions

(1) Rock fragmentation process by a single indenter was simulated by RFPA 2D. The process could be divided into four stages: powder body appeared, the formation of the powder nuclear body, the initiation and propagation of cracks, and broken blocks occurred respectively. It had a good agreement with the laboratory tests by Northeastern University of Technology in 1981. The process of rock fragmentation was mixed tensile, compressive stress and shear failure. But the dominant mechanism was tensile failure. We could distinctly see that from the picture of the numerical simulation.

(2) There was the interaction and coalescence of multiple indenters distinctly.

(3) There was the optimization of joint spacing. RFPA 2D could accurately and truly simulate the process of rock fragmentation, and carried on the disc cutter spacing optimization.

Acknowledgements

This research was supported by National Basic Research Program of China (973 Program, Grant No. 2007BAF09B01 and 2007CB209400) and the National Natural Science Foundation of China (Grant No. 50804006 and 40638040).

References

1. Liu, H.Y. Numerical Modelling of the Rock Fragmentation Process by Mechanical Tools. 2004.
2. Yu, J. Rules of rock fragmentation with mechanical methods and model of rock failure mechanism. Journal of China Coal Society, 1982, 3. 11-18.
3. Liu, H.Y., Kou, S.Q., Lindqvist, P.A. and Tang, C.A. Numerical simulation of the rock fragmentation process induced by indenters. Int. J. Rock Mech. Min. Sci., 2002, 39. 491-505.
4. Liu, D.S. Study on the Interaction between Adjacent Grooves of the Disc Cutter. Journal of Jiaozuo Institute of Technology, 1993, 3. 87-91.
5. Gong, Q.M., Jiao, Y.Y. and Zhao, J. Numerical Modelling of the Effects of Joint Spacing on Rock Fragmentation by TBM Cutters. Tunnelling and Underground Space Technology 2006, 21. 46-55.
6. Tang, C.A. Numerical Simulation of Progressive Rock Failure and Associated Seismicity. Int J Rock Mech Min Sci, 1997, 34. 249-62.
7. Lin, J.Q. Research on the Mechanism of Rock Failure and the Increment of Service Life of Disc Roller Cutter. Journal of Fuzhou University (Natural Sciences Edition), 1990, 1 (18). 109-113.

PART III

DYNAMIC BEHAVIOUR IN CIVIL ENGINEERING

STUDY OF SUBLEVEL COAL'S DISPLACEMENT MECHANICS IN EXTREMELY THICK COAL SEAMS WITH BUMP TENDENCY

HUA NAN

Department of Resources Science and Engineering, Henan Polytechnic University

Jiaozuo 454000, P.R. China

YUN-FENG LIU

Chao-hua Coal Mine, Zheng-zhou Coal Group

Xin mi, 452370, P.R. China

On the basis of bump characteristic analysis of a bump coal mine in the west of Henan Province in China, in-situ displacement experiments were conducted. The results indicate that sublevel coal's displacement in extremely thick coal seam with bump tendency has obvious three-layer-phenomena (roof action layer, short beam structure layer and support action layer). In the view of the resultant force, the top coal above the support is considered as the roof action layer which can be totally destroyed by the head abutment pressure and tensile strength from roofs rotation. Short beam structure layer is affected a little by the abutment pressure and tensile strength from the roof's rotation and support. Also, the support action layer can be fully destroyed by the raising and lowering movement of the support and is with accordance with the lab simulation results.

1 Brief Description of 21121 Longwall Panel

The Qianqiu Coal Mine, located at the center of the Yima Coal Field, was developed in 1956 and went into production in 1958. The 21121 longwall panel is designed to employ the fully mechanized top coal caving mining method. Mining depth ranges from 616.5 to 702.5 m with an average depth of 659.5 m. The coal seam, averaging 11.80 m thick, is uniform. The coal is semi-bright or dark, and prone to spontaneous combustion. The immediate roof is dark gray, tightly-cemented mudstone, from 18.23 to 29.05 m thick, and uniformly distributed. It is brittle and breaks easily with smooth surfaces. The main roof, which is very thick, is Jurassic-colored bedded conglomerate, sandstone, and powdered sandstone. The immediate floor is dark gray conglomerate with a localized floor made of coarse clay.

2 Description and Analysis of Bump

2.1 Description of Qianqiu Coal Mine's coal bump

Coal bump is a dynamic phenomenon produced by the sudden deformation energy coming from the stress balance failure of coal mass and it is one of hidden dangers of mining [1-6]. Coal bump has happened nine times since the first occurrence (happened in 14141 working face in 1988). Since then, more and more production of the Qianqiu coal mine has been made on the No.2 level; therefore, pressure burst of the coal mine has become even more serious.

2.2 Characters of Qianqiu Coal Mine's coal bump

Based on in-sit. determination and study of production record, characters of Qianqiu Coal Mine's coal bump can be summed up as following:

- (1) Paroxysm. There is no obvious evidence before the coming of coal bumping and also there is no apparent rule in coming time and it only can. expressed by the words of " out of a sudden".
- (2) Great destructiveness. Working face, tunnels and even supports and people can be ruined when coal bump happened. It is the most serious disaster for coal mine.
- (3) High speed. All things come very quickly. Working face and tunnels are destroyed with great vibration and loud voice in no time.
- (4) No gas involvement. It's proved that there is no methane content sharp raise after the coming of coal bump, so it can be only named bump.

2.3 Analysis of the influence factors of Qianqiu Coal Mine's coal bump

Generally there are many factors leading to coal bump. However, they can classified into three types which named nature factors, technology factors and management factors ^[1-3]. Based on this theory and concerning about practice situation, all of these can be summed up as following:

- (1) Mining depth. It's known that the raise of mining depth can lead to raise of gravity stress and elastic energy in coal mass, so usually danger from coal bumping can be more serious with raise of mining depth. It's proved that when the mining depth is more than 600m, there is a very sharp raising danger from coal bumping. So it's must be very careful when the mining depth is more than 600m. As it's stated before that the face's mining depth is more than 600m, so the high depth is the key reason for coal bump.
- (2) Mechanical property of coal. Based on coal bumping tendency theory, coal's mechanical property experiments are done, either 21 working section or 20 working section both are middle coal bump tendency.
- (3) Roof stratum of coal. It's known that the hard and thick roof stratum above mining coal seam can benefit the paroxysm of coal bumping and the reason is the hard and thick roof stratum can contain more elastic energy that is origin power of coal bumping. So once the hard and thick roof stratum cracked when the coal is extracted much more elastic energy is released suddenly and thus give a high occurrence of coal bump.

3 In-situ Measurement of sub-level coal's displacement

3.1 Measurement method

Trailing deep-hole base stations measurement method was used in this project. Structure of deep-hole base stations in sublevel coal can be seen from Figure 1. And installation diagram of deep-hole base stations in sublevel coal can be seen from Figure 2.

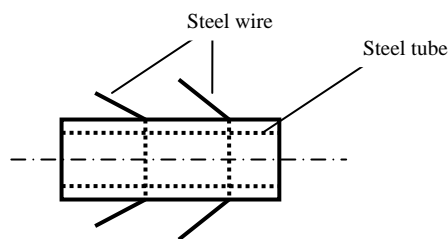


Figure 1 Structure of deep-hole base stations in sublevel coal

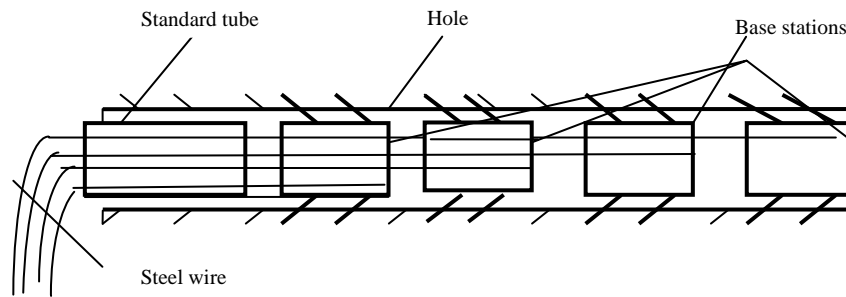


Figure2 Installation diagram of deep-hole base stations in sublevel coal

Three holes named I , II and III, were made ahead of cutting room 160m, 195m and 275m respected. Every hole has four deep-hole base stations shown by Figure 2. So the first station (A Type Station) in every hole were seated into the immediate roof about 0.7m, and the second stations (B Type Station) in very hole were seated in top coal 6.0m above tail gate's top, and the third stations (C Type Station) in very hole were seated in top coal 3.0m above tail gate's top, and the fourth stations (D Type Station) in very hole were seated in top coal 1.0m above tail gate's top.

3.2 Measurement results

Measurement results can be seen from Figure 3, Figure 4 and Figure 5.

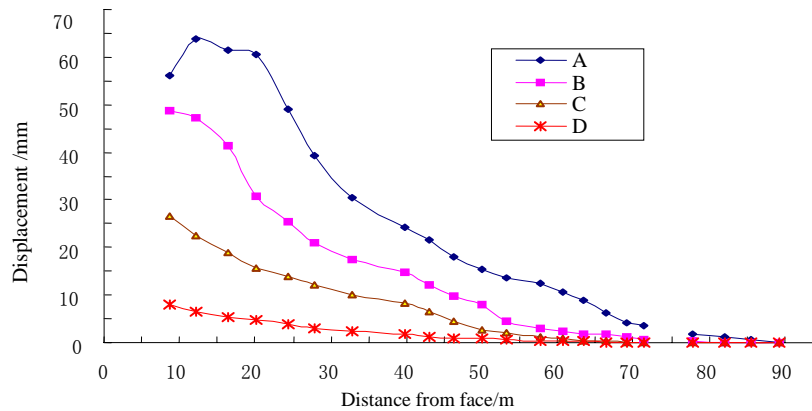


Figure 3 Relation between sublevel coal's displacement and distance of No.I measuring line

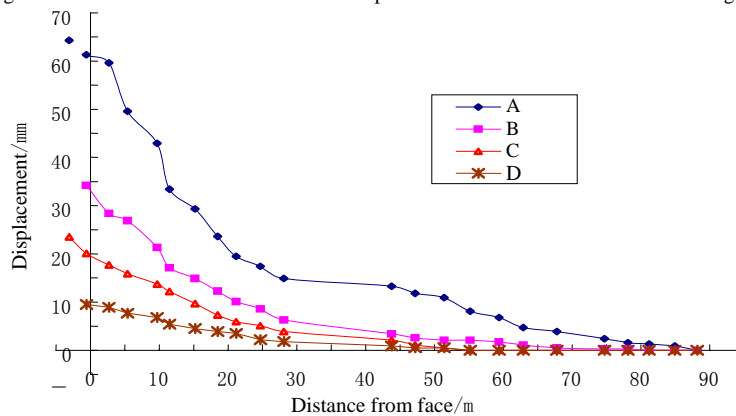


Figure 4 Relation between sublevel coal's displacement and distance of No.II measuring line

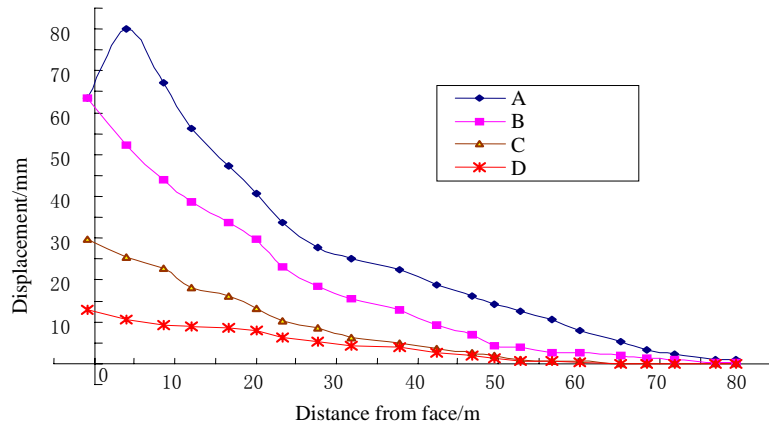


Figure 5 Relation between sublevel coal's displacement and distance of No. III measuring line

4 Theoretical Analysis

From Figure 3, Figure 4 and Figure 5, the movement of I, II and III in this face with bump tendency began at a distance ahead of face about 73m, 70m and 77m, and the average distance is 73.33m which is larger than ordinary sub-level caving face. Also it can be seen, in the area of 73.33m to 55m, the first station seated into the immediate roof about 0.7m has a displacement of 13mm, and the second stations seated in top coal 6.0m above tail gate's top has a displacement of 3mm, and the third stations in seated in top coal 3.0m above tail gate's top has a displacement of only 1mm, and the fourth stations seated in top coal 1.0m above tail gate's top has no displacement at all.

Finally, based on the displacement and failure characteristics, the extra-thick top coal with bump tendency can be divided into the following three action layers:

(1) Roof action layer. This layer can be fully destroyed by the front abutment pressure and the rotation of roof strata.

(2) Short beam layer. Because of the great thickness of top coal, the front abutment pressure and the rotation of roof strata have little effect on this layer. Nor the shield support at the face. Therefore, this layer plays an important role in the success of top coal caving method and outburst of coal bump.

(3) Support action layer. This layer starts from the bottom of short beam layer and end at the interface of coal and shield support. The front abutment pressure and rotation of roof strata have little effect on this layer. But the pressure and movement from the shield supports can make this layer fully broken up.

Obviously, the failure of short beam structure layer is critical to top coal caving mining method and outburst of coal bump. Therefore, a model was developed to investigate the failure mechanisms of short beam, as shown in Figure 6.

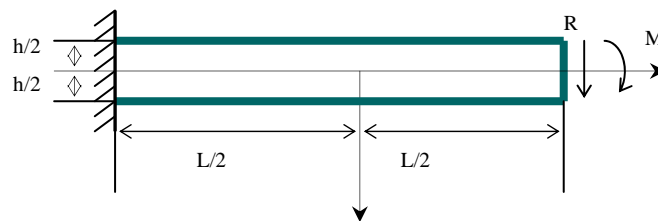


Figure 6 Mechanics of short beam model for extra-thick with bump tendency top coal

In Figure 6, h and L are the thickness and length of short beam structure layer, respectively. R and M is the force and bending moment from the roof action layer, respectively. Stresses in the beam can be calculated by equations 1-3.

$$\sigma_x = \frac{12y}{Eh^3} \left[\frac{qL}{2} \left(\frac{L}{2} - x \right) - \frac{qL^2}{12} - \frac{q}{2} \left(\frac{L}{2} - x \right)^2 \right] \quad (1)$$

$$\sigma_y = -\frac{yq}{h} - \frac{q}{2} \quad (2)$$

$$\tau_{xy} = \frac{3x(4y^2 - h^2)}{2h^3} \quad (3)$$

When the tensile stress in the beam reaches the tensile strength of the beam, the beam will fail. Therefore, at location $x=0, y=-h/2$, equation 1 is reduce to:

$$\sigma_x = \frac{qL^2}{2h^2} \quad (4)$$

when σ_x is larger than $[\sigma_t]$, the short beam structure of top coal will break down and its maximum length, L_p , can be calculated by :

$$L_p = h \sqrt{\frac{2[\sigma_t]}{q}} \quad (5)$$

It can be seen from equation 5 that: L_p is proportional to h, and related to $[\sigma_t]$ and the vertical resultant stress from the overlying roof strata. Obviously, when thickness of top coal becomes bigger, so is the thickness of short beam structure, i.e., L_p becomes bigger. A larger h or a larger L_p will be detrimental to a successful top coal caving mining.

5 Lab Analogy Simulation

This three-layer theory was proved to be true by lab analogy simulation experiments made by the authors. Results can be seen from Figure 7 and Figure 8.



Figure 7 Sub-level coal's displacement failure situation of similar analogy experiment when Sub-level coal thickness is 10.8m



Figure 8 Sub-level coal's displacement failure situation of similar analogy experiment when Sub-level coal thickness is 12.8m

6 Main conclusions

Based on the results of physical modeling and theoretical analyses, the following conclusions can be made:

- (1) The face with bump tendency has a larger scope of front abutment pressure, and more importantly the upper top coal also has a larger scope of front abutment pressure than the lower top coal.
- (2) The top coal above the shield supports is divided into three layers: roof action, short beam structure, and support action layers.
- (3) The short beam structure layer can be approximated by the short beam model, based on which the maximum thickness and length of short beam structure layer can be calculated by equation 5.

Acknowledgements

The work in this paper is funded by Grave Project of Henna Province (322020700), Education Department Project of Henna Province (133014).

References

1. Dou, L.M. and He, X.Q. Theory and technology of rock burst prevention. Press of China University of Mining, 2001.
2. Xie, G.X. and Yang, K. Surrounding rock abutment pressure distribution and thickness effect of dynamic catastrophic in fully mechanized sublevel mining. Journal of China coal society, 31(6). 731-735.
3. Chen, H.J. Stress analysis in longwall entry roof under high horizontal stress. USA: West Virginia University, 1999.
4. Nan, H. The safe system of mining extremely thick coal seam with coal bumping tendency. China paper online, 200703-340.
5. Zhang, M.T. The instability theory of rock burst and the numeration of numerical simulation. Journal of rock mechanics and engineering, 6(3). 197-204.
6. Li, X.Y. Discussion on unstability and damage of surrounding rock-coal mass system and prediction of rock burst. Journal of China university of mining & technology, 29(6). 633-636.

COAL MINING INDUCED ENVIRONMENTAL AND GEOLOGICAL PROBLEMS IN CHINA

ZHAO-PING MENG

*China Three Gorges University, Key Laboratory of Geological Hazards on Three gorges Reservoir Area,
Ministry of Education Yichang, 443002, P.R. China*

JIE-NAN PAN

*School of Resources Environment, Henan Polytechnic University
Jiaozuo 454000, P.R. China*

RUI WANG

*Department of Resources and Geosciences, China University of Mining & Technology at Beijing
Beijing, 100083, P.R. China*

China is a country with high coal production and consumption. As the main energy resource of China, coal has provided a reliable energy supply for the sustaining, development of the countries national economy. Coal in China has made a great contribution for the national economic development, but it has also caused a negative influence on the ecological environment in China. It is essential for the coal industries in China to implement sustainable development and build a new type of coal industry that will minimize the negative influence of coal mining on the remaining natural resources and ecological environment. This paper introduces the characteristics and present status of coal mining and production in China. It describes the land damage from mining subsidence, occupation of coal gangue on the land, mining field excavation and external dump of open-pit collieries. In addition, the influence and pollution from coal mining on water resources and environment are discussed. The effect of coal gas on the atmospheric environment and the influence of coal gangue on the ecological environment in mining area are analyzed. Besides, investigations of mining accidents in China with including the problems of geological disaster and ecological damage produced by coal mining are carried out.

1 Introduction

As the main energy resource of China, coal accounts for more than 70% of one-off energy sources consumption. In 2008, the full production capacity of coal in China has reached 27.16 hundred million tons and has taken the lead in the world. The demanded for coal will increase to 30 hundred million tons and account for 68% of all energy sources by 2020. With the continued development of China's economy, the ratio of coal consumption to one-off energy consumption is decreasing, but coal is still the uppermost one-off energy source. China has been on the stage of high-speed development and has the energy composition with rich coal, poor petroleum and indigent natural gas.

The major provinces rich coal in China is mainly located in the stable crustal block of the "north China platform", and the Liupan Mountain area of southwest (mainly with coal measures in the Permian), Ordos basin, northeast and northwest China (mainly with the Mesozoic coal measure strata). Many areas have good geological conditions for mining which include thicker coal seams and lower dip angles. For a long time, according to the policy of "large, medium and small collieries are coexistence; state, collective, and individual collieries are concomitance." Coal mining in China has promoted the rapid development of coal industries and

guaranteed the energy supply for the sustaining, high speed and steady development of the national economy. At the same time, by using this extensive operation of economic growth, coal mining also has resulted in large quantity of contamination and geological disasters, resulting in the pollution and destruction of the ecological environment. It mainly includes solid waste pollution, air pollution, water contamination and land subsidence of mining areas. At present, environment of coal mine has been a serious problem to deal with. Therefore, it is helpful to improving the environment of production and habitation of collieries and to promoting the healthy development of coal industries by comprehensively studying collieries environment and making corresponding protective measure and changes.

2 General situation of coal mining in China

In China there are approximately 33 thousand coal enterprises. They are divided into three main groups, state key collieries, state local collieries and township-run collieries. There are 571 state key collieries, 2000 state local collieries and 31 thousand township-run collieries employing a total of 6 million people. Since 2001 the production output of coal was increased yearly.

The total outputs of raw coal in China are 25.23 hundred million tons in 2007 and are 1.92 hundred million tons than those in 2006. The rate of increase is 8.2% in 2007. State key collieries produce 12.29 hundred million tons of coal, the increase in absolute figures is 1.09 hundred million tons and the percentage increase is 9.8%; state local collieries produce 3.37 hundred million tons of coal, the increase in absolute figures is 0.18 hundred million tons and the percentage increase is 5.55%; township-run collieries produce 9.57 hundred million tons of coal, the increase in absolute figures is 0.64 hundred million tons and the percentage increase is 7.2%. The percentages of coal outputs of the three kinds of collieries are shown in Figure 1.

Compared with the past year, in 2008, total outputs of raw coal in China have reached the record of 27.16 hundred million tons, the excess is 1.93 hundred million tons and the rate of increase is 7.6%. State key collieries produce 13.77 hundred million tons of coal, the increase in absolute figures is 1.48 hundred million tons and the percentage increase is 12.63%; state local collieries produce 4.53 hundred million tons of coal, the increase in absolute figures is 1.16 hundred million tons and the percentage increase is 34.4%; township-run collieries produce 8.86 hundred million tons of coal, the increase in absolute figures is -0.71 hundred million tons and the percentage increase is -7.4%. The percentages of coal outputs of the three kinds of collieries in 2008 are diagrammatized in Figure 2.

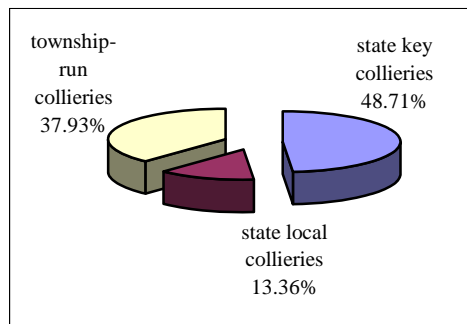


Figure 1 Structure of coal production in China in 2007

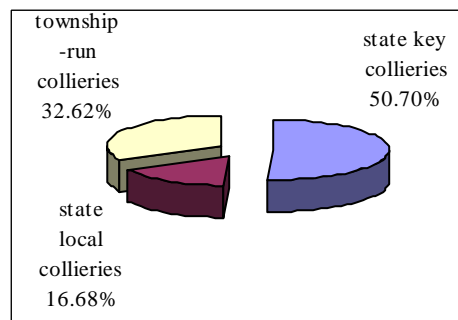


Figure 2 Structure of coal production in China in 2008

China not only is the country with the highest coal production but also takes the second place in export of coal and accounts for 11.8% in the world. The large-scale coal mining in China has provided a vital energy supply for the high speed development of national economy, but at the meantime, it also causes a serious pollution and damage of mining area's ecological environment. Moreover, with the increasing of mining depth, the accidents of collieries such as outburst, gas explosion, rock burst and water inrush are becoming a real challenge.

3 Damage to land resource of mining area from coal mining

The methods of coal mining can be divided into two kinds: underground mining and open pit mining. Different mining methods can cause various degrees of damage in different forms to the land of mining area. Generally speaking, mining subsidence and occupation of coal gangue to the land are the main damage of underground mining. Damage from open pit mining includes the open pit itself and the areas used by the dumping of excavated waste material [14, 15].

3.1. Underground mining

Damage to the land caused by underground mining is shown in Table 1 [12]. Subsidence from underground mining is the main disaster that is difficult to deal with. At present, 95% of coal output comes from underground mining in China and the basic mining method of state key coal mines is the longwall top-coal caving technology. It is measured that the greatest settlement is 0.7 time to the total thickness of coal, and the settlement area is about 1.2 times to the area of coal mining. According to the incomplete statistics [13, 21], the collapse area caused by coal mining amounts to 400,000 hectares, and equally every ten thousand tons coals may cave in 0.2 hectare. The subsidence induced by coal mining not only causes the cultivated land to rapidly reduce, but also results in soil and water loss, desertification, karst collapse, mudflow, hill creep and so on in mining area. The ecological environment of mining area encounters being destroyed seriously. For example, in Liupanshui mining areas, Guizhou, annual production of raw coal only is 500 million tons, but the area of soil and water loss caused by coal mining reaches 3270 hectares, and accounts for one-third of the whole province soil erosion area. In Shenfu-Dongsheng coal field, the large scale coal mining causes serious damage to the land resource, and the area of desertification amounts to more than 13,000 square kilometers, accounting for 81.8% of the coal field area. Thereby, the coal mining intensified the contradiction between population and the land, the coal and the agricultural; the subsidence of the west mining area accelerates soil and water loss and the land desertification. Moreover, the subsidence from coal mining also induces lots of natural disasters, such as hill body slide, collapsing, mudflow which seriously destroy the land resource and the ecological environment of the mining area. At the same time, it also brings different degrees of destruction to buildings, roadways, railway lines, bridges and electric power distribution lines. In populated areas where this occurs subsidence causes forced migration of the local inhabitants. Generally, about 2,000 inhabitants need to migrate to produce 10 million tons of coal [2]. The areas of subsidence of all the state-owned key coal mines amount to 293,681 hectares up to 2000, and among them only 14.8% of areas of subsidence got reclamation. In 2000, land reclamation rate is also only 34% (see table 2) [13].

Table 1 Reasons, characteristics and harms of damage to land from underground mining

Damage forms	Physical characteristics	Reasons	Range	Ecological harms
Subsiding basin	Caving area, slide land, seasonal or perennial accumulated water	Goaf, continual deformation on ground surface	Above goaf	Reduction and even loss of the land productivity, the soil and water resources loss, no producing of the farmland, destruction of the building or the path
Fissure and bench	Trench, fissure	Tensile strain by ground settlement	Outside edge of the subsiding basin, which is parallel to goaf boundary	
Collapse pit	Funnel	Goaf, ground surface fracture deformation	Goaf in sharp inclined coal bed	

Table 2 Damage to land caused by state-owned key coal mine and open-pit mine mining in 2000

	Total area of subsidence / ha.	Reclamation area / ha.	Subsidence area in 2000 / ha.	Reclamation area in 2000/ ha.
State-owned key coal mine	293,681.00	43,591.00	9,531.00	3,239.00

State-owned key open-pi mine	12,238.16	1,468.3	561.72	268.49
------------------------------	-----------	---------	--------	--------

3.2. Open Pit Mining

Damage to the land resources caused by open pit mining includes direct excavation of the land and external dumping from open-pit collieries. Compared with underground mining, open pit mining has the lower cost and the remarkably higher economic benefits. The flaw of open mining is that under the same conditions of mining scale, the degree and range of damage from open pit mining is much greater than those of underground mining. Large-scale open pit mining has destroyed large amount of farmland. This is a very serious problem and if left unchecked could affect agricultural production due to the fixed amount of arable land Chinas has available.

During open pit mining, to extract the coal they must first strip the surface soil and the rock layer covering the coal bed. The damage caused to the land resource from the open-air excavation field is extremely serious and even nearly fatal. According to the incomplete statistics, during open mining, for every ten thousand tons of coal mined 0.24 hectare land is lost or destroyed, 0.08 hectare from open-air excavation and 0.16 hectare is from external dump of open-pit collieries [16]. From 1991 to 2000, China plans to exploit 100 million tons raw coal one year by open mining, which will destroy about 2,400 hectares land every year and the total number amounts to 24,000 hectares in 10 years. After the year 2000, the rate of land damage annually will increase progressively 8%-9% and up to 2020 the area of the land destroyed per year will be approximately 6,600 hectares. For the next 30 years the total area of the destroyed land will amount to approximately 135,000 hectares. For example, in the west open-pit mine of Fushun [9,29], there is a deep open-air goaf 400m depth, 6.6km length and 2.2km width. Nearly 14.52 square kilometers of land was destroyed after 200 million tons of coal had been mined. In another open-air colliery, in Huaizhou in Fushun which has worked 50 years, the goaf is 350m in depth, 2km long and 4km width [7]. Because the land is thoroughly damaged by direct excavation it will have no future use or value without extensive reclamation being carried out. Similarly any open pit formed during mining may be the future cause of many other geologic disasters such as mud slides, wall collapses as well as soil and water losses induced by the local natural geological structures and ground water levels.

Open pit mining will result in a great deal of abandoned earth and stone discharge. Some of the excavated waste may be used to refill the goaf, namely inner dump earth field. Other waste materials from the mining process must be dumped in areas outside of open-air goaf, namely the external dump earth field. This material and practice occupies a lot of land resource. At present, most countries in the world with advanced coal mining technology use the inner dump area which then becomes part of the reclamation process. Because open mining with the external dumps are dominant in China, and the area of external dump earth field generally accounts for 40% ~ 50% of the total areas of the open-pit colliery. The occupation to the land in this manner and purpose is very serious. For example, in China, the west open-pit colliery of Fushun has occupied the land of 1,800 hectares, the Haizhou open-pit colliery of Fuxin has occupied 1,600 hectares and the Xinqiu open-pit colliery has occupied 867 hectares. A significant amount of land can be saved using alternate dump practices.

4 Influence on the water resources in mining area

China is a country with low fresh water resources, the fresh water resource per capita is less than 2200m³ which is only one-fourth of quantity per capita in world. This problem is made all the more problematic coupled with the fact that the water resources distribution is extremely unbalanced [20, 28, 30]. Where 81% of water resources in China are centralized in the Yangtze drainage area and south, agricultural acreage only accounts for 36% of the total cultivated area of the country. In the north of Huaihe River, agricultural acreage accounts for 64% of that of the country, but the quantity of water resources only account for 19% of that of the country.

The collieries in China are mainly concentrated in the northern areas where the climate is drier due to limited yearly rainfall. The result being many coal mining areas are severely short of water resources. According to the investigation, in the 96 national major mining areas, 71% of the mining areas lack water and

40% suffer from a serious lack of water [25]. In the Datong mining area, the water volume per capita only accounts for 9% of that of China and one to thirty-sixth of that of the world.

The entire developmental strategy of coal industries is focused in western China and the west is facing more serious problems of water resources shortage. In the Dzungar mining area, it is verified that the underground water resource may supply 122,000 t/d of water. If one ton coal consumes 10 tons of water, the daily production of raw coal is 12,200 tons, and the year productivity can only achieve 4.45 million tons. It is far from the design goal that will produce 20 million tons a year.

As previously mentioned, mining areas are lacking water. A consequence of coal mining is a lowering of existing groundwater levels. This lowering groundwater levels worsens the water situation resulting in the lack of water becoming more serious. On the other hand, because of the influence of coal mining and the draining water of mine, many water resources are destroyed and wasted in mining areas.

According to the statistics, in China mining one ton of raw coal will discharge 2 tons ground waters on an average (in North China there are 10 tons at the average, and in individual mining area it achieves 47 tons). Every year, the discharged groundwater during underground mining is approximately equal to the impoundment of 100 Shisanling reservoirs in China [3]. The water discharge of collieries in north China accounts for 19% of its natural karst water resources, but the utilization ratio of discharged water is only 30%. This kind of high strength draining water of mines, not only destroys the balance of ground water runoff and makes the ground water resources irrecoverable, but also contaminates the water quality. Once the ground water is polluted, it is also difficult to restore in the short term even if eliminating the source of pollution. According to the incomplete statistics of Shanxi Province at the beginning of 80's [4], coal mining has directly affected the drinking quality of water for 330,000 people in 18 counties, The shortage and damage of water resources have already seriously influenced the inhabitants' living in the coal mining areas, and restricts the continual, stable and healthy development of coal industries.

The effluent sewage of coal mining areas mainly includes the mine pit water, the washing coal water, the sanitary waste, the gangue leaching water and so on. The combined volume of waste sewage from coal mining account for approximately 25% of the total sewage produced in China every year. In 1996, the volume of waste sewage from all the collieries was 2.61 hundred million cubic meters. The volumes are shown in Figure 3: 22.01 hundred million m^3 of pit water, 320 million m^3 of industrial waste, 40 million m^3 of washing coal water, 50 million m^3 of sanitary sewage and other waste water [25]. In 2000, the waste sewage of national coal mines reached 2.75 billion m^3 . Details as illustrated in Figure 4: 2.3 hundred million m^3 of pit water, 350 million m^3 of industrial waste, 50 million m^3 of washing coal water and 45 million m^3 of other waste water[4, 25]. A mass of untreated mine pit water is discharged with coal fines and rock dust, which has influenced the surrounding environment of mining area.

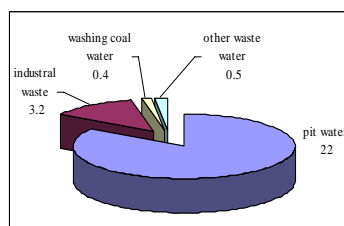


Figure 3 The waste sewage quantity of all the collieries in 1996 (hundred million m^3)

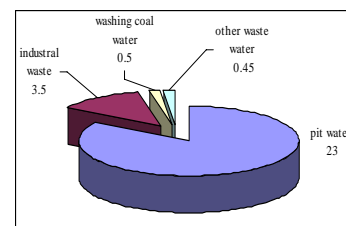


Figure 4 The waste sewage quantity of all the collieries in 2000 (hundred million m^3)

5 Influence of coal methane on atmosphere environment

During coal mining gases such as methane and carbon dioxide stored in coal are continually released into tunnels and working faces are discharged into atmosphere by the ventilation system of colliery. Methane is a

greenhouse gas whose effect is from 20 to 60 times more than carbon dioxide's, and its damage capability to ozone layer is 7 times as much as carbon dioxide's. Compared with carbon dioxide, methane is a gas with short life which can be detained in the atmosphere up to 12 years compared to carbon dioxide which can be held for more than 200 years [17, 26]. That is to say that weather associated with methane will become warmer in the several decades after it diffuses, but the action of carbon dioxide will occur gradually within several hundred years.

At present, the average content of methane in atmosphere is 1.72×10^{-6} (namely $1.72 \text{ cm}^3 / \text{m}^3$), and increases at the speed of 0.8% ~1.0% [19, 27] annually. If the content of methane only keeps increasing at the speed of 0.9% annually, and it would reach $8 \text{ cm}^3 / \text{m}^3$ by 2050. It is obvious that the influence of methane on greenhouse effect is more and more. In the following years, methane will continue the trend of the growth and its influence as a greenhouse gas will continue to increase. As a result of coal mining China discharges 19.4 hundred million m^3 of CH_4 into the atmosphere yearly which is equals to 2.26×10^8 tons of CO_2 and accounts 30% of the total amount in the world [4]. In 2008, the amount of gas extraction in collieries of China was 32 hundred million m^3 and is very lower than the amount of gas emitted into air directly. Among them the amount of utilized gas is less than 12 hundred million m^3 and the utilization ratio of gas extracted from collieries is only 37.5%. The loss of this gas is not only a waste of clean energy source but also results in serious endanger to the atmosphere environment of mining area and cause a negative influence on the global atmosphere environment.

6 Influence of coal gangue on environment

Coal gangue is the solid waste material produced in coal mining and processing, including tunneling-gangue (produced in tunneling rock way). Gangue is mined from the roof, floor and rock interlayer clipped in coal seam and washing gangue produced in the washing of coal. It is the compound composed by carbonaceous shale, carbonaceous sandstone, sandstone, shale and clay. The coal gangue is more than ten percent of coal output in coal production. According to the statistic [1, 24], there are more than 1500 gangue hills and the total accumulation of coal gangue has reach 34 hundred million tons. The quantity of gangue dump is still more than one hundred and fifty million tons every year, and the coal gangue accumulatively occupies thirteen thousand hectares of land. The accumulation of coal gangue not only occupies the land and pollutes soil, but also contaminates the water resource and atmospheric environment because of its long-term accumulation. The influence of the coal gangue on the environment during coal mining is mainly shown as: ① occupying a lot of land and polluting soil; ② contaminating water system by soluble poisonous and harmful substance; ③ polluting the atmospheric environment after long open piling and suffering from weathering, oxidizing and floating with wind; ④ easily leading to the disasters of freely burning, explosion and landslide.

Having been piled outdoors for a long time, the gangue hill gradually accumulates heat quantity. When its inner temperature reaches the ignition point of inflammable matter, the combustible matter of dump such as residual coal, carbon mudstone and waste wood can ignite by itself [18, 22]. After self-ignition, the gangue hill releases a great lot of harmful gas such as CO , CO_2 , SO_2 , H_2S and oxynitride, and a gangue hill can continue igniting for more than several decades even more time, which seriously affects the quality of atmospheric environment around gangue hill. According to the statistic [14], there are more than one thousand and five hundred gangue hills in state coal mines in China, and among them about four hundred gangue hills self-ignite chronically. By the end of 1999, 310 waste rock dumps have been treated for fire protection all over the country, but still 79 hills keep on burning and pollute the air around the mining area. Moreover, the self-ignition of coal gangue releases a lot of poisonous and harmful gas such as SO_2 , CO_2 , CO and so on, and seriously threatens the near resident health. For example, during self-igniting, the gangue releases the gas of SO_2 and H_2S at the maximum consistency daily average of 10.69 mg/m^3 in a mine of Wuda mining area, which makes the incidence of disease in this area obviously higher than that of others [22].

Being piled outdoors, the coal gangue is weathered into granule with a little coal dust, and floats with wind and pollutes atmospheric environment. Such as Laiwu mining area of Shandong province, the air pollutants of

winter are SO₂ and total suspended particle, the latter mainly comes from the dust of gangue and its pollution duty ratio is 36.15%; while in summer, the main pollutant is total suspended particle, the pollution duty ratio is 61% [3].

Besides SiO₂, Al₂O₃ and macroelements such as iron, manganese and so on, the coal gangue still contains some poisonous heavy metal elements such as lead, cadmium, hydrargyrum, arsenic and chrome. Under the action of natural weathering and rain eluviations, the coal gangue piled outdoors suffers a serial of physical and chemical changes, and produces a lot of contaminating materials. These chemical compounds are carried by rainwater then permeate the soil polluting the soil and eventually the groundwater below. With the passage of time, the range of polluted area spreads gradually and the degree of pollution becomes more and more serious. Eventually it will pollute the local water resources or that of the lower river and endangers residents' health.

7 Conclusions

The large-scale coal mining and exploitation in China not only has promoted the advance of the national economy and the development of societies, but it also has provided a reliable energy supply for the high speed development of China. Nevertheless, because the productive structure of coal is illogical and there are many small collieries to distribute widely, a mass of coal resources are occupied and badly wasted. Mining subsidence, occupation of coal gangue to land, solid waste, waste water and methane induced by coal mining have caused serious damage of land resources and water resources, and also has contaminated air of mining areas, which influences the ecological environment of mining areas. In west China especially, the ecological environment is considerably tender and the overdevelopment of coal is likely to result in the deterioration of ecological environments. Accidents in collieries from gas explosions, rock burst and water inrush cause the death of thousands of miners and the loss of property every year. In order to deal with the problem of environment pollution and ecological damage, and to create a harmonious inhabited circumstance, coal industries need to implement sustainable development and to build a new type of coal industry. That is to say, build huge modern mines and eliminate the small unproductive collieries. They must reduce the waste of natural resources; develop clean coal technology and put into practice clean production of coal and ecological construction of mining areas. The new coal industry must minimize the negative influence of coal mining on natural resources and ecological environments and resolve the conflicts between economic advances and environment protection. They must learn ways to optimize the structure of energy production and consumption and encourage developing new type of energy resources to replace coal. They must modernize the mining process using more sophisticated equipment, technologies and techniques to save coal. At the same time, it is necessary to use the means of economy, law and administration to ensure the rational coal consumption.

The national effort should be to achieve a harmonious, technical, ecological and clean working environment in the mining areas in China as well as promoting the healthy and comprehensive growth in the national coal industry.

Acknowledgements

This work is supported by the Foundation for the Author of the project sponsored by National Basic Research Program of China (973 Program)(2007CB209405) and the NSF of China (No. 40772100). The authors also sincerely thank Mr. Joseph Sawicz for his assistance with the English edition.

References

1. Bai, G.L. and Liang, B. Analysis of coal gangue leakage on the process of groundwater pollution. Journal of University of Science and Technology of China, 34(Supp). 470-475.
2. Bian, Z.F. Research on the recultivation and ecological reconstruction in coal mining area in China. Resources & Industries, 7(2). 18-24.

3. Chang, Y.X., Zhu, X.S., Song, C.B. and Wei, Z.R. Hazard of gangue and its control. *The Chinese Journal of Geological Hazard and Control*, 12(2). 39-43.
4. Cheng, H.b. and Zhang, L.X. Coal-bed methane and environment. *Coal Processing & Comprehensive Utilization*, 31(5). 6-9.
5. Cui, X.M., Li, H.X., Miao, X.X. and Su, D.G. Exploitation and utilization of water resources in China and its protection. *Chinese Mining*, 10(1). 32-35.
6. Cui, X.M. and Miao, X.X. Geological Calamity and its prevention. *Coal Mine Environmental Protection*, 14(5). 20-23.
7. Fan, J.F., Chen, W.S. and Hu, Y.J. Reclamation and reuse of stope of open pit coal mine. *Journal of Liaoning Technical University*, 22(supp). 49-50.
8. Feng, C.G. Review of accidents and disasters in China in the year 2004. *Journal of Safety and Environment*, 5(2). 1-11.
9. Feng, J.H. Study on environmental problems raised by China's opencut coal mine mining and prevention & mitigation measures. *Chinese Mining*, 11(6). 61-61.
10. Geng, D.M. Environmental problem of sustainable development of mine areas. *Journal of China Coal Economic College*, 16(3). 268-271.
11. Geng, D.M. and Jiang, F.X. Analysis of ecological environment of mines area in China. *Coal Mine Environmental Protection*, 16(6). 5-9.
12. Hu, Z.Q., Zhao, Y.L., Zhao, S., Xu, X.L. and Bate'er. Analysis of reclamation feasibility in land reclamation planning. *Transactions of the CSAE*, 20(4). 264-267.
13. Huang, S.C., Sun, X., Zhang, W.B., Zhang, B.C. and Hu, Y.H. Study on the environment influence of coal exploration and utilization in China. *The Report of Clean Energy and Environment*, 2003, 17-19.
14. Jiang, J. and Cheng, J.G. Influence of ecological disturbance induced by coal mining on sustainable development in China and its countermeasures. *Journal of Shandong University of Science and Technology (Natural Science)*, 21(1). 114-116.
15. Li, S.Z. Damage to land from coal mining and its reclamation technology in China. *Resources & Industry*, (7). 8-10.
16. Liu, H.L. Pollution and damage of open-pit collieries on ecological environment. *Journal of Heihe*, 2004. 99-100.
17. Luo, X.R. Coal-seam methane: environment, safety and resources, *China Mining*, 8(3). 20-24.
18. Ma, C., Kang, J.R. and He, W.L. Analysis of ecological environment in coal gangue dump. *Coal Mine Environment Protection*, 14(6). 71-73.
19. Milich, L. The role of methane in global warming: where might mitigation strategies be focused. *Global Environmental Change*, 9(3). 179-201.
20. Wu, W.H. An analysis of the status of water resources in China. *Land & Resource Management*, 22(4). 71-74.
21. Xiao, H.P. Important geological hazards of coal-mine and its prevention measures in China. *The Chinese Journal of Geological Hazard and Control*, 12(1). 51-54.
22. Xie, H.Q. and Zhang, G.C. Ecological environment effects and administering countermeasures of coalmine tips. *Journal of Beijing Vocational & Technical Institute of Industry*, 1(3). 27-30.
23. Xu, B. Caution of water resources crisis. *Decision & Information*, (8). 6-7.
24. Yan, Y.S. and Zhang, F.C. Coal deads and it's comprehensive utilization. *Energy Conservation*, 2. 56-58.
25. Yang, Y.R., Lu, J., Zhang, Y.Z. and Li, Z.H. Industry and environmental protection in China. *Coal Mine Environmental Protection*, 15(3). 5-9.
26. Ye, R.L. and Su, W.S. Pollution of atmosphere by coalbed gas emitted from coal mines and the countermeasures. *Mining Safety & Environmental Protection*, 1. 1-5.
27. Zhang, F.K. and Xu, L.J. Influence of methane on climate. *Mining Safety & Environment Protection*, 31(5). 6-9.
28. Zhang, J. and Xiong, B.Y. Establishing sound water circulating system in city and promoting sustainable utilization of water resources. *Journal of Shenyang Architectural and Civil Engineering University (Natural Science)*, 20(3). 204-206.
29. Zheng, M. An investigation of mining geological environment control project of WOCM in Fushun. *Geological Technoeconomic Management*, 26(6). 50-57.
30. Zhou, Y. Confinement of Water depletion to economy China. *Orient Economy*, (8). 72-73.

TIME-VARIATION STRUCTURE MODEL OF COAL BUMP INITIATION

BIN WANG, XI-BING LI and ZHI-GUO LI

School of Resource and Engineering, Central South University

Changsha 410083, P.R. China

At the present, coal bump research aims mostly at coal adjoining the laneway free surface but neglects the dynamic condition of laneway deep coal. It is based on the traditional static or dynamic theory in modelling with invariable boundaries systems. Actually, the stress state surrounding deep coal is dynamically changed with the excavation of working face or laneway, which may result in coal bump. This topic is rarely studied now. According to the representative characteristics of coal bump, the time-variation structure mechanics theory is applied to clarify the initiation mechanism of coal bump. Inherent parameters of coal self-sustaining bearing structures, such as load conditions, physics characteristics and boundaries, etc., are time-varying. The time-varying structure model is established and it can be further simplified to a mechanics model. The time-varying mechanics model indicates that the mass-decreased-with-time coal structure can give negative damping which can cause dynamic instability and lead to coal bump. By using the finite element analysis in the software ANSYS, coal bump occurrence can be well simulated when coal is softened by decreasing its elastic modulus E and poisson ratio μ . The results can be helpful in explaining the mechanism of coal bump.

Key words: coal bump; time-varying structure; negative damping; model

1 Introduction

The coal bump is one of the key areas of research in the field of mining engineering and rock mechanics. In the early 1950s research on coal bump began with a series of important theories, such as the rigidity theory, strength theory, energy theory, shock tendency theory, three criterion theory, deformation instability theory, and the rheological theory. They were put forth from different angles with the development of research on the rock bump analysis model and with laboratory work [1]. Generally speaking, all these theories are based on either rock quasi-statics theory or residual energy theory. Occurrence processes of coal bump are generally considered to be dynamic, compared to the preparation process which is relatively static [2, 3]. In essence, its preparation process is dynamic. In this paper, the time-varying mechanics theory is primarily applied to discuss the preparation and occurrence processes to analyze the coal bump from a new angle.

2 Coal bump time-varying structure model

2.1 Available coal bump structure models

Available coal bump structure models are two-dimensional models and three-dimensional models. These two kinds of models analyze the interaction between the roof and floor rocks with coal. The three-dimensional model can analyze how bilateral coal influences the coal bump. A three-dimensional model of translatory coal bump in deep mining was set up as a reference

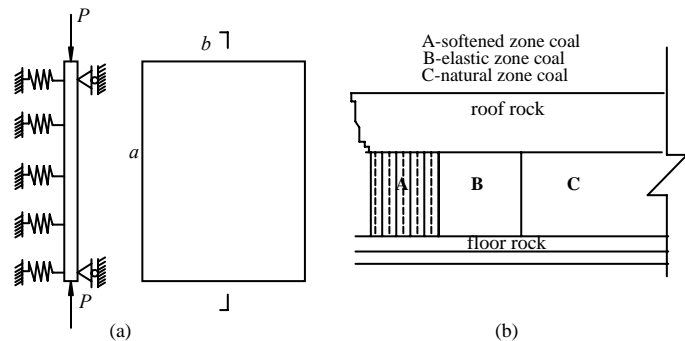


Figure.1 Available two-dimensional structure models

[4]. Three-dimensional models are complicated and are mainly used in the similar simulation and numerical simulation test. Two-dimensional plane strain models are still predominant in coal bump theoretical research and are separated into the plate girder structure model and the coal-surrounding rock structure model.

(1) In plate girder structure model shown in Figure 1(a), coal bump is suggested to be resulted from the buckling failure of thin layer separated from palisades [5, 6].

(2) Coal-surrounding rock structure model as in Figure 1(b) was firstly put forward by Cook in 1965. This kind of model considered how the roof and floor rocks act on coal. Rigidity theory came into being in 1960s, and many new theories appeared based on the model later on. The main viewpoints of this model are as follows: 1) Breakage or slippage of hard roof rock makes the sudden release of coal body energy which can induce the coal bump if reserve energy in coal is larger than cracking dissipation energy, both the roof, floor rocks and coal are hard. 2) Coal bump is a kind of coal physical instability under dynamic disturbance similar with rock rigid experiment. 3) Coal-surrounding rock system has the softening characteristics [1].

2.2 Time-varying structure characteristic of coal bump

Available coal bump structure models can be well applied to the coal bump mechanism research, but their limitation is that these models only pay more attentions to the lamination spallation zone of coal wall or how the roof and floor rocks clamp the coal, lacking of research on self-sustaining and time-varying effect of deep coal structure.

The practical engineerings prove that coal bump do not always occur even though coal compressive pressure exceeds the coal strength. When coal bump happens, the roof and floor rocks don't appear damaged or only have slight deformation, the coal body move wholly, as illustrated in Figure 2 [8], and coal seam is always hard. All of these indicate that coal body structure is composed of softened zone coal and elastic zone coal which can be self-sustaining.

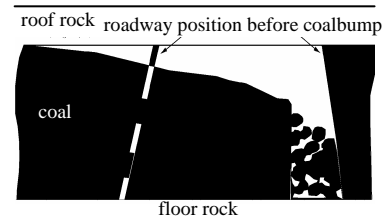


Figure 2 Rock bump phenomena in roadway[8]

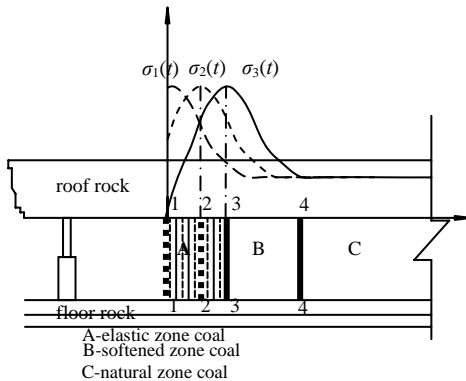


Figure 3 Coal bump time-varying effect evolvement model

To explain the time-varying effect of coal body structure, working face coal in initial excavate stage is chose to analyze. Its evolvement model is shown in Figure 3. Time-varying characteristics of coal body system inherent parameters are as follows:

(1) Coal body division boundary is variable. Generally, division boundary between softened zone and elastic zone moves rapidly or slowly from initial state line11 through middle state line22 toward goal state line33 until to the balanced in deep.

(2) Coal force condition is time-varying. Generally, with the change of coal bearing capacity, coal abutment pressure moves rapidly or slowly from initial state $\sigma_1(t)$ through middle state $\sigma_2(t)$ to goal state $\sigma_3(t)$ until to the balanced in deep. Its curve shape is variable with time, and its load state varies from uniaxial stress to triaxial stress.

(3) Coal physical and mechanical characteristics are time-varying. There are two kinds of force conditions with different characteristics in coal body: uniaxial stress near free surface and triaxial stress in deep. Failure

mode can be ductile or brittle depending on confining pressure, thus the whole strength of coal structure varies with time.

Under the condition of high stress, the coal bump possibility is pregnant with dynamic change of division boundary and abutment pressure. Coal bump will occur without external disturbances if condition satisfied, such as under blast load.

Present coal bump researches are based on the traditional static or dynamic theory with invariable boundaries systems. Its deficient is that their research objects are limited in goal state, namely division boundary line33 in Figure 3. With the rising of time-varying structure mechanics, researches on complex problems in mining engineering from the angle of variable boundary are paid more attentions to. For the advantage of its emphasis on variable structure inherent parameters, time-varying structure mechanics becomes a effective way of solving the complex problem in mining engineering.

2.3 Time-varying structure model construction

Coal body time-varying structure exists objectively. Reference [10] indicates that elastic zone coal is the main bearing structure, softened zone coal remains certain strength even though it is demolished. So these two zones are important parts of time-varying structure. In addition, Figure 4 shows that commonly softened zone coal bursts and elastic zone coal moves translatoryly. Obviously, elastic zone coal is involved in the formation of coal bump. Therefore, a new coal bump structure model which takes the influence of elastic zone coal into account is constructed as shown in Figure 4.

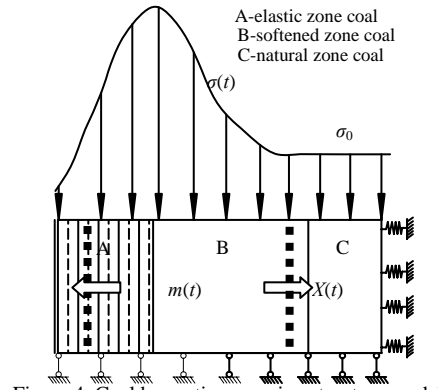


Figure 4 Coal bump time-varying structure model

Elastic zone coal and part of softened zone coal between thick broken lines in Figure 4 are the main bearing structure. Its self-sustaining capability determines whether coal bump occurs. Three parameters are introduced to analyse the coal bump, they are main bearing structure mass $m(t)$ describing the movement of division boundary, variable abutment pressure $\sigma(t)$, main bearing structure translatory displacement $X(t)$.

3 Coal bump time-varying structure analysis

3.1 Time-varying structure dynamic response

Geometry, physics, boundary parameters of most research objects in all branch subjects aren't changed with time. But if research objects have the variable characteristics with time which maybe change so much to influence the force states, time-varying mechanics shall be involved [11]. Time-varying mechanics has become a brand-new research tendency and a important modern mechanics branch, its control equation is variable coefficient mathematical equation. Vibration equation of time-varying structure system is as follow:

$$[M(t)]\{\ddot{U}(t)\} + [C(t)]\{\dot{U}(t)\} + [K(t)]\{U(t)\} = \{F(t)\} \quad (1)$$

Where $[M(t)]$ and $[C(t)]$ and $[K(t)]$ are time-dependent mass matrix and damping matrix and stiffness matrix respectively, $\{F(t)\}$ and $\{U(t)\}$ are time-dependent structure load and response respectively. If the change of all these time-varying parameters is obvious, formula (1) is called strong time-varying vibration equation [12].

Assuming that $\{X(t)\} = \{U(t), \dot{U}(t)\}^T$, then formula (1) can be taken as the form:

$$\{\dot{X}(t)\} = [A(t)]\{X(t)\} + [B(t)]\{F(t)\} \quad (2)$$

Where $[A(t)] = \begin{bmatrix} 0 & I_n \\ -[M(t)]^{-1}[K(t)] & -[M(t)]^{-1}[C(t)] \end{bmatrix}$ and $[B(t)] = \begin{bmatrix} 0 & 0 \\ 0 & [M(t)]^{-1} \end{bmatrix}$, I_n is n order matrix.

Formula (2) is state equation of n degrees of freedom time-varying vibration equation, $\{X(t)\}$ is system state vector and can describe the structure dynamic response.

To the initial condition $t=t_0$, general solutions of formula (2) is as follow:

$$\{X(t)\} = \Phi(t, t_0)\{X(t_0)\} + \int_{t_0}^t \Phi(t, \tau)[B(\tau)]\{F(\tau)\}d\tau \quad (3)$$

Where $\Phi(t, t_0)\{X(t_0)\}$ is time-varying displacement in initial state (i.e. free vibration caused by initial condition), $\int_{t_0}^t \Phi(t, \tau)[B(\tau)]\{F(\tau)\}d\tau$ is structure dynamic response caused by $\{F(t)\}$.

3.2 Time-varying structure mechanical characteristics of coal bump

Considering coal's moving horizontally when coal bumps, structure model in Figure 4 can be further simplified to be a mechanics model as Figure 5. Thus self-sustaining time-varying structure is regarded as a periodic time-varying system of single freedom degree, analysis object of which is main structure $m(t)$. $P(t)$ represents lateral load and friction force caused by abutment pressure $\sigma(t)$.

Suppose that structure system mass is $m(t)$ and its velocity is $v(t)$ at time t , then system momentum is $m(t)v(t)$. When system mass decreases with time, then at time $t+dt$, mass is $m(t)-|dm|$ and its velocity is $v+dv$. Also suppose that absolute velocity of decreased element mass dm is u , then system momentum at time $t+dt$ is $[m(t)-|dm|](v+dv)+u|dm|$. Thus according to theorem of momentum it can be inferred:

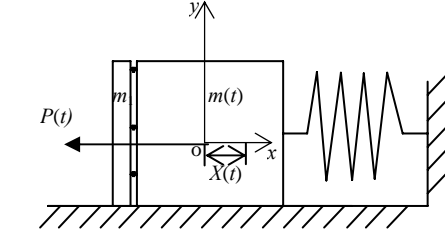


Figure 5 Time-varying mechanics model of rock bump

$$\{[m(t)-|dm|](v+dv)+u|dm|\} - mv = [P(t) - D(t)v(t) - K(t)X(t)]dt \quad (4)$$

Where $[K(t)]$ and $[D(t)]$ are system damping matrix and stiffness matrix at time t respectively,

Tiny quantities of high order dm/dt may be neglected, then forced vibration general equation of time-varying system of single freedom degree is as follow [13]:

$$m(t)\frac{d^2 X(t)}{dt^2} + \frac{dm(t)}{dt}\left[\frac{dX(t)}{dt} - u(t)\right] + D(t)\frac{dX(t)}{dt} + K(t)X(t) = P(t) \quad (5)$$

If system mass increases with time, its motion equation is still formula (2)

Exclusive of system damping, then $[D(t)]=0$, $u(t)$ is much smaller than $v(t)$ (i.e. $\frac{dX(t)}{dt}$), then let $u(t)=0$, we can get :

$$m(t)\frac{d^2 X(t)}{dt^2} + \frac{dm(t)}{dt}\frac{dX(t)}{dt} + K(t)X(t) = P(t) \quad (6)$$

Compared with formula (1), $\frac{dm(t)}{dt}$ in formula (6) is relative to viscous damping coefficient. If only free vibration considered, $\frac{dm(t)}{dt}$ has two kinds of conditions: (1) When structure mass increases with time, i.e., $\frac{dm(t)}{dt} > 0$, then structure system obtains the positive damping correspondingly. If $\frac{dm(t)}{dt}$ is large enough,

structure system can't vibrate freely. (2) When structure mass decreases with time (i.e. $\frac{dm(t)}{dt} < 0$), then structure system obtains the negative damping correspondingly, structure system can vibrate freely with a rapid increase of amplitude.

Through the analysis above, the mass change with time of time-varying system can strongly influence its dynamic response, when system mass decreases with time, structure system correspondingly obtains the negative damping and becomes a dynamic instability structure. Then the rapidly increasing amplitude of structure $m(t)$ maybe causes the ejection of free-surface mass m_1 .

3.3 Discussion on $\frac{dm(t)}{dt} < 0$

Since self-sustaining structure mass $m(t)$ is composed of elastic zone coal and part of softened zone coal, the structural stability depends on the certain proportion of coal quantity in these two zones. Under high stress some coal of these zones is demolished or weakened and loses its bearing capability. Those demolished coal can be regarded to break away from time-varying structure mass $m(t)$, so structure mass $m(t)$ decreases.

There are many factors to make the decrease of self-sustaining structure mass $m(t)$, such as crack or water. Reference [3] and reference [14] indicated that critical soften zone depth was related to elastic modulus E , and reference [15] proved that elastic modulus E felled greatly with the fall of confining pressure when confining pressure was small. In this paper, demolished or weakened coal can be described by reducing the elastic modulus E (i.e. self-sustaining structure mass decreases).

In recent years, with the rapid development of computer application technology, numerical calculating methods(boundary element method, finite element method,etc.) are widely applied, which paves the way for the research on coal bump mechanism. By finite element software ANSYS, mechanics characteristics of coal self-sustaining structure are analyzed on the condition that coal near free surface is softened to a certain extent, i.e., the decrease of elastic modulus E and poisson ratio μ . Its result can explain the coal bump.

4 Numerical analysis of time-varying structure

4.1 Calculation model and calculation parameters

Thicker the coal seam, more easily coal bursts [1], so the calculation model is a 10 m thick coal seam. Its buried depth is about 500 m, its floor and roof rock are gritstone. The physical and mechanical parameters of coal and rock used in ANSYS are as follows: (1) gritstone: elastic modulus $E = 20$ GPa, poisson ratio $\mu = 0.22$, density $\rho = 2600$ kg/m³. (2) integrated coal: elastic modulus $E = 1.9$ GPa, poisson ratio $\mu = 0.28$, density $\rho = 1800$ kg/m³. (3)softened coal: elastic modulus $E = 0.9$ GPa, poisson ratio $\mu = 0.31$, density $\rho = 1700$ kg/m³. Loading method is gravity without considering tectonic stress, failure criterion is mohr-coulomb criterion. To eliminate the influence of boundary effect, the whole model is 600 m wide and 600 m high, coal excavation span in the middle is 50 m, as shown in Figure 6.

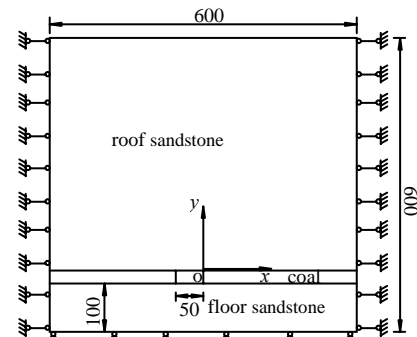


Figure 6 Coal calculation model (m)

To verify the finite element model, ANSYS static analysis of the model without coal excavation is made firstly. Compared with the abutment pressure of the top of the coal body, the result of simulation calculation is 1.7% higher than that of the engineering calculation, so the calculation model is relatively correct.

Five working conditions are calculated respectively from working condition 1 to working condition 5. They are as follow: (1) softened coal width is 2 m, (2) softened coal width is 4 m, (3) softened coal width is 6 m, (4) softened coal width is 8 m, (5) softened coal is 4 m away from the free surface and its width is still 4 m.

4.2 Results and discussions

Figure 7 and Figure 8 are Vertical stress nephogram of working condition 4 and working condition 5 respectively, Figure 9 is the abutment pressure curves of the top coal body under different working conditions. Discussions are as follow:

(1) With the increase of softened zone width, the peak value position of abutment pressure moves to the deep coal body, and its peak value decreases. When softened zone width is 8 m, the peak value is 22 % smaller than working condition 1, its position is 15.4 m away from the free surface.

(2) The abutment pressure curves of working condition 1 and working condition 2 are similar. Their peak value position are 6.24 m and 7.2 m respectively, which illuminates that coal body structure can be self-sustaining and has critical softened zone width.

(3) Working condition 5 indicates that faultage or blast loads can cause deep part of coal wall softened while free-surface part is integral, so coal body self-sustaining structure is broken. Free-surface part will suffer intensive stress concentration, its peak value of stress reaches 34.4 MPa, then coal bump will happen. Therefore, avoiding the rapid decrease of coal body structure mass and keeping its integrity can keep off the coal bump.

5 Conclusions

According to the coal bump representative characteristics, inherent parameters of the coal body self-sustaining structure (load conditions, physics characteristic and boundaries) are analysed to be time-varying. A new mechanical model for coal bump is constructed to analyze the mechanical characteristics of coal self-sustaining time-varying structure. Its results indicate that the structure system correspondingly obtains the negative damping and becomes a dynamic instability structure when its mass rapidly decreases with time. By means of finite element software ANSYS, coal bump occurrence can be well simulated when coal is softened by decreasing its elastic modulus E and poisson ratio μ .

Because time-varying structure mechanics theory is a new kind of theory which developed gradually in recent years, the authors only performed exploratory attempts to apply it to coal bump research, in order to help to advance the further study of related problems.

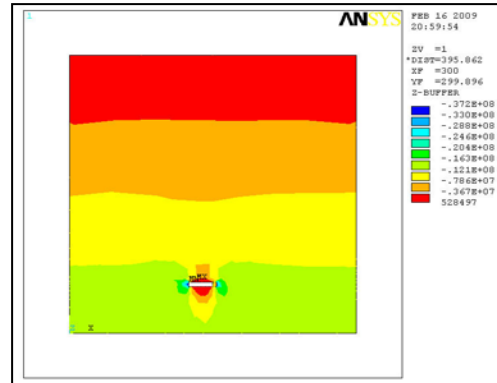


Figure 7 Vertical stress nephogram of working condition 4



Figure 8 Vertical stress nephogram of working condition 5

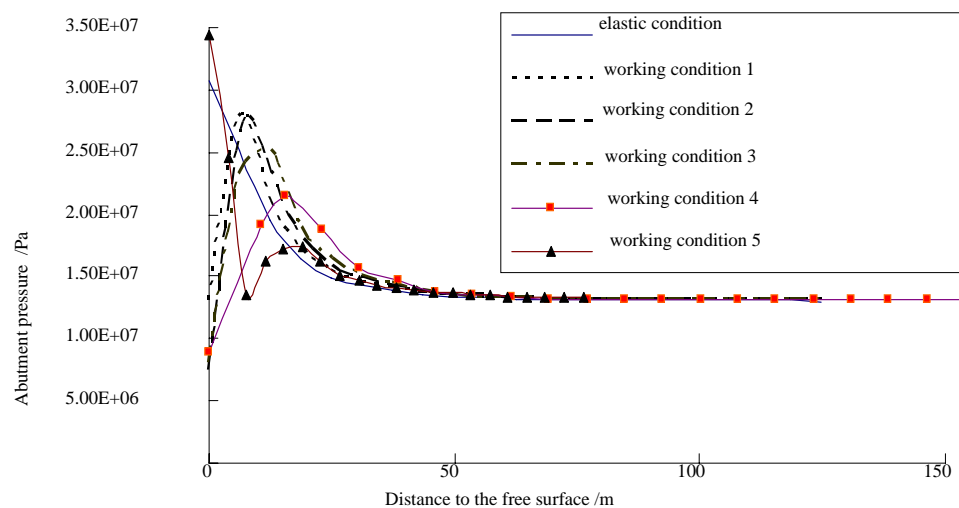


Figure 9 Abutment pressure curves of the top coal body

Acknowledgements

The authors wish to acknowledge the collaborative funding support from the National Natural Science Foundation of China Under grant nos. 50774032 and 50490274.

References

1. Qi, Q.X. and Dou, L.M. Theory and technology of coal bump. China University of Mining and Technology Press, 2008.
2. Tang, C.A. Numerical simulation of AE in rock failure. Chinese Journal of Rock Mechanics and Engineering, 1997, 16(4). 368-374.
3. Pan, Y.S. Study on rockburst initiation and failure propagation. Tsinghua University, 1999.
4. Jiang, Y.D., Zhao, Y.X., Liu, W.G., et al. Investigation on three-dimensional model of instability of translatory coal bumps in deep mining. Chinese Journal of Rock Mechanics and Engineering, 2005, 24(16). 2864-2869.
5. Wang, M.Q. and Hou, F.L. A method to determine rock burst in rock mass with plate-form damage. Rock and Soil Mechanics, 1993, 14(3). 53-59.
6. Zou, Y.J., Li, X.B., Zhao, G.Y. A catastrophe model for underground chamber rock burst under lamination spallation bucking. J. CENT. SOUTH UNIV(Science and Technology), 2005, 36(2). 311-316.
7. Cook, N, G, W. The failure of rock. Int.J, Rock Mech. Min. Sci, 1965, (2). 389-403
8. Qi, Q.X., Chen, S.B., Wang, H.X., et al. Study on the relations among coal bump, rockburst and mining tremor with numerical simulation. Chinese Journal of Rock Mechanics and Engineering, 2003, 22(11). 1852-1858.
9. Ma, Z.G., Huang, W., Gou, G.L., et al. Analysis on failure of covering rock in Ehuobulake Mine by using mechanics of systems with variable boundaries. Journal of Liaoning Technical University, 2006, 25(4). 515-517.
10. Chen, X.H., Shen, H.H. and Wang, S.Y. The research on theory and influence factors of self-sustaining structure of roadway surrounding rock. Journal of Liaoning Technical University (Natural Science), 2002,21(3). 261-263.
11. Cao, Z.Y., Zou, G.P. and Tang, S.Gg. Solution of time-variation dynamic problem by legendre polynomials. Acta Mechanica Solida Sinica, 2000, 21(2). 102-108.
12. Guan, C.S. Markov model on analysis of random time dependent structural dynamic reliability. Journal of Wuhan University of Technology, 2000, 22(2). 48-50.

13. Li, G.Q. and Li, Q.S. Theory and application of engineering structure time-varying reliability. Beijing: Science Press, 2001.
14. Liu, W.G., Jiang, Y.D., Zhou, H.W., et al. Experimental study on outburst proneness coal seam of meso character and crack destabilization. Journal of Hunan University of Science & Technology (Natural Science Edition), 2006, 21(4). 14-18.
15. Yang, Y.J., Song, Y. and Chen, S.J. Test study of coal's strength and deformation characteristics under triaxial compression. Journal of China Coal Society, 2006, 31(2). 150-153.
16. Li, X.B. and Gu, D.S. Rock impact dynamics. Changsha: Central South University of Technology Press, 1994.

RESEARCH ON THE FULL MECHANIZED TOP COAL CAVING DESIGN AND COMPREHENSIVE MEASURES OF PREVENTING ROCK BURST FOR THICK SEAMS IN LARGE EMBEDDED DEPTH

JIA-CHEN WANG

*State Key Laboratory of Coal Resource and Mine Safety, China University of Mining & Technology, Beijing
Beijing, 100083, P. R. China*

WEI-DONG PAN

*College of Resources & Safety Engineering, China University of Mining & Technology, Beijing
Beijing, 100083, P. R. China*

Based on the series characteristics in the main coal seams, such as large embedded depth, high geo-stress, compound roof, complex structure, an modern and high-tech working face was designed for the first coal mine of Juye coalfield in East China. Advanced theories and techniques were adopted on support and full mechanized top coal caving method was used. Measures of preventing rock burst were put forward through numerical simulations and on-site observations. The results showed that the anchor and truss structure with high original strength and high initial stress had expectant effect on face tunnels support and top coal caving produced smoothly. The serious hidden dangers were effectively avoided by measures of preventing rock burst. The achievements to research have important directive significance to the exploitation of whole Juye coalfield.

1 Introduction

Currently, with the rapid development of the coal industry and continuously investment of science and technology power, advanced coal mining methods, such as full mechanized top coal caving, have been widely used in the large coal enterprises. However, roadway support and rock burst are gradually being the “bottleneck” of safety mining. Data of references [1,2,3,4,5] have shown that, during the 40 years, from 1960 to 2000, the number of state-owned and rock burst coalmines grew from six to one over one hundred, and the mean frequency had increased over a thousands times, when the average mining depth increased from 400m to 800m. Therefore, the facing problems of technology security will be more severe, when exploiting the thick coal seams with large embedded depth and complicated geological conditions.

Libaosi coalmine belongs to the Feicheng Mining Group in the Shandong province of China, and was the first large modernization coalmine in the Juye coalfield. Due to the characteristics shown by production tests, such as large thickness, complicated conditions in roof, high ground stress, etc it will be a great challenge to build a forming and full mechanized top coal caving working face, which has important significance to the exploitation of the whole Juye coalfield.

2 Engineering Situations

2.1 Coal Seam Character

The research object was named 3107 working face, which main coal seam was No. 3 coal seam. The data information offered by adjacent working faces, 3115 mining face and 3111 tunnelling face, showed that the thickness of No. 3 coal seam is between 5.5 and 6.2m, 5.94 on average, the coal seam dip angle is between 6 and 12 degrees, 9 degrees on average, and the Polodyakonov coefficient f is about 1.8.

2.2 Litho logy and Characteristics of Roof and Floor

The sublevel roadways of 3107 working face were along the No. 3 coal seam floor, which height is 3m and width is 4.5m. Compound roof was composed by coal seams and rock strata, which detailed characteristics could be described as table 1 shown.

Table 1. Litho logical description of roof and floor

Category	Rock name	Thickness (m)	Cumulative thickness of roof (m)	Detailed characteristics
Roof	Grit stone	4.4	16.1	Light gray or grayish white, feldspathic quartz calcareous in the main and cementations
	fine sandstone	1.3	11.7	
	Siltstone	2.7	10.4	Shale cementation
	thin-coal	0.35	7.70	
	Siltstone	4.25	6.35	Grey black, some argillaceous composition in the upper
	Mudstone	0.10	3.1	Carbon mudstone and lowest intensity
Coal seam	No. 3 coal seam	6.0	3.0	
floor	Mudstone	1.1	1.1	Grey, pelitic texture, massive, contain some fragments fossil plants
	Siltstone	7.5	8.6	charcoal grey or grey, contain a large amount of shale cementation bands

2.3 Environmental Characteristics of Stope

The No. 3 coal seam, which relative gas emission rate is $0.871\text{m}^3/\text{ton}$ and the carbon dioxide is $0.140\text{m}^3/\text{ton}$, is low gas coal bed. It belongs to the easily spontaneous combustion coal seam, and the spontaneous combustion time is about three to six months. Coal dust has explosive hazard, and the geothermal gradient is 9.9 degree centigrade per kilometre when the ground temperature is 22 degree centigrade.

3 Support Design

Based on the especial coal occurrence condition and complicated structure of roof and floor, this chapter is going to find the difficulties and problems in support through characteristic analysis, then choose the proper supporting theory and design out the support method of sublevel roadways in final.

3.1 Characteristic Analysis of Sublevel Roadway

Because of the large embedded depth, more than 750m, and high geo-stress of No. 3 coal seam, previous and normal supporting form certainly would lead to hard maintenance and high repair rate. Meanwhile, the roof of working face is compound roof, including mudstone, carbonaceous shale and thin-coal, and the whole strength is lower. So under the influence of times mining shake, the roof is easy to break and not beneficial to roadway support, especially roof controlling.

3.2 Analysis of Support Theories

Due to the complex stress environment of compound roof, uneven loading and low strength of coal wall in roadway, supporting design had to combine with several support theories, including the theory of high strength anchor and surrounding rock strengthening, cable suspension and reinforcement effect theory, which were described as follows:

(1) The theory of high strength anchor and surrounding rock strengthening. Support of high strength anchor can heighten the cohesion and support resistance in further, after anchorage body reached the ultimate strength. Then residual strength of surrounding rock is strengthened, carrying capacity is improved, and the broken region, plastic zone and surface displacement of roadway are reduced, which is benefit for surrounding rock stability.

(2) The theories of cable suspension and reinforcement effect. Composite structure of anchor-net-girder can be slung on the stable rock above compound roof by cable, and the friction between composite structure and anchorage body can be increased by the pre-tightening force of cable. So the coal seam and strata in anchorage area can formed a new combined beam structure with large thickness, bending strength and stiffness.

3.3 Support Form Design

With the designing method of coupling support for soft rock roadway at great depth, bolt and cable truss structure system was finally chosen to support the sublevel roadway of 3107 working face. As shown in Figure 1, bolt and cable truss structure system is a linkage structure of controlling the deformation of surrounding rock, which could not only change the stress state of roof strata from two directional to three directional, but also extend the stress area and accordingly weaken the stress strength of roof strata. Meanwhile, bolt and cable truss structure system has great controlling effect on vertical joints.

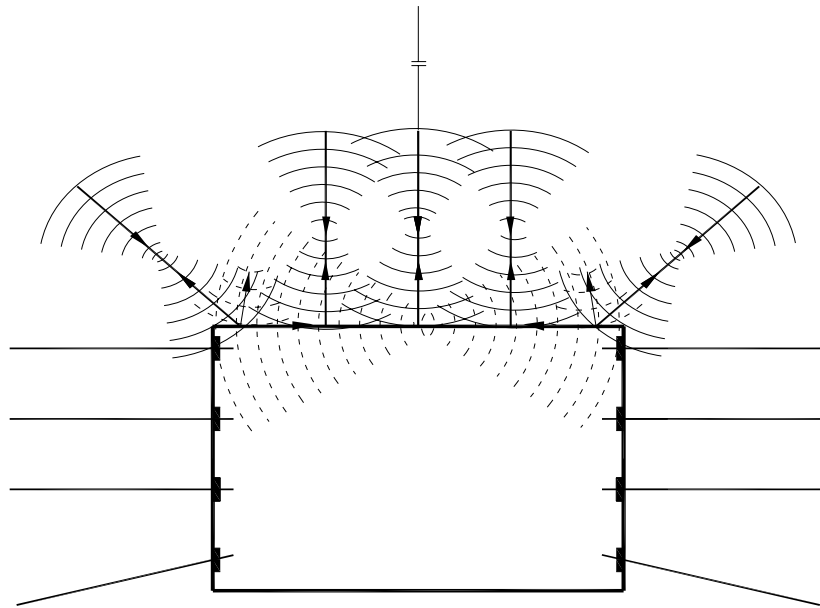


Figure 1 Action mechanism of bolt and cable truss structure system

Support materials included bolt with high strength and high pre-tightening force, W steel strip, caltrop metal net and cable with small aperture and high pre-tightening force, forming combined support system.

4 Studies on the Rock Burst Preventing

4.1 Theoretical Analysis

It is pointed out that rock burst is a structure damage process of coal and rock mass during exploitation, inducing or being accompanied with micro earthquakes and sudden release of elastic energy. Currently the common theories are Strength Theory, Energy Theory, and Rock Burst Tendency Theory. According to relevant study and practices[6,7], most of the underground coal seams have rock burst risk just with rock burst tendency and certain mining depth in the gravity field only, but the risk will be much lower if there is the internal stress field as buffer, which is shown in Figure 2(a) and 2(b).

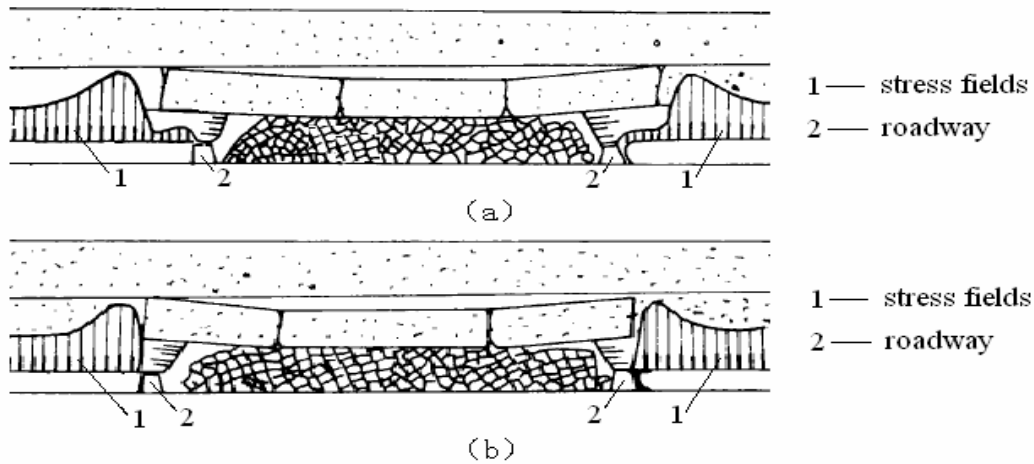


Figure 2 Effect drawing of stress distribution in stope
(a) With the internal stress field (b) Without the internal stress field

4.2 Numerical Simulation Analysis

Based on the known mechanical attributes of coal seam and rock strata, mining model of 3107 working face was built by FLAC3D(Fast Lagrangian Analysis of Continua Three-dimensional, Itasca). Stress variations of sublevel roadway surrounding rock in two periods, working face tunnelling and working face mining, were simulated and analyzed, partial results of which were shown in Figure 3(a) and 3(b).

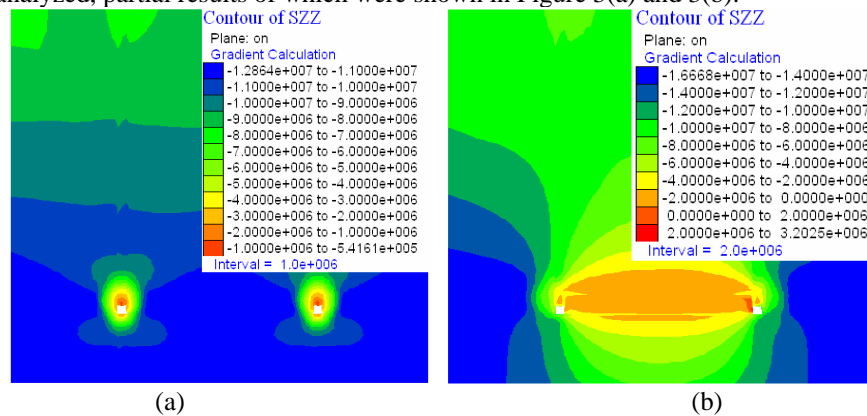


Figure 3 Distribution and diversification of vertical stress. (a) Tunnelling period of working face (b) Mining period of working face

As shown in Figure 3(a), during the tunnelling period of working face, the two sublevel roadways have similar distributing laws of vertical stress. Both roof and sides of roadway appear stress convergence, and the vertical stress of two sides is higher than that of roof, which shows that two sides are easier to break and need to strengthen support. As shown in Figure 3(b), under the influence of working face advance and mining, the outer side of the sublevel roadway appears stress convergence, and the inner side appears positive stress, in other word is pull stress, so the inner side of roadway is broken a bit seriously. But the diversification of vertical stress proves that the sublevel roadways are easy to maintain and support takes well effect.

4.3 Field Observation

Being the initial stage of mining, the advanced support pressure of 3107 working face was observed through drilling by precise hydraulic equipments, and the change trend of observation data could be shown in Figure 4.

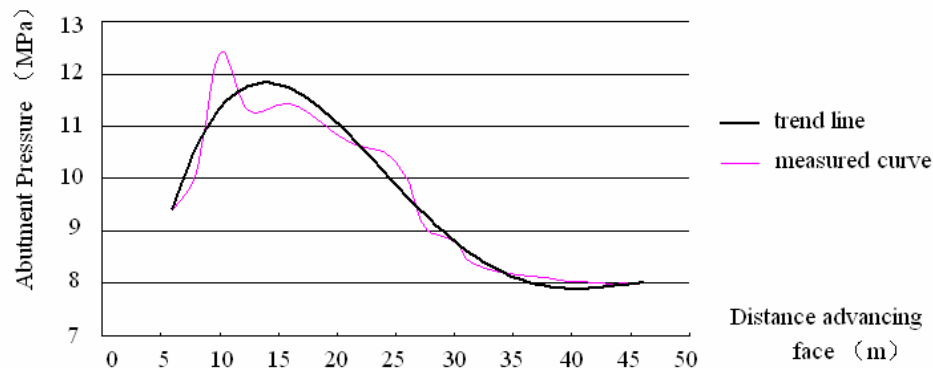


Figure 4 Change curve of advanced support pressure in 3107 working face

Through analyzing, the features of advanced support pressure in 3107 working face could be summarized as follows:

(1) The support pressure in front of working face can be divided into three areas, these are Stress increasing area, Stress decreasing area and Constant-stress area. Stress increasing area is 15m before the working face, when Stress decreasing area is from 15m to 45m and Constant-stress area is 45m far away.

(2) The change trend of support pressure showed that, there was an internal stress field in front of the working face, which was also the sign of advance breakage of top coal, so the pressure appearance obviously changed with the main roof pressure. The risk of rock burst happening could be greatly reduced by holding the persistence of internal stress field through artificial auxiliary measures.

4.4 Prevention and Treatment of Rock Burst

(1) Prediction and forecast. It's necessary to build a qualified professional staff team of rock burst preventing, to do well the mineral pressure observation, and to discern all the abnormal phenomena in daily production. Key regions should be fixed observed by professional equipment as electromagnetic radiometer, then the fatalness of mine disaster should be evaluated and predicted every day after being analyzed.

(2) Treatment of rock burst. If the advanced support pressure of working face was continued high, coal mass should be soften by boring water injection before mining. Drill hole pressure relief with large aperture or loose blasting could be used if necessary, and even vibration blasting. In other word, people produce lower degree rock burst for avoiding the big ones.

5 Conclusions

(1) Different from the previous support, the sublevel roadways of 3107 working face were supported by the bolt and cable truss structure system. Based on the series characteristics of large embedded depth, high geo-stress and compound roof, several support theories were combined, and coupling support technology of roadway was used for support designing.

(2) Stability of the roadway's surrounding rock mainly depends on the existence of the internal stress field. The result of numerical simulation showed that the two sides of the sublevel roadway were easier to break than the roof during the tunnelling period, and the damage degree of the inner side was higher than the outer side when the working face was mining.

(3) After the normal production of working face, the results of field observations showed that support designing had obtained the expected effect, and it had limited the occurrence of rock burst to some extent. By combining this with the professional measures of rock burst prevention, the requirement of safety production would certainly be met.

Acknowledgements

The research work was supported by National Basic Research Program of China (No.2007CB209402) and National Natural Science Foundation of China (No. 50834005). Many thanks to Chief engineer GAO Fa-min for the precious assistance provided during the tests.

References

1. Pan, Y.S., Li, Z.H. and Zhang, M.T. Distribution, Type, Mechanism and Prevention of Rock Burst in China. *Chinese Journal of Rock Mechanics and Engineering*, 2003, 22(11). 1844-1851.
2. Zhang, M.T. Coal Outburst Forecast and Prevention. *Journal of Liaoning Technical University*, 2001, (8). 433-435.
3. Pan, L.Y. and Niu, X.L. Knowledge of Sub-level Caving Method to Control Underground Impact Pressure. *Chinese Journal of Geotechnical Engineering*, 1999, 21(1). 14-16.
4. Wan, J.L., Zou, S.X., Nan, C., et al. Characteristics and Mechanical Analysis of Rock Burst. *Journal of Railway Engineering Society*, 1998, 58(2). 95-102.
5. Qin, Y.P., Zhang, J.F. and Wang, L. Preliminary Discussion on Theoretical Model of Rock Damage Mechanics. *Chinese Journal of Rock Mechanics and Engineering*, 2003, 22(4). 646-650.
6. Song, Z.Q., Chen, L.L. and Wang, C.Q. Knowledge on Face Working Condition in Mechanized Sub-level Caving Work Face, 1995, 20(4). 356-360.
7. Miao, X.X., Sun, H. and Wu, Z.G. Analyzed on Mechanism of Outburst at Eastern of Xuzhou Soft Rock Coal mine. *Chinese Journal of Rock Mechanics and Engineering*, 1999, 18(4). 428-431.
8. Pan, Y.S., Wang, L.G., Zhang, M.T., et al. The Theoretical and Testing Study of Fault Rock Burst. *Chinese Journal of Rock Mechanics and Engineering*, 1998, (6). 642-649.
9. Jiang, Y.D., Liu, W.G., Zhao, Y.X., et al. Study on Stability of Surrounding Rock in Deep Mining at Kailuan Group. *Chinese Journal of Rock Mechanics and Engineering*, 2005, 24 (11). 1857-1862.
10. Lippmann, H. Meckanicks of Bumpsin Coal Mines: A Discussion of Violent Deformations in the Sides of Roadways in Coal Seams. 1987, 40 (8). 1033-1043.

RESEARCH ON THE ROCK BURST MECHANISM OF THE OVERALL REMOVAL OF COAL TUNNEL WALL IN DATONG COAL MINING AREA'S "THREE HARD" COAL ROADWAY

XU-HONG WANG, LI-XUNG KANG and SHUANG-SUO YANG

College of Mining Technology, Taiyuan University of Technology

Taiyuan, 030024, China

By establishing the mathematical and mechanics model the coal tunnel wall can be pushed out overall into "three hard" coal roadways of Datong Coal Mining Area, this paper studies the mechanism of this type of rock burst. Under the condition of the separation of the seam and the roof, it is possible to have the coal wall vulnerably squeezed out and moved outward as a whole. This is because the vertical stress and the occurrence of coal as a whole is moved with very small demands.

1 Introduction

The overall removal of the coal tunnel wall is a special type of rock burst which has appeared in recent years. It takes place in the "three hard" coal seams, and poses a threat to the safe production of coal. In order to find some reasonable prevention measures, we must study its mechanism.

In section 2, the paper describes the fact that this type of rock burst has occurred in the "three hard" coal seams of the Datong Coal Mining Area and has led to security incidents. At present, such research on the mechanism of special rock burst is still a gap, so the research is of great significance.

In section 3, depending on the analysis of the limit stress and the simplified distribution of vertical stress in the rib of coal tunnel, the paper establishes the mathematical and mechanics model about the rock burst type of coal tunnel walls which can be pushed out overall in "three hard" coal seams of the Datong Coal Mining Area .

In section 4, under different conditions of whether the coal bed has been separated from the roof when the burst occurs, or whether the burst occurs at the instant of separation, the paper takes mechanical calculations and analyzes the rock burst mechanism of the overall removal of the coal tunnel wall. Under the condition of the separation of the coal bed and the roof, the vertical stress demanded by the integral removal of coal body is very small, so the coal body can be squeezed out easily and lead to the integral removal. This conclusion is in accordance with the phenomenon observed at the site.

Section 5 summarizes the conclusions of this paper.

2 Research background and its Status

The seam which is mined by Datong Coal Co. Ltd is a typical “three-hard” one and many incidents of rock burst have happened in these years. Of all the reasons, the most typical one is that coal tunnel wall has been squeezed and removed as a whole ,which causes the destruction of supports and equipments in the tunnel, and the space of the tunnel becomes less. Moverover, it can even cause incidents. This is also the character of the coal mining area with “three-hard” seam.

At present, theoretical research on the mechanism of rock burst has made great progresses, and there have been many papers on experimental research and numerical simulation analysis of rock burst phenomena, but theoretical research on the type of rock burst, that coal tunnel wall overall is pushed out, is still a blank.

The essay studies this phenomenon, in order to discover the nature mechanism of this special rock burst to seek the technical measures to prevent it and protect the security of the mining area, and to obtain efficient production.

3 The establishment of the stress-state analysis model

According to Dr Shuangsoo Yang’s analysis on the “character of mining roadway stress when two ribs are weak” [1,2], which thinks the state of the two ribs’ stress can be shown in Figure 1. When the lithology in two ribs is weaker than the ones at the roof and the floor, and the interlayer bonding intensity between the ribs and the roof as well as the floor becomes lower, the phenomenon that the coal body of two ribs is squeezed to the roadway space along the bedding is likely to be seen.

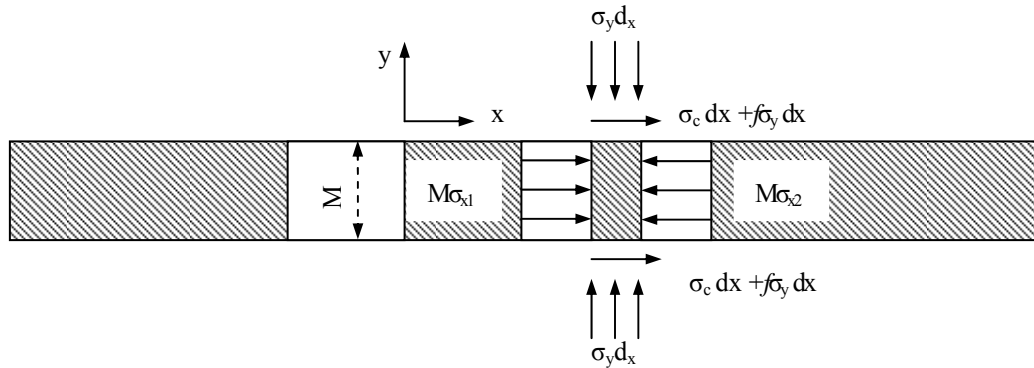


Figure 1 Limit stress analysis in the ribs

According to the analysis of limiting equilibrium under stress state as shown in Figure 1, it gets the conclusion that when the interlayer bonding force between the ribs and the roof as well as the floor disappears, the ultimate stress in the ribs should be

$$\left. \begin{aligned} \sigma_x &= R_c \frac{1 - \sin \phi}{1 + \sin \phi} \left(e^{\frac{1 + \sin \phi}{1 - \sin \phi} \frac{2f}{M} x} - 1 \right) \\ \sigma_y &= R_c \frac{1 - \sin \phi}{1 + \sin \phi} e^{\frac{1 + \sin \phi}{1 - \sin \phi} \frac{2f}{M} x} \end{aligned} \right\} \quad (1)$$

In which,

R_c —one-way compressive strength of the two ribs

f —friction coefficient between layers

M —the height of tunnel

ϕ —internal friction angle of the two ribs

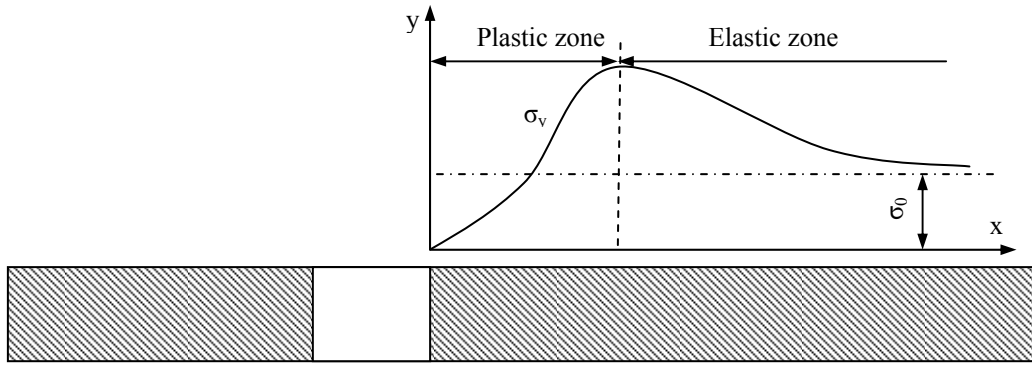


Figure 2 Vertical stress distribution in the ribs.

In the plastic zone, the deeper the coal wall goes, vertical stress σ_y is rising quantity (as shown in Figure 2) more quickly, and horizontal stress $\lambda\sigma_y$ aroused by vertical stress is also rising one [3] along with it. The horizontal tectonic stress which is vertical to the tunnel is σ_s . Supposed that the lithology of the roof and the floor is the same, according to figure 2, the horizontal combined force that the coal body whose thickness is dx bears should be

(2)

$$p_1 = M(\sigma_s + \lambda\sigma_{y2}) - 2\sigma_c dx - 2f\sigma_y dx - fMr dx - M\lambda\sigma_{y1}$$

In which, σ_c —shear strength between the rock floor and coal bed

r —bulk density of the coal bed

that is,

(3)

$$p_1 = M\lambda(\sigma_{y2} - \sigma_{y1}) + M\sigma_s - 2\sigma_c dx - f(2\sigma_y + Mr)dx$$

From (3), we know, the harder the coal bed of the two ribs in the tunnel becomes, the steeper the distribution curve of vertical stress is, the higher the peak is, the bigger the vertical stress difference ($\sigma_{y2} - \sigma_{y1}$) is, and the bigger the combined force p_1 that the coal body bears is. And especially when the bigger horizontal tectonic stress σ_s which is vertical to the tunnel is, the bigger p_1 will be, so the coal body is easily to be squeezed

and pushed outward as a whole.

If we simplify curve σ_y in plastic zone into a line, as in figure 3, the distance between the peak and coal wall is S , and the value of the peak is σ_M .

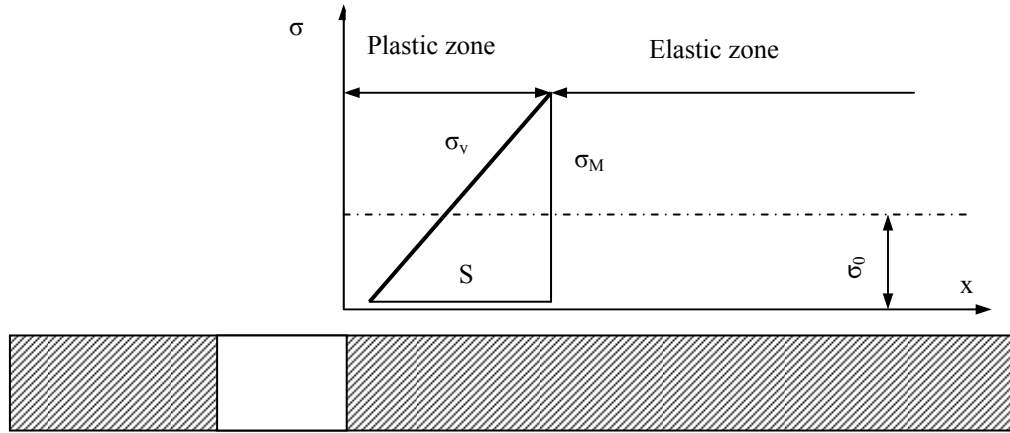


Figure 3 Vertical stress simplified distribution in the ribs

In the peak area of vertical stress, because of the effect of high stress, the vertical crack that is parallel to the working face can be found [4]. The expansion and connection of the vertical crack finally becomes to be a fracture face cutting the coal wall, which separates the coal body adjacent to the working face from the integral coal body and makes it a relatively independent part while it still has to bear the horizontal stress.

4 The analysis of rock burst mechanism

1) If, as the roof rebounds because of vibration, the coal bed has been separated from the roof and bursts at the instant of separation, in this time, the vertical stress σ_{y1} on the side of the coal wall is zero, the horizontal active force is

$$P_x = M (\sigma_s + \lambda \sigma_M) \quad (4)$$

The force that the coal body's removal has to surmount is

$$F_1 = S \sigma_c + f M r S \quad (5)$$

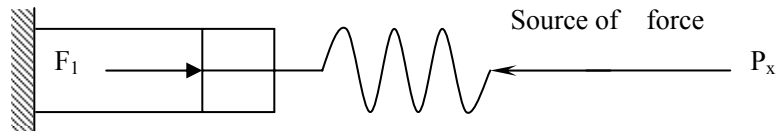


Figure 4 Mechanical model of horizontal stress distribution in the ribs.

According to Figure 4, if we want to move the coal body with the width of S , we need to satisfy the condition of $P_x \geq F_1$, that is ,

$$M(\sigma_s + \lambda\sigma_M) \geq S\sigma_c + fMrS$$

From the above, we know lest vertical stress which moves the whole coal wall is,

$$\sigma_M = (S\sigma_c + fMrS - M\sigma_s) / M\lambda \quad (6)$$

Let's take the example of circle air tunnel in working area 307, Meiyukou Coal Mining, Datong coal mining area, the thickness of coal bed (the height of the tunnel) M is 3 meters. According to actual observation ,the distance S between the vertical stress peak and the tunnel wall is 6 meters. The maximum horizontal principal stress σ_1 is 12Mpa, and the practical lateral pressure coefficient λ_1 is 1.5,so its vertical stress $\sigma_2 = \sigma_1 / \lambda_1 = 8$ Mpa. The general poisson's ratio of the coal seam is $\mu = 0.35$,and its lateral pressure coefficient $\lambda = \mu / (1 - \mu) = 0.54$,and the horizontal stress $\sigma_3 = \lambda\sigma_2 = 4.32$ Mpa caused by the vertical one,so the maximum horizontal tectonic stress $\sigma_s = \sigma_1 - \sigma_3 = 7.68$ Mpa.The shear strength between the floor and coal bed $\sigma_c = 6.5$ Mpa, $f = 0.15$, $r = 14$ KN/m³,so $\sigma_M = 11.01$ Mpa.

From (6), we know,if the vertical stress is certain, the bigger the distance S between the vertical stress peak area and coal wall is, and the bigger the minimum vertical stress σ_M demanded by the coal wall integral removal is,the less the possibility of the occurance of rock burst is. If, the bigger the horizontal tectonic stress σ_s is,the less the minimum vertical stress σ_M demanded by coal wall integral removal is , and the more the possibility of the rock burst occurring is.That is the same if it's in the opposite situation.

2) If, as the roof rebounds because of vibration, the coal bed has been separated from the roof but it doesn't burst at the instant of separation ,and it does burst after the contact of the roof and coal bed. In this time, the horizontal active force is also,

$$P_x = M(\sigma_s + \lambda\sigma_M)$$

The force that the coal body's removal has to surmount is (7)

$$F_1 = S\sigma_c + f(\sigma_M + Mr)S$$

If we want to move the coal body with the width of S , we need to satisfy the condition of $P_x \geq F_1$, that is ,

$$M(\sigma_s + \lambda\sigma_M) \geq S\sigma_c + (\sigma_M + Mr)S$$

From the above, we know the minimum of vertical stress which moves the whole coal wall is,

$$\sigma_M = (S\sigma_c + fMrS - M\sigma_s) / (M\lambda - fS) \quad (8)$$

Let's take the example of circle air tunnel in working area 307, Meiyukou Coal Mining, Datong coal mining area, if its parameters don't change, $\sigma_M = 24.79$ Mpa.

3) If, there is no separation between the coal bed and the roof, horizontal active force is also

$$P_x = M(\sigma_s + \lambda\sigma_M) \quad (9)$$

The force that the coal body's removal has to surmount is

$$F_1 = 2S\sigma_c + f(\sigma_M + Mr)S$$

If we want to move the coal body with the width of S , we need to satisfy the condition of $P_x \geq F_1$, that is ,

$$M(\sigma_s + \lambda\sigma_M) \geq 2S\sigma_c + f(\sigma_M + Mr)S$$

From the above, we know the minimum of vertical stress which moves the whole coal wall is,

$$\sigma_M = (2S\sigma_c + fMrS - M\sigma_s) / (M\lambda - fS) \quad (10)$$

The same example in Meiyukou Coal Mining, Datong coal mining area can be used here. If its parameters don't change, $\sigma_M = 78.96 \text{ Mpa}$.

From all above, we can get the result: under the condition of the separation of the coal bed and roof, the vertical stress demanded by the integral removal of coal body is very small, so the coal body can be squeezed out easily and lead to the integral removal. While if there is no separation between the coal bed and roof, the vertical stress demanded will be big, so there will be less possibility for the coal body to be squeezed out and removed integrally too.

After the study of the phenomenon that coal tunnel wall can be pushed out overall in "three hard" coal roadway of Datong Coal Mining Area, we can observe the separation of the coal bed and the roof. The roof separation can be observed in the circle air tunnel in working area 307, Meiyukou Coal Mining, and the coal wall is removed outward more than 1 meter integrally. This situation proved that the separation between the coal bed and the roof in "three hard" coal roadway can lead to the integral removal of coal wall.

5 Conclusions

The mathematical and mechanics model states that the coal tunnel wall can be pushed out overall in "three hard" coal roadways of the Datong Coal Mining Area has been established. The mechanism of this special type of rock burst has been studied. The condition of the separation of the seam and the roof will lead to the special burst phenomenon easily. The coal wall is vulnerably squeezed out and moved outward as a whole because the vertical stress that the occurrence of coal as a whole to be moved demands is very small.

References

1. Yang, S.S. Study on the Control Theory of Gate Roadway Surrounding Rock and the Support Principle of the Bolting Structure. Coal Industry Press, 2004.
2. Qi, Q.X., Shi, Y.W. and Liu, T.Q. Mechanism of Instability Caused by Viscous Sliding in Rock Burst. Journal of China Coal Society, 1997, 25:22-28.
3. Qian, M.G. and Liu, T.C. Rock Pressure and Its Control. Coal Industry Press, 1996.
4. Zhao, B.J. Rock Burst and Its Prevention and Treatment. Coal Industry Press, 1995.

STUDY LAWS OF TOP COAL'S FAILURE AND DISPLACEMENT IN EXTREMELY THICK COAL SEAM'S SUB-LEVEL CAVING MINING FACE

YING ZHOU

*Department of Resources Science and Engineering, Henan Polytechnic University
Jiaozuo 454000 ,P.R. China*

HUA NAN

*Department of Resources Science and Engineering, Henan Polytechnic University
Jiaozuo 454000 ,P.R. China*

RUI-FUG YUAN

*Department of Resources Science and Engineering, Henan Polytechnic University
Jiaozuo 454000 ,P.R. China*

The failure of top coal plays an important role in the successful sub-level mining, and also it is vital to coal bump. By using RFPA^{2D} (Rock Failure Process Analysis), the extremely thick coal seam is investigated in this paper. The extremely thick coal seam locates at the 21121 working face (fully mechanized sub-level caving longwall working face) of Qianqiu Mine, Yima Coal Mining Administration. The results keep good agreements with the consequence from the deep-hole base station in-situ displacement measurement. More important, it can be seen from RFPA^{2D} simulations that the advancing abutment distance of 21121 working face is much longer, and that the interval of top coal can generate apparent abscission layers. The obvious periodicity and beams rotation of top roofs also play a more important role in the fragmentation of the extremely thick top coal. On the basis of these characteristic analysis, the advancing abutment zone of 21121 working face with the maximum scope of 90m is divided into the following micro-zones: initial compression and plastic deformation zone, strong compression and damage zone, roofs rotation action and supports action zone. Such dividing can do great benefit to the safety and high efficient mining of the extremely thick coal seams.

1 Introduction

The top coal caving mining method is used for thick seams of more than 5.0 m . When the bottom coal is mined by the shearer and dumped into the front Army Face Conveyor (AFC), the top coal above the support will be broken up by both the ground and support pressures. Therefore, when the tail beam (or caving shield) rotates toward the rear AFC by retracting the rear hydraulic leg, the broken top coal resting on it will flow into the rear AFC.

Since the 1940s, some experiments were performed in a few countries such as France and the Soviet Union. In 1963, a perfect result was achieved in a sublevel caving mining face equipped with shield support, shear machine and AFC. Since then, sublevel caving mining became a popular technology for mining thick coal seam in Eastern Europe. However, no key progress was made in the lateral years. With society's increasing concern on environmental protection, few and fewer coal mines used this technology since the 1990s in high coal production country in the world [1,2].

In fact, sublevel caving mining technology was admired by China since its birth. There were two reasons for this: one is the fact that the reserve from coal seam of more than 5.0m can take up to one third of overall coal reserve in China; and the other is the technology is a high production technology. As a developing country, China had great need of much coal. So in 1984, the first sublevel caving mining face was born in Shenyang, located in north of China [3]. Since then, sublevel caving mining technology was widely used and was remarked as high production method in China.

The reason why sublevel caving mining technology is accepted and widely used, especially in China, is that this technology has lot of advantages [4,5,6]:

(1) Less gate roads. It's obvious that one sublevel caving mining face only need two gate roads. However, when used slices mining technology, number of gate roads will be double or even more.

(2) Higher production. In sublevel caving mining face, coal mass can not only be extracted by mining machine, but also be extracted by directed caving top coal in the same time. So sublevel caving mining face will have higher production.

(3) Less energy consumer. In sublevel caving mining face, top coal is forced to cave by ground pressure. So sublevel caving mining will cost less electricity than slices mining technology.

(4) Less utility materials consumer. Because of less gate roads, sublevel caving mining face will need less utility materials.

(5) Less face move. Because sublevel caving face has a greater mining thickness of coal seam, so as for the same amount of coal reserve, it needs few face number resulting few face move.

Since sublevel caving mining technology is a popular technology nowadays, more and more thick coal seams are mined or will be mined by this technology. However, when the coal seam is too thick, the top coal will not fully fractured and then this part of top coal will not fall onto the rear AFC in the face, but into the gob. To solve this problem, the first step is to make clear that how the top coal be fractured in the mining process.

Lot of researcher work have been done on top coal's displacement and failure[5,7,8], but as for extremely thick top coal, there is little work to have been done up to now.

By using of simulation calculation of RFFA and theory analysis, this research aims at the nature of top coal's fragmentation and failure process in mining extra-thick coal seam thick seam with sublevel caving technology, which can do great benefit to extra-thick coal seams' safe and high efficient mining.

2 Simulation experiment research

2.1 Description of Qian-qiu coal mine's 21121 working face

Qianqiu Coal Mine, located at the center of Yima Coal Field, was developed in 1956 and went into production in 1958. Since 1986, the annual production has been steady at 0.9 Mt. The coal reserve is 70 million metric tons, which is estimated to last another 60 years. Mining for the first level has completed. So production is now concentrated on the second level. The face's length along the strike direction, oriented at N86° 23'W, is 1,232m and panel width (face length) is 112m with a mineable area of 136,300m². Mining depth ranges from 617.5m to 712.5m with an average of 679.5 m. Coal seam, averaging 17.6m thick, is uniform. It strikes near the east-west direction with an average dip of 11°. Coal appears lumpy and powdery. Coal seam structure is completed. It contains 3-6 partings, 0.1-1.7m thick, including fine-grained sandstone, fine-grained sandy mudstone, and carbonaceous mudstone. The coal is semi-bright or dark, and easily susceptible to spontaneous combustion. The immediate roof is dark gray, tightly-cemented mudstone, 16.1–23.7m thick and uniformly distributed. It is brittle and breaks easily with smooth surfaces. It contains debris of plant fossils and thin streaks of fine-grained

sandstone and powdered sandstone. The main roof, being very thick, is Jurassic-colored bedded conglomerate, sandstone, and powdered sandstone. The immediate floor is dark gray conglomerate with localized floor being made of coarse clay.

2.2 Simulation experiment

The tables are designed to have a uniform style throughout the proceedings volume. It doesn't matter how you choose to place the inner lines of the table, but we would prefer the border lines to be of the style shown in table1 (width =0.5pt). For the inner lines of the table, it looks better if they are kept to a minimum. Whether top coal can be fully broken or not plays a very important role in top caving mining method. It's obvious that with thicker and thicker top coal thickness, top coal becomes more and more difficult to be fully broken up during the mining process. But how top coal act when it become thicker during mining? Based on the geological situation of 21121, the authors used RFPA to study this problem. The results can be seen from Figure 1 to 6.

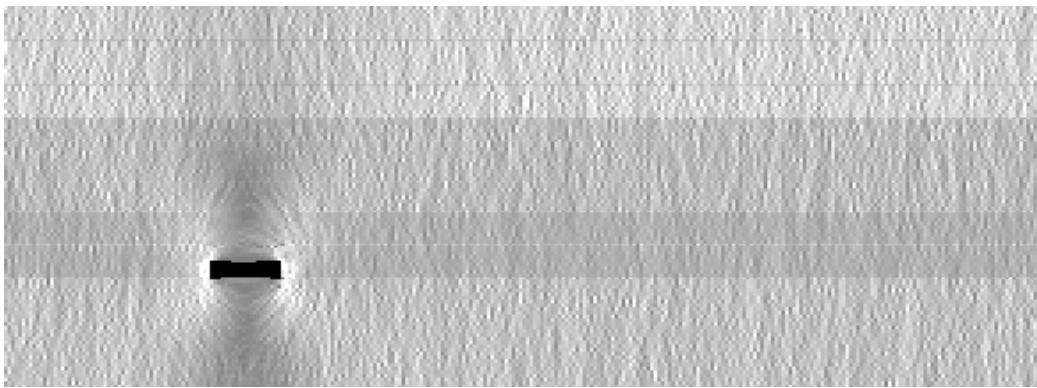


Figure 1 The No.1 simulation drawing of top coal's fragmentation and failure process for step 03

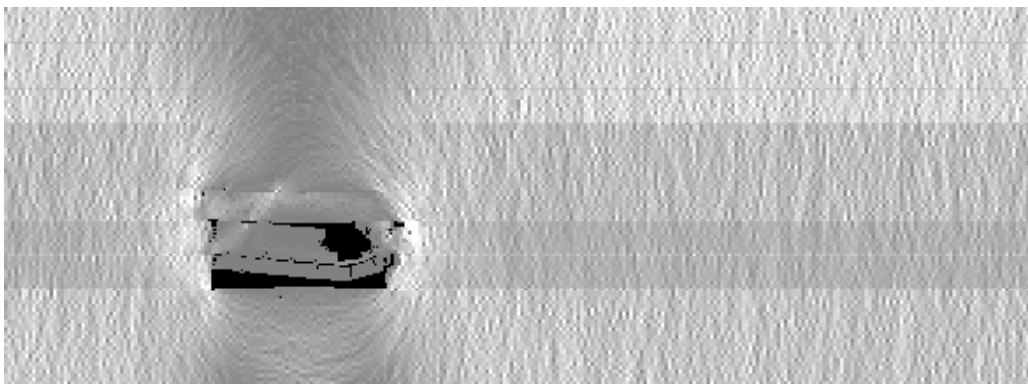


Figure 2 The No.2 simulation drawing of top coal's fragmentation and failure process for step 06

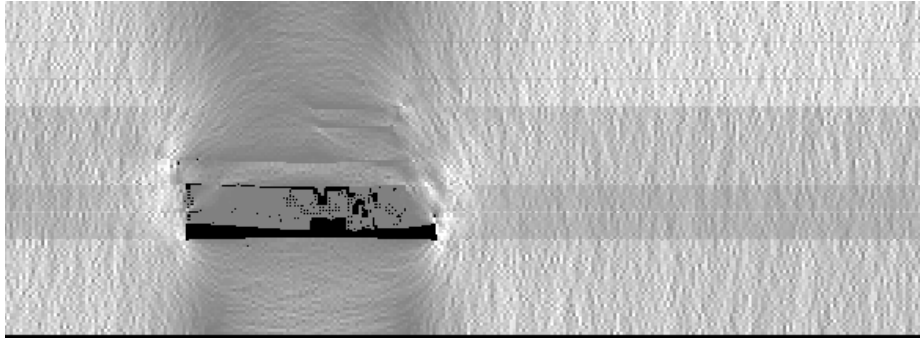


Figure 3 The No.3 simulation drawing of top coal's fragmentation and failure process for step 09

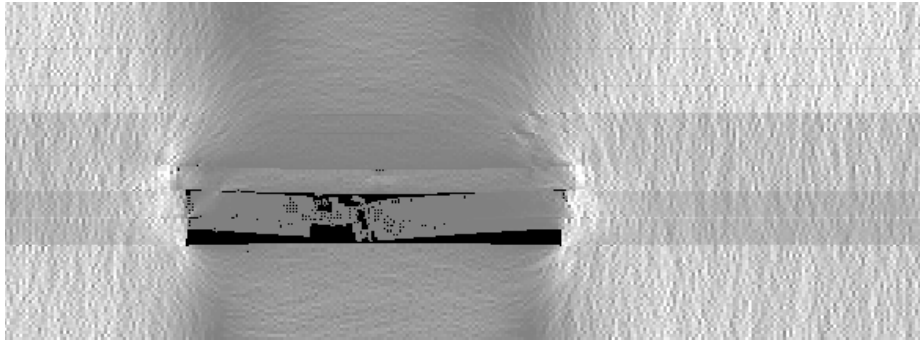


Figure 4 The No.4 simulation drawing of top coal's fragmentation and failure process for step 13

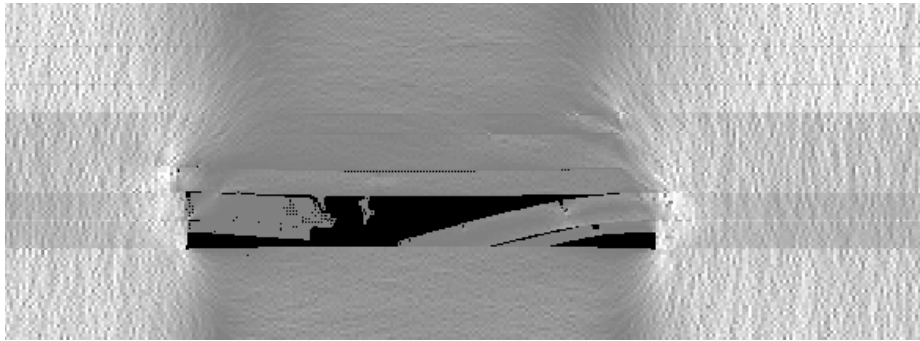


Figure 5 The No.5 simulation drawing of top coal's fragmentation and failure process for step 17

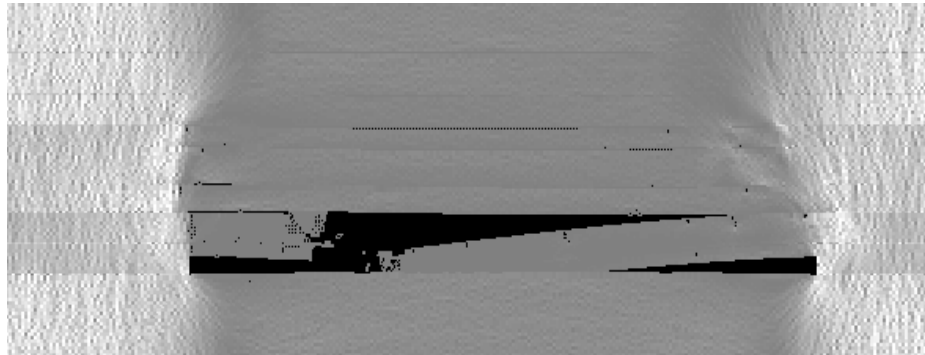


Figure 6 The No.6 simulation drawing of top coal's fragmentation and failure process for step 21

2.3 Analysis of Numerical Simulation Test's Results

From Fig.1, it can be seen that in the initial mining process the top can not caving with mining, but can form a simple supporting beam structure. With the advancing of working face, the simple supporting beam structure will be damaged at the distance of about 11m from the box cut as Fig.2 shown when the gradually increasing concentrated stress amount to 28.9MPa. With further advancing of working face, the upper top coal form a cantilever structure, which may not cave in a time, as Fig.3 shown. And also, with further advancing of working face, the cantilever structure gradually be undermined and begin gradually subside until contact the floor which can slow down the cantilever structure further damage, as illustrated in Fig.4、 Fig.5 and Fig.6.

From the numerical simulation test of top coal, it can be seen that due to the larger thickness of top coal, top coal has obvious characters of layered effect, period effect, and short beam effect. It is the short beam rotation that makes the upper top coal affected by the stretching force, so the upper top coal crush more fully. As the lower top coal is more close to the working face, the vertical direction restriction will be more decreased and support repeated supporting has more important roles to its fully broken. However, it has more difficulties to make the central top coal fully broken. To promote the central top coal fragmentation, measures to increase vertical direction deformation space like increasing cutting height or reducing residual coal in working face always have good effect.

Numerical simulation test indicates that the entire process of deformation and development of top coal is a top coal injury and continuous micro-crack's development process and finally they connect to form macro-broken crack. For the 21121 longwall panel's fully mechanized sublevel caving mining of extra-thick coal seam, although the coal seam has a large mining depth under the ground and its larger vertical stress, because of its larger thickness of nearly 18m, top coal bearing under front abutment pressure can not fully break. The main reason is, after the upper top coal under abutment pressure fragmentation, a decompression layer thus forms which can slow down the lower top coal damage. However, due to the seam's immediate roof of sandstone and siltstone with a average thickness of 25m, the broken upper top coal can easily form short beam structure and the short beam structure rotation can lead to the top coal's failure and decompression layer thickness reduction which can contribute to the lower top coal fragmentation.

3 Theory and calculation of pressure burst's layer-crack-plate model

3.1 Theory of Pressure Burst's Layer-crack-plate Model^[7-8]

Once road or working face is developed in coal mass, the original stress balance will be disturbed, and the original triaxial stress condition will become into plane stress condition or even uniaxial stress condition in distributed area of coal mass. So large amount of secondary crack is produced near high stress zone where exposing surface of road or working face. During the process of mining coal, some suitable secondary cracks develop into layer-crack-plate structure which is critical to above stratum's or coal's stability and the failure of this structure can lead to the coming of pressure burst. It's revealed that lateral stress has heavy effects on the development of secondary crack:

(1) When coal mass has high lateral stress, secondary crack develops slowly and stops at the end, so the coal mass will be stable.

(2) When coal mass has low lateral stress, secondary crack develops quickly and can lead to coal mass' split failure following Y-direction.

(3) When coal mass has reasonable lateral stress which is lower than the converting value from brittleness to plasticity, shearing strength failure will be coal mass' failure form.

On the basis of unite by use of sliding-crack theory, the critical stress of crack's developing average value can be calculated by:

$$\sigma_z^{cr} = \frac{\pi l k_k / l_0}{2 \xi(\theta) \left(1 + \frac{3 l^2}{2 h^2}\right) \sqrt{2 b \tan\left(\frac{\pi l}{2 b}\right)}} \quad (1)$$

l-----average length of secondary crack;

b-----average distance of different secondary crack;

h-----average distance from secondary crack to free face of coal;

θ ----separation angle between secondary cracks' direction and press stress; $\xi(\theta)=C\sin 2\theta\cos\theta$.

As for large scope of pressure burst, it can be simplified layer-crack-plate structure. If inter-plate effects can be ignored, the critical stress of layer-crack-plate elastic structure can be calculated by:

$$\sigma_z^{cr} = \frac{E \pi^2 h^2}{3 (1 - \nu^2) L^2} \quad (2)$$

L-----cut-through crack length.

3.2 Calculation of Pressure Burst's Layer-crack-plate Model

Based on in-sit measurement, $K_{ic}=1\text{MPa}\cdot\text{m}$, $l=2\text{mm}$, $\theta=45^\circ$, $b=10\text{mm}$, $h=5\text{mm}$, $C=1.13$, $L=120\text{mm}$, it can be calculated:

$$\sigma_z^{cr} = 30.2 \text{ (MPa)}. \quad (3)$$

4 Analysis of top Coal's Failure and Displacement

It can be seen from above that the first moving point of RFPA^{2D} is 90m before working face which is consistent with the in-sit displacement measurement result of 90m, and that the first concentrated broken stress of RFPA^{2D} is 28.9MPa which is consistent with the Layer-crack-plate model theory's calculation result of 30.2 MPa.

On the basis of above information and achievement in this area [4,5], top coal fragmentation zones can be summarized as following:

(1) The initial compression and plastic deformation zone. The initial compression of top coal begins about 90m in the front of working face. With advancing of working face the top coal will be affected by the initial coal mining, so the top coal produces plumb compressive deformation, and these deformation is mainly from the original compression of horizontal fractures of coal body. And also with the advancing of working face the ahead abutment pressure is increasing, the top coal began to produce plastic deformation and lateral expansion, and this process will make top coal internally generate some minor fissure. From the test results, it can be seen that there is no separation between immediate roof and top coal in this process.

(2) The strong compression and damage zone. It ranges from 20m to 40m in the front of working face and this scope belongs to the abutment pressure sharply increasing scope. Due to the roof's increasing pressure, the level displacement of top coal rises dramatically, the pre-existing fractures of coal body expand faster, also the initial small cracks formed in the initial compression and plastic deformation zone begin to expand. So plenty of new micro-fractures are produced and expend fast and top coal gradually becomes broken in the strong compression and damage zone. With the increasing of top coal fragmentation thickness, the immediate roof cantilever and decompression layer role becomes even more obvious.

(3) The roof's secondary rotation action zone. It ranges from 0m to 20m in the front of working face. In this zone the top coal is acted by the broken projecting beam of immediate roof, and the level displacement and moving speed increases dramatically toward working face's gob, and what's important, the side restraint of top coal from working face's gob decreases quickly, and so there is more space for fracture's expansion in top coal. So fractures in the top coal expend violently and top coal becomes more broken and begins to fall in the roof's secondary rotation action zone. So the decompression action of broken top coal decreases and the projecting beam of immediate roof becomes more concentrating which can contribute to the lower top coal fragmentation.

(4) Supports action zone. In this zone, top coal comes into the process of bulk flowing and drawing. That top coal is formed a state of bulk by the function of dropped overlying strata is the most characteristic of this zone. Each coal bulk lost intrinsic regular array and occlude relation and flows to drawing opening. However, because top coal thickness is big, lower top coal don't crash completely which make a great deal of top coal lose in the working gob in the drawing process. So supports play an important role in this region. Repeat rising and falling or horizontal movement of support can both add the crash degree of lower top coal and greatly decrease the chance of coal-coal structure and promote top coal drop smoothly. The swing of support tail bar and support bar also play a positive function in decreasing the coal-coal structure.

5 Summary

On the basis of the above work, the following summary can be made:

(1) It can be seen that the pressure, which is 28.9MPa from RFPA, is very near the pressure which is 30.4MPa from pressure burst's layer-crack-plate model. Therefore, it will be good to use RFPA to study top coal's failure and displacement, especially in the scope of the front abutment pressure

(2) The advancing abutment zone of the extremely thick coal seam can be divided into initial compression and plastic deformation zones, strong compression and damage zones, and roofs rotation action and supports action zones.

(3) There are three clear layers during the displacement and failure process of the top coal, and more importantly, the middle layer of these three layers plays a key role in the successful sub-level caving mining.

Acknowledgments

The work in this paper is funded by Grave Project of Henna Province (322020700), Education Department Project of Henna Province (133014).

References

1. Wu, J. Fifteen years retrospection of mechanized top caving technology in our country. *China Coal*, 25(1). 9-16.
2. Wang, J. CH. Fully mechanized longwall top coal caving technology in China and discussion on issues of further development. *Coal Science and Technology*, 33(1). 14-17.
3. Jiang, F.X. and Ma, Q.H. Mechanical solution of the maximum point of dynamic abutment pressure under deep long-wall working face. *Journal of China coal society*, 27(3). 273-275.
4. Wu, J. and Lu, M.X., Zhang, Y., and etc. Simulation research on stress distribution of surrounding rocks of LTCC workface. *Journal of rock mechanics and engineering*, 2(1). 2356-2359.
5. Qian, M.G., Miao, X.X. and He, F.L. Analysis of key block in the structure of voussoir beam in longwall mining. *Journal of China coal society*, 19(6). 557-563.
6. Xie, G.X. and Yang, K. Surrounding rock abutment pressure distribution and thickness effect of dynamic catastrophic in fully mechanized sublevel mining. *Journal of China coal society*, 31(6). 731-735.
7. Nan, H. and Zhou, Y. The Application of Layer-crack-plate Model in extremely Thick Coal Seam with Pressure Burst Tendency . *Proceedings in Mining Science and Safety Technology*, 2007.
8. Chen, H.J. Stress analysis in longwall entry roof under high horizontal stress. USA: West Virginia University, 1999.

POST-CLOSURE SEISMICITY IN THE MINES OF KOLAR GOLD FIELDS

C. SRINIVASAN, Y. AHNOCH WILLY and P.C. NAWANI

National Institute of Rock Mechanics

Champion Reefs-563 117, Kolar Gold Fields, India

The occurrence of rockbursts in one of the deepest mines in the world, the deep gold mining region of the Kolar Gold Fields (KGF) in Southern India was closed in 1991. Following this, when deeper levels were inundated with water, increased number of seismic events were observed at two areas where Champion mine dyke and the Mysore North fault meet the water body. Apparently, the increasing quantity of water is tending to create a super hydrostatic fluid pressure gradient at that depth. The entire mine was closed during the year 2001 and significant seismic activity continued to occur. A noticeable rockburst with magnitude 2.8 occurred on November, 2 2005 in the old and abandoned mines of KGF followed by series of seismic events. The rockburst was severe and the effect was felt by residents of adjoining areas and surrounding townships. The rockburst caused panic among people and it is reported that people came out of their houses. This paper documents the seismic activity that has occurred in this mine since closure of deeper levels and the entire mine and shows the relationships of the rate of seismic activity to the flooding within the mine.

1 Introduction

The mining district of KGF lies in the well-known schist belt of Southern Peninsular shield, whose aerial extent is about 10 km in the North-South direction along main longitudinal axis of mining region and 3 km across it. Having been the main source of gold in the country, the gold mines at KGF enjoy the distinction of being among the oldest and deepest mines of the world, which are nearly 120 years old now and the workings reached a depth of 3.3 km below ground level. However, as the richness of the ore body considerably depleted with time, especially during the past 10-15 years, mining in the deeper levels was discontinued towards the end of 1991 due to economical constraints. Thus several sections of the underground workings lie abandoned now and are filled with rainwater, which is up welling and spreading gradually. At present the water level has reached almost very near to the surface.

Not different from other hard rock underground mines in the world, one of the most severe problems related to mine safety and ground control is the phenomenon of the rockbursts in and around the mining excavations at KGF. Occurring regularly in the regions of moderate to high horizontal compressive tectonic stresses, rockbursts are commonly recognized as seismic events (mine tremors) that are caused essentially by the alteration of the virgin state of stress or rock equilibrium in the mining process to create large openings through the rock body. In case where the tectonic stresses may not be the primary driving force, redistribution of lithostatic stresses could also become a potential source of strain energy capable of triggering the mine tremors. According to early records [8] the first rockburst was reported to have occurred in a stope below 960 ft. level in the Oorgaum mine now a part of Champion reef mine and the problem of rockbursts started during beginning of 20th century.

Of late it has been observed that inundation of the abandoned KGF mines with rain water, which gradually spreads around, triggered series of mine tremors in the deeper level workings of Champion reefs. It is interesting to note that this migration of mine tremors tends to move from deeper levels to shallower levels, both

horizontally and vertically, even though no mining operations have been in vogue at those depths [11]. This is clear example of fluid induced seismicity. The details are discussed using seismic and rockburst events obtained from different seismic monitoring systems.

A regional seismic network was established in 1978 and it was operated continuously since then. The locations of geophones installed on surface and underground is shown in figure-1. The seismic data collected were in analogue form. During 1997 a three component short period seismometer was installed under a DST funded project to monitor role of prominent Mysore North fault [10]. During 1999 Broadband seismometer was installed to monitor seismicity of Peninsular India. During 2005 Strong Motion Accelerograph was installed. Seismic events from the mine were picked by both Broadband and Strong Motion seismometers due to its proximity to the mines. In the present study, the seismicity from rockburst-prone region at deeper levels of the Champion reef mine for the period 1991-1997 using analogue data, short period seismometer Digital data from 1997-1999. Broad Band Seismic data from September,1999-August,2005 and the Strong motion data from 2005-2008 from the mines of Kolar Gold Fields were analysed and interpreted.

Figure-1 Surface field plan showing locations of geophones, Broadband seismometer and Strong Motion Accelerograph.

The seismic events in and around the mine excavations were continuously monitored using 14-channel cable telemetered seismic network at Kolar Gold Fields. More than 10,000 seismic events were recorded and hypocentres of a very large number of them were determined with an accuracy of more than 50m. They are found to occur throughout the mining region and are distributed nearly parallel to the main longitudinal axis (north-south) of the Kolar Schist belt [12]. However, the seismic activity was concentrated in the vicinity of the mine workings, i.e. the deep-level workings of the Champion reef mines, Mysore mines and Nundydroog mines (Figure 2). The depth wise distribution of the rockbursts events was found to be consistent with the profile of the underground workings.

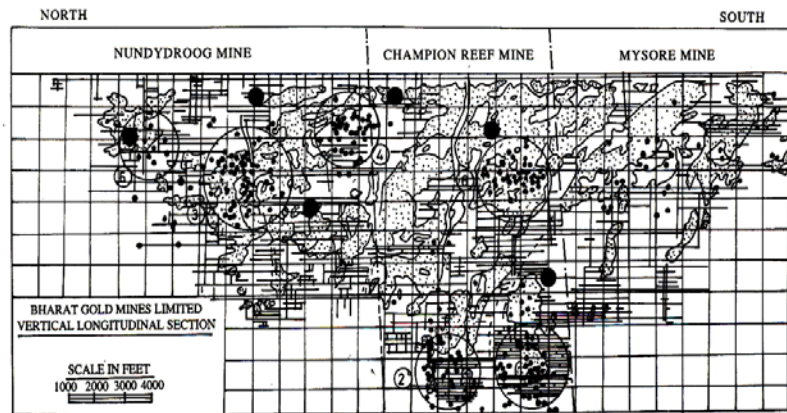


Figure. 2 Longitudinal (north-south) section through Kolar Gold Fields showing typical spatial distribution of rockbursts in one-year period (1987). Shaded areas-mined out portions; small dots –computed hypocentres of rockbursts; bigger dots-some of the geophone locations of the monitoring network; plain circles-areas enclosing bunches of rockbursts and broken line-strike of Mysore North fault(MNF). (1) Glen ore Shoot , (2) Northern Folds area, (3) HENRY'S Shaft area, (4) new Trial Shaft area, (5) Golconda Shaft area and (6) old workings.

2.2 Seismicity Observed during October,1991-September,1992 due to inundation

The Northern Folds and Glen Ore Shoot areas are deep workings of Champion Reef mine, Kolar Gold Fields from where large quantities of gold were extracted. Mining in these areas and at all other deeper levels of the Champion Reef mine was stopped from September 1991 due to economical constraints. Following this, when the deeper levels were inundated with rain water, increased number of rockbursts have been found to occur from these two areas as seen in Figure-3. The water levels during October 1991 and September 1992 are marked by dashed lines at the bottom and at the top. Majority of the major and minor rockbursts occurred above the water level during the first year off inundation. It is clearly observed that number of rockbursts in the Northern Folds area is more compared to the number of rockbursts in the Osborne's shaft area where the Mysore North Fault is present. Not much seismic activity occurred along the MNF during this period. Rockbursts have occurred above the water level as well as at the contact point near water level in this area. It is interesting to observe that these rockbursts have gradually shifted above the water level as the water level gradually increased.

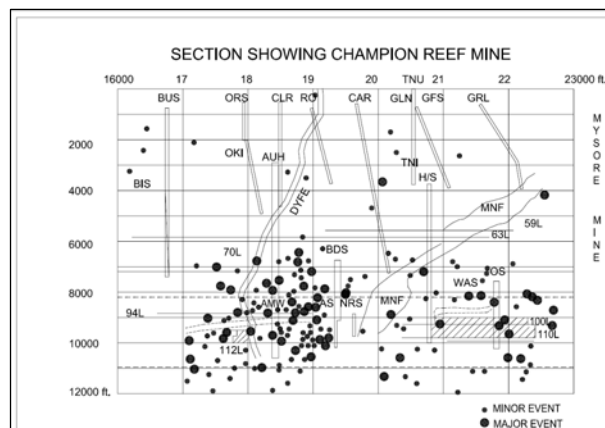


Figure-3 Plot of induced seismicity on the longitudinal section of Champion reef mine during October,1991-September,1992. vertical double lines are different mine shafts in Kolar Gold Fields. The prominent Mysore North fault (MNF) and dyke are shown. The levels of deep mine are mentioned against their respective levels.

2.3 Seismicity Observed during October,1992-September,1993 due to inundation

The seismic events occurred during this period is plotted in the Figure-4. As can be seen from the figure-4 that majority of the major rockbursts have occurred along both sides of Champion mine dyke and MNF. The seismic activity gradually shifted above vertically and horizontally. Not much seismic activity was observed in the Northern Folds and Osborn's shaft areas, which were below the water level during this period. The seismic activity migrated now and concentrated in between Champion mine dyke and MNF as a result of inundation. The seismic activity was also seen in the south side of MNF where old mine workings in Mysore mine area exist.

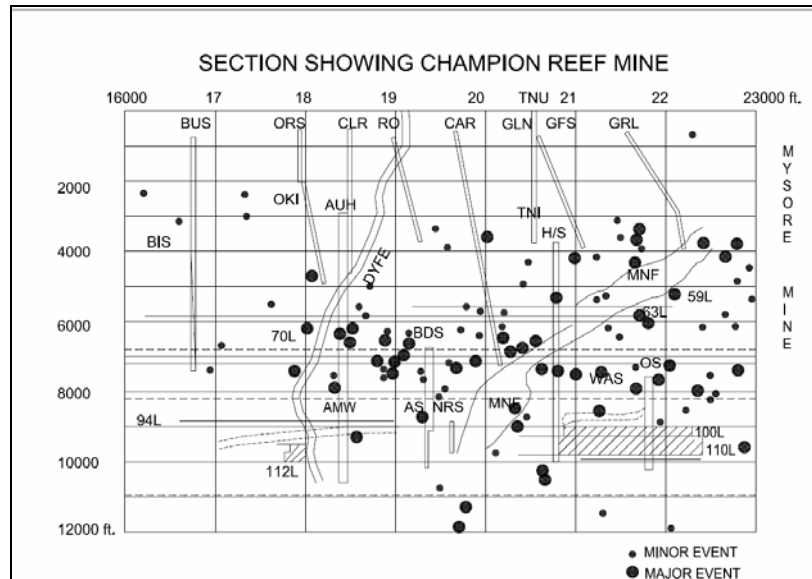


Figure 4 Plot of induced seismicity during October,1992-September,1993. The explanation of legend in Figure-1 remains the same for this figure.

2.4 Seismicity Observed during October,1993-September,1994 due to inundation

Figure-5 shows the plot of seismic events that occurred during this period. It is clearly seen that the seismic activity shifted from deeper level workings to shallow level workings. The seismic activity is concentrated below the water level and near old mine workings. Major rockbursts were found to occur on both sides of the Champion dyke and MNF, whereas the medium rockbursts were found to be near shallow mine workings including old workings. The remnant pillars left in old workings gave rise to rockbursts in addition to fluid induced seismic events at these levels.

The statistics of seismic events during the period 1991-1993 is shown in figure 6. During the month of May,1991 the deeper level was allowed to fill the levels. 7.57 lakh gallons of water filled upto November,1991, as a result, series of rockbursts triggered during the month of November and December,1991. The quantity of water collected underground during the period and the number of seismic events recorded is shown in figure-6. As the quantity of water increased, proportionately the number of rockbursts also increased indicating a very close correlation between the two parameters.

The seismicity during the period from October 1994 up to June 1997 was found to be very much low indicating a lull period. Normally lull period precedes a major rockburst. A major rockburst occurred on 29th

January, 1998 with local magnitude $M_L = 3.14$ and epicentral distance of 2265m from the Central recording station.

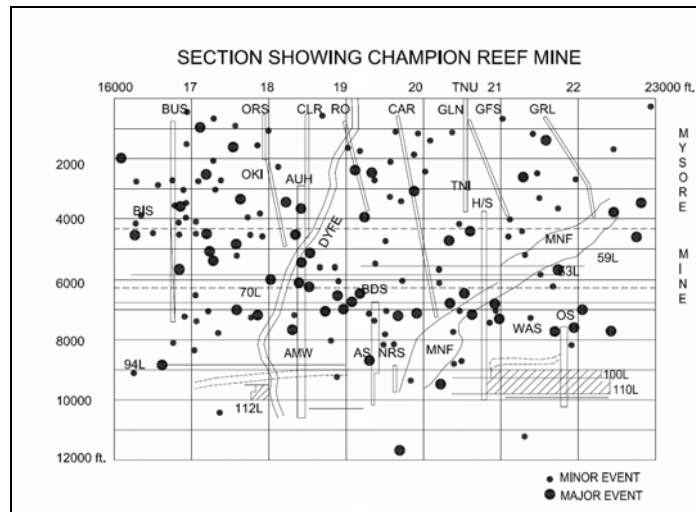


Figure-5 Plot of induced seismicity during October, 1993-September, 1994. The explanation of legend in Figure-1 remains the same for this figure.

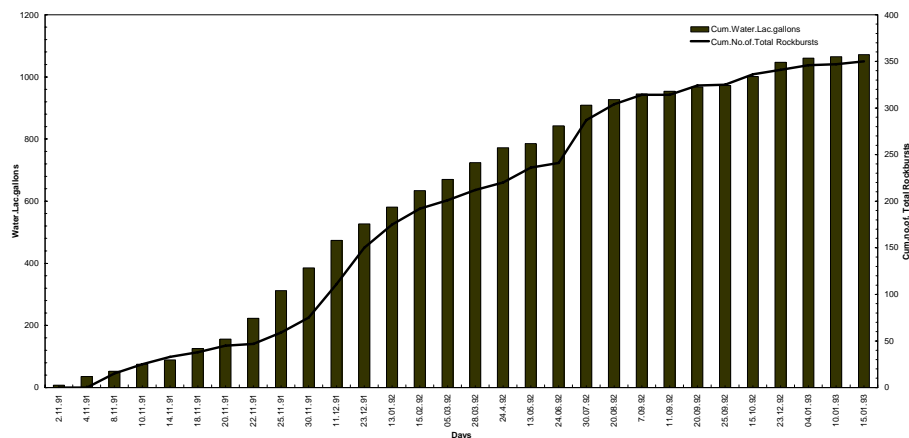


Figure-6 Plot of volume of water and the number of seismic events during the period 1991-1993

2.5 Seismicity Observed during July, 1997- July, 1999 due to inundation

The Digital Seismological System has recorded 968 seismic events which were confirmed giving an average rate of occurrence of rockbursts at 40 per month in the region of investigation. All of these detections were subjected to epicentral location using primarily the polarity of P-wave onset (First motion). In the three components Seismometer at the Central Seismic Station for determining the source azimuth and P to S time interval for epicentre distances. Local magnitude (M_L) of these events in terms of earthquake equivalent were computed using PITSA (Programmed Interactive and Physics of the Earth's Interior). It turned out that a total of 968 seismic events, all confirmed mine tremors to their vital source parameters determined as above is plotted in Figure-7. The prominent and minor geological faults crossing the region as well as the mining shafts spaced from Nundydrog mine in the North to Mysore Mine area to the South. All of these rockbursts are equivalent to microearthquakes ($M_L = 3$). Some of these rockbursts are felt appreciably. The smallest rockburst detected on

September 4, 1998 at $(\Delta) = 1867\text{m}$ has $ML = 1.65$. Majority of mine tremors, however are in the magnitude range of $ML 0.70$ and 1.2 . The rockbursts tremors are spread over distance range of 800m to 4800m from the Central Seismic recording station tending largely along the main axis (N-S) of the Kolar Schist belt.

As seen in Figure-7, the KGF mining region is traversed by a prominent NW-SE striking fault right through the center of the region together with the sub parallel minor faults (Tennant fault and Gifford fault) on either side across MNF. It appears that MNF behaves like a permeable channel for fluid discharge so that the fault plane acts as a fluid-pressure activated valve. Water induced slip along this fault seems to be triggering frequently tremors that occurred mainly in Nundydroog and Champion Reef areas. It is seen from Figure-7 that two clusters of seismic activity, one in the NW block and the other slightly away to the NE in Nundydroog mine are prominent where the two shafts (Golconda and Henry) have been operated. One other similar cluster is prominent in the NE block of Champion lode- Mysore mine section where these shafts (Tenant, Gifford and Edgar) have been operated in the past. Some rockburst activity is also present where two other shafts (Bullen and Oakley) were operative. By and large, the mine seismicity seems to follow in close proximity the strike (NW-SE) of the major MNF that passes through both old and current workings underground. On account of seepage and accumulation of water in these abandoned mines of presumably high stress zones, seismic events are frequently induced owing to reactivation of the local fault system from time to time. The present seismo tectonocity of the inundated mines causes some hazard in the region, whose systematic study is important. In the meanwhile water continues to percolate deeper and wider triggering rockburst with enhanced frequency.

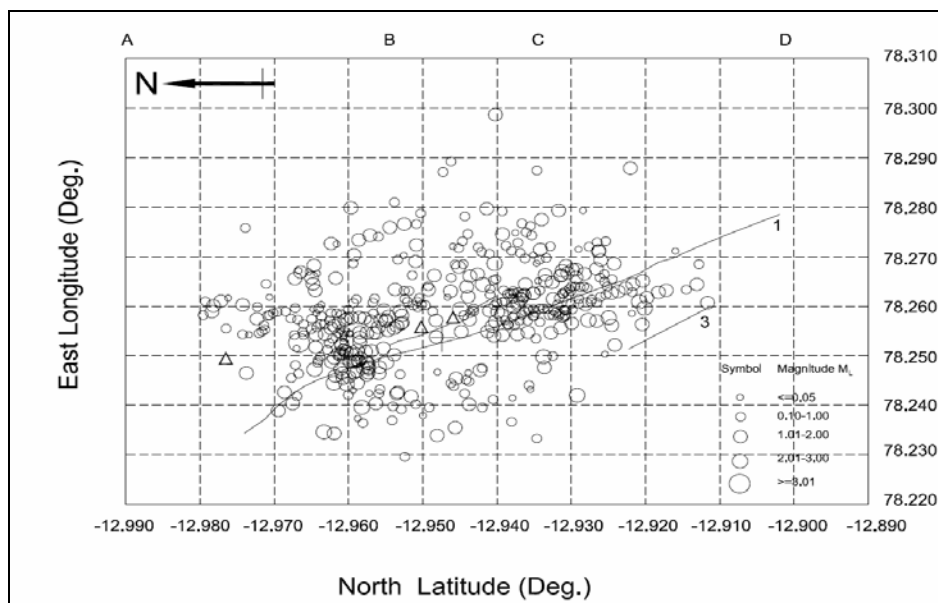


Figure-7 Distribution of computed epicentres (small circles) of rockbursts in the KGF mining region. Line traces labeled 1,2 and 3 are Mysore North Fault (MNF), tenant Fault and Gifford Fault respectively. Small triangles across the plot from north through South represent important mining shafts; Golconda, Henry (not seen due to masking), Bullen, Okley, Tennant, Gifford and Edgar (masked), plus symbol(+) in the center of the plot is the location of the centralised seismic recording station. Marked A through D at the top of the diagram, three main mining areas nundydroog (AB),Champion reef mine (BC) and Mysore Mine (CD).

2.6 Seismicity Observed during September,1999 – August,2005 due to inundation

The seismic events continued to take place and were monitored by the Broadband Seismic system installed at the Central seismic recording station (KGF Observatory). The seismic activity have been monitored using a single station broadband Seismic system and the number of seismic events were plotted month wise Figure-8.

As can be seen from the figure -8 that there are two gaps and no events reported during that period .This was due to malfunctioning of the system. Area rockbursts have been recorded sporadically. Area rockbursts are common in the mines of Kolar Gold Fields, where one major rockburst trigger more than 100 seismic events in the vicinity of the major rockburst.

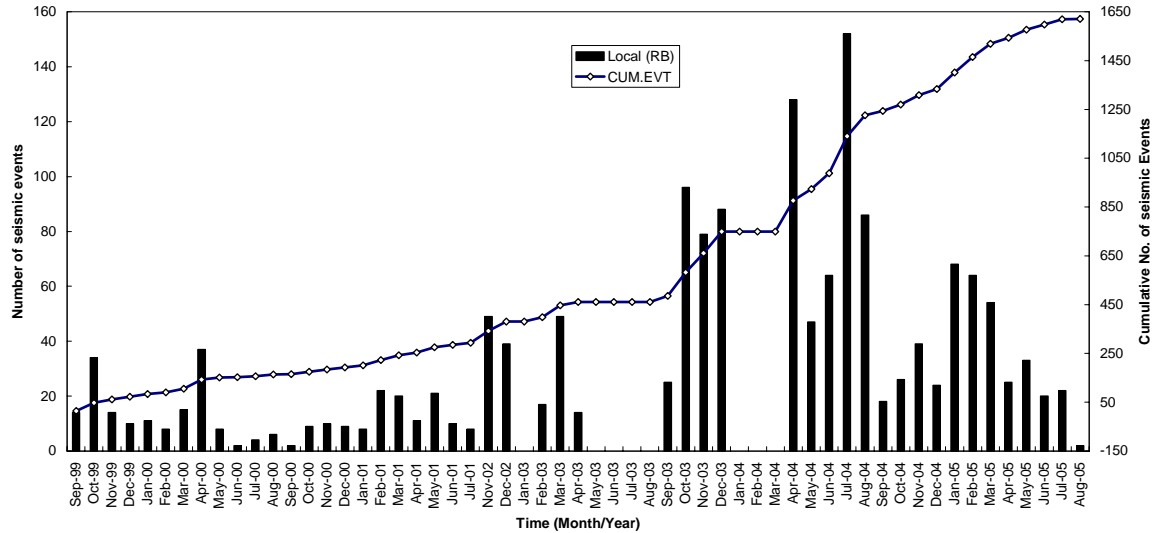


Figure-8 Plot of seismic events picked up by broadband seismic system.

2.7 Seismicity Observed during October,2005 – Decemeber,2008

In addition to the Broadband Seismic System one Strong Motion Accelerograph was installed during October,2005 and it has recorded more than 2000 seismic events as seen in Figure-9. As can be seen in the figure-9 that there were many seismic events during November,2005 .

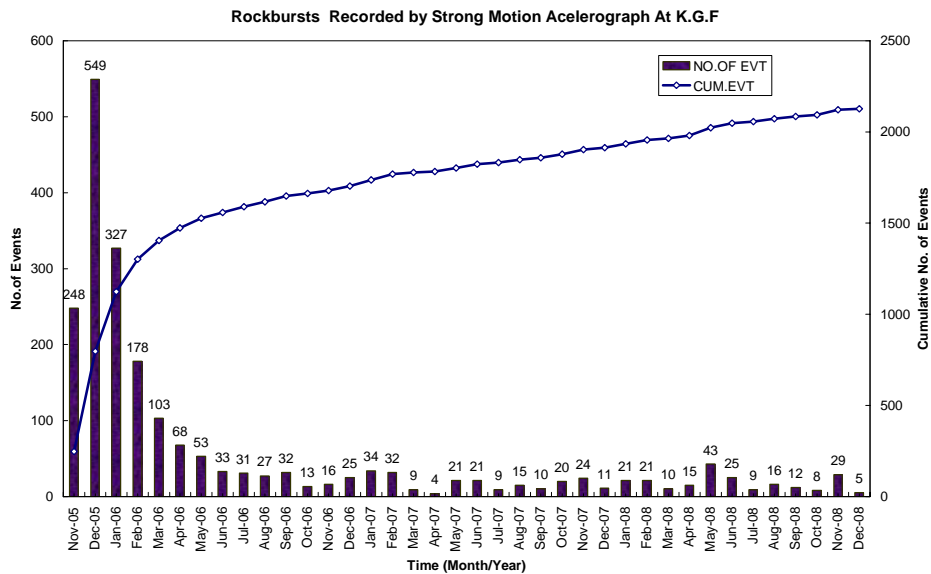


Figure-9 Plot of seismic events picked up by Strong Motion Accelerograph.

A noticeable rockburst occurred on 02.11.2005 at 23:45:00 Hrs in the old and abandoned mines of Kolar Gold Fields. The rockburst was severe and the effect was felt by residents of adjoining areas and surrounding townships. The rockburst caused panic among the residents and it is reported that the people came out of their houses. The recorded magnitude of the rockburst was highest after the closure of mines. Rockbursts were the usual phenomenon in KGF mines during mining activity [12]. However, rockbursts continued to occur even after the closure of the mines. Rising level of water in the mine workings may be one possible cause of frequent rockbursts, as was reported elsewhere in the world [3]. Normally, the frequency and severity of rockbursts are more during rainy season [6]. The peak ground acceleration recorded due to the above mentioned rockburst was 0.22g. This level of acceleration falls in the category of caution zone for houses/buildings. Many of the houses/buildings being very old are already in depilated conditions. The typical signal picked up the Strong motion Accelerograph is shown in figure-10.

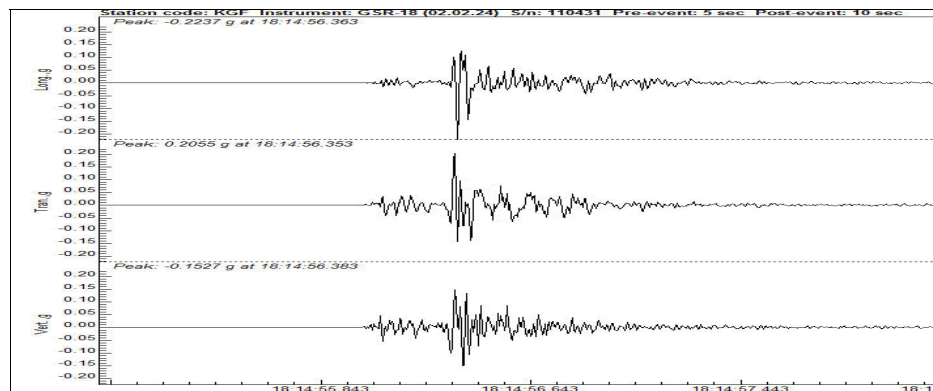


Figure-10 Typical rockburst picked up by the Strong Motion Accelerograph. Area rockburst occurred during the month of November, 2005 and December, 2005.

2.8 Characteristics of seismic events in Kolar Gold Fields

The seismic events monitored in KGF were using different seismic recording system. The short period seismometer has high frequency content compare to the broadband and strong motion seismometer. The phases of ground motion are visible; the direct P and S phases. All the seismic events are within the epicentral distance upto 5 km from the central recording station (Single station). The local magnitude range was 0.70 to 2.8. The local magnitude for analogue seismic signal was computed using coda of seismic events. Local magnitude (M_L) of short period events in terms of earthquake equivalent were computed using PITSA. The broadband seismogram was used to compute local magnitude using Seisan software. In case of strong motion data the acceleration was converted to synthetic Wood Anderson amplitude and local magnitude is being computed.

The seismic moment computed is from the spectrum of seismic events picked up by the strong motion accelerometer using Seisan software. The seismic moment has been found to be in the order of (approximately 5×10^7 Newton –Meters). The seismic moment computed for the Falconbridge events are in the same range [2]. The seismic moment of the events has been calculated from the magnitude of the events using the moment-magnitude relation for earthquakes in eastern Canada developed by [3]. Since fault slip is proportional to seismic moment, the cumulative moment release gives some indication of the overall strain deformation that has been occurring within the mine with this seismicity.

2.9 History of post-closure seismicity (Major rockburst)

Since the deeper level was closed during 1991 series of seismic events triggered and significant seismic activity continued at the mine after closure for a period of three years. The activity reduced and there was a lull period

and major event occurred during 1998. After the complete closure of the mine during 2001, there was major rockburst during 2004 and 2005. During November, 2005 there was a severe major rockburst which jolted KGF mining region. One more rockburst felt on the surface was on 8th March, 2008 as shown in figure-11. Few small events continued to occur followed by major rockburst sporadically.

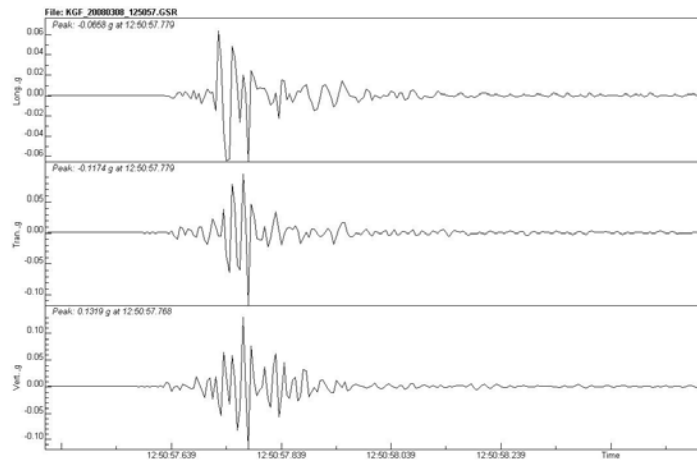


Figure 11. Felt Rockburst on 08.03.2008. 12:50:57 Hrs. $M_L = 1.85$

3 Discussion

Induced seismicity occurs when the modification of the stress system by an external stimulant is sufficient to cause failure. This can occur because of either an increase in the stresses driving the fault or a decrease in strength of the fault [1].

The strength of fault, or the shear stress required for failure, can be expressed as

$$\tau = \tau_0 + \mu(\sigma_n - P) \quad 1$$

where τ_0 is the cohesion

μ is the coefficient of friction

σ_n is the normal stress across the fault

P is the pore pressure within the fault zone

A fault may slip due to an increase in shear stress (τ) or, if the shear stress remains the same, a decrease in normal stress (σ_n) or an increase in pore pressure (P). The induced seismicity depends on the dominant factor controlling the seismicity. In some cases the isolation of a single mechanism is simple (e.g. mining, injection related seismicity and pore pressure). In others (e.g. reservoir induced) the relationship is much more complex. More than one parameter may be involved (shear stress and pore pressure).

Wetmillar [13] has reported such types of fluid induced seismic events in Falconbridge mine in Canada. The mine was closed in 1984 and from 1984 up to 1987 moderate rate of seismic activity was observed. From 1991 onwards, highest level of seismic activity was observed. The initiation of the third phase of seismic activity appears to have been triggered by flooding within the mines. All three phases of post closure seismicity at the Falconbridge mine have produced seismic events of consistent character that appear to represent a continuation of the fault-slip phase of seismic activity that was present at the mine in 1984.

There are many such studies which show that increasing the water levels in reservoirs or increasing pore pressure by pumping fluids into the ground during oil or gas recovery or waste disposal can trigger seismic activity. Board et.al [2] discusses some of the more important examples of fluid-induced seismic activity. Board also reports on a test study in a deep level South African Gold Mine where small scale seismicity was induced by injecting water along a fault surface [7]. In the mine study they found that the amount of pressure

needed to trigger seismic activity depended on the in-situ state of stress along the fault and that the magnitude of the induced events depended on the area of elevated pore pressure along the fault surface. Knoll [4] has reported the fluid-induced tectonic rockburst of March 13, 1989 in the Southwestern part of the GDR. The result of extended investigations identified the event as a fluid-induced tectonic rockburst consisting of a fluid-induced seismic event in the overburden rock strata.

In the case of rockbursts in the mines of KGF, the locations of induced rockbursts due to mining are concentrated very close to the mine workings. In the case of rockbursts due to the presence of geological weaknesses and presence of water, the location of rockbursts get distributed along the fault and in water-logged areas.

3.1. Influence of Mining excavations

Mining has a vital role in the genesis of the rockburst particularly when the mining is being practiced close to the phase of weaknesses like folds, faults, dykes etc. All these features are present in the Champion Reef mine. It is stated that whatever course of mining is adopted, there is a critical area of excavation at which major collapse will occur. This phenomenon is observed in the form of frequent occurrences of violent rockbursts on either side of the fault plane. In Champion Reef mine, it is normal practice to carry out stoping sequences simultaneously in 3-4 levels spanning approximately 30 meters. During such operations and in the event of a critical limit being reached, the entire area erupts leading into a series of rockbursts of all sizes, generally referred as Area Rockbursts [4]. However, mining being carried out in the remote region, the role of geological features need to be studied simultaneously. This type of area rockburst is observed both in the Northern Folds area and in the Glen Oreshoot area, which are on the either side of the MNF in the Champion reef mine.

3.2 Fluid Induced seismicity

The mining operations at deeper levels of Champion Reef mine has been stopped during 1991 and subsequently the other shallower working areas in the same mine. As a result of this, water was allowed to inundate the deeper level workings first. This resulted in series of rockbursts at the deeper level workings during the first three years, which are also good examples of Fluid induced seismicity.

During the period from October 1991 to September 1992 series of rockbursts have occurred at the deeper levels. The hypocentres of these rockbursts were found to be cluster near the mine workings at that time indicating the induced stresses due to mining. This process has been accentuated by the presence of water.

As the water level started increasing gradually the rockbursts locations also shifted horizontally and vertically in a gradual manner. This has been observed during the period October 1992 to September 1993. It was interesting to observe that the rockbursts concentrated on both sides of Champion mine dyke and the prominent MNF. The water tended to create a supra hydrostatic fluid pressure at that depth. It appears that the MNF is fast becoming a permeable channel way for fluid discharge and would perhaps acts as a fluid pressure activated valve in future.

The locations of rockbursts further shifted above as the water level started increasing during the period October 1993-September 1994. The occurrence of rockbursts in the shallow mine workings was due to failure of remnant pillars in old working areas. This process has also been accentuated by the presence of water as in the earlier period.

The local seismicity in the inundated mining region seems mainly due to strata failure induced by the seepage of water through the weak zones prestressed to critical limits. This is consistent with the current picture of mine tectonoseismicity where rockburst seismic sources are found to be clustering in close proximity of NW-

SE striking set of geologic faults of which MNF is most prominent. The water level has come almost very close to the surface and the seismic activity continued to take place with area rockburst occurring sporadically.

There was a lull period of seismicity from 1994-1997 and normally lull precedes a major rockburst. Accordingly major rockbursts occurred during 1998, 2004, 2005, 2007 and 2008 as discussed above.

4 Conclusions

The Champion Reef mine the second deepest mine in the world has experienced fluid induced seismicity after the closure of mining operations following inundation. During the first year, a series of major and medium rockbursts were triggered at the Northern Folds and Glen Ore Shoot mining region (October, 1991-September, 1992). Rockburst activity during the second year began in October 1992 and continued until September 1993 during which period, the rockbursts of both major and medium intensity, gradually shifted upwards horizontally and vertically. It was interesting to observe that the rockbursts concentrated in between Champion reef mine dyke and the prominent MNF and also on either side of dyke and fault. The hypocentres of rockbursts during the third year shifted upward towards shallow mine workings and old mine workings up to September 1994. There was a lull period in seismic activity after September 1994 until June 1997. The seismic activity continued further and area rockburst occurred during 2004, 2005, 2006, 2007 and 2008.

The important findings from seismic data obtained from the deeper levels of Champion reef mine and the digital seismic data from different Seismometers in Kolar Gold mining region is the identification of frequently occurring rockburst source in the presence of water. The relation between the epicentres of seismic events with respect to mine workings in general and MNF in particular is quite interesting. The cluster of seismic activity in the vicinity of both sides of MNF is significant compared to overall seismic activity in the field. This clearly indicates that the MNF has certainly a role in inducing seismic activity. The seismic monitoring in the Kolar Gold mining region needs to be continued to understand the causative factors in depth and to map the seismic hazard in the region. At present the single station broadband seismometer and single station Strong Motion Accelerometer is in operation. It is recommended to have multi channel monitoring station so that the rockbursts activity can be located in three dimensions and correlate with mining and geological conditions. This will help to mitigate understand the causative factors and mitigate seismic hazard.

Acknowledgements

The authors wish to acknowledge the funding support for Short period Seismometer, Broadband Seismometer and Strong Motion Seismograph from the Ministry of Earth Science, Government of India, New Delhi. Ministry of Mines, Government of India, New Delhi is thanked for permission to present the paper in the 7th International Symposium on Rockbursts and Seismicity in Mines to be held in China during August, 2009.

References

1. Board, M.T. Rorke, G. Williams, and Gay N., Fluid Injection for Rockbursts control in deep mining. Proc. of the U.S. Symposium on Rock Mechanics, J.R. and Wawersik, W.R. (eds), 111-121, 192, Balkema, Rotterdam.
2. Board, M.T. Review of mining conditions and Seismic data for the June 20-22, 1984, Rockburst at Falconbridge Mine, ITASCA Report to Mining Research Directorate, September, 1992, 45p.
3. Gendzwil, D.J. and Prugger A.F. Seismic activity in the flooded Saskatchewan Potash mine, Proceeding second symposium on Rockbursts and Seismicity in mines, Minnesota, (1990), US, Pp 115-120.
4. Hasegawa, H.S. Lg Spectra of local Earthquakes recorded by the Eastern Canada Telemetered network and Spectral Scaling, Bull. Seism. Soc. Am., 54, 1041-1061.

5. Knoll P., The Fluid induced tectonic rockburst of March 13, 1989, in Pottash mining area “WERRA” in GDR (first results), proc. Rock at Great Depth, Maury & Four Mantrace (eds) – 1990 Balkema, Rotterdam ISBN 9061919754.
6. Krishnamurthy R. and Gupta P.D., Rock Mechanics studies on the problem of ground control and rockbursts in the Kolar Gold Fields. Proc. Rockbursts prediction and control, Institute of Mining and Metallurgy, London (1983) Pp.67-80.
7. McGarr A. and Simpson D., Keynote lecture. A broad look at induced and triggered seismicity, Proceeding of 4th International Symposium on Rockbursts and Seismicity in mines, Poland/ 11-14 August 1997.
8. Messrs. John Taylors and Sons limited. Report of the special Committee on the occurrence of rockbursts in the mines of Kolar Gold Fields, Mysore State, India, 1955.
9. Srinivasan C, Arora S K, and Benady S., Precursory monitoring of impending rockbursts in Kolar Gold Mines from microseismic emissions at deeper levels. International .Journal of Rock Mechanics and Mining. Sciences. Vol. 36(7); (1999) 941-948.
10. Srinivasan C. and Sivakumar C.-Project Completion report, DST Project No.ESS/CA/A7-12/94.
11. Srinivasan, C. Rao, M.V.M.S. and Raju N.M., Water induced seismicity in Kolar Gold Fields, DST-Group discussions on fluid flow/ process in the earth’s crust, No.4-5,(1993), NGRI, India.
12. Srinivasan C, Arora S K, and Yaji R. K., Use of Mining and Seismological parameters as premonitors of rockbursts. International .Journal of Rock Mechanics ,Sciences. 1997; 34(6). 1001 – 1008.
13. Wetmiller, R.J., Post-closur seismicity at a hard-rock mine, Proceeding. Rockburst and Seismicity in Mines, Young (Ed) 1993, Balkema, Rotterdam, ISBN 90 5410 3205, Pp 265-274.

STUDY ON THE WORKING FACE FLOOR DAMAGE AND GAS EMISSION

FU-KUN XIAO

*Resources and Environmental Project Institute, Heilongjiang University of Science & Technology
Harbin, 150027, P.R. China*

LI-QUN DUAN

*Resources and Environmental Project Institute, Heilongjiang University of Science & Technology
Harbin, 150027, P.R. China*

In order to understand the gas emission from lower adjacent seam on this layer, the effect of working face mining on floor is discussed, and the stress condition of floor is also analyzed. It is summarized that the cause for the gas emission is the parameter of floor fracture, through which the gas rushes into exploitation bed from lower adjacent seam. The discussion on gas emission of lower adjacent seam provides theoretical direction for arrangement design of low position drilling at floor. At last, this theory has been applied in practice, and a good effect is realized.

1 Introduction

With the constant changing of coal layers and the gradual increases of gas emission quantity, gas control by drill extraction will continue to face more and more problems. Gas that diffuses into the coal face may lead to serious gas emissions when a liberated seam whose lower adjacent seam is greater and gas is exploited. It is important to study how to enhance gas drainage efficiency safely, conveniently, economically and reasonably. Consequently, the failure law of floor is needed to find the failure depth to guide gas drainage. The roof failure law is well known now and the theory of “Up Three Zone” and “Down Three Zone” has been put forward [1, 2, 3]. However, the main research purpose of main floor fracture is to determine the water conducting depth in floor that causes destruction [4]. This paper analyzes failure mechanism and form in the floor and discusses gas emission law from lower adjacent seams in view of the control gas in the adjacent seam while introducing the experiences of this theory that were applied in practice.

The strike length of the working face in the second west mining area of the Xinghua Coal Mine of Jixi Mining Industry Group is 900meters, has a inclination length of 100meters, a coal thickness of 1.5meters, and has an angle of 4 degrees. It is a 30[#] coal seam below a 28[#] coal seam from 6meters to 8 meters, and a 31[#] coal seam is 20 meters below. The measured result shows that absolute outflow of gas from the 28[#], 30[#] and 31[#] coal seams is 20-30 cubic meters, 50-60 cubic meters and 20 cubic meters respectively.

2 Bottom Pressure Destroyed by Mining

With face advances and forming process in the mined-out area, the stress distribution around the mining slope is redistributed. This causes the stress increasing zone [5] (support pressure zone) to appear in a certain range of the coal body and the floor rock may shift differently than the support pressure. (As shown in Figure 1)

Coal floor stress in the area of the coal pillar is in a rising (supercharging) condition and floor rock is in a squeezing condition. However, floor stress in a mined-out area is always in a decreasing (depressurization) condition. Floor rock has been in a swelling condition. That is, floor rock is always in squeezing(compression areaI)-swelling(expansion regionII)- recovering(depressed area) condition. And it is repeatedly found with the advancement of working face. Floor rock is easy to undergo shear deformation and occur shear failure on the juncture of the compression area and the expansion region. And it is easy to undergo cracking of separated strata in floor rock which is in swelling condition. So rock on the margin of coal pillars is most easily to produce cracks or fractures and then failure occurs. The calculated result shows that the maximum depth of mining failure in 28[#] floor is 31 meters, and it is 46 meters from the coal wall. Jacobi Simulation Experiment pressure curve is shown in figure 2. The assumed conditions are: mining depth is 800 meters, bulk density of the rock is 10 ton per cubic meter. So the contour Line 2 in the figure is equal to rock stress. From the figure it may be seen that maximum stress under coal is 4 times higher than rock stress, and the rock stress in floor rock of goaf decreases rapidly. The influence by the excavation of 28[#] coal bed changed floor stress and destroyed dynamic equilibrium of gas adsorption and desorption in 30[#] and 31[#] coal seam, which caused gas rushed through fracture in 28[#] floor to 28[#] goaf from 30[#] and 31[#] coal seam. Because of most gas rushed out of working face, the gas exceeded the limit in working face and gas drainage road.

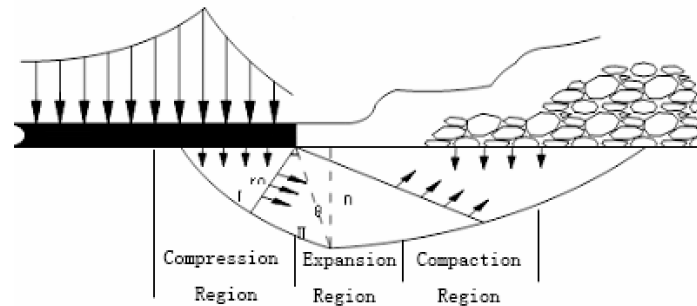


Figure 1 The schematic diagram of failure depth of seam floor caused by support pressure

3 Analysis of Gas Emission Law

Because of the very low permeability for gas in mining coal layer, mining destressing method is used to exhaust and mine gas to realize gas drainage while mining. Free state and absorption state are two forms of the gas in coal beds, and the relation between them is dynamic balance. Because of the function of the mutual attraction between molecules, gas molecules will be absorbed onto the surface in pores and cracks in coal seam when they hit them, and all this is absorption[6]. The gas in free state can be desorbed if gas molecules can overcome intermolecular attraction. It will come to dynamic balance when adsorption rate is equal to desorption rate without influence of external factors. The gas in adsorption state is 80% to 90% of the gas in coal beds, and the gas in free state is only 10% to 20%. By the coal mining, because of the change of coal and roof rock before working face, gas dynamic balance is destroyed. Then gas has been desorbed rushes through floor fracture to working face to lead gas to exceed the limit, and this is the problem needs to be solved.

4 Engineering Application

4.1 Drilling Field Arrangement

With the right first working face of 28[#] seam in Xinghua Coal Mine advancement, the gas emission and drainage volume increased significantly. Face air quantity increased to 2100 stere per minute from 1700 stere per minute. The measurement showed the absolute outflow of gas was only 22.5 stere per minute in initial

working stage. With the golf area increasing, the gas from 30[#] and 31[#] coal seam increased rapidly, Drainage method of this mine is draining gas in the fractured zone at roof. Although the drained rate is over 40%, the most gas is taken by the face air and only small part is drained. So the gas exceeds the limit in the gas going and gas drainage road. In order to assure the safety, the monthly output of the working face is controlled between 3.0 to 3.5 millions ton.

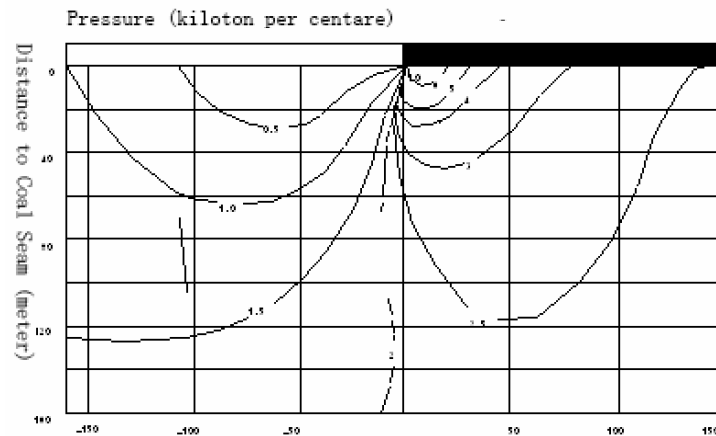


Figure 2 The stress system of floor

According the law of gas emission at the floor, this Coal Mine takes gas drainage at the floor borehole, takes floor horizontal hole drilling drainage gas from 30[#] 31[#] seam. The distance between floor lower position drilling fields is 200meters. Drilling fields were arranged at the roof of the 30[#] seam and boreholes drill were arranged in the rock pillars between 28[#] and 30[#] seams. 20 drillings were arranged in the first drilling field and 26 drillings were arranged in the second drilling field. Using the characteristics of lower density of gas and negative pressure, gas was pumed out as more as possible. And when the working face pasts upper-lower drilling field, the drilling field is supported by the wood cribs, and it is continue drilling in the golf. Borehole arrangement is shown as Figure 3.

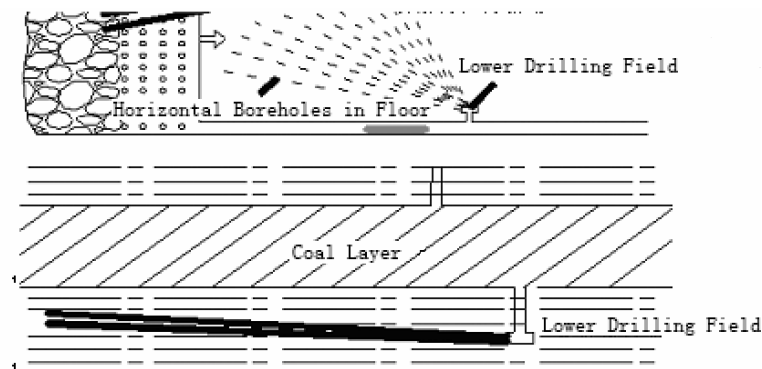


Figure 3 Low drilling field in floor

4.2 Drainage Effect

The gas concentration increased gradually after the working face pasted floor borehole over 30m, the gas drainage effect increased significantly when over 40m, and it was more significantly when over 60m. The gas concentration is 28%-100% in the borehole, the mix concentration is 40%-56%. The gas emission is increasing with the increase of working face length. The drainage volume is improving rapidly and the gas concentration is effectively controlled at every workplace. The single face output is from 3.3 million ton in the initial stage of production increases to 6.0 million ton per month, the highest output achieves 7.1 million ton per month.

5 Conclusions

1. The floor can be destroyed and fractured by the mining operation. When the bottom seam is near the working seam, the adjacent seam gas will tend to be in a free state due to the mining at adjacent seams. It may rush into the work seam through the crack and make the gas exceed the limit at the working face.

2. According to analysis of the floor failure and gas emission, the gas drainage on the floor of the lower position drilling field could not only avoid exceeding the gas content limit, but also recycle a lot of gas. At the same time, compare with the low-located drainage roadway, this method is easier for construction, more efficient in excavation and drainage, and the drilling parameters can be set flexibly according to the geological conditions etc.

Acknowledgements

The authors wish to acknowledge the funding support from the Heilongjiang provincial natural science fund (Grant No. E200610) and Heilongjiang Province Office of Education Youth backbone teachers project (Grant No. 1153G035).

References

1. Xiao, F.K. and Sun, H.R. The Study on Gas Drainage of Mining Perturbation Pressure Relief. Proceeding of the 2007, International Symposium on Safety Science and Technology, Science Press USA Inc, 2007, 1439-1441.
2. Liang, Y.P. and Wen, G.C. Comprehensive Analysis Method of "Three Zone Classification" on Mine Roof Strata. Coal Science and Technology, 2000, 5 (28). 39-42.
3. Ma, S.Z., Fan, M.C. and Yin, Q.C. Applied research on gas drainage technology with horizontal bore hole near mine roof level. Coal Science and Technology, 2002, 30 (9). 40-42.
4. Peng, S.P. and Wang, J.A. mining safely above aquifer. China coal industry publishing house, 2001.
5. Xu, Y.Q. Coal mining study. China University of Mining And Technology press, 1999, 55-65.
6. Zhou, S.N. and Li, B.Q. Coal seam gas occurrence and flow theory. China coal industry publishing house, 1999, 24-29.

ACOUSTIC EMISSION AND INFRARED CHARACTERISTICS OF COAL BURST PROCESS

DE-JIAN LI, XUE-NA JIA, JI-LI FENG, WEI-LI GONG, XIAO-MING SUN and JIN-LI MIAO

School of Mechanics and Civil Engineering, China University of Mining and Technology in Beijing, 100083, P.R. China

Strain coalburst tests of coal samples were carried out by the experimental system of rockburst to study the coal disaster mechanism at a high stress state. The acoustic emission (AE) signals and the infrared thermography for the coal samples were detected and obtained during the tests. We mainly investigated the coalburst mechanism of the coal samples by AE technique and infrared thermography from unloading to failure. The basic parameters such as the energy rate and AE events were used to transform the data between time and frequency. AE events significantly increased during unloading. There were obvious high-temperature zones before coal burst. It is concluded from the characteristics of AE and infrared thermography of coalburst process that there are the stress concentration phenomena within the coal samples and the local high-temperature zone appeared from the infrared thermography. It is indicated by the intensive AE activity that as the partial release of stress before coalburst, macro-cracks were formed and extended. Thus a large amount of energy was released, inducing coalburst

1 Introduction

The remote-sensing method that is herein referred to as the thermal-infrared and microwave was used recently to study the characteristics of thermal-infrared radiation of the rock failure process under stress. The significant change of satellite remote-sensing thermal-infrared that commonly appears on large areas in central Asia and east mediterranean sea before medium-strong earthquake was originally reported by Gorny in 1988; in which wave length ranged from 10.5 to 12.5 μm [1]. Similar phenomena in earthquake processes were also observed in China, by satellite communicate systems [2-6].

Since tectonic earthquake is closely associated with the propagation of rock cracking, it has been demonstrated that the thermal-infrared result during rock failure is strongly dependent upon cracking propagation [7-10]. It has also been revealed that the temperature of rock thermal-infrared (micro wave) radiation is changed with rock stress during loading, and the rock is prone to rupture [11-15]. The quantitative relationship between stressed rock and thermal-infrared radiation temperature, as well as mechanical energy and thermal-infrared temperature, was developed by Liu et al [16]. He studied the physical mechanism of earthquake remote sensing and thermal-infrared portent for multi-black minerals such as granodiorite, gabbro and gneiss in the Capital area under uniaxial compression from loading to rock sample rupture. It was proposed by Wu and Wang [17] that the approximate stress of 0.79 σ_c could be regarded as an alarm or critical stress for

mining stress and disaster monitoring from the experimental study of coal thermal-infrared photos and the temperature under uniaxial loading and cycle loading conditions. A theoretical model of coal failure process was derived by Zou [18], based on acoustic emission (AE) and the damage theory of continuum mechanics, as well as distribution of intrinsic defects in coal material. It was explained by Miao et al that for the failure processes of coal and granite under conditions of uniaxial compression, using the energy transform theory, to the results of thermal-infrared photos and secondary time-frequency analysis of acoustic emission data.

2 Experiment procedure

2.1 Experimental system and samples

The coal burst tests were carried out on the experimental system of rockburst simulation at great depth (He, 2004) [20] together with high-speed acquisition digital apparatus, AE monitoring system of Beijing PXWAE AE and TVS-8100MKII thermal-infrared camera system. The rockburst system is with the feature of loading independently at three directions and unloading suddenly on one face of the sample. It can also be used to conduct a uniaxial or triaxial test for rock. The AE monitoring system is with two channels to monitor the AE signal. The central frequency of transducers is 140 kHz and the sampling rate of the system is 1M, in which the sample trigger level is set at 3.6V, a magnifier of 40db is located at the front of transducers and 10 times for the signal conditioning. The thermal-infrared camera system is a TVS-8100MK II with temperature sensitivity of 0.025 °C and picture resolution of 320×240; and its acquisition rate is 60 pictures per second. The experimental system is shown in Figure 1.

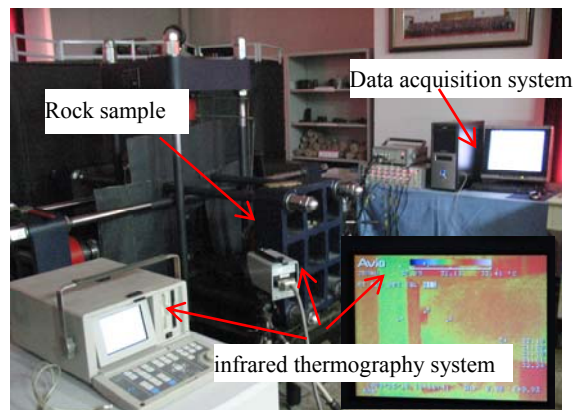


Figure 1 The experimental system of rockburst

The coal specimens used in the tests are from Nanshan mine of Hegang coal-mine in China with the underground level of 540m. Two samples were numbered by #NSV3-4 and #NSV3-5, with the size of 150×60×30mm, 1900m/s for longitudinal wave speed, which are generally intact but with some initial cracks.

2.2 Experimental method

Sample during testing will be loaded at three directions at the beginning and then one face unloading suddenly but constantly keeping loads at axial directions, in which at the same time, the infrared radiation of the rock surface is monitored during the loading process using the thermal-infrared camera system. To #NSV3-4 sample, twice shooting was done. In the first, the state of coal sample before loading as well as first unloading but holding load process was shot. In the second, second unloading to failure was recorded. To #NSV3-5 sample, the states of the sample before loading and after unloading to failure were shot. AE technique was used to detect

the time-series of acoustic emission events and characterize the change of energy in the process of sample damage.

3 Analysis of experimental results

3.1 AE character

AE events here are the signals of damage process for rock sample under loading condition. The basic character of the AE wave data for the coal samples of #NSV3-4 and #NSV3-5 at the stage of initial loading is that the AE events are relatively many more, which can be described by the approaching closeness of the original microcracks. Figure 2 represents the correlations of AE events against time and energy rate against time for two samples.

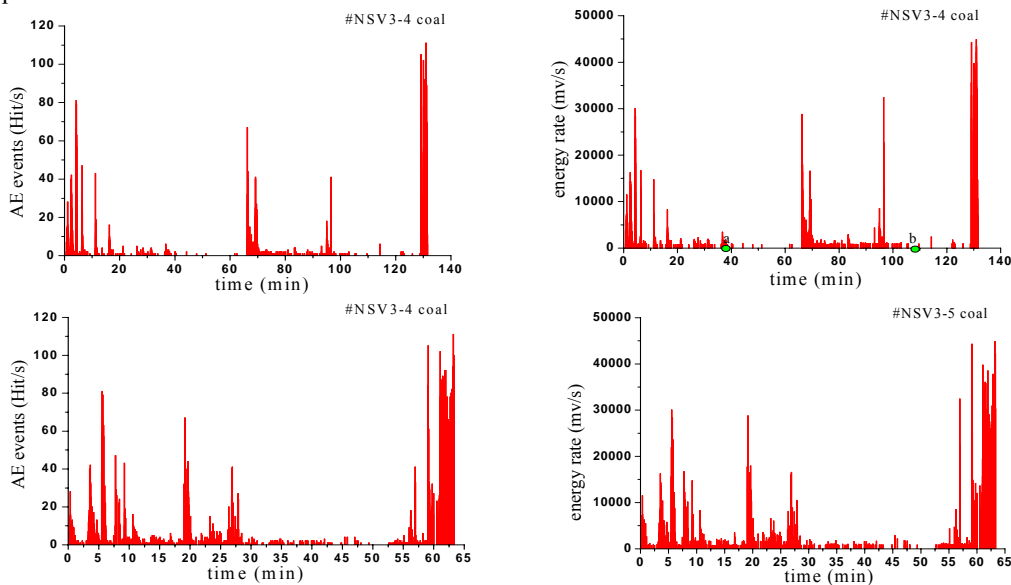


Figure 2 The AE events and their energy rates for #NSV3-4 and #NSV3-5.

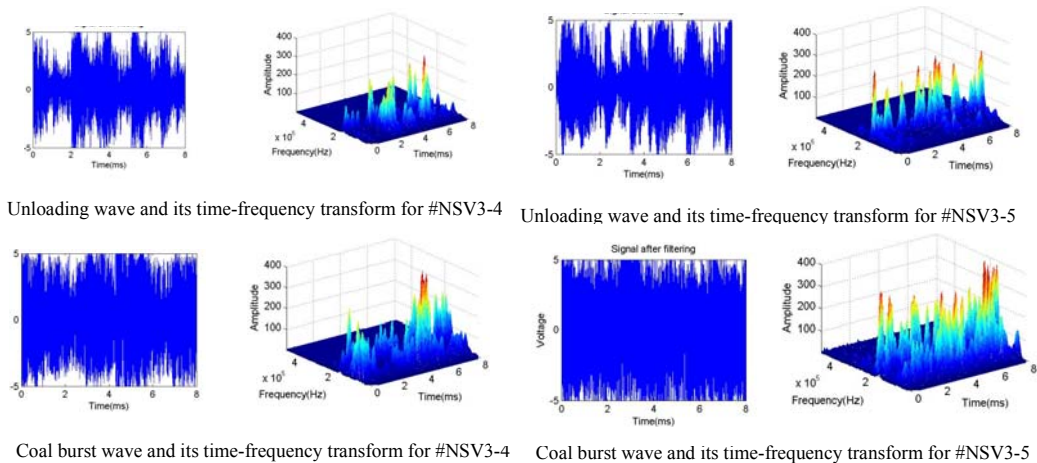


Figure 3 Waveforms and their time-frequency transform for the coal samples

As one of the most important tools to analyze unsteady signals, pseudo Wigner-Ville distribution can be regarded as one of the distributions of signal energy at the time-frequency space, which reveals the history of signal energy with time. Consequently, the three-dimensional time-frequency distributions of the AE signals for the typical waveform data of the samples are obtained by pseudo Wigner-Ville transformation. The pseudo Wigner-Ville distribution (PWD) of signal $s(t)$ is defined as follow

$$PWD_z(t, f) = \int_{-\infty}^{\infty} z(t + \frac{\tau}{2}) z^*(t - \frac{\tau}{2}) h(\tau) e^{-j2\pi f\tau} d\tau \quad (1)$$

where $z(t)$ is the analytical signal of $s(t)$.

The AE waveforms and time-frequency transform of two coal samples at two stages including unloading suddenly and coal burst are given in Figure 3, which is corresponding to either the frequency range of 100-200kHz during unloading or the frequency range of 50-220kHz during coal burst. It is readily found from the figureure that most of the amplitudes of #NSV3-5 are bigger than that of #NSV3-4, which concludes that the former coal sample in the failure process released relatively more energy than that of the later one. Further, the energy magnitudes for both samples at failure are bigger than that at the initial unloading, which represents that dissipated energy is increased with the increase of dislocation emission, slipping and shear deformation for the samples.

We here focus on the study of rockburst process under condition of unloading from one direction of the samples at the 3D stress state in laboratory experiment. To #NSV3-4 coal sample, its AE energy release rate and stress variation from unloading to coal burst is shown in Figure 4. It is found in the figureure that there are two peak values which are actually corresponding to the sample failure in the AE energy rate. The first peak in fact represents that the sample damage induced is triggered by unloading but the significant decrease of stress is not induced. The second peak indicates that the failure of the sample occurs, accompanying clearly impacted sound from the sample, which is also found from the sudden change of principal stress.

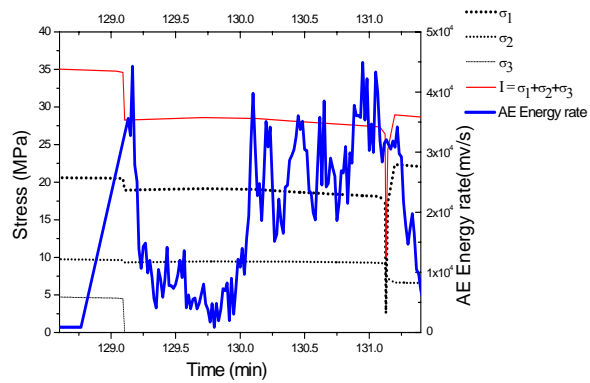


Figure 4 AE energy rate and stress paths during test.

3.2 Thermal-infrared analysis

The change of temperature field is directly associated with the moving state of molecules in materials and indirectly denotes the change state of stress field. To #NSV3-4 sample, its thermal-infrared series from last unloading to coal burst are given in Figure 5.

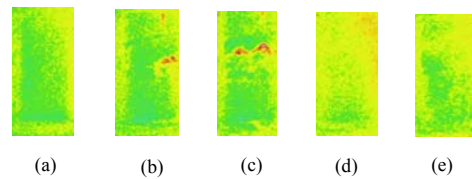


Figure 5 Thermal-infrared photos from last unloading to coal burst for #NSV3-4 coal sample.

The surface temperature of the sample after unloading is lower than that before loading, and further the one at the right hand side is higher than that at the left hand side, as shown in Figure 5(a). The stress redistribution with time is evolved after suddenly unloading from one direction of the confined sample, which can be characterized by the local high temperature zone due to the energy dissipation at different stages when cracks propagate within the sample, as indicated in Figure 5(b) and (c). The complete failure of the coal sample is with the characteristics of small grains ejecting, accompanied with the temperature decreased, as shown in Figure 5(e).

4 Conclusion

AE technique and infrared thermography have been used to investigate the failure mechanism of coal burst at the high stress state. The basic conclusions are as follows: There are more AE events and higher energy rates due to the closeness of the original cracks for coal samples at the initial loading. AE events significantly increase at the failure stage because of microcracks and defects extended through the entirety of the confined coal samples, particularly accompanied with impact sound. It is concluded from the PWD results of the key monitoring points, that much more energy can be released while the failure of coal samples occur. The infrared characteristics for #NSV3-4 coal samples from unloading damage can be described by a temperature jump or fluctuation. There is an obvious enhancement of temperature observed before failing for the coal samples, which is in good agreement with the observations of failing rock [21]. These studies may help to understand the failure mechanism of rockburst and optimize the support design of underground rockmass excavation engineering.

Acknowledgements

This work was supported by the National Basic Research Program of China (2006CB202200), the Major Program of National Natural Science Foundation of China (50490270), and Innovative Team Development Project of the Ministry of Education of China (IRT0656).

References

1. Gorny, V.I., Salman, A.G. and Tronin, A.A., et al. The Earth Outgoing IR Radiation as an Indicator of Seismic Activity. *Proc. Acad. Sci. USSR*, 1988, 30(1): 67-69.
2. Qiang, Z.J., Dian, C.G. and Li, L.Z., et al. Satellite Thermal IR Increase Temperature Anomalous Field with Imminent and Short-term Prediction before Earthquake. In: *Proc. Of IEAS'97 & IWGIS' 97*. Beijing, 1997.
3. Liu, D.F., Luo, Z.L. and Peng, K.Y. OLR Anomalous Phenomena before Strong Earthquakes. *Earthquake*, 1997, 17(2): 126-132.
4. Liu, D.F., Peng, K.Y. and Liu, W.H., et al. There are Thermal Precursors for Earthquake. *ACTA Seismologica SINICA*, 1999, 21(6): 652-656.
5. Cui, C.Y., Zhang, J.K. and Xiao, Q., et al. Monitoring the Thermal IR Anomaly of Zhangbei Earthquake Precursor by Satellite Remote Sensing Technique. In *Proc. 20th Asia RS Congress*, Hong Kong, 1999.
6. Ma, J. and Shan, X.J. An Attempt to Study Fault Activity Using Remote Sensing Technology-A Case of the Main Earthquake. *Seismology and Geology*, 2000, 22(3): 210-215.
7. Geng, N.G., Yu, P. and Deng, M.D. The Simulated Experimental Studies on Cause of Thermal Infrared

- Precursor of Earthquakes. *Earthquake*, 1998, 18(1): 83-88. (in Chinese)
8. Cui, C.Y., Deng, M.D. and Geng, N.G. The Study on Spectrum Characteristics of Rock on Different Pressure, *Chinese Science Bulletin*, 1993, 38(6): 538-541.
 9. Deng, M.D., Cui, C.Y. and Geng, N.G. Application of Principle of Remote Sensing to Earthquake Prediction and the Experimental Results. *Earthquake Research in China*, 1993, 9(2): 163-169. (in Chinese)
 10. Wu, L.X. and Wang, J.Z. Features of Infrared Thermal Image and Radiation Temperature of Coal Rocks Loaded. *Science in China*, 1998, 41(2): 158-164. (in Chinese)
 11. Wu, L.X., Liu, S.J. and Wu, Y.H., et al. Changes in IR with Rock Deformation. *Int. J. Rock Mech. & Min. Sci.*, 2002, 39(6): 825-831.
 12. Geng, N.G., Cui, C.Y. and Deng, M.D. The Proem of Remote Sensing Observation and Remote Sensing in Rock Mechanical Fracture Experiment. *Acta Seismologica Sinica*, 1992, 14: 645-652. (in Chinese)
 13. Wu, L.X. and Wang, J.Z. Infrared Radiation Features of Coal and Rocks under Loading. *Int. J. Rock Mech. & Min. Sci.*, 1998, 35(7): 969-976.
 14. Wu, L.X., Cui, C.Y. and Geng, N.G., et al. Remote Sensing Rock Mechanics (RSRM) and Associated Experimental Studies. *Int.J.Rock Mech and Min.Sci.*, 2000, 37(6): 879-888.
 15. Wu, L.X. Remote Sensing Rock Mechanics and Its Recent Achievements and Future Development. *Chinese Journal of Rock Mechanics and Engineering*, 2001, 20(2): 139-146.
 16. Liu, S.J., and Wu, L.X. Quantitative Study on the Thermal Infrared Radiation of Dark Mineral Rock in Condition of Uniaxial Loading. *Chinese Journal of Rock Mechanics and Engineering*, 2002, 21(11): 1585-1589. (in Chinese)
 17. Wu, X.L. and Wang, J.Z. The Experiment of Infrared Thermography and Radiation Temperature under Pressure of Coal. *Science in China D*, 1998, 28(1): 41-46.
 18. Zou, Y.H. Preliminary Study on Coal and Rock Acoustic Emission Mechanism and Relevant Experiments. *Mining Safety & Environmental Protection*, 2004, 31(1): 31-33. (in Chinese)
 19. Miao, J.L., Gong, W.L. and Li, D.J. Study on Failure Characteristics of Rock under Uniaxial Compression Based on Information Fusion Technology. *Mining Research and Development*, 2008, 28(3): 22-24. (in Chinese)
 20. He, M.C, and Miao, J.L. Experimental Study on Rockburst Processes of Granite Specimen at Great Depth. *Chinese Journal of Rock Mechanics and Engineering*, 2007, 26(5): 865-867. (in Chinese)
 21. Wang, X.H., Tan, Z.H. and Tang, C.A. The Experiment of Infrared Thermography about Rock Failure Process. *The 8th National Rock Mechanics and Engineering, Academic Conference Proceedings*, Beijing, 2005.

STRESS WAVE CHARACTERISTICS IN THE PROCESS OF STRAIN COALBURST EXPERIMENTS

JIN-LI MIAO, MAN-CHAO HE, DE-JIAN LI, FAN-JIANG ZENG and CHENG CHENG

School of Mechanics and Civil Engineering, China University of Mining and Technology

Beijing, 100083, P.R. China

State Key Laboratory for GeoMechanics and Deep Underground Engineering

Beijing, 100083, P.R. China

The characteristics of stress wave in the process of strain coal burst experiment are investigated in the paper from the viewpoint of interaction of stress waves through the free surface of a solid. One of the conditions triggering rockburst is interacted between strongly discontinuous waves and weakly discontinuous waves of plasticity. Tests about strain coal burst were conducted by using a real-triaxial rockburst system. It indicates that suddenly unloading one face from the coal specimen under testing is one necessary condition for rockburst. The released energy in the burst process is accompanied by the propagation of reflecting wave. Consequently, rockburst may be regarded as a result of stress wave propagation through rockmass. Rock failure, indeed, is a consequence of energy transferred unstably within rockburst, after accumulating of energy within rockmass.

1 Introductions

Strain rockburst is a nonlinear dynamic phenomenon when energy is released suddenly along with free surface excavation. Energy rockmass is here defined as one type of engineering rockmass under the action of stress fields, such as gravity and tectonic stress fields. Rock failure may actually be regarded as a result of energy transferred unstably within rock mass, after the accumulation of energy within the rock sample. In fact, rockburst often occurs in mine, underground cavern and tunnelling engineering. The frequency of rockburst occurrence is significantly higher with the increase of mining depth and the corresponding economic loss is generally great [1, 2, 3]. There is, however, there is no common accepted knowledge on the mechanism of rockburst nowadays. It is believed that the general issue on rockburst, at the present, should deal with the basic characteristics as follows [4]:

i) Rockburst is a type of sudden and violent rock failure, which may be approximately described by a process of dynamic deformation or a model of concept-cracking. However, it is different from both the roof spalling and the caving due to only gravity.

ii) The deformation of rock is usually extremely small before rockburst. Unstable deformation is the only necessary condition to make rockburst occur, but not a sufficient one.

iii) Delay and tracing are the other characteristics of rockburst. The former means that rockburst does not occur immediately after excavating or perturbing rockmass, whereas, the latter is that rockburst often occurs in the same location repeatedly. It was obtained from in-situ investigations after the excavation of hard rock that rockburst may appear generally for eight hours of excavation or so [5].

It is recognized that the multiple actions of both pressure waves and Rayleigh waves upon the free surface can lead to rockburst [6]. Thus the dynamic mechanism of rockburst was studied by the theory of stress waves

[7]. The interaction of stress waves between fracture planes that are actually being formed was investigated by Dyskin [8]. A model of layer cracking with mode II (crack under transverse shear) was developed by Feng [9].

For the feature of rockburst failure that should be characterized by the time-dependent state variables, we apply here the theory of stress wave to analyze the performance of coal burst in this paper. We also approximately calculate the velocity and thickness of coal fragment via this model to better understand the dynamic mechanism of coal failure.

2 Stress wave in rockmass

Stress wave here is a phenomenon of wave propagation induced by vibration of matter particles due to the instantaneous loading or unloading acted on the solid. Inertia and deformability are the fundamental characteristics for any solid material. While quasistatic loading be acted, stress waves will propagate and reflect and interact among the sample of rockmass [10]. On the other hand, the stress waves are also regarded as a constitution of longitudinal (pressure wave), transverse (shear wave), Rayleigh and Love wave at the surface or the rock interface. Furthermore, their speeds are generally different, in which the fastest is P wave, the second is S wave, and then is Rayleigh wave and the final is Love wave.

From the character of dynamic failure that is previously discussed, the strain rate and the inertia effect yielded by unloading suddenly must be considered. The mechanical response of rockmass at high strain rate is rather different from that of rockmass at low strain rate or without involving the effect of strain rate. From the viewpoint of solid mechanics, the displacement of particle, u , must be continuous on the wavefront from the requiring of medium continuity when stress waves propagate in the solid, but the derivative of u may be discontinuous. If the first-order derivative of u is of discontinuity, i.e., particle velocity $v (= \partial u / \partial t)$ and strain $\varepsilon (= \partial u / \partial x)$ with jump on the wavefront, then the field of velocity or strain is a so-called first-order singular surface or strong discontinuous field. However, if such a displacement and its first-order derivative are of continuity and corresponding second-order derivative, for example, the acceleration $a (= \partial v / \partial t = \partial^2 u / \partial^2 t)$ is of discontinuity, this field is called as a second-order singular surface which is also a weakly discontinuous surface [10].

The excavation of underground mine that is usually under the action of 3D stress field is similar to unloading suddenly at one or multiple directions surrounding rockmass. Therefore, the stress waves caused by such unloading considerably influence the stress redistribution within rockmass and the failure pattern of rockmass.

3 Coal burst tests and 1D theory on stress wave

The coal burst tests reported here were conducted by the following steps including 1) loading along three directions to the specimen, 2) keeping the constant loadings at three directions for a moment, generally 30 min, 3) completely unloading from one face of the specimen, and 4) maintaining other loadings to be constant or only increasing one of the two loadings. In other words, a complete process of rockburst test generally includes slowly loading at the beginning and rapidly unloading/loading at later. It is noted that the highest rate of sampling is 10000 per second during the rockburst; the rates of loading and unloading are 0.05 and 5 MPa/s, respectively. To better understand the loading path of a typical strain rockburst, one can refer to figure 1.

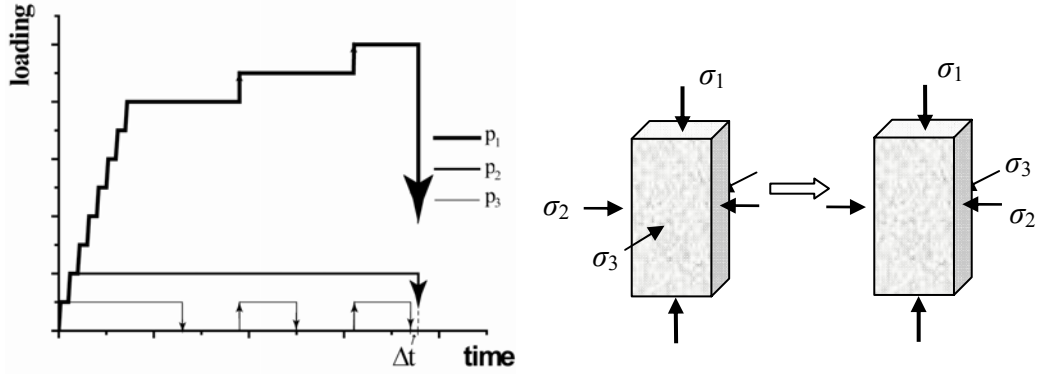


Figure 1. A history of loading and suddenly unloading in the coal specimen

In the tests, the coal samples obtained from the open-pit coalmine at Antaibao of China, in which their average weight per unit volume is about 13.4 kN/m^3 ; their uniaxial compressive strength is about 8 MPa . It is shown by the test results that the violent intensity and delay time for such coalbursts were probably associated with the stress variations of the coal samples because of unloading. Additionally, the stress redistribution is also closely related to the rockmass structure and mineral content.

It has been demonstrated in particular that the models which directly describe the dynamic failure of rockburst by 3D analytical method are not available presently. Being in mind this fact, we attempt here to approximately analyze a relatively complicated test of 3D coalburst by a 1D analytical theory of stress wave. The underlying possibility of this simplification is that if the symmetries of boundary conditions and loadings at triaxial test are taken into account, the spalling and cracking along with the unloading direction of this test could be approximately represented by a model of stress wave. The pieces are, for example, typically flaking fragments packed layer by layer due to applying some unloading, as shown in figure 2, which could be primarily explained by the 1D analytical model as discussed in detail as follows.



Figure 2. A series of fracture layers at which the thicknesses progressively varied after coalburst.

Let a coal specimen act at constant vertical and one lateral average stress. Therefore, the governing equation of stress wave propagating at the unloading direction can be represented by 1D wave theory, which includes three parts such as admissible condition or continuum equation, motion equation and constitutive relation [8].

$$\begin{cases} \frac{\partial \bar{\epsilon}}{\partial t} = \frac{\partial \bar{v}}{\partial X} \\ \rho_0 \frac{\partial \bar{v}}{\partial t} = \frac{\partial \bar{\sigma}}{\partial X} \\ \bar{\sigma} = \sigma_m + E(\bar{\epsilon} - \epsilon_m) \end{cases} \quad (1)$$

where $\bar{\varepsilon}$ is the unloading strain $\bar{\nu}$, ρ_0 is the initial density of the coal specimen, X is the Lagrange or material coordinate, $\bar{\sigma}$ is the unloading stress, σ_m is the stress corresponded by plastic strain ε_m before unloading, E is the elastic modulus of the coal specimen, respectively. During the excavation of in situ rockmass, the unloading process within rockmass is actually finished at very short time, which triggers the interaction of unloading wave (strong discontinuity) and plastic loading wave (weak discontinuity). On the other hand, strong discontinuity waves or triangle impact waves that are due to unloading from one surface of the specimen in laboratory appear.

The underlying point is that such triangle impact waves are the reason for the spalling and cracking of coal specimen. These tensile waves acted on the surfaces of coal specimen may yield rather stress in the vicinity of the surfaces where failure will not occur unless maximum stress exceeds the fracture strength of the coal, but if so, layer cracking will be appeared by the criterion of fracture [11]. Furthermore, as soon as layer cracking appears, a new surface in the coal has been yielded. Continuous stress waves that will reflect on the surface formulated newly may make next layer cracking within coal specimen. It is noted that stress wave action can be generally from a stress function with regard to time t [10]

$$\sigma(t) = \sigma_m \left(1 - \frac{C_0 t}{\lambda} \right) \quad (2)$$

If $|\sigma_m| > \sigma_{td}$ (σ_{td} , the dynamic tensile strength of the coal specimen), the thickness of first layer cracking is

$$\delta_1 = \frac{\lambda}{2} \frac{\sigma_{td}}{\sigma_m} \quad (3)$$

The departing velocity of cracking splinter, v_f , is given by

$$v_f = \frac{1}{\rho_0 \delta_1} \int_0^{\frac{2\delta_1}{C_0}} \sigma_m \left(1 - \frac{C_0 t}{\lambda} \right) dt = \frac{2\sigma_m - \sigma_{td}}{\rho_0 C_0} \quad (4)$$

where C_0 the velocity of elastic wave, λ is the wave length.

4 The calculations of velocity and thickness of coalburst fragment

It is assumed that the stress wave velocity within coal specimen is c , its frequency is f , and its wave length is λ . The stress function represented by an impulse form is $\sigma(t)$ at any point, where the wavefront reaches to this point taking time t as the initial time ($t = 0$); if the stress at the distance x from the free surface is satisfied by the fracture criterion of maximum tensile stress, layer cracking must occur, i.e.,

$$\sigma(0) - \sigma\left(\frac{2x}{c}\right) = \sigma_t \quad (5)$$

Furthermore, if the shape of stress wave is assumed to be linearly varied by a triangle form of impulse, $\sigma(t)$ can be written as

$$\sigma = \sigma_m \left(1 - \frac{ct}{\lambda} \right) \quad (6)$$

Substituting equation (5) into (4), we obtain

$$\sigma_m \left(1 - \frac{c \times 0}{\lambda} \right) - \sigma_m \left(1 - \frac{c \frac{2x}{c}}{\lambda} \right) = \sigma_t \quad (7)$$

The thickness x_1 of first layer cracking is

$$x_1 = \frac{\lambda}{2} \frac{\sigma_t}{\sigma_m} \quad (8)$$

Applying equation (8) to the coal specimen, while supposing the wave velocity (c) being 2000 m/s and the frequency being 100 kHz, the wave length is obtained to be 0.02m. It is further assumed that the tensile strength of the coal specimen is 2 MPa and the maximum amplitude of stress wave is 8 MPa, the thickness of the first layer cracking by equation (8) is about 2.5 mm. The occurrence of layer cracking is just after the beginning of stress wave reflection, t_1 , as treated as follows $t_1 = x_1/c = 0.0025/2000 = 1.25 \mu s$.

The velocity of layer cracking is approximately calculated, while its momentum equals to the impulse within the coal specimen

$$v_f = \frac{1}{\rho_0 x_1} \int_0^{\frac{2x_1}{c}} \sigma(t) dt \quad (9)$$

After considering equation (6), supposing the mass density is 1400 kg/m³, we have a simplified formulation of velocity for the coal fragment

$$v_f = \frac{2\sigma_m - \sigma_t}{\rho_0 c} \quad (10)$$

Therefore the velocity is 0.52m/s.

It has been demonstrated that the number (n) of layer cracking could be approximately estimated by a formulation, $n = \sigma_m/\sigma_t$, as referred to in detail discussion in [10]. To the coalburst specimen here, we have $\sigma_m/\sigma_t = 4$. The complete result of the thickness and velocity of each layer cracking (LC) for a typical coal specimen is presented in table 1. The sketch of layer cracking is also shown in figure 3.

Table 1 Thicknesses of fracture layers by the stress wave theory and the test

LC No.	σ_t (MPa)	σ_m (MPa)	Calculated by the theory		Observed in the laboratory
			v_f (m/s)	Thickness (mm)	Thickness (mm)
1	2	8	0.52	2.5	2.5
2	2	6	0.37	3.3	3.6
3	2	4	0.22	5.0	7.0
4	2	2	0.07	10.0	10.1

From table 1, it is readily found that the thicknesses of fracture layers predicated by the stress wave theory are good agreed with that of experimental result for the coalburst. However, the first spall layer at the coal specimen is generally of the thinnest and the longest because of boundary constraint effect. With the propagation of stress wave in coal, dissipated energy is rather different between fragments that are yielded by crack propagation in coal. Furthermore, how to evaluate the lengths of such fragments and how to develop an available criterion of cracking from the viewpoint of dynamic fracture will need further to be investigated in future. Finally, it is important to note that the extending 1D stress wave model to 2D or 3D general model in which it is difficult to deal with size effect and failure wave reflection for the treatment of rockburst urgently needs to be done.

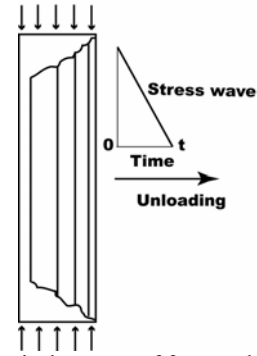


Figure 3. A typical process of fracture layer for coalburst due to suddenly unloading.

5 Conclusions

We have primarily studied the failure characteristics of the coalburst through the stress wave model and the experimental test. The main conclusions are summarized as follows.

(1) Strain coalburst occurrence is the result of stress redistribution within the coal, in which the failure development and evolution are closely associated with stress wave action that is induced by sudden unloading on one face of the specimen. It is noted that the assumption of the 1D stress wave theory is applied the theoretical calculation in all coalburst tests.

(2) The energy of ejected fragments from the specimen is the result of reflecting waves propagating through the coal specimen, which is also associated with the strain energy of the coal specimen. The thicknesses of fracture layers or fragments can be approximately evaluated by the stress wave theory. It has been observed from the coalburst tests that a series of failing or fracture layers with varied thickness can occur, in which the thicknesses are progressively decreased from the interior to the free surface due to the boundary constraint effect.

(3) How to evaluate the lengths of fragments and how to develop an available criterion of cracking from the viewpoint of dynamic fracture at the condition of 3D will need further study to be carefully investigated. Finally, careful attention must be paid to urgently develop the 3D general model to deal with the size effect and failure wave reflection for the treatment of rockburst.

Acknowledgements

This work was supported by the National Basic Research Program of China (2006CB202200), the Major Program of National Natural Science Foundation of China (50490270), and Innovative Team Development Project of the Ministry of Education of China (IRT0656).

References

1. He, M.C., Jiang, Y.D. and Zhao, Y.X. Control theory of coal blast on the principal of transform of compound energy: Beijing, Science Press, 2006, 1, 205-214.
2. He, M.C. and Qian, Q.H. Study Development on Rock Mechanics in great Depth, 9th Academic Conference of Chinese rock mechanics and Engineering, Science press, Beijing, 49-62. 2006.
3. He, M.C. Rock Mechanics and Hazard Control in Deep Mining Engineering in China, ISRM International Symposium, Fourth Asian Rock Mechanics Symposium, Rock Mechanics in Underground Construction. 8-10 November 2006, 29-46. Singapore. World Scientific Publishing Co. Ltd.
4. Cao, P., Pan, C.L. and Feng, T. Memoir and Features Analysis of Rockburst in Hard Rockmass, Proceedings of the 6th Chinese rock mechanics and engineering, Wuhan, China, 2000.
5. Tang, L.Z., Pan, C.L. and Wang, W.X. 2001 An analysis of the properties of rock burst of the working in a deep ore deposit, Mining and Metallurgical Engineering, 21(4). 19-21.
6. Huang, F. Rockburst dynamic mechanism and control in long tunnel disaster. Master thesis, Kunming, Kunming University of Science and Technology, Kunming, China, 2007.
7. Xu, Z.M., Huang, R.Q. and Luo, X.C. Limitations of Static Load Theory in Rockburst Research and Preliminary Analysis on Dynamics Mechanism of Rockburst. Chinese Journal of Rock Mechanics and Engineering, 2003, 22(8). 1255-1262.
8. Dyskin, A.V. and L.N. Germanovich, K.B. Ustinov. Asymptotic analysis of crack interaction with free boundary. International Journal of Solids and Structures, 2000, 37. 857-886.
9. Feng, T. Analysis on rockburst mechanism and protection and application PhD thesis. Central South University of Technology, Changshan, China, 1999.
10. Wang, L.L. Foundation of Wave Stress (second version), National Defense Industry Press, Beijing, 2005.
11. Tuler, F.R. and Butcher, B.M. A Criterion for the time dependence of dynamic fracture. Int. J. Fract. Mech., 2002, 4. 431-437.

RISK PREDICTION MODEL OF ROCK-BURST BASED ON COMBINED ANN

JIAN SUN, LIAN-GUO WANG, HUA-LEI ZHANG and YI-FENG SHEN

*State Key Laboratory for Geomechanics & Deep Underground Engineering, China University of Mining
& Technology, Xuzhou, Jiangsu 221008, P.R. China*

School of Sciences, China University of Mining & Technology, Xuzhou, Jiangsu 221008, P.R. China

Rock-burst is one of the coal and rock dynamical disasters that must be paid attention to when mining is carried out. At present, most risk prediction methods remain at the stage of simple statistical studies and the single factor forecast. In those methods, only the mining geology factors are considered, and the mining technical conditions are neglected. Therefore the predicted results cannot reach the desired precision. In this paper, the main influencing factors of the rock-burst risk both the mining geology factors and the mining technical conditions are comprehensively considered. Based on the sufficient existing rock-burst data, a combined artificial neural network (ANN) risk forecast model of rock-burst is proposed by utilizing the genetic algorithm to train back-propagation (BP) neural networks. It is capable for both the self-learning and strong robustness of neural networks and the global stochastically searching of genetic algorithms. Obviously, the effect of artificially determining the rock-burst risk indexes can be eliminated. The practical engineering application indicates that this method is not only precise, simple, but also intelligent. The predicted result by this method is based on the actual conditions. This model can be satisfactorily applied to the relevant engineering projects with quality results.

1 Introduction

Rock-burst is one of the coal and rock dynamical disasters, which is a serious threat to the safe production of coal mines due to its sudden, instantaneous vibratility, tremendous destructivity [1-3]. Presently, the occurrence mechanism of rock-burst is still not very clear, and the precise predicting rock-burst is the precondition of the prevention rock-burst. The prediction methods of major rock-burst include the analysis method of experience analogy, the method of drilling bits, the method of underground sound monitoring, the method of micro-seismic monitoring, the method of water content rate determination and so on[2]. As these risk prediction methods of rock-burst mostly remain simple statistical studies and single factor forecast, only considers the mining geology factors, and neglect the mining technical conditions; therefore the results predicted do not satisfied the desired precision. With the increase of mining depth, the risk of rock-burst becomes increasingly greater. How to precisely forecast and effectively prevent rock-burst is one of the important issues studied by the field of mining and geosciences, both at home and abroad.

In view of the complexity and the nonlinear dynamic characteristics of inducing factors of rock-burst [4-6], both main influencing factors of rock-burst risk, the mining geology factors and the mining technical conditions, are comprehensive considered. Based on the plentiful number of existing rock-bursts to date, we propose a combined artificial neural network (ANN) risk forecast model of rock-burst by utilizing the genetic algorithm to train back-propagation (BP) neural networks. Which behave in the ability of both self-learning and strong robustness of neural networks and the global stochastically searching of genetic algorithm; and obviously eliminate the influence of artificial determining of the rock-burst risk indexes. The practical engineering application indicates that this method is not only precise and simple, but also intelligent, with the predicted results agreeing with the actual conditions.

2 Combined ANN risk forecast model

An ANN is a type of mathematical model or computational model based on biological neural networks, which consists of a group of interactive artificial neurons and processes information by using a interconnected algorithm. In most cases, an ANN is a self-adapting, nonlinear dynamic system which has developed rapidly all over the world since the 1980s and is extensively used in many fields, such as image, speech and voice recognition, complex computation as well as trend prediction [7, 8]. Due to the complexity and the nonlinear dynamics characteristics of influencing factors of rock-burst, traditional forecasting methods are often used under conditions of severe limitations. As a newly developed method, ANN can deal with continuous and random nonlinear problems with a refined modeling agility in complex nonlinear systems and excellent ability for fitting data [9-14]. So we can use ANN to predict the risk of rock-burst.

2.1 BP network model

A BP neural network is a kind of multi-layered and feed forward ANN. A BP network changes the input/output of a group of specimens into a nonlinear optimization problem, which can be considered as mapping from a n -dimensional space ($x_k, k=1, 2, \dots, n$) to a p -dimensional space ($y_k, k=1, 2, \dots, p$). The structure of a BP neural network is shown in Figure 1, with one input layer, one output layer and one or several hidden layers, each of which includes some neurons. An input signal firstly arrives at hidden nodes where it is processed by an excitation function and is then transferred into the output layer nodes to be processed, obtaining the final output results.

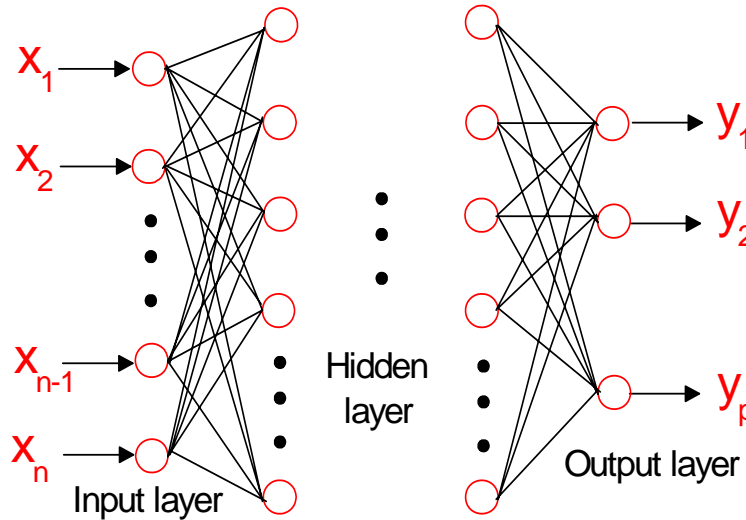


Figure 1 Structure of BP neural network

The forecast precision is directly determined by the structure of the BP neural network topology. A multi-dimensional continuous function can be approximated with any precision under the condition that the number of hidden nodes changes arbitrarily by using a sigmoid function of the three-layered BP neural network [15]. We assume that there is a multilayer feed forward neural network of any size, with the excitation function for each neural network being selected as a sigmoid function $f(x) = (1 + e^{-x})^{-1}$.

A BP neural network uses an error back propagation learning algorithm and the learning process includes the forward propagation and the back-forward propagation which alternate. If the error sum of squares of forward propagation cannot attain the forecast precision, the weight values and the threshold values would be repeatedly modified along the direction of a negative error gradient until the network global error sum of squares reaches the forecast precision.

In order to accelerate the weight convergence, a momentum factor term α is introduced into the weight correction during network learning, and the adjusted formula of weight with the momentum factor term α can be expressed as $\Delta_k W_{ji}(t+1) = \mu \cdot \delta_{kj} \cdot O_{ki} + \alpha \Delta W_{ji}(t)$. Where $w_{ji}(t+1)$ and $w_{ji}(t)$ indicate the $(t+1)$ times and (t) times iterated weight correction value, respectively, and α (generally chosen $0 < \alpha < 1$) is momentum coefficient that decides the affected degree of the past weight to the present weight, and μ (generally chosen $0 < \mu < 1$) is the learning step and δ_{kj} is the negative gradient of the error sum of squares to the weight values in BP algorithms.

BP algorithms are based on the steepest descent method [16], which has the advantage of high precision optimization. However, it also has inherent deficiencies, such as all too easily reaching local minima, a slow speed of convergence and causing an oscillating effect. The first disadvantage can be solved during the practical calculations by adjusting the initial weights, while the other two problems are often due to falling into local minima during late network training. In view of this, if a certain weight value can be obtained as the initial weight value of the BP algorithms through an effective method before carrying out the BP algorithm, both problems would be solved. We used a genetic algorithm to fulfill the earlier potential weight value search and have overcome the deficiency of BP algorithms because of their ability of macroscopic search, simple universal and strong robustness and paralleled computing characteristics. Overall, we propose a combined training algorithm which combines the genetic algorithms with the BP algorithms to form an optimizing network. That is to say, we first used the genetic learning algorithms to search for optimal values to reduce the extent of the search and then the BP neural network was used to make further searches.

2.2 Combined Network Model

The optimal model of a BP neural network risk forecast of rock-burst can be ultimately expressed as a group of optimal weights which indicate the complex mapping relation between input and output. However, the inherent limitations of BP neural networks make it impossible that all the optimal selected weights to be global optima. So the ANN risk forecast model of rock-burst can be optimized by using the genetic algorithms to compensate for the deficiency of BP neural network.

The calculation processes for combined BP neural network risk forecast model of rock-burst are described as follow:

(1) Determination of the structure of the BP neural network: We selected 12 major influencing factors as network input vectors after we statistically analyzed many field data of rock-burst, both the mining geology factors and the mining technical conditions: mining depth (m), coal seam thickness (m) and its change, coal seam pitch ($^{\circ}$) and its change, properties of roof rock, complex degree of geological structure, mining method, coal pillar (marked as 1 with coal pillar and 0 without coal pillar), roof management situation, pressure relief situation, coal noise (shooting). And for the sake of convenience, we marked the 12 influencing factors in turn as Fact.1, Fact.2, Fact.3, ..., Fact.12 (see Table 1). So, the input vector is a 12-dimensional (12D) vector. Through selecting a certain threshold value, the qualitative variable of the input vector can be quantitative expressed by "0" and "1" of quantification theory that denoting its some properties. Because the neurons number of the network output layer is 2, the output vector is a 2D vector. The risk of rock-burst is regarded as the object vector, and the different combinations of outputted vector are relative to the 4-grade of rock-burst risk, respectively. We assume that the four-grade risk (without rock burst risk, weak rock burst risk, moderate rock burst risk, strong rock burst risk) are corresponding to the four-vector of network output: (0,0), (0,1), (1,0) and (1,1) respectively. The risk of rock-burst becomes more and stronger from without rock burst to weak rock burst to moderate rock burst to strong rock burst.

We can obtain from the analysis above that the number of input nodes Q_i is 12 and 2 output node Q_j , while the number of hidden nodes Q_k is determined by the trial calculation of training samples.

(2) Determination of the coding: In general, a network can be represented as a chromosome with binary strings where each parameter in the network can be expressed by a \mathbf{P} binary system, and each network chromosome is formed by a series of parameter genes. In our model, \mathbf{P} was given 10 (having 10 binary systems), with the first place allotted sign bit (1 denotes positive, 0 denotes negative). So the coding form can be expressed as follows:

$$\underbrace{1100010111}_{W_{m1}} \underbrace{10110011010}_{W_{m2}} L \underbrace{0111010111}_{W_{mQ}}$$

where m is the number of groups, and Q the number of network parameters.

(3) Calculation of level of individual fitness (F_i): Defining the training network weight value error function is presented as $E_k = \sum_j (y_{kj} - y'_{kj})^2$ ($k=1,2,\dots,m; j=1,2,\dots,Q$). Where y_{kj} , y'_{kj} indicate the desired output and the actual output of forward training, respectively. In fact, a high level of fitness is used to be optimized, and the level of fitness function can be indicated by $F(E) = 1 - E$.

(4) Genetic operation (selection, cross, variation): We removed the chromosomes whose level of fitness is low and retained those for which it was high in order to obtain a new generation which should be superior to the earlier generation because it is selected from the former generation and inherited their good characteristics. In this step, the genetic learning algorithm was used to train the BP neural network.

(5) Iterative calculation of BP: If the network cannot attain the predetermined value of the individual level of fitness, it will return to the step (4) until F_i meets the stated requirements. At that time, the network weights and threshold value should have satisfied the predetermined requirements, and the network training should end. So it can then be used for practical forecasting purposes.

(6) We used our trained neural networks in an example where the calculated results were reduced by the standardized formulas to carry out forecasts.

3 Example Analysis

Data from rock-burst risk from 16 typical mines were selected as our training sample, shown in Table 1, including the mining geology factors and the mining technical conditions that effecting rock-burst risk (see the part of 2.2, the influencing factors were marked with Fact.1, Fact.2, Fact.3,, Fact.12, respectively). We normalized the data to establish a BP neural network in which there were 12 input-layer nodes, 2 output-layer nodes and 15 hidden-layer nodes. At the same time, genetic algorithms were used to train the BP neural network. The precision requirement of 0.01 was satisfied with 3000 generation cycle operations. Through selecting a certain threshold value, the quantitative results of samples were expressed by "0" and "1" of quantification theory, and their learning results were shown in Table 2. We know from Table 2 that the predicted results calculated by using the BP neural network are quite close to the practical conditions, indicating that the network had already learned the complex nonlinear relations among data after being trained by the genetic algorithms. The method is therefore highly accurate and reliable, making it capable to forecast the risk of rock-burst in some new workplace.

Table 1. Training samples

Sam- ples	Mining geology factors of influencing rock-burst							Mining technical conditions of influencing factors rock-burst					Practical rock- burst risk
	Fact. 1	Fact. 2	Fact. 3	Fact. 4	Fact. 5	Fact. 6	Fact. 7	Fact. 8	Fact. 9	Fact. 10	Fact. 11	Fact. 12	
1	453	1.5	fewer	29	fewer	mud	simple	short	no	better	better	less	without risk
2	532	1.3	fewer	26	fewer	mud	simple	short	no	better	worse	less	without risk
3	560	1.2	more	45	fewer	sand	simple	long	no	better	better	more	without risk
4	584	3.1	fewer	25	fewer	mud	simple	short	no	worse	better	less	without risk
5	551	0.9	fewer	32	fewer	sand	simple	long	yes	worse	better	more	weak risk
6	492	1.3	fewer	41	fewer	mud	simple	short	no	better	worse	less	weak risk
7	478	1.5	fewer	38	more	sand	simple	long	no	better	worse	less	weak risk
8	492	1.4	fewer	29	fewer	mud	simple	long	no	better	better	less	weak risk
9	713	2.5	fewer	54	fewer	sand	complex	short	no	better	better	less	moderate risk
10	562	2.8	more	68	more	sand	simple	long	yes	better	better	less	moderate risk
11	463	6.2	more	32	fewer	mud	simple	short	yes	better	worse	more	moderate risk
12	575	1.3	fewer	62	more	mud	simple	short	yes	better	better	more	moderate risk
13	852	3	more	56	more	mud	complex	short	yes	better	worse	more	strong risk
14	482	1.6	more	63	more	sand	complex	long	yes	better	worse	more	strong risk
15	512	2.3	more	62	more	sand	complex	short	yes	better	worse	more	strong risk
16	458	2.6	more	70	more	sand	complex	long	yes	better	worse	more	strong risk

Sanhejian Coal Mine of Xuzhou Mining Bureau is a new mine that has been mined at the end of the 1980s, which is designed mine with the capacity of 1.2Mt/a, and now 1.6Mt/a. Primary mineable coal seam at Sanhejian Coal Mine is Shanxi Formation 7-coal and 9-coal and their buried depth is below -420m, now the mining depth reaches below -980m. With the increase of mining depth, the stress in coal and rock mass becomes increasingly great, the coal and rock dynamical disasters becomes increasingly great, the risk of rock-burst becomes also increasingly frequent. Therefore, rock-burst is one of the major dynamical disasters in Sanhejian Coal Mine. Table 3 shows the comparison between the practical conditions and the predicted results of part workforce of Sanhejian Coal Mine. From Table 3, we can know that the predicted results calculated by the combined ANN are quite close to the practical conditions, indicating that this method can be well applied to the relevant engineering projects with satisfactory results.

Table 2 .Training samples and their learning results

Sam- ples	Mining geology factors of influencing rock-burst							Mining technical conditions of influencing rock-burst					Practical rock- burst risk	Predicted rock- burst risk
	Fact. 1	Fact. 2	Fact. 3	Fact. 4	Fact. 5	Fact. 6	Fact. 7	Fact. 8	Fact. 9	Fact. 10	Fact. 11	Fact. 12		
1	453	1.5	0	29	0	0	0	1	0	0	0	0	without risk	(0, 0)
2	532	1.3	0	26	0	0	0	1	0	0	1	0	without risk	(0, 0)

3	560	1.2	1	45	0	1	0	0	0	0	0	1	without risk	(0, 0)
4	584	3.1	0	25	0	0	0	1	0	1	0	0	without risk	(0, 0)
5	551	0.9	0	32	0	1	0	0	1	1	0	1	weak risk	(0, 1)
6	492	1.3	0	41	0	0	0	1	0	0	1	0	weak risk	(0, 1)
7	478	1.5	0	38	1	1	0	0	0	0	1	0	weak risk	(0, 1)
8	492	1.4	0	29	0	1	0	0	0	0	0	0	weak risk	(0, 1)
9	713	2.5	0	54	0	1	1	1	0	0	0	0	moderate risk	(1, 0)
10	562	2.8	1	68	1	1	0	0	0	0	0	0	moderate risk	(1, 0)
11	463	6.2	1	32	0	0	0	1	1	0	1	1	moderate risk	(1, 0)
12	575	1.3	0	62	1	0	0	1	1	1	0	1	moderate risk	(1, 0)
13	852	3	1	56	1	0	1	1	1	1	1	1	strong risk	(1, 1)
14	482	1.6	1	63	1	1	1	0	1	1	1	1	strong risk	(1, 1)
15	512	2.3	1	62	1	1	1	1	1	1	1	1	strong risk	(1, 1)
16	458	2.6	1	70	1	1	1	0	1	1	1	1	strong risk	(1, 1)

Table 3. Comparison conditions between the predicted results and the practical conditions

NO.	Workface	Outputted 2D vectors	Predicted rock-burst risk	Practical rock-burst risk
1	7109 workface	(1, 0)	moderate risk	moderate risk
2	7110 workface	(1, 0)	moderate risk	moderate risk
3	7125 workface	(0, 1)	without risk	weak risk
4	7141 workface	(1, 1)	strong risk	strong risk
5	7202 workface	(1, 0)	moderate risk	moderate risk

6	7204 workplace	(1, 1)	strong risk	strong risk
7	9101 workplace	(1, 1)	strong risk	strong risk
8	9108 workplace	(0, 0)	without risk	without risk
9	9112 workplace	(1, 1)	strong risk	strong risk
10	9202 workplace	(1, 1)	strong risk	more strong risk

4 Conclusions

In our study, we proposed a combined training algorithm which integrates the genetic learning algorithms with the BP neural network algorithms. This method possesses certain advantages, such as globe searching optimization, high precision and quick convergence. In order to test this method, a combined ANN risk forecast model of rock-burst was established by using genetic algorithms to train the ANN with massive existing engineering to date, and was then used to predict the risk of rock-burst in the Sanhejian Coal Mine. The practical application indicates that the predicted results agree with the practical conditions. Overall, this is an effective method to forecast the risk of rock-burst.

Acknowledgements

The authors wish to acknowledge the collaborative funding support from the National Natural Science Foundation of China (50874103), the National Basic Research Program of China (2006CB202210 and 2007CB209400) and the Natural Science Foundation of Jiangsu Province (KB2008135), as well as the Qing-lan Project of Jiangsu Province.

References

1. Boler, F. M., Billington, S. and Zipf, P. K. Seismological and Energy Balance Constraints on the Mechanism of a Catastrophic Bump in the Cliffs Coal Mining District. Utah, USA. International Journal Rock Mechanics Mining Sciences, 1997, 34 (1). 27-43.
2. Dou, L. M. and He, X. Q. Theory and Technology of Rock Burst Prevention. Xuzhou: China University of Mining and Technology Press, 2001, 1-17.
3. Min, C. J. and Bu, F. Q. Rockburst and the Preventable Technology in Coal Mine. Xuzhou: Press of China University of Mining & Technology, 1998.
4. Qian, M. G. and Shi, P. W. Ground Pressure and Strata Control. Xuzhou: China University of Mining and Technology Press, 2003.
5. Tang, C. A. Catastrophe in Rock Unstable Failure. Beijing: Coal Industry Press, 1988. 19-20.
6. Jiang, Y. D., Zhao, Y. X., Song, Y. Q., Liu, W. G. and Zhu, D. J. Analysis of Blasting Tremor Impact on Roadway Stability in Coal Mining. Chinese Journal of Rock Mechanics and Engineering, 2005, 24 (17). 3 131-3 136.
7. Hu, W. S. Theory of Neural Network and its Applications in Engineering. Beijing: SinoMaps Press, 2006.
8. Yuan, C. R. Artificial Neural Network and Its Applications. Beijing: TsingHua University Press, 1999.
9. Yi, G. Z., Dai, G. F., Yan, H. and Wei, Z. A. Prediction of Rockburst by Genetic Algorithm-neural Network. Rock and Soil Mechanics, 2003, 24(6). 1016-1020.
10. Feng, X.T., Zhang, Z. Q., Yang C. X. and Lin Y. M. Study on Genetic-neural Network Method of Dis-

- placement Back Analysis. Chinese Journal of Rock Mechanics and Engineering, 1999, 18(5). 529-533.
11. Feng, X. T. and Jia, M. T. Neural Network Modeling on Rock Mechanics Problems. Chinese Journal of Rock Mechanics and Engineering, 2000, 19(Supplement). 1 030-1 033.
 12. Tan, Y. L., Sun, Z. H. and Du, X. D. A Wavelet Neural Network Predicting Model for Acoustic Emission Time Series of Rock Burst, Chinese Journal of Rock Mechanics and Engineering, 2000, 19 (Supplement). 1034-1038.
 13. Wang, L. G. and Song, Y. Combined ANN Forecast of Water-inrush from Coal Floor. Chinese Journal of Geotechnical Engineering, 2001, 23(4). 502-505.
 14. Guo, D. Y., Li, N. Y., Pei, D. W. and Zhen D. F. Prediction Method of Coal and Gas Outburst Using the Grey Theory and Neural Network. Journal of University of Science and Technology Beijing, 2007, 29(4). 354-357.
 15. Hecht-Nielsen, R. Theory of Back-propagation Neural Networks. Proceedings of the International Joint Conference on Neural Networks, 1989, 1. 593-605.
 16. Zhou, X., Zhu, X. Y. and Wen, C. Y. Application of ANN to Predict the Drainage in Mine. Journal of Hydraulic Engineering, 2000, 12. 59-63.

RECOVERING ORE RESERVES IN FINAL OPEN PIT WALLS

VASILY BARYSHNIKOV and LIDIA GAKHOVA

Institute of Mining, Siberian Branch, Russian Academy of Sciences

54 Krasny Prospect, 630091 Novosibirsk, Russia

The authors analyze the geomechanical conditions of extraction of 325 m deep open pit wall reserves. Numerical modelling of the stress-strain state in the pit wall rock mass, based on the geological and geotechnical data allowed determination of strains in the pit slopes and localization of hazardous strain zones.

1 Introduction

To substantiate the optimal control over geomechanical situation in order to ensure prompt forecasting of hazardous events and to decrease their intensity, it is reasonable to model stress-strain state of a rock mass, which allows a tentative assessment of stresses and the retrace of their variation by the stages of mining. Continuous instrumental monitoring and visual examination render possible to anticipate the change in geomechanical situation in the course of mining, refine the numerical model of the rock mass, formulate safe condition criteria, validate the rock mass limit deformation parameters and, ultimately, to influence the decision-making.

2 Test site

We studied geomechanical situation in the “Aikhal” kimberlite open pit mine. The open pit depth is 325 m. It was decided to extract kimberlite reserves in the north-eastern pit wall at level +330 ÷ +205 m by horizon mining with open mined-out space (Figure 1). Final slopes after the first to third stage cutting are more than 100 m high. This made necessary to assess and forecast the state of the working excavation wall within the boundaries of the newly formed open pit walls.

3 Numerical modelling

Numerical modelling of stress-strain state of the open pit walls was based on elastic calculations with allowance for the real geometry of the open pit mine and the ore body position, by the boundary integral approach [2]. As initial, we assumed hydrostatic stress distribution ($\sigma_x^0 = \sigma_y^0 = \sigma_z^0 = -\lambda\gamma H$, where σ_y^0 , σ_x^0 , σ_z^0 are initial stresses at depth H , γ is weight of rocks, $\lambda=1$). Data on physico-mechanical properties were taken from the Book of Reference on Physico-Mechanical Properties of Host Rocks at Diamond Deposits of Yakutia, as applied to “Aikhal” open pit mine [4]. The results were plotted as isolines of horizontal stresses σ_x , σ_y and vertical stress σ_z . Axis OZ shows actual elevations, axis OY in horizontal section is perpendicular to axis OX (please refer to Figure 1b).

According to the calculations, after the second stage cutting, the south-eastern wall of the cut is completely unloaded from horizontal stresses, up to formation of tension zones at a distance 5 to 10 m from the wall (Figure 2b). The stress state only depends on the weight of a small overlying rock layer. Horizontal tension may

cause rock mass lamination and vertical fissuring. Compression stresses σ_x are low and reach $-3 \div -5$ MPa near the cross-cut end (Figure 2a).

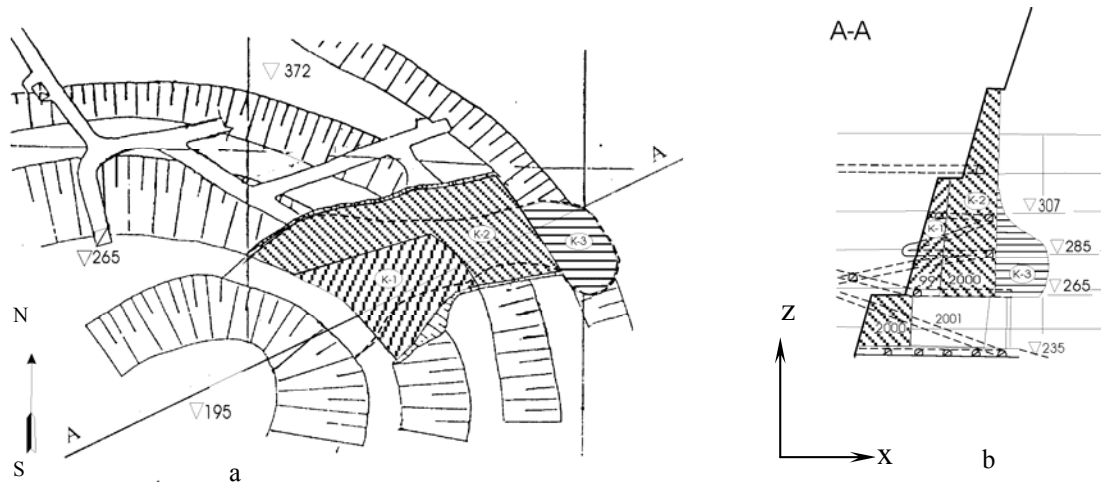


Figure 1. "Aikhal" kimberlite open pit mine, extraction of pit wall reserves:

a – integrated plan; b – profile

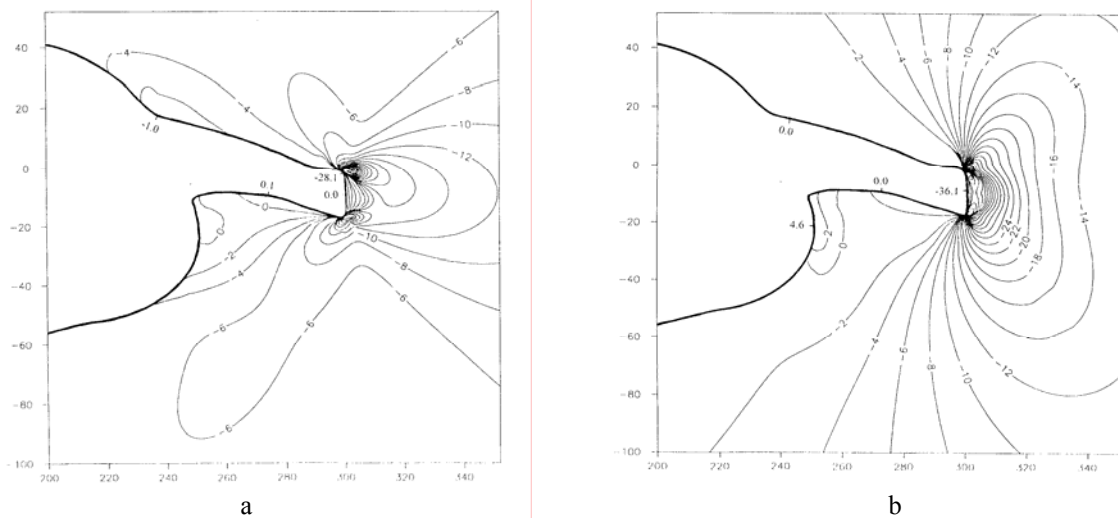


Figure 2. Horizontal stresses in section at level +265 m:

a — σ_x , b — σ_y (MPa).

Figure 2 shows isolines of σ_x and σ_y in the north-eastern pit wall, in horizontal section of level +265 m, after the second stage cutting. Stress isolines in vertical sections after the second and third stage cutting are shown in Figure 3 and 4, respectively.

The state of the north-western wall of the cut is more favourable as against the south-eastern wall. Low compression σ_x is along the wall (no tension zones arise, Figure 2a); σ_y depends on the overlying rock weight (Figure 2b). In the corners at the bottom of the cut, especially near the cross-cut end, the stress concentration is

high (Figures 2b and 3a, b). The walls and cross-cut end of the cut are free from horizontal stresses (Figure 3a, b). In the cross-cut end up, at level $+320 \div +360$ m, a zone of low tension σ_x (<0.1 MPa) appears at a distance 0.5 to 2.5 m from the contour (Figure 3b). The bottom of the cut is free from the horizontal and vertical stresses (Figure 3b, d).

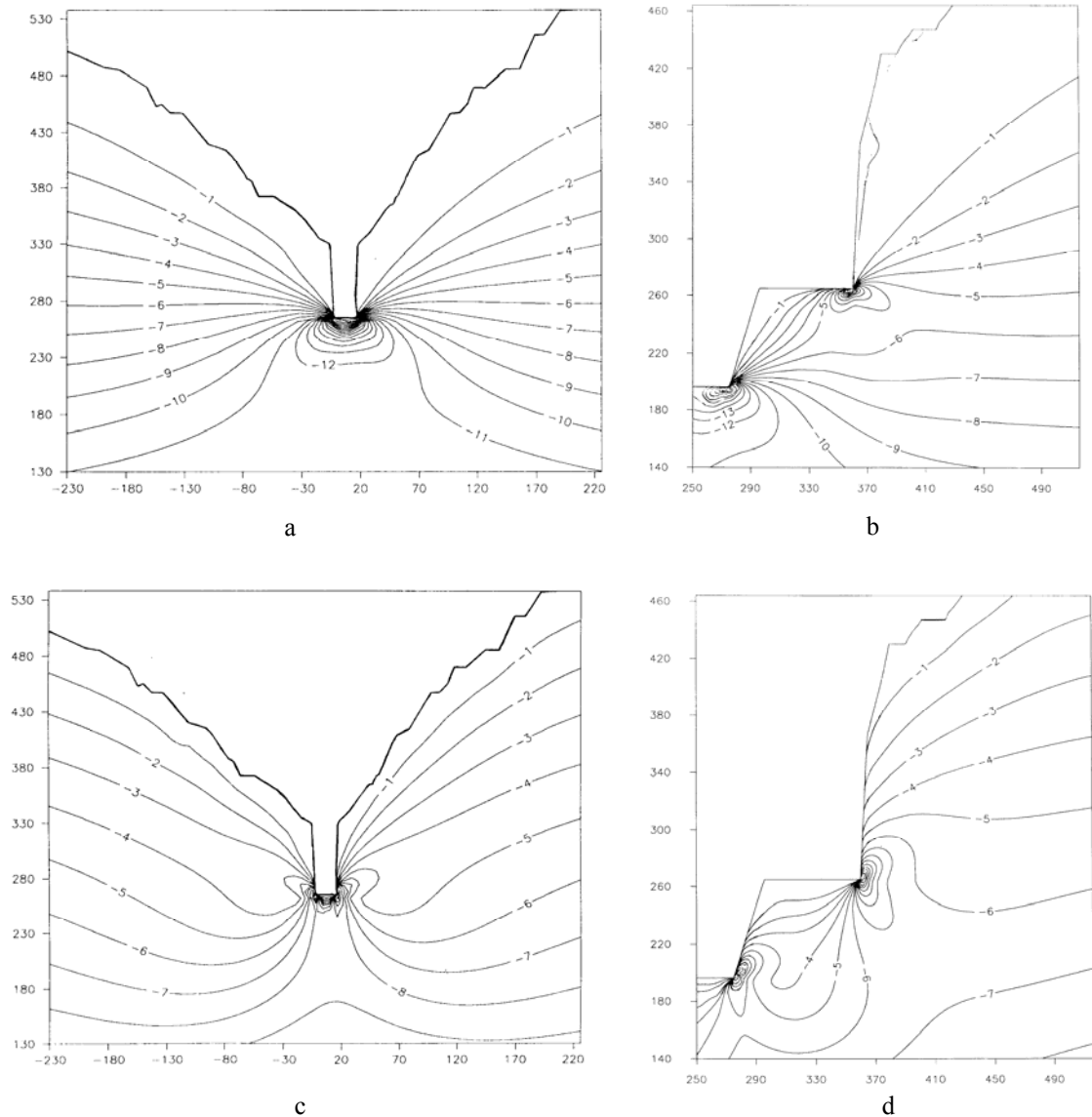


Figure 3. Stresses after the second stage cutting:

a— σ_y ; b— σ_x ; c and d— σ_z (MPa).

The state of the cross-cut end in the north-eastern wall is greatly changed after extraction of the pit wall reserves (third stage cutting, Figure 4). The zone of low horizontal tension stresses (<0.1 MPa) migrates deep down the rock mass (isoline 0 displaces by 30-40 m from the pit wall contour, Figure 4a). In the formed roof of the cut and on the bench at level $+455$ m, the horizontal tension zone occupies $\sim 15-20$ m, the tension stress equals 0.2-0.4 MPa. In the roof of the cut, at level $+300 \div +425$ m, vertical tension stresses arise: isoline 0 is up to 7 m away of the wall contour (Figure 4b).

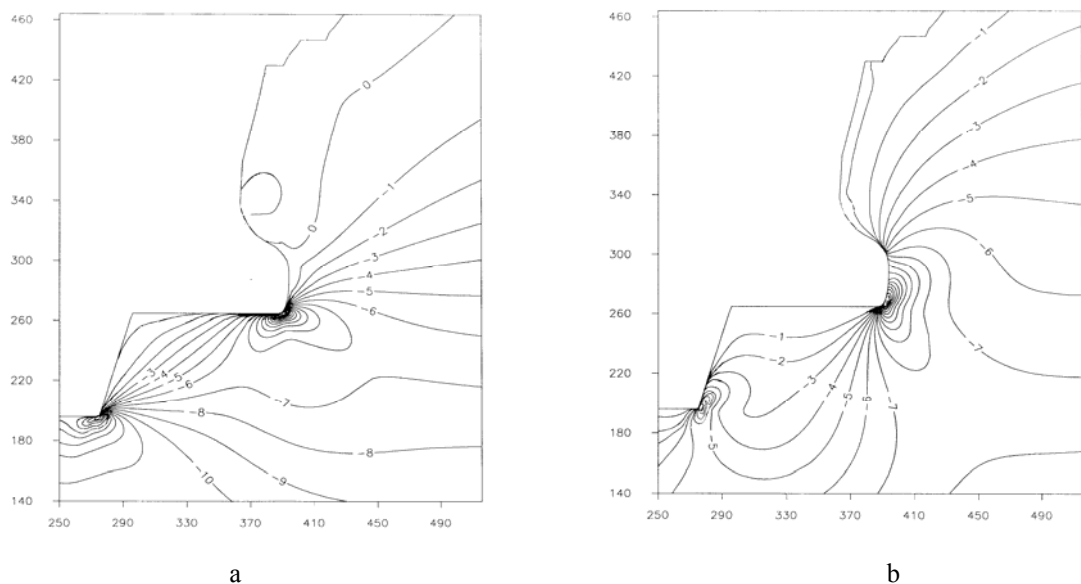


Figure 4. Stresses after the third stage cutting:

a — σ_x , b — σ_y (MPa).

4 Conclusion

Based on the study results, we have made the conclusion that the stress-strain state of the pit wall rock mass, when mining is carried out in the north-east of the open pit, with the formation of vertical slopes, indicates probable uncontrolled caving of rocks in the form of exfoliation and sloughing within the first metres from the contour. Zones of maximum compression stresses are adjacent to the cross-cut end and corners of cuts, and weaken them.

Thus, using the geomodel based on the geological and mining data, we have established the regularities of the stress state formation in the wall of “Aikhal” open pit mine in the course of the second and third stage cutting. The numerical modelling of the stress-strain state enabled detection of the potentially hazardous zones where deformation is probable. Later on monitoring of these zones was implemented to control the state of the open pit wall rocks [1, 2].

References

1. Baryshnikov, V. and Ganchenko, M., Strain control in open pit walls on the transfer from the open to underground mining. in: Contemporary Methods of Rock Mechanics in the Mining Industry, Collected Works. Nesebyr (2003).
2. Baryshnikov, V. and Gakhova, L., Stress State of the Rock Mass in the Vicinity of Underground Mining Workings, Pit Edges, and Below Its Bottom. Journal of Mining Science, 37 (5). 462-465.
3. Baryshnikov, V. and Gakhova, L., Geomechanical monitoring of the condition of pit walls in “Aikhal” open pit mine. in: Proceedings of the 3rd International GEO-Sibir-2007 Congress (Novosibirsk, 2007).
4. Book of Reference on Physico-Mechanical Properties of Host Rocks at Diamond Deposits of Yakutia. Yakutniproalmaz (Mirny, 1984).

STUDY ON MECHANISMS OF ROCKBURST INITIATION AND DEVELOPMENT AND ITS CONSTITUTIVE EQUATIONS

BIN LIU, QUAN-SHENG LIU and YUE-XIU WU

*State Key Laboratory of Geomechanics and Geotechnical Engineering,
Institute of Rock and Soil Mechanics, Chinese Academy of Science, Wuhan, 430071, P.R. China*

Essentially, microseism is considered as the reflection of energy release in the deterioration process of rock mass, which can be used to monitor and predict the position and time of occurrence of rockburst. However, the uncertainty of the mechanism of rockburst initiation and development restricts the application of microseismic monitoring method on rockburst prediction. In this paper, the mechanism of rockburst initiation and development is revealed by theoretical and experimental studies. The criterion of rockburst occurrence is proposed, which includes the failure criterion of rock mass and the criterion of the limit of energy storage. The constitutive equations of the damage and energy consumption stage and failure stage are established for the process of rockburst initiation and development, based on the least energy consumption principle and brittle plastic theory. Through the use of the microseismic monitoring method, the effective theoretical foundation provides the precise prediction of rockburst.

1 Introduction

From plenty of research at home and abroad, the conclusions are listed as the following: the accumulated energy is released in the form of microseism in the limited time, before rockburst. In the different stages before rockburst, the intensity of energy release is variable. Through the monitoring on microseism, the law of energy release can be realized, the stage of stress environment of rock mass can be inferred and the rockburst can be predicted. Through the location of microseism, the position of rockburst can be determined. In essence, microseism is the embodiment of energy release in the process of deterioration of the rock mass. Microseism is regarded as a means of predicting rockburst and is adopted more and more frequently in many countries. There are many inaccurate examples in the prediction of rockburst. The application of microseism monitoring in predicting rockburst is seriously constrained. The main reason is the theoretical insufficiency of predicting rockburst by microseism that means the lack of study on mechanism of rockburst initiation and development.

Presently, there are three methods on the study of the mechanism of rockburst initiation and development: the theory of tendency of rockburst [1], strength theory [2] and energy theory [3]. In the former two theories, the subject of rockburst occurrence is only referred to. The properties of the rupture body are the subject of rockburst occurrence. The mechanism of rockburst occurrence can not be accurately explained. Thus, there are some theoretical drawbacks using these two methods to predict rockburst. The energy theory is based on energy conservation, avoids the theoretical drawbacks of the former two methods and explains the energy problem of rockburst. However, the energy theory presently lacks quantitative indexes. The amplitude and energy storage rate of microseism can not be described in the damage process. Consequently, the deformation and damage zone of rock mass can not be predicted. To overcome the drawback of the classical energy theory, from the point of energy, through the experimental and theoretical analysis, the mechanism of rockburst occurrence and its failure criterion are studied in this paper. Adopting the least energy consumption principle, the damage evolution equation is established in the stage of rockburst initiation. The constitutive equation of rockburst is established and the theoretical foundation is provided for the precise prediction of rockburst through microseism.

2 Study on the criterion of rockburst occurrence

2.1 Integral failure criterion

Rockburst is a phenomenon of integral failure. This integral failure can not be calibrated efficiently with the current failure criterions. Heping Xie[4] analyzed the energy change in the process of deformation and damage of rock element, through definition the energy damage variable. And the relationships between energy dissipation, energy release and integral failure were described qualitatively.

Integral failure criterion:

$$(\sigma_1 - \sigma_3) [\sigma_1^2 + \sigma_2^2 + \sigma_3^2 - 2\mu(\sigma_1\sigma_2 + \sigma_2\sigma_3 + \sigma_1\sigma_3)] = \sigma_c^3 \quad (1)$$

This integral failure of rock can be calibrated with this integral failure criterion. And it is consistent with the main ideology of analysis for unstable failure from the point of energy based on the damage principle. Whether this criterion is the necessary and sufficient condition of rockburst occurrence needs to be studied advanced.

2.2 Experimental study on criterion of rockburst occurrence

Laboratory experiment study was done for the granite samples with a tendency of rockburst. Conventional triaxial compression tests were done under different confining pressures of 0, 5, 10, 20, 30, 40, 50 MPa. The compression curve under each confining pressure is shown in Figure 1. From the test, the uniaxial compressive strength of granite sample is 171 MPa, its elastic modulus is 41.8 GPa and its Poisson ratio is 0.21.

The computed integral failure strength under different confining pressure is compared with the limit failure strength obtained by experiment which is shown in table 1. the related conclusions are:

1) Only under the uniaxial compression, this criterion is the necessary and sufficient condition of rockburst occurrence. The physical meaning of integral failure strength is that: before rockburst occurrence, there is damage degradation inside the forced material. When the integral failure strength is satisfied and the integral failure structure is formed, there is no more degradation.

2) There is some difference between limit failure strength and integral failure strength. And this difference increases with the increasing of confining pressure. According to the physical meaning of integral failure strength, there is only the accumulation of elastic energy without energy dissipation. So, this stage is the stage of energy concentration. Under a certain confining pressure, after degradation of material, the integral failure structure is formed and the energy is still small to cause rockburst. So, energy concentration is needed to provide enough elastic energy for rockburst. When the elastic energy reaches some limit value, rockburst occurs. That is the limit energy storage criteria of rockburst whose mathematical expression is equation (2)

$$U^e = [U]_{\text{limit}} \quad (2)$$

3 Study on mechanism of rockburst initiation and development

3.1 Micro-damage characteristic of rockburst

In August 1998, there was rockburst at western deep levels gold mine, Witwatersrand Brasin, South Africa. After rockburst, the rockmass in the damage zone was scanned using SEM and the related photoes are shown in Figure 2.

With SEM, the tensile damage is detected (in the fault gouge)[5]. The one indicated by the white arrow, fractures parallel to the main fracture approximately and subconchoidal fractures represent the characteristic of

brittle damage. But, this macro representation of rockburst deformation is the result of shear damage (there are fault gouge and potential sliding displacement in the main shear fracture). Grodner(1996) indicated that fracture and crack propagation represented the local stress field at the moment of failure. This indicated that the failure structure had been formed by brittle tension of crack at the moment of rockburst damage. Because of the rockburst damage, the stress field will redistribute which causes another failure mode --- macro shear failure. This failure mode conceals the initial mechanism of rockburst failure.

Thus, it can be seen that there are two failure mode from the beginning of force to the accomplishment of rockburst. The first one is brittle failure and there is no plastic energy dissipation in this process. While in the second one, there is plastic energy dissipation.

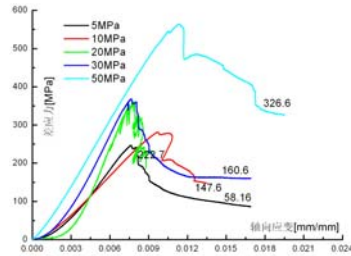


Figure 1 stress-strain curve of granite

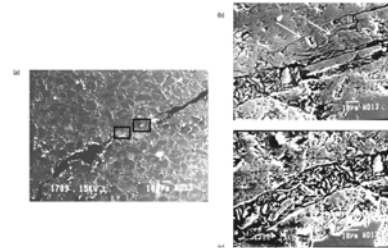


Figure 2 SEM photograph of rockburst at western deep levels gold mine, Witwatersrand Brasin, South Africa

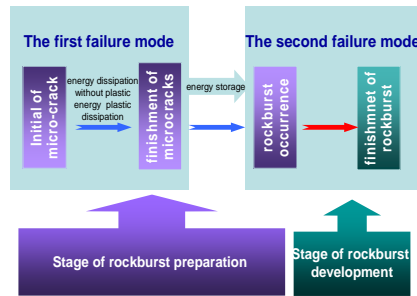


Figure 3 schematic diagram of mechanism of rockburst initiation and development

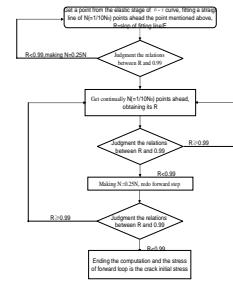


Figure 4 schematic diagram for calculation of crack initial stress

3.2 Presentation of mechanism of rockburst initiation and development

Combining with the results of SEM and laboratory experiment, mechanism of rockburst initiation and development is obtained which is shown in Figure 3. the stage of rockburst initiation begins with the generation of micro-cracks caused by force, gets the satisfaction for limit energy storage criteria and ends up with rockburst occurrence. A stage of energy dissipation without plastic energy dissipation is experienced. In this stage, degradation of rock mass is caused by the propagation of microcracks. When the integral failure strength is reached, propagation of microcracks develops to be a fracture network. Under confining pressure, rockburst doesn't occur immediately with this fracture network. Only when the elastic energy provided by the forced system satisfies limit energy storage criteria, rockburst occurs. Once that happens, the second failure mode is experienced which is different from the former mode. There is plastic energy dissipation and it causes that the macro failure mode of system is represented by shear failure mode.

4 Establishment of constitutive equations of rockburst

According to the mechanism of rockburst initiation and development, from the point of energy, constitutive equations for different stages are established respectively. Adopting the least energy consumption principle,

damage evolution equation for the first failure mode are established and its reliability is verified by the granite experiment. From the point of energy, constitutive equation for energy concentration stage is established. That is to say that constitutive equation for the whole stage of rockburst initiation is established. The deformation state after the second failure mode is simplified to be perfectly plastic and constitutive equation for the whole process of rockburst is established.

4.1 Study on constitutive equation for the stage of rockburst initiation

1) Establishment of damage evolution equation for the first failure mode

The least energy dissipation principle: In any process of energy dissipation, under a certain constraint conditions, things develop to the direction where the energy dissipation is least. The constraint conditions are the control equations and related definite conditions in the expression of energy consumption rate. The direction where the energy dissipation is least means that energy dissipation rate is the minimum of all the energy dissipation rate at any moment in the process of energy dissipation.

In the stage of first failure mode, energy dissipation is caused by the propagation of fracture and damage is used to describe this mechanism of energy dissipation. The expression of energy dissipation rate is equation (3).

$$\dot{\varphi}(t) = \frac{\dot{D}(t)}{[1-D(t)]^2} \frac{1}{E} [\sigma_1^2 + \sigma_2^2 + \sigma_3^2 - 2\mu(\sigma_1\sigma_2 + \sigma_1\sigma_3 + \sigma_2\sigma_3)] \quad (3)$$

Constraint conditions:

$$F(\sigma_1, \sigma_2, \sigma_3) = (\sigma_1 - \sigma_3) [\sigma_1^2 + \sigma_2^2 + \sigma_3^2 - 2\mu(\sigma_1\sigma_2 + \sigma_1\sigma_3 + \sigma_2\sigma_3)] - \sigma_c^3 = 0 \quad (4)$$

According to the least energy dissipation principle:

$$\frac{\partial(\dot{\varphi}(t) + \lambda F)}{\partial \sigma_i} = 0 \quad (5)$$

The damage evolution equation:

$$D = 1 - e^{-\lambda_1(\sigma_1 - \sigma_3)\varepsilon_1 - C} \quad (6)$$

Where, λ and C are the material parameters which are determined through the uniaxial stress-strain curves. Through fitting the experiment data of uniaxial compression, it can be obtained that $\lambda_1 = 5.33147E-5$, $C = -1.881932$.

Under different confining pressure, the whole failure strength obtained by whole failure criterion is compared with the crack initial stress obtained by experiment (obtained by schematic diagram Figure 4). The result is shown in table 1. With the increasing of confining pressure, the growth rate of crack initial stress of granite is more than that of whole failure strength. When confining pressure reaches a certain value, crack initial stress is larger than the whole failure strength. Because crack initial stress and whole failure strength are the starting point and ending point of the first failure mode respectively, the obtained damage evolution equation loses its physical meaning when crack initial stress is larger than the whole failure strength. Thus, when the confining pressure reaches a certain value $[\sigma_3]$ (for the experiment granite, it is 26.583Mpa.). There will be no first failure mode in the process of rockburst initiation and the established damage evolution equation can not be applied. And this process is a process of elastic energy storage, not of energy dissipation. Under low confining pressure, the application of damage evolution equation is verified through the comparasion of crack initial stress in theory with that in experiment. From table 1, the maximum error of crack initial stress is 9.5%. With the increasing of confining pressure, critical damage caused by whole failure structure decreases which is consistent

with the former research results. Thus, the application of damage evolution equation for the first failure mode is verified. After rockburst, the brittle state is experienced firstly and then the perfectly plastic state is experienced.

Table 1 comparasion of crack initial stress of granite in theory with that in experiment

Confining pressure (MPa)	0	5	10	20	30	40	50
Limit strength	171	215.3	282.5	408.2	440.8	514.5	575.6
Whole failure strength	171	173.9	176.7	181.9	186.7	193.2	203.4
Crack initial stress in experiment	75.7	100.3	127.3	160.1	198.3	210.6	—
Crack initial stress in theory	71.3	96.3	136.5	146.1	—	—	—
Error (%)	5.8	4.1	6.7	9.5	—	—	—
Maximum damage value	0.99	0.86	0.53	0.31	—	—	—

2) Determination of limit energy storage criteria and elastic module for the stage of energy storage

In the stage of energy storage: there is no any energy dissipation and it is a stage of elastic deformation. the capacity of energy storage depends on the confining pressure. Under different confining pressure, the deformation property of rock mass is determined by the critical damage value.

Mathematical expression of limit energy storage criteria is equation (7)

$$G(\sigma_1, \sigma_2, \sigma_3) = 0 \quad (7)$$

Expression of elastic module is equation (8)

$$E = (1 - D_c) E_0 \quad (8)$$

Where: D_c is the critical damage value, under different confining pressure. It can be obtained by the fitted relationship between it and confining pressure.

3) Constitutive equation for rockburst initiation

According to the study on mechanism of rockburst initiation and development, in the stage of rockburst initiation($G(\sigma_1, \sigma_2, \sigma_3) \leq 0$), including the first failure stage and energy storage stage, the research for the stage of rockburst initiation of granite is integrated and the related constitutive equation is obtained, expressed in equation(9).

$$\{d\varepsilon\} = [C]\{d\sigma\} \quad (9)$$

Where,

$$D = \begin{cases} 0 & 0 < \sigma_1 < \sigma_{fi}, \sigma_3 \leq [\sigma_3] \\ 1 - e^{-\lambda(\sigma_1 - \sigma_3)t - C} & \sigma_1 > \sigma_{fi}, F(\sigma_1, \sigma_2, \sigma_3) \leq 0, \sigma_3 \leq [\sigma_3] \\ 1 - D_c & \sigma_1 > \sigma_{fi}, F(\sigma_1, \sigma_2, \sigma_3) > 0, \sigma_3 \leq [\sigma_3] \\ 0 & \sigma_3 > [\sigma_3] \end{cases}$$

4.2 Constitutive equation for the stage of brittle failure[6]

When $G(\sigma) \leq 0$ and $G(\sigma + D\Delta\varepsilon) > 0$,

$$\left\{d\sigma_{ij}\right\} = \alpha [D] \left\{d\varepsilon_{ij}\right\} + \Delta\lambda \left\{\sigma_{ij}\right\} + (1 - \alpha) [D_{ep}] \left\{d\varepsilon_{ij}\right\} \quad (10)$$

Where, α is determined by $G(\sigma + \alpha D \Delta\varepsilon) = 0$.

$\Delta\lambda \left\{\sigma_{ij}\right\}$ is increment of stress drop corresponding to the process of stress drop.

4.3 Perfectly plastic stage

$$\left\{d\sigma_{ij}\right\} = ([D] - [D]_p) \left\{d\varepsilon_{ij}\right\} \quad (11)$$

Equation (9), (10) and (11) are the constitutive equations for the whole stage of rockburst initiation.

5 Conclusions

1) Combined with the limitations of the classical strength criterion of rockburst, the necessary conditions of rockburst occurrence is verified based on experiment. Based on this, the limit energy storage criteria of rockburst occurrence is proposed.

2) According to the SEM photos and the results of laboratory experiment, the mechanism of rockburst initiation and development is obtained: the stage of rockburst initiation begins with the generation of micro-cracks caused by force, gets the satisfaction for limit energy storage criteria and ends with rockburst occurrence. Stages of energy dissipation without plastic energy dissipation, energy storage and brittle plastic failure with the dominated plastic energy dissipation are experienced.

3) Based on the mechanism of rockburst initiation and development, the constitutive equations corresponding to different stages of rockburst initiation and development are established. An effective theoretical foundation is provided for the precise prediction of rockburst through microseism.

Acknowledgement

The financial support from The National Natural Science Foundation of China under Grant No. 40638040 and No. 90510019 is gratefully acknowledged.

References

1. Pan, Y.S. Study on Rockburst by Equivalent Material Simulation Tests . Chinese journal of Geotechnical engineering, 1997, 19(4). 49-56.
2. Yin, Y.Q. and Zheng, G.T. A cusp type catastrophic model of fault earthquake. Chinese journal of geophysics. 1988, 31(6). 657-663.
3. Tan, J.K. Rockburst. Case Record. Theory and Control. Proceedings of the international symposium on engineering in complex rock formations, 1986, 33-37.
4. Xie, H.P. Criteria for strength and structural failure of rocks based on energy dissipation and energy release principles. Chinese Journal of Rock Mechanics and Engineering, 2005, 4(17). 3003-3010.
5. Stewart, R.A. and Reimold, W.U. The nature of a deformation zone and fault rock related to a recent rockburst at Western Deep Levels Gold Mine, Witwatersrand Basin, South Arica. Tectonophysics 2001, (337). 173-190.
6. Zheng, H. and Ge, X.R. Analysis principle for rock mass with brittle-plasticity and its applications. Chinese Journal of rock mechanics and engineering, 1997, (16). 8-21.

RESEARCH ON THE MICROCOSMIC MECHANISM OF COAL-GAS OUTBURST

LIN HONG, JI-REN WANG and CUN-BAO DENG

College of Safety Science and Engineering, Liaoning Technical University, Fuxin, 123000, China

DA-GUO WANG

Center for Material Failure Modeling Research, Dalian University Dalian 116622, China

In order to obtain the mechanism of the coal-gas outburst, the quantum theory is applied to study the mutual absorption between the coal and the methane molecule. The absorption is a physical process, with an energy of 1.16KJ/mol, which can be obtained by the density functional theory. The damage of the rock results from the influence of mining stress and the subsequent changes around the mining face, which produces electromagnetic waves with a wide frequency range. The intergrowth system, which is generated by the absorption, changes from a ground state to an excited state after it absorbs the electromagnetic wave energy. Then, the methane molecule changes from an absorption state to a free state and a large number of molecules escape from the coal pores increasing the pressure. As a result, the coal-gas outburst is more likely occur at the flimsy location.

1 Introduction

Coal and gas outburst is one of the most harmful disasters which can occur in a coal mine. The disaster can damage the equipment, hurt the workers, and even cause gas explosion and coal dust explosion. For example, the gas explosion at Sunjiawan coal mine of Fuxin Coal Mine Group claimed 214 mans' lives. The explosion was caused by coal-gas outburst. The dangers of coal-gas outburst are very serious, and many measures are taken in coal mines to prevent outbursts. However, outbursts are a common occurrence. The main cause of the mechanism of coal-gas outburst is not exactly known, and the measures against outburst can't eliminate the dangers completely.

The coal-gas outburst mechanism has been researched at macroscopic level by mechanics methods for some time. However, because of the complexity of the mechanism is still not known exactly. Many people hypothesize that the burst is caused by the gas pressure and coal structure; and it is the release process of the in-situ stress and the gas potential energy. Although, this idea has not been sufficiently researched.

In this thesis, the coal-gas outburst is researched by quantum mechanics and the quantum chemistry calculation method. The essence of coal-gas outburst is revealed, and it can give theoretical instruction to people.

2 Gas adsorbed by coal

2.1 The adsorption model of coal and gas

The gas in the coal mine tunnels comes from the coal seam and the surround rock. The coal is porous media with massive porosity and specific surface, and it can adsorb a lot of gas. While coal forming, there were a lot of gas produced. Some of the gas went into the air, and the other was stored in the coal seam. The main ingredient of gas is methane. And the coal is organic macromolecule, which chemical structure is composed of

many chemical bonds and functional groups, such as methyl, ethyl and ethenyl. The coal molecule is amorphous having side chain and polycyclic aromatic hydrocarbon linked by bridge bond [1]. For the similarity of coal molecule, the coal molecule is simplified as figure 1 to simplify the calculating process, and it has one function group and has the same chemical property of coal molecule. The molecule system that coal molecule adsorbing the CH₄ molecule is optimized by density functional theory (DFT) [2] at B3LYP/6-31G calculating level. And the vibration frequency and molecule parameter of the function group is gained, such as bond length, bond angle and dihedral angle. All of above is calculated by Gaussian03 program, and the molecule is built by Gauss View program.

2.2 Calculated result of adsorption equilibrium system

After calculation, the adsorption model is gotten as figure 1, and the vibration frequency as table 1.

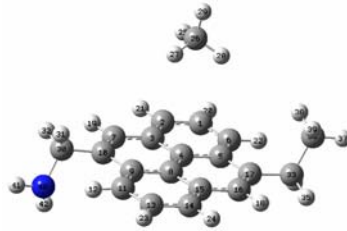


Figure 1 Geometrical equilibrium conformation of coal molecule adsorption with CH₄ molecule

Table 1. Vibration frequency of CH₄ molecule after adsorption equilibrium

parameters	ρ (CH ₄)	ν (CH ₄)	ω (CH ₄)
frequency (cm ⁻¹)	23	26	49

where: ρ is swaying vibration, ν is expansion vibration and ω is curving vibration.

The adsorption energy can be calculated as follow:

$$E_{\text{ads}} = E_{\text{M}} + E_{\text{CH}_4} - E_{\text{CH}_4/\text{M}} \quad (1)$$

E_{ads} is adsorption energy while the adsorption between coal molecule and CH₄ molecule get equilibrium status. E_{M} is the energy of coal molecule without CH₄ molecule. E_{CH_4} is the energy of CH₄ molecule before be adsorbed. $E_{\text{CH}_4/\text{M}}$ is the total energy after adsorbing.

According to the calculating, E_{CH_4} is -40.475524Hartee, E_{M} is -788.723014Hartee, and $E_{\text{CH}_4/\text{M}}$ is -829.198096Hartee. Therefore, E_{ads} is 1.16KJ/mol through formula (1), so adsorption between coal molecule and CH₄ molecule is physical adsorption.

3 The electromagnetic wave in coal mine

Before mining, the coal and rock are static, and the stress is at balancing status. When mining, some of the coal and rock are taken out of the mine, therefore there are many stress concentration regions around the tunnel. At the regions, the stress is higher than before, and the coal and rock are distorted and fracture. The research indicated that the distorting and fracturing of coal and rock can cause electromagnetic wave and infrared [3]. ZHU Yuanqing [4] considered that the distribution movement of electric charge in the crack tip end being associated with rock fracture propagation produces electromagnetic emission was brought up, and gained that the highest range of that electromagnetic wave is 1.5MHz by experiment method. CAO Huixin [5] studied the electrical signal, magnetic signal and acoustic signal produced by rock fracture with uniaxial stress, and got that the frequency range of electromagnetic emission and acoustic signal is 0~20kHz. QIAN Shuqing [6] discovered

that the electromagnetic emission band produced by rock fractured is VLF(20Hz~10kHz), MF(530kHz, 650kHz, 1.6MHz and 2.3MHz), HF(5MHz, 16MHz) and VHF(95MHz). GUO Ziqiang [7] analyzed the frequency characteristic by electric quadrupolar model, and calculated that the frequency range of electromagnetic emission varied from about 50kHz~1MHz.

The theory that the coal and rock fracturing can produce electromagnetic wave with width frequency means it has theory base to research the microcosmic mechanism of coal-gas outburst.

4 Microcosmic mechanism of coal-gas outburst

4.1 The quantum chemistry theory of gas desorbed from coal

For the adsorption between coal and gas is physical adsorption and according to the quantum chemistry theory, the energy of molecule changes after the system absorbing electromagnetic wave, and transits between different energy levels. To the intergrowth molecular system that coal molecule adsorbs CH₄ molecule, when the CH₄ molecule absorbs the electromagnetic wave, its energy increases, and CH₄ molecule changes from ground status to excited status. Thus the CH₄ molecule changes from adsorption status to free status, and a large of gas appears.

The energy of the intergrowth molecular system of coal adsorbing CH₄ molecule stably can be calculated as follow:

$$E = E_e + E_r + E_v + E_t + E_n + E_i \quad (2)$$

where: E_e is electron energy, E_r is molecule rotation energy, E_v is molecule vibration energy, E_t is molecule parallel moving energy, E_n is nucleus internal e vibration energy and E_i is group rotation energy.

When the intergrowth molecular system of coal adsorbing CH₄ molecule absorbs the energy of electromagnetic wave, CH₄ energy can transits from E_1 energy level to E_2 . For the intrinsic moving energy of molecule can be quantify, it can be learnt that the energy difference between that energy levels is the electromagnetic wave frequency, calculating as follow:

$$\nu = (E_2 - E_1)/h \quad (3)$$

The Schrödinger equation of molecule with nucleus and electron is as follow:

$$\hat{H}(R, r) = E(R, r) \quad (4)$$

where: R is the coordinate of moving nucleus and r is the coordinate of moving electron.

The Hamiton operator ignoring the interaction between spin and orbit can be as follow:

$$\hat{H} = -\sum_N \frac{\hbar^2}{2m_N} \nabla_N^2 - \sum_e \frac{\hbar^2}{2m_e} \nabla_e^2 + V_{NN} + V_{ee} + V_{eN} \quad (5)$$

In the express, the first part means energy of moving nucleus, and the second part means energy of moving electron, and V_{NN} is the electrostatic interaction between nucleuses, V_{ee} is the electrostatic interaction between electrons, V_{eN} is the electrostatic interaction between nucleus and electron.

According the speed of electron is 3 orders of the speed of nucleus, Born and Oppenheimer separated the upper equation as follow neglecting several parts of it:

$$\left[-\sum_N \frac{\hbar^2}{2m_N} \nabla_N^2 + V_{NN} + E_e(R) \right] \varphi_N(R) = E \varphi_N(R) \quad (6)$$

$$\left[-\sum_e \frac{\hbar^2}{2m_e} \nabla_e^2 + V_{ee} + V_{eN} \right] \varphi_e(R, r) = E_e(R) \varphi_e(R, r) \quad (7)$$

Formula (6) including parallel moving energy, vibration energy and rotation energy distributes the movement of molecule after absorbing electromagnetic wave, and formula (7) distributes the movement of electrons after absorbing electromagnetic wave.

4.2 Mechanism of coal-gas outburst

The stress around the work face changes for earthquake and mining in coal mine. Therefore the coal and rock mass fracture. The fracture brings electromagnetic wave with wide frequency. The energy of the adsorption CH_4 increases after absorbing the electromagnetic wave with the frequency of $23\sim 61\text{cm}^{-1}$, and the molecule changes from ground status to excited status. For the adsorption energy is very low, the CH_4 molecule can be desorbed from coal easily. And there are a great of CH_4 molecule go out to the pore, and make the gas pressure increase. That is the cause of coal-gas outburst.

5 Conclusions

The attraction between coal molecules and CH_4 molecules has been analyzed by quantum chemistry theory, and it shows that:

- (1) The attraction between the coal molecule and CH_4 molecule is physical attraction by density functional theory (DFT), and the energy of the attraction is 1.16KJ/mol .
- (2) The stress around the work face changes for earthquake and mining in coal mines causing the coal and rock mass to fracture. The fracture causes electromagnetic waves with a wide frequency. The electromagnetic wave can be absorbed by the intergrowth molecular system, and make the system change from a ground state to excited state.
- (3) The vibration frequency range of methyl molecule in the intergrowth molecular system is $23\sim 61\text{cm}^{-1}$. After the absorption of the electromagnetic wave, the methyl molecule desorbs from the surface of coal, and may cause coal-gas outburst.

Acknowledgements

The author would like to thank the financial support by the National Natural Science Foundation of P. R. China (Grant Nos. 50574047, 50809008)

References

1. Yu, J. S. Coal Chemistry. Beijing, Metallurgical Industry Press, 2003.
2. Lin, M. H. Quantum Chemistry Calculating Method. Beijing, Science Press, 2004.
3. Gong, Q. Relationship between frequency of electromagnetic radiation induced by rock fracture and the elastic parameters. Chinese Journal of Geophysics, 2006, 49(5). 1523-1528.
4. Zhu, Y. Q. A study of mechanism on electromagnetic emission associated with rock fracture. Chinese Journal of Geophysics, 1991, 34(5). 595~601.
5. Cao, H. X. Experiment Study of the Electrical Signal. Magnetic Signal and Acoustic Signal of Middle and Supper Length Band while Rock Fracture. Acta Seismologica Sinica, 1994, 16(2). 235~241.
6. Qiang, Q. S. Experiment Study of the VLF, MF, HF and VHF Frequency Properties of Electromagnetic Emission Associated with Microscopic cracking in Rocks. Acta Seismologica Sinica, 1996, 18(3). 173~177.
7. Guo, Z. Q. Frequency Properties of Electromagnetic Emission Associated with Microscopic cracking in Rocks. Chinese Journal of Geophysics, 1995, 38(2). 221~225.

EXPERIMENTAL STUDY ON WATER-INRUSH MECHANISM OF TUNNELS IN KARST AREA

LI-PING LI, SHU-CAI LI, SHU-CHEN LI and QING-SONG ZHANG

Geotechnical & Structural Engineering Research Center of Shandong University

YAN-HUI GE

Department of Civil Engineering, Shandong Jiaotong University

Jinan, 250023, P.R China

The instability of karst ground water under the disturbance of external force always results in the geological hazard of water outburst and mud gushing. It is a dynamic damage phenomenon of water and mud flowing to the tunnel face with high speed. Based on the water-rock interaction mechanism in karst tunnel, the mechanism of water inrush has been analyzed by several model tests and the theory of karst geology, engineering hydraulics and rock mechanics. It is shown that the occurrence and formation of water outburst has two steps. The first step is that the karsts water and its pressure have softening and dissolution effect on rock. It has been qualitatively studied through hydraulic fracturing experiment on rocklike material. The second step is that the water flow and its pressure have passageway expanding and flowing yield controlling effect on water inrush. It has been analyzed through the similarity test. Based on the failure characteristics of water inrush experimental tests, a mechanical model of water inrush is put forward, and the analytic solution of critical protection thickness of rock mass preventing water inrush is given. This model can be used to the calculation of safety rock mass thickness.

1 Introduction

Water inrush and mud gushing in karst areas is a dynamic damage phenomenon due to the rapid transformation of the rock condition during tunnel excavation. With characteristics of large destructibility, it brings unmeasured loss in tunnel construction at home and abroad [1-3].

The inrush in tunnels is the result of the double effect of karst water and its pressure on rock, however at present research on the inrush mechanism is limited to the latter, the pressure effect [4-8], and little test research has been done. So the current situation is that there are many inrush theories, and little attention is paid on the mechanism research of the whole process of tunnel inrush in karst area. So in this paper, by analyzing the mechanisms of pre-and post tunnel inrush respectively through hydraulic fracture test and inrush simulation test, based on the water-rock interaction, some references have been suggested for prevention work against inrush and mud gushing in karst tunnels.

2 Experiment Analysis on Potential Storage Mechanism of Karst Water-inrush

Rocklike material, which is used as simulated material, is similar to sandstone in its properties. Before the test, 10 groups of standard sandstone test blocks have been made by rocklike material, and 5 groups are taken out and immersed in water for 48 hours after maintenance. The differences of fracture characteristics and fracture pressure under soaking and non-soaking conditions have been analyzed through a hydraulic fracturing test on every test block, and the result will contribute to the analysis of the mechanism of karst water and its pressure before rock failure. The test result is given in table-1.

Table 1. Testing values of hydraulic fracture without pressure around for rock samples in lab

Group Number	Compressive Strength /M Pa	Fracture pressure /M Pa	
		Dried Block	Saturated Block
1	48.99	2.32	1.22
2	45.63	2.28	1.19
3	50.20	2.35	1.20
4	51.32	2.42	1.24
5	49.33	2.33	1.21

The test blocks are softened by water and hydraulic pressure through weak part according to the test data and irregular fracture plane appearance, and the erosion leads to changes of internal structure and low crack resistance.

There is a relation between strength of dried block and saturated block under the dissolving condition (eq-1).

$$\sigma_w = \eta k_w \sigma_0 \quad (k_w < 1) \quad (1)$$

Where η depends on the rock dissolving condition, k_w is rock softened coefficient which mainly depends on rock lithology .

The karst development origins from the erosion and expanding effects of karst water on narrow cranny in the rock, and changes of effective stress state and long-term water-rock interaction result in the weak plane which becomes the potential inrush channel.

3 Experiment Analysis on Water-inrush Instability Mechanism

3.1 Similarity Test Design

The interaction mechanism between karst water pressure and water-inrush channel is analyzed by the simulation test on different water-inrush model .In the test, rocklike material is filled in the fractured block and pressure water is injected after material solidification, the mixture of fine sand, clay and gravel has been adopted as simulation material of fault and karst conduit which intersect with tunnel.. Model test design and its device are shown as Figure 1.

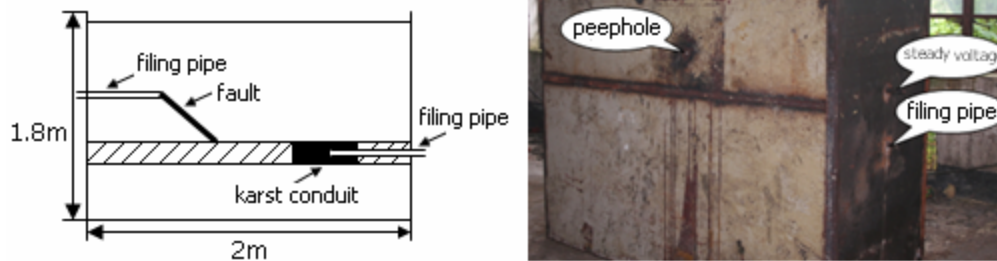


Figure 1 Model test design and its device

In the test process, miniature drilling rig of long arm has been adopted to simulate excavation of tunnel, the filing pipe intersected with fault keep constant of 0.5MPa, water inrush does not happen when the fault appears for the filing medium of water blocking performance until the sustained tunnelling. Then, the water pressure of filing pipe decreases to zero and the tunnelling stops, the water pressure of filing pipe intersected with karst conduit increases from zero to 1.6MPa, water inrush happens for the whole rock mass rupture of tunnel face.

3.2 Analysis on Experiment Observation

During the simulation test of water inrush of fault, pressure water exudates from the fault with faster flowing speed and more filling medium as the tunnelling continues, finally the water stream is clear with uniform speed when most of filled material is scoured out. In the simulation of tunnel excavation, water inrush inflow is raised rapidly when tunnel face is suddenly pushed out by high pressure water with the destruction state (Figure 2).



Figure 2 Failure model of tunnel face

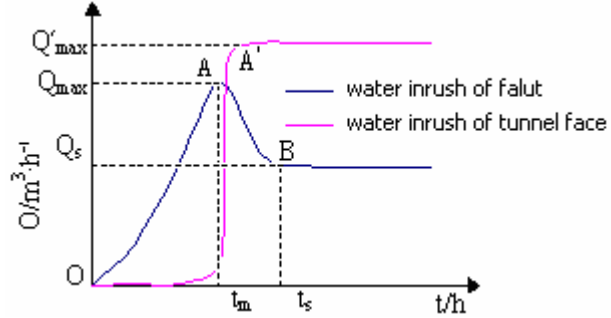


Figure 3 Correlation curve for water quantity

Mechanical function of flow in the inrush on the erosion diameter extension is reflected by the differences of the water-time curve of inflow between water inrush of fault and water inrush of tunnel face, as the Figure 3, the mechanical property of weak plane inrush that water inrush channel is gradually widened by the scouring effect is reflected by the trend of gradual increase of quantity in OA segment.

Analysis on the Test Result

3.3.1 Analysis on Water-inrush Instability Mechanism

Based on the test results, the mechanical property of water inrush channel gradually widened by the scouring effect can be described by the following mechanical model (as Figure 4).

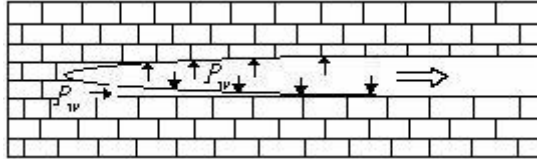


Figure 4 Mechanical model of passageway expanding by flow scouring

It is assumed that weak plane channel is treated as the ultra thin cuboid cranny, and at a certain time the crevice is with the dimensions of l, d, h , water irruption quantity is q , then flowing speed in the inrush v_τ is

$$v_\tau = q / ldh \quad (2)$$

Pressure applying on inrush channel face p_r is

$$p_r = p_w - \gamma v_\tau^2 / 2g \quad (3)$$

Eq-2 is substituted into eq-3, there is

$$p_r = p_w - \frac{\gamma q^2}{2gl^2d^2h^2} \quad (4)$$

In eq-4, obviously there is $\frac{\gamma q^2}{2gl^2d^2h^2} > 0$, so $p_r < p_w$. Inevitably there are several fracture groups around the inrush channel (Figure 6) and its water pressure is p_r . The still water in the cranny is connected with the power source in the inrush channel, and its karst pressure is p_w . So there is the pressure difference (eq-5).

$$\Delta p = p_w - p_r \quad (5)$$

And the inrush channel is enlarged when rock fractures due to the high flowing speed.

As for water inrush in karst area, the hydraulic energy at inrush point is fully consumed at overcoming resistance on the channel face and transformed into water flow energy, according to Bernoulli Energy Equation

$$z_1 + \frac{p_1}{\gamma} + \frac{v_1^2}{2g} = z_2 + \frac{p_2}{\gamma} + \frac{v_2^2}{2g} + \Delta h' \quad (6)$$

Where $\Delta h'$ is water head loss along the way, z_1 、 p_1 、 v_1 is respectively the elevation, water pressure and water flowing speed of the inrush surface, then $p_1 = p_w$, $v_1 = 0$; z_2 、 p_2 、 v_2 is respectively the elevation, water pressure, water flowing speed of the inrush nozzle and $p_2 = 0$. It is assumed that $z_1 = z_2$, then

$$v_2^2 = 2g \left(\frac{p_w}{\gamma} - \Delta h' \right) \quad (7)$$

$$v_2 = [2g(P_w / \gamma - \Delta h')]^{1/2} \quad (8)$$

As the consequence, fracture water pressure p_w determines the water irruption quantity q and shows a power control effect on it.

3.3.2 Analysis of Water-inrush Instability Mode

The destruction mode is often the extrusion of the whole rock (Figure 4) when there is no significant weak plane structure. Fracture inrush of the whole water-proofing rock occurs when release of excavation pressure induces the instability of water bearing structure system in safety protection thickness, and it could be classified into two modes according to the fracture thickness.

1. Shear Fracture

Shear fracture is a mode that the rock is entirely pushed out when the columnar contact between surrounding rock and water-proofing rock is not strong enough to resist the karst pressure (Figure 5).

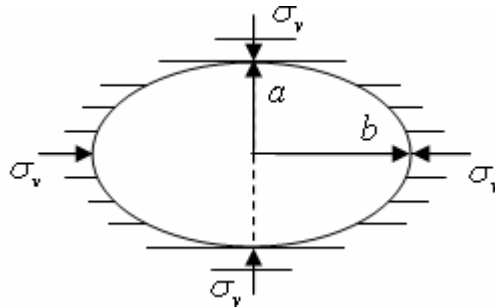


Figure 5 Shear failure model of elliptical cylinder for water inrush

It is not reasonable to establish the water inrush model of circular plate when the thickness of water-proofing rock is too large. Take the elliptical cylinder for example, the shear failure often occurs along the interface between water-proofing rock and surrounding rock. Considering the limit equilibrium between total shear force and shear resistance, the total shear force along the interface

$$F = p_w S = p_w \pi ab \quad (9)$$

In the eq-9, p_w is water pressure, S is the sectional area of elliptic, the shear force of unit length

$$f = \frac{F}{A} = \frac{p_w S}{A} = \frac{p_w \pi ab}{\pi [1.5(a+b) - \sqrt{ab}]} = \frac{p_w ab}{1.5(a+b) - \sqrt{ab}} \quad (10)$$

In the eq-10, A is the lateral area of elliptic, for the hypothesis about linear relationship between the gravity stress and buried depth, that is $\sigma_v = H\gamma_d$, then

$$\tau = h(H\gamma_d \tan \theta + c) \quad (11)$$

In the eq-10, H is the buried depth, h is the thickness of elliptic. When the limit equilibrium between total shear force and shear resistance reaches, $f = \tau$, flowing equation can be obtained

$$p_w = \frac{h(H\gamma_d \tan \theta + c)1.5[(a+b) - \sqrt{ab}]}{ab} \quad (12)$$

Eq-12 is the calculation formula of critical water pressure when the shape of water-proofing rock is elliptical cylinder. For certain water pressure eq-12 is transformed as follows

$$h = \frac{p_w ab}{(H\gamma_d \tan \theta + c)[1.5(a+b) - \sqrt{ab}]} \quad (13)$$

Eq-13 is the calculation formula of critical thickness of water-proofing rock. Based on this calculation formula, the critical water pressure is 1.53MPa in the model test.

2. Bending Destruction Mode

Circle rock bending fracture inrush is caused when rock is not strong enough to bear the bending stress caused by karst pressure, and it is simplified as thin plate bending problem to be analyzed, which is classified into bending destruction and contact shear destruction.

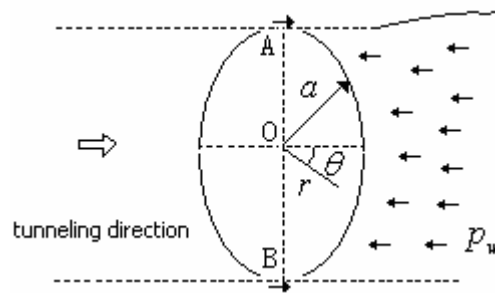


Figure 6 Water inrush model of tin plate

Based on the classical elasticity theory, it comes to the conclusion that there are shear destruction and bending destruction under the effect of karst water pressure. Among all the inrush modes, whole rock fracture inrush is usually neglected because of relatively strong anti-inrush ability, and it usually leads to the abrupt geological hazard.

4 Conclusion

Based on the simulation test and the analysis on the fracture mechanism of the surrounding rock of karst water pressure, the following conclusions are drawn:

(1) It is shown that there are two steps in the occurrence and formation of water inrush, the storage step and the instability step. These are the result of the long-term karst water pressure and surrounding rock interaction and construction external force interference.

(2) The weak plane formed in the storage step is the condition of the formation of inrush channel, and the instability step is a dynamic damage phenomenon when the water-proofing medium fractures due to the lasting effect of karst water and its pressure and the construction external force interference.

(3) The test on water fracture shows that the rupture strength is reduced 50% due to karst water and its pressure, and the test shows that the weak plane structure becomes the potential inrush channel.

(4) The test on karst inrush shows that the inrush mode is mainly determined by the structure characteristics of a water-proofing medium. For the medium with the obvious weak plane, the destruction effect is mainly reflected in the erosion, diameter extension and dynamic control of karst pressure to the water irruption quantity. The well integrity rock has two inrush forms, shear destruction inrush and bending destruction inrush. In this paper, the corresponding analytic solution is deduced out by the limit equilibrium theory, and the minimum rock safety thickness of the corresponding inrush mode is given.

Acknowledgements

The authors wish to acknowledge the funding support from the National Basic Research Program of China (973 Program, No. 2007CB209407), Natural Science Foundation of P. R. China (NO. 50874068 and 50727904) and Natural Science Foundation of Shandong Province (NO. Y2008F22 and NO. Y2006F13).

References

1. Jiang, Y. and Wang, L.H. Problems of high stress rock burst and water outburst and countermeasures in deep and long tunnels. *Chinese Journal of Rock Mechanics and Engineering*, 2002, 21(9). 1319-1323.
2. Liu, Z.W., He, M.H. and Wang, S.R. Study on karstburst mechanism and prevention countermeasures in Yuanliangshan tunnel. *Rock and Soil Mechanics*, 2006, 27(6). 228-232.
3. Zhang, X.H. and Liu, Q.W. Analysis of the features of water outburst from underground rivers and the countermeasures in Wulong tunnel. *Modern Tunnelling Technology*, 2005, 42(3). 59-63.
4. Yang, T.H., Tang, C.A., Tan, Z. H., et al. State of the art of inrush models in rock mass failure and developing trend for prediction and forecast of groundwater inrush. *Chinese Journal of Rock Mechanics and Engineering*, 2007, 26(2). 268-77.
5. Xie, X.H., Su, B.Y., Gao, Y.F., et al. Numerical study on water inrush above a confined aquifer in mining using hydro-fracturing. *Chinese Journal of Rock Mechanics and Engineering*, 2007, 24(6). 987-993.
6. Li, Z.L., Zhang, H.C., Ren, W.Q., et al. Analysis of hydraulic fracturing and calculation of critical internal water pressure of rock fracture. *Rock and Soil Mechanics*, 2005, 26 (8). 1216-1220.
7. Huang, R.Q., Wang, X.N. and Chen, L.S. Hydraulic fracturing analysis in water-spouting process in deep-lying tunnels. *Chinese Journal of Rock Mechanics and Engineering*, 2000, 19(5). 573-576.
8. Yang, T.H., Tang, C.A. and Zhu, W.C. Coupled analysis of seepage and stress in rock cracking process. *Chinese Journal of Geotechnical Engineering*, 2001, 23(4). 89-493.

NUMERICAL ANALYSIS OF THE PROCESS OF WATER INRUSH FROM THE 12TH COAL FLOOR FANGEZHUANG COAL MINE IN CHINA

HONG-LEI LIU, TIAN-HONG YANG, WAN-CHENG ZHU and QING-LEI YU

Center for Rock Instability and Seismicity Research, Box 138, Northeastern University

Shenyang, 110004, P.R. China

Based on the hydro-geological conditions of water in the Fangezhuang coal mine, the hydraulic model for rock mass in coal mining with confined water is established. The author applies the system of Coupling System of Flow & Solid in Rock Failure Process Analysis to simulate and study the whole process of the initiation of fractures, extension and formation of groundwater inrush pathway. With the analysis of damage distribution, stress and seepage field evolution, the process of the evolution from water-resisting strata to inrush pathway about the floor of complete mudstone under the condition of mining disturbance and hydraulic driving is clearly revealed, and the water rush pathways are determined. Furthermore, the effects of water rush under different water pressures in sandstone are discussed. The results show that the water inrush of 12 coal layer depends on the pressure of the water in sandstone. The water pressure has a negative correlation with water bursting coefficient in the conditions of mudstone's constant thickness, with the increasing water pressure, water inrush becomes easier. This research provides theoretical basis to forecast and prevent of water inrush at 12 coal floor.

1 Introduction

A key issue in coal mines influencing the safety of workers and production is groundwater outbursts. With the increase of mining depth and water pressure, water outbursts in deep mining are becoming increasingly more serious [1-4]. In china, a number of coal deposits are located above karsts aquifers which contain large volumes of water. Groundwater, with high pressure, can destroy the under-burden around active mine (roof or floor) panels, and burst into active mining excavations.

It is of vital importance to know when, where, and how groundwater outbursts develop during mining processes [6-9]. Rock is a heterogeneous geological material which contains natural weakness at various scales. When rock is subjected to mechanical loading, these pre-existing weaknesses can close, open, extend or induce new fractures, which can in turn change the structure of the rock and alter its fluid flow properties. Accordingly, when mining excavations are made, the re-distribution of the stress field leads to the initiation and growth of cracks, and potentially creates a highly permeable damage zone around these excavations. This damage zone creates a pathway for water flow, reduces effective stresses close to the excavation, which in turn may further extend and dilate fractures that comprise the damage zone. This reinforcing feedback may either self-arrest, or ultimately accelerate towards an inrush event. Understanding key interactions of this coupled flow-stress-damage behaviours are a key component in mitigating the occurrence and effects of outbursts. Although this phenomenon has been known for decades, the contributing mechanisms remain elusive. This knowledge gap has limited our ability to address this crucial issue for safer mining, and defines the objective of this study.

In this paper, the system of Coupling System of Flow & Solid in Rock Failure Process Analysis is presented that explicitly represents a relationship between stress, damage and permeability. Importantly, permeability evolves both with the growth of the existing fractures, and with the formation of new fractures, that result from the whole process of rock failure. This model is then applied to provide the whole process into

where, when, and how, groundwater outbursts may occur, with particular reference to mining geometries at the Fangezhuang coal mine. This is completed through explicit simulations of the evolving path of groundwater outburst as mining advances.

2 Numerical model

The Flow-RFPA model, as described above, is applied to evaluate the process of groundwater outburst in the Fangezhuang coal mine. The mine is located in Tang Shan city, Heber Province, eastern China, with an annual production of 32 million tons.

Based on the hydro-geological conditions of water in Fangezhuang coal mine, the hydraulic model for rock mass in coal mining with confined water is constructed. As shown in Figure 1, the simulation domain is 300m long and 200m high. It contains a total of 6 rock layers and the single embedded coal seam, among which the mudstone, 12# coal layer, sandstone with water, water-resisting mudstone and Ordovician limestone. The model includes a 75m long floor stratum. The water pressure of 2MPa is applied in the sandstone, and 9MPa in the Ordovician limestone. Although the water in sandstone is not large, the high water pressure in Ordovician limestone is danger to the 12# coal layer's safety mining. The average thickness of the 12# coal layer is 3.54m.

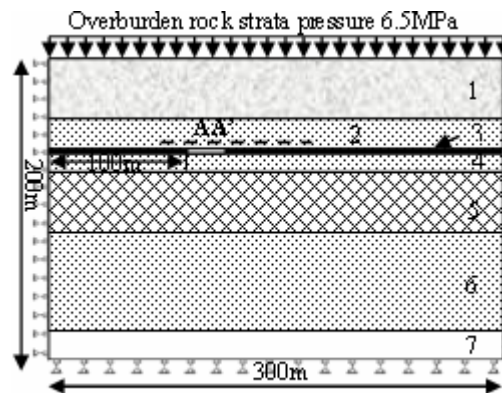


Fig.1 Numerical model for simulation

The simulation model is discretized into 300×200 elements for a total of 60000 elements. The bottom boundary of this model is constrained in the vertical direction, and both the left and the right boundaries are constrained in the horizontal direction. A pressure of 6.5MPa is applied on the top boundary of the model to simulate gravitational loading of the 400m high overburden. The four boundaries of the model are water-resisting layers. In order to simplify the mesh, and reflect the all differences in the nature of the mechanical properties and thickness distribution among rock layers, and finally combining the groups with 7 layers. Table 1 lists the averaged values of the mechanical properties of rock mass recovered from various in situ experiments.

Table 1. Calculated parameters for three different types of rock joint surface morphology

Order	Rock mass type	Thickness /m	Young's modulus/MPa	Compressive strength/MPa	Poisson's ratio	Weight Kg /m3	Hydraulic conductivity m/d
1	Overburden layer	40	20000	60	0.3	2300	0.01
2	Mudstone	20	18000	35	0.27	2630	0.01
3	12# coal seam	3	16000	25	0.3	1520	0.01
4	Mudstone	12	18000	35	0.27	2630	0.01
5	Sandstone	40	36000	100	0.15	2610	100
6	Mudstone	65	18000	35	0.27	2630	0.01
7	Ordovician	20	30000	100	0.17	3000	100

3 The results and discussion of numerical simulation

In the following, we follow the progressive evolution of the water inrush path during four-step mining sequence with the advance increment of the 25m/step. As mining advances, rock failure occurs in the surrounding rock mass. The failure initiates at isolated locations that ultimately coalesce to form a continuous failure zone. This failure zone is the potential path for groundwater in developing an outburst structure. These processes were simulated explicitly as shown in Figures2 (a)-(j).

With the first excavation to 25m from the left boundary of goaf, which lead to the surrounding rocks stress redistribution. The stress concentration occurred near the coal rib between the opening zones. The maximum compressive stress in these areas is 11.2MPa, as shown in Figures 2(a) and (d). Stress is released in the middle of the panel floor, and shear damage occurs near the corner of the coal rib but around the goaf the damaged zone is small. The roof and floor occurs the damage zones of the tension and shear, and the depth of failure is only 5m, the rock of roof and floor are still stability. The maximum vertical displacement at the centre of the excavation floor has reached 8mm, as shown in Figure 2(b).

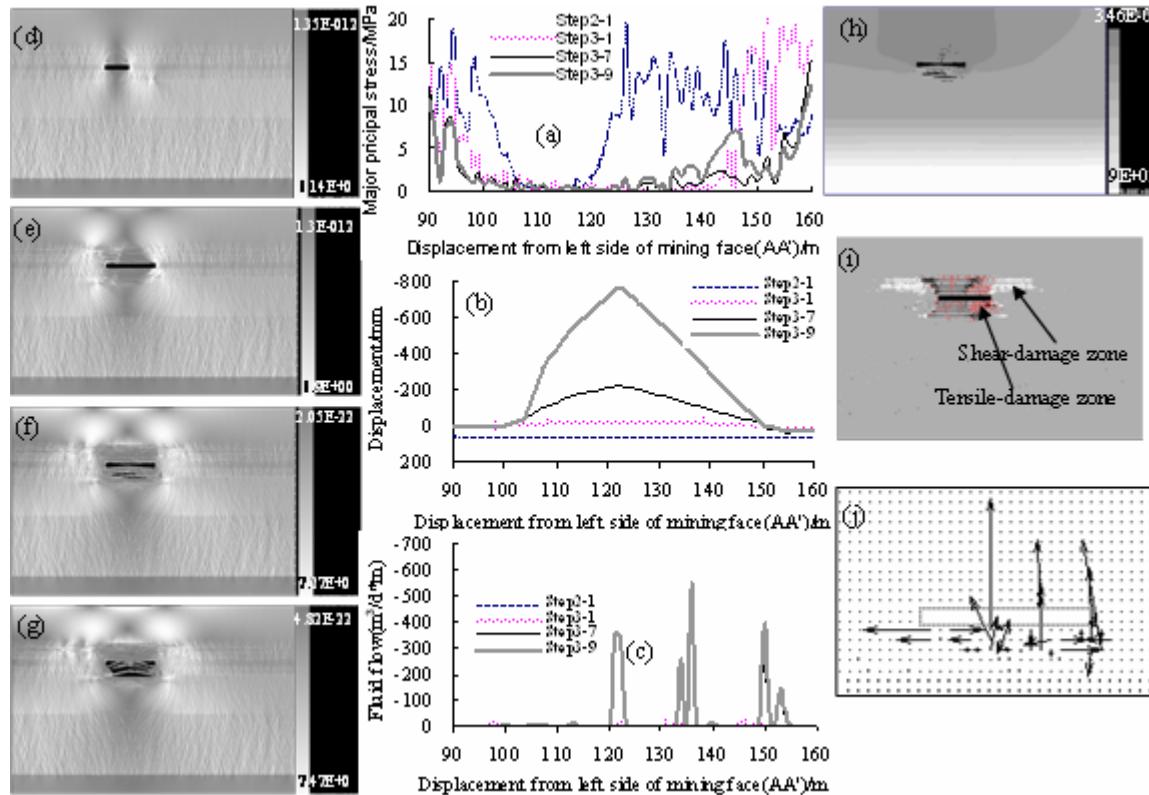


Fig.2. Numerical evolutions of stress, displacement, and flow rate during the progressive formation of a continuous groundwater outburst path linking the mining face to the aquifers. (a) Maximum principal stress distribution in the mine floor; (b) the vertical displacement in mine floor; (c) the vertical fluid flow in mine floor; (d) shear stress in mining step 2-1; (e) shear stress in mining step 3-1; (f) shear stress in mining step 3-7; (g) shear stress in mining step 3-9; (h) water head distribution in mining step 3-7; (i) damage distribution in mining step 3-9; (j) flow vector in step 3-9.

When the mining face extends to 50m in the second cut, the maximum compressive stress in these areas is 18.8MPa, as shown in Figures 2(a) and (d). The depth of roof damage zone has reached 3m and the floor damage depth of 12m. Under the interaction of pore water pressure and in-situ ground stress, the floor rock

layers appear tension and shear failure where 26m of opening from the left side of mining face. Then the water-resisting strata of mudstone occurs the aggravation of floor heaves. The stresses around the excavation adjust continuously before the initiation of the groundwater outburst path, and the tensile-shear damage accumulates in the centre of opening zone, and the mudstone grows to abscission layer, as shown in Figure 2(f). A tensile-shear failure zone also develops at the coal ribs, as shown in Figure 2(i). Figure 2(i) gives the damage distribution at step 3-9. Figure 2(g), where different colours are used to denote different damage modes: red is for the elements that are damaged in tension at current step; white is for the elements that are damaged in shear at current step; and black is for the elements that are damaged at previous steps. Figure 2(a) and Figure 2(c) indicate the location of water inrush clearly. The maximum displacement at the location of groundwater outburst is about 757mm as shown in Figure 2(b), and the flow rate is $630\text{m}^3/\text{d.m}$, as shown in Figure 2(c).

When the mining face advances to 75m in the third mining sequence, the pore pressure and fluid flow in the sandstone decrease gradually, the failure zone only connects with the sandstone layer, and the depth of outburst path does not extend further. The simulation results show that the stress concentration occurred near the coal rib between the opening zones because of mining. the floor rock layers appear tension and shear failure where 26m of opening from the left side of mining face, the damage zone extend to the next layer under the coal layer, and occurs the smaller water inrush. Under the interaction of pore water pressure and in-situ ground stress, the floor rocks layers appear failure zone where the weakest point of opening, and extend further rapidly. The water-resisting strata of mudstone occurs damage in sequence till coalescence between the 12 coal layer and sandstone. Finally, the water in the sandstone inflows the goaf from the fracture zones which in mudstone. The deeper of the damage zone, the more volume of water inrush would occur. Because of the small volume in sandstone and the fracture zone does not connect with the Ordovician limestone which contains the higher pore pressure and the more water volume, so it does not occur water inrush disastrous accidents. Conversely, when collapse column or water conductive fault exist, the water in Ordovician limestone would enter the sandstone or the excavation floor, then it would occur the water inrush disastrous accidents. For example, the 2171 mining workplace has been occurred a serious water inrush on June 2, 1984 [2].

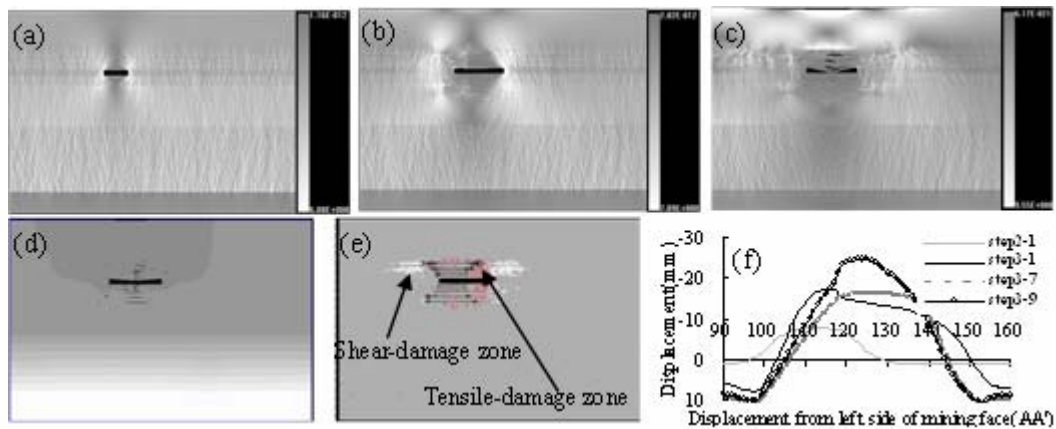


Figure 3. Numerical evolutions of stress, displacement, and flow rate during the progressive formation of a continuous groundwater outburst path linking the mining face to the aquifers. (a) shear stress in mining step 2-1; (b) shear stress in mining step 3-1; (c) shear stress in mining step 3-9; (d) water head distribution in mining step 3-9; (e) damage distribution in mining step 3-9; (f) the vertical displacement in mine floor

4 Simulation research on other working conditions

Based on the hydro-geological conditions of water and field experience in Fangezhuang coal mine, the coefficient of water inrush about 12 coal impermeable mudstone layer is presented, and the coefficient of water inrush is 0.157MPa/m for the complete mudstone floor. According to this coefficient, we can obtain 1.8MPa

which is the critical water inrush coefficient about the sandstone. We simulated three results in order to compare with other water inrush working conditions.

4.1. The water pressure of 1.7mpa in sandstone layer

With the first excavation to 25m from the left boundary of goaf, which lead to the surrounding rocks stress redistribution. The stress concentration occurred near the coal rib between the opening zones, as shown in Figures. 3(a) and (f). According to the distribution of damage zones, the damage area of excavation is smaller than the condition of 2MPa, especially the damage depth of floor only about 2m, and no bulging occur in the floor. However, the roof emerges some damage areas because effect of the overburden loading.

When the mining face advances to 50m in the second mining sequence, because the small pressure of sandstone layer, the failure area of floor is smaller than the condition of 2MPa, and have not significantly bulging deformation, as shown in Figure.3 (c)-(e). The depth of roof damage zone has reached 15m, and emerge collapsed zone, as shown in Figure.3 (e).

4.2. The water pressure of 3mpa in sandstone layer

With the first excavation to 25m from the left boundary of goaf, under the interaction of pore water pressure and in-situ ground stress, the floor and roof rock layers appear tension and shear failure, and the damage area is one time bigger than the condition of 2MPa. The depth of roof damage zone has reached 16m, in the centre of floor appear tension damage, and then the water-resisting strata of mudstone occurs the aggravation of floor heaves, as shown in Figure 4(f). The maximum displacement at the location of groundwater outburst is about 865mm as shown in Figure 4(d).

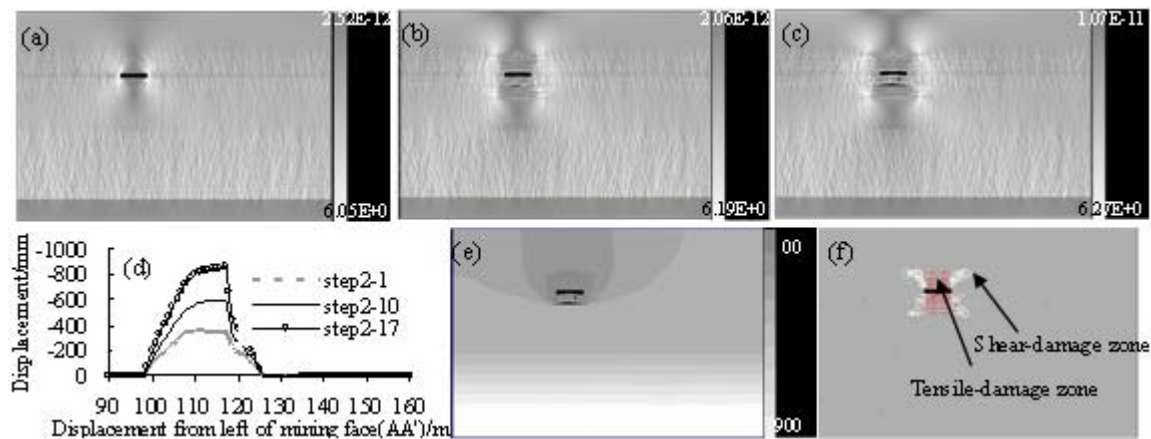


Figure 4. Numerical evolutions of stress, displacement, and flow rate during the progressive formation of a continuous groundwater outburst path linking the mining face to the aquifers. (a) shear stress in mining step 2-1; (b) shear stress in mining step 2-10; (c) shear stress in mining step 2-17; (d) the vertical displacement in mine floor; (e) water head distribution in mining step 3-17; (f) damage distribution in mining step 3-17;

5 Conclusions

Comparison of the results of the different working conditions leads to the following conclusions:

Firstly, the roof layers would failure and collapse to release the stress around the excavation when the water pressure is less than 1.8MPa in the water-bearing sandstone layer, and a groundwater inrush would not occur. But the water inrush would take place in the 12# coal floor at different stages of the excavation when the water pressure is more than 2MPa in the water-bearing sandstone layer.

Secondly, the displacement and fluid flow in the water inrush path change gradually after water outbursts, and the floor which is the water-resisting strata of mudstone has experienced the greater floor heaves. As the tensile and shear zone develops the depth of floor failure area increases gradually, leading to the failure of whole impermeable mudstone layer and in turn resulting in the connection between the working space and the water-bearing sandstone layer. Because of the protection of the permeable mudstone layer between the water-bearing sandstone and the Ordovician limestone, the failure area would not connect with the Ordovician limestone. The groundwater inrush disaster would not occur until the collapse column or water conductive fault existed to connect the water-bearing sandstone and the Ordovician limestone.

Acknowledgements

The study presented in this paper is jointly supported by the National Natural Science Foundation of China (No. 2007CB209405, 50674025, 50504005, 50874024, 10872046 and 107033).

References

1. Zhang, J.C., Zhang, Y.Z. and Liu, T.Q. Rock mass permeability and coal mine water inrush. Beijing: Geological Publishing House, 1997.
2. Wang, L.G. and Song, Y. A catastrophic model of water inrush from coal floor. *Journal of Engineering Geology*, 2002, 8(2). 160-163.
3. Wu, Q., Huang, X.L., Dong, D.L., et al. "Three maps-two predictions" method to evaluate water bursting conditions on roof coal. *Journal of China Coal Society*, 2000, 25(1). 60-65.
4. Zhang, H.R., Zhou, R.F., Guo, D.Z., et al. Investigation on predicting roof water gush in coal mines based on multi-factor analysis. *Journal of China University of Mining & Technology*, 2005, 34(1). 112-116.
5. W, J.H. and L, B.Y. Security evaluation of coal mining above the confined aquifers. *Coal Geol Explorat*, 2000.
6. Z, J.C. and S, B.H. A Coal mining under aquifers in China: a case study. *Int J Rock Mech Min Sci* 2004, 41. 629-39.
7. Wang, J.A. and Park, H.D. Fluid permeability of sedimentary rocks in a complete stress-strain process. *Eng Geol*, 2002, 63. 291-300.
8. Wang J.A. and Park H.D. Coal mining above a confined aquifer. *Int J Rock Mech Min Sci*, 2003, 40. 537-55.
9. Wu, Q., Wang, M. and Wu, X. Investigations of groundwater bursting into coal mine seam floors from fault zones. *Int J Rock Mech Min Sci*, 2004, 41. 557-71.
10. Bear, J., Tsang, C.F. and Marsily, D. Flow and contaminant transport in fractured rock. Academic Press, 1993.
11. Zhang, L. and Franklin, J.A. Prediction of water flow into rock tunnels: an analytical solution assuming a hydraulic conductivity gradient. *Int Rock Min Sci Geomech Abstr*, 1993, (1). 37-46.
12. Q, M.G., M, X.G. and X, J.L. Theoretical study of key stratum in ground control. *J China Coal Soc*, 1996, 21(3). 225-30.
13. Zhang, J.C. Stress-dependent permeability variation and mine subsidence. In: Girard, Liebman, Breeds, Doe, editors. *Pacific Rocks 2000*. Rotterdam: Balkema, 2000, p.811-6.
14. W, L.G. and Yang, S. A catastrophic model of water-inrush from coal floor. *Eng Geol*, 2000, 8(2). 160-3.

NUMERICAL ANALYSIS OF FAILURE MECHANISM OF TWO PARALLEL ROCK PILLARS

SHAN-YONG WANG and SCOTT-W SLOAN

*Centre for Geotechnical and Materials Modelling
Civil, Surveying and Environmental Engineering
The University of Newcastle
Callaghan, NSW 2308, Australia*

WAN-CHENG ZHU and TIAN-HONG YANG

*Center for Rock Instability and Seismicity Research, Box 138, Northeastern University
Shenyang, 110004, P.R. China*

CHUN-AN TANG

*Center for Rock Instability and Seismicity Research, Dalian University of Technology
Dalian, 116024, P.R. China*

Using the numerical code, RFPA2D, the progressive failure process of the parallel rock samples are simulated. The numerically simulated results show that not only the stiffness, but also the strength of rock sample in parallel models plays an important role in the instability of pillars. The damages always occur and develop in the pillar with the lower strength or lower elastic modulus. In addition, due to the Kaiser effect of rock, the stress-induced damage in a rock pillar is irreversible, and only when the previous stress state in the failed rock pillar is exceeded, the further damage will continue to occur.

1 Introduction

Pillars are in situ rock masses left between adjacent underground openings. Pillars play an important role in supporting the ground weight of overburden strata. As mining depth increases, the influence of seismic effects in a mine becomes more critical due to the progressive increase in ambient stresses on the pillars. The severest type of rock failure is rock burst. Rockbursts of pillars are sudden, explosion-like events that occur deep underground. They pose a hazard to the safety of underground miners and cause damage to mine structures. Rock bursts inside any mining excavation are due to the uncontrolled disruption of the rock equilibrium and the release of the strain energy stored in the rock mass [1].

Numerical methods are advanced design tools that allow for the consideration of complex boundary conditions and material behavior. Murali Mohan et al. used FLAC3D to simulate the failed and stable cases of pillars from Indian coal mines [2]. Chen et al. [3] and Kaiser and Tang [4] provided a double rock sample model for studying the pillar rockburst mechanism, and simulated the progressive failure process of the pillar. The numerical results confirmed that soft loading systems promote unstable failure or collapse of pillars. The focus of this present work is looking into the failure process of pillars in parallel and the corresponding stress-strain behaviors of pillars. The interaction of pillars with different strength or elastic modulus is considered.

2 Brief description of RFPA and models setup

Briefly, the code RFPA2D is a two-dimensional finite element code that can simulate the fracture and failure process of quasi-brittle materials such as rock [5, 6, 7]. To model the failure of rock material (or rock mass), the rock medium is assumed to be composed of many mesoscopic elements whose material properties are different from one to another and are specified according to a Weibull distribution. The finite element method is employed to obtain the stress fields in the mesoscopic elements. Elastic damage mechanics is used to describe the constitutive law of the meso-scale elements, and the maximum tensile strain criterion and the Mohr-Coulomb criterion are utilized as damage thresholds [8].

As we know, rock is a heterogeneous material. Statistically, it is assumed that the local mechanical parameters are distributed following a certain probability distribution, based on previous work [5, 6], Weibull distribution describes very well the experimental data obtained for the distribution of heterogeneities in rock. Here we divided the specimen into many finite elements and assumed that the elemental parameters (shear strength σ_c , elastic modulus E_c , etc.) of rock follow Weibull distribution law. That is

$$\varphi(\sigma_c) = \frac{m}{\sigma_{c0}} \left(\frac{\sigma_c}{\sigma_{c0}} \right)^{m-1} \exp \left[- \left(\frac{\sigma_c}{\sigma_{c0}} \right)^m \right] \quad (1)$$

$$\varphi(E_c) = \frac{m}{E_{c0}} \left(\frac{E_c}{E_{c0}} \right)^{m-1} \exp \left[- \left(\frac{E_c}{E_{c0}} \right)^m \right] \quad (2)$$

where σ_{c0} and E_{c0} is the average shear strength and elastic modulus, respective and m is the shape parameter. The shape parameter m is defined as the homogeneity index of the rock [8]. A larger m implies a more homogeneous material and vice versa.

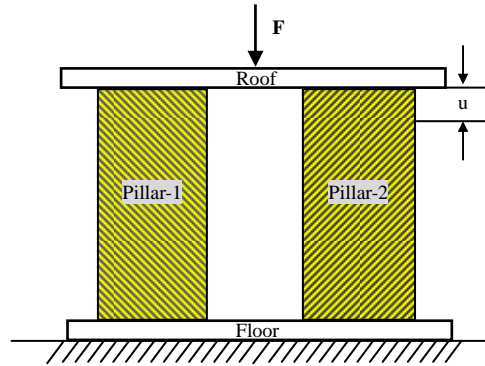


Figure 1 Serial and parallel numerical models setup for parallel pillar will different strength or elastic modulus.

Figure 1 shows the schematic models setup parallel pillars. In the current investigation, we will examine two principal parameters in equations 1 and 2, i.e. strength (σ_c) and elastic modulus (E_c). two cases of parallel pillars are numerical simulated. For case I, the elastic modulus for pillar-1 and pillar-2 are both 30GPa, while the strengths of them are different. The strength of pillar-1 and pillar-2 is 100MPa and 200MPa. For case II, the strength for pillar-1 and pillar-2 are both 200MPa, while the elastic moduli of them are different. The strength of pillar-1 and pillar-2 is 60GPa and 30GPa. Table 1 listed the detailed input parameters. The properties of floor and roof are listed in Table 2.

Table 1.Material parameters for tests of two parallel pillars

	Two parallel pillars	Case-1	Case-2
Elastic modulus	Pillar-1	30 GPa	60 GPa
	Pillar-2	30 GPa	30 GPa
Strength	Pillar-1	100 MPa	200 MPa
	Pillar-2	200 MPa	200 MPa
Poisson`s ratio	Pillar-1	0.25	0.25
	Pillar-2	0.25	0.25
Homogeneity index (m)	Pillar-1	3	3
	Pillar-2	3	3

Table 2.Material parameters for floor and roof

Elastic modulus	300 GPa
Strength	1000 MPa
Poisson`s ratio	0.25
Homogeneity index (m)	3

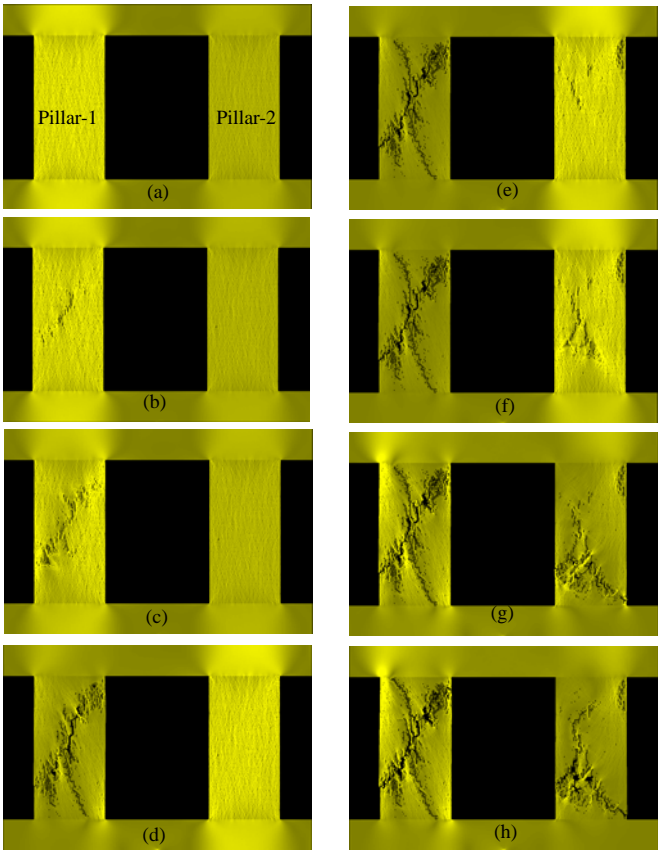


Figure 2 Failure processes of two parallel pillars with different strength but the same elastic modulus (stress distribution)

Furthermore, the size of the mesh is 200×400 with 80000 elements to simulate a specimen with a size of $4000\text{mm} \times 8000\text{mm}$. All the simulations are limited to a two-dimensional plain-strain condition. The samples are loaded in a displacement manner, something like the displacement control method in a servo-controlled laboratory test. Each increment of the displacement is regarded as a disturbance induced by mining. The pillars are loaded to failure in displacement-control mode by displacing the upper boundary vertically in increments of 0.005% of the model height.

3 Numerical results and analysis

3.1 Numerical result for case I

For case I, Figure 2 shows the failure mode development at selected stages. Figure 3 shows stress-strain relation. From Figure 2, albeit the elastic modulus of pillar-1 and pillar-2 is the same, the strength of pillar-2 is higher than pillar-1, so that the stress concentration and the initial damaged elements are firstly randomly distributed in pillar-1 (Figure 2 stage a). Afterwards, the damaged elements develop and nuclear to form a shear failure band oriented in the direction of 55° - 60° to the horizontal line (Figure 2 stages b and c). In fact, the shear failure band is composed of many small cracks. The small cracks can develop and interact into bigger crack. Along with the continuous loading, another big crack initiates from the center of the shear failure band and develops downwards (Figure 2 stage d). From Figure 3, in point d, there is a big stress drop, when pillar-1 lost its stability. During these stages (a-d), almost no damaged elements occur in pillar-2. Since pillar-1 has lost its stability, pillar-2 begins to bear the main uploading, and some failure zones start to occur (Figure 2 stage e). With the further loading, the failure zones in pillar-2 develop (Figure 2 stage f). Not until in stage g, do both pillar-1 and pillar-2 lose their stability. Stage h is the residual stage of the system.

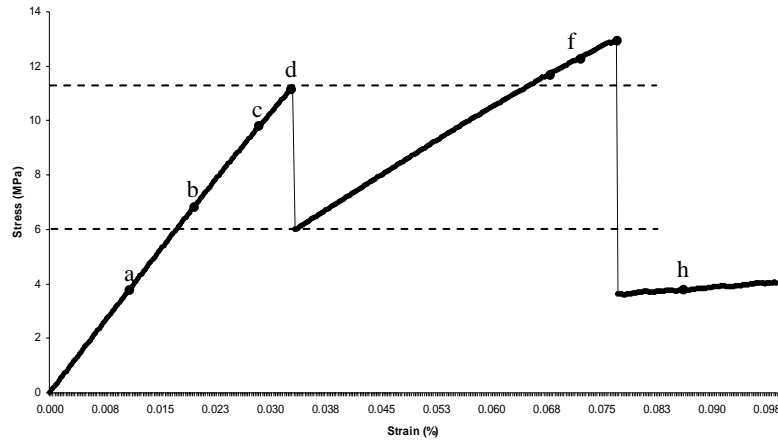


Figure 3 Stress-strain relation for two parallel pillars with different strengths but the same elastic modulus.

It should be noted that the failure zone in pillar-1 also develop from stage e to stage g. Although pillar-1 lost its stability in point d of figure 3, it still has certain strengths. As the stress-induced damage (micro-crack growth) in a rock is irreversible then it is likely that significant new damage will occur only when the previous stress state is exceeded. This is the so called Kaiser effect of rock [4]. From figure 3, with the further loading, when the stress level in point e is higher the previous highest stress level in point d, the failure zone starts to develop in pillar-1. Ultimately, the failure zone presents a shape of “X” in pillar-1.

3.2 Numerical result for case II

For case II, Figure 4 shows the failure mode development at selected stages. Figure 5 shows stress-strain relation. From Figure 4, as the strength of pillar-1 and pillar is the same, both the two pillar bear the uploading (Figure 4 stage a). With the further loading, since the elastic modulus of pillar-2 is lower than pillar-1, the initial damaged elements occur and nuclear into the failure zone in pillar-2 (Figure 4 stages b and c). During this process, almost no damaged elements occur in pillar-1. In stage d of figure 4, pillar-2 loses its stability. It corresponds to a big stress drop in the point c of figure 5. In the meantime, a failure zone occurs and develops in pillar-1. Therefore, the big stress drop and AE energy released in point c is contributed by both pillar-1 and pillar-2. Afterwards, along with the further loading, the failure zone in pillar-1 develops (stages e and f), until the system loses its stability (stage g). Stage h presents the residual strength of the system. It is noted that during the stages (e, f and g), no new damage develop in pillar-2. This is because the previous highest stress state in point d of figure 5 is not exceeded by the stress state in point g in figure 5. Similarly, due to the Kaiser effect of rock, there is no further damages occur in pillar-2.

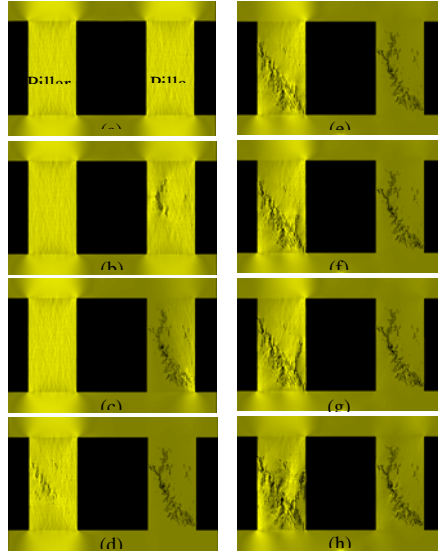


Figure 4 Failure processes of two parallel pillars with different elastic modulus but different strength (stress distribution)

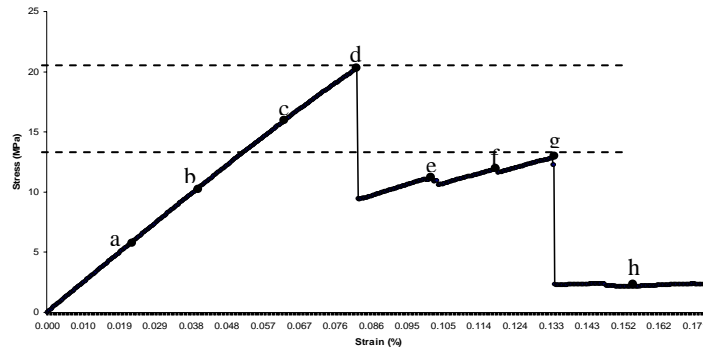


Figure 5 Stress-strain relations for two parallel pillars with different elastic modulus but the same strength

4 Conclusions

The brief description of the numerical code (RFPA2D) is presented first. Using the numerical code, RFPA2D, the progressive failure process of the parallel pillars is simulated. The whole stress-strain curves of pillars are given. The effect of two principal input parameters in the numerical model i.e. strength and elastic modulus on the failure mechanism of pillar are examined. The numerically simulated results show that, not only the stiffness, but also the strength of the rock sample in parallel models can greatly influence the stability of the two pillars. The damages always occur and develop in the pillar with the lower strength or lower elastic modulus. Furthermore, due to the Kaiser effect of rock, the stress-induced damage in a rock pillar is irreversible, and only when the previous stress state in the failed rock pillar is exceeded the further damage will continue to occur. Afterwards, both the two pillars continue to fail at the same external loading level till they lost their stability in the end.

Acknowledgements

The support from the National Science Foundation of China (Grant Nos. 50874024 and 50504005), the Program for New Century Excellent Talents in University of China (Grant No. NCET-06-0291), the Liaoning Provincial Natural Science Foundation (Grant No. 20082027), the Scientific Research Foundation for the Returned Overseas Chinese Scholars of State Education Ministry, and the Australian Research Council (Grant No. DP0881238) is greatly appreciated.

References

1. Cook, N. G. W. Seismicity associated with mining. *Eng.Geol.*, 1976, 10. 99-122.
2. Murali, M.G., Sheorey, P.R. and Kushwaha, A. Numerical estimation of pillar strength in coal mines. *International Journal of Rock Mechanics and Mining Sciences*, 2001, 38. 1185-1192.
3. Chen, Z.H., Tang, C.A. and Huang, R.Q. A double rock sample model for rockbursts. *Int. J. Rock Mech. Min. Sci.*, 1997, 34(6). 991-1000.
4. Kaiser, P.K. and Tang, C.A. Numerical simulation of damage accumulation and seismic energy release during brittle rock failure- Part II: Rib pillar collapse. *Int. J. Rock Mech. Min. Sci.*, 1998, 35(2). 123-134.
5. Tang, C.A., Hudson, J.A. and Xu, X.H. *Rock Failure Instability and Related Aspects of Earthquake Mechanisms*. China Coal Industry, 1993.
6. Tang, C.A. Numerical simulation of progressive rock failure and associated seismicity. *Int. J. Rock Mech. Min. Sci.*, 1997, 34, 249-262.
7. Tang, C.A., Chen, Z.H., Xu, X.H. and Li, C. A theoretical model of the Kaiser effect in rock. *Pure and Applied Geophysics*, 1997, 150. 203-215.
8. Zhu, W.C., Tang, C.A. Micromechanical model for simulating the fracture process of rock. *Rock Mechanics and Rock Engineering*, 2004, 37 (1). 25-56.

STUDY ON UNSTABLE FAILURE OF ROCK MASS IN KEY ROUTE OF FAULT WATER INRUSH

ZHONG-HUI CHEN, LIANG SI, ZHI-QING CAI and GUAN-HAO XUE

School of Mechanics and Civil Engineering, China University of Mining and Technology (Beijing),

Beijing, 100083, P. R. China

Water inrush of the fault is a typical dynamical disaster in the coal mines, which is the instability failure process of the rock and coal under the action of mining and pressure water. In this paper, the simplified mechanical model of the critical path was established on water inrush of the fault in allusion to the spatial relation between the fault and plasticity region of the floor. The shortest distance from the fault to plasticity region of the floor was regarded as the key route of water inrush of the fault. The limit equilibrium theory was used to study the condition of the unstable failure of rock mass in key route. The shortest distance of the key route was obtained and the prepared critical width of anti-pillar was given for tater inrush of the fault. Meantime, the rule of water inrush under the impact of the fault parameters and coal-parameter was analyzed.

1 Introduction

Water inrush in coal mines is one of the most serious disasters in coal mine production because it causes grievous casualties and heavy economic losses for coal industries. Therefore, it is a thorny problem to solve in coal mine industry at present, how to recognize the water inrush mechanism, and how to efficiently keep mine water inrush control [1]. According to statistics, many water inrush accidents occur in the coal working faces, in which 80 percent of mine water inrush accidents are related to the faults. The other 20 percent of water inrush accidents may be caused by the floor potential faults. The fault is an important water inrush channel. Its activation and slip-mutation laws under the action of mining and pressure water are significant to the occurrence and the prediction of water inrush in coal mines [2-3].

Many researchers made a study of water inrush mechanism for faults in various angles and made certain achievements. Liu found the relationship between the inclination angles, the width of the fault, offset and water inrush, and he analyzed the water inrush tendency in fault under different factors by using numerical simulation [4]. Yu estimated 171 working faces of water inrush in five mining areas, which are distributed in Shanxi, Feicheng, Zibo, Jiaozuo and Fengfeng, and he summarized that water inrush accidents influenced by faults make up 66.7 percent of the whole accidents [5]. Zhou studied the time dependency of water inrush through faults [6]. Dai, etc. analyzed the criterion of water inrush caused by the fracture of floor near faults by the methods of rock mechanics [7]. Because of the catastrophe character of the fault water-inrush, Wang used the

catastrophe theory to analyze the catastrophe of water inrush for floor and obtained the catastrophe conditions of the floor water inrush [8].

At present, the researches on water inrush mechanism for fault are mainly concentrated on activation of fault and fracture of floor. They did not involve the instability failure of the key part of water inrush through fault. In this paper, the limit equilibrium theory was used to analyze the fracture criterion of the key rock masses where water inrush through fault occurs, deduced the minimum size of key water inrush part and the theoretical formula of coal pillar preventing water inrush.

2 Model of Water Inrush through Fault

In special geological and hydrographic conditions, key reason for floor water inrush is mining and fault. Fault affects mine water inrush in three aspects: (1) water diversion and storage function of fault; (2) the fault shortens the distance between coal bed and correlative aquifer; (3) the fault decreases the strength of rock masses. Because water inrush through fault is mainly the normal fault water inrush, the main object of this paper is to study the normal fault. As shown in Fig. 1, the inclination angle of the fault is α . In mining coal seam, when the abutment pressure of the coal seam floor reaches or exceeds the critical point of the floor strength, the plastic change may occur in a certain range of rock mass of the working face floor, which makes the floor of the gob area swell. The plastic changing rock mass will move to the gob area, forming a constant face of slip field. The face of slip field, namely, slip field line, consists of two straight lines in active limiting zone, passive limiting zone and one logarithmic spiral in transitional zone [9]. In passive region the separation angle between line of slip field and horizontal level is $\beta = \frac{\pi}{4} - \frac{\varphi}{2}$, φ is the internal friction angle of floor rock mass. As shown in the Figure 1, the depth of the floor failure zone caused by mining is h .

$$h = \frac{x_a \cos \varphi}{2 \cos(\frac{\pi}{4} + \frac{\varphi}{2})} e^{(\frac{\pi}{4} + \frac{\varphi}{2}) \tan \varphi} \quad (1)$$

In the above formula, x_a is the length of yield zone for coal seam, it could be gained by practical measure at spot.

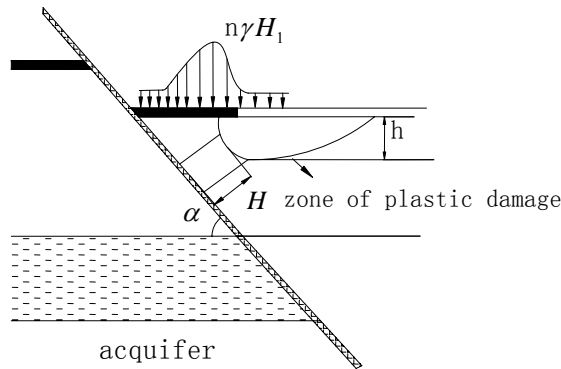


Figure 1 The sketch of key route for fault water inrush

It is supposed that the ordinary fault is transmissible fault in Figure 1, the thickness of aquiclude changes from the vertical distance from floor plastic region to aquifer into h now. It is the shortest distance from fault to floor slip line. This is the concrete manifestation that the fault shortens the distance between coal seam and aquifer. This is the shortest and the most critical way for water inrush through fault. If the aquifer water only breaks this zone, water inrush through fault will be easily formed. So the author focuses on the research of the instable failure of the regional rock mass, using traditional limit equilibrium theory and catastrophic theory to study the failure condition of the regional rock mass. The mechanical criterion can be obtained for the research of mechanism of water inrush through fault.

3 Limit Equilibrium Analysis of Fault Water-Inrush

Figure 1 illustrates the simplified geological model of water inrush through fault. To make a brief analysis, it is supposed that the floor rock mass is uniform with no tiny crack. The water inrush depends on the failure of the square regional rock mass under the action of mining and pressure water. In Figure 1, a vertical profile is chosen along H direction as Figure 2. In Figure 2, L is the length of the working face. It is subjected to fault water pressure at the bottom, horizontal stress at both left and right sides. The upper part is the floor plastic zone where is subjected to less stress so that here the stress in the upper part is supposed to be zero. In the zone, a

differential unit is chosen with the depth dz , which its stress state is as shown in illustration of Figure 2. To keep the key zone unbroken and unaltered, the condition is required to keep balance in the direction z for the unit as the following [10]. From $(\sigma_z + d\sigma_z)L - \sigma_z L - 2(C + \sigma_x \tan \varphi)dz = 0$, we can get

$$\frac{d\sigma_z}{dz} - \frac{2 \tan \varphi}{L} \sigma_x - \frac{2C}{L} = 0 \quad (2)$$

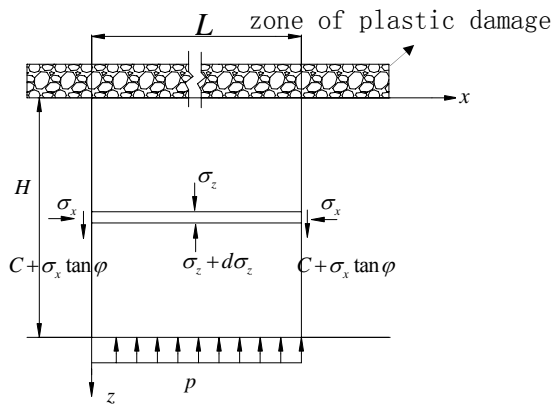


Figure 2 Limited equilibrium analysis on key route for fault water-inrush

According to the Mohr-Coulomb criterion, rock mass should follow the limit equilibrium condition when it is broken:

$$\frac{\sigma_z + C \operatorname{ctg} \varphi}{\sigma_x + C \operatorname{ctg} \varphi} = \frac{1 + \sin \varphi}{1 - \sin \varphi}$$

If $(1 + \sin \varphi) / (1 - \sin \varphi) = \lambda$

$$\text{Then } \sigma_x = \sigma_z / \lambda + (1 / \lambda - 1) C \times \operatorname{ctg} \varphi \quad (3)$$

Put Equ.3 into Equ.2, we obtain $\frac{d\sigma_z}{dz} - \frac{2 \operatorname{tg} \varphi}{\lambda L} \sigma_z = \frac{2C}{\lambda L}$. Equ.3 is concluded,

$$\sigma_z = A e^{2 \operatorname{tg} \varphi / \lambda L} - C \operatorname{ctg} \varphi \quad (4)$$

When $z = 0$, $\sigma_z = 0$, put them into Equ.4, then we can get $A = C \times \operatorname{ctg} \varphi$,

$$\text{so} \quad \sigma_z = C \operatorname{ctg} \varphi (e^{2 \operatorname{tg} \varphi / \lambda L} - 1) \quad (5)$$

When $z = H$, $\sigma_z = p$, put them into Equ.4, we can get the limited water pressure for the effective aquiclude,

$$p = C \operatorname{ctg} \varphi (e^{2 H \operatorname{tg} \varphi / \lambda L} - 1) \quad (6)$$

In the above equations, C is the cohesion of the aquiclude rock mass in kN / m^2 ; φ is the internal friction angle of rock mass; H is the minimum distance from the slip field line to the fault in m; L is the length of working face in m. The above equation can be taken as a criterion of the fault water inrush. If water pressure in the fault is stronger than limited water pressure, water inrush may occur. This is dangerous for mining so that the precautionary measures should be taken. Contrarily, if water pressure in the fault is weaker than limited water pressure, then it is safe for mining. From the above equation, we can conclude the limited length of minimum route for the fault water-inrush under the constant water pressure in the fault. That is

$$H_{\min} = \frac{\lambda L \ln(1 + \frac{p}{C \operatorname{ctg} \varphi})}{2 \operatorname{tg} \varphi} \quad (7)$$

From the above equation, it can be inferred that H_{\min} is related to the cohesion and internal friction angle of rock mass of the floor, and that H_{\min} and the length of working face exhibit directly proportional linear correlation. So the longer the working face is, the longer H is. In addition, H_{\min} also is related to water pressure in the fault. Thus the stronger the water pressure is, the longer the key route for water inrush is.

For a mine, the internal friction angle of the floor rock is 30° , the cohesion is 4MPa, water pressure in the fault is 1MPa, the length of working face is 100m. Using Equ.6, we calculated that the limited length of the minimum route for the fault water-inrush is 35m. This result corresponds to the most practically measured length.

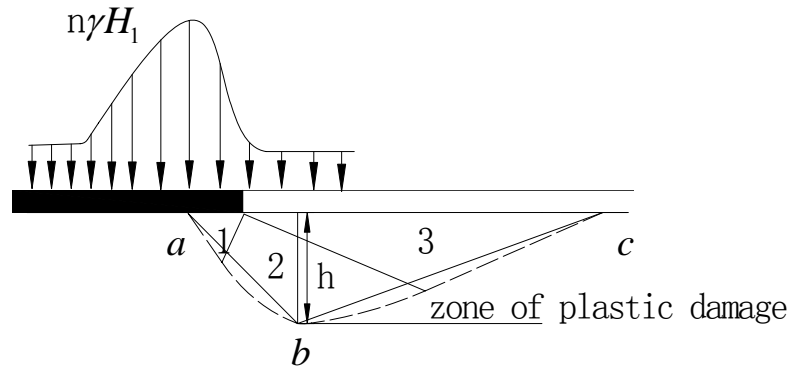


Figure 3 The simplified plastic failure zone of floor

In order to find the relationship between the anti-pillar size and H_{min} , the plastic zone of slip field in the floor of coal seam is simplified here. The slip field line of rock mass of the floor, i.e. the borderline of the plastic zone is illustrated in Figure 3. It consists of three regions: active limit region, transition region, passive limit region, namely, the dotted lines in region one, region two, and region three in the Figure [9]. The line of slip field in region one and region three is linear, in region two is a set of curves. The author simplifies the line of slip field into the triangle as shown in Figure 3.

With the change of the fault inclination angle, there are two ways for getting the size of pre-established coal pillar. When the angle between plastic failure region and horizontal line is smaller than the fault inclination angle, then the distance from point c at the triangle to the fault is the shortest. As shown in Figure 4, the length of pre-established coal pillar is

$$l = l_1 + x_a \quad (8)$$

x_a is the length of yield zone for coal seam, and according to theory of slip field, it can be inferred that x_a [9] is

$$x_a = \frac{h_0}{2\lambda_0 \tan \varphi_0} \ln \frac{n\gamma H_1 + C_0 \cot \varphi_0}{\lambda_0 C_0 \cot \varphi_0} \quad (9)$$

In the equation, h_0 is the depth of coal seam, C_0 and φ_0 is the cohesion and the friction angle of the coal seam, respectively. $n\gamma H_1$ is the top value of coal seam abutment pressure. Here, $\lambda_0 = (1 + \sin \varphi_0) / (1 - \sin \varphi_0)$.

In the triangle abc, it can be concluded by geometric relations that

$$l_1 = bc = \frac{H_{min}}{\sin \alpha} \quad (10)$$

Put Equ.9 and Equ.10 into Equ.8, the length l of the coal pillar can be calculated,

$$l = \frac{H_{min}}{\sin \alpha} + \frac{h_0}{2\lambda_0 \tan \varphi_0} \ln \frac{n\gamma H_1 + C_0 \cot \varphi_0}{\lambda_0 C_0 \cot \varphi_0} \quad (11)$$

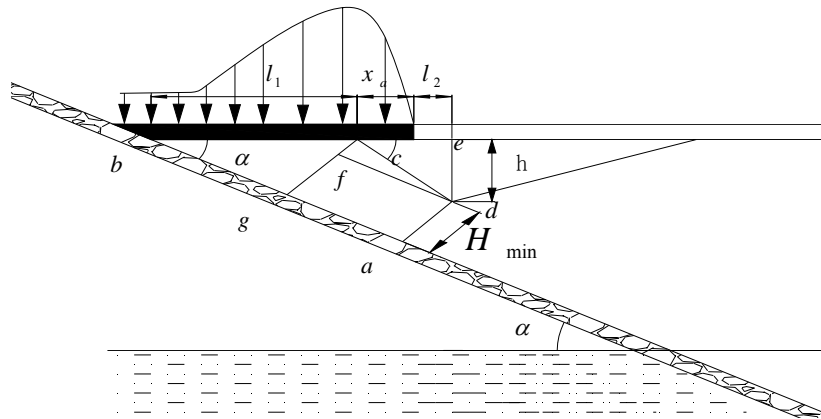


Figure 4 The sketch of obtained pillar with the big fault dip angle

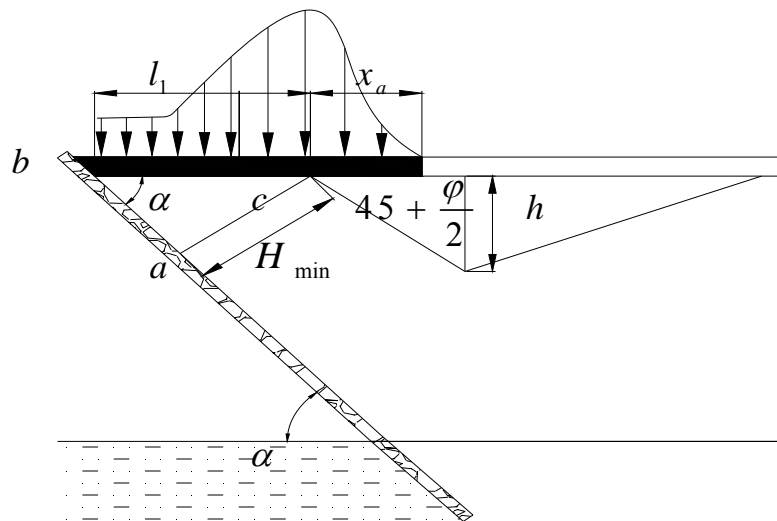


Figure 5 The sketch of obtained pillar with the small fault dip angle

If the separation angle between plastic zone and horizontal line is wider than the fault inclination angle as shown in Figure 5, the distance from the top point d of the triangle of floor plastic zone to fault is the shortest. The length of coal pillar l becomes to be $l_1 + x_a$. In order to get l_1 , two auxiliary lines are made in the quadrilateral abcd, and a vertical line of ab through point c is made and line ab is intersected at point g. A vertical line of cg through d is made and line cg is intersected at f. l_1 can be calculated by the triangle relationship.

$$l_1 = \frac{H_{\min} + \sqrt{h^2 + (x_a + l_2)^2} \cos(\frac{\pi}{4} + \alpha - \frac{\varphi}{2})}{\cos \alpha} \quad (12)$$

In the above Equation, $l_2 = x_a \tan(\frac{\pi}{2} + \frac{\varphi}{2}) e^{\frac{\pi}{2} \tan \varphi}$. So the size of the prepared coal pillar is obtained.

$$l = \frac{H_{\min} + \sqrt{h^2 + (x_a + l_2)^2} \cos(\frac{\pi}{4} + \alpha - \frac{\varphi}{2})}{\cos \alpha} + x_a \quad (13)$$

Equ.10 and Equ.12 are theoretical results for calculating the size of coal pillar in different angles of faults. It is related to the length of coal pillar yield zone, the size of floor plastic zone and Hmin.

4 Conclusions

The fault water inrush is caused by the action of mining and pressurized water. The influence of mining shows on the formation of floor plastic region and slip field, and the prepared set of anti-pillar. The influence of pressure water mainly shows on water pressure and the rock softening. In the paper, some problems are not taken into consideration including the rock softening, washing and fluid-solid coupling in water. This paper mainly focus on the key route of the occurrence process of the fault water-inrush, the limit equilibrium analysis for the shortest distance from fault to mining plastic zone of coal seam. The following is concluded:

First, according to the spatial relationship between the fault and floor plastic slip regions, the mechanical model of the key route of water inrush of the fault was established, namely, the shortest distance from the floor failure zone to the fault. If the pressure of water breaks through this zone, water inrush of the fault may occur.

Second, according to the limit equilibrium theory, the stability of the key route of the fault water inrush was discussed, and the conditions and process of the unstable failure of coal and rock mass were studied in the key route. The limiting water pressure that pressure water broke through the key route, and the minimum size of the key route for keeping stability under the water pressure action were deduced. In addition, the theoretical size of the prepared set of anti-pillars under the different inclination angles of the fault was obtained, which correspond to the practically measured size.

Acknowledgements

This work was financially supported by China 973 Program (No.2007CB209402), Natural Science Foundation of P. R. China (No. 50834005), Program for New Century Excellent Talents in University (NCET-06-201).

References

1. Yang, T., Tang C. and Tan C. State of the Art of Inrush Models in Rock Mass Failure and Developing Trend for Prediction and Forecast of Groundwater Inrush. Chinese Journal of Rock Mechanics and Engineering, 2007, 26(2). 68-77.
2. Wu, Q., Zhou, Y. and Liu, J. etc.. The Mechanical Experiment Study on Lag Mechanism of Water-bursting of Fault under Coal Seam. Journal of China Coal Society, 2003, 28(6). 61-565.

3. Li, L., Qian, M. and Li. S. Mechanism of Water-Inrush through Fault. Journal of China Coal Society, 1996, 21(2). 9-13
4. Liu, Z. and Hu, S. Solid-liquid Coupling Study on Water Inrush through Faults in Coal Mining above Confined Aquifer. Journal of China Coal Society, 2007, 32(10). 1046-1050.
5. Yu, X. Geological Structure and Underground Water Outburst from Seam Floor. Coal Engineering, 2004, 12. 34-5.
6. Zhou, R., Cheng, B. and Ye, G. etc.. Time Effect of Water Bursting in Fault Rupture Zone. Journal of Engineering Geology, 2000, 8(4). 411-15.
7. Dai, C. and He Y. Study of Floor Faultage's Water Invasion Regularity Mining on the Top of Water Pressured. Journal of Anhui University of Science and Technology (Natural Science), 2003, (4). 6-9
8. Wang, L., Song Y. and Miao, X. Study on Prediction of Water-Inrush From Coal Floor Based on Cusp Catastrophic Model. Chinese Journal of Rock Mechanics and Engineering, 2003, 22(4). 573-7.
9. Zhang, J., Zhang Y. and Liu, T. Flow in Coal Seams and Water Inrush from Seam Floor. The Geological Publishing House, Beijing, 1997.
10. Sun, W. Study on the Influence of Fault to Floor Water-Inrush, Master Degree Thesis, Shandong University of Science and Technology, 2006.

EXCAVATION & REINFORCEMENT STABILITY ANALYSIS OF UNDERGROUND ENGINEERING

HONG-DONG LI

College of architecture and civil engineering ,Heilongjiang institute of science and technology

Haerbin, 150027, P.R. China

FANG LI

Orion International Energy Ltd.

Beijing, 100190, P.R. China

There are a lot of factors, such as the order of excavation and reinforcement, the rock mass characteristics, the length and height of per excavation step and so on, that affect the stability of underground engineering. If it is underground cavern group they will affect each other, especially in the process of excavation. How to determine the stability of underground engineering is a hotspot problem at present. And the criterion index of rock mass is multiple. Now the index is varied from the single displacement, strain, plastic zone to the comprehensive index that deal with the rock displacement, stress or strain, plastic zone and so on simultaneously. In this paper, the orthogonal experiment is adopted to set up permutation and combination matrices of the factor that affect the underground stability, choosing the representative program to establish numerical model and compute it. According to the calculated result we can obtain the magnitude of displacement and plastic zone, establishing a comprehensive index to determine the underground working integer stability and getting the optimal scheme excavation and reinforcement, in order to provide reference foundation for the design.

1 Introduction

As the engineering of the underground excavations progressed certain problems appeared, such as, the depth and scope of the caves. This affected groups of caves because of the complicated geological conditions and the difficulty of construction [1]. A water power station is located on the middle part of Qing river in Badong county, in which there are four more tunnels with 300m length tail water tunnels and 9.5~11.5m diameters. This is the first water power station on the Qing river according to the tread plan of development of the Qing River. The construction of tunnel consists of two separate parts.

The calculation is carried out with the finite element model, which is established by the orthogonal plan according to the factors of the order: the length and steps, supports and the height of excavating. [2,6] The stable evaluation of the tunnel can be conducted with the index of displacement and plastic zone scope of the tunnels, after which, the optimal excavating and supporting plan can be obtained[3,5].

2 The Arrangement and the Geological Condition of Tail Water Tunnel

The water power station is designed under the right bank mountain and locates on the dam site with NE30°, which four electric generators are fixed with 1600MW total capacity. One generator capacity is 400MW. The construction of this water power station includes diversion canal, infall, pilot tunnel, main plant, installation square, generator tunnel, tail water tunnel, tail water flat, tail water channel, 500kV electric power substation, traffic tunnel, ventilation tunnel, lines tunnel and discharge water tunnel and so on[4].

The geological condition of underground cave is very complicated. Especially, the tail water tunnel has to go through varies alternate hard and soft rock strata. It is necessary to evaluate the stable state of tail water tunnel before the tunnel excavated. The tunnel axis is NE26°. The water in level is 166.8m and water out level is 188.8m. The strata of rock that tail water tunnel crosses are the first part of Xixia group(P1q1), Maan group(P1ma), Huanglong group(C2h) and Xiejing group(D3x), which strike is 235~250°<12~18°. The angle of tail water tunnel axis with stratum is 22~43°[4].

The development of shearing zone in middle part of strata is good, such as the 011#,012# zone in the first part of Xixia group(P1q1), the upper part 001# in Maan group(P1ma), the lower part F205 in Huanglong group. The characteristic of shearing zone in Huanglong group is fracture. The range of height is great which is between 5m and 12m. The grade of rock of P1q1, P1ma, D3x and C2h strata is between IV and V. The lower part of C2h is relative good which grade belong to III. Figure 1 shows the section of rock strata.

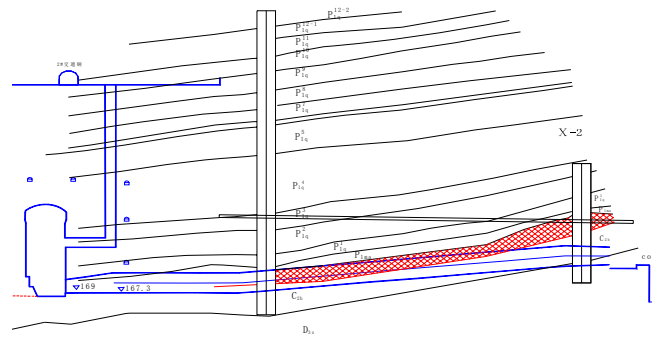


Figure 1 The section of rock strata

The axis line of number 4 tail water tunnel is vertical against the main plant. The number of tunnel is from No.1 to No.4 as the arrange of tunnels from inner side of mountain to valley of river. There are 6 parts of tunnel, that is, tail water channel, extension part of tail water channel, straight part, frontal change part, standard part and rear change part. The length of 1#~4# tunnels is 327.34m, 319.90m, 313.16m and 307.25m respectively. The total length of these 4 tunnels is 1267.65m. The width between centres of tunnels is 31m. Thickness of concrete is 1.2m. The diameter of standard tunnel is 11.5m and other parts are between 9.6m to 11.5m. All this work is separated into two parts to be constructed. The first part is from the mark to main plat (69.625M) and second part is from mark to water exit. The mark detail is shown in Figure 2.

3 The Model of Finite Element

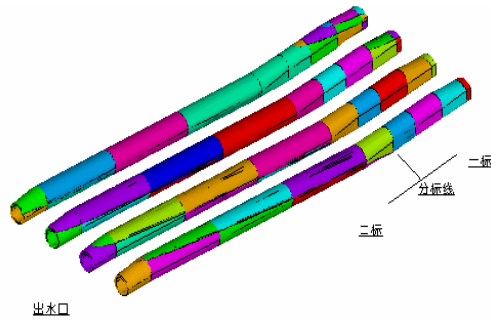


Figure 2 Tail water tunnel

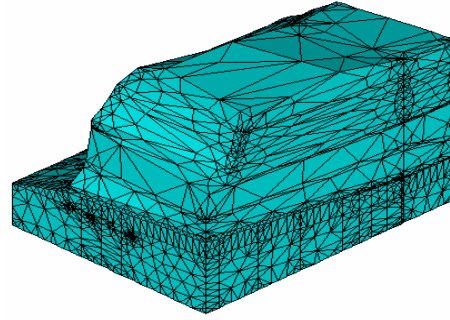


Figure 3 Meshes of model

Table 1 Parameters of rock strata

Rock groups	Density kN/m ³	Elastic ModulusE (GPa)	Poisson ratio μ	Shearing strength		Tensile strength Rt (MPa)
				C (MPa)	F	
		Range		Range	Range	Range
P1q12-4~P1m	26	10 14	0.27	0.8 1.0	1.0 1.1	0.7 1.1
P1q12-2,P1q11,P1q9, P1q7 , P1q5,P1q4 ,P1q2,C2h 上	27	15 20	0.25	1.0 1.2	1.2 1.3	1.0 1.5
P1q12-3,P1q6,P1q3,P1q1, P1q12-1,P1q6,P1q10P1q8, C2h 下	25	5 8	0.3	0.6 0.8	0.8 0.9	0.5 0.8
P1ma	22	1 2	0.35	0.3 0.5	0.5 0.6	0.2 0.5
D3x	25	3 4	0.3	0.5 0.7	0.7 0.8	0.4 0.6
D3h	25	10 12	0.27	0.8 0.9	1.0 1.1	0.7 1.1
250# concrete	24.5	26	0.167	1.8	1.8	1.7
F205 (2layer shearing zone)	0.2	0.15	0.4	0.025	0.27	0

According to the geological information from geological company, the calculated scope is $X \times Y \times Z = 350\text{m} \times 300\text{m} \times 400\text{m}$. Coordinate locates on the crossing center of No. 1 tunnel and main plant. X axes is parallel axes of main plant. Inner side of mountain is as the positive value. Y axes is vertical ground and upper direction is as positive value. Z axes is vertical to the axes of main plant and the water out direction is as the positive values. The three dimensional model has 98625 elements and 17928 nodes. Except boundary condition of river valley side is free, the other three directions are restricted in normal direction. Ground section is restricted in three directions. The meshes of model are shown in Figure 3. Only initial stress and 15 strata are considered during calculation. The mechanic parameters of each strum are listed on Table 1. The criterion of yield is applied by Drucker-Prager. The different parameters values which are employed during the simulating process excavation are listed on Table 2.

Table 2 scheme of code

Factors	A B	C	D	E
Meaning of parameters	Excavating steps for each single marking tunnel	Liner order for each tunnel	Order excavation	Height of one excavation
Possible values	1, 2, 3, 4	1, 2, 3, 4	1, 2	1, 2
The meaning of different parameters	<p>A 1, 2step excavation, first step is 20m. 2, 2step excavation, first step is 45m. 3, 3steps excavation. 4, 4steps excavation (one mark)</p> <p>B 1, 2steps excavation. 2, 3steps excavation. 3, 4 steps excavation. 4,5steps excavation (second mark)</p>	<p>1 lining front step during next step excavation.</p> <p>2 lining front two tunnels during excavating rear two tunnels and rear two tunnels are excavated by one step</p> <p>3 two tunnels are excavated by one liner</p> <p>4 liner is done after four tunnels are excavated</p>	<p>1 1#,3#tunnels are excavated first</p> <p>2 2#,4#tunnels are excavated first</p>	<p>1 whole height of tunnel</p> <p>2 half height of tunnel</p>

4 The analysis of calculation

4.1 Calculation Results

According to the schedule of calculation, the minimum calculating steps is 13 and maximum is 39 within the 16 calculating plans. It will need 30 about minutes for calculating one step by using PIV1700 computers. Some element data have to be input by hand because the excavating elements and supporting elements using concrete can not be recorded by LS document. It will need 40 days to calculating 16 different plans since it will consume a lot time to process data and output results. However, 30G dimensional space can be used to calculate plan which has the most calculating steps. The results calculated through 16 different schemes are listed in Table 3.

4.2 Optimal Calculating Scheme

The maximum displacement within 6-9cm happens in upper roof of Y axes and the minimum value within 5-7cm happens on the ground floor. The values of right and left sides within 6-8.1cm are stable relatively. The maximum difference value in the same node is about 3cm.

Table 3 computing results of orthogonal design

No. of sachems	The maximum roof displacement of liner /cm	The maximum floor displacement of liner /cm	The maximum displacement of left side liner/cm	he maximum displacement of right side liner/cm	Volume of plastic zone/M ³
11111	8.5536	7.3623	7.8796	7.9704	66069.2
12211	8.9978	6.8554	7.8798	8.0275	86480.1
13322	8.9902	6.8662	7.8713	8.0183	88978.0
14422	9.0006	6.8675	7.8747	8.0208	92150.0
21222	8.9920	6.8863	7.8723	8.0191	88581.1
22122	8.9838	6.8608	7.8655	8.0125	87670.3
23411	9.0140	8.8044	7.8782	8.0357	87888.6

24311	8.9875	6.8770	7.8756	8.0158	88706.2
31312	9.0080	6.8548	7.8793	8.0259	90140.8
32412	9.0158	6.8416	7.8792	8.0367	90941.5
33121	8.9804	6.8592	7.8639	8.0111	84449.5
34221	8.9953	6.8646	7.8714	8.0168	90426.6
41421	8.9862	8.0125	7.8741	8.0143	87625.8
42321	8.9903	6.8670	7.8726	8.0199	86034.7
43212	8.9986	6.8507	7.8739	8.0218	85168.9
44112	9.0020	8.8896	7.8821	7.9804	85024.1

The maximum value of displacement happens in the No.1 tunnel among the four tail water tunnels. The data listed on the Table 3 are processed by standardization, which the unique index can be obtained by eliminated the units of different data. The equation is $\pi_i = 0.2 + 0.6(y_{ij} - y_{imin})(y_{imax} - y_{imin})$. The equation $fitness = \min \sum [(y_{ij} - y_{imin})/y_{imin}]$ is applied by standardization process. Then the optimal schedule of excavation and support is 11111 calculating scheme, that is, the first marking part is excavated by two steps and the second marking part is also excavated by two steps. The front liner is done during the free-step excavation. The No.1 and No.3 tunnel are excavated by one step first.

The maximum roof displacement of optimal schedule is 8.5536cm, which happens on the No.1167 node in the No.1 tunnel. Its coordinate is X=-0.565m, Y=35.70m, Z=284.46m, which located on the crossing vicinity of standard part and gradual change part that the distance to water outlet is 42.88m. The maximum floor displacement is 7.3623cm, which happens on the No.1587 node that the distance to outlet is 25m. The maximum left side displacement is 7.8796cm, which happens on the No.1529 node that the distance to water outlet is 33.31m. The maximum right side displacement is 7.9704cm, which happens on the No.1557 node that the distance to water outlet is 38.1m. The maximum displacement in Z axes direction locates on the vicinity water outlet in the second marking part rather than first marking part. The displacement along the direction of water flow in the same tunnel increases gradually. The displacement of roof is much greater than that of floor in the vertical direction. All displacements of nodes can be found in Figure 5.

For whole calculating zone, the displacement decreases gradually from the highest point center of right side boundary water outlet to other parts of model, which are shown in Figure 4, Figure 5.

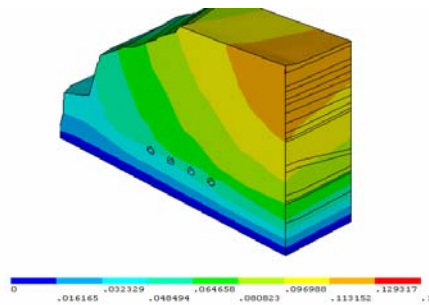


Figure 4 Contours of displacement in crosscut plane

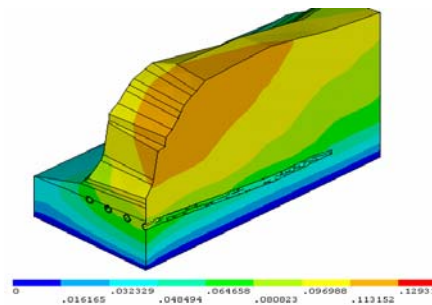


Figure 5 Contours of displacement in straight-cut plane

5 Conclusions and Expectations

(1) The displacement and deformation increase gradually from the river valley to center part of the peak along the X axes on the same level for 4 tunnels. The displacements and deformation increase gradually along the Z axes in the same tunnel, with the roof displacement being greater than that at floor. Generally speaking, the displacement decreases gradually from the highest center point of right side boundary water outlets, to other parts of tunnels.

(2) The optimal schedule of excavation is the first part executed in two steps and the second part is also executed by two steps. The next liner is done during the front step excavation. The No.1 and No.3 tunnel are primarily excavated by one step.

(3) Since the rock mass is a nonlinearity medium, all physical and mechanical changes of rocks are nonlinearity and have no reversion. The tunnel's different pattern and excavating order will result in different displacements and damages. The complex system makes for a challenging engineering job to keep the large group of underground tunnels stable. The tunnel pattern and excavating order are the two important main factors which impact the stability of the tunnels. How to distinguish the construction sequence is a comprehensive criterion which includes taking the maximum displacement and damage volume that happens on some key points (such as the points on side wall, vault, floor and so on) to be compared with the values that are given by experts and standard design. These different values, which are processed by weighted mean, can be regarded as the valued criteria. The minimum value is used as the principle for determining the sequence of excavating and supporting the tunnel.

It is a very complicated job to excavate group tunnels and impossible to correctly calculate all of the plans. The simulating work presented in this paper is a trial job. Therefore, the conclusions obtained in this paper are only primary results based on the static condition rather than the concerning affection of rock strength decreasing time passes and actual work conditions. significant time and work are needed to analyze the dynamic condition.

References

1. Zhu, W.S. and He, M.C. Rock Dynamic Construction Mechanics and Stable Analysis under Complicated Rock Strata Condition. Beijing Science Publishing House, 1995.
2. Sun J. The Theory and Practice of Designing underground Engineering. Shanghai Science Publishing House, 1995.
3. Yi, S.D. Research on Reinforcing Slipping Slope by Intelligent Method. Chinese Academy of Science, 2003.
4. The Committee of Yangtze River of Water Conservancy Ministry. Underground Power Station Bidding Report of Shuibuya Water Conservancy Construction Right Side Bank in Qing River. Hubei Province, 2002.
5. An H.G. Analysis a Large Scale of Group Caves Salability and Optimization by Using Intelligent Method. Chinese Academy of Science, 2002.
6. Publishers, Orthogonal Test Design. Shanghai Science Publishing House, 1979.

SEISMIC NETWORK OPERATIONS AT A DEEP UNDERGROUND COAL MINING DISTRICT IN WESTERN COLORADO (USA)

PETER SWANSON

*National Institute for Occupational Safety and Health, Centers for Disease Control and Prevention, Spokane Research
Laboratory, Spokane, WA 99207, USA*

WENDELL KOONTZ

West Elk Mine, Mountain Coal Company, Somerset, CO 81428, USA

JIM ABSHIRE

Bowie Mine, Bowie Resources LLC, Paonia, CO 81428, USA

An array of ten triaxial strong-motion stations has been installed on the surface above two underground longwall coal mines in western Colorado (USA). The district-scale network monitors mining-related and natural seismicity throughout an area of approximately 250 square kilometers of rugged canyon-mesa terrain. The real-time automated seismic event monitoring and notification tool features: password-protected Internet access to raw and processed data, web-client software that provides real-time graphical display of event locations, and email and paging notification of high acceleration levels and large magnitude events. This paper describes the network installation and the methods used to collect, process, and distribute seismicity information to its users and gives several examples of the collected data.

1 Background

Bowie Resources LLC, Mountain Coal Company, and the National Institute for Occupational Safety and Health (NIOSH) jointly developed a district-scale seismic monitoring network. The objectives of the network are to (i) distinguish and characterize seismic activity as either mining related or naturally occurring, (ii) implement a real-time event monitoring and notification tool, and (iii) collect data for use in research studies aimed at quantifying impacts from mining-related and natural seismicity. These potential impacts include dynamic rock mass failures such as coal bumps as well as strong shaking in the vicinity of critical structures such as impoundment dams, reservoirs, mine seals, mine openings, and steep slopes.

The first issue to be addressed in system design concerned the size of the area to be monitored. It was necessary to characterize seismicity throughout the current, former and future underground workings as well as nearby natural seismicity. It was also desirable to measure strong-ground motion in the vicinity of several earthen dams. For an array of these dimensions, conventional earthquake monitoring tools, including open-source software, could be used to characterize natural and mining seismicity and implement the real-time monitoring function. However, NIOSH's research interests require more detailed examination of failure mechanisms and strong-motion recording which necessitate additional measurements closer to the active workings. Use of temporary close-in stations that augment the district-scale network have been used to help meet this latter objective. This paper describes the development and application of the district-scale network.

1.1 Site Location

The North Fork Valley (NFV) longwall coal mines are located in western Colorado in an area where vertical elevation relief over the span of an individual mine approaches 1 km. Six minable coal seams are present with thickness ranging from 2 to 6 m. Maximum overburden in the district is approximately 0.8 km. Competent sandstone units are present with variable thickness and distance above and below most of the seams. This combination of overburden and stiff strong strata leads to the potential for coal bumps. Total yearly production from all NFV coal mines exceeds 17 million tons per year.

2 North Fork Valley (NFV) Network

2.1 Seismic Stations

Triaxial accelerometers (EpiSensors¹) and 1-Hz vertical seismometers (L4-C) are co-located at each station to record strong and weak motions, respectively. Signals are digitized by nominally 24-bit data recorders (Altus K2). The recorders are configured to continuously stream four channels of waveform data at 100 samples per second, and locally trigger and save event data to compact flash cards providing backup in case of telemetry failure. Each station is equipped with a GPS receiver for time stamping.

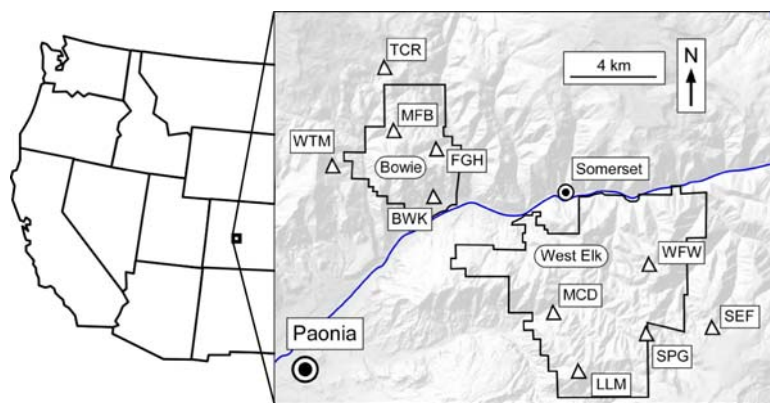


Figure 1. Seismic station locations (triangles) in North Fork Valley coal mining district of western Colorado. Lease boundaries marked by outlines.

Two groups of five seismic stations are centered around existing and/or future workings of the Bowie and West Elk mines (Figure 1) providing coverage of an area of approximately 250 square kilometers. To help constrain locations of naturally occurring earthquakes in the surrounding area, use is also made of data from a transportable array (TA) of broadband seismometers temporarily deployed as part of the EarthScope earth science project [1]. The average source to receiver distance for the nine nearest TA stations is 75 km.

2.2 Data communications

Continuous digital seismic waveform data streams are sent from each remote station to a central site in the town of Paonia equipped with a DSL Internet connection (Figure 2). Data transfer is achieved with license-free (in the U.S.) 900-MHz frequency-hopping spread-spectrum radios equipped with 10dB directional Yagi antennas. Radio interference issues have been experienced periodically with other nearby 900-MHz

¹ Mention of specific products or manufacturers does not imply endorsement by the National Institute of Occupational Safety and Health.

data-comm networks that are used for ventilation and methane drainage drillhole monitoring and other networks associated with non-mining uses. The interference has been mitigated by appropriate antenna selection, positioning and RF-power level adjustments, and/or replacement of affected links with radios in the 2.4-GHz band.

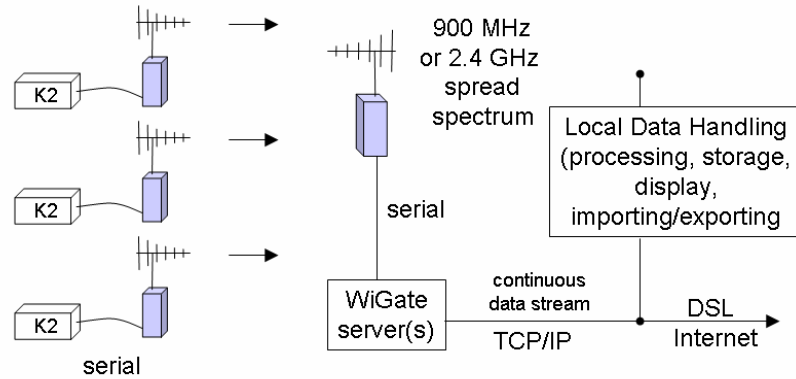


Figure 2. Data communications (serial/IP) network.

2.3 Data Processing

The open-source software Earthworm [2], developed by the U.S. Geological Survey (USGS) and other contributors, is used for a large portion of the data collection, processing, analysis and display functions. A wide variety of software modules are available, allowing one to custom build a system tailored to specific needs. Modules are available to stream real-time data from seismic instrumentation offered by numerous seismometer and recording-systems manufacturers (e.g. DAQ Systems, GeoTech Instruments, Guralp, Kinemetrics, Nanometrics, National Instruments, Reftek, Symmetric Research, Quanterra)1.

In the NFV configuration, various modules on multiple Windows platforms automatically detect, process, archive and analyze seismic events, analyze ground motion parameters, distribute waveform data for redundant processing and backup, and provide alerting services. For on-line waveform storage Winston

“waveservers” are constructed using the standard Earthworm Waveserver_V module or the MySQL-based Wave Server (WWS) Java utility [3].

Following software-based arrival-time picking, event locations are calculated using Hypoinverse [4] with a layered velocity model. Magnitude estimates are available from three separate sources: (i) the USGS’s National Earthquake Information Center (USGS/NEIC) in Golden, CO (limited to the largest events), (ii) Mesa State Seismic Network (Grand Junction, CO), and (iii) those calculated within the automated processing (Hypoinverse coda magnitude).

2.4 Distribution of Data

Raw and processed data are made available over the Internet via a password protected web page. Access can be provided to all available data or a more limited subset, depending upon user privileges. Links are provided to data products such as helicorder records (12- to 24-hour single-trace recordings similar to paper drum recordings), triggered-event waveform files, summary event location/magnitude data, and peak acceleration values. An alternative open-source interactive helicorder-style module with useful spectrum display features, Swarm - Seismic Wave Analysis and Real-time Monitor [3], is also available. Waveform data from arbitrary time periods can be manually stored to disk in a number of different formats (e.g. SAC, SUDS, mini-SEED) by accessing the waveservers from anywhere on the Internet.

2.5 Event Monitor

A separate web server provides continuous reporting of seismic activity in the vicinity of the NFV network with near real-time displays of event locations, magnitudes and times of occurrence. It receives its data from Earthworm and is based on the CISN software designed for western U.S. earthquake monitoring and emergency management 24/7 operations centers (<http://www.cisn.org/>). Modifications to this software were made to provide additional control of the location quality of the displayed events. This increases the robustness of the event reporting and reduces the display of poorly constrained events when operating under wholly automated processing conditions. However, as with any automated system, it is not immune from errant mislocations; significant events are always confirmed by experienced users through manual inspection and, if necessary, re-processing.

2.6 Alerts

Timely notice of events of particular interest is provided by email and paging. Users receive email when specified levels of acceleration are met or exceeded at a given station, providing the opportunity to inspect critical structures or initiate other actions. In practice, it has been found useful, as a simple awareness measure, to set the threshold lower than any critical, or actionable, level in order to generate a stream of email that is proportional to the rate of large-event seismic activity. This also provides periodic confirmation that the notification system is working as intended. A second system email module is used to send messages about significant events to a nationwide paging service. Individual users can customize their own notification criteria by specifying values for acceleration threshold, minimum magnitude, and distance from stations of interest.

3 Example Results and Discussion

3.1 Mining Events and Natural Earthquakes

One of the initial goals of the network was to develop a better understanding of the relative amounts of natural earthquakes versus mining-related seismicity. Locally, seismic events with $M \geq 2.8$ are fairly consistently reported by the USGS/NEIC. However, the typical location error is observed to be 8-12 km which is too large to allow discrimination between different mines in the area and discrimination from local earthquakes. Naturally occurring earthquakes ($M \leq 2.4$) have indeed been recorded throughout the region by the NFV network but they represent less than one percent of the recorded activity.

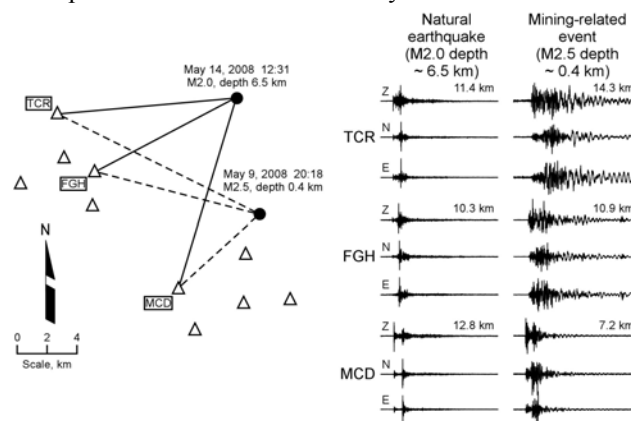


Figure 3. Comparison of waveform character observed for natural earthquakes and mining-related events.

Naturally occurring events are quite readily distinguished from the local mining events on the basis of their waveform character. Figure 3 compares waveforms observed at three strong-motion stations (TCR, FGH, and

MCD) from both a local earthquake (M2.0) and a longwall mining-related event (M2.5). The natural event displays the classic tectonic earthquake signature with distinct P and S phases. The waveform signature of the mining-related event appears different: (i) the separation between P and S phases is not nearly as well defined, (ii) there appear to be several additional phases present, or complexity that is absent in the earthquake seismogram, and (iii) the frequency content across the entire waveform is generally lower for the mining event than for the natural earthquake.

The waveform characteristics in Figure 3 are typical for natural earthquakes and mining events observed by the NFV network. While differences in source mechanisms may exist – most NFV mining events exhibit dilatational first motions, much of the difference in waveform character in Figure 3 can be attributed to propagation path effects. A far greater proportion of time is spent travelling parallel to near-surface sedimentary layers for the shallow mining event in comparison to the much deeper natural earthquake. As a result, local earthquakes show minimal surface-wave generation and mining events show the strong influence of surface waves and near-surface layering.

3.2 Distribution of Seismic Activity

From May 2007 to January 2009, approximately 20,000 events were automatically detected, processed, and located. The level of activity is a strong function of mining operations, particularly deep longwalling. The temporal distribution of the larger events with $2.0 \leq M \leq 3.4$ is shown in Figure 4.

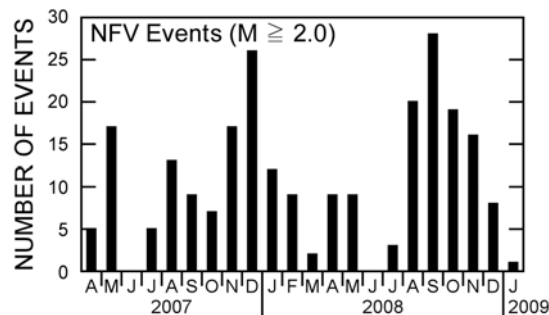


Figure 4. Temporal distribution of events in the North Fork Valley with $2.0 \leq M \leq 3.4$.

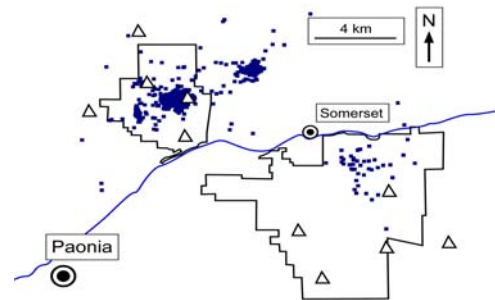


Figure 5. Distribution of event locations ($0 < M \leq 2.8$) determined by the automated processing for the month of September 2008.

An example of the distribution of event locations for a single typical month (September 2008) is shown in Figure 5. Approximately 900 events occurred with a maximum magnitude of 2.8. No naturally occurring earthquakes were detected in this area during this interval. The strong event clustering to the east of the Bowie stations occurs in the vicinity of a third NFV area coal mine.

Automatically processed event locations on the scale of an individual mine are shown in Figure 6. Approximately 6,000 events with magnitudes between 0 and 3.4 were recorded at the Bowie Mine during the 3-month period from Nov 2007 to January 2008. During this time the longwall retreated a distance of ~700 m (white outline) in the B-seam. The high level of activity is a reflection of the consistently deep cover (>500 m), near-seam brittle strata and stress interactions with the previously mined D seam 90 m above. Figures 5 and 6 display event locations without regard to constraint on the size of location error.

3.3 Performance of the Automated Processing

The automated processing is largely successful in placing events into the appropriate mine and into specific work areas (i.e. longwall versus development sections, etc.). Scatter in event locations outside the longwall panel (Figure 6) is the result of both error in automated processing and the presence of other distributed sources

such as development mining and continuation of events in old workings. There are also some outright erroneous locations due to events that occur close together in time producing overlapping arrivals which get assigned to the wrong event.

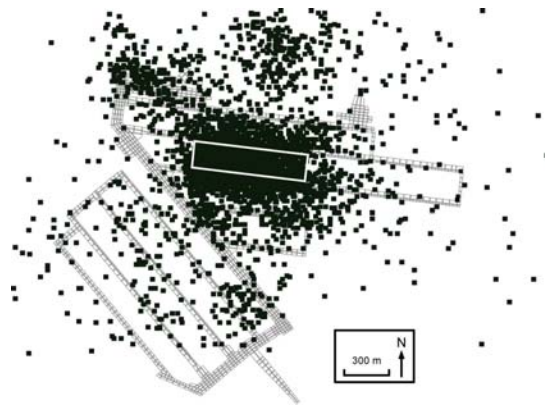


Figure 6. Automatically processed event locations for 3-month longwall retreat.

Manual arrival time picking reduces scatter in event locations, tightens up the clustering in the direct vicinity of responding mine structures, and is used when trying to maximize the understanding of the processes attending significant or damaging events. Other improvements in event locations for the automated processing are under development, including refinement of both mine-specific velocity models and station corrections and incorporation of multiple individual velocity models into the automated location process.

4 Summary

Bowie Resources LLC, Mountain Coal Company, and NIOSH have cooperated on a joint project to develop a digital wireless seismic monitoring network to collect background data on mining-related seismic activity in western Colorado and to implement a hazard monitoring tool. The ten station strong-motion array covers approximately 250 square km and provides an automated real-time monitoring capability using wireless serial and IP communications networks. To resolve details of the caving process, event depths, and interactions with specific strata in the vicinity of working faces requires augmentation of the network with a close-in fully three-dimensional distribution of additional sensors.

ACKNOWLEDGMENTS

The findings and conclusions in this report are those of the authors and do not necessarily represent the official position of the National Institute for Occupational Safety and Health.

References

1. Transportable Array of the National Science Foundation Supported EarthScope project.
2. Earle, P., Bittenbinder, A., Bogaert, B. and Johnson, C. Tune to the Worm: Seismic Network Operation Using the USGS Earthworm System. Observations and Research Facilities for European Seismology, Orfeus Newsletter, 2003, 5 (1).
3. Cervelli, D., Cervelli, P. and Murray, T. New Software for Long-Term Storage and Analysis of Seismic Wave Data. Eos Trans. AGU 85 (47), Fall Meet. 2004 (1), Abstract SF13A-0705.
4. Klein, F. User's Guide to HYPOINVERSE-2000, A Fortran Program to Solve for Earthquake Locations and Magnitudes. USGS Open-File Report 02-171, 2002, 1. 123.

SEISMIC MONITORING AND ROCK BURST HAZARD ASSESSMENT IN DEEP POLISH COAL MINES – CASE STUDY OF ROCK BURST ON APRIL 16, 2008 IN WUJEK-SLASK COAL MINE

G. MUTKE, A.LURKA and J.DUBIŃSKI

*Central Mining Institute,
40-166 Katowice, Plac Gwarkow 1, Poland*

64 channel Seismic Observation System (SOS) was developed in GIG and installed in Wujek-Slask Mine in the Upper Silesian Basin – Poland. Also software for analysis of seismic events, especially for 3D location and passive tomography has been developed and integrated with SOS system. More than 2000 seismic events were recorded in the longwall panel 2Jd using SOS seismic network, and were used to study temporal changes of P-wave field velocity images, peak particle velocity (PPV) values at the excavation boundary and seismic source parameters calculated in moving time windows.

On April 16, 2008 rock burst damage of tunnels caused by the $M=3,3$ seismic events took place. Very promising results were obtained studying changes of tomographic velocity images to determine seismic prone areas in panel 2JD in the Wujek-Slask mine. Just before rock burst, the zone of high velocity, high seismic anomaly and high gradient velocity has been observed very clearly near 2Jd gateroad. The P wave velocity increased in damaged area up to 20%. The passive tomographic velocity images turned out to be very useful as long-term precursors of seismic prone areas.

The second useful precursor was the distribution of peak particle velocity parameter (PPV) at the boundary of excavations in working area. The PPV was calculated using the empirical relationships developed for coal mines in Poland:

$\log (PPV \cdot R) = 0,66 \log M_0 - 7,4$ (Mutke 2008). The calculated peak particle velocity (PPV) in the damaged 1Jd gateroad, reached value from 0,35 m/s to 0,6 m/s. The $M=3,3$ rock burst damaged 85 m of gateroad No. 1Jd.

The seismic source parameters calculated in moving time windows were studied before rock burst event in 2Jd longwall panel. One has observed that just before strong seismic event stress drop, seismic moment and seismic energy increased significantly and was useful mid-term precursors to estimate potential seismic hazard.

1 Introduction

Rock bursts are one of the most serious natural hazards in deep Polish coal mines. Every year a few rock bursts with fatalities and a few hundred meters of damaged excavations have been occurred (Mutke and Stec 1997, Stec 2007, Mutke 2008). The strongest shocks (seismic energy $107 \div 109$ J, local magnitude $3 \div 4.5$) can cause slight damages in buildings (Mutke and Dworak 1992). Every year $1000 \div 2000$ of mining events occur with the seismic energy E greater than 105 J (local magnitude $ML > 1.5$). Seismic activity is monitored by Upper Silesian Regional Seismic Network (maintained by GIG) and by local mine seismic networks. Hypocenters of mining shocks are located in a few areas, mainly related with mining activity of deep coal seams (500m below the surface) and occur in strong sandstone complexes and in the areas of significantly developed tectonics.

In mines with high seismic hazard it is very important to determine the areas where strong bumps can occur. This can be done using numerical modeling of stresses in rocks. However our experience in Polish mines indicates that the passive tomography is very effective for finding potential places of the seismic activity (Lurka 1998, 2002; Mutke et al 2001; Dubiński and Mutke 2005). This method enables to locate overstressed zones in the rock stratum and makes it possible to estimate the distance between these zones and underground openings. Knowing additionally the magnitude one can estimate peak particle velocity (PPV) at the excavation boundary, very important parameter to assess rock burst risk level, McGarr (1991), Kidybinski (1992), Dubiński and Mutke (1996), Kaiser et al (2005), Oven (2005), Albrecht and Potvin (2005), Mutke (2008).

Study of seismic source parameters averaged in moving time windows is also useful to estimate potential seismic hazard. In Polish coal mines we have observed that just before strong seismic event stress drop, seismic moment and seismic energy averaged in time window should significantly exceed their corresponding average values for all seismic events in the area of study.

2 Profile of the Longwall Panel 2Jd/502 in Wujek-Slask Coal Mine

Wujek-Slask mine is one of the most seismically dangerous mines in Polish Upper Silesia Coal Basin. The mining has been conducted from XIX century in many coal seams. The longwall panel 2Jd in seam 502 is located 765m underground. The thickness of the coal seam vary from 7m to 10m. The natural vertical pressure reach value of 20 MPa and locally is much higher due to edges of old mining and local faults. The map of longwall 2Jd is shown in figure 1. The length of longwall face was 185m. The mining was to be stopped a few meters ahead of the big fault with throw $h=150\text{m}$. Mining-geological situation shows that we are dealing with the very difficult mining conditions. In the past very strong seismic events and even a few rock bursts took place in this area..

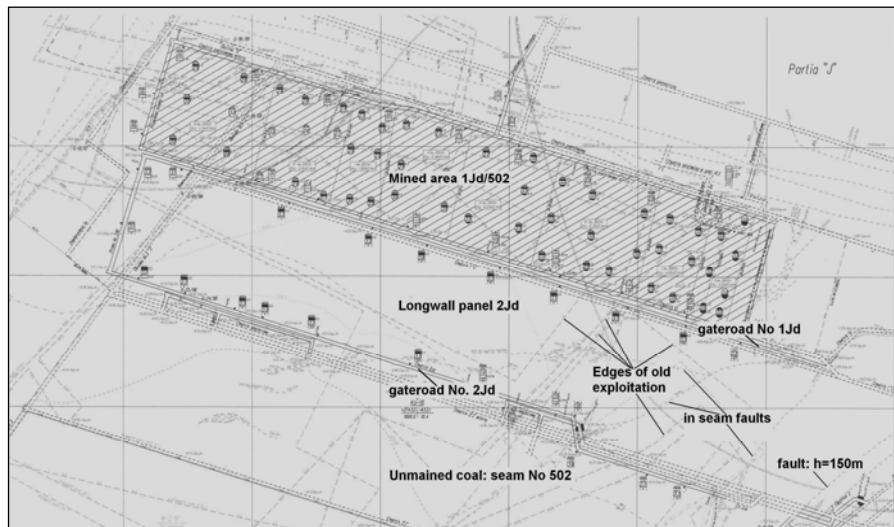


Figure 1. Plan view of working longwall panel 2Jd where microseismic monitoring was carried out.

P-wave velocity in coal seam and in surrounding hard rock was studied using seismic underground measurements (seismic in seam tomography). Velocity of seismic P-wave in coal seam varied from 1740m/s to 1840m/s and velocity of seismic P-wave in surrounding rocks varied from 3700m/s to 4400m/s - typical values for hard rocks located at a big depth ($\sim 800\text{m}$), especially for arenaceous shale. The floor of the coal seam 502 consists of shale clay, arenaceous shale and sandstone. The highest values of P-wave velocity are probably related with arenaceous shale.

The static values of the strength parameters like compressive strength and tensile strength of coal and floor rocks near the 2Jd longwall panel in seam 502 are following:

Coal in the 2Jd longwall (average P-wave velocity: 1790 m/s):

- average values of the compressive strength $R_c = 30,00 \text{ MPa}$
- average values of the tensile strength $R_t = 1,90 \text{ MPa}$

Arenaceous shale (average P-wave velocity: 4000 m/s):

- average values of the compressive strength $R_c = 38,02 \text{ MPa}$
- average values of the tensile strength $R_t = 2,44 \text{ MPa}$

3 Seismic Observation System at Field Study

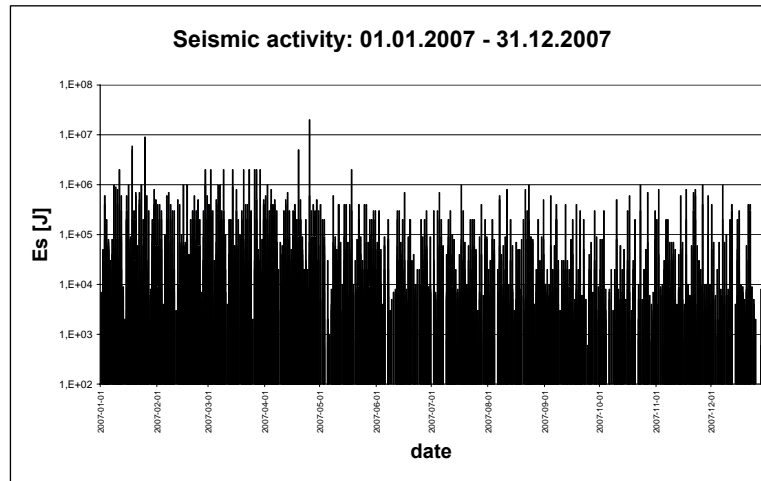


Figure 2a. Seismic activity observed from 01.01.2007 to 31.12.2007 at 2Jd longwall panel

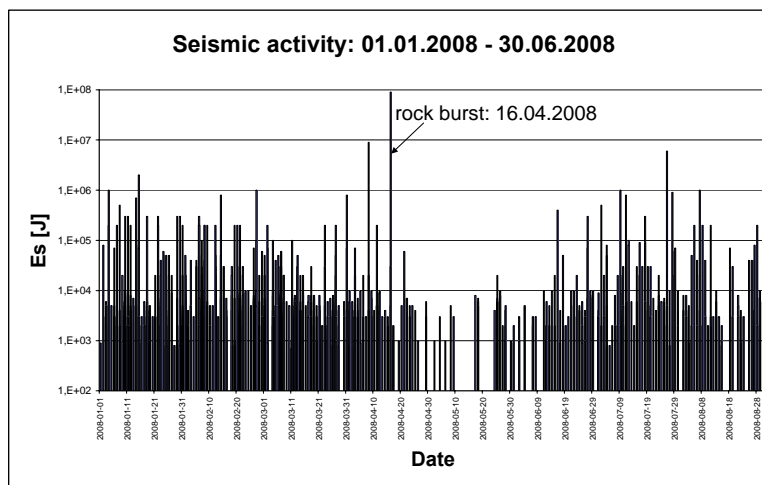


Figure 2b. Seismic activity observed from 01.01.2008 to 31.12.2008 at 2Jd longwall panel. The 9·107J (local magnitude 3,3) biggest seismic event was the reason of damaging effect in 2Jd gateroad.

64 channel flameproof Seismic Observation System was developed in Laboratory of Mining Seismology of Central Mining Institute as a management tool to evaluate rockburst hazard under ADEMA project. The Seismological Observation System “SOS” provides an efficient tool for transmission, recording and analysis of seismic events that occur in underground mines. The underground part comprises DLM measuring probes (low frequency-1Hz geophones) in combination with the transmitters for transmitting seismic signals in the form of current signals via transmission lines. The surface part comprises DLM-SO Receiving Station which is connected with the Seismic Recording System. The hardware allows to automatic trigger and record mining seismic events. Multilok and Seisgram software enable data acquisition and data processing to provide information about seismic source parameters and 3D location of seismic events. The real-time seismic monitoring system SOS has been installed in Wujek-Slask mine. During continuous measurements taken between July 2007 and

December 2008, more than 2000 strong seismic events were recorded from the panel of longwall 2JD (seismic energy: $E_s > 5 \cdot 10^2$ J, local magnitude: $ML > 0$). The seismic activity at longwall panel 2Jd is shown in figure 2. The biggest seismic events reached value of $106 \div 107$ J (local magnitude from 2,5 to 3,3). The distribution of geophones in vertical direction vary from -220m below surface level to -780m and secure good location conditions of hypocenters.

4 Analysis of tomographic velocity images to identify areas of high rock-mass instability

To study development and changes of P-wave velocity in longwall 2JD passive tomography reconstruction were performed and the evolutionary algorithm was used to find the solution of the tomographic problem (Schwefel 1995, Lurka 1996). The evolutionary algorithm is much more efficient and much more accurate than algebraic reconstruction algorithm (ART). The basic assumption of the analysis of tomographic P-wave velocity images is the increase of P-wave velocity with increase of pressure in the rock mass - Figure 3. We have observed that strong seismic events are located in zones of higher velocity and in zones of high velocity gradient. Relation between P-wave velocity and pressure is shown in figure 3 (laboratory study on samples of rock: left and field study-seismic profiling under edge: right).

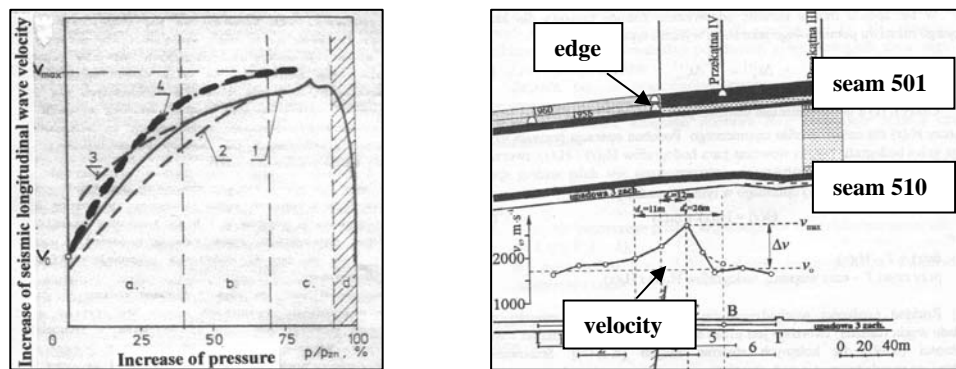


Figure 3 - Relation between P-wave velocity and vertical pressure: laboratory relation between pressure and P-wave velocity (study on samples – according to Dubinski 1989)- left and P-wave velocity seismic profiling under edge – velocity increase is seen under edge where pressure is highest – right.

Two P-wave velocity images were calculated using seismic events recorded in longwall panel 2Jd from November 1st 2007 to December 31th 2007 and from January 1st 2008 to April 15th 2008. About 200-300 hundreds of seismic event collected by SOS seismic network were used to calculate a velocity images.

The first P-wave velocity image, calculated in December 2007, shows a few zones with high value of velocity (zones I, II, III and IV in fig 4). The average P-wave seismic velocity in the area of study was 3925 m/s and 200m in front of the coal face line (zone I) is observed the highest velocity value 4700 m/s. This zone is related with edges of old mining in different coal seams (seam 411-320m, seam 413 – 190m, seam 414 – 170m and seam 502 – 3m above current mining). In the area of zone I, the highest seismic energy events took place. The stars in Figure 4 (left) indicate tremors which occurred in longwall panel 2Jd from January 2008 to March 2008 during the next 3 months after the tomographic image was calculated. Almost all seismic events took place in the highest velocity zone (see fig 4. 2D) or high gradient velocity zone (see Figure 4. 3D).

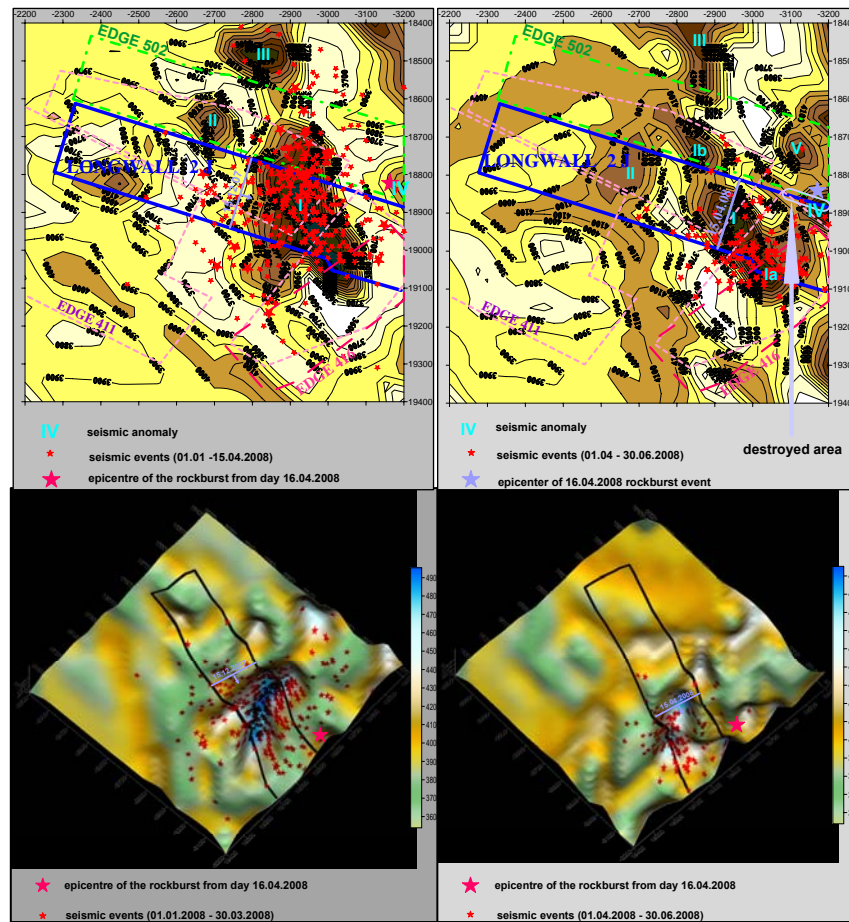


Figure 4 -Longwall 2Jd - velocity images from passive tomography based on tremors recorded between July and December 2007- the stars indicate tremors that occurred during the next 3 months (January-March 2008) – left and between January and April 2008 – the stars indicate tremors that occurred during the next 3 months (April-Jun 2008) – right

The second velocity image was calculated on 15 April of 2008, just one day before rockburst. The average P-wave seismic velocity in the area of study was 3975 m/s (50 m/s higher than 3 months ago). The highest seismic velocity values appeared just in front of coal face line (zone I – connected with edges of old mining and faults in coal seam). The next high velocity zone appeared 200m north-east of coal face at the boundary between mined and unmined area near the gallery 1Jd (zone IV). Zone I is observed in similar place like 3 months earlier. The zone IV was developed as a new one. Figure 4 shows additionally that the highest velocity values, more than 4700 m/s, are observed in zones I, Ia and IV. In zone I and Ia, a lot of seismic events took place and in zone IV the $9 \cdot 10^7$ J (local magnitude $M_L=3,3$) rockburst occurred on 16th April 2008. The rockburst caused the collapse of gallery 1Jd at the length of 85 metres (Figure 5) in the southern part of the IV zone. Serious damaging effects in the gallery 1jd took place in the high velocity and high gradient velocity zone IV.

P-wave velocity images in the longwall panel 2Jd have shown that high seismic velocity zones are moving in time. Epicenters of seismic events were located in the area of highest velocity and highest velocity gradient - figure 4. The velocity distribution indicates that migration of seismic events is related to changes of the P-wave velocities. Backward analysis of seismic activity in the longwall panel 2JD has shown that velocity images are useful to identify areas of high rock-mass instability. The basic idea of such analysis is to study temporal

changes of passive velocity images. This method enables to determine overstressed zones in the rock mass. The known positions of potentially seismic-prone zones allow us to estimate the distance between the potential seismic sources and underground openings and therefore we can use empirical relation between normalized parameter, $PPV \cdot R$, and the scalar seismic moment, M_0 , McGarr (1991), Mutke (2008). In Polish coal mines the empirical relation $\log(PPV \cdot R) = 0,66 \log M_0 - 7,4$, was obtained by Mutke (2007, 2008). Using this equation the value of peak particle velocity (PPV) in the damaged tunnel 1Jd (figure 12), reached vary from 0,35 m/s to 0,6 m/s.



Figure 5 - Picture of rock burst effect in tunnel after tremor with seismic energy 9-107 J, ($M_L=3.3$), which occurred on April 16th 2008. The gallery was damaged on segment of 85 meters and the floor was lifted up 1,5 m.

5 Tomography after Rock Burst Event

After rock burst the longwall face was moved a few meters. The average P-wave velocity in the area of study decreased to value of 3870 m/s. The velocity image calculated on December 2008 (8 months after rock burst) indicates that destressed, low velocity zone is observed in vicinity of longwall face. Two high velocity zones are seen at the galleries 1Jd and 2Jd one hundred meters in front of coal face. The P-wave velocity value in these zones is about 4200 m/s. Therefore one can conclude that seismic hazard was smaller in December 2008 than in April 2008 when the biggest high velocity zones with values greater than 4700 m/s were observed.

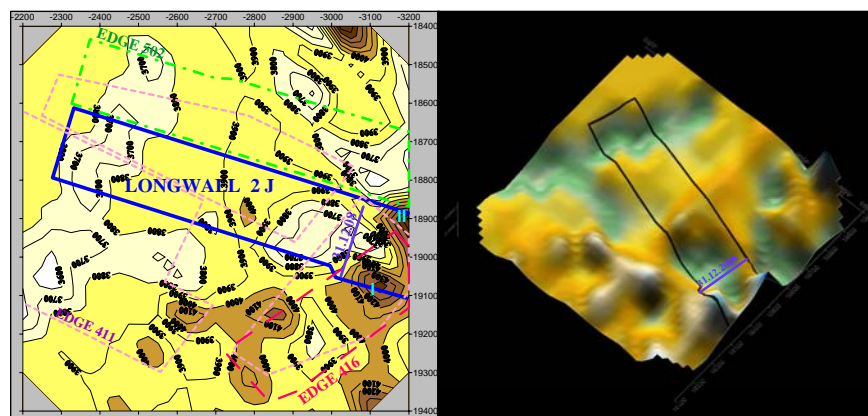


Figure 6 - Longwall 2Jd – passive tomographic velocity image based on tremors recorded between October and December 2008

6 Real Time Seismic Monitoring and Data Processing

Real time Seismic Observation System was installed in Wujek-Slask mine. During two years of continuous measurements starting from January 1st 2007 to December 31th 2008 more than 2000 seismic events in the area

of longwall panel 2Jd in seam 502 were recorded. The seismic energy varied from $E_s = 5 \cdot 10^2$ J (local magnitude 0,0) to $E_s = 8 \cdot 10^7$ J (local magnitude 3,3).

New method for processing seismic data was developed and implemented in SOS system. The developed software is based on the network architecture and works on all variants of MS WINDOWS operating system. The software is composed of two main programs: “SEISGRAM” for the analysis of seismic signals and “MULTILOK” for the analysis of tremor parameters i.e. seismic event location, seismic energy and seismic source parameters.

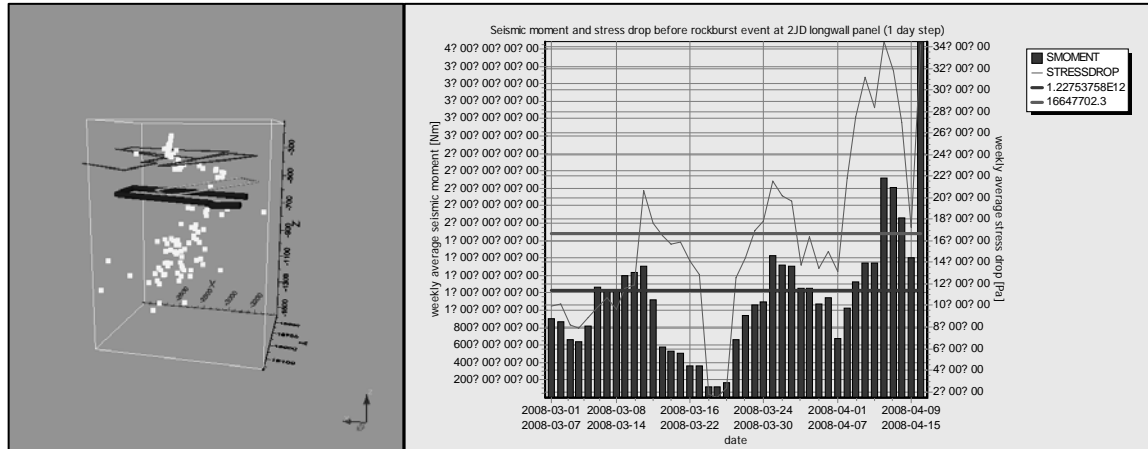


Figure 7. 3D location of seismic events in “Wujek-Slask” mine (gray dots – hypocenter of seismic events, thick line – contour of longwall 2Jd, thin lines – edges)- left. Distribution of stress drop and seismic moment before rock burst in 2Jd longwall panel (weekly average value shown) –right.

3D location of seismic events has shown that approximately 70% of the seismic sources are located below the coal seam whilst 20% were located above the seam. Most of these events occurred far from tunnels and 2Jd panel. Only a few strong seismic events were located in seam 502 in the close vicinity of 2Jd panel. One of them caused rockburst

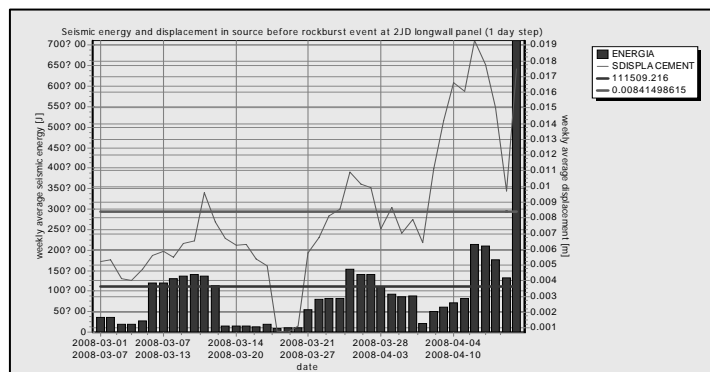


Figure 8. Distribution of seismic energy and source displacement before rock burst in 2Jd longwall panel (weekly average value shown).

3 D location of seismic events in 2Jd panel and distribution of seismic moment and stress drop before rockburst are shown in figure 7. Stress drop and seismic moment were calculated as weekly average values with 1

day step (data from 01.03.2008 to 15.04.2008). One can observe an increase of these values before rockburst dated on April 16th, 2008.

In Figure 8 the distribution of seismic energy and seismic source displacement shows also an increase of their values before the rock burst

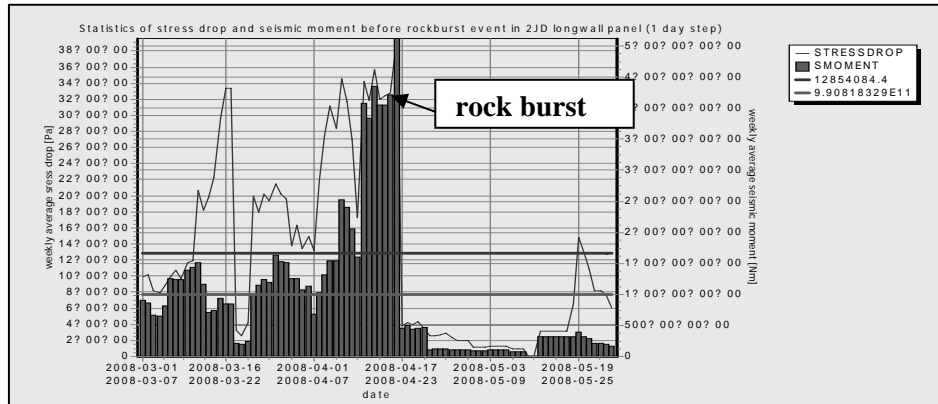


Figure 9. Distribution of stress drop and seismic moment before, during and after rock burst in 2Jd longwall panel (weekly average value shown).

In figure 9 distribution of stress drop and seismic moment in longer time interval including rock burst event is shown. One can see that after rock burst the values of stress drop and seismic moment are significantly lower than average levels (shown as straight lines). This indicates that after rock burst destressing process in rock mass around 2Jd panel is observed.

7 Peak Particle Velocity (PPV) at Excavations

In Polish coal mines one of the basic mechanisms causing rock bursts is a sudden increase of dynamic load induced by the vibrations being a result of tremors. The increase of stress is an effect of superposition of the existing static stresses in rock mass with those produced by the vibrations. As it is known, the peak particle velocity PPV is proportional to increment of stresses in rock mass (Brady and Brown 1985). The dynamic load should be known to assessment rockburst hazard and stability of excavations. To do this, the empirical formula for prediction of PPV in near field induced by mining seismic events in Upper Silesian coal mines was elaborated (Mutke 2007, 2008). The set of 65 well documented seismic events, for which PPV values were measured in near-tremor areas and the seismic moments were determined using records from the far wave field. The parameter value was used to find relations between parameter $PPV \cdot R$ (amplitude scaled with hypocentral distance increment) and scalar seismic moment M_0 . The set of data included tremors with values from $M_0 = 3 \cdot 10^{10} \text{ N}\cdot\text{m}$ to $M_0 = 4 \cdot 10^{13} \text{ N}\cdot\text{m}$. The correlation is expressed by the following empirical equation (Mutke 2008):

$$\log(PPV \cdot R) = 0.66 \cdot \log(M_0) - 7.4 \quad (1)$$

Where PPV is in m/s, R is in m and M_0 is in $\text{N}\cdot\text{m}$. Relation (1) allows predicting PPV values for vibrations in the near and middle wave field from far field records.

In their study, McGarr et al. 1981 found a relation between M_0 and PPV for the gold mines situated in the South Africa (RSA). Analyses of the two above mentioned relations show, that for seismic moment values of $1 \cdot 10^{13}$ – $1 \cdot 10^{14} \text{ N}\cdot\text{m}$ their corresponding values of scaled velocities are similar. For smaller values of seismic moment, McGarr's formula gives a bit larger values of scaled velocity $PPV \cdot R$. These differences might arise from differences in properties of the rocks in the UPCB and the RSA and the larger depth of mining in case of the mines in the RSA.

The empirical criterion for potential rock burst hazard has been developed based on the worked out relations and analysing the well documented database of rock bursts. The 120 rock bursts with damaging effects in mine excavations, occurred in the Upper Silesian Coal Basin from 1988 to 2006 were taken into account. This criterion has shown that 90% of rock bursts took place after those tremors that produced peak particle velocity (PPV) with a value from 0.05 to 1.0 m/s, and the distance between the inducing tremor and the damaged working did not exceed 100 metres (Mutke 2008). The criterion in his damage category is similar to that described by Owen 2005 and by Kaiser et al 2005.

It should be emphasised here that local state of static stresses constitutes a very important factor having an essential influence on probability of occurrence of a rock burst as a result of dynamic stresses caused by a mining tremor. Local faults, geological structure, mining conditions, supports and remains in the referred to seam, cause locally places with increased static stresses (Dubiąski 1989). Such places are much more prone to rock bursts at relatively small values of PPV. The occurrence of several rock bursts at a PPV value a bit higher than 0.05 m/s resulted probably from the presence of places with locally increased static stresses (concentration zone of stresses).

Using empirical relation (1) and far field records, the PPV values were calculated by the gateroad 1Jd in three places:

- at the beginning observed damage
- at the end observed damage
- at the face position on 16th April 2008

The highest value of PPV was observed at 16th April 2008 seismic event. In the damaged area in excavation 1Jd, the PPV reached values from 0,35 to 0,6 m/s. The same seismic event caused only 0,16 m/s at the intersection of excavation and coal face, and in that place no damaging effect was observed. The distribution of PPV values in these three places during the period 01.01.2008÷01.05.2008, are shown on pictures 1-3. PPV maximum values in destroyed area result not only because of the short distance from the shock but also from additional stresses from the edges. The PPV=0,16 m/s was harmless at the intersection of coal face and gateroad 2Jd because of lack additional stresses from edges and because of additional strengthening the support in this place. The critical values of PPV from 0,35 to 0,6 m/s is in good correlation from the empirical criterion elaborated for Upper Silesian Coal Basin region. For remaining seismic events PPV values are lower and they didn't cause damage in the 2Jd gateroad (see Figure 1-3). It means that PPV up to 0,2 m/s weren't a danger to the gateroad.

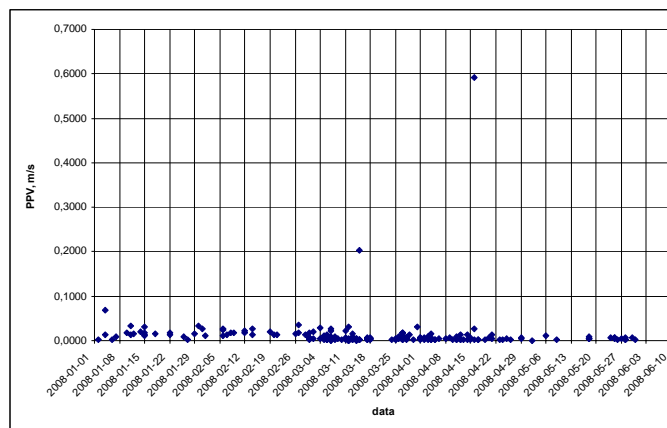


Figure 10. Distribution of PPV by 2Jd gateroad at the beginning observed damage.

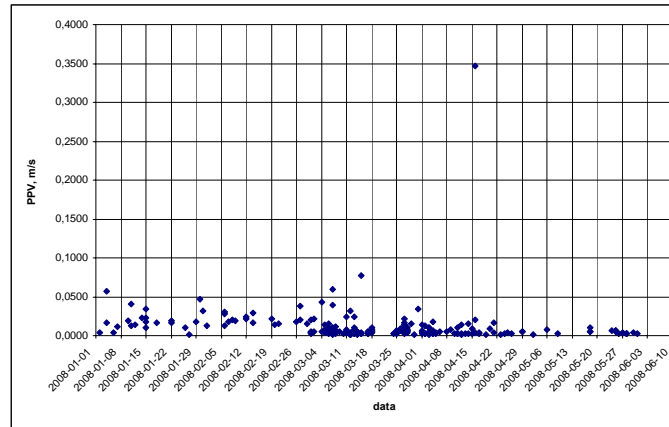


Figure 11. Distribution of PPV by 2Jd gateroad at the end observed damage.

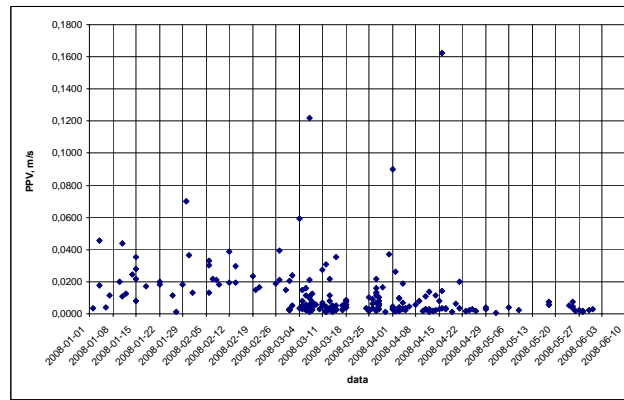


Figure 12. Distribution of PPV by 2Jd gateroad at the intersection with face position on 16th April 2008 (data of rock burst).

8 Conclusions

On April 16, 2008 rock burst caused by the $M=3.3$ seismic events damaged tunnel nearby 2Jd longwall panel in the Wujek-Ślask mine. This event gave us the opportunity to use joint analysis of passive tomographic velocity images, temporal changes of seismic source parameters and temporal changes of PPV.

The field study on the 2Jd longwall panel has shown that the multichannel seismic underground network with spatial distribution of seismic stations is fundamental in the assessment of rock burst hazard in mines. First of all such a network should allow accurate location of hypocenters.

Especially promising results were obtained studying changes of passive tomographic velocity images to determine seismic prone areas in panel 2JD in the Wujek-Ślask mine. Just before rock burst, clear zones of high velocity and high velocity gradient have been obtained nearby 2Jd gateroad. Study of seismic source parameters in moving time windows seems to be very promising mid-term precursors of rockbursts as well. An increase of the average value of the seismic moment and seismic stress drop in moving time window before rock burst dated on April 16th, 2008 was observed.

Using empirical relation based on far field records the PPV values were calculated for all the seismic events located nearby the gateroad 1Jd in three points:

- at the beginning observed damage
- at the end observed damage
- at the coal face position on 16th April 2008

The highest PPV values were obtained for seismic event recorded on 16th April 2008 that caused rock burst. In the damaged area in excavation 1Jd, the calculated PPV values varied from 0,35m/s to 0,6m/s. It is in good correlation with empirical criterion for potential rock burst hazard developed for Polish coal mines in the Upper Silesia region. Therefore PPV criterion seems to be very useful in studying rock burst hazard.

Presented results may be applied in both spatial and time table planning of mining operations under high seismicity conditions and the in the rational choice of preventive actions ensuring functionality of mine workings and improvement of work safety level.

ACKNOWLEDGMENTS

The data processed in this paper were collected as part of ADEMA project No. RFCR-CT-2005-000001 funded by Research Programme of the Research Fund for Coal and Steel.

REFERENCES

1. Brady, B.G. and Brown, E.T. Rock Mechanics for Underground Mining. George Allen and Unwin, 1985.
2. Drzewiecki, J. Movement Dynamics of Detached Roof Strata ahead of the Longwall Coalface. in Fifth International Symposium on Rockburst and Seismicity in Mines, (South African, 2001).
4. Dubinski, J. and Mutke, G. Characteristics of Mining tremors within the Near-wave Field Zone. Pageoph, 1996, 147 (2). 249-261.
5. Dubinski, J. and Mutke, G. Study of temporal changes of P-Wave velocity in Polish Copper Mines in High Seismic Activity Zones. in 6th International Symposium on Rockburst and Seismicity in Mines- Australia – Perth, (Australian, 2005).
6. Gibowicz, S.J. and Kijko, A. An Introduction to Mining Seismology. Academic Press, 1994.
7. John, C.M.St. and Zahrah T.F. Aseismic Design of Underground Structures. Agbajian Associates, Rep.No. R-8411. 1985.
8. Kaiser, P.K., Vasak, P. and Suorineni F.T. New dimensions in seismic data interpretation with 3-D virtual reality visualisation for burst-prone mines. in Sixth International Symposium on Rockburst and Seismicity in Mines Proceedings, (Australian, 2005).
9. Kowalczyk, J. and Szwejkowski, J. Relation between Anomaly of Seismic Velocity and State of Stress around Geological Structures. Geology, 1975, p.2.
10. Lurka, A. Seismic Hazard Assessment in the Bielszowice Coal Mine Using the Passive Tomography. in Proc. of Joint Japan-Poland Symp, (Kyoto, 2002).
11. Lurka A. Zwiększanie Informatywności Technik Tomograficznych w procesach eksploatacji złóż, Archiwum Górnictwa, PAN, Kraków, 2004, 495-509. (In Polish).
12. Lurka A., and Mutke G., Poprawa dokładności lokalizacji składowej pionowej hipocentrow wstrząsów górniczych (Improvement of Accuracy of Location Vertical Component mining Tremors Foci. Gospodarka Surowcami Mineralnymi (Mineral Resources Management), 2008, 24-2/3. 261-270.
13. Maxwell, S.C. and Young, R.P. A Comparison between Controlled Source and Passive Source Seismic Velocity Images. Bull. Seism. Soc. Am, 1993, 83 (6). 1813-1834.
14. Mc Garr, A., Green, R.W.E. and Spottiswoode, S.M. Strong Ground Motion of Mine Tremors. Source Implications for Near-source Ground Motion Parameters, Bull. Seismol. Soc. Am. 1981, 71. 295-319
15. Mutke, G., Lurka, A., Mirek, A., Bargiel, K. and Wrobel J. Temporal Changes in Seismicity and Passive Tomography Images. a Case Study of Rudna Copper Ore Mine-Poland. in Fifth Intern. Symp. Rockbursts and Seismicity in Mines, (South African, 2001)
16. Mutke, G. Characteristics of Near-field Ground Motion Resulting from Mining Tremors to Assessing of Rock Bursts Hazard. Prace Naukowe (Scientific Works) GIG, 2007, 87. 145.

17. Mutke G., Stability of the Underground mine Workings in the Near-field Zone of Seismic Events. in 21st World Mining Congress 2008 – New Challenges and Vision for Mining, (Poland, 2008)
18. Owen M.L. Calibrating a Semi-Quantitative Seismic Risk Model Using Rockburst Case Studies from Underground Metalliferous Mines. in Sixth International Symposium on Rockburst and Seismicity in Mines Proceedings, (Australian, 2005).
19. Albrecht J. and Potvin Y. Identifying the Factors that Control Rockburst Damage to Underground Excavations. in Sixth International Symposium on Rockburst and Seismicity in Mines Proceedings. , (Australian, 2005).
20. Schwefel H.P. Evolution and Optimum Seeking. John Wiley and Sons, 1995.
21. Stec K. Characteristics of Seismic Activity of the Upper Silesian Coal Basin in Poland. Geophysical Journal International, 2007, 168. 757–768.

STUDY ON THE MECHANISM OF SURFACE COLLAPSE ABOVE THE FOOTWALL

QING-YUN CHEN and MING ZHOU

*Department of Environment and Civil Engineering, Wuhan Institute of Technology
Wuhan, 430073, P.R. China*

SHUI-PING WANG

*Jinshandian Iron Ore Mine, Mineral & Company, Ltd. WISCO
Huangshi, 435116, P.R. China*

LIN-FANG MEI

*Daye Iron Ore Mine, Mineral & Company, Ltd. WISCO
Huangshi, 435006, P.R. China*

An underground mining strata movement dynamic analyzing model is established according to the operation process with sublevel caving method and the flowing characteristics of the collapsed strata, in which different areas and strata are given different mechanical parameters respectively and FLAC is used as a computing tool. Computing results of Jinshandian Iron Ore Mine's Yuhuasi Operation show that when mining operation is above level -150m, the footwall strata movement angle and collapse angle is small and the strata deformation becomes mild when the operation proceeds. The major factors affecting the foot wall strata deformation include the strata state, dip of the ore body, and the thickness of the ore body and mining method.

1 Introduction

Jinshandian Iron Ore Mine Yuhuasi Operation is a mine with an independent developing system and of which the open pit operation ended in the late 1970s at level $\pm 0\text{m}$. The underground operation started in 1988. When the mining activities proceeded to below -150m, the pit slope slid in a large scale on the surface above the footwall and the railway had to be shifted inward. The slide directly affected the safety of the overhaul workshop and the office building.

This phenomenon is not accidental, in fact, it is a common occurrence. From late 1990s on, with the increase of mining depth and intensity in many large and middle sized old mines in China, especially those using sublevel caving method, accidents such as fracture, inclination, and collapse happen frequently to the buildings and constructions on the surface above the footwall, which is a great menace to the safety of workers in these mines. These cases show that there exists certain risk in the practice of earmarking the surface

movement scale using engineering analogue method and arrange the general Figure on this basis in the early stage of mine establishment. So it is of great practical significance for the work safety of mines, general Figure design and land purchase to perform research into the law of footwall strata movement deformation in underground mining.

2 General situation of the mine

2.1 Geography of the Mine

Jinshandian Yuhuasi ore bed is an 800m long, 450m wide skarn magnetic iron ore mine formed by contact and metasomatism of high temperature fluid. It is situated between the south wing of Bao'an duplex anticline and the west part of the north rim of Jinshandian intruding body. Strata in the mine is primarily of Triassic Puqi group purple sand shale and Jialing river limestone spreading in the east-west direction controlled by the local tectonic control. The ore bed occurred in the unconformable contact zone of the above-mentioned strata and Yanshan epoch mid acid intrusive body and controlled by the contacting separation fracture and faulted after mineralization. The ore body mainly consists three segments. The east one, which is transmeridional and lies between line II and IV, the bottom altitude being 0m and is finished. The middle segment, about 300m long, lies between line V and VII and it's the major zone of the ore bed. It is in north-west direction, dip angle about 40~65° (the dip angle has a tendency toward flat as the depth increases). Below -200m, the direction of the ore body changed to south-north and dipping towards the west. The average thickness is 30-40m with 86~145m at most. The altitude varied between +85~-380m. The west segment is situated between line IX~X and altitude -170~-520m.

2.2 Introduction of the Operation

Sublevel caving method is adopted with stage height at 50m. The sublevel interval is 10m and above level -100m and below, 12.5m. The present operating level is -212.5m. The designed capacity is 400 kt/a and actual output reached 500 kt/a.

2.3 Mechanical Parameters of the Ore Body and Structural Face

Giving ample consideration to the connatural weak structural face of the rock mass and weathering, combining the wavelength of the longitudinal wave in the rock mass, the mechanical parameters of the rock mass are determined with reduction factor method. The mechanical parameters is achieved through calculation for the rock mass 0~100m, 100~300m and >300m below surface in Yuhuasi mine (reduction factors 0.3, 0.4, 0.5). See Table 1.

Table 1. Physical mechanical parameters of the rock mass

Lithology	depth/m	Specific gravity (kN/m^3)	Elastic modulus E (GPa)	Poisson's ratio μ	Cohesion c (MPa)	Angle of internal friction φ ($^\circ$)	Tension strength (MPa)
Hornfels	0~100	26.0	12.60	0.22	1.10	30	0.2
	100~300		16.80		3.30		0.5
	>300		21.00		5.50		2.5
Quartz diorite	0~100	27.0	13.32	0.29	1.75	36	0.2
	100~300		17.76		5.25		0.5
	>300		22.20		8.75		2.5
Iron ore	0~100	40.5	8.34	0.20	0.47	31	0.2
	100~300		11.12		1.42		0.5
	>300		13.90		2.36		2.0
Loose rock		20.0	0.012	0.14			0.0

Experimental results are adopted of the physical mechanical parameters of the rock mass structural plane without reduction. The parameters are shown in Table 2.

Table 2 Physical mechanical parameters of the rock structural plane

Sequence number	Lithology	C (MPa)	φ (MPa)
1	Hornfels	0.57	14°29'
2	Diorite	0.12	56°29'

In Yuhuasi mine, there is a structural horizontal stress field with the primary stress in the near east-west (N80°W) direction. The original stress in the horizontal direction is considered 1.4 times of its own weight stress, the effect of water being ignored in the computing.

3 FLAC numeric imitating calculation

3.1 Calculation Criteria

Movement angle and breaking angle is determined by critical deformation of the surface, according to the metallurgical mine survey standard by the former Administration of Metallurgy, for average brick and masonry constructions, the critical deformation point is defined as below:

The criteria for determination of the surface movement angle are that surface inclination ratio $i=3\text{mm/m}$, surface horizontal deformation $\varepsilon=2\text{mm/m}$ and camber of section curve $k=0.2 \times 10^{-3}/\text{m}$; for break angle, the criteria are surface inclination ratio $i=3\text{mm/m}$, surface horizontal deformation $\varepsilon=2\text{mm/m}$ and camber of section curve $k=0.2 \times 10^{-3}/\text{m}$.

In the practice of actual survey, the concept of boundary angle is introduced and the point that has 10mm of subsidence or horizontal movement is considered boundary point of the movement basin.

3.2 Section to be Calculated and the Computing Program

Through analysis of the geological ichnography and section, taking into sufficient account the extent of the affection of the mining activities underground to the constructions and buildings on the surface, and the major zones to be mined in the future, the sections VII, VI and VIE are selected in calculation. The positions and parameters of these sections are shown in Table 3.

Table 3 Positions and parameters of the sections to be calculated

Section	Azimuth angle	Space between (m)	Average thickness(m)	Dip angle
VII	125°51' 34"	72	38	65°
VI	125°12' 06"		40	60°
VIE	125°12' 06"		30	65°

According to the sublevel caving operation practice, two sublevels are in one cutting, i.e. 25m height is considered a calculating layer, the working out section being backfilled with mullock and fell wall rock. The initial balance is calculated from the end of the open pit excavation and calculates down from level 0m through the pinch-out of the ore body.

3.3 Dynamic Analyzing Modulus For Numeric Calculating

While mining large thick ore bodies with steep dip using sublevel caving method, the roof is controlled by backfilling the working out section with fell wall rock. After the working out section is fulfilled, further deformation will take place in the wall rock and leads the rocks to relax; this part of wall rock is called wall rock relaxation zone. Inside the wall rock relaxation zone, subsidence or greater movement may take place, outside the zone, however, the rock mass is likely to maintain steady through its own balance. Regressive analysis of the zone according to the radar survey result of the near surface mining geology show that the maximum movement width $L=(1.6\sim2.0)/l$ (where l is the horizontal thickness of the ore body); the rock relaxation zone is funnel-shaped in space with the tip at the boundary of the ore body being mined and progresses upward at $55^{\circ}\sim70^{\circ}$ until it reaches the maximum width of the funnel, then the relaxation progresses almost vertically until it reaches the surface. From the start point of the maximum relaxation width, drawing two diagonal lines intersecting the surface similar to the movement angle of the mine, the area between the intersection points is movement area. Initial calculating model is established on this basis.

In the course of modelling, to eliminate the boundary conditions' influence on the calculating result, sufficient length is taken in directions of the footwall, the hanging wall and the depth. To increase the precision of calculation and guarantee the smoothness of the curve, the ore body and the wall rock nearby is divided into elements of 5m by 5m, the element size in the areas away from the ore body is enlarged at a certain ratio.

Section VII and VI contains 180 by 118 elements, section VIE has 150 by 118 elements. Every functional area is signed with command MARK respectively to ensure the correctness of the calculation. In the course of calculation, backfilling is not performed until a certain deformation appeared in the wall rock after excavating and the physical mechanical parameters of the backfill is that of loose material. The calculation convergence is controlled by unbalanced force, if which is less than 10000 Pa, the calculation of the system is regarded to have reached balance, and the cutting of the next sublevel can start. Moore-kulun destruction code is adopted.

3.4 Calculating Results and Appraisal

The calculating results show that the movement angles of the three sections vary between $45^{\circ}\sim 50^{\circ}$ instead of 55° adopted in the design; mining activates in the ore body below -162.5m have little effect to the footwall strata deformation and the surface above the footwall is basically steady. Strata movement angle is not only related to lithology, but also affected by the quality of the rock mass, dip of the ore body, thickness of the ore body and mining method, etc., among which the quality of the rock mass, dip of the ore body, thickness of the ore body and mining method is most sensitive factors. The footwall strata deformation has the following characteristics:

① Strata movement angle reduces when the rock quality is weak (in comparison with the design, the same below). When mining activity was in the ore bodies above -100m, the movement angle varies between $30^{\circ}\sim 45^{\circ}$ due to the severe weathering of the rock.

② Strata movement angle reduces when the dip angle of the ore body increases. Dip angle is over 70° in the ore body above -100m, so the movement angles in all the three sections are small. Because if the dip angle is big, the slipping force of the footwall rock is great, the incline angle of the potential gliding plane decreases which in turn reduces the movement angle, and great gliding body is more likely appear. For example, the gliding body between line VIE and VI in the footwall was produced in this way. When mining activity advances to below level -162.5m, the dip of the ore body flattens and the strata deformation almost not affect the surface.

③ Strata movement angle reduces when the thickness of the ore body increases. The crests on the curve of strata movement angle about mining depth match the thick parts of the ore body.

④ Strata movement angle increases slowly when the mining depth increases. In section VIE, neither the dip angle nor the thickness varied significantly, the movement angle increases slightly as the mining depth increases.

⑤ The boundary angle and break angle has the same variation tendency with the movement angle, when mining in the near surface part, the boundary angle is about 40° and the break angle is between $50^{\circ}\sim 55^{\circ}$.

⑥ The main destruction to the footwall strata slope is tension.

⑦ The footwall strata movement angle is a combined result of effects of various factors, it is normal for the footwall movement angle and mining depth curve to have undulation.

3.5 Engineering Verification

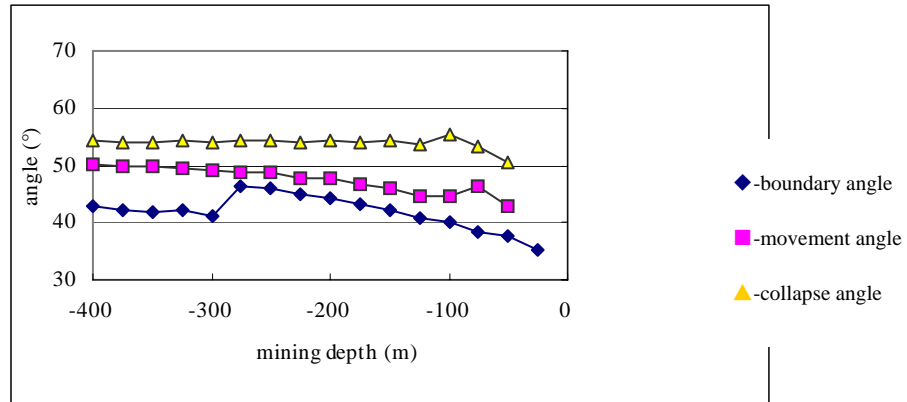


Figure 1 Footwall boundary angle, movement angle, collapse angle about mining depth in section VIE

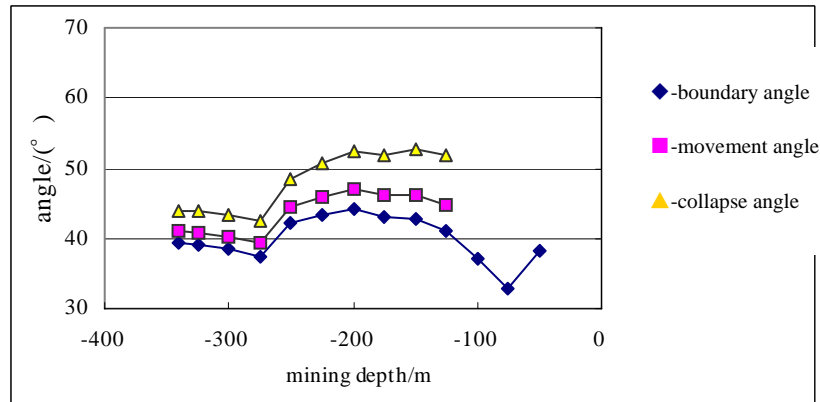


Figure 2 Footwall boundary angle, movement angle, collapse angle about mining depth in section VI

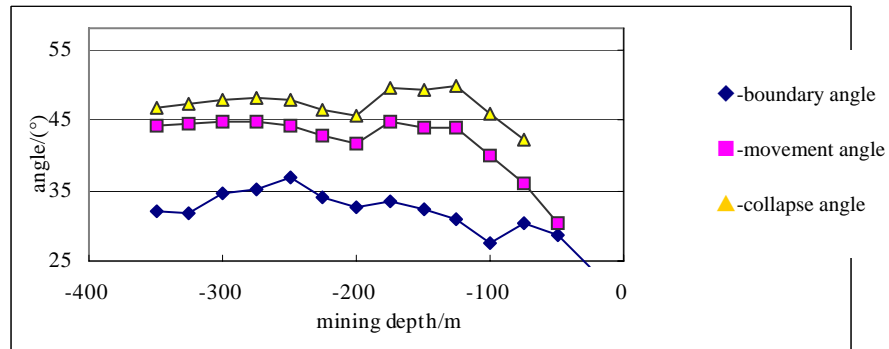


Figure 3 Footwall boundary angle, movement angle, collapse angle about mining depth in section VII

Table 4. Comparison between the results of calculation and survey (unit: °)

Section No.	Angles from FLAC calculating			Surveyed break angles	Angles in the design	
	boundary	movement	collapse		movement	collapse
VII	32.22	43.96	49.24	50.0	55	60
VI	42.92	46.12	51.85	52.1	55	60
VIE	42.33	46.04	54.29	53.8	55	60

Note: The table shows surface deformation data for mining activates in below level -150m

The result of calculation and survey is contrasted in Table 4. The difference between calculation and survey for section VIE is only 2.22%, while that for section VI is 29.3%, and 71% for section VII. The difference for section VII is large, that is because section VII is near the western bench of the open-cut pit, so there exists end effect. With the increase of mining depth and intensity, now the deformation and destruction of the western bench is severe and the footwall strata deformation rate increases obviously, it is mainly the result of the release of the deformation accumulated previously when mining in the near-surface part. On completion of this stage, the footwall strata deformation rate will decrease.

As for the large sliding body in the middle of the mining area, the fracture face is basically continued. This can testified by the fact that the tall trees and grass above was still flourishing in the severe drought in 2003. The sliding body is getting stable and this further proves that the middle of the footwall is basically steady.

4 Conclusions

The following conclusions can be drawn:

(1) The underground mining strata movement dynamic analyzing model is established according to the sublevel caving process, and the flow characteristics of the collapse wall rock satisfactorily reflects the destruction process of the footwall strata deformation.

(2) The strata movement angle is not only related to the lithology, but also affected by the quality of the rock, dip angle of the ore body, thickness of the ore body and the mining method, among which the quality of the rock, dip angle of the ore body, thickness of the ore body and mining method are the most sensitive factors.

(3) The main destruction to the footwall strata slope is tension.

(4) The footwall strata movement angle varies between 45°~50°, mining activates in the ore body below -162.5m have little effect to the footwall strata deformation, and the surface ground above the footwall is basically steady.

Acknowledgements

1. Cao, Y. Macro Collapse Characteristics of and Counter Measures to the Surface Movement in Tectonic Stress Type Mines. Mining And Metallurgy Engineering, 2002, 2. 31-33.

2. Li, T.H. On Variation of Rock Mass Characteristics about Depth. Chinese Science and Technology Press, 1994.
3. Wu, X.C. The Relationship between the Rock Mass Deformation Modulus and the Depth. Chinese Journal Of Rock Mechanics And Engineering, 1998, 5. 487-489.

ANALYSIS OF THE ENERGY RELEASING RATE IN ROCKBURST FAILURE

YAO-HUI WANG

*Wuhan Institute of Rock and Soil Mechanics, Chinese Academy of Sciences
Wuhan, 430071, P. R. China*

FENG SHEN and CONG-SHI WU

*Changsha University of Science & Technology
Changsha, P.R. China*

Rock burst is a sudden and violent failure of overstressed rock resulting in the instantaneous release of large amounts of accumulated energy. The amount and rate of the energy release can dominate the failure process in range and intensity. In this paper, the energy releasing rate in rock tunnel excavation is numerically analyzed based on the complete failure behavior of the rock. The post peak failure characteristics of the rock mass are simulated in the numerical model. In this way, the variation of the elastic energy stored in the rock mass is computed. Furthermore, the amount of the elastic energy and the releasing rate can also be evaluated simultaneously. The paper presents the numerical simulations of over excavation and loose blasting. The numerical results indicate that the risk of rock burst failure can increase if the rock mass is over excavated in tunnel projects. On the other hand, the loose blasting in the whole circular area can effectively reduce such risks. On the contrary, careful consideration should be made to adopt loose blasting in the stress concentrated area because too much reduction of the stiffness of the rock in such an area may unexpectedly increase the risk of rock burst.

1 Introduction

Rock burst is a sudden and violent failure of over-stressed rock resulting in the instantaneous release of large amounts of accumulated energy. The energy releasing behavior in fractured rock mass can dominate the dynamic failure in range and intensity. As many researchers point out, a rock burst failure is likely to happen if the released energy is greater than the energy that can be dissipated in non-dynamic fracture during excavation [1-5]. According to this point, many models were proposed to predict or describe the rock burst failure [3-5].

Numerous experimental results on the rigid testing machine illustrate that the ratio of the loading slope to the unloading slope can represent the tendency of dynamic fracture of rock samples [4-5]. As shown in Figure 1, if a rock sample is compressed to failure, much more energy can be absorbed in Type I rock than in Type II. Therefore, a dynamic burst is more likely to happen for Type II samples in compressive tests than that for Type I ones. The analysis of the complete load-displacement curves can help us to evaluate the risk of rock burst for a certain rock mass [5-6]. Furthermore, such load-displacement behaviors can also be adopted to evaluate the stability of excavation projects in rocks [7].

On the other hand, the risk of dynamic fracture is related to not only the amount of the released energy, but also the releasing rate. Based on the studies in some coal mine projects, some researchers proposed a method to evaluate the possibility of rock bursts, in which the energy releasing rate is considered as [2],

$$\frac{\alpha \left(\frac{dW_E}{dt} \right) + \beta \left(\frac{dW_s}{dt} \right)}{\frac{dW_D}{dt}} > 1 \quad (1)$$

Where, W_E is the elastic energy stored in rock mass; W_S is the elastic energy stored in coal; W_D is the dissipated energy along the coal-rock surface during the excavation; α and β are the empirical coefficients related to the ration of released energy to the stored energy in rock and coal mass.

According to this method, if the energy releasing rate is greater than the energy dissipating rate, a dynamic fracture or a rock burst can possibly happen. However, it is difficult to obtain the values of α and β in a real practice as they are highly dependent on the properties of the rock mass and the excavation operations. In order to achieve a more accurate evaluation, a numerical method is discussed in this paper to analyse the energy releasing and dissipating behaviour in tunnel excavations. The complete load-deformation curves of rock specimens are adopted to simulate the rock behaviour in this model. Furthermore, the influences of the loading rate are also considered in this method. By using such method, the variation of the energy transforming can be computed and consequently, the risk of rock burst failure can be evaluated for different cases [7-9].

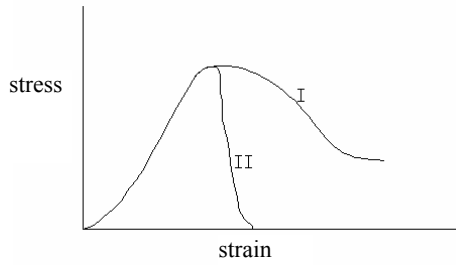


Figure 1 Typical complete stress strain curves

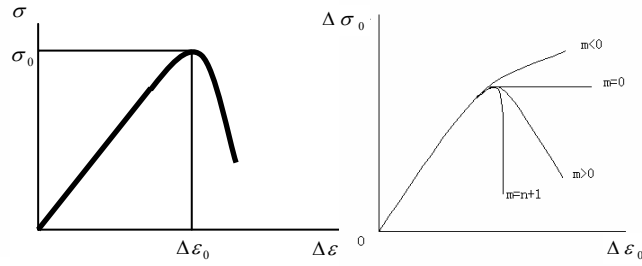


Figure 2 Okubo's constitutive model [3]

2. Numerical Method

2.1 Rock Behaviour

Lots of uniaxial testing results show that a hard rock specimen usually behaves linearly and elastically before the peak load while the post-peak behaviour is likely to be work-softening [3]. On the other hand, the deformation behaviour can also be influenced by the loading rate [6]. In order to represent such behaviour, Okubo [6] proposed a constitutive model, in which the softening behaviour and the influences of the loading rate can be considered simultaneously,

$$\left. \begin{aligned} \Delta \varepsilon^* &= \lambda^* \Delta \sigma^* \\ d\lambda^* / dt &= a(\Delta \sigma^*)^n (\lambda^*)^m \end{aligned} \right\} \quad (2)$$

where, $\lambda^* = \lambda / \lambda_0$ is the normalized compliance (λ is the compliance and, λ_0 is the initial compliance); $\Delta \sigma^* = \Delta \sigma / \Delta \sigma_0$ is the normalized stress ($\Delta \sigma$ is the shear stress, $\Delta \sigma_0$ is the shear strength); $\Delta \varepsilon^* = \Delta \varepsilon / \Delta \varepsilon_0$ is the normalized shear strain ($\Delta \varepsilon$ is the shear strain, $\Delta \varepsilon_0$ is the initial shear strain).

The coefficient a can be expressed as,

$$a = \frac{1}{t_0} \left(\frac{m}{n_0 + 1} \right)^{m / (n_0 - m + 1)} \quad (3)$$

Where, t_0 is the time to achieve the stress of $\Delta \sigma_0$ in a constant rate loading test. According to the suggestions of IRSM, the value of t_0 can be set as 120s (as shown in Figure 2).

The coefficients m and n represent the post peak behaviour for different rock specimens. The values of m and n can be back evaluated from the compressive test results. In this model, $m < 0$ can represent a work-hardening behaviour while $m > 0$ can represent a work-softening behaviour. If m is zero, a plastic behaviour can be simulated.

2.2 Energy Releasing Rate

In a compressive test, the variation of the energy in a specimen follows [6],

$$E_{diss} = W - E_{el} \quad (4)$$

Where, W is the input energy; E_{el} is the energy stored in the specimen; E_{diss} is the energy dissipated in crack generating and propagating, specimen vibrating, dynamic bursting and so on. The dissipated (released) energy will be insignificant at initial loading stage (linear elastic) as almost all the input energy can be elastically stored in the specimen. However, when the specimen behaves work-softening in post peak stage, the input energy will continually increase while the stored elastic energy will decrease. As a result, the dissipated (released) energy will significantly increase at the post peak stage (as illustrated in Figure 3).

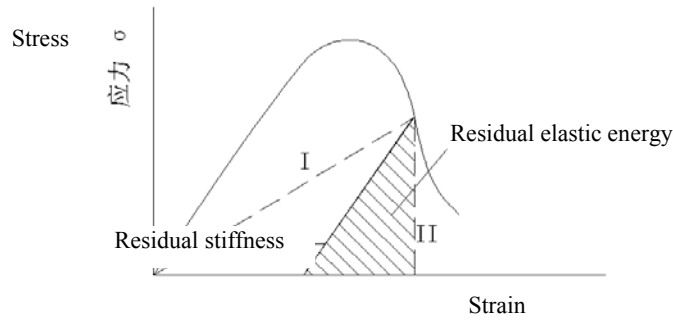


Figure 3 Stored elastic energy in rock

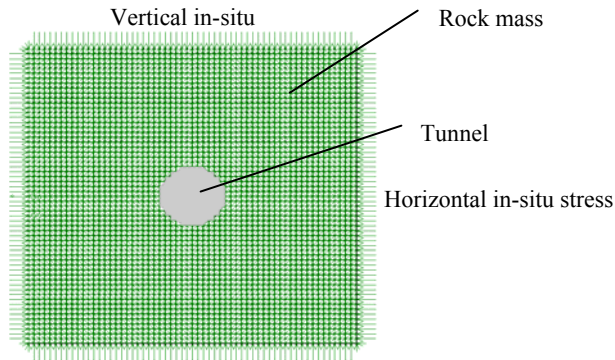


Figure 4 Numerical mesh plan

In a practical excavation project in rock mass, the input energy is nearly zero for the whole rock system [8]. However, the excavation will change the stress distribution and concentrate the stress in some areas. The rock in the stress-concentrated area will be loaded to the peak point and then behave work-softening. As a result, the stress unloading can happen in the area close to the failed points. That means a part of the stored elastic energy in the unloaded area will be released and transferred to the failed area. However, the energy input into the failed

area can not be totally stored elastically. Therefore, the “overflowed” input energy will be partly transformed into dynamic bursting (or rock burst). As mentioned above, the greater the released energy is, the greater is the risk of rock burst failure. The reason is that more energy will be dissipated in dynamic fracturing.

2.3 Numerical Model

The finite element analyses for rock excavations were widely adopted in numerous projects [8-11]. Different from those analyses on static stability of the underground structure, the simulations for the gradually fracturing in rocks were also carried out by some researchers [12-13]. In such computations, the failure progress in a rock structure is simulated as a quasi static process. In such method, the computations are performed in steps to simulate a sequence of states that are assumed as static equilibrium. The stress components are solved in each step. Based on the stress state, the deformation properties are updated after each step according to the predefined behaviour of the rock, such as complete stress-deformation behaviour. In this way, the progressive failure in the rock excavation can be numerically modelled. On the other hand, by using the method described in 2.1 and 2.2, the energy releasing can also be computed in the analysis [6-8].

For tunnelling projects, the excavation process can be numerically simulated by gradually decreasing the stiffness of the rock elements inside the tunnel at a certain rate, as shown in Figure 4. The computation can be started from the initial state for the intact rock mass (or with some existing fractures). In order to study the energy releasing process in the surrounding rocks, the computation will be further performed after the tunnel is “fully excavated” (the stiffness of the rock elements in the tunnel is decreased nearly to zero). The variation of the stored and the released energy can be computed against the excavation process in this method. The authors had used such model to study the excavation progress for some tunnelling projects [6-7]. The results showed that the obtained energy releasing rate could approximately simulate with the fracturing behaviour of the rock mass in tunnel excavations. The results also revealed that the energy releasing rate can be significantly influenced by the rock properties, the excavation rates and the in-situ stress in the rock mass [7].

As described above, the failure in rocks is likely to be initially generated in some stress concentrated areas and then propagated to the neighbourhood. Therefore, some uneven propagation can possibly be caused by the differences among the element sizes [6]. In order to avoid such unexpected effects, the numerical model is revised in this paper by setting all the elements in a same size. The adopted mesh plan is shown in Figure 4. As a further study, the numerical simulations are performed for some special cases in tunnel excavations, such as over-excavation and loose blasting.

3. Numerical Modeling

Over excavation is a very common phenomenon in tunnel excavations. It can greatly influence the stress distributions and consequently the possibility of the rock burst failure. On the other hand, the loose blasting method is usually adopted to reduce the risk of rock burst. The influences of these two factors are evaluated in the following sections.

3.1 Over Excavation

The numerical modelling for the over excavation effects is performed with the numerical model mentioned above. The diameter of the tunnel is 10m; and a 100m*100m square area is assumed as the total computed area. The parameters for the rock mass are set as following, the uniaxial strength is 35MPa; the residual strength is 10.5MPa; the Poisson’s ratio is 0.3; the Young’s modulus is 30GPa. The coefficients m and n (as described in Formula 1) are 13 and 20 respectively. The in-situ stress is assumed as 30MPa in horizontal direction and 10MPa in vertical direction. As shown in Figure 5, the locations of the over excavation are assumed as horizontal (Case I), inclined at 45° (Case II) and vertical (Case III). The over excavated area is assumed as

triangular and the depth is about 1.2m.

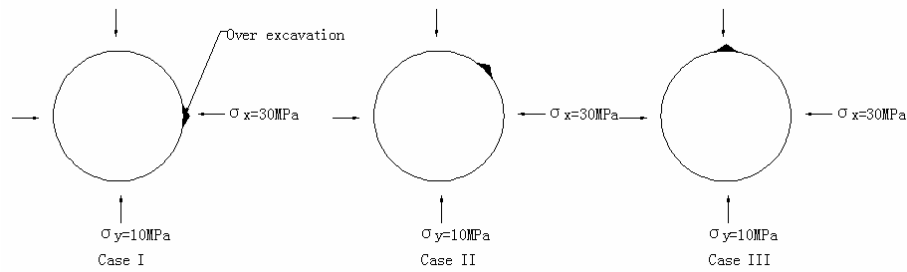


Figure 5 Cases of over excavation

By comparing the over-excavated cases with the case without any over excavation (Case original), we can find the influences on the stress distribution in rock mass (Figure 5). If the rock mass is over excavated in horizontal direction (Case I), the influences on the shear stress distribution is relatively insignificant. The over excavations inclined at 45° (Case II) can significantly enlarge the stress concentrated area while the peak value is about 3% greater than the original case. The results also show that the stress distribution can be influenced greatly by the excavation in vertical direction (Case III). In this case, the shear stress is about 10% greater than that in Case original. The comparison demonstrates that the influences of the over excavation on the shear stress distribution in the rock mass are heavily dependent on its location. The over excavation located in the stress concentration area is usually the most dangerous.

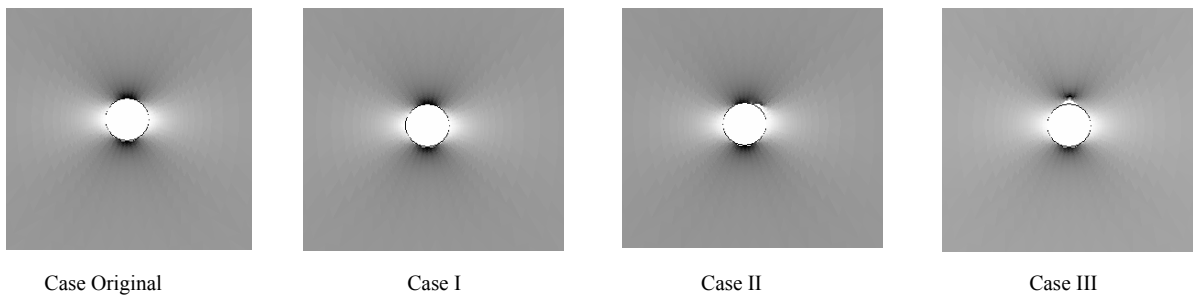


Figure 6 Distribution of shear stress influenced by over excavations

Similar results can also be observed in the computed energy releasing rates. As shown in Figure 7, the energy releasing rate in Case III is the greatest among all the cases. Therefore, the over excavating should be carefully avoided in tunnelling projects, especially in the stress concentrated area.

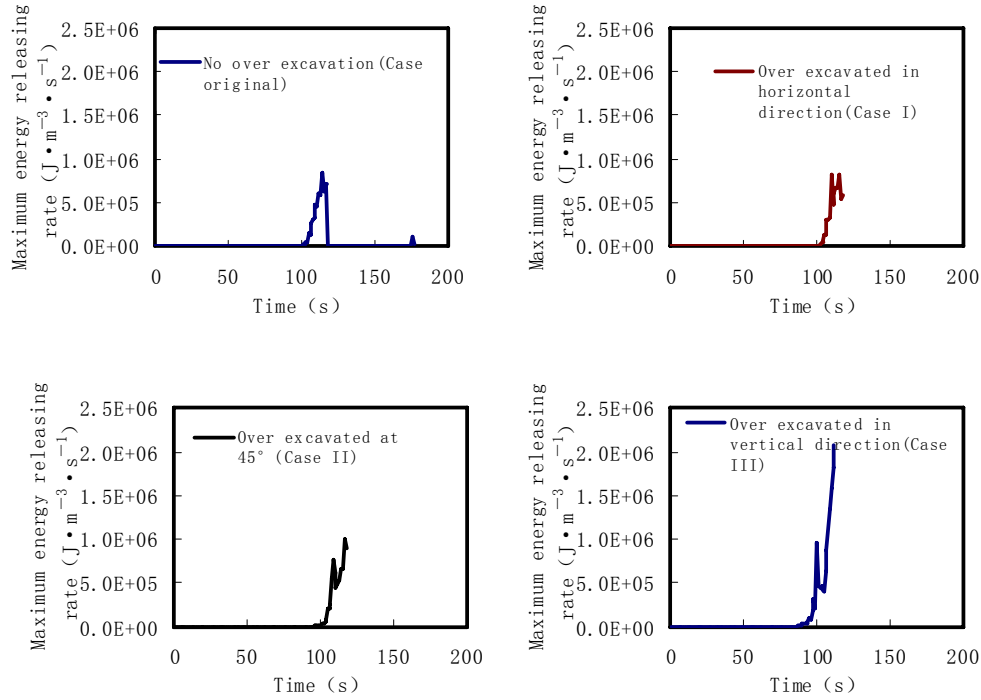


Figure 7 Energy releasing rate in different cases

3.2 Loose Blasting

The loose blasting method is widely adopted in tunnelling to reduce the stress in the rock mass and the risk of dynamic fracture. Such method can be performed in two ways, one is to soften the rock in the possibly stress-concentrated area, and the other is to soften the whole circular area near the tunnel surface. The numerical studies are performed for these two types of loose blasting. As shown in Figure 8, the rock will be loosen in the stress-concentrated area (near roof surface) in Case I, for which the loosen area is triangular with a depth of 1.2m. In Case II, the rock will be loosen in the whole circular area near the rock surface with a depth of 1.2m. For each case, the stiffness in the loosen area is assumed to be reduced to 50% and 80% of the original value.

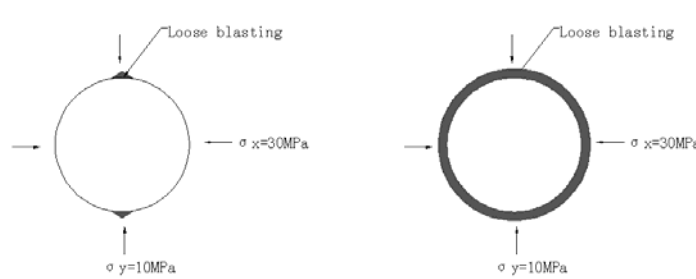


Figure 8 Energy releasing rate in different cases

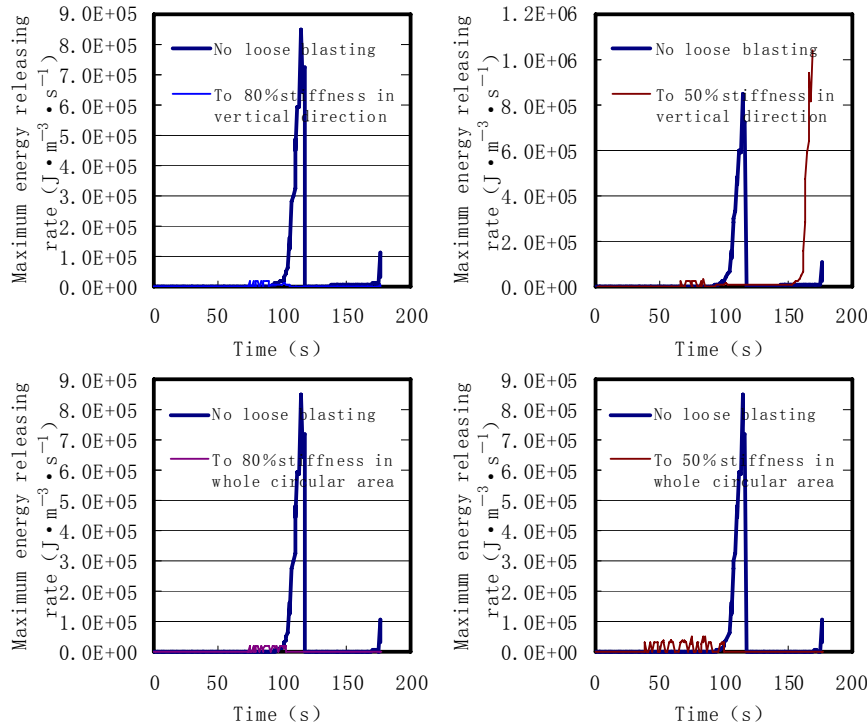


Figure 9 Energy releasing rate in different cases

The computed results show that the energy releasing rate can be significantly reduced by the loose blasting in the whole circular area near the surface (Case II, as shown in Figure 9). However, the effects for the rock partly loosen (Case I) are dependent on the softening ratio of the rocks. The energy releasing rate will be reduced significantly decreased if the rock stiffness is softened to 80% of its original value. However, if the rock stiffness is softened further to 50%, the energy releasing rate will be increased unexpectedly. The results show that the loose blasting method should be carefully operated in the stress concentrated area. If the stiffness of the rock concentrated area is too much softened, the stress concentration near the softened area may increase in an unexpected way. As a result, the energy releasing rate will increase significantly (as shown in Figure 9).

4. Discussions

This study presented a numerical method to analyze the energy releasing rate in the excavation of rock tunnels. In this model, the computed results can approximately represent the dynamic fracture process in the excavations. Furthermore, the modelling for the over excavation in tunnelling projects shows that the over excavation in the stress-concentrated area can increase the energy releasing rate. In other words, rock burst can be induced by such over excavation in some cases. Therefore, careful consideration should be taken to avoid over excavation in the rock mass, especially in the stress-concentrated area.

The study is also performed for the effects of loose blasting in rock mass. The results show that the energy releasing rate can be greatly reduced by loosening the rock in the whole circular area. However, if the rock mass is only loosened in the stress concentrated area, one should consider that too much softening of the rock in this area can unexpectedly increase the risk of rock burst.

References

1. Jaeger, J. C. and Cook, G. W. Fundamentals of Rock Mechanics. Chapman and Hall Press, 1979.
2. Linkov, A.M. Rockburst and the Instability of the Rock Masses. Int. J. Rock. Mech. Min. Sci. & Geotech. Abstr, 1996, 33 (7). 727-732.
3. Ohkubo, S. and Jin, F. Simulation of Rock Behavior around Circular Roadway by Non-linear Rheological Model. Journal of the Mining and Materials Processing Institute of Japan, 1993, 109 (3). 209-214.
4. Xu, S.L., Wu, W. and Wu, Y.S. Application of Stiff Testing Machine in Rock Mechanics Tests. in Proceedings of the International Conference on Mechanical Testing of Materials and Structure, (Hong Kong, 1998).
5. Li, S.L., Yin, X.G., Wang, Y.J. and Fang, H.Y. Studies on Acoustic Emission Characteristics of Uniaxial Compressive Rock Failure. Chinese Journal of Rock Mechanics and Engineering, 2004, 23 (15). 2499-2503.
6. Okubo, S., Nishimatsu, Y. and He.,C. Loading Rate Dependence of Class II Rock Behaviour in Uniaxial and Triaxial Compression Tests. Int. J. Rock Mech. Min. Sci. & Geomech. Abstr, 1990, 27(3). 559-562.
7. Wang, Y.H. Numerical and Laboratory Study of Rock Burst. Wuhan Institute of rock and soil mechanics, Chinese Academy of Sciences, 1999.
8. Shen Feng, Numerical Study on Rockburst in Tunnel Excavation, MPh thesis, Changsha University, 2008.
9. Wang, Y.H., Chen, L.W. and Shen, F.. Numerical Modeling of Energy Release in Rockburst. Rock and Soil Mechanics, 2008, 29 (3)790-794.
10. Oubo S. and Nishimatsu Y. Computer Modeling of Stochastic Rock Failure during Uniaxial Loading. Int. J. Rock Mech. Min. Sci., 1986, 23 (5). 363-370.
11. Zienkiewicz, O. C. The Finite Element Method(3rd edition). McGraw-Hill, New York.Stewart, 1977.
12. Jing, H.H., Guan, W.H., Ma, F.Y. and He M.C. Numerical Simulation of Rock Burst under Depth Portion Tunnel Tectonics Stress. Journal of Heilongjiang Institute of Science and Technology, 2006, 116 (1).16-18.
13. Wang, Q.H., et al. Numerical Simulation of Rock Deformation and Rock Burst of Tongyu. Tunnel. Underground Space, 2003, 23 (3). 291-295.

COMPREHENSIVE DETECTION SYSTEM OF GEOLOGICAL PRECURSORY CHARACTERISTICS FOR ROCK BURST AND WATER INRUSH

ZHEN-HAO XU, SHU-CAI LI, LI-PING LI, QING-SONG ZHANG, WAN-TAO DING,
QIN LIU, SHU-CHEN LI, YI-GUO XUE and XIAN-DA FENG

Geotechnical and Structural Engineering Research Center, Shandong University

Jinan, 250012, P.R.China

Both rock burst and water inrush are serious geological hazards in deep underground engineering, and it happened frequently in the excavation of auxiliary tunnel of Jinping Hydropower Station in China. Great damage to constructions was often caused by the geological calamities. In order to predict and control these geological hazards, a comprehensive detection system of geological precursory characteristics was established. It was proved that development degree of joint fissures was an important geological precursory characteristic, and mechanical parameters were gained by means of elastic wave techniques. According to the development characteristics of joint fractures and mechanical datum, good conclusions can be drawn about geomechanics failure patterns of rock burst, transmitting and bearing structures of water, and failure patterns of rock mass. This system reduced risk of rock burst and water inrush effectively. Finally, case studies had also been done.

1 Introduction

Hydrologic and engineering geological conditions of underground engineering are highly complex. Geological hazards often occur during construction, especially for rock burst and water inrush. This happened during the excavation of the auxiliary tunnel of Jinping Hydropower Station in China. Both rock burst and water inrush are common and disastrous geological calamities in underground constructions. Though there are great numbers of achievements on generating mechanism, monitoring and forecasting technologies of rock burst [1, 2] and water inrush [3], detection technology systems of geological precursory characteristics for the two geological hazards have not been established. The geological precursory characteristics of them are necessary and important, but have not been pointed out. This study not only solved the problems, but also studied the applicability of the detection methods mentioned, and on how to make reasonable use of the information gained from detection works. Finally, case studies of detections had also been done.

2 Detection System and Case Study

In this section, the detection system of geological precursory characteristics for rock burst and water inrush is briefly introduced. As seen in figure 1, regional geological information and survey data of the engineering site is analyzed before detection, so a macro grasp for the possibility of geological hazards is gained about the research site, and a preliminary classification of potential geological hazards is done.

If there are some potential geological hazards, detection works need to be done. By means of elastic wave techniques, both geological information and mechanical parameters can be gained. One of the most important geological facts is the development level of fractures, which plays an important role in determining the geomechanics failure patterns of rock burst, as well as the transmitting and bearing structures of water. Mechanical parameters are also very important characteristics for further prediction researches in studying the geomechanics failure patterns of rock mass which prevents rock burst or water inrush, and analyzing the

potential risk of rock burst and water inrush.

Then if there is a high risk of rock burst or water inrush, some detailed detection works have to be done, so as to get insight into the development level of fractures in potential sections of rock burst, and to find out water transmitting and bearing structures in potential sections of water inrush.

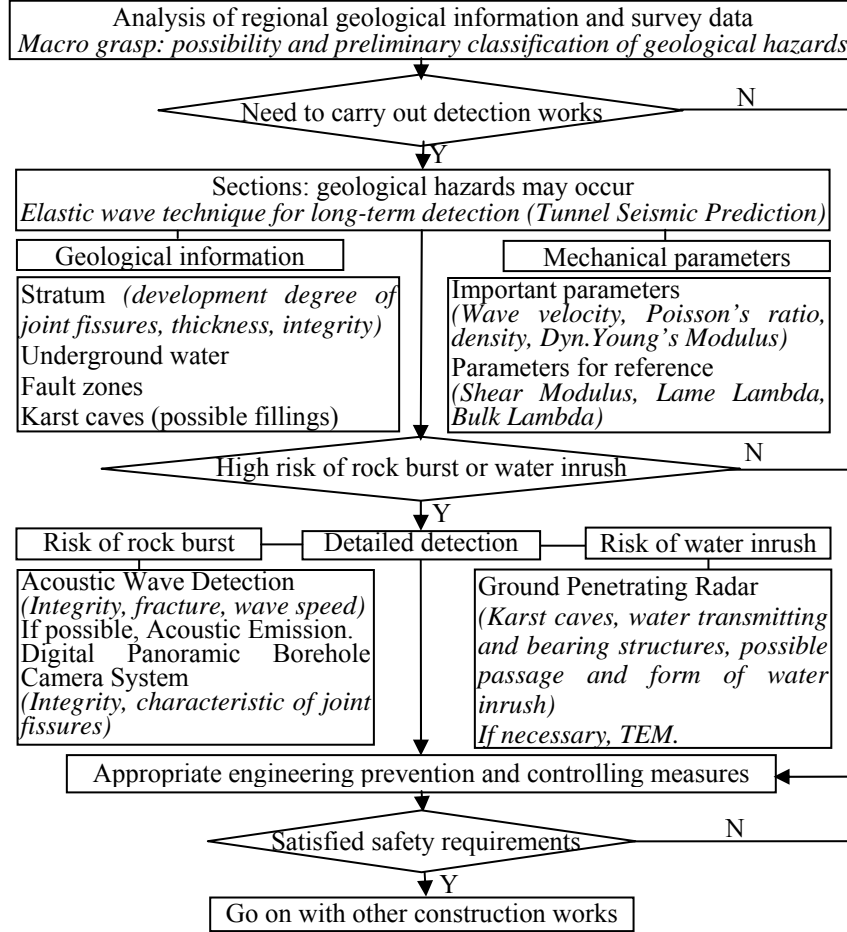


Figure 1 Comprehensive detection system of geological precursory characteristics for rock burst and water inrush

2.1 Tunnel Seismic Prediction and Case Study

Tunnel seismic prediction is a general term of seismic prediction methods, however, here it designates a new technology designed for geophysical detection in underground construction work, and it is termed Tunnel Seismic Prediction. The latest system is often called TSP 203^{PLUS}. Seismic waves are triggered by small explosive charges in 24 boreholes along the side wall of tunnel or other underground caverns, and then both direct wave and reflection wave are received by 1, 2, 3 or 4 highly sensitive seismic 3-component sensors of the TSP-203 system, as in figure 2 [4]. Because of discontinuities in strata layers, as seismic wave propagates forward, part of its energy transmits and formats transmission wave, while part reflects and formats reflection wave. The discontinuities are described in detail with the following formula (1) and (2), for different geological bodies have different wave impedance.

$$R = \frac{\rho_2 V_{p2} - \rho_1 V_{p1}}{\rho_2 V_{p2} + \rho_1 V_{p1}} = \frac{Z_2 - Z_1}{Z_2 + Z_1} \quad (1)$$

$$T = \frac{2\rho_1 V_{p1}}{\rho_2 V_{p2} + \rho_1 V_{p1}} = \frac{2Z_1}{Z_2 + Z_1} \quad (2)$$

Where R and T are the reflection and transmission ratio of the discontinuity face; ρ_1 , V_{p1} and Z_1 are the density, wave velocity and wave impedance of the inner side of the discontinuity face; ρ_2 , V_{p2} and Z_2 are the density, wave velocity and wave impedance of the outside side of the discontinuity face.

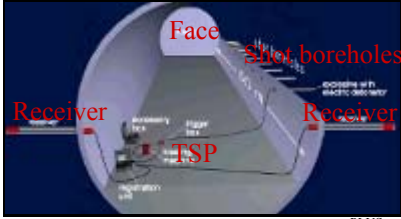


Figure 2 Layout of a standard TSP 203^{PLUS} measurement [4]

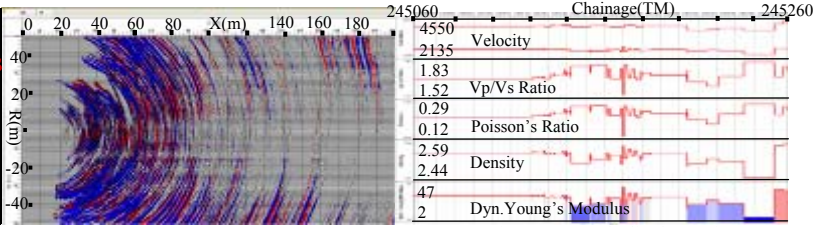


Figure 3 Result displays of P-depth migration

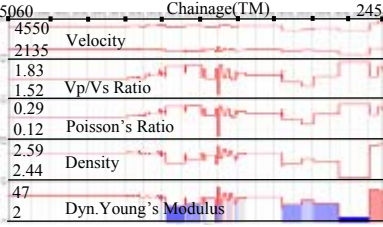


Figure 4 Result displays of 2D longitudinal and plan View

The received seismic data can be processed with wave propagation and reflection theory; and with the help of TSPwin^{PLUS} software, P wave velocity and S wave velocity can be gained. Then considerations are constricted to isotropic rock in mini zones, in which wave velocities are independent of travelling direction. Afterwards mechanical parameters are calculated via classical functions and empirical equations, and it is possible to predict the characteristic, location and size of geological bodies, however, the output of the program should be interpreted with great care sine its accuracy depends on some simplified theory and empirical formulas that can not hold for any conditions. So in order to upgrade the accuracy of interpretation and to get more useful parameters, it is necessary for interpreters to accumulate experiences, to associate with geology and to utilize other methods, such as analytic hierarchy process, fuzzy mathematical or artificial neural network (A trained artificial neural network was once used by Andisheh Alimoradi to process output datum of TSP 203 [5]).

Readers can get more detailed interpretation skills with the help of TSP operation and evaluation manual, and consult reference [6, 7]. As shown in figure 3 and 4, a case study was done by TSP 203^{PLUS} in a karst tunnel. Development extent of joint fractures, geological information and some mechanical parameters were gained. The strength of the rock mass was low, especially in the sections between K245+142~K245+160 and K245+204~K245+250. And it was abundant in joint fractures, especially in the sections between K245+120~K245+140 and K245+162~K245+182. Reflection intensity of S wave was much stronger than that of P wave in section K245+238~K245+250. Integrated with other outputs of the software and known geological information, conclusion was drawn that section K245+238~K245+250 was quite possible a karst cave and filled with water. Since there was no risk of rock burst but a high risk of water inrush, it was proposed that some cautionary measures have to be took while approaching to the milestone K245+238, especially detailed detection researches must be done near K245+220.

2.2 Acoustic Wave Detection

The basic principle of acoustic wave detection is the propagation theory of elastic wave in rock mass [8]. Detection work consists of exciting, receiving and processing of acoustic wave. Acoustic wave is triggered with certain frequency by artificial methods, and it propagates in geological medium with various waveforms. The propagation velocity dropped when the wave meet with structural plane in rock mass. And acoustic wave travels relatively faster while travels parallel to geological interface than upright to. Due to this transmitting characteristic and the propagation theory, it is possible to gain wave velocity, to get fissure abundance and distribution, and to calculate structural integrities of rock mass.

According to acoustic velocity, integrity coefficient of the rock mass can be computed as follows,

$$k_v = \left(\frac{v_p}{v_{pr}} \right)^2 \quad (3)$$

Where k_v is integrity coefficient of rock mass; v_p is the P wave velocity of rock mass; v_{pr} is the P wave velocity of fresh intact rock in the survey area.

Case studies were done at the engineering site of auxiliary tunnel of Jinping Hydropower Station. Development level of joint fissures was analyzed and studied by processing the received acoustic signal. As in figure 5, wave velocities between the two red lines is 4600 m/s~6800m/s, and there were three sections with high development degree of joint fractures, as sections 0m~1.2m, 5m~7m and 13m~14m.

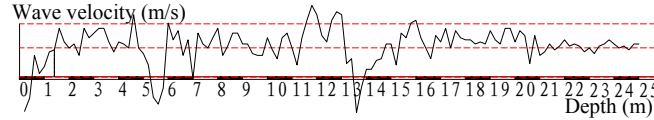


Figure 5 Relationship curve of P wave velocity and depth

2.3 Digital Panoramic Borehole Camera System

Digital Panoramic Borehole Camera System (DPBCS) is a brand new intelligence exploration technique. It is composed of two key techniques, the panoramic technique and the digital technique. The former solves a corresponding relation between 3 dimensional image and its spatial coordinates, while the latter solves problems on the formation, processing and restoration of images, the calculation and statistical analysis of geological bodies, and the establishment of expanding and 3D image of virtual core [9]. Not only can the system make it possible for real-time observation of core logging, but also can calculate the attitude, trace length and width of joint fractures, as well as structural integrities of rock mass. As in figure 6, a case study was done in a diabase cross-harbour tunnel.

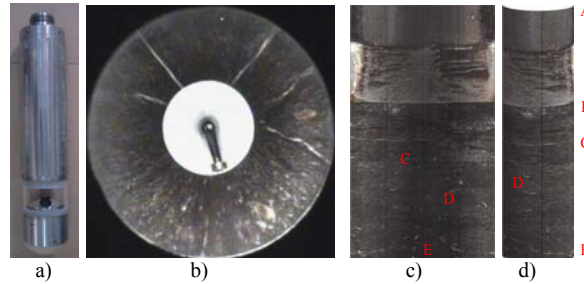


Figure 6 a) Panoramic borehole camera; b) Digital panoramic borehole image; c) Expanding image of virtual core; d) 3D image of virtual core

Where A was the outside end of the borehole orifice-pipe; B was the inside end of the borehole orifice-pipe, and it was also the joint position of the borehole orifice-pipe and the rock mass; C was a low angle fracture; D was a steep angle fracture; E was a common fracture.

Researchers can get more information about detection practice of joint fissures and other application of borehole camera or TV from references [10, 11].

2.4 Grand Penetrating Radar

Ground Penetrating Radar (GPR) is a electromagnetic detection method, and it can be used to detect the distribution of underground medium [12, 13]. Transmitter of GPR system transmits electromagnetic wave signal to the underground medium, and when the signals encounter with targets of electric difference, such as

cavity or other interface, the electromagnetic wave will partly reflect and partly penetrate. Based on processing and analyzing of the received electromagnetic waves, parameters as waveform, intensity and two-way travelling time can be gained, and information of the underground geological bodies, such as the spatial position, structure, electrical property and geometric shape can be inferred. The propagation velocity of the high frequency electromagnetic wave in the underground medium is mainly decided by the relative dielectric constant of the medium. Reflection energy depends on reflection coefficient (R) of geological interface; mathematical representation of R is,

$$R = \frac{\sqrt{\epsilon_1} - \sqrt{\epsilon_2}}{\sqrt{\epsilon_1} + \sqrt{\epsilon_2}} \quad (4)$$

Where ϵ_1 and ϵ_2 are the relative dielectric constant of the bilateral reflection interface.

It is obvious that reflection coefficient is mainly decided by the difference of the relative dielectric constant of the medium on both sides of the reflection interface, and it can be said that electric difference between geological bodies and the ambient medium makes it possible for GPR detection works. The relative dielectric constant of air is 1, rock mass between 4 and 20, and water 81, so that GPR is very sensitive to water. And according to electromagnetic wave profiles, cavities, fractures and other geological information can be gained effectively. It was found out that, while encountering with underground water, the reflection energy of electromagnetic wave increased and frequency decreased with an abnormal phase axis, sometimes with a inversion of 180 degrees. If development degree of joint fractures is high, the abnormalities and discontinuities of phase axis are even worse.

Case studies were done in a karst tunnel as in figure 7, and the circled area is abundant in joint fissures and filled with water, but without big cavities. Mating with other geological information, it was clear that there was no risk of rock burst and serious water inrush. So it released constructors from anxiety tension state, accelerated construction progress, and reduced engineering cost.

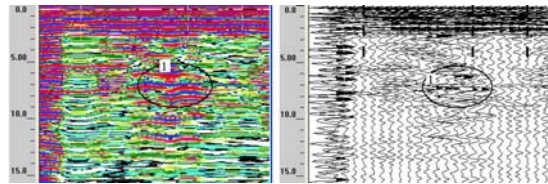


Figure 7 Electromagnetic wave profiles of GPR

3 Discussion

There are many elastic wave techniques that can provide both geological information and mechanical parameters. This paper focused on TSP for its widely use, high efficiency and long detection distance. However, the outputs of TSPwinPLUS program must be interpreted with great care, and try to amend them with experiences and empirical equations, to make full use of the known geological conditions, and to mate with geology.

4 Conclusions and Future Work

A newly comprehensive detection technology system of geological precursory characteristics for rock burst and water inrush has been brought forward in this paper. It has been successfully used at many engineering sites.

Elastic wave techniques can provide researchers both geological information and mechanical parameters. Since they are highly efficient, cost-effective, and richly informative, they are worthy of promotion in the long-distance detection system of geological precursory characteristics for rock burst and water inrush. Development level of joint fissures is an important geological precursory characteristic. Fractures can be detected briefly by

TSP, and accurately by acoustic wave detection methods and digital panoramic borehole camera systems. Together, with the gained mechanical parameters, further studies can be done to identify geomechanics failure patterns of rock burst and failure patterns of rock mass that prevents water inrush. Combine geology and make reasonable use of the outputs of TSPwin^{PLUS} software to ensure more precise and effective interpretations.

This paper focuses on the establishment of a permanent and effective detection system of geological precursory characteristics for rock burst and water inrush. It also looks at the problems of which geological precursory characteristics are of vital importance. Detailed work remains to be done in the area; on how to make more reasonable and effective use of the gained information from detection, on amelioration of the proposed techniques, and on more detailed researches of the geomechanics failure patterns of the two geological hazards.

Acknowledgements

The authors wish to acknowledge the collaborative funding support from the National Basic Research Program of China (973 Program No.2007CB209407), the National High Technology Research and Development Program of China (863 Program No.2007AA11Z131), the General Program (Key Program) of National Natural Science Foundation of China (No. 50539080), the General Program of National Natural Science Foundation of China (No.50874068), the Abroad Joint Research Fund for Young Scholars of Hong Kong (No.50729904) and Natural Science Foundation of Shandong Province (No.Y2008F22).

References

1. Feit, G. N., O. Malinnikova, N., Zykov, V. S., et al. Prediction of Rockburst and Sudden Outburst Hazard on the Basis of Estimate of Rock-Mass Energy. *Journal of Mining Science*, 2002, 38 (1). 61-63.
2. Hagan, T.O., Milev, A.M., Spottiswoode, S.M. et al, Simulated Rockburst Experiment-an Overview. *The Journal of The South African Institute of Mining and Metallurgy*, 2001, 217-222.
3. Wu, Q. and Zhou, W.F. Prediction of Groundwater Inrush into Coal Mines from Aquifers Underlying the Coal Seams in China: Vulnerability Index Method and its Construction. *Environmental Geology*, 2008, 56. 245-254.
4. Amberg Technologies AG, Regensdorf, Switzerland. Operation Manuel TSP 203^{PLUS} Field Operation & Data Acquisition, Manual Version 2.6, 2008.
5. Alimoradi, A., Moradzadeh, A., Naderi, R., et al, Prediction of Geological Hazardous Zones in front of a Tunnel Face using TSP-203 and Artificial Neural Networks. *Tunnelling and Underground Space Technology*, 2008, 23 (6). 711-717.
6. Xu, Z.H., Li, S.C., Zhang Q.S., et al. Reflection Characteristic of Seismic Wave in TSP Advance Geological Prediction. *Chinese Journal of Underground Space and Engineering*, 2008, 4 (4). 640-644.
7. Li, S.C., Li, S.C., Zhang Q.S., et al. Forecast of Karst-fractured Groundwater and Defective Geological Conditions. *Chinese Journal of Rock Mechanics and Engineering*, 2007, 26 (2). 217-225.
8. Narayan, J. P. 2.5-D Numerical Simulation of Acoustic Wave Propagation. *Pure and applied geophysics*, 1998, 151. 47-61.
9. Wang, C.Y., Ge X.R. and Bai, S.W. The Digital Panoramic Borehole Camera System and Its Application. *Rock and Soil Mechanics*, 2001, 22(4). 522-525.
10. Yang, R. L., Rocque, P., Katsabanis, P., et al. Measurement and Analysis of Near-field Blast Vibration and Damage. *Geotechnical and Geological Engineering*, 1994, 12. 169-182.
11. Miyakawa, K., Tanaka, K., Hirata, Y., et al, Detection of Hydraulic Pathways in Fractured Rock Masses and Estimation of Conductivity by a Newly Developed TV Equipped Flowmeter. *Engineering Geology*, 2000, 56. 19-27.
12. Singh, K. K. K. and Chouhan, R. K. S. Exploration of Underground Strata Conditions for a Traffic Bypass Tunnel Using Ground Penetrating Radar System -- a Case Study. *Geotechnical and Geological Engineering*. 2002, 20. 81-87.
13. Roch, K.H., Chwatal, W. and Bruckl, E. Potentials of Monitoring Rock Fall Hazards by GPR: Considering as Example the Results of Salzburg. *Landslides*, 2006, 3. 87-94.

IDENTIFICATION OF THE PREDICTIVE INFORMATION BEFORE ROCKMASS FAILURE BASED ON b -VALUE OF AE EVENTS AND ITS DEFICIENCY

RUI-FU YUAN and HUA-MIN LI

School of energy science and engineering, Henan Polytechnic University Jiaozuo

Henan, 454000, P.R China

The multi-channels acoustic emission acquiring system was employed to record the AE events in failure process of rock specimens with different lithology. Dynamic curves of AE b -value were gained by the scan-calculating method. In the early and middle phases of loading, the AE b -value generally shows ascending trend. But, there were waves with different scales and times at b -value curves before they reach peak value. Finally, the b -value descends quickly when the specimen approaches total failure. Consequently, the descending of b -value did not present the failure of rock, only AE frequency and magnitude factors could not reflect the structure status inside rock accurately, of course it could not forecast the rock dynamic disaster reliably. The mechanism of the rock dynamic failures is greatly complicated. For forecasting the rock failure more accurately, the information included in the AE signals need to be more excavated, and should conduct comprehensive analysis and investigation combined with the factors of mechanical status.

1 Introduction

Rock is a typically inhomogeneous and anisotropic material which contains many natural defects with various scales, such as microcracks, pores, fissures, joints inclusions and precipitates. Large numbers of acoustic emission (AE) signals are generated when rock is loaded till failure. Because AE signals are generated by the propagating and expanding of microcracks, each AE signal contains plentiful information of structure changing inside the rock. Therefore, it is not surprising that in the geological science, acoustic emission phenomenon has attracted much attention of rock engineering researchers. Owing to facility and technical reasons, early AE studies in rock engineering were limited to the statistic of AE number, counts, energy and magnitude [1-4]. Although great success has been achieved in the theoretical and application fields of AE monitoring technique for rock [5, 6], the accuracy to forecast the rock failure based on the AE signal needs to advance. Till now, the successful examples of forecasting rock failure disaster are very few. The main reason is that the structure and mechanical response of rock is very complex, which result in the distribution of AE signals which are also full of complexity. Therefore, the concealed information could not be excavated comprehensively by experiential estimation and conventional linear theory.

Many researchers have comprehensively researched the AE distribution in rock failure process, such as rock destroyed by compression, tension, shear, etc [7, 8]. But these researches mainly focused on the relationship of AE distribution and stress, strain of rock, and intensive analysis and exploration of distribution for AE frequency, magnitude, and location were relatively lack. Many researches had indicated rock material as fractal feature, and the AE signal which was released in the rock failure process suffer loading also has fractal features [9~11]. In this article, the fractal theory was adopted to analyze the AE b -value which reflects the frequency and magnitude of AE signal and compare to the mechanical parameters of rock, and also discuss the deficiency of b -value. The results should provide theoretic basis for microseismic technique in forecasting rock mass dynamic disaster.

2 Experimental equipment and arrangement

RMT-150B rock test machine was employed to conduct loading test. Monitoring of AE signals was achieved by using of eight piezoelectric sensors with response frequencies at 125 kHz to 750 kHz. These sensors were positioned on the sides of specimen and coupled with silicone grease. The signals were amplified by pre-amplifiers (40 dB) and main amplifiers (0~20dB, auto-adjustive). A PC with AE analyzing software is used for the acquisition and memorization of the AE waves. More detail of the experimental equipment and arrangement was presented in article [12].

3. Calculation model of AE b-value

3.1 Gutenberg-Richter Model

B-value was first advanced by Mogi in 1939 which express the magnitude-frequency relationship of earthquakes. In 1941, Guthberg and Richter given the more definite model of *b*-value and expanded the application [13]. At present, the researches on *b*-value are not limited in the seismic field. Many researchers take AE events emitted in rock when suffered loading as microseismic activity, and then investigate the regular of *b*-value in the rock failure process under different conditions. The intention is uncover the predictive feature before the rock failure, and given the basis theory for forecast the rockmass dynamic disaster.

Gutenberg-Richter model is a typical example of fractal power-law, and it closely relate to fractal dimension of seismic activity.

$$\text{Log}N=a-bm \quad (1)$$

where *m* is the magnitude of AE event, *a* and *b* are constants, the value of *b* is the aforementioned *b*-value. *N* is the number of AE events, for different application purpose, it can be count by two method which are divided-frequency and accumulative frequency. The *N* in divided-frequency is the AE events number whose magnitude are in the scale of $m-\Delta m/2$ to $m+\Delta m/2$, where Δm is dividing range of AE magnitude. This method is fit for analysis and explanation of the occurred seismic events. The *N* in accumulative frequency is the AE events number whose magnitude is lager than *m* in some region. It is usually used to predict the occurring probability of seismic whose magnitude is larger than *m* in the region.

As power law, the gradation of Gutenberg-Richter model has invariability, which let it can be used in extensive field. The AE events emitted in the rock failure process can be take as seismic events, and then AE events can be analyze AE events by *G-R* model.

3.2 Calculating Method of AE b-value

The calculation of AE *b*-value can be achieved by the calculating method of seismic *b*-value straight, such as linear least square method, exponential least square method, maximum likelihood estimation method, et al. In this article, the linear least square method was used to calculated the AE *b*-value and the AE number *N* counted by divided-frequency method, where the dividing range $\log\Delta m$ is 1. The scan range was 100, which take the AE number as sliding axis. The advantage of this method was to avoid the lack of AE event in some intervals and advance the accuracy of *b*-value.

4. Result and discussion

Fifteen specimens who were divided into three groups were tested in the experiment. The general rule of the AE distribution and *b*-value presented as: in the initial stage, there were a small quantity of AE events and their magnitude were also small; when the load stress over 40~50% of the specimens' strength, the AE number increase stably, the *b*-value was in low level, and then *b*-value showed generally ascending trend along with the

increase of loading; but in the ascending process, there were one or some waves with different scales; when the specimens closed to total failure (loading stress > 80% strength), the intensity of AE signals rise drastically, and the b -value descends quickly till the specimens were totally destroyed.

Fig1 and Fig2 show the AE rate, b -value and loading strength in the failure process of several rock specimens. The abnormality of AE signals will happen before the rock destroyed, but the AE abnormality do not absolutely predicate the rock dynamic failure will happen [15]. The AE b -value in the rock failure process also proved this opinion. Some researches indicated that the b -value of AE will descend before the rock destroyed [16, 17], but the aforementioned experimental result showed that the descending of AE b -value did not predicate the specimens will totally failure soon. In fig2, the curves of b -value show one or several waves before it reach peak value in the specimens respectively. So the prediction of rock destruction could not only achieve from the descending of b -value reliably. Consequently, it can't reflect the inside structure of rock exactly by the frequency and energy factors of AE events. For forecasting the rock failure more accurately, the information included in the AE signals need to be more excavated, and should combine with other factors which present the rock mechanical status.

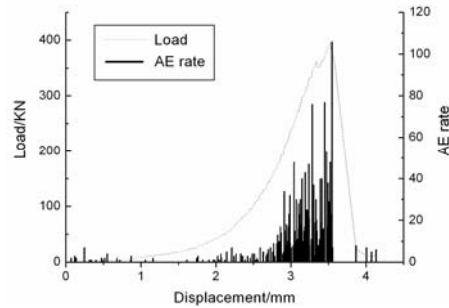


Fig1 Load, AE rate vs. displacement of granite specimen^[12]

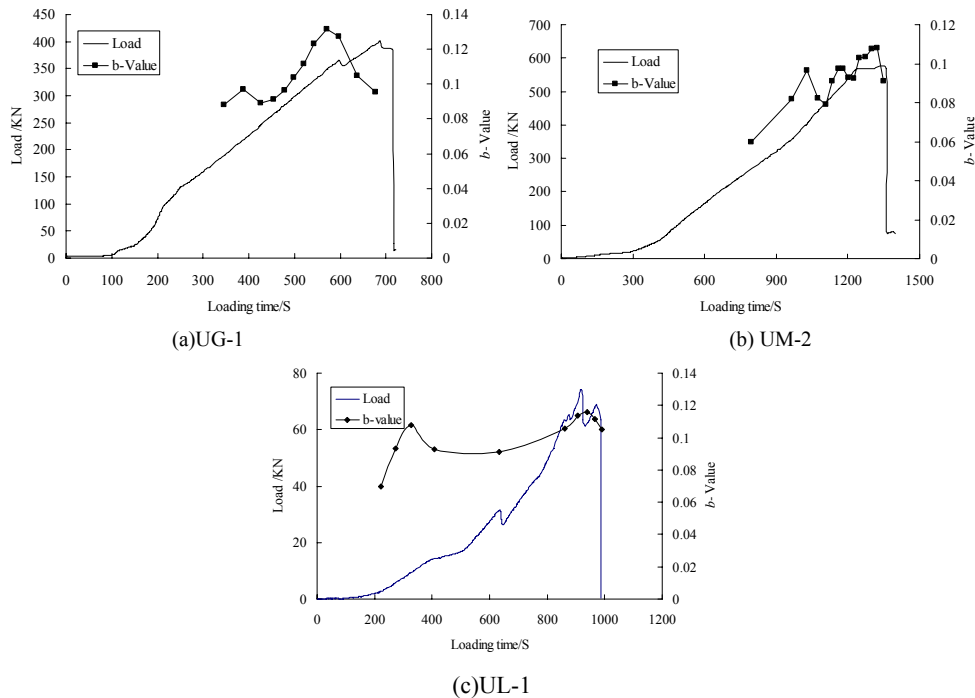


Fig2 Stress, b -value vs. time for three rock specimens

5. Conclusions

The AE experiments were conducted for 15 rock specimens which were divided into three groups with different lithologies respectively and the distribution of AE signals in the process of uniaxial compression were achieved. The b-value of AE signals were calculated by the Gutenberg-Richter model. In the early and middle phase of loading the AE b-value shows ascending trends. But, there are waves with different scales and times before b-value curves reach to peak value. Finally, the b-value descends quickly when the specimens approach total failure. Consequently, the descending of b-values can not represent the failure of rock. The factors of AE frequency and magnitude can not accurately reflect the structure status of rock independently. The mechanism of the rock dynamic failures is greatly complicated. For forecasting the rock failure more accurately, the information included in the AE signals needs to be more excavated, and must combine with mechanical factors to conduct comprehensive analysis and investigation.

Acknowledgements

The supports for this research through the Youth Science foundation of HPU (Q2008-51) and Natural Science Research Project of Henan education department (2009B440011) are gratefully acknowledged. The authors also would like to thank Mr. J. Tian, J.P. Liu and J.Y. Zhang for their help in the tests.

References

1. Lei X, L. and Satoh T, S. Indicators of Critical Point Behaviour Prior to Rock Failure Inferred from Pre-Failure Damage. *Tectonophysics*, 2007, 431. 97-111.
2. Zhao, X.D., Chen, B. and Jiang, F.B. Study of Micro-seismic Engineering Applications. *Chinese Journal of Rock Mechanics and Engineering*, 2002, 21(supp. 2). 2609-2612.(in Chinese)
3. Blake, W. *Microseismic Applications for Mining-practical Guide*. Washington: Bureau of Mines, 1982.
4. Ganne, P., Vervoort, A. and Wevers, M. Quantification of Pre-peak Brittle Damage: Correlation between Acoustic Emission and Observed Micro-fracturing. *International Journal of Rock Mechanics & Mining Science*, 2007, 44. 720-729.
5. Qin, S.Q. *An Introduction of Acoustic Emission Technology in Rock*. Publishing House of Southwest Jiaotong University, 1993 (in Chinese)
6. Acevedo, P.M. and Medrano, S.A. Characteristics of Acoustic Emission during Tests of Chilean Rocks. *Rockbursts and Seismicity in Mines*, 1993, 93. 8-9.
7. Young, R.P. Seismic and Micromechanical Studies of Rock Fracture in Granite. *Pure and Applied Geophysics*, 1995, 145(1). 3-27.
8. Li, Y.H., Yuan, R.F. and Zhao, X.D. Failure Process of Rock Sample Observed by AE Source Locating Technique under Uniaxial Compression. *Key Engineering Material*. 20006, 324-325. 567-570.
9. Li, T.J., Wang, Y.H. and Zhang, M.Y. Fractal Properties of Crack in Rock and Mechanism of Rock-burst. *Chinese Journal of Rock Mechanics and Engineering*, 2000, 19(1). 5-10.(in Chinese)
10. Xie, H.P. *An Introduction of Fractal-rock Mechanics*. Beijing: Science press, 1996. (in Chinese)
11. Hirata, T. Fractal Structure of Spatial Distribution of Microfracturing in Rock. *Geophys*, 1987. 369-374.
12. Yuan, R.F. and Li, Y.H. Fractal Analysis on Spatial Distribution of Acoustic Emission in Failure Process of Rock Specimen. *International Journal of Minerals, Metallurgy and Materials*, 2009, 16(1). 19-24.
13. Li, Q.L., Yu, T. and Hao, B. L. Temporal-scanning on Frequency-magnitude Relation of Seismicity. Beijing: Earthquake Press, 1979. (in Chinese)
14. Qu, Y. J. b-value. *Inside Earthquake*, 1989, 3(2). 187-189. (in Chinese)
15. Xie, H.P. *Fractals in Rock Mechanics*. A. A. Balkema Publishers, 1993.
16. Zhang, S.J., Liu, J.P. and Shi, C.Y. Study on Precursory Characteristics of Rock Failure Based on Acoustic Emission Experiment. *Metal Mine*, 2008, 8. 65-68. (in Chinese)
17. Yin, X.G., Li, S.L. and Tang, H.Y. Study on Strength Fractal Features of Acoustic Emission in Process of Rock Failure. *Chinese Journal of Rock Mechanics and Engineering*, 2005, 24(19). 3512-3516. (in Chinese)

STUDY ON TENDENCY ANALYSIS OF ROCKBURST AND COMPREHENSIVE PREDICTION OF DIFFERENT TYPES OF SURROUNDING ROCK

LI-XIN ZHANG and CHANG-HONG LI

*Key Laboratory of the Ministry of Education of China for High-efficient Mining and Safety of Metal Mines,
University of Science and Technology Beijing, Beijing 100083, P.R. China*

In the view of one-sidedness and the limitations in assumptions and criteria for rockburst prediction, the potential conditions of rockburst induced by deep mining of the Beiminghe iron mine are analyzed from the in-situ stress field, rock strength and elastic strain energy. Multi-index rockburst tendency for different types of surrounding rocks in deep mining such as tangential stress index(T), rock brittleness index(B), elastic energy index(Wet) and impact energy index(Acf) are analyzed by using the rock mechanics test and finite element numerical analysis. Based on the multi-indexes, fuzzy mathematics is applied for comprehensive prediction of rockburst. Prediction results show that there is no rockburst tendency for limestone and skarn, a moderate rockburst tendency for iron ore and a strong rockburst tendency for diorite in the process of deep mining. Finally, prevention and control measures of rockburst are taken from both sides of human disturbance and stress field to guarantee safe mining.

1 Introduction

Rockburst is a type of dynamic instability geological disaster with the phenomena of spalling, loosening, peeling off, ejection and even thrown etc.; caused by a re-distribution of the rock stress field due to excavation and a sudden release of elastic strain energy in the hard brittle rock under the conditions of high stress [1]. It directly threatens the safety of construction personnel and equipment and affects the project progress. It has become a worldwide problem in underground works.

Presently, many experts analyze rockburst from the strength, stiffness, energy, instability, fracture, injury, fractals, catastrophe, dynamics and so on, and present various assumptions and criteria. Only considering the impact of a single factor will bring about one-sidedness and limitations in some assumptions and criteria [2]. The occurrence of rockburst is complicated process and has many impact factors. It not only relates to the topography, lithology, rock mass structure and geological structure, but also to the size and direction of in-situ stress, external disturbance and the role of deep complex geological factors. Therefore, the authors consider that it is a more effective way to carry out a comprehensive study through current kinds of methods and means. Comprehensive prediction of rockburst is based on multi-indexes which are obtained by using the rock mechanics test and finite element numerical analysis studied through the use of the fuzzy mathematics method in this paper.

2 Potential Conditions of Rockburst

Currently, the following potential conditions of rockburst are generally accepted: ①the existence of high in-situ stress field; ②higher elastic strain energy storage in surrounding rock.

2.1 The Distribution Rules of In-situ Stress Field

Excavation in high stress area readily leads to stress concentration so that the stress of surrounding rock exceeds the limit stress of rockburst, which results in the occurrence of rockburst.

In order to obtain the distribution rules of in-situ stress field of mine area, the stress relief method was used to measure three-dimensional in-situ stress. Regression curve equations of the maximum principal stress, minimum principal stress and vertical principal stress changing with depth are as follows [3]:

$$\sigma_{h,max}=1.934+0.0478H \quad (1)$$

$$\sigma_{h,min}=0.409+0.0292H \quad (2)$$

$$\sigma_v=0.485+0.0272H \quad (3)$$

Where $\sigma_{h,max}$ is the maximal horizontal stress, MPa; $\sigma_{h,min}$ is the minimal horizontal stress, MPa; σ_v is the vertical stress, MPa; and H is the depth of measuring points, m.

Measurement results show that there is a higher in-situ stress field in mine area. At the depth of 700m, the maximum principal stress can reach 30~40 MPa. So deep mining under the conditions of high stress easily leads to the occurrence of rockburst.

2.2 Rock Strength and Elastic Strain Energy Reserved in Surrounding Rock

Rock compressive strength of different types of surrounding rock are measured by uniaxial and triaxial compression test and listed in table 1. We can see from table 1 that different types of rock have different compressive strength. The greater the confining pressure is, the greater rock compressive strength is. Uniaxial compressive strength of skarn and limestone are much lower. Diorite has the highest compressive strength and significant brittleness characteristics so that internal energy storage of rock suddenly releases in failure moment and make rockburst possible.

Table 1 Rock compressive strength of different types of surrounding rock

Rock type	Specimen No	Diameter /mm	Height /mm	Confining pressure/MPa	Compressive strength /MPa
diorite	B2-1	49.84	99.43	0	141.81
	B2-2	49.71	99.79	10.0	325.34
	B3-2	49.64	100.39	30.0	387.75
limestone	A3-1	50.51	100.27	0	53.8
	A2-2	50.41	99.59	10.0	150.85
	A3-2	50.53	98.32	30.0	258.44
skarn	S1-1	49.71	100.06	0	67.37
	S1-2	49.81	95.39	10.0	97.83
	S3-2	50.47	99.42	20.0	252.22
iron ore	F3-1	50.08	98.83	0	85.82
	F2-2	50.04	98.16	10.0	151.51
	F3-2	50.58	99.5	20.0	239.04

In order to quantitatively calculate elastic strain energy storage in surrounding rock, finite element method is applied for numerical analysis of surrounding rock stress and displacement in process of deep mining. Study at home and abroad and on-site monitoring show that when internal elastic energy reaches or exceeds 100kJ/m³, rockburst will occur [2, 4, 5].

Finite element calculations show that high elastic energy is accumulated in deep surrounding rock of mine area. When the mining depth is 510m, the maximum elastic energy of 0 #, 1 # wear vein on the vertical profile between exploration line No 7 and No +8 is 145kJ/m³ and the maximum elastic energy of 3 # wear vein on the vertical profile between exploration line No +9 and No 10 is 149kJ/m³, which exceed the above-mentioned critical value and result in the phenomenon of rockburst.

3 Multi-index Tendentious Analysis of Rockburst

3.1 Tangential Stress Criterion

Tangential stress criterion reflects rock mass stress state and rock mechanics properties [6]. Define the ratio of tangential stress σ_{\square} and uniaxial compressive strength σ_c as T .

$$T = \sigma_{\square} / \sigma_c \quad (4)$$

Where σ_{\square} is surrounding rock tangential stress, MPa; σ_c is uniaxial compressive strength, MPa

According to three-dimensional finite element simulation results and uniaxial compression test, parameter T and forecasting results of deep surrounding rock of Beiminghe iron mine are shown in table 2.

Table 2 Parameter T and forecasting results of deep surrounding rock

Rock type	σ_{\square} (MPa)	σ_c (MPa)	T	rockburst tendency
limestone	15.20	53.8	0.283	no
diorite	88.90	141.81	0.627	moderate
iron ore	59.82	85.82	0.690	moderate
skarn	32.30	67.37	0.479	weak

3.2 Rock Brittle Criterion

The ratio of rock uniaxial compressive strength and tensile strength is called brittleness coefficient, which reflects the degree of rock brittleness. The calculation formula of brittleness coefficient is as follow:

$$B = \sigma_c / \sigma_t \quad (5)$$

Where σ_c is uniaxial compressive strength, MPa; σ_t is tensile strength, MPa

Through uniaxial compression test and splitting test, parameter B and forecasting results of different types of surrounding rock of Beiminghe iron mine are shown in table 3.

Table 3 Parameter B and forecasting results of deep surrounding rock

Rock type	σ_t (MPa)	σ_c (MPa)	B	rockburst tendency
limestone	5.56	53.8	9.68	no
diorite	13.23	141.81	10.72	weak
iron ore	7.31	85.82	11.74	weak
skarn	6.70	67.37	10.06	weak

3.3 Method of Elastic Energy Index

Unload when the stress reaches 80%~90% of peak strength under uniaxial cyclic loading test and calculate

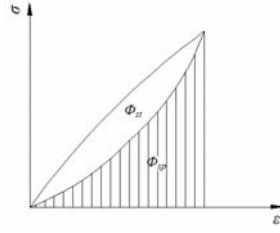


Figure 1 The calculation sketch of elastic energy index

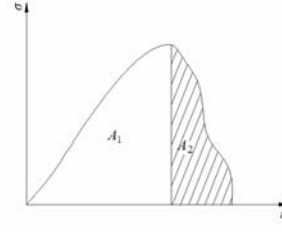


Figure 2 The calculation sketch of impact energy coefficient

elastic energy index Wet with graphical integration method as figure 1.

$$Wet = \Phi_{sp} / \Phi_{st} \quad (6)$$

Where Φ_{sp} is the area surrounded by unloading curve and ε axis, representing residual elastic strain energy; Φ_{st} is the area surrounded by loading curve and unloading curve, representing consumed strain energy.

According to the results of uniaxial cyclic loading, elastic energy index and forecasting results are shown in table 4. We can see that there is no rockburst tendency for limestone and skarn but a rockburst tendency for diorite and iron ore.

Table 4 Parameters Wet and A_{cf} and forecasting results of deep surrounding rock

Rock type	Wet	rockburst tendency	A_{cf}	rockburst tendency
limestone	1.924	no	0.986	no
diorite	3.621	moderate	3.240	strong
iron ore	2.775	weak	2.427	weak
skarn	1.101	no	1.358	no

3.4 Method of Impact Energy Coefficient

According to the theory of rockburst tendency, impact energy coefficient depends on rock complete stress-strain curve, the formula is as follow:

$$A_{cf} = A_1 / A_2 \quad (7)$$

Where A_1 、 A_2 is respective area surrounded by the part of complete stress - strain curves before and after peak strength and coordinate axes, which is shown as figure 2.

According to complete stress-strain curve of rock, the values of impact energy coefficient are calculated in table 4. It can be seen from table 4 that there are no rockburst tendency for limestone and skarn, a weak rockburst tendency for iron ore and a strong rockburst tendency for diorite.

4 Fuzzy Comprehensive Prediction of Rockburst

Fuzzy mathematics theory is introduced for better prediction of the rockburst. Four indexes of the tangential stress index (T), brittle coefficient (B), elastic energy index (Wet) and impact energy coefficient (A_{cf}) are selected to conduct comprehensive prediction of rockburst.

4.1 Establishment of Main Control Set U of Rockburst Intensity and Assessment Set V

Collection U includes n factor u_i . Theoretically, U should include all influencing factors. In fact, some most important influencing factors to easily determine are usually selected. So select four main factors for comprehensive prediction, namely,

$$U = \{T, B, Wet, A_{cf}\} \quad (8)$$

Rockburst intensity is graded by the above-mentioned indexes as a basis and divided into four grades [7] of no rockburst, weak rockburst, moderate rockburst and strong rockburst after appropriately adjusting the bound of individual criteria, namely

$$V = \{v1, v2, v3, v4\} \quad (9)$$

Four grade relations among rockburst intensity and main control factors are shown in table 5.

Table 5 Relations among rockburst intensity and main control factors

intensity grade main control factors	no rockburst	weak rockburst	moderate rockburst	strong rockburst
T	<0.3	$0.3 \sim 0.5$	$0.5 \sim 0.7$	>0.7
B	<10	$10 \sim 14$	$14 \sim 18$	>18
Wet	<2.0	$2.0 \sim 3.5$	$3.5 \sim 5.0$	>5.0
A_{cf}	<2	$2 \sim 2.5$	$2.5 \sim 3.0$	>3.0

4.2 Determination of Membership Degree of Various Factors in V and Fuzzy Relationship Matrix R

There are many methods to determine membership function. We do statistical analysis for each evaluation index value and select the k -parabolic distribution as membership function of intensity grade of rockburst by each evaluation index according to the characteristics of their distribution. The value of four indexes are obtained through test and numerical simulation and respectively substituted into standard formula [8] of membership function to get fuzzy relationship matrix R .

4.3 Determination of Weight Set A of Index Factors

Each factor can be given corresponding weight according to their important degree. Fuzzy weight of each factor can be given by expert assessment method [9] to determine weight distribution of rockburst main control factors T, B, Wet, A_{cf} so that form weight vector A as:

$$A = \{0.3, 0.2, 0.25, 0.25\} \quad (10)$$

4.4 Comprehensive Prediction Results of Rockburst Tendency

Comprehensively consider the weight and membership degree of various factors in evaluation factors set and use weight average model to make a fuzzy comprehensive evaluation for rockburst intensity tendency:

$$B = A \cdot R = \{B1, B2, B3, B4\} \quad (11)$$

Which, B corresponds to fuzzy comprehensive prediction results of rockburst tendency, B_1, B_2, B_3, B_4 corresponding to no rockburst tendency, weak rockburst tendency, moderate rockburst tendency and strong rockburst tendency.

After analysis and calculation, get matrix B of four kinds of the surrounding rock, which give the results of comprehensive prediction of rockburst:

$$B \text{ of Limestone} = \{1.0000, 0.7906, 0.1021, 0.0126\};$$

$$B \text{ of diorite} = \{0.1676, 0.0906, 0.4930, 0.8642\};$$

$$B \text{ of iron ore} = \{0.1282, 0.8210, 1.0000, 0.2707\};$$

$$B \text{ of skarn} = \{0.9974, 0.6456, 0.0027, 0\}$$

It can be seen from the results that there are no rockburst tendency for limestone and skarn, a moderate rockburst tendency for iron ore and a strong rockburst tendency for diorite when the mining depth is 510m. So we should pay close attention to the prevention and control of rockburst in deep mining.

5 Conclusions and Suggestions on Rockburst Prevention

The results of multi-index rockburst tendency analysis and comprehensive forecast for different types of surrounding rock in deep mine area shows that there is no rockburst tendency for limestone and skarn, a moderate rockburst tendency for iron ore and a strong rockburst tendency for diorite when the mining depth is 510m. Therefore during the deep mining process, rockburst should be prevented and controlled in advance (particularly for diorite and iron ore) to guarantee safe mining of the Beiminghe iron mine.

Rockburst prevention should be initiated from the causes. Since rock mass conditions and lithology exist objectively and can not be avoided or replaced, only two aspects of human disturbance and stress fields are considered for rockburst prevention and control. Measures should be taken as follows:

Optimize structure parameters and mining sequence, reasonably layout laneway and use special pressure relief projects to improve and adjust stress condition of the surrounding rock. Large distance structures of 18m, one-side mining sequence and sub-level caving method are adopted in the Beiminghe iron mine and the direction of the roadway axis is basically parallel to the direction of maximum principal stress of the tectonic stress field, which effectively improves stress concentration conditions and reduces rockburst probability. Reasonable support measures, such as bolting and shotcrete net, plastic anchor, and flexible measure or flexibility first and hardness later, etc., are applied in the key position of the chamber and surrounding rock to allow appropriate deformation of surrounding rock and gradual release of strain energy. Immediately spray water to new appearing surface of surrounding rock to reduce the capability of storage strain energy on surface of mining roadway in the section of diorite and iron ore after blasting.

Acknowledgements

The authors gratefully acknowledge the financial support received from state natural sciences fund project (No.50074002) and the specialized research fund for the doctoral program of higher education of China (No.20070008012). We wish to thank Zhang Lei and Wei Haitao for their contributions to this research project.

References

1. Yang, J. and Wang, L.J. Study on Mechanism of Rockburst by Acoustic Emission Testing. Chinese Journal of Rock Mechanics and Engineering, 2005, 24 (20).3796-3802.
2. Wang, Y.H., Li, W.D., et al. Method of Fuzzy Comprehensive Evaluations for Rockburst Prediction. Chinese Journal of Rock Mechanics and Engineering, 1998, 17 (5).493-501.
3. Ouyang, Z.H., Cai, M.F. and Li, C.H. Measuring of In-situ Stress and Disturbance Stress in Beiminghe Iron Mine of China. China mining magazine, 2005, 14 (12). 67-70.
4. Wang, Y.H., Chen, L.W. and Shen, F. Numerical Modeling of Energy Release in Rockburst. Rock and Soil Mechanics, 2008, 29 (3). 790-794.
5. Wang, G.B., Zhang, S.X. and Ren, G.F. Analysis and Prediction of Rockburst in Deep Mining of Tonglushan Copper-iron Ore. Mining Safety & Environmental Protection, 2005, 32 (5). 20-22.
6. Tang, B.Q. and Cao, P. Discussions on Stress Criteria of Rockburst. Hunan Nonferrous Metals, 2001, 3 (2). 1-3.
7. Hou, F.L., Liu, X.M. and Wang, M.Q. Re-analysis of the Causes of Rockburst and Discussion of Intensity Classification. in Rock dynamics of the Third National Conference Papers, (Beijing, 1992).
8. Yang, L.B. and Gao, Y.Y. Principle and Application of Fuzzy Math. Press of South China University of Technology, 2002.
9. Du, Z.J., Xu, M.G., et al. Laboratory Integrated Evaluation Method for Rockburst of Engineering Wall Rock. Gold, 2006, 27 (11).26-29.

STABILITY ANALYSIS OF SURROUNDING ROCK AND RETAINING STRUCTURE DURING EXCAVATION OF TUNNEL GROUP AND OPERATION UNDER SEISMIC LOADING

XIAO-WEN LIU and GONG ZHANG

School of Architectural Engineering ,Nanchang University

Jiangxi ,330031,P.R China

Using the branch tunnel group of the power tunnel from a hydropower station as the object of study, with the method of static simulation of seismic loads, stress and deformation law of surrounding rock and the retaining structure are analysed with two-dimensional finite element analysis method considering the concrete lining and the anchor rod using separate model during digging and operation. The results show that the most adverse loading condition is a full water tunnel during an earthquake. Compared with the normal condition, the first principal stress value of the lining structure adds 0.3MPa~0.5MPa. For a circular cross-section, the largest tensile stress of lining occurs in the lining arch inside and in the interface between a fault and lining structure; the largest tensile stress of an anchor rod has a certain increase under seismic loading. For the profile through the fault, seismic loading can increase lining damage much more. Regarding to selecting the profile of the calculation, the surrounding supporting structure's stability and security can be guaranteed; the results of the project provide a basis for the stability analysis of the surrounding rock and retaining structure.

1 Introduction

There are a lot of hydropower projects in earthquake-prone areas which are under construction or have been built, these projects have large branch tunnel groups in the power tunnel which have large cross-section size, short distance between the hole group axis, and complex geological and operating conditions. If damaged, it will result in enormous economic losses, which may lead to serious secondary disasters. Therefore, it is very important for people to do some research about the stability of surrounding rock and supporting structure in large branch tunnel groups during the period of construction for earthquake-prone areas.

Seismic design methods for underground structure's calculations are generally divided into static, quasi-static and the dynamic response method. In china, seismic research about tunnels has increased lately. In the 50's, the Chinese developed code for the seismic design of railway tunnels by referring to foreign research experience and built anti-seismic norms using the static method; which was the practice until now [1]. The static method is so rough that it has been basically eliminated now. Dynamic response analysis method has high accuracy, and many scholars have in-depth research results applied to the projects. There is a detailed analysis of the seismic design of underground structures as well as the lining of the dynamic response of the structure in literature [2]. The literature [3] using the time-history analysis method, by entering the four typical seismic waves, obtained the time of the internal forces (axial force, bending moment and shear force) according to dynamic interaction between the tunnel and soil, and proposed the largest internal forces and its distribution. The literature [4] studied the changes of rock parameters and the effect of dynamic response by setting up the damping layer and grouting reinforcement of tunnel lining structure, and gave some laws. It is hard to make a assessment of the calculated results, because the dynamic response analysis methods required deeper, various

professional knowledge and skills [5]. Therefore, people often use the quasi-static calculation method, except for particularly important projects or complex structures and special soil conditions [6] .

By the method of static simulation of seismic loads, stress and deformation law of surrounding rock and the retaining structure are analysed with two-dimensional finite element analysis method considered the concrete lining and the anchor rod using separate model during digging and operation for a branch tunnel group of power tunnel from a hydropower station. The paper provides some guidance about designing underground tunnels safely.

2 Project Summary

The power station tunnels are on the right bank ,arranged two parallel tunnels, the total distance of left tunnels (that is I tunnel) is about 3400m, the distance of right tunnels (that is II tunnel) is about 3300m.The diameter of a single tunnel is 8m, and each tunnel after the surge shaft is divided into two branch tunnels which diameter is 6m, the concrete lining thickness is 0.5m,nine bases $\phi 22$ mm bolts are arranged in 180 degree semi-circular framework during the early supporting time, the length of each anchor rod is 4.2m, spacing 1.2m,and 15cm thick concrete lining is applied to surrounding rock; the distance of each two adjacent hole axes is 16.7m.

According to the known 6 grade earthquake happened in this district, the near field is considered that may still happen around 6 earthquake. According to 1:400 million, "China ground motion parameters zoning map" (GB18306-2001),the ground motion peak acceleration is 0.15g in the project area, correspondingly, the basic earthquake intensity is VII, the characteristics of ground motion response spectrum period is 0.45s.The peak ground acceleration of hole posture is 0.10g by finite element of stability analysis.

3 Computing Model

3.1 Model Boundary

According to geological features, select a typical cross-section. Calculation model is 140 meters width ,118.9 meters high; Four-node mesh is applied to rock mass and late support concrete structures, and anchor rods and the primary support use two-node mesh. A total of 11601 nodes and 12187 element mesh are produced in finite element analysis. Model on both sides of the border for the horizontal direction imposed sliding supports, at the end of the border in the vertical direction also has imposed supports, the calculation model is shown in Figure 1. Layers of rock of model are soil cover, strong weathering, the upper part of the weak weathering, the lower part of weak weathering and slight weathering from the top down.

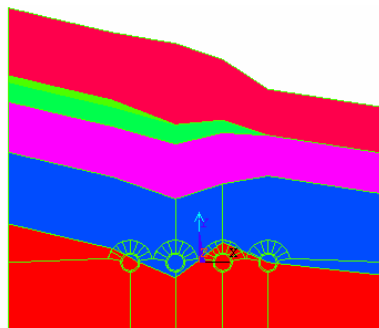


Figure 1 Finite element calculation model

Physical and mechanical parameters are shown in Table 1.

Table 1 Physical and mechanical parameters

Lithology	Density (kg/m ³)	The elastic modulus (GPa)	Poisson's ratio	Cohesion (MPa)	Friction angle (°)
Cover layer	2100	0.03	0.35	0.005	22
Strongly weathering layer	2600	3.0	0.3	0.3	31
Upper part of the weak weathering	2650	6.5	0.28	0.75	39.5
lower part of the weak weathering	2650	7.5	0.26	0.75	46
Slight weathering layer	2650	10.5	0.24	0.93	48
C20 Concrete	2349	26	0.2	/	/
C25 Concrete	2449	28.5	0.2	/	/
φ 22 anchor rod	7959	170	0.3	/	/
Fracture	2200	2.0	0.35	0.035	22

3.2 Calculation Conditions

Calculation condition mainly includes construction period and operation period, and different period is corresponding to different load combination. Conditions corresponding to various load combination on construction period are shown in Table 2.

Table 2 Calculation condition on construction period

Calculation condition of construction period	load combination
hole without any support	initial self-weight stress field + excavation load
hole with the early initial support	initial self-weight stress field + excavation load
hole with the early and late support	initial self-weight stress field + excavation load

In operation conditions, conditions corresponding to various load combination are shown in Table 3.

Table 3 Calculation condition hole water diversion and power generation on operation period

Calculation condition of operation peration	load combination
Two-hole full of water operating conditions	the initial self-weight stress field + excavation load + external water pressure + two-hole full of water inside the water pressure
Single-hole full of water operating conditions	the initial self-weight stress field + excavation load + external water pressure + single-hole full of water inside the water pressure
Two-hole full of water operating conditions + seismic loading	the initial self-weight stress field + excavation load + external water pressure + two-hole full of water inside the water pressure + earthquake loading
Single-hole full of water operating conditions + seismic loading	the initial self-weight stress field + excavation load + external water pressure + single-hole full of water inside the water pressure + earthquake loading

The water pressure acted on the tunnel lining outer edge is known as the external water pressure, according to survey data, external water pressure is 10m, the average inner water pressure is 29.5m.

4 Calculation Results

4.1 The Deformation and Stability of Surrounding Rock on Construction

Calculations show the total maximum of displacement reaches 0.18cm (branch hole 1) when the initial support is not taken on profile, the total amount of subsidence is very small. The total displacement is 0.167cm (branch hole 1) when immediately implement support at this early stage; while, if immediately implement primary support and late support are imposed after the formation of bare-hole, then the total value of displacement is only 0.086cm (branch hole 1). The fact that plastic zone does not appear after rock excavation shows surrounding rock is steady.

4.2 The Deformation and Stability of Surrounding Rock on Operation

The total maximum displacement of surrounding rock, the maximum shear stress, first principal stress, as well as the third principal stress are slightly smaller in full of water operating conditions than those in non-operating mode, the reason is that under the operating condition of full of water, surrounding rock stress conditions have improved due to active tolerance made by late support, and no tensile stress appears. Whether it is single-hole or double-hole operates, there is no tensile stress. Non-operation condition is the most unfavorable condition.

4.3 The Forces of Supporting Structure on the Operational Phase

Calculations show the axial stress of tunnel anchor rod and lining initial of supporting structure are reduced under the operational condition of full water rather than a state of non-full water tunnel condition. The maximum anchor rod stress under operational phase is 32.1MPa, far less than the designed tensile strength value of anchor rod. The largest tensile stress of lining structure is 1.57MPa (tensile stress of branch hole I under the operational condition of full water), the maximum of compressive stress of late lining is 12.2MPa, all are smaller than the standard value of concrete tensile strength and compressive strength (for the C25 concrete, and its standard value of axis tensile strength is 1.75MPa, the standard value of axial compressive strength is 17MPa). According to 《hydraulic tunnel design specifications》 (SL279-2002), for 3th grade tunnel, under the basic load combination condition, the tensile safety factor of lining concrete is 1.8, 1.6 under special conditions, under the basic load combination, the allowed tensile stress of concrete lining can be calculated to 0.972MPa, 1.09MPa under special conditions, but greater than the concrete tensile stress allowed, the concrete lining will be cracking, but it will not damage.

The largest tensile stress of late lining in other conditions of branch hole is between 0.006 and 0.88MPa, and can meet the permitted requirements of tensile stress of concrete lining.

4.4 The Forces of Supporting Structure under the Conditions of Earthquake

Under seismic conditions, the most unfavorable condition is the full load of water + earthquake working condition (see Table 4, Table 5). For the profiles, compared with the normal working condition, the first principal stress value of lining increases no more than 0.3MPa. The first principal stress maximum of late Lining is between -0.006 and 1.83MPa; the tensile stress maximum of lining of branch hole 1 under full-water conditions is 1.83MPa, greater than the value of standard axial tensile strength of concrete, indicating that the concrete lining will be destroyed. The maximum tensile stress of lining of other branch holes meets the allowed tensile stress of concrete requirements in various conditions. Therefore, for the section, with the exception of branch hole 1, the existing support parameters can guarantee the security of supporting structure under the conditions of earthquake.

Because of space limitations, finite element analysis results about the fault through the cross-section are not listed, calculated results can be drawn the largest tensile stress of lining occurred in the interface of fault

structure and lining; the largest tensile stress of anchor rod has also increased to some extent when a earthquake happen. For profiles passed through by the fault , seismic loading can increase the lining damage.

5 Conclusion

The finite element method can be easily simulate stress and displacement fields of rock and the lining structure during tunnel excavation process and operating course for seismic load; and is a quantitative analysis of the stability of surrounding rock and the tunnel optimizing the support structure. The results show that the most adverse loading condition is the tunnel full of water + earthquake condition under seismic loads. Compared with the normal working conditions, the first principal stress value of the lining structure increases between 0.3MPa and 0.5MPa. For the circular cross-section, the largest tensile stress of lining occurred in the vault inside. Regarding to selecting the profile of the calculation, the surrounding supporting structure's stability and security can be guaranteed; the results can be used as a reference for design and construction.

Table 4 Force and deformation of supporting structure for operation period under normal condition

project condition			the most value of bolt axial stress (MPa)		he most value of the initial axial force lining (KN)		maximum bending moment of the initial lining (KN • m)		the late maximum first principal stress of lining (MPa)	
			Numerical	Location	Numerical	Location	Numerical	Location	Numerical	Location
Tunnel I running	Tunnel I	Branch 1	23.7	Vault	-211	Vault	1.98	Vault Lumbar arch	1.57	Vault
			-14.2	Lumbar arch	-17.3	Lumbar arch				
	Tunnel II	Branch 2	20.9	Vault	-192	Vault	0.91	Vault Lumbar arch	0.88	Vault
			-14.3	Lumbar arch	-8.2	Lumbar arch				
	Tunnel II	Branch 3	23.6	Vault	-319	Vault	1.1	Lumbar arch	0.025	Vault Backpla -ne
			-2.8	Lumbar arch	-172	Lumbar arch				
Tunnel II running	Tunnel I	Branch 1	32.1	Vault	-410	Vault	2.2	Vault	0.12	Vault.
			-6.0	Lumbar arch	-206	Lumbar arch				
	Tunnel II	Branch 2	29. 4	Vault	-400	Vault	1.0	Vault Lumbar arch	-0.006	Vault Backpla -ne
			-5.9	Lumbar arch	-112	Lumbar arch				
	Tunnel II	Branch 3	16.4	Vault	-141	Vault	0.83	Vault Lumbar arch	0.72	Vault.
			-8.3	Lumbar arch	-74	Lumbar arch				
Two Tunnels running	Tunnel I	Branch 1	23.6	Vault	-214	Vault	1.98	拱肩	1.52	Vault.
			-14.2	Lumbar arch	-15.5	Lumbar arch				
	Tunnel II	Branch 2	20.8	Vault	-199 .3	Vault	0.88	Vault Lumbar arch	0.76	Vault.
			-14.2	Lumbar arch	-4.9	Lumbar arch				
	Tunnel II	Branch 3	16.4	Vault	-136.1	Vault	0.80	Vault Lumbar arch	0.58	Vault.
			-8.3	Lumbar arch	-68.3	Lumbar arch				
		Branch 4	17.1	Vault	-159.1	Vault	0.67	Vault Lumbar arch	0.20	Vault.
			-10.9	Lumbar arch	-5.4	Lumbar arch				

Table 5 Force and deformation of supporting structure for operation period under seismic condition

project condition			the most value of bolt axial stress (MPa)		he most value of the initial axial force lining (KN)		maximum bending moment of the initial lining (KN • m)		the late maximum first principal stress of lining (MPa)	
			Numerical	Location	Numerical	Location	Numerical	Location	Numerical	Location
Tunnel I running + earthquake	Tunnel I	Branch 1	23.9	Vault	192.3	Vault	1.99	Vault Lumbar arch	1.83	Vault.
			-14.4	Lumbar arch	-12.8	Lumbar arch				
	Tunnel II	Branch 2	20.9	Vault	-185.2	Vault	0.92	Vault Lumbar arch	0.99	Vault.
			-14.3	Lumbar arch	-6.6	Lumbar arch				
		Branch 3	23.5	Vault	-326.9	Vault	1.1	Vault Lumbar arch	0.026	Vault. Backpla-ne
			-2.9	Lumbar arch	-172.1	Lumbar arch				
Tunnel II running + earthquake	Tunnel II	Branch 4	25.5	Vault	-372.3	Vault	0.81	Vault Lumbar arch	0.0031	Vault
			-2.5	Lumbar arch	-105.2	Lumbar arch				
	Tunnel I	Branch 1	31.9	Vault	-429.9	Vault	2.13	Vault Lumbar arch	0.12	Vault
			-6.1	Lumbar arch	-208.8	Lumbar arch				
	Tunnel II	Branch 2	29.3	Vault	-407.1	Vault	0.98	Vault Lumbar arch	-0.008	Vault
			-5.9	Lumbar arch	-112.7	Lumbar arch				
Two tunnels running + earthquake	Tunnel I	Branch 3	16.5	Vault	-136.9	Vault	0.82	Vault Lumbar arch	0.79	Vault
			-8.3	Lumbar arch	-74.4	Lumbar arch				
	Tunnel II	Branch 4	17.3	Vault	-141.2	Vault	0.69	Vault Lumbar arch	0.45	Vault
			-10.8	Lumbar arch	-3.7	Lumbar arch				
	Tunnel I	Branch 1	23.9	Vault	-194.8	Vault	1.99	Vault Lumbar arch	1.79	Vault
			-14.1	Lumbar arch	-11.1	Lumbar arch				
Two tunnels running + earthquake	Tunnel II	Branch 2	20.1	Vault	-192.0	Vault	0.9	Vault Lumbar arch	0.86	Vault
			-10.4	Lumbar arch	-3.4	Lumbar arch				
	Tunnel I	Branch 3	16.4	Vault	-145.1	Vault	0.81	Vault Lumbar arch	0.52	Vault
			-8.3	Lumbar arch	-68.6	Lumbar arch				
	Tunnel II	Branch 4	16.8	Vault	-174.7	Vault	0.65	Vault Lumbar arch	0.046	Vault
			-11.1	Lumbar arch	-8.7	Lumbar arch				

References

1. GB50157-2003 Code for the Design of Metro. China Planning Press, 2003. (in Chinese)
2. Hashash, Y.M.A., Hook, Jeffrey, J., Schmidt, B., Yao, J.I.C. Seismic design and analysis of underground structures. Tunnelling and Underground Space Technology, 2001, 16(4). 247-293.
3. Gao, F. and Shi, Y.C. et al. Tunnel Study Two Damping Measures. Journal of Rock Mechanics and Engineering, 2005, 24 (2). 222-229.
4. Liu, R.S., Hu, S.Q. and Shi, H.B. Study on Seismic Loading of Pseudo-static Approach Used in the Seismic Design of Underground Structure. Chinese Journal of Geotechnical Engineering, 2007, 29(2). 237-242.
5. Zhou, J., Su, Y. and Dong, P. Current Situation of Earthquake Resistance of Subway and Underground Structures in Soft Soil. Underground Space, 2003, 23(2). 173-178. (in Chinese)
6. KAWAJIMA, K. A Seismic Design of Underground Structure. Japan: Kajima Institute Publishing Co., Ltd. 1994. (in Japanese)

RELATIONSHIP OF TEXTURAL STRESS AND ROCK FAILURE ON THE DIVERSION OF THE TUNNEL

LING-QIANG YANG, YUAN-YUAN LI and QING-LIAN SHU

*School of Civil Engineering and Architecture, University of Ji'nan,
Ji'nan 250022, P.R. China*

The textural stress has great effect on the stability of rock. According to the measured geo-stress data, through FEM and combined with the linear multivariate regression method, the geo-stress field was analyzed. Based on Yu Maohong's generalized twin-shear strength theory, the failure type was classified into the generalized tension, the generalized compression and the generalized shear. Using these methods, the stress distribution, peculiarity and process of failure in a diversion tunnel of a large-scale hydropower station was analyzed. It was shown that the stress concentration was located at the bottom of the wall and the arch top, the stress in the wall was small and the failure happened at the bottom of the wall and the arch top, and then the bottom board and some areas far from the tunnel. Under the condition without considering textural stress, the stress concentration area located in the wall and the failure happened at the bottom of the wall, then in the middle of the wall and at the arch top, the failure elements were around the tunnel. Based on the deformation observation, it is indicated the textural stress could reflect the real failure process of tunnels.

1 Introduction

The stress state of the rock mass in engineering is one of key factors to analyze the safety of engineering, slope stability, and basement's stability. The rock mass is a part of the geologic mass and the stress state is very complex because of a long history of geological action. Based on previous researchers' results and engineering experience, the stress state in rock mass is not consistent with the quiet hydro press which was supported previously. The stress state not only relates to dead-load stress, but also to geologic textural stress created by long time geological action [1]. As a result of the engineering scale becoming larger and larger, the conditions of geologic textural stress will be more obvious. Consequently, more importance is paid to the geologic stress. The diversion tunnel is a typical hydro-projection located in a complex geologic environment with its safety being affected significantly by geologic textural stress. In different geologic conditions, the specialty and failure mode differs, which leads to the importance of the study of geologic textural stress in diversion tunnel engineering.

2 Projection Information and Numerical Model

Hydroelectric engineering arranges three diversion tunnels in the left bank. N.O 1 and N.O. 2 tunnels are located outside of the workshop. The axis of orientation of one tunnel is S38°E - S11.5°E. The altitude in the inlet and outlets are 600m and 578m respectively with the length at 3678m. The distance of two-tunnel axis is 65 meter at upstream, but 61 meter at downstream. The altitude of N.O. 3 tunnel in inlet and outlet are 660m and 639m respectively. There are four faults in the hydroelectric station dam region. The strike of F1 is N15°-30°E. The dip of F1 is NW56°-82°. The width of F1 is 13-23 m. The length of F1 is 7500m. The strike of F3 is N14°-50°E. The dip of F3 is NW80°-90°. The width of F3 is 2-6 m. The length of F3 is 1000m. The strike of F5

is N18°-25°E. The dip of F5 is NW60°-80°. The width of F5 is 1-3 m. The length of F5 is 1200m. The strike of F15 is N30°-42°W. The dip of F15 is SW55°-70°. The width of F15 is 0.5-6 m. The length of F15 is 500m. Using hole deformation method to measure the initial stress of rock mass in 5 points as in Table.1.

Table 1. Measured values of the initial stress state

Position	σ_1/MPa	$\alpha_1/(\text{°})$	$\beta_1/(\text{°})$	σ_2/MPa	$\alpha_2/(\text{°})$	$\beta_2/(\text{°})$	σ_3/MPa	$\alpha_3/(\text{°})$	$\beta_3/(\text{°})$
PD204(302 m)	10.87	N71.2E	22.5	5.13	N0.3E	-38.3	1.86	S41.7E	-43.3
PD204(502 m)	7.39	N65.4E	25.2	6.4	N6.6E	-47.7	-1.26	S41.3E	-31.4
PD204(685 m)	6.49	N56.6E	38.2	4.63	S39.4E	-7.6	2.47	N41.3E	-50.8
PD204(215 m)	8.00	N38.7E	48.8	2.52	S46.0E	4.6	1.19	N47.9E	-40.9
PD204(380 m)	7.18	N30.1E	56.1	3.08	N40.1E	-33.4	-0.97	S52.9E	4.60

Where: α is dip direction. β is dipangle.

Based on the topography, physiognomy and measure point location, the numerical model region is 5000m at vertical stream direction, 3000m at stream direction, 3000m at vertical direction. The geologic rock include upper of weak weather rock mass, lower of weak weather rock mass, fleabite weather rock mass and flesh rock. The geologic numerical model of finite element is Figure 1.



Figure 1 Model of finite element

3 Geologic Textural Stress

The stability of rock mass is close relating to it's stress state. In some condition, the stress state can be control factor. So it is nessary to study geologic textural stress in engineering rock mass to ascertain its direction and quantity. Of course the analysis method used in geologic mechanics is often used in practice engineer. The method of projecting to equatorial plane is also used in some engineer. From Table 1 and the four fault's strike, the direction of geologic textural stress is N30.1°-71.2°E, the tip of geologic textural stress is 22.5°-56.1°[2].

The linear multivariate regression method was used to calculate the strike and tip of geologic textural stress in order to validate above qualitative result. The 3-D initializing stress state is composed of dead-load stress and geologic textural stress state. In elastic state, the initial stress can be express as [3]

$$\sigma = L'_1\sigma_z + L'_2\sigma_{g1} + L'_3\sigma_{g2} + \dots + L'_n\sigma_{gn} + \varepsilon_k \quad (1)$$

Where, $L'_1, L'_2 \dots$ are regression coefficient. ε_k is observation error. Its mean value is 0.

Suppose there are m measure points. Least squares fitting method with consideration of the residuals was used to determine the cohesion of fault.

$$S_c = \sum_{k=1}^m \sum_{j=1}^6 (\sigma_{jk}^* - \sum_{i=1}^n L_i' \sigma_{jk}^i)^2 \quad (2)$$

Where, σ_{jk}^* is measured stress ponderance of k point j-th ponderance. σ_{jk}^i is calculted stress ponderance of k point j-th ponderance. Based Least squares fitting method, the regression coefficient can be calculated.

The disserted square sum can reflect the departure of measure point, i.e

$$S_{00} = \sum_{k=1}^m \sum_{j=1}^6 (\sigma_{jk}^* - \bar{\sigma}_j^*)^2 \quad (3)$$

$$\text{where, } \bar{\sigma}_j^* = \frac{1}{m} \sum_{k=1}^m \sigma_{jk}^*$$

The regression square sum can express as $S_h = S_{00} - S_c$. The effect of regression can be measured by relation coefficient R.

$$R = \sqrt{S_h / S_{00}} \quad (4)$$

Based on field measured stress value, using add one unit displacement in stream-direction and vertical stream direction to modify geologic textural stress. The regression equation is

$$\sigma = 1.0\sigma_z + 0.252\sigma_{g1} - 0.0231\sigma_{g2} \quad (5)$$

Used the value of point 2 and 4 to check Eq. (5) in Table 2. The relation coefficient R is 0.8753. So the regression equation is rather good.

Table 2 Comparison between measured and computed stresses

Stress /MPa		σ_x	σ_y	σ_z	τ_{yz}	τ_{zx}	τ_{xy}
1	measured	3.8	9.62	4.44	2.78	1.27	-1.10
	calculated	3.96	6.85	6.21	2.76	1.22	-1.09
4	measured	3.23	3.43	5.06	2.74	-2.01	-0.80
	calculated	3.62	3.71	5.76	2.62	-1.96	-0.80

4 Concepts of Progressive Slope Failure and Strength Theory

The stress states of points in the slope are different, so the point with bigger stress will break after it exceeds its strength limit (or shear deformation limit). In this sense, slope failure is a progressive failure progress. Firstly the effect field and reliability index field of slope are analyzed by FEM, and the minimum value of reliability index and its failure probability are logged. Then, after the minimum reliability index is specified, under which the element will break, the stress originally sustained by the element will be transferred to other unbroken elements in the field, and the stress is then redistributed. Thus the stiffness matrix relevant to that element is recalculated, and the overall stiffness matrix is assembled accordingly. After that, the effect field and reliability index field of slope are analyzed again. Correspondingly, the minimum value of reliability index and its corresponding failure probability and conditional probability need to be recorded too. Therefore, when specified again is the minimum reliability index under which the element will break, the failure will continue element after element until the slope fails and slides after the failure of m elements. When this takes place, it becomes a mechanism, or its serviceability is affected since excessive deformation occurs. The geometrical location of

these m failure elements constitute the most possible sliding plane, and these m values of conditional probability compose the probability vector of possible sliding of this sliding plane[4,5].

$$P_f = [p_{f1} \quad p_{f2} \quad \dots \quad p_{fm}] \quad (6)$$

The following is the k th element of the above probability vector

$$P_{fk} = \prod_{i=1}^k P_{f0i} \quad (7)$$

When k equals 1, it is the probability of initial sliding of slope; when k equals m , it is the probability of failure. If the sliding failure of slope is considered a parallel system, this track will be the most possible one.

Based on YUMaohong's strength theory[6] .

$$\text{If } \sigma_2 \leq \frac{\sigma_1 + \alpha\sigma_3}{1 + \alpha} \quad Z = f_t - (\sigma_1 - \frac{\alpha}{2}(\sigma_2 + \sigma_3)) \quad (8)$$

$$\text{If } \sigma_2 \geq \frac{\sigma_1 + \alpha\sigma_3}{1 + \alpha} \quad Z = f_t - (\frac{1}{2}(\sigma_1 + \sigma_2) - \alpha\sigma_3) \quad (9)$$

Where, $\alpha = f_t/f_c$. f_t and f_c are tension and pressure strength in one axis. σ_1 , σ_2 and σ_3 are the first, second and third master stress. If $Z < 0$, the element will failure.

5 Tunnel Stress Distribution Under Geologic Textural Stress

The stress state of tunnel has relation to tunnel type and excavation processor. In the calculation processor, sub-model was used to introduce initial stress field firstly. Then calculation was done in different surrounding rock type. Some conclusion that has action to engineering was been drawn. Because of print space limitation, only city gate tunnel in third surrounding rock was analysis as example. There are no big faults in the type surrounding rock. There are some joint spacing between 1.0-2.0 m. So the joint was not simulated solely. Its action reflects through modifying the mechanics parameter of element.

The calculating flow is as follow. First take out typical tunnel section as sun-model. Initial stress field put through the boundary condition[7,8]. Then using air element simulated excavation. The other calculating mode also was done without considering geologic textural stress for contrast[9]. The stress state of two model is Figure 2 and Figure 3. From these we can see that when considering geologic textural stress, the shear stress at arch top is more then that of without considering geologic textural stress. The region of stress focus is larger than that of without considering geologic textural stress. Tension stress happen at bottom of the tunnel when considering geologic textural stress.

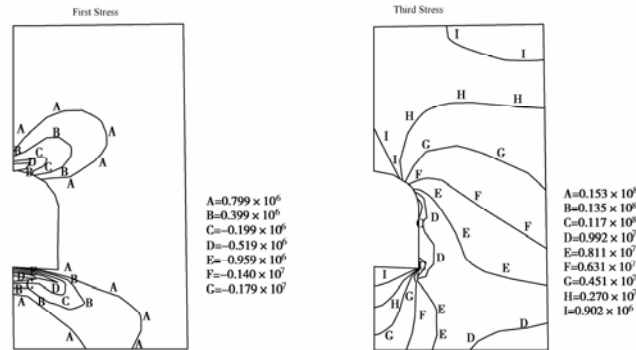


Figure 2 Stress state on section considering textural stress (unit: Pa)

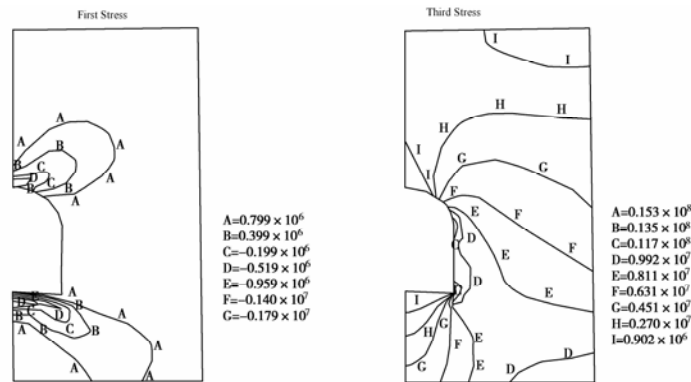


Figure 3 Stress state on section without textural stress (unit: Pa)

6 Processor of Tunnel Failure

Cracking trajectory method was used to find out the failure processor. At first the element with biggest stress or least value of strength criterion will be forced to crack or to be failure no matter it failure or not. Then the element stiff matrix will be modified according to reference (Yang L.Q. 2003)[10]. Then another element with biggest stress or least value of strength criterion will be forced to be failure. And so on. In the paper there were 25 elements be forced to be failure as in Figure 4. The strength criterion value of the 25 elements shows in Figure 5. From the two figures, we can see that when considering the geologic textural stress, the processor is wall corner fist failure for stress concentrate. The next is arch top failure for shear stress. At last the bottom was failure for general compression. The failure of tunnel is suddenly for the stress is very large. And strength criterion value is very lower. The processor is consistent with Specification for design of hydraulic tunnel[11]. Without considering geologic textural stress, the processor is wall corner, then wall, then arch top. The processor is different with field observation.

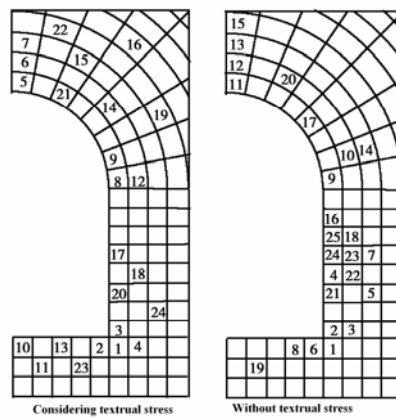


Figure. 4 Failure sequence of element

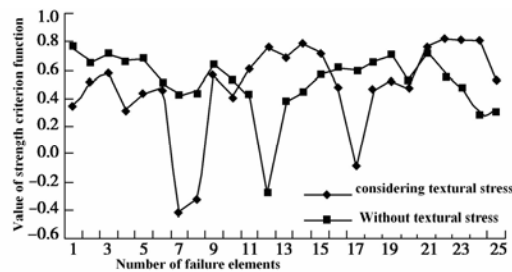


Figure. 5 Criterion function of failure element

6 Conclusions

From above analysis, the follow conclusion could be drawn.

The geologic textural stress is a key factor to estimate the stability of the rock surrounding the tunnel because of its close relation to stability.

The geologic textural stress not only affects the stress value of the tunnel, but also changes the stress distribution and region of the stress concentrate.

The method of projecting to the equatorial plane can ascertain the direction of geologic textural stress, but could not make out the value of the geologic textural stress. The linear multivariate regression method can determine the direction and value of geologic textural stress.

Reference:

1. Sun, G.Z. Theory and Appliance of Geological Engineering. Seismological Press, 1996.
2. Sun, G.Z. Basic of Geology Mechanics. Science Press, 1984.
3. Guo, H.Z, Ma, Q.C. and Xue, X.C. Analysis of Rock Initial Stress Field. Chinese Journal of Geotechnical Engineering, 1983, 5 (3). 64–75.
4. Chen, Z.and Chen, S. Probability Vector of Cracking Trajectories of Arch Dam and Stochastic Finite Element Analytical Method. in Proceedings of CCCBE-VII, ASCE, (Berlin, 1995).
5. Chen, Z.P. Probability Analysis of Linear Cracking Trajectories of Arch Dam. Journal of Hydraulic Engineering, 2000, (2). 41–48.
6. Yu, M.H. Engineering Strength Theory. Higher Education Press, 2002.
7. Wang, H.J., Zhang, S.R.and Lian, J.J. Rock Stabilization Analysis of Diversion Tunnel of a Large-scale Hydropower Station. Chinese Journal of Geotechnical Engineering, 2006, 28 (7). 869–873.
8. Wang, X.C.and Shao, M. The Basic Theory and mMethod of FEM. Tsinghua University Press, 1997.
9. Hou, Y.M., Wang, J.H. and Chen, J.J. 3D FEM Analysis of Oversize & dDeep Excavation. Chinese Journal of Geotechnical Engineering, 2006, 28 (S): 1374–1377.
10. Yang, L.Q., Lian, J.J, Zhang, S.R., et al. Analysis of Bcreaking and Overloading of Arch Dam. Journal of Hydraulic Engineering, 2003 (3). 55–63.
11. SL279-2002. Specification for Design of Hydraulic Tunnel. 2003.

STUDY OF FLOOR HEAVE IN SOFT ROADWAY

HOU-QUAN ZHANG, LI-JUN HAN, YONG-NIAN HE, BING-SONG JIANG and JI-ZONG XIA

*State Key Laboratory for Geomechanics and Deep Underground Engineering, School of Architecture and Civil
Engineering, China University of Mining and Technology*

Xuzhou, 221008 P.R. China

LIAN-HUA LI and YAN-JIE LIN

Xinlu Freezing and Installation Company of Yanzhou Mining Group

Yanzhou, 273500 China

A sump of a certain coal mine at -400m level is located in a complicated geological structure zone and its floor strata have a very high dilatability when encountered by water. Under high tectonic stress, high in-situ stress and high expansion stress, previous common anchoring-netting-shotcreting and pre-stressed cabling support can not at all keep its indispensable stability of surrounding rock in the sump. Based on the analysis of in-situ geological conditions and surrounding rock failure reasons, and combined with the shortcomings of previous support design, a full-face reinforced concrete arch walling approach was adopted for the sump support. A kind of long distance pumping concrete technology was used in the concrete arch walling support, which fetched up the shortages of common manual arch walling. Good technical effects and economic benefits were obtained. The research results show that it is very difficult to keep the stability of sump in soft surrounding rock with great expansively only through anchoring-netting-shotcreting and pre-stressed cabling support. It can improve the loading capability and integrity of support structure effectively through grouting for large broken zone of surrounding rock. The support structure formed by full-face reinforced concrete arch walling can control the heavy floor heave of roadways effectively.

1 Introduction

Floor heave is a common failure phenomenon in soft roadways [1]. Heavy floor heave will result in the convergence of the whole transect of roadways, interrupting material transportation and personnel traffic, hindering the ventilation, even inducing the abandonment of the whole roadway. It has a great destructive influence on normal production and necessary safety in coal mines. Nearly 50% of roadway maintenance expense is often spent on the control and treatment of floor heave [2]. Therefore, floor heave is one of the most difficult problems in roadway support.

A great deal work has been focused on the producing mechanism in recent decades, and general results were obtained. Soviet scholar, Цимбаревич found that the mechanism of floor heave was consistent with that of incompact soil extrusion under two compressive stiff mouldings and worked out the compressive stress counteracted on the floor heave strata according to limit equilibrium theory [3]. German scholar, Oldengott carried out some similar material simulation on roadway failure and found that a great deal compressive breakage under vertical stress occurred at first in two sidewalls of the roadway and then floor heave induced by horizontal stress followed [2]. Haramy considered floor strata as a rock beam fixed at two ends and computed its loading capability and stability [4]. Kang performed some analytical discussion and found that rock dilation under deviatoric stress, rock expansion encountered by water and flexible deformation of floor strata were three main reasons for floor heave; moreover, 67% of floor heave resulted from the flexible deformation [5,6]. He also made a special research on the relationship between expansive rock and floor heave and drew a conclusion

that volumetric expansion and strength degradation were two primary sources to cause floor heave [7]. HE Yongnian observed roadway deformation and recorded the data in Maoming mining area. He found that the compaction sinkage of sidewalls accounted for a great deal of the floor heave deformation and the reinforcement of sidewalls can prevent sidewall inrush and help to control the floor heave [8].

To sum up, floor heave in different roadways have different mechanisms. According to the producing mechanism, a lot of techniques to control floor heave have been put forward, for example, the retractive close steel bracket [9], concrete reverse arching [10], grouting, anchoring in roof strata [11], sidewalls [12,13] and floor strata [14], pressure release by blasting, grooving in floor strata [14]. These methods have great instructive effect on the control of floor heave. However, with the increase of mining depth, the ground pressure increases and the rock lithologies become more complicated. A lot of recent research results show that there are many differences in engineering mechanics between shallow mining and deep mining [15]. Therefore, floor heave support should be designed based on the different geological conditions of surrounding rock and its stress circumstances in practice.

This study presents a floor heave in a sump of a coal mine located in a complicated geological structure zone and its floor strata with great dilatibility when encountered by water. A new approach of full-face reinforced concrete arch walling with a long distance pumping concrete technology was adopted for the sump support according to the practical conditions. Good technical effects and economic benefits are obtained.

2 Engineering Conditions

The coal mine is located in High-Tech Zone, Jining city, Shandong Province. Its 1160 mining area is located in a syncline structure zone full of many faults, foldings and fractures. Therefore, high tectonic stress exists in this mining area. According to the measurement of in-situ stress, the horizontal stress is three times as high as that vertical one. At the same time, this area is located at -400m level; the vertical ground pressure by its self-weight of overburden strata is very high.

Roof strata of the sump is mainly composed of medium sandstone and siltstone but roof strata have embedded many weak and soft interlayers, showing representative lamination characteristics, see in figure 1(a). Moreover, quite a few faults and fragments exist in local regions. Therefore, the stability of roof strata is very poor.



Figure 1 rock lithologies of roof and floor strata

Most of immediate floor strata are degenerative clay rock. 95% of mineral ingredients are argillaceous mineral while the other is organic matter. The diameter of argillaceous mineral is about 0.05~0.1mm and the interval of mineral grains is about 0.05mm, as shown in figure 1(b). Therefore, the clay rock has a high porosity. When subjected to water, it is highly expansive, softening and mudding. Therefore, the mechanical properties of floor strata are very degenerative. Under the long-term erosion effect of underground water in the sump, heavy

weathering deterioration happened in the surrounding rock, showing representative characteristics of exceptional soft rock mass.

3 Floor Heave Mechanism

The heavy floor heave under previous bolting-shotcreting and pre-stressed cabling support is shown figure 2. Based on spot field investigation of geological conditions and the detailed analysis of failure reasons, it can be concluded that the floor heave is mainly resulted from these four aspects as follows: (1) high stress conditions, including high tectonic stress (in a complicated geological structure zone), high in-situ stress and high expansion stress; (2) unstable rock lithologies, including expansive, softening and mudding deterioration of clay rock; (3) underground deposited water circumstance, (4) unreasonable support, bolting-shotcreting and pre-stressed cabling can't close up the surrounding rock and prevent water erosion on expansive clay rock. According to the above reasons, a full-face reinforced concrete arch walling method was adopted for the sump support.



Figure 2 Rock deformation and fracturing situation after previous common bolting support

4 Support Design and Technical Parameters

4.1 Grouting Reinforcement

Due to large broken zone surrounding the sump under previous ineffective bolting-netting-shotcreting and pre-stressed cabling support, the first step is to enhance the mechanical properties of the fractured surrounding rock by grouting. Drilling and stalling the internal grouting bolt in roof strata and sidewalls and then grouting in time.

The internal grouting bolt ($\Phi 22 \text{ mm} \times 2000 \text{ mm}$) with pressed thread is made of seamless steel pipe. The end of bolt was screwed so as not to leak cement mortar, as shown in figure 3. The bolts were radially placed along the whole opening of sump. The distribution of anchors was 1600 mm (column) \times 1600 (row). The bolt was fastened by a roll of 3530 type resin power stick at the end. Final anchoring force should reach above 60 kN, the pre-stress is not blow 10 kN. The grouting was obtained from the mixture of concrete and soluble glass. The ratio of water and concrete power was 0.8~1.0. The dosage of soluble glass was 3~5% of the concrete weight. Grouting pressure was limited in 2.0 MPa. The grouting bolt was screwed tightly by standard screw cap and a high strength of steel salver [16]. The support structure after bolting-grouting is shown in figure 4.

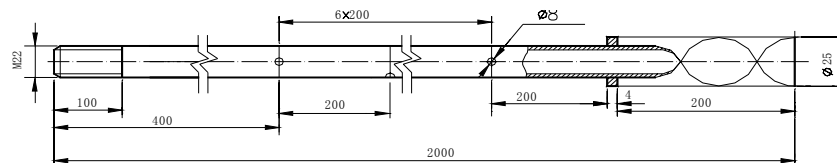


Figure 3 Grouting bolt configuration

After grouting for the whole sump transect and hanging the wire net, shotcreting were carried out again to close off the surrounding rock. The shotcreting thickness was about 50 mm. The total thickness of shotcreting layer added up to 200 mm.

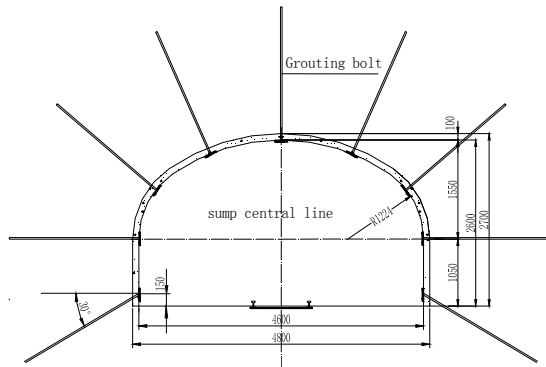


Figure 4 Bolting-grouting Structure

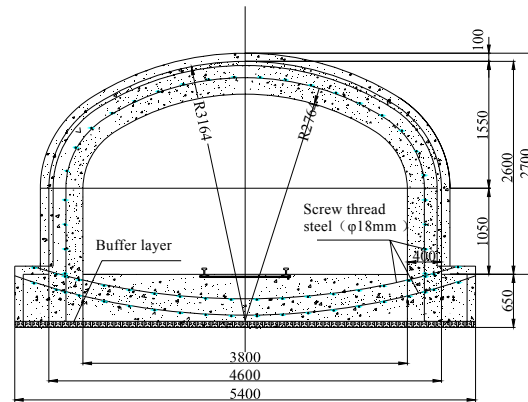


Figure 5 Full-face arch walling

4.2 Full-face Arch Walling

(1) Digging down and reverse arch walling in floor strata.

After grouting in roof strata and sidewalls, scooping up the floor heave and digging down into floor strata at a depth of 750 mm, excavating out from sidewalls for a thickness of 400 mm, as shown in figure 5. The hollowing part of sidewalls was temporarily supported by shotcreting. The frame construction of reverse arch structure with a buffer layer and concrete pouring were followed on the floor.

A) Laying out of buffer layer. After cleaning floating gauge and draining off the deposited water, laying out of buffer layers can be processed. Buffer layer is made of 75 mm thick polyethylene foam. The buffer layer setting required the tight connection with the floor surface.

B) Binding of steel rebars. The foundation steel was designed for double layers. The steel space between two layers was 400 mm. The lower layer of steel was 100 mm away from the buffer layer. Screw thread steel ($\phi 18\text{mm}$) was adopted and arranged along the longitudinal direction. The steel rebars were prepared in an arc shape, consistent with the radian of gross floor. A distance of 600 mm at two ends of steel rebars was designedly left for lap connection. Screw thread steel ($\phi 8\text{mm}$) was chosen for the lapping steel for the connection purpose of every two basic steel rebars ($\phi 18\text{mm}$) at a distance of 600 mm. The lapping steel rebar was curved at two ends and placed in the longitudinal direction. A 22# wire was selected for the colligation of steel rebars at lapping points. The distribution of steel rebar was 300 mm (column) \times 300 mm (row).

C) Concrete pouring. After binding of steel rebars, concrete pouring was implemented for a thick layer of 650 mm, as seen in figure 5. For the high density and close packing, concrete vibrating should be performed one time every 300–400 mm when concrete pouring. It is appropriate to vibrate until cement slurry came out from the surface.

It should be noted that a kind of long distance pumping concrete technology was used in the arch walling support for the huge workload of concrete pouring because the highly fractured sump is 980 m long. This kind of technology have many merits compared with common manual arch walling, for example, the high compactness, high contact quality for two segments of concrete pouring and high impermeability, operation agility and high speed construction, etc. Good technical effects and economic benefits were obtained.

(2) Arch walling in shoulder and roof parts and sidewalls.

A) Binding of steel rebars. The single-layer reinforced steel rebar ($\phi 18\text{mm}$) was selected and reserved a length of 600mm at two ends for lapping. Screw thread steel ($\phi 8\text{mm}$) was chosen for the lapping steel for the connection purpose of every two basic steel rebars ($\phi 18\text{mm}$) at a distance of 600 mm. The lapping steel rebar was curved at two ends and placed in the longitudinal direction. A 22# wire was selected for the colligation of steel rebars at lapping points. The distribution of steel rebar was 300 mm (column) \times 300 mm (row).

B) Moulding board installation. Stable standing columns in square timber (200mm) were fixed in the floor strata. Every two standing columns at an interval of 1.5m were fastened by square timber (100mm) on its bottom and sides. Arched girders were placed on the tops of standing columns and moulding boards were tied on the girders. The moulding boards are made of 10# channel steel 6.0 m long.

C) Concrete pouring. After finishing the installation of moulding board, concrete pouring for a thick layer of 400 mm was implemented, as seen in figure 5. Concrete pouring should be vibrated for the purpose of high density and close packing. Construction height of two walls' pouring exceeded 100 mm from arch baseline. Arch pouring should be performed symmetrically to prevent moulding boards from deviating towards one side.

The pouring concrete strength is 30 MPa. Rubble particle in reasonable gradation is about 10~20mm in diameter. Medium-coarse sand in reasonable gradation and Po. 42.5R type common Portland cement of high early strength were selected. MF-1 type water pumping agent with water reducing function was appended and its dosage accounts for 2.5% of cement weight.

Concrete mixture ratio of cement: sand: stone: water = 1: 2.01: 3.89: 0.51. The corresponding material weight ratio of every cubic metre concrete was 324 kg: 651.24 kg: 1260.36 kg: 165.24 kg. Concrete slump was 80~160mm.

The good stability of sump after full-face reinforced concrete arch walling is shown in figure 6.



Figure 6 The stability of sump after full-face arch walling

5 Conclusions

This study presents a floor heave in a sump of a coal mine located in a complicated geological structure zone and its floor strata with great dilatibility when encountered by water. A new approach of full-face reinforced concrete arch walling with a long distance pumping concrete technology was adopted for the sump support. This arch walling method can cover the shortcomings of common manual arch walling and good technical effects and economic benefits were obtained. The results show that it is very difficult to keep the stability of sump in soft surrounding rock with great expansivity only through anchoring-netting-shotcreting and pre-stressed cabling support. It can improve the loading capability and integrity of support structure effectively through grouting for large broken zone of surrounding rock. The support structure formed by full-face reinforced concrete arch walling can control heavy floor heave of roadways effectively.

Acknowledgements

This study was supported by NSFC (Nos: 50804046, 50774082 and 50490273) and Scientific Research Fund for youths of CUMT (No: 0B080240).

References

1. Jiang, Y.D., Zhao, Y.X., Liu, W.G., Li, Q. Research on Floor Heave of Roadway in Deep Mining. Chinese Journal of Rock Mechanics and Engineering, 2004, 23(14). 2396-2401.
2. Oldengott, M. Prevention and Treatment of Roadway Floor Heave. Translated by Wang, M.S., China Coal Industry Press, 1985.
3. Цимбаревич, П.М. Mine Support. China Coal Industry Press, 1953.
4. Haramy, K. Floor Heave Analysis in a Deep Coal Mine. Proc. of the 27th U.S. Symposium on Rock Mechanics, Balkema AA, 1986, 520-525.
5. Kang, H.P. An Analysis on the Mechanism of Roadway Floor Heave. Chinese Journal of Rock Mechanics and Engineering, 1991, 10(4). 362-373.
6. Kang, H.P. Mechanism and Treatment of Soft Roadway Floor Heave. China Coal Industry Press, 1993.
7. Kang, H.P. Swelling Rock and Opening Floor Heave. Journal of Fuxin Mining Institute (Natural Science), 1994, 13(2). 44-48.
8. He, Y.N., He, Y.N. Analyses of the Measured Results on the Floor Heave in Maoming Mine. Chinese Journal of Geotechnical Engineering, 1994, 16(4). 40-46.
9. Hou, C.J. and Zhang, S.D. Control of Gate Floor Lifts by New Type Ring Supports. Journal of China Institute of Mining and Technology, 1985, 3. 49-57.
10. Zhou, Y.J. Treatment of Floor Heaves in Roadways by Reverse Rching. Ground Pressure and Strata Control, 1998, 3. 58-60.
11. Li, X.H., Wang, W.J. and Hou, C.J. Controlling Floor Heave with Strengthening Roof in Gateway by Numerical Analysis. 2003, 32(4). 436-439.
12. Wang, W.J. and Feng, T. Study on Mechanism of Reinforcing Sides to Control Floor Heave of Extraction Opening. Chinese Journal of Rock Mechanics and Engineering, 2005, 24(5). 808-811.
13. Hou, C.J., He, Y.N. and Li, X., et al. Reinforcing Sidewalls and Corners of Gateway to Control Floor Heave. Journal of China Coal Society, 1995, 20(3). 229-234.
14. Li, Y.S. Control Technique and New Support Method of Floor Heave in West Germany. Coal Science and Technology, 1982, 6. 52-55.
15. He, M.C., Xie, H.P., Peng, S.P. and Jiang, Y.D. Study on Rock Mechanics in Deep Mining Engineering. Chinese Journal of Rock Mechanics and Engineering, 2005, 24(16). 2803-2813.
16. Zhang, H.Q., He, Y.N., Han, L.J., et al. Dynamic Superposition "Tri-anchor" Support Technology at Tunnel Junction under Complex Rock Strata. in Cai, M.F. and Wang, J.A. eds. Boundaries of Rock Mechanics, Taylor & Francis Group, 2008. 743-747.

PREDICTION OF ROCKBURST IN THE NIBA MOUNTAIN EXPRESS HIGHWAY TUNNEL

LIN DENG, RONG-GUI DENG and BAO-JUN YUAN

Department of Geological Engineering, Southwest Jiaotong University

Chengdu, 610031, P.R China

JIANG SHAO

Highway Investigation and Design Institute of the Traffic Department of Sichuan Province

Chengdu, 610031, P.R China

Niba mountain tunnel in Yaan-Lugu highway, with a depth about 1650m and a length about 10km, will be the deepest and longest tunnel in Sichuan Province after construction. Rockburst is serious problem during the tunnel excavation. Two primary factors lead to rockburst: the internal cause is the characteristics of rock, and external factor is the ambient stress field. The rockmass geo-stress is determined according to hypocenter mechanism, hydraulic fracturing method, regressed by 3D finite element method (FEM), Kaiser Effect of the rock. The characteristics of rock structure is educed by field geological survey, strength of rock mass is studied in laboratory. The probability and intensity of rockburst along tunnel were predicted according to the comprehensive analyse based on the geology, energy theory and strength theory. The results indicate that moderate-intensity rockburst will occur in the tunnel, but high-intensity rockburst seldom occurs.

1 Introduction

The deep-seated and super long tunnel is a large-scale project with a large duration of construction and investment of money. Also, construction is difficult due to the geology problems such as rockburst and high ground stress. Precisely predicting rockburst is of the key problem directly affecting the success or failure of the investment and construction.

The Niba mountain tunnel on the Yaan-Lugu highway is part of the Beijing –Kunmin highway, with a depth of about 1650m and a length of about 10km, making it the deepest and longest tunnel in Sichuan Province. The hazard of rockburst may be encountered in the tunnel and it is extremely necessary to study the rockburst intensity.

2 Engineering geologic Condition in Tunnel Area

The tunnel is located in the Niba Mountain on the border of the Yingjing and Hanyuan county in Ya'an Sichuan, near the "Y" tectonic belt formed by the Xianshuihe, Longmen mountain and An'ninghe fault zones. Due to the multi-period tectonic movement, the geologic structure is very complex; fault and plains type fold is quite common. Geological structural settings in tunnel area are shown in Fig 1.

The settings are: the Emei subzone of the upper Yangtze Region, connected to the Kangding subzone in the west, connected to the Chengdu subzone in the east, connected to the Jiudingshan subzone in the north. Lithology outcropped in tunnel area is simple. The rock surrounding the tunnel consists of primarily rhyolite with andesite and dolostone secondarily in the simian system.

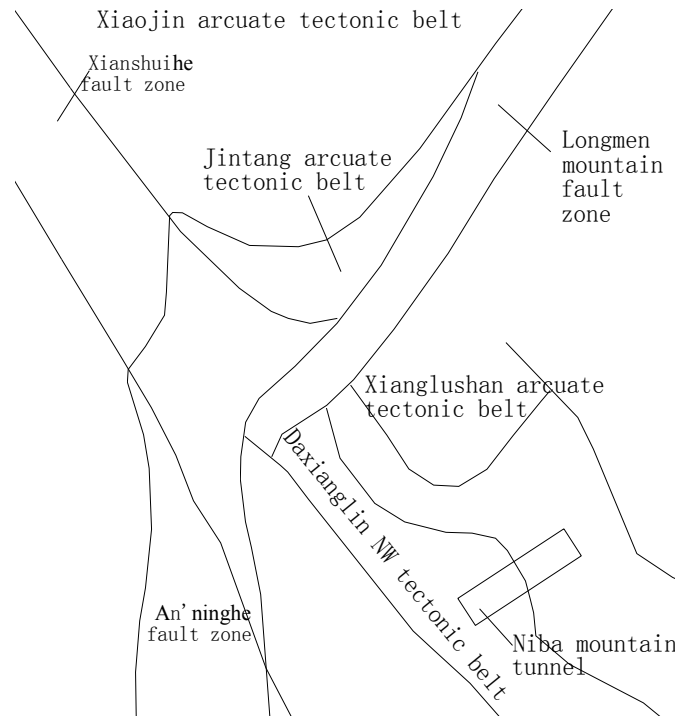


Fig 1 Geological structural settings in tunnel area

3 Charcter of the Geostress Field of Tunnel

The rockmass geostress is determined according to hypocenter mechanism, hydraulic fracturing method, regressed by 3D finite element method (FEM), Kaiser effect of the rock. Charcter of the geostress field shown as follows [1]:

- (1) The direction of max principal stress in tunnel area is $N55^{\circ}\sim 65^{\circ}W$, but the axis of the tunnel is $N47^{\circ}E$. It show that principal stress strongly influence the stability of surrounding rocks.
- (2) Geostress increases vertically with depth, similar to linear relationship
- (3) Ground stress consists of horizontal tectonic principal stress primarily and self-weight stress secondly of the tunnel entrance, in the exit pay equal attention to tunnel.
- (4) Value of the tectonic max horizontal principal stress is about 50MPa near the buried depth of tunnel, min horizontal principal stress is about 21MPa, vertical stress is about 45MPa.

4 Predictive of Rockburst in the Tunnel

4.1 Geological comprehensive analysis

According to characters of rockburst in engineering practice and the rockburst mechanism, essential condition of rockburst is the character of principal stress field and surrounding rock, other factors affecting rockburst is microscopic structures and features certain change, ground water, ground temperature, tunnel boundary and technology for construction. Based on the environmental geology condition, author comprehensive analysis the characters of rockburst.

4.1.1 Conditions of the Geostress

Based on the previous analysis, tunnel produced the preconditions for high ground stress. The most part of the depth of burial over 1000m, gravity stress is high. Tunnel is in high stress condition, as is shown in two high-drilled rock core, it is split as pie. Principal stress is about 50MPa near the buried depth of tunnel, according to test result. The length of tunnel is about 8km, which the ground stress beyond 20MPa, and be about 5.15km beyond 30MPa. Tunnel produced the preconditions of stress field for rockburst.

4.1.2 Lithologic Character

Tunnel surrounding rock is rhyolite and andesite mostly, the other is the secondary rock by the tectonic setting. The autochthonous rock is lava, it is hard and brittle. The character of the deformation fracture of the rock is shown in following Fig 2. Deformation curve of stress-strain is nonsteady mostly, the curve is quite irregular following initiated breakage. It is indicated that rock will gusty burst if loaded continue after yield. Rockburst will come into being dead easy during the excavation.

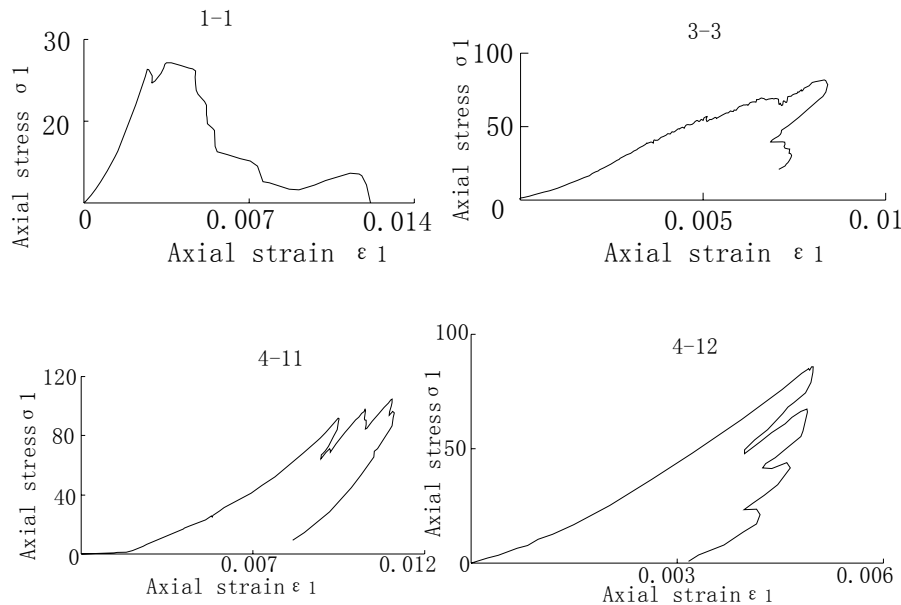


Fig 2 Typical complete stress-strain curves in uniaxial compression test

4.1.3 Geological Comprehensive Condition

There is no high ground temperature by means of the field investigation. It is make no difference to rockburst.

Plenty fracture water will weaken rockburst, but the hydrophilicity of rhyolite and andesite is poor. There is no rockburst near the zone of faulting, but there is easy to generate stress concentration near the zone of hard and soft contact, it is probably occur rockburst [2]. From the geological condition, the possibility for rockburst is great. Rockburst intensity require further study. Many method is used to forecast the intensity, Outline these theory, there is three process-driven methodologies. one is theory of strength, other is energy theory, and the other is rigidity theory. Theory of strength and energy theory are adopted mostly in practical work.

4.2 Analysis by Energy Theory

Energy theory is used to predict the rockburst intensity based on the relationship between the damage characteristics of surrounding rocks and the different energy change in the process of deformation. There are three main approaches: elastic strain energy index; energy impact index; brittleness coefficient[3,4,5].

4.2.1 Elastic Strain Energy Index

Elastic strain energy index(Wet) is being raised by Kidybinshi [3]. It is defined as the ratio of the elastic strain energy accumulate to dissipated, as shown in format (1). Determination method is shown as follows: Use uniaxial compressive strength test, when the load reach to per 70~80 of the peak strength, then unloading. computation module is shown in Fig 3.

$$Wet = \frac{\phi_{sp}}{\phi_{st}} \quad (1)$$

In the format: ϕ_{sp} is the accumulated elastic strain energy, the area of AOC namely, ϕ_{st} is the dissipated elastic strain energy, the area of AOB namely as shown in Fig 3. The smaller the elastic strain energy index, the less the elastic strain energy accumulate, the less the energy released during the late stages of instability disruptive, the lower the intensity. According to many engineering practice evaluation criterion used as following [3]: $Wet \geq 5.0$, serious rockburst; $Wet = 2.0 \sim 4.9$, feeble to moderate rockburst. The evaluation results are shown as Table 1.

4.2.2 Energy Impact Index

Energy impact index (K_E) is defined as the ratio of the energy accumulates during loading to the energy dissipated during damage, as shown in format (2). According to engineering practice, there will be rockburst if $K_E > 1$. Computation module is shown in Fig 4. The evaluation results shown as Table 1

$$K_E = \frac{F_1}{F_2} \quad (2)$$

In the format: F_1 is the accumulated energy, the area of OAC namely, F_2 is the energy dissipated, the area of ACED namely, as shown in Fig 4.

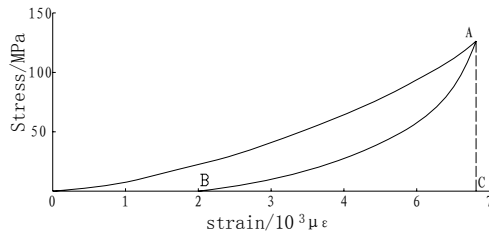


Fig 3 Typical complete stress-strain curves in uniaxial unloading test

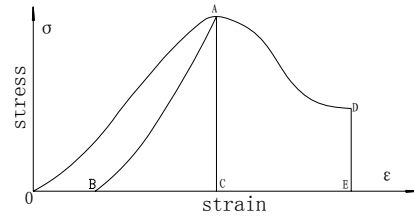


Fig 4 Complete stress-strain curves

4.2.3 Brittleness Coefficient

Zhang and Li [6] and Tan [7] believe that brittleness of rock has much to do with rockburst after detailed analyses by scanning electron microscopy. The stronger the brittleness, the higher the risk. Tang [8] pointed out that the ratio of uniaxial compressive strength to uniaxial tensile strength can show the accumulation performance of elastic deformation energy, the ratio of total strain before peak strength to total strain after peak strength can show the relation between energy accumulation and energy dissipation. The brittleness coefficient(B) is defined as the product of the two ratios, as shown in format (3). According to many engineering practice evaluation criterion used as following[8,9,10]: $B \geq 5$, serious rockburst; $3 < B < 5$, feeble rockburst; $B \leq 3$, none. The evaluation results are shown as Table 1.

$$B = \alpha \frac{\sigma_c \varepsilon_f}{\sigma_t \varepsilon_b} \quad (3)$$

In the format: α is modified coefficient(choose 0.1), σ_c is the uniaxial compressive strength; σ_t is the uniaxial tensile strength; ε_f is strain before peak strength; ε_b is total strain after peak strength.

Table 1 Predicting outcomes by energy theory

Number	Lithology	Bury/m	Elastic strain energy index		Energy impact index		Brittleness coefficient	
			Wet	Rockburst intensity	K_E	Rockburst intensity	B	Rockburst intensity
ZK4-6	rhyolite	425	3.6	moderate	18.2	serious	44	serious
ZK4-7	rhyolite	425	2.0	feeble	/	/	/	/
ZK3-1	rhyolite	100	/	/	21.9	serious	3.5	feeble
ZK3-2	rhyolite	100	/	/	4.4	serious	3.6	feeble
ZK4-1	rhyolite	345	/	/	8.4	serious	3.1	feeble
ZK4-23	rhyolite	1100	/	/	14.1	serious	59	serious
ZK5-3	rhyolite	700	/	/	20.7	serious	55	serious

There will be serious rockburst in this tunnel, according to the internal causes.

4.3 Analysis by Theory of Strength

Theory of strength include two areas: one is the actual stress, the other is the strength. There are two ways to predict rockburst. one is strength-stress ratio($W_b = \sigma_c / \sigma_1$). The ratio of uniaxial compressive strength(σ_c) to the max principal stress(σ_1) namely, the other is stress-strength ratio($W_b = \sigma_0 / R_b$). the ratio of the max tangential stress(σ_0) to the saturated uniaxial compressive strength(R_b). According to many engineering practice evaluation criterion used as following[11,12,13]: $W_b \geq 0.7$, serious rockburst; $0.5 \leq W_b < 0.7$, moderate rockburst; $0.3 \leq W_b < 0.5$, feeble rockburst; $W_b < 0.3$, none. The evaluation results are shown as Table 2.

Table 2 Predicting outcomes by theory of strength

Range	max tangential stress σ_0 /MPa	Saturated uniaxial compressive strength R_b /MPa	W_b	Rockburst intensity
K55+720~56+160	52	60	0.87	serious
K56+220~56+778	60	60	1	serious
K56+858~57+330	72	60	1.2	serious
K57+960~58+480	76	60	1.26	serious
K58+580~58+945	70	60	1.16	serious
K59+085~59+450	74	102.49	0.72	moderate~feeble
K59+630~60+757	72	102.49	0.70	moderate~feeble
K60+937~61+405	58	102.49	0.56	feeble~moderate
K61+787~62+570	43	102.49	0.42	feeble

There have differences between the predicting outcomes by theory of strength and practical engineering. Because theory of strength not be included rock mass structure, the other reason is the tunnel in triaxial position but the strength is uniaxial. Combining the energy theory and theory of strength, and comprehensive analysis, the results shown as Table 3

Table 3 Predicting outcomes by comprehensive analysis

Range	Bury/m	Tangential	Lithology	Energy theory	Theory of strength	Comprehensive
K55+100~55+700	360~700	36~46	Rhyolite, Kakirite	none ~serious	none~ feeble	none ~ feeble
K55+700~56+100	700~800	46~55	Rhyolite, Andesite	none ~serious	feeble	feeble ~ moderate
K56+100~56+300	800~910	55~60	Fault rock Kakirite	none	feeble	none ~ feeble
K56+300~56+720	910~1210	60~79	Andesite	moderate	feeble	feeble ~ moderate
K56+720~56+900	1210~1350	79~84	Fault rock, Kakirite	none	none~ feeble	none~ feeble
K56+900~57+260	1350~1470	84~89	Andesite	moderate	feeble	feeble ~ moderate
K57+260~58+000	1280~1490	73~96	Fault rock, Kakirite	none ~ feeble	none ~ eeble	none ~ feeble
K58+000~58+420	1410~1570	84~90	Andesite	moderate	moderate	moderate
K58+420~58+620	1570~1650	91~94	Fault rock, Kakirite	none ~ feeble	none	none ~ feeble
K58+620~59+000	1540~1650	88~93	Andesite	moderate	moderate	moderate
K59+000~59+180	1430~1540	82~85	Fault rock, Kakirite	none ~ feeble	feeble	none ~ feeble
K59+180~59+460	1250~1430	71~78	Rhyolite	serious	moderate ~ serious	moderate ~ serious
K59+460~59+660	1210~1250	68~70	Fault rock,	none ~ feeble	none ~ feeble	none ~ feeble

K59+660~60+740	1110~1390	63~78	Rhyolite	serious	serious	moderate ~ serious
K60+740~60+940	1110~1170	63~64	Fault rock,Kakirite	none	none ~ feeble	none ~ feeble
K60+940~61+360	850~1130	48~60	Rhyolite	moderate	moderate ~ serious	feeble ~ moderate
K61+360~62+560	370~850	32~60	Kakirite, Rhyolite	none ~serious	none ~ moderate	none ~ feeble

5 Discussions

There is a significant threat of rockburst in this tunnel. The rock strength, rockmass structure, geostress, and form of construction are influences on rockburst. The larger the area of disturbance, the larger the probability and intensity of rockburst will be. The use of smooth blasting and pre-splitting blasting reduces the rockburst intensity. Tunneling near the Longmen mountain fault zones the value of the geostress will be reduced because of the “5.12” earthquake. The influence of the earthquake on rockburst needs to be researched further.

Acknowledgements

My deepest gratitude to Communication Administration Subject (2006318000104) and Southwest Jiaotong University Doctor Creation funds in 2008 for their financial support.

References

1. Highway Investigation and Design Institute of the Traffic Department of Sichuan Province, Southwest Jiaotong University. The Forecasting of Surrounding Rockburst and Fault Water Gush or Ejection for the Niba Mountain Tunnel in Daxingling.2009.
2. Wang, X.B., Hai, L., Song, W.Y.,etc. Fault Rockburst is Snap-back due to Shear Strain Localization. Chinese Journal of Rock Mechanics and Engineering, 2004, 23 (18). 3102-3105.
3. Kidybinski, A. Bursting Liability Indices of Coal. Int.J.Rock Mech.Min.Sci. Geomech. Abstr, 1981, 18 (2). 295-304.
4. Xu. Z.M.and Huang, R.Q. Judgement and Preventing Ggeological Disaster of Long Tunnels with Great Buried. Southwest Jiaotong University Press, 2000.
5. Singh, S.P. Technical Note: Burst Energy Release Endex. Rock Mechanics and Rock Engineering, 1988, 21 (2).149-155.
6. Zhang, M.Y., Yuan, J.X., Li, T.J., etc Mechanism of Deformation and Failure for Rock in Uniaxial Compression Test. Chinese Journal of Rock Mechanics and Engineering, 1998, 17 (1). 1-8
7. Tan, Y.A. Study on Formation Mechanism of Rockburst. Hydrogeology and Engineering Geology, 1989, (1). 34-38.
8. Tang, L.Z. and Wang, W.X. New Rockburst Proneness Index. Chinese Journal of Rock Mechanics and Engineering, 2002, 21 (6).874-878.
9. Kwasniewski, M. and Wang, J.A. 3-D Numerical Modeling and Study of Mine Tremors Associated with coal Mining in Vicinity of Major Faults.Pupls.Inst.Geophys.1999,M22 (310). 351-364.
10. Cai, M.F., Wang, J.A. and Wang, S.H. Analysis on Energy Distribution and Prediction of Rockburst during Deep Mining Excavation in LingLong Gold Mine. Chinese Journal of Rock Mechanics and Engineering, 2001,20 (1):38-42.

- 11 Liang, Z.Y., Liu, H.C., Shi, Y.C.,etc. Probability Model for Rockburst Prediction. Chinese Journal of Rock Mechanics and Engineering, 2004, 23 (18). 3098~3101.
- 12 Russnes, B.F. Analyses of Rockburst in Tunnels in Valley Sides. Norwegian Inst.of Technology,1994
- 13 Xu, L.S. and Wang, L.S. Study on the Laws of Rockburst and Its Forecasting in the Tunnel of Erlang Mountain Road. Chinese Journal of Geotechnical Engineering, 1999, 21 (5). 569-572

SCALE EFFECT OF JOINTED ROCKS IN FAILURE

ZHENG-ZHAO LIANG, LIAN-CHONG LI, CHUN-AN TANG and HAO-YU CHEN

School of Civil and Hydraulic Engineering, Dalian University of Technology

Dalian, People's Republic of China, 116024

The problem of scale effect of jointed rock masses is an important issue in civil and mining engineering. The scale/size effect of the rock mass specimens containing ideally distributed joints subjected to uniaxial compression is studied numerically by using a numerical code. Unlike other numerical models, complete failure process can be obtained, and also the heterogeneous nature of material in mesoscopic scale can be taken into consideration. By varying the dip angle of the joints, the numerical rock mass specimens show a strong anisotropic feature. Numerical results confirm that scale effect or size effect for jointed rock masses maybe originates from the joint distribution, the strength of joints and rocks. The strength of the jointed rock masses decreases with the increasing of the scale/size, which can be predicted by a negative exponential formula. The failure mode of the jointed rock masses can be classified into tensile fracture perpendicular to the joints or shear fracture parallel to the joints. The results will give help to understand the mechanical behaviour of jointed rock masses.

1 Introduction

Jointed rock masses are often encountered during excavation in civil engineering and mining engineering. The design of high rock slopes, typical of open pits, and tunnel excavation often requires the evaluation of the rock mass strength containing joints. Many failures of underground openings during excavation are reported closely relate to joints. Joints usually occur in sets which are more or less parallel and regularly spaced. And also there are usually several sets in very different directions so that the rock mass is broken up into a blocky structure [1].

The importance of scale effect for the design of rock masses as well as other heterogeneous materials is a well debated issue. The combination of the Weibull statistical theory of random strength and energetic theory is one of the promising approaches to explain the phenomena of scale effect. Scale effect rises originally from microstructures of brittle materials. Many explanations have been put forward to predict the strength and fracture behavior of brittle materials, such as rock, concrete and ceramics et al. Based on experiments on fatigue fracture of metals and heuristic arguments, Weibull [2] introduced his probability distribution into the theory of fatigue failure of metals and ceramics and obtained the first power law for the statistical scale effect. For about half of a century, almost all experimentally observed scale effects in all materials are attributed to Weibull theory.

If it is only attributed to the heterogeneous nature of the material, Weibull theory seems provides a satisfactory answer [3]. However, serious discrepancies appear from experiments conducted on quasi-brittle materials [4], which lack plasticity and are characterized by gradual softening in a fracture process zone that cannot be negligible compared to structure size. The deterministic energetic scale effect is obtained for not too large structure sizes, and the Weibull statistical scale effect is obtained as the asymptotic limit for very large structures [3]. Scale effect of jointed rocks can be studies by analytical analysis, experimental study and empirical investigation. Jaeger proposed an empirical formula to predict the rock mass strength. Numerical study has been come to be a useful tool to better understand the failure process as well as scale effect of brittle materials nowadays. A direct approach to studying the scale effect phenomenon in a heterogeneous material, such as concrete, is based on the square lattice network. Bazant et al. [3,4], and Schlangen and van Mier et al [5] modified the Herrmann approach in several ways in order to apply it to concrete.

In this paper, progressive failure process of the heterogeneous jointed rock specimen is simulated by a two dimensional numerical micromechanics model with a view to study the scale effect in strength. The rock mass specimens containing pre-existing layered joints are represented to undertake uniaxial compressive loading tests, and the specimens have the similar shape but different sizes. The size effect on peak strength, deformation and fracture patterns is discussed.

2 Numerical Modelling

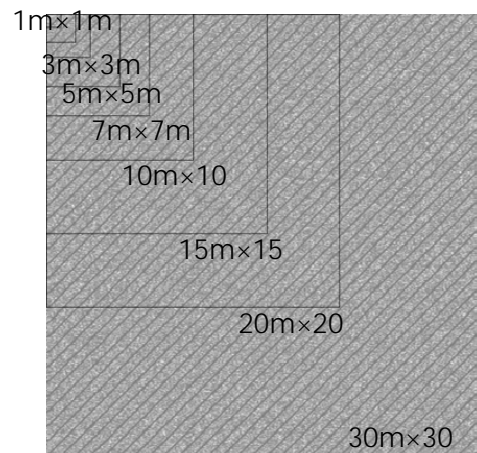


Figure 1 Sketch of jointed rock specimens with different scales

In this study, three kinds of rock masses are considered. For one kind of rock masses, layered joints with the dip angle 30° , 45° and 60° are arranged, and the scales of the specimens are $1\text{m} \times 1\text{m}$, $2\text{m} \times 2\text{m}$, $3\text{m} \times 3\text{m}$, $5\text{m} \times 5\text{m}$, $7\text{m} \times 7\text{m}$, $10\text{m} \times 10\text{m}$, $15\text{m} \times 15\text{m}$, $20\text{m} \times 20\text{m}$ and $30\text{m} \times 30\text{m}$. In order to investigate the anisotropic mechanical behaviour of jointed rocks, the specimens of $5\text{m} \times 5\text{m}$ and $10\text{m} \times 10\text{m}$ are prepared by varying the joint dip angle from 0° , 15° , 75° , to 90° . There are totally 32 cases for this kind of rock mass containing layered joints. Only uniaxial compressive loading is applied on the top of the specimens when the bottom of them is fixed in vertical direction. Compressive loading is implemented by using a constant rate of displacement increment. In the numerical model, both the rocks and the joints are considered to be heterogeneous. The heterogeneity index for

the rocks is assumed to be 2.0, and the index for joints, which are much more heterogeneous than rocks, is assumed to be 1.5. The parameters used in the simulation are listed in Table 2. The jointed rock specimen containing one set of joints with the dip angle 45 is shown in Figure 1. The joints have the heterogeneity index 1.5, which are more heterogeneous than the rocks. Due to the small elastic modulus, the joint elements can have a large deformation relatively along the joints surface even though they can not slide far way. However, the failed joint elements will get a high stiffness if they are compressed to reach the maximal strain coefficient. The high stiffness will prevent the imbedding problem.

3 Numerical Simulation and Results

In each loading step, 0.0002 times of the specimen height is applied. When there is any failure in the elements in the current step, the strength and elastic modulus of the failed elements will be reduced to a certain value determined by the residual strength coefficient, and then the stress will be recalculated by FEM program to obtain the redistributed stress field. A combined failure criterion, Mohr-Coulomb shear failure criterion and maximal tensile strength failure criterion, is utilized to justify the failure of the elements in the model, so there will be two failure mode for each elements. If there is no new failure, it will be continued to apply the increment in next step.

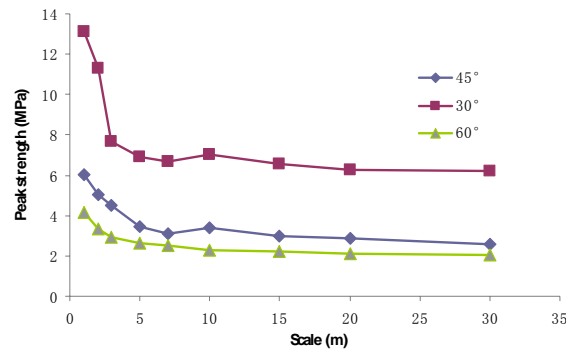


Figure 2 Relation between the peak strength and the specimen scale of the specimens containing layered joints with different dip angle.

3.1 Scale Effect

The peak strength of the specimens tested is obtained as shown in Figure 2. As found by other investigators, the peak strength under uniaxial compressive loading decreases with the increasing of jointed specimen scale. When the scale grows larger and reaches to a critical value, the peak strength tends to be a constant. The critical scale can be regarded as REV (Representative Elementary Volume). When the scale of the specimens increases to 20m, the peak strength will never decrease any more. The mechanical parameters of the specimen with this critical scale are much important for the evaluation of the total rock engineering. The relation of the peak strength and specimen scale can be well fitted by a negative exponential function. The function can be described as $y = a + be^{-cx}$, where y represents the peak strength and x is the specimen scale. Parameter a , b and c are all constant. When the scale tends to be zero, the peak strength will be an unexpected large value, and if it tends to be large enough, the peak strength will be a constant value, which represents the critical value REV. Many authors have given this function to describe the size rule of brittle materials [1-3, 5].

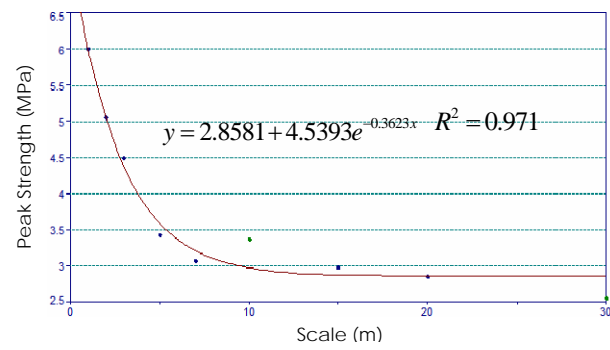


Figure 3 Scale effect of rock masses containing joints of 45°

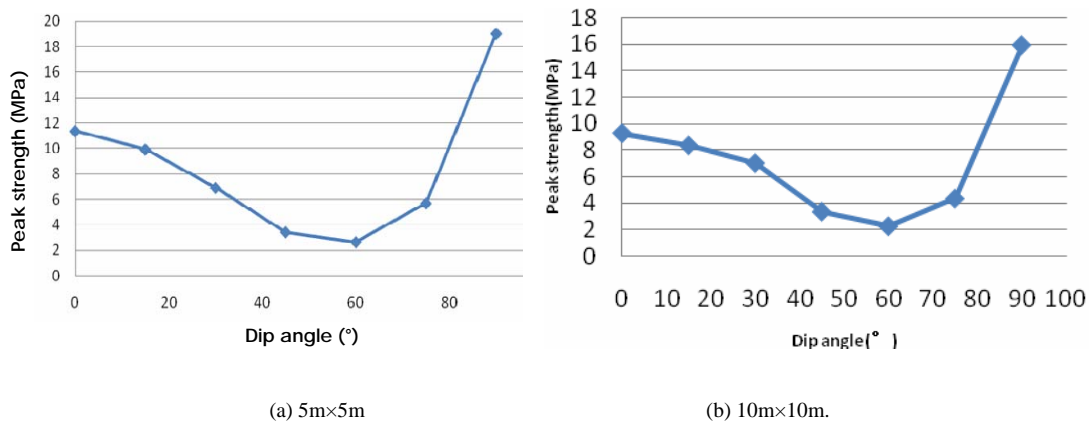
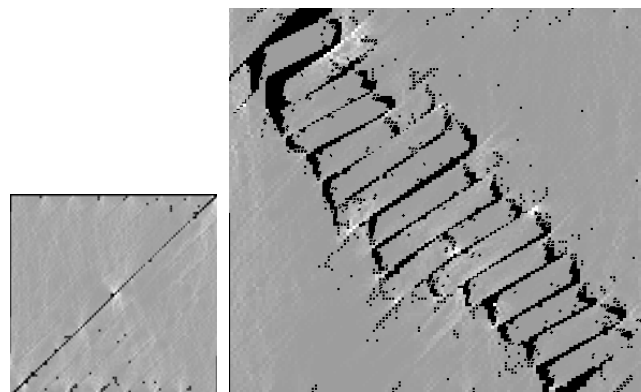


Figure 4 Plots of peak strength vs. the dip angle.



(a) Shear failure (5m×5m, 45°) (b) Tensile failure (10m×10m, 45°)

Figure 5 Different fracture modes for different scale.

3.2 Anisotropic Feature of Peak Strength

If we keep the scale unchanged and vary the dip angle, we can get the relation between peak strength and the dip angle. Figure 4 shows the simulated results of the specimens with the scale of $5\text{m} \times 5\text{m}$ and $10\text{m} \times 10\text{m}$. Both curves show a V shape. The peak strength decreases as dip angle increases to 60° . However, when the angle increases further, the peak strength increases. The specimens with the joints of 60° give the minimal peak strength, while the specimens with the joints of 90° have the maximal peak strength.

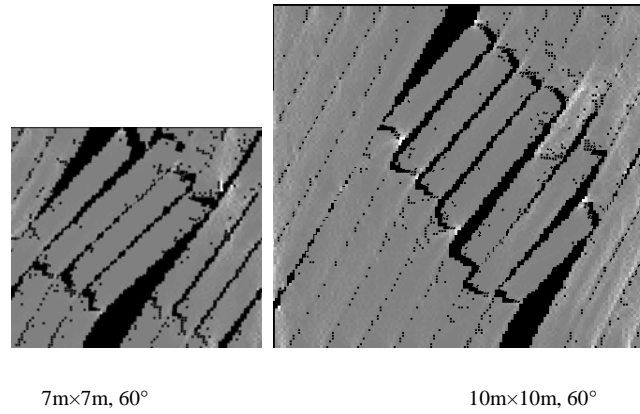


Figure 6 Fracture patterns of the rock mass specimens containing layered joints with dip angle 60°

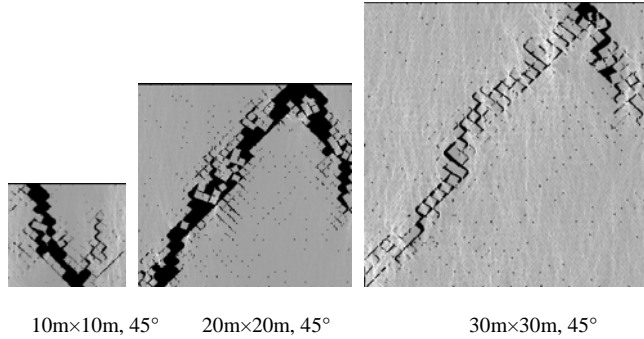


Figure 8. Fracture patterns of the rock mass specimens containing two sets of joints with dip angle 45°

3.3 Fracture Patterns

It is very interesting to find that there are two different fracture patterns for the jointed specimens with dip angle 45° . When the scale is less than 10m , the fracture of the specimens is dominated by shear slide along a single joint surface. The strength of the specimens depends on the strength of the joints (Figure 5(a)). When the scale is larger than or equal to 10m , shear fractures along joints are observed at the beginning loading stage, while the vital fractures are found perpendicular to the surfaces of the joints. The failure shows a tensile fracture mode. In these cases, the coalescence of these tensile fractures leads to the final failure of the jointed rock masses. In this fracture mode, the peak strength will not depend on the shear strength of the joints, as shown in Figure 5(b). When the dip angle changes to be 60° , there exists another fracture mode between tensile fracture mode and shear fracture mode. As shown in Figure 6 for the specimen with joints angle 60° . Both shear fractures and

tensile fractures are observed in the specimen of 7m×7m. It is difficult to determine which fracture dominates the coalescence of the specimen. It is interesting to find that the fracture patterns for the specimens of different sizes containing two sets of perpendicular joints have different fracture pattern from one set of joints.

4 Discussion

Scale effect or size effect for jointed rock masses maybe originates from the joint distribution, the strength of joints and rocks, and the boundary condition. Many researchers considered heterogeneities in rocks and other materials was the key factor of scale effect. The distribution of joints, including joint density, length, width as well as depth in three-dimension, can be regarded as one of the heterogeneities contained in rocks. As shown by the numerical simulation, the strength of jointed rocks is influenced by the strength of rocks and joints. It should be noted that in this study only uniaxial compressive tests are undertaken to investigate the scale effect. It can be predicted that the fitted formulas will be different more or less and the scale effect of jointed rocks under confining pressure will be not so obvious as the results under uniaxial loading. The strength of the jointed rock masses decreases with the increasing of the scale/size, which can be predicted by a negative exponential formula. In our simulation, a power function $y = a + bx^c$ is also optional for the effect. The failure mode of the jointed rock masses can be classified into tensile fracture perpendicular to the joints or shear fracture parallel to the joints. In relatively smaller specimens, rock specimens containing fewer joints have a higher strength, so the peak strength depends on the shear strength of the joints. However, in relatively larger specimens, rock specimens containing more joints, due to the interaction between shear fractures appearing at the beginning loading stage, the coalescence of these shear fractures induced by tensile stress will predominate in the failure. Only idealized joint distribution is considered in this paper. The scale effect of rock masses containing randomly distributed joints implemented by Monte Carlo method will be presented in another paper.

Acknowledgements

This research was supported by National Basic Research Program of China (973 Program, Grant No. 2007BAF09B01 and 2007CB209400) and the National Natural Science Foundation of China (Grant No. 50804006 and 40638040).

References

1. Jaeger, C. Rock Mechanics and Engineering (2nd Edition). Cambridge University Press, 1979.
2. Weibull, W. The Phenomenon of Rupture in Solids. Proc Rswed Inst Engng Res (Ing Akad Handl Sweden). 1939, 153. 1-55.
3. Bazant, Z.P. and Yavari, A. Is the Cause of Size Effect on Structural Strength Fractal or Energetic-Statistical? 2005, Engineering Fracture Mechanics, 72. 1-31.
4. Bazant, Z.P., Tabbara, M.R., Kazemi, M.T. and Pijaudier, C.G. Random Particle Model for Fracture of Aggregate or Fibre Composites. ASCE J Engng Mech 1990, 116. 1686-705.
5. Schlangen, E. and Van, M.J. Experimental and Numerical Analysis of Micromechanisms of Fracture of Cement-Based Composites. Cement Concrete Comp, 1992, 14. 105-18.

STUDY OF STRENGTH AND DEFORMATION OF AIR ENTRAINED CONCRETE UNDER BIAXIAL COMPRESSION AFTER FREEZING AND THAWING CYCLES

FENG ZHANG , SHU-CAI LI ,SHU-CHENG LI ,JING-PENG ZHU and BO ZHANG

*School of Civil and Hydraulic Engineering, Shandong University
Jinan, 250061, P.R. China*

DE-LONG LUO

*Shandong Expressway Group Co., Qingdao High-speed Ltd.
Qingdao,26601, P.R. China*

Properties of air-entrained concrete under compressive loads with constant confined stress after 0, 100, 200, 300 cycles of freeze–thaw were studied. Concrete cubes were tested under biaxial compressive stresses. Four constant confined stresses and four different cycles of freeze–thaw were the main variables. Static compressive strengths were examined. Failure modes of specimens were also described. The experimental results show that the effect of freezing and thawing cycles on plain concrete do not change the failure modes. The formula of the biaxial compressive strength, biaxial tension-compression strength and biaxial tensile strength in principal stress space is proposed. It provides the experimental and theory foundations for strength analysis of air-entrained concrete structures subject to complex loads in cold environment.

1 Introduction

As more and more concrete structures are being built in deeper seas, the demand for durable concrete has increased. Durability [1–3] is a key function for materials which are used in severe environments, and heightened durability of concrete is necessary as it is one of the most demanding engineering materials used by mankind. It has been a significant scientific and technical problem to improve the durability and to prolong the service life of concrete. It is used commonly for bridges, dams and offshore structures. In cold environments, freezing and thawing can be harmful for a porous brittle material such as concrete when it is subjected to lower temperatures. Plain concrete subjected to repeated cycles of freezing and thawing may deteriorate rapidly, and failure of the material may take the form of loss of strength and crumbling.

Hence, the freezing and thawing action can be looked upon as a very complex fatigue crack propagation process. Forster [4] stated that freezing and thawing results differ depending on the original aggregate type. Mulheron and O'Mahony[5] reported that the durability of lean concrete, made using recycled aggregates, appeared to be better than or similar to an equivalent control concrete made with natural gravel when subjected to freezing and thawing conditions. Sun [6] investigated damage and damage resistance of high strength concrete under the action of flexural load and freeze–thaw cycles. Jacobsen [7] investigated the effect of internal cracking on ice formation for high strength concrete. Marzouk and Jiang [8] investigated the tension properties of high strength concrete after freezing and thawing cycles. Soroushian and Nagi [9] reported that the durability of lightweight carbon fiber reinforced cement composites after different cycles of freeze–thaw. The strength and deformation of air entrained concrete subjected to freezing and thawing cycles under biaxial stress conditions need to be investigated, but these types of studies were rare.

2 Experimental procedures

2.1. Materials and mix proportions

The cementations materials used for this investigation are same to that used at Qing-Dao bay bridge.. Coarse aggregates were crushed stone (diameter ranging from 5 mm to 20 mm). The water–cement ratio for the mixture of concrete was 0.34. The air entrain admixture of the specimen was 4.7% after mixing. Table 1 shows the mix proportions by weight of the mixture.

Table 1 The gradients per cubic meter air-entrained concrete and characteristic of concrete(kg/m³)

cement	mineral powder	coal ash	sand	coarse aggregate	water	water reducing agent	anti-corrosion agent	air entrained agent
164	212	94	737	938	155	4.47	6	0.0118

2.2. Samples and testing programs

Concrete specimens were 100 mm cubes and 100 mm×100 mm×400 mm prisms cast in steel molds and compacted by a vibrating table. The cubes were used to measure the strength and strain, and the prisms were used to measure the weight loss subjected to freeze–thaw cycles. All specimens were removed from the molds 48h after casting and then cured in a normal condition of 20±3 °C and 95%RH(relative humidity) for 23 days according to "The test method of long-term and durability on ordinary concrete" BJ82-85[10].

Some specimens were then immersed in water for 4 days before being exposed to the freezing and thawing cycles; these specimens were put to the freeze–thaw apparatus, and were used to measured the strength, strain, weight loss after 100,200,300 freezing and thawing cycles respectively. Freeze-thaw apparatus were shown in Figure 1.The other specimens were cured in a normal condition up to 28 days; these specimens were used to measured the strength and strain prior to the freezing and thawing cycles.



Figure 1 Freezing and throwing apparatus

In this paper, the freeze–thaw cycling test was performed according to GBJ82-85. The temperature of the concrete samples was controlled by a Pt sensor embedded in the center of a concrete. In a single cycle, the temperature of the specimens cools from 8°C to –17 °C and then warms to 8 °C all within approximately 2.5–3 h. The specimen is insufficient to resist freezing–thawing if its RDME drops to 60%, its loss of weight exceeds 5.0% before the 300th cycle.

The freeze–thaw tests were performed in a freeze–thaw apparatus. The mechanical tests were conducted in a tri-axial testing machine (designed by the Geotechnical and Structural Engineering Research Center of Shandong University) that is capable of developing three independent compressive or tensile forces. Three layers of butter and three layers of plastic membrane were used as friction-reducing pads to measure the biaxial

compressive strength. A minimum of three specimens were tested for each batch. The tests were performed under constant confined stress ratios ($\sigma_2=0.0\text{MPa}$, 10.8MPa , 14.4MPa , 18.8MPa), It was shown in Figure 2. The three principal stresses and the three principal strains are expressed as $\sigma_1 \geq \sigma_2 \geq \sigma_3$, $\varepsilon_1 \geq \varepsilon_2 \geq \varepsilon_3$ (tension denoted as positive). In order to get the tension yield stress of concrete, splitting tension test of concrete cubes were executed. It was shown in Figure 3. In the same time ,uniaixal compression test of concrete cubes were completed, as was shown in Figure 4. The loads and deformations in the two principal directions under biaxial compression were monitored and recorded after 0,100,200and 300cycles of freeze–thaw respectively.



Figure 2 Splitting test



Figure 3 Biaxial test of concrete cubes

3 Results and discussions

3.1. Experimental results

The weight loss of plain concrete after different cycles of freezing and thawing are given in Table 2.

Table 2 The weight loss of concrete after different cycle of freezing and thawing

Number of freeze-thaw cycle(N)		0	100	200	300
Weight loss (%)	No.1	0	0.58	1.46	2.39
	No.2	0	0.47	1.34	2.31
	No.3	0	0.55	1.41	2.36

The experimental results of plain concrete under biaxial compression are listed in Table 3. The loading speed was 0.003mm/s in the direction of σ_3 . The compressive stresses σ_2 and σ_3 were calculated by dividing the compressive loads by the area of loading (0.01 m^2).

Table 3 The experimental results of plain concrete under biaxial compression (MPa)

σ_2/Mpa	Freeze-thaw cycles(N)			
	0	100	200	300
10.8	66.546	55.483	26.07	31.436
	59.964	48.044	52.003	37.476
	63.634	51.276	46.945	36.861
	53.9	66.034	41.887	36.471
	64	55.528	54.476	38.359
14.4	60	42.82	38.339	36.446
	65			
	67			
	63			
18.8	74.5	59.214	27.833	39.783

	55.672	54.798	56.719	34.887
	68.71	50.539	53.034	36.879
	53.066			

The experimental results of plain concrete under tension are listed in Table 4.

Table 4 The experimental results of plain concrete under tension (MPa)

Freeze-thaw cycles (N)	Splitting tension load (kN)	Splitting tension stress (Mpa)	Mean value (MPa)
0	84.231	5.366	5.424
	93.387	5.949	
	77.822	4.957	
50	83.773	5.336	4.550
	53.584	3.413	
	76.907	4.899	
	73.702	4.695	
100	66.378	4.228	4.437
	68.896	4.389	
	86.749	5.526	
200	51.450	3.277	4.130
	56.306	3.587	

The experimental results of plain concrete under tension are listed in Table 5.

Table 5 The experimental results of plain concrete under uniaxial compression(MPa)

Freeze-thaw cycles (N)	Specimen number	Uniaxial compression stress (Mpa)
0	1	60.22065
0	2	53.949
0	3	44.427
50	1	43.969
50	2	44.816
50	3	45.274
50	4	54.269
50	5	63.746
100	1	34
100	2	38
100	3	39.9
100	4	40
100	5	52
100	6	62
200	1	36.302
200	2	37.56
300	1	26.734
300	2	29.73
300	3	31.9
300	4	27.329

3.2. Failure modes

The failure modes of the concrete specimens under biaxial compressive loading subjected to the action of freezing and thawing cycles are shown in Figure 4.



Figure 4 Failure model of concrete cubes at biaxial stress

Although the modes of failure under uniaxial and biaxial loading were different, the splitting tensile strain along the unload plane was the cause of failure for both. This finding on the failure modes obtained for plain concrete under biaxial compression conditions is in agreement with a previous study [11]. It was obvious that the influence of freezing and thawing cycles on plain concrete did not change the tensile splitting mode from occurring.

3.3. Failure criterion

The biaxial strength envelopes of concrete presented by Kupfer—Gerstle is divided into three regions, as is biaxial compression, biaxial tension and tension compression regions. The criterion expression is given by

$$(\sigma_1 < 0, \sigma_2 < 0, 0 \leq \alpha = \frac{\sigma_1}{\sigma_2} \leq 1)$$

$$\begin{aligned} \sigma_{2c} &= \frac{1+3.65\alpha}{(1+\alpha)^2} f_c \\ \sigma_{1c} &= \alpha \sigma_{2c} \end{aligned} \quad (1)$$

$$(\sigma_1 > 0, \sigma_2 < 0, \alpha = \frac{\sigma_1}{\sigma_2} \leq 0)$$

$$\begin{aligned} \sigma_{1t} &= \left(1 - 0.8 \frac{\sigma_2}{f_c} \right) f_t \\ \sigma_{1t} &= \alpha \sigma_{2c} \end{aligned} \quad (2)$$

$$(\sigma_1 > 0, \sigma_2 > 0, 1 \leq \alpha = \frac{\sigma_1}{\sigma_2} \leq \infty)$$

$$\sigma_{1t} = \sigma_{2t} = f_t \quad (3)$$

Using regression analysis, the test results of the plain concrete after different numbers of freezing and thawing cycles (with three layers of butter used as a friction reducing pad) led to the formula of the biaxial compressive strength, taking the following form:

$$(\sigma_1 < 0, \sigma_2 < 0, 0 \leq \alpha = \frac{\sigma_1}{\sigma_2} \leq 1)$$

$$\begin{aligned}\sigma_{2c} &= \exp(a_1 N) \frac{1 + 3.65\alpha}{(1 + \alpha)^2} f_c \\ \sigma_{1c} &= \alpha \sigma_{2c}\end{aligned}\quad (4)$$

where: $\alpha = \sigma_1/\sigma_2$ (for $0 < \alpha < 1$), N is the number of freezing and thawing cycles; α is the stress ratio; f_c is the uniaxial compressive strength of plain concrete prior to the freezing and thawing cycles. a_1 is parameter to be calibrated by test results.

Based on test results of table 3 and Levenberg-Marquardt(L-M) optimizing algorithm, a_1 value are get.

The failure criterion of biaxial compression considering stress ratio α ($\alpha = \sigma_1/\sigma_2$) and freeze-thaw cycles N is given by the expression

$$\begin{aligned}(\sigma_1 < 0, \sigma_2 < 0, 0 \leq \alpha = \frac{\sigma_1}{\sigma_2} \leq 1) \\ \sigma_{2c} &= \exp(-0.002N) \frac{1 + 3.165\alpha}{(1 + \alpha)^2} f_c \\ \sigma_{1c} &= \alpha \sigma_{2c}\end{aligned}\quad (5)$$

Figure 5 gives the comparison of proposed model and the test values.

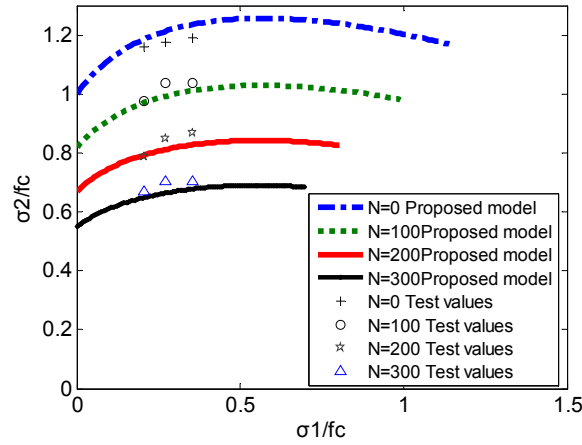


Figure 5 Failure envelopes in principal stress space of concrete under biaxial compression subjected to freezing and thawing cycles

Using regression analysis, the test results of the plain concrete in Table 4 and Table 5 led to the formula of the biaxial tensile strength, taking the following form:

$$\begin{aligned}(\sigma_1 > 0, \sigma_2 > 0, 1 \leq \alpha = \frac{\sigma_1}{\sigma_2} \leq \infty) \\ \sigma_1 = \sigma_2 = 1.369 f_{ts0} (-0.001N + 0.9448) (f_c e^{-0.002N})^{-0.0833}\end{aligned}\quad (6)$$

where: f_{ts0} is the splitting strength of plain concrete prior to the freezing and thawing cycles.

Using regression analysis, the test results of the plain concrete after different numbers of freezing and thawing cycles led to the formula of strength under tension-compression condition, taking the following form:

$$(\sigma_1 > 0, \sigma_2 < 0, \alpha = \frac{\sigma_1}{\sigma_2} \leq 0)$$

$$\sigma_1 = 1.369 f_{ts0} (-0.001N + 0.9448) (f_c e^{-0.002N})^{-0.0833} \left(1 - 0.8 \frac{\sigma_2}{f_c e^{-0.002N}} \right) \quad (7)$$

$$\sigma_1 = \alpha \sigma_2$$

4 Conclusion

Based on the test results, the following conclusions can be drawn:

1. The effect of freezing and thawing cycles on plain concrete did not change the failure modes.
2. The failure criterion of biaxial compression considering stress ratio α ($\alpha = \sigma_1/\sigma_2$) and freeze-thaw cycles N is given by the expression

$$(\sigma_1 < 0, \sigma_2 < 0), 0 \leq \alpha = \frac{\sigma_1}{\sigma_2} \leq 1)$$

$$\sigma_{2c} = \exp(-0.002N) \frac{1 + 3.165\alpha}{(1 + \alpha)^2} f_c$$

$$\sigma_{1c} = \alpha \sigma_{2c}$$

3. The formula of the biaxial tensile strength, taking the following form:

$$(\sigma_1 > 0, \sigma_2 > 0, 1 \leq \alpha = \frac{\sigma_1}{\sigma_2} \leq \infty)$$

$$\sigma_1 = \sigma_2 = 1.369 f_{ts0} (-0.001N + 0.9448) (f_c e^{-0.002N})^{-0.0833}$$

4. The formula of strength under tension-compression condition, taking the following form:

$$(\sigma_1 > 0, \sigma_2 < 0, \alpha = \frac{\sigma_1}{\sigma_2} \leq 0)$$

$$\sigma_1 = 1.369 f_{ts0} (-0.001N + 0.9448) (f_c e^{-0.002N})^{-0.0833} \left(1 - 0.8 \frac{\sigma_2}{f_c e^{-0.002N}} \right)$$

$$\sigma_1 = \alpha \sigma_2$$

Acknowledgements

The authors wish to acknowledge the funding support from Post-Doctoral Innovative Projects In Shandong Province Under grant no. 200703702.

References

- 1 Mather, B. Concrete Durability. Cement & Concrete Composites, 2004, 26.3-4.
- 2 Maltais, Y., Samson, E. and Marchand, J. Predicting the Durability of Portland Cement Systems in Aggressive Environments—Laboratory Validation, Cement and Concrete Research, 2004, 34. 1579– 1589.
- 3 Alexander, M.G. and Magee, B.J. Durability Performance of Concrete Containing Condensed Silica Fume. Cement and Concrete Research, 1999, 29. 917–922.

- 4 Forster, S.W., Moore, S.P. and Simon, M.J. Behavior of Recycled Concrete as Aggregate in Concrete. in Supplementary Papers of Third CANMET/ACI International Conference on Durability of Concrete, (France, 1994).
- 5 Mulheron, M. and O'mahony, M. The Durability of Recycled Aggregates and Recycled Aggregate Concrete. in Proceedings of the Second International Symposium (RILEM) on Demolition and Reuse of Concrete and Masonary, (Tokyo, 1988).
- 6 Sun, W. and Zhang, Y.M. Yan, H.D. and Mu, R. Damage and damage Resistance of High Strength Concrete under the Action of Load and Freeze–thaw Cycles. Cement and Concrete Research, 1999, 29. 1519–1523.
- 7 Jacobsen, S., Sellevold, E.J. and Frost, S.M. Durability of High Strength Concrete: the Effect of Internal Cracking on Ice Formation. Cement and Concrete Research, 1999, 66. 919–931.
- 8 Marzouk, H. and Jiang, D. Effects of Freezing and Thawing on the Tension Properties of High-strength Concrete. ACI Material Journal, 1995, 91. 577–586.
- 9 Soroushian, P., Nagi, M. and Okwuegbu, A. Freeze–thaw durability of lightweight carbon fiber reinforced cement composites, ACI Material Journal, 1992, 89, 491–494.
- 10 GBJ82-85. National Standard of the People's Republic of China. The Test Method of Long-Term and Durability on Ordinary Concrete. Beijing, 1997.
- 11 Song, Y.P. Failure Criteria and Constitutive Relations of Concrete. Water Power Press, 2002.

STUDY ON ZONAL DISINTEGRATION OF SURROUNDING ROCK IN DEEP CROSS ROADWAY UNDER HIGH STRESS

CHUN-JIANG SUN

Xin Wen Mining Group Corp.

Xin Tai ,Shan Dong, China

JIAN-GUO NING, YUN-LIANG TAN, HAI-TAO LI

Key Laboratory of Mine Disaster Prevention and Control, Shandong University of Science & Technology Qingdao,

Shan Dong, China

Based on geological and mining conditions of -530 rail roadways in the E Zhuang coal mine of the Xin Wen mine group, zonal disintegration phenomenon of deep cross-roadway surrounding rock mass with high-stress is inspected through employment of the strata exploring instrument. According to failure information inside roof rock strata recorded by the strata exploring instrument, rock failures in each drill are respectively drawn in one graph, and failure regions with the distance less than 0.2m are regarded as one partition. The study shows that because of stress field superposition and road excavated section increment of cross roadway under deep and high-stress conditions, large subsidence of the rock mass is caused, the fissure and slice come into being in cross roadway rock strata interface, subsequently zonal disintegration named complete failure zone and loose strip zone forms under the rock strata, and the higher the stress is, the higher the amount of zonal disintegration and radius.

1 Guidelines

With the increase of energy demand and mining depth and the gradual decrease of shallow resources, a lot of countries subsequently face the problem of deep resource mining conditions. According to incomplete statistics, there are more than 80 coal mines with mining deeper than 1000m abroad, among which most are distributed in South Africa and Russia. In china, some 53% coal resources in the detected coal reserves are buried at a depth exceeding 1000m abroad presently, and mining depth increases by 8~12m per year in terms of contemporary mining methods [1]. With the increase of mining depth, engineering disasters becomes more frequent, especially the deformation failure and support of deep roadways with high in situ stress. Some studies show that expansion and compression regions (or failure region and undamaged region) occur alternately in deep surrounding rock, and width increases gradually according to the ratio of equality, which is called the zonal disintegration phenomenon [2].

I.Shemyakin ect. found zonal disintegration phenomenon in deep mine with the use of electrical resistivity apparatus at 1980s, and further demonstrated existence of the phenomenon[3]. D. F. Malan and S. M.

Spottiswoode, by present data, analyzed the formation and development of roof strata zonal disintegration along with working time and mining activity, and searched the relevance between rock burst and zonal disintegration of the roof rock[4]. E. J. Sellers and P. Klerck studied, by experiment, the influence of surrounding rock discontinuous surface on zonal disintegration in immersed tunnel, found that zonal disintegration of tunnel surrounding rock might be formed by discontinuous surface when a certain condition was met[5]. In China, Fang Zulie found zonal disintegration phenomenon for the first time in Jin Chuan nickel mine, when detecting deep roadways surrounding rock deformation by multiple-point displacement apparatus[6]. Recently, advocated by Qian Qihu, zonal disintegration phenomenon has been further studied by many scholars. Such as Gu Jincai and Pan Yishan have proved zonal disintegration by model experiment[7,8]. Tang Chun'an, Zhou Xiaoping, Li Shuchen ect. have studied zonal disintegration characteristic of surrounding rock within deep roadway by numerical simulation[9,10,11]. According zonal disintegration characteristic of tunnel surrounding rock, He Yongnian ect. have revealed new balance process and stability form of deep tunnel surrounding rock[12]. Zhou Xiaoping and Qian Qihu, regarding deep roadway excavation as dynamic problem and using movement equation in the form of displacement potential function, have determined residual strength of rock mass and formation time of zonal disintegration, and further determined the number and the width of zonal disintegration and integration by elastic and fracture mechanic[13]. By field detection, Li Shucai has found the relation between the radius of failure partitions and roadways radius of γ is $\gamma^{2(i-1)/2}$ ($i=1, 2, 3, 4$) and that 4 disintegration zones occurred in surrounding rock[14].

Scholars above-mentioned have got some achievements, separately from model experiment, field detection and theory. At present the mechanism of deep roadways surrounding rock zonal disintegration is not still completely understood, and zonal disintegration under specific conditions is not studied. Based on geological and mining conditions in Xinwen mine group, employing advanced strata exploring instrument, surrounding rock failure and slice of cross- roadways with high stress are detected, in order to reveal the development law of the zonal disintegration of cross roadways. It is important and realistic to safe mining of deep resource.

2 Detecting Project Conditions

Observation station is arranged in -530 rail roadway of E Zhuang coal mine in Xinwen mining group corp., which lies to south of mining area 6, west of -530 west roadways and cross-cut, the buried depth of which is between -825.6m ~ -817.8m. -530 rail roadways is excavated along strike, then advance along cross-cut through from siltstone of coal seam 17 bottom to siltstone of coal seam 5 roof, meeting at 202 cable roadway. "grouting-bolt-mesh- grouting" support is used and the section shape of -530 rail roadway is semicircle arched-type, the net sectional area of which is 14.78m^2 , and the net sectional area of cross-roadways at cross point is 28.32m^2 . Figure 1 shows -530 rail roadway arrangement.

Observation roadway is in coal seam 7, surrounding rocks of which are mainly composed of medium sandstone, siltstone and coal. The thickness of coal seam 7 is 1.1~2.0 m. The characteristic of coal, which is mainly vitrain and bright coal, is black, massive, visible strip structure, lustrous type, abundant joint inner, brittle and fragile, and hardness factor f of which is 2. The thickness of siltstone is about 3~5 m and the rock has characteristic of grey, condensation, fragile, shelly fracture, fragment containing plant leaf fossil, partly silt-medium sandstone interlayer, and hardness factor f of which is 3~4. the thickness of medium sandstone is

about 10~20m, iron grey, the main component of which is quartz and orthoclase secondary, with the characteristics of argillaceous cement, oblique bedding, not water, and hardness factor f is 5. The bottom is siltstone with the characteristics of dark grey, condensation, fragile, shelly fracture, breakable, easily weathered, siderite subcutaneous node, and hardness factor f of which is 3. Figure 2 is rock stratum columnar section.

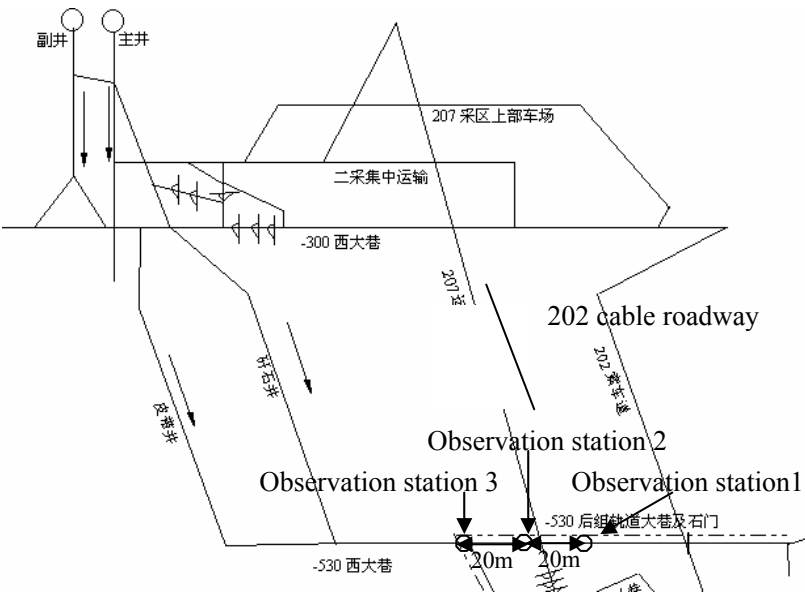


Figure.1 -530 rail roadway arrangement

Name	Schematic Drawing	Thickness	Characteristic
Medium Sandstone		10~20	Iron grey, the main component is quartz and orthoclase secondary, not water-bearing, and hardness factor f is 5
Siltstone		3~5	Grey, abundant joint inner, hardness factor f is 3~4
Coal		1.1~2.0	Black, massive, luminous type, abundant joint inner, brittle and fragile, hardness factor f is 2
Siltstone		4.0~5.0	Fragile, shelly fracture, hardness factor f is 3

Figure 2 Rock stratum columnar sections

3 Research Method and Observation Station Arrangement

Together, 3 observation stations are arranged, among of which the 1st station locates at the cross of 202cable car roadway and -530m rail roadway, the 2nd and 3rd stations are 20m and 40m separately away from the former, (seen from Figure 1), and one drill is arranged in roof at each station, keeping dip angle 90^0 against horizontal plane. With cable machine drilling, the depth of drill 8.0m and diameter is ϕ 28mm.

Strata exploring instrument of YTJ20 produced by Zhong Kuang Hua Tai is adopted for inspecting the zonal disintegration inside roof strata, consisting of photograph detector, video frequency transmission line, guide pole, depth counter and host computer etc. (Figure 3). Strata exploring instrument of YTJ20 is able to clearly record the depth, interface of coal seam and strata, interface of strata and strata, failure extent and formation of surrounding rock. Figure 4 shows the video frequency graphs in some drills. In response to extent and formation of failure, they are divided into complete facture, loose fracture, crack, fissure and slice. According to internal information of surrounding rock recorded by Strata exploring instrument, rock failures in each drill were drew respectively in one graph from inside to outside, and failure regions whose distance were less than 0.2m were regarded as one zone, They are respectively defined as zone 1, zone 2, zone 3, etc., which is joined together, and full of cross shaped budding grid different depth failure zones are formed.

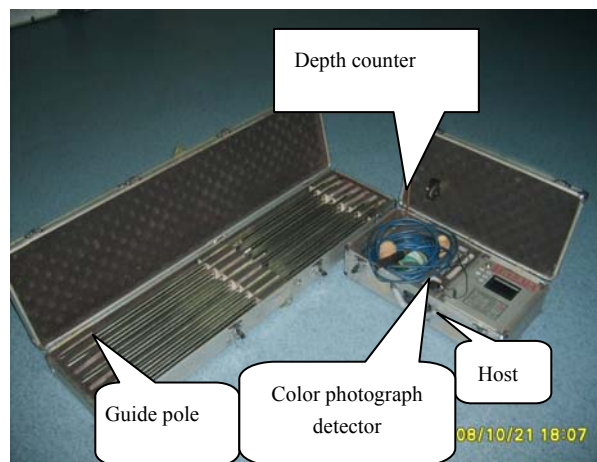
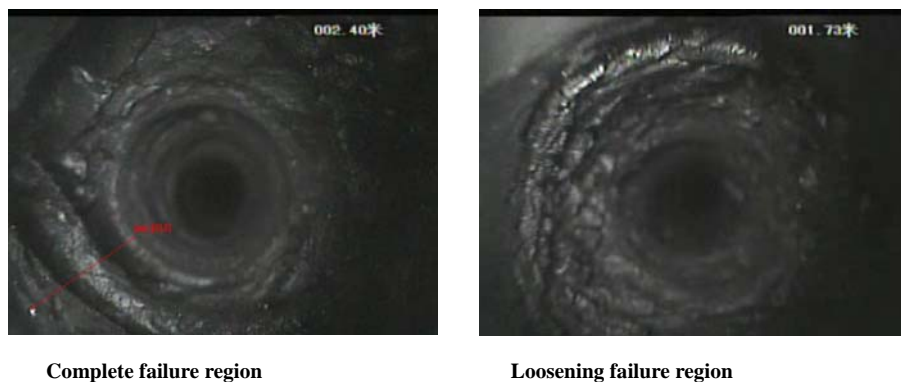


Figure.3 Components of Strata exploring instrument



Complete failure region

Loosening failure region

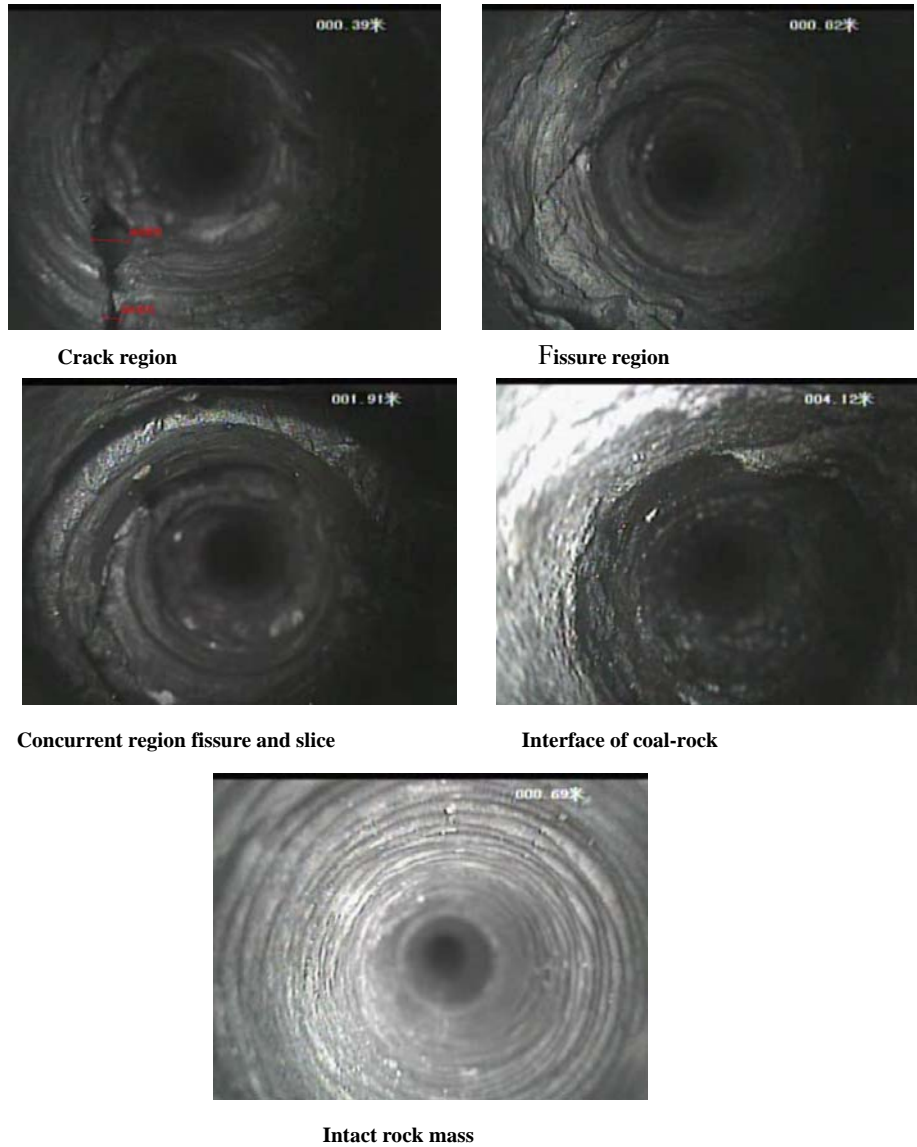


Figure.4 Video frequency graphs in some drills

4 Result and analysis of drilling detection

Figure 5 shows zonal disintegration of different depth at each station in roof of -530 rail roadways. Through it, there are 5 disintegration zones in roof of station 3, 3 disintegration zones in roof of station 2 and 1, and intact region between each disintegration, which shows the number of zonal disintegration in roof of station 1 and 2 less than that in station 3. And table 1 describes the radius of disintegration zone in the roof of each station, by which it is seen that the radius of disintegration zone in roof of station 1 and 2 less than that in station 3.

Table 1 The radius of disintegration zone in the roof of each station

observation station	Zone 1	Zone 2	Zone 3	Zone 4	Zone 5
station 1	0~1.6	2.0~2.2	2.6~3.4	3.7~4.0	4.2~4.8
station 2	1.2~1.4	1.6~1.8	2.6~2.8		
station 3	0.4~0.6	0.8~1.0	3.5~3.7		

According to internal information of each drill recorded by Strata exploring instrument, the position of interface between medium siltstone and medium sandstone in roof is determined, which is 4.2m above roof at station 1, some 3.0m at station 2 and 4.0m at station 3. Additionally, the range of the 1st, 2nd and 3rd zonal disintegration at station 3 is bigger, and failure in the zones mainly are serious damage, which is called complete failure region, denoted respectively S₁, S₂, S₃ in Figure 5. the 4th zonal disintegration is called crack region with the characteristic of few longitudinal crack and the average width of 7.2m, and denoted S₄ in Fig.5. The 5th zone is called concurrent region of fissure and slice, denoted S₅ in Fig.5. The 5th and the 4th zone nearly lie at interface between medium sandstone and medium siltstone. At station 2 and 3, the 1st and 2nd zonal disintegration are considered as complete failure, denoted respectively H₁, H₂, in Fig.5, and the 3rd is the concurrent region of crack and separation, denoted H₃ in Fig.5, with the same position as the 4th and 5th of the station1.

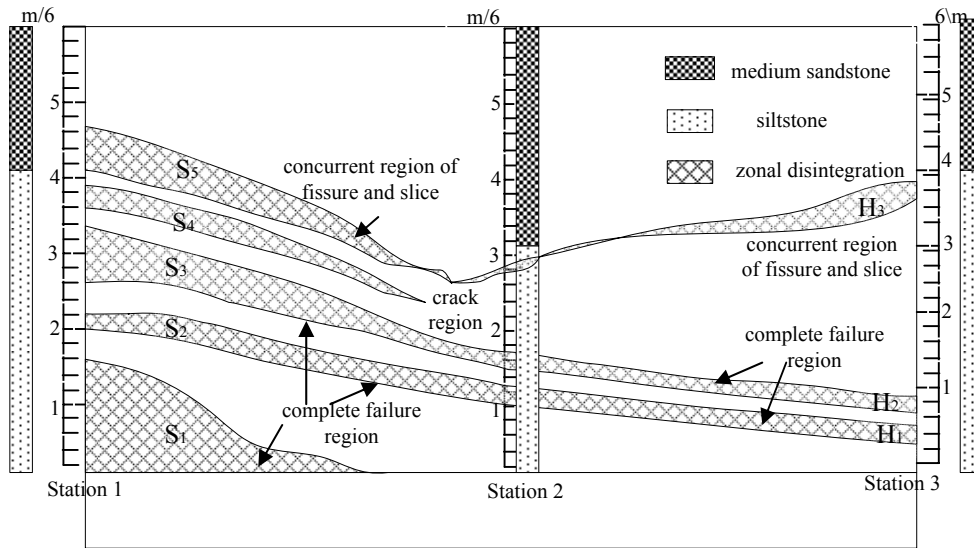


Figure.5 Zonal disintegration of the roof surrounding rock in -530rail roadway

5 Mechanism discussions

So far, there are different views on mechanism of zonal disintegration formation in roof surrounding rock. Through this detection, stress field superposition and roadway excavated section increment of cross roadway under deep and high-stress condition form zonal disintegration formation in roof surrounding rock, namely that surrounding rock pressure is several times, even nearly ten times than original rock pressure at the cross, therefore, the number of zonal disintegration is 5 and the radius of failure partition also increases at station 1.

Because of stress field superposition and roadway excavated section increment of cross roadway, large subsidence of in rock strata interface is caused, the fissure and slice come into being in cross roadway rock strata interface, seen from zone S₄ and S₅ in roof of station 1 and zone H₃ of station 2 and 3 in Figure 5, subsequently zonal disintegration named complete failure zone and loose strip zone forms under rock strata, seen from zone S₁, S₂ and S₃ of station 1 and zone H₁ and H₂ of station 2 and 3 in Figure 5, the higher the stress is, the more the number of zonal disintegration is, and the larger the radius is, Meanwhile, rock property has important impact on zonal disintegration, Compared with sandstone with high strength, zonal disintegration easily happens in brittle siltstone with low strength.

6 Conclusions

(1) Due to stress field superposition and excavation of roadway section increments of cross roadway which are deeply buried and under high stress, surrounding rock pressure is several, even ten times the original rock pressure. This induces increases of the number and enlargement of the radius of zonal disintegration at the cross point of roadways.

(2) The fissure and slice come into being in the cross roadway rock strata interface under high stress. Subsequently zonal disintegration named complete failure zone and loose strip zone forms under rock strata. The higher the stress is, the larger the number of zonal disintegration and the radius will be.

(3) If the bolt-cable anchor support system is adopted to support deep crossing roadways under high stress, the complete and loose failure region in the roof of roadways are key strata in the process of the support design.

Acknowledgements

The study is supported by Open Foundation Subject of Key Laboratory of Mining Disaster Prevention and Control(04000010302), Research Project of "SUST Spring Bud"(06540040104), China Natural Science Fund (No. 50534080, No. 50674063), Shandong Province Natural Science Fund (Z2008F01), Project No. J06N04 of Educational Department of Shandong Province, Key Laboratory of Mine Disaster Prevention and Control of Education Ministry, Tai'shan Scholar Engineering Construction Fund of Shandong Province of China.

References

1. Qian, Q.H. Key Scientific Problems for Deep underground Space Excavation. Nanjing: Engineering Institute of Engineering Corps, PLA University of Science and Technology, 2004.
2. Qian, Q.H. and Li, S.C. A Review of Research on Zonal Disintegration Phenomenon in Deep Rock Mass

- Engineering. Chinese Journal of Rock Mechanics and Engineering, 2008, 27 (6), 1278-1284.
3. Shemyakin, I., Fisenko, G. L., Kurlenya, M. V., et al. Zonal Disintegration of Rocks around Underground Workings. I. Data Of In-situ Observations. Soviet Mining Science, 1986, 22 (3). 157–168.
 4. Malan, D.F. and Woode, S.M. Time-dependent Fracture Zone Behaviour and Seismicity Surrounding Deep Level Stopping Operations. in Proceedings of Rock Bursts and Seism City in Mines, (Rotterdam, 1997).
 5. Sellers, E.J. and Klerck, P. Modelling of the Effect of Discontinuities on the Extent of the Fracture Zone Surrounding Deep Tunnels. Tunnelling and Underground Space Technology, 2000, 15 (4), 463–469
 6. Fang, Z.L. Maintenance Principle and Controlling Measure of Soft rock. Chian Coal Industry Publishing House, 1996.
 7. Gu, J.C., Gu, L.Y., Chen, A.M., et al. Model Test Study On Mechanism Of Layered Fracture within Surrounding Rock of Tunnels in Deep Stratum. Chinese Journal of Rock Mechanics and Engineering, 2008, 27 (3). 1433-1438.
 8. Pan, Y.S., Li, Y.J., Tang, X., et al. Study on Zonal Disintegration of Rock. Chinese Journal of Rock Mechanics and Engineering, 2008, 26 (supp.1).3335–3341.
 9. Tang, C.A. and Zhang, Y.B. Discussion on Mechanism and Evolution Laws of Fracture Spacing in Rock mass. Chinese Journal of Rock Mechanics and Engineering, 2008, 27 (7), 1362-1369.
 10. Zhou, X.P. and Qian, Q.H. Discussion on Mechanism of Zonal Disintegration around Deep Underground Works. Chinese Journal of Rock Mechanics and Engineering, 2007, 26 (5), 877-885.
 11. Li, S.C., Qian, Q.H., Li, S.C. et al. Numerical Model of the Zonal Disintegration for the Rock Mass around Deep Underground Works. Chinese Journal of Rock Mechanics and Engineering, 2008, 27 (8). 1457-1460.
 12. He, Y.N. and Zhang, H.Q. Discussion on Theory and practice of Zonal Disintegration in Surrounding Rocks of Deep Roadways. Chinese Journal of Rock Mechanics and Engineering, 2008, 27 (11). 2369-2375.
 13. Zhou, X.P. and Qian, Q.H. Zonal Fracturing Mechanism in Deep Tunnel. Chinese Journal of Rock Mechanics and Engineering, 2007, 26 (5). 877-885.
 14. Li, S.C., Wang, H.P., Qian, Q.H., et al. In-situ Monitoring Research on Zonal Disintegration of Surrounding Rock Mass in Deep Mine Roadways. Chinese Journal of Rock Mechanics and Engineering, 2008, 27 (8). 1545-1553.

TUNNEL EXCAVATION MECHANICS RESPONDING SENSIBILITY PARAMETERS ANALYSIS BASED ON SEEPAGE-STRESS COUPLING 3D MODEL

JUN XING and JING-PING QIU

*School of Resources & Civil Engineering, Northeastern University
Shenyang, 110004, P.R. China*

AN-NAN JIANG

*Institute of Highway and Bridge , Dalian Maritime University
Dalian, 116026, P.R. China*

The tunnel excavation in underground water environment destroys the balance of the original seepage field and stress . The whole process includes unloading stage, non-state seepage stage and consolidation stage. Meanwhile, this process concerns multitudinous parameters. How these parameters affect the mechanical response of tunnel is an important problem to be solved. In this study, based on the equifinality porous seepage-stress coupling theory of tunnel, the parameters analysis method by combining orthogonal test and 3D numerical simulation is provided. The flowchart of parameters sensitivity analysis method is also introduced. In terms of the excavation of small clear space mountain ridge tunnels in Shenzhen city, the 3D numerical analysis of solid-fluid coupling is carried out. The safety degree of lining and displacements of top and bottom of tunnel is selected as outputting responding indices. For the input parameters including Young's modulus, Poisson ratio, Cohesion strength, internal friction angle, coefficient of permeability, and coefficient of Boit, the paper adopts the orthogonal test numerical simulation and analyzes the parameters sensibility. It indicates that the parameters analysis method is feasible and the analyzed result has reference value for similar engineering.

1 Introduction

Water-rock interaction and unloading rock mechanics are hotspot problems in the field of rock mechanics. Along with the rock excavation deformation, the seepage-stress coupling process companied with loading or unloading action, which brings detrimental effects, even makes the disasters of the water invasion and downfall. According to statistics, one third of the tunnels constructed in China have water disease damage. The wealthy water region tunnels such as the subaqueous tunnel, mining tunnel, hydrotechnics tunnel and mountain trench, all have the water-rock interaction problems[1-4].

Terzaghi firstly proposed effect stress theory of saturated rock soil body. Biot proposed real three dimensional consolidation theory. In China, Shen Zhujiang firstly used the FEM Boit consolidation theory to analyze consolidation problems. The real rock mass is a fracture medium, and single fissure-plane is the basic element of rock mass. Zheng Shaohe, Zhao Yangsheng et used tri-axial apparatus to test and study the single fissure-plane rock. They believe that there is a power exponent relation between the coefficient of permeability and equifinality normal stress [2]. Zhou Chuangbing studied the generalized seepage cube law of rock joints[5].

The underground water seepage models of fractured rock mass include multiple medium model, discrete crack network model and equifinality continuous medium model. Based on strong application background, many researchers adopt solid-fluid theory to compute the tunnel engineering[6-7]. However, there are too many parameters in solid-fluid coupling system (including stress field and seepage field), there is uncertainty in the geological body. For example, how to select the parameters is an important problem.

2 The Seepage-stress Coupling Theory of Underground Engineering

Along with the excavation unloading and surrounding rock deformation, water flows to air face, water loading and seepage stress must affect the displacement of solid matrix, the deformation of solid matrix also changes pore water stress and coefficient of permeability, then influences the seepage. Above coupling process accompanied with dynamic loading or unloading. The excavation in rock soil body with underground water disturbed original balance of seepage-stress field, through the unloading, unstable seepage and consolidation actions, reached at a new multiple fields balance.

Because the rock mass structure is difficult to be described, so it is important to construct equifinality penetration properties in REV size scope. Regarded the rock mass as equifinality continuous medium, based on the rock excavation theory and solid-fluid interaction theory, that can be computed. The unstable seepage flow difference equations considering compressible water and rock soil matrix are as follows.

$$\frac{\partial}{\partial x}(k_x \frac{\partial h}{\partial x}) + \frac{\partial}{\partial y}(k_y \frac{\partial h}{\partial y}) + \frac{\partial}{\partial z}(k_z \frac{\partial h}{\partial z}) = \rho g(\alpha + n\beta) \frac{\partial h}{\partial t} = S_s \frac{\partial h}{\partial t} \quad (1)$$

In above formula, h is hydraulic head function, x, z are space coordination, t is time coordination. k_x , k_z are coefficients of permeability respectively along x and z directions. S_s is the unit water-storage capacity. Boit theory directly from elastic theory, satisfied the soil balance equations, elastic stress-strain relation and deform compatibility condition. So in consolidation process, the sum of principal stresses change continually. The seepage consolidation theory is as follows.

$$C_{v3} \nabla^2 u = \frac{\partial u}{\partial t} - \frac{1}{3} \frac{\partial \theta}{\partial t} \quad (2)$$

$$C_{v3} = \frac{kE'}{3\gamma_w(1-2\nu')} \quad (3)$$

In above formula, C_{v3} is consolidation coefficient of three direction consolidation. θ is the sum of normal stresses of a point. The equation reflects the adjusting process of stress-seepage coupling. Based on above formulas, combining rock excavation mechanics theory, plastic constitutive model and strength criterion, the solid-fluid coupling underground engineering can be calculated.

3. The Sensitivity Analysis Method Based on Orthogonal Design and Numerical Test

Compared with conventional tunnel excavation analysis, the solid fluid coupling rock excavation analysis concerns more complex parameters, study how the parameters affect the displacements and the stability of surrounding rock has important sense.

Figure 1 is the sensitivity analysis process sketch. Orthogonal test design is a method of utilizing orthogonal table to arrange and analyze multiple factors test. The orthogonal test design has the basic characters of orthogonality, representation and syntheses comparability. It uses part tests to instead of full tests, through the results of part tests to grasp the full tests. Range analysis method computes the range which is the maximal difference of the sum of each level result. The bigger the factor corresponds to the range, the more the factor affects the test result. According to range of the factors, the sensitivity factors can be determined.

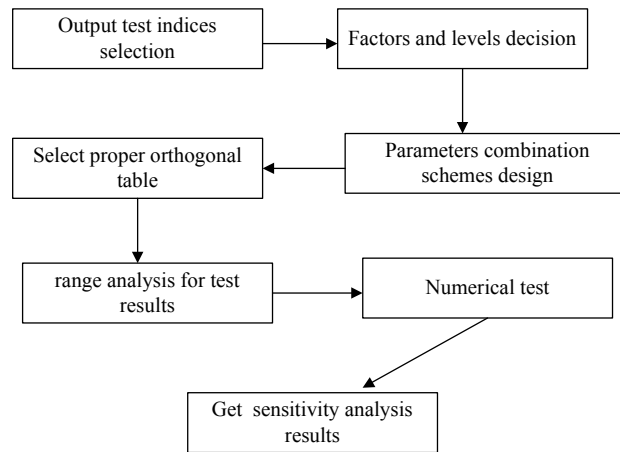


Figure 1 Sensitivity analysis process

However, the laboratory test expends much manpower and resource, and it is difficult to realize the complex seepage-stress process. So the numerical simulation is carried out to analyze the parameters sensibility. The software FLAC3D is used and the mechanism of solid-fluid interaction follows the formula (1-3). FLAC3D simulates water flow in rock by pore water press dissipation inducing structure displacement. While fluid flowing through solid matrix, the pore water pressure, seepage flow change.

In the coupling compute process, from statistic mechanics balance state, each step of water-stress coupling includes one or more steps of fluid computation, until the statistic balance equations are coincident. At the same time, because of the water flow, the increase of pore water should be calculated in seepage circle step, and the contribution to volume strain should be calculated in mechanics circle step. Then the volume strain result as region values are distributed to each node, so the fluid –solid coupling is realized.

4 Engineering Application

4.1 Engineering Introduction.

There is an underground tunnel in Shenzhen city. The original physiognomy is table land and hill, the ground elevation is between 20.6m and 99.9m, the strata are made of ground layer, moulding gravel, clay soil silt, silty clay, migmatite and coarse-grained granite including full, strong, suffer and slight weathering rocks. The classes of surrounding rock are from II to VI. Ground water is mostly fracture water of bedrock, occurring in slightly

weathered rock. The level of underground water is between 16.20 m and 88.00m. Supporting structure type is leading long tube shed and leading tubule supporting for V~VI class of surrounding rock. The bolt and spray supporting for IV class of surrounding rock. The quadric lining is adopted for all surrounding rock. According to the provided geological data, the study region is selected from k5+150 to k5+250, the mining design method is used. The geology section is shown in Figure2.

4.2 Numerical Simulation.

The cavern section shape is three centers circles and straight wall invert arch, the arc wall clear height is 7.8m, the clear width is 9.46m, the designed spray thickness is 30 centimeters and the lining thickness is 50cm. The full section excavation is simulated. According to actual tunnel excavation sequence, the tunnel construction is simulated. The numerical model is shown in Figure 2. In the coordination, z axis is the tunnel axis direction, x-y plane is normal to tunnel axis, the scope is 120×130×100 m, which is from -60 m to 60 m in x direction, from -30m to 100m in y direction and from 0 to 100m in z direction. The model is divided as 18600 tetrahedral elements and 21142 nodes. It is shown in Figure3. The strata are generalized to three layers (1, 2 and 3).

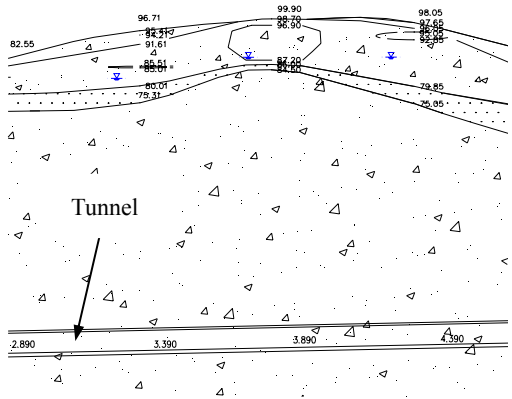


Figure 2 Engineering geology section of K5+100~K5+300

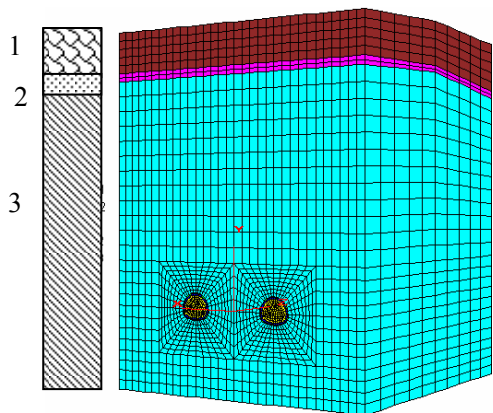


Figure 3 Computation model of tunnel

The rock of layer 3 is the main part affecting the tunnel stability, according to prior exploration, the density is 2.71 g/cm³. The other 6 parameters (E, c, Φ , μ , k, a) of stratum 3 are adopting random variables. E is Young's modulus, c is cohesion, ϕ is inner friction angle, u is passion ratio, k is permeability coefficient and a is Boit coefficient. The parameters of stratum I and II are listed in Table 1, the statistical characterization of the parameters are shown in Table 2.

Table 1 Physic-mechanical and fluid parameters of rock

Stratum	Crude density ρ (g/cm ³)	Inner friction Φ (°)	Cohesion Strength (KPa)	Elastic Modulus (MPa)	Passion Ratio	Osmotic Coefficient k(m/d)	Porosity (%)
1	1.9	28	80	90	0.29	0.5~1.5	10
2	2.53	36	1500	100	0.27	1.0~2.0	5

Table 2 Statistical data of random variable for stratum 3

<i>random variable</i>	<i>unit</i>	<i>Average value</i>	<i>standard deviation</i>	<i>dispersion pattern</i>
Elastic Modulus (E)	GPa	4.5	0.45	normal distribution
Cohesion (c)	MPa	5.5	0.55	normal distribution
Inner friction angle (ϕ)	°	41	0.41	normal distribution
Passion ratio (μ)	non dimension	0.21	0.021	normal distribution
permeability coefficient (k)	$\text{e}^{-15} \times \text{m}^2/(\text{pa} \cdot \text{sec})$	6.0	0.6	normal distribution
Boit coefficient (a)	non dimension	0.8	0.033	normal distribution

The surrounding rock adopts elastic-plastic constitutive model and the criterion is Mohr-Coulomb. The criterion is described as follows.

$$f(\sigma_1, \sigma_2, \sigma_3) = \frac{1}{2}(\sigma_1 - \sigma_3) - \frac{1}{2}(\sigma_1 + \sigma_3) \sin \phi - c \cos \phi = 0 \quad (4)$$

In formula, σ_1 、 σ_3 are respectively maximal and minimal principal stress, c, ϕ are respectively cohesion strength and inner friction angle of material. Generally, the lining is divided by many elements. For each element based on elastic model, according to Mohr-Coulomb theory, the safety factor express of lining element is gotten as formula (5).

$$F_s = \left(c \cos \phi + \frac{\sigma_1 + \sigma_3}{2} \sin \phi \right) / \left(\frac{\sigma_1 - \sigma_3}{2} \right) \quad (5)$$

4.3 The numerical computing results based on average parameters

The computation includes 5 steps in total and each step excavating 20m along z direction. Each step expends 1×10^5 s (about one day), and after 5 excavation steps finished, the time of 1×10^5 s is also simulated, then the total time is 6×10^5 s. When the first stage is excavated, the pre-spray and supporting are installed, after 1×10^5 s, the second stage is excavated, and at the same time, the first stage second lining is installed. In the solid-fluid coupling process, hydraulic seal is installed between pre-spray layer and second lining, so it is thought that the second lining is hydraulic seal.

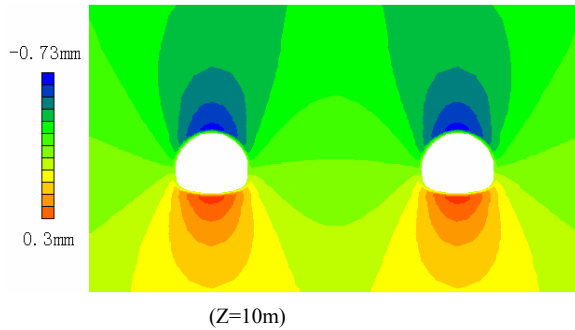


Figure 4 Contour of Y-displacement

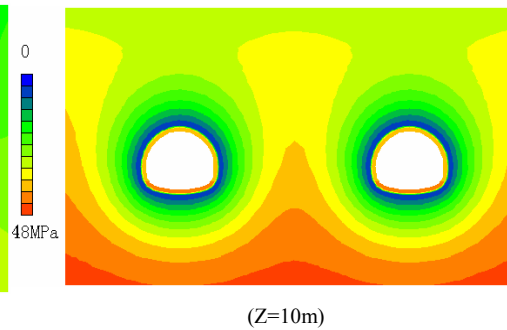


Figure 5 Contour of pore-pressure (Z=10m)

The solid-fluid interaction simulation time is 6e5s, along with the tunnel excavation and pore water pressure dissipation, the stress of surrounding rock readjusted. As time goes on, the consolidation proceeds and effect stress changes. The simulation stress contour of section Z=10m shows that at both sides of arch wall there occurs compressive stress concentration and at top arc occurs tension stress concentration. The maximal tension stress is 0.3 MPa, the maximal compress stress is 4.93 MPa. Figure 4 is the contour of Y-displacement, it is shown that in section of Z=10m the maximal top arc subsidence is 0.73mm, the maximal soleplate up moving is 0.3mm. Figure 5 is the pore-pressure contour at section of Z=10m, it is shown that near the air face the pore water pressure approaches zero, the farther the distance from air face, the smaller the pore pressure dissipation is.

4.4 Sensibility analysis

According to Table 2, each random variable adopt 5 levels, ie $1(X-3\sigma)$, $2(X-1.5\sigma)$, $3(X)$, $4(X+1.5\sigma)$, $5(X+3\sigma)$. X , σ are respectively the mean and standard error of random variable. According to orthogonal experimental design method, the test design of 5 levels and 6 factors is adopted, the numerical computing platform FLAC3D is used to fluid-solid coupling numerical simulation. The random parameters of Table 2 is the slightly weathering layer of migmatite corresponding to the III layer of Figure 2. The mechanics respond indices are displacements of arc top and bottom plate of right hole, the average of safety coefficients of second lining (36 elements in total). The orthogonal schemes calculation results are in Table3.

Table.3 Orthogonal schemes calculation results

Test No.	Factor Coding						Top Deform (mm)	Bottom Deform (mm)	Safety Factor	Test No.	Factor Coding						Top Deform (mm)	Bottom Deform (mm)	Safety Factor
	E	C	Φ	μ	K	a					E	C	Φ	μ	K	a			
1	1	1	1	1	1	1	-1.024	0.629	2.26	14	3	4	1	3	5	2	-0.754	0.400	3.52
2	1	2	2	2	2	2	-0.930	0.559	1.74	15	3	5	2	4	1	3	-0.727	0.400	3.78
3	1	3	3	3	3	3	-0.997	0.603	2.73	16	4	1	4	2	5	3	-0.717	0.373	3.53
4	1	4	4	4	4	4	-0.984	0.590	2.87	17	4	2	5	3	1	4	-0.693	0.373	4.00
5	1	5	5	5	5	5	-0.971	0.577	2.84	18	4	3	1	4	2	5	-0.693	0.365	4.22
6	2	1	2	3	4	5	-0.836	0.300	3.12	19	4	4	2	5	3	1	-0.683	0.363	4.20
7	2	2	3	4	5	1	-0.818	0.300	3.31	20	4	5	3	1	4	2	-0.719	0.381	3.20
8	2	3	4	5	1	2	-0.789	0.400	3.30	21	5	1	5	4	3	2	-0.660	0.325	4.64
9	2	4	5	1	2	3	-0.855	0.300	2.58	22	5	2	1	5	4	3	-0.658	0.318	4.64
10	2	5	1	2	3	4	-0.846	0.300	2.84	23	5	3	2	1	5	4	-0.689	0.335	3.50
11	3	1	3	5	2	4	-0.725	0.400	3.75	24	5	4	3	2	1	5	-0.668	0.335	3.97
12	3	2	4	1	3	5	-0.752	0.389	1.63	25	5	5	4	3	2	1	-0.662	0.332	4.38
13	3	3	5	2	4	1	-0.756	0.400	3.19										

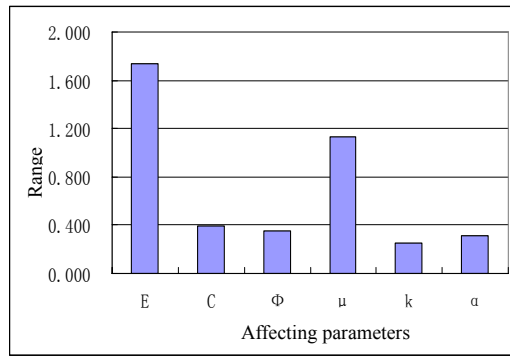


Figure 6 Sensitivity analysis of safety factor

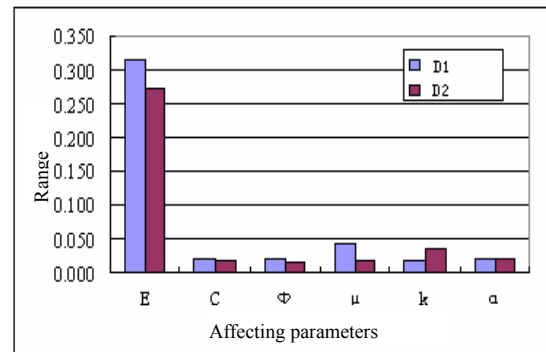


Figure 7 Analysis of vertical displacements

According to the factors sensibility analysis results, the elastic modulus E is the most sensitive factor affecting lining safety degree, the range value R is 1.740. Secondly is Passion ratio, the range value is 1.128. The range values of Cohesion, inner friction angle, permeability coefficient and Boit coefficient are respectively 0.397、0.353、0.255、0.309, which are equalization in values and smaller than elastic modulus E and Passion ratio u . The factors affecting lining safety degree is shown in Figure6. In underground engineering, the vertical displacements of tunnel are major monitoring data. This paper monitors the displacements of arc top and bottom plate of right hole and analyze how the factors affects the displacements. It is shown from the sensibility analysis results(Figure 7, D1 is displacement of arc top, D2 is displacement of bottom plate), elastic modulus E has the most obvious affection to displacements, the range values are respectively 0.314、0.272. The other factors are less than 0.043. The range value of elastic modulus E has an order of magnitude larger than other parameters.

5 Conclusion

The tunnel excavation in an underground water environment behaves as changing the original seepage field-stress field balance to a new one, experiencing the process of unloading mechanics, non-state seepage and consolidation. The process concerns multitudinous parameters.

The paper is based on the introduction of excavation mechanism of stress-seepage coupling, constructs the parameters sensibility analysis method based on integration orthogonal experimental design principle and seepage-stress coupling 3D numerical simulation. Compared with full test, orthogonal experimental design decreases the number of numerical calculation and keeps the representation, and it also saves a lot of calculation time.

Carried out three dimensional fluid-solid coupling numerical simulation and takes lining safety degree, displacements as output respond, the paper adopts orthogonal experimental design and sensibility analysis for a mountain tunnel with two holes of small clear distance, verifies the method feasibility. According to the sensibility analysis results, the elastic modulus E and Passion ratio u are the most sensitive factors affecting the lining safety degree. The range values of Cohesion, inner friction angle, Boit coefficient are equalization in values and smaller than elastic modulus E and Passion ratio u . To the displacements of top arc and bottom plate,

The range value of elastic modulus E has an order of magnitude larger than other parameters. The results had guiding and referencing meaning to similar solid-fluid coupling tunnel parameters study.

Acknowledgments

The paper partially supported by the State Program of National Natural Science of China (Grant No. 50574022, 50508007) and Chinese postdoctoral fund (20070420205).

Reference

1. M.oda and An Y.Hatsuyama and Ohnishi, Y. Numerical Experiments on Permeability Tensor and Its Application to Jointed Granite at Stripa Mine, Sweden.J.Geophys., Res., 1987, 92 (B8): 8037-8048.
2. Zheng, S.H., Zhao, Y.S. and Duan K.L. An Experimental Study on the Permeability Law of Natural Fracture under 3-D Stress. Chinese Journal of Rock Mechanics and Engineering, 1999, 18 (2). 133-136.
3. Liang, B., Sun ,K.M. and Xue, Q. The Research of Fluid-solid Coupling in the Ground Engineering. Journal of Liaoning Technical University, 2001, 20 (2). 129-134.
4. Zhou, C.B. and Xiong W.L. A Generalized Cubic Law for Percolation in Rock Joints. Rock and Soil Mechanics, 1996, 17 (4). 1-7.
5. Li, T.C., Li, S.C., Chen W.Z., et al. Comparison of Computing Results with and without Water Coupled in Simulation on Subsea Tunnel Stability. Chinese Journal of Rock Mechanics and Engineering, 2003, 22 (Supp.1). 2159-2163.
6. Ji, X.M. and Ren, W.X. Geological Environment of Tunnel Ground and Depiction of the Excavation Process. 2006, 2 (4). 615-620.

STUDY ON EFFECT OF INTERMITTENT JOINT ON ARCH ROADWAY STABILITY

ZHE ZHANG, SI-LI CHEN, ZHI-QIANG HUANG and QING LI

School of Architecture and Civil Engineering, Shenyang University of Technology

Shenyang 110178, China

When the roadway was excavated, the stress state of rock mass around roadway periphery changed from triaxial to biaxial stress conditions. While the stress in roadway surrounding rock is higher than the strength of wall rock, the damage zone will occur in roadways surrounding rocks with intermittent joints. The shape of the damage zone is circular or oval. This study is more useful and significant for further understanding of the stability of roadway in rock mass on the theoretical and practical aspects. It is the deformation and nonlinear progressive failure characteristics in deep rock mass as well as the displacement and the stress variation of the key position in roadway periphery that were numerically analyzed.

1 Introduction

With the development of society, the demand for mineral resources and the increase of excavation depth, geological environments have become more and more complicated. Overseas, the valley tunnel construct of Norway reached the length of 24.5km, and the Gotthard tunnel of the Switzerland reached the length of 16.3 km. In our country, considering the relatively lagging economy, highway tunnel construction fell behind, tunnel build technology is relatively backward by comparison with developed country, but recent years, highway tunnel build scale and quantity need to develop majorly. These tunnels act the important function to promote our national economy and ameliorate trafficking environment aspect [1]. In order to conform to tunnel engineering and construction technical develop, many engineers and scholar have the theory studied, and the experimental investigation on tunnel wall rock stability proceeds method. Tunnel stability analysis mostly includes: finite element method [2, 3], boundary element method [4], coupling analysis method [5], semi-resolve numerical method, neural net, and the systems engineering method. Go with computer technology develop and finite element analysis technical maturity. Finite element method should be known for clear comprehensive application at geotechnical engineering stability analysis, which can contribute to the solution to a number of very practical problems. In these previous studies, the primary objectives are needed to explain abundant field observations through analytical models and to better understand the stress-dependent mechanism through finite element analyses.

In this study, the stability safety factor is defined as wall rock practice shear strength and fold subtract rear critical damage shear strength ratio in this text, syntheses handle finite element, intensity fold subtraction and

optimization theory about tunnel wall rock stability analysis research tunnel wall rock. We conduct this research through two logical steps. Firstly, we validate the numerical code by comparing the stress states between field experiment and numerical model. Secondly, we analyse different tunnel section model. We also analyze the number of final fractures with the total number of acoustic event occurrences assuming that a relation between the acoustic event and the micro-fracture formation exists. The results show this study can predict the fractures in tunnel surrounding rock. This may have significant applications in a number of engineering areas.

2 Numerical Simulation

It is well known that rock deformation is nonlinear in macroscopic, however, the functions defined above are only adapted to continuous, isotropic and linearly elastic materials. In fact, the nonlinear deformation of rock is aroused by heterogeneity in microscopic level, and the continually failures of elements with loading added are the essential reason. There are large different between macroscopic and microcosmic level of rock due to extremely heterogeneity, i.e. rock deformation behaves nonlinear characters at macroscopic level and linearly elastic characters of microcosmic elements can be used at macroscopic level. Considering the heterogeneity of rock at a microcosmic level, all the small elements own its property, maybe same or different. By introducing the statistical method, we assume that the element parameters of rock.

Numerical model was given in figure.1 the model grid size was 20m * 20m. The diameter of circle roadway was 2m. The thickness of intermittent joint is 5cm. The vertical distance between intermittent joints was 2.5m. The model has been considered into a 200 *200 (40,000) mesh. Plane strain assumption was used in the modelling. First, we applied 0Mpa ambient pressure and excavated the roadway. Then gradualness made load on model through two equal loads from horizontal and vertical. It was withal displacement increment mode proceed applied, displacement increment equal 0.1 mm, until wall rock body crippling, thereby learn stress distribution, transfer and crackle initiation, spread course as well about that load.

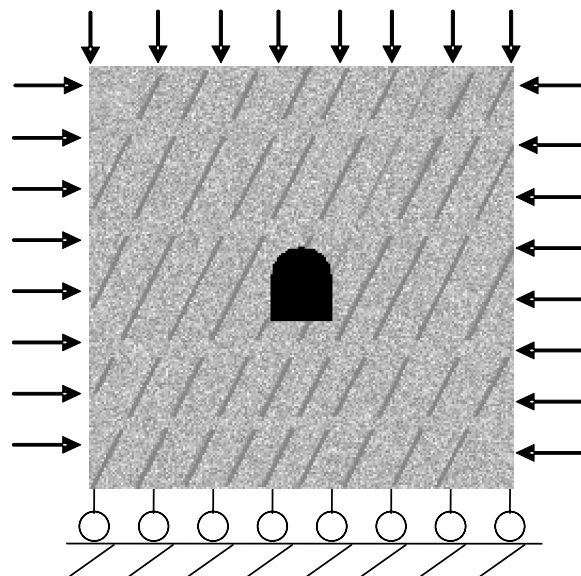


Figure.1 Numerical model

Materials mechanics properties parameters (such as Young's modulus, compressive strength) were given in table 1.

Table 1 Materials mechanics properties

Parameter	Rock mass	Joints
Homogeneity index	10	10
Young's modulus /GPa	10	2
Poisson's ratio	0.3	0.25
Friction angle /°	32	25
Compressive strength /MPa	50	5
Tension Strength /MPa	10	1

3 Simulation Result and Analysis

Figure.2 (a-c) show rock mass failure mode with shear stress. From the theoretical solutions, it is generally concluded that crack will initiate under peak load. The maximum tensile stress at the surface of centre hole is calculated and considered as the tensile strength of rock. It is actually assumed that the rock has attained its peak loading capacity and lost its loading capacity when crack initiates at the surface of the tunnel. As a matter of fact, when the crack initiates near the surface of tunnel, the stress concentration will be released, the stress in the rock will be redistribution to attain a new equilibrium conditions and the load applied on the model can also be increased with the propagation of crack. Therefore, the initiation of fracture around of tunnel when stresses attain the tensile strength the crack is fully developed.

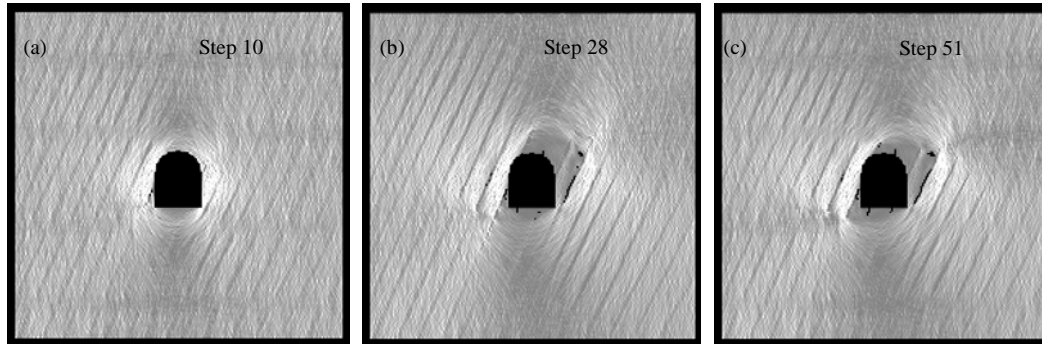


Figure.2 Rock mass failure mode with shear stress

As can be seen from figure.2, we simulate numerically the evolution process of the progressive failure leading to sudden fracture by using the Rock Failure Process Analysis code which allows us to examine the progressive failure process visually on a continuous basis during the loading process, when the applied boundary displacement increases, the micro-seismic events occurred as shown in figure.2 (b-c). Several micro-seismic events occur randomly and non-interacting fractures are observed. Some small clusters of micro-seismic form, extend or coalescence. The principal characteristic of this stage would be associated with

disorder and heterogeneity in the entire rock mass.

Figure.3 show seismic source location during rock mass failure. As we know, one important method of observing damage during the rock deformation experiments is monitoring the acoustic emissions (AE). There is generally a good correlation between AE counts and inelastic strain rate so that the AE rate can be used to quantify damage accumulation occurring in the rock. It can be seen from figure.3 (b). An abrupt stress drop and the maximum rate of AE events appear in the step 51. It indicates that the initiation and propagation of microscopic fracturing which precedes the final stage macroscopic fracture development has occurred in the rock.

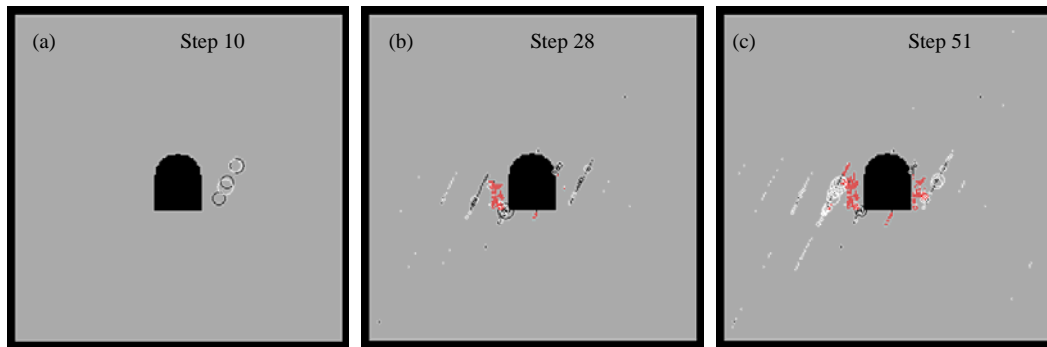
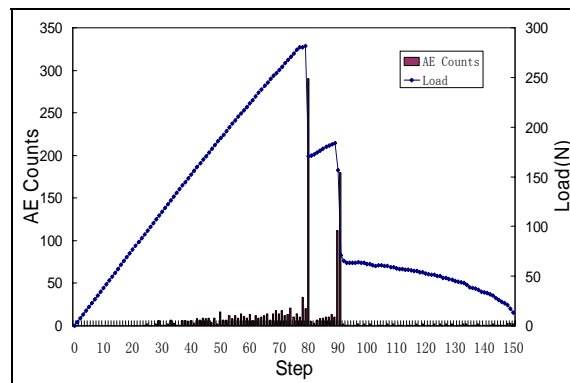


Figure.3 Seismic source location during rock mass failure

The results show that the maximum AE event or main shock emitting from rock can be regarded as the precursor of fracture of rock. When the tensile stress concentration at this edge is released and the tensile stress concentration is transferred to the opposite edge. At last the bottom and top boundary failure. This pattern exists commonly in tunnel as actual.

Figure.4 show stress-strain, seismic event and seismic energy release during loading. As the boundary displacement continues to increase, the micro seismic events will become dense enough to begin interacting. After some further shearing, the left pillar fails in the same failure mode during a single loading step. This pillar failure is associated with more energy release because a more extensive shear zone forms than during the failure of the first pillar.



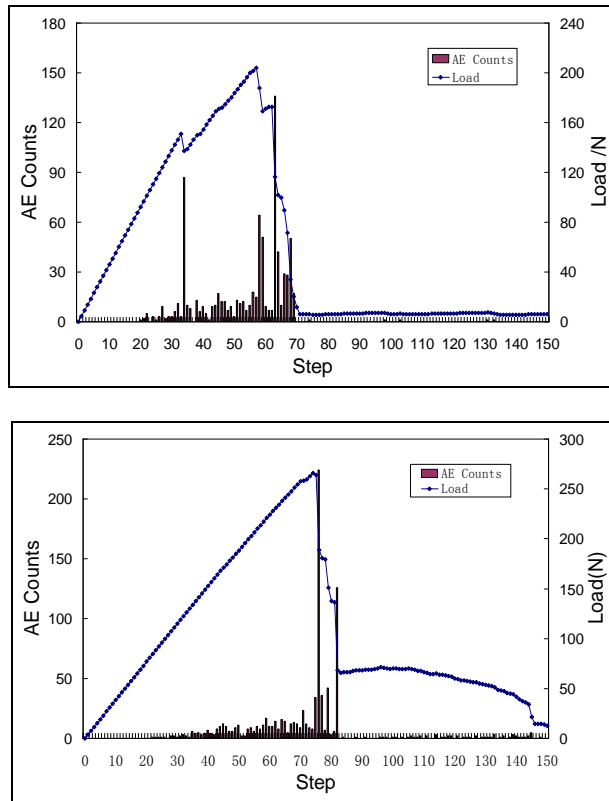


Figure.4 Stress-strain, seismic event and seismic energy release during loading

It is apparent that before the two big rock failures, there are always little micro-seismic events occurring, which is similar to the quiescence of seismic activity, and it is also found that following the big rock failure, there is a relatively long time quiescence of seismic activity for the large energy release.

4. Conclusion

The stress transfer, crack initiation, propagation and coalescence in deep rock mass induced by excavation. Also the plastic zone formed under hydrostatic pressure, stress transfer and crack initiation, coalescence were numerically simulated. The stability of roadway was studied by observing roadway deformation characteristics.

With an increase in loading, linear elasticity deformation phase, joint plane slippage, stress concentration on the tips of the joints, stress concentration between rock bridges and crack initiation, propagation and coalescence continuously occur. The deformation and failure possess deep rock masses with intermittent joints that have several obvious phases.

References

1. Wu, M.J., Chen, Z.G., Xu, X.B., et al. The present and prospect of highway tunnel surrounding rock stability. 2003, 22(2). 24–28.

2. Zhang, Z., Tang, C.A., Ma, T.H. and Duan, D. Numerical Investigation of Fracture Behavior of Tunnel by Excavation Loading. *Journal of Coal Science & Engineering*. 2007, 13(4). 484-488.
3. Zhu, H.H., Zhang, C.M., Wang, J.X., et al. Dynamic displacement back analysis and prediction of longshan two-arcade twin tunnel. *Chinese Journal of Rock Mechanics and Engineering*, 2006, 25(1): 67-73.
4. Wang, Z.L., Li, X.Y. and Hou, J.X. The jointed rock stability and parameters back analysis of one tunnel engineering with BME. *Geotechnical Engineering Technique*, 2001, 3. 176-179.
5. Wang B. and Zhang, M.X. The method of coupling infinite elements with finite elements and its application to structure analysis of a road tunnel. *Journal of Gansu Sciences*, 1994, 6(2). 1-6.

STUDY OF THE FATIGUE DEGRADATION OF ROCK SLOPE UNDER CYCLIC LOADING

WEN-BIN JIAN, RUN LI, JUN PENG and XIU-FENG FAN

Institute of Geotechnical and Geological Engineering, Fuzhou University

Fuzhou, 350108, China

One concern to rock slopes in open pit mining and civil engineering is the potential for the gradual deformation of a large slope to develop into a fast moving catastrophic slide. The process must be considered as a potential threat where large deforming slopes occur. The degradation of rock mass strength is a factor in the process. In this paper, through the fatigue tests of moderately weathered sandstone sampled from a rock slope, the S-N curve equation of rock fatigue strength is established and the fatigue degradation of rock slopes under cyclic loading is further studied by finite element simulation. The results show that fatigue accumulation damage will be generated in rock mass of slope under cyclic loading. The geotechnical parameters and slope stability factor are gradually decreased with the cyclic fatigue loading. Consumption of slope fatigue life is not sensitive to geotechnical parameters and stability factor at the initial stage of fatigue, however, at the later stage sensitivity increases. When the threshold value of accumulation of fatigue damage is achieved, the rock slope failure occurs abruptly.

1 Introduction

One of the threats to rock slopes in open pit mining and civil engineering is the potential for the gradual deformation of a large slope to develop into a fast moving catastrophic slide. The process must be considered as a potential threat where large deforming slopes occur. The degradation of rock mass strength is a factor in the process. Fatigue degradation of material occurs widely in various fields of civil engineering [1-3]. With the extension and development of high-grade highways, railways and other construction activities in mountainous area, as foundation, roadbed, dam foundation and slope, tunnel wall rock and other engineering structures, the long-term stability problem of rock and soil mass is becoming increasingly more important. The roadbed or slope of highway and railway is subject to cyclic loading with variations in frequency, amplitude and duration. Under the long-term cycle loading, the fatigue damage and degradation will occur in the engineering rock, soil mass for the subgrade, and slope. Thus the deformation and instability may be further engendered.

Under cyclic loading, the rock will be subject to repeated stress and strain. In such circumstances, even if the load is lower than the static load strength, the damage or lapse will be also generated in rock. In this regard, the corresponding research is carried by Ge Xiurun et al.[4], Singh.S.K[1], Tien.YM et al.[5], Li.G. et al.[6], Ishizuka et al. [7], Royer.G. et al.[8], XI Daoying et al.[9], Fan Xiufeng et al. [10-12], and certain results have been achieved. However, under the traffic load the deformation, the instability of slope rock and soil mass are complex. The study of the fatigue damage mechanism and the prevention of fatigue destruction are one of the more advanced subjects for geotechnical researchers [13,14] and have important theoretical significance. The engineering application value for the evaluation of long-term stability of highway and railway slopes under

traffic load is important to correctly study the fatigue effect of rock slope and its influence. Slope stability under traffic load is useful to reduce or avoid rock and soil disaster caused by various types of environmental vibration.

2 Rock Fatigue Test

2.1 Rock Specimen and Test Parameters

The fatigue analysis of rock slope is based on fatigue properties of slope rock material. In order to analysis rock fatigue, it is necessary to obtain accurate fatigue curve of the rock material by test. A sandstone rock slope is located at Shaxian, 205-provincial road in Fujian Province. The slope height is 20m with two grades, 10m for each, the slope rate is 1:1; the width of middle roadway is 10m. The typical profile of the slope is as shown in figure 1:

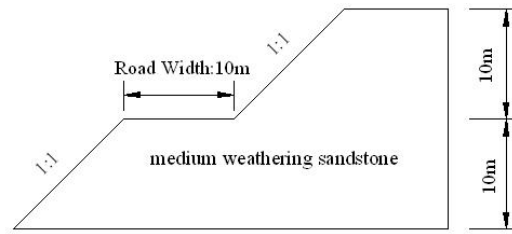


Figure 1 Typical profile of slope in research site

The moderately weathered sandstone with greyish-white, blocky structure for the test is sampled from the slope. The specimen is cuboid with the size of 50 mm × 50 mm × 100 mm. The test is carried by equiamplitude for three groups, 5 specimens for each group.

The rock samples are tested by INSTRON1304 electro-hydraulic servocontrolled fatigue testing machine in *Instrumentation Analysis and Measurement Center of Fuzhou University*. The fatigue damage test is controlled by load and the sine curve is chosen as load waveform. By electro-hydraulic servocontrolled system, the sine dynamic signal is transformed into cyclic loading and loaded to specimens, so that the excitation of system are finished; the specimen is deformed under the force (that is, response of system), the responded dynamic deformation signals are outputted by displacement sensor of INSTRON1304 testing machine. The strain data is collected and processed by the INVSA-8 dynamic strain gauge and 306DF intelligent signal collecting and processing system.

The characteristic parameters of load waveform are shown in figure 2. Among them, σ_{\max} as the upper limit stress of cyclic loading, σ_{\min} as the lower limit stress of cyclic loading, $\Delta\sigma = \sigma_{\max} - \sigma_{\min}$, $\Delta\sigma$ as load amplitude; T as the cycle, f as frequency, $f = 1/T$. In the test, the lower limit stress is fixed, whereas the upper limited stress could be changed. Stress S is presented by stress ratio (stress ratio indicates the ratio of the stress parameters fixed in the test to the rock static intensity σ_c).

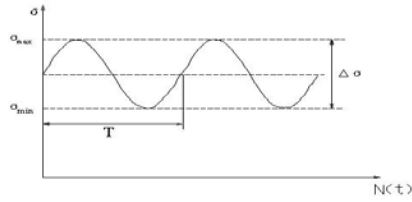


Figure 2 Cyclic load waveform

The load mode is uniaxial compression, the uniaxial compressive strength of sandstone specimen is $\sigma_c = 20.02 MP_a$, the load upper limit stress ratio of equiamplitude fatigue test is 0.8-0.9, and the lower limit stress ratio is kept at 0.1. The load frequencies in fatigue test are 5 Hz.

2.2 Results of Rock Fatigue Test

The equiamplitude fatigue life are obtained by test. The issue of rock fatigue strength is usually concluded to the S-N curve equation (also known as Wohler equation). The relation between stress level S and the fatigue life N is described by the S-N curve, its mathematical expression as follows:

$$S = A - B \lg N \quad (1)$$

Where A and B are the corresponding coefficients.

Through the indoor fatigue test for rock specimen, under equiamplitude cyclic loading, the fatigue strength S-N relation of moderately weathered sandstone is obtained, that is:

$$S_{\max} = 1.326 - 0.109 \lg N_f \quad R = -0.997 \quad (2)$$

There into: S_{\max} as upper limit stress ratio, N_f as fatigue life (time), R as correlation coefficient.

3 Fatigue Degradation of Rock Slope under Cyclic Loading

3.1 Establishment of Calculation Model

In order to further reveal the fatigue degradation of rock slope under cyclic loading, the physical and mechanics parameters of sandstone rock sampled from the slope is tested. The results are shown in table 1.

Table 1. Physical and mechanics parameters of sandstone rock

Material model	Unit weight $\gamma(kN/m^3)$	Young modulus $E(GPa)$	Poisson ratio ν	Cohesion $C(kPa)$	Angle of internal friction $\phi(^{\circ})$	Angle of dilatancy $\psi(^{\circ})$
Drucker-Prager	25.8	20	0.25	380	33	0

When the fatigue analysis of slope is carried, the required fatigue curve of slope rock material is the same as the equation (2).

The calculation region: The extension is double of slope height around the slope; the extension below is the same height of the slope; the boundary conditions are set as follows: 1)the top of the border: free surface; 2)the

bottom of the border: displacement constraints on horizontal and vertical directions; 3) both sides of the border: displacement constraint on horizontal direction.

The slope model is simplified to plane strain problem, and 4-node quadrilateral element is adopted.

3.2 Degradation of Slope Rock and Attenuation of Stability Factor

As to the problem of slope fatigue stability considering fatigue effects, the geotechnical parameters are degraded and stability factors are attenuated with the consumption of slope fatigue life. Based on finite element strength reduction method, the above fatigue failure process of rock slope under traffic load, as well as the relations and change laws among geotechnical parameters, stability coefficient and fatigue life are simulated.

(1) The original geotechnical parameters ($c_1=380$ kPa, $\varphi_1=33^\circ$) of slope are reduced according to equi-proportional strength. By stepwise approximation, when the strength reduction factor is 7.63, the calculation of slope finite element is not convergent, so the reduction factor is the slope stability factor. From that, the initial slope stability factor $K_{f1}=7.63$ is obtained; this stability factor is corresponded to one time fatigue loading cycle; by geotechnical parameters (c_r, φ_r), the corresponding fatigue life of slope is acquired. The original fatigue life of slope is obtained by the initial geotechnical parameters ($c_1=380$ kPa, $\varphi_1=33^\circ$), that is, $N_{f1} = 11760000$ (times).

(2) The finite element strength reduction method indicates, when the limit equilibrium state of the slope is achieved, the geotechnical parameters are reduced from $c_1=380$ kPa, $\varphi_1=33^\circ$ to $c_n=49.80$ kPa, $\varphi_n=4.33^\circ$; the corresponding safety factor is reduced to limit state $K_m=1.00$, so the corresponding stability factor of limit state is $K_m=1.00$ at that time. The geotechnical parameters $c_n=49.80$ kPa, $\varphi_n=4.33^\circ$ are multiplied by the stability factor K_{fr} ($1 \leq K_{fr} \leq 7.63$) to obtain the corresponding geotechnical parameters (c_r, φ_r), here ($1 \leq r \leq n$).

The damage D is defined to be the ratio of consumed fatigue life N_{dr} to initial fatigue life N_{f1} , that is,

$D_r = N_{dr} / N_{f1}$. When damage cumulates to $D = 1$, the fatigue failure is occurred.

Therefore, the relationships among “geotechnical parameters - stability factor - fatigue life” can be established, and the corresponding geotechnical parameters (c_r, φ_r) and fatigue life N_{fr} could be calculated for different stability factors. The results are shown in table 2.

Table 2 The relationships among geotechnical parameters - stability factor - fatigue life – accumulation damage

Stability factor K_f	Cohesion C (kPa)	Angle of internal friction φ (°)	Fatigue life N_f (time)	Consumed life N_d (time)	Accumulation damage D
7.63	380	33.00	11760000	1	0.000
7.51	374.00	32.52	10660000	1100000	0.094
7	348.62	30.28	7973000	3787000	0.322

6.44	320.71	27.89	6395000	5365000	0.456
6	298.82	25.95	5481000	6279000	0.534
5	249.02	21.63	3857000	7903000	0.672
4	199.21	17.30	2458000	9302000	0.791
3	149.41	12.98	1412000	10348000	0.880
2	99.61	8.65	521300	11238700	0.956
1.8	89.64	7.79	297600	11462400	0.975
1.6	79.68	6.93	134900	11625100	0.989
1.4	69.72	6.06	83540	11676460	0.993
1.2	59.76	5.20	6472	11753528	0.999
1	49.80	4.33	509	11759491	1.000
≤ 1	-	-	0	11760000	1.000

3.3 Degradation Characteristics of Slope Rock

From table 2, the instability of slope induced by fatigue of rock is controlled by damage accumulation and presented as fatigue life consumption; with the fatigue life consumption, the geotechnical parameters are degraded and stability factors are attenuated at the same time; when damage accumulation D is 1, the fatigue life is exhausted, the geotechnical parameters are degraded to limit equilibrium state and stability factor is attenuated to 1; if the fatigue loading is continued, the instability and damage of slope will be generated. Geotechnical parameters and the stability factor are gradually decreased with the fatigue loading cycle.

The consumption of fatigue life is not sensitive to geotechnical parameters and stability factor at initial stage, but at later stage, the sensitivity is increased. When the stability factor is reduced to 2, the slope will rapidly develop to be damaged, this characteristic indicates that when the threshold value for accumulation of fatigue damage is achieved, the rock slope failure occurs abruptly.

4 Conclusions

(1) Under cyclic loading, the fatigue accumulation damage will be generated in rock and soil mass. Rock fatigue strength is concluded through the S-N curve equation, and the relationship between stress level S and the fatigue life N is described by the S-N curve.

(2) Geotechnical parameters and the stability factor are gradually decreased with the fatigue loading cycle. The instability of slope fatigue is controlled by damage accumulation and presented as fatigue life consumption. With the fatigue life consumption, the geotechnical parameters are degraded and stability factors are attenuated at the same time. If the fatigue loading is continued, the instability and damage of slope will occur.

(3) The consumption of slope fatigue life is not sensitive to geotechnical parameters and stability factor at initial stage, but at later stage, the sensitivity is increased. When the stability factor is reduced to 2, the slope will rapidly develop to be damaged; this characteristic indicates that when the threshold value for accumulation of fatigue damage is achieved, the rock slope failure occurs abruptly.

Acknowledgements

This work is kindly supported by NSFC (National Natural Science Foundation of China) , No. 40672176 and the authors wish to express their deep gratitude to Professor Wu Weiqing in Instrumentation Analysis and Measurement Center of Fuzhou University for his kind help during the indoor test.

References

1. Singh, S.K. Relationship among Fatigue Strength, Mean Grain Size and Compressive Strength of a Rock. *Rock Mechanics and Rock Engineering*, 1988, 21 (4). 271-276.
2. Jian, W.B., Huang, C.X., Wu, W.Q., et al. Research on Fatigue Behavior of Cement-sodium-silicate-grouted soil. *Chinese Journal of Rock Mechanics and Engineering*, 2004, 23 (11). 1949-1953.
3. Shang, D.Z. Methods to Calculate Soil Fatigue in Pile Driving. *China Harbor Engineering*, 2007, (1). 20-22.
4. Ge, X.R., Jiang, Y., Lu, Y.D., et al. Testing Study on Fatigue Deformation Law of Rock under Cyclic Loading . *Chinese Journal of Rock Mechanics and Engineering*, 2003, 22 (10). 1581-1585.
5. Tien, Y.M., Lee, D.H. and Juang, C.H. Strain. Pore Pressure and Fatigue Characteristics of Sandstone under Various Load Conditions. *International Journal of Rock Mechanics and Mining Sciences & Geomechanics Abstracts*, 1990, 27 (4). 283-289.
6. Li, G., Moelle, K.H.R. and Lewis, J.A. Fatigue Crack Growth in Brittle Sandstones. *International Journal of Rock Mechanics and Mining Sciences & Geomechanics Abstracts*, 1992, 29 (5). 4677- 4694.
7. Ishizuka, Y., Abe, T., Koyama and Hiroshi. Effects of Strain Rate and Frequency on Fatigue Strength of Rocks. in *Doboku Gakkai Rombun-Hokokushu/Proceedings of the Japan Society of Civil Engineers*, (Japan, 1993).
8. Royer-Carfigni, G. and Salvatore, W. Localized Fatigue Damage of Carrara marble. in *Proceedings of the International Conference on Damage and Fracture Mechanics, Computer Aided Assessment and Control*, (1998)
9. Xi, D.Y., Liu, Y.P., Liu, X.Y., et al. Influence of Fatigue Loading on Physical Mechanical Characteristics of Rock. *Chinese Journal of Geotechnical Engineering*, 2001, 23 (3). 292-295.
10. Fan, X.F. and Jian W.B. Prospect of Rock Fatigue Damage and Corresponding Ultrasonic Surveying Test and Data analysis. in *Proceedings of the 9th National Conference on Rock Mechanics and Engineering*, (Shenyang, 2006).
11. Fan, X.F. and Jian W.B. Numerical Analysis for Damage Process of Rock-soil under Fatigue Loading. *Rock and Soil Mechanics*, 2007, 28 (S). 85-88.
12. Fan, X.F. and Jian, W.B. Experimental Research on Fatigue Characteristics of Sandstone using Ultrasonic Wave Velocity Method. *Journal of Rock Mechanics and Engineering*, 2008, 27 (3). 557- 563.
13. Gong, X.N. Prospects for the Development of Geotechnical Engineering in the 21th Century. *Chinese Journal of Geotechnical Engineering*, 2000, 22 (2). 238-242.
14. Sun, W., Shen X.K. and Zhang , Z.M. Prospect of Geotechnical Engineering Investigation 10 Years Hereafter. *Geotechnical Investigation & Surveying*, 2001, (3): 66-69.

ANALYZING MINING TUNNELLING ROCK FAILURE PROBABILITY BASED ON PARTICLE SWARM OPTIMIZATION- SUPPORT VECTOR MACHINE

JUN XING and JING-PING QIU

*School of Resources & Civil Engineering, Northeastern University
Shenyang, 110004, P.R. China*

AN-NAN JIANG and CHUN-YAN BAO

*Institute of Highway and Bridge , Dalian Maritime University
Dalian, 116026, P.R. China*

Since the mining tunnel geological body has characteristics of uncertainty and randomness, and the conventional certainty calculation has limitations. Moreover, the numerical simulation method expends much time and can not express the relation between parameters and responding value. It brings difficulties in uncertain calculation. Aiming at these problems and general responding surface method limitations, this paper proposed a surrounding rock failure probability calculation method based on particle swarm optimization (PSO)- support vector machine(SVM). According to random distribution of each parameter, adopts orthogonal and uniformity design principles and produces data samples by numerical tests, constructs support vector machine model mapping parameters and responding values which is taking advantage of the nonlinear generalization ability of SVM. The PSO is used to search the parameters of SVM which affecting the forecast accuracy. Afterwards, the PSO-SVM mapping model combined with Monte-Carlo sampling method can be used to calculate rock failure probability which can directly use the current large scale numerical simulation software. Applying the method to Jinshandian Ore Mine tunnel analysis, the analyzed results show this method is feasible.

1 Introduction

Nowadays, the certainty calculation method for underground engineering sees mechanical parameters as deterministic values. However, the geological body has characteristics of uncertainty and randomness. Also, the safety coefficient method can not reflect the discreteness of parameters and the safety margin. The difference between calculation parameters and that of true engineering can not ignored, that weakens the rationality of calculation. Therefore, considering the uncertainty characteristic of the geological body, calculating the failure probability of the surrounding rock becomes a concerned subject [1-5].

Analytic method only deals with the conditions of simple boundary and media characteristics, and can not be applied to complex engineering. The numerical calculation method can simulate complex geological bodies and engineering structures, and it has strong adaptability in underground engineering. However, numerical simulation expends too much time and can not express the mapping relation between parameters and responding, so there is limitation in rock failure probability analysis. Responding surface method (RSM) has been developed to solve these problems; the basic thinking is fitting the test samples by polynomial function or artificial neural

network (ANN). But ANN is the method based on experience risk minimization, occurring experience dependence, and extra learning problems.

Support vector machine (SVM) is the machine learning tool which occurred in 1995, which is based on structure risk minimization and solves small sample, nonlinear and localization minimization problems[6]. Arbitrary precision fitting function can be gotten by SVM because of its strong generalizing ability. The paper combines numerical simulation, orthogonal design, PSO-SVM, and Mont-Carlo sampling method, proposed a rock failure probability calculation method. Then applied the method to a tunnel of Jinshandian Ore Mine to prove the feasibility of this method.

2 The Theory of Support Vector Machine and Particle Swarm Optimization

2.1 Support Vector Machine

Support vector machine is the machine learning tool that is based on statistics learning theory and in order to solve multi-dimension function. The fitting SVM theory is as follows.

Firstly using linear regression function $f(x)=w \cdot x+b$ to fit data $\{x_i, y_i\}$, $i=1, \dots, N, x_i \in R^d, y_i \in R$, and supposing that all trained data may be fitted within tolerated precision ε with the linear function. Using nonlinear relation mapping the dada samples from original space to high dimensional characteristic space: $\varphi(x) = (\varphi(x_1), \varphi(x_2), \dots, \varphi(x_N))$, in the highly dimensional space constructing optimal decision function $f(x)=w \cdot \varphi(x)+b$, thus the complex nonlinear estimation function changes to linear estimation function in high dimensional space. The standard support vector machine of Vapnik[7] and least square support vector machine[8] select respectively different allowed slack variables, the former selects ξ and the latter selects two norm of ξ . For least square support vector machine, the optimization problem becomes:

$$\begin{aligned} \min J(w, \xi) &= \frac{1}{2} w^T \cdot w + c \sum_{i=1}^N \xi_k^2 \\ s.t : y_k &= \varphi(x_k) \cdot w^T + b + \xi_k, k = 1, \dots, N. \end{aligned} \quad (1)$$

Solving the optimization problem by Lagrange method:

$$\begin{aligned} L(w, b, \xi, a) &= \frac{1}{2} w^T \cdot w + \\ & c \sum_{k=1}^N \xi_k^2 - \sum_{k=1}^N a_k (w^T \cdot \varphi(x_k) + b + \xi_k - y_k) \end{aligned} \quad (2)$$

In above formula, $a_k, k=1, \dots, N$, are Lagrange multipliers. According to the optimization conditions, solve partial derivatives for w, b, ξ, a , and make them equate zero, then:

$$\begin{aligned} w &= \sum_{k=1}^N a_k \varphi(x_k), \sum_{k=1}^N a_k = 0, a_k = c \xi_k, \\ w^T \cdot \varphi(x_k) + b + \xi_k - y_k &= 0 \end{aligned} \quad (3)$$

Define $k(x_i, x_j) = \varphi(x_i) \cdot \varphi(x_j)$, $k(x_i, x_j)$ are symmetrical function matching Mercer conditions. According to formula (4), the optimization problem changes to solve the system of linear equation.

$$\begin{bmatrix} 0 & 1 & \cdots & 1 \\ 1 & k(x_1, x_1) + 1/c & \cdots & k(x_1, x_l) \\ \vdots & \vdots & \ddots & \vdots \\ 1 & k(x_N, x_N) & \cdots & k(x_N, x_N) + 1/c \end{bmatrix} \begin{bmatrix} b \\ a_1 \\ \vdots \\ a_N \end{bmatrix} = \begin{bmatrix} 0 \\ Y_1 \\ \vdots \\ Y_N \end{bmatrix} \quad (4)$$

Finally the nonlinear model has been gotten as follows:

$$f(x) = \sum_{k=1}^N a_k k(x, x_k) + b \quad (5)$$

The system of linear equations can be solved by least square method, so the LS-SVM has been named for the training method; it has faster training speed than standard SVM. In formula (7), there are three kernel functions: polynomial kernel function, Gauss kernel function and sigmoid kernel function. Research states that Gauss kernel function can get good calculation result, so the paper adopts Gauss kernel function as kernel function.

2.2 Particle Swarm Optimization

The research stated that penal factor c and kernel parameter affect the forecast precision evidently. But SVM theory did not provides the method of parameters ascertaining. So the paper introduced global optimization algorithm -particle swarm optimization to search them. Particle swarm optimization is an evolutionary computing technology simulating the birds flying and preying food. PSO shares many similarities with evolutionary computation techniques such as genetic algorithm, and in the different, it has not “Crossover” and “Mutation” operations, but making particles swarm move to higher fitting function value with gradient descent algorithm. Supposing there are m particles in a population, one of the particles is denoted with $x_i = [x_{i1}, x_{i2}, \dots, x_{il}]$, ($i \leq m$) in l -dimension space, judged by fitting function, then the particles are iterated as following formulas:

$$v_{id}^k = w_i v_{id}^{k-1} + c_1 * rand_1 * (pbest_i - x_{id}^{k-1}) + c_2 * rand_2 * (gbest - x_{id}^{k-1}) \quad (6)$$

$$x_{id}^k = x_{id}^{k-1} + v_{id}^k \quad (7)$$

In above equations, $i=1,2,\dots,m$; $d=1,2,\dots,l$. where k is current iteration step, c_1 and c_2 denote two different positive constants, $rand_1$ and $rand_2$ are two independent random between 0 and 1, $pbest_i$ is local optimal solution of the i th particle in current iteration, $gbest$ is global optimal solution of current iteration, w_i is momentum item coefficient, which may change search ability by adjusting its value.

3. The Mining Tunnel Failure Probability Analysis Based on PSO-SVM

For most complex underground engineering, mechanics behavior need numerical simulation (Finite element, Finite difference, discrete element et), the most problem of rock failure calculation based on numerical simulation is the functional equation can not be expressed explicitly, and time consumption of numerical simulation brings difficulties in the Monte-Carlo arithmetic and numerical simulation while the failure probability is small. Artificial neural network is based on experience risk minimization principle, having

extra-learning problem. General support vector machine has the human blindness in parameters selection. Aiming at above problems, the paper proposed an integration method combining support vector machine, Monte-Carlo arithmetic, numerical simulation and orthogonal design principle, constructed the flowchart of mining tunnel surrounding rock failure probability analysis. The process of the analysis method is as follows(Figure 1):

1)According to the survey and test information of rock, select random parameters and ascertain their distribution, constructs orthogonal and uniformity design schemes and carry out the numerical simulation calculation. Construct learning and test samples for SVM by normalization.

2) Adopts particle individual that is corresponding to penalty factor and kernel parameter, constructs the learning and forecast model by support vector machine. Calculates the fitness value $f(i)$ of each particle individual, so as to reflect the generalizing ability. The fitness function is as follows:

$$f(i) = \min(\max\left\{\frac{|x_j - x'_j|}{x'_j}\right\}, j = 1, 2, \dots, l)) \quad (8)$$

In formula, x_j is the j th test sample forecast value, x'_j is the j th test sample actual value. $j=1, 2, \dots, l$, l is the number of test samples.

3) According to particle swarm optimization, compare fitness value of particle with $fpbest_i$ - the best one of its experience, if $f_i < fpbest_i$, instead $fpbest_i$ with f_i , and instead the prior iteration particle with new particle, ie $fpbest_i = f_i$, $pbest_i = x_i$.

4) Compare the best fitness value of each particle ($fpbest_i$)with the best fitness value of all particles ($fgbest_i$). If $fpbest_i < fgbest_i$, Instead the best fitness value of all particle($fgbest_i$) with $fpbest_i$. At the same time, keep the particle position.

5) Judge if the fitness value or iteration number fitting the convergence criterion, if not continue the new iteration, the particles are flying according to formula(6)(7), get the new particles, and turn to step 2. If fitting the criterion, the calculation ends and output the parameters of SVM. Generally, the iteration number or forecast err is the convergence criterion.

6) Adopt the parameters of SVM, training the forecast model. According to the distribution regulation of random parameters, using Monte-Carlo sampling method to produce the responding indices. Input the responding indices to functional equation Z , calculate the number of times that $Z \leq 0$.

7)Calculate and get the failure probability P_f of surrounding rock, output the calculate result.

4 Engineering Application

The Jinshandian ore mine of Wuhan Steel Processing Company Limited in China is one of the large-scale underground metal mine inland. The mine tri-phase - under 270 mining design is going to adopt large scale structure parameters: sublevel height of 14 m, drift interval of 16 m, tunnel width of 3.6 m and tunnel height of 3.2 m. Surrounding rock security problem is much more serious, as the increase of the setting depth and parametric of tri- phase project. The supporting of the tunnel is cables and lining. That includes arch square

edge wall, the net horizontal width is 3.0m, abutment wall is a height of 2.1~2.3 mm (including embedded part for 2.8m) , arch height is 1.0m, shoring shell thickness is 0.5m and reinforcing cage concrete structure is adopted[5]. The plane strain numerical model is constructed based on studying geologic examination information and design data (Figure 1), the calculation region is between – 270m to – 340m of the mining zone. The original stresses are according to prior research of the Ore Mine as follows:

$$\sigma_x = k_x \sigma_z, \quad \sigma_y = k_y \sigma_z \quad (9)$$

In above formula, k_x is the x horizontal direction stress coefficient which equates 0.8728, k_y is the y horizontal direction stress coefficient which equates 1. σ_z is the vertical ground stress[5].

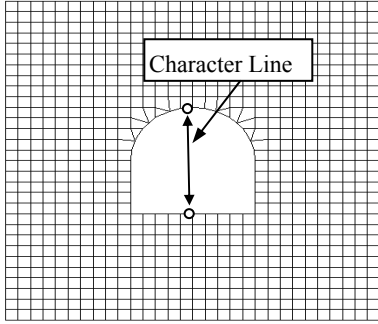


Figure 1 Calculation grid

Table2 Statistical data of random variable

Random variable	Unit	Average value	Standard deviation	Dispersion pattern
Elastic modulus(E)	GPa	5.0	0.60	normal
Cohesion (C)	MPa	1.3	0.45	normal
Friction angle (Φ)	°	45	0.4	normal

There mostly Scarn rock in the computing zone, the elastic-plastic model of Mohr-Coulomb is adopted which is described as follows:

$$f_s = \sigma_1 - \sigma_3 \frac{1 + \sin \phi}{1 - \sin \phi} - 2c \sqrt{\frac{1 + \sin \phi}{1 - \sin \phi}} \quad (10)$$

σ_1 、 σ_3 in the formula are respectively maximal and minor principal stress, c 、 ϕ are respectively cohesive force and internal friction angle of material. According to prior laboratory tests, the elastic modulus, cohesive strength and angle of internal friction vary relatively bigger, the random distribution is shown in Table 2. Other parameters have small discreteness and adopt constant values as Poisson ratio μ equates 0.32, strength of extension equates 1.2Mpa and rock densities is 2600kg/m³. The spray bolt scheme is according to designed parameters that is 10cm of concrete thickness, 2 m of bolt length and 20 cm of bottom plate.

Surrounding rock displacement relative convergence criteria is one of the most used criterions to evaluate the stability of tunnel. Because of the monitoring is necessary in the tunnel construction, this criterion is also used normally. The limiting state equation of tunnel stability evaluation as follows:

$$Z = g(x) = [u] - u(\gamma, E, c, \phi) = 0 \quad (11)$$

In the formula , $[u]$ is top-bottom limit convergence displacement, which belongs to resisting power, referring to norm and empiric value, it is adopted as 50mm in the calculation example. u is the actual value of

top- bottom displacement (functional equation), which is the term of loads, the relation between u and each stochastic variables is unable to express explicitly because of numerical modeling characters.

Also because the numerical simulation expends time, considering the parameters in Table2, respectively according to the orthogonal experimental design table and uniformity design table of 3 factors and 5 levels and carrying out calculation, we get 25 groups of data samples for learning and 5 groups of data samples for forecast. In order to overcome the discreteness of samples, change the original sample data into standard data between 0.2 to1. according to formulae as follows:

$$s = 0.8 \times (d_i - d_{\min}) / (d_{\max} - d_{\min}) + 0.2 \quad (12)$$

in the formula, s is sample of normalization, dmax is the peak value of sample data, and dmin is the minimal value. Studying the samples by PSO-SVM algorithm introduced in the paper which developed by MATLAB, we acquired the optimal SVM model corresponding to kernel parameter σ of 37.89, and penal factor is 321.58. Used this model to forecast the samples, the results are listed in Table2, the samples of 1-25 are learning samples, the samples of 26-30 with star are forecast test samples .

Table2 Comparison between PSO – SVR forecast and numerical calculation for the samples

Test	Displacement of Point A		Relative error	Test	Displacement of Point A		Relative error
No.	PSO-SVR forecast	Numerical simulation	(%)	No.	PSO-SVR forecast	Numerical simulation	(%)
1	0.98	1	2.00	21	0.241	0.233	3.43
2	0.574	0.583	1.54	22	0.278	0.290	4.14
3	0.519	0.526	1.33	23	0.437	0.425	2.82
4	0.564	0.542	4.06	24	0.309	0.317	2.52
5	0.312	0.326	4.29	25	0.394	0.388	1.55
11	0.351	0.361	2.77	26*	0.417	0.402	3.73
12	0.523	0.507	3.16	27*	0.263	0.257	2.33
13	0.207	0.200	3.5	28*	0.486	0.502	3.19
14	0.261	0.253	3.16	29*	0.492	0.479	2.71
15	0.207	0.212	2.36	30*	0.552	0.527	4.74

It is shown in Table2 that the forecast values approach to the numerical calculation results, which means the PSO-SVM model can reflect functional nonlinear relation correctly. The convergence curve of particle swarm optimization is shown in Figure2, which states that it has searched the optimal parameters of SVM rapidly. Figure 3 is how the different kernel parameters affect the forecast accuracy while the penal factor is fixed. The curve shows that it is reasonable that PSO searched parameter and PSO is necessary for improving SVM forecast precision.

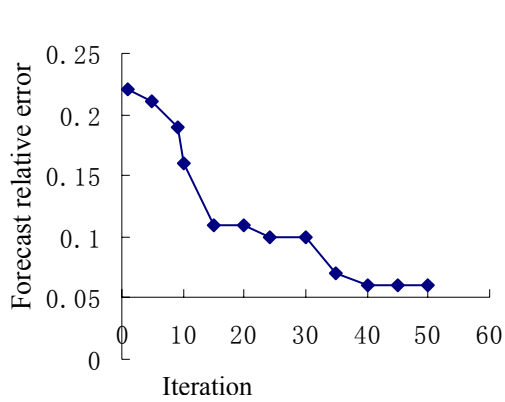


Figure2 The convergence curve of PSO

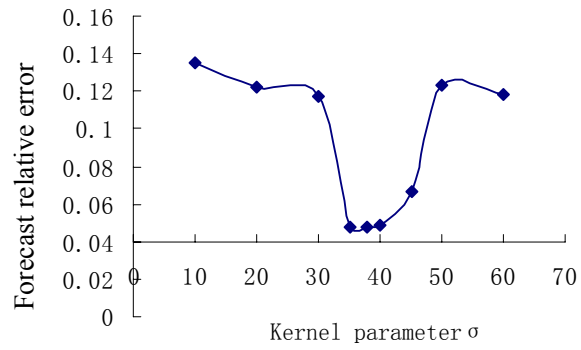


Figure3 Penal factor affecting the forecast accuracy (c=321.58)

After the SVM model has been acquired, according to the distribution of each parameter, random sampling points are produced by Monte – Carlo method. The PSO-SVM sampling number is 105, ie, input 105 groups of parameters to the SVM model and get the corresponding outputting convergence displacements, substitute them to the limit state equation Z which is shown in formula (9), find out the number of samples that according to $Z < 0$, then, we can get failure probability $P_f = 0.027$. Monte – Carlo and numerical simulation direct sampling is the relative accurate method to calculate failure probability, which is shown as testing standard method, however it expends too much time. In the paper, the 2 D numerical model combining Monte – Carlo sampling is adopted for 104 times to calculate the failure probability, which is used to be compared with the PSO-SVM method. The results are shown in Table 3. It is shown that there is small difference between them. That states the PSO-SVM responding surface method is feasible.

Table3 surrounding rock failure probability obtained from computation

Sampling calculation method	Surrounding rock failure probability	Sampling number
Mont-Carlo PSO-SVM	0.027	10^5
Mont-Carlo numerical simulation	0.031	10^4

5 Conclusion

(1) Support vector machine is a machine learning tool based on VC dimension statistics theory which is applied to the structural risk minimization principle. It can overcome the extra-learning problem of artificial neural network. Also, it adopts support vector machine to the surrounding rock failure probability of mining tunnels, and the SVM responding surface description overcomes the problems of conventional mapping methods. Particle swarm optimization arithmetic is adopted to select the SVM parameters, avoiding the human blindness of SVM parameters selection, improving the forecast precision.

(2) For the mining tunnels that do not have explicit function equations, the mining tunnel rock failure probability based on PSO-SVR is a promising method. The application states that it is feasible, and the calculation result is satisfied. The method can directly combine the numerical calculating programs such as ANSYS、FLAC3D、ADINA, etc, and the ability to do this is very practical and helpful.

(3) The representation of samples is the necessary condition that guarantees the fitting or generalizing precision of SVM; the schemes of orthogonal design and uniformity design adopting less testing schemes and get better representation, which are good methods to produce samples. The paper adopts plan models, and the calculations are not very complex. For a more complex calculation, such as a 3D model, in order to guarantee the fitting accuracy of the nonlinear functional equation, the samples number and how to select samples need more research.

Acknowledgements

The authors would like to deeply appreciate the Project supported by the State Program of National Natural Science of China (Grant No. 50574022, 50508007) and Chinese postdoctoral fund (20070420205).

Reference

1. Jing, S.T.. The Research Development of Probability Analysis of Underground Structure. Journal of Shijiazhuang Railway Institute, 1995, 18 (2).13-19.
2. Zhao, G.F. The Theory and Application of Engineering Structure. Press of Dalian Technology University, 1996.
3. Xu, J., Zhang, L.M. and Zheng, Y.R. Reliability Calculation Method Based on Numerical Simulation and BP Network. Chinese Journal of Rock Mechanics and Engineering, 2003, 22 (3). 395-399.
4. Chen, J.K., Zhu, D.F., Zhao, W.Q., et. Structure Reliability Analysis of Underground Cavern Based on Response Surface Method, 2005, 24 (2). 351-356.
5. University of Science and Technology Beijing. Researching the Dynamic Pressure and Control Technology of Mine Stope tunnels in Hard Mining Orebody, 2003,12. 115-128.
6. Zhao, H.B., Feng, X.T. and Yin, S.D.. Classification of Engineering Rock Based on Support Vector Machine. Rock and Soil Mechanics, 2002, 23 (6). 698-701.
7. Vapnik, V.N. An Overview of Statistical Learning Theory. IEEE Trans Neural Network, 1999, 10 (5). 988-999.
8. Suykens, J.A.K. and Vandewalle, J. Least Square Support Vector Machine Classifiers. Neural Processing Letters, 1999, 9 (3). 293-300.

STUDY ON EXTENICS PREDICTION OF ROCKBURST IN HIGH GROUND STRESS ZONE OF DEEP BURIED TUNNEL

YI-GUO XUE, SHU-CAI LI, YAN ZHAO, MAO-XIN SU and HAI-YAN LI

Geotechnical & Structural Engineering Research Center of Shandong University

No.73 Jingshi Road, 250061, Jinan, P.R. China

Deep buried tunnel in mining is operated under complex geological environments with "three high and one disturbance" [1], namely the high in-situ stress, high ground temperature, high karst hydraulic pressure, and intense mining disturbance for long time, which significantly changed the rock mass structures, physical properties and mechanical responses. In this case, rockburst, which is usually characterized by the high burstiness, serious perniciousness and no obvious omen, becomes a common geologic hazard in deep buried tunnel. This paper firstly gathered the distinguishing standards for predicting rockburst in deep buried tunnel both domestically and internationally. The matter-element is then applied to improve the function with extenics. A matter-element model is finally proposed to forecast rockburst. Throughout this study, it is proved that the method developed in this paper is reliable, precise and useful for predicting rockburst in deep buried tunnel.

1 Introduction

The rockburst has been a world-class problem since first reported in Britain in 1738 [2]. Many scholars have done a lot of work to try and fix the problem. They have made various criteria to analyze rockburst intensity, energy, stiffness, fracture damage, power disturbances, fractal and mutation [3]. For example: the Norway Russense criterion(I_s/σ_{mas}), the former Soviet Union Turchaninov criterion ($\sigma_c/(\sigma_t+\sigma_l)$), the South Africa Hock criterion($\sigma_\theta+\sigma_c$), the Poland Kidybinski energy criterion($W_{ET}=\Phi_{SP}/\Phi_{ST}$), the Sweden Anderson criterion($\sigma_{\theta max}/\sigma_c$), the China's Lu Jia-you criterion($[\sigma_\theta]\geq K_s[\sigma_c]$), the criteria made by JIA Yu-ru, Wang Yuan-han and WANG Lan-sheng, XU Lin-sheng's, geological prediction method, SHAN Zhi-gang's lithology criteria($\sigma_\theta/\sigma_c>K_s$), HOU Fa-liang's depth prediction critical($H_{cr}=0.318R_b(1-\mu)/(3-4\mu)\gamma$). All of the above scholars have made in-depth studies of the theory about rockburst, and also have achieved a certain degree of prediction. However, the emergence of rockburst is combined results affected by many factors. Only the individual factor of criteria above rockburst is discussed, which would lead to one-sidedness and limitations.

Therefore, in recent years, some of the latest and modern methods of science and technology have been applied to forecast rockburst. For example, WAGN Yuan-han [4] and TAN Yi-an[5] adopted a fuzzy mathematics comprehensive evaluation method to forecast occurrence of rockburst and the intensity or size of the forecast. FENG Xia-ting[6] use artificial neural networks to predict rockburst. XIE He-ping[7] made fractal analysis about mines in forecasting rockburst. Although the scholars have put forward a variety of theories, criteria and methods of rockburst, the existing prediction method on rockburst is hard to meet the needs of engineering due to the complexity of rock mass itself and a variety of geo-environmental factors. Therefore, the new method combined many factors is need to predict rockburst.

2 Theory Exterics

The extenics[8-11] is a new subject, created by Professor Cai Wen of China in 1983, which is a method of dealing with problems from both qualitative and quantitative. Extenics theoretical system includes elementary theory, logical extension and extension set theory.

2.1 Matter-Element Theory

In Matter-element theory, the triples group includes things, characteristics and value between things, and characteristics, recorded as R-(things, characteristics, value), which can be stated by easy way.

$$R = R_i(N_i, c_i, v_i) = \begin{bmatrix} N_i & c_1 & v_1 \\ & c_2 & v_2 \\ & \dots & \dots \\ & c_n & v_n \end{bmatrix} \quad (1)$$

Where R is n-dimensional matter-element, N is the name of things, c is the characteristics, v is value of corresponding c-characteristics, which are the three elements of matter-element.

2.2 Classical Domain

Based on matter-element theory, the classical domain can be defined as follows:

$$R_{0j} = (N_{0j}, C_i, V_{0ji}) = \begin{bmatrix} N_{0j} & C_1 & V_{0j1} \\ & C_2 & V_{0j2} \\ & \vdots & \vdots \\ & C_n & V_{0jn} \end{bmatrix} = \begin{bmatrix} N_{0j} & C_1 & \langle a_{0j1}, b_{0j1} \rangle \\ & C_2 & \langle a_{0j2}, b_{0j2} \rangle \\ & \vdots & \vdots \\ & C_n & \langle a_{0jn}, b_{0jn} \rangle \end{bmatrix} \quad (2)$$

Where N_{0j} is the first j levels of division quality; C_i is the characteristics of quality grade N_{0j} ; X_{0ji} is the provisional scope of N_{0j} about C_i .

2.3 Section Domain

The section of the domain can be expressed as follows:

$$R_p = (P, C, V_{pi}) = \begin{bmatrix} P & C_1 & V_{p1} \\ & C_2 & V_{p2} \\ & \vdots & \vdots \\ & C_n & V_{pn} \end{bmatrix} = \begin{bmatrix} P & C_1 & \langle a_{p1}, b_{p1} \rangle \\ & C_2 & \langle a_{p2}, b_{p2} \rangle \\ & \vdots & \vdots \\ & C_n & \langle a_{pn}, b_{pn} \rangle \end{bmatrix} \quad (3)$$

Where P is all of the quality and grade; V_{pi} is the section domain of P .

2.4 Matter-element to be evaluated

The collected data or the results of the analysis can be indicated by matter-element about assessment project P_0 .

$$R_0 = (P, C, V_{pi}) = \begin{bmatrix} P_0 & C_1 & X_1 \\ & C_2 & X_2 \\ & \vdots & \vdots \\ & C_n & X_n \end{bmatrix} \quad (4)$$

Where P_0 is assessment project, X_i is value of P_0 about C_i .

2.5 Weighted Coefficient

The weighted coefficient is quantization coefficient of importance of the quantitative factor reflected Evaluation criteria, and different weights coefficient will be different results. In order to reasonably determine the weights in this paper a simple method of correlation function to determine weights coefficient.

$$r_{0ji}(v_i, V_{0ji}) = \begin{cases} \frac{2(v_i - a_{0ji})}{(b_{0ji} - a_{0ji})} & v_i \leq \frac{a_{0ji} + b_{0ji}}{2} \\ \frac{2(b_{0ji} - v_i)}{(b_{0ji} - a_{0ji})} & v_i \geq \frac{a_{0ji} + b_{0ji}}{2} \end{cases} \quad (i=1, 2, 3, \dots, n; j=1, 2, 3, \dots, m) \quad (5)$$

2.6 The Quality Level of Correlation to be evaluated

The correlation about all levels j of individual evaluation indicators v_i in evaluation district as follows:

$$K_{0j}(v_i) = \begin{cases} \frac{\rho(v_i, V_{0ji})}{\rho(v_i, V_{pi}) - \rho(v_i, V_{0ji})} & \rho(v_i, V_{pi}) - \rho(v_i, V_{0ji}) \neq 0 \\ -\rho(v_i, V_{pi}) - 1 & \rho(v_i, V_{pi}) - \rho(v_i, V_{0ji}) = 0 \end{cases} \quad (6)$$

2.7 Calculating Correlation of all levels of Matter-Element to be evaluated

The correlation District level j of District P to be evaluated as follows:

$$K_{0j}(p) = \sum_{i=1}^m \alpha_i K_{0j}(v_i) \quad (7)$$

2.8 Evaluated Levels to determine

If $K_{j\max}(p) = \max_{j \in \{1, 2, 3, \dots, m\}} K_{0j}(p)$, then p belongs to level j .

$$\bar{K}_{0j}(p) = \frac{K_{0j}(p) - \min_j K_{0j}(p)}{\max_j K_{0j}(p) - \min_j K_{0j}(p)}, \quad j^* = \frac{\sum_{j=1}^m j \cdot \bar{K}_{0j}(p)}{\sum_{j=1}^m \bar{K}_{0j}(p)} \quad (8)$$

Then j^* is eigenvalue-level variables of P .

2.9 Improved Matter-Element Model of Comprehensive Evaluation

Improved matter-element model of comprehensive evaluation is given about rockburst evaluation; the correlation function expression of classic matter-element model of comprehensive evaluation can be fully retained, only the distance expression is changed.

(1) The indicators is better while the value is smaller t

$$\rho(X_i, X_{0ji}) = \begin{cases} a_{0ji} - X_i, & X_i < a_{0ji} \\ X_i - b_{0ji}, & X_i \geq a_{0ji} \end{cases} \quad (9)$$

(2) The indicators is better while the value is bigger

$$\rho(X_i, X_{0ji}) = \begin{cases} a_{0ji} - X_i, & X_i \leq b_{0ji} \\ X_i - X_{0ji}, & X_i > b_{0ji} \end{cases} \quad (10)$$

(3) The indicators with appropriate value to level range

$$\rho(X_i, X_{0ji}) = \begin{cases} a_{0ji} - X_i, & X_i < S_i \\ X_i - b_{0ji}, & X_i \geq S_i \end{cases} \quad (11)$$

Where S_i is appropriate value, and its value is $a_{0ji} \leq S_i \leq b_{0ji}$, when $S_i = a_{0ji}$, it points to (1); when $S_i = b_{0ji}$, it points to (2), when $S_i = 1/2(a_{0ji} + b_{0ji})$, it points to classic situation. This shows the classic case and (1), (2) the circumstances are special case of (3).

3 Extenics Forecasting Examples about Rockburst

3.1 Project Overview

The Jinping Stage two Hydropower Station is located in the main stream of Yalong river bend. The region have suffered Indo-China, Yanshan, especially the Himalayan movement since Mesozoic, and have formed a series of tile-shaped again and again thrust fault, stratigraphic inversion, "A"-type lying folds and stretching lineations and klippe formed along the fault structure. Rocks exposed are follows: the Lower Paleozoic is clastic rocks;The Upper Paleozoic and Mesozoic metamorphism are carbonate rocks, clastic rocks and basalt,volcaniclastic rocks; And the metamorphic rocks, Paleozoic carbonate rocks, clastic rocks and the Emeishan basalt, Mesozoic clastic rocks, clay rock in former Sinian. The project area is located in height stress district. The tunnel depth is 1500 ~ 2000m, the maximum depth is about 2500m.

3.2 Project Overview

The rockburst criterion is four categories as followings:

(1) σ_θ/σ_c , The emergence of rockburst is correct to the stress, σ_θ is the largest tangential stress, σ_c is uniaxial compressive strength of rock. The ratio the greater, the possibility of rockburst occurred the greater. (2) σ_c/σ_t , the emergence of rockburst is related to lithology, and σ_t is the uniaxial tensile strength of rock, the ratio smaller, the intensity of rockburst larger. (3) W_{et} , the emergence of rockburst is related to energy, W_{et} is elastic energy index, and its value the greater the energy release when damaging is also more, which reflects the existence of rockburst and its intensity. (4) I_s , the rock will sharp fracture after the peak strength, which can be expressed by degrees of brittle. The rock brittleness index is the ratio of total peak intensity before deformation to permanent deformation. The greater the ratio, the higher the brittleness. Taking these four criteria of rockburst, the relationship between rockburst intensity and master can be taken as follows:

Table 1 relation between rockburst and the control factors

	no rockburst	weak rockburst	intermediate rockburst	strong rockburst
σ_θ/σ_c	<0.3	0.3~0.5	0.5~0.7	>0.7
σ_c/σ_t	>40	40~26.7	26.7~14.5	<14.5
W_{et}	<2.0	2.0~3.5	3.5~5.0	>5.0
I_s	<3.5	3.5~5.5	5.5~7.0	>7

3.3 Establishment of matter-element model of rockburst

The rockburst active type of matter-element can be described:

$$R = (N, C, V) = \begin{bmatrix} N & c_1 & v_1 \\ & c_2 & v_2 \\ & c_3 & v_3 \\ & c_4 & v_4 \end{bmatrix} = \begin{bmatrix} \text{rockburst intensity} & \text{rock stress} & \sigma_\theta / \sigma_c \\ & \text{lithology} & \sigma_c / \sigma_t \\ & \text{engery} & W_t \\ & \text{deformation ratio} & I_s \end{bmatrix} \quad (12)$$

According to intensity in table 1, the rockburst can be divided into four categories: non-rockburst, weak rockburst, intermediate rockburst and strong rockburst, which were recorded as " N_{01} ", " N_{02} ", " N_{03} " and " N_{04} ".

3.4 Determining the Classical Domain, Section Domain and Matter-element to Be Evaluated.

(1) Classical domain,

Based on table 1, the classical domain matter-element is constructed as follows:

$$\begin{aligned}
R_{01} = (N_{01}, C, X_{01}) &= \begin{bmatrix} N_{01}, & c_1, & \langle 0,0.3 \rangle \\ & c_2, & \langle 40,50 \rangle \\ & c_3, & \langle 1.0,2.0 \rangle \\ & c_4, & \langle 2,3.5 \rangle \end{bmatrix} & R_{02} = (N_{02}, C, X_{02}) &= \begin{bmatrix} N_{02}, & c_1, & \langle 0.3,0.5 \rangle \\ & c_2, & \langle 26.7,40 \rangle \\ & c_3, & \langle 2.0,3.5 \rangle \\ & c_4, & \langle 3.5,5.5 \rangle \end{bmatrix} \\
R_{03} = (N_{03}, C, X_{03}) &= \begin{bmatrix} N_{03}, & c_1, & \langle 0.5,0.7 \rangle \\ & c_2, & \langle 14.5,26.7 \rangle \\ & c_3, & \langle 3.5,5.0 \rangle \\ & c_4, & \langle 5.5,7.0 \rangle \end{bmatrix} & R_{04} = (N_{04}, C, X_{04}) &= \begin{bmatrix} N_{04}, & c_1, & \langle 0.7,1.0 \rangle \\ & c_2, & \langle 10,14.5 \rangle \\ & c_3, & \langle 5.0,10.0 \rangle \\ & c_4, & \langle 7.0,10.0 \rangle \end{bmatrix}
\end{aligned} \quad (13)$$

(2) Section domain and its matter-element is expressed as:

$$R_p = (P, C, X_p) = \begin{bmatrix} P, & c_1, & \langle 0,1 \rangle \\ & c_2, & \langle 10,50 \rangle \\ & c_3, & \langle 1.0,10.0 \rangle \\ & c_4, & \langle 2,10 \rangle \end{bmatrix} \quad \begin{bmatrix} P, & c_1, & X_{p1} \\ & c_2, & X_{p2} \\ & c_3, & X_{p3} \\ & c_4, & X_{p4} \end{bmatrix} = \begin{bmatrix} P, & c_1, & \langle a_{p1}, b_{p1} \rangle \\ & c_2, & \langle a_{p2}, b_{p2} \rangle \\ & c_3, & \langle a_{p3}, b_{p3} \rangle \\ & c_4, & \langle a_{p4}, b_{p4} \rangle \end{bmatrix} \quad (14)$$

Where P is all the levels of rockburst activities, that is, P includes no rockburst, rockburst weak, intermediate and strong rockburst, C_i is the characteristic parameters of P , which is on behalf of all range of C_i , that is, the domain section.

(3) Matter-element to be evaluated

The parameters of activity level in tunnel are judged by matter-element:

$$R_x(m) = (N_x(m), C, X) = \begin{bmatrix} P, & c_1, & X_1(m) \\ & c_2, & X_2(m) \\ & c_3, & X_3(m) \\ & c_4, & X_4(m) \end{bmatrix} \quad (15)$$

Where $N_x(m)$ is the first m sites, C_i is rockburst activity of this site, Parameters X_i is parameter value.

3.5 Correlation of Calculation Prediction Samples with Various Levels.

The correlation of rockburst activity parameters of samples to be evaluated with various levels.

$$K_j(X_i(m)) = \begin{cases} \frac{-\rho(X_i(m), X_{0ji})}{|X_{0ji}|}, & X_i(m) \in X_{0ji} \\ 0.5, \text{ while } X_i(m) = a_{0ji} \quad \text{or} \quad b_{0ji} \\ \frac{\rho(X_i(m), X_{0ji})}{\rho(X_i(m), X_{pi}) - \rho(X_i(m), X_{0ji})}, & \text{while } X_i(m) \notin X_{0ji} \end{cases} \quad (16)$$

Where

$$\begin{aligned}
\rho(X_i(m), X_{0ji}) &= |X_i(m) - 0.5 \times (a_{0ji} + b_{0ji})| - 0.5 \times (b_{0ji} - a_{0ji}) \\
\rho(X_i(m), X_{pi}) &= |X_i(m) - 0.5 \times (a_{pi} + b_{pi})| - 0.5 \times (b_{pi} - a_{pi}) \\
K_j(N_x(m)) &= \sum_{i=1}^4 \alpha_{ij}(m) K_j(X_i(m)), \quad j=1,2,3,4, \quad \sum_{i=1}^4 \alpha_{ij}(m) \leq 1
\end{aligned} \quad (17)$$

Where i is parameter, $i=1,2,3,4$; j is rockburst level, $j=1,2,3,4$; m is sample.

3.6 Correlation of Calculation Prediction Samples with Various Levels

In order to verify the effectiveness above-mentioned matter-element model, Selecting AK11+100~AK10+100 of the transport tunnel from in Jinping as example. The paragraph is a marble lithology. Result shows that the weaker sections may occur strong rockburst. The actual excavation of the situation that the rockburst occurred(Figure 1).

The method in accordance with the above extension is used to comprehensively evaluate rockburst. The weights coefficient $\omega_1 = 0.3$, $\omega_2 = 0.2$, $\omega_3 = 0.3$, $\omega_4 = 0.2$. The evaluation results and the actual situation are in the basic line. This method of forecasting accuracy rate of 89.1 percent, The result shows that the matter-element model is effect in forecasting rockburst



Figure 1 Rockburst photo

4 Conclusions and Future Work

In this paper, the matter-element model within extenics is used to predict rockburst. The author gathered the distinguishing standard of rockburst in a deep buried tunnel at home and abroad, used the way of Extenics, and applied matter-element to improve the function. He set up a matter-element model to forecast rockburst. The result shows that the matter-element model can predict rockburst with an accuracy rate of 82.1 percent. It has been proven that this method is reliable and precise. At the same time it provided useful experience to prevent rockburst to endanger the tunnel, and was helpful to perfect the forecast of rockburst in a deep buried tunnel. However, the methods still need many improvements.

Acknowledgements

The work described in this paper was substantially supported by a grant from the National Basic Research Program of China(973) (No. 2007CB209407), China Natural Science Fund(No. 50539080), National high-tech research and development technologies (863) (No. 2007AA11Z131) and Hong Kong, Macao Joint Research Fund for Young Scholars Project(No. 50729904).

References

1. He, M.C. Xie, H.P., Peng, S.P., et al. Study on Rock Mechanics in Deep Mining Engineering. Chinese Journal of Rock Mechanics and Engineering, 2005, 24 (16). 2803-2813.
2. Xu, Z.M, Huang, R.Q., Fan, Z.G., et al. Progress in Research on Rockburst Hazard of Longtunnel with Large Section. Journal of Natural Disasters, 2004,13 (2). 16-24.
3. Zhang, Z.Y., Song, J.B. and Li, P.F. Rockburst Comprehensive Forecasting Method for the Chamber Group of Underground Power House. Advance in Earth Sciences, 2004, 19(3). 451-456.
4. Wang, Y.H., Li, W.D., LEE, P K K, et al. Method of Fuzzy Comprehensive Evaluations for Rockburst Prediction. Chinese Journal of Rock Mechanics and Engineering, 1998, 17 (5).493-501.
5. Tan, Y.A. The Character of Rockburst and the Structure Effect of Rockmass. Science in China(Series B), 1991, (9). 985-991.
6. Feng, X.T. Introduction of Intelligent Rock Mechanics. Beijing: Science Press, 2000.
7. Xie,H.P. Fractal Characteristics and Mechanism of Rocks. Chinese Journal of Rock Mechanics and Engineering, 1993, 12 (1). 28-37.
8. Cai, W., Yang, C.Y. and Lin, W.C. Extension Engineering technique. Technology Literature Press, 1997.
9. Yuan, G.H., Chen, J.P. and Ma, L. Application of Extenics Inevaluating of Engineering Quality of Rock Masses. Chinese Journal of Rock Mechanics and Engineering, 2005, 24 (9). 1539-1544.
10. Qiu, D.H., Chen, J.P., Zhang, B.H., et al. Study on Rockburst Prediction and Prevention in Deep and Over-length Highway Tunnel.Chinese Journal of Underground Space and Engineering, 2006, 2 (6). 950-956.
11. Wang, Y.W. Extension and Fuzzy Method in Evaluating the Engineering Quality of Rock Masses in Underground Mining. Chinese Journal of Rock Mechanics andEngineering, 2002, 21 (1).18-22.

SPOT MONITORING OF BIFURCATION TUNNEL AND COUNTERMEASURES OF CONSTRUCTION TECHNOLOGIES

LI-YUAN YU and SHU-CAI LI

*Research Center of Geotechnical and Structural Engineering, Shandong University
Jinan, 250061, P.R. China*

XIAO-HONG GUO

*CCCC Second Highway Consultants Co,Ltd
Wuhan, 430056, P.R. China*

MING-BIN WANG

*School of Science, Shandong Jianzhu University
Jinan, 250101, P.R. China*

With less unitary cost for joint bridge-tunnel projects, bifurcation tunnel looks promising in the construction of transportation infrastructure. As a new type of tunnel, the excavation manner and support style of bifurcation tunnelling should be adequately investigated in order to ensure the structural stability. Along with the case of the Baziling tunnel, the contents, technique and method of spot monitoring system for bifurcation tunnel are described in detail. The focus of the work is on the surface subsidence, rock deformation, bolt axial stress, and so on. The properties of the deformation and stress in the surrounding rock and supporting system are further analyzed. Blasting dynamic characteristics of rock vibration for the neighborhood segment are also presented. Numerical analysis is done to find out the least appropriate thickness of interval rock column. Finally, the countermeasures for the construction technologies of the bifurcation tunnel are listed.

1 Introduction

As a new type of tunnel which is developed along with construction of transportation infrastructure in the west of China, a bifurcation tunnel consists of four segments namely open-tunnel, large-span-tunnel, multi-arch-tunnel and neighborhood-tunnel. Since the bifurcation tunnel can reduce holistic cost for joint bridge-tunnel projects, there are three tunnels which adopt this structural type in the Hubei Province part of speedway engineering from Shanghai City to Chengdu City.

Bifurcation tunnel simultaneity has characteristics of four types of tunnels. Moreover the corresponding design codes and construction standards have not come forth yet. So, it is very necessary to carry on the spot monitoring job in the construction course. One side, dynamic construction response of surrounding rock and supporting system can be obtained via the site monitoring. Then based on this, design schemes and construction technics may be modified to insure engineerings safe and economical. On the other hand, field monitoring can provide essential data for back analysis of parameters and numerical calculation, so correlative research can be performed favorably^[1-3].

Most of mountain tunnels are excavated with the drill-and-blast construction method in China. So there are many problems that should be studied to protect rock stability when the neighborhood part is dug. For example,

how to find out the least appropriate thickness of interval rock column and the maximal charge amount per delay interval. The linings of constructed tunnels had crazed and flaked due to excavations of the subsequent ones with drill-and-blast method in such as Locoo Colio Tunnel (Italy) and Xiang Shui Gou Tunnel (China)^[4]. Generally, there are two ways that we can use to solve these problems. One is spot vibration velocity monitoring, and the other is numerical simulation.

In this paper, the field monitoring method of bifurcation tunnels is introduced according to the spot measuring job of Baziling Tunnel. Surrounding rock and supporting system are analyzed based on results of site monitoring. Then suitable countermeasures of construction technologies are put forward.

2 Background of Baziling Tunnel

Baziling Tunnel which is one of the most important and difficult engineering of the whole speedway is located at the junction of Yichang City and Enshi City. The exit end of Baziling Tunnel is connected to Sidu River Outsize Bridge. In order to minish width of the bridge and consequently reduce unitary cost, the creationary bifurcation tunnel is designed for the exit segment of Baziling Tunnel. Bifurcation tunnel concretely is that two separate tunnels turn into a single large span tunnel gradually (as shown in Fig.1).

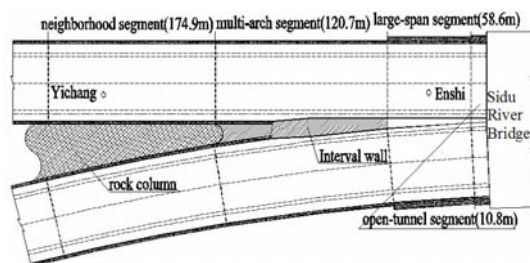


Figure 1 Layout of Baziling bifurcation tunnel

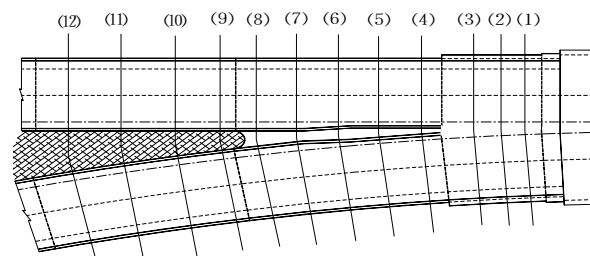


Figure 2 Layout of site monitoring sections

Different segments of the bifurcation tunnel are constructed in different methods. The large-span tunnel is excavated with upper-lower-bench method, while multi-arch-tunnel and neighborhood-tunnel is dug with full-face driving method. The arch part of the tunnel is built with smooth blasting method, while the side-wall parts are excavated by the presplitting blasting method. Smooth and presplitting blasting methods can protect surrounding rock as soon as possible.

The bifurcation tunnel is supported by the complex lining system which is composed of the initial support and subsequent concrete lining. The initial support consists of rock bolt, shotcrete, reinforced net and rigid support. The subsequent concrete lining is designed to bear residual load when the surrounding rock and initial support have come steady basically, so the construction opportunity of subsequent concrete lining must be chosen according to information of spot monitoring. The invert part of subsequent concrete lining is required to construct in the wake of the initial support in weak geological environment.

3 Schemes of Spot Monitoring

3.1 Synthetical Monitoring Transects

Synthetical monitoring transects shown in Fig.2 are designed according to the structural trait, construction technics and geological conditions of Baziling Tunnel. Monitoring transects of left tunnel and right tunnel are laid in the same axial position in multi-arch segment and neighborhood segment so as to observe dynamic response of the tunnel by reason of the construction process

Section 1~3 are located in large-span segment, and their interval is 20m. The layout of measuring points for section 3 is shown as Fig.3. The vault sinkage term is set in the same cross-section with the bolt axial stress term and horizontal convergence term. So metrical results of these three terms could validate each other.

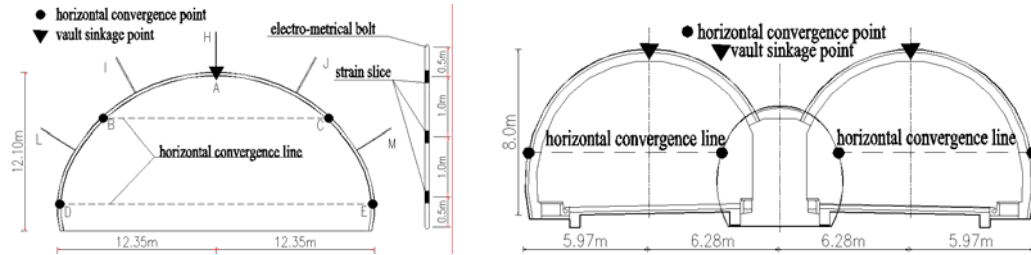


Figure 3 Layout of measuring points in large-span segment and multi-arch segment

Section 4~8 are located in multi-arch segment, and their interval is 25m. The layout of measuring points for section 6 is shown as Fig.3. The bolt axial stress term is not arranged in multi-arch segment.

Section 9~12 are located in neighborhood segment, and their interval is 30m. Their layouts of measuring points that are similar with the multi-arch segment are not presented.

3.2 Surface Subsidence Monitoring Transect

Obvious surface subsidence occurs in the shallow large-span segment when the tunnel is excavated by the sequence 1→2→3 shown in Fig.4. And the subsidence will be observed and recorded in virtue of monitoring points in Fig.4.

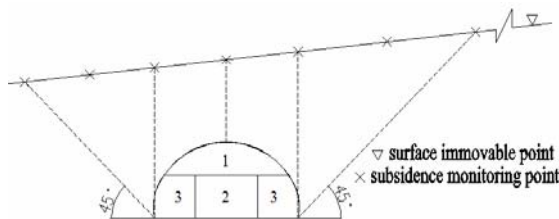


Figure 4 Layout of surface subsidence monitoring points

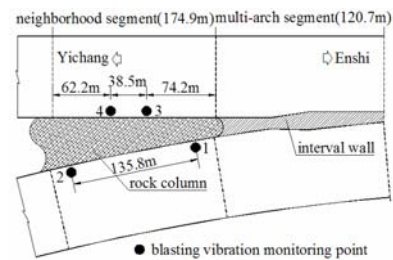


Figure 5 Layout of vibration monitoring points

3.3 Blasting Vibration Test

In order to insure surrounding rock steady, especially to keep rock column of neighborhood segment impervious, the peak value of vibration velocity must be less than certain limit. The rock vibration velocity depends on dynamite quantity charged when the tunnel is excavated. Generally millisecond delay blasting method is adopted, so the maximal charge amount per delay interval could be adjusted by spot vibration velocity test. Arrangement of monitoring points in the longitudinal profile is shown as Fig.5, and that of the vertical cross-section is laid to overlap the horizontal convergence point.

4 Result of Spot Monitoring

4.1 Displacement Monitoring Inside The Tunnel

Deformation of surrounding rock is a macroscopical measurement which is relative to its stabilization tightly. Result of displacement monitoring is the state information of surrounding rock when the tunnel is excavated^[5].

(1) longitudinal characteristic of deformation

The longitudinal deformation curves are shown as Fig.6. The x-coordinate represents distances between monitoring transects and the exit end of Baziling Tunnel, while the y-coordinate denotes the final cumulative values of monitoring terms for each transect. So these curves generally reflect the longitudinal characteristic of tunnel deformation.

Some conclusions can be drawn through Fig.6. Trends of horizontal convergence curve and vault sinkage curve are consistent basically. The two curves both achieve maximal value at the junction of multi-arch segment and neighborhood segment(Section.9), and values of the two terms are also comparatively great at adjoining sections. This means that the junction part of the tunnel is relatively weak. The maximal final cumulative values of the horizontal convergence term and vault sinkage term are 5.81cm and 9.12cm respectively, and these are less than restrictions in relevant codes. So the tunnel engineering is quite steady.

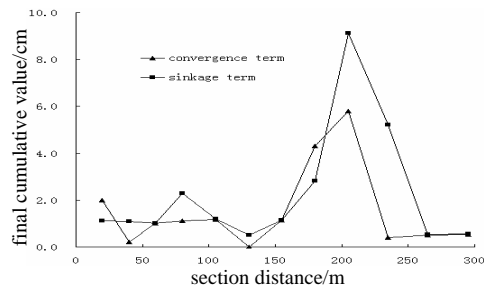


Figure 6 Longitudinal deformation curve of the tunnel

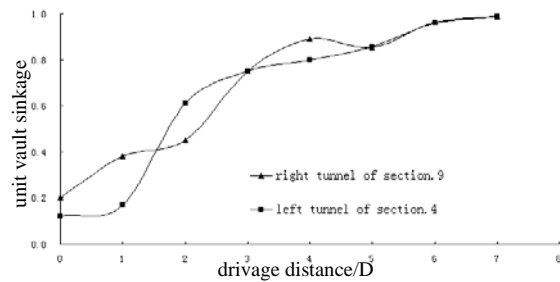


Figure 7 Influence of working faces on vault sinkage curve

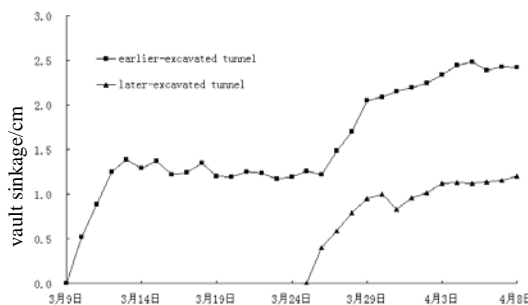


Figure 8 Interaction between left and right tunnels on vault sinkage curve

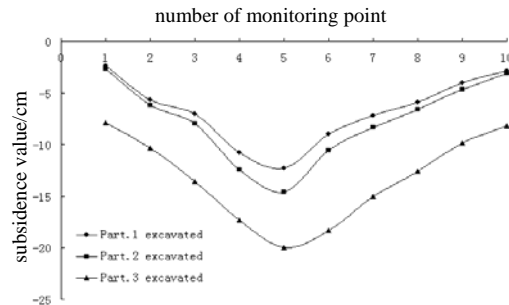


Figure 9 Representative surface subsidence curves

(2) spatial effect of working face

The working face can restrain surrounding rock move inside the tunnel room when the drivage is executed, and this is called "spatial effect of working face". Then surrounding rock which lies in certain range behind the working face could keep steady during some period of time despite no supporting system. Stress release of surrounding rock is stepwise rather than instantaneous owing to spatial effect of working face^[6-9]. The thickness

of interval rock column between right and left tunnels of Baziling Tunnel is very small, so there is not only intense spatial effects but also interaction between spatial effects of the two tunnels.

The mutative curves of vault sinkage term for representative sections along with advancing of working faces are shown as Fig.7, and visible spatial effect of working face is displayed through it. The curve for the earlier-excavated left tunnel of Section.4 becomes smooth when the working face is 5D ahead, while it is 4D for the earlier-excavated right tunnel of Section.9 (D is the span of tunnel). Both are longer than the corresponding distance for single tunnel (3D)^[9]. The causation is interaction between spatial effects of the two adjacent tunnels. The stabilization of a certain section in the earlier-excavated tunnel is influenced by not only working face of this tunnel but also working face of the later-excavated adjacent tunnel.

The curves of vault sinkage term for Section.10 of right and left tunnels are shown as Fig.8, and obvious superposition of spatial effects of working faces is demonstrated through it. The earlier-excavated tunnel becomes stable when stress displacement is completed basically after construction of supporting system. The stress state of surrounding rock suffers once more adjustment when the later-excavated tunnel is dug.

4.2 Surface Subsidence Monitoring

The result of surface subsidence monitoring is shown as Fig.9, and a few conclusions can be educed as follows.

1. Rapid surface subsidence occurs when Part.1 (as Fig.5) is excavated. There are two primary reasons. One is the biggish acreage of excavation, the other is the delayed supporting system as a result of constructional difficulties.
2. The surface subsidence owing to excavation of Part.2 is quite mild. And the reason is that Part.2 is not a load-bearing part despite its large area.
3. Second sharp surface subsidence takes place while Part.3 is excavated. This part lies at arch abutment, so it is very important for stabilization of the tunnel.
4. The surface subsidence curve always appears funnelform at each constructional stage. The subsidence mainly occurs just on top of the tunnel. And this phenomena is consistent with Peck Curve^[10].

4.3 Analysis of Bolt Axial Stress Term

The layout of bolt axial stress monitoring and constitution of electro-metrical bolt are presented as Fig.3. The strain slices which lie near the boundary of tunnel for each electro-metrical bolt are put forward to compare one another mutually (Fig.10)^[11]. A few conclusions can be elicited as follows.

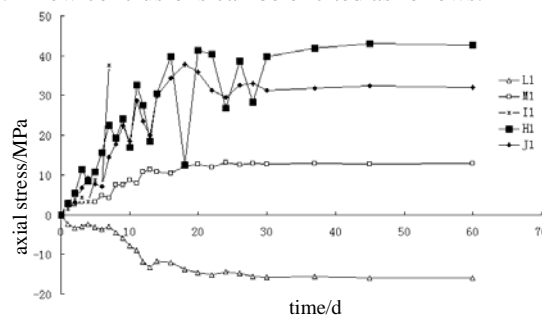


Figure 10 Temporal curves of bolt axial stresses

1. The large-span segment is shallow. Moreover its geological condition is rather weak. So the stress state is adjusted tempestuously when the tunnel is excavated, and vault sinkage value is quite large. The hanging

function of bolts is pretty distinct. The maximal value of tensile stress for H_1 reaches 43Mpa. Tensile stress for J_1 which lies at right spandrel ascends acutely soon after the excavation.

2. All the curves become flat gradually about 30 days after the excavation, and this phenomenon predicates that surrounding rock gradually becomes a new stable state. The strain slice marked as I_1 can not work 8 days after the excavation. The reason is that the slice lies unluckily at cracked zone, and extendibility of the crack leads invalidation of the slice.

3. Axial stresses of bolts located at the skewback part are both small. Additionally the slice marked as L_1 is situated in compression area. Both stress curves of Slice M_1 and L_1 rise lenitively.

4.4 Analysis of Blasting Vibration

(1) blasting vibration test

Blasting vibration test is executed with the scheme shown in Fig.5. Then 7 groups of data are recorded as Table.1.

Table 1. Blasting vibration velocities for monitoring points

NO	Q/kg	1			2			3			4		
		R/m	hor/cm/s	ver/cm/s	R/m	hor/cm/s	ver/cm/s	R/m	hor/cm/s	ver/cm/s	R/m	hor/cm/s	ver/cm/s
1	160	126	0.155	0.107	23	5.497	4.032	110	0.313	0.149	40	3.432	1.983
2	160	109	0.105	0.078	6	-	-	93	0.540	0.489	23	4.733	4.041
3	150	129	0.406	0.346	26	4.098	3.782	113	0.359	0.257	43	2.718	1.857
4	144	112	1.157	0.419	9	6.937	6.781	96	1.124	1.071	26	-	-
5	150	135	0.289	0.549	32	3.130	3.132	119	0.551	0.311	49	2.341	1.623
6	144	138	0.452	-	35	3.071	3.094	122	0.399	0.177	52	2.921	1.392
7	99	105	0.512	-	18	4.926	4.331	105	0.475	0.874	35	3.605	2.757

Data of blasting vibration test can be dealt with the regression formula as follows ^[12].

$$v = K \left(Q^{1/3} / R \right)^{\alpha} \quad (1)$$

Where v is the particle peak vibration velocity (cm/s), Q is the charge amount per delay interval (kg), R is the distance between monitoring point and center of charge (m), K is the coefficient connected with field condition, and α is the attenuation coefficient.

The two following regression equations can be calculated via results of spot blasting vibration test.

$$\text{Horizontal:} \quad v = 172 \left(Q^{1/3} / R \right)^{1.644} \quad (2)$$

$$\text{Vertical:} \quad v = 191 \left(Q^{1/3} / R \right)^{1.48} \quad (3)$$

(2) thickness of interval rock column

In order to find out the least appropriate thickness of interval rock column, the Flac^{3D} Program is used to simulate blasting vibration. Five cases of the thickness are introduced to establish numerical models. The particle peak vibration velocity of the node which lies at the position marked as 1 in Fig.11 is recorded for each case to compare one another mutually (shown as Table.2). Vibration velocity curves of this node for the case 2.5m are displayed as Fig.12. Considering all factors synthetically, 2.5m is chosen as the least appropriate thickness of interval rock column.

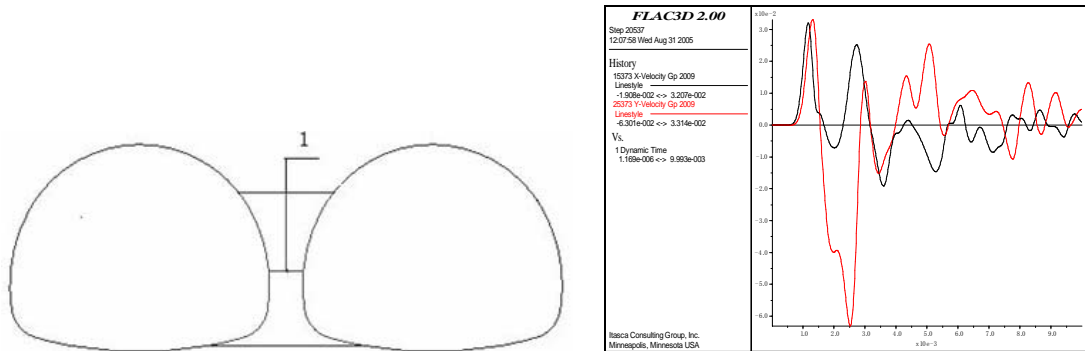


Figure 11 Sketch map for position of key node Figure 12 Temporal curves of x-velocity and y-velocity for the case 2.5m

Table 2. Peak vibration velocities for key node

thickness	1.5m	2.0m	2.5m	3.0m	3.5m
hor/cm/s	6.86	4.74	3.21	3.08	2.84
ver/cm/s	11.77	7.57	6.30	6.22	3.23

5 Countermeasures of Construction Technologies

The following countermeasures of construction technologies are proposed based on results and analysis of spot monitoring of Baziling Tunnel.

- (1) Supporting system of the neighborhood segment should be strengthened because of the large displacements of surrounding rock.
- (2) Construction organization of the large-span segment should be improved due to repetitious adjustments of stress state.
- (3) Working faces of right and left tunnels for multi-arch and neighborhood segments should keep a certain distance which can be given by results of spot monitoring so as to weaken spatial effect of working face.
- (4) The two regression equations could be used to calculate the maximal charge amount per delay interval, and the least appropriate thickness of interval rock column could adopt 2.5m. Technologies of presplitting blasting and smooth blasting are suggested to avoid bad effects of blasting vibration.

References

1. Wang, J., Xia, C.C. and Zhu, H.H. Site Monitoring and Analysis of Non-symmetrical Multi-arch Highway Tunnel. Chinese Journal of Rock Mechanics and Engineering, 2004, 23 (2). 267-271.
2. Schubert, P., Xie, Z.H. and Tang, F.L. Explanation of Monitoring Data during Tunnel Excavation. Journal of Geoscience Translation, 1995, 12 (3). 92-96.
3. Yang, Z.F. and Wang, S.J. A New Research Orientation of Engineering Geology. Journal of Geological Hazards and Environment Preservation, 1996, 7 (1). 1-6.
4. Wang, M.N., Pan, X.M., Zhang, C.M., et al. Study of Blasting Vibration Influence on Close-spaced Tunnel. Rock and Soil Mechanics, 2004, 25 (3). 412-414.
5. Xu, L.S. Displacements Monitoring and Application to Tunnel Engineering. Highway Tunnel, 2000, (2). 1-6.

6. Ozbek, A., Turkmen, S. and Gul, M. The Deformation Evaluation of Kızılac T3A Tunnel. *Engineering Geology*, 2003, 67 (3-4). 309-320.
7. Jeon, J.S., Martin, C.D., Chan, D.H., et al. Predicting Ground Conditions ahead of the Tunnel Face by Vector Orientation Analysis. *Tunnelling and Underground Space Technology*, 2005, 20 (4). 344-355.
8. Kontogianni, V.A. and Stiros, S.C. Induced Deformation during Tunnel Excavation: Evidence from Geodetic Monitoring. *Engineering geology*, 2005, 79. 115-126.
9. Sun, J. and Zhu, H.H. Mechanical Simulation and Analysis of Behaviour Of Soft and Weak Rocks in the Construction of a Tunnel Opening. *Rock and Soil Mechanics*, 1994, 15 (4). 20-33.
10. Peck, R.B. Deep Excavations and Tunneling in Soft Ground. in *Proceedings of 7th International Conference of Soil Mechanics & Foundation Engineering*, (Mexico, 1969).
11. Yao, X.C., Li N. and Chen, Y.S. Theoretical Solution for Shear Stresses on Interface of Fully Grouted Bolt in Tunnels. *Chinese Journal of Rock Mechanics and Engineering*, 2005, 24 (13). 2272-2276.
12. Yang, N.H. and Liu, H. Vibration Field at Tunnel Contour Induced by a Close-in Blasting. *Engineering Blasting*, 2000, 6 (2): 6-10.

RESEARCH ON SAFETY CRITERION OF VIBRATION BY DRILL-BLAST IN SUBWAY TUNNEL ENGINEERING

AI-YUAN ZHENG^{1, 2, 3}, MENG-SHU WANG¹ and YONG-SHENG LIU¹

1 school of civil engineering of Beijing Jiao tong university, Beijing, 100044, P. R. China

2 China Railway Tunnel Group Ltd, Luoyang. 471009, P. R. China

3 Shenzhen Metro Co. Ltd, Shenzhen, 518026, P. R. China

Based on the theoretical research and field test, the failure criteria for blasting vibration on subway tunnel engineering are summarized in the paper. It proposes the calculation formulas of the maximum allowable vibration velocity on intact and fractured rocks, on which the maximum allowable vibration velocity are given about the intact rock and fractured rocks. The safety criterion and effect of blasting vibration in tunnel are studied, as well as the safety control and vibration effect on ground buildings by blasting excavation. On the other hand, the attenuation pattern of seismic waves is diversity under different methods of blasting excavation.

1 Introduction

The blasting excavation is an important practical method, because of its economic and fast characteristics for hard rock tunnels. The blasting vibration damage is catholically regarded as the most damaging characteristic of blasting, and the seismic waves from blasting construction are propagated by the stress waves caused by explosive conditions that can disturb the surrounding rock. The peak value of stress waves is higher than the tensile strength of rock nearby, so that the rock is damaged, and produces different zones such as the crushed and fractured zones. The peak value of stress waves is lower than the tensile strength of rock in the zones far from the source, the elastic waves, so-called blasting seismic wave caused particles to vibrate elastically, which induces the ground to vibrate. Some ground buildings may be damaged when the vibration intensity reaches a certain point. To establish reasonable safety criterion, study and application of new technology for blasting becomes the key of solving the contradiction between blasting constructions and blasting damage.

2 Safety Standard and Criterion for the Blasting Vibration of Subway Tunnel

The stability of the rock tunnel and underground roadway should be evaluated under blasting construction of urban subway. Mass test data and engineering experience^[1,2,3] shows that the vibration speeds of the particle is used for safety criterion for ground buildings, except for some special cases. For example, the new building far from the blasting source is damaged, but some old ground buildings are still undamaged. It is thought that the vibration frequency decreases with increasing distance. Occurrence of the reason of this phenomenon lies in the difference of their natural frequency. It is necessary to adopt the parameters including the vibration velocity and

frequency, not just merely the frequency. The safety standard of blasting vibration from several countries is listed in the Table 1.

Table 1. Failure criterion on vibration of underground engineering

authors	Peak value of vibration velocity of mass points(mm/s)	damage
Hendron 1977	900~1800 460	Damage standard—intermittent damage The minimum peak value of velocity of damaged mass points
Persson 1990	700~1000	Hard rock tunnel
Siskind 1997	305	New fracture or damage caused by tunnel vibration
Fourie and Green 1993	110 390	Minor underground damage Serious tensile damage
Singheta 1995	48	No flaking from roof or pillar

3 Calculation of Maximum Allowable Vibration Velocity for Different Surrounding Rock

Maximum allowable vibration velocity for different surrounding rock is different on the process of blasting construction. The allowable vibration velocity of intact rock is higher, while the one of the fractured rock is lower. Generally for the fractured rock, blasting vibration may cause the tensile stress on the top of the initial fracture, which may lead to larger fracture. Theory of the maximum tensile stress may be used to control the condition of the rock damage. Intensity factor by tensile stress is:

$$K = \sqrt{\pi a \sigma_{\theta}} \quad (1)$$

Where, the tensile stress σ_{θ} on the fracture top can be calculated

$$\sigma_{\theta} = K_{\sigma} \rho C_p V_p \quad (2)$$

Where:

k_{θ} —coefficient of site characteristic; taking 1, when rock mass structure is approximate and structure size and shape is same,

ρ —medium density, kg/m³;

C_p —p-wave velocity in medium, m/s;

V_p —vibration speed consistent with wave propagation direction, for tunnel vault direction of V_p is same with the radial directions of tunnel, m/s.

According to formula (1) and formula (2), the condition of controlling fracture can be give, and can calculate the maximum allowable vibration velocity for the fractured rock. For the fractured rock, when the fracture toughness of the fracture is 1.22 MPa.m^{1/2}, p-wave velocity of the one is 3550m/s, rock density is 2500kg/m³, so on the basis of the different fracture length in surrounding rock, the table 2 can be given:

Table 2. Allowable vibration velocity under different initial fracture length in Rocks of Grade V

initial fracture length/m	0.05	0.1	0.15	0.2
---------------------------	------	-----	------	-----

Maximum Allowable vibration velocity /cm/s	34	24	19.5	17
---	----	----	------	----

According to the data from the table 2, Maximum Allowable vibration velocity of the fractured rock is related with p-wave velocity of rock, density as well as the length of the length of initial fracture. The calculating result in table 2 is approximate with the result (30.5cm/s) of the Siskind(1997) which is brought out based on the new fracture, so the calculating result is credible.

For the intact rock, it can be considered that the stress by blasting may lead tensile failure in the micro fissure. The fracture criterion can be showed:

$$\sigma_{\theta} \geq [\sigma]_{ten} \quad (3)$$

Substituting equation (2) into the equation (3), the maximum allowable vibration velocity is 84cm/s, if the rock tensile strength 12.2MPa, rock density 2650 kg/m³, and p-wave velocity in rock 5500m/s. The calculating result is coincident with the result that given by Persson (1990) under that the vibration velocity is about 70~100cm/s, so the calculating result is credible.

4 Effect and Test Analysis of The Blasting Vibration of Subway Tunnel

The most damage is the blasting vibration effect on the ground buildings. In order to judge the safety of the ground buildings, it is necessary to monitor the vibration velocity of the particle by the seismic effect of blasting construction, and to feedback design and construction and adjust and to optimize the blasting parameters to ensure the safety of the grounding buildings.

Measuring points are mainly arranged on the foundation and column of the important buildings on the blasting construction zone. The test data of blasting vibration is enumerated in Table 3, and Figure 1 is the diagram of vibration velocity of vertical and horizontal direction from 10 m of the blasting source. The allowable vibration velocity of the reinforced concrete is 5cm·s⁻¹, with the distance of 10m from the blasting source. The attenuation law of the test data adopting the method of regression analysis is

$$V = 168.5(Q^{1/3} / R)^{1.54} \quad (6)$$

Adopting the equation (6) , maximum vibration velocity of particles on the tested reinforced concrete is 2.17cm·s⁻¹, with R=10m, and Q=35Kg. The spectrum analysis is adopted by spectrum of the blasting seismic waves tested, based on the fast FFT. The natural frequency of vertical and horizontal vibration is between 100 Hz and 150Hz.

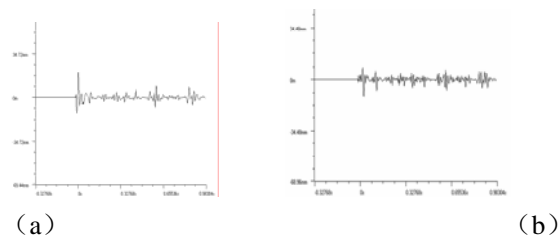


Figure 1 diagram of vibration velocity (a----vertical direction, b---- horizontal direction)

Table 3 test data of blasting vibration of a subway tunnel

serial number	Distance from the blasting source/m	channel	Maximum quantity explosive per segment /kg	Maximum vibration velocity /cm·s ⁻¹	dominant frequency Hz	Direction of vibration velocity
1	10	1#	29.7	2.01	132.51	Vertical
		2#		0.81	137.00	horizontal
		3#		0.78	125.69	vertical
2	11	1#	25	1.54	137.67	vertical
		2#		0.94	131.08	vertical
		4#		1.13	129.85	horizontal
3	15	1#	34	1.18	98.94	vertical
		3#		0.5	107.5	vertical
		4#		0.7	117.8	horizontal
4	10	1#	30	2.14	145.36	vertical
		2#		0.86	145.36	vertical
		3#		0.66	116.92	horizontal
5	11	1#	31	1.97	119.03	vertical
		3#		1.34	109.06	vertical
		4#		0.89	119.09	horizontal

5 Conclusion and future work

The blasting vibration damages and harm are necessary if the drilling and blasting method is adopted in construction of subway tunnels. It is necessary to pay attention to the blasting seismic waves and research the effect of various mediums, buildings and structures in order to fully understand the economic benefit of adopting the blasting technology and reduce the vibration effect from blasting construction. In order to guide blasting construction, the test data and the safety criterion must be paid full attention.

Acknowledgements

The authors wish to thank Professor Huang Ming-Li, Professor Wang Yong-Hong, and Professor Tan Zhong-Sheng from school of civil engineering of Beijing Jiao Tong University for their contributions to this research project.

References

1. Niue, Q. Rock Blasting Mechanism. Northeast Institute of Technology Press, 1986.
2. Zhang, Q.Z. Standard Extract of Regulations of Blasting Safety. Standards Press of China, 1993.
3. Yang, X.L. Harm and Damage on Surrounding Rock from Blasting. Work Report of Postdoctoral Research. Beijing Jiao Tong University, 2001.

NUMERICAL PROCEDURE FOR MODELLING DYNAMIC FRACTURE OF ROCK BY BLASTING

H. Y. LIU, D. J. WILLIAMS and D. M. PEDROSO

Golder Geomechanics Centre, The University of Queensland, St Lucia QLD 4072, Australia

WEI-MIN LIANG

School of Civil Engineering, Henan Polytechnic University, Jiaozuo City Henan Province, China

A generic nonlinear and dynamic finite element modelling technique is implemented to simulate rock fragmentation by blasting. The element elimination method, together with a brittle failure material model, is used as a means to simulate the initiation and growth of fractures in the rock under the effect of a blast-induced dynamic pressure pulse. The blasthole pressure profile after blasting is described using an equation of state, incorporating parameters relating volume, energy and pressure of detonation. Blasting a single borehole in an unbounded rock medium and in a rock mass with one free surface is firstly modelled and compared with the published literatures to calibrate the developed modelling procedure. The method is then applied to investigate simultaneous blasting and consecutive blasting with various detonation delays, in order to improve blast efficiency.

1 Introduction

Blasting has been widely employed in the mining industry for many centuries and it remains a popular method of rock fragmentation to the present day. However, many studies have shown that the situation in current mining production blasting is far from the optimum fragmentation because of the complexities associated with explosives and rock in blasting [1]. It is generally impossible to directly observe more than the final size and shape of the crater or pile of fragments. The space for improving production blasting in mining engineering is huge and the economic potential is enormous. Under this scenario, further accumulation of extensive experimental database is pressing, and the investigation of the fracture and fragmentation mechanism through numerical approaches is also essential. Considerable efforts have been directed towards developing finite, discrete and finite-discrete element methods to simulate rock blasting [2-6] so that the effect of various blast design parameters and explosive types can be studied while limiting the number of field experiments. For the

discrete / finite-discrete element methods, the rock mass is represented by an assembly of jointed elements, i.e. blocks or particles and a fracture is initiated when the joint between the discrete elements exceeds a critical value. However, it requires large amount of data about the spatial distribution, geometrical and mechanical properties of the rock joints, which are normally not readily available. It is the purpose of this paper to model a series of cases in rock blasting using finite element method in order to contribute to a better understanding of the mechanism of rock blasting due to the detonation of an explosive charge and then improve the blasting efficiency.

2 Numerical Methods

In this section we firstly briefly review the explicit dynamic modelling method. An equation of state (EOS) is then introduced to describe the explosive dynamic loads after blasting. After that, a brittle failure material model is employed to model the fracture of rock under impact loads caused by blasting.

2.1 Explicit dynamic modelling method

Simulation of the fracture process of rock by blasting essentially involves the solution of the equations of motion. In a dynamic finite element method, the equations of motion with respect to time t can be written in the following incremental displacement form:

$$M\ddot{U}(t) + C\dot{U}(t) + KU(t) = R(t) \quad (1)$$

where M , C and K are the mass, damping and stiffness matrices, respectively; \ddot{U} , \dot{U} and U are the acceleration, velocity and displacement vectors, respectively; and R is the external load vector. In practical finite element analysis, the equations of motion can be solved by either explicit or implicit integration methods. In this study, the explicit integration method will be used since it has a number of advantages in modelling dynamic fracture of rock by blasting compared with the implicit integration methods such as the Houbolt, Wilson and Newmark methods. In order to outline the advantages, the central difference method, which is one of the most effective explicit integration methods and will be used in this study, is briefly reviewed. The central difference method assumes that

$$\ddot{U}(t) = \frac{1}{\Delta t^2} [U(t - \Delta t) - 2U(t) + U(t + \Delta t)] \quad (2)$$

$$\dot{U}(t) = \frac{1}{2\Delta t} [-U(t - \Delta t) + U(t + \Delta t)] \quad (3)$$

The displacement solution for time $t + \Delta t$ is obtained by considering the equations of motion at time t , i.e. substituting Eqs. 2 and 3 into Eq. 1:

$$\left(\frac{1}{\Delta t^2}M + \frac{1}{2\Delta t}C\right)U(t + \Delta t) = \hat{R}(t) \quad (4)$$

$$\hat{R}(t) = R(t) - \left(K - \frac{2}{\Delta t^2}M\right)U(t) - \left(\frac{1}{\Delta t^2}M - \frac{1}{2\Delta t}C\right)U(t - \Delta t) \quad (5)$$

It should be noted that the solution of $u(t + \Delta t)$ is thus based on using the equilibrium conditions at time t . For this reason, the integration procedure is called explicit. The explicit integration schemes do not require a factorization of the stiffness matrix in the step-by-step solution. If the mass matrix is diagonal and the system has no physical damping, Eq. 4 can be solved without factorizing a matrix, i.e. only matrix multiplications are required to obtain the right-hand side load vector after which the displacement components are obtained.

$$U_i(t + \Delta t) = \hat{R}_i(t) \left(\frac{\Delta t^2}{m_{ii}}\right) \quad (6)$$

where $U_i(t + \Delta t)$ and $R_i(t)$ denote the i th components of the vector $U(t + \Delta t)$ and $\hat{R}(t)$, respectively, and m_{ii} is the i th diagonal element of the mass matrix. If neither the stiffness nor the mass matrix of the element assemblage is to be triangularized, it is also not necessary to assemble K and M , which means that the quantities in Eq. 5 can be calculated on the element level by summing the contributions from each element to the right-hand side load vector $\hat{R}(t)$

$$\hat{R}(t) = R(t) - \sum_i K_i U(t) - \sum_i \frac{1}{\Delta t^2} M_i [U(t - \Delta t) - 2U(t)] \quad (7)$$

where it is important to note that the products $K_i U(t)$ and $M_i [U(t - \Delta t) - 2U(t)]$ are evaluated using K_i and M_i in compacted form, i.e. elemental matrices K_i^e and M_i^e are employed. Since no stiffness and mass matrices of the complete element assemblage need to be calculated, the solution can essentially be carried out on the element level and relatively little high-speed storage is required. The method becomes even more effective if element stiffness and mass matrices of subsequent elements are the same, because in that case it is only necessary to calculate or read from back-up storage the matrices corresponding to the first element in series. Considering the shortcomings of the explicit method, it must be recognized that the integration method is conditionally stable, which requires that the time step Δt must be smaller than a critical value Δt_{cr} . However, the small time step makes the explicit method be especially suitable for the rock blasting modelling since the small time steps ensure numerical accuracy and the duration of rock blasting is very short, i.e. in the order of milliseconds.

2.2 Equation of state for explosive dynamic loads

For rock blasting analysis, the modelling of the interaction behaviour between the detonation products and the surrounding rock mass is a major requirement. In most of existing methods for rock blasting, the pressure-time histories generated from empirical equations are used to model the detonation-induced pressure [2, 4-7]. The approach has many limitations and uses various crude approximations: e.g. it does not take into account any confinement, the shape of the explosive charge, shadowing by intervening objects, and so on. In this study, the pressure of the detonation product depends on the expansion of the blast chamber, which in turn is related to the properties of the surrounding rock mass. The instantaneous pressure of the explosion gases at any time during the expansion process is calculated using the Jones-Wilkens-Lee (JWL) equation of state (EOS) since it is widely used due to its simplicity in hydrodynamic calculations and experimental basis [8]. JWL EOS contains parameters describing the relationship among the volume, energy and pressure of detonation products, which can be written as the following:

$$P = A \left(1 - \frac{w\rho}{R_1\rho_0} \right) \exp \left(-R_1 \frac{\rho_0}{\rho} \right) + B \left(1 - \frac{w\rho}{R_2\rho_0} \right) \exp \left(-R_2 \frac{\rho_0}{\rho} \right) + \frac{w\rho^2}{\rho_0} E_{m0} \quad (9)$$

where P is the pressure, A , B , R_1 , R_2 and w are material constants, ρ_0 and ρ are the densities of the explosive and the detonation products, respectively. The reaction and initiation of the explosive modelled using JWL EOS are determined by a geometric construction using the detonation wave speed and the distance of the material point from the detonation points.

2.3 Brittle failure material model

The tensile failure is the overwhelming failure mode of brittle material under either mode-I, mode-II or mixed-mode loading conditions as defined in fracture mechanics. On the basis of observations using the scanning electron microscope, Tapponnier and Brace [9] concluded that most microcracks are tensile in nature. In the present study, a brittle failure material model coupled with an erosion algorithm based on critical cracking opening displacement is used to describe the brittle failure behaviour of rock under impacting loads caused by the detonation of explosive. In the brittle failure material model, a crack forms when the maximum principal tensile stress at a material point exceeds the tensile strength of the brittle material. Cracking is irrecoverable. However, crack closing and reopening may take place along the directions of the crack surface normals. The brittle failure material model uses the smeared crack model, i.e. it does not track individual macrocracks. Instead, constitutive calculations are performed independently at each material point of the finite element model. The presence of cracks enters into these calculations by the way in which the cracks affect the

stress and material stiffness associated with the material point. Once cracks exist at a point, the components of all vector- and tensor-valued quantities are rotated so that they lie in the local system defined by the crack orientation vectors. The strain rate of the brittle failure material model is decomposed into elastic and cracking strain rates

$$d\boldsymbol{\varepsilon} = d\boldsymbol{\varepsilon}^{el} + d\boldsymbol{\varepsilon}^{ck} \quad (11)$$

where $d\boldsymbol{\varepsilon}$ is the total mechanical strain rate, $d\boldsymbol{\varepsilon}^{el}$ is the elastic strain rate representing the uncracked material, i.e. the continuum between the cracks, and $d\boldsymbol{\varepsilon}^{ck}$ is the cracking strain rate associated with any existing cracks. Since a crack direction is introduced at a material point after a crack forms, it is convenient to define a local Cartesian coordinate system (n, t, s) that is aligned with the crack direction. The transformation between global strains $\boldsymbol{\varepsilon}$ and local strain \boldsymbol{e} and that between local stresses \boldsymbol{t} and global stresses $\boldsymbol{\sigma}$ can be written as

$$\boldsymbol{\varepsilon} = \boldsymbol{T}\boldsymbol{e} \text{ and } \boldsymbol{t} = \boldsymbol{T}^T \boldsymbol{\sigma} \quad (12)$$

where \boldsymbol{T} is a transformation matrix constructed from the direction cosines of the local cracking coordinate system. The relation between the local stresses and the cracking strains at the crack interfaces is written in rate form as

$$d\boldsymbol{t} = \boldsymbol{D}^{ck} d\boldsymbol{e}^{ck} \quad (13)$$

where \boldsymbol{D}^{ck} is a diagonal cracking matrix that depends on the state of the existing cracks. The rate constitutive equations of the brittle failure material model can then be written as

$$d\boldsymbol{\sigma} = \boldsymbol{D}^{el} (d\boldsymbol{\varepsilon} - \boldsymbol{T} d\boldsymbol{e}^{ck}) \quad (14)$$

Pre-multiplying Eq. 14 by \boldsymbol{T}^T and substituting Eq. 12 and 13 into the resulting left-hand side, we can get

$$d\boldsymbol{e}^{ck} = (\boldsymbol{D}^{ck} + \boldsymbol{T}^T \boldsymbol{D}^{el} \boldsymbol{T})^{-1} \boldsymbol{T}^T \boldsymbol{D}^{el} d\boldsymbol{\varepsilon} \quad (15)$$

Substituting Eq. 15 into Eq. 14, we can finally obtain the stress-strain rate equations

$$d\boldsymbol{\sigma} = \left[\boldsymbol{D}^{el} - \boldsymbol{D}^{el} \boldsymbol{T} (\boldsymbol{D}^{ck} + \boldsymbol{T}^T \boldsymbol{D}^{el} \boldsymbol{T})^{-1} \boldsymbol{T}^T \boldsymbol{D}^{el} \right] d\boldsymbol{\varepsilon} \quad (16)$$

In order to simulate the physical fracture of rock in the numerical model, the so-called erosion algorithm is used, which has the capability of treating the excessive element distortion problem. The element is immediately deleted when the material response in an element reaches certain erosion criterion. The deletion process is irreversible, which means when the applied load is reversed, the deleted material will not be able to offer further resistance. This technique can be employed to capture the physical fracture process if no significant reverse loading occurs. There may be a variety of criteria governing the erosion of the material. In the brittle failure material model, when the local direct cracking displacement components at a material point reach the value

defined as the failure displacement, the material point fails and all the stress components are set to zero. If all of the material points in an element fail, the element is removed from the mesh. In this way, the physical separation of rock can be simulated.

3 Calibration of the Numerical Method

In this section, the numerical method described above and available in ABAQUS [10] will be calibrated by modelling the stress wave propagation and fracture process due to blasting in an infinite rock mass and in a rock mass with one free surface, and comparing the results with those well documented in literatures.

3.1 Stress wave propagation and fracture process by blast in an infinite rock mass

Fig. 1 shows the geometrical and numerical models for the simulation of blasting in an infinite rock mass. The model consists of a borehole with a radius of 50 mm in a rock mass (Fig. 1 a). The boundaries of the model are put far away from the interested area, i.e. the vicinity of the borehole, to avoid the influence of the reflected stress waves. The model is simplified as two-dimensional plane strain problem and is discretized into triangular elements. As shown in Fig. 1b, dense elements are used in the vicinity around the borehole, which is the interested area for blasting in an infinite rock mass.

The modelled temporal and spatial distribution of the tangential stress wave and failure by blasting in an infinite rock are depicted in Fig. 2. The stress distributions in the pictures correspond to the major principal stress, which can be referred as the tangential direction stress in terms of the borehole. The grey represents the size of the major principal stress, as shown by the colour label in Fig. 2 a). In Fig. 2 b), the black colour indicates crack and the white colour represents the intact rock mass. In the immediate vicinity of the hole, the wave energy is highly concentrated and produces extensive breakage. This significantly modifies the hole boundary on which the gas pressure subsequently acts. Notice from Fig. 2 a) that the stress field in compression as well as the tensile stresses radiate from the borehole after the detonation, but the stress level decreases as the time increases, which is consistent with the photoelastic results in the PMMA material conducted by Fournery et al. [11]. This decrease is due both to material damping and geometric dispersion. In the leading edge of the stress wave, a biaxial compressive state exists. That is, both the radial stress (not shown in Fig. 2 since it is easily understood) and the tangential stresses (as shown by the colour close to the black end in Fig. 2 a) are compressive, and the radial stress is several times larger than the tangential stress. In the trailing part of the outgoing wave, both stress components are tensile (as shown by the colour close to the white end in Fig. 2a). Since the tangential stresses are the most tensile, the majority of cracks will propagate in the radial direction. Compared with the typical fracture pattern caused by a fully contained explosion [7], it can be seen that the numerical modelling captures the main features around a borehole, i.e. a dense crushed zone immediately around the borehole, a radially fracture zone, followed by a ring of wider spaced radial cracks.

3.2 Stress wave propagation and fracture process by blast in a rock mass with one free surface

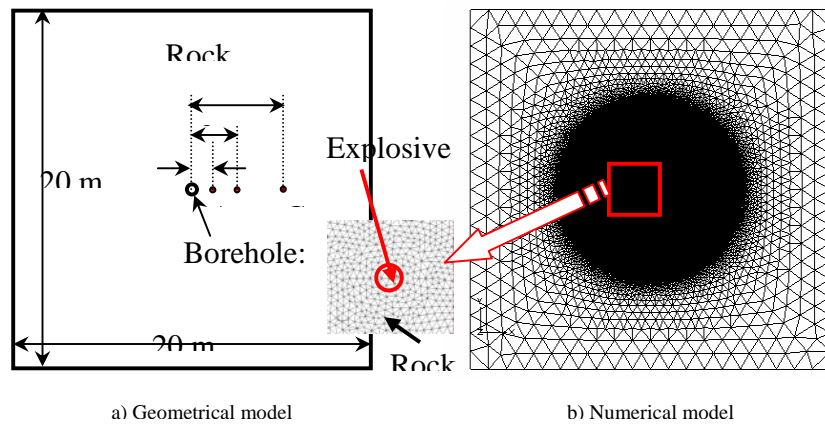


Figure 1 Geometrical and numerical models for blast in an infinite rock mass

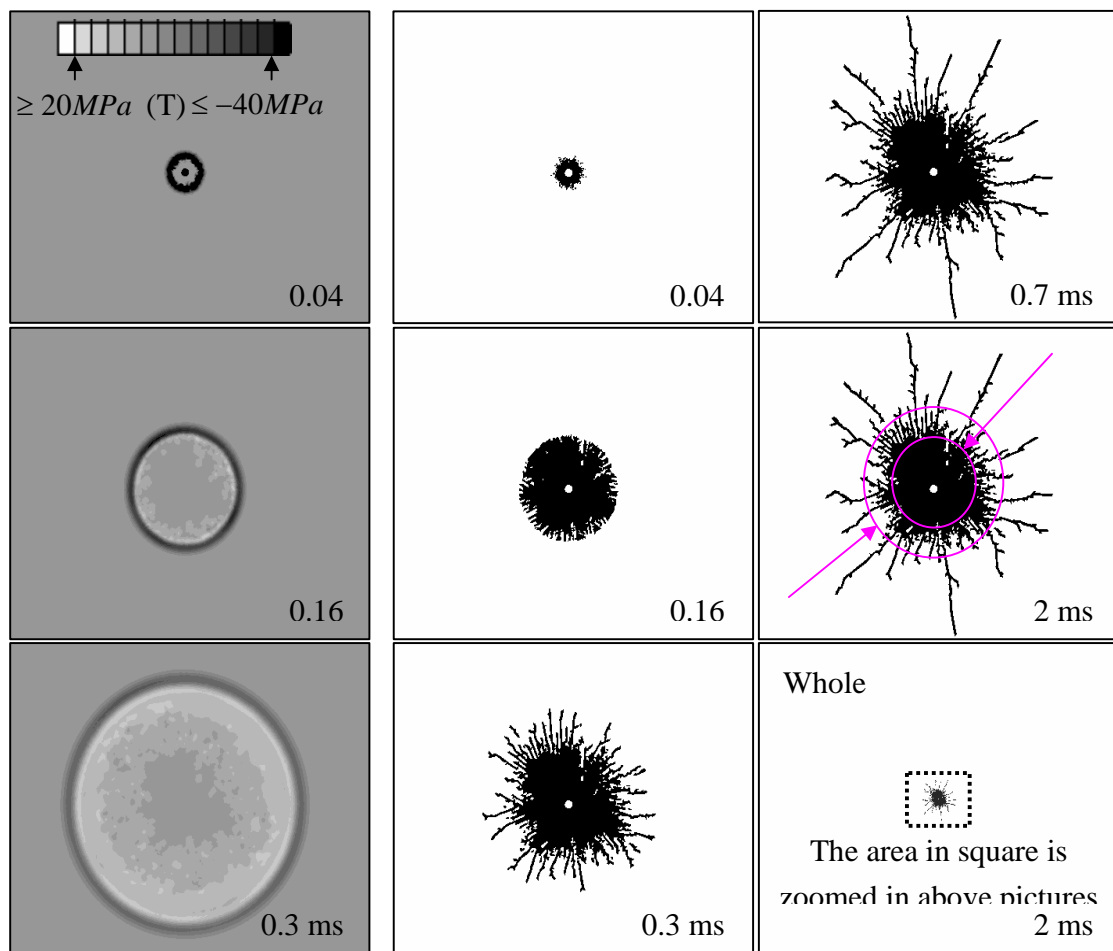


Fig. 2 Stress wave propagation and failure process by blast in an infinite rock

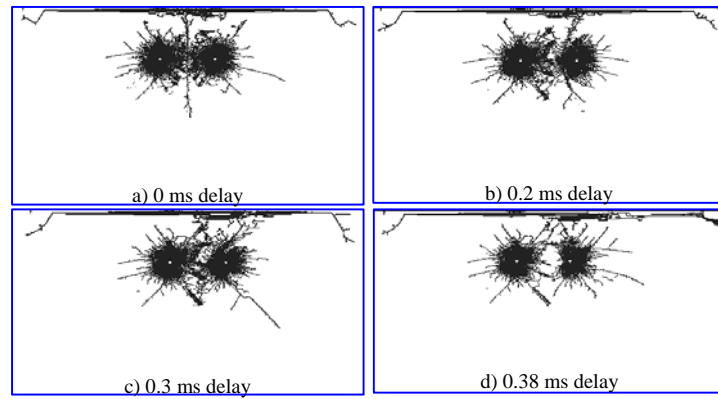


Figure 4 Simultaneous and consecutive blastings

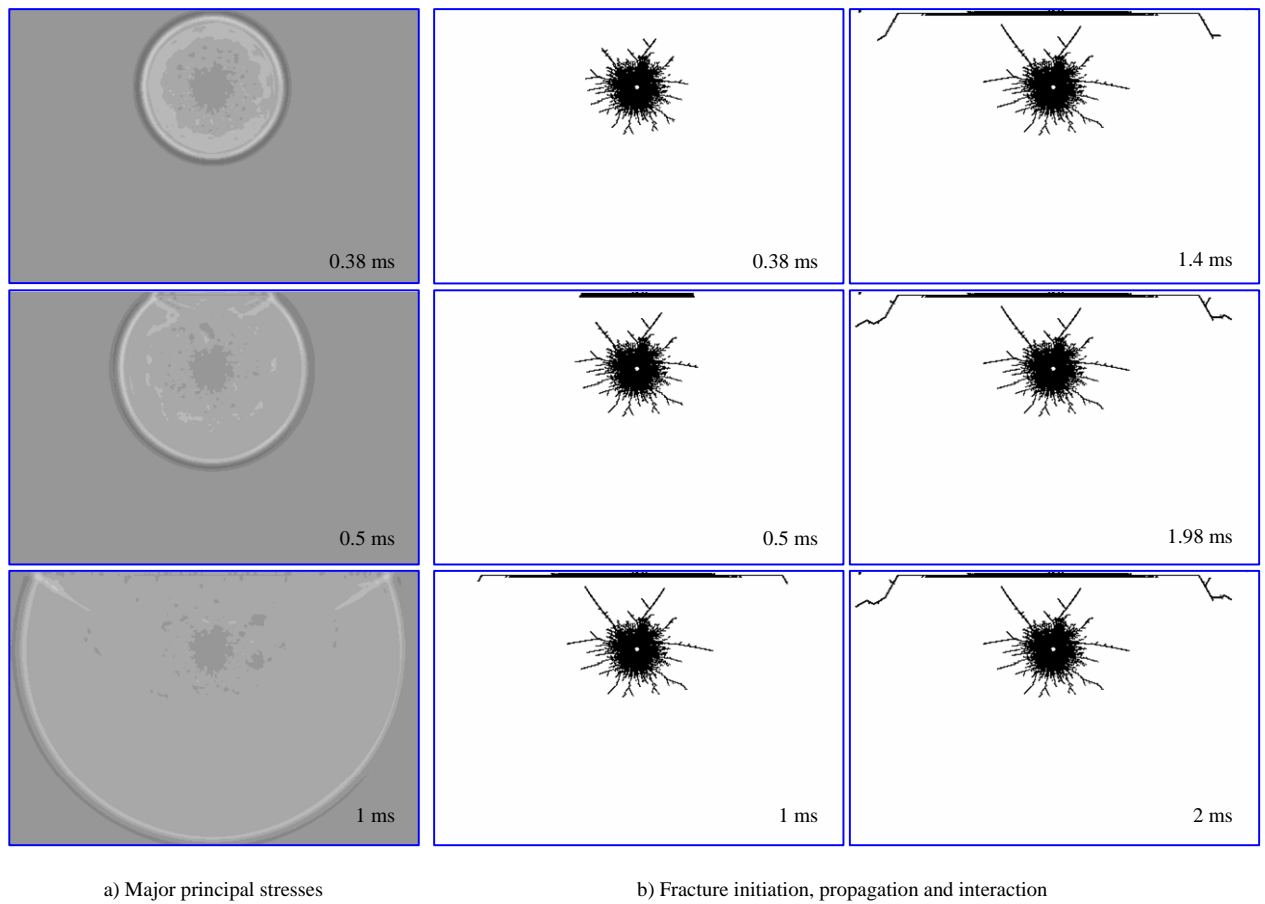


Fig. 3 Stress wave propagation and fracture process by blast in a rock mass with one free face (burden: 2 m)

In this section, the numerical method is applied to model the stress wave propagation and fracture process by blast in a rock with a burden of 2 m and the corresponding results are depicted in Fig. 3. It can be seen before

the stress wave approaches the free surface, the stress wave propagation sequence and failure process are similar to those observed in the infinite rock mass in Fig. 2. At the time of $t = B/c_d$ (around 0.38 ms), the wavefront of the compressive stress wave reach the free boundary. Upon reaching the free face the biaxial compression in the leading edge of the wave is converted into biaxial tension and this tensile wave travels back into the model towards the borehole. The tensile stress in the inward travelling wave exceeds the dynamic tensile strength of the rock and fracturing spalling occurs near the free surface, as shown in Fig. 3 at the times of 0.5 ms. It is especially clear in the pictures at the time till 1.4 ms. At 1.98 ms, the fracture pattern becomes stable. The calculation is continued till 2 ms to be sure that the final fracture pattern is obtained.

4 Simultaneous Blasts and Consecutive Blasts

The final fracture patterns induced by simultaneous blasts and consecutive blasts with various delays are compared in Fig. 4. It can be seen that with a very shorter delay time, the fracture pattern is closer to that by simultaneous blast. With a relatively longer time, the fracture pattern around the second borehole is greatly influenced by the blast in the first borehole. When simultaneous initiation is used, the blast waves from neighbouring holes meet half way between the contour holes and superimpose, which means that the amplitude of the blast waves will double, and this is expected to increase the blast-induced damage due to ground vibrations. In order to investigate whether there could be an optimal time delay in contour blasting, the influence of the delay time between the contour holes on the radial crack length and fragmentation by a number of researchers in Sweden. It is reported by Rustan [12] that short delay blasting produced a 33% longer mean maximum radial crack length from each blasthole compared with simultaneous initiation

5 Conclusions

The numerical modelling of blasting in an infinite rock mass indicates that the numerical method reproduces the stress wave propagation sequence and fracture progressive process caused by blast in a confined blasting. Moreover, the numerical method successfully simulates the spalling and crater formation by blasting in a rock mass with one free surface. Therefore, it is reasonable to conclude that the numerical method described in this study can simulate the rock blasting. Finally, simultaneous blasts and consecutive blasts with various delays, which have not received many attentions and are not well understood, are investigated using the calibrated numerical method. The results discussed in this paper have practical significance in that it has been demonstrated that control of the reflected stress wave and the delay time regulates the fragmentation process. The surface shape and condition of the rock face are clearly important in that they affect the reflected wave. Similarly, with multiple charge firing, the positioning, sequence of firing, pulse duration and choice of explosive are all important factors. Further studies are needed in these areas.

Acknowledgements

The first author would like to thank Dr. Penny Stewart at Golder Associates Pty Ltd for inviting him to conduct a pre-study on precision blasting control for the narrow vein mining research project initiated by her. Besides, the financial support of the UQ FirstLink project is greatly appreciated.

References

1. Ouchterlony, F., Olsson, M, Kou, S.Q., Evertsson. M., Wang, Y.M. and Forssberg, E. Kartläggning av FoU inom fragmenteringsområdet i Sverige och omvärlden. GHRR project report, 2004.
2. Donze, F.V., Bouchez, J., Magnier, S.A. Modelling Fractures in Rock Blasting. *Int J Rock Mech Min Sci*, 34 (8). 1153-1163.
3. Mortazavi A. and Katsabanis, P.D. Modelling Burden Size and Strata Dip Effects on the Surface Blasting Process. *International Journal of Rock Mechanics and Mining Sciences*, 2001, 38: 481-498.
4. Cho, S.H., Kaneko, K. Influence of the Applied Pressure Waveform on the Dynamic Fracture Processes in Rock. *International Journal of Rock Mechanics and Mining Sciences*, 2004, 41. 771-784.
5. Saharan, M.R., Mitri, H.S. Numerical Procedure for Dynamic Simulation of Discrete Fracture due to Blasting. *Rock Mechanics and Rock Engineering*, DOI 10.1007/s00603-007-0136-9
6. Ma, G.W. and An, X.M. Numerical Simulation of Blasting-induced Rock Fractures. *International Journal of Rock Mechanics and Mining Sciences*, 2008, 45. 966-975.
7. Kutter, H.K. and Fairhurst, C. On the Fracture Process in Blasting. *International Journal of Rock Mechanics and Mining Sciences*, 1971, 8. 181-202 .
8. Etoh, S., Hamashima, H., Murata, K. and Kato, Y. Determination of JWL Parameters from Underwater Explosion Tests.in: the 12th International Detonation Symposium, (San Diego, 2002).
9. Tapponnier, P. and Brace, W.F. Development of Stress-induced Microcracks in Westerly Granite. *International Journal of Rock Mechanics, Mining Sciences and Geomechanics Abstracts*, 1976, 13: 103-112.
10. ABAQUS. ABAQUS User Manual. 2001.
11. Fournery, W.L., Dick, R.D., Wang, X.J. and Wei, Y. Fragmentation Mechanism in Crater Blasting. *International Journal of Rock Mechanics and Mining Sciences*, 1993, 30 (4). 413-429.
12. Rustan, A.P. Micro-sequential Contour Blasting – How Does It Influence the Surrounding Rock Mass. *Engineering Geology*, 1998, 49. 303-313.

STUDY ON EVOLUTION LAWS OF ZONAL DISINTEGRATION IN DEEP ROCK MASS AROUND PARALLEL TUNNELS

MING-SHAN GENG, CHUN-AN TANG and YONG-BIN ZHANG

Center for Rock Instability and Seismicity Research, Dalian University of Technology

Dalian, 116024, P.R. China

Under the influence of the so called "Three high and one disturbance", namely the high geostress, high ground temperature, high karst hydraulic pressure, and intense mining disturbance, the engineering response of deep rock mass shows some new characteristic scientific phenomena. In comparison with responses of the shallow rock engineering, these new characteristic scientific phenomena have distinctive features, and can't be explained by traditional continuum mechanics satisfactorily, such as the phenomena of zonal disintegration. Based on this background, the results of numerical tests on mechanism and evolution laws of zonal fracture are put forward with RFPA. The phenomena and laws of zonal fracturing are briefly introduced, which has great theoretical and practical significance to deep rock engineering in China.

1 Introduction

With the fast development of national economic construction and national defense construction, the development of underground space is becoming deeper step by step. The intensity of resource extraction continued to increase, mining extraction are deeper more than 1000 meters now. The most deep underground gold deposit of South Africa, India has reached 4000m. China's Hongtoushan copper mine has reached the depth of 1300m, which is the deepest metal mine in the exploitation of mines. Large hydraulic engineering, transportation engineering (road, rail), Pumped Storage Project and the West Route of South-to-North Water Transfer Project under construction in the present or in the future has involved the construction of ultra-large-scale underground chambers and deep over-long-distance underground tunnel project, the majority of projects required below the depth of 500m, with the West Route of South-to-North Water Transfer Project, the longest tunnel is 73km long and the maximum depth reached 1150m. Besides, the deep geological disposal project of radioactive waste in National Defense construction, the large underground reserves in national energy resource inventory and the deep underground protective project are all related to the excavation problem in deep underground chambers, such as the protection of the North American Aerospace Defense Command under 700 meters rock mass [1,2,3]. And so deep mining is the development trend of the future. The engineering response of deep rock mass shows a series of new characteristics of scientific phenomena, such as rock-burst and large deformation of extrusion, the relationship between high geostress and zonal disintegration hasn't been clearly yet [2]. Compared to responses of shallow rock engineering, these features of scientific phenomena are distinctive. The traditional continuum mechanics theory can't be given a satisfactory explanation. It attracts the attention of international experts and engineers in the fields of rock mechanics and geotechnical engineering in

the entire world during the past decades, and becomes the focus of the research in this field. The research on deep rock mechanics and engineering response has great theoretical and practical significance to both deep coal mining engineering and other associated engineering in China, and will involve many new areas of scientific research; the research methods and research results will be useful to other studies of scientific problems.

The most distinguished difference between deep and shallow levels is so called high geostress. The failure of the shallow rock mass is brittle failure; the failure of the deep rock mass may be brittle failure or ductile failure that depends on the property of rock mass and the geostress state. The mechanical behaviours of rock mass in deep tunnel are different from those in shallow tunnel. The surrounding rock in shallow tunnel is classified into loose zone, plastic zone and elastic zone; while the surrounding rock around deep tunnel is classified into fractured zone and non-fractured zone, which occur alternatively and called zonal disintegration [4-11]. The mechanism of the phenomenon is not clear as yet.

The zonal disintegration phenomenon in deep rock mass around tunnel reveals another kind of balance process and a new form of balance stability of deep rock mass. The significance of recognizing this phenomenon consists in the evidence that it can provide for modern nonlinear scientific theory, namely, the seemingly disorderly and unsystematic rock fracture under high geostress will form a regular and orderly structure [11]. As resources exploitation in our country extends to the deep of the Earth, developing further research on basic mechanical problems of deep rock mass is very significative, and it is a new challenge and opportunity that human are faced with in the new century [12].

Based on the study of the geostress state and the deformation characteristic of surrounding rock of tunnels in deep stratum, the mechanism of the layered fracture within the surrounding rock is put forward by Gu Jincai [13]. He pointed that: for the geostress in deep stratum is very high and the orientation of the maximum stress is possibly parallel to the axes of the tunnel, the radial tensile strain within surrounding rock of tunnels will occur under higher axial compressive stress, and the value of this tensile strain is smaller at the wall of tunnels but higher in rock mass at some distances from the wall of tunnels. The tensile failure of rock mass around tunnels is created when the tensile strain exceeds its ultimate value. Consequently one or more layered fractures are created within rock mass around tunnels; and the range of layered fractures is determined by the magnitude of the axial compressive stress.

Prof. Tang Chun'an and Zhang Yongbin [14, 15] classify the fracture spacing phenomenon into three patterns: parallel fracture spacing (parallel crack), net fracture spacing (crack) and ring fracture spacing (zonal disintegration). Fracture spacing in stratum, earth shrinkage and fracture spacing(zonal disintegration) in rock mass around deep tunnel are all belong to fracture spacing. They carried out a series of numerical tests on three-dimensional failure process of rock samples containing one hole with RFPA-Parallel system, reproducing fracture spacing (zonal disintegration) observed from rock mass around deep tunnels. They got a conclusion that fracture spacing is the result of circular tensile within surrounding rock mass under the loading of principal stress in the tunnel direction.

Based on the results of Tang Chun'an, a series of numerical tests on rock samples containing double holes are carried out with RFPA-3D, reproducing zonal disintegration surrounding deep chambers. The phenomena and laws of zonal fracturing are briefly introduced.

2 Method and Model Building

As we know, the rock is a very complex material with heterogeneous microstructure or texture, micro cracks and weak interfaces [16]. So we should take the heterogeneity into consideration. Here, the Weibull statistical distribution is used to characterize the rock heterogeneity. The density of Weibull distribution function can be expressed as Eq. 1:

$$f(\alpha) = \frac{m}{\alpha_0} \cdot \left(\frac{\alpha}{\alpha_0} \right)^{m-1} \cdot e^{-\left(\frac{\alpha}{\alpha_0} \right)^m} \quad (1)$$

Where: α --- Rock microstructure nature parameter (Strength, elasticity coefficient, and so on);

α_0 --- The mathematical expectation value;

m --- The shape parameter describing distribution function, The physical meaning of m can reflect the rock's homogeneity;

$f(\alpha)$ --- Mechanical properties of rock microstructure α , statistical distribution density.

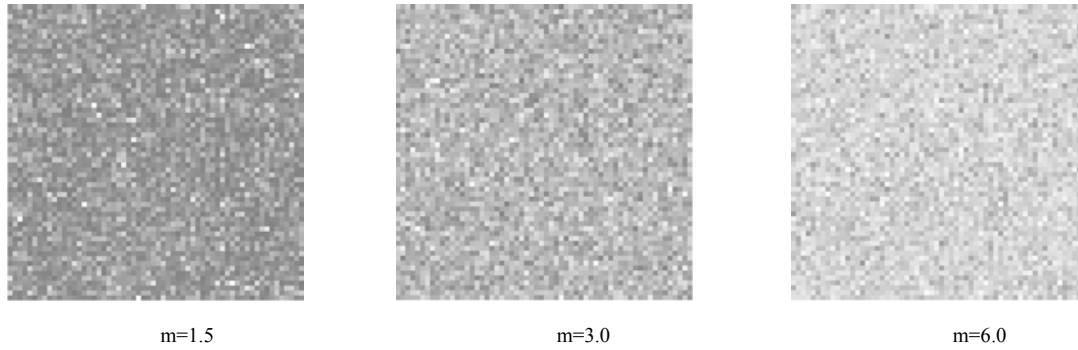


Figure 1 Numerical samples generated by RFPA with different homogeneity indexes

Figure 1 shows three numerical samples consisting of 60×60 elements generated randomly according to Weibull distribution with different homogeneity indexes m . In the Figure 1, the different shades of gray correspond to different magnitudes of elements strength. It can be found that the strength of the elements is concentrated and close to α_0 with the increase of homogeneity index [17]. The higher homogeneity index leads to more homogeneity numerical samples. In general, it is assumed that Young's modulus and strength conform to two individual distributions with the same homogeneity index; and Poisson's ratio usually doesn't vary much, so it isn't treated with variation distributions. Each element is assumed to be isotropic and homogeneous. The effects of the homogeneity index on the macroscopic mechanical response have been discussed by Tang Chun'an et al [17, 18].

In the paper, the numerical tests on three-dimensional failure process of rock samples containing double holes are carried out with RFPA-3D. To get the evolution laws of zonal fracture, assigning different values to

the distance of two holes s with $d/2$, d and $2d$ (where d represents the diameter of the hole and s represents the distance of two holes).

As illustrated in Figure 2, the model with geometry of $180\text{mm} \times 180\text{mm} \times 25\text{mm}$ consists of $180 \times 180 \times 25$ brick elements, contains two holes parallel to z -axis, whose radius is 5mm . As boundary conditions, a constant displacement increment rate is imposed on the vertical model boundaries of $z=25\text{mm}$, and a constant restriction is applied normal to the other boundaries, to model the far field tectonic loading. The displacement increment rate is 0.005mm per step.

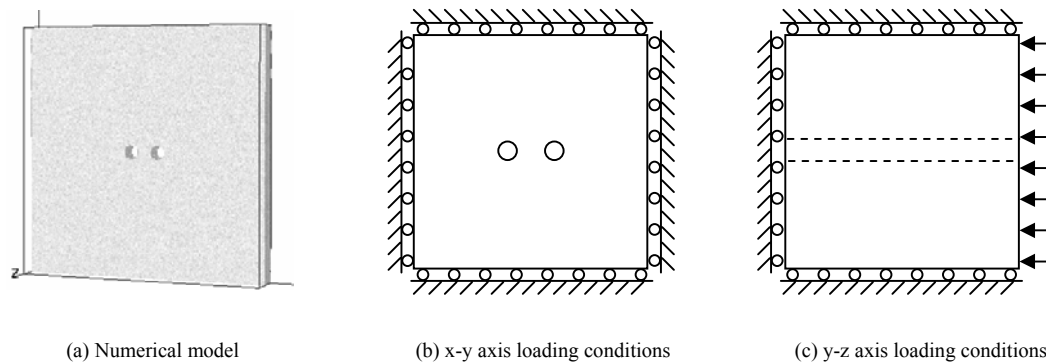


Figure 2 Numerical model and loading conditions

3 Numerical Test Analysis of RFPA Model

As illustrated in Figure 3, results showed that the cracks initiation and growth while the distance of two holes s equals to $d/2$. It has been observed cracks initiation mechanism and zonal disintegration phenomena in rock mass around deep tunnel.

According to the numerical results, it can be seen that, micro-cracks firstly appear around the holes (Figure 3a), with the continual increase of load, the approximate ring fracture form around the holes (Figure 3b-c), and it expands spiral (Figure 3d-e). According to the results of Gu Jincai [13], when the geostress in deep stratum is very high and the orientation of the maximum stress is possibly parallel to the axes of the tunnel, the zonal fracture phenomenon may generates in the rock mass around roadway. Since the rock mass under the greater axial stress will have a transverse expansion, and could only expand to the inner tunnel. The radial tensile strain within surrounding rock of tunnels will occur under higher axial compressive stress, and the value of this tensile strain is smaller at the wall of tunnels but higher in rock mass at some distances from the wall of tunnels. The tensile failure of rock mass around tunnels is created when the tensile strain exceeds its ultimate value. Consequently one ring fracture created within rock mass around tunnels. When the first fracture occurs in the rock mass surrounding tunnel, a greater tunnel generates, a new fracture process occurs in the larger one under the greater axial stress. The fracture process occurred repeatedly (Figure 3f-i), and then more ring cracks generate in the surrounding rock.

Figure 3 is the forming process of zonal fracture, which is obtained by numerical simulation of RFPA. Micro-cracks firstly appear and grow around the two holes (Figure 3a). The continual loading increase results in the emergence of approximate ring fracture around two holes, and it expands in shape of helix gradually (Figure

3b-e). Besides, a fracture appears separately in the upper while the first spiral fracture is developing (Figure 3e). Subsequently, the inactive fracture zone and newly induced fracture zone link up, forming a completed spiral line of fracture (Figure 3f). When the first fracture forms around the holes, a greater hole generates, the fracture process occurred repeatedly (Figure 3g-i), and then more ring cracks generate in the surrounding rock.

Results showed the cracks initiation and growing process while the distance of two holes centers s equals to d in Figure 4 and the process while the distance equals to $2d$ in Figure 5.

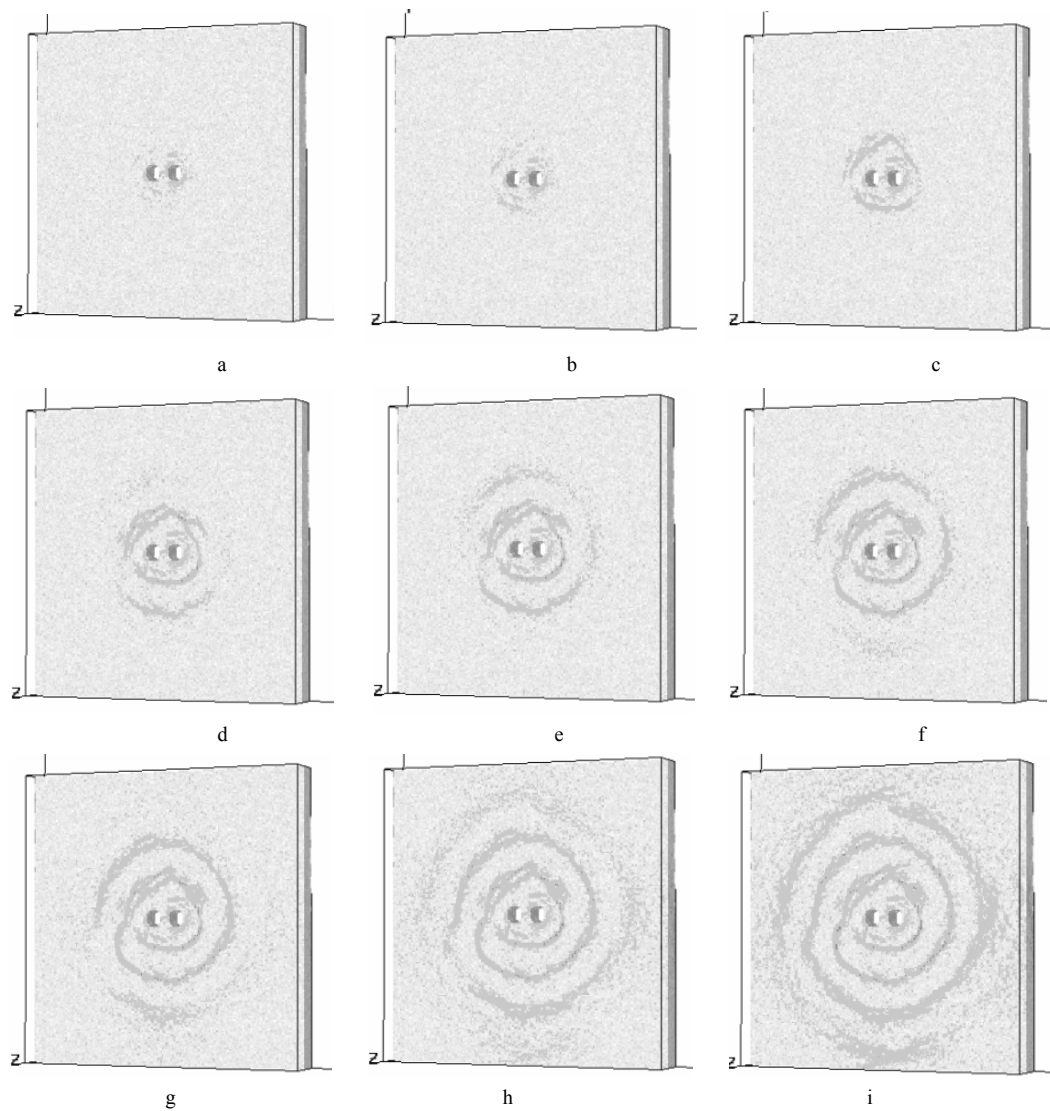


Figure 3 Zonal fracture forming process obtained by RFPA($s=d/2$)

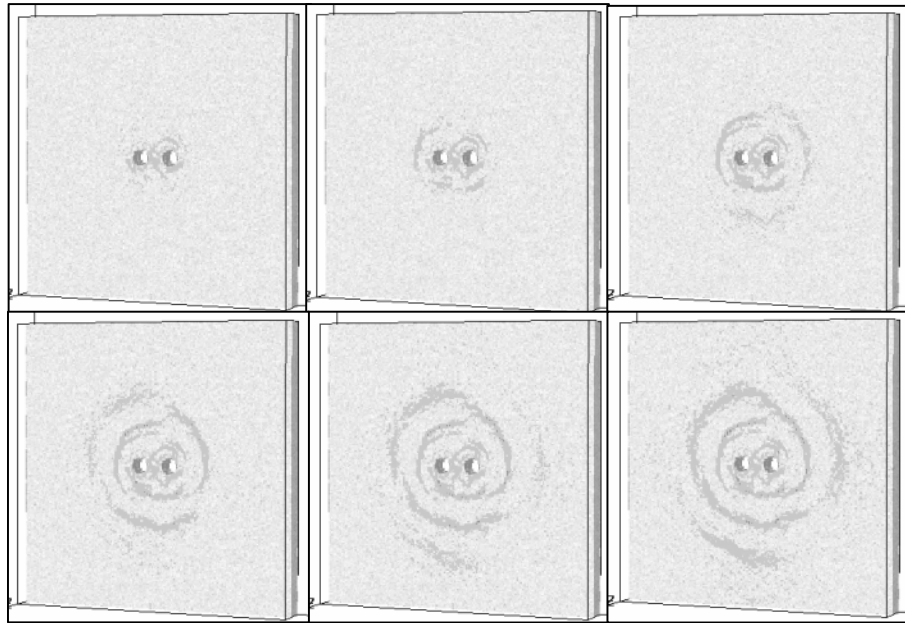


Figure 4 Zonal fracture forming process obtained by RFPA($s=d$)

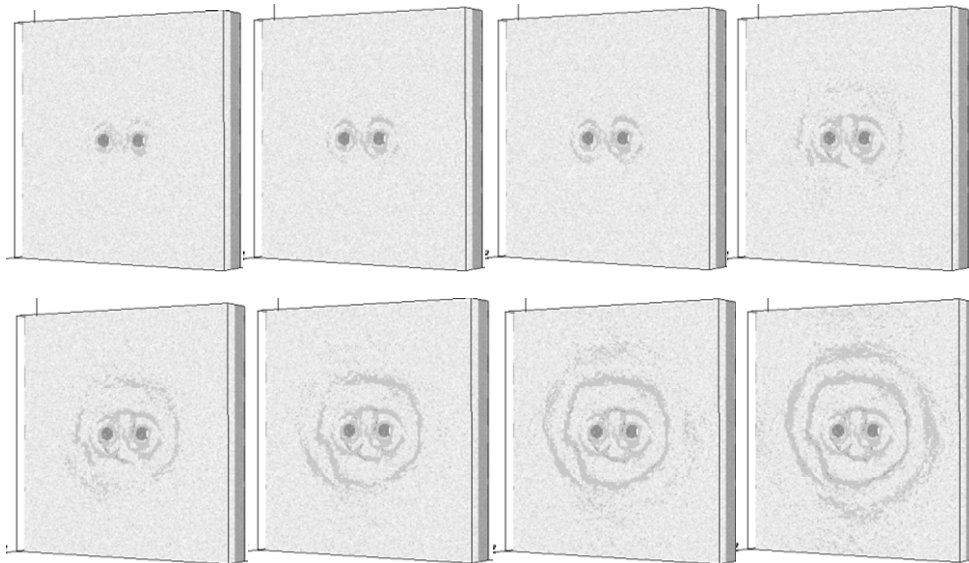


Figure 5 Zonal fracture forming process obtained by RFPA($s=2d$)

As illustrates in Figure 4 and Figure 5, with the increasing of the distance of the two holes, there are one or two ring fractures growing around each hole. While the distance of the two holes is small enough, we can see that the ring fractures firstly appear and grow around the two holes in Figure 3. And so, the distance between two holes has certain influence on the form of zonal disintegration.

At the same time, it can be also found that, not entirely in accordance with standard spiral, the spiral fracture doesn't develop away from border of the hole; contrarily, the cracks turn to develop around the border of the hole, forming a closed loop of fracture. Figure 4 shows that, because spiral fracture develops in pattern of non-continuity, although the first fracture stops developing, a new fracture is induced again. Subsequently, the inactive fracture zone and newly induced fracture zone link up, forming a completed spiral line of fracture. Both the non-uniformity of materials and boundary conditions are important factors to the emergence of non-continuous fracture.

The evolvement of the cracks is discontinuous, maybe evolve into the inner arc-cracks to create an integrated circle fracture; or evolve into the outer arc-cracks to create a integrated spirals fracture. The fracture evolvement of initiation, propagation and coalescence is a random process, it cannot really create an integrated circle fracture. Tang Chun'an [14] believes that the phenomena so-called zonal disintegration is the artificial graphics been linked by the stress data got from the limited boreholes in surrounding rock of deep tunnel. The graphics can't reflect the true situation of the fracture shape actually. This point is approved again in this paper.

4 Conclusions

In the paper, we give one kind of numerical models that the sample with double holes. The numerical tests are carried out with RFPA-3D system. The phenomena and laws of zonal fracturing are briefly introduced. The following conclusions could be derived from the test results presented in this paper.

(1)The evolvement of the cracks is discontinuous, maybe evolve into an integrated circle fracture; or create a spiral fracture. The evolvement process of fracture is a random process;

(2)The distance between two holes has certain influence on the form of zonal disintegration. While the distance is small enough, the ring fractures firstly appear and grow around two holes, with the increasing of the distance, there will be one or two ring fractures growing around each hole;

(3)Study on analysis of zonal fracture phenomenon in deep rockmass with RFPA system is feasible;

There are a number of factors affecting on the zonal disintegration phenomenon, the further research will focus on several crucial affecting factors, such as loading state, rock mass conditions and excavation sequence. The associated research will be carried out in the later numerical test.

Acknowledgements

The authors wish to acknowledge the collaborative funding supports from National Natural Science Foundation of China (No.50809012 and 10672028) and National Basic Research Program of China "973 Program" (No.2007CB209400).

References

1. Qian, Q.H. Key Science Problems for Deep Underground Space Excavation. in the 230th Xiangshan Science Conference, (Beijing, 2004).

2. Qian Q.H. Zonal Disintegration Phenomenon around Rock Mass in Deep Tunnel Engineering. China Science and Technology Press, 2008.
3. Liao, M.C., Guo, Z.K., Liu, F. and Chen, W.X. Determination of the Specimen Size for Model Experiment on Zonal Fracturing of Deep Rock-mass. *Journal of Disaster Prevention and Mitigation Engineering*, 2006, 26 (1). 58-62.
4. Shemyakin, E.I., Kyrlenya, M.V. and Reva, V.N. Effect of Zonal Disintegration of Rocks around Underground Workings. *Dokl. Akad. Nauk. USSR*, 1986, 289 (5). 1088-1094.
5. Shemyakin, E.I., Kyrlenya, M.V. and Reva, V.N. USSR discovery No.400, Phenomenon of Zonal Disintegration of Rocks around Underground Workings. *Byull. Izobret*, 1992, (1). 7-15.
6. Kyrlenya, M.V. and Oparin, V.N. Problems of Nonlinear Geomechanics (part I). *Fiz. Tekh. Probl. Razrab. Polezn. Iskop*, 1999, (3). 1-22.
7. Guzev, M.A., and Paroshin, A.A. Non-Euclidean Model of the Zonal Disintegration of Rocks around Underground Working. *Journal of Applied Mechanics and Technical Physics*, 2001, 42 (1). 131-139.
8. Reva, V.N. Stability Criteria of Underground Workings under Zonal Disintegration of Rocks. *Fiz. Tekh. Probl. Razrab. Polezn. Iskop*, 2002, (1). 35-38.
9. Wang, M.Y., Song, H., Zheng, D.L. and Chen, S.L. On Mechanism of Zonal Disintegration within Rock Mass around Deep Tunnel and Definition of Deep Rock Engineering. *Chinese Journal of Rock Mechanics and Engineering*, 2006, 25 (9). 1771-1776.
10. Li, Y.J., Pan, Y.S. and Li, Z.H. Analysis of Mechanism Of Zonal Disintegration Of Rocks. *Chinese Journal of Geotechnical Engineering*, 2006, 28 (9). 1124-1128.
11. He, Y.N., Han, L.J., Shao, P. and Jiang, B.S. Some Problems of Rock Mechanics for Roadways Stability in Depth. *Journal of China University of Mining & Technology*, 2006, 35 (3). 288-295.
12. Jia, P. Numerical Study on Failure Mechanics of Tunnel under the Influence of Structural Planes Based on Strength Reduction Method. Shenyang: Northeastern University, 2008.
13. Gu, J.C., Gu, L.Y. and Chen, A.M. Model Test Study on Mechanism of Layered Fracture within Surrounding Rock of Tunnel in Deep Stratum. *Chinese Journal of Rock Mechanics and Engineering*, 2008, 27 (3). 433-438.
14. Tang, C.A. and Zhang, Y.B. Discussion on Mechanism and Evolution Laws of Fracture Spacing in Rock Mass. *Chinese Journal of Rock Mechanics and Engineering*, 2008, 27 (7). 1362-1369.
15. Tang, C.A., Zhang, Y.B. and Liang, Z.Z. Numerical Test research with RFPA on Fracture Spacing with Rock Mass around Deep Tunnel. in *The 7th Cross-Strait Tunnel and Underground Engineering and Technology Seminar*, (Dalian, 2008).
16. Tang, C.A., Wang, S.H. and Fu, Y.F. Numerical Test of Rock Failure. Science Press, 2003.
17. Li, L.C., Tang, C.A. and Li, C.W. Slope Stability Analysis by SRM-based Rock Failure Process Analysis (RFPA). *Geomechanics and Geoengineering*, 2006, 1 (1). 51-62.
18. Tang, C.A. and Liu, H.Y. Numerical Studies of the Influence of Microstructure on Rock Failure in Uniaxial Compression Part I: Effect of heterogeneity. *Int. J. Rock Mech. Miner. Sci.*, 2000, 37 (4). 555-569.

AN EXPERIMENTAL STUDY IN ROCK SLOPES AGAINST DYNAMIC FLEXURAL TOPPLING FAILURE

MEHDI AMINI

*School of Mining Engineering, Tehran Universit
, Tehran, Iran*

ÖMER AYDAN

*School of Marine Civil Engineering, Tokai Universit,
Shimizu, Japan*

ABBAS MAJDI

*School of Mining Engineering, Tehran University
Tehran, Iran*

KATSUMI OHKUBO

*Naka-Nihon Expressway Company (NEXCO)
Tokyo, Japan*

Flexural toppling failure is one of common instability modes of rock masses that may occur in a wide range of layered rock strata in open pit mines and rock slopes. This failure occurs due to bending of layers with or without cross joints. The active flexural toppling failure is well known and it occurs under mainly gravitational loading with or without water pressure and seismic loading. However, the passive flexural toppling can also occur when an overload due to topsoil and/or glacial load in the past and seismic loads act. In this paper, first, a brief review of current studies on flexural toppling failure is presented. Then, the results of dynamic experimental modelling of single column with potential of flexural toppling failure are presented. Finally, brief results of physical modelling of rock slopes with potential of dynamic flexural toppling failure are explained.

1. Introduction

Flexural toppling failure is one of the most probable instability modes of open pit mines and rock slopes (Figures 1 & 2). The toppling failure was first mentioned by Müller in 1968 [1]. Between 1968 till 1976, many articles were published on the toppling failure using physical model tests in laboratory and case histories [2, 3, 4]. In 1976, Goodman and Bray classified the toppling failure into four principal types: flexural, blocky, blocky-flexural and secondary toppling [5]. Aydan and Kawamoto was first to present a theoretical method to analyze slopes and underground openings prone to flexural toppling failures, on the basis of limiting equilibrium method utilizing the bending theory of cantilever beam in 1987, 1988 and 1992 with the consideration of gravity, earthquake and water pressure [6,7,8,9]. In 1996, Adhikary et al. tried another approach based on the Cosserat type modeling [10]. This model is incapable of taking into account the interlayer slip between layers. In 2008, Amini et al. proposed another approach based on the displacement compatibility of between layers [11]. However, all these methods consider the active mode of failure. In 1987,

Aydan presented first theoretical treatment for active and passive modes sliding and toppling failures of a single block and discontinuous rock slopes [12]. In 1989, these theoretical relations were later published in a paper by Shimizu et al. [13]. Aydan presented a first example of passive flexural toppling of rock slope nearby Ergenli-Bayindir (Turkey) within Menderes metamorphic massive in one of his articles on flexural toppling failure and his doctorate thesis [7,8]. In this paper, the results of some experimental modeling of flexural toppling failure of single column and rock slopes are presented. Then, the experimental results are compared with the results of existing analytical equations.

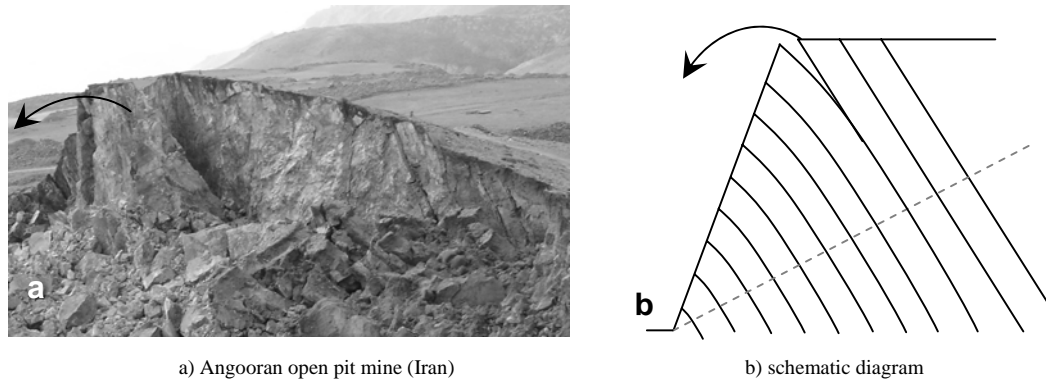
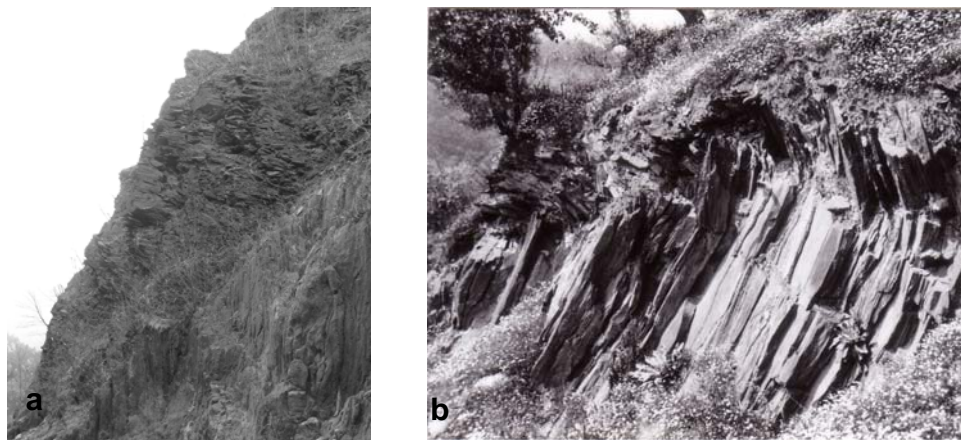


Figure 1 Active flexural toppling failure (picture by Amini)



(a) Akamizu Water Fall in Abe Valley (Japan) (b) Ergenli - Bayindir (Turkey) [7,8,9]

Figure 2 Examples of passive flexural toppling failure from Japan and Turkey (pictures by Aydan)

2. Engineering Properties of Materials

Columns used in preparing physical models of a single column and layered rock slopes were created through the consolidation of a special powder mixture under a given pressure. Various researchers determined the properties of this solid material [6,7,9,14,15]. In this experimental study, some new samples prepared under a consolidation pressure of 600 kPa. Frictional angle, unit weight, tensile and compressive strength of these samples have been measured in the laboratory and the results are summarized in Table 1.

Table 1- Engineering properties of materials with 600kPa consolidation pressure

Parameters	UCS (<i>kPa</i>)	Tensile strength (<i>kPa</i>)	Density <i>kN / m³</i>	Fictional angle (<i>Degree</i>)
Values	50-110	15-35	17-22.3	35-40

3. Mechanism of Dynamic Flexural Toppling Failure

As was mentioned in abstract, flexural toppling failure occurs due to bending of rock layers. Body force of the rock layers and water pressure are the primary cause of bending. Hence, if dip direction of layers is approximately the same as that of the slope, the rock mass will not have a potential of flexural toppling failure. However, bending moment on rock layers is caused by weight and seismic forces under dynamic condition. Therefore, the potential of flexural toppling failure is much greater under dynamic condition than that under static condition. Accordingly, flexural toppling failure may be classified into 2 types as follows:

- Passive: Dip direction of discontinuities and slope are the same ($0 < \delta < 90$).
- Active: Discontinuities dip steeply against the slope ($90 \leq \delta < 180$).

Where δ is inclination of the layers (figure 3).

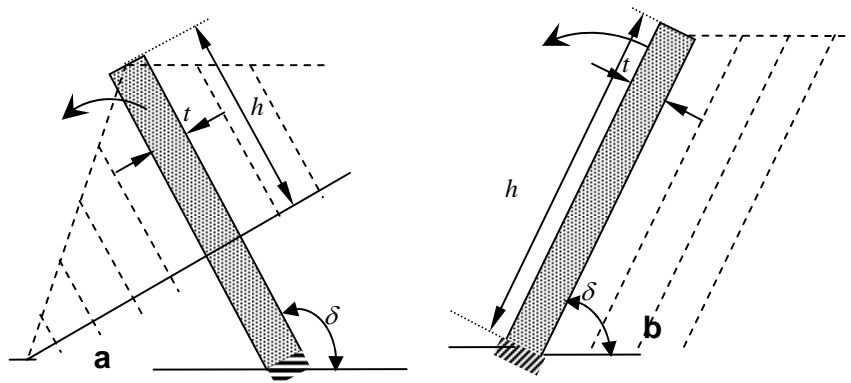


Figure 3 Models of a single column with potential of active (a) and passive (b) flexural toppling failure

4. Physical modeling of a single column

Active flexural toppling failure was theoretically and experimentally studied by some researchers [2,6,7,8,9]. Although Aydan and Kawamoto [9] considered the seismic load in modeling flexural toppling failure in active mode, there are no theoretical and experimental studies on flexural toppling failure in passive mode in literature. In this research, models of single columns and layered rock slopes were prepared to study the active and passive flexural toppling failure and tested on shaking tables in Aydan's laboratory and Structural Mechanics Laboratory of Marine Civil Engineering Department of Tokai University. For physical modeling, some samples were prepared using a consolidation pressure of 600 kPa. Then, the end of samples was firmly fixed on the shaking table. The acceleration of shaking table was increased up to the maximum capacity of the shaking tables, gradually. During the test, the acceleration of the shaking table, deformation of the sample and crack initiation were monitoring by accelerometer, laser transducer and AE (acoustic omission) sensors, respectively.

The results of these experiments have been compared with analytical results for column inclinations (δ) of 60, 90 and 120 (Figures 4, 5 and 6). The analytical bounds can be found on the basis of bending theory of cantilever beams for single column using the seismic coefficient method. As it can be seen from these figures, good correlations between theoretical and experimental results are found.

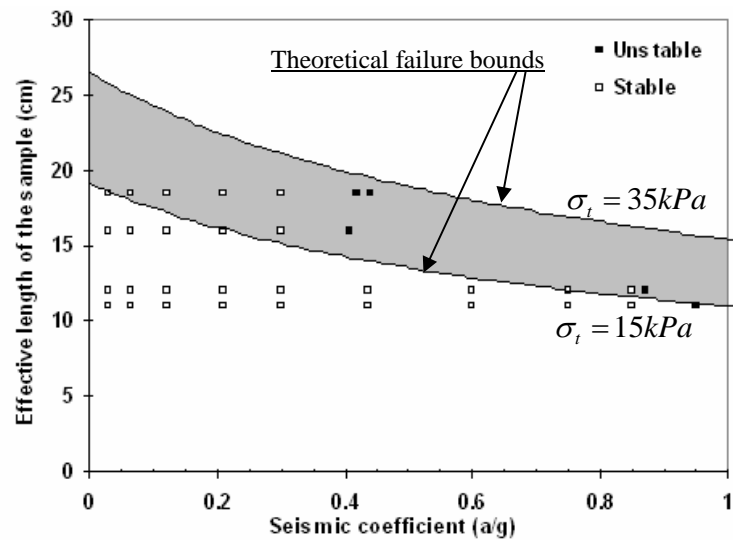


Figure 4 Results for a single column with an inclination of 120 for flexural toppling failure

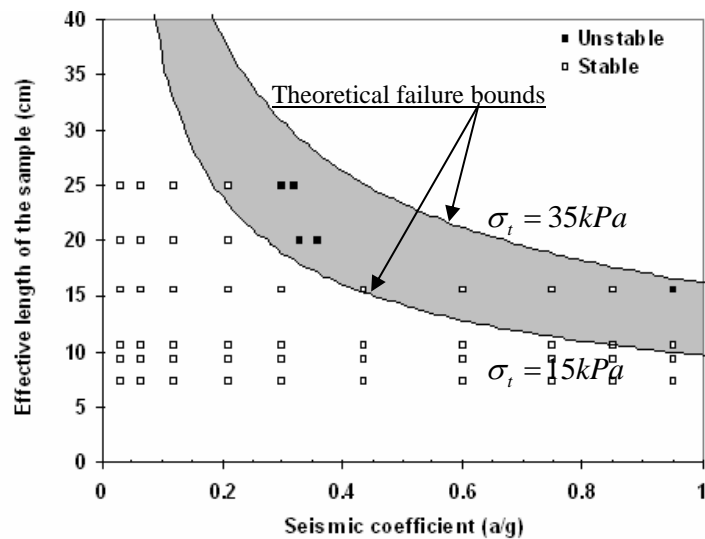


Figure 5 Results for a single column with an inclination of 90 for flexural toppling failure

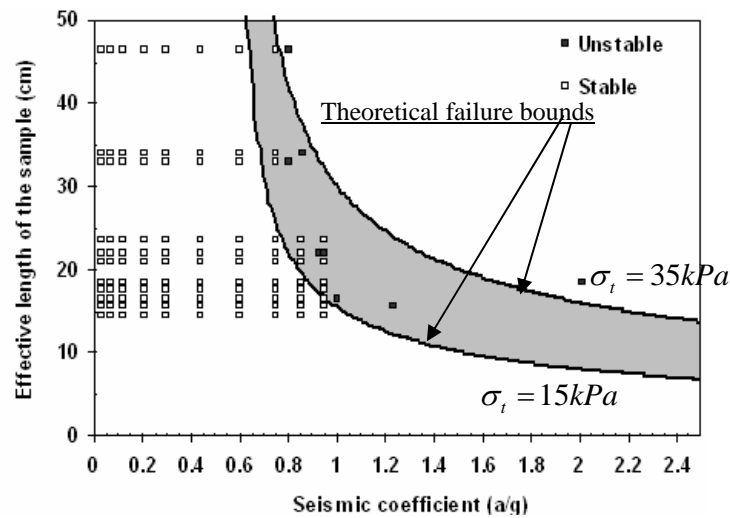


Figure 6 Results for a single column with an inclination of 60 for flexural toppling failure

5. Physical Modeling of Slope

A series of experimental modeling were performed to clarify the mechanism of flexural toppling failure in rock slopes and open pit mines under dynamic condition. The inclination of layers is selected as 45, 60, 90, 120 and 135. These tests have been still continuing. A schematic view and photo of a physical rock slope model for a layer inclination of 90 are shown in Figure 7. Before forcing the models to failure in each test, vibration responses of some observation points in the slope were measured with the purpose of investigating the natural frequency of slopes and amplification. Also, deflection of the slope surface and crack initiation were monitored by laser and acoustic emission sensors. The records of base acceleration and deflection of slope surface of the model are shown in Figure 8 for a layer inclination of 90 as an example. The experimental results of model slopes for layer inclination of 90 are compared with the analytical predictions for a single column (Figure 9). As it can be seen from these figures there are good correlations between theoretical and experimental results for this particular case.

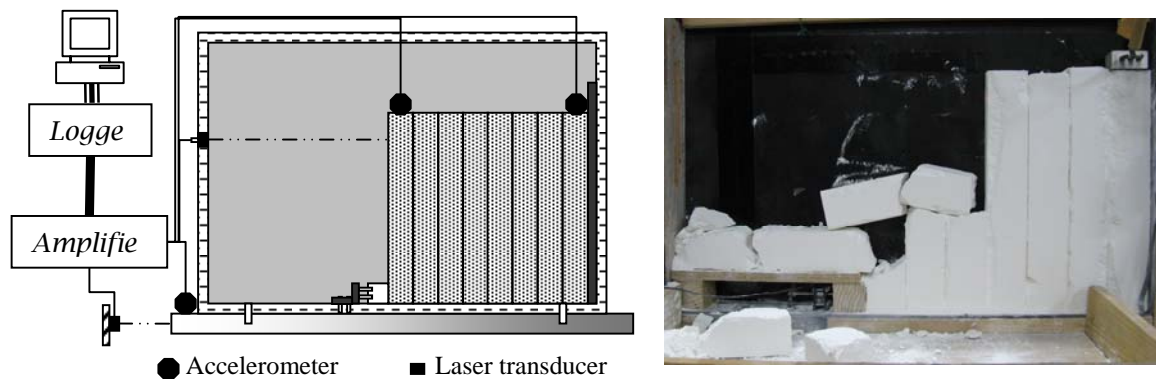


Figure 7 Physical model of rock slopes with a layer inclination of 90

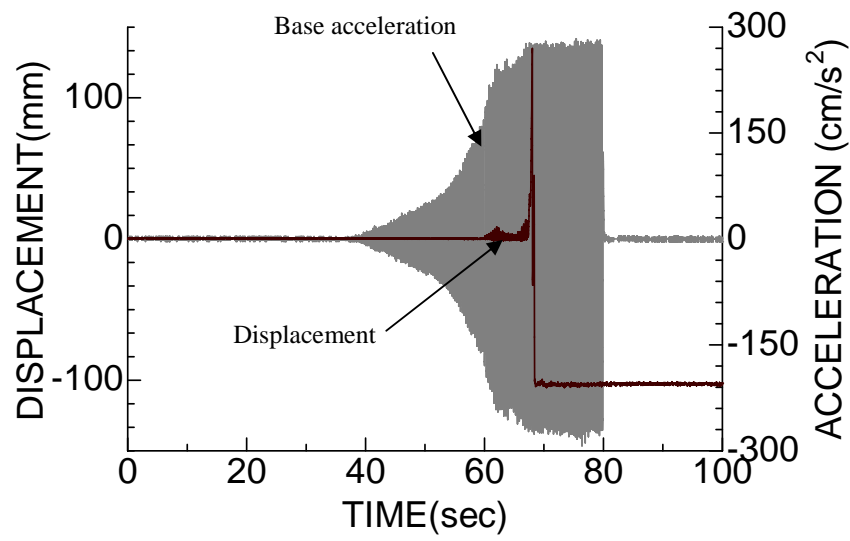


Figure 8 Base acceleration and displacement responses of a rock slope model with layer inclination of 90

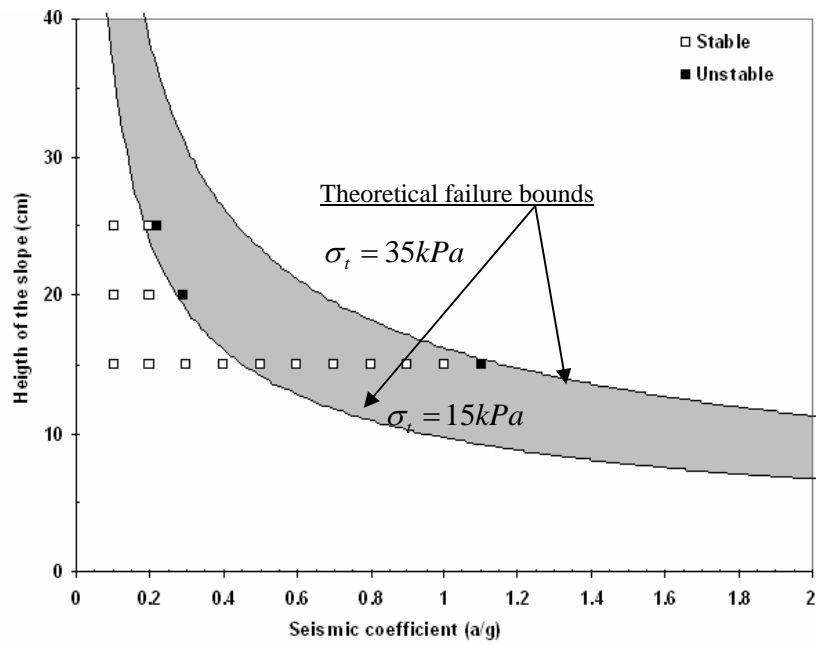


Figure 9 Comparisons between theoretical and experimental results for dynamic flexural toppling failure

6. Conclusions

Although this study has been still continuing, the preliminary outcomes of this research can be summarized as follows:

1. If dip direction of layers discontinuities is approximately the same as dip direction of the slope, the rock mass will not have a potential of flexural toppling failure under static condition.
2. Flexural toppling failure under dynamic condition can be classified into 2 modes: active and passive.
3. Experiments indicated that the required seismic coefficient is much higher for single column subjected to passive toppling as compared with that of columns subjected to active toppling.
4. The experiments on model rock slopes also indicated that the required seismic coefficient is much higher for slopes subjected to passive toppling as compared with that of slopes subjected to active toppling.
5. Preliminary predictions of seismic coefficient for the initiation of flexural toppling failure of a single column under active or passive modes by analytical method are close to experimental results.

Acknowledgements

The first author would sincerely like to acknowledge the scholarship provided by the Ministry of Science, Research and Technology of Iran for his studies in The Marine Civil Engineering Department of Tokai University and Tokai University for the kind permission for this study in its education and experimental premises. The experiments reported in this article have been carried out at the Aydan's laboratory and structural laboratory of Marine Civil Engineering of Tokai University and it is gratefully acknowledged.

References

1. Müller, L. New Considerations on the Vajont Slide. *Rock Mech. Eng. Geol.* 1968,6. 1-91.
2. Erguvanli, K. and Goodman, R. E.: Applications of Models to Engineering Geology for Rock Excavations. *Bull. assoc. Eng. Geologists* 9. 1970.
3. De Freitas, M. H. and Watters, R. J.: Some Field Examples of Toppling Failure. *Geotechnique*, 1973, 23 (4), 495-514.
4. Bukovansky, M., Rodriguez, M. and Cedrun, G. Three Rock Slides in Stratified and Jointed Rocks. in: *Proc. of 3rd Int. Congr. on Rock Mechanics*, (1974).
5. Goodman, R. E., and Bray, J. W. Toppling of Rock Slopes. in *ASCE Specialty Conference on Rock Engineering for Foundations and Slopes*, (Boulder Colorado, 1976).
6. Aydan, Ö. and Kawamoto, T. Toppling Failure of Discontinuous Rock Slopes and Their Stabilization (in Japanese). *Journal of Japan Mining Society*, 1987, 103 (1197). 763-770.
7. Aydan, Ö., Kyoya, T., Ichikawa, Y. and Kawamoto, T. Flexural Toppling Failures in Slopes and Underground Openings. in *The 9th Western Japan Rock Engineering Symposium*, (Japan, 1988).
8. Aydan, Ö. *The Stabilisation of Rock Engineering Structures by Rockbolts*. Nagoya University, 1989.
9. Aydan, Ö. and Kawamoto, T., (1992): Stability of slopes and underground openings against flexural toppling and their stabilization, *Rock Mech. Rock Engng.* 25 (3), 143-165.
10. Adhikary, D. P., Dyskin, A. V., and Jewell, R. J. Numerical Modelling of the Flexural Deformation of Foliated Rock Slopes. *Int. J. Rock Mech. Min. Sci. Geomech. Abstr.*, 1996, 33 (6), 595-600.
11. Amini M., Majdi A., and Aydan Ö. Stability Analysis and the Stabilization of Flexural Toppling Failure. *Rock Mech. Rock Engng.*, 2008, DOI 10.1007/s00603-008-0020-2. (2008)
12. Aydan, Ö. A Note on the Seismic Stability of Discontinuous Rock Slopes. Interim report, December 7, Geotechnical Engineering Department, Nagoya University, 16 pages. 1987.
13. Shimizu, Y. Aydan, Ö., Ichikawa, Y., and Kawamoto, T. The Stability and Failure of Discontinuous Rock Slopes (in Japanese). *Journal of Civil Engineering, Geotechnical Division*, 1988, 400-III-10, 189-198.
14. Kawamoto, T., Obara, Y. and Ichikawa, Y. A Base Friction Apparatus and Mechanical Properties of a Model Material (in Japanese). *J. Min. Metall. Inst. of Japan*, 1983, 99, 1-6.

15. Egger, P. A New Development in the Base Friction Technique. Coll. Phys. Geomech. Models, ISMES, 67-87, Bergamo. 1983.

A NEW IDEA TO ANALYZE THE FAILURE MECHANISM OF DEEP EARTH ROCKS

JIE WEI

Institute of Geotechnolgy, Hohai University

Nanjing, 210098, P.R. China

Jiangsu Province Geotechnical Surveying Institute of Jianyuan Co.,LTD

No.20 Cibeishe Huaqiao Road, Nanjing, 210029, P.R. China

The failure mechanism of the deep earth's rocks under transient loading is analysed in this paper according to the different stress condition and mechanical behaviour of the rocks in the deep part to that on the upper part of the crust. It is obtained as a result in this paper that the intact rocks behaves very high compressive strength in the deep part of the crust, the limited compressive strength $\sigma_f \geq (\sigma_c + \gamma H) / \lambda$, in contrast, when the intact rocks is broken, the limited compressive strength will be enormously reduced, $\sigma_f \leq \sigma_c$, and the former is nearly 20 times larger than the latter or more sometimes. The rock explosion and its spreading wave of detonation would be occurred as the failure mode of the deep intact rocks in such conditions due to the so larger fall in the limited compressive strength of the rocks. This idea and conclusion in this paper may provide a new way to the further research.

1 Introduction

The descriptions to the mechanical behaviour of rocks are apt in a large amount up to now to the rocks distributed on the upper of the earth's crust, however, the research results on the deep earth's rocks are relatively less. Fortunately a academic sharon on "zoning effect on rupture of adjacent rocks in deep earth's rock engineering" was organized jointly by the academic department of association of science and technology of China and Chinese society for rock mechanics and engineering from 22 to 24 June 2008. The mechanical behaviour of the rocks under the depth of thousand meters scale was discussed at the sharon, and then, the zoning phenomenon of rupture of the deep rocks was researched also that rock rupture in deep behaves as rupture zones and non-rupture zones occurred turn by turn.

The research in this paper primarily is focused on the mechanical behaviour of rocks in ten thousand meters scale under the earth's surface. The loads to the rocks this paper discussed come from tectonic stress、earthquake effects etc., and belong to category of geodynamics. The stress conditions and mechanical behaviours of rocks under the depth of ten thousand meters scale are different from that of thousand meters scale, and especially different from that on the earth's surface, however, they have some relationship with each other. The latter are paid attention to mainly by experts in rock mechanics and engineering, and the former is focused on by scholars of geodynamics.

2 Analysis On Mechanical Behaviour Of Deep Rocks

2.1 Differences Of Stress State Between Rocks In Deep And On The Upper Earth

The rock on upper earth's crust is in a state of very low surrounding pressure or no surrounding pressure of rocks. The surrounding pressure of the rocks in deep earth's crust has two kinds of stress state, for intact rocks

and for fissured rocks separately. The intact rocks are borne by high surrounding pressure with long-term loading duration, the fissured rocks are exerted by uneven surrounding pressure and the regions of faults or fissures are loaded with lowest surrounding pressure that can be neglected in some way. Refer to table 1.

2.2 Differences Of Mechanical Characters Between Rocks In Deep And On The Upper Earth

The mechanical character of rocks on the upper earth's crust behaves elastic-brittle, the strength theory of which is based on the theory of elastics-brittle, such as Mohr-Coulomb theory etc. However, the mechanical character in deep earth's crust behaves both elastic-brittle and rheological behaviour, and in the local region, the two behaviours distributes in turn. The intact rocks under transient loading also show elastic-brittle, however the intact rocks under long-term loading show rheological behaviour. The rocks near the fault zone and fissured rock show elastic-brittle when under transient loading ; and show the character between elastic-brittle and rheological behaviour. Such "dual property" of rock mechanical character depends on the amount of surrounding pressure and loading term of duration. Refer to table 1.

2.3 The Features Of Loading Mode

The "dual property" of the mechanical character of rocks are determined by the features of loading mode, which means that the same intact rocks under high surrounding pressure and long-term loading show rheological behaviour, and under low surrounding pressure and short-term loading show elastic-brittle behaviour. The loading mode of rocks on the upper earth's crust involve static and dynamic load, and the loading duration is relatively short. The loading mode of rocks in deep earth's crust involve three ways: static load、transient load and waving load. The static load may be analysed by the rheological behaviour under long-term loading and high surrounding pressure of rock, and the transient load is equivalent to the static load on the upper earth's crust, and correspondingly, the rocks show elastic-brittle behaviour. The mechanical behaviour of rocks under transient load in deep earth's crust is researched in this paper. Refer to table 1.

table 1. The primary difference of the mechanical behaviours between rocks in deep and on the upper earth

Characters of rocks	The stress state of rocks	Loading modes	Mechanical characters of rocks
Rocks on the upper earth's crust	low or no surrounding pressure of rock	static and dynamic loading; with short-term loading duration	elastic-brittle
Intact rocks in deep earth's crust	high surrounding pressure of rock; with long-term loading duration	static loading; with long-term loading	rheological behaviour.
		transient loading; nearly equivalent to the static loading to the rocks on the upper earth's crust	elastic-brittle
		waving loading	elastic-brittle
Fissured rocks in deep earth's crust	Uneven surrounding pressure of rock; lowest surrounding pressure is on the faults and fissures of rocks	static loading	between elastic-brittle and rheological behaviour
		transient and waving loading; nearly equivalent to the static and dynamic loading to the rocks on the upper earth's crust	elastic-brittle

3 Analysis On Failure Mechanism Of Deep Rocks Under Transient Loading

3.1 Analysis On Failure Mechanism Of Deep Intact Rocks

Suppose the unit this paper studied on is at the depth H under the crust surface, the scale of studied unit of intact homogeneous rocks is large enough compared to its deformation to neglect the effect of the boundary of the

intact rocks, the uniaxial tension strength of the intact rocks is σ_t , the uniaxial compression strength of it is σ_c , λ is the lateral pressure coefficient of the intact rocks, γ is the unit weight of the above layers.

According to the presume above, when the intact homogeneous rocks were loaded a main horizontal pressure stress σ_1 , the lateral pressure stress is σ_3 , $\sigma_3 = \lambda \sigma_1$. σ_3 was composed by two parts of stress, one is gravity pressure of above rock layers, the other can be considered as the rock's passive strength some way. When σ_1 reaches to the limited compressive strength σ_f , the rock's lateral passive strength will not be less than the uniaxial compression strength of the rocks σ_c . Thus, we have:

$$\sigma_3 \geq \sigma_c + \gamma H \quad (1)$$

$$\sigma_f = \sigma_1 = \sigma_3 / \lambda \geq (\sigma_c + \gamma H) / \lambda \quad (2)$$

In formula (2), if γH nearly be zero, for the condition at the surface of the earth's crust, λ can ordinary take the data 1/4, we have:

$$\sigma_f = \sigma_c / \lambda = 4\sigma_c \quad (3)$$

Formula (3) is rather consistent to result of triaxial compression test of intact rocks. When σ_1 is larger than the limited compressive strength σ_f , the rock would be broken become fissured rock with a large amount of fissures, the fissured rock newly formed would change the stress condition of effective surrounding pressure instead of the uniaxial loading condition. The limited compressive strength σ_f would be not more than the uniaxial compression strength of the rocks σ_c . If $\sigma_c = 60$ MPa, $H = 10000$ m, $\gamma = 25$ kPa, $\lambda = 1/4$, according to formula (2), we have $\sigma_f \approx 20 \sigma_c$, i.e., the limited compressive strength of the intact rocks is about 20 times larger than the strength of the rocks after being failed. The analysis result can be described as fig.1.

3.2 Analysis On Failure Mechanism Of Deep Fissured Rocks

The paper only analyse one special situation that unit studied was near the fault or some boundary line as follows. In this situation, the uniaxial compression strength σ_c would be instead by the uniaxial tension strength of the rocks σ_t , if the rocks were relatively near intact, take the uniaxial tension strength of the intact rock; if the rocks were relatively broken or fissured, take the uniaxial tension strength of the fissured rocks that the strength would be rather low near zero. For the condition of relatively intact rocks, formula (2) can be become to formula (4), and refer to fig.1:

$$\sigma_f = \sigma_1 = \sigma_3 / \lambda \geq (\sigma_t + \gamma H) / \lambda \quad (4)$$

For above case, the failure mode of the rocks is mainly tension type, different from the failure mode discussed in paragraph 3.2, that the failure mode of intact rocks is mainly compression type. However, there is still shear type and mixed type of failure for specific condition.

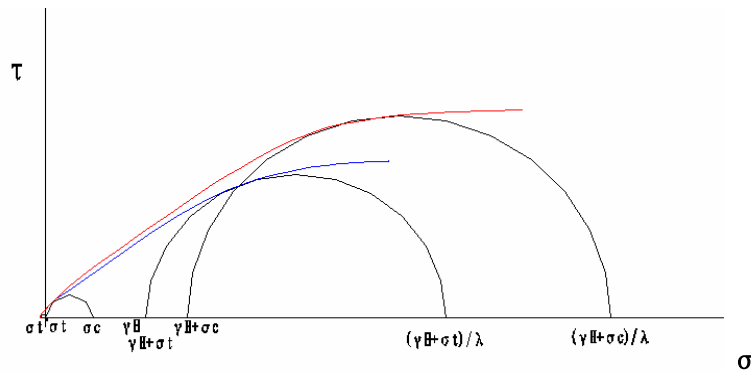


Fig.1 stress and strength of the deep rocks

3.3 Special Broken Manner Of The Deep Intact Rocks

In 3.1, when the rock failed, it would be happen suddenly that the volume of the breaking rocks expanded rapidly, the density of the intact rocks reduced rapidly also. The enormous reduce of the strength and density of the breaking rocks will produce rock explosion and detonation wave to spread. This is the main special characteristics of the "deep rocks".

4 Conclusions

The stress condition of the deep rocks is different from the rock distributed on the surface of the crust. The behaviour of the deep rocks show the dual property that elastics-brittle behaviour and rheological behaviour occurred due specific condition for same rocks. The enormous reduce of the strength when deep intact rocks breaking would produce a series sudden change as well as matter phase change. The rock explosion and its spreading wave of detonation would occurred in specific condition. The author of the paper insists on that the idea and some results of the paper will become some basis or new way to solve many puzzled problems in the discussed areas.

References

1. Goodman, R. E. Introduction To Rock Mechanics. Second Edition. New York: John Wiley & Sons, 1989
2. Xie, H.P. and Chen, Z.H. Rock Mechanics. Science Press, Beijing, 2008.
3. Yun, S.R. and Zhao, H.Y. Mechanics of Explosion. National Defense Industry Press, Beijing, 2005.
4. Ge, X.B. and Zhang, J.C. Blasting Engineering. China Communications Press, Beijing, 2007.

EFFECT OF CRACK-STOPPING HOLE ON SHEAR FRACTURE OF ROCK

QIUHUA RAO, HAIFENG XIE, QIANG XIE, ZHI WANG

College of Civil Engineering and Architecture, Central South University

Changsha, Hunan, 410083, P.R.China

raoqh@mail.csu.edu.cn

Effect of crack-stopping hole on shear (Mode II) fracture of rock is studied numerically and experimentally. Finite element method through the displacement approach is used to calculate the shear stress intensity factors of the specimens with and without symmetrical double holes, K_{II} and K_{II0} . Shear-box test and new electrometric method with conductive glue are adopted to measure the maximum shear stress intensity factor (K_{IIC}), stable shear crack propagation rate (V) and time (T) of these specimens in order to find out optimal double holes for shear crack-stopping. Results show that the effect of crack-stopping hole on shear fracture of rock specimen depends on its location and size, which can be denoted by a regression equation about the ratio of K_{II}/K_{II0} and the three parameters, radius (R), distance away from the notch tip (L) and distance between the two holes (S). The more the R and L , the larger the K_{II}/K_{II0} and the easier to fracture the rock specimen. However, the more the S , the smaller the K_{II}/K_{II0} and the more difficult to propagate the shear crack. When R and L are the smallest and S is the largest, the specimen with double holes has the largest values of K_{IIC} and T and the smallest value of V , which is most favourable to shear crack-preventing. Adding optimal double holes symmetrical with respect to the original crack plane is an effective method for shear crack arresting of brittle rock.

1 Introduction

In rock engineering, pre-existing cracks or discontinuities in rock masses are seldom directly subjected to tensile loading, but rather to compressive, shear or mixed mode loading. For example, the fracture of rock bridges between two adjacent discontinuities in rock masses is of the shear (i.e. Mode II) fracture in some cases, especially in underground excavation and in the toe of a rock slope. Therefore, shear crack growth and arrest have attracted increasing attention of researchers in the world. Theoretical work is focused on the principle of crack arrest and establishment of crack arrest criteria, by means of stress intensity factor^[1-2] and strain energy release rate^[3]. In order to satisfy the crack arrest condition, two methods are adopted in engineering, based on enhancement of fracture toughness of material^[4] and decrease of maximum stress in fracture zone by using additional structures such as crack-stiffened panel^[5] and bolted stiffener^[6-8]. Unfortunately, these methods of crack-stopping are less applied for rock material. Currently available literatures are mainly for tensile rather than shear crack growth and arrest.

In this study effect of crack-stopping hole on shear (Mode II) fracture of rock is investigated numerically and experimentally. Finite element method through the displacement approach is used to calculate the shear stress intensity factors of the specimens with and without symmetrical double holes. Shear-box test and new electrometric method with conductive glue are adopted to measure the maximum shear stress intensity factor, stable shear crack propagation rate and time of these specimens in order to find out optimal methods of shear crack-stopping for rock materials.

2 Numerical analysis

2.1 FEM model

Fig.1 shows the single-notched specimen with double holes under shear-box loading, where P_σ and P_τ are compressive and shear load. The specimen is 50mm×50mm×50mm in size and the notch is 25mm long and 1mm wide. Double holes are located ahead of the notch tip and symmetrically with respect to the original notch plane. Table 1 lists the dimensions of the double holes, where R , L and S are radius, distance away from the notch tip and distance between the two holes, respectively.

A finite element software, MSC.Marc2005, was used to calculate shear stress intensity factors of the specimens with and without double holes, K_{II} and K_{III} . Since the distribution of the stress applied to the specimen surface was unknown in the shear box, the specimen and loading set-up were modelled as a whole. Eight-node hexahedral elements with isotropic properties were adopted and mesh refinement was performed in the vicinity of the notch tip to improve the accuracy of calculation. Fig.2 shows the finite element meshes as well as the Cartesian and polar coordinate systems at the crack tip. The rock material is sandstone and its elastic modulus E and Poisson's ratio ν are 10.7GPa and 0.27. Boundary conditions were defined by applying uni-axial compressive stress on the upper loading plane and zero vertical displacements on the bottom support plane.

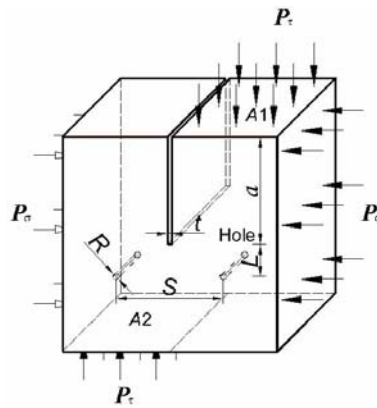


Figure1 Single-notched specimen with double holes.

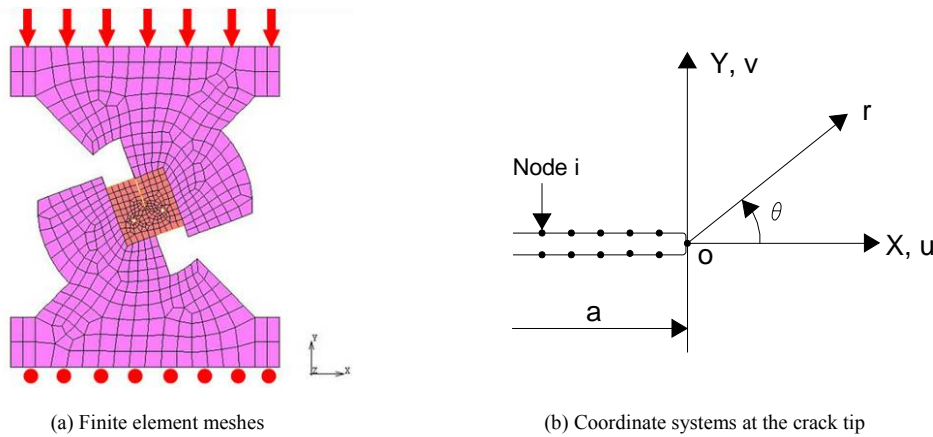


Figure 2 Numerical calculation.

Table 1 Dimensions of the single-notched specimens with double holes.

Specimen No.	R/mm	L/mm	S/mm	K_{II}/K_{III}
A11	7.5	1.5	13	1.00
A12			19	0.99
A13			25	0.97
A14		2.5	13	1.03
A15			19	1.01
A16			25	1.00
A17		4.0	13	1.16
A18			19	1.03
A19			25	1.01
A21	12.5	1.5	13	0.94
A22			19	1.00
A23			25	0.97
A24		2.5	13	1.01
A25			19	1.04
A26			25	1.00
A27		4.0	13	1.14
A28			19	1.05
A29			25	0.98
A31	17.5	1.5	13	0.98
A32			19	0.99
A33			25	1.00
A34		2.5	13	1.03
A35			19	1.00
A36			25	1.00
A37		4.0	13	1.12
A38			19	1.07
A39			25	1.02

2.2 Calculation of shear stress intensity factor

Shear stress intensity factors, K_{II} and K_{III} , can be calculated with the finite element method through the displacement approach, which is based on Irwin's crack tip displacement equations.

For the sake of generality, a crack under any planar loading was considered. In the Cartesian coordinate system, the X-direction (i.e. shear) displacement u is given by Irwin's equation:

$$u = \frac{K_I}{4G} \sqrt{\frac{r}{2\pi}} \left[(2k-1) \cos \frac{\theta}{2} - \cos \frac{3\theta}{2} \right] + \frac{K_{II}}{4G} \sqrt{\frac{r}{2\pi}} \left[(2k+3) \sin \frac{\theta}{2} + \sin \frac{3\theta}{2} \right] \quad (1)$$

where G is shear elastic modulus and k is $(3-4\nu)/(1+\nu)$ for plane stress and $3-4\nu$ for plane strain.

Generally, the nodes are selected on the crack-free surfaces, i.e. $\theta = \pm 180^\circ$. In this case, Equation (1) becomes

$$\begin{aligned} u_i^+ &= \frac{K_{II}^i}{2G} \sqrt{\frac{r_i}{2\pi}} (k+1), \quad \text{at } \theta = 180^\circ \\ u_i^- &= -\frac{K_{II}^i}{2G} \sqrt{\frac{r_i}{2\pi}} (k+1), \quad \text{at } \theta = -180^\circ \end{aligned} \quad (2)$$

where K_{II}^i is shear (i.e. Mode II) stress intensity factor at the node i .

The relative X-direction displacement of the node i on the crack-free surfaces, U_i , is defined as

$$U_i = u_i^+ - u_i^- = \frac{K_{II}^i}{G} \sqrt{\frac{r_i}{2\pi}} (k+1) \quad (3)$$

and thus K_{II}^i is obtained by

$$K_{II}^i = \frac{G}{k+1} \sqrt{\frac{2\pi}{r_i}} U_i \quad (4)$$

Obviously, K_{II}^i depends on the distance r_i from the crack tip. Since the shear stress intensity factor K_{II} is a crack tip parameter requiring r to be extremely small in comparison with the crack length a , i.e. $r \ll a$, the determination of K_{II} from K_{II}^i requires an extrapolation of K_{II}^i back to the crack tip, i.e. $r=0$.

Based on the displacement approach, the shear stress intensity factors of the specimens without and with double holes, K_{II0} and K_{II} , can be calculated. K_{II0} is 81.61 N.m^{-1.5}. Table 1 lists the ratios of K_{II0} to K_{II} of the specimens with different double holes. A regression equation can be obtained by linearly fitting the plotted points of K_{II0}/K_{II} versus the three parameters of the double holes, R , L and S .

$$\frac{K_{II}}{K_{II0}} = 1.0118 + 0.03250R + 0.00031L - 0.00432S \quad (5)$$

From the Equation (5), it is seen that the effect of R , L and S on the shear fracture of rock depends on the sign and magnitude of its coefficient. The more the R and L , the larger the K_{II0}/K_{II} and thus the easier to fracture the rock specimen. However, S is opposite. That is probably because the larger double holes enhance the stress concentration of the specimen and facilitate the shear fracture. When the double holds are farther away from the notch tip, they are closer to the boundary of the specimen and increase the stress concentration, which is helpful for shear crack propagation. If the double holds have larger distance apart, they are farther away from the original notch plane and decrease the stress concentration, which is favourable for shear crack arrest in the original plane. Obviously, the weight relationship among R , L and S for shear crack arrest is $S > L > R$. Therefore, the double holes of smaller R , smaller L and larger S could help to prevent the shear fracture of rock specimen.

3 Experimental Study

3.1 Testing Arrangement

Shear-box test was used to obtain the shear fracture of rock^[9]. The scheme of the loading device is illustrated in Fig. 3. The cubic specimen of 50mm×50mm×50mm in size was placed between two bevelled dies at an inclination angle of 70° to the horizontal direction. A new electrometric method with conductive glue was designed to continuously measure the shear crack propagation rate, where a thin layer of conductive glue was glued parallel to the original notch plane on the surface of specimen^[10].



Figure 3 Single-notched specimen with double holes.

Rock material is sandstone. Table 2 lists its mechanical properties including the tensile strength σ_t , uniaxial compressive strength σ_c , cohesion C , internal friction angle φ , elastic modulus E , Poisson's ratio ν and tensile (Mode I) fracture toughness K_{IC} , which were measured by ISRM (the International Society for Rock Mechanics) standard testing methods.

Table 2. Mechanical properties of the tested rock

Rock type	σ_t /MPa	σ_c /MPa	C /MPa	φ /°	E /GPa	ν	$K_{IC}/\text{N}\times\text{m}^{-1.5}$
Sandstone	2.20	66.0	14.0	35.1	10.7	0.27	0.55

Typically, four kinds of single-notched specimens with different double holes, A13 (of the smallest R and L , and the largest S), A18 (of the largest R , the smallest L and medium S), A25 (of medium R , L and S), A34 (of the largest L and S , and medium R), were adopted to study the effect of the double holes on shear fracture of rock. Also, a single-notched specimen without any hole, A0, was tested for comparison. The straight-through notch and double holes must be carefully machined using a diamond disc saw and drilling bit in order to avoid any damage to the specimens.

All of tests were carried out on a servo-controlled Instron closed-loop press, with a capacity of 2000 KN under position control. The loading rate was 0.5mm/min. The tests included the measurement of the peak load, maximum shear stress intensity factor, stable shear crack propagation rate and time.

3.2 Results and discussions

Fig.4 shows fracture trajectory of the specimen with double holes. It is seen that under the shear-box loading, new crack is initiated at the notch tips of the specimen and propagated along the original notch plane, which is of shear (i.e. Mode II) fracture.

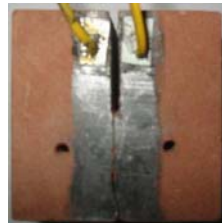


Figure 4 Fracture trajectory of the specimen with double holes

Table 3 lists the test results of the peak load P_m , maximum shear stress intensity factor K_{IIIC} , stable shear crack propagation rate V and shear crack propagation time T for the specimens with different double holes (A13, A18, A25, A34) as well as the specimen without any hole (A0). It is found that the effect of symmetrical double holes on the shear fracture of rock specimen depends on its size and location. Compared with A0 (without any hole), both A13 and A18 have larger values of P_m , K_{IIIC} and T and the smaller value of V , while A25 and A34 are opposite. Obviously, when R and L are the smallest and S is the largest for the specimens with double holes (e.g. A13), P_m , K_{IIIC} and T are the largest and V is the smallest, which is most favourable to crack-preventing. The experimental results are in good agreement with the numerical results. Therefore, adding optimal double holes symmetrical with respect to the original crack plane is an effective method for shear crack-arresting of brittle rock.

Table 4. Test results of the specimens with and without double holes

Specimen No.	P_m/kN	$K_{IIIC}/\text{N}\times\text{m}^{-1.5}$	$V/\text{m/s}$	T/s
A0	21.71	1.52	1.86×10^{-4}	29.60
A13	25.00	1.75	1.07×10^{-4}	35.64
A18	22.14	1.55	1.77×10^{-4}	31.27
A25	21.45	1.50	1.90×10^{-4}	28.80
A34	20.70	1.45	2.48×10^{-4}	28.64

4 Conclusions

- 1) Effect of crack-stopping hole on shear fracture of rock specimen depends on its location and size, which can be denoted by a regression equation about the ratio of K_{II}/K_{II0} and the three parameters, radius (R), distance away from the notch tip (L) and distance between the two holes (S).
- 2) The more the R and L , the larger the K_{II}/K_{II0} and the easier to fracture the rock specimen. However, the more the S , the smaller the K_{II}/K_{II0} and the more difficult to propagate the shear crack. When R and L are the smallest and S is the largest, the specimen with double holes has the largest values of K_{IIIC} and T and the smallest value of V , which is most favourable to shear crack-preventing.
- 3) Adding optimal double holes symmetrical with respect to the original crack plane is an effective method for shear crack arresting of brittle rock.

Acknowledgements

The financial supports from the National Natural Science Foundation of China (Grant No. 50374073) and the Natural Science Foundation of Hunan Province, China (Grant No. 08JJ3119) are gratefully acknowledged.

References

1. Liu, Z.H., Xie D. and Wang Y.H. Dynamics of Engineering Fracture. Huazhong University of Science and Technology Press, 1996.
2. Xie, H.P., Peng, R.D., Ju, Y. Research Progress on Strength Theory of Rock Based on Fracture Mechanics and Damage Mechanics. Progress in Natural Science, 2004, 14(10): 1086-1092.
3. Bai, X.Z., Hu, Y. D. and Tan W.F. Advance of the Study of Crack Prevention by the Electromagnetic Heat Effect. Advances in Mechanics, 2000, 30(4):546-557.
4. Chen, F.L. and Shuai J. Arrest Structure and Ductile Determine Methods of Ductile Fracture for Gas Transportation Pipeline. Pressure Vessel Technology, 2006, 7: 39-43.
5. Sethuraman R. and Maiti S. K. Determination of Mixed Mode Stress Intensity Factors for a Crack-stiffened Panel. Engineering Fracture Mechanics, 1989, 33(3): 355-369.
6. Yahşi, O.S., Karakurt, A.O. The Effect of a Stiffener on a Cracked Plate under Skew-symmetric Loading. International Journal of Pressure Vessels and Piping, 1988, 33(5): 385-403.
7. Tsamasphyros, G. and Dimou, G. Stress Intensities in a Strip Reinforced by Stiffeners at the Edges. Engineering Fracture Mechanics, 1995, 51(6): 897-914.
8. Güngör, S., Nurse, A.D. and Patterson, E.A. Experimental Determination of Stress Intensity Factors of Cracks in Sheet Structures with Bolted Stiffeners. Engineering Fracture Mechanics, 1996, 53(4): 561-565.
9. Rao, Q.H., Sun, Z.Q., Stephansson, O., Li, C.L. and Stillborg, B. Shear Fracture (Mode II) of Brittle Rock. International Journal of Rock Mechanics and Mining Sciences, 2003, 40(3):355-375.
10. Xie, H.F. Theoretical and Experimental Study on Shear Fracture and Crack Arrest of Brittle Rock at High Temperature. PhD Thesis, Central South University, 2008.

STUDY ON BLASTING DISTURBANCE AND ITS INFLUENCE ON ROCK BURST DURING DEEP BURIED TUNNEL

PENG YAN

*East China Investigation and Design Institution Under CHECC
Hang zhou, 310014, P.R. China*

PENG YAN and TIAN-BIN LI

*State Key Laboratory of Geohazard Prevention and Geoenvironment Protection, Chengdu University of
Technology, Chengdu, 610059, P.R. China*

PENG YAN and WEN-BO LU

*State Key Laboratory of Water Resources and Hydropower Engineering Science, Wuhan University
Wuhan, 430072, P.R. China*

HONG-TAO XU

*Dongfang Electric Corporation
Chengdu, 610036, P.R. China*

In this paper, the Excavation-induced Disturbance (ED) under high geo-stress conditions is studied through the use of a method combining theoretical calculation and field vibration analysis. The influence of every component of ED on the initiation and propagation of cracks and formation of rock burst is studied as well. The results show that the vibration monitored during blasting-excavation under high in-situ stress conditions consists of Vibration Induced by Blasting load (VIB) and Vibration Induced by in-situ stress transient Unloading (VIU). VIU becomes the main part of ED under a certain level of in-situ stress as it surpasses VIB. Both components of ED can make the cracks that extend paralleling to the free face; however, their mechanisms are different from one another. The blasting load rapidly reaches its peak value and then unloads in tens of milliseconds due to its character of impact. The tensile stress in the radial direction, induced by the unloading of the blast load, leads to initiation and extension of the circumferential cracks in the rocks around the blast holes. However, in the process of geo-stress transient unloading, radial stress unloads first and then rebounds, while tangential stress increases when the wave-front of transient unloading stress wave goes through. The combination of them makes the dynamic shearing stress increase and directly leads to the initiation and propagation of circumferential cracks. Therefore, sufficient attention should be paid to the unloading effect of geo-stress during blasting under high in-situ stress conditions.

1 Introduction

Rock burst is one of main geological hazards encountered during excavation of deep lying tunnels and it is a dynamic failure phenomenon induced by human activity with common forms of rock ejection and lager scale collapse or mining-induced earthquake, and so on. The elementary results of experiments on the relationship between underground engineering blasting, stress waves, rock burst and earthquakes were reported in 1950s. With the development of drilling and blasting methods, especially the increasing of drilling footage and charge weight per round, the influence of blasting-induced dynamic disturbance on rock burst is becoming stronger and stronger. The rock bursts, reported in several projects both at home and abroad, such as the Tian Sheng Qiao, the Tai Ping Yi, Er Tan Hydropower station, Qing Ling train tunnel, and Sima Hydropower station in Norway; almost took place in a certain time quantum after blasting. The high risk area of rock burst is usually in the distance of 2~50m away from tunnel face. The intensity of rock burst decays with the lapse of time [1]. After studying the occurrence of conditions of rock burst reported both in home and abroad, professor Guan Bao-shu pointed out that if the drilling and blasting method is adopted in tunnel excavation, rock burst may take place; however, if the TBM is used in the same tunnel, rock burst may be avoided. So blasting disturbance can be regarded as an important exciting or trigger factor of rock burst, and more importantly, it can also be a significant controlling factor of rock burst under certain conditions [2]. Wang Xian-neng also revealed that blasting-induced disturbance is not only a trigger factor of rock burst, but also affects the scale of it seriously [3]. Xie Yong-mou, Li Tian-bing, et al [4], and Xu Ze-ming, Huang Run-qiu, et al [5], indicated that the cracks in all directions caused by P wave and Rayleigh wave induced by blasting are important basis of rock burst and slabbing or spalling.

All of the studies above have confirmed that blasting excavation-induced disturbance has significant importance to rock burst, but the excavation response of surrounding rock under high geo-stress condition has not been paid sufficient attention to and the response difference caused by different unloading rate of in-situ stress also should be taken into adequate account. J.Miklowitz took notice of the dynamic unloading effect induced by the process of punching a circular hole in the center of a stretched disk in 1960s [6]. Hou Fa-liang, et al, indicated that in true tri-axial test, the unloading rate is faster, the strength of rock sample is lower [7]. Zhang Li-ming, et al, revealed that if the stress unloads suddenly in one direction, the rock sample may break in low stress level condition and rock burst may happen during this unloading process [8]. Luo Xian-qi pointed out that the tunnel excavation in hard rock is equal to the sudden unloading on excavation boundary in brittle material mass in compression field. The unloading stress wave travels from the unloading boundary to inner part of rock mass. If the energy deposited in the compressed rock mass is large enough, the shear fractures on unloading wave front would extend unstably and cause rock burst [9].

In this paper, the different mechanisms of circumferential cracks extension induced by different component of excavation disturbance are compared, and some interesting conclusions are obtained. The results of this paper have certain theoretical significance and engineering application value.

2 Composition of Blasting Excavation-Induced Disturbance

Generally speaking, the blasting excavation-induced disturbance means the vibration of surrounding rock induced by blasting load during excavation. But in the process of blasting excavation of large scale dam foundation and high rock slope and wide-span underground opening group under high geo-stress condition, serious problems of rock mass stability or deformation control induced by in-situ stress unloading would be encountered excepting for blasting load. Since recent ten or twenty years, in-situ stress unloading and its mechanical effects have always been the hot issues in rock mechanism study and engineering fields domestic and abroad.

LU Wen-bo, et al [10], confirmed that the unloading process of in-situ stress during blasting is a dynamic process and would activize dynamic unloading stress wave in surrounding rock of an underground opening. This transient unloading effect could explain the loosening mechanism of joint rock during carven or high slope excavation. Yi Chang-ping, Lu Wen-bo and Yan Peng [11-14] studied the characters of blasting load and transient unloading of in-situ stress respectively, the result indicates that the average blasting load on the excavation contour and the geo-stress are in the same magnitude order. So comparing with blasting load, the influence of the in-situ stress dynamic unloading on the stability of surrounding rock should not be ignored. Further more, the Vibration Induced by Blasting load (VIB) and Vibration Induced by in-situ stress dynamic (or transient) Unloading (VIU) were compared by Lu and Yan in the process of excavation of a circular tunnel under hydro-static stress condition [12], the result is shown in Figure 1 (BL and IS represent blasting load and in-situ stress respectively, and the values following IS represent the level of in-situ stress).

It could be seen in Figure 1 that VIU could exceed VIB and become the main component of total vibration under certain level of in-situ stress (for example 20MPa shown in Figure 1) from certain distance away the excavation contour in surrounding rock.

The calculation result has been verified by field vibration monitored during blasting excavation. Six parallel inlet tunnels are arranged with a center distance of 28.9m in a certain hydropower station located in western China. The diameter of circular inlet tunnels is 10.7m, and in-situ stress in the construction area is about 10 Mpa. Surrounding rock of tunnel is granite with a measured longitudinally sonic velocity of about 4500m/s. For the poor condition of surrounding rock, the length of boreholes in the advancing section of diversion tunnel 3# is only 1.5 m. Overall charge is 48 kg, and is divided into three micro-delays, the maximum single-shot explosive of which is 20 kg. The initiation sequence is followed by center cut holes, breakage holes and contour smooth blasting holes. The measure radial blasting vibration curve is shown in Figure 2. BL-blasting induced vibration, IS- unloading of in-situ induced vibration, MS1~MS5-delay numbers for detonators

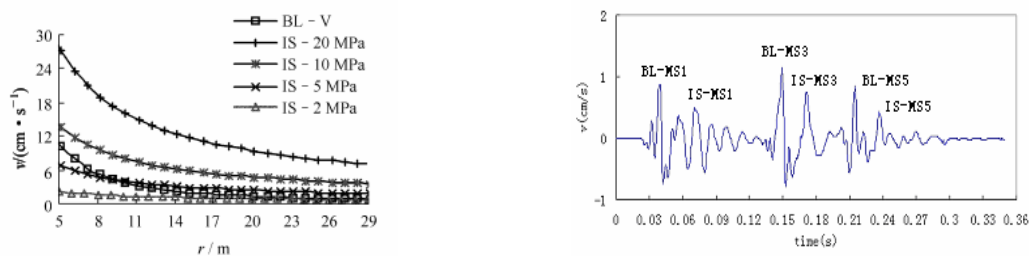


Figure 1 peak particle velocity induced by initial stress
dynamic unloading and blast load respectively [12]

Figure 2 Monitored vibration curve versus time in inlet-water tunnel [14]

Since the arrangement of vibration monitors is designed specially for tunnel face, it can be inferred that the Rayleigh wave is not included in the vibration wave monitored. From the Figure 2, it could be clearly seen that, the total vibration curve includes three parts corresponding to three delays, which were initiated in time 24.5ms, 132.0ms and 201.0ms respectively. By estimating propagation time for P wave, S wave or R wave induced respectively, it could be deduced that, peaks BL-MS1, BL-MS3 and BL-MS5 be induced by blasting loads ,and peaks IL-MS1, IL-MS3 and IL-MS5 be caused by the transient unloading of in-situ stress [14]. (In figure 2, BL is blast induced vibration, IS is the vibration induced by the transient unloading of in-situ stress, and the number after MS shows the stage of millisecond detonator.)

The geo-stress measurements and blasting-induced vibration monitoring in Longtan hydropower station, carried out by ZHANG Zheng-yu, et al, also indicated that the dynamic effect induced by blasting process includes two aspects, they are blasting impact and in-situ stress transient unloading [15].

3 Mechanism of Rock Burst Induced by Excavation Disturbance

3.1. Propagation of Cracks and Occurrence of Rock Burst During Excavation

After excavation, the micro-cracks in surrounding rock of underground opening would extend and coalesce with each other paralleling to form circumferential cracks under stress concentration or excavation disturbance, as shown in Figure 3. Rock sheets generates because of propagation and coalescence of circumferential cracks. And some studies have demonstrated that these rock sheets would fail unstably and break violently when certain conditions are satisfied, and then rock burst happens [16].

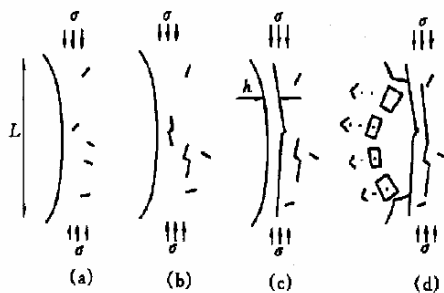


Figure 3 Qualitative description of mechanism of rock burst [16]

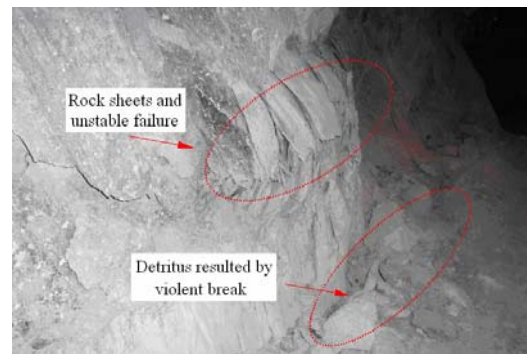


Figure 4 Rock burst on the wall of tunnel after blasting excavation

As shown in Figure 4, the rock burst, which took place in left spandrel and side wall of a deep buried tunnel after blasting excavation, verified the mechanism of rock sheet unstable failure mentioned above excellently. So it could be concluded that the circumferential cracks (or cracks paralleling to the free surface of tunnel) in surrounding rock of an underground opening have important significance on the occurrence of rock burst.

3.2. Extension Mechanism of Cracks Caused by Excavation Disturbance

In order to simplify the analysis processes, circular tunnel with a diameter of 10.0m is employed in theoretical analysis, and it is assumed that full face drilling and blasting is employed during tunnel excavating, as shown in Figure 5. Type of the surrounding rock of tunnel is granite with a density of 2700kg/m^3 , elastic modulus of 64.2GPa , Poisson ratio of 0.23 and longitudinally sonic velocity of 5250m/s .



Figure 5 Full section excavation of circular tunnel

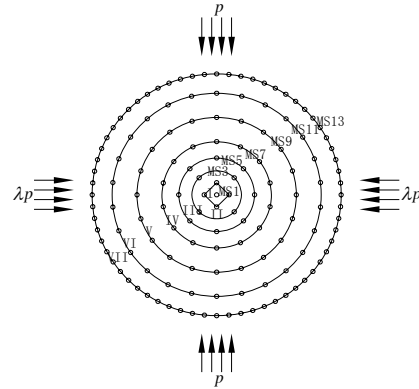


Figure 6 Blast design of circular tunnel excavation

The blasting design for the full face tunnel excavation is shown in Figure 6, where cut blasting with middle parallel blast holes is adopted. The diameter of blast hole is 42 mm , and emulsion with a density of 1000kg/m^3 and a detonate velocity of 3400m/s is used. From the inner to contour, blast holes of 2 rounds of cut, 3 rounds of breakage, 1 round of buffering and finally smooth blasting holes are arranged on the excavation work face, which are initiated in sequence with milliseconds-delay detonators named as MS1, MS3, MS5, MS7, MS9, MS11 and MS13.

(1) Influence of blasting load on circumferential cracks

Through Laplace transformation and Stehfest numerical inversion, the dynamic stress field in elastic rock medium around the cylindrical cavity (blast holes) under inner explosion load is calculated [17]. The blasting load adopted in calculation is shown in Figure 7, and the ascending time of blasting load $t_r = 50\text{ }\mu\text{s}$, Yang's modulus of rock mass $E = 50\text{ GPa}$, Poisson's ration of rock mass $\nu = 0.25$, density of rock mass $\rho = 2400\text{Kg/m}^3$. Curves of radial stresses corresponding to different unloading rate of blasting load are shown in Figure 8, and curves 1, 2 and 3 are corresponding to $t_s = 100\text{ }\mu\text{s}$ 、 $150\text{ }\mu\text{s}$ 、 $200\text{ }\mu\text{s}$, respectively.

From Figure 8 we can arrive at a conclusion that during the unloading process, radial stresses around blast holes would change from compressive stresses into tensile stresses, and the higher unloading rate is, the higher tensile stresses are. This result could be explained as follows.

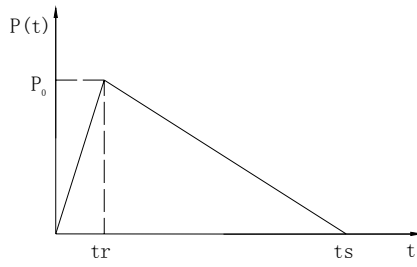


Figure 7 Curve of explosive load on cavity wall

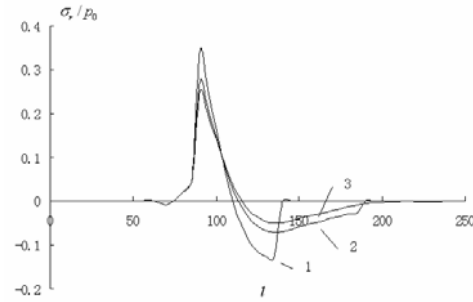


Figure 8 Curve of radial stresses of different unloading rate while $p(t)$ attenuating linearly

After detonation, under the blasting induced shock waves and stress waves, rock mass around the charge cavity suffer violent compression, and a crushed zone will appear and radial cracks will arise in the cracked zone in an extremely short time. At the same time, a large amount of elastic potential energy is accumulated in rock media in the elastic zone. Following the blasting shock waves, particles around the cavity will outspread radially, and last for a while, which result in negative pressure in the cavity with the addition of other reasons such as the venting of explosive gases and the spread of radial cracks, etc. and then cause the unloading of blasting load. Because the time of blasting load attenuating from the magnitude of several ten thousands or several hundred thousands atmosphere pressure to a comparatively lower average pressure (i.e. the quasi-static pressure of explosive gases) is so short that it can be counted by millisecond, so the unloading speed is rather high and can be regarded as instantaneous unloading generally. During such a high speed unloading process, the elastic potential energy stored in rock media previously will release sharply and unloading waves are induced, which induce a rather high amplitude value of tensile stresses and causes radial stresses to change from compressive stresses to tensile stresses. If the radial tensile stresses are larger than dynamic tensile strength of rock, rock will be split open by tension and then circumferential cracks arise. So we think it's a sound explanation to the generation of circumferential cracks in rock mass.

(2) Influence of in-situ stress transient unloading on circumferential cracks

Because blast holes on excavation work face are initiated in a sequence of round by round, the disturbed in-situ stress which is also called as the excavation load of surrounding rock corresponding to different blasting sequences could be calculated with formula of elastic cylinder with an infinite thickness, that is

$$\sigma_r = \left(1 - \frac{r_0^2}{r^2}\right)P \quad (1)$$

Where r_0 is the inner radius of cylinder, P is the initial in-situ rock stress. Shown in Figure 9, for sequence V, before it initiates, the initiations of series I,II,III and IV should have been carried out, so a cylinder with a inner free surface has formed, then the excavation load corresponding to blasting sequence V should be equal to the disturbed in-situ stress of rock.

For simplifying, the unloading mode of initial geo-stress is supposed to be linearity [14]. The stress change on unloading surface versus time during blasting is taken as fold line ① shown in figure 10, which is the superposition of the far-off in-situ stress (line ②) and unloading course (fold line ③) [6].

The duration time t_0 of in-situ stress unloading could be estimated by the propagation velocity of crack driven by explosion load [18], which is set as 2ms in this paper.

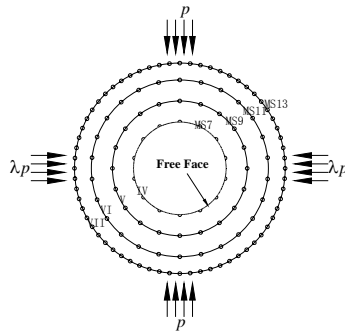


Figure 9 Determination of unloading stress

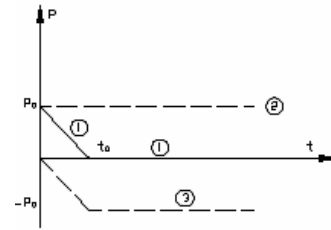
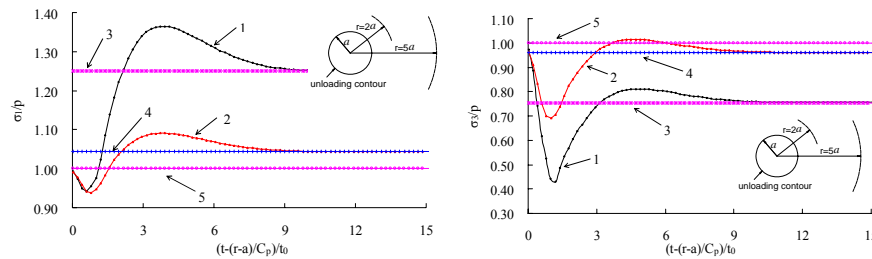


Figure 10 Transient unloading process of surrounding rock stress

The curves of the maximum and minimum principal stresses versus time at certain distance in surrounding rock of the tunnel with lateral pressure coefficient $\lambda = 1$ and unloading time $t_0 = 2ms$ are presented in Figure 12. The number 1 and 3 or 2 and 4 represent the transient unloading stress and quasi-static unloading stress at distance $r=2a$ and $r=5a$ respectively, a is the radius of excavation tunnel. The quasi-static stress could be calculated using Formula (1). Number 5 in the pictures represents in-situ stress.



(a) Maximum principle stress σ_1 (Tangential stress)

(b) Minimum principle stress σ_3 (Radial stress)

(1,2-transient unloading stress at $r=2a$, $r=5a$ respectively; 3,4- quasi-static unloading stress at $r=2a$, $r=5a$ respectively; 5- in-situ stress)

Figure 11 The stress of dynamic unloading when $\lambda = 1$

As shown in Figure 11, the in-situ dynamic unloading-induced disturbance transmits with a velocity of C_p (the longitudinally sonic velocity) in surrounding rock of the tunnel, and when the unloading stress wave arrives, the balanced stress state is affected. Both of the maximum and minimum principle stress (σ_1 and σ_3) unload first and then rebound, and finally converge to the quasi-static unloading stress.

Following the result presented above, the differences of principle stress ($\sigma_1 - \sigma_3$) induced by transient and quasi-static unloading respectively are calculated and shown in Figure 12, including stress curves versus time at two different distances ($r=2a$ and $r=5a$) in surrounding rock.

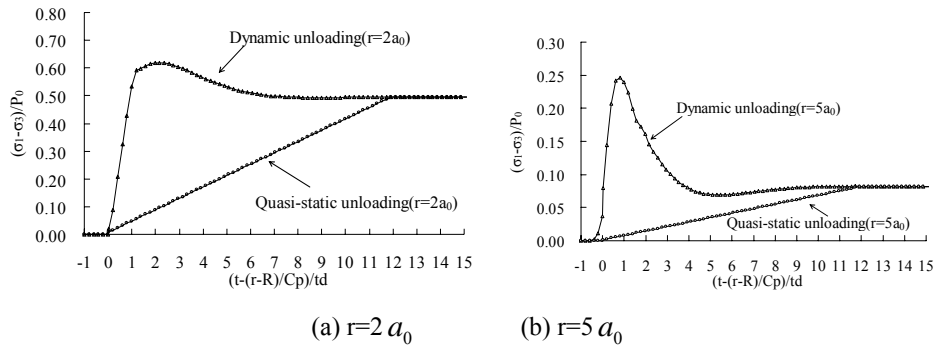


Figure 12 Difference between maximum and minimum principle stress during quasi-static and dynamic unloading [13]

It could be seen from Figure 12 that, comparing with quasi-static unloading, the transient unloading of in-situ stress could cause much larger principle stress difference, which would make the tangential stress increases when the wave-front of transient unloading stress wave goes through. The circumferential cracks would initiate and propagate when the dynamic tangential stress is larger than dynamic strength of rock.

4 Conclusions

Through aforementioned analysis and discussion of excavation disturbance and rock burst, the following conclusions could be made:

- (1) The blasting excavation disturbance is not only an inducing factor of rock burst, but also an important controlling and forming factor of it. Excavation disturbance seriously influences the intensity and scale of rock burst, although it is not necessary for the occurrence of rock burst.
- (2) Both theoretical calculation and analysis to the monitoring vibration indicate that the vibration induced by the excavation of a tunnel under high in-situ stress is the result of superposition of blasting-induced vibration (VIB) and the transient unloading of in-situ stress induced vibration (VIU). VIU can exceed VIB and become the main component of total vibration under certain levels of in-situ stress from certain distances away from the excavation contour in the surrounding rock.
- (3) The initiation and propagation of circumferential cracks, which have important significance on the forming of rock burst, could be induced both by blasting load and in-situ stress transient unloading, but with different driving mechanisms. The blasting load reaches its peak value rapidly and then unloads in about tens of milliseconds due to its character of impact. This unloading process of the blasting load would give birth to tensile stress in the radial direction, which would give birth to circumferential cracks in surrounding rock if the tensile stress is larger than the dynamic strength of rock. However, in the process of geo-stress transient unloading, the radial stress unloads first and then rebounds and the tangential stress increases when the wave-front of transient unloading stress wave goes through. So the dynamic shearing stress is strengthened and directly leads to the initiation and propagation of circumferential cracks.

(4) According to the results mentioned above, sufficient attention should be paid to the unloading effect of geo-stress during blasting under high in-situ stress conditions.

Acknowledgements

The authors wish to express their thanks to Joint support from Special Research fund of State Key Laboratory of Geohazard Prevention and Geoenvironment Protection (Chengdu University of Technology) (Support No. GZ2009-15) and China National Science Foundation and Yalongjiang Development Corporation(Support No. 50639100)to the work.

References

1. Xu, Z.M. and Huang R.Q. Progress in Research on Rock Burst Hazard of Long Tunnel with Large Section. *Journal of Natural Disasters*, 2004, 13(2). 16-24.
2. Guan, B.S. and Zhang, Z.Q. The Basic Condition of Rock-Burst in Tunnels. *Journal of Railway Engineering*, 1998, (supplement). 326-330.
3. Wang, X.N. and Huang, R.Q. Analysis of Deformation and Failure Features Characteristics of Rock under Unloading Conditions and Their Effects on Rock Burst. *Journal of Mountain Research*, 1998, 16(4). 281-285.
4. Xu, Z.M., Huang, R.Q., Luo X.C., et al. Limitations of Static Load Theory in Rock Burst Research and Preliminary Analysis on Dynamics Mechanism of Rock Burst. *Chinese Journal of Rock Mechanics and Engineering*, 2003, 22(8). 1255-1262.
5. Xie, Y.M. and Li, T.B. Primary Discussion on Blast's Affection on Rock Burst. *The Chinese Journal of Geological Hazard and Control*, 2004, 15(1). 61-64.
6. Miklowitz, J. Plane-Stress Unloading Waves Emanating From a Suddenly Punched Hole in a Stretched Elastic Plate. *Journal of Applied Mechanics*, 1960, 27. 165-171.
7. Hou, F.L., Liu, X.M., et al. Second Analysis to the Mechanism of Rock-Burst and Its Intensity. *The proceedings of the third national conference of rock dynamics*, (Guilin, 1992).
8. Zhang, L.M., Wang, Z.Q. and He, J.Z. Analysis of Failure Characteristics of Rock under Unloading Conditions and Their Effects on Rock Burst. *J1 Xi'an Univ. of Arch. & Tech*, 2007, 39(1). 111-114.
9. Luo, X.Q. and Shu, M.X. Dynamic Fracture Criterion of Rock Blasting-d Criterion. *The Chinese Journal of Geological Hazard and Control*, 1996, 7(2). 1-5.
10. Lu, W.B. Study on the Mechanism of the Loosing of the Jointed Rock Mass Caused by the Dynamic Unloading of Initial Stress during Rock Blasting. *Chinese Journal of rock mechanics and engineering*, 2005, 24(1). 4653-4657.
11. Yi, C.P., Lu, W.B., Xu, H.T., et al. The Dynamic Unloading Effect Study of Initial Stress Field in Excavation Process of Large-Scale Rock Mass Structure. *Chinese Journal of Rock Mechanics and Engineering*, 2005, 24(s1). 4750-4754.
12. Lu, W.B., Chen, M., Yan, P., et al. Study on the Characteristics of Vibration Induced by Tunnel Excavation under High In-Situ Stress. *Chinese Journal of Rock Mechanics and Engineering*, 2007, 26(s1). 3329-3334.
13. Yan, P. Study on Mechanism of the Vibration Induced by Dynamic Unloading during Rock Excavation.

Wuhan: Doctoral Dissertation of Wuhan University, 2008.

14. Lu, W.B., Peng Y., and Zhou C.B. Dynamic Response Induced by the Sudden Unloading of Initial Stress during Rock Excavation by Blasting. In Proceedings of the 4th Asian Rock Mechanics Symposium (ISRM International Symposium 2006), World Scientific Publishing, (Singapore, 2006).
15. Zhang, Z.Y., Liu, Y. and Zhang, W.X. Study on Blasting Vibration Effect of Underground Powerhouse of Dongfeng Power Station. The 5th conference of engineering blasting, 1993, 299-305.
16. Dyskin, A.V. and Germanovich, L.N. Model of Rock Burst Caused by Cracks Growing Near Free Surface. Rock-bursts and Seismicity in Mines. Rotterdam: Balkema, 1993, 169-174.
17. Xu, H.T., Lu, W.B. and Zhou, Y.F. Study on the Mechanism of the Formation of Circumferential Cracks in Drilling Blasting. Engineering Blasting, 2003, 9(3). 7-11.
18. Zhang, Z.C., Xiao, Z.X., Guo, X.B., et al. Experiment Study of High-Speed Photography of Crack Development in Fracture Control Blasting. Journal of Southwest China Institute of Technology, 2001, 16(2). 53-57.
19. Wu, L. Study on Mechanism and Fracture Criterion of Rock Crack Propagation Driven by Blasting Load. Wuhan: Doctoral Dissertation of Wuhan University, 2007.

PHYSICAL MODEL FOR ROCKBURST BASED ON ACOUSTIC EMISSION

XU-BIAO DENG, WEN-FENG DU and GANG XU

*School of Safety and Resource Engineering, China University of Mining and Technology (Beijing),
Beijing 100083, P.R. China*

XU-BIAO DENG, WEN-FENG DU and GANG XU

*State Key Laboratory of Coal Resources and Mine Safety, China University of Mining and Technology, Beijing
100083, P.R. China*

Rockburst is one drastic type of rock failure and a hazard to the production and safety of underground mining and tunnelling. It is a difficult problem to describe the mechanism of rockburst. From the point of solid physics and mesomechanics, a bond spring model of rock failure (BSMRF) was given upon acoustic emission (AE) of rock damage and a virtual bond spring, which represents the elastics and plastics of compression and tension and rotation of rock bond. Applied to the analysis of damage development and energy change of rock failure, the model gives a criterion of fracture development, which is called virtual remaining energy. According to the AE pattern of rock failure, the paper gives three types of rock failure, i.e. whole-course-pattern, end-course-pattern, and burst-pattern. The burst-pattern rock failure is rockburst. Through analysis of three rock samples based on BSMRF, it was found that AE during the loading, ruptured particle distribution, and their surface area of rockburst are very distinctive. It indicates that the failure of the last series of bond spring has decisive influence to rock failure. In one pattern of rock failure, the ratio of the last bond springs of rockburst has a sharp difference from the common, which took more than a half of the total. When the result is applied to the explanation of size effect, confining pressure effect, and some other rockburst phenomena, it is found that reasonable explanation can be obtained.

Rockburst is a drastic type of rock failure, called bump in mining, and is one of the biggest geology disasters in coal mining. The sudden failure of rock is also called rock destabilizing failure by lecturers. Rockburst is the most drastic rock failure. Based on the rock destabilizing model, scientists provided different models of rockburst [1]. This paper provides a bond spring model of the micro mechanism of rock loading. According to the AE pattern of rock failure, a bond-spring model of rock failure (BSMRF) was created to describe the character of rockburst and explain some relative problems with it.

1 Micro Mechanical Character of Rock and Bond Spring

There are numerous papers and theories on the subject of mechanical and engineering behaviors of rock, however, little of them are concerned with the micro mechanism of these behaviors and studied them together. Generally, it was thought necessary to study the innate characteristics of rock mechanics in micro-sizes and meso-sizes since it was a same type of rock failure for different sizes and must have some similarities. Therefore, the rock mechanical behaviours in macro size may be induced from the micro character of bond.

The interaction and potential energy of atoms in a solid was sketched by figure 1 [2]. In figure 1, the distance between the two atoms is r_0 is called the equivalent distance because the attraction is equivalent to the repulsion forces between atoms. When the distance is closer than r_0 , because of compression, the repulsion becomes bigger than the attraction and exponentially bigger as r gets smaller. The attraction will become larger when r gets bigger because of tension forces. The interaction of atoms is called a bond. One distinctive

characteristic is that the attractive action has a peak value as r gets bigger, which indicates that the only way for a bond to break is to increase r .

Basically, the mechanical state of a rock is determined by its characteristics of its micro atom bond. The elastic force is produced when the distance of atoms is changed under certain limits of compression or tension from loading and disappears as loading is taken off. As indicated in figure 1, the repulsive reaction of a bond is unlimited but the attraction has a peak. The bond has to rotate to a smaller energy position to break when the rock is compressed to deform. The bond rotation is proposed to be the reason for plastic property of material, of which the change is irrecoverable. From the energy point, the elastic energy of a rock is bigger than the plastic and the energy accumulated by compression is much larger than by tension, which leads to many kinds of geology disaster. Therefore, the plastic has been neglected and the compression failure of a rock is illustrated in this paper, which is typical and can be applied to other loading form.

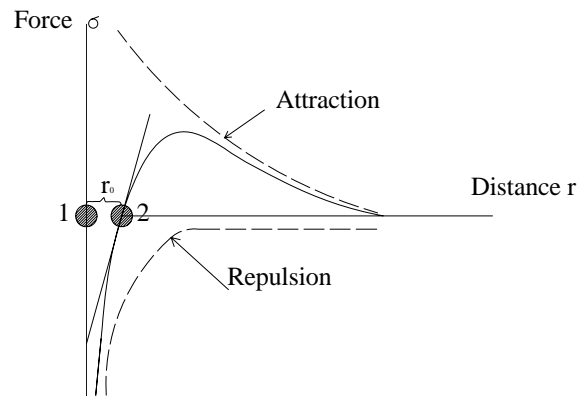


Figure 1 Sketch for relationship of two atoms and its potential energy change (Cited from ZI-QIANG GUO, 1982, modified.)

The above analysis from bond theory in micro size complies well with phenomena of rock mechanical failure in meso-size and macro-size. Firstly, the compression strength of a rock is far bigger than the tension strength and both have strain limits. Secondly, the failure pattern of a rock is thought to be a tension one despite that some scientists suggest that the shear failure is also one pattern [3]. Finally, the fracture development of rock determines the rock failure [3].

It is coincidence that the bond action is very similar to a spring except the latter cannot rotate. Thus a virtual bond spring can be made to represent bond action between atoms. The tension limit of a bond spring in rock is smaller than the compression limit. When the spring reached its limit under a compression loading it will not destroy directly but rotate to a free direction to reach its tension limit and destroy. The rotation strain is irreversible and consumes little energy. If unload when bond spring rotating, the elastic strain will recover and the rotation part is a plastic change. The following physical model of rock failure is made up by this bond spring.

2 Physical Model for Rock Failure

A solid rock has deficiency of all kinds in different size level such as fault, fractures and pores, dislocations. The stress concentrations around deficiency make the rock mechanical state very complex. In addition, the state is influenced by other factors such as size effect, confining pressure effect and loading rate, which interact each other and make the problem more complicated. It is the reason that the model made in past can just represent some characters of rock [4,5]. When damage mechanics introduced to rock mechanics, the deficiency has been considered only by an equivalent way in macro size. The size effect which produced by fractures and pores in meso-size is an unsolvable problem for damage mechanics [6]. Some scientists considered the size effect of

deficiency, but confined in a pattern of fixed possibility distribution such as Weibull distribution [7,8,9]. A good model to represent all these characters of rock is desperately in need.

It is studied frequently of a rock failure under uniaxial compression. Many rock parameters are calculated from the experiment data. The following characters are found by experiments. The failure always happened with the production, development and breakthrough of fractures, appeared to be several main rupture faces [3] and the rupture particles are in different size [4]; The AE is consistent to the production, development and breakthrough of fractures in the usual loading form and different from the rock states, classified as five patterns by Z. G. YIN [10] and three patterns by C. A. TANG [8].

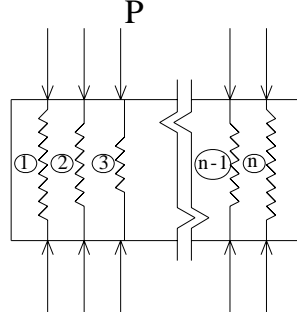


Figure 2 The bond spring model of rock failure

Considering above characters of rock failure and AE, a physical model is established. It was supposed that a rock structured by n bond springs in parallel, which have the same coefficient of elasticity, different compression limits and the same tension limits, sketched by figure 2. When loading, the smaller limits of bond springs reach their limits and broke first and then the bigger ones. The broke of a bond spring is corresponded to one AE, which indicates the production or development of a fissure. The rock failure means that all bond springs of the model are broke. The fissure development has different energy stages, which increase as the strain increases. The springs in one stage are called one series of bond springs, which corresponds to a series of AE. Generally, the failure of a bond spring influences only his series, which was called localization [11]. Rock in different states has different AE series. If the model has α series and β_i springs in each series then it has $n = \sum_{i=1}^{\alpha} \beta_i$. The above model is called bond spring model of rock failure (BSMRF). The following part is a detail analysis.

It is supposed that the main ruptured faces of a rock failure are formed by $n \Gamma_i$, which was a bond spring with elastic limit x_{ci} before it emerged. The elastic coefficient of bond springs is η . The elastic energy of a bond spring when a fissure produced or developed is

$$U_{ei} = \frac{1}{2} \eta x_{ci}^2 \quad (1)$$

The left bond spring has the following elastic energy

$$U_i^k = \frac{1}{2} \eta x_i^2 \quad (2)$$

It easy to get the remaining energy after the fissure development

$$V_i = U_{ei} - \Gamma_i \quad (3)$$

For a rock, the compression limit is usually bigger than the tension limit. So it has $U_{ei} > \Gamma_i$ and $V_i > 0$, which indicates that a face of Γ_i consumes only a larger part of the bond spring energy. The remaining energy V_i will flow to the adjacent springs of his series and caused a series production or development of fissures. It was supposed that there is m bond springs in the series and the beginning springs is k . The failure lasted until the last bond spring. For a given time of $k+j-1$, j of the left bond springs has elastic energy of

$$U_{k+j}^{(k+j)} = U_{k+j}^k + \sum_{i=1}^j \frac{V_{k+i-1}}{m-i} \quad (4)$$

The $k+j$ bond spring has a virtual remaining energy as following

$$V_{k+j}^{(k+j)} = U_{k+j}^{(k+j)} - U_{ek+j} \geq 0 \quad (5)$$

There is an assumption in formula (4) that the transferring speed of energy is much faster than the work done by exogenic force. It is reasonable since the energy transferred in elastic wave and only a detonation loading has a close speed. Formula (5) is the necessary and sufficient condition for the production or development of a fissure. If the spring energy satisfied formula (5) then the fissure will develop from the k step to $k+j$ step. Or the development of fissure will stop. If $k+j=n$ then the rock deformed entirely. In formula (4), if the last series of a rock has many bond springs, the remaining energy will accumulate to a high standard at the last second of failure, and a rockburst happen.

Formula (5) can also be written as

$$V_i^{(i)} = U_i^{(i)} - U_{ei} \quad (6)$$

$V_i^{(i)}$ in formula (6) is named as virtual remaining energy (VRE), a criteria for the production or development of a fissure. When $V_i^{(i)} < 0$, the development need more energy, $V_i^{(i)} = 0$ indicates a stable fissure development, and $V_i^{(i)} > 0$ do a speeding development.

Table1 Quantitative statistics of AE from rock rupture for three pattern

Parameter	Failure Pattern		
	Burst	End Course	Whole Course
R_{AE}	≈ 1	< 0.5	< 0.25

It is induced from the past rock mechanical and AE experiment that the “ n ” steps and α series of fissure development which formed the main faces is limit and despite of the rock size and loading form. Both steps and series correspond to AE. According to statistics from the past experiments about sandstone, limestone and granite, etc. [8,10,12,13,14], sedimentary rock, metamorphic rock and magmatic rock correspond roughly to three patterns of failure, i.e. whole course pattern, end course pattern and burst pattern, illustrated by R_{AE} in table 1. R_{AE} is the AE ratio of the last series and total bond springs. Obviously, the end course pattern has an AE intension between the burst and the whole course one.

3 Rockburst Analysis Based on Bond Spring Model of Rock Failure

Rockburst is commonly geology disaster in mining that happened not only on pillar but also on working face of mining and tunnelling, and more fluent and drastic as depth increases. It is a big influence to mining and miner safety, which made it an important research subject. According to BSMRF, rockburst is a burst failure of rock and difficult prediction object for AE. It is necessary to make further study and find the way to prevent or predict the occurrence of rockburst. More study put on the hard rock or coal but we get a rockburst on sandstone

clay during a uniaxial compression test about rock. Contrast by other failure pattern of rocks, it appear to be outstanding of rockburst.

3.1 Data from the rockburst test

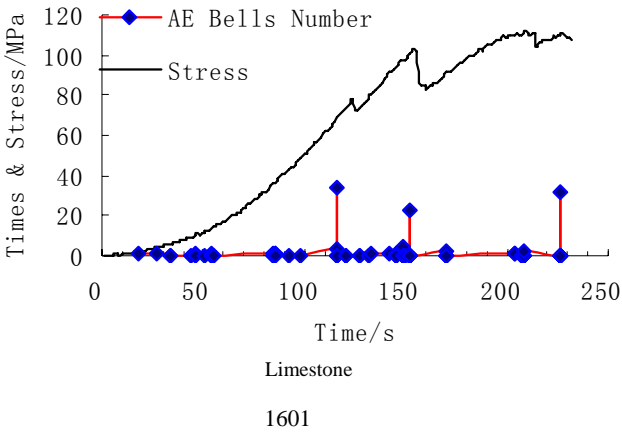
The test carried out in Laboratory of Rock Mechanics and Control of Engineering disaster in Depth, China University of Mining and Technology (Beijing), China. Rock is loaded by triaxial rock loading machine with electrohydraulic servo controlled by computer. AE is detected by digital full wave AE detector. The particles from the rock failure were analyzed in size. Two rock samples that were not burst were chosen to be contrast with the burst one. The usual parameters were listed in table 2. The pictures of rock after failure showed in figure 3. Figure 4 gives relationship of time and bells number of AE.

Table 2 Basic parameters of rock samples

Rock Samples	Mass /g	Height /mm	Diameter /mm	Density /g.cm ³	SW's Speed /m.s ⁻¹	PW's Speed /m.s ⁻¹	Uniaxial Strength /Mpa	Elastic Ratio /Mpa	Poisson Ratio
Limestone	431.31	84.85	48.86	2.69	3367	4396.4	59.6	24.24	0.11
Sandstone Clay 1	426.77	85.12	49.00	2.65	1984	3236.5	98.59	25.3	0.12
Sandstone Clay 2	429.04	85.09	48.99	2.64	2753.6	5034.7	124.36	36.53	0.13



Figure 3 The pictures of rock after and before failure



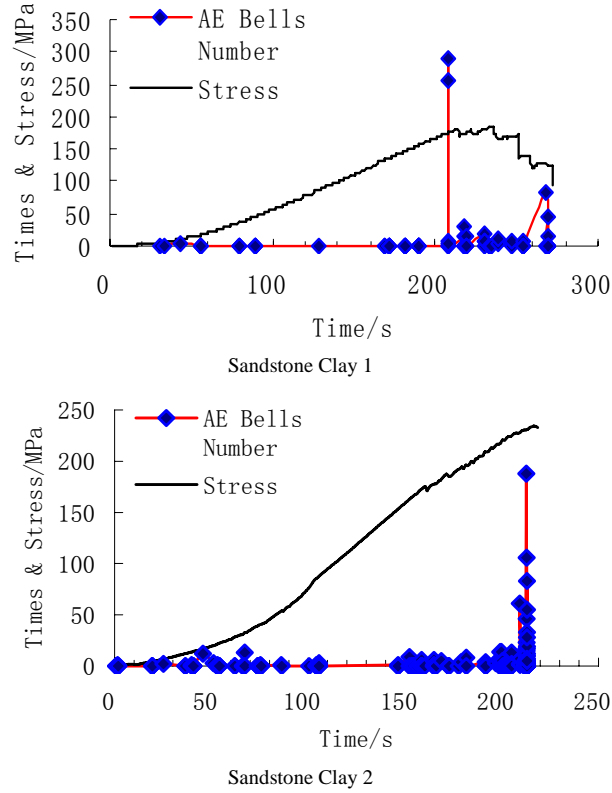


Figure 4 Relationship between time, AE bells number and stress

Obviously, the rockburst has more crush particles, more complete failure and more intensive AE bells that has been proved by tests and engineering [12,13]. But the interrelation and energy character of these phenomena is still uncovered.

3.2 Rock Outburst Analysis Based on BSMRF

From the theoretical analysis about bond spring model of rock failure (BSMRF), the total energy of the last series of bond springs before rockburst is

$$U_n^{(n)} = U_n^k + \sum_{i=1}^{n-k} \frac{V_{k+i-1}}{n-k-i} \quad (7)$$

The total remaining energy is

$$\sum_{i=1}^{n-k} V_{k+i-1} = \sum_{i=1}^{n-k} (U_{ek+i-1} - \Gamma_{k+i-1}) \quad (8)$$

Whatever the complexity of the rockburst or its influenced factors, the dominant energy of rockburst is determined by parameters of the last bond springs. Beside the universal ones such as elastic coefficient η and elastic limit x_g , the number of last series bond springs $n-k$ is also very important. Accordingly, it would be easy to describe the failure character of rockburst and explain the complex phenomena in tests and engineering about it.

As a reasonable hypothesis there is no kinetic energy existed in rock since the development and breakthrough of fissures happened in inner rock. Thereby, all energy of bond springs has to be consumed to

produce the new face of particles and thus determines the particle distribution. Data analyzed from the tests listed in table 3. It is clear that ratios of AE bells number, mass and surface area of particles smaller than 40mm and the total are very close, which suggest that the main faces breakthrough and particles distribution of rock failure was determined by the last series of bond springs. Consequently, it can be induced rationally that the rock failure is determined by the last series of bond springs. As one pattern of rock failure, the ratio of the last bond springs of rockburst has a sharp difference from the common, which took more than a half of the total. This is a quantitative description of rockburst and might be a new criteria to the happen of rockburst.

Table 3 Statistics about AE bells number and crush particles

Rock Samples	AE Bells Number/times			Mass of Crush Particles/g			Surface Area of Crush Particles/cm ²		
	Total	Last	Last/Total	Total	<40	(<40)/Total	Total	<40	(<40)/Total
Limestone	112	32	0.29	431.31	120.71	0.28	706.35	198.14	0.28
Sandstone Clay 1	821	143	0.17	426.77	64.09	0.15	726.66	123.35	0.17
Sandstone Clay 2	959	727	0.76	429.04	284.37	0.66	864.47	584.75	0.68

The size increase of a sample would probably increase the α series at the same time, accordingly, decrease the number of the last series $n-k$. Therefore, it might be a safe method to determine the happen of a rockburst through a small sample test if carried properly. Confining pressure for a rock can enlarge elastic limit χ_d and increase the number $n-k$ of last series of bond springs, which makes it easy to happen a rockburst with big energy. One face unloading when true triaxial loading frequently produce a rockburst because the rotations of bond springs are in same direction make more bond springs deformed at the same time.

In mining engineering, the rupture of hard rock roof, local intensive stress and blast digging often solely or assembly lead to production of a bump with complex phenomena [14]. If make the tunnelling or mining a system of bond springs, it might be possible to illustrate the happen of a bump. A big impulse force load on the rock or coal seam when the hard rock roof ruptured that makes many bond springs reach their elastic limits and deformed at the same time and produce a bump. The blast digging is much like a one-face unloading when true triaxial loading discussed above. The more mass dig, the easier a bump happen. If the dig mass is not that much then a bump would delay or not happen. In a local intensive stress zone there is much energy existed with the confining pressure, which if release in a sudden way would frequently lead to a bump. Some reported rockbursts happened on a rock pillar, which happened to be the same condition of the one in the tests of this paper. If the width of the pillar increased the last series of bond springs would decrease as discussed in the last paragraph, which was thought to be a feasible method to reduce the energy before a rock failure and prevent a rockburst from happening [15].

4 Conclusions

1) A bond spring model of rock failure was established through the theoretical and experimental analysis of the rock failure in macro, meso and micro sizes, and its AE. Three failure patterns were found to be whole-course, end course and burst, and rockburst.

2) By contrast analysis of the phenomena from burst rock and two non-burst rocks under uniaxial loading, it was found that rockburst has a more complete destruction and a more drastic and intensive AE during the loading end, with more ruptured particles (<40mm).

3) With quantitative analysis of energy based on BSMRF, it is indicated that the failure of the last series of bond spring has a decisive influence on rock failure, determined by the elastic coefficient, elastic limit and number of the last bond spring series. As one pattern of rock failure, the ratio of the last bond springs of rockburst has a sharp difference from common occurrences, which is more than a half of the total. Apply the

results to the explanation of the effect of size, confining pressure effect, and some relative engineering facts of rockburst, it seems to be reasonable.

Acknowledgements

The authors wish to acknowledge the collaborative funding support from items of Chinese 973 project (2009CB219603, 2006CB202209, 006CB202210, 2005CB221501), major items of Chinese national natural science foundation project (40874071、50490271、40672104), items of Chinese national support science projects (2006BAK03B01). In particular we wish to thank YONG-JUN LI, KAI ZHANG, GANG XU and staff in Laboratory of Rock Mechanics and Control of Engineering disaster in Depth, China University of Mining and Technology (Beijing), China, for their help in preparing the sample and carrying out the experiment.

References

1. Tang, C.A. Fracture, instability and rockburst of rocks. in centurial achievement of rock mechanics and engineering in Nanjing, China. (Ed. by WANG Sijing, YANG Zhifa, FU Bingjun ed.). Hohai University Press, Nanjing, China, 2004, 324-335
2. Guo, Z.Q. Wave in solid. Seismos Publishing House, Beijing, China, 1982.
3. Lin J.M. Study on the mesoscopic characteristics of rock damage under compressive loading. Journal of Tongji University, 21(2). 219-226
4. Xie, H.P. Approach to mechanics of fractal-rock. Science Press, Beijing, China, 1997.
5. Huang, X.H., Feng, X.T. and Chen, B.R. Discussion on parameters determination of viscoelastic model in creep test. Chinese Journal of Rock Mechanics and Engineering, 2007, 26(6). 1226-1231
6. Xie, H.P. Damage mechanics of rock and concrete. China University of Mining and Technology Publishing House, Xuzhou, China, 1990.
7. Ling, J.M. and Sun, J. On meso-crack damage of brittle rocks and its time-dependent characters. Chinese Journal of Rock Mechanics and Engineering, 12(3). 304-312
8. Tang, C.A. Catastrophe during Rock Rupture. Beijing: Coal Industry Press, 1993
9. Yang, Y.Q. Continuum damage mechanics analysis on strength of rock. Chinese Journal of Rock Mechanics and Engineering, 18(1). 23-27.
10. Yin, Z.G. Experimental study on acoustic emission and damage during the failure of rock. Master Dissertation, Central South University, Chang Sha, China, 2005.
11. Fan, H.J., Xiao, S.X. and Peng K. Study on constitutive model of rock sample in uniaxial compression based on strain localization. Chinese Journal of Rock Mechanics and Engineering, 25(Add. 1). 2635-2641.
12. He, M.C, Miao, J.L. and Li, D.J. Experimental study on rockburst processes of granite specimen at great depth. Chinese Journal of Rock Mechanics and Engineering, 26(5). 865-876.
13. Li, X.W. Working face AE model of rockburst and application. Master Dissertation. Shandong University of Science and Technology, Jinan, Shan Dong, China, 2004.
14. Zhao, B.J. and Tang, X.J. Rock burst and its cure. Coal Industry Press, Beijing, China, 1995.
15. Han, S.P. Study on size effects and slenderness ratio effects of rock mass characteristics. Taiyuan University of Technology, Tai Yuan, Shan Xi, China, 2007.